Transactions of the ASME®

Technical Editor, LEWIS T. WHEELER (1997)

Department of Mechanical Engineering,
University of Houston,
Houston, TX 77204-4792

APPLIED MECHANICS DIVISION

Chairman, L. B. FREUND
Secretary, C. T. HERAKOVICH
Associate Technical Editors,
R. ABEYARATNE (1994)
T. R. AKYLAS (1994)
D. M. BARNETT (1996)
S. A. BERGER (1994)
I. M. DANIEL (1996)
G. J. DVORAK (1995)
E. J. HAUG, JR. (1996)
S. LICHTER (1995)
W. K. LIU (1996)
X. MARKENSCOFF (1994)
D. M. PARKS (1995)
J. N. REDDY (1995)
J. W. RUDNICKI (1994)
W. N. SHARPE, JR. (1996)
S. W. SHAW (1997)
C. F. SHIH (1995)
P. D. SPANOS (1994)
M. TAYA (1996)
F. Y. M. WAN (1994)

BOARD ON COMMUNICATIONS

Chairman and Vice-President
R. D. ROCKE

Members-at-Large
T. BARLOW, T. DEAR, L. M. KEER, J. KITTO,
W. MORGAN, E. M. PATTON, S. PATULSKI,
R. E. REDER, R. SHAH, A. VAN DER SLUYS,
F. M. WHITE, J. WHITEHEAD

OFFICERS OF THE ASME
President, J. H. FERNANDES
Exec. Director
D. L. BELDEN
Treasurer
R. A. BENNETT

PUBLISHING STAFF
Mng. Dir., Publ.,
CHARLES W. BEARDSLEY
Managing Editor,
CORNELIA MONAHAN
Production Editor,
JUDITH SIERANT
Production Assistant,
MARISOL ANDINO

Transactions of the ASME, Journal of Applied Mechanics (ISSN 0021-8936) is published quarterly (Mar., June, Sept., Dec.) for $165.00 per year by The American Society of Mechanical Engineers, 345 East 47th Street, New York, NY 10017. Second class postage paid at New York, NY and additional mailing office. POSTMASTER: Send address changes to Transactions of the ASME, Journal of Applied Mechanics, c/o THE AMERICAN SOCIETY OF MECHANICAL ENGINEERS, 22 Law Drive, Box 2300, Fairfield, NJ 07007-2300.

CHANGES OF ADDRESS must be received at Society headquarters seven weeks before they are to be effective. Please send old label and new address.

PRICES: To members, $40.00, annually: to nonmembers, $165.00. Add $24.00 for postage to countries outside the United States and Canada.

STATEMENT from By-Laws. The Society shall not be responsible for statements or opinions advanced in papers or . . . printed in its publications (B7.1, Par. 3).

COPYRIGHT © 1994 by The American Society of Mechanical Engineers. Authorization to photocopy material for internal or personal use under circumstances not falling within the fair use provisions of the Copyright Act is granted by ASME to libraries and other users registered with the Copyright Clearance Center (CCC) Transactional Reporting Service provided that the base fee of $3.00 per article is paid directly to CCC, 27 Congress St., Salem, MA 01970. Request for special permission or bulk copying should be addressed to Reprints/Permission Department.

INDEXED by Applied Mechanics Reviews and Engineering Information, Inc. Canadian Goods & Services Tax Registration #126148048

Journal of Applied Mechanics

Published Quarterly by The American Society of Mechanical Engineers

VOLUME 61 • NUMBER 2 • JUNE 1994

TECHNICAL PAPERS

231 The Buckling of an Elastic Layer Bonded to an Elastic Substrate in Plane Strain
T. W. Shield, K. S. Kim, and T. T. Shield

236 Bifurcation Effects in Ductile Metals With Nonlocal Damage
J. B. Leblond, G. Perrin, and J. Devaux

243 Circularly Cylindrical and Plane Layered Media in Antiplane Elastostatics
T. Honein, E. Honein, and G. Herrmann

250 Two-Dimensional Contact on an Anisotropic Elastic Half-Space
Hui Fan and L. M. Keer

256 Transient Response of an Elastic Homogeneous Half-Space to Suddenly Applied Rectangular Loading
F. Guan and M. Novak

264 A Novel Boundary Element Method for Linear Elasticity With No Numerical Integration for Two-Dimensional and Line Integrals for Three-Dimensional Problems
A. Nagarajan, E. Lutz, and S. Mukherjee

270 A Strip Element Method for Stress Analysis of Anisotropic Linearly Elastic Solids
G. R. Liu and J. D. Achenbach

278 Static Axisymmetric Hertzian Contacts Subject to Shearing Forces
R. L. Munisamy, D. A. Hills, and D. Nowell

284 Isotropy of Strain Energy Functions Which Depend Only on a Finite Number of Directional Strain Measures (94-WA/APM-2)
D. Elata and M. B. Rubin

290 A Hypoelastic Model for Computing the Stresses in Center-Wound Rolls of Magnetic Tape
N. Zabaras, S. Liu, J. Koppuzha, and E. Donaldson

296 Large Amplitude Vibrations of Strings
A. W. Leissa and A. M. Saad

302 Random Vibrational Response and Stability Study of Long-Span Bridges
K. Y. R. Billah and M. Shinozuka

309 Ultrasonic Evaluations of Stiffness Tensor Changes and Associated Anisotropic Damage in a Ceramic Matrix Composite
B. Audoin and S. Baste

317 Vibration of Circular Rings With Local Deviation
Jin Sun Hong and Jang Moo Lee

323 Reflection of Waves at the Free Edge of a Laminated Circular Cylinder
N. Rattanawangcharoen, A. H. Shah, and S. K. Datta

330 Excitation of Guided Waves in Generally Anisotropic Layers Using Finite Sources
J. J. Ditri and J. L. Rose

339 An Exact Stiffness Method for Elastodynamics of a Layered Orthotropic Half-Plane
Y. Wang and R. K. N. D. Rajapakse

349 Effective Elastic Moduli of Two-Dimensional Brittle Solids With Interacting Microcracks, Part I: Basic Formulations
J. W. Ju and Tsung-Muh Chen

358 Effective Elastic Moduli of Two-Dimensional Brittle Solids With Interacting Microcracks, Part II: Evolutionary Damage Models
J. W. Ju and Tsung-Muh Chen

367 Optimal Cool Down in Nonlinear Thermoviscoelasticity With Application to Graphite/Peek (APC-2) Laminates
K. Lee and Y. Weitsman

375 Integrated Damping Mechanics for Thick Composite Laminates and Plates
D. A. Saravanos

384 Asymptotic Stress Field of a Mode III Crack Growing Along an Elastic/Elastic Power-Law Creeping Bimaterial Interface
C.-Y. Hui and M. T. A. Saif

390 Two-Dimensional Grained Composites of Extreme Rigidity
S. Vigdergauz

395 Effect of Constitutive Parameters on Formation of a Spherical Void in a Compressible Nonlinear Elastic Material
Shiro Biwa, Elji Matsumoto, and Toshinobu Shibata

402 Electron Beam Moire Study of Fracture of a Glass Fiber Reinforced Plastic Composite
D. T. Read and J. W. Dally

410 Free-Edge Effects in Anisotropic Laminates Under Extension, Bending and Twisting, Part I: A Stress-Function-Based Variational Approach
W.-L. Yin

416 Free-Edge Effects in Anisotropic Laminates Under Extension, Bending and Twisting, Part II: Eigenfunction Analysis and the Results for Symmetric Laminates
W.-L. Yin

422 Biaxial Ratcheting Under Strain or Stress-Controlled Axial Cycling With Constant Hoop Stress
Z. Xia and F. Ellyin

(Contents continued on Inside Back Cover)

Downloaded 04 May 2010 to 171.66.16.52. Redistribution subject to ASME license or copyright; see http://www.asme.org/terms/Terms_Use.cfm

CONTENTS (CONTINUED)

429 **Asymptotic Viscoelastic Rays in a Thick Plate**
R. L. Weaver and W. Sachse

434 **Imposition of Constraints**
S. Djerassi

440 **Motion and Force Prediction of a Pushed Object by Maximum Dissipation Method**
Hiroshi Sakurai

446 **Maximal Lyapunov Exponent and Almost-Sure Stability for Coupled Two-Degree-of-Freedom Stochastic Systems**
N. Sri Namchchivaya, H. J. Van Roessel, and S. Talwar

453 **On the Boltzmann-Hamel Equations of Motion: A Vectorial Treatment**
J. G. Papastavridis

460 **Generalized Reynolds Equation for Solid-Liquid Lubricated Bearings**
F. Dai and M. M. Khonsari

BRIEF NOTES

Accurate Data for Stress Intensity Factors at Infinitesimal Kinks — **S. Melin** — 467

On the Use of Variational Principles to Derive Beam Boundary Conditions — **Hui Fan and G. E. O. Widera** — 470

On the Double Cantilever Beam Specimen for Mode-I Interface Delamination — **B. Balendran** — 471

Electroelastic Field Concentrations In and Around Inhomogeneities in Piezoelectric Solids — **M. L. Dunn and M. Taya** — 474

Material Instability for Fiber Composites — **R. M. Christensen** — 476

Stability of a Fluid-Conveying Pipe With Flow-Dependent Support Stiffness — **A. Guran and R. H. Plaut** — 477

Both Bounds to Buckling Loads and Fundamental Frequencies — **R. Schmidt** — 479

Finite Element Simulation of the Hardness Testing of Ion-Implanted Materials — **J. P. Blanchard** — 480

483 Torsion of Rectangular Bars With Multiple Cylindrical Reinforcement or Cavities
A. K. Naghdi

487 Diffusive Transport Across a Wavy Plate Composed of Annular Sectors
C. Y. Wang

489 Torsion of Tube With Longitudinal Corrugations
C. Y. Wang

491 The Buckling Behavior of Rectangular-Bar Helical Compression Springs
L. E. Becker and W. L. Cleghorn

493 Longitudinal Impact of a Shaped Projectile on a Hopkinson Bar
C. Bacon

495 Longitudinal Shear and Torsion of Bimaterial Solids
Xiangzhou Zhang and Norio Hasebe

497 Bending of Plates on Thin Compressible Foundations
C. W. Bert

499 Identities for Torsion of Cylinders
Zhengxian Bai and R. T. Shield

DISCUSSION

501 **On the Approximate Solution of Nonclassically Damped Linear Systems, by J. H. Hwang and F. Ma—Discussion by S. M. Shahruz with Author's Closure**

BOOK REVIEWS

503 ***Mechanics of Composite Structures*, by Valery V. Vasiliev** . . . Reviewed by **C. W. Bert**

503 ***Introduction to the Thermodynamics of Solids*, by J. L. Eriksen** . . . Reviewed by **Yi-Chao Chen**

ANNOUNCEMENTS AND SPECIAL NOTES

255 19th International Congress of Theoretical and Applied Mechanics—Announcement

301 9th International Conference on Numerical Methods in Laminar and Turbulent Flow—Call for Papers

383 Thermal Stresses '95—Announcement

401 Change of Address Form

421 Europe-U.S. Workshop on Fracture of Quasibrittle Materials—Announcement

428 International Conference on Mechanics of Solids and Materials Engineering—Call for Papers

439 Eighth International Conference on Pressure Vessel Technology

502 9th International Conference on Numerical Methods for Thermal Problems—Call for Papers

504 Books Received by the Office of the Technical Editor

505 Worldwide Mechanics Meetings List

507 Information for Authors

Downloaded 04 May 2010 to 171.66.16.52. Redistribution subject to ASME license or copyright; see http://www.asme.org/terms/Terms_Use.cfm

T. W. Shield
Department of Aerospace Engineering and Mechanics, University of Minnesota, Minneapolis, MN 55455
Assoc. Mem. ASME

K. S. Kim
Division of Engineering, Brown University, Providence, RI 02912
Mem. ASME

R. T. Shield[1]
Department of Theoretical and Applied Mechanics, University of Illinois, Urbana, IL 61801
Fellow ASME

The Buckling of an Elastic Layer Bonded to an Elastic Substrate in Plane Strain

The solution for buckling of a stiff elastic layer bonded to an elastic half-space under a transverse compressive plane strain is presented. The results are compared to an approximate solution that models the layer using beam theory. This comparison shows that the beam theory model is adequate until the buckling strain exceeds three percent, which occurs for modulus ratios less than 100. In these cases the beam theory predicts a larger buckling strain than the exact solution. In all cases the wavelength of the buckled shape is accurately predicted by the beam model. A buckling experiment is described and a discussion of buckling-induced delamination is given.

Introduction

Buckling of layers bonded to elastic substrates has recently gained importance in the semiconductor industry. Increasing the level of circuit integration leads to large numbers of dissimilar layers bonded together. These layered structures are assembled at elevated temperatures and then cooled. The different coefficients of thermal expansion can cause a layer to buckle as shown in Fig. 1. Buckling of a layer can lead to delamination. This will be discussed later.

Historically, interest in this problem was motivated by the buckling of the sandwich panels in aircraft. Previous works have all used beam theory (plate theory with a single axis of bending) models for the layer. Here we present a two-dimensional solution for the stresses in both the layer and the substrate. The results obtained are compared to those obtained using beam theory for the layer. Original work on this type of problem was done by Gough, Elam, and De Bruyne (1940). They considered eight geometrical cases experimentally and theoretically. Their model ignores the compression in the substrate and assumes that the tangential interface displacements are zero. This approximation agrees with the plate theory model for stiff layers (compared to the substrate) and small loads. Their approximations do not allow them to recover the Euler buckling load for a sandwich beam. Their experiments considered metals sandwiched between Onazote (expanded ebonite) foam. By sandwiching the stiff layer between the foam they avoided the possibility of delamination that is discussed below. However, the foam was permanently deformed by the metal during buckling and because no bond was made, the foam only provided compressive stresses across the interface.

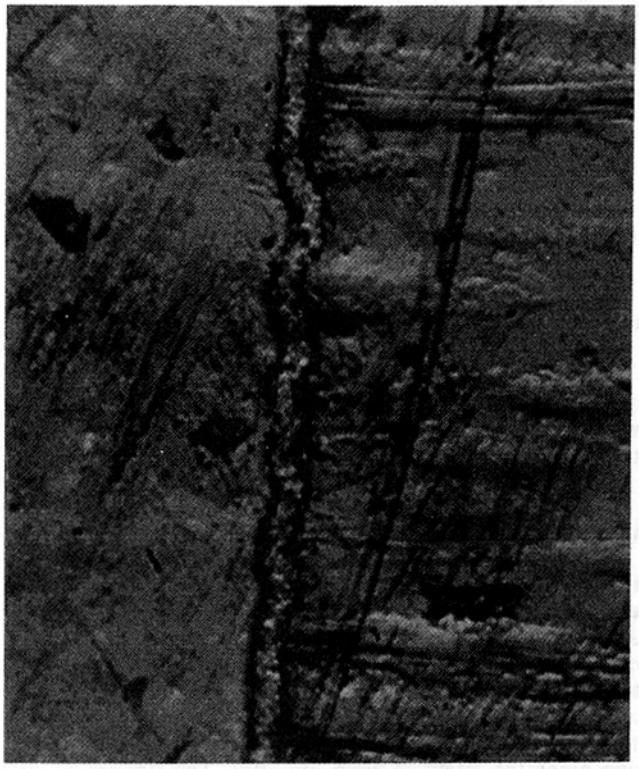


Fig. 1 Copper film of 10 μm thickness in polymide substrate, buckling probably occurred during manufacture before top substrate was added. Here $\lambda/h \approx 4$ and $E_L/E \approx 35$. (Specimen courtesy of IBM).

[1]Current address: P.O. Box 834, Oriental, NC 28571.

Contributed by the Applied Mechanics Division of THE AMERICAN SOCIETY OF MECHANICAL ENGINEERS for publication in the JOURNAL OF APPLIED MECHANICS.

Discussion on this paper should be addressed to the Technical Editor, Professor Lewis T. Wheeler, Department of Mechanical Engineering, University of Houston, Houston, TX 77204-4792, and will be accepted until four months after final publication of the paper itself in the JOURNAL OF APPLIED MECHANICS.

Manuscript received by the ASME Applied Mechanics Division, Aug. 1, 1991; final revision, May 12, 1993. Associate Technical Editor: A. K. Noor.

Copyright © 1994 by ASME
Downloaded 03 May 2010 to 171.66.16.20. Redistribution subject to ASME license or copyright; see http://www.asme.org/terms/Terms_Use.cfm

The problem of buckling of sandwich panels was approached using energy methods by Hoff and Maunter (1945). They took Poisson's ratio of the substrate to be zero and their calculations provide an upper bound on the buckling load. However, their calculations predict the energy of a skew mode of deformation that is greater than that in a symmetric mode of deformation, which is not correct. Furthermore, they do not recover the Euler buckling load as a limiting case. Their experiments also used a cellular substrate with a relative layer stiffness of about 2000. Chung and Testa (1969) considered fibers in a composite using beam theory for the fibers and ignored the contribution of the energy in the core to correctly predict the lower energy of the symmetric mode of deformation compared to the skew mode.

Goodier (1946) considered cylindrical buckling of sandwich plates using a form of Biot's equations (1965) for the initially stressed core and beam theory for the layer. This method leads to a reasonable approximate answer. However, his assumption that the tangential displacement is zero on the interface is too restrictive to recover the Euler buckling mode. Biot's equations are not derivable from a strain energy, but the terms omitted are of the same order as those ignored elsewhere in the analysis.

Stability of a Layered on a Half-Space: Two-Dimensional Solution

In order to treat the stability of a body under compression, we first consider an elastic body which in the reference state is in a state of initial stress S_{ij} referred to rectangular Cartesian axes x_i. For equilibrium of the reference state,

$$S_{ij,j}=0 \text{ and } S_{ij}=S_{ji}$$

throughout the body. The Lagrangian stress tensor T_{ij} in the deformed state is such that the stress vector T_i, measured per unit area of the reference state, is given by

$$T_i=T_{ji}n_j,$$

where n_i is the unit normal to the surface element in the reference state. For an elastic material we have

$$T_{ji}=\partial W/\partial u_{i,j},$$

where the strain energy W per unit volume of the reference state is a function of the Cauchy strains e_{ij} given by

$$e_{ij}=\frac{1}{2}(u_{i,j}+u_{j,i}+u_{r,i}\,u_{r,j})$$

in terms of the displacements u_i. Since T_{ij} is equal to S_{ij} in the reference state, we take

$$W=S_{ij}\,e_{ij}+W_0(\mathbf{e}),$$

and for linear behavior W_0 is taken to be given by

$$W_0=\frac{1}{2}\,c_{ijkl}\,e_{ij}\,e_{kl},$$

with the coefficients c_{ijkl} satisfying the usual symmetry relations. The stresses T_{ij} then become

$$T_{ji}=S_{ij}+S_{jr}\,u_{i,r}+c_{ijkl}\,u_{k,l} \tag{1}$$

if we ignore second-order terms in $u_{i,j}$.

We now consider an elastic half-space of homogeneous isotropic material with a stiffer layer of isotropic material of uniform thickness h bonded to its surface (Fig. 2(*a*)). We assume conditions of plane strain and consider stability under compression parallel to the layer. The compression is assumed to induce the same uniform compressive strain ϵ in the layer and in the half-space and we take the compressed state to be the reference state. We use x and y for x_1 and x_2 with the x-axis along the interface as in Fig. 2(*a*). The stresses S_{yy} and S_{xy} are zero while S_{xx} has the values $-P_L$ and $-P$ in the layer and in the half-space, respectively, given by

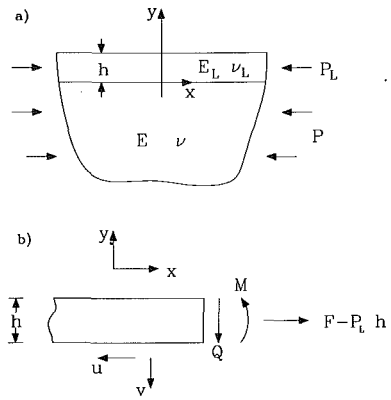


Fig. 2 (*a*) **The geometry of the layer buckling problem;** (*b*) **the sign conventions and notation used for the plate model for the layer**

$$P=\epsilon\,E/(1-\nu^2),\ P_L=\epsilon\,E_L/(1-\nu_L^2),$$

where E and ν denote Young's modulus and Poisson's ratio for the materials. The stiffness ratio K is defined as

$$K=\frac{E_L(1-\nu^2)}{E(1-\nu_L^2)}=\frac{\mu_L(1-\nu)}{\mu(1-\nu_L)}=\frac{P_L}{P},$$

where μ is the shear modulus. We look for the lowest value of ϵ for which an adjacent position of equilibrium is possible with the upper surface of the layer traction-free and with no body force.

For infinitesimal deformations from the compressed state we use the stress-strain relation (1) together with the approximation that W_0 has the isotropic form of the strain energy for the materials in the unstressed state. This assumes that the effect of the compression on the elastic moduli can be neglected and it is called the "engineering approximation" by Pearson (1956). For equilibrium of a perturbed state $T_{ji,j}=0$ and for the half-space this leads to

$$\mu\nabla^2 u+(\lambda+\mu)(u_x+v_y)_x-Pu_{xx}=0$$
$$\mu\nabla^2 v+(\lambda+\mu)(u_x+v_y)_y-Pv_{xx}=0, \tag{2}$$

where u_x, etc., and derivatives of the displacements u, v and λ is Lamé's constant. If we look for solutions of (2) for which u and v are proportional to sin x and cos x, respectively, we obtain the solution

$$u=(-Aa\mathbf{e}^{ay}+B\omega\mathbf{e}^{by})\sin\omega x,$$
$$v=(A\omega\mathbf{e}^{ay}-Bb\mathbf{e}^{by})\cos\omega x, \tag{3}$$

where A and B are arbitrary constants and a and b are given by

$$a=\omega(1-P/\mu)^{1/2},\ b=\omega[1-P(1-2\nu)/\mu(1-\nu)]^{1/2}. \tag{4}$$

The solution (3) is similar in form to the solution for a Rayleigh wave on the surface of a half-space with P replacing ρc_R^2, where ρ is the density and c_R is the Rayleigh wave speed. The displacements go to zero as y goes to negative infinity. The tractions on the interface $y=0$ are T_{yx} and T_{yy} and if we adjust the constants in the solution (3) so that

$$u=hU\sin\omega x,\ v=hV\cos\omega x,\ \text{on } y=0, \tag{5}$$

then we find that in terms of the amplitudes U, V we have on $y=0$

$$T_{xy}=\mu(\gamma U+\delta V)\sin\omega x,\ T_{yy}=\mu(\alpha U+\beta V)\cos\omega x, \tag{6}$$

where

$$\alpha=\delta=-\Omega(\Omega^2+\xi^2-2\xi\eta)/\Delta,\ \beta=\xi(\Omega^2-\xi^2)/\Delta,$$
$$\gamma=b\beta/a,\ \Delta=\Omega^2-\xi\eta,\ \Omega=\omega h,\ \xi=ah,\ \eta=bh. \tag{7}$$

Equality of the coefficients α and δ is related to the fact that Eqs. (2) are self-adjoint and a Reciprocal Theorem holds.

Downloaded 03 May 2010 to 171.66.16.20. Redistribution subject to ASME license or copyright; see http://www.asme.org/terms/Terms_Use.cfm

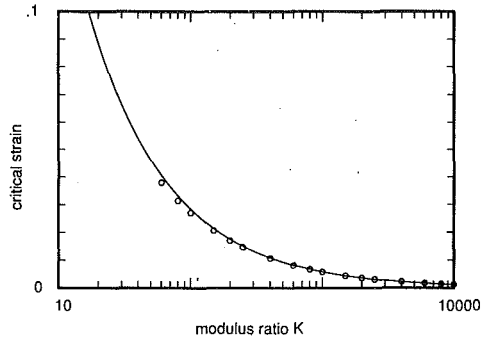


Fig. 3 The buckling strain as a function of the layer modulus ratio. Comparison of the full elasticity results Eq. (9) (circles) and the approximate plate theory results of (16) (solid curves) for $\nu = 0.25$

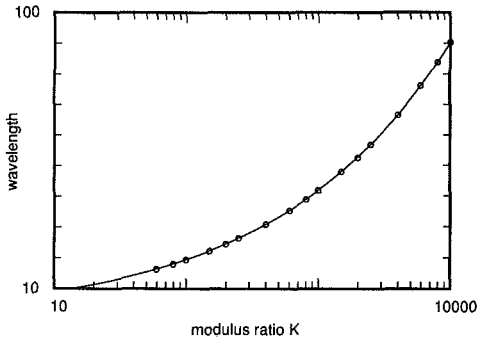


Fig. 4 The wavelength of the buckled shape as a function of the layer modulus ratio. Comparison of the full elasticity results Eq. (9) (circles) and the approximate plate theory results of (17) (solid curves) for $\nu = 0.25$.

Equations similar to (2) apply in the layer. We can change the signs of a and b in (3) and still have a solution of Eqs. (2). Combining the solutions for the layer we can choose the four constants in the solutions so that the upper surface of the layer is free from traction and so that the displacements on the lower surface have the values (5). We then find the stresses T^L_{yx} and T^L_{yy} in the layer at the interface $y=0$ are given by (6) with μ replaced by μ_L and α, β, γ, δ replaced by α_L, β_L, γ_L, δ_L where

$$\alpha_L = \delta_L = \Omega\{[(\xi_L^2+\Omega^2)^2 - 4\xi_L\eta_L\Omega^2] \times (\eta_L^2+\Omega^2-2\xi_L\eta_L)\sinh\xi_L \sinh\eta_L - 2\xi_L\eta_L(\xi_L^2+\Omega^2)(\xi_L^2+3\Omega^2)[\cosh(\xi_L-\eta_L)-1]\}/\Delta_L$$

$$\beta_L = \xi_L(\xi_L^2-\Omega^2)[4\xi_L\eta_L\Omega^2\sinh\xi_L\cosh\eta_L - (\xi_L^2+\Omega^2)^2\sinh\eta_L\cosh\xi_L]/\Delta_L$$

$$\gamma_L = \eta_L(\xi_L^2-\Omega^2)[4\xi_L\eta_L\Omega^2\sinh\eta_L\cosh\xi_L - (\xi_L^2+\Omega^2)^2\sinh\xi_L\cosh\eta_L)]/\Delta_L$$

$$\Delta_L = \xi_L\eta_L(\xi_L^2-\Omega^2)\cosh\xi_L\cosh\eta_L - \Omega^2(\xi_L^2+\Omega^2-2\xi_L\eta_L)\sinh\xi_L\sinh\eta_L + 4\xi_L\eta_L\Omega^2(\xi_L^2+\Omega^2)[\cosh(\xi_L-\eta_L)-1]. \quad (8)$$

In these equations ξ_L and η_L have the values a_Lh, b_Lh where a_L and b_L are given by expressions of the same form as (4) but evaluated using P_L and the material constants for the layer.

In order that the solutions for the layer and the half-space represents an adjacent position of equilibrium, we must impose continuity of the tractions T_{yx}, T_{yy} across the interface $y=0$. This leads to two homogeneous linear equations for U, V and in order for a solution for U, V to exist the determinant of the coefficients must be zero. This gives

$$(\mu_L\alpha_L - \mu\alpha)^2 - (\mu_L\beta_L - \mu\beta)(\mu_L\gamma_L - \mu\gamma) = 0. \quad (9)$$

For given values of the material constants this equation is a relation between $\Omega = \omega h$ and the compressive strain ϵ for which adjacent equilibrium solutions exist. The critical value ϵ_c at which the layer will buckle is found from (9) by determining the value of Ω for which ϵ is a minimum.

The circles in Fig. 3 show the buckling strain ϵ_c versus the stiffness ratio K for the case when $\nu = \nu_L = 0.25$. The nondimensional buckling wavelength $\lambda_c/h = 2\pi/\Omega$ is shown by the circles in Fig. 4.

Beam Approximation for the Layer

When the buckling wavelength is large compared to the thickness of the layer, the behavior of the layer can be described approximately by using beam theory (plate theory with a single axis of bending). We assume that after deflection of the compressed layer, an axial force $F - P_Lh$, a moment M and a shear force Q act on a section of the layer, as indicated in Fig. 2(*b*), and the lower surface of the layer has tractions T_{yx}, T_{yy}. The displacements at the lower surface are denoted by u, v. With the assumption that plane sections remain plane, the vertical displacement at the central line will be v and the horizontal displacement will be $u - hv_x/2$. The moment and additional axial force are then given by

$$M = \frac{E_Lh^3}{12(1-\nu_L^2)}\, v_{xx},\quad F = \frac{E_Lh}{(1-\nu_L^2)}\left(u_x - \frac{h}{2}\, v_{xx}\right). \quad (10)$$

For equilibrium of the layer

$$\frac{dM}{dx} + P_Lhv_x - Q - \frac{h}{2}\, T_{yx} = 0$$

$$\frac{dQ}{dx} + T_{yy} = 0,\quad \frac{dF}{dx} - T_{yx} = 0, \quad (11)$$

where the effect of the geometry change on the action of the force P_Lh has been taken into account. If we differentiate the first of Eqs. (11) to eliminate Q and use the values (10) for M and F we find that

$$\frac{E_Lh^2}{(1-\nu_L^2)}\left(\frac{h}{3}\, v_{xxxx} - \frac{1}{2}\, u_{xxx}\right) + P_L\, hv_{xx} + T_{yy} = 0$$

$$\frac{E_Lh}{(1-\nu_L^2)}\left(u_{xx} - \frac{h}{2}\, v_{xxx}\right) - T_{yx} = 0. \quad (12)$$

If we assume that u and v are given by (5) and use expressions (6) for T_{yx} and T_{yy} in Eqs. (12), we get two homogeneous linear equations for U, V, and in order for a solution to exist we must have

$$\left[\alpha + \frac{K\Omega^3}{(1-\nu)}\right]^2 - \left[\beta + \frac{2K\Omega^2}{(1-\nu)}\,(\Omega^2/3 - \epsilon)\right]\left[\gamma + \frac{2K\Omega^2}{(1-\nu)}\right] = 0. \quad (13)$$

The limiting values of the coefficients α, . . . as P/μ goes to zero are

$$\alpha = \delta = -2\Omega\,\frac{(1-2\nu)}{(3-4\nu)},\quad \beta = \gamma = 4\Omega\,\frac{(1-\nu)}{(3-4\nu)} \quad (14)$$

and they are the response coefficients for an isotropic half-space with surface displacements (5). If we use these values as approximations for α, . . . in (13) we find that the strain ϵ for which an adjacent equilibrium solution exists is given approximatly by

$$\epsilon = \left\{\frac{(3-4\nu)K}{24(1-\nu)^2}\,\Omega^2 + \frac{1}{\Omega} + \frac{(1-2\nu)}{2(1-\nu)} + \frac{\Omega}{3} + \frac{1}{2K\Omega^2}\right\} \times \left\{\frac{(3-4\nu)K}{2(1-\nu)^2} + \frac{1}{\Omega}\right\}^{-1}. \quad (15)$$

The minimum value of ϵ is the buckling strain. For K greater

Downloaded 03 May 2010 to 171.66.16.20. Redistribution subject to ASME license or copyright; see http://www.asme.org/terms/Terms_Use.cfm

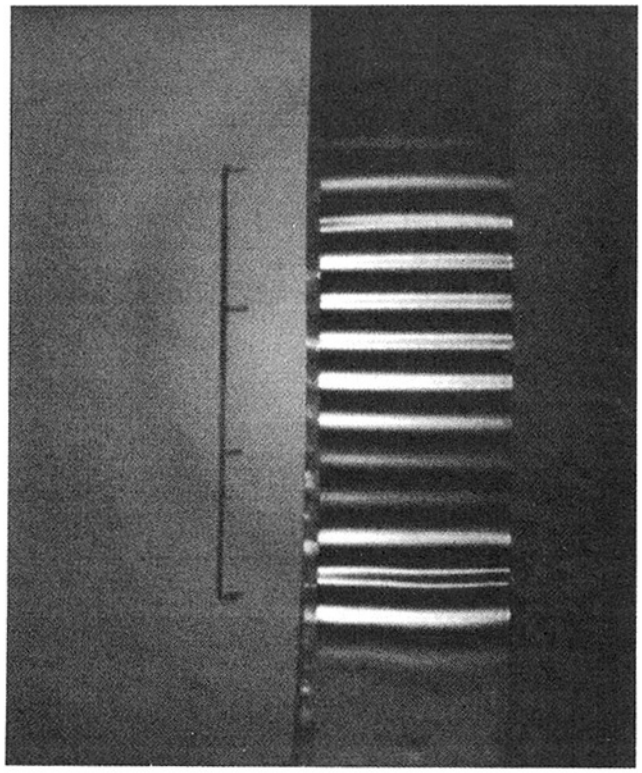


Fig. 5 A top view of the buckled configuration of a mylar film on a rubber substrate, $K = 2140$ and $h = 44$ μm, centimeter scale shown

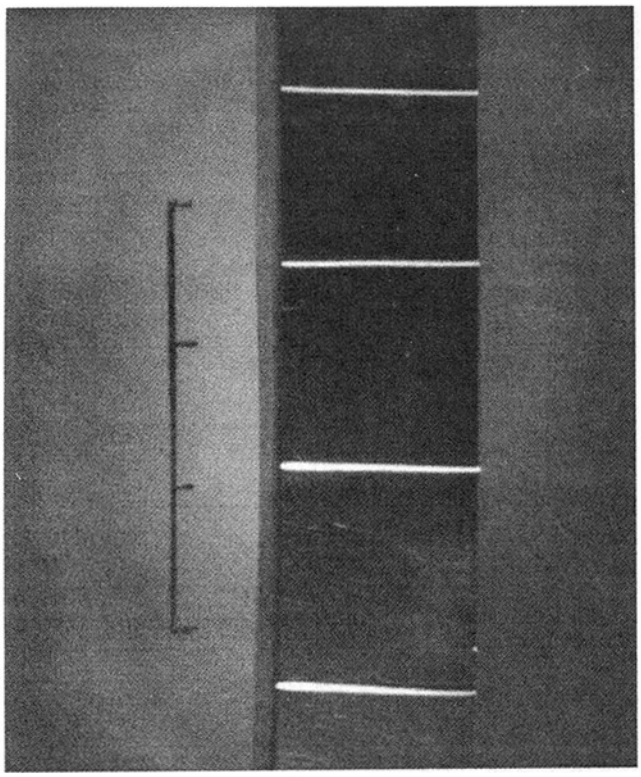


Fig. 6 Post-buckling delamination pattern of a mylar film bonded to a rubber substrate, $K = 465$, centimeter scale shown

than $(3-4\nu)/(1-\nu)(1-2\nu)$ it can be shown that the equation $d\epsilon/d\Omega = 0$ has at most one positive root. For large values of the stiffness ratio K, ϵ is a minimum when

$$\Omega_c^3 = \frac{12(1-\nu)^2}{K(3-4\nu)} \tag{16}$$

and with this value of Ω, (15) gives

$$\epsilon_c = \frac{\Omega_c}{12}\left\{3 + \frac{(1-2\nu)}{(1-\nu)}\Omega_c + \frac{2}{3}\Omega_c^2 + \frac{(3-4\nu)}{12(1-\nu)^2}\Omega_c^2\right\}\left\{1 + \frac{\Omega_c^2}{6}\right\}^{-1} \tag{17}$$

as an approximation to the buckling strain. For $\nu = \nu_L = 0.25$ and $K \geq 100$, the value of Ω_c given by (16) differs by less than one percent from the value which minimizes ϵ determined from Eq. (9), and the approximation for the critical strain given by (16) and (17) overestimates ϵ_c determined from (9) by less than five percent. The theory assumes small strains so it is less reliable for smaller values of K when the values predicted for the critical strain are rather large (over 2.5 percent for $K \simeq 100$). For $K > 1000$, ϵ_c from (16) and (17) is within one percent of ϵ_c determined from (9) so that the approximation (16), (17) is accurate enough. These results are shown by the solid curves in Figs. 3 and 4 $\nu = 0.25$. The Euler buckling value of ϵ_c for a strip in plane strain with the same buckling wavelength is $\Omega^2/12$; for large K, Ω is small and (17) is close to three times the Euler value.

Similar approximations to those of this section are made by Gough, Elam, and de Bruyne (1940) but their analysis assumes that there is no horizontal displacement at the interface and the effect of the interfacial shear stress on the equilibrium of the layer is ignored. The plane stress value for the buckling strain given by Gough, Elam, and de Bruyne when converted to plane strain is $\Omega^2/4$ with Ω given by (16), in agreement with the approximation (17) for small values of Ω.

Discussion

Figure 5 shows the buckled configuration of a mylar film on a rubber substrate. The modulus ratio, K, is 2140 for these materials and the layer thickness is 44 μm. Poisson's ratio for the substrate is close to 0.5. The relative wavelength, λ/h, of the buckled shape is approximately 57, which compares well to the value of 54 predicted by (16). The buckling strain for this configuration was roughly the magnitude of that predicted by (17) but was not measured accurately enough to report here. The modulus of the substrate used in this case was very low. Attempts were made to use a stiffer rubber substrate with a modulus ratio $K = 465$. The result of this experiment is shown in Fig. 6. Unlike Fig. 5, the configuration in Fig. 6 is in the unloaded state. The periodic bright lines correspond to narrow regions of delamination of the mylar from the rubber substrate and are kinks in the film. These kinks formed after buckling occurred in the film.

The process that formed the periodic delaminations in Fig. 6 is as follows. Due to local imperfections, buckling first occurs in a small region of the film. However, the interface cannot support the tensile normal stresses that occur during buckling. Thus the film delaminates in a small region, this immediately relieves the compressive strain in the system and the characteristics wavelength of the buckled film disappears. The kink in the film effectively cuts the film into two parts that must now be treated as film segments bonded to the substrate. Further loading will cause the axial strain to again increase in the film, however the strain in the film will not reach the value of the strain in the substrate near the delamination. There is a characteristic distance from the delamination for the strain in the film to build up to a large percentage of the strain in the substrate. This distance can be predicted by considering beam segments bonded to a half-space as in Shield and Kim (1992). At this distance from the first delamination, the film again

Downloaded 03 May 2010 to 171.66.16.20. Redistribution subject to ASME license or copyright; see http://www.asme.org/terms/Terms_Use.cfm

buckles and caused another delamination kink. This process was repeated three times to arrive at the configuration shown in Fig. 6 with periodic delaminations separated by the characteristic distance defined above.

Buckling-induced delamination is characteristic of film/substrate combinations with low modulus ratios and hence large buckling strains. In is very difficult to construct such a system with an interface that can withstand the stresses in the buckled configuration. One solution this problem is to sandwich a layer between two substrates as in Gough, Elam, and de Bruyne (1940). The only change to the analysis for this case is that the quantity h defined above would be the half thickness of the layer. The delamination behavior discussed here shows the importance of considering the possibility of elastic buckling of thin films. Such buckling is highly probable in polymer-based electronic devices made up of conducting thin films that have high stiffness and polymeric substrates that may undergo a large shrinkage. The shrinkage strain may be caused by either polymerization or thermal contraction during cooling. Although the buckled configuration may never be observed, it still may be the original cause of delamination and failure of the film.

Acknowledgment

TWS and KSK would like to thank IBM for support during this research through the University of Illinois agreement number 148/FE206101Z. RTS acknowledges support from the National Center for Composite Materials Research at the Department of Theoretical and Applied Mechanics of the University of Illinois.

References

Biot, M. A., 1965, *Mechanics of Incremental Deformations*, John Wiley and Sons, New York.

Chung, W.-Y., Testa, R. B., 1969, "The Elastic Stability of Fibers in a Composite Plate," *J. Comp. Mat.*, Vol. 3, pp. 58–80.

Goodier, J. N., 1946, "Cylindrical Buckling of Sandwich Plates," ASME JOURNAL OF APPLIED MECHANICS, Vol. 13, pp. A253–A260.

Gough, G. S., Elam, C. F., and de Bruyne, N. A., 1940, "The Stabilization of a Thin Sheet by a Continuous Supporting Medium," *J. Royal Aero. Soc.*, Vol. 44, pp. 12–43.

Hoff, N. J., and Mautner, S. E., 1945, "The Buckling of Sandwich-Type Panels," *J. Aero. Sci.*, Vol. 12, pp. 285–297.

Pearson, C. E., 1956, "General Theory of Elastic Stability," *Quart. Appl. Math.*, Vol. 14, pp. 133–144.

Shield, T. W., and Kim, K.-S., 1992, "Beam Theory Models for Thin Film Segments Cohensively Bonded to an Elastic Half Space," *Int. J. of Solids and Structures*, Vol. 29, No. 9, pp. 1085–1103.

Downloaded 03 May 2010 to 171.66.16.20. Redistribution subject to ASME license or copyright; see http://www.asme.org/terms/Terms_Use.cfm

J. B. Leblond
Laboratoire de Modélisation en Mécanique,
Université Pierre et Marie Curie,
Tour 66, 4 place Jussieu,
75005 Paris, France

G. Perrin[1]
Laboratoire de Mécanique des Solides,
Ecole Polytechnique,
91128 Palaiseau, France

J. Devaux
FRAMASOFT + CSI,
10 rue Juliette Récamier,
69398 Lyon Cedex 03, France

Bifurcation Effects in Ductile Metals With Nonlocal Damage

The purpose of this paper is to investigate some bifurcation phenomena in a porous ductile material described by the classical Gurson (1977) model, but with a modified, nonlocal *evolution equation for the porosity. Two distinct problems are analyzed theoretically: appearance of a discontinuous velocity gradient in a finite, inhomogeneous body, and arbitrary loss of uniqueness of the velocity field in an infinite, homogeneous medium. It is shown that no bifurcation of the first type can occur provided that the hardening slope of the sound (void-free) matrix is positive. In contrast, bifurcations of the second type are possible; nonlocality does not modify the conditions of first occurrence of bifurcation but does change the corresponding bifurcation mode, the wavelength of the latter being no longer arbitrary but necessarily infinite. A FE study of shear banding in a rectangular mesh deformed in plane strain tension is finally presented in order to qualitatively illustrate the effect of finiteness of the body; numerical results do evidence notable differences with respect to the case of an infinite, homogeneous medium envisaged theoretically.*

1 Introduction

It has been long recognized that introduction of strain softening in a constitutive law for such materials as porous metal or brittle concrete raises problems from both the mathematical and physical points of view. The main mathematical drawback is the occurrence of bifurcations with an infinite number of bifurcated branches, which raises the problem of selecting the relevant one, especially in numerical computations. The major physical drawback is the strain localization phenomenon, which results in a zero energy dissipation at failure.

It thus appears necessary to introduce some "localization limiter." In order to do so, some authors have introduced a small viscosity coefficient; but the latter appears as a mere mathematical artifact void of physical meaning. In the present authors' view, the most convincing (or rather, least artificial) approach is to use the *nonlocal* concept. A formulation in which all state variables were nonlocal was proposed by Bažant et al. (1984); however this formulation led to serious complications. It was later recognized by Pijaudier-Cabot and Bažant (1987) that considerable simplifications could be achieved without losing the essential features of the nonlocal concept by assuming the damage parameter to be the only nonlocal variable. The power of this approach to represent complex, experimentally observed phenomena has been demonstrated by Bažant and Ožbolt (1990).

Theoretical studies of the properties of nonlocal models have been carried out in the context of instability and bifurcation problems. Instability studies include the works of Bažant and Pijaudier-Cabot (1988) and Bažant and Lin (1989) on strain localization in rods and three-dimensional solids. Bifurcation problems were considered in the work of Pijaudier-Cabot and Bode (1991). The question studied by these authors was that of bifurcation into a sinusoidal mode in an infinite, homogeneous body deformed in plane strain and obeying the Lemaître-Chaboche (1989) damage model. They found that for a *given orientation* of the wave vector of the bifurcated solution, the *magnitude* of this vector at bifurcation is fixed in a nonlocal medium, in contrast to the case of a local medium where it can take arbitrary values. (In fact, Pijaudier-Cabot and Bode derived this only with a certain assumption on the orientation of the wave vector, but this restriction was unnecessary and could easily be removed.) This result suggests that the nonlocal concept does allow for the settlement of the problem of the infinite number of bifurcated branches encountered in local media.

In this paper, we shall study bifurcation phenomena in a nonlocal medium obeying the Gurson (1977) model for porous ductile metals. Two problems will be investigated theoretically, namely appearance of a discontinuous velocity gradient in an arbitrary (finite, inhomogeneous) body and arbitrary bifurcation in an infinite, initially homogeneous medium. In both cases, the usual hypothesis of absence of elastic unloadings will be made. The second problem is strongly connected with that studied by Pijaudier-Cabot and Bode (1991), in spite of the differences between the constitutive models considered. The present analysis will go somewhat deeper in that we shall seek the orientation of the wave vector that leads to easiest

[1] Current address: Division of Applied Sciences, Pierce Hall, Harvard University, 29 Oxford Street, Cambridge, MA 02138.

Contributed by the Applied Mechanics Division of THE AMERICAN SOCIETY OF MECHANICAL ENGINEERS for publication in the ASME JOURNAL OF APPLIED MECHANICS.

Discussion on this paper should be addressed to the Technical Editor, Professor Lewis T. Wheeler, Department of Mechanical Engineering, University of Houston, Houston, TX 77204-4792, and will be accepted until four months after final publication of the paper itself in the ASME JOURNAL OF APPLIED MECHANICS.

Manuscript received by the ASME Applied Mechanics Division, Jan. 31, 1991; final revision, Apr. 16, 1993. Associate Technical Editor: C. F. Shih.

Copyright © 1994 by ASME
Downloaded 03 May 2010 to 171.66.16.20. Redistribution subject to ASME license or copyright; see http://www.asme.org/terms/Terms_Use.cfm

bifurcation; this will allow for the study of the influence of nonlocality on the conditions of first occurrence of bifurcation and on the corresponding bifurcated solution. A finite element study of shear banding in a rectangular mesh loaded in plane strain tension will finally be carried out in order to illustrate the influence of boundary conditions in a real, finite body.

2 Discontinuity of the Velocity Gradient in an Arbitrary Body

We consider a porous material obeying the classical Gurson (1977) yield criterion (as improved by Tvergaard, 1981) and associated flow rule:

$$\Phi(\sigma_{eq},\ \sigma_m,\ \bar{\sigma},\ f)=\frac{\sigma_{eq}^2}{\bar{\sigma}^2}+2qf\cosh\left(\frac{3\sigma_m}{2\bar{\sigma}}\right)-1-q^2f^2=0;$$
$$D_{ij}^p=\eta\Phi_{,\sigma_{ij}},\ \eta\geq 0, \tag{1}$$

where σ_{eq} is the equivalent stress, σ_m the mean stress, $\bar{\sigma}$ the yield stress of the unvoided matrix, f the porosity, q the Tvergaard parameter, $\mathbf{D}^p$ the plastic strain rate, and η the plastic multiplier. The usual evolution equation for $\bar{\sigma}$ is also supposed to be obeyed:

$$\boldsymbol{\sigma}:\mathbf{D}^p=(1-f)\bar{\sigma}\,\dot{\bar{\epsilon}}=(1-f)\frac{\bar{\sigma}\,\dot{\bar{\sigma}}}{d\bar{\sigma}/d\bar{\epsilon}}, \tag{2}$$

where $\bar{\epsilon}$ and $d\bar{\sigma}/d\bar{\epsilon}$ denote the equivalent plastic strain and (supposedly positive) hardening slope of the unvoided matrix. However, the classical evolution equation for f is modified through convolution with some weight function φ:

$$\dot{f}(\mathbf{x})=\frac{1}{A(\mathbf{x})}\int_\Omega[1-f(\mathbf{y})]D_{kk}^p(\mathbf{y})\varphi(\mathbf{x}-\mathbf{y})d^3\mathbf{y},$$
$$A(\mathbf{x})\equiv\int_\Omega\varphi(\mathbf{x}-\mathbf{y})d^3\mathbf{y}, \tag{3}$$

where Ω denotes the volume studied; φ is assumed to be indefinitely differentiable (this means in particular that it does not involve any infinite, Dirac-like peak at the point $\mathbf{O}$), isotropic ($\varphi(\mathbf{y})\equiv\varphi(|\mathbf{y}|)$), and normalized $\left(\int_{\mathbb{R}^3}\varphi(\mathbf{y})d^3\mathbf{y}=1\right)$. Note that the normalization factor $A(\mathbf{x})$ in Eq. (3) is not necessarily unity since the integral defining it is taken over Ω instead of $\mathbb{R}^3$.

We shall now see that in spite of the nonlocal character of the constitutive equations, the *jumps* of the stress and strain rates through any surface are connected by a *local* relation; this is the key feature that makes the analysis possible. Indeed, the consistency condition $\dot{\Phi}=0$ (which results from the hypothesis of absence of elastic unloadings) reads

$$\Phi_{,\sigma_{eq}}\dot{\sigma}_{eq}+\Phi_{,\sigma_m}\dot{\sigma}_m+\Phi_{,\bar{\sigma}}\dot{\bar{\sigma}}+\Phi_{,f}\dot{f}=0.$$

Now $\dot{f}$, being given by the integral expression (3_1), is *continuous*. The same is true of the partial derivatives of Φ at the inception of the discontinuity, since they only depend on the mechanical fields and not on their time-derivatives. Thus, considering the jump of the preceding equation at that instant and taking Eqs. (1_2), (2) into account, one gets

$$\Phi_{,\sigma_{eq}}[\![\dot{\sigma}_{eq}]\!]+\Phi_{,\sigma_m}[\![\dot{\sigma}_m]\!]+\Phi_{,\bar{\sigma}}[\![\dot{\bar{\sigma}}]\!]=0\Rightarrow[\![\eta]\!]=$$
$$-\frac{(1-f)\bar{\sigma}(\Phi_{,\sigma_{eq}}[\![\dot{\sigma}_{eq}]\!]+\Phi_{,\sigma_m}[\![\dot{\sigma}_m]\!])}{\Phi_{,\bar{\sigma}}\sigma_{k\ell}\Phi_{,\sigma_{k\ell}}\dfrac{d\bar{\sigma}}{d\bar{\epsilon}}}$$

where the symbol $[\![\ ]\!]$ denotes the jump of any quantity. Using again Eq. (1_2) and taking elasticity into account, one then obtains the expression of the jump of the total strain rate $\mathbf{D}$:

$$[\![D_{ij}]\!]=\frac{1+\nu}{E}[\![\dot{\sigma}_{ij}]\!]-\frac{\nu}{E}\delta_{ij}[\![\dot{\sigma}_{kk}]\!]$$
$$-\frac{(1-f)\bar{\sigma}(\Phi_{,\sigma_{eq}}[\![\dot{\sigma}_{eq}]\!]+\Phi_{,\sigma_m}[\![\dot{\sigma}_m]\!])\Phi_{,\sigma_{ij}}}{\Phi_{,\bar{\sigma}}\sigma_{k\ell}\Phi_{,\sigma_{k\ell}}\dfrac{d\bar{\sigma}}{d\bar{\epsilon}}},$$

where E and ν are Young's modulus and Poisson's ratio. (A small strain formulation is used here for the law of elasticity, following the classical approach of strain localization of Rudnicki and Rice (1975), who showed that replacement of the ordinary time-derivative by an objective one modifies the critical hardening modulus only by a very small term.)

From now on, Rudnicki and Rice's classical treatment can be applied with almost no modifications. In the first place, the preceding equation can be put under the form used by these authors:

$$2[\![D'_{ij}]\!]=\frac{[\![\dot{\sigma}'_{ij}]\!]}{G}+\frac{1}{h}\left(\frac{\sigma'_{k\ell}[\![\dot{\sigma}_{k\ell}]\!]}{2\tau}+\beta'\frac{[\![\dot{\sigma}_{kk}]\!]}{3}\right)\frac{\sigma'_{ij}}{\tau};$$
$$[\![D_{kk}]\!]=\frac{[\![\dot{\sigma}_{kk}]\!]}{3K}+\frac{\beta}{h}\left(\frac{\sigma'_{k\ell}[\![\dot{\sigma}_{k\ell}]\!]}{2\tau}+\beta'\frac{[\![\dot{\sigma}_{kk}]\!]}{3}\right), \tag{4}$$

where $3K$ and G are the elastic bulk and shear moduli, h, β, β' coefficients (the symbol β' is preferred to Rudnicki and Rice's original notation μ because of the possible confusion with the elastic shear modulus), $\mathbf{D}'$ and $\boldsymbol{\sigma}'$ the deviators of the strain rate and the stress, and τ the equivalent stress divided by $\sqrt{3}$. The values of β, β' and h are

$$\beta=\beta'=\frac{1}{\sqrt{3}}\frac{\Phi_{,\sigma_m}}{\Phi_{,\sigma_{eq}}};$$
$$h=-\frac{\Phi_{,\bar{\sigma}}(\Phi_{,\sigma_{eq}}\sigma_{eq}+\Phi_{,\sigma_m}\sigma_m)}{3(1-f)\bar{\sigma}\Phi_{,\sigma_{eq}}^2}\frac{d\bar{\sigma}}{d\bar{\epsilon}} \tag{5}$$

(the formula $\Phi_{,\sigma_{ij}}=(3\sigma'_{ij}/2\sigma_{eq})\Phi_{,\sigma_{eq}}+(\delta_{ij}/3)\Phi_{,\sigma_m}$ has been used to derive these expressions). Secondly, this equation can be inverted to the form $[\![\dot{\sigma}_{ij}]\!]=\mathfrak{L}_{ijk\ell}[\![D_{k\ell}]\!]$ where the expression of $\mathfrak{L}_{ijk\ell}$ is given in Rudnicki and Rice (1975). Thirdly, the jump of the velocity gradient being necessarily of the form $\mathbf{g}\otimes\mathbf{n}$ where $\mathbf{n}$ is the unit vector normal to the surface of discontinuity and $\mathbf{g}$ an arbitrary nonzero vector, the incremental equilibrium equation leads to the condition $\operatorname{Det}_{i,k}\mathfrak{L}_{ijk\ell}n_jn_\ell=0$, which is equivalent to an equation of the form $h=\tilde{h}(\mathbf{n})$ where the expression of $\tilde{h}(\mathbf{n})$ is again to be found in Rudnicki and Rice (1975). Fourthly, though the notation does not emphasize it, both h and $\tilde{h}(\mathbf{n})$ vary with time, h being originally greater than $\tilde{h}(\mathbf{n})$ for all values of $\mathbf{n}$; the possibility of a discontinuous velocity gradient appears when h reaches $\tilde{h}(\mathbf{n})$ for some $\mathbf{n}$ for the first time, and this occurs when h takes the critical value $h_c=\operatorname{Max}_{\mathbf{n}}\tilde{h}(\mathbf{n})$.

Now it has been shown in the paper of Rudnicki and Rice (as completed by Perrin and Leblond, 1993) that when $\beta=\beta'$, the expression of h_c is

$$\frac{h_c}{G}=-\frac{1+\nu}{2}\left(N+\frac{2\beta}{3}\right)^2$$
$$\text{if}\quad N_{\min}+(1-\nu)N<\frac{2(1+\nu)\beta}{3}<N_{\max}+(1-\nu)N;$$
$$=-\frac{1+\nu}{1-\nu}\left(\frac{N_{\max}}{2}-\frac{2\beta}{3}\right)^2-\frac{1}{4}(N-N_{\min})^2$$
$$\text{if}\quad N_{\max}+(1-\nu)N\leq\frac{2(1+\nu)\beta}{3};$$

Downloaded 03 May 2010 to 171.66.16.20. Redistribution subject to ASME license or copyright; see http://www.asme.org/terms/Terms_Use.cfm

$$= -\frac{1+\nu}{1-\nu}\left(\frac{N_{\min}}{2}-\frac{2\beta}{3}\right)^2 - \frac{1}{4}(N_{\max}-N)^2$$

$$\text{if } N_{\min}+(1-\nu)N \geq \frac{2(1+\nu)\beta}{3}, \quad (6)$$

where $N_{\max}=\sigma'_I/\tau$, $N=\sigma'_{II}/\tau$, $N_{\min}=\sigma'_{III}/\tau$, σ'_I, σ'_{II}, σ'_{III} denoting the principal ordered values of $\boldsymbol{\sigma}'$ ($\sigma'_I \geq \sigma'_{II} \geq \sigma'_{III}$). It follows that h_c is *nonpositive*. On the other hand, h is *positive*; this results from (5_2), (1) and the assumed positiveness of $d\bar{\sigma}/d\bar{\epsilon}$. Hence, the equality of h and h_c is impossible, which means that *a discontinuous velocity gradient is impossible in the material considered*. The basic reason for this is the continuity of the porosity rate arising from its nonlocal (integral) expression.

3 Arbitrary Bifurcation in an Infinite, Homogeneous Medium

We now study the possibility of an arbitrary loss of uniqueness of the velocity field in an infinite, initially homogeneous medium. We shall use the method of Fourier transforms, which is especially appropriate for such geometries; the Fourier transform of a function $g(\mathbf{x})$ will be denoted with a caret:

$$g(\mathbf{x}) = \frac{1}{(2\pi)^3}\int_{\mathbb{R}^3} \hat{g}(\mathbf{p}) e^{ip.x} d^3\mathbf{p};$$

$$\hat{g}(\mathbf{p}) = \int_{\mathbb{R}^3} g(\mathbf{x}) e^{-ip.x} d^3\mathbf{x}. \quad (7)$$

Also, we shall simply denote $\dot{\boldsymbol{\sigma}}$, $\mathbf{D}\ldots$ the various rates corresponding to the *difference* of two possible solutions.

Applying Eqs. (1_2), (2) to two possible solutions and taking the Fourier transform of the difference, we obtain at the instant of incipient bifurcation when the mechanical fields are still homogeneous:

$$\hat{D}^p_{ij}(\mathbf{p}) = \hat{\eta}(\mathbf{p})\Phi_{,\sigma_{ij}}; \quad \boldsymbol{\sigma}:\hat{\mathbf{D}}^p(\mathbf{p}) = (1-f)\frac{\overline{\boldsymbol{\sigma}\hat{\boldsymbol{\sigma}}}(\mathbf{p})}{d\bar{\sigma}/d\bar{\epsilon}}.$$

Also, taking the Fourier transform of Eq. (3) (noting that the normalization factor $A(\mathbf{x})$ is unity for an infinite medium), we get

$$\hat{f}(\mathbf{p}) = (1-f)\hat{\mathbf{D}}^p_{kk}(\mathbf{p})\hat{\varphi}(\mathbf{p}).$$

Insertion of these equations into the Fourier transform of the consistency condition yields the value of $\hat{\eta}(\mathbf{p})$:

$$\hat{\eta}(\mathbf{p}) = -\frac{\Phi_{,\sigma_{eq}}\hat{\sigma}_{eq}(\mathbf{p}) + \Phi_{,\sigma_m}\hat{\sigma}_m(\mathbf{p})}{\Phi_{,\bar{\sigma}}\dfrac{\sigma_{k\ell}\Phi_{,\sigma_{k\ell}}}{(1-f)\bar{\sigma}}\dfrac{d\bar{\sigma}}{d\bar{\epsilon}} + (1-f)\Phi_{,f}\Phi_{,\sigma_{kk}}\hat{\varphi}(\mathbf{p})}.$$

Accounting for elasticity (using a small strain formulation), we then get

$$\hat{D}_{ij}(\mathbf{p}) = \frac{1+\nu}{E}\hat{\sigma}_{ij}(\mathbf{p}) - \frac{\nu}{E}\hat{\sigma}_{kk}(\mathbf{p})\delta_{ij} - \frac{[\Phi_{,\sigma_{eq}}\hat{\sigma}_{eq}(\mathbf{p}) + \Phi_{,\sigma_m}\hat{\sigma}_m(\mathbf{p})]\Phi_{,\sigma_{ij}}}{\Phi_{,\bar{\sigma}}\dfrac{\sigma_{k\ell}\Phi_{,\sigma_{k\ell}}}{(1-f)\bar{\sigma}}\dfrac{d\bar{\sigma}}{d\bar{\epsilon}} + (1-f)\Phi_{,f}\Phi_{,\sigma_{kk}}\hat{\varphi}(\mathbf{p})},$$

which can again be put under the form (4) (the $[\![\,]\!]$ symbols being replaced by carets) by defining β and β' as above (Eq. (5_1)) and $h \equiv h(\mathbf{p})$ by

$$h(\mathbf{p}) = -\frac{1}{3\Phi^2_{,\sigma_{eq}}}\left[\frac{\Phi_{,\bar{\sigma}}(\Phi_{,\sigma_{eq}}\sigma_{eq} + \Phi_{,\sigma_m}\sigma_m)}{(1-f)\bar{\sigma}}\frac{d\bar{\sigma}}{d\bar{\epsilon}} + (1-f)\Phi_{,f}\Phi_{,\sigma_m}\hat{\varphi}(\mathbf{p})\right]. \quad (8)$$

Inversion then yields $\hat{\sigma}_{ij}(\mathbf{p}) = \mathfrak{L}_{ijk\ell}(\mathbf{p})\hat{D}_{k\ell}(\mathbf{p})$ where the expression of $\mathfrak{L}_{ijk\ell}(\mathbf{p})$ is again given in Rudnicki and Rice (1975) (with $h \equiv h(\mathbf{p})$).

Now let $\mathbf{U}$ denote the difference of the velocity fields. The Fourier transform of the incremental equilibrium equation reads

$$\mathfrak{L}_{ijk\ell}(\mathbf{p})p_j p_\ell \hat{U}_k(\mathbf{p}) = 0.$$

We are looking for the nonzero Fourier components $\hat{\mathbf{U}}(\mathbf{p})$ of $\mathbf{U}$. For such a component, the condition $\underset{i,k}{\text{Det}}\,\mathfrak{L}_{ijk\ell}(\mathbf{p})p_j p_\ell = 0$ must be satisfied. The vector $\mathbf{p}$ can be assumed to be nonzero, because the Fourier component $\hat{\mathbf{U}}(\mathbf{0})$ represents an uninteresting translatory movement. Hence we can define

$$p = |\mathbf{p}|; \quad \mathbf{n} = \mathbf{p}/p, \quad (9)$$

and the preceding condition is equivalent to $\underset{i,k}{\text{Det}}\,\mathfrak{L}_{ijk\ell}(\mathbf{p})n_j n_\ell = 0$. This condition, which is of the same type as in classical bifurcation studies except for the dependence upon $\mathbf{p}$, yields an equation for h of the type

$$h(\mathbf{p}) \equiv h(p) = \tilde{h}(\mathbf{n}) \quad (10)$$

where the expression of $\tilde{h}(\mathbf{n})$ is to be found in Rudnicki and Rice (1975). (The fact that h depends on $\mathbf{p}$ only through its norm p results from Eq. (8) and the assumed isotropy of φ and $\hat{\varphi}$). We shall now discuss the solutions of this equation, the function $\hat{\varphi}(p)$ being assumed to decrease toward zero for $p \to +\infty$ (this is, for instance, true if φ is Gaussian).

Let us first suppose that the vector $\mathbf{n}$ *is fixed.* $h(p)$ being a monotone function (see Eq. (8)), Eq. (10) can have at most one solution in p. Thus, for a fixed orientation of the wave vector, the wavelength of the bifurcated mode (difference between the possible solutions) is determined uniquely; this contrasts with the case of a local medium where it can take arbitrary values. (This case is easily recovered by equating φ to Dirac's δ-distribution: then $\hat{\varphi} \equiv 1$ so that h is independent of p and Eq. (10) puts no condition upon this parameter.) This fundamental feature is exactly identical to that evidenced by Pijaudier-Cabot and Bode (1991) in the case of the Lemaître-Chaboche model. Also, the wavelengths allowed by Eq. (10) are bounded from below; i.e., p is bounded from above; indeed, with $\hat{\varphi}(+\infty) = 0$, the value of $h(p)$ given by (8) tends to that given by (5_2) for $p \to +\infty$, and it has been shown that the equality $h = \tilde{h}$ is impossible for such an expression of h.

Let us now let the orientation $\mathbf{n}$ *of the wave vector* $\mathbf{p}$ *vary* in order to investigate the conditions of first appearance of a bifurcation and the corresponding bifurcated solution. At the beginning of the loading, $h(p)$ is greater than $\tilde{h}(\mathbf{n})$ for all p's and $\mathbf{n}$'s. A bifurcation becomes possible when (10) is verified for the first time for some values of p and $\mathbf{n}$, hereafter denoted p_0 and $\mathbf{n}_0$. Now consider Fig. 1, which represents both h and $\tilde{h}$ as functions of p for $\mathbf{n} = \mathbf{n}_0$ (case *a*) and as functions of $\mathbf{n}$ for $p = p_0$ (case *b*), at the beginning of the loading and when (10) is satisfied for the first time. If, in Fig. (1*a*), h were not minimum at the point of contact of the curves at the latter instant, some point of the h-curve would lie below the $\tilde{h}$-horizontal line and thus, by continuity, the curves would cross each other somewhat earlier. Hence p_0 must correspond to the absolute minimum of $h(p)$. A similar reasoning shows that $\tilde{h}(\mathbf{n})$ must be maximum at the point of contact of the curves in Fig. (1*b*). Thus the condition determining both the first occurrence of a bifurcation and the corresponding parameters p_0 and $\mathbf{n}_0$ reads

$$\min_p h(p) = h(p_0) = \max_{\mathbf{n}} \tilde{h}(\mathbf{n}) = \tilde{h}(\mathbf{n}_0). \quad (11a)$$

In order to make this condition more explicit, let us study the function $h(p)$ defined by (8). Using Eq. (1_1) and the inequalities $\cosh(3\sigma_m/2\bar{\sigma}) \geq 1$ and $qf < 1$ (the latter property follows from the fact that if qf reaches unity, the yield locus reduces to the single point (0, 0) in the (σ_{eq}, σ_m) plane), one

Downloaded 03 May 2010 to 171.66.16.20. Redistribution subject to ASME license or copyright; see http://www.asme.org/terms/Terms_Use.cfm

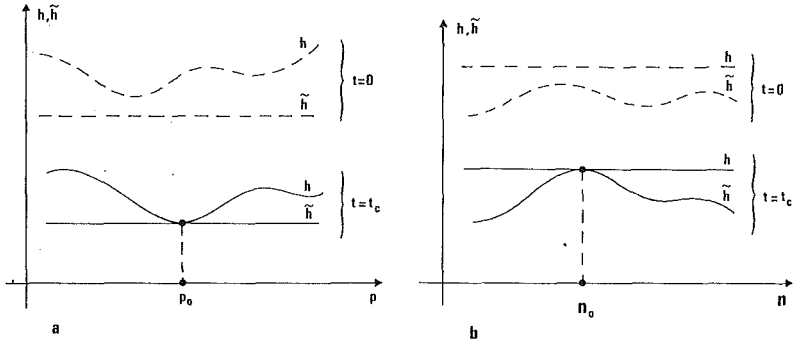


Fig. 1 Plots of h and $\tilde{h}$, (*a*) versus p for $n = n_0$ and (*b*) versus n for $p = p_0$, at the beginning of the loading ($t = 0$) and at the instant when (10) becomes satisfied for the first time ($t = t_c$).

easily checks that Φ_f is positive. If σ_m is nonpositive, $\Phi_{,\sigma_m}$ is also nonpositive, and $h(p)$ is a nonincreasing function; hence (11*a*) can be written $h(+\infty) = \operatorname{Max}_{\mathbf{n}} \tilde{h}(\mathbf{n})$; but, as remarked above, this equality is impossible. Therefore *no bifurcation can occur in compression* ($\sigma_m \leq 0$). We shall therefore assume σ_m to be positive hereafter. Then $\Phi_{,\sigma_m}$ is also positive, $h(p)$ is an increasing function and (11*a*) becomes

$$h(0) = \operatorname{Max}_{\mathbf{n}} \tilde{h}(\mathbf{n}). \tag{11b}$$

Now $\hat{\varphi}(\mathbf{0}) = 1$ because of the normalization condition of φ. Therefore the value of $h(0)$ is identical to that of h for a *local material* (corresponding to $\hat{\varphi} \equiv 1$). It follows that *the condition* (11*b*) *of first occurrence of a bifurcation is exactly the same as for a local medium*. On the other hand, *nonlocality does have an effect on the first bifurcation mode, the wavelength of the latter being necessarily infinite* ($p_0 = 0$) *in a nonlocal medium*, instead of being arbitrary as in a local one.

In fact, the first bifurcation mode corresponds to a mere translatory movement. It nevertheless deserves interest in that it marks the onset of loss-of-uniqueness phenomena (new bifurcation modes with finite, gradually decreasing wavelengths appear immediately after the first one).

Let us finally derive the fully explicit form of condition (11*b*), which is easily done by using the expression (6) of $h_c = \operatorname{Max}_{\mathbf{n}} \tilde{h}(\mathbf{n})$. Disregarding the particular case corresponding to $2(1+\nu)\beta/3 \leq N_{\min} + (1-\nu)N$ because, as remarked by Perrin and Leblond (1993), it implies a nonpositive β and hence, by Eqs. (5_1) and (1_1), a nonpositive σ_m, and evaluating β and $h(0)$ with the aid of (5_1), (8), and (1_1), one gets

$$\frac{6\bar{\sigma}}{E} q^2 f(1-f) sh(ch - qf) - \frac{4}{(1-f)E} \frac{d\bar{\sigma}}{d\bar{\epsilon}} \left(\frac{\sigma_{eq}^2}{\bar{\sigma}^2} + \frac{3qf\sigma_m}{2\bar{\sigma}} sh \right)^2$$

$$= \begin{cases} \left(\dfrac{3\sigma_{II}'}{\bar{\sigma}} + qfsh \right)^2 & \text{if } qfsh < \dfrac{3[\sigma_I' + (1-\nu)\sigma_{II}']}{(1+\nu)\bar{\sigma}} \\ \dfrac{2}{1-\nu} \left(\dfrac{3\sigma_I'}{2\bar{\sigma}} - qfsh \right)^2 + \dfrac{9(\sigma_{II}' - \sigma_{III}')^2}{2(1+\nu)\bar{\sigma}^2} & \text{otherwise,} \end{cases} \tag{11c}$$

where "*sh*" and "*ch*" are short notations for $\sinh(3\sigma_m/2\bar{\sigma})$ and $\cosh(3\sigma_m/2\bar{\sigma})$, respectively, and σ_I', σ_{II}', σ_{III}' denote the principal ordered values of the stress deviator $\boldsymbol{\sigma}'$ as above. In fact there is nothing new, in principle, in this condition, since it is identical to that for a local material which has already been studied by a number of authors, notably Yamamoto (1978); the novelty here lies only in the use of Perrin and Leblond's (1993) correction of the Rudnicki-Rice formula in the particular case where $qfsh \geq 3[\sigma_I' + (1-\nu)\sigma_{II}']/((1+\nu)\bar{\sigma})$.

4 Finite Element Study of Shear Banding in a Rectangular Mesh

This section is essentially illustrative; its aim is to evidence, using a finite element simulation, some of the differences which may arise between the highly idealized case of an infinite, homogeneous medium and that of a real, finite one.

We shall consider a rectangle of dimensions 10×12 mm divided into 120 quadratic subintegrated square elements, deformed in plane strain tension in its largest, vertical dimension; the boundary conditions are as follows:

$$\boldsymbol{\sigma}.\mathbf{n} = \mathbf{0} \quad \text{for} \quad X = 0 \quad \text{and} \quad 10 \text{ mm};$$

$$\sigma_{XY} \equiv \mathbf{e}_X.\boldsymbol{\sigma}.\mathbf{e}_Y = 0 \quad \text{for} \quad Y = 0 \quad \text{and} \quad 12 \text{ mm};$$

$$U_Y = 0 \quad \text{for} \quad Y = 0 \text{ mm}, \quad U_Y = U_0 \quad \text{for} \quad Y = 12 \text{ mm},$$

where X and Y denote the initial horizontal and vertical coordinates. The material constants are $E = 200{,}000$ MPa, $\nu = 0.3$, $\bar{\sigma} = 450$ MPa and $d\bar{\sigma}/d\bar{\epsilon} = 0$. The initial porosity is $f_0 = 0.1$ in all elements (except for a single one indicated by a cross in the figures below, which simulates an imperfection aimed at "triggering" the bifurcation). This value is admittedly quite large (it has been chosen so in order to enhance the influence of the porosity), but it does occur in practice in those zones where coalescence of voids takes place. The value $q = 4/e = 1.47\ldots$ of the Tvergaard parameter determined by Perrin and Leblond (1990) by a *self-consistent* method is adopted. In order to evidence the influence of nonlocality of the porosity rate, calculations are performed both with a local model and with a Gaussian weight function $\varphi(\mathbf{y}) \equiv \varphi(|\mathbf{y}|) = e^{-|\mathbf{y}|^2/\ell^2}/(\pi\ell^2)$, where $\ell = 2$ mm. Numerical experience has shown that the ratio h/ℓ, where h is the element size, is then small enough (0.5) for the results to be independent of h.

The computation uses the "Large Strain Plasticity" option of the SYSWELD software developed by the FRAMASOFT + CSI Company. The formulation employed is identical to that described above in the context of small strains except for the replacement of the ordinary time-derivative $\dot{\boldsymbol{\sigma}}$ by a Green-Naghdi derivative. Its numerical implementation is described in detail in Leblond (1992) and may be summarized as

Downloaded 03 May 2010 to 171.66.16.20. Redistribution subject to ASME license or copyright; see http://www.asme.org/terms/Terms_Use.cfm

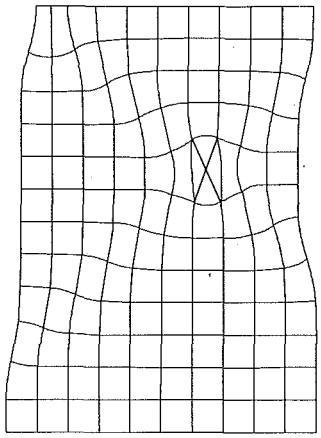


Fig. 2 Deformed mesh for a 0.83 percent logarithmic strain in the vertical direction (the displacements are magnified by a factor of 15); local model

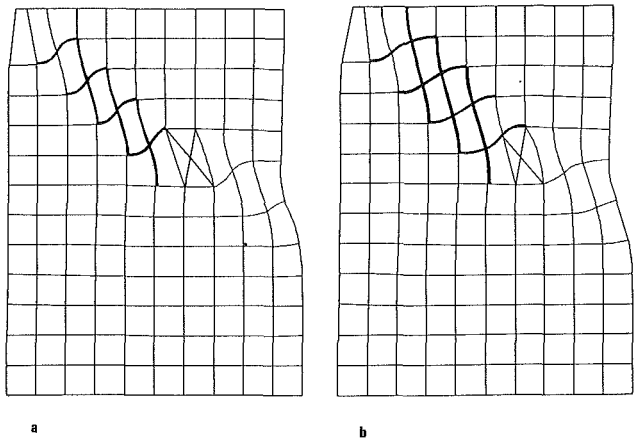


Fig. 3 Deformed mesh for a 8.0 percent logarithmic strain in the vertical direction (no magnification of the displacements); (*a*) local model, (*b*) nonlocal model

follows. The equilibrium equations and constitutive laws are solved using the same iterative procedure as in classical plasticity, the only novelties being that the stress tensor is projected onto the Gurson yield locus instead of that of Von Mises and that the calculation of the evolution of the porosity has a nonlocal character. The operation of projection onto the yield locus uses an algorithm which is implicit with respect to the stress-tensor (i.e., the normality rule is written using the final, unknown normal $\Phi_{,\sigma_{ij}}$ to the yield locus) but explicit with respect to the porosity; in order to increase the accuracy of the scheme, we do not use for f the value corresponding to the beginning of the time step but an estimate of its value at the mid-interval deduced by extrapolation from the preceding results. Local values of $[1-f(\mathbf{y})]D^p_{kk}(\mathbf{y})$ at all Gauss points are also evaluated simultaneously with corrected stresses. Once convergence is reached, a double "DO" loop is performed over all Gauss points, using these values, to evaluate the integrals of Eqs. (3). (Nothing special occurs near boundaries, except that the value of the normalization factor $A(\mathbf{x})$ decreases because the intersection of the volume studied and the region where $\varphi(\mathbf{x}-\mathbf{y})$ takes appreciable values becomes smaller.) The porosity increments calculated in that way are finally used to update the porosity at all Gauss points.

Preliminary calculations performed with a small imperfection showed no sign of the formation of shear bands, even for notable overall strains. On the other hand, it is easy to evaluate the bifurcation criterion (11*c*) numerically, and the results show that the latter is fulfilled almost instantaneously. The only possible explanation of this "contradiction" is that condition (11*c*), which was derived for an infinite medium, applies badly to the finite geometry considered here, because the boundary conditions are incompatible with the strain and stress states that would prevail in shear bands (the effect of the imperfection cannot be invoked here since it is known to facilitate, rather than prevent, bifurcations).

We thus decided to perform calculations with a large imperfection, and took a value of 0.5 for the initial porosity in the crossed element. Such large porosity inhomogeneities can be met in the final stages of ductile fracture, when zones where moderate coalescence of voids has occurred coexist with almost completely ruined ones. Figure 2 shows the deformed mesh obtained for a small strain imposed, in the case of the local model. Shear bands conspicuously appear here; one of them ends on the lateral traction-free surfaces on both sides, while the other one ends on a free surface on one side and on the upper surface subject to a prescribed displacement on the other side (because of this difference, it may be anticipated that the system will "choose" one shear band during the subsequent loading and that the other one will cease developing). However, it is important to note that the occurrence of these shear bands cannot be interpreted as due to some bifurcation, since the latter should then be observable no matter how small the imperfection; the observed behavior is much more similar to that of a Von Mises material containing a hole, for which the effect of concentration of the deformation in narrow bands does occur but strongly depends upon the importance of the perturbation.

The analogous figure for the nonlocal model is not shown because it is indistinguishable from the preceding one; this means that the effect of nonlocality of the porosity rate on the deformation is very small at the beginning of the loading. It is natural to wonder whether this does not simply arise from a lack of influence of the *porosity* itself. A computation has been performed with $f_0=0$ (except in the imperfection) in order to clear up this question. The deformed mesh obtained then is indeed almost the same, in the early stages of the loading, as in the case where $f_0=0.1$ (for both the local and nonlocal models). This confirms that the formation of shear bands arises primarily from the almost empty crossed element and not from the porosity, and thus that the observed behavior is closer to that of a Von Mises medium containing a hole rather than to that of a softening material exhibiting a bifurcation.

Figure 3 shows the deformed mesh at a later stage of the loading, for both the local and nonlocal models. Though the two meshes look relatively similar at first sight, the shear band is in fact notably wider in the case of the nonlocal material: this is emphasized by bold lines which show that it extends over three elements (in both the horizontal and vertical directions) in that case, instead of two for the local material. The difference would become more dramatic if a finer mesh were used, because in the case of the local model the band width is essentially determined by the element size. Thus the nonlocality of the porosity rate, and a fortiori the porosity itself, now have a significant influence on the deformation.

Another noteworthy point on Fig. 3 is the fact that the shear band with one end on the upper surface has now completely prevailed over the other one. It is quite surprising that the system has preferred to "select" this band; indeed it clearly appears on Fig. 2 that the condition of prescribed displacement generates a higher distorsion of the shear band than that of zero traction, and it thus seems that it should hinder its normal development in a more significant way.

Figures 4 and 5 show the isoporosity curves for the same deformation as in Fig. 2, for the local and nonlocal models, respectively. Even at that early stage of the deformation, the porosity distribution appears to be notably affected by nonlocality, contrary to the deformation.

Downloaded 03 May 2010 to 171.66.16.20. Redistribution subject to ASME license or copyright; see http://www.asme.org/terms/Terms_Use.cfm

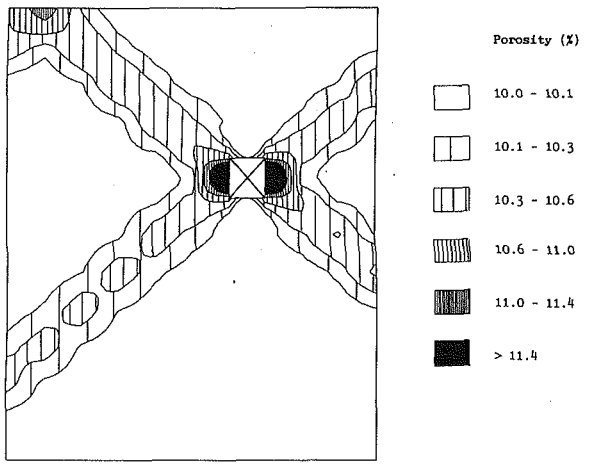


Fig. 4 Isoporosity curves on the deformed mesh (no magnification of the displacements), for a 0.83 percent logarithmic strain in the vertical direction; local model

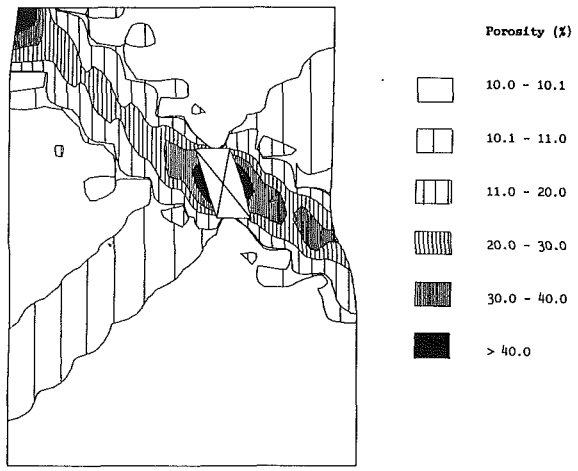


Fig. 6 Isoporosity curves on the deformed mesh (no magnification of the displacements), for a 8.0 percent logarithmic strain in the vertical direction; local model

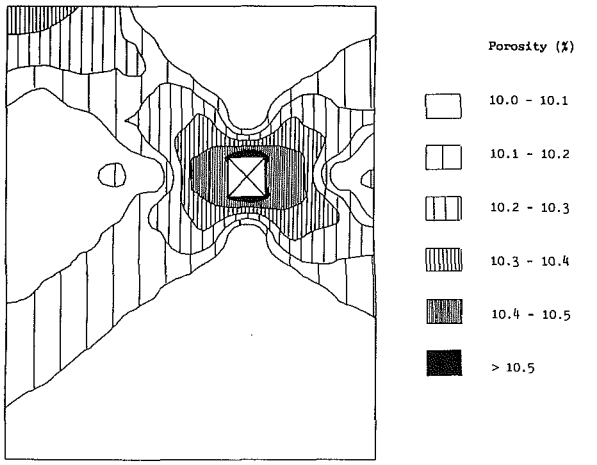


Fig. 5 Same as Fig. 4, but for the nonlocal model

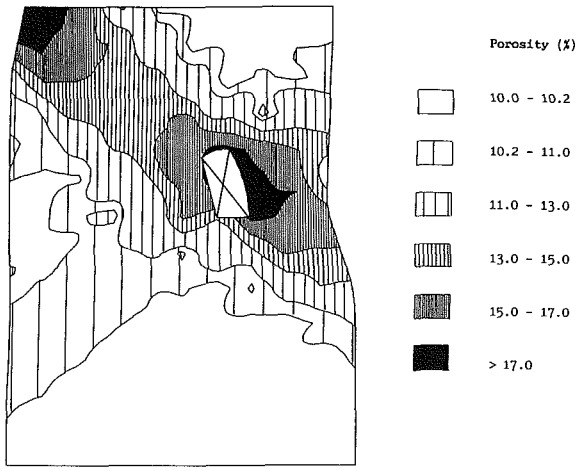


Fig. 7 Same as Fig. 6, but for the nonlocal model

Finally, Figs. 6 and 7 show the isoporosity curves for the same deformation as in Fig. 3. The influence of nonlocality is now dramatic, the porosity being concentrated in a much narrower zone, and its maximum value being considerably higher, for the local material than for the nonlocal one. The "tentacles" emanating laterally from the shear band in the local case indicate a strong influence of the discretization. Also, these figures make it clear that the minor shear band with both ends on free surfaces has not been erased in the late stages of the loading, but that its development has simply been "frozen" by that of the major one.

In conclusion, the main difference between an ideal, infinite body and the finite one considered in this section is that although shear bands and voids coexist in both media, void growth occurs in the former before the onset of shear bands and triggers the bifurcation, whereas in the latter, shear bands appear first due to the large porosity inhomogeneity, in the absence of any bifurcation, and govern the beginning of void growth. (As a result, in the nonlocal material, the size of the shear band is almost independent of the characteristic distance ℓ during the early stages of the loading.) Studying other types of loadings, not corresponding to plane strain conditions, would certainly lead to confirmation of the conclusion that bifurcations are unlikely in the finite medium, since plane strain conditions are known to greatly favor bifurcations. On the other hand, the geometry studied here is quite small (the characteristic distance in the weight function and the size of the inhomogeneity are only about 5 times smaller than the dimensions of the specimen), which enhances the hindering effect of boundary conditions upon bifurcations; thus the occurrence of the latter cannot be excluded in larger bodies.

Note. Since the first draft of this paper was written, an analogous study (Pijaudier-Cabot and Benallal, 1992) of bifurcations in a medium obeying a nonlocal version of the Lemaître-Chaboche damage model (Lemaître and Chaboche, 1989) has been forwarded to the authors. The conclusions of this study are essentially similar to those of the present paper, in spite of the differences between the constitutive models considered.

References

Bažant, Z. P., Belytschko, T. B., and Chang, T. P., 1984, "Continuum Theory for Strain-Softening," *ASCE Journal of Engineering Mechanics*, Vol. 110, pp. 1666–1692.

Bažant, Z. P., and Lin, F. B., 1989, "Stability Against Localization of Softening into Ellipsoids and Bands: Parameter Study," *International Journal of Solids and Structures*, Vol. 28, pp. 1483–1498.

Bažant, Z. P., and Ožbolt, J., 1990, "Nonlocal Microplane Model for Fracture, Damage, and Size Effect in Structures," *ASCE Journal of Engineering Mechanics*, Vol. 116, pp. 2484–2504.

Bažant, Z. P., and Pijaudier-Cabot, G., 1988, "Nonlocal Continuum Damage, Localization Instability and Convergence," ASME JOURNAL OF APPLIED MECHANICS, Vol. 55, pp. 287–293.

Downloaded 03 May 2010 to 171.66.16.20. Redistribution subject to ASME license or copyright; see http://www.asme.org/terms/Terms_Use.cfm

Gurson, A. L., 1977, "Continuum Theory of Ductile Rupture by Void Nucleation and Growth: Part I—Yield Criteria and Flow Rules for Porous Ductile Media," ASME *Journal of Engineering Materials and Technology*, Vol. 99, pp. 2–15.

Leblond, J. B., 1992, "Nouveau modèle de rupture ductile—Numérisation et mise en données," FRAMASOFT + CSI Internal Report No. LTSW.92/2027 (in French).

Lemaître, J., and Chaboche, J. L., 1989, *Mechanics of Solid Materials*, Cambridge University Press, Cambridge, U.K.

Perrin, G., and Leblond, J. B., 1990, "Analytical Study of a Hollow Sphere Made of Porous Plastic Material and Subjected to Hydrostatic Tension—Application to Some Problems in Ductile Fracture of Metals," *International Journal of Plasticity*, Vol. 6, pp. 677–699.

Perrin, G., and Leblond, J. B., 1993, "Rudnicki and Rice's Analysis of Strain Localization Revisited," ASME JOURNAL OF APPLIED MECHANICS, Vol. 60, pp. 842–846.

Pijaudier-Cabot, G., and Bažant, Z. P., 1987, "Nonlocal Damage Theory," *ASCE Journal of Engineering Mechanics*, Vol. 113, pp. 1512–1533.

Pijaudier-Cabot, G., and Benallal, A., 1992, "Strain Localization and Bifurcation in a Nonlocal Continuum," submitted to *International Journal of Solids and Structures*.

Pijaudier-Cabot, G., and Bode, L., 1991, "Two-Dimensional Analysis of Strain Localization with Nonlocal Continuous Damage," paper presented at the 8th ASCE Engineering Mechanics Specialty Conference, Colombus, OH.

Rudnicki, J. W., and Rice, J. R., 1975, "Conditions for the Localization of Deformation in Pressure-Sensitive Dilatant Materials," *Journal of the Mechanics and Physics of Solids*, Vol. 23, pp. 371–394.

Tvergaard, V., 1981, "Influence of Voids on Shear Band Instabilities under Plane Strain Conditions," *International Journal of Fracture*, Vol. 17, pp. 389–407.

Yamamoto, H., 1978, "Conditions for Shear Localization in the Ductile Fracture of Void-Containing Materials," *International Journal of Fracture*, Vol. 14, pp. 347–365.

Downloaded 03 May 2010 to 171.66.16.20. Redistribution subject to ASME license or copyright; see http://www.asme.org/terms/Terms_Use.cfm

Circularly Cylindrical and Plane Layered Media in Antiplane Elastostatics

T. Honein[1]
Postdoctoral Research Affiliate.

E. Honein
Research Associate,
Assoc. Mem. ASME

G. Herrmann
Professor of Applied Mechanics,
Honorary Mem. ASME.

Division of Applied Mechanics,
Stanford University,
Stanford, CA 94305-4040

In this paper we consider, within the framework of the linear theory of elasticity, the problem of circularly cylindrical and plane layered media under antiplane deformations. The layers are, in the first instance, coaxial cylinders of annular cross-sections with arbitrary radii and different shear moduli. The number of layers is arbitrary *and the system is subjected to* arbitrary *loading (singularities). The solution is derived by applying the heterogenization technique recently developed by the authors. Our formulation reduces the problem to solving linear functional equations and leads naturally to a group structure on the set* t *of real numbers such that* $-1 < t < 1$. *This allows us to write down the solution* explicitly *in terms of the solution of a corresponding homogeneous problem subjected to the same loading. In the course of these developments, it is discovered that certain types of inclusions do not disturb a uniform longitudinal shear. That these inclusions, which may be termed "stealth," are important in design and hole reinforcements is pointed out. By considering a limiting case of the aforementioned governing equations, the solution of plane layered media can be obtained. Alternatively, our formulation leads, in the case of plane layered media, to linear functional equations of the finite difference type which can be solved by several standard techniques.*

Introduction

In this paper we are concerned, within the framework of the linear theory of elasticity, with the heterogeneous problem of circularly cylindrical or plane layered media under antiplane deformations.

One such medium is composed, in the first instance, of an inclusion whose cross-section consists of many concentric circles (or parallel straight lines, in the limiting case) bounding isotropic and homogeneous materials of different elastic moduli. The inclusion is inserted into a matrix of infinite extent (see Fig. 1). We assume that the bond between the different materials is perfect, i.e., it ensures the continuity of tractions and displacements across the boundaries. The system is subjected to arbitrary singularities which generate out-of-plane displacement fields but are otherwise arbitrary.

We propose to express the solution of this problem in terms of the solution of the corresponding much simpler problem of an infinite homogeneous body subjected to the same loading.

In order to illustrate in as simple a setting as possible the ideas and techniques involved in carrying out such an analysis, we will assume that all singularities lie in the matrix. These ideas and techniques constitute a new procedure which was termed *heterogenization*, and which was advanced and implemented recently by the authors in a series of papers (1988,

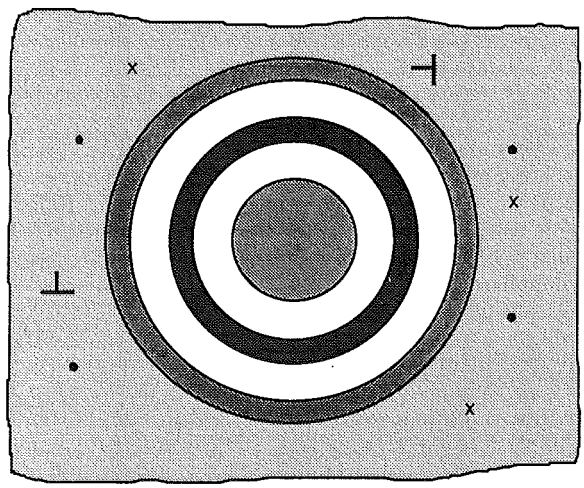


Fig. 1 A circularly cylindrical layered inclusion inserted into a matrix, of infinite extent, subjected to arbitrary loading

[1]Current address: General Science and Technology, Inc., 491 Macara Avenue, Suite 1007, Sunnyvale, CA 94086-2822.

Contributed by the Applied Mechanics Division of THE AMERICAN SOCIETY OF MECHANICAL ENGINEERS for publication in the ASME JOURNAL OF APPLIED MECHANICS.

Discussion on this paper should be addressed to the Technical Editor, Professor Lewis T. Wheeler, Department of Mechanical Engineering, University of Houston, Houston, TX 77204-4792, and will be accepted until four months after final publication of the paper itself in the ASME JOURNAL OF APPLIED MECHANICS.

Manuscript received by the ASME Applied Mechanics Division, Dec. 1, 1991; final revision, Dec. 10, 1992. Associate Technical Editor: R. Abeyaratne.

Copyright © 1994 by ASME
Downloaded 03 May 2010 to 171.66.16.20. Redistribution subject to ASME license or copyright; see http://www.asme.org/terms/Terms_Use.cfm

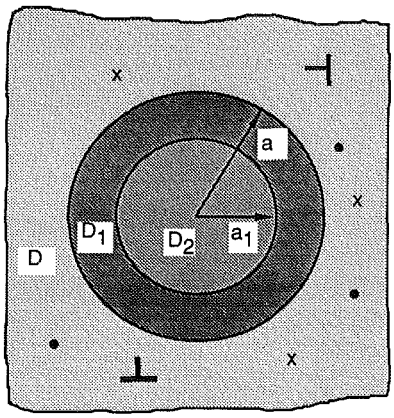


Fig. 2 A circularly cylindrical layered inclusion, consisting of two layers, inserted into a matrix, of infinite extent, subjected to arbitrary loading

1990a, 1990b, 1992a, 1992b). Heterogenization refers roughly to the methodology whereby the solution of a heterogeneous problem is sought in terms of a transformation performed on the solution of the corresponding homogeneous problem. It is to be noted in this regard that the transformation involved must be independent of the loading considered. In the present case, our methodology will reduce the problem for three materials (or more) to solving a linear functional equation relating the values of a function at two (or more) distinct points. This governing equation can be simply solved analytically by different means, such as iterations or power series expansions, as will be seen later.

In the literature, some special cases, involving lamellar materials under special loading, have been solved for the antiplane case by exploiting the "method of images," which is widely used in electrostatics. In this regard, it might be worthwhile emphasizing that our procedure differs from the classical "method of images" in many respects. We would like to mention the more notable ones.

First, the "method of images" associates with each source generating the deformation an image source, and therefore the sources, which produce the elastic field, as well as their locations, must be known in advance, while in our procedure we operate on the elastic field of the homogeneous body, thus obtaining universal equations, which are independent of the nature and locations of the sources.

Second, while the "method of images" generates a single representation of the solution, our procedure leads to several representations, and therefore to deeper insight into the problem. Indeed, if the governing linear functional equation is solved by iterations it yields, in a systematic and routine fashion, the same representation as the one obtained by the "method of images." However, for some cases this might not be the most effective representation.

Third, in the presence of many layers, the "method of images" becomes very cumbersome and therefore impractical, while in our procedure, we can relate the governing functional equation for the case when the boundaries consist of $n + 1$ circular cylinders to the governing equation for the case when the boundaries consist of n circular cylinders. This leads thus to an inductive scheme, which can be exploited very efficiently, as will be demonstrated in the sequel. The key step is to use a group structure on the set t of real numbers such that $-1 < t < 1$. Employing the group operation allows us to write down the solution *explicitly* as an infinite series in terms of the solution to a corresponding homogeneous problem.

Last, but not least, our procedure can be extended and applied to two and three-dimensional elastostatics, as well as to other field theories. However, as these topics will involve a much more complicated algebra, they will be deferred to forthcoming papers.

It was decided, in formulating the problem at hand, to employ the complex representation of antiplane elastostatics. This allows for lucidity and compactness in our formulation. The relevant notations are established at the beginning of Section 1. The remainder of that section is devoted to the treatment of the problem with cross-section consisting of a circular ring, whose inner boundary is perfectly bonded to a circular domain, and whose outer boundary is perfectly bonded to a matrix, of infinite extent, subjected to arbitrary loading. In Section 2, these results are extended to the case of many rings leading to the complete treatment of circularly cylindrical layered media. Then, in Section 3, the results for plane layered media are worked out. In Section 4, some further examples are presented and finally in Section 5, we draw some conclusions and indicate possible extensions and further applications of the results achieved.

1 A Simple Circularly Cylindrical Layered Medium

In this section, we consider the system, shown in Fig. 2, whose cross-section consists of a circular ring D_1, with outer and inner radii designated by a and a_1, respectively, and which is occupied by a material of shear modulus μ_1. Its inner boundary is perfectly bonded to a circular domain D_2 which is occupied by a material of shear modulus μ_2. Its outer boundary is perfectly bonded to a matrix D, of infinite extent, occupied by a material of shear modulus μ and subjected to arbitrary singularities. These latter generate out-of-plane displacement but are otherwise arbitrary.

We propose to express the solution to this problem in terms of the solution to the corresponding much simpler problem of a homogeneous material of shear modulus μ occupying the whole space and subjected to the same loading (singularities). Since it is most convenient, in treating these problems, to use the complex formulation of antiplane elastostatics, we briefly recall here the basic notions.

Under antiplane deformations, the displacement field satisfies

$$u_1 = u_2 \equiv 0, \quad u = u_3 = u_3(x_1, x_2), \tag{1}$$

i.e., the only nonvanishing component of displacement, with respect to a Cartesian coordinate system $Ox_1x_2x_3$, is $u = u_3$ which is a function of the coordinates x_1 and x_2 only.

As is well known, the displacement field u can be expressed, in the case of antiplane elastostatics, in terms of an analytic complex function ϕ of a complex variable $z = x_1 + ix_2$, namely

$$u = \frac{1}{\mu} \operatorname{Im}\{\phi(z)\}, \tag{2}$$

where μ is the shear modulus and Im stands for the imaginary part of the argument. Then the nonvanishing stress components, in Cartesian coordinates, are related to ϕ by

$$\sigma_{23} + i\sigma_{13} = \phi', \tag{3}$$

and, in polar coordinates, by

$$\sigma_{\theta 3} + i\sigma_{r3} = e^{i\theta}\phi', \tag{4}$$

where, throughout this paper, prime indicates differentiation with respect to the complex variable z.

Now, let the solution to the homogeneous problem be represented by the complex potential ϕ. We seek the solution to the heterogeneous problem in the form:

$$\text{in } D: \quad \Phi = \phi + \mathcal{K}_a(f) \tag{5}$$

$$\text{in } D_1: \quad \Phi_1 = \phi + \phi_1 + \mathcal{K}_{a_1}(f_1) \tag{6}$$

$$\text{in } D_2: \quad \Phi_2 = \phi + \phi_2 \tag{7}$$

The transformation $\mathcal{K}_a$ is the "hat" transformation defined by

Downloaded 03 May 2010 to 171.66.16.20. Redistribution subject to ASME license or copyright; see http://www.asme.org/terms/Terms_Use.cfm

$$\mathcal{K}_a(f)(z) = \overline{f\left(\frac{a^2}{\bar{z}}\right)}.$$

The functions ϕ_2 and f_1 are analytic in D_2, while ϕ_1 and f are analytic in the disk $r < a$. We wish to determine these functions in terms of ϕ. The idea of the solution procedure is the following:

First, we use the continuity of tractions and displacements across the interface $r = a$, to express ϕ_1 and f_1 in terms of f and ϕ.

Second, we use continuity of tractions across the interface $r = a_1$ to express ϕ_2 in terms of ϕ_1, f_1, and ϕ, and hence ϕ_2 in terms of f and ϕ.

Finally, having expressed ϕ_1, f_1, and ϕ_2 in terms of f and ϕ, the continuity of displacements across $r = a_1$ yields a governing equation for f. It turns out that this equation is a linear functional equation relating the values of f at two distinct points, namely z and $q_1 z$, where $q_1 = a_1^2/a^2$. This is easily solved analytically by considering, for example, a power series representation for f.

In the following the solution procedure outlined above will be implemented.

(*1*) *Continuity of tractions across* r = a. It follows from Eq. (4) that the σ_{3r} component of the stress tensor may be represented as

$$\sigma_{3r} = \mathrm{Im}(e^{i\theta}\phi'), \tag{8}$$

where ϕ is the complex potential for antiplane elastostatic problems.

On substituting the expressions for Φ and Φ_1 given by Eqs. (5) and (6) into (8), and using the fact that

$$(\mathcal{K}_a f)' = -\frac{a^2}{z^2}\mathcal{K}_a(f'), \tag{9}$$

and that along the interface $r = a$ we have

$$e^{i\theta} = z/a, \tag{10}$$

we can easily verify that the tractions will be continuous across $r = a$ provided the following relation holds:

$$\phi_1(z) + f_1(q_1 z) = f(z), \tag{11}$$

where, we recall that, $q_1 = a_1^2/a^2$.

(*2*) *Continuity of displacements across* r = a. The displacement field is expressed as

$$u = \frac{1}{\mu}\mathrm{Im}\{\Phi\}, \tag{12}$$

where μ is the shear modulus.

A substitution of Eqs. (5) and (6) into (12), yields readily the result that the displacement field will be continuous across the interface $r = a$ provided the following relation holds:

$$\phi_1(z) - f_1(q_1 z) = (m_1 - 1)\phi(z) - m_1 f(z), \tag{13}$$

where m_1 is defined by

$$m_1 = \frac{\mu_1}{\mu}. \tag{14}$$

We now add and subtract Eqs. (11) and (13), to obtain, for ϕ_1 and f_1 the following expressions, in terms of f and ϕ:

$$2\phi_1(z) = (m_1 - 1)(\phi(z) - f(z)), \tag{15}$$

and

$$2f_1(q_1 z) = (1 - m_1)\phi(z) + (1 + m_1)f(z). \tag{16}$$

(*3*) *Continuity of tractions across* r = a_1. On substituting the expressions of Φ_1 and Φ_2 given by Eqs. (6) and (7) into Eq. (8), it can be readily seen that the tractions will be continuous across the interface $r = a_1$, provided the following relation holds:

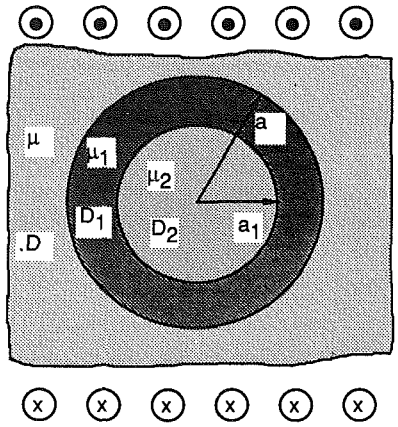


Fig. 3 A circularly cylindrical layered medium, subjected to remote uniform shear

$$\phi_2(z) = \phi_1(z) + f_1(z). \tag{17}$$

The substitution of Eqs. (15) and (16) into (17) provides the expression for ϕ_2, in terms of f and ϕ, as

$$2\phi_2(z) = (m_1 - 1)(\phi(z) - f(z)) + (1 - m_1)\phi(q_1^{-1}z) + (1 + m_1)f(q_1^{-1}z). \tag{18}$$

(*4*) *Governing equation for* f. All we need now is an expression for f, but this is determined by requiring that the displacements across $r = a_1$ be continuous. This gives

$$\phi_2(z) = (m_2 - 1)\phi(z) + m_2(\phi_1(z) - f_1(z)), \tag{19}$$

where $m_2 = \mu_2/\mu_1$.

We substitute ϕ_1, f_1, and ϕ_2 by their values and we use Eqs. (15), (16), and (18), into Eq. (19), to find that f must satisfy the following relation:

$$(m_1 + 1)(m_2 + 1)f(z) + (m_1 - 1)(m_2 - 1)f(q_1 z) = (m_1 - 1)(m_2 + 1)\phi(z) + (m_1 + 1)(m_2 - 1)\phi(q_1 z), \tag{20}$$

which can be written as

$$f(z) + \alpha_1\alpha_2 f(q_1 z) = \alpha_1\phi(z) + \alpha_2\phi(q_1 z), \tag{21}$$

where we have defined α_i by

$$\alpha_i = \frac{m_i - 1}{m_i + 1}, \quad i = 1, 2. \tag{22}$$

Equation (21) is a linear functional equation relating the values of f at two distinct points, namely z and $q_1 z$. Before we discuss its general solution and some of its ramifications, we would like to make some remarks and discuss a simple but important example.

Remarks.

(1) For a homogeneous material, we have $\alpha_1 = \alpha_2 = 0$, we find, from Eqs. (21), (15), (16), and (17), that $f = \phi_1 = f_1 = \phi_2 = 0$ and the solution is simply ϕ, as expected.

(2) For a single elastic inclusion with relative modulus α_1, we find, after putting $\alpha_2 = 0$ in Eq. (21)

$$f(z) = \alpha_1\phi(z), \tag{23}$$

and

$$\phi_1(z) = \alpha_1\phi(z), \tag{24}$$

which are well-known results.

1.1 Example.

Case of Uniform Remote Shear. Consider now the application of uniform remote shear τ (see Fig. 3). The complex potential ϕ, for the corresponding homogeneous problem, is given by $\phi = \tau z$, and it is readily seen that the solution of Eq. (21) is given by

Downloaded 03 May 2010 to 171.66.16.20. Redistribution subject to ASME license or copyright; see http://www.asme.org/terms/Terms_Use.cfm

$$f(z)=\frac{\alpha_1+\alpha_2 q_1}{1+\alpha_1\alpha_2 q_1}\,\tau z. \tag{25}$$

This means that, as far as the stress field in the matrix is concerned, the combination D_1, D_2 is equivalent to a single inclusion with relative modulus given by

$$\alpha=\frac{\alpha_1+\alpha_2 q_1}{1+\alpha_1\alpha_2 q_1}. \tag{26}$$

From Eqs. (15)–(17) and (25), we readily obtain the following expressions:

$$\phi_1(z)=\frac{(m_1-1)(1-\alpha)}{2}\,\tau z, \tag{27}$$

$$f_1(z)=\frac{\tau z}{2q_1}\,\{(1-m_1)+(1+m_1)\alpha\}, \tag{28}$$

and

$$\phi_2(z)=\frac{\tau z}{2}\left\{(m_1-1)(1-\alpha)+\frac{1}{q_1}\,[(1-m_1)+(1+m_1)\alpha]\right\}. \tag{29}$$

This leads to the solution in terms of the complex potentials as

$$\text{In } D:\quad \Phi(z)=\tau z+\alpha\tau a^2/z. \tag{30}$$

$$\text{In } D_1:\quad \Phi_1(z)=\tau z+\frac{(m_1-1)(1-\alpha)}{2}\,\tau z+\frac{\tau a^2}{2z}\,\{(1-m_1)+(1+m_1)\alpha\}. \tag{31}$$

$$\text{In } D_2:\quad \Phi_2(z)=\tau z+\frac{\tau z}{2}\left\{(m_1-1)(1-\alpha)+\frac{1}{q_1}\,[(1-m_1)+(1+m_1)\alpha]\right\}. \tag{32}$$

The interface stresses are calculated, in cylindrical coordinates, to be at $r = a$

$$\sigma^D_{\theta 3}=\tau(1-\alpha)\cos\theta, \tag{33}$$

$$\sigma^D_{r3}=\sigma^{D_1}_{r3}=\tau(1+\alpha)\sin\theta, \tag{34}$$

$$\sigma^{D_1}_{\theta 3}=m_1(1-\alpha)\tau\cos\theta, \tag{35}$$

and at $r = a_1$

$$\sigma^{D_1}_{\theta 3}=\tau\cos\theta\left\{1+\frac{(m_1-1)(1-\alpha)}{2}-\frac{1}{2q_1}\,[(1-m_1)+(1+m_1)\alpha]\right\}, \tag{36}$$

$$\sigma^{D_1}_{r3}=\sigma^{D_2}_{r3}=\tau\sin\theta\left\{1+\frac{(m_1-1)(1-\alpha)}{2}+\frac{1}{2q_1}\,[(1-m_1)+(1+m_1)\alpha]\right\}, \tag{37}$$

$$\sigma^{D_2}_{\theta 3}=\tau\cos\theta\left\{1+\frac{(m_1-1)(1-\alpha)}{2}+\frac{1}{2q_1}\,[(1-m_1)+(1+m_1)\alpha]\right\}. \tag{38}$$

It is remarkable to note that there are some combinations of D_1, D_2 which do not disturb the stress field in the matrix, for such combinations we must have

$$\alpha=0, \tag{39}$$

and therefore

$$\alpha_1=-\alpha_2 q_1. \tag{40}$$

Such inclusions do not interact with each other in the presence of a uniform shear stress.

Now consider the special case, where the region D_2 is a hole, and suppose we wish, as a design requirement, that the region around the cavity remains unperturbed.

We recall that the largest stress amplification factor at a point of the free edge of the cavity is 2.

Equation (40) implies, with $\alpha_2 = -1$, that $\alpha_1 = q_1 = a_1^2/a^2$. We can now choose the (stiffer) material μ_1 for a hollow cylindrical inclusion of thickness $a - a_1$, which will achieve the desired goal. However, this will occur at the expense of higher stress amplification in the cylinder. These amplification factors may be calculated to be m_1 $(= \mu_1/\mu)$ at $r = a$ and even $m_1 + 1$ at $r = a_1$. Other cases, depending on the design requirements, can be investigated as well.

1.2 Discussion of the General Solution of Eq. (21). It is readily seen, by considering power series expansions, that the general solution of Eq. (21) can be written as

$$f(z)=\sum_{k=0}^{+\infty}\frac{\alpha_1+\alpha_2 q_1^k}{1+\alpha_1\alpha_2 q_1^k}\,\frac{\phi^{(k)}(0)}{k!}\,z^k, \tag{41}$$

where $\phi^{(k)}$ designates the kth derivative of ϕ.

Note that

$$\left|\frac{\alpha_1+\alpha_2 q_1^n}{1+\alpha_1\alpha_2 q_1^n}\right|<1$$

and therefore the radius of convergence of the series given by Eq. (41) is at least as large as that of ϕ which has a convergent Taylor's series in the disk $|z| < a$.

Equation (41) implies that $\mathcal{JC}_a(f)$ will be asymptotic (up to a discarded constant), for large z, to

$$\mathcal{JC}_a(f)=\frac{\alpha_1+\alpha_2 q_1^k}{1+\alpha_1\alpha_2 q_1^k}\,\frac{\overline{\phi^{(k)}(0)}}{k!}\,\frac{a^{2k}}{z^k}+O(z^{-k-1}), \tag{42}$$

where k is the order of the first nonvanishing derivatives of ϕ at the origin.

We can deduce from Eq. (42) that the far stress field is given by

$$\sigma_{\theta x_3}+i\sigma_{rx_3}=-k\,\frac{\alpha_1+\alpha_2 q_1^k}{1+\alpha_1\alpha_2 q_1^k}\,\frac{\overline{\phi^{(k)}(0)}}{k!}\,\frac{a^{2k}}{z^{k+1}}+O(z^{-k-2}). \tag{43}$$

We see from Eq. (43) that the far stress field decays rapidly if k is large, and we conclude, from the coefficient of the dominant term, that the equivalent relative modulus will be given by

$$\alpha=\frac{\alpha_1+\alpha_2 q_1^k}{1+\alpha_1\alpha_2 q_1^k}, \tag{44}$$

which equals approximately α_1 if k is large and D_1 is not too thin.

Another representation of the solution of Eq. (21) can be achieved as follows:

Introduce an operator $\mathcal{Q}_1$ defined by

$$\mathcal{Q}_1(f)(z)=f(q_1 z). \tag{45}$$

Then Eq. (21) takes the form

$$(\mathcal{I}+\alpha_1\alpha_2\mathcal{Q}_1)f=(\alpha_1\mathcal{I}+\alpha_2\mathcal{Q}_1)\phi, \tag{46}$$

where $\mathcal{I}$ is the identity operator defined by $\mathcal{I}(f)(z) = f(z)$.

Equation (46) has the formal solution

$$f=(\mathcal{I}+\alpha_1\alpha_2\mathcal{Q}_1)^{-1}(\alpha_1\mathcal{I}+\alpha_2\mathcal{Q}_1)\phi. \tag{47}$$

This last result leads us to introduce the operator $\mathcal{R}_2$ defined by

$$\mathcal{R}_2=(\mathcal{I}+\alpha_1\alpha_2\mathcal{Q}_1)^{-1}(\alpha_1\mathcal{I}+\alpha_2\mathcal{Q}_1), \tag{48}$$

which we call the image operator associated with D_1, D_2, relative to D, for obvious reasons.

Noting that

$$(\mathcal{I}+\alpha_1\alpha_2\mathcal{Q}_1)^{-1}=\sum_{k=0}^{+\infty}(-\alpha_1\alpha_2\mathcal{Q}_1)^k, \tag{49}$$

Downloaded 03 May 2010 to 171.66.16.20. Redistribution subject to ASME license or copyright; see http://www.asme.org/terms/Terms_Use.cfm

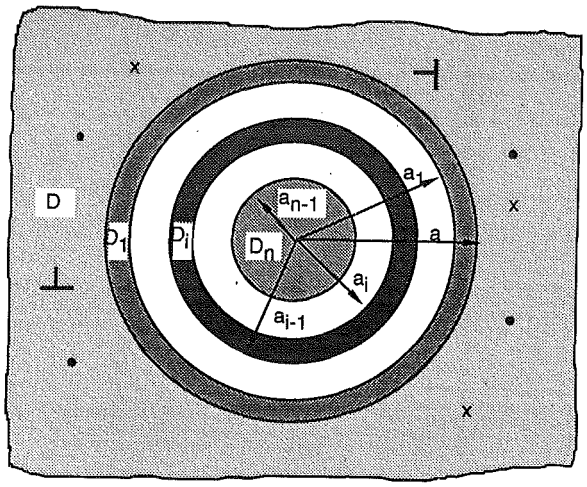


Fig. 4 A circularly cylindrical layered inclusion, consisting of *n* layers, inserted into a matrix subjected to arbitrary loading

we can write $\mathcal{R}_2$ as

$$\mathcal{R}_2=\alpha_1\mathcal{I}+\alpha_2(1-\alpha_1^2)\sum_{k=1}^{+\infty}(-\alpha_1\alpha_2)^{k-1}\mathcal{Q}_1^k, \tag{50}$$

and the solution $f(z)$ as

$$f(z)=\alpha_1\phi(z)+\alpha_2(1-\alpha_1^2)\sum_{k=1}^{+\infty}(-\alpha_1\alpha_2)^{k-1}\phi(q_1^k z). \tag{51}$$

The solution given by Eq. (51) offers an obvious geometric interpretation in terms of the method of images.

2 Case of an Arbitrary Number of Layers

In this section, we consider the system shown in Fig. 4 whose cross-section consists of $n-1$ concentric circular rings $D_1, \ldots, D_{n-1}$ perfectly bonded along their common boundaries. The innermost boundary is perfectly bonded to a circular domain D_n, while the outermost boundary, a circle of radius a, is perfectly bonded to a matrix D, of infinite extent, occupied by a material of shear modulus μ and subjected to arbitrary loading. The domain D_i is occupied by a material of shear modulus μ_i, $i=1, \ldots, n$, the outer radius of D_i is a_{i-1}, $i=1, \ldots, n$, while its inner radius is a_i, $i=1, \ldots, n-1$.

Let ϕ be the solution to the corresponding homogeneous problem. We seek the solution to the heterogeneous problem in the form

$$\text{in } D: \quad \Phi=\phi+\mathcal{H}_a(f), \tag{52}$$

$$\text{in } D_i: \quad \Phi_i=\phi+\phi_i+\mathcal{H}_{a_i}(f_i), \quad i=1, \ldots, n-1, \tag{53}$$

$$\text{in } D_n: \quad \Phi_n=\phi+\phi_n. \tag{54}$$

The functions ϕ_1 and f are analytic in the disk $r<a$, while ϕ_{i+1} and f_i are analytic in the disk $r<a_i$, for $i=1, \ldots, n-1$.

We define

$$m_1=\mu_1/\mu, \quad q_1=a_1^2/a^2,$$

and

$$m_i=\mu_i/\mu_{i-1}, \quad q_i=a_1^2/a_{i-1}^2, \quad i=2, \ldots, n,$$
$$\alpha_i=(m_i-1)(m_i+1)^{-1}, \quad i=1, \ldots, n.$$

Let $\mathcal{R}_n$ be the image operator associated with $D_1, \ldots, D_n$ relative to D, and $\mathcal{R}_{n-1}$ be the image operator associated with $D_2, \ldots, D_n$ relative to D_1. We wish to establish a relation between $\mathcal{R}_n$ and $\mathcal{R}_{n-1}$.

It follows from the definition that

$$f_1=\mathcal{R}_{n-1}(\phi+\phi_1). \tag{55}$$

On the other hand, we have

$$f=\mathcal{R}_n(\phi). \tag{56}$$

Using Eqs. (15) and (16) we obtain

$$\mathcal{Q}_1\mathcal{R}_{n-1}((m_1+1)\phi-(m_1-1)\mathcal{R}_n(\phi))=(1-m_1)\phi+(1+m_1)\mathcal{R}_n(\phi), \tag{57}$$

which yields

$$(m_1+1)\mathcal{R}_n(\phi)+(m_1-1)\mathcal{Q}_1\mathcal{R}_{n-1}\mathcal{R}_n(\phi)=(m_1-1)\phi+(m_1+1)\mathcal{Q}_1\mathcal{R}_{n-1}(\phi). \tag{58}$$

Hence

$$(\mathcal{I}+\alpha_1\mathcal{Q}_1\mathcal{R}_{n-1})\mathcal{R}_n=\alpha_1\mathcal{I}+\mathcal{Q}_1\mathcal{R}_{n-1}, \tag{59}$$

which implies

$$\mathcal{R}_n=(\mathcal{I}+\alpha_1\mathcal{Q}_1\mathcal{R}_{n-1})^{-1}(\alpha_1\mathcal{I}+\mathcal{Q}_1\mathcal{R}_{n-1}). \tag{60}$$

The last equation expresses the image operator of n domains in terms of that of $n-1$ domains.

We note that the operations in Eq. (60) are the same which are involved in evaluating the "equivalent relative modulus" (see Eq. (26)).

This last remark suggests the following rule for writing down the governing equation for f in the presence of an arbitrary number of layers.

Rule: *Calculate "the equivalent relative modulus" of* D_n, $D_{n-1}, \ldots, D_1$ *in this order*

$$((\ldots D_n * D_{n-1}) * D_{n-2} \ldots) * D_1)$$

where $D_i * D_{i-1}$ *indicates that we calculate the equivalent relative modulus of* D_i, D_{i-1} *relative to* D_{i-2}.

The final result can be written as

$$A(q_1, \ldots, q_{n-1})B^{-1}(q_1, \ldots, q_{n-1})$$

where A and B are polynomials in $q_1, \ldots, q_{n-1}$.

Then the governing equation for f is

$$B(\mathcal{Q}_1, \ldots, \mathcal{Q}_{n-1})f=A(\mathcal{Q}_1, \ldots, \mathcal{Q}_{n-1})\phi, \tag{61}$$

where $\mathcal{Q}_i$ $(i=1, \ldots, n-1)$ *designates the following operator*:

$$\mathcal{Q}_i(f)(z)=f(q_i z). \tag{62}$$

Finally, ϕ_i and f_i can be obtained by induction according to

$$2\phi_{i+1}=(m_{i+1}-1)\phi+(m_{i+1}+1)\phi_i+(1-m_{i+1})f_i, \tag{63}$$

and

$$2\mathcal{Q}_{i+1}f_{i+1}=(1-m_{i+1})\phi+(1-m_{i+1})\phi_i+(m_{i+1}+1)f_i. \tag{64}$$

These last relations have been obtained by enforcing the continuity of tractions and displacements across the boundary common to D_i and D_{i+1}.

The foregoing considerations prompt us to study in detail the operation $*$. To this end we consider the set $I=(-1, 1)$ of real numbers t such that $-1<t<1$. On this set, we define $x * y$ by

$$x*y=\frac{x+y}{1+xy}, \tag{65}$$

and note that the equivalent relative modulus of two inclusions can now be written as (see Eq. (26))

$$\alpha=\alpha_1*(\alpha_2 q_1). \tag{66}$$

The operation $*$ defines the structure of an Abelian group on the set I, i.e., $*$ has the same properties as the operation of addition $+$ on the set $\mathbf{R}$ of real numbers. In fact $(I, *)$ and $(\mathbf{R}, +)$ are isomorphic, that is there is a one-to-one correspondence between I and $\mathbf{R}$ which transforms $*$ into $+$. Indeed from the definition of $*$, we can readily obtain

$$\tanh^{-1}(x*y)=\tanh^{-1}(x)+\tanh^{-1}(y), \tag{67}$$

where tanh is the hyperbolic tangent function (see Abramowitz

Downloaded 03 May 2010 to 171.66.16.20. Redistribution subject to ASME license or copyright; see http://www.asme.org/terms/Terms_Use.cfm

and Stegun, 1965). In particular $*$ is associative and commutative. Moreover, it can be verified that the solution of (61) when $\phi = a_k z^k$ is given by

$$f = \alpha_1 * q_1^k(\alpha_2 * q_2^k(\alpha_3 * \ldots)\ldots)a_k z^k. \tag{68}$$

Hence, when $\phi = \Sigma_{k=0}^{+\infty} a_k z^k$, the solution of (61) is given by

$$f(z) = \sum_{k=0}^{+\infty} \alpha_1 * q_1^k(\alpha_2 * q_2^k(\alpha_3 * \ldots)\ldots)a_k z^k, \tag{69}$$

which can also be written as

$$f(z) = \sum_{k=0}^{+\infty} \tanh(\tanh^{-1}(\alpha_1) + \tanh^{-1}(q_1^k(\tanh(\tanh^{-1}(\alpha_2) + \tanh^{-1}(q_2^k(\ldots)\ldots). \tag{70}$$

Note that the series given by Eq. (69) is convergent for it has the convergent power series $\Sigma_{k=0}^{\infty} a_k z^k$ as majorant since $|\alpha_1 * q_1^k(\alpha_2 * q_1^k(\alpha_3 * \ldots)\ldots| < 1$.

Equations (69) or (70) provide an explicit solution of the heterogeneous problem, with an arbitrary number of layers, in terms of that of the homogeneous one.

2.1 Example.

The case when n = 3. In this case, the equivalent relative modulus of D_3, D_2 relative to D_1 is given by

$$\tilde{\alpha}_2 = \frac{\alpha_2 + \alpha_3 q_2}{1 + \alpha_2 \alpha_3 q_2}. \tag{71}$$

The equivalent relative modulus of D_3, D_2, D_1 according to the order indicated in the rule is

$$\tilde{\alpha}_1 = \frac{\alpha_1 + \tilde{\alpha}_2 q_1}{1 + \alpha_1 \tilde{\alpha}_2 q_1} = \frac{\alpha_1 + \alpha_2 q_1 + \alpha_1 \alpha_2 \alpha_3 q_2 + \alpha_3 q_1 q_2}{1 + \alpha_1 \alpha_2 q_1 + \alpha_2 \alpha_3 q_2 + \alpha_1 \alpha_3 q_1 q_2}. \tag{72}$$

Therefore

$$A = \alpha_1 + \alpha_2 q_1 + \alpha_1 \alpha_2 \alpha_3 q_2 + \alpha_3 q_1 q_2 \tag{73}$$

and

$$B = 1 + \alpha_1 \alpha_2 q_1 + \alpha_2 \alpha_3 q_2 + \alpha_1 \alpha_3 q_1 q_2. \tag{74}$$

Hence the governing equation for f is

$$f + \alpha_1 \alpha_2 f(q_1 z) + \alpha_2 \alpha_3 f(q_2 z) + \alpha_1 \alpha_3 f(q_1 q_2 z) = \alpha_1 \phi + \alpha_2 \phi(q_1 z) + \alpha_1 \alpha_2 \alpha_3 \phi(q_2 z) + \alpha_3 \phi(q_1 q_2 z). \tag{75}$$

The solution to this equation is

$$f(z) = \sum_{k=0}^{+\infty} \alpha_1 * q_1^k(\alpha_2 * q_2^k \alpha_3) a_k z^k, \tag{76}$$

where $\phi = \Sigma_{k=0}^{+\infty} a_k z^k$.

3 Plane Layered Media

As mentioned previously, the case of straight boundaries can be treated as a limiting case. For example, one can solve for circular boundaries and by fixing parallel tangents to the circles let the center tend to infinity. This limiting procedure should, however, be performed on the governing equation since the solution is not uniformly convergent. An alternative way is to follow the same lines of arguments used for the circular boundaries and then arrive at the governing equation. Consider the system shown in Fig. 5 where now D occupies the left half-plane and D_i ($i = 1, \ldots, n-1$) is an infinite strip of thickness t_i. In this instance, all the previous calculations remain valid provided we replace the operators $\mathfrak{Q}_i$ ($i = 1, \ldots, n-1$) by the operators $\mathfrak{I}_i$ defined by

$$\mathfrak{I}_i(f)(z) = f(z - 2t_i). \tag{77}$$

Then the governing equation for f is obtained by replacing, in Eq. (61), $\mathfrak{Q}_i$ by $\mathfrak{I}_i$.

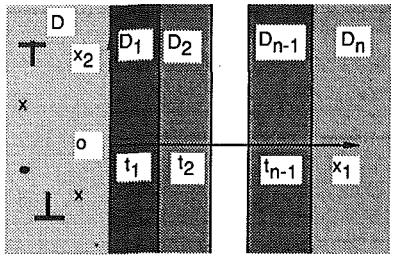


Fig. 5 A plane layered medium subjected to arbitrary matrix singularities or loading

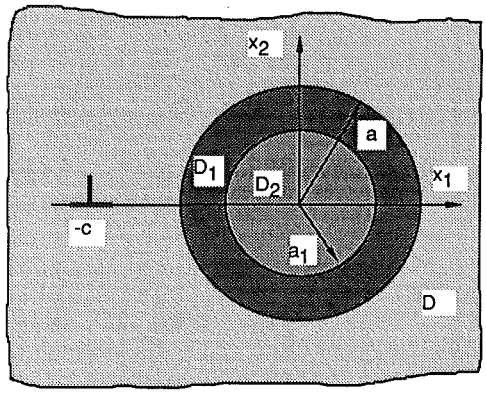


Fig. 6 A circularly cylindrical layered medium subjected to a point force or screw dislocation at the point (− c, 0)

For example, the governing equation for f when $n = 2$ is

$$f(z) + \alpha_1 \alpha_2 f(z - 2t_1) = \alpha_1 \phi(z) + \alpha_2 \phi(z - 2t_1), \tag{78}$$

which is a linear functional equation of the finite difference type governing f.

There are several methods available to solve Eq. (78). For example, the solution to this equation can be written down following the arguments leading to (51) as

$$f(z) = \alpha_1 \phi(z) + \alpha_2(1 - \alpha_1^2) \sum_{n=1}^{+\infty} (-\alpha_1 \alpha_2)^{n-1} \phi(z - 2nt_1), \tag{79}$$

which converges uniformly on compact sets since ϕ is bounded and $|\alpha_1 \alpha_2| < 1$.

4 Example

In this section, we consider the example of a point force or a screw dislocation interacting with circular cylindrical inclusions.

We consider the case $n = 2$ and a point force or a screw dislocation located at the point $-c$ of the x_1-axis where $c > a$ (see Fig. 6).

The complex potential of the homogeneous problem is given by

$$\phi = b \ln(z + c) \tag{80}$$

where b is a purely imaginary constant for a point force and a real constant for a screw dislocation. In the domain $r < a$, ϕ has the expansion

$$\phi = b \sum_{k=1}^{\infty} (-1)^{k-1} \frac{z^k}{kc^k}. \tag{81}$$

Thus

$$f = b \sum_{k=1}^{\infty} (-1)^{k-1} \frac{\alpha_1 + \alpha_2 q_1^k}{1 + \alpha_1 \alpha_2 q_1^k} \frac{z^k}{kc^k}. \tag{82}$$

Downloaded 03 May 2010 to 171.66.16.20. Redistribution subject to ASME license or copyright; see http://www.asme.org/terms/Terms_Use.cfm

And we obtain, for the material forces expressed by the J_1, J_2 integrals (see, for example, Budiansky and Rice, 1973) around the point force or screw dislocation, the following expression:

$$J_1 - iJ_2 = -\frac{\pi}{\mu} |b|^2 \sum_{k=0}^{\infty} \frac{\alpha_1 + \alpha_2 q_1^k}{1 + \alpha_1 \alpha_2 q_1^k} \left(\frac{a}{c}\right)^{2k}. \quad (83)$$

The solution for n layers is given by

$$f = b \sum_{k=1}^{\infty} (-1)^{k-1} \alpha_1 * q_1^k (\alpha_2 * q_2^k (\alpha_3 * \ldots) \ldots) \frac{z^k}{k c^k}, \quad (84)$$

and the expression for the J_1, J_2 integrals is

$$J_1 - iJ_2 = -\frac{\pi}{\mu} |b|^2 \sum_{k=0}^{\infty} \alpha_1 * q_1^k (\alpha_2 * q_2^k (\alpha_3 \ldots) \ldots) \left(\frac{a}{c}\right)^{2k}. \quad (85)$$

This result yields the material force (or the Peach-Koehler force, in the case of a screw dislocation) acting on the point singularity.

The series given by Eq. (85) is convergent for it has a convergent geometric series as a majorant since $|\alpha_1 * q_1^k(\alpha_2 * q_2^k(\alpha_3 * \ldots)\ldots)| < 1$.

5 Conclusions

In this paper, novel methods were introduced to derive an analytical solution, in antiplane elastostatics, for circularly cylindrical or plane layered media, formed by an arbitrary number of layers and subjected to arbitrary loading.

The formulation introduced leads to a governing functional equation relating the values of a function at two or more distinct points. An inductive scheme was used to obtain a relation between the governing equation for n layers to that of $n - 1$ layers. This relation is closely connected with a group structure on the set t of real numbers such that $-1 < t < 1$. We exploited this connection to arrive at an *explicit* solution (as an infinite series) of the problem. Similar results could be achieved for the case of plane elastostatics. These, however, will be presented separately in a forthcoming paper.

Acknowledgments

This work was performed with the support of the U.S. Department of Energy and the National Science Foundation. This support is gratefully acknowledged.

References

Abramowitz, M., and Stegun, I., Eds., 1965, *Handbook of Mathematical Functions*, Dover, New York.

Budiansky, B., and Rice, J. R., 1973, "Conservation Laws and Energy Release Rates," ASME JOURNAL OF APPLIED MECHANICS, Vol. 40, pp. 201–203.

Honein, E., Honein, T., and Herrmann, G., 1992a, "On Two Circular Inclusions in Harmonic Problems," *Quarterly of Applied Mathematics*, Vol. L, No. 3, Sept. 1992, pp. 479–499.

Honein, E., Honein, T., and Herrmann, G., 1992b, "Further Aspects of the Elastic Field of Two Circular Inclusions in Antiplane Elastostatics," ASME JOURNAL OF APPLIED MECHANICS, Vol. 59, pp. 774–779.

Honein, T., and Herrmann, G., 1988, "The Involution Correspondence in Plane Elastostatics for Regions Bounded by a Circle," ASME JOURNAL OF APPLIED MECHANICS, Vol. 55, pp. 566–573.

Honein, T., and Herrmann, G., 1990a, "A Circular Inclusion with Slipping Interface in Plane Elastostatics," *Micromechanics and Inhomogeneity*, G. J. Weng et al., eds., Springer-Verlag, New York, pp. 127–136.

Honein, T., and Herrmann, G., 1990b, "On Bonded Inclusions with Circular or Straight Boundaries in Plane Elastostatics," ASME JOURNAL OF APPLIED MECHANICS, Vol. 57, pp. 850–136.

Downloaded 03 May 2010 to 171.66.16.20. Redistribution subject to ASME license or copyright; see http://www.asme.org/terms/Terms_Use.cfm

Two-Dimensional Contact on an Anisotropic Elastic Half-Space

Hui Fan[1]

L. M. Keer
Fellow ASME

Department of Mechanical Engineering,
Northwestern University,
Evanston, IL 60208

The two-dimensional contact problem for a semi-infinite anisotropic elastic media is reconsidered here by using the formalism of Eshelby et al. (1953) and Stroh (1958). The approach of analytic function continuation is employed to investigate the half-space contact problem with various mixed boundary conditions applied to the half-space. A key point of the solution procedure suggested in the present paper is its dependence on a general eigenvalue problem involving a Hermitian matrix. This eigenvalue problem is analogous to the one encountered when investigating the behavior of an interface crack (Ting, 1986). As an application, the interaction between a dislocation and a contact strip is solved. The compactness of the results shows their potential for utilization to solve the problem of contact of a damaged anisotropic half-space.

1 Introduction

The most well-known systematic study in the area of two-dimensional anisotropic elasticity is the formulation due to Lekhnitskii (1961), which also summarized the accumulated Russian literature from 1930–1950. Lekhnistkii's formulation can be considered as an extension of the stress function approach used in isotropic elasticity, and many anisotropic elasticity problems corresponding to the solution given by Muskhelishvili (1953) have been documented there. Eshelby et al. (1953) independently developed their own formulation using displacement functions. Their scheme, further modified by Stroh (1958), derived elegant representations which have been proven to be simpler for dislocation and wave propagation problems in an anisotropic medium (Hirth and Lothe, 1979).

Recently, the broad applications of composite materials in industrial and other application have developed new interest into the research of anisotropic elasticity. Investigations of interfacial crack behavior have been the subject of several recent anisotropic elastic studies. Most papers follow the Stroh formulation, e.g., Ting (1986), Qu and Bassani (1989), Suo (1990), and Gao et al. (1992). Although the general solution for anisotropic media is expressed by three complex variables (see Section 2), Ting (1986), and Qu and Bassani (1989) retain real functions in their matrix formulation. Suo (1990) studied interfacial crack behavior using the analytic function continuation approach, and some results reported in Qu and Bassani (1989) were presented by Suo in a simpler manner. There is no doubt that the analytic function continuation approach is a simpler procedure. There is no doubt that the analytic function continuation approach is simpler for some configurations, such as the half-space and joined half-spaces of dissimilar anisotropic materials.

The present paper considers two-dimensional contact on an anisotropic elastic half-space by the analytic function continuation approach. Some results for an anisotropic half-space contact are available in the literature. Using the Radon transform, Willis (1966) studied the three-dimensional Hertz contact on an anisotropic half-space. A solution of the two-dimensional contact problem has been given in Green and Zerna (1954). Almost all the subsequent papers involving two-dimensional contact have followed Green and Zerna. Recently Klintworth and Strong (1990) provided a numerical result for the indentation of a rigid punch on an anisotropic half-space. However, these formulations appear complicated because the notation used is an extension of that used for isotropic elasticity and is not suitable for general anisotropic materials. In addition, the Green and Zerna (1954) approach was a solution for in-plane deformation, which will be the general case of two-dimensional anisotropic elasticity due to coupling between the in-plane and antiplane deformations. The notation of Eshelby et al. (1953) is used here to reconsider the two-dimensional contact problem of an anisotropic half-space. In addition, the analytic function continuation approach has been found to be the most appropriate for considering the anisotropic half-space. Suo (1990) and Gao et al. (1992) showed that this approach is powerful and compact when applied to the interface crack problem. The contact problem, as a related mixed boundary value problem, can be treated in a similar manner used for the interface crack. The results in Section 3 show how various boundary conditions can be treated in a simple and elegant form. A detailed derivation is given to the case where all displacement components are prescribed, and the coupled Hilbert problems, which have been encountered in investigations of interfacial cracks (Ting, 1986; and Suo, 1990), are decoupled

[1]Current address: School of Mechanical and Production Engineering, Nanyang Technological University, Singapore 2263.

Contributed by the Applied Mechanics Division of THE AMERICAN SOCIETY OF MECHANICAL ENGINEERS for publication in the ASME JOURNAL OF APPLIED MECHANICS.

Discussion on this paper should be addressed to the Technical Editor, Professor Lewis T. Wheeler, Department of Mechanical Engineering, University of Houston, Houston, TX 77204-4792, and will be accepted until four months after final publication of the paper itself in the ASME JOURNAL OF APPLIED MECHANICS.

Manuscript received by the ASME Applied Mechanics Division, June 1, 1992; final revision, Mar. 8, 1993. Associate Technical Editor: D. B. Bogy.

Copyright © 1994 by ASME
Downloaded 03 May 2010 to 171.66.16.20. Redistribution subject to ASME license or copyright; see http://www.asme.org/terms/Terms_Use.cfm

by consideration of a general eigenvalue problem. As an example of the approach, the Green's function for the interaction between a dislocation in a half-space with a surface strip having prescribed displacements is given in closed form in Section 4.

Although anisotropic two-dimensional contact problems have been considered as a soluble problem for many years, the results in the literature are not in general comprehensive. It is the recent progress in anisotropic two-dimensional elasticity via the Stroh formalism that makes the analysis of the coupled in-plane and antiplane contact problem possible. It should be pointed out that the present research is motivated by the study of a cracked anisotropic half-plane under contact fatigue. The compact solution obtained in the present paper can be used as a kernel in the integral equations for the damaged half-space under contact (Bryant et al., 1984; Bower, 1989).

2 Stroh Formalism for Anisotropic Elasticity

First, the formulation of Eshelby for linear anisotropic elasticity is developed. The displacements are given as u_i and the relation between strain ϵ_{ij} and displacement is

$$\epsilon_{ij}=\frac{1}{2}(u_{i,j}+u_{j,i}). \tag{1}$$

Hooke's law, relating the stress σ_{ij} and the strain is

$$\sigma_{ij}=C_{ijkl}\epsilon_{kl} \text{ or } \epsilon_{ij}=S_{ijkl}\sigma_{kl} \tag{2}$$

where C_{ijkl} are the stiffnesses and S_{ijkl} the compliances. Substituting (2*a*) into (1) and applying the equilibrium equation

$$\sigma_{ij,j}=0, \tag{3}$$

the equation of equilibrium is

$$C_{ijkl}u_{k,lj}=0. \tag{4}$$

Assume that

$$u_k=a_k f(x+py), \tag{5}$$

and substitute (5) into (4), which leads to the next equations

$$(C_{i1k1}+p(C_{i1k2}+C_{i2k1})+p^2C_{i2k2})\ a_k=0. \tag{6}$$

The requirement of a nonzero solution for a_k leads to the following eigenvalue equation:

$$\det(C_{i1k1}+p(C_{i1k2}+C_{i2k1})+p^2C_{i2k2})=0. \tag{7}$$

It has been proved by Lenkniskii and Eshelby et al., utilizing the positive definite character of the strain energy density, that all roots of (7) cannot be real. One may take

$$p_i=\overline{p}_{i+3} \quad (i=1, 2, 3) \tag{8}$$

with

$$\text{Im}(p_i)>0.$$

It is seen that the solution (5) can be expressed in terms of complex functions. In the sequel the following terminology involving complex function theory will be used, where the equations for anisotropic elasticity can be considered as an extension of the already well established complex variable theory for isotropic elasticity. The variables z and its complex conjugate $\overline{z}$ are defined as follows:

$$z=x+py=x+\alpha y+i\beta y=X+iY$$
$$\overline{z}=x+\overline{p}y=x+\alpha y-i\beta y=X-iY \tag{9}$$

where

$$p=\alpha+i\beta \quad \text{and} \quad X=x+\alpha y,\ Y=\beta y. \tag{10}$$

A generalized complex function in Eq. (5) may be written in the form

$$f(z)=f(X+pY)=u(X, Y)+iv(X, Y). \tag{11}$$

The function $f(z)$ is analytic when it has continuous first-order partial derivatives and the Cauchy-Reimann conditions are satisified, i.e.,

$$u_{1,Y}=-u_{2,X} \quad u_{1,X}=u_{2,Y}$$

which corresponds to $df(z)/d\overline{z}=0$. In addition, if a function $f(z)$ is analytic in the upper half-plane (S_1), then the function $f(\overline{z})$ in also analytical in the lower half-plane (S_2).

The following results (see, for instance, Stroh, 1958), which allow the analysis to be abbreviated, are introduced next:

$$u_i=2\text{Re}\left[\sum_{j=1}^{3}A_{ij}f_j(z_j)\right],$$
$$\sigma_{2i}=2\text{Re}\left[\sum_{j=1}^{3}L_{ij}f_j'(z_j)\right],\ \sigma_{1i}=-2\text{Re}\left[\sum_{j=1}^{3}L_{ij}\mu_j f_j'(z_j)\right] \tag{12}$$

where

$$z_j=x+p_jy \qquad \mathbf{A}=(\mathbf{a}_1, \mathbf{a}_2, \mathbf{a}_3)$$

and

$$L_{ij}\sum_{k=1}^{3}(C_{i2kl}+p_j C_{i2k2})\ A_{kj}.$$

Each of the **a**'s is determined by the eigenvalue problem (Eqs. (6) and (7)) to within a complex valued normalization constant.

When the roots p_j are distinct, Stroh (1958) proved that the matrices **A** and **L** are nonsingular. By consideration of the properties possessed by two of these matrices, another matrix can be defined as

$$\mathbf{B}=i\mathbf{A}\mathbf{L}^{-1}. \tag{13}$$

The utilization of the expressions of **A** and **L** allowed Stroh (1958) to prove that **B** is a Hermitian matrix, i.e.,

$$\overline{\mathbf{B}}^{\,T}=\mathbf{B}$$

where the superscript "T" stands for the transpose of the matrix.

In addition, Stroh calculated the energy of a dislocation in an anisotropic medium, which leads to the conclusion that $\mathbf{B}+\overline{\mathbf{B}}$ is a positive definite symmetric matrix, provided that the strain energy is positive definite. Due to its importance in all types of anisotropic elasticity problems, the matrix **B** has been studied in detail. After it was introduced by Ingebrigtsen and Tonning (1969), Barnett and Lothe (1985) and their coworkers made an extensive study of the dynamic version of this matrix. The provided properties of this matrix will be used without any further discussion of its history.

Expression (12) may break down if the roots of Eq. (7) are degenerate. A well-known example is for an isotropic material, where $i=\sqrt{-1}$ is a triple root. A more systematical consideration on the degenerate cases for the roots has been given by Ting and Hwu (1987). They classified the degenerate cases as semi-simple and non-semi-simple. In the former case, **A** and **L** are still nonsingular, while in the latter case both **A** and **L** become singular. Readers are referred to their paper for a detailed discussion on this matter.

In order to avoid confusion the summation convention will not be used in the sequel. Instead, matrix and vector expressions will be denoted by bold letters. For example, a vector function is defined as

$$\mathbf{f}(z)=\{f_1(z), f_2(z), f_3(z)\}^T$$

where the argument has the generic form $z=x+py$. Once the solution of $\mathbf{f}(z)$ is obtained for a boundary value problem, a replacement of z_1, z_2 and z_3 should be made for each component function to calculate the displacement and stress from Eq. (12). This observation, which was pointed out by Suo (1990), makes the analytic function continuation possible.

3 Rigid Indenter on an Anisotropic Elastic Half-Space

Solutions to this problem have been documented in Green

Downloaded 03 May 2010 to 171.66.16.20. Redistribution subject to ASME license or copyright; see http://www.asme.org/terms/Terms_Use.cfm

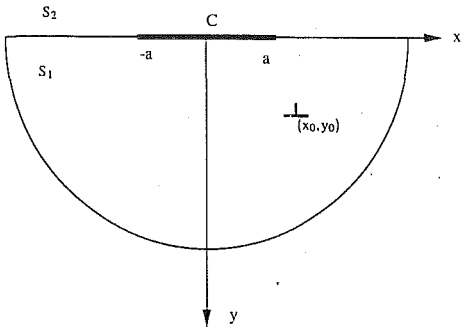


Fig. 1 An anisotropic half-space

and Zerna (1954), Klintworth and Strong (1990), and others. In addition to a derivation that is cumbersome, their formulation cannot solve problems that involve coupled in-plane and antiplane deformation. By reconsidering this problem from the point of view of the Eshelby approach, the genuine simplicity inherent in the problem becomes evident. Instead of a term-by-term expansion of all the stress and displacement components, the present formulation involves only the three important matrices, **A**, **L**, and **B**.

In the present section four types of boundary conditions prescribed on the strip C (Fig. 1) are considered; the remainder of the x-axis is considered free of tractions.

Case (1). All stress components are prescribed on C.

Case (2). All the displacements are prescribe on C, which corresponds to a nonslip high friction case or adhesion.

Case (3). Some of the stresses and displacements are prescribed on C.

Case (4). The values, $u_{2,1}$ and $t_1(x)=\mu t_2(x)$ are prescribed on C, since the coefficient of friction is not sufficiently large to prohibit slip as in Case (2).

Case (1). From Eq. (12), the traction on $y=0$ is given as

$$\mathbf{L}\mathbf{f}'(x)+\overline{\mathbf{L}\mathbf{f}'(x)}=\mathbf{t}(x) \quad x\epsilon(-\infty,\infty) \tag{15}$$

where $\mathbf{t}(x)$ is a known function along the x-axis. Introduce a function $\mathbf{h}(z)$ as follows:

$$\mathbf{h}(z)=\mathbf{L}\mathbf{f}'(z) \quad \text{for } z \text{ in } S_1 \tag{16a}$$

$$\mathbf{h}(z)=-\overline{\mathbf{L}\mathbf{f}'(\bar{z})} \quad \text{for } z \text{ in } S_2 \tag{16b}$$

Equation (15) can be written in terms of $\mathbf{h}(z)$ as

$$\mathbf{h}^+(x)-\mathbf{h}^-(x)=\mathbf{t}(x). \tag{17}$$

The solution of (17) can be easily found as

$$\mathbf{h}(z)=\frac{1}{2\pi i}\int_{-a}^{a}\frac{\mathbf{t}(x)}{x-z}\,dx. \tag{18}$$

Case (2). This case is not as straightforward as the previous one. The mixed boundary conditions, here displacements are prescribed in segment C and the remainder of the surface is traction free, can be written as

$$\mathbf{A}\mathbf{f}(x)+\overline{\mathbf{A}\mathbf{f}(x)}=\mathbf{d}(x) \quad \text{for } x\epsilon C \tag{19a}$$

$$\mathbf{L}\mathbf{f}'(x)+\overline{\mathbf{L}\mathbf{f}(x)}=0 \quad \text{for } x\notin C. \tag{19b}$$

With the definitions of Eq. (16), Eq. (19*b*) is converted to

$$\mathbf{h}^+(x)-\mathbf{h}^-(x)=0 \quad \text{for } x\notin C. \tag{20}$$

Equation (19*a*) is rewritten by use of definitions (13) and (16) as

$$\mathbf{h}^+(x)+\mathbf{B}^{-1}\overline{\mathbf{B}\mathbf{h}}^-(x)=i\mathbf{B}^{-1}\mathbf{d}'(x) \quad \text{for } x\epsilon C. \tag{21}$$

When the **B** matrix is real, the solution of the Hilbert problem, Eq. (21), can be obtained as

$$\mathbf{h}(z)=\frac{\chi(z)}{2\pi}\int_{-a}^{a}\frac{(\mathbf{B}^{-1}\mathbf{d}'(x))}{\chi^+(x)(x-z)}\,dx+\chi(z)\;Q(z) \tag{22}$$

where

$$\chi(z)=(z^2-a^2)^{-1/2} \tag{23}$$

and $Q(z)$ is a polynomial with an appropriate singularity at infinity determined from consideration of the resultant force in C. It is assumed that the stress vanishes as $O(1/z)$ as $z\to\infty$. Thus,

$$Q_i(z)=Q_{0_j},$$

since $\chi(z)\to 1/z$ as $z\to\infty$.

In general **B** is a complex matrix, and a special procedure to transform the matrix $\mathbf{B}^{-1}\overline{\mathbf{B}}$ in Eq. (21) into a diagonal matrix is required to uncouple the three equations. Consider the following eigenvalue problem:

$$\overline{\mathbf{B}}\mathbf{p}=\lambda\mathbf{B}\mathbf{p} \tag{24}$$

By taking the complex conjugate of (24), we have

$$\overline{\mathbf{B}}\overline{\mathbf{p}}=\mathbf{B}\overline{\mathbf{p}}/\overline{\lambda}. \tag{25}$$

Equations (24) and (25) show that if λ is an eigenvalue of the problem, then $1/\overline{\lambda}$ is also an eigenvalue. Since the matrix **B** is 3×3, there are three distinct eigenvalues, λ, $1/\overline{\lambda}$, and 1 (-1 is neglected as will be discussed later), which leads to the result that the eigenvalue problem (24) has a complete eigenvector set. Furthermore, it can be concluded that the $\mathbf{B}^{-1}\overline{\mathbf{B}}$ matrix can be diagonalized. A similar eigenvalue problem was first discussed by Ting (1986) to study an interfacial crack.

Recall that **B** is Hermitian and $\mathbf{B}+\overline{\mathbf{B}}$ is a positive definite matrix. One may write

$$\mathbf{B}=\mathbf{D}+i\mathbf{W} \tag{26}$$

where

$$\mathbf{D}=\mathbf{D}^T \text{ and } \mathbf{W}=-\mathbf{W}^T \tag{27}$$

are all real matrices.

By substituting Eq. (26) into Eq. (24) and utilizing the conditions of Eq. (27), the eigenvalues of the problem can be determined from

$$\det(\overline{\mathbf{B}}-\lambda\mathbf{B})=0 \tag{28a}$$

or

$$\det(\mathbf{W}+i\delta\mathbf{D})=0 \tag{28b}$$

where

$$\delta=\frac{1-\lambda}{1+\lambda} \text{ or } \lambda=\frac{1-\delta}{1+\delta}$$

with $\lambda\neq -1$. The case that $\lambda=-1$ leads to the conclusion from Eq. (28*a*) that $\det(\mathbf{D})=0$, which is not consistent with the positive definiteness of the matrix.

The eigenvalues of Eq. (28*b*) have been obtained by Ting (1986) as

$$\delta_{1,2}=\pm\left(-\frac{1}{2}\,\mathrm{tr}(\mathbf{D}^{-1}\mathbf{W})^2\right)^{1/2} \text{ and } \delta_3=0 \tag{29}$$

Ting has shown that all the roots are real (Ting, 1986, Appendix). There is no direct proof that all λ positive, although some hints provided by the studies of interfacial cracks (Ting, 1986 and Suo, 1990) show that λ should be positive. The present derivation will take all λ to be positive.

With a complete set of eigenvalues, there are three independent eigenvectors that form the matrix

$$\mathbf{P}=(\mathbf{p}_1,\ \overline{\mathbf{p}_1},\ \mathbf{p}_3)$$

which correspond, respectively, to λ, $1/\lambda$, and 1. This matrix diagonalizes $\mathbf{B}^{-1}\overline{\mathbf{B}}$ as

$$\mathbf{B}^{-1}\overline{\mathbf{B}}=\mathbf{P}\Lambda\mathbf{P}^{-1} \tag{30}$$

where

$$\Lambda=\mathrm{diag}\left(\lambda,\frac{1}{\lambda},1\right). \tag{31}$$

Downloaded 03 May 2010 to 171.66.16.20. Redistribution subject to ASME license or copyright; see http://www.asme.org/terms/Terms_Use.cfm

Finally, Eq. (21) is decoupled as

$$\mathbf{P}^{-1}\mathbf{h}^{+}(x)+\mathbf{\Lambda}\mathbf{P}^{-1}\mathbf{h}^{-}(x)=i\mathbf{P}^{-1}\mathbf{B}^{-1}\mathbf{d}'(x). \tag{32}$$

By introducing

$$\hat{\mathbf{h}}(z)=\mathbf{P}^{-1}\mathbf{h}(z) \quad \hat{\mathbf{d}}'(\mathbf{x})=\mathbf{P}^{-1}\mathbf{B}^{-1}\mathbf{d}'(x),$$

a solution of (32) can be written as

$$\hat{h}_1(z)=\frac{\chi_1(z)}{2\pi}\int_{-a}^{a}\frac{\hat{d}_1'(x)\,dx}{\chi_1^{+}(x)(x-z)}+\chi_1(z)\,Q_1(z)$$

$$\hat{h}_2(z)=\frac{\chi_2(z)}{2\pi}\int_{-a}^{a}\frac{\hat{d}_2'(x)\,dx}{\chi_2^{+}(x)(x-z)}+\chi_2(z)\,Q_2(z)$$

$$\hat{h}_3(z)=\frac{\chi_3(z)}{2\pi}\int_{-a}^{a}\frac{\hat{d}_3'(x)\,dx}{\chi_3^{+}(x)(x-z)}+\chi_3(z)\,Q_3(z) \tag{33}$$

where

$$\chi_1(z)=(z^2-a^2)^{-1/2}\left(\frac{z-a}{z+a}\right)^{i\epsilon}$$

$$\chi_2(z)=(z^2-a^2)^{-1/2}\left(\frac{z+a}{z-a}\right)^{i\epsilon}$$

$$\chi_3(z)=\chi(z)=(z^2-a)^{-1/2} \tag{34}$$

and

$$\epsilon=\frac{\ln\lambda}{2\pi}$$

which is called oscillation index in the interface crack papers. It is well known that displacement at the edge of the indenter will also show oscillation if the index is nonzero. Since this oscillatory zone is very small compared to the entire contact region, the solutions given by Eq. (33) and (34) still hold. Treatment and models to account for this oscillation have been used in the research of the interface crack and will not be pursued further.

From Eq. (32), it is clear that $\lambda=1$ is the triple root corresponding to $\mathbf{B}=\overline{\mathbf{B}}$ as was deduced at the beginning of the discussion of Case (2).

Cases (3) and (4). For these cases some of the stress components are prescribed while the remaining component(s) are the prescribed displacement(s). The analytic function continuation approach may not be the simplest way to solve the problem because some new matrices are introduced into the formulation that allow stress and displacements to appear together. These matrices may not be of a proper form to allow the analytic continuations as in the previous discussions. The authors suggest that the singular integral equation approach may be a better alternative for these cases.

From Eq. (17) and (21), the displacement and traction in the contact area can be expressed

$$\mathbf{h}^{+}(x)-\mathbf{h}^{-}(x)=\mathbf{t}(x) \tag{17}$$

$$\mathbf{B}\mathbf{h}^{+}(x)+\overline{\mathbf{B}}\mathbf{h}^{-}(x)=i\mathbf{d}'(x). \tag{21}$$

Eliminating $\mathbf{h}^{-}(x)$ from above two equations, it follows that

$$(\mathbf{B}+\mathbf{B})\mathbf{h}^{+}(x)-\overline{\mathbf{B}}\mathbf{t}(x)=i\mathbf{d}'(x) \tag{35}$$

Furthermore, the Plemelj formulae give

$$\mathbf{h}^{+}(x)=\frac{1}{2}\left(\mathbf{t}(x)+\frac{1}{\pi i}\int_c\frac{\mathbf{t}(\xi)}{\xi-x}\,d\xi\right). \tag{36}$$

With Eq. (36), a direct calculation will put Eq. (35) into the form

$$\frac{(\mathbf{B}+\overline{\mathbf{B}})}{2\pi i}\int_c\frac{\mathbf{t}(\xi)}{\xi-x}\,d\xi+\frac{(\mathbf{B}-\overline{\mathbf{B}})}{2}\,\mathbf{t}(x)=i\mathbf{d}'(x). \tag{37}$$

This is a set of singular integral equations for the unknown traction in C. For more insight, consider materials with the $x-y$ plane as a plane of symmetry. Under these assumptions the solutions of plane and antiplane problems can be uncoupled. The $\mathbf{B}$ matrix for the in-plane deformation in (Suo, 1990)

$$\mathbf{B}=\begin{pmatrix} s_{11}\,\mathrm{Im}(p_1+p_2) & -i(p_1p_2s_{11}-s_{12}) \\ i(\overline{p_1}\,\overline{p_2}\,s_{11}-s_{12}) & -s_{22}\,\mathrm{Im}(1/p_1+1/p_2)\end{pmatrix}.$$

Note that s_{ij} in the above matrix is applicable for the state of plane stress and can easily be converted to the plane strain state as

$$s_{ij}'=s_{ij}-\frac{s_{i3}\,s_{j3}}{s_{33}}.$$

For the case of an isotropic material, it is interesting to note that the $\mathbf{B}$ matrix has a regular behavior when the roots of Eq. (7) are degenerate, while the matrices $\mathbf{A}$ and $\mathbf{L}$ are singular. For an isotropic material, the matrix $\mathbf{B}$ is expressed as follows:

$$\mathbf{B}=\begin{pmatrix} 2s_{11} & i(s_{11}+s_{12}) \\ -i(s_{11}+s_{12}) & 2s_{11}\end{pmatrix}.$$

and Eq. (37) reduces to the integral equations for isotropic materials as given by Johnson (1985, p. 29) as

$$\int_c\frac{t_1(\xi)}{\xi-x}\,d\xi=\frac{\pi(1-2\nu)}{2(1-\nu)}\,t_2(x)-\frac{\pi(1-\nu^2)}{2E}\,d_1'(x)$$

$$\int_c\frac{t_2(\xi)}{\xi-x}\,d\xi=-\frac{\pi(1-2\nu)}{2(1-\nu)}\,t_1(x)-\frac{\pi(1-\nu^2)}{2E}\,d_2'(x) \tag{37'}$$

For Case (3), either $u_1(x)$, $t_2(x)$ or $u_2(x)$, $t_1(x)$ are prescribed in C. The integral Eqs. (37) for the unknown traction component $t_1(x)$ or $t_2(x)$ are decoupled. There is no additional difficulty for this case except that a solution of a Fredholm integral equation of the second kind rather the first kind is required.

Case (4) is important to investigations of constant fatigue, and for this reason a solution given in detail is presented next. An in-plane deformation is considered, and the boundary conditions for this case are the following:

$t_1(x)=\mu t_2(x)$ and $u_{2,1}(x)=d_2'(x)$ are prescribed in C.

Equation (37) is rewritten using the above boundary conditions as

$$\frac{(\mathbf{B}+\overline{\mathbf{B}})}{2\pi i}\begin{pmatrix}\mu\\1\end{pmatrix}\int_c\frac{t_2(\xi)}{\xi-x}\,d\xi+\frac{(\mathbf{B}-\overline{\mathbf{B}})}{2}\begin{pmatrix}\mu\\1\end{pmatrix}t_2(x)=i\mathbf{d}'(x). \tag{38}$$

The second equation is

$$\frac{k_1}{\pi}\int_{-a}^{a}\frac{t_2(\xi)}{\xi-x}\,d\xi+k_2t_2(x)=-d_2'(x) \tag{39}$$

where

$$k_1=\frac{1}{2}\left(\mu(B_{21}+\overline{B}_{21})+(B_{22}+\overline{B}_{22})\right)$$

$$k_2=\frac{i}{2}\left(\mu(B_{21}-\overline{B}_{21})+(B_{22}-\overline{B}_{22})\right)$$

When $k_2\neq 0$, the solution of Eq. (39) can be found in Johnson (1985, Ch. 2). Thus

$$t_2(X)=-\frac{d_2'(X)}{(1+q^2)k_2}$$

$$-\frac{q}{(1+q^2)k_2}\frac{1}{\pi(1-X^2)^{1/2}}\left(\frac{1+X}{1-X}\right)^{\gamma}\int_{-a}^{a}(1-S)^{1/2}\left(\frac{1+S}{1-S}\right)^{\gamma}$$

$$\times\frac{d_2'(S)}{S-X}+\frac{q}{(1+q^2)k_2}\frac{1}{\pi(1-X^2)^{1/2}}\left(\frac{1+X}{1-X}\right)^{\gamma}\frac{F_2}{a}\,ds$$

Downloaded 03 May 2010 to 171.66.16.20. Redistribution subject to ASME license or copyright; see http://www.asme.org/terms/Terms_Use.cfm

where

$$e^{2\pi i\gamma}=\frac{iq-1}{iq+1},\quad q=-k_1/k_2\quad F=\int_{-1}^{1} t_2(X)dX.$$

When $k_2=0$, Eq. $(37)_2$ is simplified as

$$\frac{k_1}{\pi}\int_{-a}^{a}\frac{t_2(\xi)}{\xi-x}\,d\xi=-d_2'(x)$$

and this condition corresponds to $\mathbf{B}=\overline{\mathbf{B}}$ or $\mu=0$ for an isotropic material. The solution of this equation is given next

$$t_2(x)=\frac{1}{\pi(a^2-x^2)^{1/2}k_1}\int_{-a}^{a}(a^2-\xi^2)^{1/2}\frac{d_2'(\xi)}{\xi-x}+\frac{F_2}{\pi(a^2-x^2)^{1/2}k_1}.$$

If the shape of the indenter $d_2(x)$ is a polynomial, then the stress distribution will be in a closed form.

4 Dislocation Interaction

The half-space Green's function that characterizes the interaction between a dislocation and a finite surface strip is useful for consideration of subsurface damage near a sliding or sticking contact. The study and application for one class of solutions for an isotropic material has been given by Bryant et al. (1984). As a preliminary result the solution for a dislocation in a traction-free half-space is required for deriving the interaction between the dislocation and contact loading. The solution for a single dislocation in a traction-free half-space, which was obtained by analytic function continuation approach, was given by Suo (1990).

The complex potential in a closed form is given as

$$\mathbf{f}_D(z)=\mathbf{f}_0(z)-\mathbf{L}^{-1}\overline{\mathbf{L}}\,\overline{\mathbf{f}_0(\bar{z})} \tag{40}$$

where

$$f_{0j}(z)=q_j\ln(z-s_j)\text{ and }s_j=x_0+p_jy_0 \tag{41}$$

is the solution for a dislocation in the whole space. The determination of $\mathbf{q}$ has been documented in detail by Hirth and Lothe (1982) as

$$\mathbf{q}=\frac{1}{2\pi}\mathbf{L}^{-1}(\mathbf{B}+\overline{\mathbf{B}})^{-1}\mathbf{b} \tag{42}$$

where $\mathbf{b}$ is the Burgers vector; the branch cut is chosen in the negative x-direction and the phase angle is measured from the positive x-direction. It is worthwhile to mention again that the positive definiteness of $\mathbf{B}+\overline{\mathbf{B}}$ was obtained from the solution of (42) by Stroh (1958).

We will use as an example the boundary conditions for Case (2), which has displacements only prescribed in C. This case is relevant to the problem of adhesive wear. The disturbance produced by the dislocation on the solution is determined by introducing into Eq. (22) or (34) a negative displacement calculated from (40) on $y=0$ as follows:

$$-\mathbf{d}_D'(x)=2\,\mathrm{Re}\,[i\mathbf{B}\,(\mathbf{L}\mathbf{f}_0'(x)-\overline{\mathbf{L}\mathbf{f}_0'(x)})] \tag{43}$$

where the subscript D denotes the disturbance of the dislocation.

When the matrix $\mathbf{B}$ is real

$$\mathbf{h}_D(z)=\frac{\chi(z)}{2\pi i}\int_{-a}^{a}\frac{-2(\mathbf{L}\mathbf{f}_0'(x)-\overline{\mathbf{L}\mathbf{f}_0'(x)})}{\chi^+(x)(x-z)}\,dx. \tag{44}$$

The contour integral required to evaluate (44) can be found in Erdogan (1961). Without presenting the detailed calculation required for this contour integral, the solution of the disturbance of a dislocation interacting with indenter with no slip is given as

$$\mathbf{h}_D(z)=-\mathbf{L}\mathbf{F}(z) \tag{45}$$

where

$$F_j(z)=q_j\left(\frac{1}{z-s_j}\left(1-\frac{\chi(z)}{\chi(s_j)}\right)-\frac{1}{z-\bar{s}_j}\left(1-\frac{\chi(z)}{\chi(\bar{s}_j)}\right)\right). \tag{46}$$

The total solution for the interaction between a dislocation and an indenter with no slip is therefore the summation of

$$\mathbf{h}(z)_{\text{total}}=\mathbf{h}(z)+\mathbf{h}_D(z)+\mathbf{L}\mathbf{f}'_D(z) \tag{47}$$

where the first term is obtained from Eq. (22) with the indenter shape prescribed and the second and third terms are given, respectively, by (45) and (40). Cases that involve other boundary conditions, e.g., Case (4), which is appropriate to sliding friction, can be solved using a similar procedure.

5 Concluding Remarks

The two-dimensional contact problem for an anisotropic half-space is formulated using the Stroh formalism (Stroh, 1958) and the analytic function continuation approach (Suo, 1990). The Stroh formulation, which solved the coupled in-plane and antiplane two-dimensional problem, is more general than the Green and Zerna (1954) formulation, which was only for in-plane deformation. The compactness of the present results shows a great potential to be used in the other problems.

As mentioned earlier, the expression, Eq. (12), may break down if the roots of Eq. (7) are degenerate (non-semi-simple, Ting and Hwu, 1986), as for example, in isotropic materials. The solution of Eq. (34) for Case (2) will not hold for the degenerate case. Fortunately, Eq. (37) holds for all cases, including isotropic materials. Thus, the solution of Case (2) in the degenerate case can be obtained by solving the integral equations without difficulty (Johnson, 1985). The symmetry of the matrix $\mathbf{B}+\overline{\mathbf{B}}$ in Eq. (37) allows the iteration procedure to be avoided for this case. In addition, the complex variable approach developed for isotropic materials (e.g., England, 1971; Muskhelishvili, 1953) can be considered to be more straightforward for these degenerate cases.

Acknowledgment

The present research was partially supported by National Science Foundation.

References

Barnett, D. M., and Lothe, J., 1985, "Free Surface (Rayleigh) waves in Anisotropic Elastic Half Space: the Surface Impendance Method," *Proc. Roy. Soc. Lon.*, Vol. A402, pp. 135-151.

Bower, A. F., 1988, "The Influence of Crack Face Friction and Trapped Fluid on Surface Initiated Rolling Contact Fatigue Cracks," ASME *J. Tribology*, Vol. 110, pp. 704-711.

Bryant, M. D., Miller, G. R., and Keer, L. M., 1984, "Line Contact Between a Rigid Indenter and a Damaged Elastic Body," *Quar. J. Mech. Appl. Math.*, Vol. 37, Part 3, pp. 467-478.

England, A. H., 1971, *Complex Variable Methods in Elasticity*, John Wiley and Sons, London, U.K.

Erdogan, F., 1961, "On the Stress Distribution in Plates with Collinear Cuts Under Arbitrary Loads," *Proceedings of the Fourth U.S. National Congress of Applied Mechanics*, pp. 547-553.

Eshelby, J. D., Read, W. T., and Shockley, W., 1953, "Anisotropic Elasticity with Applications to Dislocation Theory," *Acta Met.*, Vol. pp. 251-259.

Gao, H., Addudi, H., and Barnett, D. M., 1992., "Interfacial Crack-Tip Field in Anisotropic Elastic Solids," *J. Mech. Phys. Solids*, Vol. 40, No. 2, pp. 393-416.

Green, A. E., and Zerna, W., 1954, *Theoretical Elasticity*, Clarendon Press, Oxford, U.K.

Hirth, J. P., and Lothe, J., 1982, *Theory of Dislocations*, 2nd ed., John Wiley and Sons, London, U.K.

Ingebrigtsen, K. A., and Tonning, A., 1969, "Elastic Surface Waves in Crystal," *Physical Review*, Vol 184, No. 3, pp. 942-951.

Johnson, K. L., 1985, *Contact Mechanics*, Cambridge University Press, Cambridge, U.K.

Klintworth, J. W., and Stronge, W. J., 1990, "Plane Punch Indentation of Anisotropic Elastic Half-Space," ASME JOURNAL OF APPLIED OF MECHANICS, Vol. 57, pp. 84-90.

Lekhnitskii, S. G., 1963, *Theory of Elasticity of an Anisotropic Body*, Holden-Day, San Francisco.

Downloaded 03 May 2010 to 171.66.16.20. Redistribution subject to ASME license or copyright; see http://www.asme.org/terms/Terms_Use.cfm

Muskhelishvili, N. I., 1953, *Some Basic Problems of the Mathematical Theory of Elasticity*, Leydon, Noordhoff.

Qu, J., and Bassani, J. L., 1989, "Cracks on Bimaterial and Bicrystal Interfaces," *J. Mech. Phys. Solids*, Vol. 37, No. 4, pp. 417–433.

Stroh, A. N., 1958, "Dislocation and Cracks in Anisotropic Elasticity," *Phil. Mag.*, Ser. 8, Vol. 3, pp. 625–646.

Suo, Z., 1990, "Singularity, Interface and Crack in Dissimilar Anisotropic Media," *Proc. Roy. Soc. Lon.*, Vol. A427, pp. 331–358.

Ting, T. C. T., 1986, "Explicit Solution and Invariance of the Singularities at an Interface Crack in Anistotropic Composite," *Int. J. Solids and Stuctures*, Vol. 22, pp. 965–983.

Ting, T. C. T., and Hwu, C., 1987, "Sextic Formalism in Anisotropic Elasticity for Almost Non-Semisimple Matrix N," *Int. J. Solids Structures*, Vol. 24, No. pp. 65–76.

Willis, J. R., 1966, "Hertzian Contact of Anisotropic Bodies," *J. Mech. Phys. Solids*, Vol. 14, pp. 163.

Downloaded 03 May 2010 to 171.66.16.20. Redistribution subject to ASME license or copyright; see http://www.asme.org/terms/Terms_Use.cfm

Transient Response of an Elastic Homogeneous Half-Space to Suddenly Applied Rectangular Loading

F. Guan

M. Novak

Department of Civil Engineering,
The University of Western Ontario,
London, Ontario N6A 5B9, Canada

A closed-form solution of transient response to suddenly applied loading distributed over a rectangular area on the surface of an elastic homogeneous half-space is developed for special purposes such as analysis of dynamic soil-structure interaction or contact problems. The solution is obtained using Laplace transform with respect to time and Fourier transform with respect to space. Inverse Laplace transform is implemented analytically. As extreme cases of rectangular loading, the solutions for a point force or finite line load can also be obtained. The advantages of this solution over most other solutions by numerical analyses are that the multiple integrations are reduced by one order, the singularity is removed from the integral kernel, and no additional discretization in the vicinity of the region of interest is required.

1 Introduction

The great advantage of transient analysis in the time domain is its ability to simulate nonlinear behavior of structures and to elucidate real wave propagation characteristics. In engineering practice, many structures can be considered as resting on subsoils that extend to practical semi-infinity. For the transient numerical analyses of such soil-structure systems to external or seismic loading, most of the difficulties arise in the simulation of the half-space. Therefore, the development of a transient fundamental solution, which can be applied efficiently, is important from a practical point of view.

The first treatment of dynamic half-space problems was due to Lamb (1904). Since then, numerous papers have been published on the topics concerned with the problem. A similarity solution was obtained by Smirnov and Sobolev (1932) for surface line loading, which was identical to that given by Lamb (1904). Pekeris (1955a, b) solved the responses due to a surface or buried force normal to the medium boundary for Poisson's ratio $\sigma = 0.25$. Ang (1960) studied the wave pattern in a half-space due to line loading moving on its surface. Chao (1960) presented the response of a half-space loaded by a point force parallel to the boundary. Eason (1964) derived the response of a half-space due to a torsional body force. Again, Eason (1966) derived the displacements in a half-space for point or disk loads applied normally to the surface. Payton (1967) derived the surface displacement due to buried sources for two-dimensional problems. Johnson (1974) derived the Green function for a three-dimensional half-space. The response of a half-space subjected to a moving point loading was presented by Gakenheimer and Miklowitz (1969). Mooney (1972) extended the work by Pekeris (1955a) for arbitrary Poisson's ratios. All the solutions described above are based on Cargniard technique (1962) or its modified version, Cargniard-de Hoop technique by de Hoop (1960). More recently, Mamoon developed frequency and transient Green's functions (1990) for a half-space extending Mindlin's method for the corresponding static solution (1936).

As an alternative to Green's function due to point/line loading, the displacement induced by distributed loading has been of interest for many years. Mitra (1962) solved the problems of uniformly distributed strip loadings normal to the half-space. Then Mitra (1964) gave a solution outside a circular area loaded with impulsive normal pressure. Eason (1964) presented the solution due to distributed torsional loadings on a half-space. Craggs (1959) solved the problem of a uniformly distributed strip loading traveling with a constant velocity. Cruse (1968a,b) formulated the elastodynamic boundary-initial value problem in terms of singular integral equations in Laplace transform domain and the numerical results were represented by numerical inverse Laplace transform. Norwood (1969) gave the response of the half-space to vertical uniform loading distributed over one of its quarters. With this solution, the response due to finite rectangular, normal loading can also be obtained; however, the solution for the rectangular impulses given by Norwood is not as complete as those given here and no numerical results are presented in his paper. In the afore-

Contributed by the Applied Mechanics Division of The American Society of Mechanical Engineers for publication in the ASME Journal of Applied Mechanics.

Discussion on this paper should be addressed to the Technical Editor, Professor Lewis T. Wheeler, Department of Mechanical Engineering, University of Houston, Houston, TX 77204-4792, and will be accepted until four months after final publication of the paper itself in the ASME Journal of Applied Mechanics.

Manuscript received by the ASME Applied Mechanics Division, June 29, 1992; final revision, Feb. 3, 1993. Associate Technical Editor: T. R. Akylas.

Copyright © 1994 by ASME
Downloaded 03 May 2010 to 171.66.16.20. Redistribution subject to ASME license or copyright; see http://www.asme.org/terms/Terms_Use.cfm

mentioned work, no solution is given in the form of Green's function.

For the numerical analysis of the dynamic response of surface structures encountered in engineering practice, it is convenient to develop a solution that can be applied directly. The solution for loadings with distributions in both space and time is preferred to the solutions for line/point loadings with Dirac delta time function. Motivated by this, a transient solution for a half-space subjected to horizontal/vertical impulsive loadings over a rectangular area is developed in a double integral form. With the aid of Laplace transform with respect to time and Fourier transforms with respect to horizontal coordinates, the solution is obtained in the transform domain. As the limiting cases, the solutions for point/finite line loadings can also be obtained directly. The solution developed in this paper can be readily applied to other problems in engineering practice such as the transient response of surface foundations. To the best of the authors' knowledge, no analytical or numerical results are given for the rectangular distributed impulsive loadings in the form of Green's function.

It is worth mentioning that, although the problem stated above can be solved by other available fundamental solutions, the advantages of the solution presented herein are considerable. In the procedure employing the full-space transient Green functions, the region in the vicinity of the loaded area has to be discretized and both displacement and stress kernels are involved. The solution can also be obtained by integrating the solutions given by Pekeris (1955a) and Chao (1960); however, these are expressed by triple integrals instead of double integrals employed here.

An indirect way to solve the transient problem is to study it first in the frequency domain and then to obtain the time domain solution by the FFT technique, as many do in practice. The solution in the frequency domain is simpler and can be dealt with as its static counterpart. However, this technique is limited to linear problems and the high-frequency components may be difficult to Fourier transform. For the nonlinear problems it is difficult to use the frequency domain solutions. In addition, although, in general, the frequency domain solution is easier to treat numerically compared with the time domain solution, it is not always so and in some cases of transient response, direct time domain solutions are preferable.

The applications of the solution presented here are promising for cases of soil-structure interaction, dynamic contact problems, and the transient response of multifoundations with though-soil coupling between foundations. The response to general transient loading can be readily obtained from the response to the Heaviside step function type of loading assumed here.

2 General Formulation of the Problem

2.1 Wave Equations. The half-space as shown in Fig. 1 is assumed isotropic and elastic, described by shear modulus μ, mass density ρ, and Poissons' ratio σ with P, SV, and Rayleigh wave velocities, denoted as α, β, C_R, respectively. The Lamé potentials satisfy the following governing equations in the absence of body forces (see, e.g., Achenbach, 1973)

$$\nabla^2\phi-\frac{1}{\alpha^2}\frac{\partial^2\phi}{\partial t^2}=0 \tag{1a}$$

$$\nabla^2\varphi_j-\frac{1}{\beta^2}\frac{\partial^2\varphi_j}{\partial t^2}=0 \tag{1b}$$

where $j = x, y, z$ and

$$\nabla^2=\frac{\partial^2}{\partial x^2}+\frac{\partial^2}{\partial y^2}+\frac{\partial^2}{\partial z^2}=0. \tag{2}$$

The potentials ϕ_x, ϕ_y, and ϕ_z are divergence-free,

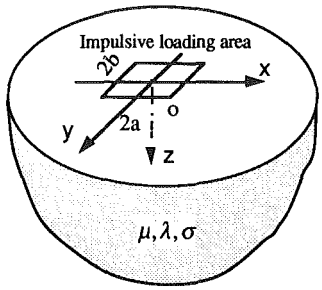


Fig. 1 Geometry of the problem

$$\frac{\partial\varphi_x}{\partial x}+\frac{\partial\varphi_y}{\partial y}+\frac{\partial\varphi_z}{\partial z}=0. \tag{3}$$

The displacements and stresses can be expressed in terms of Lamé potentials.

By taking the radiation condition at infinity into account, the solutions of (1) in Laplace and Fourier transform domains (in x and y directions) are

$$\phi=Ae^{-k_\alpha z} \tag{4a}$$

$$(\varphi_x,\varphi_y,\varphi_z)=(B,C,D)\ e^{-k_\beta z} \tag{4b}$$

$$k_\alpha=\sqrt{p^2/\alpha^2+k_x^2+k_y^2},\ k_\beta=\sqrt{p^2/\beta^2+k_x^2+k_y^2}\ (\mathrm{Re}(k_a,k_\beta)\geq 0)$$

where p, k_x, and k_y are the Laplacian parameter and wave numbers in the x and y directions, respectively.

2.2 Boundary Conditions. The impulsive loading of unit magnitude is assumed to be applied over a rectangular area on the free surface. Hence, the boundary conditions may be described as

$$(\tau_{xz},\tau_{yz},\tau_{zz})=\begin{cases}\dfrac{-H(t)}{4ab} & |x|\leq a \text{ and } |y|\leq b\\ 0 & |x|>a \text{ and } |y|>b\end{cases} \tag{5}$$

where $H(t)$ is a Heaviside step function defined as

$$H(t)=\begin{cases}1 & t>0\\ 0 & t\leq 0\end{cases} \tag{6}$$

and their counterpart in the transform domain

$$(\tilde{\tau}_{xz},\tilde{\tau}_{yz},\tilde{\tau}_{zz})=-\frac{\sin(k_xa)\sin(k_yb)}{abk_xk_y}\frac{1}{p}. \tag{7}$$

Then the displacements and stresses can be expressed as

$$\begin{Bmatrix}\tilde{u}\\ \tilde{v}\\ \tilde{w}\end{Bmatrix}=\begin{bmatrix}-ik_x & 0 & k_\beta & -ik_y\\ -ik_y & -k_\beta & 0 & ik_x\\ -k_\alpha & ik_y & -ik_x & 0\end{bmatrix}\begin{Bmatrix}A\\ B\\ C\\ D\end{Bmatrix} \tag{8}$$

and

$$\mu\begin{bmatrix}k_\beta^2+k_x^2+k_y^2 & -2ik_\beta k_y & 2ik_\beta k_x & 0\\ 2ik_\alpha k_y & k_\beta^2+k_y^2 & -k_xk_y & -ik_\beta k_x\\ 2ik_\alpha k_x & k_xk_y & k_\beta^2+k_x^2 & ik_\beta k_y\\ 0 & ik_x & ik_y & k_\beta\end{bmatrix}\begin{Bmatrix}A\\ B\\ C\\ D\end{Bmatrix}=\begin{Bmatrix}\tilde{\tau}_{zz}\\ \tilde{\tau}_{yz}\\ \tilde{\tau}_{xz}\\ 0\end{Bmatrix}, \tag{9}$$

respectively, where $i=\sqrt{-1}$ is the imaginary unit.

The coefficients can be solved by inverting the coefficient matrix in (9) (see Guan and Novak, 1992). Substituting the coefficients into (8), the solution in space-time domain is

Downloaded 03 May 2010 to 171.66.16.20. Redistribution subject to ASME license or copyright; see http://www.asme.org/terms/Terms_Use.cfm

$$\begin{Bmatrix} u(x,y,t) \\ v(x,y,t) \\ w(x,y,t) \end{Bmatrix} = \frac{-1}{8\pi^3 i} \int_0^{2\pi} \int_0^{\infty} \int_{\gamma-i\infty}^{\gamma+i\infty} k\tilde{\Delta}(k,\theta,p) e^{pt} e^{-ik(x\cos\theta + y\sin\theta)} \begin{Bmatrix} \tilde{\tau}_{xz} \\ \tilde{\tau}_{yz} \\ -\tilde{\tau}_{zz} \end{Bmatrix} d\theta dk dp \qquad (10)$$

in which

$$\tilde{\Delta} = \tilde{\Delta}' - \tilde{\Delta}''$$

where

$$\tilde{\Delta}' = \begin{bmatrix} \frac{-p^2/\beta^2 k_\beta}{\mu\Delta_R}\cos^2\theta & \frac{-p^2/\beta^2 k_\beta}{\mu\Delta_R}\sin\theta\cos\theta & \frac{k_\beta^2 + 2k^2 - 2k_\alpha k_\beta}{\mu\Delta_R} i\cos\theta \\ \frac{-p^2/\beta^2 k_\beta}{\mu\Delta_R}\sin\theta\cos\theta & \frac{-p^2/\beta^2 k_\beta}{\mu\Delta_R}\sin^2\theta & \frac{k_\beta^2 + 2k^2 - 2k_\alpha k_\beta}{\mu\Delta_R} i\sin\theta \\ \frac{k_\beta^2 + 2k^2 - 2k_\alpha k_\beta}{\mu\Delta_R} i\cos\theta & \frac{k_\beta^2 + 2k^2 - 2k_\alpha k_\beta}{\mu\Delta_R} i\sin\theta & \frac{p^2/\beta^2 k_\alpha}{\mu\Delta_R} \end{bmatrix} \qquad (11)$$

and

$$\tilde{\Delta}'' = \begin{bmatrix} \frac{\sin^2\theta}{\mu k_\beta} & \frac{-\sin\theta\cos\theta}{\mu k_\beta} & 0 \\ \frac{-\sin\theta\cos\theta}{\mu k_\beta} & \frac{\cos^2\theta}{\mu k_\beta} & 0 \\ 0 & 0 & 0 \end{bmatrix} \qquad (12)$$

In these equations, $\tilde{\Delta}'$ and $\tilde{\Delta}''$ are symmetric matrices representing the in-plane and antiplane motions, respectively.

The Laplace integration is executed first as in Eason (1966) in (10). The inverse Laplace transform can be implemented on the p-complex plane (see Guan and Novak, 1992). The integration of the terms in (10) with respect to p can be found in the Appendix. The integral with respect to k can be evaluated analytically for the loadings described here.

and

$$\delta_{jk} = \begin{cases} 1 & j = k \\ 0 & j \neq k. \end{cases}$$

The functions χ_{jk} and $G_{jk}^{(i)}$ depend on the spatial and time distributions of the loading, respectively. The expressions of $G_{jk}^{(i)}$ can be found in the Appendix.

The integration with respect to θ can be obtained analytically or numerically depending on the type of loading (see Guan and Novak, 1992). Here only the responses due to rectangular loading, and one of its limiting cases, finite line loading, are considered.

2.3 Rectangular loading. The integration of (10) over k can be obtained analytically. The related integration is of the form (Gradshteyn and Ryzhik, 1980, p. 433)

$$\chi_{jl}(x,y,\theta,c,t) = \int_0^{\infty} \frac{\sin(ak\cos\theta)\sin(bk\sin\theta)(1-\cos(kct))}{abk^2\sin\theta\cos\theta} \begin{Bmatrix} \sin(k(x\cos\theta + y\sin\theta)) \\ \cos(k(x\cos\theta + y\sin\theta)) \end{Bmatrix} dk$$

$$= \frac{1}{4ab\sin\theta\cos\theta} \sum_{m,n}^{2} (-1)^{m+n+1} \begin{cases} f_{mn}(x,y,\theta,c,t) & j=3, l\neq 3 \text{ or } j\neq 3,\ l=3 \\ g_{mn}(x,y,\theta,c,t) & \text{otherwise} \end{cases} \qquad (16)$$

After the evaluation of the integrals with respect to k and p, the Green's function can be written in double integral form

$$\Delta_{jk}(x,y,t) = \int_0^{2\pi} \Delta_{jk}^{(1)} \chi_{jk}(x,y,\theta,C_R,t)d\theta + \int_0^{2\pi}\int_{\beta}^{\alpha} \Delta_{jk}^{(2)}\chi_{jk}(x,y,\theta,\eta,t)d\eta d\theta + \int_0^{2\pi}\int_{\alpha}^{\infty} \Delta_{jk}^{(3)}\chi_{jk}(x,y,\theta,\eta,t)d\eta d\theta \qquad (13)$$

in which $\Delta_{jk}^{(i)}$ can be expressed as

$$\Delta_{jk}^{(i)} = \begin{cases} G^{(i)}(\delta_{jk} - \delta_j\delta_k) - G_{jk}^{(i)}\delta_j\delta_k & j\leq 2 \text{ and } k\leq 2 \\ -G_{jk}^{(i)}\delta_j\delta_k & \text{otherwise} \end{cases} \qquad (14)$$

where

$$G_{11}^{(i)} = G_{22}^{(i)} = G_{12}^{(i)} = G_{21}^{(i)}$$

$$G_{31}^{(i)} = -G_{13}^{(i)},\ G_{32}^{(i)} = -G_{23}^{(i)}$$

$$G_{13}^{(i)} = G_{23}^{(i)}$$

$$\delta_1 = \cos\theta,\ \delta_2 = \sin\theta,\ \delta_3 = 1 \qquad (15)$$

where

$$f_{mn}(x,y,\theta,c,t) = \frac{c_{mn}}{2}\ln\left|\frac{c_{mn}^2 - c^2t^2}{c_{mn}^2}\right| + \frac{ct}{2}\ln\left|\frac{c_{mn}+ct}{c_{mn}-ct}\right| \qquad (17a)$$

$$g_{mn}(x,y,\theta,c,t) = \begin{cases} \frac{\pi}{2}(ct - |c_{mn}|) & |c_{mn}| \leq ct \\ 0 & |c_{mn}| \geq ct \end{cases} \qquad (17b)$$

$$c_{mn} = (x + (-1)^m a)\cos\theta + (y + (-1)^n b)\sin\theta. \qquad (17c)$$

As can be seen, the singularity in the above formula occurs when c_{mn} equals to ct. However, this singularity is removable, which can readily be proved by inspecting (17a).

The present solution has many advantages over other solutions available. The solution for the problem can be obtained by two different approaches. One is to solve the problem by means of transient Stokes' solution. However, in this scheme, the region in the vicinity of the loading area is to be discretized and both the displacement and stress kernels are involved. Another way is to integrate the solution obtained by Pekeris and Chao. This leads to the solutions in the form of triple integrals.

2.4 Finite Line Loading. This case can also be treated as

Downloaded 03 May 2010 to 171.66.16.20. Redistribution subject to ASME license or copyright; see http://www.asme.org/terms/Terms_Use.cfm

an extreme case of the rectangular loading with $b \to 0$ or $a \to 0$. Then the transformed boundary conditions become

$$(\tilde{\tau}_{xz}, \tilde{\tau}_{yz}, \tilde{\tau}_{zz}) = -\frac{\sin(k_y b)}{b k_y} \frac{1}{p} \quad (a \to 0) \tag{18}$$

for uniform distribution (Fig. 2(*a*)) and

$$(\tilde{\tau}_{xz}, \tilde{\tau}_{yz}, \tilde{\tau}_{zz}) = -\frac{(1-\cos(k_y b))}{b^2 k_y^2} \frac{1}{p} \tag{19}$$

for triangular distribution (Fig. 2 (*b*)).

For the uniformly distributed finite line loading, the integration with respect to k is found to be (Gradshteyn and Ryzhik, 1980, p. 480)

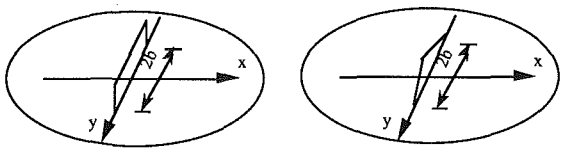
$$\chi_{jl}(x,y,\theta,c,t) =$$

$$= \int_0^\infty \frac{\sin(bk\sin\theta)(1-\cos(kct))}{bk\sin\theta} \begin{Bmatrix} \sin(k(x\cos\theta + y\sin\theta)) \\ \cos(k(x\cos\theta + y\sin\theta)) \end{Bmatrix} dk$$

$$= \frac{1}{4b\sin\theta} \sum_m^2 (-1)^{m+1} \begin{cases} f_m(x,y,\theta,c,t) & j=3, l\neq 3 \text{ or } j\neq 3, l=3 \\ g_m(x,y,\theta,c,t) & \text{otherwise} \end{cases} \tag{20}$$

where

$$f_m(x,y,\theta,c,t) = \ln \left| \frac{c_m^2 - c^2 t^2}{c_m^2} \right| \tag{21a}$$



(a) uniform loading (b) triangular loading

Fig. 2 Distributed finite line loadings

$$g_m(x,y,\theta,c,t) = -\operatorname{sign}(c_m) \begin{cases} \pi & ct > |c_m| \\ \frac{\pi}{2} & ct = |c_m| \\ 0 & ct < |c_m| \end{cases} \tag{21b}$$

$$c_m = x\cos\theta + (y + (-1)^m b)\sin\theta \tag{21c}$$

The integrations remaining in (10) are performed by a numerical integration scheme. Corresponding to the solution in the frequency domain for the same problem, there is also integration with respect to the wave number. It is found that no additional computational effort is required for the solution in the time domain compared with its counterpart in the frequency domain. Therefore, it is not recommended to obtain the transient solution using the numerical Laplace transform or Fourier transform techniques for the problems considered here. The most important aspect is that, for nonlinear analyses, the solution in the time domain is necessary, while the numerical transform technique is limited to the cases of linear or equivalent linear problems.

3 Numerical Results

3.1 Finite Line Loading. In many cases, this solution is better suited than the often adopted assumption of a line loading infinitely long in one direction leading to a two-dimensional problem. Herein, the wave propagation characteristics of both the finite line loading and infinite line loading are investigated.

The displacement responses at (2*b*,0) due to finite loadings distributed over $-b < y < b$ and those due to infinite line loadings with the same density $1/2b$ are plotted in Fig. 3, where the arrival and departure of the P, S, and Rayleigh waves are denoted by *P*, *S* and *R*, respectively. Before the P wave generated by the loading outside $-b < y < b$ arrives at the receiving station, the responses to finite and infinite line loadings are identical; then the curves for the two responses separate. The components u_{kk} due to line loading increase as the time goes by since the waves generated outside the range $-b < y < b$

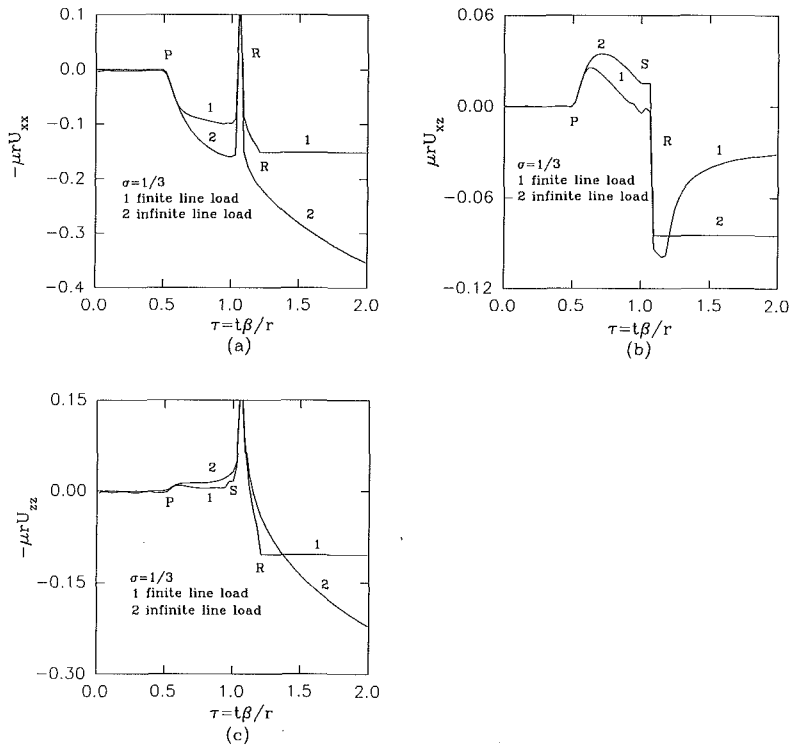


Fig. 3 Comparisons between displacements at point (2*b*,0) due to finite and infinite loadings for Poisson's ratio σ = 1/3

Downloaded 03 May 2010 to 171.66.16.20. Redistribution subject to ASME license or copyright; see http://www.asme.org/terms/Terms_Use.cfm

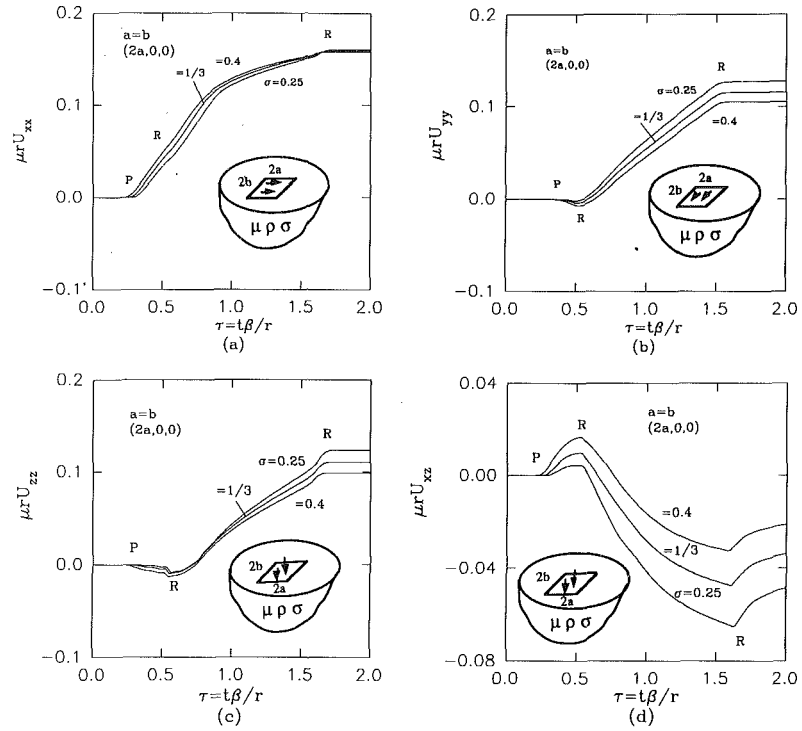


Fig. 4 Displacements at point (2*a*,0,0) due to rectangular loadings (*b* = *a*) versus nondimensional time τ

contribute to the responses continuously. This explains why, for the line loading, the static solutions u_{kk} are not defined . Therefore, the infinite line loading represents an idealized case that is not realistic. The response u_{zx} to finite line loading remains constant for a while just around the time the Rayleigh wave arrives and leaves, then decreases with time until all the waves pass by. In contrast with this, the component u_{zx} due to infinite line loading remains constant once the Rayleigh wave arrives. The components u_{kk} due to both loadings become infinite when Rayleigh wave arrives since they have a logarithmic type of singularity.

Another interesting difference between the responses to finite and infinite line loadings may be noted. For the finite line loading, the components u_{kk} remain constants after the Rayleigh wave arrives, while for the infinite line loading, the responses $u_{jk}(j \neq k)$ assume their static values. (The slight oscillations visible in some parts of the response are due to numerical inaccuracies.)

3.2 Rectangular loading. The formula for the response of a half-space subjected to rectangular loading with delta-function time-dependence applied normally to the surface was presented by Norwood (1969). However, no numerical results are given in his paper. Here numerical results are presented for various Poisson's ratios, dimensionless ratios b/a, and receiving stations to study the wave propagation due to distributed loading. For the static solution, an excellent agreement has been obtained between the present results and those by Thomson and Kobori (1963).

Figure 4 illustrates the surface displacement responses of a half-space for the location (2*a*,0). It is observed that the differences in u_{xx} for various Poisson's ratios are slight except for time delays in the dimensionless arrival time. The effects of the Rayleigh wave on the displacement components are dominant. This can be seen from the responses. For instance, in Fig. 4(*d*), the displacements u_{xz} go up after the P waves arrive, then they decrease after the Rayleigh wave arrives. When the Rayleigh waves are leaving, the trends of the displacement curves change again. The signs of the velocities also change at the time when the Rayleigh wave arrives and leaves. The arrival and leaving times of the Rayleigh wave correspond to the first and last arrival times of the wave fronts generated by the front and rear edges of the rectangular loading, respectively.

The responses for other cases are shown in Figs. 5 to 7. Figs. 5(*b*) and (*c*) show that velocity discontinuities arise when the Rayleigh wave arrives and passes by. After the Rayleigh waves arrive, the responses go up or fall down, then assume their static values or go gradually to their static values. For the response u_{zz} during the time the Rayleigh wave passes through, there are only slight differences for different Poisson's ratios. However, the differences become more distinct when the Rayleigh waves pass by and the static values are attained.

Comparing Fig. 4 and Fig. 5, or Fig. 6 and Fig. 7, one may note that the contribution of the Rayleigh wave is also characterized by the distance of the receiving station from the source. The farther the receiving station, the more marked the change in the displacement responses when the Rayleigh wave arrives and leaves. That is, for farther receiving stations, the response component due to Rayleigh waves is significant, as might be expected.

The displacement responses due to both point loading and rectangular loading are greatly affected by Rayleigh waves and SV waves. For the point loading, the displacements become discontinuous (infinite or finite jumps) when Rayleigh and SV wave fronts arrive (see Guan and Novak, 1992). For the distributed loading, the Rayleigh wave fronts are not singular but arrive continuously. Consequently, some of the displacements are dominated by Rayleigh waves while they last at the receiving station.

The data in Karabalis and Beskos (1984) cannot be compared directly with the results presented here. However, the accuracy of the present solution is verified at least to some extent. To investigate the accuracy of the numerical solutions, the response during the time before the P wave arrives is also evaluated. The numerical solutions yield almost no response before the P waves arrives, although very slight oscillations occur around zero in some cases.

Downloaded 03 May 2010 to 171.66.16.20. Redistribution subject to ASME license or copyright; see http://www.asme.org/terms/Terms_Use.cfm

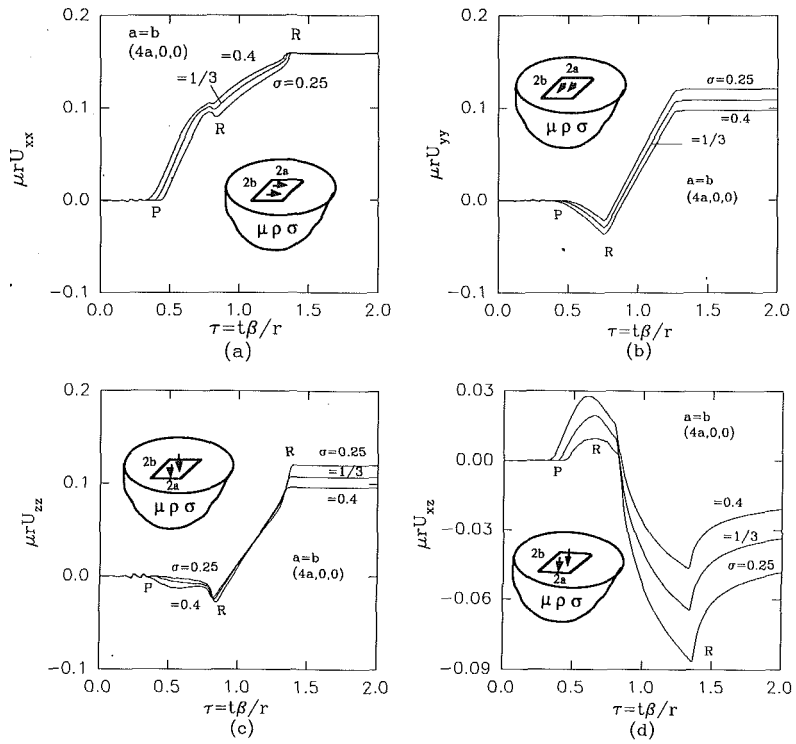


Fig. 5 Displacements at point (4*a*,0,0) due to rectangular loadings (*b* = *a*) versus nondimensional time τ

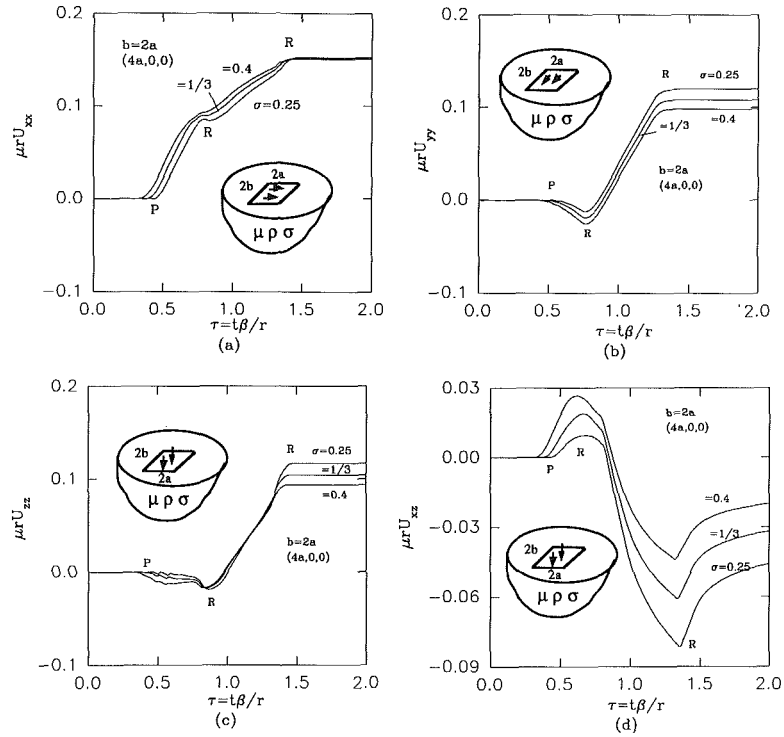


Fig. 6 Displacements at point (4*a*,0,0) due to rectangular loadings (*b* = 2*a*) versus nondimensional time τ

4 Conclusions

The integral form of Green's functions due to rectangular and finite line loadings is developed, and some numerical results are presented. Based on the studies, the following conclusions can be made:

(1) The contribution of Rayleigh waves to the surface response is significant and increases with the distance from the receiving station. For the rectangular loading, sudden changes in velocity may arise when the Rayleigh wave arrives and leaves.

(2) For the finite line loading, discontinuities occur in some displacements when the SV wave arrives.

(3) The computational work involved in the finite line loading is equivalent to that required by the integration of the formulae presented by Pekeris (1955) and Chao (1960). In-

Downloaded 03 May 2010 to 171.66.16.20. Redistribution subject to ASME license or copyright; see http://www.asme.org/terms/Terms_Use.cfm

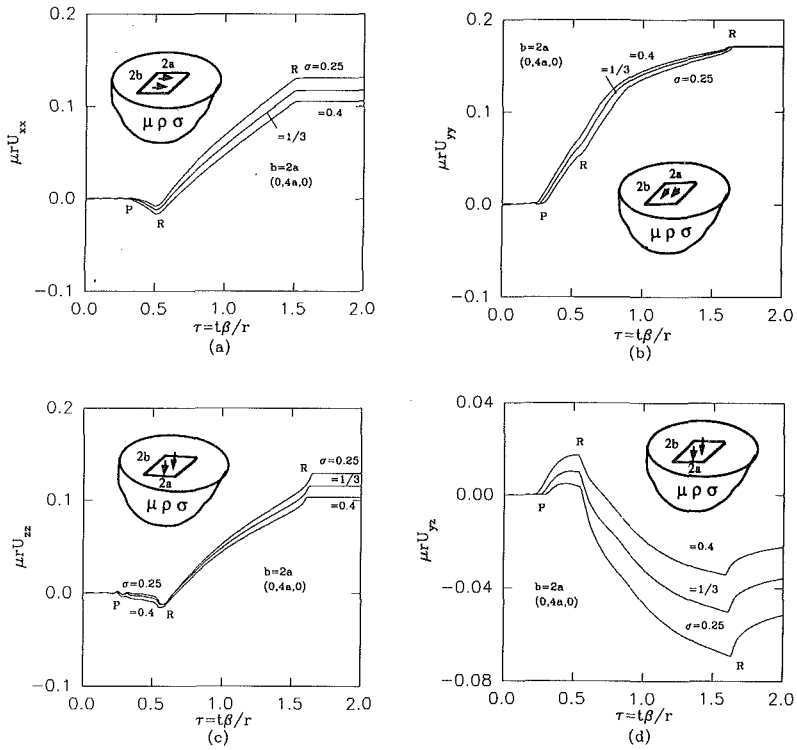


Fig. 7 Displacements at point (0,4*a*,0) due to rectangular loadings ($b = 2a$) versus nondimensional time τ

accuracy may be expected in the response if the singularity in the integral kernel is not treated properly.

(4) After the P wave generated outside the range loaded with the finite line source arrives at the receiving station, the responses due to finite line loading and infinite line loading are quite different.

(5) The present solution for uniform rectangular loadings is expressed in double integral form instead of triple integration form obtained from the solutions due to Pekeris (1955) and Chao (1960).

(6) The solution for uniform rectangular loadings is amenable to numerical computation. No singularity arises in the integral kernel.

(7) Further applications of the solution are possible, e.g., in the analyses of dynamic soil-structure interaction, and in contact problems of a structure in contact with soil represented by a half-space.

Acknowledgments

The support by the National Sciences and Engineering Research Council of Canada is appreciated.

References

Achenbach, J. D., 1973, *Wave Propagation in Elastic Solids*, North-Holland, Amsterdam.

Ang, D. D., 1960, "Transient Motion of a Line Load on the Surface of an Elastic Halfspace," *Quart. Appl. Math.*, Vol. 18, pp. 251–256.

Clenshaw, C. W., and Curtis, A. R., 1960, "A Method for Numerical Integration on an Automatic Computer," *Numer. Math.*, Vol. 2, pp. 197–205.

Cruse, T. A., and Rizzo, F. J., 1968a, "A Direct Formulation and Numerical Solution of the Transient Elastodynamic Problems, I," *J. Math. Anal. Appl.*, Vol. 22, pp. 244–259.

Cruse, T. A., 1968b, "A Direct Formulations and Numerical Solution of the Transient Elastodynamic Problems, II" *J. Math. Anal. Appl.*, Vol. 22, pp. 341–351.

Cargniad, L., 1962, *Reflection and Refraction of Progressive Seismic Waves*, McGraw-Hill, New York.

Chao, C. C., 1960, "Dynamic Response of an Elastic Halfspace due to Tangential Surface Loadings," ASME JOURNAL OF APPLIED MECHANICS, Vol. 27, pp. 559–567.

Graggs, J. W., 1959, "On Two-Dimensional Waves in an Elastic Halfspace," *Camb, Philos. Soc.*, Vol. 56, pp. 269–283.

de Hoop, A. T., 1959-1960, "The Surface Line Source Problem," *Appl. Sci. Res.*, Vol. B8, pp. 349–356.

Eason, G., 1966, "The Displacements Produced in an Elastic Halfspace by a Suddenly Applied Surface Force," *J. Inst. Maths Applics.* Vol. 2, pp. 299–326.

Eason, G., 1964, "On the Torsional Impulsive Loading of an Elastic Halfspace," *Quart. J. Mech. Appl. Mathe.*, Vol. 17, pp. 279–292.

Eringen, A. C., and Suhubi, E. S., 1975, *Elastodynamics*, Vol. II. Academic Press, New York.

Gakenheimer, D. G., and Miklowitz, J., 1969, "Transient Excitation Of An Elastic Halfspace By A Point Loading Travelling On The Surface," ASME JOURNAL OF APPLIED MECHANICS, Vol. 36, pp. 505–515.

Gradshteyn, I. S., and Ryzhik, I. M., 1980, *Table of Integrals, Series and Products*, Academic Press, New York.

Guan, F., and Novak, M., 1992, "Transient Response of an Elastic Homogeneous Halfspace to Suddenly Applied Rectangular Loading," Geotechnical Research Report, No.Geot-10-92, Dept. of Civil Engineering, The University of Western Ontario, London, Ontario, Canada.

Johnson, L. R., 1974, "Green's Function for Lamb's Problem," *Geophys. J. R. Astr. Soc.*, Vol. 37, pp. 99–131.

Karabalis, D. L., and Beskos, D. E., 1984, "Dynamic Response of 3-D Rigid Surface Foundations by Time Domain Boundary Element Method," *Earthq. Engrg. and Struct. Dyn.*, Vol. 12, pp. 73–93.

Lamb, H., 1904, "On the Propagation of Tremors on the Surface of an Elastic Solid," *Philos. Trans. Royal Soc., London*, Vol. A203, pp. 1–42.

Mamoon, S. M., 1990, "Dynamic and Seismic Behavior of Deep Foundations," Ph.D. Thesis, State University of New York at Buffalo, Buffalo NY.

Mindlin, R. D., 1936, "Force at a Point in the Interior of a Semi-infinite Solid," *J. of Appl. Phy.*, Vol. 7, pp. 195–202.

Mitra, M., 1962, "Note on the Disturbance Produced in an Elastic Halfspace by Transient Pressure Applied over a Portion of the Boundary," *Pro. Nat. Inst. Sci. India Sec.*, Vol. A28, pp. 199–205.

Mitra, M., 1964, "Disturbance Produced in an Elastic Halfspace by Impulsive Normal Pressure," *Proc. Camb. Phil. Soc.*, Vol. 60, pp. 683–696.

Mooney, H. M., 1974, "Some Numerical Solutions for Lamb's Problem," *Bull. Seis. Soc. Am.*, Vol. 64, pp. 473–491.

Norwood, R. D., 1969, "Exact Transient Response of an Elastic Halfspace Loaded Over a Rectangular of Its Surface," ASME JOURNAL OF APPLIED MECHANICS, Vol. 36, pp. 516–522.

Payton, R. G., 1968, "Transient Motion of an Elastic Halfspace due to a Moving Surface Line Load," *Int. J. Engrg. Sci.*, Vol. 5, pp. 49–79.

Pekeris, E., 1955a, "The Seismic Surface Pulse," *Proc. Nat. Acad. Sci.*, Vol. 41, pp. 469–480.

Pekeris, E., 1955b, "The Seismic Surface Pulse," *Proc. Nat. Acad. Sci.*, Vol. 41, pp. 629–639.

Downloaded 03 May 2010 to 171.66.16.20. Redistribution subject to ASME license or copyright; see http://www.asme.org/terms/Terms_Use.cfm

Smirnov, V. I., and Sobolev, S., 1932, "On a New Method in the Problem of Elastic Vibrations," *Akad. Nauk.*, SSSR Seism. Institute, Trudy. 20.

Thomson, W. T., and Kobor, T., 1963, "Dynamic Compliance of Rectangular Foundations on an Elastic Halfspace," ASME *Journal of Applied Mechanics*, Vol. 30, pp. 579–584.

APPENDIX

The inverse Laplace transform can be performed by integrations along the path as indicated in Fig. A1. For the terms in Eq. (10), the results are (see Guan and Novak, 1992)

$$\frac{1}{2\pi i}\int_{\gamma-i\infty}^{\gamma+i\infty}\frac{-p^2/\beta^2 k_\beta}{\mu\Delta_R}e^{pt}dp=\frac{C_R^2/\beta^2\sqrt{1-C_R^2/\beta^2}}{2\mu K(C_R)}\sin kC_Rt-$$
$$-\frac{2}{\pi\mu}\int_\beta^\alpha\frac{\eta^2/\beta^2(2-\eta^2/\beta^2)^2\sqrt{\eta^2/\beta^2-1}}{(2-\eta^2/\beta^2)^4+16(1-\eta^2/\alpha^2)(\eta^2/\beta^2-1)}\sin k\eta t d\eta-$$
$$-\frac{2}{\pi\mu}\int_\alpha^\infty\frac{\eta^2/\beta^2\sqrt{\eta^2/\beta^2-1}}{(2-\eta^2/\beta^2)^2+4\sqrt{\eta^2/\beta^2-1}\sqrt{\eta^2/\alpha^2-1}}\sin k\eta t d\eta \tag{A1}$$

$$\frac{1}{2\pi i}\int_{\gamma-i\infty}^{\gamma+i\infty}\frac{k_\beta^2+2k^2-2k_\alpha k_\beta}{\mu\Delta_R}e^{pt}dp$$
$$=\frac{C_R^2/\beta^2(2-C_R^2/\beta^2)}{4\mu K(C_R)}\sin ktC_R-$$
$$-\frac{4}{\pi\mu}\int_\beta^\alpha\frac{\eta^2/\beta^2(2-\eta^2/\beta^2)\sqrt{1-\eta^2/\alpha^2}\sqrt{\eta^2/\beta^2-1}}{(2-\eta^2/\beta^2)^4+16(1-\eta^2/\alpha^2)(\eta^2/\beta^2-1)}\sin kt\eta d\eta \tag{A2}$$

$$\frac{1}{2\pi i}\int_{\gamma-i\infty}^{\gamma+i\infty}\frac{-k_\alpha p^2/\beta^2}{\mu\Delta_R}e^{pt}dp=\frac{C_R^2/\beta^2\sqrt{1-C_R^2/\alpha^2}}{2\mu K(C_R)}\sin ktC_R-$$
$$-\frac{8}{\pi\mu}\int_\beta^\alpha\frac{\eta^2/\beta^2(1-\eta^2/\alpha^2)\sqrt{\eta^2/\beta^2-1}}{(2-\eta^2/\beta^2)^4+16(1-\eta^2/\alpha^2)(\eta^2/\beta^2-1)}\sin kt\eta d\eta-$$
$$-\frac{2}{\pi\mu}\int_\alpha^\infty\frac{\eta^2/\beta^2\sqrt{\eta^2/\alpha^2-1}}{(2-\eta^2/\beta^2)^2+4\sqrt{\eta^2/\beta^2-1}\sqrt{\eta^2/\alpha^2-1}}\sin kt\eta d\eta \tag{A3}$$

$$\frac{1}{2\pi i}\int_{\gamma-i\infty}^{\gamma+i\infty}\frac{1}{\mu k_\beta}e^{pt}dp=-\frac{2}{\pi\mu}\int_\beta^\infty\frac{1}{\sqrt{\eta^2/\beta^2-1}}\sin kt\eta d \tag{A4}$$

where $K(C_R)$ denotes

$$K(C_R)=C_R\left\{\frac{1}{\beta^2}\left(2-\frac{C_R^2}{\beta^2}\right)-\frac{1}{\alpha^2}\frac{\sqrt{1-C_R^2/\beta^2}}{\sqrt{1-C_R^2/\alpha^2}}-\frac{1}{\beta^2}\frac{\sqrt{1-C_R^2/\alpha^2}}{\sqrt{1-C_R^2/\beta^2}}\right\}. \tag{A5}$$

This is the response due to loading with delta time-dependence. For the loading by the Heaviside step function in terms of time, the solutions are the same except that the term $\sin(k\eta t)$ is replaced by $(1-\cos(k\eta t))/\eta k$.

Therefore, the expressions of $G_{jk}^{(l)}$ in the (14) take on the form

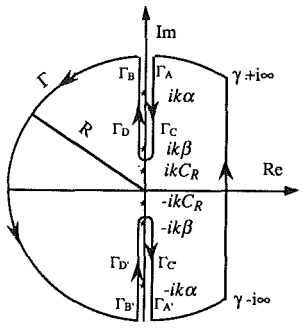


Fig. A1 Integration contour on *p*-complex plane

$$G_{11}^{(1)}=\frac{C_R^2/\beta^2\sqrt{1-C_R^2/\beta^2}}{2\mu K(C_R)}$$

$$G_{11}^{(2)}=-\frac{2}{\pi\mu}\frac{\eta^2/\beta^2(2-\eta^2/\beta^2-1}{(2-\eta^2/\beta^2)^4+16(1-\eta^2/\alpha^2)(\eta^2/\beta^2-1)}$$

$$G_{11}^{(3)}=-\frac{2}{\pi\mu}\frac{\eta^2/\beta^2\sqrt{\eta^2/\beta^2-1}}{(2-\eta^2/\beta^2)^2+4\sqrt{\eta^2/\beta^2-1}\sqrt{\eta^2/\alpha^2-1}} \tag{A6}$$

$$G_{13}^{(1)}=\frac{C_R^2/\beta^2(2-C_R^2/\beta^2)}{4\mu K(C_R)}$$

$$G_{13}^{(2)}=-\frac{4}{\pi\mu}\frac{\eta^2/\beta^2(2-\eta^2/\beta^2)\sqrt{1-\eta^2/\alpha^2}\sqrt{\eta^2/\beta^2-1}}{(2-\eta^2/\beta^2)^4+16(1-\eta^2/\alpha^2)(\eta^2/\beta^2-1)} \tag{A7}$$

$$G_{13}^{(3)}=0$$

$$G_{33}^{(1)}=\frac{C_R^2/\beta^2\sqrt{1-C_R^2/\alpha^2}}{2\mu K(C_R)}$$

$$G_{33}^{(2)}=-\frac{8}{\pi\mu}\frac{\eta^2/\beta^2(1-\eta^2/\alpha^2)\sqrt{\eta^2/\beta^2-1}}{(2-\eta^2/\beta^2)^4+16(1-\eta^2/\alpha^2)(\eta^2/\beta^2-1)}$$

$$G_{33}^{(2)}=-\frac{2}{\pi\mu}\frac{\eta^2/\beta^2\sqrt{\eta^2/\alpha^2-1}}{(2-\eta^2/\beta^2)^2+4\sqrt{\eta^2/\beta^2-1}\sqrt{\eta^2/\alpha^2-1}} \tag{A8}$$

$$G^{(1)}=0$$

$$G^{(2)}=-\frac{2}{\pi\mu}\frac{1}{\sqrt{\eta^2/\beta^2-1}} \tag{A9}$$

$$G^{(3)}=G^{(2)}.$$

Downloaded 03 May 2010 to 171.66.16.20. Redistribution subject to ASME license or copyright; see http://www.asme.org/terms/Terms_Use.cfm

A. Nagarajan
Graduate Student,
Department of Theoretical and Applied Mechanics,
Cornell University,
Ithaca, NY 14853

E. Lutz
402 Richard Place,
Ithaca, NY 14850

S. Mukherjee
Professor,
Department of Theoretical and Applied Mechanics,
Cornell University,
Ithaca, NY 14853
Fellow ASME

A Novel Boundary Element Method for Linear Elasticity With No Numerical Integration for Two-Dimensional and Line Integrals for Three-Dimensional Problems

This paper presents a novel application of the boundary element method to solve problems in linear elasticity. The new method is called the Boundary Contour Method. This approach requires no numerical integration at all for two-dimensional problems and numerical evaluation of line integrals only for three-dimensional problems; even for curved line or surface boundary elements of arbitrary shape! Numerical results are presented for some two-dimensional problems.

Introduction

The conventional boundary element method for linear elasticity usually requires numerical evaluation of line integrals for two-dimensional and surface integrals for three-dimensional problems (see, for example, Mukherjee, 1982). Here, by using the diverge free property of the usual boundary element method intergrand, a new approach is proposed that achieves a further reduction in dimension. Thus, three-dimensional problems can be reduced to numerical evaluation of line integrals over closed contours and two-dimensional problems to merely evaluation of functions at points on the boundary of the body. This is true even for curved line (for two-dimensional problems) and curved surface (for three-dimensional problems) boundary elements of arbitrary shape! Numerical results are presented here for some two-dimensional elasticity problems using this approach.

Theory

Lutz (1991) and Lutz et al. (1992) observed that, for the Laplace equation in two-dimensions or three-dimensions, the usual boundary element method formulation

$$\int_{\partial B} [u(Q)\nabla G(P, Q) - G(P, Q)\nabla u(Q)]\cdot d\mathbf{S} = \alpha u(P) \quad (1)$$

with u the unknown function, G the Green's function, ∇ the gradient operator, $d\mathbf{S} = \mathbf{n}dS$ a vector surface element ($\mathbf{n}$ is a unit outward normal to ∂B at Q), and P and Q source and field points, respectively, on ∂B, and α the included angle at a corner (solid angle for three-dimensions), has the property

$$\nabla\cdot\mathbf{F} = \nabla_Q\cdot(u\nabla G - G\nabla u) = 0 \quad (2)$$

everywhere in the domain except when the point Q coincides with the point P. $\mathbf{F}$ is clearly a vector field which varies with both P and Q since G is a function of both P and Q. The divergence in Eq. (2) is taken with respect to the field Q for a fixed source point P.

This property of $\mathbf{F}$ ensures the existence of a vector function $\mathbf{V}$ such that

$$\mathbf{F} = \nabla\times\mathbf{V} \quad (3)$$

(for proof see Kaplan, 1984). The integral in Eq. (1) is a surface integral in three-dimensions and a line integral in two dimensions. As a direct consequence of Eq. (3), in three dimensions, surface integrals over elements on the boundary of a domain can be reduced to contour integrals around the elements, using Stoke's theorem, so that

$$\int_S \mathbf{F}\cdot d\mathbf{S} = \int_S \nabla\times\mathbf{V}\cdot d\mathbf{S} = \oint_C \mathbf{V}\cdot d\mathbf{r}$$

where S is a surface patch and C is its boundary. For two-dimensional problems, it is sufficient to seek $\Phi(x, y)$ with $\mathbf{V} = \Phi\mathbf{e}_3$ ($\mathbf{e}_i$ are unit, orthogonal base vectors). To $\mathbf{V}$ any function $\mathbf{V}_0$, whose curl is zero, can be added. In three dimensions, again using Stokes's theorem, it is easy to see that this arbitrary function does not contribute to the integral on a closed contour. In two-dimensions there is an arbitrary constant of integration which gets added and subtracted at opposite end points on a boundary element, thereby making no net contribution to the definite integral.

Contributed by the Applied Mechanics Division of THE AMERICAN SOCIETY OF MECHANICAL ENGINEERS for publication in the ASME JOURNAL OF APPLIED MECHANICS.

Discussion on this paper should be addressed to the Technical Editor, Professor Lewis T. Wheeler, Department of Mechanical Engineering, University of Houston, Houston, TX 77204-4792, and will be accepted until four months after final publication of the paper itself in the ASME JOURNAL OF APPLIED MECHANICS.

Manuscript received by the ASME Applied Mechanics Division, Sept. 9, 1992; final revision, Mar. 29, 1993. Associate Technical Editor: A. K. Noor.

Copyright © 1994 by ASME
Downloaded 03 May 2010 to 171.66.16.20. Redistribution subject to ASME license or copyright; see http://www.asme.org/terms/Terms_Use.cfm

This idea can be extended to elasticity problems. The starting point here is the standard boundary element method formulation for linear elasticity (Rizzo, 1967) (it is assumed here that there are no physical body forces)

$$c_{ik}(P)u_i(P) = \int_{\partial B} [U_{ik}(P, Q)\tau_i(Q) - T_{ik}(P, Q)u_i(Q)]dS \tag{4}$$

where $\mathbf{U}$ and $\mathbf{T}$ are the usual Kelvin kernels, $\mathbf{u}$ and τ are displacement and traction, respectively, and $\mathbf{c}$ is the corner tensor. The integral in Eq. (4) is interpreted in the Cauchy principal value sense.

Writing

$$\tau_i = \sigma_{ij}\,\eta_j \tag{5}$$

$$T_{ik} = \Sigma_{ijk}\eta_j \tag{6}$$

where σ is the stress tensor, the integrand on the right-hand side of Eq. (4) can be written as

$$(\sigma_{ij}U_{ik} - \Sigma_{ijk}u_i)\mathbf{e}_j \cdot (\mathbf{n}dS). \tag{7}$$

Here k is a free index. Let $k=1$ and define

$$\overset{*}{u}_i = U_{i1};\ \overset{*}{\sigma}_{ij} = \Sigma_{ij1}. \tag{8}$$

Now let

$$\mathbf{F} = F_j\mathbf{e}_j = (\sigma_{ij}\,\overset{*}{u}_i - \overset{*}{\sigma}_{ij}\,u_i)\mathbf{e}_j. \tag{9}$$

It is easy to show that

$$\nabla\cdot\mathbf{F} = (\sigma_{ij}\,\overset{*}{u}_i - \overset{*}{\sigma}_{ij}\,u_i)_{,j} = (\sigma_{ij}\,\overset{*}{\epsilon}_{ij} - \overset{*}{\sigma}_{ij}\,\epsilon_{ij}) + (\sigma_{ij,\,j}\,\overset{*}{u}_i - \overset{*}{\sigma}_{ij,\,j}\,u_i) \tag{10}$$

where $\epsilon_{ij} = 1/2\ (u_{i,j} + u_{j,\,i})$ and similarly for $\overset{*}{\epsilon}_{ij}$.

The quantity $\nabla\cdot\mathbf{F}$ vanishes everywhere except at the point of singularity provided that $(\mathbf{u}, \sigma)$ correspond to a body force free elastostatic state with the same elastic constants as the Kelvin solution. This property is a direct outcome of Betti's reciprocal theorem which is the basis for the boundary element method formulation for liner elasticity. However, $\nabla\cdot\mathbf{F} = 0$ demonstrates the existence of a vector function $\mathbf{V}$ such that $\mathbf{F} = \nabla\times\mathbf{V}$, where $\mathbf{F}$ is the usual boundary element method integrand given by Eq. (9). Again, as in the case of Laplace's equation, given $\mathbf{F}$ (in both two and three dimensions), one can find a vector function $\mathbf{V}$ such that Eq. (3) is satisfied. Thus, the dimensions of the usual boundary element method integral can be reduced by one in elasticity also.

The situation in two-dimensions is quite simple. Here, with $\mathbf{V} = \Phi\mathbf{e}_3$, Eq. (3) gives

$$F_1 = \frac{\partial\Phi}{\partial y},\ F_2 = -\frac{\partial\Phi}{\partial x} \tag{11}$$

so that

$$\int_1^2 \mathbf{F}\cdot d\mathbf{S} = \int_1^2 \mathbf{F}\cdot\mathbf{n}dS = \Phi(x_2, y_2) - \Phi(x_1, y_1) \tag{12}$$

The same calculations can be easily carried out for values of the free index k (in Eq. (7)) equal to two (for two dimensions).

Thus, in two dimensions, one has the result $(k=1, 2)$

$$\int_{Q_1}^{Q_2} [U_{ik}(P, Q)\tau_i(Q) - T_{ik}(P, Q)u_i(Q)]dS = \Phi_k(Q_2) - \Phi_k(Q_1). \tag{13}$$

The above integral is path-independent!

It is important to observe that the above integrand contains unknown functions $\mathbf{u}$ and τ on ∂B which must satisfy the equations of elasticity. Thus, local shape functions for $\mathbf{u}$ must be chosen such that they satisfy the Navier-Cauchy equations and the shape functions for τ must be derived from those of $\mathbf{u}$.

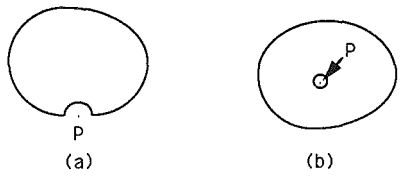


Fig. 1

Generalization

A generalization of the aforementioned proof can be carried out as follows.

Suppose $\mathbf{F}$ is a two-point vector valued function in two or three dimensions such that

$$\int_{\partial B} \mathbf{F}(P, Q)\cdot d\mathbf{S}_Q = 0 \quad \text{for } P \notin B.$$

This is generally the case for many problems in mechanics such as potential theory, plate bending, and linear elasticity.

The preceding equality is also valid for the cases:

(*a*) $P \epsilon \partial B$, provided that the contour is slightly indented locally at P and so as to exclude P from B. (Fig. 1(*a*)).

(*b*) $P \epsilon B$, provided that ∂B is the boundary of a multiply connected region that excludes an infinitesimal circle (for two-dimensions) or sphere (for three-dimensions) centered at P. (Fig. 1(*b*)).

Applying Gauss' theorem to the above, one gets

$$\int_B \nabla_Q\cdot\mathbf{F}(P, Q)dV = 0$$

where, for case (*a*), B is the indented and for (*b*) the punctured domain.

Since B is arbitrary,

$$\nabla_Q\cdot\mathbf{F}(P, Q) = 0$$

at every point P except at the point of singularity $P=Q$. This result is intrinsically linked to boundary element method formulations for linear problems.

Related Work

Recent work by Zienkiewicz and his co-workers on applications of the Trefftz method in boundary elements should be mentioned here. Jin, Cheung, and Zienkiewcz (1990) have applied the method to planar elasticity problems based on the stress function approach while Cheung, Jin, and Zienkiewicz (1989, 1991) have solved the harmonic and Helmholtz equations, respectively.

In the work on linear elasticity (Jin, Cheung, and Zienkiewicz, 1990), the authors set up a boundary element system of equations in which the weighting and/or trial functions are derived from complete solutions for the stress function in the domain of the body (hence the Trefftz method). This avoids the use of singular kernels in the boundary element method equations. The rest of the treatment follows the usual boundary element method approach in that interpolation functions must be chosen for the boundary element geometries and the physical variables on the boundary, and integrations must be carried out over boundary elements. This work of Zienkiewciz's group is analogous to the present work to the extent that global solutions in the domain of the body are also used in their work. The present work, however, is quite different from that of Zienkiewcicz's group in the sense that no numerical integration over boundary elements is required here.

Other related work for two-dimensional problems, this time using complex variables, is due to Piltner and Taylor (1990) and Lee (1993). In the both cases, the starting point is the use of complex stress and displacements potentials based on the classical work of Muskhelishvili (1963). The complex potentials

Downloaded 03 May 2010 to 171.66.16.20. Redistribution subject to ASME license or copyright; see http://www.asme.org/terms/Terms_Use.cfm

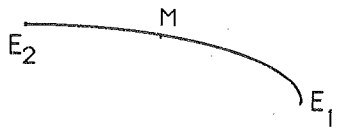


Fig. 2 Boundary element

are represented in terms of basis functions by the Cauchy integral formula. These unknown complex basis functions are discretized on boundary elements and nodal unknowns are solved for by using standard collocation methods. Piltner and Taylor (1990) carry out closed-form integrals of the basis shape functions on straight boundary elements. Lee (1993) realizes that these complex integrals on boundary elements are, in fact, path independent (provided suitable branch cuts are used). In this sense, Lee's work is analogous to the work presented in this paper. Lee's work, however, is based on complex variables theory and is restricted to two-dimensional problems. The present paper uses real variables and the idea is valid for two as well as for three-dimensional problems.

Two-Dimensional Plane Strain With Linear Shape Functions

Consider a general curved boundary element with E_1 and E_2 the end points and M the middle point of the element (Fig. 2).

Linear shape functions for $\mathbf{u}$ are chosen for each element such that

$$\mathbf{u} = (a_1 + b_1 x + c_1 y)\mathbf{e}_1 + (a_2 + b_2 x + c_2 y)\mathbf{e}_2 \tag{14}$$

where, as before, x and y are coordinates with respect to a global coordinate system.

From the equations of elasticity (e.g., Timoshenko and Goodier, 1970)

$$\tau = \{[(\lambda + 2\mu)b_1 + \lambda c_2]n_1 + \mu(b_2 + c_1)n_2\}\mathbf{e}_1 + \{\mu(b_2 + c_1)n_1 + [(\lambda + 2\mu)c_2 + \lambda b_1]n_2\}\mathbf{e}_2 \tag{15}$$

where λ and μ are the Lamé constants for the material.

Higher-order approximations for $\mathbf{u}$, which also satisfy the Navier-Cauchy equation, can be obtained systematically from the Papkovitch-Neuber potentials.

The six constants in Eq. (14) are related to six "primary" physical quantities on a boundary element by a transformation matrix T

$$\{p\} = [T]\{c\} \tag{16}$$

where $p^T = (u_1^{(E_1)}\ u_2^{(E_1)}\ \tau_1^{(M)}\ \tau_2^{(M)}\ u_1^{(E_2)}\ u_2^{(E_2)})$ and $c^T = (a_1\ b_1\ c_1\ a_2\ b_2\ c_2)$. The elements of the matrix $\mathbf{T}$ depend on the nodal coordinates and the normal at M. The variables in $\mathbf{p}$ are chosen such that the matrix $\mathbf{T}$ is invertible.

For convenience, a new coordinate system (ξ, η), centered at a source point E_1 on a boundary element, is introduced. The ξ and η axes are parallel to the global x and y-axes. The shape functions in Eq. (14) remain linear in ξ and η with new constants $\hat{a}_1$ and $\hat{a}_2$ instead of a_1 and a_2. Thus,

$$\mathbf{u} = (\hat{a}_1 + b_1\xi + c_1\eta)\mathbf{e}_1 + (\hat{a}_2 + b_2\xi + c_2\eta)\mathbf{e}_2. \tag{17}$$

It is easy to show that $\hat{a}_1 = a_1 + b_1 x_1 + c_1 y_1$ and $\hat{a}_2 = a_2 + b_2 x_1 + c_2 y_1$, where (x_1, y_1) are the coordinates of the source point with respect to the x and y-axes. Combining this with Eq. (14),

$$\mathbf{u} = ([a_1 + b_1 x_1 + c_1 y_1] + b_1\xi + c_1\eta)\mathbf{e}_1 + ([a_2 + b_2 x_1 + c_2 y_1] + b_2\xi + c_2\eta)\mathbf{e}_2. \tag{18}$$

This representation is used in the numerical implementation. The traction τ retains the same form as in Eq. (15).

The shape function in Eq. (18) can be be expressed as a linear combination of six linearly independent solutions of the Navier-Cauchy equations:

$$\begin{aligned}
&(1)\quad u_1 = 1,\ u_2 = 0\\
&(2)\quad u_1 = \xi,\ u_2 = 0\\
&(3)\quad u_1 = \eta,\ u_2 = 0\\
&(4)\quad u_1 = 0,\ u_2 = 1\\
&(5)\quad u_1 = 0,\ u_2 = \xi\\
&(6)\quad u_1 = 0,\ u_2 = \eta.
\end{aligned} \tag{19}$$

Potential functions must be obtained for each of these six states, for each of the directions $k = 1$ and $k = 2$ in Eq. (13). Let ϕ_i, $i = 1, 6$ denote potentials for the above six states, for $k = 1$. These correspond to the Kelvin force in the $\mathbf{e}_1$ direction. The function Φ_1 in Eq. (13) is a linear combination of ϕ_i, $i = 1, 6$. The ϕ_i's can be calculated individually by using Eq. (11), with ϕ_i replacing Φ and ξ and η replacing x and y, respectively. Clearly, F_1 and F_2 should be expressed as functions of ξ and η. As an example, for ϕ_1, $F_1 = -\Sigma_{111}$ and $F_2 = -\Sigma_{121}$, where Σ is defined in Eq. (6).

Similarly, let ϕ_i, $i = 7, 12$ denote potentials for the six states above for $k = 2$. Now Φ_2 in Eq. (13) is a linear combination of ϕ_i, $i = 7, 12$. The potentials ϕ_i have been calculated in closed form using the independent solutions from Eq. (19). For example, the functions ϕ_1 and ϕ_4, in terms of these local coordinates, are

$$\phi_1 = \frac{1}{2\pi}\tan^{-1}\frac{\eta}{\xi} + \frac{1}{4\pi(1-\nu)}\frac{\eta\xi}{r^2} \tag{20}$$

$$\phi_4 = \frac{1}{4\pi(1-\nu)}\left[\frac{\eta^2}{r^2} + (1-2\nu)\ln r\right] \tag{21}$$

where $r^2 = \xi^2 + \eta^2$ and ν is Poisson's ratio.

The functions ϕ_i, $i = 1, 12$ are given in the Appendix. It should be noted that Φ_1 in Eq. (13) is composed of ϕ_i, $i = 1, 6$ and Φ_2 is composed of ϕ_i, $i = 7, 12$.

Discretized Equations

The boundary ∂B is discretized, as usual, into N elements. These elements can be curved as mentioned before. The shape functions for $\mathbf{u}$ and τ are given by Eqs. (18) and (15). The boundary element method equations are enforced only at the end points of elements and not at their midpoints M.

The integral over an element

$$\int_{E_1}^{E_2} \mathbf{F}\cdot d\mathbf{S} \text{ (with } k = 1 \text{ in Eq. (13))}$$

is a linear combination of $\phi_i(E_2) - \phi_i(E_1)$, $i = 1, 6$ with a_j, b_j, c_j, $j = 1, 2$ as coefficients. Similarly, with $k = 2$ in Eq. (13), one gets linear combinations of $\phi_i(E_2) - \phi_i(E_1)$, $i = 7, 12$, again with a_j, b_j and c_j, $j = 1, 2$ as coefficients. It should be emphasized again that these expressions are obtained from numerical evaluations of the potentials ϕ_i, $i = 1, 12$, at E_1 for each element, and no numerical integration is necessary.

The foregoing integrals, for one element, can be written as products of known row vectors and the column vector $\mathbf{c}$ defined below Eq. (16). Such integrals, over all the elements, are assembled in the form

$$[L]\{c\}.$$

Next, Eq. (16) is used to express the vector $\mathbf{c}$ in terms of the physical quantities in the vector $\mathbf{p}$. The global system of equations is condensed out to reflect continuity of displacements across elements in the usual way. This gives a discretized form of the right-hand side of Eq. (4). The left-hand side vector of Eq. (4) contains contributions from the terms $c_{ik}u_i$ and these are moved over to the right-hand side.

It is instructive at this stage to consider the number of equations and unknowns that result from discretization. As an example, Fig. 3 illustrates a quarter of a plate with a cutout

Downloaded 03 May 2010 to 171.66.16.20. Redistribution subject to ASME license or copyright; see http://www.asme.org/terms/Terms_Use.cfm

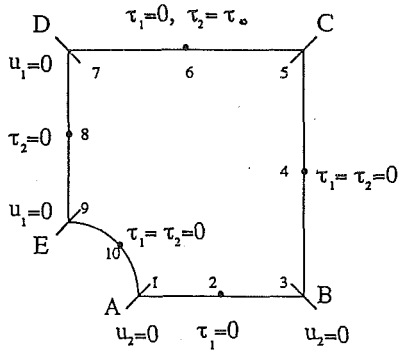


Fig. 3 A plate with a cutout with $n_1=n_2=n_3=n_4=n_5=1$. Prescribed quantities are shown in the figure.

under remote uniaxial stress. *AB* and *DE* are symmetry lines. The modeling of corners is very easy in this formulation since only displacement components are prescribed at corners and traction jumps around corners, if any, are taken care of by the formulation.

Suppose the number of boundary elements on the sides *AB*, *BC*, *CD*, *DE*, and *EA* in Fig. 3 are n_1, n_2, n_3, n_4, and n_5, respectively. (Figure 3 shows only one element on each segment for clarity.) The situation regarding equations and unknowns can be viewed in two different but equivalent ways.

(*a*) The total number of elements $=n_1+n_2+n_3+n_4+n_5=n$.

The unknowns are a_i, b_i, c_i $i=1, 2$, on each element.

Therefore, the number of unknowns $=6n$.

The number of prescribed physical quantities on the sides *AB*, *BC*, *CD*, *DE*, and *EA* are $2n_1+1$, $2n_2$, $2n_3$, $2n_4+1$ and $2n_5$, respectively.

Hence, the total number of prescribed quantities $=2n+2$.

Displacement continuity equations (two at the start of each element) $=2n$.

Boundary element method equations (two at the start of each element) $=2n$.

Finally, the total number of equations and prescribed quantities $=6n+2$.

Thus, one gets two extra equations in this case.

(*b*) The total number of physical quantities (two displacement components at starts and two traction components at the midpoints of elements) $=4n$.

The total number of prescribed physical quantities $=2n+2$.

Therefore, the total number of physical unknowns $=2n-2$.

The total number of boundary element method equations $=2n$.

Again, one has two extra equations.

The assembled system of equations involves only the physical quantities as in (*b*) above. Thus, in this example one would have $2n$ equations and $2n-2$ unknowns. In general, the system of equations can be overdetermined.

Finally, after the usual switching of columns, the result is

$$[k]\{x\}=\{y\} \tag{22}$$

where **x** contains the unknown boundary quantities and **y** is known in terms of prescribed boundary quantities and geometrical and material data of the problem.

Post-Processing for Other Physical Variables

There are other physical quantities, namely tractions at the ends of elements and displacements at their middle points, which have not figured in the calculations so far. These quantities, however, can be easily calculated at a post-processing step. The idea here is to use Eq. (16) to calculate the vector **c** from **p** and then use Eqs. (14) and (15) to find the remaining quantities, namely **u** at midpoints of elements and τ at the end points.

The boundary stresses σ_{ij}, in this formulation, can be obtained directly from the displacement shape functions by using Hooke's law:

$$\sigma_{ij}=\lambda\, u_{k,\,k}\,\delta_{ij}+\mu(u_{i,\,j}+u_{j,\,i}) \tag{23}$$

where δ_{ij} is the Kronecker delta. This step is justified since the shape functions for **u** are valid not just on an element, but in its neighborhood as well. Also, tractions have already been derived based on this assumption (see Eq. (15)).

Evaluation of strain components at points inside a body require transformation of the strain boundary element method equation at an internal point *p* (see, for example, Mukherjee, 1982) to an integrated form analogous to Eq. (13). This can be done since the integrand is again divergence free. Stress calculations would then follow from Hooke's law.

Numerical Results

In all the following examples, $E=2.5$ (in consistent units) and $\nu=0.3$.

(a) Examples Involving Displacement Fields. Two numerical examples, for plane strain linear elasticity have been solved using this approach. In each case, the region of interest is a circle of unit radius centered at the point (2, 2) in the (x, y) plane. The boundary of the circle is divided into N elements with $N=20$ and $N=30$, respectively. Displacement fields, which are exact solutions of the Navier-Cauchy equations of elasticity, have been imposed at suitable nodes on the boundary of the circle. The expressions used for the boundary normals are exact.

The two displacement fields chosen for this purpose are

(*a*) $u_1=-2(1-2\nu)xy$, $u_2=x^2$

(*b*) $u_1=\dfrac{x}{x^2+y^2}$, $u_2=\dfrac{y}{x^2+y^2}$.

It is interesting to note that case (b) is a "perfect planar" problem, in the sense that $u_3=0$ (from the plain strain assumption) and $\sigma_{33}=0$ as well.

Numerical results for the tractions on the boundary of the circle are compared against exact solutions, in Figs. 4–5. The numerical plots are obtained from the calculated values of τ_1 and τ_2 at the midpoints of the boundary elements. The results are seen to agree very well, especially for $N=30$.

(b) Plates With Cutouts. A plate with an elliptical cutout is loaded biaxially by remote tractions S_1 and S_2. Only a quarter of the plate is modeled here due to symmetry. The plate geometry, boundary element method mesh, and loading are shown in Fig. 6. (The midpoints of elements are not shown in this figure). Calculation of c_{ij} at corners and $O(1/r)$ singular integrals are avoided by using rigid-body translation (see, for example, Mukherjee, 1982).

Several cases are considered here:

(1) $S_1=0$, $S_2=1$ (i.e., unaxial loading) for $a/b=4/3$ and $a/b=2$, respectively. The normalized tangential stress σ_{tt}/S_2, around the quarter ellipse, is shown as a function of $2\theta/\pi$ (where θ is the eccentric angle of the ellipse) in Fig. 7. The boundary element method numerical solutions show excellent agreement with the analytical solutions in both cases. The analytical solution used here is the one for an elliptical hole in an infinite plate (Timoshenko and Goodier, 1970), which is

$$\sigma_{tt}=S_2\,\frac{1+2m-m^2+2\cos 2\theta}{1+m^2+2m\cos 2\theta}$$

where $m=(b-a)/(b+a)$.

(2) In this case, $a/b=2$, $S_1=1$ and $S_2=1/2$. This is an interesting case, where, using the methods of Muskhelishvili (1963), one can show that the tangential stresses around the

Downloaded 03 May 2010 to 171.66.16.20. Redistribution subject to ASME license or copyright; see http://www.asme.org/terms/Terms_Use.cfm

ellipse is uniform. Its value is $\sigma_{tt}/S = 1.5$ in this case (see, for example, Banichuk, 1983).

A uniform mesh with ten boundary elements is used around the quarter ellipse. The rest of the mesh is the same as shown in Fig. 6. The boundary element method results for σ_{tt}, computed at the midpoints of the elements on the elliptical cutout, are again very accurate. Most errors (compared to the analytical solution) are less than 0.5 percent. The worst error, at $\theta = 5$ deg, is 1.3 percent.

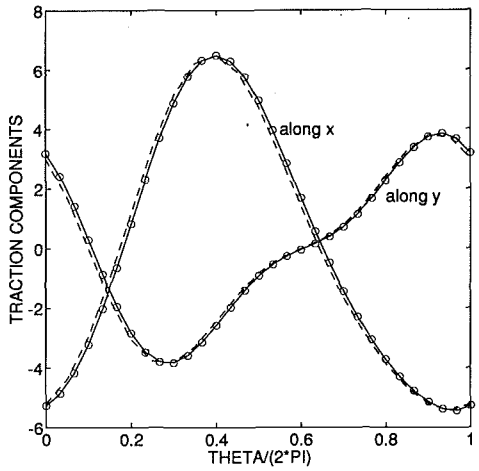


Fig. 4 Traction components along the x and y directions for example (a); ——— *exact solution,* - - - - - *with 20 elements,* o o o o *with 30 elements*

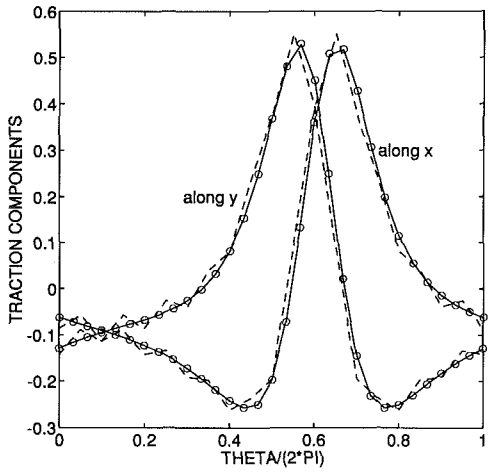


Fig. 5 Traction components along the x and y directions for example (b); ——— *exact solution,* - - - - - *with 20 elements,* o o o o *with 30 elements.*

Conclusions

A new boundary element method is presented in this paper for linear elasticity. This method requires no numerical integration, even for general curved elements in two-dimensions, and only requires numerical evaluation of contour integrals for three-dimensional problems. Numerical results for some two-dimensional problems show that the method performs very well.

One of the interesting applications of this work lies in adaptive meshing. The finite element method requires meshing of three-dimensional regions for three-dimensional and two-dimensional regions for two-dimensional problems. The standard boundary element method for linear elasticity requires meshing of only two-dimensional regions for three-dimensional problems and curves for two-dimensional problems. There is, for example, a very nice recent paper by Guiggiani (1990) on the subject of adaptive meshing, for two-dimensional problems, by the standard boundary element method.

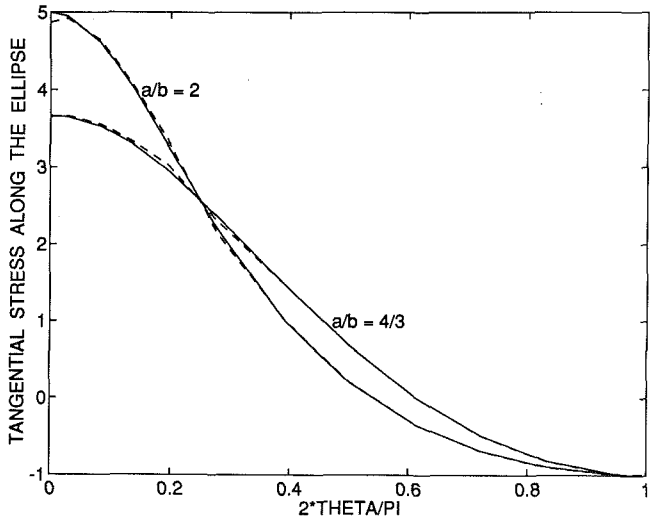


Fig. 6 Plate with an elliptical cutout. Dimensions, mesh, and boundary conditions.

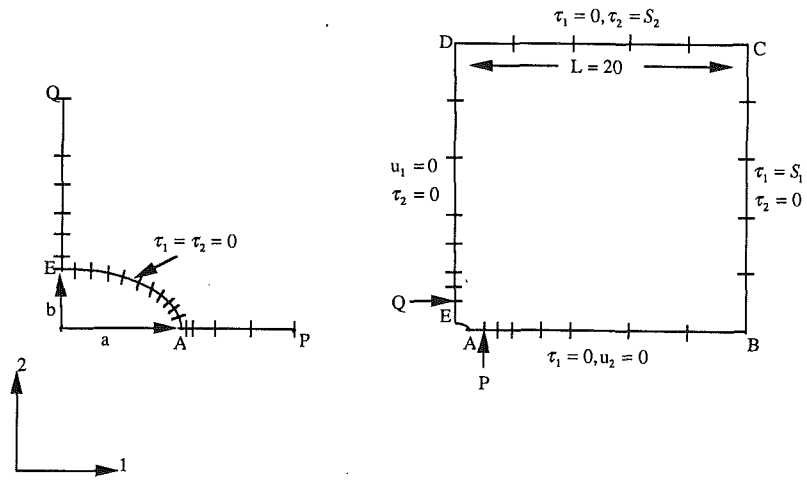


Fig. 7 Normalized tangential stress around the quarter ellipses; ——— *exact solution,* - - - - - *boundary element method solution.*

Downloaded 03 May 2010 to 171.66.16.20. Redistribution subject to ASME license or copyright; see http://www.asme.org/terms/Terms_Use.cfm

The method presented in this paper requires only the evaluation of contour integrals for three-dimensional problems. For adaptive meshing, although surface elements will still have to be subdivided, only line integrals around their boundaries need to be evaluated. This is expected to be a big advantage compared to any other method.

Acknowledgments

This research has been supported by NSF Grant Number MSS-8922185 to Cornell University and the University of Arizona.

References

Banichuk, N. V., 1983, *Problems and Methods of Optimal Structural Design*, Plenum Press, New York.

Cheung, Y. K., Jin, W. G., and Zienkiewicz, O. C., 1989, "Direct Solution Procedure for Solution of Harmonic Problems Using Complete, Non-Singular, Trefftz Functions," *Communications in Applied Numerical Methods*, Vol. 5, pp. 159–169.

Cheung, Y. K., Jin, W. G., and Zienkiewicz, O. C., 1991, "Solution of Helmholtz Equation by Trefftz Method," *International Journal for Numerical Methods in Engineering*, Vol. 32, pp. 63–78.

Guiggiani, M., 1990, "Error Indicators for Adaptive Mesh Refinement in the Boundary Element Method—A New Approach," *International Journal for Numerical Methods in Engineering*, Vol. 29, pp. 1247–1269.

Jin, W. G., Cheung, Y. K., and Zienkiewicz, O. C., 1990, "Application of the Trefftz Method Plane Problems," *International Journal of Numerical Methods in Engineering*, Vol. 30, pp. 1147–1161.

Kaplan, W., 1984, *Advanced Calculus*, 3rd ed., Addison-Wesley.

Lee, K. J., 1993, "A Boundary Element Technique for Plane Isotropic Elastic Media Using Complex Variable Techniques," *Computational Mechanics*, Vol. 11, pp. 83–91.

Lutz, E. D., 1991, "Numerical Methods for Hypersingular and Near Singular Boundary Integrals in Fracture Mechanics," Ph.D. Thesis, Department of Computer Science, Cornell University, Ithaca, New York.

Lutz, E. D., Back, A., Gray, L., and Ingraffea, A., 1992, *Systematic Conversion of Boundary Integrals to Contour Integrals*, Technical Report, 92-6, April 1992, Structural Engineering, School of Civil and Environmental Engineering, Cornell University, Ithaca, NY.

Mukherjee, S., 1982, *Boundary Element Methods in Creep and Fracture*, Elsevier Applied Science, London, UK.

Muskhelishvili, N. I., 1963, *Some Basic Problems of the Mathematical Theory of Elasticity*, Noordhoff, Groningen, The Netherlands.

Piltner, R., and Taylor, R. L., 1990, "A Boundary Element Algorithm Using Compatible Boundary Displacements and Tractions," *International Journal for Numerical Methods in Engineering*, Vol. 29, pp. 1323–1341.

Rizzo, F. J., 1967, "An Integral Equation Approach to Boundary Value Problems of Classical Elastostatics," *Quarterly of Applied Mathematics*, Vol. 25, pp. 83–95.

Timoshenko, S. P., and Goodier, J. N., 1970, *Theory of Elasticity*, 3rd ed., McGraw-Hill, New York.

Zhang, Q., and Mukherjee, S., 1991, "Design Sensitivity Coefficients for Liner Elastic Bodies with Zones and Corners by the Derivative Boundary Element Method," *International Journal of Solids and Structures*, Vol. 27, pp. 983–998.

APPENDIX

$$\phi_1(\xi, \eta) = \frac{1}{4\pi(1-\nu)}\left[2(1-\nu)\tan^{-1}\left(\frac{\eta}{\xi}\right) + \frac{\xi\eta}{r^2}\right]$$

$$\phi_2(\xi, \eta) = \frac{-1}{4\pi(1-\nu)} \times \left[\frac{\eta^3}{r^2} + \frac{(1-\nu)(3-4\nu)\eta\,\ln(r) - (4\nu^2-9\nu+4)\eta}{(1-2\eta)}\right]$$

$$\phi_3(\xi, \eta) = \frac{-1}{4\pi(1-\nu)}\left[(1-2\nu)\xi + \frac{\xi^3}{r^2} - \frac{(3-4\nu)}{2}\,\xi\,\ln(r)\right]$$

$$\phi_4(\xi, \eta) = \frac{-1}{4\pi(1-\nu)}\left[\frac{\eta^2}{r^2} + (1-2\nu)\,\ln(r)\right]$$

$$\phi_5(\xi, \eta) = \frac{-1}{4\pi(1-\nu)}\left[\frac{\xi^3}{r^2} - \frac{(3-4\nu)}{2}\,\xi\,\ln(r)\right]$$

$$\phi_6(\xi, \eta) = \frac{1}{4\pi(1-\nu)}\left[\frac{\eta^3}{r^2} - \frac{\nu(3-4\nu)\eta\,\ln(r) - \nu\eta}{(1-2\nu)}\right]$$

$$\phi_7(\xi, \eta) = -\phi_4(\eta, \xi)$$

$$\phi_8(\xi, \eta) = -\phi_6(\eta, \xi)$$

$$\phi_9(\xi, \eta) = -\phi_5(\eta, \xi)$$

$$\phi_{10}(\xi, \eta) = -\phi_1(\eta, \xi)$$

$$\phi_{11}(\xi, \eta) = -\phi_3(\eta, \xi)$$

$$\phi_{12}(\xi, \eta) = -\phi_2(\eta, \xi)$$

Downloaded 03 May 2010 to 171.66.16.20. Redistribution subject to ASME license or copyright; see http://www.asme.org/terms/Terms_Use.cfm

A Strip Element Method for Stress Analysis of Anisotropic Linearly Elastic Solids

G. R. Liu

J. D. Achenbach
Fellow ASME.

Center for Quality Engineering and Failure Prevention, Northwestern University, Evanston, IL 60208-3020

A new numerical method, the strip element method, is presented for the stress analysis of anisotropic linearly elastic solids. For two-dimensional problems the domain is discretized in one direction into strip elements. By using the principle of virtual work, approximate governing differential equations are derived for the field dependence in the second direction. These differential equations can be solved analytically. For infinite bodies, some special features such as infinite elements and nonreflecting boundary conditions are introduced and a viscoelastic nonreflecting boundary is also presented. Numerical results for static and dynamic problems are presented and compared with exact solutions. Very good agreement is observed. The strip element method maintains the advantages of the finite element method, but it requires much less data storage. The technique can easily be extended to solids that are inhomogeneous in one direction.

1 Introduction

A new technique is presented for dynamic stress analysis of anisotropic and/or inhomogeneous solids. The technique, which is called the strip element method, has definite advantages over the finite element method and the boundary element method.

A disadvantage of the finite element method is the need for a large memory. To solve the memory problem, many storage techniques have been developed, such as bandwidth storage (see, e.g., Meyer, 1973, 1975) and sky-line storage techniques (see, e.g., Bathe et al., 1976; Felippa, 1975; Jennings, 1966). In another approach a special finite element method, the finite strip method, has been developed for plate analysis (Cheung, 1976). The finite strip method has also been used to investigate harmonic waves in anisotropic laminated strips (Liu et al., 1990b). In the finite strip method, the problem domain is divided into elongated elements, and series expansions with a few terms are taken in the direction of elongation. The memory required in the finite strip method is usually much smaller than for the finite element method, at least for problems with simple boundaries and certain special boundary conditions. Even though these special approaches may reduce the required memory, data storage problems may still reduce the accuracy of solutions or may force a reduction of the scale of the computation.

Another technique to reduce data storage is to combine the finite element method with Fourier integral methods (Liu et al., 1991b). In this technique three-dimensional problems are reduced to two-dimensional ones by discretization in one direction. The FFT and modal analysis techniques can be used for the solution in the other two directions. This technique is very efficient for laminated anisotropic infinite plates.

The boundary element method (see, e.g., Beskos, 1987) usually requires only a boundary surface discretization. This makes the boundary element method more efficient than the finite element method for many problems. The boundary element method has been successfully used for a great variety of problems. Achenbach et al. (1991) and Ahn et al. (1991) have used the boundary element method to solve very complicated wave propagation problems for the geometry of a line-focus acoustic microscope. The boundary element method is, however, difficult to apply for anisotropic and inhomogeneous solids, because there are no simple Green's function for such materials.

There are advantages in combining the finite element method and the boundary element method to create optimum numerical schemes. Recently, Liu et al. (1992) have presented a finite element method/boundary element method technique to analyze the wave fields generated by a line-focus acoustic microscope on the surface of anisotropic-layer/substrate configurations.

For wave propagation problems in unbounded laminated plates, Liu et al. (1990c) have discussed the dispersion of Lamb waves in anisotropic laminated plates. An exact transcendental dispersion equation for laminated plates was obtained and this equation was solved by using a search procedure to find the frequency for a given wave number. Recently, scattered Lamb waves have been investigated by Al-Nassar et al. (1991) and Karunasena et al. (1991), who used a combined finite element

Contributed by the Applied Mechanics Division of THE AMERICAN SOCIETY OF MECHANICAL ENGINEERS for publication in the ASME JOURNAL OF APPLIED MECHANICS.

Discussion on this paper should be addressed to the Technical Editor, Professor Lewis T. Wheeler, Department of Mechanical Engineering, University of Houston, Houston, TX 77204-4792, and will be accepted until four months after final publication of the paper itself in the ASME JOURNAL OF APPLIED MECHANICS.

Manuscript received by the ASME Applied Mechanics Division, Sept. 23, 1992; final revision, Feb. 23, 1993. Associate Technical Editor: D. K. Datta.

Copyright © 1994 by ASME
Downloaded 03 May 2010 to 171.66.16.20. Redistribution subject to ASME license or copyright; see http://www.asme.org/terms/Terms_Use.cfm

and Lamb wave modal expansion method. Dispersion equations for Lamb waves were obtained by an exact method. The Lamb modes were found by using Müller's method, a numerically complex roots search procedure, which calculates the wave number for a given frequency. Another efficient way to find Lamb wave modes for unbounded laminated media is to use the infinite layer element method (see, e.g., Dong et al., 1972; Waas, 1972; Nelson et al., 1973; Dong et al., 1985; Kausel, 1986; Datta et al., 1988; Liu et al., 1991c). In this method, the dispersion relation becomes an eigenvalue equation, hence it can be solved easily to find the frequency for a given wave number or to find the wave number for a given frequency.

In this paper a new numerical method, the strip element method is presented. In this method, the problem domain is first divided into a set of strip elements. Then a dimension-reduced system of approximate differential equations is derived for the strip elements by using the principle of virtual work. The equations are solved analytically. This method keeps many advantages of the finite element method and boundary element method, but it requires much less data storage. Just like the finite element method, it can be used for anisotropic solids, but like the boundary element method, it only requires a small memory. A similar idea has been presented by Liu et al. (1990a, 1991a) for harmonic wave modes in anisotropic laminated bars. However, in the present paper the approach is extended into a general numerical method. To deal with infinite bodies, some special features, such as infinite elements and nonreflecting boundary conditions, are introduced. A viscoelastic nonreflecting boundary is also presented. The accuracy and efficiency of the strip element method are demonstrated by static and dynamic examples.

2 Formulation

Consider two-dimensional dynamic problems for an anisotropic solid. Following Kausel's formulation (Kausel, 1986), the system of governing differential equations is expressed as

$$\mathbf{W}=\rho\ddot{\mathbf{U}}-\mathbf{L}^T\sigma=\mathbf{0}, \tag{1}$$

where a dot indicates differentiation with respect to time, and a superscript "T" denotes the transposed matrix or vector. The differential operator matrix $\mathbf{L}$ may be written as

$$\mathbf{L}^T=\begin{bmatrix}\dfrac{\partial}{\partial x} & \mathbf{0} & \dfrac{\partial}{\partial y}\\ \mathbf{0} & \dfrac{\partial}{\partial y} & \dfrac{\partial}{\partial x}\end{bmatrix}. \tag{2}$$

Also

$$\sigma^T=\{\sigma_{xx}\ \sigma_{yy}\ \sigma_{xy}\},\quad \epsilon^T=\{\epsilon_{xx}\ \epsilon_{yy}\ \epsilon_{xy}\}, \tag{3}$$

$$\sigma=\mathbf{c}\epsilon,\quad \epsilon=\mathbf{L}\mathbf{U},\quad \mathbf{U}^T=\{u\ v\}, \tag{4}$$

where σ_{ij} $(i, j=x, y)$ and ϵ_{ij} are the stress and strain tensors, while u and v are the displacement components in the x and y directions, respectively. In Eq. (4) $\mathbf{c}=(c_{ij})$, $i,j=1, 2, 3$, defines the matrix of elastic constants. Using Eqs. (3) and (4), Eq. (1) can be rewritten as

$$\mathbf{W}=\rho\ddot{\mathbf{U}}-\mathbf{L}^T\mathbf{c}\mathbf{L}\mathbf{U}=\mathbf{0}. \tag{5}$$

Next, the operator matrix $\mathbf{L}$ is written as

$$\mathbf{L}=\mathbf{L}_x\frac{\partial}{\partial x}+\mathbf{L}_y\frac{\partial}{\partial y}, \tag{6}$$

where the matrices $\mathbf{L}_x$ and $\mathbf{L}_y$ can be obtained from Eq. (2) by inspection. By using this definition of $\mathbf{L}$ the expansion of the product, $\mathbf{L}^T\mathbf{c}\mathbf{L}$ may be written as

$$\mathbf{L}^T\mathbf{c}\mathbf{L}=\mathbf{D}_{xx}\frac{\partial^2}{\partial x^2}+2\mathbf{D}_{xy}\frac{\partial^2}{\partial x\partial y}+\mathbf{D}_{yy}\frac{\partial^2}{\partial y^2}, \tag{7}$$

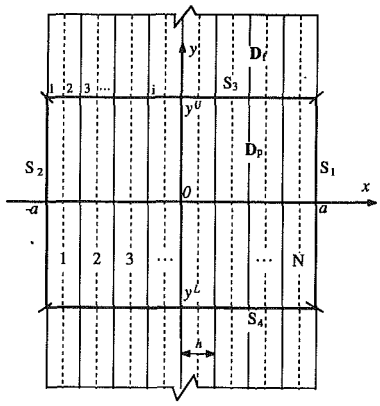


Fig. 1 Problem domain and coordinate system

where the matrices $\mathbf{D}_{xx}$, $\mathbf{D}_{xy}$, and $\mathbf{D}_{yy}$ are given in the Appendix.

The stresses acting on a plane $y=$ constant can be written as

$$\mathbf{R}_y=\mathbf{L}_y^T\mathbf{c}\mathbf{L}\mathbf{U}, \tag{8}$$

and the stresses acting on a plane $x=$ constant can be written as

$$\mathbf{R}_x=\mathbf{L}_x^T\mathbf{c}\mathbf{L}\mathbf{U}. \tag{9}$$

3 The Basic Idea of the SEM

Consider a domain $\mathbf{D}_f$ defined by $x=\pm a$, $-\infty<y<\infty$, which includes the domain of problem definition $\mathbf{D}_p$ with boundaries S_1, S_2, S_3, and S_4 as shown in Fig. 1. The domain $\mathbf{D}_f$ is divided into N infinite strip elements. The displacement field in an element is assumed to be of the form

$$\mathbf{U}(x, y)=\mathbf{N}(x)\mathbf{V}(y)\exp(-i\omega t), \tag{10}$$

where $i=\sqrt{-1}$. The variables t and ω are, respectively, time and angular frequency. The matrix $\mathbf{N}$ and the vector $\mathbf{V}$ are given by

$$\mathbf{N}=\left[\left(1-3\frac{x}{h}+2\frac{x^2}{h^2}\right)\mathbf{I}\quad 4\left(\frac{x}{h}-\frac{x^2}{h^2}\right)\mathbf{I}\quad \left(-\frac{x}{h}+2\frac{x^2}{h^2}\right)\mathbf{I}\right], \tag{11}$$

$$\mathbf{V}^T=\{\mathbf{V}_L^T\ \mathbf{V}_M^T\ \mathbf{V}_R^T\}. \tag{12}$$

In Eq. (11), h is the width of the strip element, and the matrix $\mathbf{I}$ is the 2 by 2 identity matrix. In Eq. (12), $\mathbf{V}_L$, $\mathbf{V}_M$, and $\mathbf{V}_R$, which denote the displacement amplitude vectors on the left, middle, and right node lines of the element, are functions of y.

Applying the principle of virtual work to the strip element, we have

$$\delta\mathbf{V}^T\mathbf{T}=\delta\mathbf{V}^T\mathbf{S}+\int_o^h\delta\mathbf{U}^T\mathbf{W}dx, \tag{13}$$

where $\mathbf{T}$ is the external traction vector acting on the three node lines of the element, and $\mathbf{S}$ is the stress vector on the boundary lines of the element, where

$$\mathbf{S}^T=\{\mathbf{R}_x^T|_{x=o}\ \mathbf{0}_M^T\ \mathbf{R}_x^T|_{x=h}\}. \tag{14}$$

The external traction is taken in the form

$$\mathbf{T}=\overline{\mathbf{T}}\exp(-i\omega t), \tag{15}$$

where $\overline{\mathbf{T}}$ is the amplitude vector. Substituting Eqs. (10)–(12) and (14)–(15) into Eq. (13), integrating over the thickness of the element, and requiring that the result is valid for arbitrary virtual displacements $\delta\mathbf{V}$, we obtain the following set of approximate differential equations for an element.

$$\overline{\mathbf{T}}=\left[-\mathbf{A}_2\frac{\partial^2\mathbf{V}}{\partial y^2}+\mathbf{A}_1\frac{\partial\mathbf{V}}{\partial y}+\mathbf{A}_0\mathbf{V}-\omega^2\mathbf{M}\mathbf{V}\right], \tag{16}$$

where the matrices $\mathbf{A}_i$ $(i=0, 1, 2)$ and $\mathbf{M}$ are given in the

Downloaded 03 May 2010 to 171.66.16.20. Redistribution subject to ASME license or copyright; see http://www.asme.org/terms/Terms_Use.cfm

Appendix. Assembling all the strip elements of domain $\mathbf{D}_f$, a system of approximate differential equations for the whole domain $\mathbf{D}_f$ is obtained as

$$\overline{\mathbf{T}}_t = \left[-\mathbf{A}_{2t} \frac{\partial^2 \mathbf{V}_t}{\partial y^2} + \mathbf{A}_{1t} \frac{\partial \mathbf{V}_t}{\partial y} + \mathbf{A}_{0t}\mathbf{V}_t - \omega^2 \mathbf{M}_t \mathbf{V}_t \right], \quad (17)$$

where the subscript "t" denotes matrices or vectors for the total domain. The matrices $\mathbf{A}_{it}$ $(i=0, 1, 2)$, $\mathbf{M}_t$ and the vectors $\mathbf{T}_t$, $\mathbf{V}_t$ can be obtained by assembling the corresponding matrices and vectors of adjacent elements just like is done in the finite element method.

Equation (17) represents a set of second-order differential equations. It can be solved exactly as follows. Assuming

$$\mathbf{V}_t = \mathbf{d}_t \exp(iky), \quad (18)$$

$$\overline{\mathbf{T}}_t = \mathbf{P}_t \exp(iky), \quad (19)$$

and substituting these expressions into Eq. (17), we obtain

$$\mathbf{P}_t = [k^2 \mathbf{A}_{2t} + ik\mathbf{A}_{1t} + \mathbf{A}_{0t} - \omega^2 \mathbf{M}_t]\mathbf{d}_t. \quad (20)$$

Vector $\mathbf{P}_t$ is the amplitude vector of external forces acting on the node lines of domain $\mathbf{D}_f$. In this paper, we only discuss the case of $\mathbf{P}_t = \mathbf{0}$, therefore the following eigenvalue equation with respect to k can obtained.

$$\mathbf{0} = [k^2 \mathbf{A}_{2t} + ik\mathbf{A}_{1t} + \mathbf{A}_{0t} - \omega^2 \mathbf{M}_t]\mathbf{d}_t \quad (21)$$

For a given frequency, Eq. (21) can be changed to a standard eigenvalue equation (Dong, 1977).

$$\mathbf{0} = \left(\begin{bmatrix} \mathbf{0} & \mathbf{I} \\ \omega^2 \mathbf{M}_t - \mathbf{A}_{0t} & -i\mathbf{A}_{1t} \end{bmatrix} - k \begin{bmatrix} \mathbf{I} & \mathbf{0} \\ \mathbf{0} & \mathbf{A}_{2t} \end{bmatrix} \right) \begin{Bmatrix} \mathbf{d}_t \\ k\mathbf{d}_t \end{Bmatrix} \quad (22)$$

Solving this equation by using a general eigenvalue solving subroutine, $2M$ $(M = 4N+2)$ eigenvalues k_j $(j = 1, 2M)$ and eigenvectors can be obtained. If the part of the jth eigenvector corresponding to $\mathbf{d}_t$ is denoted by ϕ_j,

$$\phi_j^T = \{\phi_{1j} \ \phi_{2j} \cdots \phi_{Mj}\}, \quad (23)$$

then the displacement can be written by superposition of these eigenvectors as

$$\mathbf{V}^t = \sum_{j=1}^{2M} C_j \phi_j \exp(ik_j y) = \mathbf{G}(y)\mathbf{C} \quad (24)$$

where C_j are constants. Equation (24) is a fundamental solution for domain $\mathbf{D}_f$. The constant vector $\mathbf{C}$ can be determined by using the boundary conditions on S_3 and S_4 to obtain a special solution for domain $\mathbf{D}_p$. There are M nodes and $2M$ boundary conditions on S_3 and S_4 to determine $2M$ constants C_j. For half-space problems in the domain $y \le 0$, there is no boundary S_4, hence only M boundary conditions can be used. However, as $y \to \infty$, the displacement must be bounded. Therefore, only the eigenvalues which satisfy $\mathrm{Im}(k_j) \ge 0$ need to be taken, and for eigenvalues with $\mathrm{Im}(k_j) = 0$, a condition $\mathrm{Re}(k_j) \le 0$ has to be added to ensure that the waves propagate in the negative y-direction. Consequently only M eigenvalues need to be chosen, which just equals the number of the available boundary conditions on the boundary S_3. A process to determine $\mathbf{C}$ and to derive a relationship between the displacement and stress vectors on the boundaries S_3 and S_4 will now be discussed.

Using Eq. (24) the constant vector $\mathbf{C}$ can be expressed in terms of the displacement vector at the node point on boundaries S_3, and S_4

$$\mathbf{C} = \mathbf{G}_d^{-1}\mathbf{V}_{bt} = \begin{bmatrix} \mathbf{G}_U \\ \mathbf{G}_L \end{bmatrix}^{-1} \mathbf{V}_{bt} \quad (25)$$

where

$$\mathbf{V}_{bt} = \{\mathbf{V}_{bt}^U \ \mathbf{V}_{bt}^L\} = \{u_1 \ v_1 \ u_2 \ v_2 \cdots u_M \ v_M\}, \quad (26)$$

$$\mathbf{G}_U = \begin{bmatrix} \phi_{11}Y_1^U & \phi_{12}Y_2^U & \cdots & \phi_{1L}Y_L^U \\ \phi_{21}Y_1^U & \phi_{22}Y_2^U & \cdots & \phi_{2L}Y_L^U \\ \vdots & \vdots & \ddots & \vdots \\ \phi_{M1}Y_1^U & \phi_{M2}Y_2^U & \cdots & \phi_{ML}Y_L^U \end{bmatrix}, \quad (27)$$

$$Y_j^U = \exp(ik_j y^U), \quad (28)$$

where the superscripts "U" and "L" indicate the matrices or variables on the upper boundary S_3 and the lower boundary S_4, respectively. In Eq. (26) u_i and v_i are the displacement components in the x and y directions at point i on the boundaries S_3 and S_4. In Eq. (28) y^U is the y-coordinate of the upper boundary S_3. Matrix $\mathbf{G}_L$ is the same as $\mathbf{G}_U$ but Y_j^U is replaced by $Y_j^L = \exp(ik_j y^L)$, where y^L is the y-coordinate of the lower boundary S_4.

Using Eq. (8), the stress vector at any point in an element can be given by

$$\mathbf{R}_y = \mathbf{D}'_{yx} \frac{\partial \mathbf{U}}{\partial x} + \mathbf{D}_{yy} \frac{\partial \mathbf{U}}{\partial y}, \quad (29)$$

where the matrices $\mathbf{D}'_{yx}$ and $\mathbf{D}_{yy}$ are given in the Appendix. With the help of Eqs. (11) and (12), we have

$$\mathbf{R} = \{\mathbf{R}_y|_{x=0} \ \mathbf{R}_y|_{x=h/2} \ \mathbf{R}_y|_{x=h}\}^T = \mathbf{R}_1\mathbf{V} + \mathbf{R}_2 \frac{\partial \mathbf{V}}{\partial y}, \quad (30)$$

where $\mathbf{R}_1$ and $\mathbf{R}_2$ are given in the Appendix. Using matrices $\mathbf{R}_1$ and $\mathbf{R}_2$ of all the strip elements, the stress vector for all the node lines, $\mathbf{R}_t$, can be obtained as

$$\mathbf{R}_t = \mathbf{R}_{1t}\mathbf{V}_t + \mathbf{R}_{2t} \frac{\partial \mathbf{V}_t}{\partial y}, \quad (31)$$

where $\mathbf{R}_{1t}$ and $\mathbf{R}_{2t}$ can be obtained by combining $\mathbf{R}_1$ and $\mathbf{R}_2$ of all the elements. It may be mentioned that at the interface node, the stresses are given by the average stresses obtained from the right and left elements. Using Eqs. (24), (25), and (31) we finally have

$$\mathbf{R}_{bt} = \mathbf{K}\mathbf{V}_{bt}, \quad (32)$$

where $\mathbf{R}_{bt} = \{\mathbf{R}_{bt}^U \ \mathbf{R}_{bt}^L\}^T$ is the external traction vector on boundaries S_3 and S_4, and

$$\mathbf{K} = \begin{bmatrix} \mathbf{R}_{1t} & \mathbf{0} \\ \mathbf{0} & \mathbf{R}_{1t} \end{bmatrix} + \begin{bmatrix} \mathbf{R}_{2t}\mathbf{G}'_U\mathbf{G}_d^{-1} \\ \mathbf{R}_{2t}\mathbf{G}'_L\mathbf{G}_d^{-1} \end{bmatrix}, \quad (33)$$

is a stiffness matrix in which matrices $\mathbf{G}'_U$ and $\mathbf{G}'_L$ have the same forms as matrices $\mathbf{G}_U$ and $\mathbf{G}_L$ but $\mathbf{Y}_j^U$ and $\mathbf{Y}_j^L$ in $\mathbf{G}_U$ and $\mathbf{G}_L$ have to be replaced by $Y_j'^U = ik_j \exp(ik_j y^U)$ and $Y_j'^L = ik_j \exp(ik_j y^L)$, respectively.

Equation (32) gives the relationship between the tractions and the displacements on the boundaries S_3 and S_4. For given $\mathbf{R}_{bt}$, $\mathbf{V}_{bt}$ can be solved from Eq. (32). Next the total displacement can be obtained by using Eqs. (10), (24), and (25), and finally the stress fields can be obtained by using Eqs. (8) and (9).

4 Numerical Examples

A strip element method program was written in FORTRAN 77. The program was first used to demonstrate the strip element method for three classical problems (one static and two dynamic) for which exact solutions are available. The static problem is Flamant's problem, i.e., an isotropic half-space subjected to a normal line load. The dynamic problems are for the two-dimensional full-space Green's function problem (an unbounded solid subjected to a time-harmonic line load), and for Lamb's problem (a half-space subjected to a normal time-harmonic line load). The line loads are acting at the origin of the coordinate system. Because of symmetry considerations only a quarter-space needs to be divided into N vertical strip

Downloaded 03 May 2010 to 171.66.16.20. Redistribution subject to ASME license or copyright; see http://www.asme.org/terms/Terms_Use.cfm

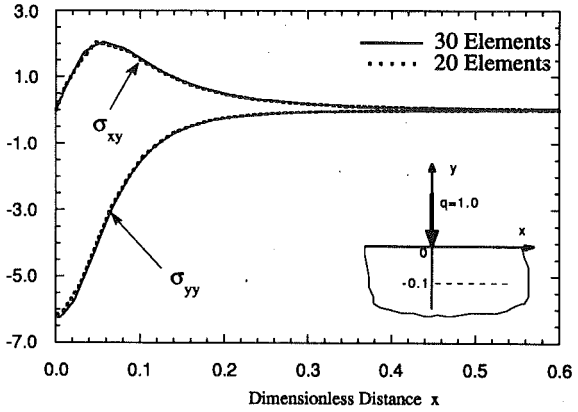


Fig. 2 Convergence of stress distributions on $y=-0.1$ for an isotropic half-space subjected to a static line load, computed by the strip element method with an infinite element at $x=0.7$

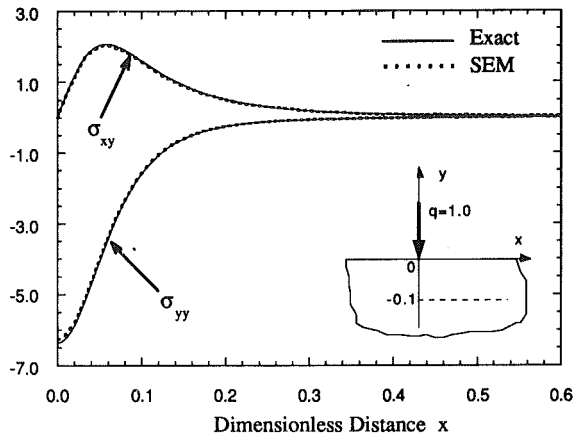


Fig. 3 Stress on $y=-0.1$ for an isotropic half-space subjected to a static line load. Comparison of exact and strip element method results, with an infinite element at $x=0.7$ for the strip element method.

elements for each problem. The line loads are modeled as triangular distributions of tractions acting on the boundary S_3 of the one element which contains the origin. The widths of all elements are the same except for the width of the first element at the origin, h_1, which is chosen to be very small to simulate the line load. For static problems $h_1=0.001$, and for dynamic problems $h_1=0.05\,\lambda_0$ (for the full-space $\lambda_0=\lambda_t$, where λ_t is the wave length of the transverse wave; for the half-space, $\lambda_0=\lambda_r$, where λ_r is the wavelength of the Rayleigh wave). The elastic properties of a steel, which can be found in a paper by Liu et al. (1992), were used for the isotropic problems.

In addition the strip element method was used to compute the surface displacement for a half-space of MgO, which is an anisotropic material. The material constants of MgO can be found in a paper by Kim et al. (1992). The computations have been carried out on a HP700 workstation. The results are discussed in the following two subsections.

4.1 Static Problems (Flamant's Problem). For the static problem, the one change is that the terms containing time and frequency become zero. To simulate the semi-infinite body in the strip element method, a half-space infinite element is used at $x\geq a$. The infinite element is developed by using an interpolation function (see, e.g., Zienkiewicz et al., 1989). The stiffness and the mass matrices, which are derived in the same way as for regular elements, are given in the Appendix. In the strip element method, a quarter space with the following boundary conditions is considered:

At $x=0$:

$$\sigma_{xy}=0, \quad u=0. \tag{34}$$

And at $y=0$:

$$\sigma_{yy}=\frac{q_0}{h_1}\left(\frac{x}{h_1}-1\right), \text{ when } x\leq h_1; \quad \sigma_{yy}=0, \text{ when } x>h_1;$$

$$\sigma_{xy}=0, \text{ when } x\geq 0. \tag{35}$$

The exact solution of Flamant's problem, which can be found in texts on elasticity theory, is

$$\sigma_{xx}=\frac{-2q_0x^2y}{\pi(x^2+y^2)^2} \quad \sigma_{xy}=\frac{-2q_0xy^2}{\pi(x^2+y^2)^2} \quad \sigma_{yy}=\frac{-2q_0y^3}{\pi(x^2+y^2)^2}. \tag{36}$$

Figure 2 shows the stress distributions on the line $y=0.1$, $x>0$. The results are obtained by the strip element method using 20 and 30 elements, and an infinite element is attached at $x=0.7$. The convergence is very good. In Fig. 3 the results obtained by using 30 elements are compared with the exact solutions given by Eq. (36), and very good agreement is observed.

4.2 Dynamic Problems. To reduce the domain of discretization for dynamic problems in infinite bodies, so-called nonreflecting boundaries have to be used. A good review of nonreflecting boundary conditions has been given by Givoli (1991). Three nonreflecting boundary conditions for elastic waves have been used with the present strip element method. A general form of the three nonreflecting boundary conditions can be written as

$$\left.\frac{\partial \mathbf{U}}{\partial x}\right|_{x=a}=\mathbf{B}\mathbf{U}|_{x=a}. \tag{37}$$

The matrix $\mathbf{B}$ takes different forms for the first, second, and third nonreflecting boundary conditions, namely

$$\mathbf{B}=i\begin{bmatrix} k_l & 0 \\ 0 & k_t \end{bmatrix}, \tag{38}$$

$$\mathbf{B}=i\mathbf{B}_0-ik\mathbf{B}_1+ik^2\mathbf{B}_2, \tag{39}$$

and

$$\mathbf{B}=i\begin{bmatrix} k_r & 0 \\ 0 & k_r \end{bmatrix}, \tag{40}$$

respectively. Equations (38) and (39) correspond to the first and the second-order nonreflecting boundary conditions given by Clayton et al. (1977). The matrices $\mathbf{B}_i$ $(i=0, 1, 2)$ in Eq. (39) have been given by Clayton et al. (1977) and Engquist et al. (1979). The third nonreflecting boundary condition is obtained by replacing c_l and c_t by c_r, where c_r is the velocity of the Rayleigh wave. This modification was proposed by Bamberger et al. (1988) for the absorption of Rayleigh waves.

Equation (37) gives the relationship between the derivative of the displacement with respect to x and the displacement itself on the boundary line $x=a$. With the help of Eq. (4), the stress vector at $x=a$ can be expressed in terms of the displacement vector at $x=a$. Substituting the boundary stress vector into Eq. (20), a modified eigenvalue equation for the infinite body is obtained, and fundamental solutions for the domain $\mathbf{D}_f$ where the nonreflecting boundary condition is used can be obtained. Finally, the displacement can be obtained from Eq. (32) by using the boundary conditions on the boundaries S_3 and S_4.

As will be shown, the three nonreflecting boundary conditions do not work in a satisfactory manner for the half-space case. We have, therefore, constructed a new viscoelastic nonreflecting boundary by attaching a few artificial viscoelastic elements at $x=a$. By letting the viscosity of the elements increase slightly as x increases, these viscoelastic elements can very efficiently absorb waves with any incident angle to the

Downloaded 03 May 2010 to 171.66.16.20. Redistribution subject to ASME license or copyright; see http://www.asme.org/terms/Terms_Use.cfm

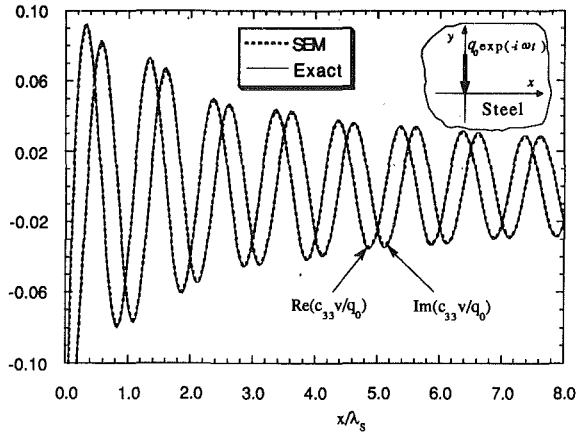


Fig. 4 Comparison of elastodynamic displacements on $y=0$ for an isotropic full-space subjected to a time-harmonic line load. Comparison of exact and strip element method results, with a viscoelastic nonreflecting boundary for the strip element method.

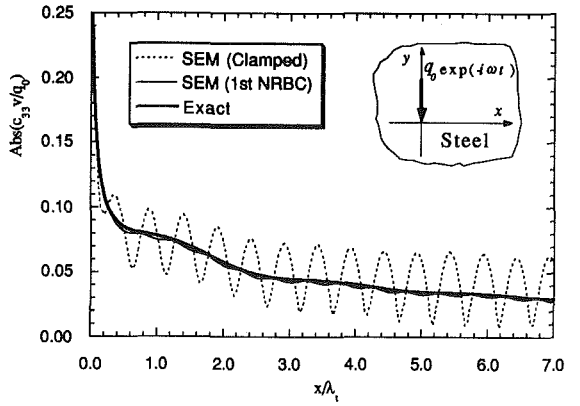


Fig. 5 Elastodynamic displacements on $y=0$ for an isotropic full-space subjected to a time-harmonic line load. Comparison of exact and strip element method results, with different artificial boundaries for the strip element method.

boundary. In this paper, the material constant matrix of the kth viscoelastic element, $\mathbf{c}_k^{ve}$, is assumed to be

$$\mathbf{c}_k^{ve} = \mathbf{c} - i\alpha_0\beta^{k-1}\mathbf{c}, \tag{41}$$

where $\mathbf{c}$ is the elastic constant matrix defined by Eq. (4). In the following calculations, the factors α_0 and β in Eq. (41) are chosen to be 0.01 and 1.624, respectively. A total of 120 elements are used in the range of $0 \le x \le 15\lambda_0$. As x increases 100 elements are elastic, and 20 elements to the right of the 100 elastic elements are viscoelastic.

4.2.1 Full Space. The elastodynamic response of an unbounded body to a time-harmonic line load is the well-known two-dimensional Green's function which can be found, for example, in Chapter 4 of a book edited by Beskos (1987). To apply the strip element method, only a quarter space with the following boundary conditions has to be considered:

At $x=0$:

$$\sigma_{xy}=0, \quad u=0. \tag{42}$$

And at $y=0$:

$$\sigma_{yy}=\frac{q}{2h_1}\left(\frac{x}{h_1}-1\right), \text{ when } x \le h_1;$$

$$\sigma_{yy}=0, \text{ when } x>h_1; \quad u=0. \tag{43}$$

Thus, the line load is again approximated by a triangular distribution of tractions. The time-harmonic term has been omitted.

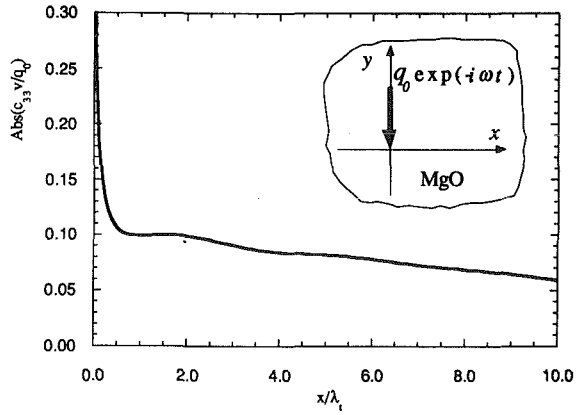


Fig. 6 Elastodynamic displacements on $y=0$ for an isotropic full-space subjected to a time-harmonic line load, obtained by the strip element method with a viscoelastic nonreflecting boundary

Figure 4 shows the displacement v on the line $y=0$ $(x>0)$. The solid line is obtained by the exact method, and the dashed line is obtained by the strip element method with the viscoelastic nonreflecting boundary. Excellent agreement is observed. Figure 5 shows the displacements obtained by the strip element method by using the first nonreflecting boundary condition and by using a clamped boundary at $x=7\lambda_t$, together with the exact results. Quite good results are obtained by using the first nonreflecting boundary condition. Very poor results are obtained by using the clamped boundary condition because of the reflection of incident waves from the clamped boundary. It is also found that very good results can be obtained by using the second nonreflecting boundary condition.

An important feature of the strip element method is its applicability to anisotropic solids. For anisotropic solids, no simple form of the exact solution nor an artificial boundary like the second nonreflecting boundary condition are available. Figure 6 shows the displacement distribution at $x=0$ for an anisotropic full-space (single crystal MgO) obtained by the strip element method with the viscoelastic nonreflecting boundary. The single crystal MgO is cubic symmetric, and its anisotropic factor is about 1.5. The time-harmonic line periodic load is acting in the [001] direction.

4.2.2 Half-Space (Lamb's Problem). For an isotropic half-space subjected to a normal time-harmonic line load, there is no closed-form exact elastodynamic solution. However, the following integral representations follow from an application of the exponential Fourier transform:

$$\frac{c_{33}}{q_0}u=\frac{1}{2\pi}\int_{-\infty}^{\infty}\frac{i\xi[(k_t^2-2\xi^2)\exp(-\beta y)+2\alpha\beta\exp(-\alpha y)]}{(2\xi^2-k_t^2)^2-4\xi^2\alpha\beta}\times\exp(-i\xi x)d\xi, \tag{44}$$

$$\frac{c_{33}}{q_0}v=\frac{1}{2\pi}\int_{-\infty}^{\infty}\frac{i\beta[(k_t^2-2\xi^2)\exp(-\beta y)+2\xi^2\exp(-\alpha y)]}{(2\xi^2-k_t^2)^2-4\xi^2\alpha\beta}\times\exp(-i\xi x)d\xi, \tag{45}$$

where

$$\alpha=\sqrt{\xi^2-k_l^2}, \quad \beta=\sqrt{\xi^2-k_t^2},$$

and k_l and k_t are the wave numbers of the longitudinal and transverse waves. In this paper, Eqs. (44) and (45) are evaluated numerically. Special techniques have to be used in the numerical evaluation. Near the two poles $\xi=\pm k_r$, where k_r is the wave number of the Rayleigh wave, the integral path should be changed from the real axis to a complex integral path $\eta=-\text{sign}(\xi)i\epsilon+\xi$ in which the ϵ should be given a very small value (10^{-6} in this paper). The integrands vary very rapidly

Downloaded 03 May 2010 to 171.66.16.20. Redistribution subject to ASME license or copyright; see http://www.asme.org/terms/Terms_Use.cfm

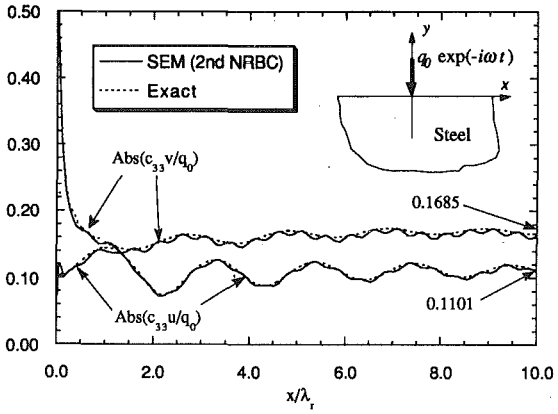


Fig. 7 Elastodynamic displacements on the surface of an isotropic half-space subjected to a time-harmonic line load. Comparison of exact and strip element method results, with the second nonreflecting boundary condition for the strip element method.

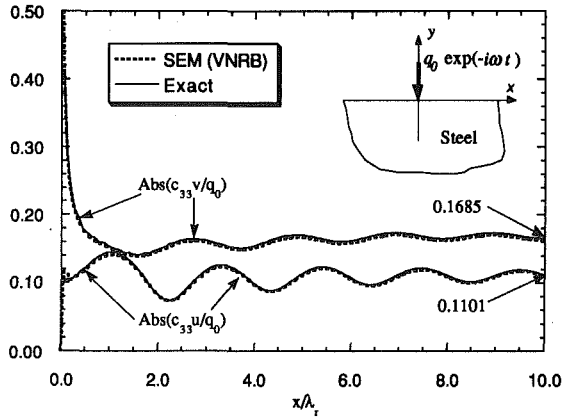


Fig. 8 Elastodynamic displacements on the surface of an isotropic half-space subjected to a time-harmonic line load. Comparison of exact and strip element method results, with a viscoelastic nonreflecting boundary for the strip element method.

near $\eta = \text{sign}(\xi)(k_r - i\epsilon)$, hence a subroutine which can integrate over rapidly varying integrands has to be used near these points. The integrand also oscillates at a very high frequency when $\xi \to \pm\infty$, hence again a subroutine for integrations over rapidly oscillating functions has to be used.

In the strip element method, the domain for the numerical calculations is a quarter space. The boundary conditions are as same as Eqs. (34) and (35). The time-harmonic term has been omitted.

Figure 7 shows the displacement distribution on the surface of a steel half-space subjected to a time-harmonic normal line load. The dashed lines are obtained by the numerical evaluation of Eqs. (44) and (45), and the solid lines are obtained by the strip element method with the second nonreflecting boundary condition. Even though good agreement is obtained, small oscillations are observed in the strip element method curves, because the second nonreflecting boundary condition cannot completely absorb waves that are incident on the artificial boundary with large angles of incidence (cf., Clayton et al., 1977). The displacements have also been computed by using the first nonreflecting boundary condition, but these results are much worse than for the second nonreflecting boundary condition. The third nonreflecting boundary condition is as good as the second nonreflecting boundary condition, because the major wave reflections are for Rayleigh waves, and the third nonreflecting boundary condition absorbs the Rayleigh waves quite well. Figure 8 shows the distribution of the absolute value of the displacement obtained by the strip element method

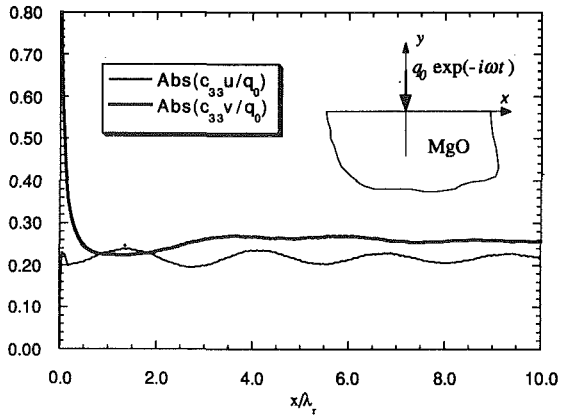


Fig. 9 Elastodynamic displacements on the surface of an anisotropic half-space (MgO) subjected to a time-harmonic line load, computed by the strip element method with a viscoelastic nonreflecting boundary

with the viscoelastic nonreflecting boundary, together with the exact solutions. Excellent agreement is observed. The curves obtained by the strip element method are a little lower than the exact curves (see Figs. 7 and 8), because the line load is treated as a distributed traction, as given by Eq. (35). It has been checked that the strip element method results more closely approach the exact curves as the width of the first element becomes smaller.

Another check is that the absolute values of the two displacement components approach constant values when $x \to \infty$. In this case the constants are $\text{Abs}(c_{33}u/q_0) = 0.1101$, $\text{Abs}(c_{33}v/q_0) = 0.1685$ as shown in Figs. 7 and 8.

For anisotropic half-space problems, there is no exact solution. Figure 9 shows the displacement distribution on the surface of an anisotropic half-space (single crystal MgO) obtained by the strip element method with the viscoelastic nonreflecting boundary. The normal line load is acting at the origin in the [001] direction.

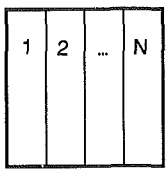
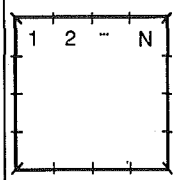
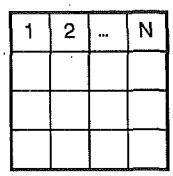
5 Comments on Numerical Calculations

The discretization for the finite element method produces a large number of node variables, and hence the matrix size in a finite element method problem is usually very large. In the boundary element method, a fundamental problem for a full-space is first solved exactly, and then the fundamental solutions (Green's functions) are used to derive boundary integral equations that are solved by discretizing the boundary. In the strip element method, the problem domain is first discretized into strip elements to obtain approximate governing equations that are solved analytically. Because of the lower levels of discretization the matrix size in both the boundary element method and the strip element method is very small as compared with the finite element method. Table 1 gives a simple example to show how much memory can be saved by using the strip element method. In Table 1 a square domain is considered and linear interpolation functions are used in the strip element method, the boundary element method, and the finite element method. Table 1 shows that the largest matrix size in the boundary element method is four times that of the strip element method, and that if 100 elements in the horizontal direction are needed to solve the problem, the largest matrix size in the finite element method is more than 50 times that of the strip element method, even if the bandwidth storage technique would be used in the finite element method.

To use the strip element method efficiently, some special numerical techniques should be used, based on the following considerations: (1) Since the main computation in an strip element method program has to deal with large size matrices, it is advisable to use vectorization techniques to reduce the

Downloaded 03 May 2010 to 171.66.16.20. Redistribution subject to ASME license or copyright; see http://www.asme.org/terms/Terms_Use.cfm

Table 1 Comparison of matrix sizes for the strip element method (SEM), boundary element method (BEM), and finite element method (FEM)

SEM	BEM	FEM
		
N elements N+1 node lines Matrix size: $M_s = 16(N+1)^2$	4N elements 4N nodes Matrix size: $64N^2 \approx 4M_s$	N^2 elements (N+1)(N+1) nodes Matrix size: (Bandwidth storage) $(8N+22)(N+1)^2 \approx (N/2)M_s$

computation time. (2) Since the matrices given before Eq. (22) are narrow band symmetric or asymmetric matrices (cf. Appendix), it is recommended to used bandwidth storage techniques to reduce the storage and the computation time. (3) Since the matrices after Eq. (22) are usually full and complex-valued matrices, and since some of them contain exponential functions, it is strongly recommended to use subroutines for solving linear algebraic equations instead of subroutines for solving inverse matrices, to save computation time and maintain accuracy. (4) If the matrices contain exponential functions (which are often very large or very small), an efficient way to avoid loss of precision is to normalize these matrices before computation. Otherwise, wrong results may be obtained due to loss of accuracy. (5) Since the computation time in an strip element method program is mainly consumed by solving Eq. (22) to obtain eigenvalues and eigenvectors, an efficient eigenvalue solving subroutine is required. The most efficient method is to first calculate eigenvalues using an eigenvalue solving subroutine from Eq. (22), and then to calculate the corresponding eigenvectors from Eq. (21) by using a subroutine for solving linear algebraic equations, because the number of equations in Eq. (21) is a half that of Eq. (22).

6 Conclusions

A strip element method has been presented. Its application has been demonstrated for static and dynamic linearly elastic problems. The method has the following features.

(1) It can be used for elastic or viscoelastic stress-analysis problems of anisotropic materials. It can easily be extended to solids that are inhomogeneous in one direction.

(2) It can be used not only for bounded bodies but also for bodies of infinite extent. For static loading of bodies of infinite extent, an infinite element is used. For dynamic loading, three nonreflecting boundaries have been introduced for use with the strip element method, as well as a viscoelastic nonreflecting boundary. The viscoelastic nonreflecting boundary proved to be the best nonreflecting boundary for the examples considered in this paper.

(3) Compared to the finite element method, the strip element method requires a significantly smaller computer memory.

Acknowledgment

This research was partially supported by the office of Naval Research under contract N00014-89-J-1362, and partially by the Science and Technology Agency of Japan.

References

Achenbach, J. D., Ahn, V. S., and Harris, J. G., 1991, "Wave Analysis of the Acoustic Material Signature for the Line Focus Microscope," *IEEE Trans. Ultrason. Ferroelec. Freq. Contr.*, Vol. 38, No. 4, pp. 380–387.

Ahn, V. S., Achenbach, J. D., Li, Z. L., and Kim, J. O., 1991, "Numerical Modeling of the $V(z)$ Curve for a Thin-Layer/Substrate Configuration," *Res. Nondestr. Eval.*, Vol. 3, pp. 183–200.

Ahn, V. S., Harris, J. G., and Achenbach, J. D., 1992, "Numerical Analysis of the Acoustic Signature of a Surface-Breaking Crack," *IEEE Trans. Ultrason. Ferroelec. Freq. Contr.*, Vol. 39, No. 1, pp. 112–118.

Al-Nassar, Y. N., Datta, S. K., and Shah, A. H., 1991, "Scattering of Lamb Waves by a Normal Rectangular Strip Weldment," *Ultrasonics*, Vol. 29, pp. 125–132.

Bamberger, A., Chalinder, B., Joly, P., Roberts, J. E., and Teron, J. L., 1988, "Absorbing Boundary Conditions for Rayleigh Waves," *SIAM Journal on Scientific and Statistical Computing*, Vol. 9, No. 6, pp. 1016–1049.

Bathe, K.-J., and Wilson, E. L., 1976, *Numerical Methods in Finite Element Analysis*, Prentice-Hall, Englewood Cliffs, New Jersey.

Beskos, D. E., 1987, *Boundary Element Methods in Mechanics*, North-Holland, Amsterdam.

Cheung, Y. K., 1976, *Finite Strip Method in Structural Analysis*, Pergamon Press, Oxford, U.K.

Clayton, R., and Engquist, B., 1977, "Absorbing Boundary Conditions for Acoustic and Elastic Wave Equations," *Bull. Seismol. Soc. Amer.*, Vol. 67, No. 6, pp. 1529–1540.

Datta, S. K., Shah, A. H., Bratton, R. L., and Chakraborty, T., 1988, "Wave Propagation in Laminated Composite Plates," *J. Acoust. Soc. Am.*, Vol. 83, No. 6, pp. 2020–2026.

Dong, S. B., and Nelson, R. B., 1972, "On Natural Vibrations and Waves in Laminated Orthotropic Plates," ASME JOURNAL OF APPLIED MECHANICS, Vol. 39, pp. 739–745.

Dong, S. B., 1977, "A Block-Stodola Eigensolution Technique for Large Algebraic Systems with Non-symmetrical Matrices," *Int. J. Numer. Methods Eng.*, Vol. 11, pp. 247–267.

Dong, S. B., and Huang, K. H., 1985, "Edge Vibrations in Laminated Composite Plates," ASME JOURNAL OF APPLIED MECHANICS, Vol. 52, pp. 433–438.

Engquist, B., and Majda, A., 1979, "Radiation Boundary Conditions for Acoustic and Elastic Wave Calculations," *Commun. Pure Appl. Math.*, Vol. 32, pp. 313–357.

Felippa, C. A., 1975, "Solution of Linear Equations with Skyline-Stored Symmetric Matrix," *Comp. Struct.*, Vol. 5, pp. 13–30.

Givoli, D., 1991, "Non-Reflection Boundary Conditions," *J. Comput. Phys.*, Vol. 94, No. 1, pp. 1–29.

Jennings, A., 1966, "A Compact Storage Scheme for the Solution of Symmetric Simultaneous Equations," *Comp. J.*, Vol. 9, pp. 281–285.

Karunasena, W. M., Shah, A. H., and Datta, S. K., 1991, "Plane-Strain-Wave Scattering by Cracks in Laminated Composite Plates," *ASCE Journal of Engineering Mechanics*, Vol. 117, No. 8, pp. 1738–1754.

Kausel, E., 1986, "Wave Propagation in Anisotropic Layered Media," *Int. J. Numer. Methods Eng.*, Vol. 23, pp. 1567–1578.

Kim, J. O., and Achenbach, J. D., 1992, "Line-Focus Acoustic Microscopy to Measure Anisotropic Acoustic Properties of Thin Films," *Thin Solid Films*, Vol. 214, pp. 25–34.

Liu, G. R., Achenbach, J. D., Kim, J. O., and Li, Z. L., 1992, "A Combined Finite Element Method/Boundary Element Method Technique for $V(z)$ Curves of Anistropic-Layer/Substrate Configurations," *J. Acoust. Soc. Am.*, Vol. 92, No. 5, pp. 2734–2740.

Liu, G. R., Tani, J., Ohyoshi, T., and Watanabe, K., 1991a, "Characteristics of Surface Wave Propagation Along the Edge of an Anistropic Laminated Semi-Infinte Plate," *Wave Motion*, Vol. 13, pp. 243–251.

Liu, G. R., Tani, J., Ohyoshi, T., and Watanabe, K., 1991b, "Transient Waves in Anistropic Laminated Plate, Part 1: Theory; Part 2: Application," ASME *Journal of Vibration and Acoustics*, Vol. 113, pp. 230–239.

Liu, G. R., Tani, J., Ohyoshi, T., and Watanabe, K., 1991c, "Characteristic Wave Surfaces in Anistropic Laminated Plates," ASME *Journal of Vibration and Acoustics*, Vol. 113, pp. 279–285.

Liu, G. R., Tani, J., Watanabe, K., and Ohyoshi, T., 1990a, "A Semi-Exact Method for the Propagation of Harmonic Waves in Anistropic Laminated Bars of Rectangular Cross Section," *Wave Motion*, Vol. 12, pp. 361–371.

Liu, G. R., Tani, J., Watanabe, K., and Ohyoshi, T., 1990b, "Harmonic Wave Propagation in Anistropic Laminated Strips," *Journal of Sound and Vibration*, Vol. 139, No. 2, pp. 313–324.

Liu, G. R., Tani, J., Watanabe, K., and Ohyoshi, T., 1990c, "Lamb Wave Propagation in Anistropic Laminates," ASME JOURNAL OF APPLIED MECHANICS, Vol. 57, No. 2, pp. 923–929.

Meyer, C., 1973, "Solution of Equations; State-of-the-Art," *J. Struct. Div. ASCE*, Vol. 99, No. 7, pp. 1507–1526.

Meyer, C., 1975, "Special Problems Related to Linear Equation Solvers," *J. Struct. Div. ASCE*, Vol. 101, No. 4, pp. 869–890.

Nelson, R. B., and Dong, S. B., 1973, "High Frequency Vibrations and Waves in Laminated Orthotropic Plates," *Journal of Sound and Vibration*, Vol. 30, pp. 33–44.

Waas, G., 1972, "Linear Two-Dimensional Analysis of Soil Dynamics Problems in Semi-Infinite Layer Media," Ph.D. Thesis, University of California, Berkeley, CA.

Downloaded 03 May 2010 to 171.66.16.20. Redistribution subject to ASME license or copyright; see http://www.asme.org/terms/Terms_Use.cfm

Zienkiewicz, O. C., and Taylor, R. L., 1989, *The Finite Element Method*, 4th ed., Vol. 1, Chapter 8, McGraw-Hill, New York.

APPENDIX

Matrices in Eqs. (16) and (30):

$$\mathbf{D}_{xx}=\begin{bmatrix} c_{11} & c_{13} \\ c_{13} & c_{33} \end{bmatrix}, \quad \mathbf{D}_{xy}=\frac{1}{2}\begin{bmatrix} 2c_{13} & c_{33}+c_{12} \\ c_{33}+c_{12} & 2c_{23} \end{bmatrix},$$

$$\mathbf{D}_{yy}=\begin{bmatrix} c_{33} & c_{23} \\ c_{23} & c_{22} \end{bmatrix}, \quad \mathbf{D}'_{xy}=\begin{bmatrix} c_{13} & c_{12} \\ c_{33} & c_{23} \end{bmatrix}, \quad \mathbf{D}'_{yx}=\begin{bmatrix} c_{13} & c_{33} \\ c_{12} & c_{23} \end{bmatrix}$$

$$\mathbf{A}_0=\frac{1}{3h}\begin{bmatrix} 7\mathbf{D}_{xx} & -8\mathbf{D}_{xx} & \mathbf{D}_{xx} \\ & 16\mathbf{D}_{xx} & -8\mathbf{D}_{xx} \\ \text{sy.} & & 7\mathbf{D}_{xx} \end{bmatrix},$$

$$\mathbf{A}_1=\frac{1}{3}\begin{bmatrix} 3(\mathbf{D}_{xy}-\mathbf{D}'_{xy}) & -4\mathbf{D}_{xy} & \mathbf{D}_{xy} \\ & 0 & -4\mathbf{D}_{xy} \\ \text{asy.} & & 3(\mathbf{D}_{xy}-\mathbf{D}'_{xy}) \end{bmatrix}$$

$$\mathbf{A}_2=\frac{h}{30}\begin{bmatrix} 4\mathbf{D}_{yy} & 2\mathbf{D}_{yy} & -\mathbf{D}_{yy} \\ & 16\mathbf{D}_{yy} & 2\mathbf{D}_{yy} \\ \text{sy.} & & 4\mathbf{D}_{yy} \end{bmatrix}, \quad \mathbf{M}=\frac{\rho h}{30}\begin{bmatrix} 4\mathbf{I} & 2\mathbf{I} & -\mathbf{I} \\ & 16\mathbf{I} & 2\mathbf{I} \\ \text{sy.} & & 4\mathbf{I} \end{bmatrix}$$

$$\mathbf{R}_1=\frac{1}{h}\begin{bmatrix} -3\mathbf{D}'_{yx} & 4\mathbf{D}'_{yx} & -\mathbf{D}'_{yx} \\ -\mathbf{D}'_{yx} & \mathbf{0} & \mathbf{D}'_{yx} \\ \mathbf{D}'_{yx} & -4\mathbf{D}'_{yx} & 3\mathbf{D}'_{yx} \end{bmatrix}, \quad \mathbf{R}_2=\begin{bmatrix} \mathbf{D}_{yy} & \mathbf{0} & \mathbf{0} \\ \mathbf{0} & \mathbf{D}_{yy} & \mathbf{0} \\ \mathbf{0} & \mathbf{0} & \mathbf{D}_{yy} \end{bmatrix}.$$

Matrices in Eqs. (16) and (30) for infinite elements for static problems:

$$\mathbf{A}_0=\frac{1}{15x_{QC}}\begin{bmatrix} 46\mathbf{D}_{xx} & -52\mathbf{D}_{xx} & 6\mathbf{D}_{xx} \\ & 64\mathbf{D}_{xx} & -12\mathbf{D}_{xx} \\ \text{sy.} & & 6\mathbf{D}_{xx} \end{bmatrix},$$

$$\mathbf{A}_2=\frac{x_{QC}}{6}\begin{bmatrix} \mathbf{D}_{yy} & -2\mathbf{D}_{yy} & -\mathbf{M}^1_\infty \\ & 16\mathbf{D}_{yy} & \mathbf{M}^1_\infty \\ \text{sy.} & & \mathbf{M}^2_\infty \end{bmatrix}$$

$$\mathbf{R}_1=\frac{1}{2x_{QC}}\begin{bmatrix} -12\mathbf{D}'_{yx} & 16\mathbf{D}'_{yx} & -4\mathbf{D}'_{yx} \\ -\mathbf{D}'_{yx} & \mathbf{0} & \mathbf{D}'_{yx} \\ \mathbf{0} & \mathbf{0} & \mathbf{0} \end{bmatrix}.$$

Matrices $\mathbf{A}_1$ and $\mathbf{R}_2$ are the same as the regular matrices, $x_{QC}=2a$.

Downloaded 03 May 2010 to 171.66.16.20. Redistribution subject to ASME license or copyright; see http://www.asme.org/terms/Terms_Use.cfm

R. L. Munisamy

D. A. Hills

D. Nowell

Department of Engineering Science,
Oxford University,
Parks Road,
Oxford OX1 3PJ, U.K.

Static Axisymmetric Hertzian Contacts Subject to Shearing Forces

A numerical method is used to resolve the classic Mindlin-Cattaneo partial slip problem for contact between similar and between dissimilar bodies. It is shown that, for similar bodies, the surface frictional energy dissipation is concentrated off the plane of symmetry although the overall dissipation is similar to that predicted by the classical solution. This effect is enhanced for certain combinations of dissimilar materials, where the process of frictional shakedown leads to a displaced contact and hence additional shear compliances.

1 Introduction

The first solutions to the problem of pressing together two bodies to form a Hertzian contact and then applying a shearing force in the plane of the contact, but less than that needed to cause sliding, were published independently in the first half of this century by Cattaneo (1938) and by Mindlin (1949). These solutions are both developed in a way appropriate to a general elliptical Hertzian contact, and rely on a superposition of the solutions for the surface displacements induced under *sliding* conditions, a concise explanation of which is provided by Johnson (1985). However, although the Cattaneo-Mindlin solution is exact for the contact of cylinders it has long been recognized that for a general elliptical or circular contact, the relative displacement of surface particles within the slip zone has a component perpendicular to the direction of the applied tangential force. This violates the requirement that, within a slip zone, the frictional tractions must be directed so as to oppose an increment of relative displacement. This discrepancy seems particularly marked in the case of an applied shearing force acting at an angle to the axes of the contact ellipse (Szalwinski, 1985).

The intention of the present article is first to re-evaluate the partial slip problem for the case of a circular contact formed between two elastically similar bodies, and in particular to examine the regions of maximum frictional energy expenditure to throw more light on the question of how fretting contacts induce crack initiation. Thus, although, for example, we do not expect the overall tangential compliance to differ greatly from the Mindlin case, we do expect significant local differences and we hope to determine in detail the distribution and direction of surface shearing tractions. From this preliminary calculation we will briefly consider the shearing traction distribution under sliding conditions, and proceed to resolve the partial slip problem for elastic contact between elastically *dissimilar* bodies. The influence of the shear tractions on the normal pressure distribution will be neglected for these cases. Both the transitory and steady-state solutions will be found, the two-dimensional equivalents of which are already known (Nowell et al., 1988).

2 Formulation

First, we will restrict our attention to the case of contact between elastically similar bodies. Two spheres are pressed into contact by normal load P (see Fig. 1), giving rise to a Hertzian pressure distribution:

$$p(x, y) = p_0\sqrt{1-\left(\frac{r}{a}\right)^2} \quad r^2 = x^2 + y^2 \le a^2 \tag{1}$$

where

$$p_0 = \frac{3P}{2\pi a^2} \tag{2}$$

and a is the contact radius. Subsequently, a tangential force

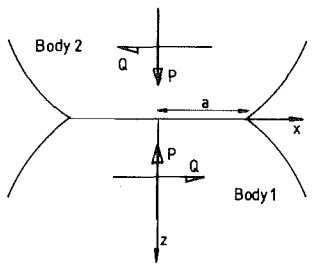


Fig. 1 Overall geometry of the problem: Two spheres pressed together by a normal force P followed by a tangential force Q

Contributed by the Applied Mechanics Division of THE AMERICAN SOCIETY OF MECHANICAL ENGINEERS for publication in the ASME JOURNAL OF APPLIED MECHANICS.

Discussion on this paper should be addressed to the Technical Editor, Professor Lewis T. Wheeler, Department of Mechanical Engineering, University of Houston, Houston, TX 77204-4792, and will be accepted until four months after final publication of the paper itself in the ASME JOURNAL OF APPLIED MECHANICS.

Manuscript received by the ASME Applied Mechanics Division, Aug. 3, 1992; final revision, Mar. 4, 1993. Associate Technical Editor: F. Y. M. Wan.

Copyright © 1994 by ASME
Downloaded 03 May 2010 to 171.66.16.20. Redistribution subject to ASME license or copyright; see http://www.asme.org/terms/Terms_Use.cfm

Q, whose magnitude is insufficient to cause gross sliding, is applied incrementally to the bodies parallel to the x-axis. A distant point in the undeformed region of one body is thus displaced relative to one in the other by δ_x (symmetry dictates that the relative transverse displacement is zero), while at the surface of the lower body, tangential elastic displacements due to the shearing tractions alone are (Johnson, 1985)

$$u_{x1}(x, y) = \frac{1}{4\pi\mu_1} \iint_S \left[q_x(\zeta, \eta) \left\{ \frac{2(1-\nu_1)}{\rho} + \frac{2\nu_1(\zeta-x)^2}{\rho^3} \right\} - q_y(\zeta, \eta) \frac{2\nu_1(\zeta-x)(\eta-y)}{\rho^3} \right] d\zeta d\eta \quad (3)$$

$$u_{y1}(x, y) = \frac{1}{4\pi\mu_1} \iint_S \left[q_y(\zeta, \eta) \left\{ \frac{2(1-\nu_1)}{\rho} + \frac{2\nu_1(\eta-y)^2}{\rho^3} \right\} + q_x(\zeta, \eta) \frac{2\nu_1(\zeta-x)(\eta-y)}{\rho^3} \right] d\zeta d\eta \quad (4)$$

where

$$\rho^2 = (\zeta-x)^2 + (\eta-y)^2, \quad (5)$$

$q_x(x, y)$ and $q_y(x, y)$ are the x and y-components of tangential traction $\mathbf{q}(x, y)$, μ_1 and ν_1 are the modulus of rigidity and Poisson's ratio, respectively, of body 1, and the region of integration S is the area of contact. Since body 2 has the same elastic properties as body 1 but the tangential tractions act on it in the opposite sense, u_{x2} and u_{y2} are equal in magnitude but of opposite sign to u_{x1} and u_{y1}. Hence, the components of *relative* displacement $\mathbf{s}(x, y)$ within the contact are

$$s_x(x, y) = \delta_x - (u_{x1} - u_{x2}) = \delta_x - 2u_{x1} \quad (6)$$

$$s_y(x, y) = -(u_{y1} - u_{y2}) = -2u_{y1}. \quad (7)$$

We note that the contribution to relative tangential displacements resulting from the normal tractions is zero as the bodies are elastically similar. For the same reason, the shearing tractions have no effect upon the pressure distribution and the problem is "uncoupled."

The contact is composed of regions of stick and micro-slip. Within a stick zone the shear tractions cannot exceed the limiting frictional value:

$$|\mathbf{q}(x, y)| \le fp(x, y), \quad (8)$$

where f is the coefficient of Coulomb friction, and for a monotonically increasing shear force Q, the relative incremental displacements are zero:

$$\frac{d}{dQ} s_x = 0 \quad (9)$$

$$\frac{d}{dQ} s_y = 0. \quad (10)$$

Hence, from Eqs. (6) and (7)

$$2\frac{d}{dQ} u_{x1} = \frac{d}{dQ} \delta_x \quad (11)$$

$$2\frac{d}{dQ} u_{y1} = 0. \quad (12)$$

Within a slip zone the shearing traction takes its limiting value

$$|\mathbf{q}(x, y)| = fp(x, y), \quad (13)$$

and opposes the relative incremental displacement, giving the requirement

$$\frac{\mathbf{q}(x, y)}{|\mathbf{q}(x, y)|} = -\frac{d}{dQ} \frac{\mathbf{s}(x, y)}{|\mathbf{s}(x, y)|}. \quad (14)$$

This is met when the ratios of the x and y components of the two vectors are equal, which after cross multiplying may be written as

$$q_x \frac{d}{dQ} s_y - q_y \frac{d}{dQ} s_x = 0, \quad (15)$$

and the corresponding components of each vector act in opposite directions, i.e.,

$$q_x \frac{d}{dQ} s_x \le 0 \quad (16)$$

$$q_y \frac{d}{dQ} s_y \le 0. \quad (17)$$

In order to find an approximate solution for the tangential tractions subject to the constraints of either (8), (11), and (12) or (13), (15), (16), and (17) it is convenient to discretize the contact into a mesh of m square, uniform traction elements of unknown magnitudes q_{xj}, q_{yj}. This technique has been applied successfully to a sliding contact problem (Munisamy et al., 1992) and similar methods have previously been used by Kalker (1990). The relative displacements at the center of square i located at (x_i, y_i) may now be written in discretized form:

$$s_{xi} = \delta_x - \sum_{j=1}^{m} (2I_{ij}^x q_{xj} - 2I_{ij}^t q_{yj}) \quad (18)$$

$$s_{yi} = -\sum_{j=1}^{m} (2I_{ij}^y q_{yj} + 2I_{ij}^t q_{xj}) \quad (19)$$

where the influence functions are recorded in full in Munisamy (1994).

As the tangential tractions are history dependent, we propose to solve the incremental problem by increasing the load in small finite steps and recording the relative displacements s_{xi}, s_{yi} at the end of each. In fact, we shall take the displacement δ_x (whose increments are δ_x^{inc}) as the independent variable and integrate over the contact to find Q_x a posteriori.

When the solution has been found the loads required for the imposed displacement may be evaluated by summing the forces acting on each element. The cumulative density of energy dissipated within the contact may be found by summing the products of the components of relative displacement and tangential tractions at each square within the slip zone: they must be collinear by virtue of Eq. (14).

The situation is somewhat more complex when two spheres which have dissimilar elastic properties are pressed into contact. In general, there is coupling between the normal and shearing tractions. Any normal tractions within the contact give rise to tangential displacements at the surface of each body in proportion to the combination of material constants $(1 - 2\nu)/\mu$. If friction is present, shearing tractions are generated at the interface which tend to oppose any relative tangential displacement. These shearing tractions in turn produce normal displacements proportional to the same parameter $(1 - 2\nu)/\mu$. For two-dimensional and axisymmetric contacts, the magnitude of the coupling phenomenon caused by Poisson's effect and difference in the direct compliance, $2(1 - \nu)/\mu$, of each body is conveniently quantified by Dundurs' constant

$$\beta = \frac{(1-2\nu_1)/\mu_1 - (1-2\nu_2)/\mu_2}{2(1-\nu_1)/\mu_1 + 2(1-\nu_2)/\mu_2}. \quad (20)$$

The present problem falls into neither of these categories and Dundurs' contraction of dissimilar elastic constants cannot immediately be made. This will be discussed more fully later, but first the initial problem of normal loading, which *is* axisymmetric, is now considered, as a prelude to the full problem.

We note that the limiting value of the shearing tractions is the fraction f of the normal pressure. Hence, when the coefficient of friction is small, the coupling effect of the normal tractions on the tangential ones is much greater than vice versa. This trend is compounded in normal loading because the tangential tractions are self-equilibrating, i.e., have no resultant. We exploit this fact to make the approximation, first used by

Downloaded 03 May 2010 to 171.66.16.20. Redistribution subject to ASME license or copyright; see http://www.asme.org/terms/Terms_Use.cfm

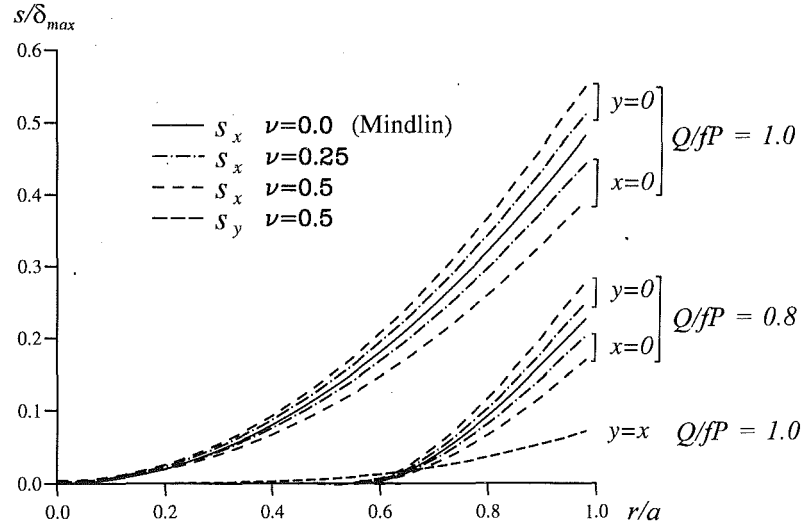


Fig. 2 Components of relative slip for Mindlin-type contact

Goodman (1962), that the pressure distribution is little different from that given by the Hertz theory. This contact problem has been solved by Spence (1975) and Hills and Sackfield (1987) who found the distribution of shearing tractions, ignoring their effect on the normal pressure, in closed form. In the rest of this section r and the stick radius, c, have been normalized with respect to the radius of contact, a.

$$\frac{q_r(r)}{fp_0}\,\mathrm{sgn}\beta=\sqrt{1-r^2}-rH(c-r)\int_r^c\frac{\Psi(t,\,c)}{t^2\sqrt{1-t^2}}\,dt\quad 0<r<1 \tag{21}$$

where $H(r)$ is Heaviside's step function,

$$\Psi(r,\,c)=\frac{2wr}{\pi}\,\Pi\left(n,\,\frac{\pi}{2},\,c'^2\right)-\frac{2cK(c')}{\pi r}\left\{\frac{w}{c'}-\frac{\ln\dfrac{1+w}{1-w}}{\ln\dfrac{1+c}{1-c}}\right\} \tag{22}$$

$$w^2=\frac{c^2-r^2}{1-r^2} \tag{23}$$

$$c'^2=1-c^2 \tag{24}$$

$$n=\frac{1-c^2}{1-w^2}, \tag{25}$$

and $K(c)$ and $\Pi(n,\,\pi/2,\,c)$ are the complete elliptic integrals of the first and third kinds, respectively. Near the center of the contact the tangential tractions are below their limiting value and prevent relative slip to radius c, which is related to the material properties by

$$\frac{\beta}{f}=\frac{cK(c')}{\ln\dfrac{1+c}{1-c}}. \tag{26}$$

To determine whether Goodman's approximation can be justifiably made when the tangential load is applied, it is instructive to consider the extreme case of gross sliding between two elastically dissimilar spheres. The authors have shown (Munisamy et al., 1992) that when the product βf is less than 0.1 there is little difference in either the boundary of the contact or the pressure distribution compared with Hertz' solution. Hence, throughout the cycle of tangential loading, we will assume that the normal tractions are given by Eq. (1).

After the normal load has been applied, but prior to any tangential loading, in contrast to the elastically similar problem, a degree of relative prestraining is produced. However, the direction of subsequent shearing tractions depends only on the *incremental* change in surface displacements, and since the tangential displacements caused by the normal tractions remain constant, they may be ignored from the analysis. The tangential tractions do, of course, vary and the initial relative displacements they cause may be found by distributing them over the full mesh and using modified versions of Eqs. (18) and (19) incorporating the difference in elastic mismatch.

3 Results: The Mindlin Problem

We shall first apply the technique to a re-evaluation of the Mindlin problem for elastically dissimilar bodies. In Mindlin's analysis (Mindlin, 1949), an approximate solution was found by a superposition of the stress field associated with a sliding Hertzian contact. Specifically, the traction distribution is taken as

$$\tau_{zx}(x,\,y)=fp_0\left[\sqrt{1-\left(\frac{r}{a}\right)^2}-\left(\frac{\bar{c}}{a}\right)\sqrt{1-\left(\frac{r}{\bar{c}}\right)^2}\right] \tag{27}$$

where $\bar{c}$ is the radius of the stick zone and p_0 the peak Hertzian contact pressure. The stick zone size, $\bar{c}$, is found by imposing equilibrium in the x-direction giving

$$\left(\frac{\bar{c}}{a}\right)^3=1-\frac{Q}{fP}. \tag{28}$$

The surface strains and hence displacements within the slip zone corresponding to tractions (27) may be found by using the solutions for the state of stress produced by a sliding Hertzian contact (see, for example, Hamilton and Goodman, 1966). These reveal an inconsistency in that, for nonzero Poisson's ratio, there is a finite relative displacement in the y-direction. Johnson (1955) neglects this in comparison with the component of relative displacement in the x-direction which he approximates as

$$s_x(r)\approx\frac{3fP}{32a}\left(\frac{2-\nu_1}{\mu_1}+\frac{2-\nu_2}{\mu_2}\right)\times\left\{\left(1-\frac{2}{\pi}\sin^{-1}\frac{\bar{c}}{r}\right)\left(1-2\frac{\bar{c}^2}{r^2}\right)+\frac{2}{\pi}\frac{\bar{c}}{r}\left(1-\frac{\bar{c}^2}{r^2}\right)^{1/2}\right\}\frac{r^2}{a^2}. \tag{29}$$

This displacement is, of course, independent of θ, and is included in Fig. 2 which is a comparison of slip, s_x, for two cases of loading: first, for the case when there is incipient sliding, and secondly when the imposed tangential displacement is about 70 percent of the value at the onset of sliding,

Downloaded 03 May 2010 to 171.66.16.20. Redistribution subject to ASME license or copyright; see http://www.asme.org/terms/Terms_Use.cfm

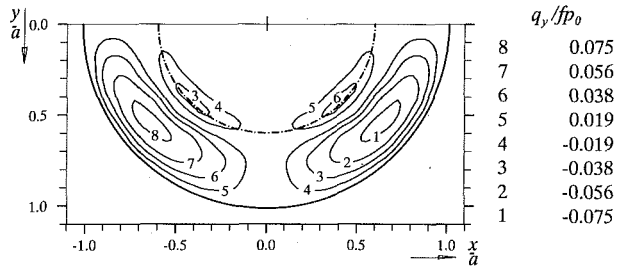


Fig. 3 Transverse shearing tractions in the contact for two incompressible bodies ($\nu = 0.5$) when $Q/fP = 0.8$. A chain line encloses stick zone.

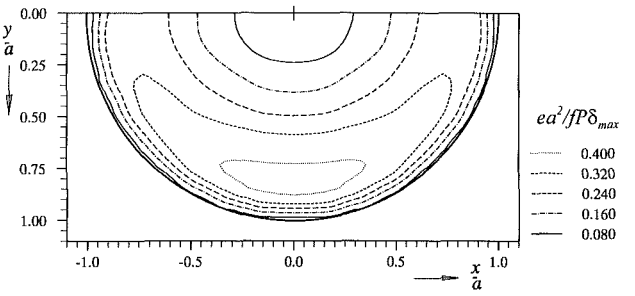


Fig. 4 Plan of frictional work dissipation for $Q/fP = 1.0$ and $\nu = 0.5$

which corresponds to a Q/fP value of 0.8. It is exact for components exhibiting no Poisson's effect, i.e., $\nu = 0$. Also shown in Fig. 2 are the corresponding results using the present numerical method, for the cases when Poisson's ratio is 0.25 and 0.5. The larger value of ν represents the greatest discrepancy between the numerical and Mindlin's solutions. For nonzero values of Poisson's ratio relative *transverse* displacements result within the slip zone and are maximum along the lines $y = \pm x$. An example is included in Fig. 2 for incipient sliding with $\nu = 0.5$. The magnitude of the y-displacement at the edge of the contact is 15 percent of the magnitude of the x-displacement predicted by Eq. (28). Mindlin gave the bulk relative tangential displacement of the two bodies as

$$\delta_{\text{mind}} = \frac{3fP}{16a}\left(\frac{2-\nu_1}{\mu_1}+\frac{2-\nu_2}{\mu_2}\right)\left\{1-\left(1-\frac{Q}{fP}\right)^{2/3}\right\} \qquad (30)$$

and the displacements in the figures are normalized by $\delta_{\max}$, which corresponds to δ_{mind} when $Q/fP = 1.0$.

Of course there are no transverse shear tractions in the Mindlin solution, but significant values do arise in the numerical scheme. These are shown, again for an incompressible material, in Fig. 3 for the case of $Q/fP = 0.8$. It will be noted that the maximum transverse tractions occur on the lines $y = \pm x$, and that they are larger in the partial slip case than under incipient sliding conditions.

The overall force-displacement history for a full-cycle of shear loading was calculated. For any value of Poisson's ratio, the numerical results are imperceptibly different from the Mindlin approximation. The total energy dissipated during a cycle—equivalent to the area of the hysteresis loop traced out—is therefore independent of ν. However, of much greater practical interest in the application of these data to the study of fretting fatigue is the localized density of the frictional energy expenditure $e(x, y)$. In the Mindlin case, because the solution is axisymmetric, the work expended per unit area is also the same along all radial lines. A plot of the frictional energy expenditure over the contact area per cycle for $Q/fP = 1.0$ is given in Fig. 4. It will be noted that the amount of work dissipated per unit area is about 50 percent higher in the crescent shaped areas on "either side" of the plan compared with the value on the plane of symmetry.

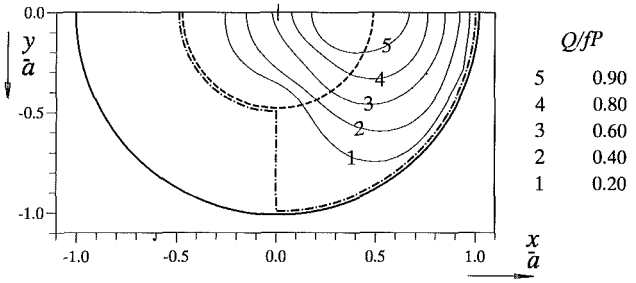


Fig. 5 Evolution of stick zone for contact between dissimilar elastic materials. Broken line corresponds to normal loading alone and chain line to a subsequent infinitesimal tangential force.

It may be remarked that the surface shearing tractions are not precisely directed in the direction of gross motion under sliding conditions, except when both bodies have a Poisson's ratio of zero. However, a consideration of the factors affecting the direction of slip reveals that the effect is not as great as that in the Mindlin problem. If we follow a particle as it passes through the contact in the sliding case, it experiences varying local tractions, which give rise to elastic displacements U_x, U_y that must be added to the gross relative motion of the two bodies. However, these displacements are small and the gradient of relative slip is given by $\partial U_y/\partial x$, which has an order of magnitude of a/R where R is the relative radius of curvature of the contacting bodies and Hertz theory assumes this to be small.

In the Mindlin case, we assume that the change in position of each particle within the contact is sufficiently small for it to experience no change in normal pressure. This can be justified because, even on the verge of sliding, the normalized rigid-body displacement, δ_x/a is of the order of magnitude of a/R. Any relative transverse displacement results from the change in the frictional tractions as the tangential load is increased. Hence, the gradient of relative slip is $(\partial U_y/\partial Q)/(\partial U_x/\partial Q)$, which, in contrast to sliding, is not a second-order effect.

4 Results: Partial Slip of Dissimilar Bodies

We now turn our attention to the problem of two elastically dissimilar bodies pressed together to form a Hertzian contact and with a subsequent shearing force imposed parallel to the plane of contact. A previous solution to this problem has been found for the case of plane contact (Nowell et al., 1988) and hence we shall concentrate on a nominally axisymmetric contact (although the presence of the shearing tractions may render the contact noncircular). As was stated in the formulation we shall assume that $\beta f < 0.1$, which allows us to ignore the influence of the shearing tractions on the normal surface displacement; hence, the contact pressure remains Hertzian (Goodman, 1962).

The first step in the solution to the problem is to determine the surface traction distribution when the normal contact force only is applied. This is given in Eq. (21) and is associated with an annular region of slip surrounding a circular region of stick. Its radius is $0.485a$ when $\beta/f = 1.0$ and is shown in Fig. 5 by the broken line. We then impose an infinitesimal shear force, which gives rise to the stick zone shown by the chain line in Fig. 5. It will be readily seen that within this zone the increment of slip opposes the direction of the shearing traction. As a finite shear force is imposed, the stick zone recedes as indicated.

In order to present a comprehensive set of results, it is essential to consider how the material properties affect the contact problem. To do this let us write down the full integral equations expressing the relationship between the tractions and relative surface displacements. If we include, for the time being, *all* terms we see (Johnson, 1985),

Downloaded 03 May 2010 to 171.66.16.20. Redistribution subject to ASME license or copyright; see http://www.asme.org/terms/Terms_Use.cfm

$$u_z(x,y)=\frac{1}{4\pi}\iint_S\left[\left(\frac{1-\nu_1}{\mu_1}+\frac{1-\nu_2}{\mu_2}\right)\frac{2}{\rho}p(\zeta,\eta)-\left(\frac{1-2\nu_1}{\mu_1}-\frac{1-2\nu_2}{\mu_2}\right)\times\left\{\frac{\zeta-x}{\rho^2}q_x(\zeta,\eta)+\frac{\eta-y}{\rho^2}q_y(\zeta,\eta)\right\}\right]d\zeta d\eta \quad (31)$$

$$u_x(x,y)=\frac{1}{4\pi}\iint_S\left[\left(\frac{1-\nu_1}{\mu_1}+\frac{1-\nu_2}{\mu_2}\right)\frac{2}{\rho}q_x(\zeta,\eta)+\left(\frac{\nu_1}{\mu_1}+\frac{\nu_2}{\mu_2}\right)\left\{\frac{2(\zeta-x)^2}{\rho^3}q_x(\zeta,\eta)-\frac{2(\zeta-x)(\eta-y)}{\rho^3}q_y(\zeta,\eta)\right\}-\left(\frac{1-2\nu_1}{\mu_1}-\frac{1-2\nu_2}{\mu_2}\right)\frac{\zeta-x}{\rho^2}p(\zeta,\eta)\right]d\zeta d\eta \quad (32)$$

$$u_y(x,y)=\frac{1}{4\pi}\iint_S\left[\left(\frac{1-\nu_1}{\mu_1}+\frac{1-\nu_2}{\mu_2}\right)\frac{2}{\rho}q_y(\zeta,\eta)+\left(\frac{\nu_1}{\mu_1}+\frac{\nu_2}{\mu_2}\right)\left\{\frac{2(\eta-y)^2}{\rho^3}q_y(\zeta,\eta)+\frac{2(\zeta-x)(\eta-y)}{\rho^3}q_x(\zeta,\eta)\right\}-\left(\frac{1-2\nu_1}{\mu_1}-\frac{1-2\nu_2}{\mu_2}\right)\frac{\eta-y}{\rho^2}p(\zeta,\eta)\right]d\zeta d\eta. \quad (33)$$

Normalizing these by dividing both sides by p_oaA we obtain

$$\frac{u_z(x,y)}{p_0aA}=\frac{1}{2\pi p_0 a}\iint_S\left[\frac{1}{\rho}p(\zeta,\eta)-\beta\left\{\frac{\zeta-x}{\rho^2}q_x(\zeta,\eta)+\frac{\eta-y}{\rho^2}q_y(\zeta,\eta)\right\}\right]d\zeta d\eta \quad (34)$$

$$\frac{u_x(x,y)}{p_oaA}=\frac{1}{2\pi p_0 a}\iint_S\left[\frac{1}{\rho}q_x(\zeta,\eta)+\left\{\frac{(\zeta-x)^2}{\rho^3}q_x(\zeta,\eta)-\frac{(\zeta-x)(\eta-y)}{\rho^3}q_y(\zeta,\eta)\right\}-\beta\frac{\zeta-x}{\rho^2}p(\zeta,\eta)\right]d\zeta d\eta \quad (35)$$

$$\frac{u_y(x,y)}{p_oaA}=\frac{1}{2\pi p_0 a}\iint_S\left[\frac{1}{\rho}q_y(\zeta,\eta)+\left\{\frac{(\eta-y)^2}{\rho^3}q_y(\zeta,\eta)+\frac{(\zeta-x)(\eta-y)}{\rho^3}q_x(\zeta,\eta)\right\}-\beta\frac{\eta-y}{\rho^2}p(\zeta,\eta)\right]d\zeta d\eta \quad (36)$$

where

$$A=\frac{1-\nu_1}{\mu_1}+\frac{1-\nu_2}{\mu_2} \quad (37)$$

$$\gamma=\left(\frac{\nu_1}{\mu_1}+\frac{\nu_2}{\mu_2}\right)\Big/A. \quad (38)$$

These equations reveal that the normalized problem is uniquely defined by the two material parameters β and γ, and the friction law relating the shearing tractions to the normal ones (e.g., a ratio whose limiting coefficient is f).

Our formulation is somewhat more specific than the general one outlined above. In particular, the shearing tractions are assumed to have no influence upon the normal tractions, which eliminates all but the first term from the integral of Eq. (34) and determines that the frictional tractions (normalized by fp_0) after normal loading depend upon the ratio β/f alone. In addition, the subsequent displacements are evaluated incrementally, which removes the constant normal tractions from Eqs. (35) and (36) and so the normalized shearing tractions are dependent only upon their previous values and the material parameter γ.

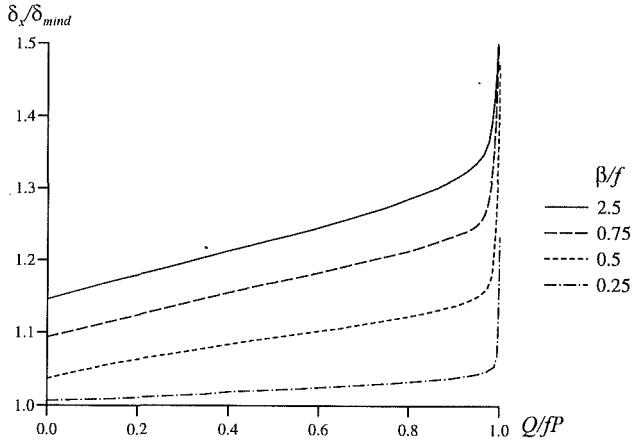


Fig. 6 Initial tangential compliance of the numerical scheme compared with Mindlin's approximation

As can be seen from Eq. (30), Mindlin's prediction of the gross relative displacement of the two bodies attempts to account for material dissimilarity. In order to facilitate the comparison of our results with his, we elect to use δ_{max} (Mindlin's approximation when Q/fP 1.0) as the normalizing length. Quite fortuitiously the ratio of $(2-\nu_1)/\mu_1 + (2-\nu_2)/\mu_2$ to A is a linear function of γ, so no further normalization is necessary. The first observed difference of the numerical scheme is a reduction in the stiffness of the contact when the tangential load is applied in a monotonically increasing manner. This property depends critically upon β/f but is unaffected by changing γ. Figure 6 shows the displacement resulting from the numerical analysis compared with that given by Eq. (30) as Q/fP is increased for representative values of β/f. When elastically dissimilar spheres are loaded normally and then tangentially the shear tractions, which are initially radial, retain a radial component as the tangential load is increased; the result is that the bodies experience gross sliding before $Q/fP = 1.0$ and this is responsible for the apparent dramatic reduction in stiffness as sliding is approached.

When the tangential load is applied in a cyclic manner the *global*, force-displacement characteristic appears to "shakedown" after the first cycle; however, a study of the *local* shear tractions reveals that an actual steady-state is not achieved until several more cycles are completed. In every case studied the modification of the force-displacement history compared with Mindlin's results is independent of γ and depends on the ratio β/f and the magnitude of the tangential force alone. After the first loading cycle the shearing tractions within the slip zone gradually take up an orientation parallel to the applied load. During this process the magnitude of the oscillations is the same as that predicted by Mindlin. However, the *midpoint* of these oscillations is displaced from the original center of the contact, adding to the tangential compliance.

After shakedown, the area of the force-displacement hysteresis is identical to Mindlin's approximation. This implies that the normalized total energy dissipated, as in the case of similar materials, is independent of the material properties. However, the localized energy density is affected by the material parameter γ, but not β. The ratio of the maxima along the lines $x = 0$ and $y = 0$ is plotted in Fig. 7 which shows

Downloaded 03 May 2010 to 171.66.16.20. Redistribution subject to ASME license or copyright; see http://www.asme.org/terms/Terms_Use.cfm

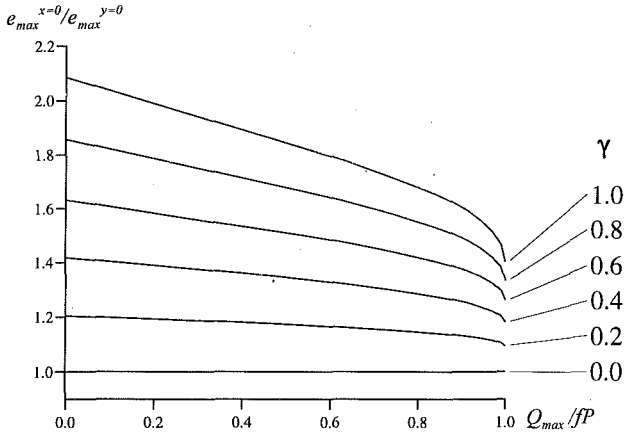


Fig. 7 Ratio of maximum energy density dissipated per cycle along $x = 0$ and $y = 0$

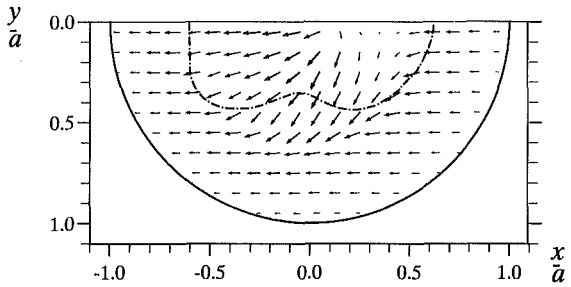


Fig. 8 Orientation and magnitude of surface shearing tractions after two cycles for $\beta/f = 1.0$, $\gamma = 0.0$ and $Q/fP = 0.8$

how it increases with γ and decreases with $Q_{\max}/fP$. Since this property is not dependent on β, the graph is valid for all material combinations, including similar materials.

Finally, Fig. 8 shows a typical distribution of shear tractions (magnitude and direction) for $\beta/f = 1.0$ and $|Q_{\max}/fP| = 0.8$ after two complete cycles. This is part of the transition stage between the initial force displacement and the steady-state. The shape of the stick zone, shown by the chain line, merits further discussion. With each oscillation of the tangential force, the transverse component of tractions within the slip zone is reduced. Initially, this slip zone includes two areas at its edge on each side of the axis of symmetry. Within these regions, the remaining radial component of traction is just sufficient to produce minute micro-slip, but insufficient to affect the local energy dissipation or the force-displacement characteristic. Eventually the tractions there align more closely with the applied tangential load, they no longer experience relative displacement, and the stick zone expands to include them. After about ten complete cycles, the stick zone becomes the circle predicted by Mindlin. Within the stick zone the shearing tractions retain a radial component, but outside it they are aligned with the tangential force. At this stage the material dissimilarity is in evidence only by the offset of the midpoint of the oscillations; the other properties depend upon γ alone.

5 Conclusion

Considering, first, the re-evaluation of contact between elastically similar bodies, it is clear that the transverse shear tractions and displacements are not insignificant, and may not safely be ignored in a study of surface damage. The density of frictional energy dissipation is considerably localized either side of the plane of symmetry, in contrast to the Mindlin solution which predicts an axisymmetric dissipation. The tangential compliance is not significantly affected.

Turning to the corresponding problem for contact between dissimilar materials, it is clear that the pre-existing tractions, present after normal indentation, have a profound effect on the stick zone size and location during the first cycle of loading. This ultimately gives rise to an offset force-displacement history. It is noteworthy, however, that the ratio β/f has an insignificant effect on the distribution of energy dissipated after the first cycle. In our formulation of the problem, in which the influence of shearing tractions on surface normal displacements is neglected, the contact pressure remains Hertzian, and it is shown that the solution is characterized by the two dimensionless ratios β/f and γ. This reduced dependence on the elastic constants permits comprehensive results to be displayed.

References

Cattaneo, C., 1938, "Sul contatto di due corpi elstici: Distribuzione locale degli sforzi," *Reconditi dell Accademia natzionale dei Lincei*, Vol. 27, pp. 342–348, 434–436, 474–478.

Goodman, L. E., 1962, "Contact Stress Analysis of Rough Spheres," ASME JOURNAL OF APPLIED MECHANICS, Vol. 84, pp. 515–522.

Hamilton, G. M., and Goodman, L. E., 1966, "The Stress Field Created by a Circular Sliding Contact," ASME JOURNAL OF APPLIED MECHANICS, Vol. 109, pp. 8–14.

Johnson, K. L., 1955, "Surface Interaction between Elastically Loaded Bodies under Tangential Forces," *Proc. Roy. Soc., London*, Vol. A230, p. 531.

Johnson, K. L., 1985, *Contact Mechanics*, Cambridge University Press, Cambridge, U.K.

Kalker, J. J., 1990, *Three dimensional elastic bodies in rolling contact*, Kluwer, Dordrecht, The Netherlands.

Mindlin, R. D., 1949, "Compliance of Elastic Bodies in Contact," ASME JOURNAL OF APPLIED MECHANICS, Vol. 16, pp. 259–268.

Munisamy, R. L., 1994, "A Study of Dry Frictional Contacts With Emphasis on Material Dissimilarity," D.Phil. Thesis, University of Oxford, Oxford, U.K.

Munisamy, R. L., Hills, D. A., and Nowell, D., 1988, "A Numerical Analysis of an Elastically Dissimilar Three-dimensional Sliding Contact," *Proc. I. Mech. E.*, Part C, Vol. 206, pp. 203–211.

Nowell, D., Hills, D. A., and Sackfield, A., 1988, "Contact of Dissimilar Elastic Cylinders under Normal and Tangential Loading," *Int. Jnl. Mech. Phys. Solids*, Vol. 36, No. 1, pp. 59–75.

Spence, D. A., 1975, "The Hertz Contact Problem with Finite Friction," *Jnl. Elasticity*, Vol. 3-4, pp. 297–398.

Szalwinski, C. M., 1985, "Flexibility of a Contact Area of an Isotropic Body," ASME JOURNAL OF APPLIED MECHANICS, Vol. 52, pp. 62–66.

Downloaded 03 May 2010 to 171.66.16.20. Redistribution subject to ASME license or copyright; see http://www.asme.org/terms/Terms_Use.cfm

Isotropy of Strain Energy Functions Which Depend Only on a Finite Number of Directional Strain Measures

D. Elata[1]

M. B. Rubin
Mem. ASME

Faculty of Mechanical Engineering,
Technion—Israel Institute of Technology,
32000 Haifa, Israel

Motivated by studies of low-density materials and fiber-dominated composites, we consider an elastic material whose strain energy function depends only on a finite number of directional strain measures, which correspond to the strains of material fibers in specific material directions. It is shown that an arbitrary set of six distinct direction vectors can be used to define six symmetric base tensors which span the space of all symmetric second-order tensors. Using these base tensors and their reciprocal tensors we develop a representation for the strain tensor in terms of six directional strain measures. The functional form of the strain energy of a general anisotropic nonlinear elastic material may then be expressed in terms of these directional strain measures. Next, we consider general nonlinear isotropic response by developing explicit functional forms for three independent strain invariants in terms of these directional strain measures. Finally, with reference to previous work, we discuss isotropy of specific functional forms of directional strain measures associated with up to 15 directions in space.

1 Introduction

In the study of low-density materials with open cells and of fiber-dominated matrix composites, it appears useful to model the material as a continuum composed of a collection of one-dimensional struts, each having only axial stiffness. Christensen (1986) used this approach in his analysis of low-density materials where he considered the struts to be randomly oriented. Christensen (1987) also used this approach to determine sufficient symmetry conditions for isotropy of the elastic moduli tensor where he considered six struts oriented normal to six pentagonal faces of a regular dodecahedron. This causes the continuum to have six axes of five-fold symmetry. Furthermore, Christensen (1987, p. 773) emphasized that the symmetry characteristics of the continuum should not be confused with the symmetry characteristics of the cell architecture.

From a macroscopic continuum point of view it is possible to use the strain tensor at a given material point to calculate the axial strain of a material fiber oriented in any given direction. In both of his studies Christensen (1986, 1987) used the affine assumption that the strain in any given one-dimensional strut is equal to the axial strain of a material fiber oriented in the direction of the strut. In this sense the representative cell consisting of the collection of struts is considered to experience homogeneous deformation. Confining attention to linear elastic response and using the affine assumption Christensen (1986, 1987) derived stress-strain relations for the continuum by summing the contributions of the individual struts. Since the struts used in his analysis were presumed to exhibit uniaxial stress in the direction of the strut, the resulting continuum equations were equivalent to the theory of Poisson and Cauchy with one elastic constant and Poisson's ratio $\nu = 1/4$.

In his analysis of open-cell architecture Christensen (1986) also used the affine assumption and considered a collection of 30 struts oriented along the edges of a regular dodecahedron. Kimmel et al. (1986) and Budiansky and Kimmel (1987) also considered a similar collection of struts in their analysis of lung tissue, but they assumed the struts were connected by pin joints so they analyzed the mechanics of the resulting truss structure. The important distinction between these two approaches is that Kimmel et al. (1986) and Budiansky and Kimmel (1987) do not use the affine assumption.

The main objective of this paper is to reconsider the question of isotropy of continuum materials of the type considered by Christensen (1986, 1987) from the simpler point of view of analysis of the associated strain energy function. To this end we use the affine assumption and consider an elastic material

[1]Presently at Lawrence Livermore Laboratory, Livermore, CA.

Contributed by the Applied Mechanics Division of THE AMERICAN SOCIETY OF MECHANICAL ENGINEERS for presentation at the International Mechanical Engineering Congress and Exhibition, the Winter Annual Meeting of The ASME, Chicago, IL, Nov. 13-18, 1994.

Discussion on this paper should be addressed to the Technical Editor, Professor Lewis T. Wheeler, Department of Mechanical Engineering, University of Houston, Houston, TX 77204-4792, and will be accepted until four months after final publication of the paper itself in the ASME JOURNAL OF APPLIED MECHANICS.

Manuscript received by the ASME Applied Mechanics Division, Oct. 12, 1992; final revision, Apr. 22, 1993. Associate Technical Editor: G. J. Dvorak.

Paper No. 94-WA/APM-2.

Copyright © 1994 by ASME
Downloaded 03 May 2010 to 171.66.16.20. Redistribution subject to ASME license or copyright; see http://www.asme.org/terms/Terms_Use.cfm

whose strain energy depends only on a finite number of directional strain measures, which correspond to the strains of material fibers in specific material directions. Here we generalize the work of Christensen (1987) in the following two ways: (1) we consider large deformation nonlinear elastic response; and (2) we consider a more general dependence of the strain energy function on the directional strain measures, so the resulting elastic continuum will be more general than a Poisson-Cauchy material.

With regard to the generalization (2) we should mention that Christensen (1987) analyzed the question of isotropy from the point of view of stress-strain relations rather than the strain energy. Nevertheless, his work (Christensen, 1987) corresponds to the assumptions that each strut has the same constant Young's modulus E_m, the strain energy of each elastic strut is proportional to the square of the directional strain in the direction of the strut, and that the total strain energy is the sum of the strain energies of all the struts. Within the context of his assumptions Christensen (1987) concluded that a model of six struts (oriented normal to six pentagonal faces of a regular dodecahedron) exhibited isotropic response. In this work we emphasize that isotropy of the material response depends on both the functional form of the strain energy and on the particular directions chosen for the directional strain measures. In particular we will show that the restriction of isotropy imposes a restriction on the functional form of the strain energy which may be satisfied even if the directions associated with the directional strains are not oriented in the directions considered by Christensen (1987).

Throughout this work the summation convention applies on repeated indices unless: (i) the notation (no sum) appears by the equation, or (ii) the term with repeated indices is contained within a summation symbol (Σ). Boldfaced symbols will be used to indicate tensors (including vectors) in Euclidean three-space and indices will take the range ($i = 1, 2, \ldots, n$) when we consider a collection of n directional strain measures.

In the following sections we show that only six directional strain measures are needed to model a general anisotropic elastic material and that the directions associated with these strain measures need only be distinct in a sense defined later. In developing these results we consider some mathematical preliminaries associated with convenient representations of general symmetric second-order tensors. After developing representations of the strain invariants we exhibit the functional form of the strain energy for isotropic elastic response with directional strain measures in six arbitrary distinct directions. As a special case we consider the six directions used by Christensen (1987) and develop the strain energy function for a general isotropic elastic material with an arbitrary (within the usual bounds) value of Poisson's ratio. Next, we consider additional sets of directional strain measures. For convenience some of the mathematical results are recorded in the Appendix.

2 Representations of Elastic Materials

By way of background, consider a body embedded in Euclidean three-space and refer the position of material points in the body to a fixed Cartesian coordinate system with the orthogonal base vectors $\{\mathbf{e}_1, \mathbf{e}_2, \mathbf{e}_3\}$. Let $\mathbf{X}$ locate the position of a material point in the reference configuration and $\mathbf{x}$ locate the position of the same material point in the present configuration, at time t. Furthermore, let $\mathbf{F} = \partial\mathbf{x}/\partial\mathbf{X}$ be the deformation gradient, $\mathbf{C} = \mathbf{F}^T\mathbf{F}$ be the right Cauchy-Green deformation tensor, and $\mathbf{E} = (1/2)(\mathbf{C} - \mathbf{I})$ be the Lagrangian strain tensor, where $\mathbf{I}$ is the unit tensor.

For the elastic materials under consideration here, we assume that the strain energy is a function of a collection of n directional strain measures. These directional strain measures correspond to the strains of material fibers, which in the reference configuration, are oriented in the unit vector directions $\mathbf{N}_i$ ($i = 1, 2, \ldots, n$). To this end, it is convenient to define associated symmetric second-order tensors $\mathbf{B}_i$, called direction tensors, by the formulas

$$\mathbf{B}_i = \mathbf{N}_i \otimes \mathbf{N}_i \quad \text{(no sum on } i\text{)} \quad (i = 1, 2, \ldots, n), \tag{1}$$

where the symbol $\otimes$ denotes the tensor product. Notice that each direction tensor is insensitive to the attitude of the direction vector on which it is based [$\mathbf{B}_i = \mathbf{N}_i \otimes \mathbf{N}_i = (-\mathbf{N}_i) \otimes (-\mathbf{N}_i)$]. Consequently, each direction tensor is characterized by the orientation of a line in space rather than one of the two opposing directions along that line. The directional strain measure E_i in the $\mathbf{N}_i$ direction is

$$E_i = \mathbf{B}_i \cdot \mathbf{E} = \mathbf{N}_i \cdot (\mathbf{E}\mathbf{N}_i) \quad \text{(no sum on } i\text{)} \quad (i = 1, 2, \ldots, n), \tag{2}$$

where the symbol ($\cdot$) denotes the dot product between two tensors. For example, $\mathbf{A} \cdot \mathbf{B}$ denotes the usual scalar product between two vectors when $\mathbf{A}$, $\mathbf{B}$ are first-order tensors, and it denotes $\mathrm{tr}(\mathbf{A}\mathbf{B}^T)$ when $\mathbf{A}$, $\mathbf{B}$ are two second-order tensors. The strain measures E_i are valid for large deformations and their associated forms for small deformations are well known.

Since the strain tensor $\mathbf{E}$ is symmetric ($\mathbf{E} = \mathbf{E}^T$) it follows that it has only six independent components. This means that it is possible to completely characterize the strain at a point with only six directional measures of strain E_i if the six directions $\mathbf{N}_i$ are distinct and the six direction tensors $\mathbf{B}_i$ are independent, in the sense defined presently. Specifically, the six directions tensors $\mathbf{B}_i (i = 1, 2, \ldots, 6)$ will span the space of all symmetric second-order tensors if they are linearly independent and therefore satisfy the condition that

$$\alpha_i \mathbf{B}_i = 0 \quad \text{only if} \quad \alpha_i = 0 \quad (i = 1,2, \ldots, 6), \tag{3}$$

where α_i are constants. For our present purposes it is convenient to define the symmetric metric β_{ij} ($i, j = 1, 2, \ldots, 6$) of a six-dimensional space through the formula

$$\beta_{ij} = \mathbf{B}_i \cdot \mathbf{B}_j = (\mathbf{N}_i \cdot \mathbf{N}_j)^2 \quad (\beta_{ij} = \beta_{ji}) \quad (i,j, = 1,2, \ldots, 6). \tag{4}$$

Assuming that $\mathbf{B}_i$ are linearly independent then the condition (3) holds and (4) may be used to deduce the results

$$\alpha_i \beta_{ij} \alpha_j = (\alpha_i \mathbf{B}_i) \cdot (\alpha_j \mathbf{B}_j) > 0 \quad \text{if any } \alpha_i \neq 0$$

$$(i,j, = 1,2, \ldots, 6), \tag{5a}$$

$$\alpha_i \beta_{ij} \alpha_j = (\alpha_i \mathbf{B}_i) \cdot (\alpha_j \mathbf{B}_j) = 0 \quad \text{only if all } \alpha_i = 0$$

$$(i,j, = 1,2, \ldots, 6), \tag{5b}$$

which indicate that β_{ij} is positive definite and therefore invertible. If on the other hand we have

$$\det(\beta_{ij}) \neq 0, \quad (i,j, = 1,2, \ldots, 6), \tag{6}$$

then β_{ij} is invertible so that $\alpha_i \beta_{ij}$ vanishes only when all α_i vanish. Consequently, in view of the quadratic form (5) it follows that β_{ij} is positive definite and the condition (3) must hold so that again $\mathbf{B}_i$ are linearly independent. In this sense the directions $\mathbf{N}_i$ are said to be distinct and the direction tensors $\mathbf{B}_i$ are linearly independent if $\det(\beta_{ij})$ is positive.

Given that $\det(\beta_{ij})$ is positive, the inverse of β_{ij} exists and can be denoted by β^{ij} such that

$$\beta_{ik}\beta^{kj} = \beta^{jk}\beta_{ki} = \delta_i^j \quad (i,j = 1,2, \ldots, 6), \tag{7}$$

where δ_i^j is the Kronecker delta in six-dimensional space and β^{ij} is symmetric. We now define the six reciprocal tensors $\mathbf{B}^i$ by

$$\mathbf{B}^i = \beta^{ij}\mathbf{B}_j \quad (i,j = 1,2, \ldots, 6), \tag{8}$$

so that the six direction tensors $\mathbf{B}_i$ and their reciprocal tensors $\mathbf{B}^i$ satisfy the relations

$$\mathbf{B}_i \cdot \mathbf{B}^j = \mathbf{B}^j \cdot \mathbf{B}_i = \delta_i^j \quad (i,j = 1,2, \ldots, 6). \tag{9}$$

It also follows from (4), (7), and (8) that

$$\mathbf{B}^i \cdot \mathbf{B}^j = \beta^{ij} \quad (i,j = 1,2, \ldots, 6). \tag{10}$$

Downloaded 03 May 2010 to 171.66.16.20. Redistribution subject to ASME license or copyright; see http://www.asme.org/terms/Terms_Use.cfm

We note that although the direction tensor $\mathbf{B}_i$ may be represented as the simple tensor product of the direction vector $\mathbf{N}_i$ with itself ($\mathbf{B}_i = \mathbf{N}_i \otimes \mathbf{N}_i$, no sum on i) the reciprocal tensor $\mathbf{B}^i$ cannot be represented in such a simple form.

Given six distinct direction vectors $\mathbf{N}_i$, the direction tensors $\mathbf{B}_i$ and their reciprocal tensors $\mathbf{B}^i$ may each be used as a basis for representing an arbitrary symmetric second-order tensor. For example, the strain tensor $\mathbf{E}$ admits the representations

$$\mathbf{E} = E_i \mathbf{B}^i \quad \text{where } E_i = \mathbf{E} \cdot \mathbf{B}_i \quad (i = 1,2, \ldots, 6), \tag{11a}$$

$$\mathbf{E} = E^i \mathbf{B}_i \quad \text{where } E^i = \mathbf{E} \cdot \mathbf{B}^i \quad (i = 1,2, \ldots, 6). \tag{11b}$$

It follows from (11) that with reference to a six-dimensional space, E_i and E^i may be thought of as the covariant and contravariant components of $\mathbf{E}$, respectively. Similarly, $\mathbf{B}_i$ and $\mathbf{B}^i$ may be thought of as covariant and contravariant base tensors, respectively. However, unlike the directional strain measure E_i, the physical meaning of E^i is not simple.

On the basis of (11a), we conclude that the strain energy of any nonlinear anisotropic elastic material may be represented as a function of six directional strain measures associated with the direction is $\mathbf{N}_i$ if the condition (6) is satisfied. In particular, given an elastic material characterized by the strain energy function $\psi = \hat{\psi}(\mathbf{E})$ we may write

$$\psi = \hat{\psi}(E_i \mathbf{B}^i) = \overline{\psi}(E_1, E_2, \ldots, E_6), \tag{12}$$

where $\overline{\psi}$ is a different function from $\hat{\psi}$. It now follows from (12) and the representation (11a) that the symmetric Piola-Kirchhoff stress tensors $\mathbf{S}$ becomes

$$\mathbf{S} = \frac{\partial \hat{\psi}}{\partial \mathbf{E}} = \frac{\partial \overline{\psi}}{\partial E_i} \frac{\partial E_i}{\partial \mathbf{E}} = \frac{\partial \overline{\psi}}{\partial E_i} \mathbf{B}_i \quad (i = 1,2, \ldots, 6), \tag{13}$$

where the strain energy ψ is measured per unit reference volume.

It is well known that for nonlinear isotropic elastic materials, the strain energy is a function of the strain $\mathbf{E}$, only through three independent invariants of $\mathbf{E}$. Here, we use the three invariants

$$\Phi_I = \mathbf{E} \cdot \mathbf{I}, \quad \Phi_{II} = \mathbf{E} \cdot \mathbf{E}, \quad \Phi_{III} = \det(\mathbf{E}) = \frac{1}{6} (\mathbf{E} \times \mathbf{E}) \cdot \mathbf{E}, \tag{14a, b, c}$$

where the cross product $\mathbf{E} \times \mathbf{E}$ between two tensors is defined in the Appendix. Using the representation (11a) these three invariants may be expressed as functions of the six directional strain measures E_i by the formulas

$$\Phi_I = E_i \mathbf{B}^i \cdot \mathbf{I}, \tag{15a}$$

$$\Phi_{II} = E_i E_j \mathbf{B}^i \cdot \mathbf{B}^j = E_i E_j \beta^{ij}, \tag{15b}$$

$$\Phi_{III} = \frac{1}{6} (\mathbf{E} \times \mathbf{E}) \cdot \mathbf{E} = \frac{1}{6} E_i E_j E_k (\mathbf{B}^i \times \mathbf{B}^j) \cdot \mathbf{B}^k. \tag{15c}$$

Therefore, the strain energy of a general isotropic elastic material may be represented in the form

$$\psi = \tilde{\psi}(\Phi_I, \Phi_{II}, \Phi_{III}) = \overline{\overline{\psi}}(E_1, E_2, \ldots, E_6). \tag{16}$$

where Φ_I, Φ_{II}, Φ_{III} are given by (15).

For a given set of six distinct direction vectors $\mathbf{N}_i$, we can regard (15) as functions of the six directional strain measures E_i. Since these functions are invariants of $\mathbf{E}$, they are insensitive to rigid rotations of the direction vectors $\mathbf{N}_i$. In general, $\mathbf{N}_i$ can be any set of six vectors which are distinct in the sense that (6) is satisfied, so the functions (15) may be rather complicated. However, with the intention of simplifying these functional forms we are intuitively led to consider an "isotropic" set of directions $\mathbf{N}_i$. To this end, consider the intersection points of a spherical surface and a set of different lines that pass through the center of the sphere. If the intersection points are uniformly distributed over the spherical surface (i.e., the distances between all neighboring intersection points are equal), then the set of lines is said to be "equi-spaced." If every line is described by a single unit vector, the set of unit vectors is called an "equi-spaced set of directions." The problem of distributing n points uniformly over the sphere (so that the distances between all neighboring points are equal) is identical to the problem of the construction of a regular polyhedron that has n vertices. Jacobs (1970) presents a simple argument showing that there are only five regular polyhedra. Consequently, it can be shown that there are only four[2] independent equi-spaced sets of directions in three-dimensional space. One of these sets is described in the following section, and the other three sets are described in Section 4.

3 Six Axes of Five-Fold Symmetry

The following six unit vectors define six nonparallel lines in space. These lines are defined by either: normals to the faces of a regular dodecahedron; or lines passing through opposing vertices of a regular icosahedron (Fig. 1)

$$\mathbf{N}_1 = \mathbf{e}_1, \qquad \mathbf{N}_2 = \frac{1}{\sqrt{5}} \mathbf{e}_1 + \frac{2}{\sqrt{5}} \mathbf{e}_2, \tag{17a, b}$$

$$\mathbf{N}_3 = \frac{1}{\sqrt{5}} \mathbf{e}_1 + \frac{1}{2}\left(1 - \frac{1}{\sqrt{5}}\right) \mathbf{e}_2 + \sqrt{\frac{1}{2}\left(1 + \frac{1}{\sqrt{5}}\right)}\ \mathbf{e}_3, \tag{17c}$$

$$\mathbf{N}_4 = \frac{1}{\sqrt{5}} \mathbf{e}_1 - \frac{1}{2}\left(1 + \frac{1}{\sqrt{5}}\right) \mathbf{e}_2 + \sqrt{\frac{1}{2}\left(1 - \frac{1}{\sqrt{5}}\right)}\ \mathbf{e}_3, \tag{17d}$$

$$\mathbf{N}_5 = \frac{1}{\sqrt{5}} \mathbf{e}_1 - \frac{1}{2}\left(1 + \frac{1}{\sqrt{5}}\right) \mathbf{e}_2 - \sqrt{\frac{1}{2}\left(1 - \frac{1}{\sqrt{5}}\right)}\ \mathbf{e}_3, \tag{17e}$$

$$\mathbf{N}_6 = \frac{1}{\sqrt{5}} \mathbf{e}_1 + \frac{1}{2}\left(1 - \frac{1}{\sqrt{5}}\right) \mathbf{e}_2 - \sqrt{\frac{1}{2}\left(1 + \frac{1}{\sqrt{5}}\right)}\ \mathbf{e}_3. \tag{17f}$$

The set of equi-spaced directions exhibit six axes of five-fold symmetry and is the same one used by Christensen (1987). It may be shown that the related six direction tensors $\mathbf{B}_i$ are linearly independent, that the related metric β_{ij} and its inverse β^{ij} are given by

$$\beta_{ij} = \frac{1}{5} \begin{pmatrix} 5 & 1 & 1 & 1 & 1 & 1 \\ 1 & 5 & 1 & 1 & 1 & 1 \\ 1 & 1 & 5 & 1 & 1 & 1 \\ 1 & 1 & 1 & 5 & 1 & 1 \\ 1 & 1 & 1 & 1 & 5 & 1 \\ 1 & 1 & 1 & 1 & 1 & 5 \end{pmatrix},$$

$$\beta^{ij} = \frac{1}{8} \begin{pmatrix} 9 & -1 & -1 & -1 & -1 & -1 \\ -1 & 9 & -1 & -1 & -1 & -1 \\ -1 & -1 & 9 & -1 & -1 & -1 \\ -1 & -1 & -1 & 9 & -1 & -1 \\ -1 & -1 & -1 & -1 & 9 & -1 \\ -1 & -1 & -1 & -1 & -1 & 9 \end{pmatrix}, \tag{18a, b}$$

and that the determinant of β_{ij} is

$$\det(\beta_{ij}) = \frac{2^{11}}{5^5} > 0. \tag{19}$$

Using the definition (8) and the result (18b), it may easily be shown that for these direction vectors the functions (15a, b) may be expressed as

[2]Every set of equi-spaced directions can be related to more than one regular polyhedron.

Downloaded 03 May 2010 to 171.66.16.20. Redistribution subject to ASME license or copyright; see http://www.asme.org/terms/Terms_Use.cfm

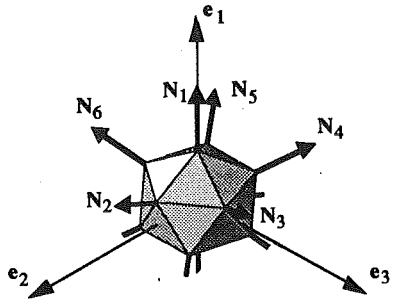


Fig. 1 The vertices of a regular icosahedron

$$\Phi_I=\frac{1}{2}\sum_{i=1}^{6}E_i,\quad \Phi_{II}=\frac{5}{4}\sum_{i=1}^{6}E_i^2-\frac{1}{8}\left(\sum_{i=1}^{6}E_i\right)^2. \qquad (20a,\ b)$$

Furthermore, using the definition (8) and the expression (18*b*), it can be shown that the reciprocal tensors $\mathbf{B}^i$ have the simpler forms

$$\mathbf{B}^i=\frac{10}{8}\mathbf{B}_i-\frac{1}{8}\sum_{j=1}^{6}\mathbf{B}_j=\frac{5}{4}\mathbf{B}_i-\frac{1}{4}\mathbf{I}\quad (i=1,2,\ldots,6). \qquad (21)$$

However, to calculate the term $(\mathbf{B}^i\times\mathbf{B}^j)\cdot\mathbf{B}^k$ in (15*c*) it seems most convenient to first calculate the expression $(\mathbf{B}_i\times\mathbf{B}_j)\cdot\mathbf{B}_k$. To this end, we use the definition (1) and write (see Eq. (A2) of the Appendix)

$$(\mathbf{B}_i\times\mathbf{B}_j)\cdot\mathbf{B}_k=(\mathbf{N}_i\times\mathbf{N}_j\cdot\mathbf{N}_k)^2. \qquad (22)$$

In view of the properties of the scalar triple product of three vectors the cross and dot operations may be interchanged so that $(\mathbf{B}_i\times\mathbf{B}_j)\cdot\mathbf{B}_k$ is seen to be insensitive to any permutations of its indices. Furthermore, with reference to Fig. 1 and the expression (22), it may be observed that the term $(\mathbf{B}_i\times\mathbf{B}_j)\cdot\mathbf{B}_k$ is related to the volume of the tetrahedron defined by the vectors $\{\mathbf{N}_i, \mathbf{N}_j, \mathbf{N}_k\}$. Using this notion as well as the fact that $(\mathbf{B}_i\times\mathbf{B}_j)\cdot\mathbf{B}_k$ is insensitive to the attitude (sign) of $\mathbf{N}_i$ it follows that the only nontrivial tetrahedrons separate into two distinct groups of the type defined by either $\{\mathbf{N}_1, \mathbf{N}_2, \mathbf{N}_3\}$ or $\{\mathbf{N}_1, \mathbf{N}_2, \mathbf{N}_4\}$. Thus, the scalars $(\mathbf{B}_i\times\mathbf{B}_j)\cdot\mathbf{B}_k$ may be seen to take the values

$$(\mathbf{B}_i\times\mathbf{B}_j)\cdot\mathbf{B}_k=\begin{cases}0 & \text{for } i=j \text{ or } i=k \text{ or } j=k, \quad (23a)\\ \frac{2}{5}\left(1+\frac{1}{\sqrt{5}}\right) & \text{for Condition A,} \quad (23b)\\ \frac{2}{5}\left(1-\frac{1}{\sqrt{5}}\right) & \text{for Condition B,} \quad (23c)\end{cases}$$

where Conditions A and B are defined by: *Condition A:* The lines associated with $\mathbf{N}_i$, $\mathbf{N}_j$, $\mathbf{N}_k$ are different and pass through the three corners of a single triangular surface of the icosahedron (Fig. 1) so that the indices $\{i, j, k\}$ may be all permutations of the sets of numbers {1, 2, 3}, {1, 2, 6}, {1, 3, 4}, {1, 4, 5}, {1, 5, 6}, {2, 3, 5}, {2, 4, 5}, {2, 4, 6}, {3, 4, 6}, {3, 5, 6}; *Condition B:* The lines associated with $\mathbf{N}_i$, $\mathbf{N}_j$, $\mathbf{N}_k$ are different and do not pass through the corners of a single triangular surface of the icosahedron (Fig. 1) so that the indices $\{i, j, k\}$ may be all permutations of the set of numbers {1, 2, 4}, {1, 2, 5}, {1, 3, 5}, {1, 3, 6}, {1, 4, 6}, {2, 3, 4}, {2, 3, 6}, {2, 5, 6}, {3, 4, 5}, {4, 5, 6}. Now we may use (8) to compute the values $(\mathbf{B}^i\times\mathbf{B}^j)\cdot\mathbf{B}^k$ from the formula

$$(\mathbf{B}^i\times\mathbf{B}^j)\cdot\mathbf{B}^k=\beta^{il}\beta^{jm}\beta^{kn}(\mathbf{B}_l\times\mathbf{B}_m)\cdot\mathbf{B}_n, \qquad (24)$$

where β^{ij} is given in (18*b*). It can be seen from (24) that in view of the symmetry of the quantity $(\mathbf{B}_l\times\mathbf{B}_m)\cdot\mathbf{B}_n$ the term $(\mathbf{B}^i\times\mathbf{B}^j)\cdot\mathbf{B}^k$ is also insensitive to permutations of its indices. Specifically it may be shown that the term $(\mathbf{B}^i\times\mathbf{B}^j)\cdot\mathbf{B}^k$ has four distinct values which are recorded in the Appendix.

In order to compare with previous work it is convenient to consider two additional functions of the directional strain measures of the forms

$$\phi_1=\sum_{i=1}^{6}E_i,\quad \phi_2=\sum_{i=1}^{6}E_i^2. \qquad (25a,\ b)$$

Using the expressions (15) and (20) it follows that the functions ϕ_1 and ϕ_2 are scalar invariants which can be represented in the alternative forms[3]

$$\phi_1=2\Phi_I=2\mathbf{E}\cdot\mathbf{I},\quad \phi_2=\frac{2}{5}\Phi_I^2+\frac{4}{5}\Phi_{II}=\frac{2}{5}[(\mathbf{E}\cdot\mathbf{I})^2+2\mathbf{E}\cdot\mathbf{E}]. \qquad (26a,\ b)$$

A simple nonlinear generalization of the strain energy of an isotropic linear elastic material may be represented in the form

$$\psi=\frac{1}{2}[\lambda(\mathbf{E}\cdot\mathbf{I})^2+2\mu\mathbf{E}\cdot\mathbf{E}], \qquad (27)$$

where λ and μ are Lame's constants. Using the result (26*b*) it may be shown that a nonlinear form of the strain energy associated with Christensen's (1987) six strut linearly elastic model can be written in the form

$$\psi=\frac{1}{2}\mu[(\mathbf{E}\cdot\mathbf{I})^2+2\mathbf{E}\cdot\mathbf{E}]=\frac{5}{4}\mu\phi_2, \qquad (28)$$

with only one elastic constant $\lambda=\mu$ and Poisson's ratio $\nu=1/4$ (see Christensen, 1987, Eqs. (4)). This is not surprising because the strain energy (28) can be seen to depend only on a single strain invariant ϕ_2. However, by including dependence on the two invariants ϕ_1 and ϕ_2 in the form

$$\psi=\frac{1}{8}(\lambda-\mu)\phi_1^2+\frac{5}{4}\mu\phi_2, \qquad (29)$$

we obtain a two-parameter isotropic elastic model of the type (27). This shows the importance of including an independent measure of volume change ϕ_1 in the strain energy of a non-Poisson-Cauchy material with an arbitrary (within the usual bounds) value of ν.

4 Additional Sets Of Direction Vectors

In this section we generalize the functions ϕ_1 and ϕ_2 in (25) to be applicable to a set of n different direction vectors $\mathbf{N}_i$ such that

$$\phi_1=\sum_{i=1}^{n}E_i,\quad \phi_2=\sum_{i=1}^{n}E_i^2, \qquad (30a,\ b)$$

where E_i are the directional strain measures defined by (2). Here we will consider different sets of direction vectors and will examine whether or not the functions (30) are isotropic functions of the strain $\mathbf{E}$. In addition, we will present explicit representations of the isotropic functions in terms of invariants of $\mathbf{E}$.

As mentioned in Section 2, there are only four independent equi-spaced sets of directions in three-dimensional space. These sets of equi-spaced directions are denoted as *D*3, *D*4, *D*6, and *D*10, where the number next to the letter *D* corresponds to the number of lines defining the set. Each of the direction vectors associated with these sets will be represented in terms of the rectangular Cartesian base vectors $\mathbf{e}_i$. Specifically, set *D*3 is defined by the three lines normal to the faces of a cube, with $\mathbf{N}_i$ given by

$$\mathbf{N}_1=\mathbf{e}_1,\quad \mathbf{N}_2=\mathbf{e}_2,\quad \mathbf{N}_3=\mathbf{e}_3. \qquad (31a,\ b,\ c)$$

The set *D*4 is defined by the four lines normal to the faces of a regular tetrahedron, or normal to faces of a regular oc-

[3]It is interesting to note that the function $\Sigma_{i=1}^{6}E_i^3$ is not an invariant of $\mathbf{E}$.

Downloaded 03 May 2010 to 171.66.16.20. Redistribution subject to ASME license or copyright; see http://www.asme.org/terms/Terms_Use.cfm

tahedron, or by lines passing through opposing vertices of a cube, with $\mathbf{N}_i$ given by

$$\mathbf{N}_1=\mathbf{e}_1, \qquad \mathbf{N}_2=-\frac{1}{3}\mathbf{e}_1+\frac{2\sqrt{2}}{3}\mathbf{e}_2, \tag{32a, b}$$

$$\mathbf{N}_3=-\frac{1}{3}\mathbf{e}_1-\frac{\sqrt{2}}{3}\mathbf{e}_2+\sqrt{\frac{2}{3}}\mathbf{e}_3, \quad \mathbf{N}_4=-\frac{1}{3}\mathbf{e}_1-\frac{\sqrt{2}}{3}\mathbf{e}_2-\sqrt{\frac{2}{3}}\mathbf{e}_3. \tag{32c, d}$$

The set $D6$ is defined by Eqs. (17). The set $D10$ is the last equi-spaced set and is defined by ten lines normal to faces of a regular icosahedron, or by ten lines passing through opposing vertices of a regular dodecahedron, with $\mathbf{N}_i$ given by

$$\mathbf{N}_1=\mathbf{e}_1, \qquad \mathbf{N}_2=\frac{\sqrt{5}}{3}\mathbf{e}_1+\frac{2}{3}\mathbf{e}_2, \tag{33a, b}$$

$$\mathbf{N}_3=\frac{\sqrt{5}}{3}\mathbf{e}_1-\frac{1}{3}\mathbf{e}_2+\frac{1}{\sqrt{3}}\mathbf{e}_3, \quad \mathbf{N}_4=\frac{\sqrt{5}}{3}\mathbf{e}_1-\frac{1}{3}\mathbf{e}_2-\frac{1}{\sqrt{3}}\mathbf{e}_3, \tag{33c, d}$$

$$\mathbf{N}_5=\frac{1}{3}\mathbf{e}_1+\frac{\sqrt{5}}{3}\mathbf{e}_2+\frac{1}{\sqrt{3}}\mathbf{e}_3, \quad \mathbf{N}_6=\frac{1}{3}\mathbf{e}_1+\frac{1}{3\tau^2}\mathbf{e}_2+\frac{\tau}{\sqrt{3}}\mathbf{e}_3, \tag{33e, f}$$

$$\mathbf{N}_7=\frac{1}{3}\mathbf{e}_1-\frac{\tau^2}{3}\mathbf{e}_2+\frac{1}{\tau\sqrt{3}}\mathbf{e}_3, \quad \mathbf{N}_8=\frac{1}{3}\mathbf{e}_1-\frac{\tau^2}{3}\mathbf{e}_2-\frac{1}{\tau\sqrt{3}}\mathbf{e}_3, \tag{33g, h}$$

$$\mathbf{N}_9=\frac{1}{3}\mathbf{e}_1+\frac{1}{3\tau^2}\mathbf{e}_2-\frac{\tau}{\sqrt{3}}\mathbf{e}_3, \quad \mathbf{N}_{10}=\frac{1}{3}\mathbf{e}_1+\frac{\sqrt{5}}{3}\mathbf{e}_2-\frac{1}{\sqrt{3}}\mathbf{e}_3, \tag{33i, j}$$

where $\tau = (1 + \sqrt{5})/2$ is known as the Golden ratio.

Since there are only five regular polyhedra, it is impossible to *uniformly* distribute more than 20 points over the surface of a sphere, so there are no sets with more than ten equi-spaced directions. In spite of this, we will consider a non-equi-spaced set of 15 direction vectors denoted by $d15$ which is defined by fifteen lines parallel to the edges of a regular dodecahedron or parallel to the edges of a regular icosahedron, with $\mathbf{N}_i$ given by

$$\mathbf{N}_1=\mathbf{e}_1, \quad \mathbf{N}_2=\mathbf{e}_2, \quad \mathbf{N}_3=\mathbf{e}_3, \tag{34a, b, c}$$

$$\mathbf{N}_4=\frac{\tau}{2}\mathbf{e}_1+\frac{1}{2}\mathbf{e}_2+\frac{1}{2\tau}\mathbf{e}_3, \quad \mathbf{N}_5=\frac{1}{2\tau}\mathbf{e}_1-\frac{\tau}{2}\mathbf{e}_2+\frac{1}{2}\mathbf{e}_3, \quad \mathbf{N}_6=\frac{1}{2}\mathbf{e}_1-\frac{1}{2\tau}\mathbf{e}_2-\frac{\tau}{2}\mathbf{e}_3, \tag{34d, e, f}$$

$$\mathbf{N}_7=\frac{\tau}{2}\mathbf{e}_1-\frac{1}{2}\mathbf{e}_2+\frac{1}{2\tau}\mathbf{e}_3, \quad \mathbf{N}_8=\frac{1}{2}\mathbf{e}_1+\frac{1}{2\tau}\mathbf{e}_2-\frac{\tau}{2}\mathbf{e}_3, \quad \mathbf{N}_9=\frac{1}{2\tau}\mathbf{e}_1+\frac{\tau}{2}\mathbf{e}_2+\frac{1}{2}\mathbf{e}_3, \tag{34g, h, i}$$

$$\mathbf{N}_{10}=\frac{\tau}{2}\mathbf{e}_1-\frac{1}{2}\mathbf{e}_2-\frac{1}{2\tau}\mathbf{e}_3, \quad \mathbf{N}_{11}=\frac{1}{2\tau}\mathbf{e}_1+\frac{\tau}{2}\mathbf{e}_2-\frac{1}{2}\mathbf{e}_3, \quad \mathbf{N}_{12}=\frac{1}{2}\mathbf{e}_1+\frac{1}{2\tau}\mathbf{e}_2+\frac{\tau}{2}\mathbf{e}_3, \tag{34j, k, l}$$

$$\mathbf{N}_{13}=\frac{\tau}{2}\mathbf{e}_1+\frac{1}{2}\mathbf{e}_2-\frac{1}{2\tau}\mathbf{e}_3, \quad \mathbf{N}_{14}=\frac{1}{2}\mathbf{e}_1-\frac{1}{2\tau}\mathbf{e}_2+\frac{\tau}{2}\mathbf{e}_3, \quad \mathbf{N}_{15}=\frac{1}{2\tau}\mathbf{e}_1-\frac{\tau}{2}\mathbf{e}_2-\frac{1}{2}\mathbf{e}_3. \tag{34m, n, o}$$

It can be seen from (34) that the set $d15$ is actually a combination of five differently oriented $D3$ sets of orthonormal vectors $(\mathbf{N}_1, \mathbf{N}_2, \mathbf{N}_3)$, $(\mathbf{N}_4, \mathbf{N}_5, \mathbf{N}_6)$, . . . , $(\mathbf{N}_{13}, \mathbf{N}_{14}, \mathbf{N}_{15})$. The set $d15$ is considered because the directional strain measures associated with it are the same strain measures used by Christensen (1986) in his analysis of open cell architecture.

Table 1 Alternative representations of the functions ϕ_1 and ϕ_2

Set	n	ϕ_1	ϕ_2
D3	3	$\frac{3}{3}\mathbf{E}\cdot\mathbf{I}$	not an invariant
D4	4	$\frac{4}{3}\mathbf{E}\cdot\mathbf{I}$	not an invariant
D6	6	$\frac{6}{3}\mathbf{E}\cdot\mathbf{I}$	$\frac{6}{15}\left[(\mathbf{E}\cdot\mathbf{I})^2+2\mathbf{E}\cdot\mathbf{E}\right]$
D10	10	$\frac{10}{3}\mathbf{E}\cdot\mathbf{I}$	$\frac{10}{15}\left[(\mathbf{E}\cdot\mathbf{I})^2+2\mathbf{E}\cdot\mathbf{E}\right]$
d15	15	$\frac{15}{3}\mathbf{E}\cdot\mathbf{I}$	$\frac{15}{15}\left[(\mathbf{E}\cdot\mathbf{I})^2+2\mathbf{E}\cdot\mathbf{E}\right]$

Using a computer program for symbolic mathematical manipulations we were able to determine exact representations of the functions ϕ_1 and ϕ_2 in (30) associated with these sets of directions and the results are presented in Table 1. Since the sets $D3$ and $D4$ have less than six direction vectors, they cannot be used to represent the function ϕ_2 as an invariant of the strain tensor. Nevertheless, they can be used to express ϕ_1 in terms of the first invariant of strain. This means that they could be used to represent the strain energy of a linearly elastic isotropic material that responds only to volume changes and is insensitive to distortional changes[3]. As can be seen from Table 1, the sets $D6$, $D10$, and $d15$ can be used to express the functions ϕ_1 and ϕ_2 in terms of invariants of strain. It follows that a strain energy of the form (28) with ϕ_2 being determined for the set $d15$ will represent an isotropic material. Consequently, the result for ϕ_2 associated with set $d15$ presented in Table 1 proves that Christensen's (1986) dodecahedral open-cell model exhibits isotropic response.

Acknowledgment

The authors would like to acknowledge helpful discussions with Prof. E. Altus and Dr. G. Iosilevskii.

References

Budiansky, B., and Kimmel, E., 1987, "Elastic Moduli of Lungs," ASME JOURNAL OF APPLIED MECHANICS, Vol. 54, pp. 351–358.

Christensen, R. M., 1986, "Mechanics of Low Density Materials," *Journal of the Mechanics and Physics of Solids*, Vol. 34, pp. 563–578.

Christensen, R. M., 1987, "Sufficient Symmetry Conditions for Isotropy of the Elastic Moduli Tensor," ASME JOURNAL OF APPLIED MECHANICS, Vol. 54, pp. 772–777.

[4]For nonlinear deformations the function ϕ_1 is sensitive to distortional changes of the body.

Downloaded 03 May 2010 to 171.66.16.20. Redistribution subject to ASME license or copyright; see http://www.asme.org/terms/Terms_Use.cfm

Jacobs, H. R., 1970, *Mathematics: A Human Endeavor*, W. H. Freeman, San Francisco, pp. 209–212.

Kimmel, E., Kamm, R. D., and Shapiro, A. H., 1987, "A Cellular Model Of Lung Elasticity," ASME *Journal of Biomechanical Engineering*, Vol. 109, pp. 126–131.

APPENDIX

Consider two second-order tensors $\mathbf{A} = A_{ij}\,\mathbf{e}_i \otimes \mathbf{e}_j$ and $\mathbf{B} = B_{ij}\,\mathbf{e}_i \otimes \mathbf{e}_j$ with components A_{ij} and B_{ij} referred to the rectangular Cartesian base vectors $\mathbf{e}_i\,(i = 1, 2, 3)$. The cross product $\mathbf{A} \times \mathbf{B}$ is defined by the second-order tensor

$$\mathbf{A}\times\mathbf{B} = (A_{ij}\mathbf{e}_i\otimes\mathbf{e}_j)\times(B_{lm}\mathbf{e}_l\otimes\mathbf{e}_m),$$

$$= A_{ij}B_{lm}(\mathbf{e}_i\times\mathbf{e}_l)\otimes(\mathbf{e}_j\times\mathbf{e}_m) = A_{ij}B_{lm}\epsilon_{ilk}\epsilon_{jmn}\mathbf{e}_k\otimes\mathbf{e}_n, \quad \text{(A1)}$$

where ϵ_{ilk} is the permutation symbol and all indices in (A1) have the range (1, 2, 3). It follows from the definition (1) of the main text that

$$\mathbf{B}_i\times\mathbf{B}_j = (\mathbf{N}_i\otimes\mathbf{N}_i)\times(\mathbf{N}_j\otimes\mathbf{N}_j) = (\mathbf{N}_i\times\mathbf{N}_j)\otimes(\mathbf{N}_i\times\mathbf{N}_j)$$

(no sum on i, j)

$(i, j = 1,2, \ldots, n)$. (A2)

For the special case of the six direction vectors of Section 3 the values of the terms $(\mathbf{B}^i \times \mathbf{B}^j) \cdot \mathbf{B}^k$ are given by

$$(\mathbf{B}^i\times\mathbf{B}^j)\cdot\mathbf{B}^k = \frac{3}{8} \quad \text{for } i=j=k, \quad \text{(A3}a\text{)}$$

$$-\frac{1}{4} \quad \text{for } i=j\neq k \text{ or } i=k\neq j \text{ or } j=k\neq i, \quad \text{(A3}b\text{)}$$

$$\frac{7+5\sqrt{5}}{32} \quad \text{for Condition A,} \quad \text{(A3}c\text{)}$$

$$\frac{7-5\sqrt{5}}{32} \quad \text{for Condition B,} \quad \text{(A3}d\text{)}$$

where Conditions A and B are described in the main text just after Eqs. (23).

Downloaded 03 May 2010 to 171.66.16.20. Redistribution subject to ASME license or copyright; see http://www.asme.org/terms/Terms_Use.cfm

N. Zabaras
Assoc. Professor,
Sibley School of Mechanical
and Aerospace Engineering,
188 Engineering and Theory Center,
Cornell University,
Ithaca, NY 14853
ASME Mem.

S. Liu
Senior Engineer,
CAE Application and Development,
Hardgoods and Electronic Support Division,
3M Center Building 260-6A-08,
3M Company,
St. Paul, MN 55144
ASME Mem.

J. Koppuzha
Senior Research Physicist,
National Media Laboratory,
3M Information and Imaging
Technologies Sector,
3M Center Building 235-3B-30,
3M Company,
St. Paul, MN 55144

E. Donaldson
Manager,
CAE Application and Development,
Hardgoods and Electronic Support Division,
3M Center Building 260-6A-08,
3M Company,
St. Paul, MN 55144
ASME Mem.

A Hypoelastic Model for Computing the Stresses in Center-Wound Rolls of Magnetic Tape

A hypoelastic finite element model for the calculation of continuous internal stress and deformation distributions in wound rolls used in center winding is presented. The stress problem is formulated as an initial boundary value problem and its solution satisfies continuity of deformation as one rewinds more layers on the growing roll. Hypoelasticity is shown to be a natural way to account for the growing body nature of a magnetic tape during winding. Several cases are examined with constant and radial stress dependent radial elastic modulus. The agreement with Hakiel's model and experimental data obtained through the sandwiched pull strip method is very good. The results for the static linear and nonlinear cases examined found to be weakly dependent on the winding speed. The present analysis is more versatile than previous models in simulating the growing nature of the tape pack and it can naturally be extended to include nonlinear time and history-dependent phenomena.

Introduction

The long-term integrity of a tape pack depends mainly on how well the pack was wound. The roll pressure distribution is a good indicator of the winding quality of the tape pack. Lack of tension causes winding defects such as cinching and spoking, while excessive pressure can lead to an increased creep and stress relaxation phenomena. Thus, knowledge of the stress distribution in a wound roll is important for understanding the mechanisms of roll defects. Altmann (1968) assuming plane stress conditions and an orthotropic roll calculated in an integral form the pressure and the in-roll tension distribution. Yogoda (1980) used Altmann's calculations to find a closed-form solution for the stresses by assuming a power series expansion of the winding tension in terms of the radial location. Yogoda (1981) also extended Altmann's formulas to plane strain. These solutions treat the roll as a homogeneous orthotropic disk with constant elastic moduli in both the radial and tangential directions. Experimental results show that the radial elastic modulus E_r depends on the interlayer pressure. Pfeiffer (1979) modeled the interlayer pressure as a function of the radial strain, while Hakiel (1987) modeled E_r as a polynomial function of pressure. Willett and Poesch (1988) considered the radial strain to be a polynomial function of the interlayer pressure.

The current analyses of center-wound rolls (tapes) are based on a sequence of assumptions that will now be briefly reviewed in order to put the hypoelastic analysis in the right perspective. Let us suppose that one wants to calculate the stress increment that is added to the stress distribution of a tape consisting of $(n-1)$ layers while one is currently winding the nth model

Contributed by the Applied Mechanics Division of THE AMERICAN SOCIETY OF MECHANICAL ENGINEERS for publication in the ASME JOURNAL OF APPLIED MECHANICS.

Discussion on this paper should be addressed to the Technical Editor, Professor Lewis T. Wheeler, Department of Mechanical Engineering, University of Houston, Houston, TX 77204-4792, and will be accepted until four months after final publication of the paper itself in the ASME JOURNAL OF APPLIED MECHANICS.

Manuscript received by the ASME Applied Mechanics Division, June 11, 1992; final revision, Apr. 7, 1993. Associate Technical Editor: F. Y. M. Wan.

Copyright © 1994 by ASME
Downloaded 03 May 2010 to 171.66.16.20. Redistribution subject to ASME license or copyright; see http://www.asme.org/terms/Terms_Use.cfm

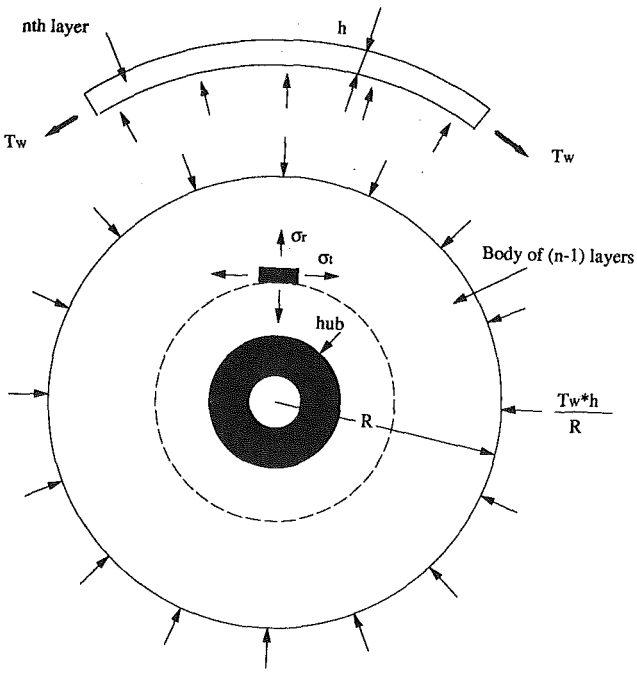


Fig. 1 A traditional way for looking at the stress problem during tape winding

layer. The term "model layer" is here used to describe a collection of several physical tape layers. Then it is customary to follow three steps (for example, Pfeiffer, 1979):

(1) Apply equilibrium of the nth layer assuming that it is under prescribed tension and calculate the traction forces (pressure) acting on its bottom surface. In this step one solves a statically determinate problem, i.e., no consideration of the deformation of the nth layer comes into the analysis. To start this step, it is assumed that the nth layer tension is at the given winding tension T_w (Fig. 1).

(2) Solve a boundary value problem for the (continuum) body consisting of $(n-1)$ layers with prescribed displacement boundary conditions on the hub and traction boundary condition on the top of the $n-1$ layer (Fig. 1). This last boundary condition is the pressure that was calculated from step (1) above.

(3) Using the solution of step (2) one can calculate the tangential stress on the top surface of the $(n-1)$ layer body and then return to step (2) above by updating the tension of the nth layer.

The above procedure generates a sequence of ordinary differential equations for σ_r that are solved starting out at the hub and progressing to the outer layer. The interlayer pressure is obtained via linear superposition by summing the radial stress increments found from the solutions of these ordinary differential equations. Finally, the tangential stress is found from the stress equilibrium equations based on the calculated solution for σ_r.

Several serious drawbacks are associated with the above analyses. Even though one solves sequences of two separate problems, one for the nth layer and another one for the body of $(n-1)$ layers, one is still interested in satisfying equilibrium and compatibility for the continuum body consisting of n layers. Satisfaction of this condition requires continuity of tractions and displacements as we pass from the top surface of the $(n-1)$ layer to the bottom surface of the nth layer. To correct this problem one could, for example, include a fourth step (4) where the information from steps (1) and (2) is used to solve a new boundary value problem defined by the continuum consisting of all n layers.

To account for these difficulties special attention has to be given to the fact that a magnetic tape is not a fixed body, but a body which grows during winding. We propose a completely new way of thinking of the winding process. Instead of solving a boundary value problem we will consider an *initial boundary value problem*. This will allow us to account for the fact that each new tape layer that is added to the existing layers has some initial stresses at the time it becomes part of the tape pack (zero radial and prescribed tangential stresses). Due to this initial stress condition, the strain tensor does not satisfy the compatibility condition, even though the compatibility condition is satisfied when it is expressed in terms of strain rates. In this sense, it is natural to express all governing equations that involve strain in a rate form. As a result, classical elasticity is not appropriate for analyzing the deformation of growing bodies and hypoelastic deformations must be considered instead (stress rates proportional to strain rates). This form of elasticity introduces history of deformation since each layer becomes part of the tape pack at different times. Due to this history involvement, one will calculate residual stresses at the end of winding even when the elastic moduli of each layer are constant. This idea of hypoelasticity has been shown to be very appropriate for other growing body problems (Zabaras et al., 1991). It will still require knowledge of the elastic properties of the stack of tape layers. Measurement of elastic properties of magnetic tapes is a complicated issue. These measurements are strongly affected by the amount of air trapped between layers, the amount of friction, previous winding conditions, humidity, temperature, thickness of stack, and other factors. The problem is even more complicated considering, for example, that the air trapped between layers is itself a function of the stress distribution in the stack of tape layers. To avoid some of these complications and in order to treat the stack of tape layers as a homogeneous body, the elastic properties of a stack of tape layers are generally considered to be functions of the radial stress in a way similar to that introduced earlier by Pfeiffer (1979), Hakiel (1987), and others.

The present paper starts with a brief review of the governing equations and a detailed presentation of the hypoelastic model. The FEM implementation of this model is then given together with the algorithm. Several detailed examples are presented and the results are compared with those obtained from Hakiel's model as well as with experimental data. The potential of the present model in analyzing time and history-dependent deformations is discussed.

The Hypoelastic Analysis

The hypoelastic formulation introduces a new variable, time, to the tape winding problem. In hypoelastic analysis, each material point in the tape becomes part of the tape pack at different times. The radius of the tape pack increases with time as more tape layers are wound into the pack during the winding operation. The stresses in the whole tape pack are affected by the initial stresses induced by winding tension in newly wound tape. The radius of the tape pack at time t, $R(t)$, and its rate $\dot{R}(t)$ are usually known in a winding operation.

Governing Equations. The tape pack is modeled as collection of concentric hoops of tape. Radially symmetric geometry is assumed, and the stresses and displacements in the tape pack are assumed to be functions of radial but not of circumferential and axial locations. The kinematics are expressed in a rate form as follows:

$$\left.\begin{aligned}\dot{\epsilon}_r &= \frac{d\dot{u}}{dr}\\ \dot{\epsilon}_t &= \frac{\dot{u}}{r}\end{aligned}\right\} \tag{1}$$

where $(\dot{\ })$ denotes a time derivative, ϵ_r and ϵ_t are strains in radial and circumferential directions, respectively, and u is the

Downloaded 03 May 2010 to 171.66.16.20. Redistribution subject to ASME license or copyright; see http://www.asme.org/terms/Terms_Use.cfm

radial displacement. The equilibrium equation has the form

$$r\frac{d\sigma_r}{dr}+\sigma_r-\sigma_t=0 \tag{2}$$

where σ_r and σ_t are the radial and circumferential stresses, respectively.

For numerical reasons, the equilibrium equation is not expressed in a rate form (Zabaras et al., 1991). Indeed, satisfying the rate of equilibrium equation can numerically lead to stresses that slowly deviate from their equilibrium values.

The hypoelastic constitutive equations are introduced as

$$\left.\begin{aligned}\dot{\sigma}_r&=\frac{E_r}{1-\nu_{rt}\nu_{tr}}\dot{\epsilon}_r+\frac{\nu_{tr}E_r}{1-\nu_{rt}\nu_{tr}}\dot{\epsilon}_t\\ \dot{\sigma}_t&=\frac{\nu_{rt}E_t}{1-\nu_{rt}\nu_{tr}}\dot{\epsilon}_r+\frac{E_t}{1-\nu_{rt}\nu_{tr}}\dot{\epsilon}_t\end{aligned}\right\} \tag{3}$$

where following familiar notation E_r, E_t, ν_{rt}, and ν_{tr} are the moduli of elasticity and Poisson's ratios, respectively. E_r and E_t are generally assumed to be functions of temperature and pressure. Their rates do not appear in the particular hypoelastic model (Zabaras et al., 1991). In this sense, the model (3) is distinct from the rate model that results from the time differentiation of the (hyper) elastic model that will include time derivatives of the elastic moduli.

The stresses at a material point at time t_n, $n=1, 2, \ldots$ can be evaluated from the stress rates at that point by performing the following backward integration scheme:

$$\left.\begin{aligned}\sigma_r(t_n)&=\dot{\sigma}_r(t_n)\Delta t^*+\sigma_r(t_{n-1})\\ \sigma_t(t_n)&=\dot{\sigma}_t(t_n)\Delta t^*+\sigma_t(t_{n-1}),\end{aligned}\right\} \tag{4}$$

where $\sigma(t_{n-1})$ is the stress of the particular material point at time t_{n-1}, $\dot{\sigma}(t_n)$ denotes the stress rate at the same point at time t_n, and Δt^* is a time step defined as follows:

(a) if a material point was part of the tape pack at both t_n and t_{n-1}, $\Delta t^*=t_n-t_{n-1}$ and $\sigma(t_{n-1})$ is the stress of the material point in the tape pack at time t_{n-1}.

(b) if the material point just became part of the tape at time t_n, $\Delta t^*=0$ and $\sigma(t_{n-1})$ is the initial stress of the material point when it became part of the tape pack. These initial stresses are

$$\left.\begin{aligned}\sigma_r^0&=0\\ \sigma_t^0&=T_w\end{aligned}\right\} \tag{5}$$

where T_w is the winding tension at time t_n.

(c) if a material point becomes part of the tape at time t^* with $t_{n-1}<t^*<t_n$, then $\Delta t^*=t_n-t^*$, and $\sigma(t_{n-1})$ is given as in Eq. (5).

The tape pack is considered at all times to be a continuum governed by Eqs. (1)–(5) with appropriate boundary conditions at its inner and outer surfaces. At the outer surface of the core, that is, at the inner surface of the tape pack, $r=R_{in}$, continuity of the displacement and normal stress, gives the following boundary condition:

$$u=\frac{\sigma_r}{E_c}R_{in} \quad \text{at} \quad r=R_{in} \tag{6}$$

where E_c is the known effective stiffness of the core.

At the outer surface of the pack at time t, $r=R(t)$, the radial stress is zero, i.e.,

$$\sigma_r=0 \quad \text{at} \quad r=R(t). \tag{7}$$

In summary, in order to calculate the residual stresses in a tape of final radius $R(t_{\max})$ due to the winding process, one must solve a sequence of initial boundary value problems defined by Eqs. (1) and (2), with the constitutive model of Eq. (3), the boundary conditions from Eqs. (6) and (7), and the initial conditions given from Eq. (5).

Finite Element Formulation and Implementation. A Galerkin type of weak formulation of equilibrium Eq. (2) is developed for a finite element method implementation. At any time t has the following form

$$\int_{R_{in}}^{R(t)}\delta u\left(r\frac{d\sigma_r}{dr}+\sigma_r-\sigma_t\right)dr=0 \tag{8}$$

where δu is a kinematically admissible variation of the displacement u. With integration by parts and noting that $\sigma_r(R(t))=0$ at the outer surface of the tape pack, and that since $u(R_{in})$ is prescribed, $\delta u(R_{in})=0$, we can finally write the weak form of the equilibrium equation as

$$\int_{R_{in}}^{R(t)}(\delta\epsilon_r r\sigma_r+\delta u\sigma_t)dr=0. \tag{9}$$

The region $[R_{in}, R(t)]$ is now divided into finite elements. In each element Ω_e, the displacement is expressed as

$$u^e=\sum_{i=1}^{N^e}u_i^e\phi_i^e \tag{10}$$

where N^e is the total number of nodes in the element, u_i^e is the displacement at the node i, and ϕ_i^e is the shape function corresponding to node i. Substituting Eqs. (10) into (9) and using the fact that δu_i^e is arbitrary, one can finally show that

$$\sum_{e=1}^{E}\int_{\Omega_e}\left(r\sigma_r\frac{d\phi_i^e}{dr}+\sigma_t\phi_i^e\right)dr=0 \quad i=1, 2, \ldots N^e. \tag{11}$$

Let us use Eqs. (1) and (3) to express σ_r and σ_t in Eq. (11) in terms of $\dot{u}$. At each time t_n, one can then write the following assembled equations in terms of $\dot{u}$:

$$K_{IJ}\dot{u}_J=F_I \quad I,J=1, 2, \ldots M \text{ (sum on } J) \tag{12}$$

where I and J are the global nodal numbers corresponding to element nodes i and j, respectively, and $M(t)$ is the total number of nodes for the tape pack at time t.

In Eq. (12),

$$K_{IJ}=\sum_{e=1}^{E}k_{ij}^e, \quad \text{and} \quad F_I=\sum_{e=1}^{E}f_i^e,$$

where E is the total number of elements. The element expressions of k_{ij}^e and f_i^e are as follows:

$$k_{ij}^e=\int_{\Omega_e}\left[\frac{E_r}{1-\nu_{rt}\nu_{tr}}r\frac{d\phi_i^e}{dr}\frac{d\phi_j^e}{dr}+\frac{\nu_{tr}E_r}{1-\nu_{rt}\nu_{tr}}\frac{d\phi_i^e}{dr}\phi_j^e+\frac{\nu_{rt}E_t}{1-\nu_{rt}\nu_{tr}}\phi_i^e\frac{d\phi_j^e}{dr}+\frac{E_t}{1-\nu_{rt}\nu_{tr}}\phi_i^e\frac{\phi_j^e}{r}\right]\Delta t^*\,dr \tag{13}$$

$$f_i^e=-\int_{\Omega_e}\left[r\frac{d\phi_i^e}{dr}\sigma_r(t_{n-1})+\phi_i^e\sigma_t(t_{n-1})\right]dr. \tag{14}$$

Numerical integration of Gauss method is used in k_{ij}^e and f_i^e calculations. In each Gauss integration point of the element e, Δt^* is expressed as

$$\Delta t^*=\sum_{i=1}^{N^e}\Delta t_i^{*e}\phi_i^e \tag{15}$$

where Δt_i^{*e} is the Δt^* of the material particle located at node i, and ϕ_i^e are the same shape functions as those used in Eq. (10). It is important to note that Eq. (12) is not the discretized version of the rate equilibrium equations. The rates have been appeared only because of the hypoelastic constitutive model. Also note that Δt^* appears inside the integral in Eq. (13). If E_r is considered a function of σ_r, then iteration on σ_r is necessary to solve Eq. (12).

Solution Procedure. In summary, the following algorithm

Downloaded 03 May 2010 to 171.66.16.20. Redistribution subject to ASME license or copyright; see http://www.asme.org/terms/Terms_Use.cfm

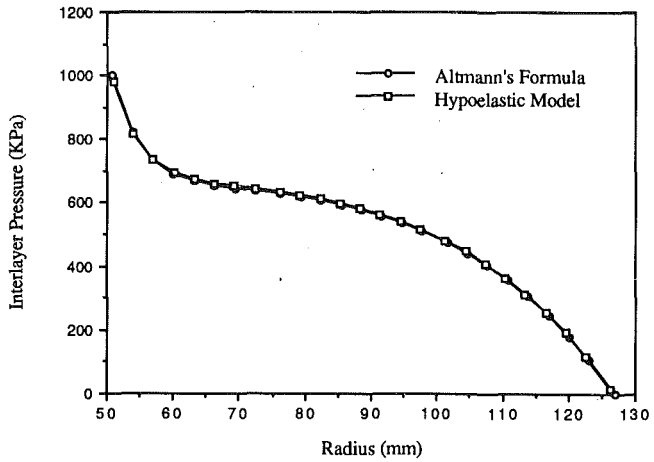


Fig. 2 Interlayer pressure of a linear orthotropic tape pack with constant E_r

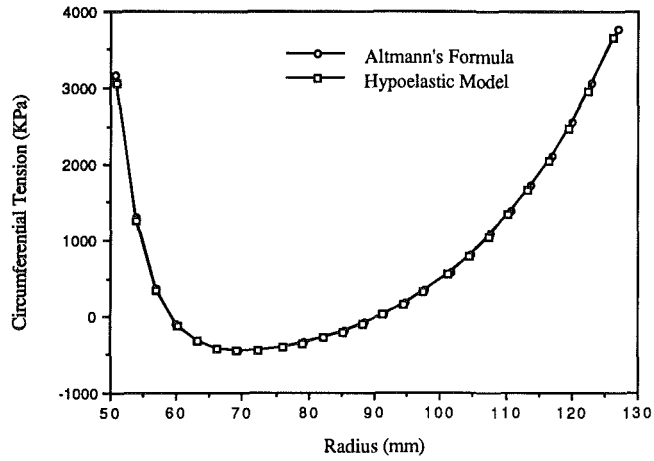


Fig. 3 Circumferential tension of a linear orthotropic tape pack with constant E_r

must be followed in the finite element method implementation of the hypoelastic analysis of the tape winding problem.

1 Calculate the Δt needed to wind the new model layer according to the winding conditions (note that each model layer has the same number of physical tape layers).

2 Add new finite elements to the pack for the newly added layer.

3 Compute the f_i^e by Eq. (14) and assembly it into F_I as in Eq. (12).

4 Start iteration for σ_r, set σ_r for first iteration.

5 Calculate E_r as function of σ_r at each Gauss point.

6 Compute k_{ij}^e by Eq. (13) and assembly them into K_{IJ} as in Eq. (12).

7 Apply boundary conditions Eq. (6) and (7) to Eq. (12) and solve Eq. (12) for $\dot{u}_J$ ($J=1, 2, \ldots, M$).

8 Use $\dot{u}_J$ and constitutive Eq. (3) to get $\dot{\sigma}_r$ and $\dot{\sigma}_t$.

9 Integrate $\dot{\sigma}_r$ and $\dot{\sigma}_t$ to get σ_r and σ_t by using Eq. (4).

10 Check the maximum difference between the σ_r components of the current and previous iterations. If the difference $>$ tolerance, update σ_r and go to 5. If the difference $<$ tolerance, go to 11.

11 If all the layers have been wound, then stop and print the results. If more layers needed to wind, add a new layer and go to 1.

Note that if the material properties are considered as constants, steps 4, 5, and 10 are skipped.

In the numerical computations reported here, linear finite elements have been used. Each layer is modeled with one finite element except the current winding layer, where a fine mesh (five elements) is used. After the calculations at each time step are completed, the newly added layer of five finite elements is represented by one finite element where all stresses and displacements are mapped. As such, at the final pack, a uniform finite element mesh is obtained. It is assumed that the tape is wound to the pack at a constant linear tangential speed, V_0. If the physical thickness of the tape is h, the relationship between the current pack radius, $R(t)$, and time t can be derived as

$$\pi(R^2(t) - R_{in}^2) = V_0 ht \tag{16}$$

where R_{in} is the inner radius of the tape pack, and $R(t=0) = R_{in}$. The time needed to wind a layer of tape at current radius $R(t)$ is

$$\Delta t = \frac{\pi}{V_0}[2R(t) + nh]n \tag{17}$$

where n is the number of physical tape layers in each model layer. Note that the relation, $R(t+\Delta t) - R(t) = nh$ has been applied in deriving Eq. (17). Also note that Δt changes with time and is such that at each time step a fixed number of physical layers are always wound to the tape roll. The calculation starts at time $t=0$ and radius $R=R_{in}$. For each new wound layer, new elements are added to the pack and Δt is calculated by Eq. (17) The finite element method mesh density was found to be important in the nonlinear cases examined and finer meshes were required to obtain good solutions.

Examples

Example 1: Linear Orthotropic Tape Pack With Constant E_r. In this example, the magnetic tape pack is modeled as a linear orthotropic structure. The pack inside radius is $R_{in} = 50.8$ mm, while the final pack outside radius is $R_0 = 127.0$ mm. The thickness of the tape is 0.0254 mm, there are 3000 physical layers in the final pack, and each model layer consists of 30 physical layers. The tape Young's modulus in the tangential direction is given by Willett and Poesch (1988) as $E_t = 6.200 \times 10^3$ MPa. Typical values in the magnetic tape industry also suggest $E_r = 1.379 \times 10^2$ MPa. The effective modulus for an aluminum core is $E_c = 2.127 \times 10^4$ MPa and the tape Poisson's ratio $\nu_{tr} = 0.3$. The ν_{rt} value can be estimated from $\nu_{rt} = \nu_{tr}E_r/E_t$. Finally, the winding speed is 508 mm/sec and the winding tension is 3.771 MPa. The results of the computations with constant E_r are shown in Figs. 2 and 3, together with Altmann's analytical solution (Altmann, 1968). Both interlayer pressure and circumferential tension computed by the hypoelastic model are in excellent agreement with Altmann's solution. Figures 4(a) and 4(b) also show the calculated radial displacement at the end of winding. This calculation is not directly available to the other techniques that are stress based. In Fig. 4(a), "relative displacement" of a material layer, is the radial displacement of the layer with zero displacement reference its position at the deformed roll at the time when the particular layer became part of the roll. This relative displacement is calculated by adding the displacement increments as they are calculated from the displacement rates (Eq. (12)). In Fig. 4(b), "absolute displacement" is the radial displacement of a layer with reference to its position at a rigid roll (as if the winding process was without deformation). Note that using the present hypoelastic model, the obtained stresses and displacements were found to weakly depend upon the winding speed.

From this example it follows that the classical elasticity approach is adequate as far as the stress distributions are concerned. The hypoelastic model becomes important when the growing aspect of the tape pack is modeled. However, even when only stresses are needed, the present model is more ver-

Downloaded 03 May 2010 to 171.66.16.20. Redistribution subject to ASME license or copyright; see http://www.asme.org/terms/Terms_Use.cfm

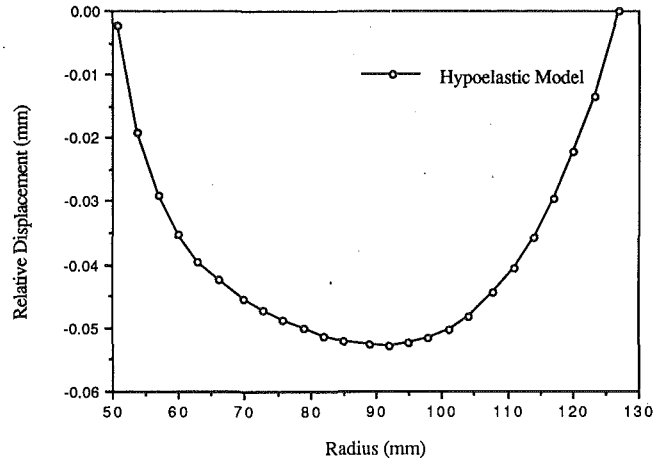


Fig. 4(*a*) Relative displacement in the radial direction of a linear orthotropic tape pack

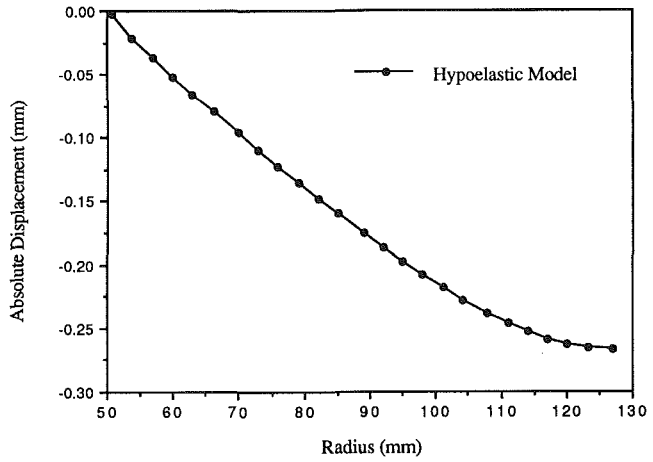


Fig. 4(*b*) Absolute displacement in the radial direction of a linear orthotropic tape rack

satile and it can easily be implemented in general purpose FEM deformation algorithms.

Example 2: Comparison With Experimental Data. Winding experiments were performed at 3M's National Media Laboratory for nontensilized magnetic tape to verify the proposed model. The interlayer pressure and core pressure were measured and compared against the modeled results.

The elastic modulus of a stack of film in the thickness direction (radial modulus E_r) was determined by compressing the stack and measuring the load and deflection data as suggested by Pfeiffer. Several compression tests were performed to determine E_r for different types of tapes. Specifically, circular tape samples of diameter of about 1.8 cm were punched and stacked to a height of about 3 to 4 cm. This stack was then inserted into a steel tube of slightly larger diameter and compressed by a piston of diameter 1.6 cm using a computerized Instron and load cell arrangement. When samples are cut, it is possible to have irregular and distorted edges and these edge effects are avoided by compressing the samples with a piston of smaller diameter than the sample diameter. A dead mass (weight) of 500 gm was used to squeeze out most of the air of the stack. It was found that for a given load the deflection values during loading and unloading are different, indicating the existence of a hysteresis loop. From the slope of the stress/strain plot, the radial modulus (stack modulus) for that particular film is computed for various stress values and an empirical expression for E_r as a function of radial stress was

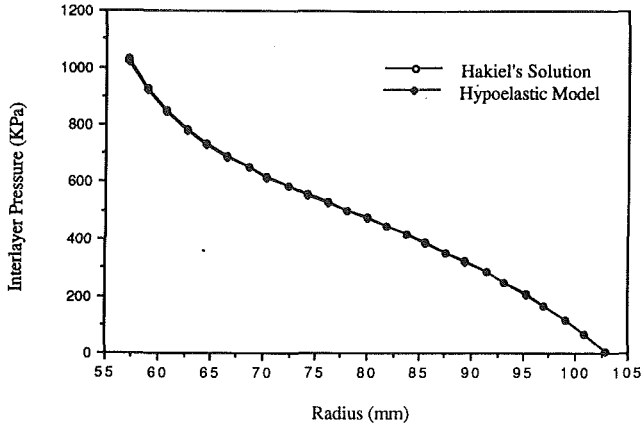


Fig. 5 Interlayer pressure in a tape pack of nontensilized films

developed by fitting the data. Separate expressions for E_r as a function of radial stress (pressure p) were developed for loading and unloading cases. Five stacks of a nontensilized coated film were compressed and quadratic expressions of the form $E_r = C_1 p + C_2 p^2$, were determined for each case. The values of C_1 and C_2, were determined by fitting the test data. The obtained expression for E_r using the average coefficients is given as $E_r = 490.8923p - 0.52345 \times 10^{-4} p^2$, for the loading case, and $E_r = 673.5635p - 0.59767 \times 10^{-4} p^2$, for the unloading case. Here E_r and p are in Pascals.

The nontensilzed coated tape has a modulus 5.0573×10^9 Pascals in the machine direction and is 1.9 cm wide and 2.54×10^{-3} cm thick. The tape was wound with 170 gm tension at a winding speed of 0.254 meters per second on an aluminum hub of inner diameter 8.89 cm and outer diameter 11.43 cm ($E_c = 1.833 \times 10^4$ MPa). The tape Poisson's ratio $\nu_{tr} = 0.3$ and the ν_{rt} value was estimated from $\nu_{rt} = \nu_{tr} E_r / E_t$. No experimental validation of this equation is available. However, it is widely used in the tape industry and its use preserves the symmetry of the stiffness matrix. The outer diameter of the pack was 20.574 cm. There are 3600 physical layers in the final pack and 300 model layers were used. For modeling purposes, the expression for E_r for the loading case mentioned above was used along with the given tape properties and winding conditions.

The interlayer pressure inside a tape pack was measured after winding using a special device called "the Sandwiched Pull Strip" (SPS) developed at 3M's National Media Laboratory (Koppuzha, 1992). Here, a strip of stainless steel (25 cm long, 0.25 cm wide, and 0.0025 cm thick) is sandwiched between two pieces of stainless steel shim stocks (2.5 cm long, 2 cm wide, and 0.00125 cm thick). The SPS is precalibrated by applying known pressure on it and measuring the force required to pull the strip back and forth using a force gauge. During winding, five or six SPS devices are inserted between layers at different radii and after winding the interlayer pressure at each location is determined by measuring the pull strip force at that location. Some of the advantages of this device over the conventional pull tab, are what we do not have to determine the coefficient of friction between the tape and tab surfaces, and also that the strip remains inside the pack maintaining the integrity of the tape pack, where when pull tabs are pulled out, voids are created within the pack that can perturb the pressure profile.

With a final finite element method mesh of 300 elements, the interlayer pressure and circumferential tension are calculated and compared with the solution obtained using an implementation of Hakiel's model (Figs. 5 and 6). Figure 7 shows modeled versus measured interlayer pressure distribution data (SPS data) from the same winding experiment. The agreement

Downloaded 03 May 2010 to 171.66.16.20. Redistribution subject to ASME license or copyright; see http://www.asme.org/terms/Terms_Use.cfm

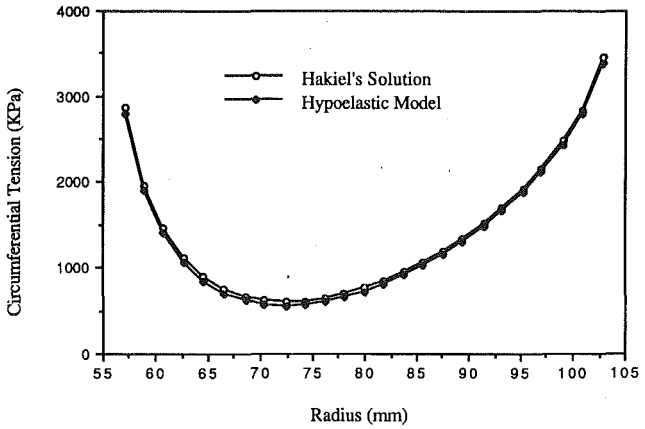


Fig. 6 Circumferential tension in a tape pack of nontensilized films

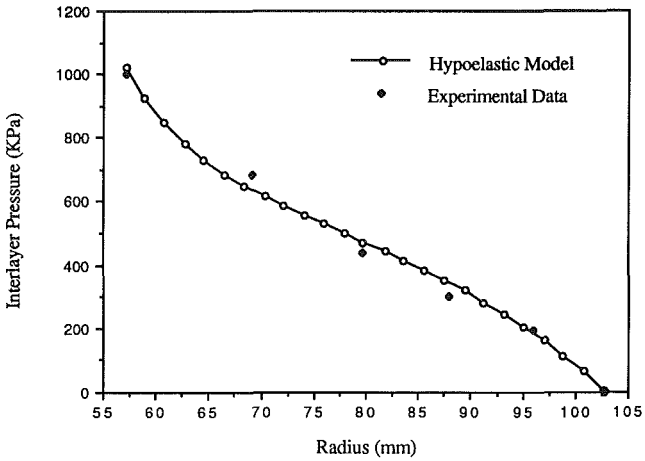


Fig. 7 Interlayer pressure in a pack of nontensilized tapes

of the hypoelastic solution with both experimental data and Hakiel's solution is very good.

The core pressure could be accurately determined by mounting a strain gauge on the inner side of the hub. The strain gauge should be precalibrated by applying known radial pressure on the hub and measuring the signal voltage for each applied pressure. During the winding process, strain gauge data is taken by stopping the winding process at various radii of winding. Figure 8 depicts modeled versus measured data for core pressure (strain gauge data) from a winding experiment. Again the agreement is very good. In this experiment a strain gauge was mounted on the inner side of an aluminum hub of inner diameter 7.62 cm and outer diameter 8.89 cm ($E_c = 1.0542 \times 10^4$ MPa). The magnetic tape used in this test is the nontensilized tape whose properties were defined earlier in this section.

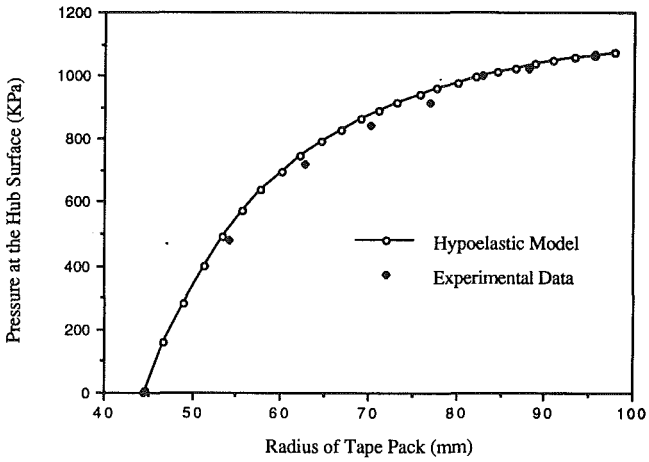


Fig. 8 Pressure at the hub/tape pack interface as the radius of the tape pack increases

Conclusions

A new way of thinking of the winding process was introduced. A sequence of initial boundary value problems has been proposed. A hypoelastic constitutive model was shown to naturally account for the incompatibility of strains and for the fact that each tape layer joins the tape pack with some initial stresses. The attachment time at which each layer joins the tape pack is well defined by the winding process. Such an analysis produces continuous deformations and it can naturally be extended to include rate phenomena like creep and relaxation. It remains a challenge to develop accurate experimental techniques for measuring elastic properties and understanding the effect of the air trapped between layers on the long-term integrity of magnetic tapes. Tests are currently being conducted at the National Media Laboratory to develop a rigorous hypoelastic-viscoplastic constitutive model for magnetic tapes that could be used at different loading, temperature, humidity, and cyclic conditions.

References

Altmann, H. C., 1968, "Formulas for Computing the Stresses in Center-Wound Rolls," *J. of Technical Association of the Paper and Pulp Industry (TAPPI)*, Vol. 51, No. 4, pp. 176–179.

Hakiel, Z., 1987, "Non Linear Model for Wound Roll Stresses," *J. of Technical Association of the Paper and Pulp Industry (TAPPI)*, Vol. 70, No. 5, pp. 113–117.

Koppuzha, J. K., 1992, "A Novel Method for Roll Pressure Measurement," *J. of Advances in Information Storage Systems*, Vol. 4, pp. 73–78.

Pfeiffer, J. D., 1979, "Prediction of Roll Defects from Roll Structure Formulas," *J. of Technical Association of the Paper and Pulp Industry (TAPPI)*, Vol. 62, No. 10, pp. 83–88.

Yogoda, H. P., 1980, "Resolution of a Core Problem in Wound Rolls," ASME Journal of Applied Mechanics, Vol. 47, pp. 847–854.

Yogoda, H. P., 1981, "Generalized Formulas for Stresses in Wound Rolls," *J. of Technical Association of the Paper and Pulp Industry (TAPPI)*, Vol. 64, No. 2, pp. 91–93.

Willet, M. S., and Poesch, W. L., 1988, "Determining the Stress Distributions in Wound Rolls of Magnetic Tape Using a Nonlinear Finite Difference Approach," ASME Journal of Applied Mechanics, Vol. 55, No. 2, pp. 365–371.

Zabaras, N., Ruan, Y., and Richmond, O., 1991, "On the Calculation of Deformations and Stresses During Axially Symmetric Solidification," ASME Journal of Applied Mechanics, Vol. 58, pp. 865–871.

Downloaded 03 May 2010 to 171.66.16.20. Redistribution subject to ASME license or copyright; see http://www.asme.org/terms/Terms_Use.cfm

Large Amplitude Vibrations of Strings

A. W. Leissa
Fellow ASME.

A. M. Saad

Department of Engineering Mechanics,
Ohio State University,
Columbus, OH 43210

The study of nonlinear, free, undamped transverse vibrations of a stretched string may be traced back to an equation of motion developed by Kirchhoff more than a century ago. Subsequent studies have typically assumed small slopes and done little to incorporate longitudinal coupling effects. In the present work a new set of coupled equations is derived. These highly nonlinear equations are solved by means of a newly developed Galerkin procedure which determines variations of the transverse and longitudinal displacements in both space and time. Time variation is determined by incremental use of polynomials. Validity of solutions is verified by independent finite difference solutions. Numerical results are presented for three example problems wherein the string is displaced transversely into a half-sine wave, and released from rest. The problems include: (1) moderate strain ($\epsilon_o = 0.005$) in the straight line equilibrium position and moderate transverse displacement ($\delta = 0.1L$), (2) moderate strain and large displacement ($\delta = 0.4L$), and (3) small strain ($\epsilon_o = 10^{-5}$) and moderate displacement. Plots of transverse and longitudinal displacement with time are shown for all three examples. From these plots it is seen that higher modes are generated when only a single mode is initiated, and that the motion is definitely nonperiodic.

Introduction

The problem of the free, undamped, transverse vibrations of a perfectly flexible, initially stretched string was first studied more than two centuries ago. The following assumptions are made in the classical analysis:

(1) motion of the string is strictly transverse, and in a plane.
(2) the tension (T_o) in the static equilibrium position is large, and the transverse displacement (w) during vibration is small, so that the tension may be taken as constant during the motion.
(3) the slope of the string at all points is small during vibration.
(4) the mass per unit length of string remains constant (ρ_o) during the motion.

With these assumptions, summing forces in the transverse (z) direction on a differential element of the string yields the classical, linear one-dimensional wave equation

$$T_o w_{,xx} = \rho_o w_{,tt} \tag{1}$$

where x is the longitudinal coordinate and t is time. The solution of this equation is often the first problem taken up in a standard text on boundary value problems.

The effect of significantly changing tension due to the transverse displacement was considered by Kirchhoff (1876) more than a century ago. He proposed the following nonlinear integro-differential equation for the string:

$$\left(T_o + \frac{EA_o}{2L}\int_0^L w_{,x}^2\, dx\right) w_{,xx} = \rho_o w_{,tt} \tag{2}$$

where E is Young's modulus, and A_o and L are the cross-sectional area and length of the string in its stretched, equilibrium position, respectively. The second term in the parentheses represents the increase in string tension, which increases the free vibration frequency.

Carrier (1945, 1949) a half-century ago took up the nonlinear problem in a more rigorous manner. He considered longitudinal displacement (u), as well as transverse, and obtained a set of equations of motion

$$\begin{aligned}(T\sin\theta)_{,x} &= \rho_o w_{,tt}\\ (T\cos\theta)_{,x} &= \rho_o u_{,tt}\end{aligned} \tag{3}$$

where $\tan\theta$ is the slope of the deformed string; that is,

$$\sin\theta = \frac{w_{,x}}{\sqrt{(1+u_{,x})^2 + w_{,x}^2}}, \quad \cos\theta = \frac{1+u_{,x}}{\sqrt{(1+u_{,x})^2 + w_{,x}^2}}. \tag{4}$$

Assuming that the material of the string deforms according to Hooke's Law, the tension depends upon the displacements as

$$T = T_o + EA_o[\sqrt{(1+u_{,x})^2 + w_{,x}^2} - 1]. \tag{5}$$

Substituting Eqs. (4) and (5) into (3), it is seen that two highly nonlinear partial differential equations result, which are cou-

Contributed by the Applied Mechanics Division of THE AMERICAN SOCIETY OF MECHANICAL ENGINEERS for publication in the ASME JOURNAL OF APPLIED MECHANICS.

Discussion on this paper should be addressed to the Technical Editor, Professor Lewis T. Wheeler, Department of Mechanical Engineering, University of Houston, Houston, TX 77204-4792, and will be accepted until four months after final publication of the paper itself in the ASME JOURNAL OF APPLIED MECHANICS.

Manuscript received by the ASME Applied Mechanics Division, June 17, 1992; final revision, Mar. 11, 1993. Associate Technical Editor: F. Y. M. Wan.

Copyright © 1994 by ASME
Downloaded 03 May 2010 to 171.66.16.20. Redistribution subject to ASME license or copyright; see http://www.asme.org/terms/Terms_Use.cfm

pled in u and w. Instead of the fixed and conditions $u(0, t) = u(L, t) = 0$, the following was used:

$$\int_0^L u_{,x}dx = 0. \tag{6}$$

To reduce the complexity of the nonlinear system, Carrier (1945, 1949) assumed a perturbation solution based upon small amplitude motions that yielded the Eq. (2) previously derived by Kirchhoff. Equation (2) was also obtained by Narasimha (1968) using another approach. Generalizations of Eq. (2) to include viscous damping (Anand, 1969a, 1969b) and flexural rigidity (Lieber, 1975; Morioka, 1978, 1979, 1980) were also made. The solution of Eq. (2) received attention (Christie and Sanz-Serna, 1984), as well as the existence and uniqueness of such solutions (Nishida, 1971). Further generalization was made by Mote (1966) and by Ames, Lee, and Zaiser (1968) who analyzed the nonlinear vibration of an axially moving string. The moving string problem received considerable subsequent attention (Bapat and Srinivasan, 1967, 1971; Shih, 1971; Kim and Tabarrok, 1972; Ghangrekar, 1975; Moustafa and Salman, 1976; Korde, 1985).

Although Eq. (2) has been widely derived and used, it requires that: (1) the tension, although changing with time, is constant along the length of the string, (2) the slope is small, and (3) the longitudinal displacement is neglected. If one assumes that the string vibrates in sine wave mode shapes, as for the linear problem, i.e., $w(x, t) = W(t) \sin(m\pi x/L)$, with m an integer, then Eq. (2) straightforwardly yields the well-known Duffing equation

$$\ddot{W} + \frac{T_o}{\rho_o}\left(\frac{m\pi}{L}\right)^2 W + \frac{EA}{4\rho_o}\left(\frac{m\pi}{L}\right)^4 W^3 = 0 \tag{7}$$

for hard spring, free vibration behavior. This has a solution which is periodic in time.

Still other attempts to formulate two-dimensional equations of motion have been made (Muller, 1953; Bauer, 1969; Arya and Lardner, 1974; Arya, 1978). However, to the authors' knowledge, no thorough study of the problem has previously been made, especially when the effects of longitudinal displacement, and of large amplitude in the transverse displacement, are included. The present work begins with the derivation of a proper set of governing equations of motion. Accurate solutions of these nonlinear equations are carried out by a recently developed numerical procedure which utilizes an incremental form of the Galerkin method with time as a variable (Saad, 1992). Correctness of the solutions is verified by finite difference results.

A New Derivation of the Equations of Motion

Figure 1 shows a string displaced from its straight line, equilibrium position. A typical point P undergoes displacements u and w in the longitudinal (x) and transverse (z) directions, respectively. In the equilibrium position its length is L.

In Fig. 2 an infinitesimal element of deformed length ds is shown. In the equilibrium position its length is dx, while its unstretched length is dx_o. The total strain in the element is

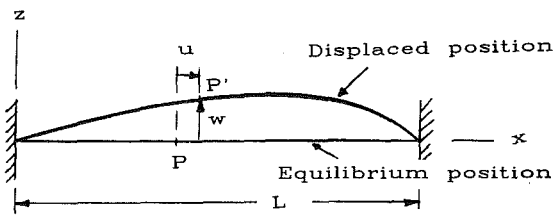


Fig. 1 Vibrating string with displacement components

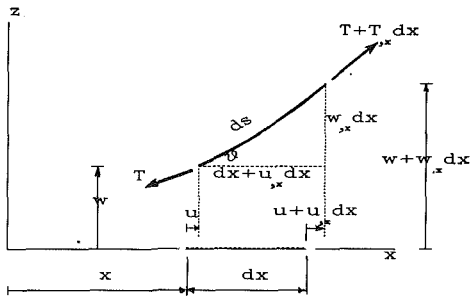


Fig. 2 Displaced string element

$$\epsilon = \frac{ds - dx_o}{dx_o} = \frac{ds}{dx}\frac{dx}{dx_o} - 1. \tag{8}$$

However,

$$\frac{dx}{dx_o} = 1 + \epsilon_o \tag{9}$$

where ϵ_o is the equilibrium position strain and, from Fig. 2,

$$\frac{ds}{dx} = \sqrt{(1 + u_{,x})^2 + w_{,x}^2}. \tag{10}$$

Assuming that the string remains linearly elastic during its motion, the tension-displacement relation becomes

$$T = EA_o\epsilon = EA_o[(1 + \epsilon_o)\sqrt{(1 + u_{,x})^2 + w_{,x}^2} - 1]. \tag{11}$$

Because the tension in the equilibrium position is $T_o = EA_o\epsilon_o$, Eq. (11) differs from that of Eq. (5) used by Carrier. For moderate longitudinal displacement gradient and moderate slope ($w_{,x}$) the difference is significant.

Summing force components in Fig. 2 in the transverse and longitudinal directions, one obtains for the string element:

$$(T \sin\theta)_{,x}dx = \rho w_{,tt}ds$$

$$(T \cos\theta)_{,x}dx = \rho u_{,tt}ds \tag{12}$$

where ρ is the mass per unit length of string in the displaced position. This changes as the string is stretched during displacement. Conservation of mass requires that

$$\rho ds = \rho_o dx_o = \rho_o \frac{dx_o}{dx}dx = \frac{\rho_o}{1 + \epsilon_o}dx \tag{13}$$

when Eq. (9) is utilized. Thus, the equations of motion become

$$(T \sin\theta)_{,x} = \frac{\rho_o}{1 + \epsilon_o} w_{,tt}$$

$$(T \cos\theta)_{,x} = \frac{\rho_o}{1 + \epsilon_o} u_{,tt} \tag{14}$$

which differ from Eqs. (3) used by Carrier by the presence of the equilibrium position strain, ϵ_o. This difference is typically very small.

Substituting Eqs. (4) and (11) into (14), the equations of motion become

$$EA_o(1 + \epsilon_o)^2 w_{,xx} - EA_o(1 - \epsilon_o)\frac{(1 + u_{,x})^2 w_{,xx} - w_{,x}(1 + u_{,x})u_{,xx}}{[(1 + u_{,x})^2 + w_{,x}^2]^{3/2}} = \rho_o w_{,tt}$$

$$EA_o(1 + \epsilon_o)^2 u_{,xx} - EA_o(1 + \epsilon_o)\frac{w_{,x}^2 u_{,xx} - w_{,x}(1 + u_{,x})w_{,xx}}{[(1 + u_{,x})^2 + w_{,x}^2]^{3/2}} = \rho_o u_{,tt} \tag{15}$$

This system of coupled, nonlinear, partial differential equations describes the large amplitude, planar, free vibrations of the elastic string. It is subjected to the boundary conditions

Downloaded 03 May 2010 to 171.66.16.20. Redistribution subject to ASME license or copyright; see http://www.asme.org/terms/Terms_Use.cfm

$$w(0, t) = w(L, t) = u(0, t) = u(L, t) = 0. \quad (16)$$

Potential and kinetic energies associated with this motion are:

$$V = \frac{1}{1+\epsilon_o} \int_0^L [T_o(\epsilon - \epsilon_o) + \frac{1}{2} EA_o(\epsilon - \epsilon_o)^2] dx \quad (17)$$

$$K = \frac{\rho_o}{2(1+\epsilon_o)} \int_0^L (w_{,t}^2 + u_{,t}^2) dx \quad (18)$$

Substituting Eqs. (8)–(10) into (17), and applying Hamilton's principle, the same equations of motion (15) are obtained (Saad, 1992).

Solution by the Galerkin Method

The nonlinear equations of motion may be solved by a recently developed numerical procedure (Saad, 1992) which utilizes the Galerkin method incrementally in time. For the present problem, solutions are assumed in terms of series of functions which are sinusoidal in space and polynomials in time, over the intervals $0 \le x \le L$ and $t_i \le t \le t_i + k$, where k is the time step over the interval:

$$w(x, t) = \sum_{m=1}^{M} \sum_{n=0}^{N} A_{mn} \sin \frac{m\pi x}{L} \cdot \hat{t}^n \quad (19a)$$

$$u(x, t) = \sum_{p=1}^{P} \sum_{n=0}^{N} B_{pn} \sin \frac{p\pi x}{L} \cdot \hat{t}^n \quad (19b)$$

where $\hat{t} = t - t_i$ and the A_{mn} and B_{pn} are coefficients which are determined straightforwardly by the Galerkin method. These functions satisfy the boundary conditions (16) at all times. The first two coefficients of each time polynomial, A_{mo}, A_{m1}, B_{po}, and B_{p1} are chosen so as to satisfy the initial conditions at the beginning of each time step.

Writing the equations of motion (15) in the forms

$$\bar{L}_1(w, u) = 0, \quad \bar{L}_2(w, u) = 0, \quad (20)$$

the Galerkin orthogonalizing equations are constructed for each time step:

$$\int_0^k \int_0^L \bar{L}_i(w, u) \cdot \sin \frac{m\pi x}{L} \hat{t}^n dx d\hat{t} = 0 \quad (i = 1, 2). \quad (21)$$

This yields a system of $(M + P)(N - 1)$ nonlinear algebraic equations in A_{mn} and B_{pn} for each time step. A numerical solution is obtained by iteration.

The validity and accuracy of the numerical procedure described above has been established (Saad, 1992) on three problems which have exact solutions available for comparison:

(1) viscously damped, free vibration of a particle,
(2) large oscillation of a pendulum, and
(3) the Duffing equation.

The last two problems involve nonlinear equations. For all three problems it was shown that correct convergence in time is obtained by increasing either the degree of the polynomial (N) or the number of time steps.

From the one-dimensional (time) studies described above, and from additional convergence studies made for the vibrating string (Saad, 1992), it was determined that accurate time response was obtained for the present problem by choosing N in the range from 3 to 5, and k in the range from 1/200 to 1/100 of the approximate oscillation period.

Solution by Finite Differences

The solution of the large amplitude, nonlinear string vibration problem was also carried out by means of the finite difference method, using a predictor-corrector iterative algorithm. The derivatives in both space and time appearing in the equations of motion (15) were represented by first order, central finite differences. The predictor-corrector algorithm was used to obtain convergence in time over each time step, k. The maximum time step which may be used is determined by onset of numerical instability. Finite difference intervals of $L/100$ in space were found to be sufficient for accurate solutions. Accurate results were obtained for a variety of values of initial displacements and equilibrium tension T_o, which agreed with those of the incremental Galerkin procedure described previously. Details of the finite difference procedure are available in a recent dissertation (Saad, 1992).

Example Results

Let the string be displaced transversely into a half-sine wave and released from rest. That is,

$$w(x, 0) = \delta \sin \frac{\pi x}{L}, \quad w_{,t}(x, 0) = 0. \quad (22)$$

The initial longitudinal displacement is chosen to satisfy the equation derived by Anand (1969a), applied to the static situation

$$u_{,x} + \frac{1}{2} w_{,x}^2 = 0. \quad (23)$$

Under this condition, the tension in the statically displaced string is almost constant (Saad, 1992). Substituting Eq. (22) into (23), integrating twice, and applying the boundary conditions (16) yields

$$u = -\frac{\pi}{8} \frac{\delta^2}{L} \sin \frac{2\pi x}{L}. \quad (24)$$

The initial longitudinal velocity ($u_{,t}$) is taken to be zero.

In solving the problem by the Galerkin method, three transverse modes are used. That is, because of the symmetry present, $m = 1, 3, 5$ in Eq. (19a), to allow some higher modes to develop freely during the motion. Similarly, for the longitudinal displacement, p is taken as 2, 4, 6, 8, 10 in Eq. (19b). These numbers of transverse and longitudinal modes were found to be sufficient for accurate solutions of the problems described below (Saad, 1992).

Consider first a string stretched to a moderate value of strain at equilibrium, $\epsilon_o = 0.005$ (which would cause large stresses in metallic wires), and given a half-sine wave transverse displacement of moderate amplitude, $\delta = 0.1L$. The total transverse displacement of a point at the middle ($x = L/2$) is observed in Fig. 3. Nondimensional displacement is plotted versus nondimensional time, the former obtained by dividing by L and the latter by dividing by the period of classical, linear (small amplitude) vibration. The transverse displacement appears to be simple harmonic motion, but it is not, as may be seen by the behavior of the third mode ($m = 3$), shown in Fig. 4. The

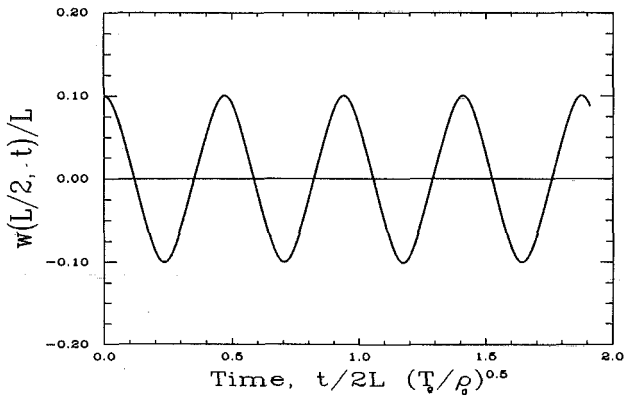


Fig. 3 Transverse displacement at the midpoint ($\epsilon_o = 0.005$, $\delta/L = 0.1$)

Downloaded 03 May 2010 to 171.66.16.20. Redistribution subject to ASME license or copyright; see http://www.asme.org/terms/Terms_Use.cfm

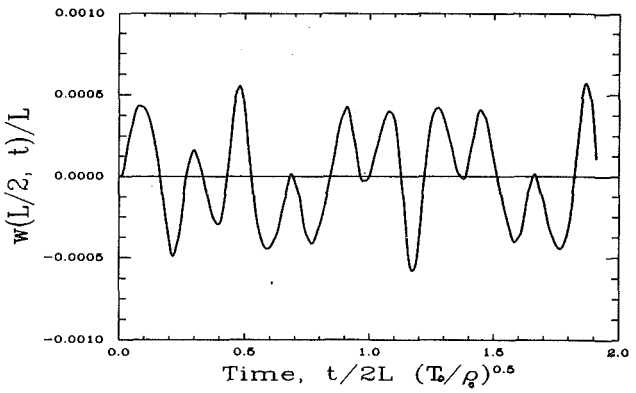


Fig. 4 Contribution of the third mode (sin $3\pi x/L$) to the transverse displacement of Fig. 3

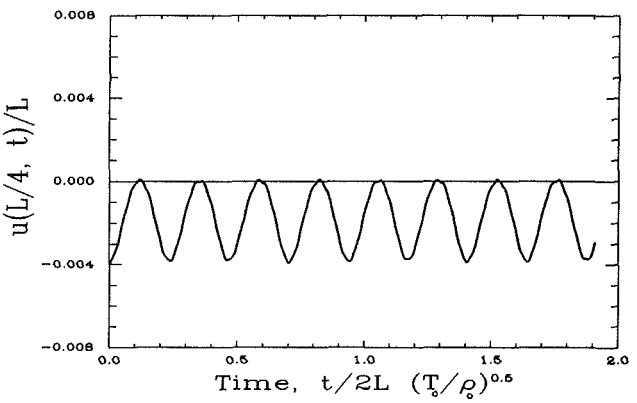


Fig. 5 Longitudinal displacement at the quarter-point (ϵ_o = 0.005, δ/L = 0.1)

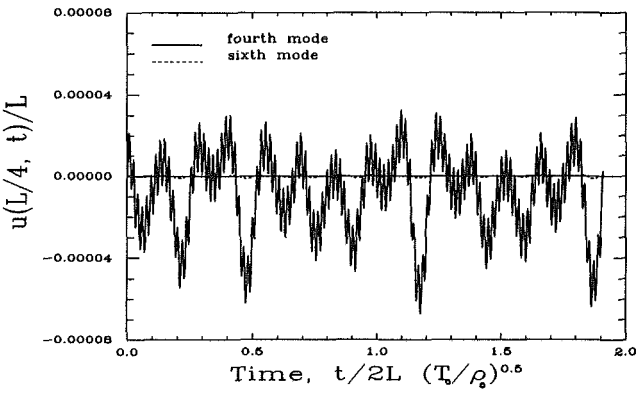


Fig. 6 Fourth and six mode contributions to the longitudinal displacement of Fig. 5

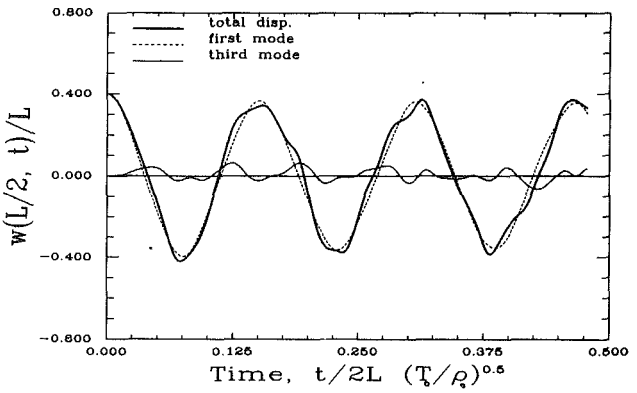


Fig. 7 Transverse displacement at the midpoint (ϵ_o = 0.005, δ/L = 0.4)

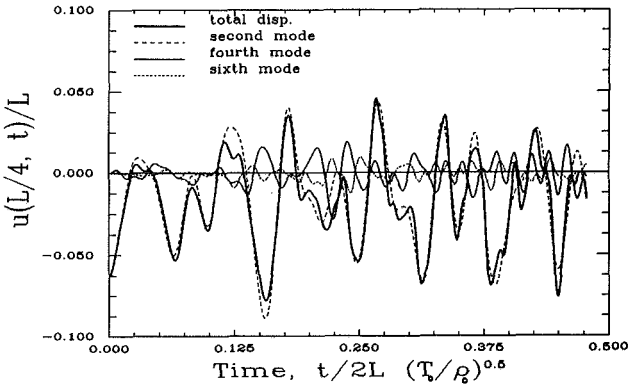


Fig. 8 Longitudinal displacement at the quarter-point (ϵ_o = 0.005, δ/L = 0.4)

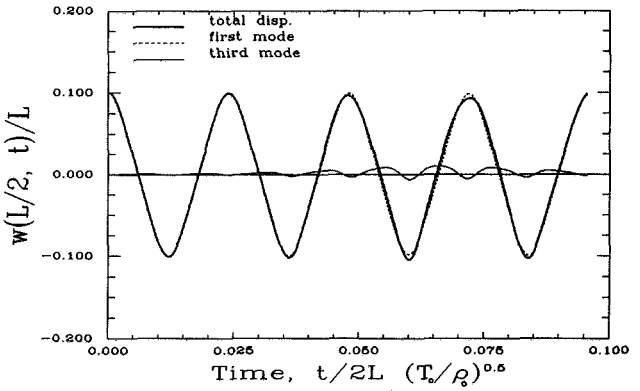


Fig. 9 Transverse displacement at the midpoint ($\epsilon_o = 10^{-5}$, δ/L = 0.1)

amplitudes of the third and fifth transverse modes are only 0.55 and 0.01 percents of the total displacement, δ. Thus, the transverse motion is almost periodic, but not quite.

The longitudinal displacement observed at the quarter-point ($x = L/4$), is also nearly periodic, but with twice the frequency, and is shown in Fig. 5. (Longitudinal displacement at the midpoint is zero at all times with the symmetric initial conditions.) It is dominated by the second mode (sin $2\pi x/L$). Amplitudes of the fourth and sixth modes are 1.7 and 0.1 percents of the total longitudinal displacement. Time variations of the second and fourth mode contributions are seen in Fig. 6.

For the second example, the equilibrium strain is retained at ϵ_o = 0.005, but a large initial transverse displacement, $\delta = 0.4L$, is given to the string. In this case, the motion is much less periodic, as seen in Fig. 7. The individual mode responses themselves are not periodic, which is clearly observed in the behavior of the third mode. Amplitudes of the third and fifth transverse modes are 15 and 7 percents of the total displacement. The longitudinal displacement, shown in Fig. 8, has large contributions of the higher (fourth and sixth) modes to the total displacement. The total displacement is seen to be highly nonperiodic.

For the last example, the string in its equilibrium position is nearly slack ($\epsilon_o = 10^{-5}$). The initial transverse displacement is moderate ($\delta = 0.1L$). The amplitude of the third mode is observed to grow (Fig. 9) and then diminish. This causes the amplitude of the total displacement to fluctuate. Amplitude of the fifth mode is small, being only 0.3 percent of the total

Downloaded 03 May 2010 to 171.66.16.20. Redistribution subject to ASME license or copyright; see http://www.asme.org/terms/Terms_Use.cfm

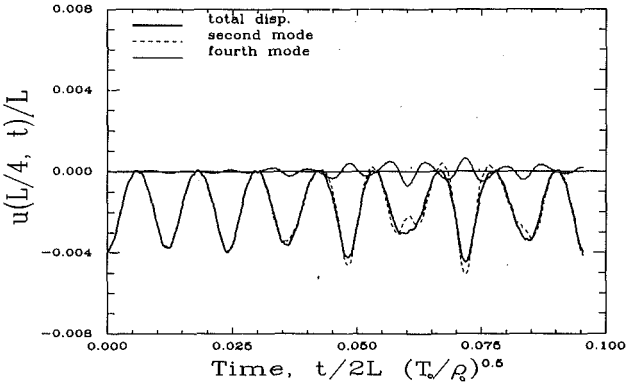


Fig. 10 Longitudinal displacement at the quarter-point ($\epsilon_o = 10^{-5}$, $\delta/L = 0.1$)

displacement. Simultaneously, as the third transverse mode grows, the longitudinal displacement becomes distorted (Fig. 10).

It may be noted that the "periods" of the quasi-periodic motion seen in the transverse displacements of Figs. 3, 7, and 9 are all less than that for the classical, linear solution ($2L\sqrt{\rho_o/T}$). Thus, the ratio of the nonlinear to the linear frequency is seen to increase in going from Fig. 3 to 7 to 9; that is, as the initial amplitude increases and the equilibrium strain decreases.

Finally, it should be mentioned that the nonperiodic response and coupling of higher modes demonstrated above is contrary to the expectations set forth by the previous researchers mentioned in the Introduction. The nonperiodicity of the motion, or the generation of higher modes during the motion has not been dealt with or mentioned explicitly by any of them. Indeed, many of them sought periodic solutions to their equations of motion and/or assumed that modes which are not initially excited would not appear subsequently during the motion (Anand, 1969; Mote, 1966; Bapat and Srinivasan, 1967, 1971; Ghangrekar, 1975; Korde, 1985; and Nishida, 1971).

Concluding Remarks

An accurate set of equations of motion have been derived representing the large amplitude, undamped, transverse vibrations of string. The effects of large slopes and coupling between transverse and longitudinal displacement during the motion were included. Three restricting assumptions were made, viz., (1) the string has no flexural stiffness, (2) stretching deformation is linearly elastic, and (3) motion occurs in a single plane. While it has been shown by some researchers that motion initiated in a plane will, in time, involve the other transverse displacement component, such behavior typically requires considerable time and many cycles before the coupling becomes significant. Moreover, even in this situation, the present equations should reasonably represent the motion in a plane which rotates.

By solving the equations of motion, two phenomena have been clearly identified which have not been previously established in the published literature: (1) nonperiodic motion; (2) higher modes being generated when only a single (linear) mode is initiated. Moreover, although many researchers have derived forms of equations of motion which involve coupling between the longitudinal and transverse displacements, none of them have demonstrated clearly the magnitude of the coupling by determining the relative amplitudes of these displacements during vibration.

It has been demonstrated that if the string is at least moderately strained ($\epsilon_o = 0.005$) in its static equilibrium position, displaced transversely in a half-sine wave (the fundamental mode for the linearized problem) of small amplitude ($\delta = 0.1L$) and released from rest, the subsequent motion is almost periodic. This is because the higher vibration modes are scarcely excited. That is, for this situation, the integro-differential Eq. (1) of Kirchhoff which increases the frequency to account for tension increase due to vibratory displacement is reasonably valid. However, for either large amplitude ($\delta = 0.4L$) or small equilibrium strain ($\epsilon_o = 10^{-5}$) mode coupling becomes significant, and the motion is definitely nonperiodic.

The numerical results shown in this work were for an initial condition given by Eq. (24) which, when combined with the half-sine wave of Eq. (22), yields nearly uniform initial tension in the string. Three other cases of initial conditions have also been investigated (Saad, 1992):

(1) zero initial longitudinal displacement ($u = 0$),
(2) zero initial longitudinal external force, and
(3) zero initial tangential external force.

Applying moderate initial strain ($\epsilon_o = 0.005$) and large initial transverse displacement ($\delta = 0.4L$), as in the second example studied in the present work, it was found that the motion was nonperiodic in each case. Higher transverse modes were also generated in each case, especially for Cases 2 and 3, and significant longitudinal motions ensued, even for Case 1.

Further studies with large amplitudes and the present equations of motion have revealed small intervals of string length and time where the changing tension becomes negative (Saad, 1992). Because the string has no flexural stiffness, it would buckle in those intervals. A more precise, although much more complicated, numerical study in these situations would require substitution of equations with zero tension in these intervals. However, even for the large amplitude used ($\delta = 0.4L$), it is not expected that such a complicated analysis would alter the results drastically.

References

Ames, W. F., Lee, S. Y., and Zaiser, J. N., 1969, "Nonlinear Vibration of a Travelling Threadline," *International Journal of Nonlinear Mechanics*, Vol. 3, pp. 449–469.

Anand, G. V., 1969a, "Large Amplitude Damped Free Vibration of a Stretched String," *Journal of the Acoustical Society of America*, Vol. 45, pp. 1089–1096.

Anand, G. V., 1969b, "Stability of Nonlinear Oscillations of Stretched Strings," *Journal of the Acoustical Society of America*, Vol. 46, pp. 667–677.

Arya, J. C., 1978, "The Effect of Kinematical Nonlinearities on the Vibration Frequencies of a Damped String," *Acta Mechanica*, Vol. 29, pp. 159–167.

Arya, J. C., and Lardner, R. W., 1974, "The Effect of Kinematical Nonlinearities on the Vibration Frequencies of a Stretched String," *Utilitas Mathematica*, Vol. 6, pp. 307–320.

Bapat, V. A., and Srinivasan, P., 1967, "Nonlinear Transverse Oscillations in Traveling Strings by the Method of Harmonic Balance," ASME JOURNAL OF APPLIED MECHANICS, Vol. 34, pp. 775–777.

Bapat, V. A., and Srinivasan, P., 1971, "Nonlinear Transverse Oscillations in Traveling Strings by a Direct Linearization Method," *Journal of the Indian Institute of Science*, Vol. 53, pp. 120–125.

Bauer, H. F., 1969, "Nichtlineares Verhalten einer schwingenden Saite," *Zeitschrift für Angewandte Mathematik und Mechanik*, Vol. 49, pp. 699–701.

Carrier, G. F., 1945, "On the Nonlinear Vibration Problem of the Elastic String," *Quarterly of Applied Mathematics*, Vol. 3, pp. 157–165.

Carrier, G. F., 1949, "A Note on the Vibrating String," *Quarterly of Applied Mathematics*, Vol. 7, pp. 97–101.

Christie, I., and Sanz-Serna, J. M., 1984, "A Galerkin Method for a Nonlinear Integro-Differential Wave System," *Computer Methods in Applied Mechanics and Engineering*, Vol. 44, pp. 229–237.

Ghangrekar, S. G., 1975, "On Nonlinear Oscillation of Moving String," *Labdev Journal of Science and Technology: Physical Sciences*, Vol. 13A, pp. 255–257.

Kim, Y. I., and Tabarrok, B., 1972, "On the Nonlinear Vibration of Travelling Strings," *Journal of the Franklin Institute*, Vol. 293, pp. 381–399.

Kirchhoff, G., 1876, *Vorlesungen Uber Mathematische Physik*: Mechanik, Leipzig.

Korde, K. R., 1985, "On Nonlinear Oscillation of Moving String," ASME JOURNAL OF APPLIED MECHANICS, Vol. 52, pp. 493–494.

Leissa, A. W., and Saad, A. M., (recently submitted for publication), "An Incremental Galerkin Method with Time as a Variable".

Lieber, E., 1975, "Moderne Theorie über die Physik der schwingenden Saite und ihre Bedeutung für die musicalische Akustik," *Acustica*, Vol. 33, No. 5, pp. 324–335.

Downloaded 03 May 2010 to 171.66.16.20. Redistribution subject to ASME license or copyright; see http://www.asme.org/terms/Terms_Use.cfm

Morioka, M., 1978, "Nonlinear Vibration of String with Elastically Restrained Mass," *Japan National Congress of Applied Mechanics*, Vol. 26, pp. 289–299.

Morioka, M., 1979, "Coupled Oscillations of Stiff String and a Beam," *Japan National Congress of Applied Mechanics*, Vol. 27, pp. 385–398.

Morioka, M., 1980, "Nonlinear Coupled Oscillations of Stiff Strings with an Elastically Restrained Mass," *Japan National Congress of Applied Mechanics*, Vol. 28, pp. 355–368.

Mote, C. D., 1966, "On the Nonlinear Oscillation of an Axially Moving String," ASME JOURNAL OF APPLIED MECHANICS, Vol. 33, pp. 463–464.

Moustafa, M. A., and Salman, F. K., 1976, "Dynamic Properties of a Moving Thread Line," ASME *Journal of Engineering for Industry*, pp. 868–875.

Müller, V. H., 1953, "Zur nichtlinearen Theorie der schwinginden Saite," *Annalen Physik*, Leipzig, Vol. 12, pp. 398–400.

Narasimha, R., 1968, "Nonlinear Vibratiokn of an Elastic String," *Journal of Sound and Vibration*, Vol. 8, pp. 134–155.

Nishida, T., 1971, "A Note on the Nonlinear Vibrations of the Elastic String," *Memoirs of the Faculty of Engineering*, Kyoto University, Vol. 33, pp. 329–341.

Saad, A. M., 1992, "Nonlinear Free Vibration Analysis of Strings by the Galerkin Method," Ph.D. Dissertation, Ohio State University.

Shih, L. Y., 1971, "Three Dimensional Nonlinear Vibration of a Traveling String," *International Journal of Non-Linear Mechanics*, Vol. 6, pp. 427–434.

Downloaded 03 May 2010 to 171.66.16.20. Redistribution subject to ASME license or copyright; see http://www.asme.org/terms/Terms_Use.cfm

Random Vibrational Response and Stability Study of Long-Span Bridges

K. Y. R. Billah
Department of Civil, Environmental, and Coastal Engineering,
Stevens Institute of Technology,
Hoboken, NJ 07030

M. Shinozuka
Department of Civil Engineering and Operations Research,
Princeton University,
Princeton, NJ 08544
Fellow ASME

A random vibrational response study of a dynamical system is presented. In particular, suspension bridge stability analysis in the presence of turbulence is addressed. The effects of turbulence on the well-understood deterministic stability of section models using aerodynamic functions are explored emphasizing governing physical mechanisms. For this purpose, the primary emphasis is placed on the nonlinear control parameter (square of the upstream flow velocity) and the resulting nonlinear noise term. To this end, it is pointed out that the introduction of "nonwhite" nonlinear noise for the excitation forces is of paramount importance. Further, it is concluded that this invoking of nonwhite noise is necessary to avoid inconsistencies involved with the usual assumption of Gaussian white noise. Finally, numerical simulation of nonwhite, nonlinear noise and subsequent integration of the single-degree-of-freedom torsional equation of motion involving varying "time scales" are carefully carried out. The numerical tests for sample stability provide some new results that are consistent with existing experimental observations.

1 Introduction

The stability of motion of long-span bridges under strong winds has generated much interest in the last three decades. Numerous studies to date have provided a wealth of information that have clarified much confusion created after the collapse of the Tacoma Narrows bridge in 1940 (e.g., Petroski, 1991; Scanlan, 1976; Billah and Scanlan 1991). Much of the present understanding has come from experimental studies in wind tunnel and from the flutter derivative concept incorporated in the "Scanlon functions" (Scanlan and Tomko, 1971; Scanlan, 1977).

The interest in this problem lies fundamentally in the stability issue arising from a flow that could be practically turbulence-free as well as one in which turbulence is important. As far as present understanding is concerned, the mechanism of instability when the upstream flow is smooth is much better understood than when fluctuations are present in the environment.

When turbulence is present in the upstream flow, experimental observations suggest that a change of stability character may occur from the deterministic state (Huston 1986; Scanlan and Huston 1986; Huston et al. 1988). Although full-scale three-dimensional model studies have been carried out to determine these changes, generally the section-model tests (in which changes are identified with the character of the flutter derivatives) have been more appealing and popular. This has been so not only because of the relative simplicity of its analytical formulation, but also because it is possible to implement detailed experiments using this model.

A number of papers have been published (Beliveau et al. 1977; Lin and Ariaratnam 1980; Bucher Lin, 1988; Tsiatis and Gasparini 1987; Tsiatis and Sarkar 1988; Lin 1979) which do analytically predict some broad trends of the observed experimental changes. Some difficulties, however, still remain. For example, in these studies for single-degree-of-freedom torsional mode, only destabilization under turbulence is obtained. In reality, however, both destabilization and stabilization have been observed in section model tests.

The present work was primarily motivated by the lack of a satisfactory interpretation of the *duality in a single-degree-of-freedom torsional instability* within the present state of art. The present authors believe that two important factors, namely the correlation time of the turbulence and the nonlinear fluctuations that occur, have been excluded so far in the formulation. The authors hold that these could introduce substantial changes in stability studies from existing analytical results. It is known from studies in related fields (Gardiner 1985; Moss and McClintock 1989), where fluctuations play an important role, that this parameter may have substantial effects on response characteristics and more so on the nature of stability since "memory" effects are imparted to the noise. It is pertinent to point out that in existing studies it is agreed that the ambient noise is in reality "band-limited," but due to the so-called *relaxation time* (Moss and McClintock, 1989; Stratonovich, 1963) concept (see later discussion), the approximation of white noise can be justified. In the present paper the authors will venture a different interpretation.

Contributed by the Applied Mechanics Division of THE AMERICAN SOCIETY OF MECHANICAL ENGINEERS for publication in the ASME JOURNAL OF APPLIED MECHANICS.

Discussion on this paper should be addressed to the Technical Editor, Professor Lewis T. Wheeler, Department of Mechanical Engineering, University of Houston, Houston, TX 77204-4792, and will be accepted until four months after final publication of the paper itself in the ASME JOURNAL OF APPLIED MECHANICS.

Manuscript received by the ASME Applied Mechanics Division, June 11, 1991; final revision, Oct. 22, 1992. Associate Technical Editor: P. D. Spanos.

Copyright © 1994 by ASME
Downloaded 03 May 2010 to 171.66.16.20. Redistribution subject to ASME license or copyright; see http://www.asme.org/terms/Terms_Use.cfm

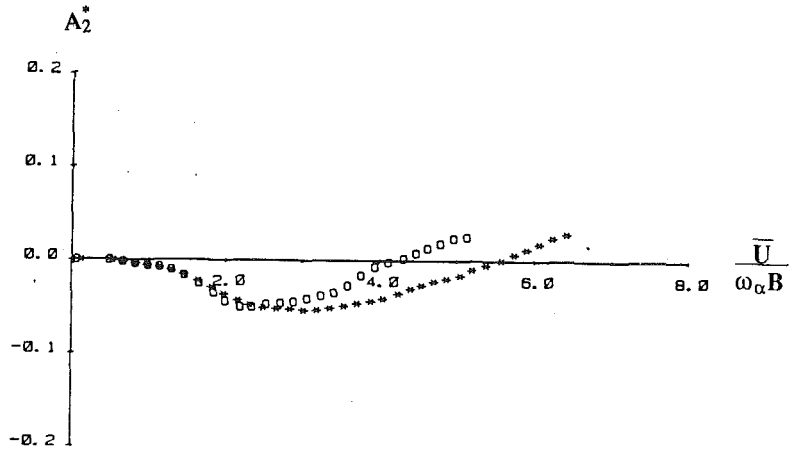


Fig. 1(*a*) The effect of turbulence on A_2^* coefficient; destabilized under turbulence; (* * *)—laminar, (□ □ □)—turbulent (from Huston, 1986)

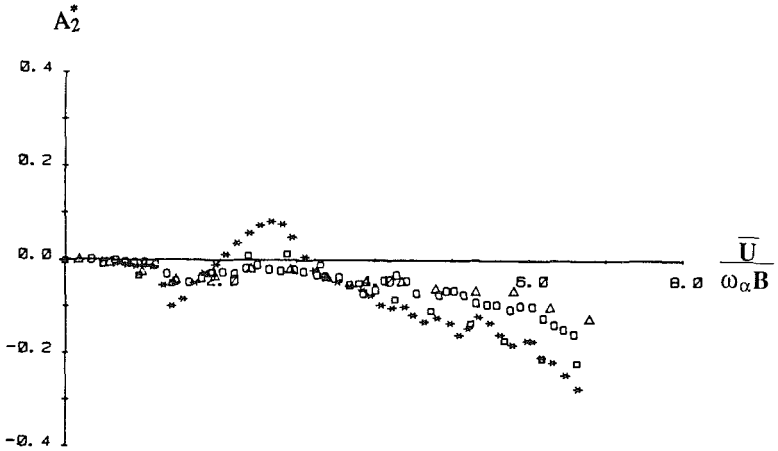


Fig. 1(*b*) The effect of turbulence on A_2^* coefficient; stabilized under turbulence; (* * *)—laminar; others—varying degree of turbulence (from Huston, 1986)

2 Turbulence and Stability of Suspension Bridges

The analytical study of the effect of turbulence begins with the modeling of the noise and its effect on deterministic bifurcation. Near this bifurcation point in parameter space, fluctuations become very important. The interplay of potentially unstable system and the environmental randomness may cause a shift of the deterministic instability point (or in the case of nonlinear state variables, may create new noise-induced states).

When turbulence is present two types of load are considered: buffeting and self-excitation (Scanlan, 1976; Scanlan and Lin, 1979). In the governing equations, the self-excited loads appear as parametric and the buffeting effects appear as nonhomogeneous forcing terms. These nonhomogeneous terms cannot cause motional instability and thus they are usually disregarded when the goal is to determine the change in stability condition.

Consider the section model which is constrained to move only in torsional mode. Then the equation of motion is given by (Scanlan and Tomko, 1971; Scanlan, 1977)

$$I[\ddot{\alpha}+2\zeta\omega_\alpha\dot{\alpha}+\omega_\alpha^2\alpha] = 1/2\rho U^2(2B^2)\left[KA_2^*(K)\frac{B\dot{\alpha}}{U}+K^2A_3^*(K)\alpha\right] \quad (1)$$

where α = torsional angle; I = torsional moment of inertia per unit length, ω_α = natural frequency of dominant torsional mode, ζ = damping ratio, ρ = air density, B = width of bridge deck, U = total horizontal wind velocity (mean plus random fluctuation), $K=B\omega_\alpha/U$ (reduced frequency), and $A_2^*(K)$ and $A_3^*(K)$ are nondimensional coefficients which are functions of K.

Equation (1) is written in a mixed time and frequency domain form. When a particular section model is considered, however, the frequency in Eq. (1) represents the torsional frequency ω_α in which the bridge primarily vibrates. In this sense Eq. (1) is not really written in a mixed form. Indeed, it is in this sense that the same representation has been used in aeronautical engineering as well as in some notable publications on bridges (Scanlan and Huston, 1991; Simiu and Scanlan, 1986).

The change in the critical deterministic speed is identified by experimentally observing the shift in the A_2^* curve when the flow becomes turbulent. This is shown in Fig. 1 (Huston, 1986); in Fig. 1(*a*), for turbulent flow, the curve shifts towards the left (smaller wind speed) indicating a destabilizing effect, while in Fig. 1(*b*), the curves shift toward the right (higher wind speed) indicating a stabilizing effect.

The effect of turbulence on self-excited loads is generally accounted theoretically in the random oscillation of the dynamic pressure $1/2\rho U^2$, where U is the *control parameter* (Gardiner, 1985).

For the long-span bridge problem, the flow is usually simplified to be horizontally perpendicular to the bridge span and

Downloaded 03 May 2010 to 171.66.16.20. Redistribution subject to ASME license or copyright; see http://www.asme.org/terms/Terms_Use.cfm

the turbulence considered spanwise smooth (Davenport, 1961, 1962; Simiu and Scanlan, 1986). Effect of wakes (the so-called signature turbulence) or vortex shedding is usually not considered. It should be added that all the above conditions and assumptions do not necessarily depict the natural wind condition over a suspension bridge (Simiu and Scanlan, 1986). For the experimental section-model tests, however, they are consistent. And since comparison of the present work will be done with such laboratory test results, it is also appropriate to introduce such assumptions.

3 Work to Date

In the study on the effect of turbulence on the flutter derivatives and hence stability carried out by Scanlan and Lin (1979), the effect of turbulence was incorporated by determining the flutter derivatives corresponding to a mean wind velocity. This provided an empirical means to determine the effect of turbulence on stability.

Lin and Ariaratnam (1980) analyzed the problem considering fluctuations in flow velocity (in terms of white-noise intensity D) directly in the equation of motion for a single-degree-of-freedom torsional motion. They obtained stochastic differential equations and found that the stability condition changed under turbulence. For all practical white-noise intensity, this work and related work (Lin, 1979) showed that turbulence always has a destabilizing effect on the single-degree-of-freedom model. It may be added here that this destabilization obtained is essentially due to the "adding" of a correction factor (the Wong-Zakai correction) in the "drift part" of the equation to have a Stratonovich interpretation (Gardiner, 1985) for state-dependent white-noise excitation.

To predict stabilization, Tsiatas and Gasparini (1987) introduced spanwise correlation of the fluctuation and did obtain some result which showed stabilization. However, as pointed out by Huston et al. (1986), this does not explain the observed stabilization in two-dimensional section model test.

In a more recent study of interest, Bucher and Lin (1988) asserted that stabilization could be the effect of energy transfer from an unstable torsional mode to the stable vertical mode. On this premise, they introduced the coupled torsional and vertical motion formulation. Although this is intuitively appealing, conceptual difficulties are encountered because of the vastly different time scales of motion for the stable and the unstable degrees-of-freedom (Sri Namachchivaya and Hilton, 1988; Mangel, 1979). Through this formulation, they obtained in a limited region of parameter space (white-noise intensity D and flow speed U) "coupled flutter" stabilization effect. This coupled flutter formulation, however, leaves unresolved the experimentally observed stabilization under turbulence for section models restrained to move only in torsional degree of motion (Huston, 1986; Scanlan and Huston, 1991).

4 Nonlinear and Nonwhite Noise

All physical fluctuations are correlated. The correlation time, τ_c, of a stochastic process model for such a fluctuation indicates the general time scale within which the fluctuation behaves more or less regularly. The relaxation time for a system near instability becomes very long compared with τ_c, and for this reason the external noise can be simplified as white noise.

However, there are other time scales of the system (e.g., that of the inertia) which has to be compared with the correlation time of the external noise. If the correlation time of the noise approaches one of these other time scales it may not act as a noise but more like a deterministic variation. Comparison of noise time scale with scales other than the relaxation time is usually not made because of the complexity involved. But as theoretically shown and numerically verified (Billah and Shinozuka, 1991), the existence of such time scales changes calculation results substantially.

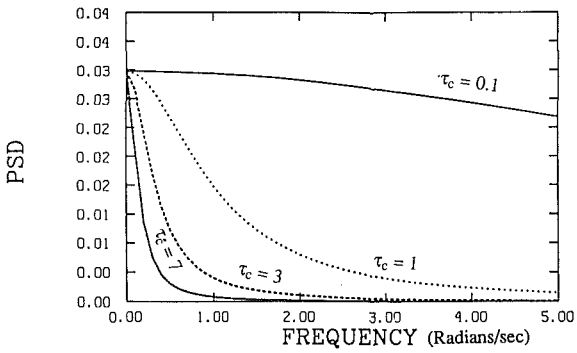


Fig. 2 Power spectral density for the exponentially correlated noise for $D = 0.1$ and different values of τ_c

Furthermore, due to the fundamental quadratic relation that exists between the flow velocity (U) and dynamic pressure ($1/2\rho U^2$), the assumption of white noise has to be made with extreme care. In this regard, the standard treatment of this feature in the existing literature is as follows: Since

$$U = \overline{U}[1 + \xi(t)] \tag{2}$$

it is obvious that

$$U^2 = (\overline{U})^2[1 + 2\xi(t) + \xi^2(t)], \tag{3}$$

where $\xi(t)$ is the nondimensional fluctuating component of the wind speed. Then, it is argued that since "ξ is small compared to unity" (Lin and Ariaratnam, 1980; Bucher and Lin, 1988; Tsiatas and Gasparini, 1987; Tsiatas and Sarkar, 1988; Lin, 1979), $\xi^2(t)$ can be neglected (this approximation is made before specifying the nature of the fluctuations) in Eq. (3). After this approximation, the assumption is usually made that the fluctuations are Gaussian and "white" and thus amenable to solution by standard Markovian theory.

However, Eq. (3) is not proper for white noise since $\xi^2(t)$ has no meaning for white noise (Gardiner, 1985; Gard, 1988; Billah and Shinozuka, 1990b). This enforces reconsideration of the white-noise assumption in section-model studies of bridge instability problems. The general conclusion that can be drawn at this point is that when fluctuations are introduced, these have to be modeled as colored noise. Also, the square term $\xi^2(t)$ should be retained since, as will be shown later, the square term affects the stability characteristics of the system significantly.

The above comments regarding the inability of white noise to approximate the turbulence effects and the necessity to retain the square term pertain to the present instability problem only. The authors are aware of the utility and usefulness of the assumption of external noise as white and neglecting the square term for some vibrational problems of practical significance.

4.1 Correlated Noise. For the present study, noise with *exponential correlation function* (Gardiner, 1985; Gard, 1988) is chosen as colored noise. It has the following two properties:

$$\langle \xi(t) \rangle = 0$$

$$\langle \xi(t)\xi(t') \rangle = \frac{D}{\tau_c} \operatorname{Exp}\left[\frac{-|t-t|}{\tau_c}\right] \tag{4a, b}$$

where D/τ_c is the intensity (mean square value) of the fluctuating component of wind speed and τ_c is by definition the correlation time.

Note that the white-noise limit is obtained in Eq. (4) when τ_c approaches zero with D fixed

$$\langle \xi(t)\xi(t') \rangle = 2D\,\delta(t-t'). \tag{5}$$

For sufficiently small τ_c, Eq. (4) is effectively a white noise as shown in Fig. 2.

Downloaded 03 May 2010 to 171.66.16.20. Redistribution subject to ASME license or copyright; see http://www.asme.org/terms/Terms_Use.cfm

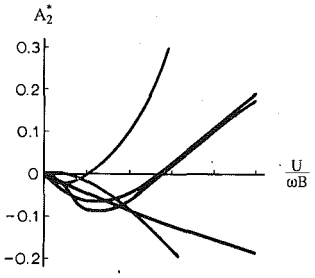


Fig. 3 Experimentally obtained values for A_2^* coefficient (from Scanlan and Tomko, 1971)

It is noted that the colored noise as defined in Eq. (4) has a mean square value D/τ_c, which for a fixed D changes (Simiu and Scanlan, 1986) depending on the value of τ_c. However, the standard practice (Gardiner, 1985; Sancho et al., 1982, Billah and Shinozuka, 1991) is such that experimental results are reported in terms of the white-noise intensity D and hence in the present work the results are summarized under fixed value of D with τ_c as a varying parameter.

5 Analysis of the Equation of Motion

5.1 Formulation. The single-degree-of-freedom equation of torsional motion (Eq. (1)) can be rewritten as

$$I[\ddot{\alpha}+2\zeta\omega_\alpha\dot{\alpha}+\omega_\alpha^2\alpha]=CU^2[a_1(K)\dot{\alpha}+a_2(K)\alpha] \qquad (6)$$

where $C=1/2\rho(2B^2)$, $a_1(K)=KA^*{}_2(K)\ B/U$ and $a_2(K)=K^2A_3^*(K)$ are empirical coefficients. In the present analysis $a_1(K)$ and $a_2(K)$ are considered to be given.

At the critical wind speed U_{cr} for a given cross-section under laminar flow,

$$F=2I\zeta\omega_\alpha-CU_{cr}^2\beta_1=0 \text{ or } U_{cr}^2=\frac{2I\xi\omega_\alpha}{C\,\beta_1}, \qquad (7a, b)$$

where β_1 is obtained using the value $|A_2^*(K)|_{\text{crit}}$ from a typical experimental results as shown in Fig. 3. Under turbulent flow, however, U in Eq. (6) should be replaced by

$$\overline{U}[1+\xi(t)].$$

5.2 Present Method of Analysis. For a non-Markovian dynamics generated by nonwhite noise, no tailored theory can be applied, as theoretical solutions are in general difficult to obtain, even in approximation. In fundamental physics, various attempts have been made (and still continue) to develop Fokker-Planck type of equation (Van Kampen, 1989; Sancho et al., 1982) for systems driven by colored noise. Most of the methods have been confined to a one-variable (1/2 degree-of-freedom) problem and linear noise. Even then conflicting results are sometimes obtained (Moss and McClintock, 1989).

For the present problem with available experimental results, there is a pressing need to verify more realistic physical modeling—starting with the inclusion of the ideas outlined above. In the face of nonavailability of theoretical tools, verifications of these stated assertions become of paramount importance as they can differ substantially from existing ones.

To achieve this goal, a simulation study was carried out the results of which represents the essence of this paper. The results can be considered as experimental in numerical sense and from that point of view complements the experimental ones. Obviously, a welcome priority persists to formulate the problem realistically and solve it theoretically. For the kind of problem where instability resulting from nonlinear colored noise is the issue, there seems to be no immediate possibility for a theoretical solution, however.

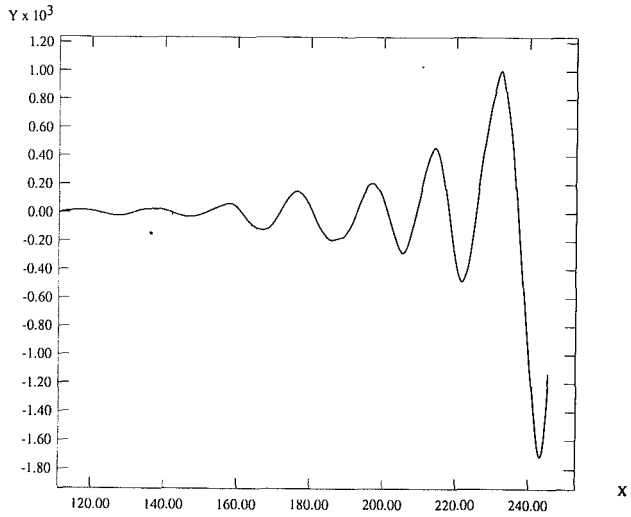


Fig. 4 Typical anamalous increase of response

For numerical solution the turbulence is generated using the well-developed method of simulating stochastic processes from a given nonwhite power spectra, giving careful consideration to the different time scales involved and the proper integration of the differential equations, and results may be obtained that check reasonably well with experimental results.

The numerical method of stability analysis has the advantage in that it can simulate experimental observations quite easily. The instability involved in the section model study is a *sample stability* (Huston, 1986; Scanlan and Huston, 1986; Kozin, 1969; Scanlan and Huston, 1991) as the observations are made on each sample run. The concept of moment stability, which is an ensemble averaging, is difficult to relate to these experimental undertakings.

In the existing bridge stochastic stability studies properties are often associated with moments and probabilities (Lin and Ariaratnam, 1980; Bucher and Lin, 1988; Tsiatas and Gasparini, 1987; Tsiatas and Sarkar, 1988; Lin, 1979), rather than on the study of sample stability properties. As observed by Kozin (1969): "This is somehow strange when it is realized that upon observing a system in operation it is a sample that is witnessed not an average or a probability." In fact, this has also been the viewpoint in fundamental physics; ". . . the phenomena of bifurcation might be missed entirely if one only looks at ensemble averages (Lebowitz et al., 1988)."

For a system which is linearly unstable a particular trajectory has an anomalous increase in response value with time (Agu, 1983; Mangel, 1979). In the present case if the square of the response along a generated trajectory is numerically calculated, its anomalous increase will indicate instability and the corresponding flow speed will be the critical speed under turbulence (Fig. 4). It is to be noted that this method of calculating limits of sample stability is consistent with the experimental method (Huston, 1986; Scanlan and Huston, 1986; Huston et al., 1988; Scanlan and Huston, 1991) which is deemed as the criteria of judgment of the undertaking. For a critical comparison of the sample stability boundary and the commonly used moment stability boundary please see Kozin and Sugimoto (1977).

5.3 Numerical Simulation. For the present method a stochastic process $f_s(t)$ is simulated by the following series (Shinozuka and Jan, 1972; Shinozuka and Deodatis, 1990), with a large value of N:

$$f_s(t)=\sqrt{2}\sum_{n=1}^{N}\sqrt{2S_f(\omega_n)\Delta\omega}\cdot\cos(\omega t\Phi_n) \qquad (8)$$

where $\omega_n=n\Delta\omega;\ n=1, 2, 3, \ldots . N$ and $\Delta\omega=\omega_u/N$. This

Downloaded 03 May 2010 to 171.66.16.20. Redistribution subject to ASME license or copyright; see http://www.asme.org/terms/Terms_Use.cfm

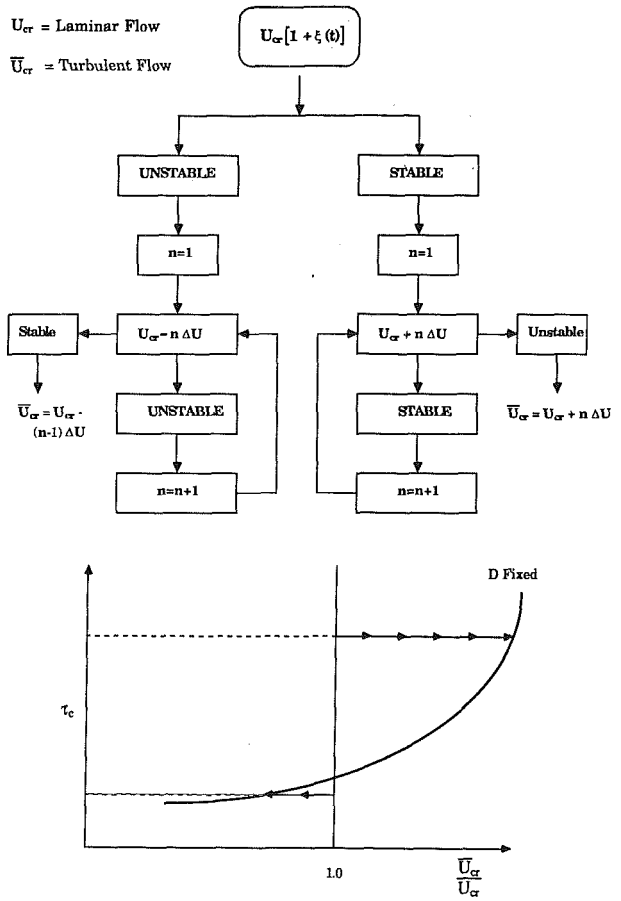


Fig. 5 The method of stability analysis by means of simulation

method was chosen for the advantages it offers over others for application to nonlinear and unstable systems (Billah and Shinozuka, 1990a).

In the above equation ω_u represents an upper cutoff frequency for the two-sided power spectral density function in such a way that beyond ω_u its value may be taken to be zero. The Φ_l's in Eq. (8) are independent random phase angles uniformly distributed over the interval [0, 2π]. Equation (8) provides a simulated stochastic process $f_s(t)$ which is asymptotically Gaussian as $N\rightarrow\infty$ due to the central limit theorem. Furthermore, it can be shown that each sample run is ergodic in the mean as well as in the correlation and that the simulated stochastic process repeats itself with a period $T_s=2\pi/\Delta\omega$. To take advantages of the FFT technique, Eq. (8) is rewritten in the following form for a sample function $f(i)$:

$$f^{(i)}(p\cdot\Delta t)=\mathrm{Re}\left\{\sum_{n=0}^{M-1} b_n e^{\frac{inp2\pi}{M}}\right\};\ p=0,1,\ldots.M-1 \quad (9)$$

where $b=\sqrt{2}\sqrt{2S_f(n\Delta\omega)\Delta\omega}\ e^{i\phi^{(i)}_n}$; $n=0, 1, \ldots M-1$, and $\phi_n{}^{(i)}$ is the ith realization of a sequence of random variable Φ_n. For simulation, three parameters of Eq. (9) namely N, M, and ω_u are pivotal; N controls, amongst other things, the accuracy of Gaussianness of the simulated process, M controls the digitized time step of the stochastic process: by varying M, wind turbulence at desired time interval can be generated; and ω_u controls the upper cut off point (Shinozuka and Deodatis, 1990) as mentioned earlier.

The two-sided power spectral density for exponentially correlated noise is (Fig. 2)

$$S_f(\omega)=\left(\frac{D}{\tau_c}\right)\frac{(1/\tau_c)^2}{\omega^2+(1/\tau_c)^2}. \quad (10)$$

Turbulence corresponding to the above power spectral density was generated by using Eq. (9), and Eq. (6) was numerically integrated by the Runga-Kutta method.

The method of stability analysis by means of simulation used in this study is summarized in Fig. 5 and can be described as follows:

(1) Given a cross-section, identify U_{cr} under laminar flow corresponding to the structural parameters ω_α, ξ, and I.

(2) Let $\overline{U}_{cr}$ be the critical mean wind speed under turbulence. Assume $\overline{U}_{cr}=U_{cr}$ to initiate the iterative process involving numerical calculation ($n=1$).

(3) Solve Eq. (6) with turbulent component (for a given D and τ_c) added to check whether response is stable or unstable; $U=U_{cr}[1+\xi(t]$ in Eq. (6).

(4) Case (a): If stable, modify current value of U_{cr} to $U_{cr}+\Delta U$. Case (b): If unstable, modify current value of U_{cr} to $U_{cr}-\Delta U$.

(5) Step (3) is repeated until for: (i) Case (a) unstable response is observed or (ii) Case (b) stable response is observed.

The value of the mean velocity at which the incipient unstable condition is obtained gives the $\overline{U}_{cr}$ value for a given D and τ_c.

(6) Steps (3) to (5) are repeated for different values of D and τ_c.

It is to be noted that this method of determining the effect of fluctuation around the deterministic stable condition is a common practice in the physical sciences (Moss and McClintock, 1989) as is in the case of suspension bridge stability studies (Huston, 1986; Scanlan Huston, 1986; Lin Ariaratnam, 1980; Bucher and Lin, 1988; Tsiatas and Gasparini, 1987; Tsiatas and Sarkar, 1988; Lin, 1979) where the deterministic coefficients (the $A_2^*(K)$ coefficients, as shown in Fig. 3) are used. This method, in effect, predicts the stability character under turbulence if only the deterministic stability analysis is available (Lefever and Turner, 1986; Gardiner, 1984) and in the present case circumvents the use of flutter derivatives under turbulence.

This numerical procedure is consistent with the experimental one used in the wind tunnel (Scanlan and Tomko, 1971; Scanlan and Huston, 1986; Scanlan and Huston, 1991). The numerical values used for the parameters were $\omega_a=2.0$ rad/sec, $\xi=0.05$, $I=857{,}000\text{lb/sec}^2$.

6 Results and Conclusion

Two types of simulation were carried out; the first involved both linear and nonlinear noise and the second neglecting nonlinear noise. Figures 6 and 7 show the simulation results for different values of D and τ_c for the two cases. In each case, the figures divide the wind speed value into destabilized region lying to the left and stabilization to the right of $\overline{U}_{cr}=U_{cr}$, where $\overline{U}_{cr}$ is the critical mean wind speed under turbulent condition.

The stability results obtained in this study for a particular type of noise namely, one having a exponential correlation function, are summarized below.

Figure 6 is plotted for *linear and nonlinear colored noise* in which case stabilization is observed for large τ_c and destabilization is obtained with small τ_c.

Figure 7 is plotted for *linear colored noise only* (solid curves) where for very small value of τ_c destabilization (i.e., as turbulence approaches "white noise") and for large τ_c stabilization is obtained (more so than in the case of including nonlinear noise)

In the numerical calculations the highest values of τ_c plotted is about 5.5 (arbitrary time unit). Some calculations were done for very large τ_c which showed expected shifting of the curves toward $\overline{U}_{cr}/U_{cr}=1$ (expected because, as τ_c increases, the flow becomes more laminar). But calculations for such asymptotic plots are not trival matter and they are deferred to future study.

The above summaries are consistent with existing experimental observation and our assertion that

Downloaded 03 May 2010 to 171.66.16.20. Redistribution subject to ASME license or copyright; see http://www.asme.org/terms/Terms_Use.cfm

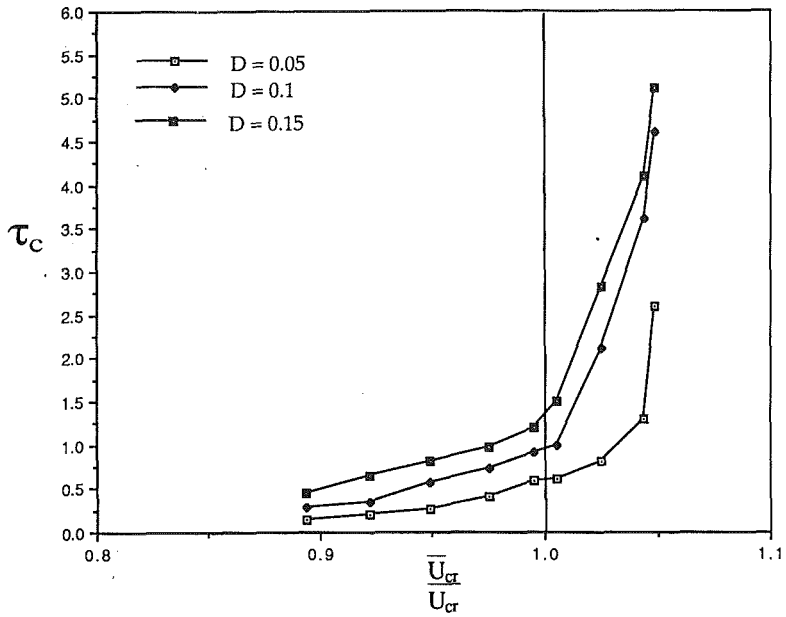


Fig. 6 Mean instability wind speed versus correlation time considering both linear and nonlinear noise

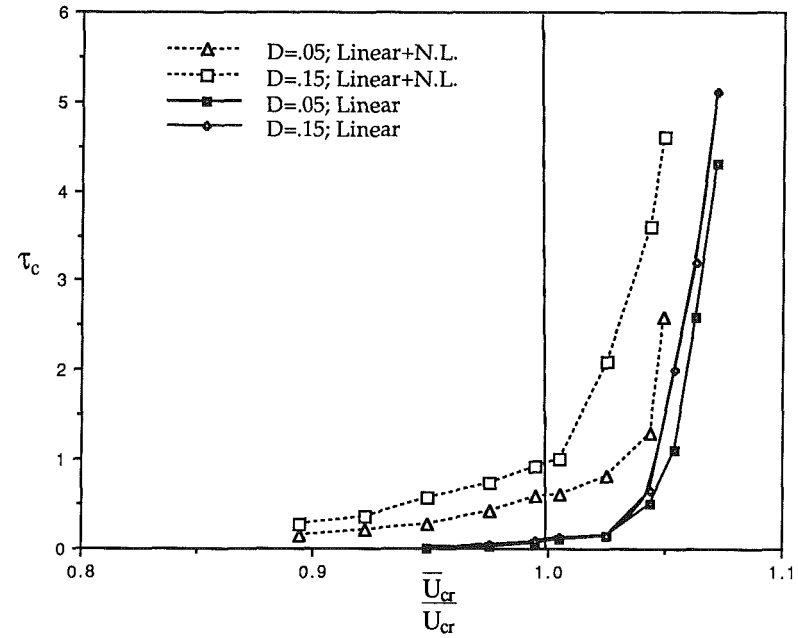


Fig. 7 Mean instability wind speed versus correlation time for linear noise. (Values for the both linear and nonlinear case, i.e., Fig. 6 are also given for comparison.)

(i) in general, colored noise influences the system stability quite differently from white noise,
(ii) finite correlation time can stabilize the torsional motion, pushing $\overline{U}_{cr}$ to larger values,
(iii) the square term of the noise can play a significant part in the stability analysis,
(iv) a single-degree-of-freedom model can effectively portray change (from the deterministic condition) to stability as well as instability under turbulence,
(v) the Stratonovich interpretation of stochastic differential equations (which gives the destabilizing effect in existing studies) is not the only possible physical interpretation; the correct interpretation can only be known from the underlying physical mechanisms (please refer to Gardiner (1985); Moss and McClintock (1989), Billah and Shinozuka (1991), Gardiner (1984) for related discussion on this important assertion and conclusion), and
(vi) the results shown in Fig. 6 and 7 cannot be obtained by analytical methods at this time.

Note added in proof: A recent paper (Lin, Y. K., and Li, Q. C., 1993, "New Stochastic Theory for Bridge Stability in Turbulent Flow," *J. of Engineering Mech.*, Vol. 119, pp. 113–127) presents an analytical study of bridge stability considering some of the issues discussed here and in Billah and Shinozuka (1990b). The study emphasizes the use of nonwhite turbulence, sample stability and considers a single-degree-of-freedom model. However, only stabilization in the torsional motion is obtained.

Downloaded 03 May 2010 to 171.66.16.20. Redistribution subject to ASME license or copyright; see http://www.asme.org/terms/Terms_Use.cfm

References

Agu, M., 1983, "A Method for Identification of Linear or Nonlinear System With the Use of Externally Applied Random Force," *J. Applied Physics*, Vol. 54, No. 3, pp. 1193–1197.

Beliveau, G., Vaicaitis, R., and Shinozuka, M., 1977, "Motion of Suspension Bridge Subject to Wind Loads," *Journal of Structural Division*, ASCE, Vol. 103, pp. 1189–1205.

Billah, K. Y., and Scanlan, R. H., 1991, "Resonance, Tacoma Narrows Bridge Failure and Undergraduate Physics Textbooks," *American Journal of Physics*, Vol. 59, pp. 118–124.

Billah, K. Y. R., and Shinozuka, M., 1991, "Stabilization of a Nonlinear System by Multiplicative Noise," *Physical Review A*, Vol. 44, pp. R4779–R4781.

Billah, K. Y. R., and Shinozuka, M., 1990a, "Fluctuations in Dynamic Pressure and the White Noise Assumption in Flow-Induced Vibration," *Journal of Sound and Vibration*, Vol. 147, No. 1, 1991, pp. 179–183.

Billah, K. Y. R., and Shinozuka, M., 1990b, "A Method of Color Noise Generation and its Application to Bistable System," *Physical Review A15*, Vol. 2, pp. 7492–7494.

Bucher, C. G., and Lin, Y. K., 1988, "Stochastic Stability of Bridges Considering Coupled Modes," *Journal of Engineering Mechanics*, Vol. 114, pp. 2055–2071.

Davenport, A. G., 1962, "The Response of Slender, Line-Like Structures to a Gusty Wind," *Proc. Institute of Civil Engineers*, Vol. 23, pp. 389–407.

Davenport, A. G., 1961, "The Application of Statistical Concepts to Wind Loading of Structures," *Proc. Institute of Civil Engineers*, Vol. 19, pp. 449–472.

Gard, T. C., 1988, *Introduction to Stochastic Differential Equations*, Marcel Dekker, New York.

Gardiner, C. W., 1985, *Handbook of Stochastic Methods*, 2nd ed., Springer-Verlag, Berlin.

Gardiner C. W., 1984, "Adiabatic Elimination in Stochastic Systems I. Formulation of Methods and Application to Few Variable Systems," *Physical Review A*, Vol. 29, pp. 2814–2821.

Huston, D. R., Bosch, H. R., and Scanlan, R. H., 1988, "The Effect of Fairings and of Turbulence on the Flutter Derivatives of a Notably Unstable Bridge Deck," *J. of Wind Engineering and Industrial Aero.*, Vol. 29, pp. 339–349.

Huston, D. R., 1986, "The Effect of Upstream Gusting on the Aeroelastic Behavior of Long-Suspended Span Bridge," Ph.D. Thesis, Princeton University.

Kozin, F., and Sugimoto, S., 1977, "Relations Between Sample and Moment Stability for Linear Stochastic Differential Equations," *Proc. Conf. on Stochastic Differential Equations*, D. Mason ed., Academic Press, New York, pp. 145–162.

Kozin, F., 1969, "A Survey of Stability of Stochastic Systems," *Automatica*, Vol. 5, pp. 95–112.

Lebowitz, J. L., Presulti, E., and Spohn, H., 1988, "Microscopic Models of Hydrodynamic Behaviour," *J. Stat. Physics*, Vol. 51, pp. 841–861.

Lefever, R., and Turner, J. Wm., 1986, "Sensitivity of a Hopf Bifurcation to Multiplicative Colored Noise," *Physical Review Letters*, Vol. 56, pp. 1631–1634.

Lin, Y. K., and Ariaratnam, S. T., 1980, "Stability of Bridge Motion in Turbulent Winds," *Journal of Structural Mechanics*, Vol. 8, pp. 1–15.

Lin, Y. K., 1979, "Motion of Suspension Bridges on Turbulent Winds," *J. Engineering Mechanics Div.*, ASCE, Vol. 105, pp. 921–932.

Mangel, M., 1979, "Uniform Treatment of Fluctuations at Critical Points," *Physica A*, Vol. 97, pp. 597–615.

Moss, F., and McClintock, P. V. E., 1989 *Noise in Nonlinear Dynamical Systems*, Vol. 1–3, Cambridge University Press, Cambridge, England.

Petroski, H., 1991, "Still Twisting," *American Scientist*, Vol. 79, No. 5, pp. 398–401.

Sancho, J. M., San Maguel, M., Katz, S. L., and Gunta, J. D., 1982, "Analytical and Numerical Studies of Multiplicative Noise," *Physical Review A*, Vol. 26, pp. 1589–1609.

Scanlan, R. H., and Huston, D., 1991, personal communication.

Scanlan, R. H., and Huston, D. R., 1986, "Change in Bridge Deck Flutter Derivatives Caused by Turbulence, in Dynamic Response of Structures," *G. Hart and R. Nelson, eds., Proc. ASCE Specialty Conf.*, Los Angeles, Mar., pp. 382–384.

Scanlan, R. H., and Lin, W. H., 1978, "Effects of Turbulence on Bridge Flutter Derivatives," *J. of Engineering Mechanics Div.*, ASCE, Vol. 100, pp. 657–672.

Scanlan, R. H., 1977, "The Action of Flexible Bridges Under Wind: I. Flutter Theory," *Journal of Sound and Vibration*, Vol. 60, pp. 187–194.

Scanlan, R. H., 1976, "On the State of Stability Consideration for Suspended Span Bridge under Wind," *Proc. IUTAM-IAHR Symposium*, Karlsruhe, Germany, Paper F1, pp. 595–618.

Scanlan, R. H., and Tomko, J. J., 1971, "Airfoil and Bridge Deck Flutter Derivative," *J. Eng. Mech.*, Vol. 97, pp. 1717–1737.

Shinozuka, M., and Jan, C. M., 1972, "Digital Simulation of Random Process and Its Application," *Journal of Sound and Vibration*, Vol. 25, pp. 111–128.

Shinozuka, M., and Deodatis, G., 1990, "Stochastic Processes by Spectral Representation," *Applied Mechanics Review*, Vol. 44, Apr. 1991, pp. 191–203.

Simiu, E., and Scanlan, R. H., 1986, *Wind Effects on Structures*, 2nd ed., John Wiley and Sons, New York.

Sri Namachchivaya, N., and Hilton, H. H., 1988, "Stochastically Perturbed Bifurcation," *Nonlinear Stochastic Dynamics Engineering System*, F. Ziegler, and G. I. Schuëller, eds., Springer-Verlag, pp. 169–180.

Stratonovich, R. L., 1963, *Topics in the Theory of Random Noise*, Vol. 1-2, Gordon Breach, New York.

Tsiatas, G., and Sarkar, P. P., 1988, "Motion Stability of Long-Span Bridges Under Gusty Winds," *Journal of Engineering Mechanics*, Vol. 114, pp. 257–276.

Tsiatas, G., and Gasparini, D. A., 1987, "Torsional Response of Long Span Bridges in Presence of Turbulence," *Journal of Engineering Mechanics*, Vol. 113, pp. 303–314.

van Kampen, N. G., 1989, "Langevin-Like Equation with Colored Noise," *J. Stat. Physics*, Vol. 54, pp. 1289–1308.

Downloaded 03 May 2010 to 171.66.16.20. Redistribution subject to ASME license or copyright; see http://www.asme.org/terms/Terms_Use.cfm

Ultrasonic Evaluation of Stiffness Tensor Changes and Associated Anisotropic Damage in a Ceramic Matrix Composite

B. Audoin

S. Baste

Laboratoire de Mecanique Physique,
URA CNRS No. 867,
Universite Bordeaux I,
351, Cours de la Liberation,
33405-Talence Cedex, France

After describing the crucial role of microcracking in the behavior of ceramic matrix composites, we introduce a phenomenological model in the framework of continuum damage mechanics, where damage is defined as the change of the tensor of elasticity. For damage identification, we have developed a specific ultrasonic device. This immersion set-up was connected to a suitable data processing system for an optimum recovery of the stiffness matrix coefficients from convenient sets of velocity measurements. Linked to a tensile machine, it enabled us to measure the stiffness changes and the anisotropic damage induced by a uniaxial tensile test.

1 Introduction

Damage is conventionally defined as the progressive deterioration of materials due to nucleation and growth of microcracks. The purpose of the damage concept (Kachanov, 1958) is to take into account the microscopic deterioration of the material in its macroscopic constitutive law. In composite materials, the microcracks have a preferential orientation and the damage variable depends on the direction of measurement (Onat and Leckie, 1988). Nonlinear analysis of such materials must consider this anisotropy by introducing a tensorial damage variable in the constitutive equations. For applications of continuum damage mechanics to composites (Talreja, 1985a; Daniel and Charewicz, 1986), damage was introduced as an internal state variable whose tensorial nature depends on assumptions about cracks geometry. An extensive review of the damage models has been given by Krajcinovic (1989). The main difficulties when dealing with anistropic description of damage are both to identify the introduced parameters (Litewka, 1985; Wang et al., 1986) and to be able to perform the measurements which test the predictions of the proposed model.

Numerous methods lead to the formulation of the constitutive laws of damaged materials. The micromechanical approach consists in analyzing the microscopic phenomena to predict the macroscopic behavior. The microdefects are defined by their geometrical parameters: crack lengths, discontinuity spacing, . . ., for the calculation of the properties of the continuous equivalent damaged medium (Budiansky and O'Connel, 1976; Hoenig, 1979; Onat, 1984; Horri and Nemat-Nasser, 1985; Laws and Dvorak, 1987). But the microscopic level is unsuitable for modeling the global behavior of an actual material in which microdefects usually present a disordered geometry. The description of damage by a macroscopic approach leads to a more convenient analysis and identification of the behavior, for structural computations.

The purpose of this paper is the macroscopic representation of the inelastic behavior of a ceramic matrix composite. Those materials exhibit a highly nonlinear behavior under load due to the growth of microcracks. In Section 2, this microscopic phenomenon is represented by an internal variable which describes the effect of these microdefects on the macroscopic scale. A general description of damage is proposed for which no assumption on microcracks geometry is required. The calculation of the dissipation due to damage and the account of the associated thermodynamical restrictions provide the admissible range of variation of the damage tensorial variable. This representation requires that the changes of each stiffness coefficient be identified.

The feasibility of the ultrasonic evaluation of damage has already been shown (Waynes et al., 1989; El Guerjouma and Baste, 1989). The ultrasonic technique makes it possible to measure the stiffness tensor of an anisotropic material (Markham, 1970; Roux et al., 1985; Roux, 1990; Baste and Hosten, 1990). The use of an immersed interferometer with a tensile machine leads to the identification of the elastic tensor changes during a tensile test. In Section 3, the numerical processing of the wave velocities data, which leads to the identification, is briefly described.

Results derived from the measurements made, as well as the analysis of damage tensor evaluation in the ceramic matrix composite submitted to a tensile test, are presented in Section 4. Stiffness changes corroborate the anisotropy of damage and emphasize the necessity of the independent measurement of each coefficient.

Contributed by the Applied Mechanics Division of THE AMERICAN SOCIETY OF MECHANICAL ENGINEERS for publication ASME JOURNAL OF APPLIED MECHANICS.

Discussion on this paper should be addressed to the Technical Editor, Professor Lewis T. Wheeler, Department of Mechanical Engineering, University of Houston, Houston, TX 77204-4792, and will be accepted until four months after final publication of the paper itself in the ASME JOURNAL OF APPLIED MECHANICS.

Manuscript received by the ASME Applied Mechanics Division, Feb. 28, 1992; final revision, May 27, 1993. Associate Technical Editor: W. N. Sharpe, Jr.

Copyright © 1994 by ASME
Downloaded 03 May 2010 to 171.66.16.20. Redistribution subject to ASME license or copyright; see http://www.asme.org/terms/Terms_Use.cfm



Fig. 1 Woven structure of the SiC-SiC 2-D material

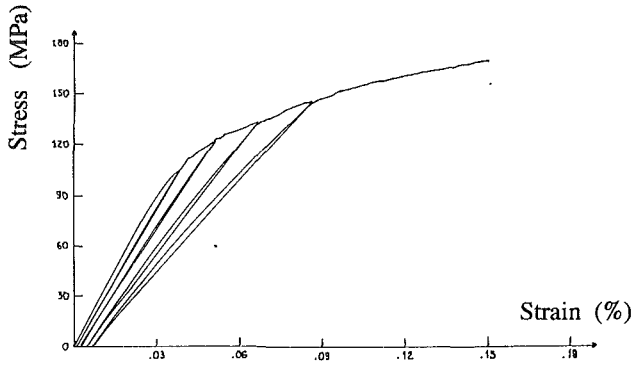


Fig. 2 Damaged elastic behavior of the SiC-SiC 2-D material

2 *Continuum Damage Mechanics*

2.1 Mechanical Behavior of the Brittle Matrix Composites. The material studied is a bi-directional ceramic-ceramic composite. It consists of SiC fibers which are reinforced with a SiC matrix. It is fabricated from performs built up from multiple layers of SiC cloths. The SiC matrix was added by a chemical vapor infiltration process which resulted in samples with a porosity of about 20 percent (Inghels and Lamon, 1988). The woven structure and the porosity of the material are shown in Fig. 1.

Though both of the constituents, the fibers and the matrix, display a brittle behavior the composite shows a ductile one. During a uniaxial tensile test, it exhibits some nonlinearities depicted on the typical stress-strain curve of Fig. 2. When this tensile test is performed by cycles, the unloadings return to a strain equal to zero, even if the nonlinearity threshold is exceeded. Above this limit, the stress-to-strain ratio of the cycles then decreases. It appears that the nonlinearity of the behavior is not due to plasticity but to the reduction of the elastic properties. To the anisotropy of the virgin material, an anisotropic reduction of its stiffness properties is added due to the solicitation undergone by the composite. This degradation is caused by the existence and the propagation of complex microcracking of the brittle matrix.

2.2 Damage Variable. The internal structure change, which occurs in certain materials under stress, affects their physical and mechanical properties. Degradation of one of these properties is an indirect measurement of damage. It is now commonly recognized that the change in elasticity is the direct measure of damage (Ortiz, 1985; Krajcinovic, 1989). The values of the elastic compliances themselves can be taken as a characterization of the state of damage of the material. The elasticity tensor can be written in an additive form:

$$\mathbf{C} = \mathbf{C}_0 - \mathbf{C}_c, \tag{1}$$

in terms of the stiffness tensor $\mathbf{C}_0$ of the uncracked material and of the loss of stiffness $\mathbf{C}_c$ due to the microcracks. The variation of the stiffness tensor

$$\omega = \mathbf{C}_c = \mathbf{C}_0 - \mathbf{C} \tag{2}$$

is selected as an internal variable representing the current state of the microcracking of the material. Like the initial elasticity tensor $\mathbf{C}_0$, the effective stiffness is a fourth rank symmetrical tensor, and the damage variable ω shows the same properties. With the introduction of usual abbreviated subscripts notation, (2) becomes

$$\omega_{IJ} = C^0_{IJ} - C_{IJ}, \quad I, J = 1 \text{ to } 6. \tag{3}$$

The components of this tensor have a clearly identifiable physical meaning, they form a finite set of data and a fully anisotropic behavior can be described.

Traditionally, in phenomenological models based on the thermodynamics of continuous media, the damage parameter varies from zero for the initial state to the critical value $d = 1$ at the failure of the volume element (Lemaitre and Chaboche, 1978; Chaboche, 1988). To this end it is necessary to normalize the components of the damage tensor to their thermodynamically admissible maximum values $\omega^{\lim}_{IJ}$ such that the elasticity tensor remains a definite positive operator, i.e., the volume free energy of the damaged material is still positive (Baste and Audoin, 1991). The components of the normalized damage tensor are then given by

$$D_{II} = \frac{\omega_{II}}{\omega^{\lim}_{II}} = 1 - \frac{C_{II}}{C^0_{II}}, \quad I = 1 \text{ to } 6, \text{ no sum}, \tag{4}$$

$$D_{IJ} = \frac{\omega_{IJ}}{\omega^{\lim}_{IJ}} = \frac{C^0_{IJ} - C_{IJ}}{C^0_{IJ} + \text{Sign}\,(C^0_{IJ} - C_{IJ})\sqrt{C^0_{II}(1 - D_{II})\,C^0_{JJ}(1 - D_{JJ})}}, \quad I, J = 1, \ldots, 6, \; I \neq J, \tag{5}$$

2.3 Thermodynamic Restrictions on the Stiffness Variations Induced by Damage. Damage being a dissipative phenomenon, it is customary, within the generalized standard framework (Germain et al., 1983), to introduce a threshold function governing damage evolution, i.e., a dissipative law connecting the damage variable to its dual force.

The state variable ω being specified, the volume free energy, taken as the thermodynamic potential

$$W_e = \frac{1}{2}\,\sigma : \epsilon^e = \frac{1}{2}\,\sigma : (\mathbf{C}_0 - \omega)^{-1} : \sigma, \tag{6}$$

defines the local state of the material as a function of an observable variable, the elastic strain ϵ^e, and of an internal variable ω. The symbol : denotes the contracted product on two subscripts and σ is the stress tensor. The thermodynamic force $\mathbf{Y}$ conjugate to the variable ω (Marigo, 1981; Mazars, 1986),

Downloaded 03 May 2010 to 171.66.16.20. Redistribution subject to ASME license or copyright; see http://www.asme.org/terms/Terms_Use.cfm

$$\mathbf{Y} = \frac{\partial W_e}{\partial \omega}, \tag{7}$$

has the same tensorial nature as ω, i.e., is a fourth rank symmetrical tensor.

Dissipation due to damage is the product of the force $\mathbf{Y}$ by the damage flux variable

$$\Phi = \mathbf{Y} :: \dot{\omega}, \tag{8}$$

which must be positive according to the Clausius-Duhem inequality. The symbol :: denotes the contracted product on four subscripts. From (2), one gets the relation

$$\dot{\omega} = -\dot{\mathbf{C}}, \tag{9}$$

from which the inequality which connects the damage force to the flux variable $\dot{\mathbf{C}}$ is then

$$\mathbf{Y} :: \dot{\mathbf{C}} < 0. \tag{10}$$

This equation can be written as follows for an uniaxial loading in direction 3 (Baste and Audoin, 1991):

$$A_{33}\dot{\Delta} - \Delta \dot{A}_{33} < 0 \tag{11}$$

where Δ is the determinant of the matrix $\mathbf{C}_{IJ}$ and A_{33} the cofactor of C_{33}. Noting that the change of the compliance S_{33} is given by

$$\dot{S}_{33} = \frac{\Delta \dot{A}_{33} - A_{33}\dot{\Delta}}{\Delta^2}, \tag{12}$$

we conclude that dissipation due to damage is positive if the following inequality is verified:

$$\dot{S}_{33} > 0. \tag{13}$$

The only constraint imposed by dissipativity applies to the evolution of the axial compliance which must increase, i.e., the Young's modulus E_3 must decrease. No other thermodynamic restriction exists on the variations of the other elasticity constants.

3 Ultrasonic Device

The interest of the description of damage presented above consists in its generality and in its purely phenomenological character. The price to pay for its simplicity is the requirement of developing a specific identification device. The ultrasonic evaluation technique makes it possible to measure the nine stiffness coefficients describing completely the elasticity of an orthotropic material.

3.1 Ultrasonic Characterization of an Orthotropic Material. In anisotropic solids exhibiting an elastic behavior, the stress-strain relationship using or not using the abbreviated subscripts notation

$$\sigma_I = C_{IJ}\epsilon_J, \quad I, J = 1 \text{ to } 6 \quad \text{or} \quad \sigma_{ij} = C_{ijkl}\epsilon_{kl}, \quad i, j = 1, 2, 3, \tag{14}$$

can be written in term of the small displacement field of an elastic plane wave (Auld, 1973). It leads to the wave equation, which we write in its Christoffel form

$$(\Gamma_{ij} - \rho v^2 \delta_{ij}) P_j = 0, \text{ with } \Gamma_{ij} = C_{ijkl} n_k n_l, \quad i, j = 1, 2, 3, \tag{15}$$

where ρ is the density, $\mathbf{P}$ the polarization vector, $\mathbf{n}$ the direction of propagation, v the velocity, and δ_{ij} Kronecker's symbol. The velocities are the solutions of the secular equation

$$\det(\Gamma_{ij} - \rho v^2 \delta_{ij}) = 0. \tag{16}$$

The ultrasonic characterization purpose is to solve the inverse problem of the secular Eq. (16). Stiffnesses have to be recovered as the coefficients of Eq. (16) from suitable sets of experimental values of its roots ρv^2 in various directions $\mathbf{n}$ (Castagnède et al., 1990). Let N be the number of these directions of measurements. The question is one of solving an overdetermined system of N nonlinear equations (with $N > 9$) whose unknowns are the nine stiffness coefficients. This recovering of the stiffness coefficients from the experimental velocities is solved by an optimization inversion method. It minimizes, in the least square sense, the shift between the experimental values, and the one calculated from Eq. (16) for the optimum values of the stiffnesses. In order to ensure the convexity of the process, the optimization scheme is broken in three parts:

- identification of C_{11}, C_{22}, C_{12}, C_{66} (in axes of Fig. 3) using experimental values of the velocities issued from a propagation test in plane (1, 2),
- identification of C_{11}, C_{33}, C_{13}, C_{55} (in axes of Fig. 3) using experimental values of the velocities issued from a propagation test in plane (1, 3),
- identification of the two remaining coefficients C_{23} and C_{44} using the previously identified coefficients and the experimental velocities measured in a non principal plane of symmetry, plane (1, 4). Axis 4 is defined as the bisecting line of the axes 2 and 3 (see Fig. 3).

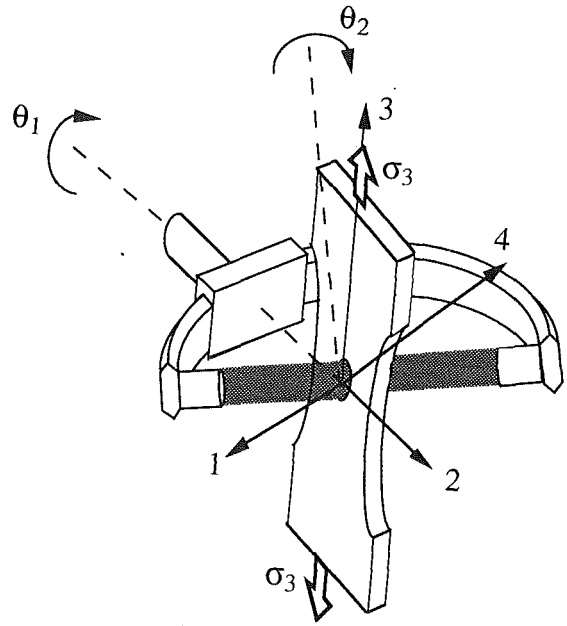


Fig. 3 Under-load ultrasonic characterization device. The transducers are moved by a combination of two rotations (θ_1 and θ_2) while the sample is loaded along direction 3.

Wave speed measurements are performed by using ultrasonic pulses which are refracted through a plate sample immersed in water (Markham, 1970). Because of the signal distortion due to the propagation in a porous media (Walter et al., 1988), a special signal processing method was developed (Audoin and Roux, 1990). It leads to the correct measurement of the phase velocity of the pulses through the porous sample.

An estimation of the confidence interval associated to each identified constant can be calculated (Audoin et al., 1991) by means of a statistical analysis of the set of the velocity measurements in each plane of propagation. As it requires some assumptions on the angular repartition of the off-set between the measured and the calculated velocities, it does not provide an exact calculation. Nevertheless, it enabled us to establish the ultrasonic characterization reliability by means of the comparison of the identification with classical mechanical measurements of Young's modulus (Audoin, 1991).

3.2 Stiffness Coefficients of the SiC-SiC 2-D. Because of its bi-directional structure, the material possesses three perpendicular planes of symmetry and it satisfies the hypothesis of an orthorhombic symmetry required by the ultrasonic technique. For the three SiC-SiC 2-D samples studied, the stiff-

Downloaded 03 May 2010 to 171.66.16.20. Redistribution subject to ASME license or copyright; see http://www.asme.org/terms/Terms_Use.cfm

Table 1 Stiffness coefficients (in GPa) and associated 90 percent confidence interval of the three tested samples

sample	32-3	32-2	30-1
plate	32	32	30
density	2.78	2.80	2.85
C_{11}	169 ± 2	144 ± 2	177 ± 1
C_{22}	295 ± 19	457 ± 25	374 ± 8
C_{33}	318 ± 12	466 ± 20	387 ± 14
C_{12}	48 ± 4	60 ± 4	60 ± 2
C_{13}	51 ± 3	66 ± 3	63 ± 3
C_{23}	145 ± 30	324 ± 4	214 ± 35
C_{44}	93 ± 24	42 ± 4	37 ± 35
C_{55}	60 ± 2	53 ± 2	69 ± 1
C_{66}	57 ± 2	58 ± 2	64 ± 1

nesses before load, and their 90 percent confidence interval are shown in Table 1.

The SiC-SiC 2-D material possesses a coarse texture and a significant porosity. In such a sample the thickness is only 3.5 mm along normal axis 1 and the texture periodicity is about 0.5 mm in this direction. Therefore, with the signal frequency used, which is equal to 2.25 MHz, we are close to the limit of the scales of homogeneity required to interpret the wave propagation. Then, the ultrasonic wave velocity measurement is of lesser quality than when dealing with homogeneous materials or organic matrix composites (Audoin et al., 1991). Nevertheless, the accuracy estimated from the confidence interval is about eight percent at worst for the coefficients identified from propagation in a principal plane of symmetry. Because of numeric difficulties, the accuracy of the identification of C_{23} and C_{44} from measurements in plane (1, 4) is lower (Audoin, 1991).

Two samples, referred to as 32-2 and 32-3, have been cut out from the same plate of material, while the third one, 30-1, has been extracted from another plate. The dispersion of the stiffness values measured is as important for samples cut of the same plate, as it is when taken out from different plates (see Table 1). This variation is caused by the high sensitivity of the material properties to the porosity level and to the non homogeneous distribution of the porosity which is due to the manufacture process (Caputo et al., 1987).

3.3 Under Load Characterization Device. The ultrasonic evaluation of damage requires that the samples are submitted to a tensile stress increasing by steps: during each step, the stress is controlled to remain constant, and the angular investigation in the three planes (1, 2), (1, 3), and (1, 4) is performed. For that purpose, we have built a specific immersed interferometer which is incorporated into a tensile machine. The tank laying on the lower traversing saddle is crossed by the tensile axis and supports the positioning system of the transducers. This later device generates two degrees of rotation, the Euler angles (Fig. 3), and it positions the transducers on a sphere surrounding the material under test. In particular, it makes it possible to perform the angular incrementation in the three required planes.

The specific dog-bone shape of the samples locates the damage in the part investigated by the ultrasonic beam. It also ensures that the stress state is homogeneous in that zone. Three samples have been submitted to a tensile test in the direction 3.

4 Measurement of Damage

The ultrasonic measurements of damage presented above require that the material keeps its orthorhombic symmetry during the degradation process. This condition is satisfied if the direction of crack growths correspond with the bi-directional texture of the composite (Talreja, 1985b).

The damage parameters plotted in Fig. 7 are calculated from the stiffness changes using Eq. (4) and (5). For these calculations, the coefficients of the undamaged material C^0_{IJ} are supposed to be those of the samples before tensile test.

4.1 Stiffness Tensor Variation During a Single Tensile Test. Two samples referred 32-2 and 30-1 in Table 1 have been tested during a monotonic tensile test until fracture. About 20 steps of stress have been applied and the fracture occurred around 230 MPa. The results of the stiffness tensor identifications and their relative confidence intervals are plotted in Fig. 4. This plot describes three behaviors.

- Up to a 90 MPa stress, none of the stiffness coefficients vary in a significant manner. This stress value is the damage threshold. Up to this value, the behavior is purely elastic.
- Afterwards, the matrix microcracking begins and the stiffness moduli decrease. The stress to failure of the matrix has been exceeded (Bernhart et al., 1985; Veltri et al., 1989). Since D_{33} exhibits an increase of 0.5 (see section 4.3), the cracks grow preferentially in the plane transverse to the loading direction (Laws and Dvorak, 1987). Because of the composite texture (Kuo and Chou, 1991), they also propagate along the fibers: C_{11} also decreases heavily. It is worth noting that this microcracking has also an important effect on the shear moduli, and particularly on those relative to the planes which contain the loading direction (see C_{55} in Fig. 4). The damage level reached by the parameters relative to those shear moduli ($D_{55} \approx 0.4$) are similar to the one reached by C_{33} ($D_{33} \approx 0.5$).
- When a 130 MPa stress has been reached, the evolution of the stiffness coefficients becomes much slower. Microcracking of the matrix has reached its saturation level. A second more diffused degradation mechanism seems to propagate inside the bundles (Quenisset, 1988). Beyond 130 MPa, the damage increases slowly and the elasticity of the material is close to that of the fibers. Their failure occurs suddenly around 230 MPa.

Note that despite the dispersion of their initial values, the stiffness coefficients are comparable when the fracture occurs, in particular those whose variation is important and which seem to command the failure, i.e., C_{33}, C_{55}, C_{13}, C_{23}.

4.2 Stiffness Tensor Variation During a Double Tensile Test. The third sample, referred to as 32-3, has been submitted to a tensile test realized in two stages—a first loading up to 180 MPa with 17 steps for characterization and a second test up to failure preceded by a return to a zero load. The variations of the stiffness coefficients measured during this double tensile test are plotted in Fig. 6.

From 0 to 20 MPa a transverse hardening appears which is mainly apparent on C_{22} but also on C_{12}, C_{66}, and C_{23}. The variation of C_{22} is about 150 GPa and the parameter D_{22} is initially nonzero ($D_{22} = 0.35$). This variation has been observed twice: during the first loading test, and during the second one.

The Young's modulus in the tensile direction, obtained from the inversion of the stiffness matrix, does not increase significantly with regard to the precision of its calculation (Fig. 5). The transverse hardening observed is then thermodynamically admissible (Section 2.3). It is due to the closure by the Poisson effect of pre-existing cracks and porosities whose volume along the transverse directions is small. The presence of those pre-existing cracks is confirmed by the low values of the stiffness coefficients of this sample before load shown in Table 1. Such a transverse hardening has already been provided by numerical

Downloaded 03 May 2010 to 171.66.16.20. Redistribution subject to ASME license or copyright; see http://www.asme.org/terms/Terms_Use.cfm

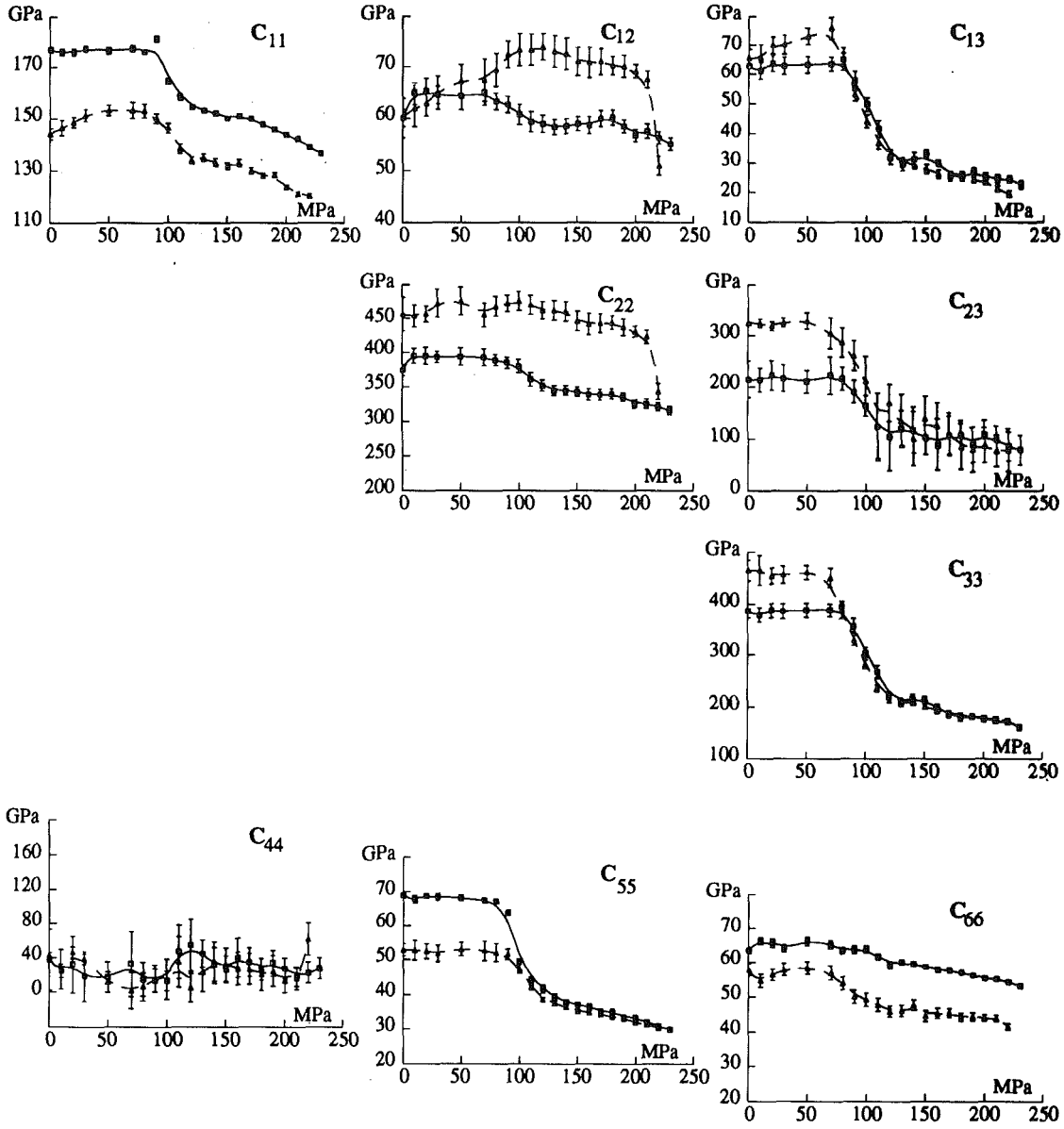


Fig. 4 Variation of the stiffness tensor coefficients and their 90 percent relative confidence interval with the tensile stress in direction 3, samples 30-1 (squares) and 32-2 (triangles)

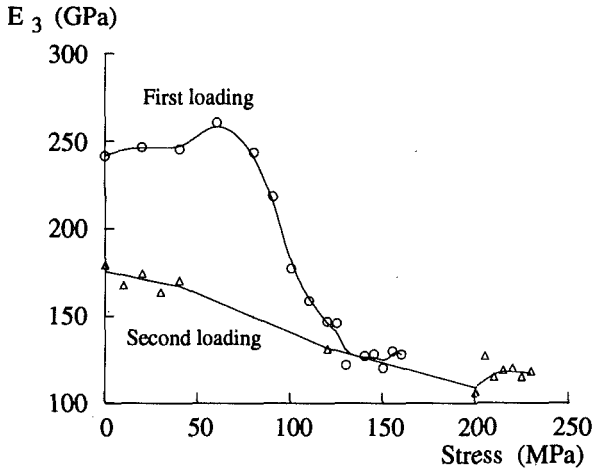


Fig. 5 Variation of Young's modulus E_3 in the tensile direction of sample 32-3 calculated from ultrasonic data

simulations based on micromechanic concepts (Ortiz, 1985; Andrieux et al., 1986).

Beyond a 20 MPa stress and until fracture, the sample behaves similarly to samples 32-2 and 30-1 considered previously. It exhibits the same three specific zones described above. When the sample is unloaded, the values of the stiffness coefficients are similar to those attained during the first load at 180 MPa, if we do not consider the cracks opening and closure effects (Ortiz, 1985). During the second tensile test, as the pre-stress is included in the third characteristic stress interval, the variation of the coefficients between 0 and 180 MPa is as linear as it was between 120 and 230 MPa for the virgin samples.

4.3 Damage Coefficients. The overlaying of the damage parameters plotted in Fig. 7 shows the reproducibility of the behaviors of the three samples. The parameters whose variation are most important are those which are affected by cracks normal to the tensile axis 3. Indeed, the damage parameter D_{33}, but also the parameter relative to the modulus C_{55}, reach the value 0.7 when the fracture occurs. The other parameters

Downloaded 03 May 2010 to 171.66.16.20. Redistribution subject to ASME license or copyright; see http://www.asme.org/terms/Terms_Use.cfm

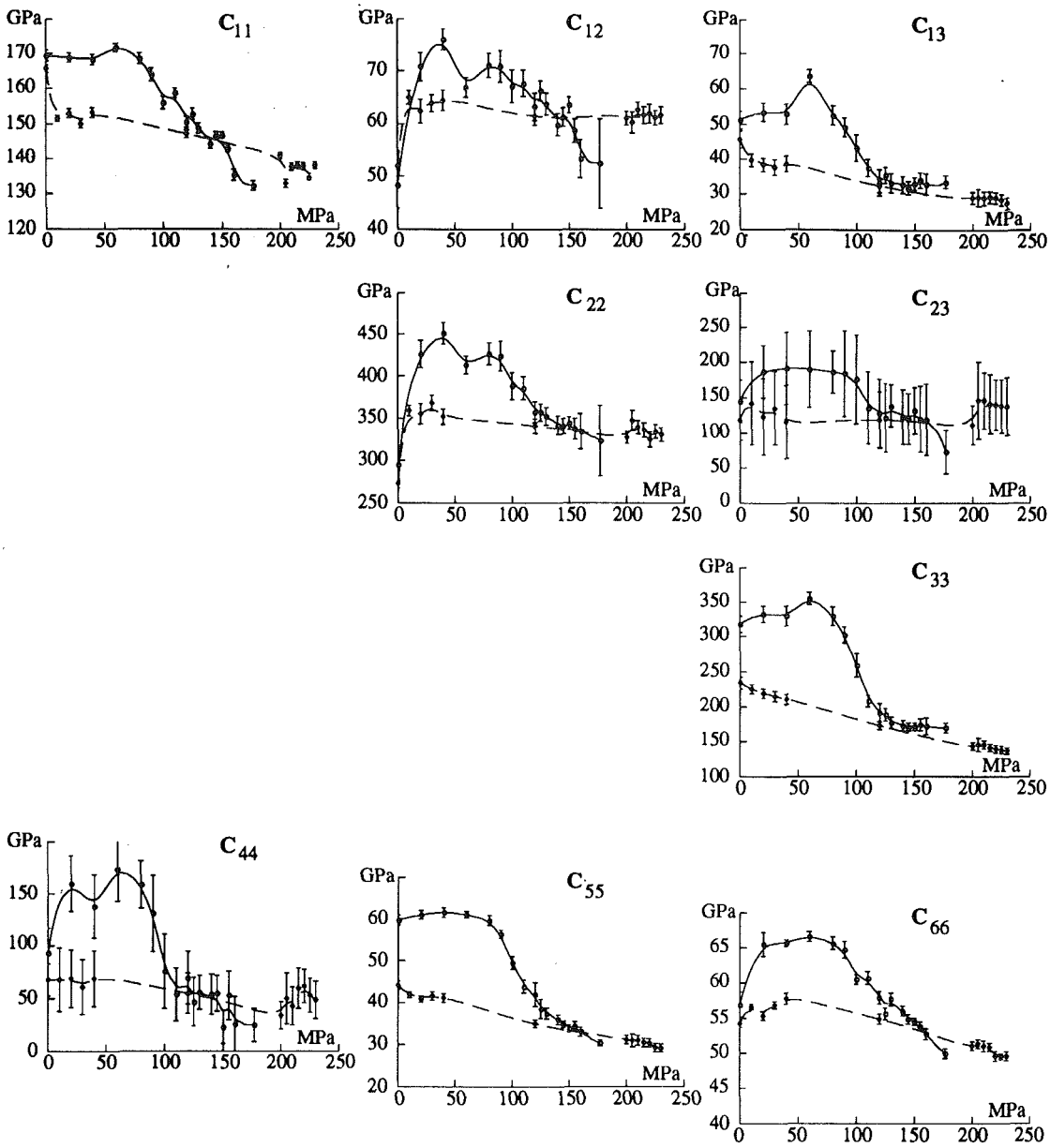


Fig. 6 Variation of the stiffness tensor coefficients and their 90 percent relative confidence interval with the tensile stress in direction 3 during the first loading (circles) and the second one (diamond), sample 32-3

values are then about 0.3 except D_{12} which does not vary. The poor precision of the identification of the coefficient C_{44} does not allow the plotting of the variation of its associated damage parameter. Nevertheless, Fig. 7 establishes that the two directions orthogonal to the tensile axis are equivalent from the damage point of view. The parameters D_{11}, D_{22} on the one hand, and D_{13}, D_{23} on the other hand, appear to be equal considering their relative identification precision.

4.4 Construction of the Stress-Strain Curves. From the inversion of the stiffness matrix measured above, the calculation of the Young's modulus E_3 relative to axis 3 has been done. With the hypothesis of an elastic damage behavior, the strain in the tensile direction has been calculated for each level of stress. The stress-strain curves, which are often plotted when dealing with classical gauge measurement, are reported in Fig. 8.

Despite of the low accuracy of the calculation of the Young's modulus E_3, which requires the inversion of a matrix whose coefficients are identified with different accuracies, the behavior appears to be similar to the one measured on this material (Bernhart et al., 1985). Between 90 and 130 MPa the nonlinearity appears corresponding to the stiffness moduli decrease plotted in Fig. 5.

5 Conclusion

The development and the growth of microcracks highly affect the macroscopic behavior of brittle matrix composites. This deterioration is measured, at the macroscopic scale, by the changes of the stiffnesses. Since cracks have overriding propagation directions, the effect is highly anisotropic and the variations of the whole stiffness tensor must be studied. As classical measurement methods lead to a partial identification of these tensor variations, an ultrasonic device has been connected to a tensile machine to perform the measurements of stiffness tensor changes during a tensile test. The assumption required for this identification is that the material keeps its orthorhombic symmetry during the degradation process. With this phenomenological approach, damage is directly defined as the stiffness variation.

Downloaded 03 May 2010 to 171.66.16.20. Redistribution subject to ASME license or copyright; see http://www.asme.org/terms/Terms_Use.cfm

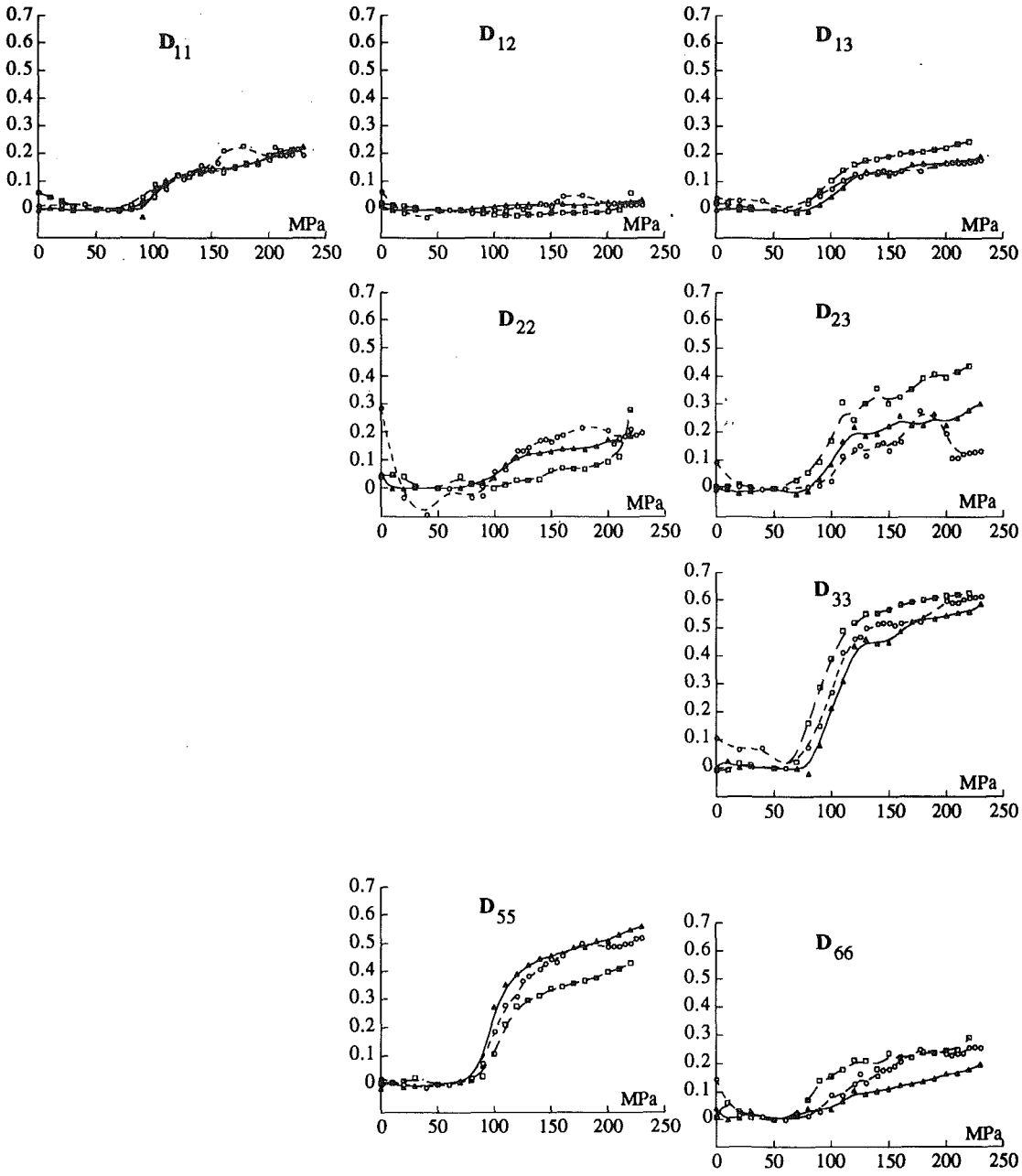


Fig. 7 Evolution of damage tensor coefficients of the three samples

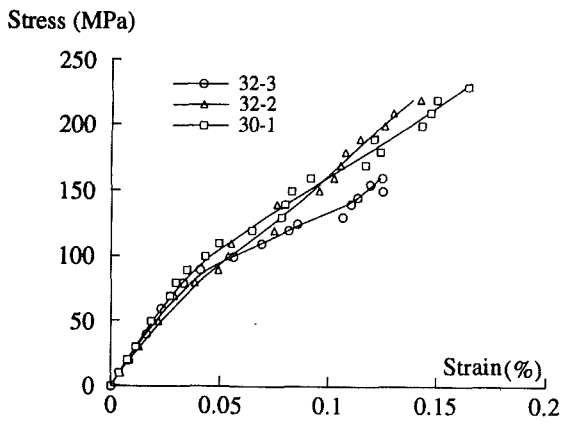


Fig. 8 Stress/axial-strain curves restored from ultrasonic data

The measurements have been performed with a SiC-SiC 2-D composite which presents a damaged elastic behavior since no residual deformation is observed on its typical cycled stress-strain curves. The different variations of damage parameters characterize the anisotropy of the damaging process and justify the requirement of the independent identification of each stiffness coefficient. These measurements show that the damage associated to the shear modulus C_{55} is as critical as the one associated to the stiffness C_{33} in the tensile direction. Also, the tridimensional effect of a pre-stress higher than the damage threshold has been measured.

This approach appears to be efficient when the material has no microcracks in its initial state, and when the loading is applied in a monotonic manner. The experiments on the third sample 32-3, which is cycled back to zero stress once, reveal that the damage does not relate to the intrinsic state of the material, but that it is a function of the applied stress. Thus this global description shall be divided using two internal vari-

Downloaded 03 May 2010 to 171.66.16.20. Redistribution subject to ASME license or copyright; see http://www.asme.org/terms/Terms_Use.cfm

ables: one relating to the accumulated and growing damage resulting to the initiation and propagation of microcracks and the second relating to the opening closing of existing microcracks without propagation (Baste et al., 1992).

In addition, the microcracking effect may be totally characterized when the response of the material to any stress has been measured. For that purpose, the wide area of off-diagonal solicitation must still be investigated.

Acknowledgment

This work was partially supported by Société Européenne de Propulsion (SEP) through Grant No. 451957. The composite samples were supplied by SEP.

References

Andrieux, S., Bamberger, Y., and Marigo, J. J., 1986, "Un modèle de matériau microfissuré pour les bétons et les roches," *J. Mec. Theory. Appl.*, Vol. 5, pp. 471–513.

Audoin, B., 1991, "Evaluation ultrasonore de l'endommagement anisotrope d'un composite à matrice fragile," Ph.D Thesis, Université de Bordeaux I.

Audoin, B., and Roux, J., 1990, "Traitement de signal ultrasonore adapté à l'évaluation non destructive de matériaux dispersifs," *Revue Phys. Appl.*, Vol. 25, pp. 1011–1017.

Audoin, B., Baste, S., and Castagnède, B., 1991, "Estimation de l'intervalle de confiance des constantes d'élasticité identifiées à partir des vitesses de propagation ultrasonores," *C. R. Acad. Sci. Paris*, Vol. 312, Series II, pp. 679–686.

Auld, B. A., 1973, *Acoustic Fields in Solids*, Vol. 1, John Wiley and Sons, New York.

Baste, S., and Hosten, B., 1990, "Evaluation de la matrice d'élasticité des composites orthotropes par propagation ultrasonore en dehors des plans principaux de symétrie," *Revue Phys. Appl.*, Vol. 25, pp. 161–168.

Baste, S., and Audoin, B., 1991, "On Internal Variables in Anisotropic Damage," *Eur. J. Mech. A/Solids*, Vol. 10, No. 6, pp. 587–606.

Baste, S., El Guerjouma, R., and Audoin, B., 1992, "Effect of Microcracking on the Macroscopic Behavior of Ceramic Matrix Composites, Ultrasonic Evaluation of Anisotropic Damage," *Mechanics of Materials*, Vol. 14, pp. 15–31.

Bernhart, G., Lamicq, P., and Macé, J., 1985, "Fiabilité des Composites Céramiques Céramiques," *L'industrie Céramique*, Vol. 790, pp. 51–56.

Budiansky, B., and O'Connel, R. J., 1976, "Elastic Moduli of a Cracked Solid," *Int. J. Solids Struct.*, Vol. 12, pp. 81–97.

Caputo, A. J., Stinton, D. P., Lowden, R. A., and Besmann, T. M., 1987, "Fiber-Reinforced SiC Composites with Improved Mechanical Properties," *Am. Ceram. Soc. Bull*, Vol. 66, No. 2, pp. 368–372.

Castagnède, B., Jenkins, J. T., Sachse, W., and Baste, S., 1990, "Optimal Determination of Elastic Constants of Composite Materials from Ultrasonic Wave-Speed Measurements," *J. Appl. Phys.*, Vol. 67, No. 6, pp. 2753–2761.

Chaboche, J.-L., 1988, "Continuum Damage Mechanics," Parts I and II, *J. Appl. Mech.*, Vol. 55, pp. 59–72.

Daniel, I. M., and Charewicz, A., 1986, "Fatigue Damage Mechanisms and Residual Properties of Graphite/Epoxy Laminates," *Eng. Fract. Mech.*, Vol. 25, pp. 793–808.

El Guerjouma, R., and Baste, S., 1989, "Evaluation of Anisotropic Damage in Ceramic-Ceramic (SiC-SiC) Composite by Ultrasonic Method," Ultrasonics International 89, Madrid, July, pp. 895–900.

Germain, P., Nguyen, Q. S., and Suquet, P., 1983, "Continuum Thermodynamics," ASME JOURNAL OF APPLIED MECHANICS, Vol. 50, pp. 1010–1020.

Hoenig, A., 1979, "Elastic Moduli of a Non-Randomly Cracked Body," *Int. J. Solids Struct.*, Vol. 5, pp. 137–154.

Horii, H., and Nemat-Nasser, S., 1985, "Elastic Fields of Interacting Inhomogeneities," *Int. J. Solids Struct.*, Vol. 21, pp. 731–745.

Inghels, E., and Lamon, J., 1988, "Caractérisation de l'endommagement de composites tissés à matrice SiC," *Revue Phys. Appl.*, Vol. 23, pp. 193–200.

Kachanov, L. M., 1958, "Time of Rupture Process Under Creep Conditions," *Izv. Akad. Nauk S.S.R. Otd. Tekh. Nauk.*, Vol. 8, pp. 26–61.

Krajcinovic, D., 1989, "Damage Mechanics," *Mechanics of Material*, Vol. 8, pp. 117–197.

Kuo, W.-S., and Chou, T.-W., 1991, "Modeling of Nonlinear Constitutive Relations of Woven Ceramic Composites," *Ceram. Eng. Sci. Proc.*, Vol. 12, pp. 1556–1573.

Laws, N., and Dvorak, G. J., 1987, "The Effect of Fiber Breaks and Aligned Penny-Shaped Cracks on the Stiffness and Energy Release Rates in Unidirectional Composites," *Int. J. Solids Struct.*, Vol. 23, pp. 1269–1283.

Lemaître, J., and Chaboche, J. L., 1978, "Aspect Phénoménologique de la Rupture par Endommagement," *J. Meca. Appl.*, Vol. 2, No. 3, pp. 167–189.

Litewka, A., 1985, "Effective Material Constants for Orthotropically Damaged Elastic Solid," *Arch. Mech.*, Vol. 37, pp. 631–642.

Marigo, J. J., 1981, "Formulation d'une loi d'endommagement d'un matériau élastique," *C. R. Acad. Sci. Paris*, Vol. 292, pp. 1309–1312.

Markham, M. F., 1970, "Measurement of the Elastic Constants of Fibre Composites by Ultrasonics," *Composites*, Vol. 1, pp. 145–149.

Mazars, J., 1986, "A Description of Micro- and Macro-scale Damage of Concrete Structures," *Eng. Fract. Mech.*, Vol. 25, pp. 729–737.

Onat, E. T., 1984, "Effective Properties of Elastic Materials that Contain Penny Shaped Voids," *Int. J. Engng. Sci.*, Vol. 22, pp. 1013–1021.

Onat, E. T., and Leckie, F. A., 1988, "Representation of Mechanical Behavior in the Presence of Changing Internal Structure," ASME JOURNAL OF APPLIED MECHANICS, Vol. 55, pp. 1–10.

Ortiz, M., 1985, "A Constitutive Theory for the Inelastic Behavior of Concrete," *Mechanics of Materials*, Vol. 4, pp. 67–93.

Quenisset, J. M., 1988, "Mécanismes d'endommagement des matériaux composites," *Endommagement et rhéologie des solides*, Proceedings of 23e G. F. R., Bordeaux, France, Oct., pp. 2.1–2.41.

Roux, J., 1990, "Elastic Wave Propagation in Anisotropic Materials," IEEE 1990 Ultrasonics Symposium, Honolulu, HI, D., pp. 1065–1073.

Roux, J., Hosten, B., Castagnède, B., and Deschamps, M., 1985, "Caractérisation Mécanique des Solides par Spectro-Interférométrie Ultrasonore," *Revue Phys. Appl.*, Vol. 20, pp. 351–358.

Talreja, R., 1985a, "A Continuum Mechanics Characterization of Damage in Composite Materials," *Proc. R. Soc. Lond.*, Vol. A399, pp. 195–216.

Talreja, R., 1985b, "Transverse Cracking and Stiffness Reduction in Composite Laminates," *J. Compos. Materials*, Vol. 19, pp. 355–375.

Veltri, R. D., Condit, D. A., and Galasso, F. S., 1989, "Chemical Vapor Deposited SiC Matrix Composites," *J. Am. Ceram. Soc.*, Vol. 72, No. 3, pp. 478–480.

Walter, J. B., Lott, L. A., and Telschow, K. L., 1988, "Ultrasonic Characterisation of Ceramic-Ceramic Composites," *Review of Progress in Quantitative NDE*, Vol. 7B, D. O. Thompson and D. E. Chimenti, eds., Plenum Press, New York, pp. 971–978.

Wang, S. S., Chim, E. S.-M., and Suemasu, H., 1986, "Mechanics of Fatigue Damage and Degradation in Random Short-Fiber Composites, Part II—Analysis fo Anisotropic Property Degradation," ASME JOURNAL OF APPLIED MECHANICS, Vol. 53, pp. 347–353.

Waynes, P. R., Issacs, J., and Nemat-Nasser, S., 1989, "Effect of Microstructural Damage on Ultrasonic Velocity and Elastic Moduli of Partially Stabilized Zirconia," *Review of Progress in Quantitative Non Destructive Evaluation*, Vol. 8B, D. O. Thompson and D. E. Chimenti, eds., Plenum Press, New York, pp. 1827–1833.

Downloaded 03 May 2010 to 171.66.16.20. Redistribution subject to ASME license or copyright; see http://www.asme.org/terms/Terms_Use.cfm

Jin Sun Hong
Asst. Professor,
Department of Precision Mechanical Engineering,
Kangnung National University,
Kangnung-si, Kangwondo 210702, Korea

Jang Moo Lee
Professor,
Department of Mechanical Design and Production Engineering,
Seoul National University,
Kwanak-ku, Seoul 151 Korea
Assoc. Mem. ASME

Vibration of Circular Rings With Local Deviation

An analytical method is presented for predicting the effects of local deviations such as a point mass, a sharp decrease in stiffness and variation of thickness on the free in-plane bending vibration characteristics of nearly axisymmetric rings. The approach is based on the Laplace transformation method and the expression of local deviation as the variation of heaviside unit step function. The effects of local deviation on the natural frequencies and mode shapes of the rings are predicted for the proposed nondimensional mass and stiffness parameters. The validity of the approach was examined through modal testings and/or finite element computation.

1 Introduction

The occurrence of slight irregularity of shape, material property, or local defects to otherwise perfectly axisymmetric rings or shells causes the vibration analysis difficult and the study on the approximately axisymmetric rings or shells has been of active interest. Practical examples are found in oriental bells (Ansari et al., 1985), welded cylinders, ring gyroscopes, and rings with cracks.

In this study, the in-plane vibration of rings is analytically investigated for the cases where local deviations of mass and stiffness exist in the rings. The purpose of this study is to analytically evaluate the effects of the local deviation on the free vibration characteristics such as natural frequencies and mode shapes of the rings.

Various types of rings or shells, deviated slightly from axisymmetry, were studied by many authors (Allaei et al., 1986; Allaei et al., 1987; Celep, 1990; Rossi, 1989). However, the mathematical approach shown in this paper is different from those presented in the previous investigation. The free vibration behavior of circular of rings with attached grounded spring, attached torsional spring, and/or a point mass was studied (Allaei et al., 1986; Allaei et al., 1987) used the receptance method which cannot be applied to the rings with thickness variation. We used the Laplace transformation method and were able to solve the free vibrations of rings with a small cut and thickness variation. In-plane vibration of circular rings on a tensionless foundation was studied (Celep, 1990), which used the harmonic approximation for the deflection function of the ring and Lagrange equation. He treated the vibration of rings with changing contact surface and did not consider either a point mass or a thickness variation in the ring. In-plane vibration of circular rings of nonuniform cross-section was studied (Rossi, 1989) which used the finite element method where explicit expressions for the stiffness and mass matrix were derived for a generic element of the ring's circular central axis. In our study, we do not need to derive stiffness and mass matrices and we cannot treat only the vibration of the rings with thickness variation but must also treat the vibration of rings with a point mass and pure stiffness variation, i.e., rings with a sharp cut.

In this paper, the Laplace transformation method was utilized to analytically solve the eigenvalue problem of the in-plane vibration of rings with rather general local derivations. The effects of mass and/or stiffness local variation were evaluated with nondimensional parameters and the validity of the approach was examined through experiments and/or finite element analysis. The analysis discussed in this paper can also be applied to beams and plates and the dynamic modification of slight-asymmetric rings and shells can also be investigated using the results of the present study.

2 Analysis

The equation of motion of a circular ring vibrating in a plane is known as

$$\frac{\partial^3 M_b}{\partial \theta^3}+\frac{\partial M_b}{\partial \theta}=R^2\frac{\partial^2}{\partial t^2}\left[mv-\frac{\partial}{\partial \theta}(mu)\right] \tag{1}$$

where R and m denote the radius and mass per unit length of a circular ring, and u and v are the radial (toward the center) and circumferential component of displacement, respectively. The relationship between the bending moment M_b and displacement can be expressed as

$$M_b=\frac{EI}{R^2}\left(\frac{\partial^2 u}{\partial \theta^2}+\frac{\partial v}{\partial \theta}\right). \tag{2}$$

And the condition of inextensional motion is known as follows:

$$u=\frac{\partial v}{\partial \theta}. \tag{3}$$

Contributed by the Applied Mechanics Division of THE AMERICAN SOCIETY OF MECHANICAL ENGINEERS for publication in the ASME JOURNAL OF APPLIED MECHANICS.

Discussion on this paper should be addressed to the Technical Editor, Professor Lewis T. Wheeler, Department of Mechanical Engineering, University of Houston, Houston, TX 77204-4792, and will be accepted until four months after final publication of the paper itself in the ASME JOURNAL OF APPLIED MECHANICS.

Manuscript received by the ASME Applied Mechanics Division, June 2, 1994; final revision, Jan. 15, 1993. Associate Technical Editor: R. L. Huston.

Copyright © 1994 by ASME
Downloaded 03 May 2010 to 171.66.16.20. Redistribution subject to ASME license or copyright; see http://www.asme.org/terms/Terms_Use.cfm

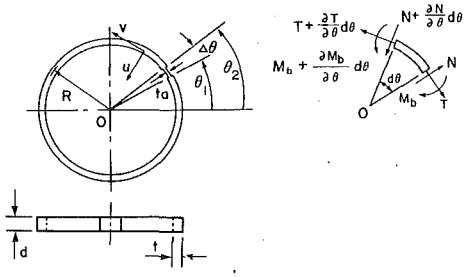


Fig. 1 Circular ring with local deviation (Model 2)

Now, consider a circular ring with local stiffness deviation and/or mass as shown in Fig. 1. We can express stiffness and mass per unit length as follows:

$$EI = (EI)_u + (EI)_a[H(\theta-\theta_1) - H(\theta-\theta_2)] \tag{4}$$

$$m = m_u + m_a[H(\theta-\theta_1) - H(\theta-\theta_2)] \tag{5}$$

where $H(\theta)$ is the heaviside unit step function and the subscript "a" denotes added properties. Equations (1)-(5) constitute the equation of motion of a circular ring with local deviation.

Assuming $v(\theta,t) = V(\theta)e^{j\omega t}$, we can derive the eigenvalue problem from these equations:

$$\begin{aligned}[V^{(6)} + 2V^{(4)} + V'' - \lambda(V'' - V)] \\ - \lambda \frac{m_a}{m_u}[V'' - V)(H_1 - H_2) + V'(\delta_1 - \delta_2)] \\ + \frac{(EI)_a}{(EI)_u}[(V^{(6)} + 2V^{(4)} + V'')(H_1 - H_2) \\ + (3V^{(5)} + 4V''' + V')(\delta_1 - \delta_2)] \\ + (3V^{(4)} + 3V'')(\delta_1' - \delta_2') + (V''' - V')(\delta_1'' - \delta_2'') = 0\end{aligned} \tag{6}$$

where the primes denote derivatives with respect to θ, and λ, H_1, δ_1, etc., are defined as

$$\lambda = \frac{m_u R^4 \omega^2}{(EI)_u}$$

$$H_1 = H(\theta-\theta_1), \quad \delta_1 = \delta(\theta-\theta_1), \ldots . \tag{7}$$

The matching boundary conditions are

$$V^{(n)}(0) = V^{(n)}(2\pi), \quad n = 0, 1, \ldots, 5. \tag{8}$$

Displacement components and bending moments should be continuous at $\theta = \theta_1$. If we denote θ_1^+ and θ_1^- as the limits of $\theta_1 + \epsilon$ and $\theta_1 - \epsilon$ as ϵ approaches zero, respectively, the following equations must be satisfied:

$$\begin{aligned}V(\theta_1^+) &= V(\theta_1^-) \\ V'(\theta_1^+) &= V'(\theta_1^-) \\ V'''(\theta_1^+) + V'(\theta_1^+) &= \frac{(EI)_u}{(EI)_u + (EI)_a}[V'''(\theta_1^-) + V'(\theta_1^-)],\end{aligned} \tag{9}$$

and the conditions of continuity at $\theta = \theta_2$ are analogous. With the aid of these continuity additions, we can take the Laplace transform of Eq. (6).

$$\begin{aligned}[S^6 + 2S^4 + (1-\lambda)S^2 + \lambda]\bar{V}(S) \\ - [S^5 + 2S^3 + (1-\lambda)S]V(0) + [S^4 + 2S^2 + (1-\lambda)]V'(0) \\ + (S^3 + 2S)V''(0) + (S^2 + 2)V'''(0) + SV^{(4)}(0) + V^{(5)}(0) \\ + M^*\lambda e^{-S\theta_0}[S\hat{V}'(\theta_0) - \hat{V}(\theta_0)] \\ - (EI)^* e^{-S\theta_0}(S^3 + S)[\hat{V}'''(\theta_0) - \hat{V}'(\theta_0)]\end{aligned} \tag{10}$$

where

$$\hat{V}^{(n)}(\theta_0) = \frac{1}{2}[V^{(n)}(\theta_1^-) + V^{(n)}(\theta_2^+)], \; n = 0, 1, 3 \tag{11}$$

$$M^* = \frac{m_a \cdot \Delta\theta}{m_u} \tag{12}$$

$$(EI)^* = \frac{(EI)_a \cdot \Delta\theta}{(EI)_u + (EI)_a}. \tag{13}$$

If we express stiffness and mass per unit length as $EI = (EI)_u + (EI)_u(EI)_a[(EI)_u + (EI)_a]^{-1} \cdot \Delta\theta \cdot \delta(\theta-\theta_0)$ and $m = m_u + m_a \cdot \Delta\theta \cdot \delta(\theta-\theta_0)$ in place of Eq. (4) and (5), we can arrive at the same result as Eq. (10).

The inverse transform of this equation can be obtained by the residue theorem. Assuming $e^{S\theta}$. $\bar{V}(S)$ to have simple poles at $S = \pm Z_1$, $\pm Z_2$, and $\pm Z_3$, (Z_i's are complex numbers), we can show that

$$\begin{aligned}V(\theta) = \sum_{i=1}^{3}[A_i \cosh(Z_i\theta) + B_i \sinh(Z_i\theta)] \\ + H(\theta-\theta_0)\sum_{i=1}^{3}\{C_i \cosh[Z_i(\theta-\theta_0)] + D_i \sinh[Z_i(\theta-\theta_0)]\}\end{aligned} \tag{14}$$

where

$$\begin{aligned}A_i &= \frac{1}{Q_i}\{[Z_i^5 + 2Z_i^3 + (1-\lambda)Z_i]V(0) \\ &\quad + (Z_i^3 + 2Z_i)V''(0) + Z_i V^{(4)}(0)\} \\ B_i &= \frac{1}{Q_i}\{[Z_i^4 + 2Z_i^2 + (1-\lambda)]V'(0) + (Z_i^2 + 2)V'''(0) + V^{(5)}(0)\} \\ C_i &= \frac{Z_i}{Q_i}\lambda M^* \hat{V}'(\theta_0) - \frac{Z_i^3 + Z_i}{Q_i}(EI)^*[\hat{V}'''(\theta_0) + \hat{V}'(\theta_0)] \\ D_i &= -\frac{1}{Q_i}\lambda M^* \hat{V}(\theta_0) \\ Q_i &= 3Z_i^5 + 4Z_i^3 + (1-\lambda)Z_i, \quad i = 1, 2, 3.\end{aligned} \tag{15}$$

If we apply the matching boundary conditions (8) to Eq. (14), the results are

$$\begin{bmatrix} 1 & 1 & 1 \\ Z_1^2 & Z_2^2 & Z_3^2 \\ Z_1^4 & Z_2^4 & Z_3^4 \end{bmatrix}\begin{bmatrix} F_{11} & F_{12} \\ F_{21} & F_{22} \\ F_{31} & F_{32} \end{bmatrix} = \begin{bmatrix} 0 & 0 \\ 0 & 0 \\ 0 & 0 \end{bmatrix} \tag{16}$$

where

$$\begin{aligned}F_{i1} &= (a_i - 1)A_i + b_i B_i + c_i C_i + d_i D_i \\ F_{i2} &= b_i A_i + (a_i - 1)B_i + d_i C_i + c_i D_i \quad \text{(no summation)} \\ a_i &= \cosh(2\pi Z_i) \\ b_i &= \sinh(2\pi Z_i) \\ c_i &= \cosh[Z_i(2\pi - \theta_0)] \\ d_i &= \sinh[Z_i(2\pi - \theta_0)].\end{aligned} \tag{17, 18}$$

As Z_i's are assumed to be different from one another, all F_{ij} in Eq. (16) should be zero.

$$\begin{bmatrix} a_i - 1 & b_i \\ b_i & a_i - 1 \end{bmatrix}\begin{Bmatrix} A_i \\ B_i \end{Bmatrix} = -\begin{bmatrix} c_i & d_i \\ d_i & c_i \end{bmatrix}\begin{Bmatrix} C_i \\ D_i \end{Bmatrix}, \quad i = 1, 2, 3. \tag{19}$$

From these equations we can consider two forms of solutions. First consider the case where some of the Z_i's are nj (n is an integer, $j = \sqrt{-1}$). In this case, all C_i's and D_i's become zero, so that

$$V(\theta) = C\cos[n(\theta - \phi)] \tag{20}$$

where, C and ϕ are constants. Now, if $M^* \neq 0$ only the trivial solution can be obtained as $\hat{V}(\theta_0) = \hat{V}'(\theta_0) = 0$. And the constant ϕ becomes θ_0 if $M^* = 0$ and $(EI)^* \neq 0$.

The second case arises when any of the Z_i's are not nj. In

Downloaded 03 May 2010 to 171.66.16.20. Redistribution subject to ASME license or copyright; see http://www.asme.org/terms/Terms_Use.cfm

this case, A_i and B_i can be expressed as functions of C_i and D_i. Then, from Eq. (14), we can obtain $V(\theta)$ as

$$V(\theta)=\sum_{i=1}^{3}\left\{-C_i\frac{\sinh[Z_i(\theta-\theta_0+\pi)]}{2\sinh(\pi Z_i)}-C_i\frac{\cosh[Z_i(\theta-\theta_0+\pi)]}{2\cosh(\pi Z_i)}\right\}+H(\theta-\theta_0)\sum_{i=1}^{3}\{C_i\cosh[Z_i(\theta-\theta_0)]+D_i\sinh[Z_i(\theta-\theta_0)]\}. \quad (21)$$

Displacement components are continuous at $\theta=\theta_0$ if

$$\sum_{i=1}^{3}C_i=\sum_{i=1}^{3}Z_iD_i=0 \quad (22)$$

is satisfied. From Eq. (11), (15), and (21) we can derive the following equation:

$$\begin{bmatrix}(p-1) & 0 & 0\\ 0 & (q+r-1) & q\\ a & (s+t) & (s-1)\end{bmatrix}\begin{Bmatrix}\hat{V}(\theta_0)\\ \hat{V}'(\theta_0)\\ \hat{V}'''(\theta_0)\end{Bmatrix}=\begin{Bmatrix}0\\0\\0\end{Bmatrix} \quad (23)$$

where the elements of the coefficient matrix are functions of Z_i's as shown as follows:

$$p=-\sum_{i=1}^{3}\frac{1}{2Q_i\tanh(\pi Z_i)}\lambda M^*$$

$$q=\sum_{i=1}^{3}\frac{Z_i^2(Z_i^2+1)}{2Q_i\tanh(\pi Z_i)}(EI)^*$$

$$r=-\sum_{i=1}^{3}\frac{Z_i^2}{2Q_i\tanh(\pi Z_i)}\lambda M^*$$

$$s=\sum_{i=1}^{3}\frac{Z_i^4(Z_i^2+1)}{2Q_i\tanh(\pi Z_i)}(EI)^*$$

$$t=-\sum_{i=1}^{3}\frac{Z_i^4}{2Q_i\tanh(\pi Z_i)}\lambda M^*$$

$$a=-\sum_{i=1}^{3}\frac{Z_i^3}{2Q_i}\lambda M^*. \quad (24)$$

If $\hat{V}(\theta_0)=\hat{V}'(\theta_0)=\hat{V}'''(\theta_0)=0$, then only the trivial solution is obtained. Therefore, the following equation must be satisfied:

$$(p-1)(qt-rs+q+r+s-1)=0. \quad (25)$$

This is the characteristic equation of a circular ring with local stiffness deviation and/or mass. Since the Z_i's are roots of $S^6+2S^4+(1-\lambda)S^2+\lambda=0$, at least one of Z_i's is imaginary. If we denote $Z_1=j\alpha$ where α is a real number, we have the following equations:

$$\lambda=\frac{\alpha^2(\alpha^2-1)^2}{\alpha^2+1} \quad (26)$$

$$Z_2^2=\frac{1}{2}\left\{-(\alpha^2-2)^2+\left[(\alpha^2-2)^2-\frac{4\lambda}{\alpha^2}\right]^{1/2}\right\} \quad (27)$$

$$Z_2^2=\frac{1}{2}\left\{-(\alpha^2-2)^2-\left[(\alpha^2-2)^2-\frac{4\lambda}{\alpha^2}\right]^{1/2}\right\}. \quad (28)$$

For the given value of M' and $(EI)^*$, we can obtain α and thus λ from the Eqs. (24)-(28). If λ is known from the above characteristic equation, then the mode shape can be obtained easily. If $qt-rs+q+r+s-1=0$,

$$V(\theta)=\sum_{i=1}^{3}\left\{-\frac{\sinh[Z_i(\theta-\theta_0+\pi)]}{2\sinh(\pi Z_i)}+H(\theta-\theta_0)\cosh[Z_i(\theta-\theta_0)]\right\}C_i \quad (29)$$

$$U(\theta)=\sum_{i=1}^{3}\left\{-\frac{\cosh[Z_i(\theta-\theta_0+\pi)]}{2\sinh(\pi Z_i)}+H(\theta-\theta_0)\sinh[Z_i(\theta-\theta_0)]\right\}Z_iC_i \quad (30)$$

where

$$C_i=\left[\frac{Z_i}{Q_i}\lambda M^*+\frac{Z_i^3+Z_i}{Q_i}\cdot\frac{r-1}{q}(EI)^*\right]\hat{V}'(\theta_0). \quad (31)$$

and if $p-1=0$,

$$V(\theta)=\sum_{i=1}^{3}\left\{-\frac{\cosh[Z_i(\theta-\theta_0+\pi)]}{2\sinh(\pi Z_i)}+H(\theta-\theta_0)\sinh[Z_i(\theta-\theta_0)]\right\}D_i \quad (32)$$

$$U(\theta)=\sum_{i=1}^{3}\left\{-\frac{\sinh[Z_i(\theta-\theta_0+\pi)]}{2\sinh(\pi Z_i)}+H(\theta-\theta_0)\cosh[Z_i(\theta-\theta_0)]\right\}Z_iD_i \quad (33)$$

where

$$D_i=-\frac{1}{Q_i}\lambda M^*V(\theta_0). \quad (34)$$

From Eqs. (29) and (30), we can verify that $U(\theta_0+\epsilon)=U(\theta_0-\epsilon)$ and $V(\theta_0+\epsilon)=-V(\theta_0-\epsilon)$ for any ϵ. Thus these equations represent symmetric modes with respect to the diameter passing through the point of local deviation, θ_0. Similarly, the modes represented by Eqs. (32) and (33) are antisymmetric with respect to the same diameter.

If $M^*=0$, the modes represented by Eq. (32) and (33) do not exist as $p=0$. As mentioned in Eq. (20), the antisymmetric modes in this case are

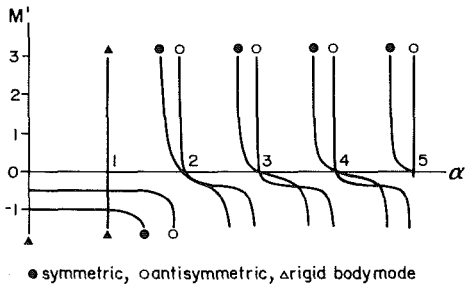
$$V(\theta)=C\cos[n(\theta-\theta_0)] \quad (35)$$

$$U(\theta)=-nC\sin[n(\theta-\theta_0)],\quad n=2,\ 3,\ 4,\ \ldots. \quad (36)$$

3 Results and Verification of the Analysis

Natural frequencies and mode shapes of a circular ring which has local deviation are calculated by using the analytical method discussed previously. To verify the results of this analysis, the results of this analysis are compared with the results obtained by experiment and/or finite element method.

(a) Case 1—Mass Effects. As the first case, only local deviation of mass per unit length is considered. Figure 2 shows



● symmetric, ○antisymmetric, ▲rigid body mode

Fig. 2 Characteristic curves of a circular ring with concentrated mass attached

Downloaded 03 May 2010 to 171.66.16.20. Redistribution subject to ASME license or copyright; see http://www.asme.org/terms/Terms_Use.cfm

Table 1 Data of Model 1

Material	Mild Steel
Young's modulus	2.1×10^{11}dyne/mm^2
Mass of ring	181 g
concentrated mass	12.6 g
D_1	307 mm
D_2	317 mm
d	4.75 mm

Table 2 Natural frequencies of Model 1

Mode \ Mass Ratio	0.0696 Experiment	0.0696 Present Analysis	0.000 Analysis[7]
1-1	125 Hz	125.0 Hz	
			131.5 Hz
1-2	130 Hz	129.9 Hz	
2-1	350 Hz	352.9 Hz	
			372.0 Hz
2-2	370 Hz	369.8 Hz	
3-1	657 Hz	678.1 Hz	
3-2	710 Hz	710.8 Hz	713.2 Hz

Table 3 Data of Model 2

Material	Mild Steel
Density	7.775×10^{-3}g/mm^3
Young's modulus	2.1×10^{11}dyne/mm^2
R	172.7 mm
t	7.0 mm
d	11.1 mm
$\Delta\theta$	3 deg
t_a	$0.5t$

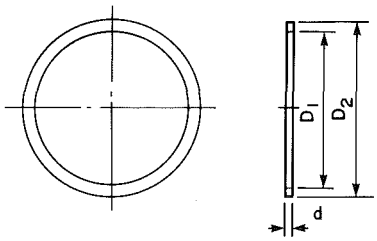


Fig. 3 Circular ring (Model 1)

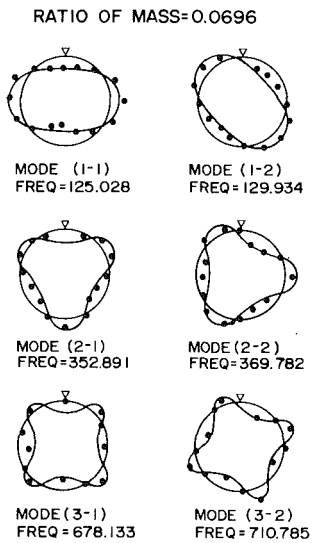
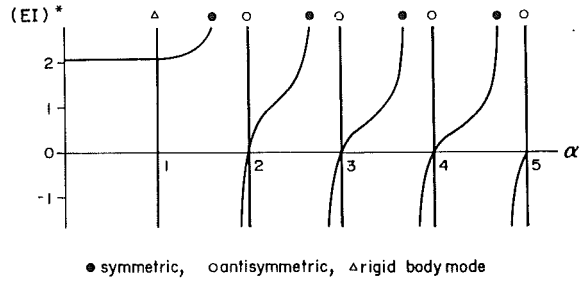


Fig. 4 Mode shape of a circular ring with concentrated mass attached (▽; concentrated mass, —; present analysis, •; experiment)

Table 4 Natural frequencies of Model 2 considering only stiffness effect

Mode \ Stiff Ratio	$(EI)^*=-0.3665$ Present Analysis	$(EI)^*=-0.3665$ FEM	$(EI)^*=0$ Analysis[7]
1-1	143.3 Hz	143.3 Hz	
			150.4 Hz
1-2	150.4 Hz	150.4 Hz	
2-1	406.7 Hz	406.6 Hz	
			425.3 Hz
2-1	425.3 Hz		
3-1	782.3 Hz	781.8 Hz	
			815.5 Hz
3-2	815.5 Hz	814.7 Hz	



● symmetric, ○antisymmetric, △rigid body mode

Fig. 5 Characteristic curves of a circular ring with local deviation of stiffness

the characteristic curves for this case. The characteristic curves show the effect of local deviation [M' or $(EI)^*$] on the characteristic value α of Eq. (26) and thus the natural frequencies and the mode shapes. In this figure, M' is the ratio of added (or deprived) point mass to the mass of a uniform circular ring ($M'=M^*/2\pi$) and $j\alpha=Z_1$. From this figure, we can know that if $M'=0$, $\alpha=2, 3, 4, \ldots$, which correspond to the natural frequencies of a uniform circular ring. As the value of M' increases, α decreases and separates. The model made for the experiment is shown in Fig. 3 and the properties of this model are in Table 1. After attaching a point mass of 12.6 g ($M'=0.0696$) at point 1, an impact test was carried out. Mode shapes obtained are shown in Fig. 4. Natural frequencies obtained by the present analysis are shown in Table 2 and this shows good agreement with experiment (within one percent).

(b) Case 2—Stiffness Effects. Here, only the local deviation of stiffness was considered. The characteristic curves were calculated as shown in Fig. 5. In this figure it can be noticed that if the "corresponding stiffness ratio" $(EI)^*$ equals zero, $\alpha=2, 3, 4, \ldots$, then this corresponds to the natural frequencies of a uniform circular ring. If the value $(EI)^*$ is not zero, then α separates as was shown in case 1.

To verify the results obtained by the present analysis, a finite element analysis was performed. Model 2 of Fig. 1 shows a circular ring with a slight cut. For this model, we neglected the mass which is deprived of and considered to have stiffness deviation only. 124 straight beam elements (no shear effect) were used in the finite element analysis by ADINA. The comparison of natural frequencies are in Table 4. Figure 6 shows the mode shapes of this model obtained by the present analysis.

(c) Case 3—Combined Effects. As the last case, mass and stiffness effects were considered simultaneously. For the Model 2 of Fig. 1, natural frequencies and mode shapes were obtained by the analysis and impact test. Figure 7 shows mode shapes obtained by the present analysis and the experiment and it shows good agreement. The comparison of natural frequencies obtained by the present analysis and the experiment are shown in Table 5. From this table, we know that the maximum deviation is about 1.5 percent.

Downloaded 03 May 2010 to 171.66.16.20. Redistribution subject to ASME license or copyright; see http://www.asme.org/terms/Terms_Use.cfm

Table 5 Natural frequencies of Model 2

Mode	Model 2 Present Analysis	Model 2 Experiment	Uniform ring Analysis[7]
1-1	143.0 Hz	145 Hz	
1-2	150.5 Hz	152.5 Hz	150.4 Hz
2-1	408.9 Hz	410 Hz	
2-2	425.5 Hz	427.5 Hz	425.3 Hz
3-1	787.0 Hz	787.5 Hz	
3-2	815.7 Hz	817.5 Hz	815.5 Hz

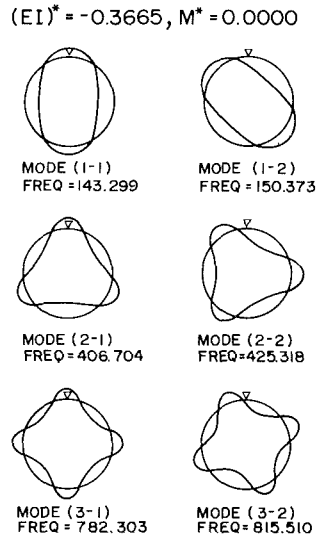


Fig. 6 Mode shapes of a circular ring with local deviation of stiffness (▽; point of local deviation of stiffness)

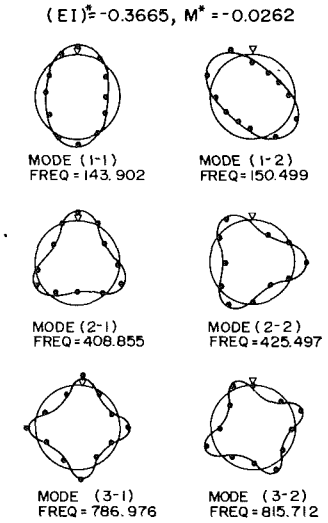


Fig. 7 Mode shape of a circular ring with local deviation of mass and stiffness (▽; concentrated mass, ·; present analysis, •; experiment)

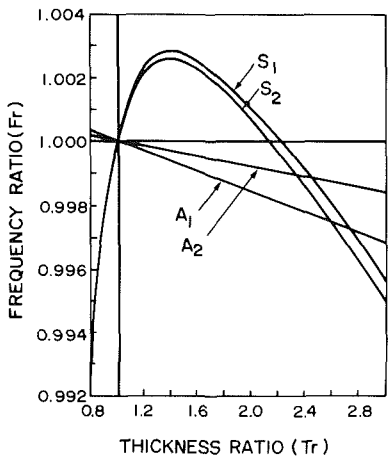


Fig. 8 Frequencies of a circular ring with local deviation ($\Delta\theta = 3$ deg, S_i; i-th symmetric mode, A_i; ith antsymmetric mode)

4 Discussion

Up to now, we have shown the effects of local deviation of stiffness and mass on the free vibration characteristics of a circular ring. Under these effects, one mode of a uniform ring separates into two modes. One is symmetric and the other is asymmetric with respect to the diameter passing through the point of local deviation. And the phenomenon of beat occurs if the amount of deviation is small.

Since there is no point on a ring where displacement is identically zero, natural frequencies of asymmetric modes, as well as those of symmetric modes, decrease under mass effect. On the other hand, natural frequencies of asymmetric modes do not vary under stiffness effect because the bending moment is zero at the point of local deviation and the local variance of stiffness plays no role in the free vibration characteristics of a circular ring.

Let us consider a circular ring with a rectangular cross-section. If we denote $T_r = t_a/t$ as the ratio of thickness of the nonuniform part to that of the uniform part, the free vibration characteristics of this ring depend only on the thickness ratio T_r and the angle $\Delta\theta$ (refer to Fig. 1).

Figure 8 shows the variation of natural frequencies with respect to the thickness ratio when $\Delta\theta = 3$ deg. In this figure, the frequency ratio F_r means natural frequency of this ring divided by the natural frequency of the same mode of a uniform ring. As the thickness ratio increases, natural frequencies of symmetric modes decreases almost proportionally. On the other hand, natural frequencies of symmetric modes increase until the thickness ratio reaches about 1.4, but decrease after that value. So there are certain thickness ratios at which frequencies of symmetric and antisymmetric mode coincide. As an example, if $T_r = 2.78$, natural frequencies of the first symmetric mode and the first antisymmetric mode coincide, so that the modes are identical and no beat phenomenon occurs.

As discussed previously, natural frequencies of antisymmetric modes are affected by only mass effect, but those of symmetric modes are affected not only by mass effect, but also by stiffness effect. These effects on the first symmetric mode are shown in Fig. 9. As the thickness ratio increases, the curve S shows saturation. This saturation is due to the fact that $(EI)^*$ converges with the limit of T_r (refer to Eq. (13)).

5 Conclusions

This paper has presented an analytical method for obtaining the free-vibration characteristics of vibrations of circular rings which have local deviation of mass and/or stiffness. It describes how to formulate the local mass and stiffness. As a concentrated mass can be represented by $m_a \cdot \Delta\theta \cdot \delta(x)$, it was proven that the local stiffness can be represented by $(EI)_u(EI)_a[(EI)_u + (EI)_a]^{-1} \cdot \Delta\theta \cdot \delta(x)$ where $\Delta\theta$ is the angle of local deviation.

If axisymmetry is not satisfied by local deviation, natural mdoes separate into pairs, such as symmetric and antisymmetric modes. And the point of local deviation becomes a nodal point (strictly speaking, only the radial component of

Downloaded 03 May 2010 to 171.66.16.20. Redistribution subject to ASME license or copyright; see http://www.asme.org/terms/Terms_Use.cfm

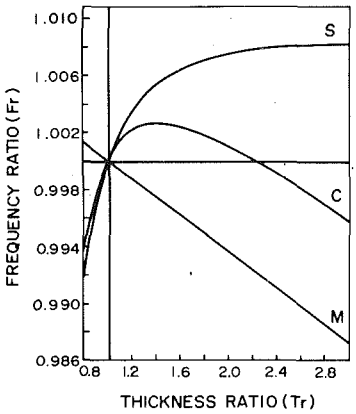


Fig. 9 Effects of stiffness and mass on the first symmetric mode (*S*; stiffness effect, *M*; mass effect, *C*; combined effect)

displacement is zero) for antisymmetric modes and antinodal point for symmetric modes.

Using the results of this paper, dynamic modification of slight-asymmetric shells will be further investigated.

Acknowledgment

This study is carried out under the support of the Independent Project Pursuits of the Korean Ministry of Education and the Long Range Basic Research Project by Korean Agency for Defence Development.

References

Allaei, D., Soedel, W., and Young, T. Y., 1986, "Natural Frequencies and Modes of Rings That Deviate from Perfect Axisymmetry," *Journal of Sound and Vibration*, Vol. 111, No. 1, pp. 9–27.

Allaei, D., Soedel, W., and Young, T. Y., 1987, "Eigenvalues of Rings with Radial Spring Attachments," *Journal of Sound and Vibration*, Vol. 121, No. 3, pp. 547–561.

Ansari, J., Yum, Y. H., and Lee, J. M., 1985, "A Study on the Vibrations of Axisymmetric Shells," *Proceedings of the 3rd International Modal Analysis Conference*, pp. 1138–1144.

Celep, Z., 1990, "In-Plane Vibrations of Circular Rings on a Tensionless Foundation," *Journal of Sound and Vibration*, Vol. 143, No. 3, pp. 461–471.

Hong, J. S., Lee, J. M., Park, Y. I., and Pak, C. H., 1989, "Free Vibration Analysis of Circular Rings with Slight Irregularities," *Proceedings of the 7th International Modal Analysis Conference*, pp. 124–130.

Love, A. E. H., 1944, *A Treatise on the Mathematical Theory of Elasticity*, 4th ed.

Rossi, R. E., 1989, "In-Plane Vibrations of Circular Rings of Non-Uniform Cross-Section with Account Taken of Shear and Rotatory Inertia Effects," *Journal of Sound and Vibration*, Vol. 135, No. 3, pp. 443–452.

Strutt, J. W., and Rayleigh, B., 1945, *The Theory of Sound*, Vol. 1, Dover.

Downloaded 03 May 2010 to 171.66.16.20. Redistribution subject to ASME license or copyright; see http://www.asme.org/terms/Terms_Use.cfm

N. Rattanawangcharoen

A. H. Shah

Department of Civil and Geological Engineering, University of Manitoba, Winnipeg, Manitoba R3T 2N2, Canada

S. K. Datta

Department of Mechanical Engineering, University of Colorado, Boulder, CO 80309-0427
Fellow ASME

Reflection of Waves at the Free Edge of a Laminated Circular Cylinder

A wave function expansion method is employed to solve the reflection problem of time-harmonic elastic waves incident upon the free edge of a semi-infinite laminated circular cylinder. Wave functions are obtained using a propagator matrix approach for laminated isotropic cylinders and by a Rayleigh-Ritz type approximation for laminated composite cylinders. The least-square technique as well as the variational method are employed to evaluate the complex amplitudes and the energy flux associated with the reflected waves. To validate the solutions and present algorithm, results are compared with analytical solutions whenever available. Examples include free-end reflection of waves in an isotropic solid rod, a two-layered isotropic cylinder, and a four-ply [+15/−15/+15/−15] graphite/epoxy cylinder. Numerical experimentation shows that the least-square method provides poor results for the laminated anisotropic cylinder compared to those obtained through the variational technique.

1 Introduction

The use of laminated composite materials is increasing at a rapid rate in various fields. This is reflected by the growing theoretical research and laboratory development in these areas. Cracks and delamination are major problems for the use of these laminated composites. New technology development using wave scattering plays an important role in identifying cracks and delamination. One approach to solve the wave scattering problem theoretically is to represent the scattered field by wave function expansion, as reported by Karunasena et al. (1991a) for cracks in plates. The free edge of a cylinder can be considered as a through-thickness crack. The present study of free-end reflection in laminated composite cyclinders will help in contriving suitable techniques to analyze more complicated problem of wave sccattering due to cracks and delamination in composite cylinders.

When a wave travels along a semi-infinite cylinder and strikes at the free end of the cylinder, an infinite number of reflected waves is generated. These reflected waves may have real, imaginary, or complex wave numbers. Only a finite number of these waves, with real wave numbers, propagates the energy. The imaginary and complex modes carry no energy and their amplitudes exponentially decay with the distance. However, these nonpropagating and evanescent modes, the imaginary and complex modes, respectively, are as significant as the propagating modes at the edge of the cylinder in satisfying the traction free-end condition.

The free-end reflection of axisymmetric waves in a homogeneous isotropic elastic solid rod was first investigated experimentally by Oliver (1957). By employing the approximate three-mode theory, McNiven (1961) predicted the existence of an end resonant frequency which differed from Oliver's result by 13 percent. Analogous to the work of McNiven, Zemanek (1972) considered the problem using the five, seven, and nine-mode approximations. It was found that his predicted value of the end resonant frequency with the nine-mode approximation differed by 0.5 percent as compared to that obtained by Oliver. However, the Poisson's ratio employed in his study was 0.3317 against 0.29 which was used by McNiven. Recently, Kim and Steele (1989) and Gregory and Gladwell (1990) investigated the problem analytically. Kim and Steele proposed a solution procedure which exploits the asymptotic behavior for higher harmonics in the radial direction to solve the problem. Gregory and Gladwell employed a least-square technique to minimize the difference between the energy of the incident wave and that of the reflected waves. The end resonance phenomenon was also investigated and was found to depend strongly upon the Poisson's ratio. In their work, they predicted the end resonant frequency at the Poisson's ratio of 0.29 which differed from Oliver's result by 2.5 percent.

The free-end reflection of the extensional waves in homogeneous, isotropic, elastic hollow cylinder was studied by McNiven and Shah (1967). The approximate three-mode theory was employed to predict the resonant frequency. They found that the frequency of the end resonance for hollow cylinders was lower than that for solid rod.

To our knowledge, the free-end reflection of waves in laminated anisotropic cylinders has not yet been reported. In this

Contributed by the Applied Mechanics Division of THE AMERICAN SOCIETY OF MECHANICAL ENGINEERS for publication in the ASME JOURNAL OF APPLIED MECHANICS.

Discussion on this paper should be addressed to the Technical Editor, Professor Lewis T. Wheeler, Department of Mechanical Engineering, University of Houston, Houston, TX 77204-4792, and will be accepted until four months after final publication of the paper itself in the ASME JOURNAL OF APPLIED MECHANICS.

Manuscript received by the ASME Applied Mechanics Division, Feb. 10, 1992; final revision, Jan. 13, 1993. Associate Technical Editor: L. M. Keer.

Copyright © 1994 by ASME
Downloaded 03 May 2010 to 171.66.16.20. Redistribution subject to ASME license or copyright; see http://www.asme.org/terms/Terms_Use.cfm

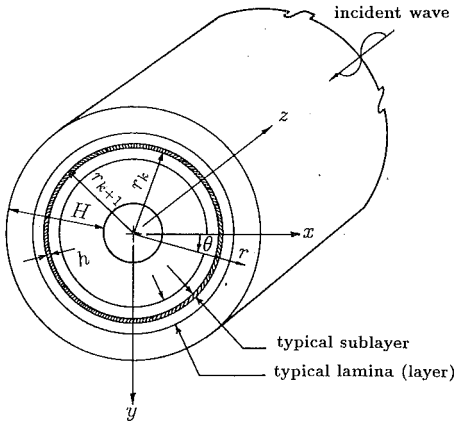


Fig. 1 Geometry of semi-infinite laminated cylinder

paper, the free-end reflection of harmonic waves in a semi-infinite cylinder is considered. The cylinder is composed of composite layers perfectly bonded together. The reflected wave field is represented by the modal sum of a finite number of wave functions (eigenfunctions). To obtain these eigenfunctions at discrete points through the thickness, the propagator matrix approach (Karunasena et al., 1991b) based upon the three-dimensional elastic theory is applied for laminated isotropic cylinders. On the other hand, the Rayleigh-Ritz type approximate method (Huang and Dong, 1984; Rattanawangcharoen et al., 1992) is used where the analytical solution is unattainable. The amplitudes of the wave functions are determined by satisfying the traction-free edge conditions by the least-square and variational methods.

The validation and the accuracy of the methods are demonstrated by comparing the results with existing results for a homogeneous isotropic elastic solid rod. The comparison between the results obtained from the Rayleigh-Ritz type approximation and the propagator matrix approach illustrates the applicability of the Rayleigh-Ritz type approximation in the free-end reflection problem. Numerical results for a two-layered isotropic hollow cylinder and for a four-ply graphite/epoxy hollow cylinder are presented.

2 Formulation

A semi-infinite laminated cylinder considered occupies the region $z \geq 0$ in the cylindrical coordinates r, θ, and z as shown in Fig. 1. The layers or laminae may have distinct mechanical properties as well as different thicknesses. The thickness of the cylinder, H, is discretized into N sublayers to model the radial inhomogeneity and to compute the eigenvectors at discrete points. The cylinder is excited at $z = +\infty$ which generates the incident wave with angular frequency of ω and wave number ξ_{in}. This time-harmonic guided wave travels in the negative z-direction and impinges upon the free end $z = 0$ of the cylinder.

2.1 Wave Functions. Wave functions required for the reflection analysis are obtained by considering the elastic wave propagation in the corresponding infinite cylinder. Two approaches are employed in the present paper, viz. the propagator matrix approach (Karunasena et al., 1991c) for laminated isotropic cylinders and the Rayleigh-Ritz type approximation for laminated anisotropic cylinders (Huang and Dong, 1984; Rattanawangcharoen et al., 1992). Since the details of these two methods can be found in the existing publications, only a brief summary of them is presented herein.

2.1.1 The Propagator Matrix Approach. For laminated isotropic cylinder, the propagator matrix is employed to evaluate the wave functions. Consider kth isotropic sublayer bounded by $r = r_k$ and $r = r_{k+1}$ surfaces. Based upon the three-dimensional elastic theory, the displacement components u, v, and w in r, θ, and z directions, respectively, can be written as (Armenàkas et al., 1969):

$$u = \left[f' + \frac{im}{r} g_2 + \xi g_1 \right] e^{im\theta} e^{-i(\xi z - \omega t)},$$

$$v = \left[\frac{im}{r} f - i\xi g_1 - g_2' \right] e^{im\theta} e^{-i(\xi z - \omega t)},$$

$$w = \left[-i\xi f - i\left\{ g_1' + \frac{(m+1)}{r} g_1 \right\} \right] e^{im\theta} e^{-i(\xi z - \omega t)}, \quad (1)$$

where

$$f(r) = C_1 H_m^{(1)}(\alpha r) + C_2 H_m^{(2)}(\alpha r),$$

$$g_1(r) = C_3 H_{m+1}^{(1)}(\beta r) + C_4 H_{m+1}^{(2)}(\beta r),$$

$$g_2(r) = C_5 H_m^{(1)}(\beta r) + C_6 H_m^{(2)}(\beta r), \quad (2)$$

and

$$\alpha^2 = \frac{\omega^2}{v_p^2} - \xi^2; \quad \beta^2 = \frac{\omega^2}{v_s^2} - \xi^2. \quad (3)$$

The prime denotes the differentiation with respect to r. m is the circumferential wave number, ξ is the wave number in the z-direction, t denotes the time, and $i = \sqrt{-1}$. $H_m^{(1)}$ and $H_m^{(2)}$ are Hankel functions and $C_i (i = 1 - 6)$ are arbitrary complex constants for the layer. v_p and v_s are the velocities of dilatational and torsional waves and are in the forms of

$$v_p^2 = \left(\frac{\lambda + 2\mu}{\rho} \right); \quad v_s^2 = \frac{\mu}{\rho}, \quad (4)$$

where λ and μ are Lamé's constants and ρ is the mass density.

The displacement and the stress components at the interface $r = r_k$ can be presented in terms of the six unknown constants, C_i, and the Hankel functions by employing Eq. (1) and using the linear stress-strain and strain-displacement relations. Similarly, the displacement and the stress components at the interface $r = r_{k+1}$ of the kth sublayer can also be evaluated in terms of these six unknown constants and the Hankel functions. After some algebraic manipulations, the following relation can be obtained:

$$\{\hat{q}\}_{k+1} = [P_k]\{\hat{q}\}_k, \quad (5)$$

where

$$\{\hat{q}\}_k^T = \langle u_k \;\; v_k \;\; w_k \;\; \sigma_{rrk} \;\; \sigma_{r\theta k} \;\; \sigma_{rzk} \rangle. \quad (6)$$

The vector quantity $\{\hat{q}\}_k$, which is yet unknown, represents the displacement and traction components at $r = r_k$. Superscript T denotes the transpose. $[P_k]$ is the propagator matrix for the kth sublayer and is defined in Appendix A. Repeated application of Eq. (5) for every sublayer in a cylinder consisted of N sublayers results in

$$\{\hat{q}\}_{N+1} = [P]\{\hat{q}\}_1, \quad (7)$$

where

$$[P] = [P_N][P_{N-1}] \ldots [P_1]. \quad (8)$$

By invoking the zero-traction conditions at the inner and the outer surfaces of the cylinder, Eq. (7) yields

$$\begin{bmatrix} P_{41} & P_{42} & P_{43} \\ P_{51} & P_{52} & P_{53} \\ P_{61} & P_{62} & P_{63} \end{bmatrix} \begin{Bmatrix} u_1 \\ v_1 \\ w_1 \end{Bmatrix} = \begin{Bmatrix} 0 \\ 0 \\ 0 \end{Bmatrix}. \quad (9)$$

The exact dispersion relation can then be obtained by equating the determinant of the complex coefficient matrix in Eq. (9) to zero. This relation can be used to evaluate ω for a given ξ, or alternately, for a given ω it can be solved for ξ.

Downloaded 03 May 2010 to 171.66.16.20. Redistribution subject to ASME license or copyright; see http://www.asme.org/terms/Terms_Use.cfm

2.1.2 The Rayleigh-Ritz Type Approximation. For laminated composite cylinders, the wave functions cannot be determined analytically. In that case, the Rayleigh-Ritz type approximation (Huang and Dong, 1984) is employed.

Consider the kth anisotropic sublayer bounded by $r=r_k$ and $r=r_{k+1}$ surfaces. The displacement components u, v, and w are approximated by interpolation polynomials in the radial direction as

$$\{U\}=[N]\{\tilde{q}\}, \tag{10}$$

where

$$\{U\}^T=\langle u\ v\ w\rangle, \tag{11}$$

$$\{\tilde{q}\}^T=\langle u^b\ v^b\ w^b\ u^m\ v^m\ w^m\ u^f\ v^f\ w^f\rangle, \tag{12}$$

$$[N]=\begin{bmatrix} n_1 & 0 & 0 & n_2 & 0 & 0 & n_3 & 0 & 0 \\ 0 & n_1 & 0 & 0 & n_2 & 0 & 0 & n_3 & 0 \\ 0 & 0 & n_1 & 0 & 0 & n_2 & 0 & 0 & n_3 \end{bmatrix}. \tag{13}$$

In Eqs. (11)–(13) the generalized displacements u^b, u^m, u^f are taken at the back (inner), middle, and front (outer) nodal surfaces of the sublayer. The interpolation polynomials n_i are quadratic functions given by

$$n_1=1-3\eta+2\eta^2;\ n_2=4\eta-4\eta^2;\ n_3=-\eta+2\eta^2, \tag{14}$$

where $\eta=(r-r_k)/h_k$, h_k being the thickness of the kth sublayer.

By using Hamilton's principle, the governing equation for the entire cylinder is found to be

$$[K_1]\{\tilde{Q}\}''+[K_2]\{\tilde{Q}\}'-[K_3]\{\tilde{Q}\}-[M]\ddot{\{\tilde{Q}\}}=0. \tag{15}$$

Here $[K_1]$ and $[M]$ are real symmetric, $[K_2]$ is skew-hermitian, and $[K_3]$ is hermitian. The prime denotes differentiation with respect to z and the overdot denotes differentiation with respect to t. The vector $\{\tilde{Q}\}$ contains the generalized nodal coordinates for the cylinder.

A solution representing harmonic wave propagation for Eq. (15) can be assumed in the form

$$\{\tilde{Q}\}=\{Q_0\}e^{-i(\xi z-\omega t)}e^{im\theta}, \tag{16}$$

where $\{Q_0\}$ represents the nodal amplitude vector. Substitution of Eq. (16) into Eq. (15) results in a set of linear homogeneous equations as

$$\{-\xi^2[K_1]-i\xi[K_2]-[K_3]+\omega^2[M]\}\{Q_0\}=0. \tag{17}$$

For a nontrivial solution $\{Q_0\}$ the determinant of the coefficient matrix must be zero and this results in a quadratic algebraic eigenvalue problem. This equation serves as the dispersion relation for the cylinder.

2.2 Reflected Wave Field and Incident Field. The reflection occurs after the wave strikes the edge $z=0$ of the cylinder. The reflected waves consist of a finite number of waves with real wave number and an infinite number of waves with imaginary and complex wave numbers. These reflected waves can be obtained by either one of the aforementioned approaches. The displacement vector corresponding to these reflected waves $\{q_z\}_{re}$ at any arbitrary z have the form of

$$\{q_z\}_{re}=\sum_{j=0}^{\infty}A_j\{q_j\}e^{-i(\xi_j z-\omega t)}e^{im\theta},\quad z\geq 0, \tag{18}$$

where

$$\{q_j\}^T=\langle u_{1j}v_{1j}w_{1j}\ldots u_{kj}v_{kj}w_{kj}\ldots u_{(NP)j}v_{(NP)j}w_{(NP)j}\rangle, \tag{19}$$

NP being the number of nodal points. The displacements u_{kj}, v_{kj}, and w_{kj} at the kth nodal point associated with the jth mode can be obtained from Eq. (5) or (17). The complex amplitude A_j of the jth mode is to be determined so that the associated stress field satisfies the free-end condition. The factor $e^{i\omega t}e^{im\theta}$ will be suppressed in the following formulation.

For the purpose of numerical evaluation, the series in Eq. (18) is truncated to J terms. Only the modes corresponding to the wave numbers with a small negative imaginary part are superposed (Gregory and Gladwell, 1990). The wave numbers having a positive imaginary part are unbounded for large z and, therefore, they are not admissible.

The reflected wave field at the edge $z=0$, $\{q_0\}_{re}$, with J modes approximation can then be written as

$$\{q_0\}_{re}=[G]\{A\}, \tag{20}$$

where

$$[G]=[\{q_1\}\{q_2\}\ldots\{q_j\}\ldots\{q_J\}], \tag{21}$$

$$\{A\}^T=\langle A_1A_2\ldots A_j\ldots A_J\rangle. \tag{22}$$

The stress components (σ_{rz}, $\sigma_{\theta z}$, and σ_{zz}) at discrete points on the surface $z=$ constant of the kth sublayer can be obtained by the stress-strain and the strain-displacement relations. Note that $\sigma_{\theta z}$ and σ_{zz} may not be continuous at the interfaces between sublayers. The stress vector containing these stress components due to the reflected field at the free end can be formulated as

$$\{R\}_{re}=[F]\{A\}, \tag{23}$$

where

$$[F]=[\{S_1\}\{S_2\}\ldots\{S\}_j\ldots\{S\}_J], \tag{24}$$

$$\{S_j\}^T=\langle\sigma_{rz1j}\sigma_{\theta z1j}\sigma_{zz1j}\ldots\sigma_{rzkj}\sigma_{\theta zkj}\sigma_{zzkj}\ldots\sigma_{rz(NP)j}\sigma_{\theta z(NP)j}\sigma_{zz(NP)j}\rangle. \tag{25}$$

Similarly, the stress vector due to the incident field at the free edge can be written in the form of

$$\{R\}_{in}=A_{in}\{F_{in}\}, \tag{26}$$

where A_{in} is the amplitude of the incident mode. The stress vector $\{F_{in}\}$ is calculated from the wave corresponding to the propagating incident mode.

The traction-free condition at $z=0$ requires that

$$\{R\}=\{R\}_{re}-\{R\}_{in}=\{0\}. \tag{27}$$

By minimizing the sum of the squares of the residuals of $\{R\}$, the least-square solution for complex amplitude $\{A\}$ is obtained as

$$\{A\}=A_{in}\left[\int_{r_i}^{r_o}[\bar{F}]^T[F]rdr\right]^{-1}\left[\int_{r_i}^{r_o}[\bar{F}]^T\{F_{in}\}rdr\right], \tag{28}$$

where r_i and r_o represent the inner and the outer radii of the cylinder, respectively. Superscript -1 and overbar denote the inverse and the complex conjugate of the matrix, respectively.

An alternate approach of determining the complex amplitude $\{A\}$ is to employ the variational principles (Wu and Plunkett, 1967). Using the principle of virtual displacement one obtains

$$\delta\{\bar{q}_0\}^T\{R\}=0, \tag{29}$$

where δ represents variation. The total displacement field $\{q_0\}$ at the free end of the cylinder is

$$\{q_0\}=\{q_0\}_{in}+\{q_0\}_{re}, \tag{30}$$

in which

$$\delta\{q_0\}=\delta\{q_0\}_{re}, \tag{31}$$

where $\{q_0\}_{in}$ is the incident field. The solution is obtained by substituting Eqs. (20), (27), and (31) into Eq. (29). This leads to

$$\{A\}=A_{in}\left[\int_{r_i}^{r_o}[\bar{G}]^T[F]rdr\right]^{-1}\left[\int_{r_i}^{r_o}[\bar{G}]^T\{F_{in}\}rdr\right]. \tag{32}$$

The normalized amplitude B_j is defined by

$$B_j=\frac{A_j}{A_{in}}. \tag{33}$$

Downloaded 03 May 2010 to 171.66.16.20. Redistribution subject to ASME license or copyright; see http://www.asme.org/terms/Terms_Use.cfm

Once the amplitude $\{A\}$ is known, the displacement and stress fields anywhere in the cylinder can be computed.

2.3 Energy flux. One of the physical quantities of interest is the mean total energy flux. Reflected energy is carried only by the various propagating modes which can exist at that particular frequency. The time-averaged value of the energy flux associated with the jth reflected propagating mode through the cylinder section is given by

$$E_j = \omega |A_j|^2 \mathrm{Im}\left[\int_{r_i}^{r_o} [\{F_j\}^T \cdot \{\bar{q}_j\} r dr]\right]; \quad j \le N_{pr}, \tag{34}$$

where N_{pr} represents the number of propagating modes in the reflected field. The mean total energy flux is obtained from the sum of the energy fluxes carried by reflected propagating modes. This is given by

$$E_{re} = \sum_{j=1}^{N_{pr}} E_j. \tag{35}$$

The energy flux of the incident field can be written in a similar form as

$$E_{in} = \omega |A_{in}|^2 \mathrm{Im}\left[\int_{r_i}^{r_o} [\{F_{in}\}^T \cdot \{\bar{q}_{in}\} r dr]\right], \tag{36}$$

where $\{q_{in}\}$ is the vector of displacements corresponding to the propagating incident mode.

The proportion of the incident energy transferred into the jth reflected propagating mode is

$$I_j = \frac{E_j}{E_{in}}. \tag{37}$$

Since the free-end condition requires no energy dissipation when the wave reflects, the percentage difference in energies carried by the incident and reflected fields is then given by

$$|\epsilon| = |[E_{in} - E_{re}] 100 / E_{in}|. \tag{38}$$

The principle of energy conservation requires that $|\epsilon| = 0$. The smallness of the value of $|\epsilon|$ is an useful index to assess the accuracy of the numerical results.

3 Numerical Evaluation and Discussion

Methods to evaluate the roots of dispersion relations (Eqs. (9) and (17)) and the numerical results for the reflection problem for three examples are presented in this section.

3.1 Wave Number Determination. The quadratic eigenvalue problem can be manipulated in a standard algebraic eigenvalue form for the evaluation of the roots from the Rayleigh-Ritz type approximation (Huang and Dong, 1984). Muller's method (Muller, 1956) is employed for the evaluation of the eigenvalues by the propagator matrix approach. At the first step, beginning with the lowest frequency of interest, the cylinder is discretized into a sufficiently large number of sublayers and the approximate roots are obtained via the Rayleigh-Ritz type approximation. These approximate roots are used as initial guesses in the Muller's method to recover the exact roots. It should be noted that the division into sublayers is not required to obtain the exact roots, but is used to compute the eigenvectors in the modal expansion method. At the next step, ω is increased by a small increment and the exact roots from the previous step are taken as initial guesses at the current step. The process is repeated until the frequency range of interest is scanned. As a check, at some intermediate frequencies, approximate roots from Rayleigh-Ritz type approximation are used as initial guesses in the Muller's method to obtain the exact roots. After obtaining the wave numbers, ξ_j, for each frequency, only J number of roots are chosen. The selected roots must include all the propagating modes. The real roots are ordered in the descending order of the magnitude while the nonpropagating and evanescent roots are ordered in the ascending order of magnitude of their imaginary parts.

It must be mentioned here that when the circumferential wave number, m, is not equal to zero, the wave number ξ_j and ξ_j' for propagating modes in the positive and negative z-directions, respectively, are not the same for a laminated composite cylinder unless the material properties are symmetric with respect to θ. Once the wave number, ξ_j', for the incident mode has been selected, it was found convenient to evaluate the incident field quantities in the (r, θ', z') coordinates where $\theta' = -\theta$ and $z' = -z$.

3.2 Numerical Results. To validate and to assess the accuracy and applicability of the methods, the following three numerical examples are considered:

1 a homogeneous isotropic elastic rod,
2 a two-layered isotropic hollow cylinder, and
3 a four-ply $[+15/-15/+15/-15]$ graphite/epoxy hollow cylinder.

In all examples, H and R are the total thickness and mean radius of the cylinder, respectively. The frequency and wave number, whenever referred, are the normalized frequency Ω and normalized wave number γ with the forms of

$$\Omega = \frac{\omega}{\omega_{\mathrm{ref}}}; \quad \gamma = \frac{\xi}{\xi_{\mathrm{ref}}},$$

where ω_{ref} and ξ_{ref} are the reference frequency and the reference wave number, respectively.

The total number of sublayers N used to compute the discrete eigenvectors and the number of modes J used in the modal expansion are very important factors for the accuracy of the method. Reasonably good values of N and J are chosen in such a way that the amplitude $\{A\}$ in Eq. (28) or (32) and the proportion of the energy carried by each reflected mode I_j in Eq. (37) converge.

Example 1. The reflection of the first axisymmetric wave in a solid rod with Poisson's ratio ν of 0.25 is considered. The reference frequency and the reference wave number are, respectively,

$$\omega_{\mathrm{ref}} = \frac{v_p}{H}; \quad \xi_{\mathrm{ref}} = \frac{1}{H}.$$

A full discussion of the frequency spectra for this case was given by Onoe et al. (1962). The first three cutoff frequencies are $\Omega = 1.931$, 2.069, and 2.212. The propagator matrix approach with 20 sublayers (corresponding to 42 degrees-of-freedom) and 21 modes are employed in this example. Figures 2(a) and 2(b) show the normalized amplitude B_j and the proportion of energy I_j of each reflected mode. The comparison of proportion of energy obtained by the present method with that of Gregory and Gladwell (1990) is made. It can be seen that the present method yields results that are in excellent agreement with those obtained by Gregory and Gladwell. For the range of Ω in Fig. 2, $|\epsilon|$ is less than 0.5 percent. From the numerical experimentation, it is observed that there is no discrepancy between the results obtained by the least-square method and those obtained by the variational technique, Eqs. (28) and (32), respectively, in this example.

The numerical results confirmed that the end resonant frequency for this rod is 1.644 which is identical to the one obtained by Gregory and Gladwell.

Example 2. The reflection of the first propagating mode in a two-layered isotropic cylinder is considered. The properties of the two layers are (Armenàkas, 1971): $\nu_1 = \nu_2 = 0.30$; $\mu_1/\mu_2 = 1$; $\rho_1/\rho_2 = 2$; $h_1/h_2 = 1$. The subscripts 1 and 2 represent the inner and the outer layer, respectively. The ratio of the thickness to the mean radius of the outer layer, h_2/R_2, is 0.20.

Downloaded 03 May 2010 to 171.66.16.20. Redistribution subject to ASME license or copyright; see http://www.asme.org/terms/Terms_Use.cfm

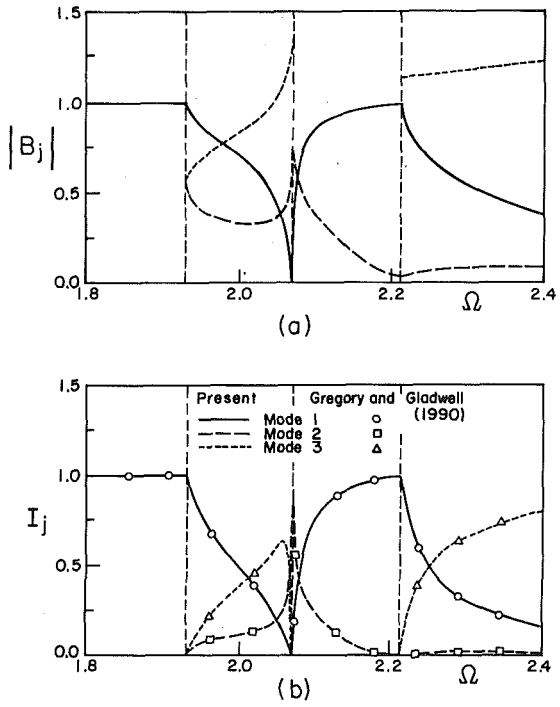


Fig. 2 Reflection in isotropic elastic solid rod; (*a*) the normalized amplitude $|B_j|$, (*b*) the proportion of energy I_j

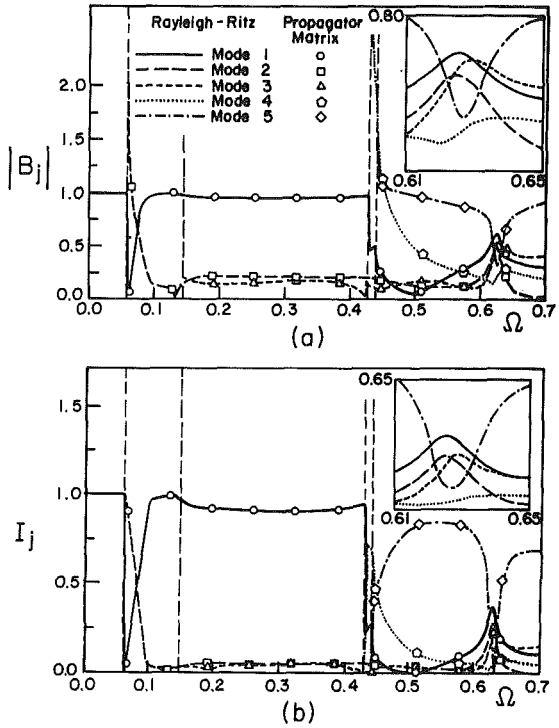


Fig. 3 Reflection in two-layered isotropic cylinder; (*a*) the normalized amplitude $|B_j|$, (*b*) the proportion of energy I_j

The circumferential wave number m is 1. The reference frequency and the reference wave number are, respectively,

$$\omega_{\text{ref}}=\frac{2\pi v_{s2}}{H};\quad \xi_{\text{ref}}=\frac{2\pi}{H}.$$

The frequency spectrum for this cylinder was presented by Armenàkas (1971). The first four cutoff frequencies are $\Omega=0.059$, 0.145, 0.428, and 0.438. The propagator matrix approach and the Rayleigh-Ritz type approximation are employed in this example to illustrate the applicability and the accuracy of the Rayleigh-Ritz type approximation for the reflection problem. In order for the two methods to be comparable, the discretizations are made in such a way that both methods have the same number of degrees-of-freedom. It is found that 99 degrees-of-freedom (corresponding to 32 and 16 sublayers for the propagator matrix approach and the Rayleigh-Ritz type approximation, respectively) and 30 modes provide reasonably good results.

Figures 3(*a*) and 3(*b*) illustrate the normalized amplitude B_j and the proportion of energy I_j of each reflected mode, respectively. It can be observed that the results from both methods are in excellent agreement. For the frequencies lower than the first cutoff frequency, only one reflected propagating mode is possible. This mode has the same absolute amplitude as that of the incident wave and will carry all of the energy back. At the first cutoff frequency, the second propagating mode becomes predominant. The amplitude of this second mode is comparatively large. This phenomenon, however, is not very stable as the frequency is shifted away from the first cutoff frequency. The first propagating mode recovers its dominacy as the frequency increases. This mode is also predominant in the frequency range between the second and third cutoff frequencies. Between the third and fourth cutoff frequencies, the fourth propagating mode has very high amplitude. However, its amplitude is not high enough to consider it as a resonance phenomenon. For the frequency greater than the fourth cutoff frequency, the fifth propogating mode predominants all other modes except in a small region around $\Omega=0.62$ as shown in the inserts in the figures. An investigation in this region reveals that the first mode is the breathing mode, the second and the fourth modes are torsional modes while the third and the fifth modes are the mode coupling of the longitudinal motions.

For the range of Ω considered in Figs. 3, $|\epsilon|$ is less than 0.5 percent. Similar to the first example, the results obtained from the least-square method and those obtained by the variational technique show negligible discrepancy.

Example 3. The reflection of the first incoming propagating mode in a four-ply $[+15/-15/+15/-15]$ graphite/epoxy is considered. The elastic properties for each ply relative to their natural elastic axes are (Huang and Dong, 1984):

$$E_L=13.9274\times10^{10}\ \text{N/m}^2;\quad E_T=1.5169\times10^{10}\ \text{N/m}^2;$$

$$G_{LT}=G_{TL}=0.5861\times10^{10}\ \text{N/m}^2;\quad \nu_{LT}=\nu_{TT}=0.21,$$

where L denotes the fiber direction and T the transverse direction. The normalized frequency and the normalized wave number are given by

$$\omega_{\text{ref}}=\frac{v_L}{H};\quad \xi_{\text{ref}}=\frac{\pi}{H},$$

where

$$v_L=\left[\frac{E_L}{\rho}\right]^{1/2}.$$

The circumferential wave number m and H/R are 1 and 0.667, respectively. As mentioned earlier, when the waves travel in the anisotropic cylinder with the circumferential wave number greater than zero, the wave number of wave traveling in the positive z-direction differs from that of the wave traveling in the negative z-direction. Figure 4 shows the frequency spectrum for this cylinder. The solid lines represent the waves traveling in the positive z-direction, while the dashed lines illustrate the waves traveling in the negative z-direction. The incident wave must be chosen from one of the waves traveling in the negative z-direction. The first four cutoff frequencies are $\Omega=0.215$, 0.295, 0.696, and 0.760.

Since the analytical solution is unattainable for laminated

Downloaded 03 May 2010 to 171.66.16.20. Redistribution subject to ASME license or copyright; see http://www.asme.org/terms/Terms_Use.cfm

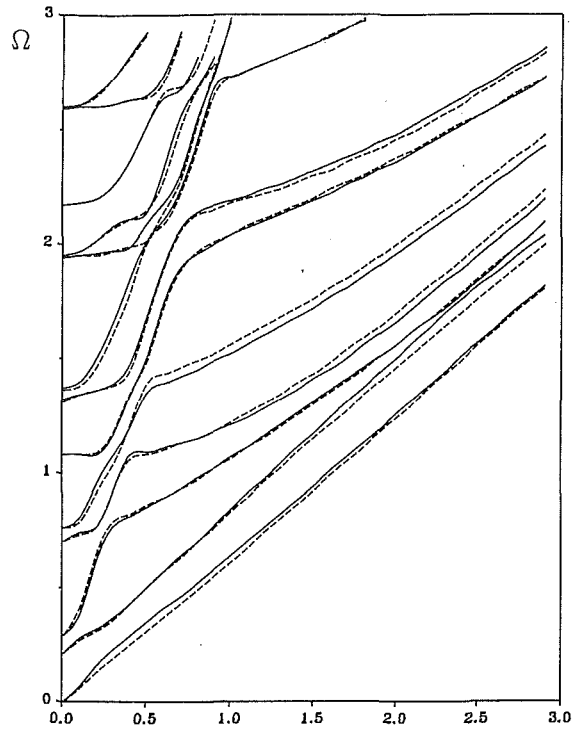


Fig. 4 Frequency spectrum for the four-ply [+15/−15/+15/−15] graphite/epoxy cylinder

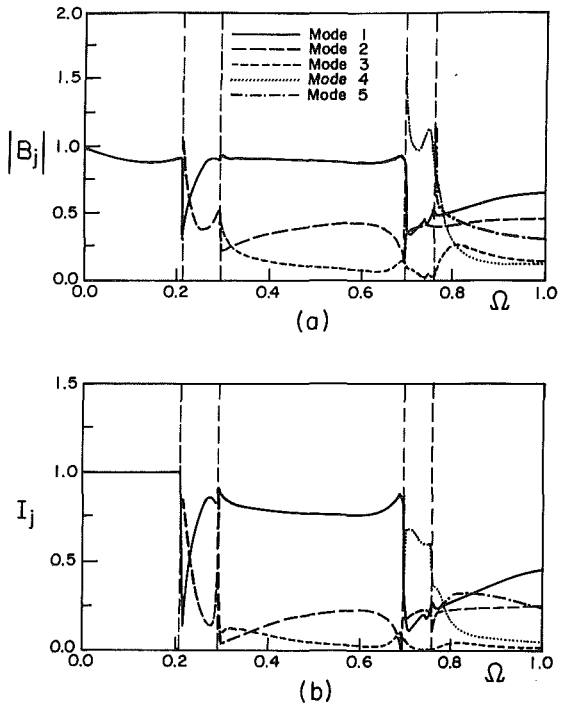


Fig. 5 Reflection in the four-ply [+15/−15/+15/−15] graphite/epoxy cylinder; (*a*) the normalized amplitude $|B_j|$, (*b*) the proportion of energy I_j

composite cylinders, the Rayleigh-Ritz type approximation is employed in this example. The cylinder is discretized into 16 sublayers (corresponding to 99 degrees-of-freedom) and 30 modes are considered.

Figures 5(*a*) and 5(*b*) show the normalized amplitude and the proportion of energy of each reflected mode. Unlike in the previous example, the propagating modes in the positive and in the negative z-directions are different. Therefore, for the frequencies of lower than the first cutoff frequency, the normalized absolute amplitudes of the reflected wave need not be unity. However, the conservation of the energy still holds; i.e., the energy carried by the incident wave is totally transferred to the reflected propagating wave as seen in Fig. 5(*b*). Similar to the case of layered isotropic cylinder, at the first cutoff frequency, the second mode becomes predominant. In the range between the second and third cutoff frequencies, all three propagating waves are essential in carrying energy back. Between the third and fourth cutoff frequencies, the patterns of both the normalized amplitude and the proportion of energy are very irregular. After the fourth cutoff frequency, all propagating modes in the reflected waves are contributing in the transfer of the energy. In this example, it is observed that the numerical results obtained by the least-square method are very inaccurate. For the range of Ω considered here, the variational technique yields the $|\epsilon|$ of less than 0.5 percent while the least square method gives $|\epsilon|$ up to 15 percent. The reason for the anomalous results is that the least-square method does not have a physical basis unlike the variational method in which the energy is minimized. Although the sum of the squares of the residuals is minimized in the least-square method, the minimized residual sum could be large which results in large error in $|\epsilon|$.

A careful search was made for the end resonant frequency in examples 2 and 3 but none could be found in the range of the frequency considered and no attempt was made to search for the end resonant frequency outside this range.

4 Conclusion

The free-end reflection of waves in laminated cylinders is studied by the wave function expansion method. To obtain the required eigenfunctions at the discrete points through the thickness of the cylinder, the propagator matrix approach is employed when the analytical solution is obtainable and the Rayleigh-Ritz type approximation is used when the analytical solution is unattainable. Numerical results confirm the applicability and accuracy of the exploitation of the Rayleigh-Ritz type approximation in the free-end reflection problem in laminated isotropic cylinders. The least-square technique as well as the variational method are employed in determining the complex amplitudes of the reflected waves. It is found that the results from the least-square method are not reliable for the laminated anisotropic case.

Acknowledgment

The work presented in this paper is supported by the Natural Science and Engineering Research Council of Canada by Grant No. OGP007988.

References

Armenàkas, A. E., 1971, "Propagation of Harmonic Waves in Composite Circular Cylindrical Shells, Part II Numerical Results," *AIAA Journal*, Vol. 9, pp. 599–605.

Armenàkas, A. E., Gazis, D. C., and Herrmann, G., 1969, *Free Vibrations of Circular Cylindrical Shells*, Pregamon Press, Oxford, U.K.

Gregory, R. D., and Gladwell, I., 1989, "Axisymetric Waves in a Semi-infinite Elastic Rod," *Quarterly Journal of Mechanics and Applied Mathematics*, Vol. 42, pp. 327–337.

Huang, K. H., and Dong, S. B., 1984, "Propagation Waves and Edge Vibrations in Anisotropic Composite Cylinders," *Journal of Sound and Vibration*, Vol. 96, pp. 363–379.

Karunasena, W. M., Shah, A. H., and Datta, S. K., 1991a, "Plain-Strain-Wave Scattering by Cracks in Laminated Composite Plates," *Journal of Engineering Mechanics, ASCE*, Vol. 117, No. 8, pp. 1738–1754.

Karunasena, W. M., Shah, A. H., and Datta, S. K., 1991b, "Reflection of Plain Strain Waves at the Free Edge of a Laminated Composite Plate," *International Journal of Solids and Structures*, Vol. 27, No. 8, pp. 949–964.

Karunasena, W. M., Shah, A. H., and Datta, S. K., 1991c, "Wave Propagation in a Multi-Layered Laminated Cross-Ply Composite Plates," ASME Journal of Applied Mechanics, Vol. 58, pp. 1028–1032.

Kim, Y. Y., and Steele, C. R., 1989, "End Effects and Time-harmonic Longitudinal Wave Propagation in a Semi-Infinite Solid Cylinder," ASME Journal of Applied Mechanics, Vol. 56, pp. 334–346.

Downloaded 03 May 2010 to 171.66.16.20. Redistribution subject to ASME license or copyright; see http://www.asme.org/terms/Terms_Use.cfm

McNiven, H. D., 1961, "Extensional Waves in a Semi-Infinite, Elastic Rod," *Journal of Acoustical Society of America*, Vol. 33, pp. 23–27.

McNiven, H. D., and Shah, A. H., 1967, "The Influence of the End Mode on the Resonant Frequencies of Finite, Hollow, Elastic Rods," *Journal of Sound and Vibration*, Vol. 6, pp. 8–19.

Muller, D. E., 1956, "A Method for Solving Algebraic Equations Using an Automatic Computer," *Mathematical Tables and Aids to Computation*, Vol. 10, pp. 208–215.

Oliver, J., 1957, "Elastic Wave Dispersion in a Cylindrical Rod by a Wide-band, Short-duration Pulse Technique," *Journal of Acoustical Society of America*, Vol. 29, pp. 189–194.

Onoe, M., McNiven, H. D., and Mindlin, R. D., 1962, "Dispersion of Axially Symmetric Waves in Elastic Rods," ASME JOURNAL OF APPLIED MECHANICS, Vol. 29, pp. 729–734.

Rattanawangcharoen, N., Shah, A. H., and Datta, S. K., 1992, "Wave Propagation in Laminated Composite Circular Cylinders," *International Journal of Solids and Structures*, Vol. 29, No. 6, pp. 767–781.

Wu, C. H., and Plunkett, R., 1967, "On the Solutions of Plates, Strips, Rods and Cylinders Subjected to Arbitrary Dynamic Edge Load," *SIAM Journal of Applied Mathematics*, Vol. 15, pp. 107–119.

Zemanek, 1972, "An Experimental and Theoretical Investigation of Elastic Wave Propagation in a Cylinder," *Journal of Acoustical Society of America*, Vol. 51, No. 1, pp. 265–283.

APPENDIX A

Defining

$$D(1,1)=\frac{m}{r}Z_m(\alpha r)-\alpha Z_{m+1}(\alpha r),$$

$$D(1,2)=\xi Z_{m+1}(\beta r),$$

$$D(1,3)=\frac{im}{r}Z_m(\beta r),$$

$$D(2,1)=\frac{im}{r}Z_m(\alpha r),$$

$$D(2,2)=-i\xi Z_{m+1}(\beta r),$$

$$D(2,3)=\beta Z_{m+1}(\beta r)-\frac{m}{r}Z_m(\beta r),$$

$$D(3,1)=-i\xi Z_m(\alpha r),$$

$$D(3,2)=-i\beta Z_m(\beta r),$$

$$D(3,3)=0,$$

$$D(4,1)=\mu\left\{\left(\frac{2m(m-1)}{r^2}+(\xi^2-\beta^2)\right)Z_m(\alpha r)+\frac{2\alpha}{r}Z_{m+1}(\alpha r)\right\},$$

$$D(4,2)=2\mu\xi\left\{\beta Z_m(\beta r)-\frac{(m+1)}{r}Z_{m+1}(\beta r)\right\},$$

$$D(4,3)=\frac{2i\mu m}{r}\left\{\frac{(m-1)}{r}Z_m(\beta r)-\beta Z_{m+1}(\beta r)\right\},$$

$$D(5,1)=\frac{2i\mu m}{r}\left\{\frac{(m-1)}{r}Z_m(\alpha r)-\alpha Z_{m+1}(\alpha r)\right\},$$

$$D(5,2)=i\mu\xi\left\{\frac{2(m+1)}{r}Z_{m+1}(\beta r)-\beta Z_m(\beta r)\right\},$$

$$D(5,3)=\mu\left\{\left(\beta^2-\frac{2m(m-1)}{r^2}\right)Z_m(\beta r)-\frac{2\beta}{r}Z_{m+1}(\beta r)\right\},$$

$$D(6,1)=2i\mu\xi\left\{\alpha Z_{m+1}(\alpha r)-\frac{m}{r}Z_m(\alpha r)\right\},$$

$$D(6,2)=i\mu\left\{(\beta^2-\xi^2)Z_{m+1}(\beta r)-\frac{\beta m}{r}Z_m(\beta r)\right\},$$

$$D(6,3)=\frac{\mu m\xi}{r}Z_m(\beta r), \tag{A1}$$

where $Z_m=H_m^{(1)}$. The other three columns, i.e., $j=4, \ldots, 6$, can be obtained from the first three columns by replacing the Hankel functions $H_m^{(1)}$ by $H_m^{(2)}$. The propagator matrix for the kth sublayer in Eq. (5) is defined by

$$[P_k]=[D_{k+1}][D_k]^{-1} \tag{A2}$$

where $[D_k]$ is $[D]$ evaluated at $r=r_k$ and $[D_{k+1}]$ is $[D]$ evaluated at $r=r_{k+1}$.

Downloaded 03 May 2010 to 171.66.16.20. Redistribution subject to ASME license or copyright; see http://www.asme.org/terms/Terms_Use.cfm

Excitation of Guided Waves in Generally Anisotropic Layers Using Finite Sources

J. J. Ditri
Assoc. Mem. ASME.

J. L. Rose
Assoc. Mem. ASME.

Engineering Science and Mechanics Department, Pennsylvania State University, State College, PA 16802

The excitation of guided wave modes in generally anisotropic layers by finite sized strip sources placed on the surfaces of the layer is examined. The general problem of arbitrarily applied harmonic surface tractions is first solved using the normal mode expansion technique in conjunction with the complex reciprocity relation of elastodynamics. This general solution is then specialized to loading situations modelling those commonly used to excite guided waves in layers for use in nondestructive evaluation. The amplitudes of the generated modes are written as the product of an "excitation function" which depends only on the distribution of the applied tractions and an "excitability function" which depends only on the properties of the specific mode(s) being excited and which determines how receptive the modes are to the applied tractions. Expressions are obtained for the −9 dB wave number and phase velocity bandwidths (σ_β and σ_v, respectively) which determine the widths of the wavenumber or phase velocity excitation spectra at the −9 dB generation point. Finally, the problem of transient loading is addressed by superimposing time harmonic solutions via an integration over the dispersion curves of the layer.

Introduction

Guided waves are finding an increased usage among the nondestructive evaluation (NDE) community for both defect detection and material characterization (Spetzler and Datta, 1990; Rokhlin et al., 1990; Karim et al. 1990; Guo and Cawley, 1992; Mal et al., 1992 and Pilarski and Rose, 1992). The unique properties of the individual guided wave modes which exist in the layer offer a host of possibilities for nondestructively probing the material of which the layer is composed. Because of the different field distributions of the different modes, they each interact differently with the material composing the layer, and hence each carries useful information about the constitution and/or state of the layer.

Before one can fully utilize the diverse nature of the different modes, however, it is necessary to understand fully the manner in which the individual guided wave modes can be introduced into the layer by applied surface tractions. The goal of this paper is to determine the amplitude of each of the propagating modes generated in an anisotropic layer due to arbitrarily applied surface tractions, and to relate the amplitudes of the generated modes to the properties of the tractions used to excite them. After the results are obtained for arbitrary loading, specific loading conditions, typical of those used in nondestructive evaluation techniques for generating waveguide modes, are examined in detail.

The problem of the excitation of an arbitrarily anisotropic layer due to arbitrarily applied time-harmonic surface tractions is solved by utilizing the Normal Mode Expansion Technique (Auld and Kino, 1971; Kino, 1987; Auld, 1990b). In this technique, the fields in the loaded layer are expanded in terms of the "normal modes" of the layer (i.e., the mode fields in the free layer) multiplied by unknown complex amplitudes. The goal is then to determine, from the applied tractions, the expansion amplitudes necessary for evaluation of the fields in the loaded waveguide. Such expansion techniques have been successfully used to solve *edge* load problems for plates (Folk and Herczynski, 1986) and solid circular cylinders (Herczynski and Folk, 1989), as well as side excitation problems for hollow circular cylinders (Ditri and Rose, 1992). The key to the success of the technique is the establishment and use of an orthogonality condition between the free waveguide modes, analogous to the orthogonality of the trigonometric functions used in Fourier Series expansions.

Starting with the expansion amplitudes for the harmonic excitation case, the more general problem of arbitrary time-dependence loading can be treated by linear superposition of harmonic solutions. This type of approach leads to solutions (expansion amplitudes) which are identical in *form* for isotropic or generally anisotropic layers. The difference is accounted for when evaluating the quantities appearing in the solutions. Because of this, the true physical nature of the excitation process becomes clear, unobstructed by the peculiarities of a particular material.

Contributed by the Applied Mechanics Division of THE AMERICAN SOCIETY OF MECHANICAL ENGINEERS for publication in the ASME JOURNAL OF APPLIED MECHANICS.

Discussion on this paper should be addressed to the Technical Editor, Professor Lewis T. Wheeler, Department of Mechanical Engineering, University of Houston, Houston, TX 77204-4792, and will be accepted until four months after final publication of the paper itself in the ASME JOURNAL OF APPLIED MECHANICS.

Manuscript received by the ASME Applied Mechanics Division, July 14, 1992; final revision, Dec. 16, 1992. Associate Technical Editor: S. K. Datta.

Copyright © 1994 by ASME
Downloaded 03 May 2010 to 171.66.16.20. Redistribution subject to ASME license or copyright; see http://www.asme.org/terms/Terms_Use.cfm

Normal Modes

The governing equations for wave propagation in flat, linearly elastic, nonpiezoelectric and generally anisotropic layers, for zero body forces, can be written as

$$\frac{\partial T_{ij}}{\partial x_j} = \rho \frac{\partial^2 u_i}{\partial t^2} \tag{1a}$$

$$T_{ij} = C_{ijkl} \frac{\partial u_k}{\partial x_l} \tag{1b}$$

where $\mathbf{T}$ denotes the Cauchy stress tensor, $\mathbf{u}$ denotes the particle displacement vector, $\mathbf{C}$ denotes the stiffness tensor, and ρ denotes the mass density. Summation convention over repeated subscripts is assumed.

Along with the governing equations, Eqs. (1*a–b*), the normal modes of the layer are required to satisfy traction-free boundary conditions

$$t_i \equiv T_{ij} n_j = 0 \tag{2}$$

at both the upper and lower surfaces of the layer. n_i denotes the components of a unit vector normal to the surfaces of the layer. Solutions to the boundary value problem, Eqs. (1) and (2), can be found in the literature for layers of various classes of anisotropy (Solie and Auld, 1972; Nayfeh et al., 1988; Li and Thompson, 1990).

When propagating in an anisotropic layer, the characteristics of the normal modes (i.e., phase and group velocities, field distributions, etc.) are in general very dependent on the orientation between the wave vector of the mode and the natural or crystallographic coordinate system of the media, when such preferred axes exist (see for instance Datta et al., 1988). In all of the derivations to follow, it is assumed that the "z" coordinate is aligned with the wave vector of the generated mode and that the "y" axis is transverse to the layer (i.e., in the thickness direction). For anisotropic layers, this will generally necessitate a coordinate transformation of the elastic stiffness tensor since, in general, the principal axes of the anisotropic medium will not coincide with the chosen coordinate axes. With this choice of coordinate system (and the subsequent transformation of the elastic stiffness tensor), the fields associated with any given mode are uniform in the "x" coordinate direction. This serves to make the problem one of plane strain in the $y - z$ plane (i.e., $\epsilon_{xx} = \epsilon_{xy} = \epsilon_{xz} \equiv 0$ and $\epsilon_{ij} = \epsilon_{ij}(y, z, t)$ where $i, j \in \{y, z\}$).

The fields caused by the waveguide modes can then be written in the general form

$$\xi(y, z, t) = \bar{\xi}(y) e^{j(\omega t - \beta z)} \tag{3}$$

where $\bar{\xi}(y)$ represents the "modal distribution" or "y" variation of the field, ξ. β is the wave number of the mode which, for a given frequency ω, is determined by a generalized Rayleigh-Lamb type of equation whose form depends on the type of anisotropy exhibited by the layer (Li and Thompson, 1990). Just as in the isotropic case, the wave number β can be real, imaginary, or complex for a given real and positive frequency ω.

Problem Statement and Solution

The problem to be addressed is shown in Fig. 1. A linearly elastic, generally anisotropic layer (i.e., having up to 21 independent elastic moduli) is loaded over a finite portion of its top surface by a traction force

$$\mathbf{t}(z) e^{i\omega t} = [t_z(z)\hat{\mathbf{e}}_z + t_y(z)\hat{\mathbf{e}}_y] e^{i\omega t}, \tag{4}$$

where $\hat{\mathbf{e}}_i$ denotes a unit vector in the x_i coordinate direction. The tractions are assumed to be independent of the x-coordinate and therefore actually represent loading along a strip of infinite width in the x-direction.

We start the analysis from the purely acoustic form of the

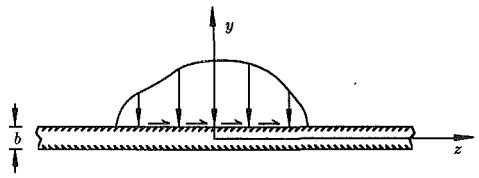


Fig. 1 Loading of an anisotropic layer by harmonic surface tractions

complex reciprocity relation (Auld, 1990b, pp. 154–155), relating any two solutions, 1 and 2, to the governing field equations (Eq. (1)). This relation can be written in differential form as

$$\nabla \cdot (\tilde{\mathbf{v}}_2 + \mathbf{T}_1 + \mathbf{v}_1 \cdot \tilde{\mathbf{T}}_2) = 0 \tag{5}$$

where $\mathbf{v}$ represents the particle velocity field and the tilde represents complex conjugation. In Eq. (5) both solutions, 1 and 2, are assumed to have the same frequency, ω, and the $e^{i\omega t}$ dependence of all field variables will be dropped for brevity.

The fields in the loaded waveguide are then expressed as a summation over all of the normal modes of the free layer, specified by index μ, multiplied by unknown, generally complex and z-dependent amplitudes, $A_\mu(z)$. For the field variables appearing in Eq. (5), these expansions are of the form

$$\mathbf{v}(y, z) = \sum_\mu A_\mu(z) \mathbf{v}_\mu(y) \tag{6a}$$

and

$$\mathbf{T}(y, z) = \sum_\mu A_\mu(z) \mathbf{T}_\mu(y). \tag{6b}$$

To determine the unknown mode amplitudes $A_\mu(z)$, in Eqs. (6*a–b*), the reciprocity relation, Eq. (5), is invoked with solution "1" being $\mathbf{v}$ and $\mathbf{T}$ appearing in Eqs. (6*a*) and (6*b*), and solution "2" being the νth mode of the free layer. That is

$$\mathbf{v}_2 = \mathbf{v}_\nu(y) e^{-i\beta_\nu z} \tag{7a}$$

$$\mathbf{T}_2 = \mathbf{T}_\nu(y) e^{-i\beta_\nu z}. \tag{7b}$$

Substituting Eqs. (6*a–b*) and (7*a–b*) into the reciprocity equation, Eq. (5), integrating the resulting equation across the waveguide thickness $-b/2 \le y \le b/2$ and making use of the fact that the normal modes satisfy traction-free boundary conditions results in a first-order ordinary differential equation which governs the amplitudes of the generated modes. For propagating modes, the wave number β_ν is real, and it can be shown by specializing a general equation in (Auld, 1990b, pg. 162) that, for the case considered here, the equation governing the amplitude of the generated modes reduces to the form

$$4P_{\nu\nu}\left(\frac{d}{dz} + i\beta_\nu\right) A_\nu(z) = \tilde{\mathbf{v}}_\nu(b/2) \cdot \mathbf{t}(z) \tag{8}$$

where the quantity $P_{\nu\nu}$ has been defined as

$$P_{\nu\nu} = \Re e\left(-\frac{1}{2}\int_{-b/2}^{b/2} \tilde{\mathbf{v}}_\nu \cdot \mathbf{T}_\nu \cdot \hat{\mathbf{e}}_z dy\right) \tag{9}$$

and $\Re e(\ )$ denotes real part of the quantity in brackets. From the definition of the acoustic Poynting vector (Auld, 1990a, pg. 155), this is recognized as the time-averaged power flow carried by the νth mode in the z-direction per unit waveguide width (in the x-direction) and has typical units of [Watts/m]. It should be remembered that, since the amplitudes of the modal fields themselves ($\mathbf{v}_\nu$ and $\mathbf{T}_\nu$) can be arbitrarily assigned (within the restrictions of infinitesimal elasticity theory), the power carried by the modes, Eq. (9), is also arbitrary, depending on the assigned amplitude. We will see that this indeterminacy will disappear in the final result, which will be independent of the arbitrary amplitude which may be assigned to $\mathbf{v}_\nu$ and $\mathbf{T}_\nu$.

Downloaded 03 May 2010 to 171.66.16.20. Redistribution subject to ASME license or copyright; see http://www.asme.org/terms/Terms_Use.cfm

Equation (8) is a first-order ordinary differential equation and can therefore be integrated using standard techniques. The solution can be written

$$A_\nu(z) = \frac{e^{-i\beta_\nu z}}{4P_{\nu\nu}} \int_c^z e^{i\beta_\nu \eta} \tilde{\mathbf{v}}_\nu(b/2) \cdot \mathbf{t}(\eta) d\eta, \tag{10}$$

where c is a constant used to satisfy the boundary condition on $A_\nu(z)$. Supposing that the external tractions, $\mathbf{t}$, are only nonzero in the interval $-L \le z \le L$, and using the boundary condition

$$A_\nu(z) = 0 \quad z \le -L \tag{11}$$

gives, for the amplitude of the rightward travelling modes,

$$A_\nu(z) = \frac{e^{-i\beta_\nu z}}{4P_{\nu\nu}} \int_{-L}^{L} e^{i\beta_\nu \eta} \tilde{\mathbf{v}}_\nu(b/2) \cdot \mathbf{t}(\eta) d\eta \quad z \ge L. \tag{12}$$

The corresponding expression for the leftward propagating modes can be obtained from Eq. (12) by replacing $P_{\nu\nu}$ by $-P_{\nu\nu}$, $\tilde{\mathbf{v}}_\nu$ by $\tilde{\mathbf{v}}_{-\nu}$, the wave number β_ν by $-\beta_\nu$ and finally by using the boundary condition $A_{-\nu} = 0$ for $z \ge L$. The result is

$$A_{-\nu}(z) = \frac{e^{i\beta_\nu z}}{4P_{\nu\nu}} \int_{-L}^{L} e^{-i\beta_\nu \eta} \tilde{\mathbf{v}}_{-\nu}(b/2) \cdot \mathbf{t}(\eta) d\eta \quad z \le -L. \tag{13}$$

Since the applied tractions vanish outside the interval $|z| > L$, the integration limits in Eqs. (12) and (13) can be extended indefinitely, i.e., to plus and minus infinity. The two equations can also be combined into

$$A_{\pm\nu}(z) = \frac{e^{\mp i\beta_\nu z}}{4P_{\nu\nu}} \tilde{\mathbf{v}}_{\pm\nu}(b/2) \cdot \int_{-\infty}^{\infty} e^{\pm i\beta_\nu \eta} \mathbf{t}(\eta) d\eta. \tag{14}$$

Having determined the expansion amplitudes, $A_{\pm\nu}(z)$, of the propagating modes (real β_ν), the fields in the loaded layer due to the propagating modes follow from the original expansions Eqs. (6*a*, *b*). For instance, the particle velocity field in the loaded layer can be written

$$\mathbf{v}(y, z) = \sum_\nu \left\{ \frac{e^{\mp i\beta_\nu z}}{4P_{\nu\nu}} \tilde{\mathbf{v}}_{\pm\nu}(b/2) \cdot \int_{-\infty}^{\infty} e^{\pm i\beta_\nu \eta} \mathbf{t}(\eta) d\eta \right\} \mathbf{v}_{\pm\nu}(y) + \sum_\nu A^e_{\pm\nu}(z) \mathbf{v}_{\pm\nu}(y). \tag{15}$$

For $z \ge L$, only the summation over the positive travelling (or decaying) modes (+) contribute whereas for $z \le -L$, only the summation over the negative travelling (or decaying) modes (−) contribute. The first summation represents the contribution of the propagating modes (real wave number, β_ν) and the second represents the contribution of the evanescent modes (imaginary and/or complex wave numbers) with expansion amplitudes $A^e_{\pm\nu}(z)$. Since the evanescent modes decay exponentially away from the source which excites them, the contribution from the second summation becomes smaller as z becomes larger. The actual distance from the source at which the amplitude of an evanescent mode becomes negligible depends on the magnitude of the imaginary part of its wave number.

Once the applied tractions, $\mathbf{t}(z)$, are specified, Eq. (14) can be used to determine the amplitudes of the forward and backward traveling modes which, when substituted into the original normal mode expansion, Eqs. (6*a*, *b*), gives that part of the total field in the loaded layer due to the propagating modes. The part of the total field due to the nonpropagating modes can also be determined by this procedure but their contribution is of less importance in nondestructive evaluation purposes since they decay exponentially from the source which excites them. Their amplitudes are not, however, given by Eq. (14), which is valid only for propagating modes. For the evanescent modes, the differential equation governing the amplitudes, Eq. (8), must be modified.

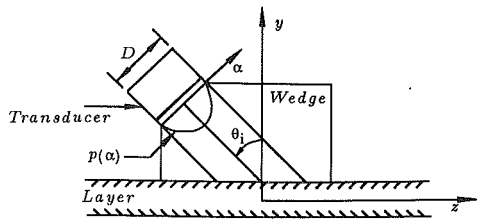


Fig. 2 Model of the "wedge method" of exciting guided waves. The transducer, of length, *D*, is mounted to a wedge and produces a plane wave with arbitrary pressure distribution, $p(\alpha)$, which impinges on the layer.

Specific Cases

It is now assumed that the tractions produced at the upper surface of the layer are due to loading by an ultrasonic transducer mounted to an angle beam "wedge" as shown in Fig. 2. The ultrasonic transducer is assumed to produce a time-harmonic plane stress wave which travels within the wedge and strikes the layer at a given angle θ_i. Beam spreading and beam shifting upon striking the layer are neglected, and the wedge is assumed to be coupled to the layer by a thin layer of nonviscous liquid. As a result, only normal tractions, $t_y(z)$, are assumed to be transferred, the shear tractions, $t_z(z)$, vanishing. Finally, the transducer is allowed to have an arbitrary pressure distribution, $p(\alpha)$, across its face. A similar problem, for isotropic layers and piston-like transducer, was solved using Fourier Integrals by Viktorov (1967).

Projecting $p(\alpha)$ on the the layer surface, the traction produced on the top of the layer is assumed to be of the form (neglecting an unnecessary phase factor and the $e^{i\omega t}$ dependence)

$$\mathbf{t}(z) = \begin{cases} p(z \cos\theta_i) |R(\theta_i)| e^{-ik_w \sin\theta_i z} \tilde{\mathbf{e}}_y, & \text{if } |z| \le L \\ 0, & \text{if } |z| > L \end{cases} \tag{16}$$

where $|R(\theta_i)|$ is a numerical factor introduced to account for the fact that the actual traction at the wedge-layer interface will in general be different than that due solely to the incident wave. It is assumed, however, that this factor is frequency independent and a discussion of this result, along with limited experimental verification, can be found in Ditri (1992). In Eq. (16), k_w represents the wave number of the incident wave in the wedge, numerically equal to ω/V_w, V_w representing the velocity of longitudinal waves in the wedge material.

Substituting this assumed form of surface traction into the general result, Eq. (14), gives, after some manipulation,

$$A_{\pm\nu}(z) = \frac{|R(\theta_i)|}{4} \frac{\tilde{v}_{\pm\nu y}(b/2)}{P_{\nu\nu}} \frac{e^{\mp i\beta_\nu z}}{\cos(\theta_i)} \int_{-\infty}^{\infty} p(\alpha) e^{\pm i\chi_\pm \alpha} d\alpha \tag{17}$$

where

$$\chi_+ \equiv \frac{\beta_\nu - k_w \sin\theta_i}{\cos\theta_i} \tag{18a}$$

$$\chi_- \equiv \frac{\beta_\nu + k_w \sin\theta_i}{\cos\theta_i} \tag{18b}$$

and $\tilde{v}_{\pm\nu y}$ represents the complex conjugate of the y-component of the particle velocity field of positive (+) and negative (−) propagating modes.

The appearance of the factor $P_{\nu\nu}$ in the denominator of Eq. (17) for the amplitudes ensures that the final result is independent of the arbitrarily chosen amplitude of $\mathbf{v}_\nu$. This is so because when A_ν of Eq. (17) is substituted into the normal mode expansions, Eqs. (6*a*, *b*), they contain products of the form $v_{\nu y}(b/2)\mathbf{v}_\nu(y)/P_{\nu\nu}$ and $v_{\nu y}(b/2)\mathbf{T}_\nu(y)/P_{\nu\nu}$. If $\mathbf{v}_\nu$ is replaced by $\alpha\mathbf{v}_\nu$ where α is an arbitrary complex constant, then owing to the linearity of the governing elasticity equations, $\mathbf{T}_\nu$

Downloaded 03 May 2010 to 171.66.16.20. Redistribution subject to ASME license or copyright; see http://www.asme.org/terms/Terms_Use.cfm

is also multiplied by the same factor. It follows that the terms $v_{\nu y}(b/2)\mathbf{v}_\nu(y)$ and $v_{\nu y}(b/2)\mathbf{T}_\nu(y)$ are multiplied by α^2. However, reference to Eq. (9) shows that $P_{\nu\nu}$ is also proportional to the product $\mathbf{v}_\nu(y)\cdot\mathbf{T}_\nu(y)$ and is therefore also multiplied by α^2. This ensures that the ratios $v_{\nu y}(b/2)\mathbf{v}_\nu(y)/P_{\nu\nu}$ and $v_{\nu y}(b/2)\mathbf{T}_\nu(y)/P_{\nu\nu}$ remain the same. Therefore, the final fields caused in the layer by the individual modes, Eqs. (6*a*, *b*), are independent of the arbitrarily assigned amplitudes of the modal fields which appear in their definitions. One could have started the normal mode expansion technique by expanding the fields in the loaded layer in terms of the power normalized normal modes, $\mathbf{v}_\nu/\sqrt{P_{\nu\nu}}$ and $\mathbf{T}_\nu/\sqrt{P_{\nu\nu}}$, which are already independent of the arbitrarily chosen multiplicative amplitudes for $\mathbf{v}_\nu$ and $\mathbf{T}_\nu$. In this case, $A_{\pm\nu}$ would have a $\sqrt{P_{\nu\nu}}$ factor instead of $P_{\nu\nu}$ in its denominator.

The integral appearing in Eq. (17) can be interpreted as the Fourier transform of the pressure distribution function $p(\alpha)$ with transform parameter χ given by Eqs. (18*a*) or (18*b*). It clearly exhibits the influence of the transducers pressure distribution on its guided wave generation characteristics.

In order to manifest clearly the physics of the excitation phenomenon, Eq. (17) is written in the form

$$A_{\pm\nu}(z) = \mathcal{G}\mathcal{F}^{(+)}E_{\pm\nu}e^{\mp i\beta_\nu z} \tag{19}$$

where

$$\mathcal{G} \equiv \frac{|R(\theta_i)|}{4} \tag{20a}$$

$$E_{\pm\nu} \equiv \frac{\tilde{v}_{\pm\nu y}(b/2)}{P_{\nu\nu}} \tag{20b}$$

$$\mathcal{F}^{(\pm)} \equiv \frac{1}{\cos(\theta_i)}\int_{-\infty}^{\infty} p(\alpha)e^{\pm i\chi\pm\alpha}d\alpha. \tag{20c}$$

The function $\mathcal{G}$ represents a numerical factor which depends solely on the output power of the transducer. The function $E_{\pm\nu}$, termed the "excitability" function of mode ν is seen to depend only on properties of the mode which is being excited and *not* on the properties of the source used for excitation. The function $\mathcal{F}^{(\pm)}$ is seen to depend only on properties of the transducer and wedge used to excite the layer. The product function, $\mathcal{F}\mathcal{G}$, which is also dependent only on transducer parameters, is termed the "excitation" function of the source. The amplitude with which guided waves are generated is therefore seen to be proportional to the product of the excitation function, $\mathcal{F}\mathcal{G}$, determined by transducer and wedge parameters, and the excitability function, $E_{\pm\nu}$, which depends on which mode is excited and where on its dispersion curve it is excited.

The actual pressure distribution of a transducer, $p(\alpha)$, depends essentially on how the transducer is manufactured. The simplest approximation to an actual pressure variation is the piston source defined by

$$p(\alpha) = \begin{cases} \sigma_o, & \text{if } |\alpha| \le \dfrac{D}{2} \\ 0, & \text{if } |\alpha| > \dfrac{D}{2} \end{cases}. \tag{21}$$

If this pressure variation is substituted into Eq. (17), the resulting expression for the excitation amplitudes is found to be

$$A_{\pm\nu}(z) = \frac{\sigma_o|R(\theta_i)|}{4}\frac{\tilde{v}_{\pm\nu y}(b/2)}{P_{\nu\nu}}\,2\,\frac{\sin\left(\dfrac{(\beta_\nu \mp k_w \sin\theta_i)D}{2\cos\theta_i}\right)}{(\beta_\nu \mp k_w \sin\theta_i)}\,e^{\mp i\beta_\nu z} \tag{22}$$

where the positive amplitudes are valid for $z \ge L$ and the negative amplitudes for $z \le -L$. Comparing Eq. (22) with Eq. (19) shows that for a piston source transducer, $\mathcal{G} = \sigma_o|R(\theta_i)|/4$, $E_{\pm\nu} = \tilde{v}_{\pm\nu y}(b/2)/P_{\nu\nu}$ and

$$\mathcal{F}^{(\pm)}_{\text{Piston}} = 2\,\frac{\sin\left(\dfrac{(\beta_\nu \mp k_w \sin\theta_i)D}{2\cos\theta_i}\right)}{(\beta_\nu \mp k_w \sin\theta_i)}, \tag{23}$$

which is, except for notation, identical to the result found by (Viktorov, 1967, pp. 83–93) when treating the problem of the excitation of isotropic layers using piston sources by Fourier integral techniques. It is interesting to note from Eq. (22) that, unlike the case of infinite plane wave excitation, Snell's law is not rigorously applicable in describing the generation process of Lamb waves when using finite sources since the amplitude function is nonzero for a range of wave numbers (or phase velocities) instead of being nonzero for just the single wave number determined by Snell's law (Eq. (25)). The most common method found in the literature of determining the appropriate shoe angle to use when trying to generate a Lamb wave mode of phase velocity V_{ph} is the use of Snell's law,

$$\theta_i = \sin^{-1}\left(\frac{V_w}{V_{\text{ph}}}\right), \tag{24}$$

where V_w is the longitudinal wave velocity in the shoe material (or coupling fluid if immersion is used). In terms of wave numbers, this relation can be written

$$\beta = k_w \sin\theta_i, \tag{25}$$

that is, it is usually assumed that, given an incident angle, θ_i, and incident wave number, k_w, only a single wave number, given by Snell's law, can be generated, or will at least be the dominant wave number of the generated waves.

Although the function $\mathcal{F}^{(+)}_{\text{Piston}}$ is strictly not defined when Eq. (25) is satisfied, it can be defined as the limit,

$$\mathcal{F}^{(+)}_{\text{Piston}}|_{\beta=k_w\sin\theta_i} \equiv \lim_{\beta\to k_w\sin\theta_i}\mathcal{F}^{(+)}_{\text{Piston}} = \frac{D}{\cos\theta_i}, \tag{26}$$

in which case $\mathcal{F}^{(+)}_{\text{Piston}}$ will be continuous for all β and have a maximum at the Snell's law wave number $\beta = k_s \sin(\theta_i)$. Equation (22) then shows that for $\beta_\nu \ne k_w \sin\theta_i$, $\mathcal{F}^{(-)}_{\text{Piston}}$ and $\mathcal{F}^{(+)}_{\text{Piston}}$ do not vanish identically, even though they decrease as β_ν becomes different than $k_w \sin(\theta_i)$. Therefore, even if the Snell's Law angle is not used, the mode can still be generated, albeit less efficiently.

We can define a "wave number bandwidth," σ_β, associated with the piston transducer as the value of $\beta - k_s \sin\theta_i$ where the function $\mathcal{F}^{(+)}_{\text{Piston}}$ decreases to say $1/e$ (≈ -9dB) its maximum, that is, $\mathcal{F}^{(+)}_{\text{Piston}}(\beta - k_s\sin\theta_i = \pm\sigma_\beta) = \mathcal{F}^{(+)}_{\text{Piston}}(0)/e$. This value is given, approximately, by

$$\sigma_\beta \approx \frac{4.398\cos\theta_i}{D}. \tag{27}$$

As can be seen from Eq. (27), as $D \to \infty$, $\sigma_\beta \to 0$, i.e., for plane wave incidence (infinite diameter transducer) the wave number bandwidth is zero, so only one value of wave number can be excited as given by Snell's Law, Eq. (25). For a finite-sized piston source transducer, we see that the wave number bandwidth is inversely proportional to the diameter D. The bandwidth is directly proportional to $\cos\theta_i$ which in the interval $0 \le \theta_i < 90$ deg decreases monotonically from 1.0 to 0.0. Recognizing $D/\cos\theta_i$ as the length of the loaded region (see Fig. 2), we can conclude that the wave number bandwidth *decreases* as the size of the insonification region *increases*.

Figure 3 is a parametric plot of $\mathcal{F}^{(+)}_{\text{Piston}}$ with the size of the loading region, $D/\cos\theta_i$ as the parameter (in all plots, $\omega = 2$ [rad/μsec]). As can be seen, as the insonification region becomes larger, the transducer-wedge source becomes more and more selective to the Snell's Law wave number $k_w \sin(\theta_i)$.

A somewhat more realistic model of an actual ultrasonic

Downloaded 03 May 2010 to 171.66.16.20. Redistribution subject to ASME license or copyright; see http://www.asme.org/terms/Terms_Use.cfm

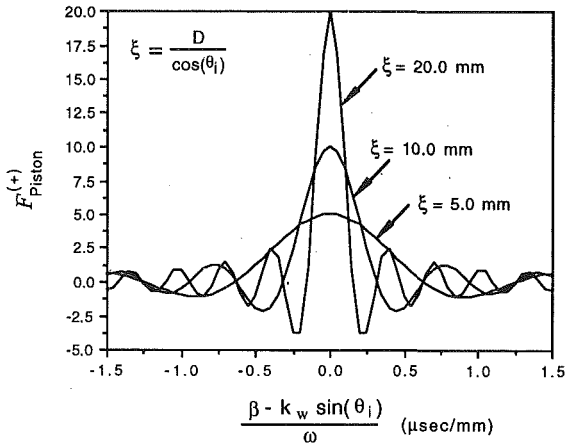


Fig. 3 Parametric plots of the $\mathcal{F}^{(+)}_{Piston}$ with the size of the loading region as the parameter (ω = 2 rad/μsec)

transducer is a parabolic pressure distribution. In this case, the pressure distribution function $p(\alpha)$ can be written

$$p(\alpha) = \begin{cases} \sigma_o\left(1 - \dfrac{\alpha^2}{(D/2)^2}\right), & \text{if } |\alpha| \le \dfrac{D}{2} \\ 0, & \text{if } |\alpha| > \dfrac{D}{2} \end{cases} \tag{28}$$

where σ_o now represents the maximum pressure which occurs at the center of the transducer face, $\alpha = 0$.

Substituting Eq. (28) into Eq. (17) and comparing the result with Eq. (19) shows that

$$\mathcal{F}^{(+)}_{Parabolic}(\chi_+) = \frac{8}{D\cos(\theta_i)\chi_+^2}\left[\frac{2\sin\left(\chi_+ \dfrac{D}{2}\right)}{D\chi_+} - \cos\left(\chi_+ \frac{D}{2}\right)\right], \tag{29}$$

where χ_+ is defined in Eq. (18*a*).

Again, we can define the wave number bandwidth of the parabolic source transducer, σ_β, to be the value of $\beta - k_s \sin\theta_i$ at which $\mathcal{F}^{(+)}_{Parabolic}$ drops to $1/e$ its maximum value (at $\chi_+ = 0$). Performing the calculations results in, approximately,

$$\sigma_\beta \approx \frac{5.852\cos\theta_i}{D}. \tag{30}$$

Comparing this bandwidth with that obtained for the Piston source, Eq. (27), shows that the parabolic source has a somewhat *wider* wave number bandwidth. The dependence of σ_β on the transducer diameter, D, and the incident angle, θ_i, is the same as for the piston transducer.

It is important to know how the transducer parameters (or equivalently the wave number bandwidth) influences the range of *phase velocities* which may be generated by the applied source. Due to the finite size of the loading region, there is actually a range of phase velocities within which the magnitude of $\mathcal{F}^{(+)}$ (for both piston and parabolic sources) remains above, say -9dB of its maximum value. As a result, it should be expected that any mode who's dispersion curve passes through this phase velocity region (for the given frequency ω) may be excited by the source while modes whose dispersion curves are far from this region should contribute less to the total generated field. How strongly each mode is generated also depends on the value of its excitability function E_ν at this frequency.

To get an estimate of the range of phase velocities within which significant excitation may occur, we can use the definition of the wave number bandwidth σ_β. Recalling that σ_β is

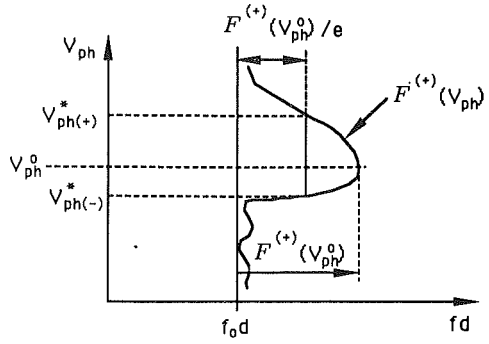


Fig. 4 Definitions of the lower, $V^*_{ph(-)}$, and upper, $V^*_{ph(+)}$, phase velocities where $\mathcal{F}^{(+)}$ drops by approximately 9 dB

the value of $\beta - k_s \sin\theta_i$ where the function $\mathcal{F}^{(+)}$ drops to $1/e$ ($\approx -9dB$) its maximum value (at $\beta = k_w \sin\theta_i$), we have

$$\mathcal{F}^{(+)}(\beta - k_s \sin\theta_i) = \mathcal{F}^{(+)}(0)/e \Rightarrow \beta - k_w \sin\theta_i = \pm\sigma_\beta$$

$$\Rightarrow \omega\left(\frac{1}{V^*_{ph}} - \frac{1}{V^o_{ph}}\right) = \pm\sigma_\beta \tag{31}$$

where V^*_{ph} is the phase velocity at which $\mathcal{F}^{(+)}$ drops by 9 *dB* of its maximum value and $V^o_{ph} = V_w/\sin\theta_i$. Considering the plus and minus signs in the above equality we can solve for two values of V^*_{ph} which we denote by $V^*_{ph(-)}$ and $V^*_{ph(+)}$. These are given by

$$V^*_{ph(-)} = \frac{\omega V^o_{ph}}{\omega + \sigma_\beta V^o_{ph}} \tag{32}$$

and

$$V^*_{ph(+)} = \frac{\omega V^o_{ph}}{\omega - \sigma_\beta V^o_{ph}}. \tag{33}$$

These velocities, under certain conditions to be developed shortly, represent the values of phase velocity at which the function $\mathcal{F}^{(+)}$ (considered as a function of phase velocity) drops by 9 dB of its maximum value which occurs at $V_{ph} = V^o_{ph}$. $V^*_{ph(-)}$ represents the velocity *smaller than* V^o_{ph} at which $\mathcal{F}^{(+)}$ drops by 9 dB and $V^*_{ph(+)}$ represents the velocity *larger than* V^o_{ph} at which $\mathcal{F}^{(+)}$ drops by 9 dB (Fig. 4).

Having $V^*_{ph(-)}$ and $V^*_{ph(+)}$, we can calculate the range of phase velocities over which significant excitation may occur, $V^*_{ph(+)} - V^*_{ph(-)}$. As a percent of the Snell's Law velocity, V^o_{ph} (at which $\mathcal{F}^{(+)}$ is maximum), this range is given by

$$\sigma_v \equiv \frac{V^*_{ph(+)} - V^*_{ph(-)}}{V^o_{ph}} = \frac{2\sigma_\beta\left(\dfrac{V^o_{ph}}{\omega}\right)}{1 - \sigma_\beta^2\left(\dfrac{V^o_{ph}}{\omega}\right)^2}. \tag{34}$$

The quantity σ_v will hereafter be called the "-9 dB Phase Velocity Bandwidth" or (-9 dB PVB) of the transducer-wedge combination. Equation (34) for the -9 dB PVB is only valid in the range $0 \le \sigma_\beta \le \omega/V^o_{ph}$. This is due to the fact that, while $V^*_{ph(-)}$ remains valid for $0 \le \sigma_\beta < \infty$ (i.e., for any value of σ_β it represents the value of phase velocity, smaller than V^o_{ph}, at which $\mathcal{F}^{(+)}$ drops by 9 dB), $V^*_{ph(+)}$ is only defined for $0 \le \sigma_\beta < \omega/V^o_{ph}$. As σ_β approaches ω/V^o_{ph}, the upper velocity at which $\mathcal{F}^{(+)}$ drops by 9 dB (i.e., $V^*_{ph(+)}$) quickly approaches infinity. For $\sigma_\beta > \omega/V^o_{ph}$, $V^*_{ph(+)}$ becomes negative and there is no longer an upper value of phase velocity at which $\mathcal{F}^{(+)}$ will drop by 9 dB. Instead, it asymptotically approaches some finite value *above* the -9 dB values as $V_{ph} \to \infty$. Therefore, the -9 dB phase velocity bandwidth approaches infinity as $\sigma_\beta \to \omega/V^o_{ph}$ and we will say that it is infinite for $\sigma_\beta > \omega/V^o_{ph}$

Downloaded 03 May 2010 to 171.66.16.20. Redistribution subject to ASME license or copyright; see http://www.asme.org/terms/Terms_Use.cfm

with the understanding that this means that there is no upper velocity at which $\mathcal{F}^{(+)}$ drops by 9 dB of its maximum value.

Making use of the relation $V^o_{\text{ph}}/\omega = \lambda^o/2\pi$ and the fact that the wave number bandwidths of both the piston and parabolic sources can be written as $\sigma_\beta = K\cos(\theta_i)/D$ (see Eqs. (27) and (30)), the -9 dB phase velocity bandwidth can be written

$$\sigma_v = \frac{\dfrac{K}{\pi}\left(\dfrac{\lambda^o}{D}\right)}{1-\left(\dfrac{K}{2\pi}\right)^2\left(\dfrac{\lambda^o}{D}\right)^2}, \tag{35}$$

where $\overline{D} \equiv D/\cos(\theta_i)$ represents the length of the insonification region, $\lambda^o \equiv 2\pi V^o_{\text{ph}}/\omega$, and $K = 4.398$ for piston sources or 5.852 for parabolic sources.

Equation (35) shows that, for a given source, the -9 dB PVB depends *only* on the ratio of the length of the insonification region to the wavelength at the chosen phase velocity and frequency and that the -9 dB PVB approaches zero as this ratio approaches infinity.

Physically, this is a manifestation of the fact that if the wavelength is very small compared to the size of the insonification region, the waveguide modes generated in the layer can properly "phase match" to the incident wave field and hence, due to destructive interference, will have a narrow phase velocity spectrum. On the other hand, for large wavelengths compared to the size of the insonification region, the generated wave modes cannot properly phase match to the incident field and the generated modes may be excited over a significant range of phase velocities. Because the guided wave modes are more or less excitable at different points of their dispersion curves (determined by their excitability functions), this means that the modes may actually be generated more strongly at phase velocities other than that given by Snell's Law even though the excitation function $\mathcal{F}^{(+)}$ is maximum at the Snell's Law phase velocity.

Transient Loading

The results presented thus far were for harmonic excitation at a single but arbitrary frequency ω. The excitation amplitudes, $A_{\pm\nu}$, are therefore frequency dependent. If the transducer mounted to the wedge actually has a frequency spectrum, say $\hat{g}(\omega)$, then, by linear superposition, the total fields in the loaded waveguide can be expressed as integrals over frequency (times thickness product) $\Omega \equiv fd$. For instance, the velocity field in front of $(+)$ or behind $(-)$ the transducer due to the propagating modes, $\mathbf{v}_p$, can be written (Ewing et al., 1957) as

$$\mathbf{v}_p^{(\pm)}(y, z, t) = \int \left(\sum_\mu A_{\pm\mu}(z, \Omega, V_{\text{ph}})\mathbf{v}_{\pm\mu}(y, \Omega, V_{\text{ph}})e^{i\frac{2\pi\Omega}{d}t}\right)d\Omega \tag{36}$$

where now $\mathcal{G}$ which appears in the definition of $A_{\pm\nu}$ is given by $\mathcal{G} = \hat{g}(\Omega)|R(\theta_i)|/4$ and since we are considering only propagating modes, the limits of the integration extend from the cutoff fd of the given mode to infinity. Also, the index μ is taken to include only the propagating modes of the structure at a given frequency thickness product Ω.

Since there are only a finite number of propagating modes at any frequency thickness product, the summation in Eq. (36) contains a finite number of terms. We can therefore interchange the summation and integration, in which case, Eq. (36) can be written

$$\mathbf{v}_p^{(\pm)}(y, z, t) = \sum_\mu \int A_{\pm\mu}(z, \Omega, V_{\text{ph}})\mathbf{v}_{\pm\mu}(y, \Omega, V_{\text{ph}})e^{i\frac{2\pi\Omega}{d}t}d\Omega$$

$$= \sum_\mu \int \mathcal{G}(\Omega)E_{\pm\mu}\mathcal{F}^{(\pm)}(V_{\text{ph}}, \Omega)\mathbf{v}_{\pm\mu}(y, \Omega, V_{\text{ph}})e^{i\left(\frac{2\pi\Omega}{d}t\mp\beta_\mu z\right)}d\Omega. \tag{37}$$

Since the phase velocity V_{ph} and frequency thickness Ω of a given mode μ are restricted to lie on that modes' dispersion curve, each of the integrals in Eq. (37) are actually along the dispersion curves of the individual modes. It is interesting to note that even when integral transform techniques are used to solve waveguide loading problems, a similar form (i.e., summation of dispersion curve integrals) results for the excited fields (Achenbach, 1973; Miklowitz, 1978). However, the present technique gives a direct physical interpretation to the integrand whereas the integral transform technique does not. Some limited experimental verification of Eq. (37), comparing

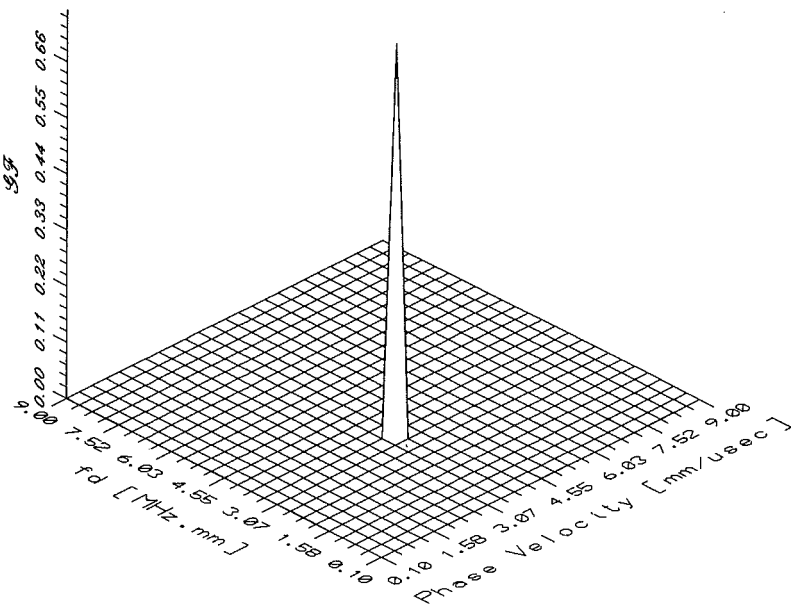


Fig. 5 Plot of the magnitude of the excitation function, $|\mathcal{G}\mathcal{F}^{(+)}_{\text{Piston}}|$ for a transducer of length $1 \cdot 10^5$ mm (3,937 in.), central frequency of 3.5 MHz, -9 dB frequency bandwidth of .5 MHz, mounted to a wedge of angle 45 deg with longitudinal velocity 2.7 mm/μsec

Downloaded 03 May 2010 to 171.66.16.20. Redistribution subject to ASME license or copyright; see http://www.asme.org/terms/Terms_Use.cfm

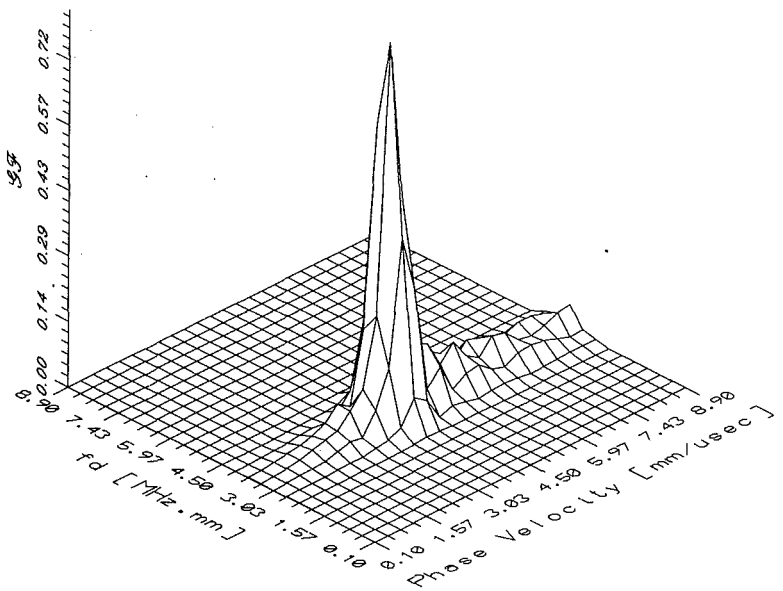


Fig. 6 Same as Fig. 5, except for a transducer length of 6.35 mm (1/4 in.)

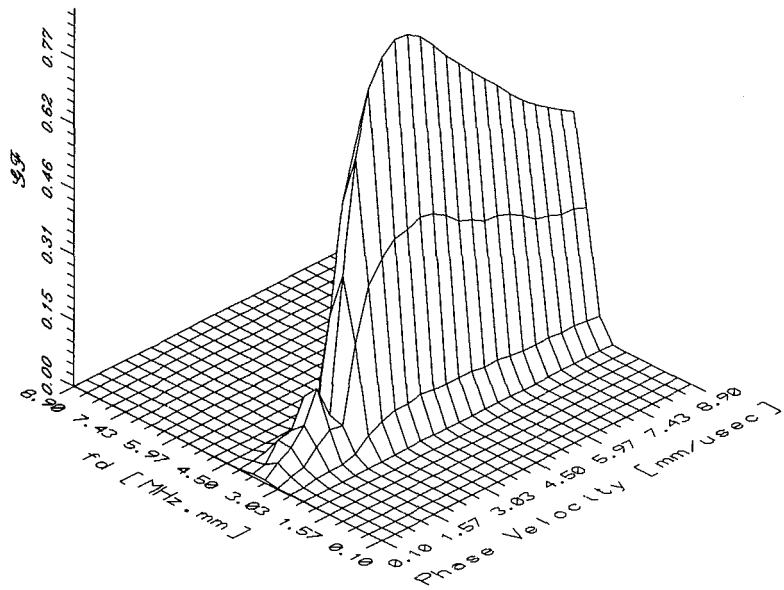


Fig. 7 Same as Fig. 5, except for a transducer length of 0.77 mm (1/33 in.)

experimentally obtained RF signals with the numerical evaluation of Eq. (37) for specific y and z can be found in Ditri, (1992).

The two functions $\mathcal{G}(\Omega)$ and $\mathcal{F}(V_{\text{ph}}, \Omega)$ determine the region in the phase velocity-frequency thickness plane in which the transducer-wedge combination is most capable of exciting waveguide modes.

Figures 5 through 7 illustrate the effect of the transducer diameter, D, on the excitation function $\mathcal{G}(\Omega)\mathcal{F}(V_{\text{ph}}, \Omega)$, and hence, on the selectivity of the transducer-wedge combination to a particular phase velocity and frequency. The transducer is assumed to have a Gaussian frequency spectrum

$$\hat{g}(\Omega) = Ae^{-\left(\frac{\Omega-\Omega_o}{\sigma_t}\right)^2}, \tag{38}$$

where the central frequency is taken as 3.5 MHz and the frequency bandwidth, σ_t, is taken as 0.5 MHz (for a 1 mm thick layer). The transducer is also assumed to generate a piston pressure profile and therefore $\mathcal{F}^{(+)}$ represents $\mathcal{F}^{(+)}_{\text{Piston}}$ given by Eq. (23). The figures are surface plots of the magnitude of the excitation function, $|\mathcal{G}(\Omega)\mathcal{F}(V_{\text{ph}}, \Omega)|$, over the phase velocity $-fd$ plane. The figures show the effect of varying the diameter of the transducer for fixed incident angle, frequency, and frequency bandwidth, and hence, varying the ratio $\overline{D}/\lambda^o$. The constant parameters in all the plots are a center frequency of 3.5 MHz, a frequency bandwidth (σ_t) of 0.5 MHz, an incident angle of 45 deg, and a shoe with longitudinal velocity, V_w, of 2.7 mm/μsec (Plexiglass). This gives a wavelength, λ^o, at the peak frequency, 3.5 MHz, of 1.09 mm. The parameter which is varied is the diameter of the transducer (D) and hence the size of the loading region on the layer, $\overline{D} = D/\cos\theta_i$. Since the wavelength, λ^o, remains the same for each plot, decreasing $\overline{D}$ decreases the ratio $\overline{D}/\lambda^o$. The diameters used in Figs. 5–7, as well as the calculated wave number and phase velocity bandwidths are given in Table 1.

In each of the plots, one should imagine the dispersion curves

Downloaded 03 May 2010 to 171.66.16.20. Redistribution subject to ASME license or copyright; see http://www.asme.org/terms/Terms_Use.cfm

of the particular layer under consideration as being superimposed on the underlying grid of phase velocity versus fd. Then, the amplitude with which each mode, μ, is generated at each particular point of its dispersion curve is given by the product of the excitability of the mode at that point, $E_\mu(\Omega, V_{ph})$, with the amplitude of the $\mathcal{GF}$ surface at that point. Therefore, the sharper the peak of the $\mathcal{GF}$ surface, the more selective the transducer-shoe combination is to a particular mode at a particular point on its dispersion curve.

As can be seen from Figs. 5-7 and Table 1, the selectivity of the transducer-wedge combination to a particular phase velocity becomes worse and worse as the ratio of the insonification region to the wavelength at the central frequency, $\overline{D}/\lambda^o$ is decreased. Figure 5 is used to illustrate the fact that if a plane wave is incident (extremely large D), then there is essentially only one value of phase velocity which can be generated with any appreciable intensity and it is given by Snell's Law once the material properties of the wedge and the incident angle are known. Figure 6 illustrates that when $\overline{D}/\lambda^o \sim 10$ the selectivity of the transducer-wedge combination is still highly peaked at the Snell's Law phase velocity but that the width of the peak (in the phase velocity direction) at the -9 dB point is now around 17 percent of the Snell's Law velocity. Finally, Fig. 7 shows that when $\overline{D}/\lambda^o \sim 1$, the transducer-wedge combination has virtually no selectivity to phase velocity since the excitation function remains over -9 dB of its maximum over a 275 percent velocity range.

An illustration of the fact that it is the ratio $\overline{D}/\lambda^o$ and not merely the size of the transducer, which determines the selectivity of the transducer to a particular phase velocity, Fig. 8 and 9, are parametric plots where the diameter and all frequency parameters are kept the same as in the previous figures while the incident angle is varied. This has the effect of varying the Snell's Law phase velocity, V^o_{ph}, and hence the wavelength $\lambda^o \equiv 2\pi V^o_{ph}/\omega$. For a given diameter transducer, the insonified region, $\overline{D}$, increases as the incident angle does. The net result is that although the transducer diameter, D, is kept constant in all plots, the ratio of loading length to wavelength, $\overline{D}/\lambda^o$ is being varied. The incident angles used in Figs. 8-9 are given in Table 2 along with the calculated Snell's Law phase velocities, and wave number and phase velocity bandwidths.

It can be seen from Figs. 8-9 that a given diameter transducer, with a given central frequency and frequency bandwidth, can be more or less selective in phase velocity depending on the incident angle θ_i. This is actually a manifestation of the fact that the ratio of loading region to wavelength $\overline{D}/\lambda^o$ increases with increasing incident angle.

Conclusions

The problem of the excitation of generally anisotropic layers by applied surface tractions has been analyzed using the normal mode expansion technique. Two loading configurations, typical of those used in nondestructive evaluation for generating waveguide modes, have been examined in detail. It has been shown how the relevant parameter in determining the selectivity of the source to a specific phase velocity is the ratio of the length of the loaded region, $\overline{D}$, to the wavelength in the phase velocity-frequency thickness plane, λ^o. It was demonstrated that for $\overline{D}/\lambda^o$ greater than approximately 10, the significant excitation (above -9 dB of the maximum) may occur over an approximately 17 percent range, whereas for $\overline{D}/\lambda^o \sim 1$ there is virtually no selectivity to a particular phase velocity.

Acknowledgments

Thanks are given to the Federal Aviation Agency in Atlantic City, NJ, and to the NASA Lewis Research Center, Cleveland, OH, for partial support of this work. Special thanks are given to Dave Galella of the FAA and Alex Vary of NASA.

Table 1 Parameters used in Figs. 5 through 7

Figure	D (mm) (in.)	$\overline{D}/\lambda^o$	σ_β (1/mm)	σ_v • 100 percent
5	$1.0 \cdot 10^5$ (3937)	$3.29 \cdot 10^6$	$1.22 \cdot 10^{-6}$	$4.233 \cdot 10^{-5}$
6	6.35 (1/4)	8.24	0.490	17.13
7	0.77 (1/33)	1.00	4.035	274.57

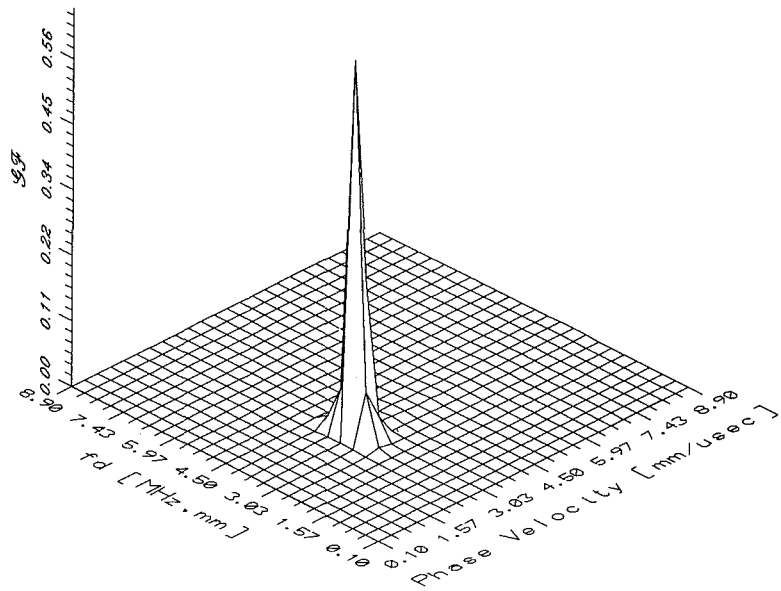


Fig. 8 Plot of the magnitude of the excitation function, $|\mathcal{GF}^{(+)}_{Piston}|$ for a transducer of length 25.4 mm (1 in.), central frequency of 3.5 MHz, -9 dB frequency bandwidth of .5 MHz, mounted to a wedge of angle 80 deg with longitudinal velocity 2.7 mm/μsec

Downloaded 03 May 2010 to 171.66.16.20. Redistribution subject to ASME license or copyright; see http://www.asme.org/terms/Terms_Use.cfm

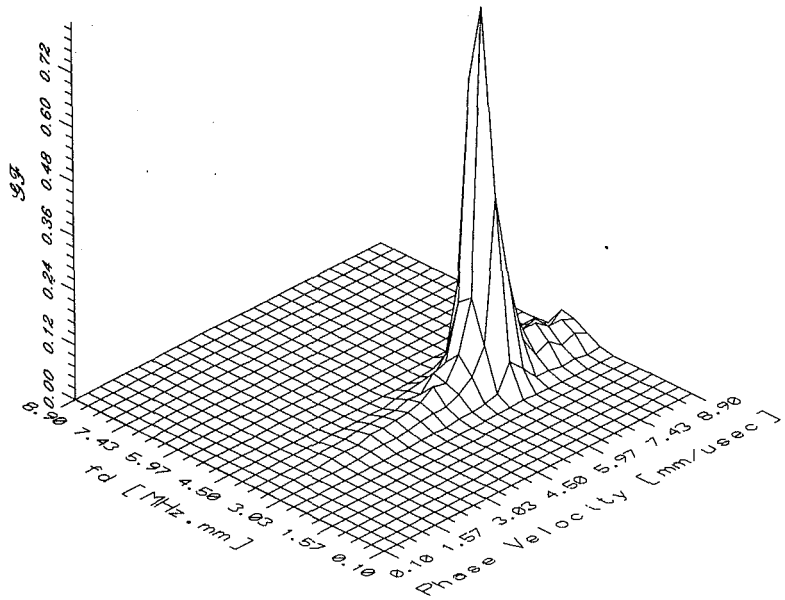


Fig. 9 Same as Fig. 8, except for an incident angle of 25 deg

Table 2 Parameters used in Figs. 8 and 9

Figure	D (mm)	θ_i (Deg)	V^o_{ph}	$\overline{D}/\lambda^o$	σ_β (1/mm)	σ_v • 100 percent
8	25.40	80	2.74	186.73	0.024	0.59
9	25.40	25	6.38	15.35	0.286	16.76

References

Achenbach, J. D., 1973, *Wave Propagation in Elastic Solids*, Elsevier, New York, NY, pp. 331–342.

Auld, B. A., and Kino, G. S., 1971, "Normal Mode Theory for Acoustic Waves and Their Application to the Interdigital Transducer," *IEEE Trans.* Vol. ED-18, pp. 898–908.

Auld, B. A., 1990a, *Acoustic Fields and Waves in Solids*, Vol. I, 2nd ed., Kreiger, FL.

Auld, B. A., 1990b, *Acoustic Fields and Waves in Solids*, Vol. II, 2nd ed., Kreiger, FL.

Bendec, F., Peretz, M., and Rokhlin, S. I., 1984, "Ultrasonic Lamb Wave Method for Sizing of Spot Welds," *Ultrasonics*, Vol. 22, No. 2, pp. 78–84.

Datta, S. K., Shah, A. H., Chakraborty, T., and Bratton, R. L., 1988, "Wave Propagation in Laminated Composite Plates: Anisotropy and Interface Effects," *Wave Propagation in Structural Composites*, AMD-Vol. 90, A. K. Mal, and T. C. T. Ting, eds., ASME, New York, pp. 39–52.

Ditri, J. J., and Rose, J. L., 1992, "Excitation of Guided Elastic Wave Modes in Hollow Cylinders by Applied Surface Tractions," *J. Appl. Phys.*, Vol. 72, No. 7, pp. 2589–2597.

Ditri, J. J., 1992, "Some Theoretical and Experimental Aspects of the Generation of Guided Elastic Waves Using Finite Sources," Ph.D. Thesis, Drexel University, Philadelphia, PA.

Ewing, W. M., Jardetsky, W. S., and Press, F., 1956, *Elastic Waves in Layered Media*, McGraw-Hill, New York, pp. 61–62.

Folk, R., Herczynski, A., 1986, "Solutions of Elastodynamic Slab Problems Using a New Orthogonality Condition," *J. Acoust. Soc. Am.*, Vol. 80, No. 4, pp. 1103–1110.

Herczynski, A., and Folk, R., 1989, "Orthogonality Conditions for the Pochammer—Chree Modes," *Q. Jl. Mech. Appl. Math.*, Vol. 42, Pt. 4, pp. 523–536.

Karim, M. R., Mal, A. K., and Bar-Cohen, Y., 1990, "Determination of the Elastic Constants of Composites Through Inversion of Leaky Lamb Wave Data," *Review of Progress in Quantitative NDE*, D. O. Thompson and D. E. Chimenti, eds., Vol. 9.

Kino, G. S., 1987, *Acoustic Waves: Devices, Imaging and Digital Signal Processing*, Prentice-Hall, Englewood Cliffs, NJ.

Li, Y., Thompson, R. B., 1990, "Influence of Anisotropy on the Dispersion Characteristics of Guided Ultrasonic Plate Modes," *J. Acoust. Soc. Am.*, Vol. 87, No. 5, pp. 1911–1931.

Mal, A. K., Gorman, M., and Prosser, W., 1992, "Material Characterization of Composite Laminates Using Low Frequency Plate Wave Dispersion Data," *Review of Progress in Quantitative NDE*, D. O. Thompson and D. E. Chimenti, eds. , Vol. 11B, pp. 1451–1458.

Miklowitz, J., 1978, *The Theory of Elastic Waves and Waveguides*, North-Holland, New York, pp. 409–430.

Nayfeh, A. H., Taylor, T. W., and Chimenti, D. E., 1988, "Theoretical Wave Propagation in Multilayered Orthotropic Media," ASME, *Wave Propagation in Structural Composites*, AMD-Vol. 90, A. K. Mal, and T. C. T. Ting, eds., ASME, New York, pp. 17–27.

Pilarski, A., and Rose, J. L., 1992, "Utility of Subsurface Longitudinal Waves in Composite Material Characterization," *Journal of Nondestructive Evaluation*, to be published.

Rokhlin, S. I., Wu, C. Y., and Wang, L., 1990, "Application of Coupled Ultrasonic Plate Modes for Elastic Constant Reconstruction of Anisotropic Materials," *Review of Progress in Quantitative NDE*, D. O. Thompson and D. E. Chimenti, eds., Vol. 9, pp. 1403–1410.

Solie, L. P., and Auld, B. A., 1972, "Elastic Waves in Free Anisotropic Plates," *J. Acoust. Soc. Am.*, Vol. 54, No. 1, pp. 50–65.

Spetzler, H., and Datta, S., 1990, "Experimental Flaw Detection by Scattering of Plate Waves," *Elastic Waves and Ultrasonic Nondestructive Evaluation*, S. K. Datta, J. D. Achenbach, and Y. S. Rajapakse eds., Elsevier, New York, pp. 135–141.

Viktorov, I. A., 1967, *Rayleigh and Lamb Waves, Physical Theory and Applications*, Plenum Press, New York.

Downloaded 03 May 2010 to 171.66.16.20. Redistribution subject to ASME license or copyright; see http://www.asme.org/terms/Terms_Use.cfm

An Exact Stiffness Method for Elastodynamics of a Layered Orthotropic Half-Plane

Y. Wang

R. K. N. D. Rajapakse

Department of Civil Engineering,
University of Manitoba,
Winnipeg, R3T 2N2 Canada

A method is presented in this paper to compute displacements and stresses of a multilayered orthotropic elastic half-plane under time-harmonic excitations. The half-plane region under consideration consists of a number of layers with different thicknesses and material properties. Exact layer stiffness matrices describing the relationship between Fourier transforms of displacements and tractions at the upper and bottom surface of each layer are established explicitly by using the analytical general solutions for displacements and stresses of a homogeneous orthotropic elastic medium. The global stiffness matrix which is also symmetric and banded is assembled by considering the traction continuity conditions at the interface between adjacent layers of the multilayered half-plane. The numerical solution of the global stiffness equation results in the solutions for Fourier transform of displacements at layer interfaces. Thereafter displacements and stresses of the multilayered plane can be obtained by the numerical integration of Fourier integrals. Only negative exponential terms of Fourier transform parameter are found to appear in the elements of layer stiffness matrices. This ensures the numerical stability in the solution of the global stiffness equation. In addition, the size of the final equation system is nearly one-half of that corresponding to the conventional matrix approach for layered media based on the determination of layer arbitrary coefficients. The present method provides accurate solutions for both displacements and stresses over a wide range of frequencies and layer thicknesses. Selected numerical results are presented to portray the influence of layering, material orthotropy, and frequency of excitation on the response of five layered systems. Time-domain solutions are also presented to demonstrate the features of transient surface displacements due to a surface loading pulse applied to layered orthotropic half-planes.

Introduction

The study of dynamic response of multilayered media under time-harmonic loadings is of fundamental importance to several disciplines such as geophysics, earthquake engineering, geomechanics, composites, nondestructive testing, etc. The consideration of different materials and layers of different thickness in a multilayered domain results in insurmountable algebraic difficulties in obtaining an explicit analytical solution. A number of semi-analytical and numerical methods have been developed over the last 40 years to evaluate the static and dynamic response of an isotropic multilayered medium. The earliest approach is the transfer matrix method based on the determination of layer arbitrary coefficients developed by Thomson (1950) and Haskell (1953, 1960, 1962). A procedure similar to the transfer matix method was also reported independently by Pestel and Leckie (1963). The Thomson-Haskell technique has significant drawbacks in the numerical implementation due to the presence of certain exponential terms. Improved formulations were developed later by Knopoff (1964), Gilbert and Backus (1966), Watson (1970), and Schwab (1970). A finite-element-type approximation has been proposed by Waas (1972), Waas (1980), Kausel and Peek (1982), and Oner and Dong (1988) to determine the response of an isotropic multilayered medium. In this approach the medium is divided into a number of thin layers within which the displacements have prescribed variations in the vertical direction (e.g., linear). A comprehensive and rigorous treatment of Green's functions of an isotropic layered medium has been presented by Luco and Apsel (1983) and Apsel and Luco (1983). Applicability and accuracy of these Green's functions in the boundary element method has also been reported in the literature (Apsel and Luco, 1987). More recently Mal (1988a) presented a different manipulation of the matrix approach

Contributed by the Applied Mechanics Division of THE AMERICAN SOCIETY OF MECHANICAL ENGINEERS for publication in the ASME JOURNAL OF APPLIED MECHANICS.

Discussion on this paper should be addressed to the Technical Editor, Professor Lewis T. Wheeler, Department of Mechanical Engineering, University of Houston, Houston, TX 77204-4792, and will be accepted until four months after final publication of the paper itself in the ASME JOURNAL OF APPLIED MECHANICS.

Manuscript received by the ASME Applied Mechanics Division, Sept. 25, 1991; final revision, Dec. 3, 1992. Associate Technical Editor: S. K. Datta.

Copyright © 1994 by ASME

Downloaded 03 May 2010 to 171.66.16.20. Redistribution subject to ASME license or copyright; see http://www.asme.org/terms/Terms_Use.cfm

based on layer arbitrary coefficients to yield a matrix formulation which is free from numerically unstable terms but has the same size as that of conventional matrix procedures. In Mal's approach the basic unknowns consist of a combination of layer arbitrary coefficients and displacements at the surface and the bottom layer half-space interface.

A review of the literature reveals that studies related to dynamics of multilayered orthotropic media are limited. Payton (1984) presents an excellent treatment of elastodynamics of a transversely isotropic material and a review of the existing literature. Solutions for point loads acting inside a full space and a surface load on a half-space are also presented by Payton (1984). A recent study by Rajapakse and Wang (1991) presents explicit solutions in terms of the Fourier integrals for Green's functions corresponding to point loads acting inside an orthotropic elastic half-plane. Mal (1988b) extended the matrix approach presented earlier (Mal, 1988a) to include anisotropy. Seale and Kausel (1989) presents an extension of the thin layer method (Waas, 1980; Kausel and Peek, 1982) to study the dynamics of a multilayered cross-anisotropic elastic half-space.

In this paper, a technique is presented to compute displacements and stresses of a multilayered orthotropic elastic half-plane subjected to time-harmonic loadings. The exact general solutions of a homogeneous orthotropic elastic medium are used to construct explicit layer stiffness matrices which describe the relationship between Fourier transform of displacements and tractions at the upper and bottom surface of a layer. The layer stiffness matrix, being 4×4 for a plane problem, is symmetric and its elements involve only negative exponentials and other numerically stable terms of the Fourier transform parameter. The stiffness matrix of the underlying half-plane is a 2×2 matrix and is also derived explicitly by using the general solutions. The global stiffness matrix of the multilayered plane is assembled by using layer stiffness matrices and by considering the continuity of tractions at each interface. The global stiffness matrix is a banded symmetric matrix which is also constrained against rigid-body displacements due to the consideration of regularity conditions at $z\to\infty$ in the derivation of the stiffness matrix of the underlying half-plane. The size of the global equation system is nearly one-half of that corresponding to the conventional matrix approach based on layer arbitrary coefficients. The numerical solution of the global stiffness equation system for discrete values of the Fourier transform parameter results in the Fourier transform of displacements at layer interfaces. Thereafter, displacements and stresses can be computed by numerical integration of Fourier integrals. Due to the explicit derivation of exact layer stiffness matrices which involve only exponentially decaying terms of the Fourier transform parameter it is found that the present scheme is numerically very stable. The present scheme can be applied over a wide range of frequencies and layer thicknesses. Selected numerical results for displacements and stresses of corresponding to five layered orthotropic systems are presented in this study to portray the influence of layering, degree of material anisotropy, and the frequency of excitation on the response. Selected time-domain solutions are also presented for layered orthotropic half-planes subjected to a vertical loading pulse.

General Solutions of Orthotropic Half-Plane

Consider a homogeneous orthotropic elastic medium with a Cartesian coordinate system (x, y, z) defined as shown in Fig. 1. The stress-strain relationship of a homogeneous orthotropic elastic material can be expressed as (Lekhnitskii, 1963)

$$\sigma_{xx}=c_{11}\epsilon_{xx}+c_{12}\epsilon_{yy}+c_{13}\epsilon_{zz} \tag{1}$$

$$\sigma_{yy}=c_{12}\epsilon_{xx}+c_{22}\epsilon_{yy}+c_{23}\epsilon_{zz} \tag{2}$$

$$\sigma_{zz}=c_{13}\epsilon_{xx}+c_{23}\epsilon_{yy}+c_{33}\epsilon_{zz} \tag{3}$$

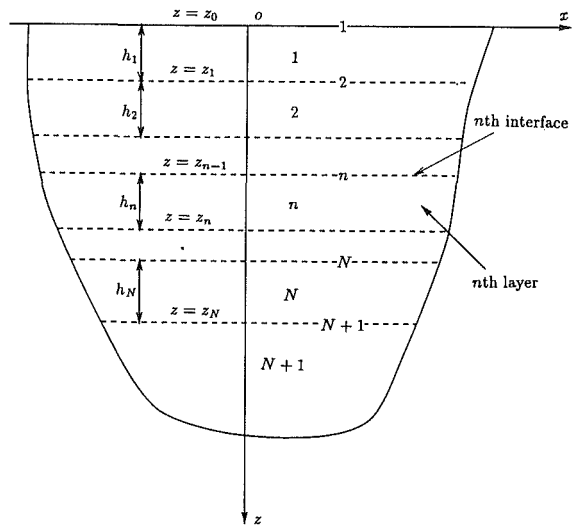


Fig. 1 Geometry of a multilayered system

$$\sigma_{xy}=2c_{55}\epsilon_{xy} \tag{4}$$

$$\sigma_{xz}=2c_{44}\epsilon_{xz} \tag{5}$$

$$\sigma_{yz}=2c_{66}\epsilon_{yz} \tag{6}$$

where c_{11}, c_{12}, c_{13}, c_{22}, c_{23}, c_{33}, c_{44}, c_{55}, and c_{66} are material constants. It is assumed that the deformations are plane strain in the xz-plane. Therefore, $\epsilon_{yy}=\epsilon_{yz}=\epsilon_{xy}=0$ and c_{12}, c_{22}, c_{55}, and c_{66} do not appear in subsequent manipulations. It is noted that constitutive equations for plane-strain problems corresponding to orthotropic materials are identical to those corresponding to a transversely isotropic material with the xy-plane as the plane of isotropy.

A set of nondimensional parameters α, β, κ, and γ are introduced as follows to simplify subsequent algebraic manipulations (Payton, 1984):

$$\alpha=\frac{c_{33}}{c_{44}},\quad \beta=\frac{c_{11}}{c_{44}},\quad \kappa=\frac{c_{13}+c_{44}}{c_{44}},\quad \gamma=1+\alpha\beta-\kappa^2. \tag{7}$$

Define the Fourier transforms (Sneddon, 1951) of function $\phi(x, z)$ with respect to the x-coordinate as

$$\bar{\phi}(\lambda, z)=\frac{1}{\sqrt{2\pi}}\int_{-\infty}^{\infty}\phi(x, z)e^{-i\lambda x}dx \tag{8}$$

and the inverse formula is given by

$$\phi(x, z)=\frac{1}{\sqrt{2\pi}}\int_{-\infty}^{\infty}\bar{\phi}(\lambda, z)e^{i\lambda x}d\lambda. \tag{9}$$

It is assumed that the motions under consideration are time-harmonic of the form $e^{i\omega t}$, where ω is the circular frequency and the term $e^{i\omega t}$ is omitted in the sequel. Let u_i and σ_{ij} $(i, j=x, z)$ denote the displacement and stress components, respectively. It can be shown that the Fourier transforms of displacements and stresses with respect to the x-coordinate can be expressed as (Rajapakse and Wang, 1991)

$$i\bar{u}_x(\zeta, x)=s_1Ae^{-\delta\xi_1 z}-s_1Be^{\delta\xi_1 z}+s_2Ce^{-\delta\xi_2 z}-s_2Ee^{\delta\xi_2 z} \tag{10}$$

$$\bar{u}_z(\zeta, z)=Ae^{-\delta\xi_1 z}+Be^{\delta\xi_1 z}+Ce^{-\delta\xi_2 z}+Ee^{\delta\xi_2 z} \tag{11}$$

$$\bar{\sigma}_{xx}(\zeta, z)=\eta_1Ae^{-\delta\xi_1 z}-\eta_1Be^{\delta\xi_1 z}+\eta_2Ce^{-\delta\xi_2 z}-\eta_2Ee^{\delta\xi_2 z} \tag{12}$$

$$i\bar{\sigma}_{xz}(\zeta, z)=\eta_3Ae^{-\delta\xi_1 z}+\eta_3Be^{\delta\xi_1 z}+\eta_4Ce^{-\delta\xi_2 z}+\eta_4Ee^{\delta\xi_2 z} \tag{13}$$

$$\bar{\sigma}_{zz}(\zeta, z)=\eta_5Ae^{-\delta\xi_1 z}-\eta_5Be^{\delta\xi_1 z}+\eta_6Ce^{-\delta\xi_2 z}-\eta_6Ee^{\delta\xi_2 z} \tag{14}$$

where $A(\zeta)$, $B(\zeta)$, $C(\zeta)$, and $E(\zeta)$ are arbitrary functions to be determined by invoking appropriate boundary and/or continuity conditions relevant to a given problem and the parameters δ and ζ are defined as

Downloaded 03 May 2010 to 171.66.16.20. Redistribution subject to ASME license or copyright; see http://www.asme.org/terms/Terms_Use.cfm

$$\delta^2=\rho\omega^2/c_{44};\quad \zeta=\lambda/\delta, \tag{15}$$

while ρ denotes the mass density. In addition,

$$\xi_1(\zeta)=\frac{(\gamma\zeta^2-1-\alpha+\sqrt{\Phi})^{1/2}}{\sqrt{2\alpha}};$$

$$\xi_2(\zeta)=\frac{(\gamma\zeta^2-1-\alpha-\sqrt{\Phi})^{1/2}}{\sqrt{2\alpha}} \tag{16}$$

$$\Phi(\zeta)=(\gamma\zeta^2-1-\alpha)^2-4\alpha(\beta\zeta^4-\beta\zeta^2-\zeta^2+1) \tag{17}$$

$$s_1=\frac{\alpha\xi_1^2+1-\zeta^2}{\kappa\xi_1\zeta};\quad s_2=\frac{\alpha\xi_2^2+1-\zeta^2}{\kappa\xi_2\zeta} \tag{18}$$

$$\eta_1=\frac{c_{44}\delta}{\kappa\xi_1}[(\gamma-1+\kappa)\xi_1^2+\beta(1-\zeta^2)];$$

$$\eta_2=\frac{c_{44}\delta}{\kappa\xi_2}[(\gamma-1+\kappa)\xi_2^2+\beta(1-\zeta^2)] \tag{19}$$

$$\eta_3=\frac{-c_{44}\delta}{\kappa\zeta}[(\alpha\xi_1^2+1)+(\kappa-1)\zeta^2];$$

$$\eta_4=\frac{-c_{44}\delta}{\kappa\zeta}[(\alpha\xi_2^2+1)+(\kappa-1)\zeta^2] \tag{20}$$

$$\eta_5=\frac{c_{44}\delta}{\kappa\xi_1}[(\kappa-1)(1-\zeta^2)-\alpha\xi_1^2];$$

$$\eta_6=\frac{c_{44}\delta}{\kappa\xi_2}[(\kappa-1)(1-\zeta^2)-\alpha\xi_2^2]. \tag{21}$$

In Eq. (16), radicals ξ_1 and ξ_2 are selected such that $\mathrm{Re}(\xi_1, \xi_2)>0$ in order to satisfy regularity conditions as $z\to\infty$. The branch points of ξ_1 and ξ_2 are given by

$$\zeta_p=\pm 1/\sqrt{\beta};\quad \zeta_s=\pm 1. \tag{22}$$

In the classical matrix approach the general solutions given by Eqs. (10)–(14) are used for each layer and a set of complex linear simultaneous equations based on the boundary conditions at the top surface, and continuity conditions at layer interfaces are established to determine arbitrary coefficients corresponding to the system shown in Fig. 1 (four coefficients for each layer and two coefficients for the underlying half-plane resulting in a total of $4N+2$ unknowns). The numerical solution of the simultaneous equation system for discrete values of the Fourier transform parameter ζ results in the solutions for arbitrary coefficients corresponding to each layer and the underlying half-plane. Thereafter Eqs. (9)–(14) can be used to compute displacements and stresses by using numerical integration procedures. Thomson (1950) presented a matrix decomposition of the simultaneous equation system by taking into consideration the block diagonal form of the system. A systematic numerical implementation of Thomson's procedure for layered media was given by Haskell (1953, 1960). The Thomson-Haskell algorithm becomes numerically unstable for short wavelengths due to the presence of certain exponential terms. As an alternative to the classical approaches (Haskell, 1953; Knopoff, 1964; Mal, 1988a,b), based on the determination of layer arbitrary coefficients, the authors present a numerically stable and computationally efficient exact stiffness matrix approach in the ensuing sections to evaluate the dynamic response of layered orthotropic half-planes.

Layer and Half-Plane Stiffness Matrices

A multilayered orthotropic elastic half-plane with a total of N layers of finite thickness is considered (Fig. 1). Layers and interfaces are numbered as shown in Fig. 1. Let $\bar{u}_i^{(n)}$ denote the Fourier transform of displacements of the nth interface and $\bar{\sigma}_{ij1}^{(n)}$ and $\bar{\sigma}_{ij2}^{(n)}$ denote the Fourier transform of stress components σ_{ij} at the top and bottom surface of the nth layer, respectively. Then, the following relationships can be established for the nth layer of the system shown in Fig. 1.

$$\bar{\mathbf{u}}^{(n)}=\mathbf{G}^{(n)}\mathbf{a}^{(n)},\quad n=1, 2, \ldots, N \tag{23}$$

$$\bar{\boldsymbol{\sigma}}^{(n)}=\mathbf{F}^{(n)}\mathbf{a}^{(n)},\quad n=1, 2, \ldots, N \tag{24}$$

where

$$\bar{\mathbf{u}}^{(n)}=\langle i\bar{u}_x^{(n)}\ \ \bar{u}_z^{(n)}\ \ i\bar{u}_x^{(n+1)}\ \ \bar{u}_z^{(n+1)}\rangle \tag{25}$$

$$\bar{\boldsymbol{\sigma}}^{(n)}=\langle -i\bar{\sigma}_{xz1}^{(n)}\ \ -\bar{\sigma}_{zz1}^{(n)}\ \ i\bar{\sigma}_{xz2}^{(n)}\ \ \bar{\sigma}_{zz2}^{(n)}\rangle \tag{26}$$

$$\mathbf{a}^{(n)}=\langle A^{(n)}\ \ B^{(n)}\ \ C^{(n)}\ \ D^{(n)}\rangle \tag{27}$$

$$\mathbf{G}^{(n)}=\begin{pmatrix} s_1e_{1,n}^{-1} & -s_1e_{1,n} & s_2e_{2,n}^{-1} & -s_2e_{2,n} \\ e_{1,n}^{-1} & e_{1,n} & e_{2,n}^{-1} & e_{2,n} \\ s_1e_{1,n+1}^{-1} & -s_1e_{1,n+1} & s_2e_{2,n+1}^{-1} & -s_2e_{2,n+1} \\ e_{1,n+1}^{-1} & e_{1,n+1} & e_{2,n+1}^{-1} & e_{2,n+1} \end{pmatrix} \tag{28}$$

$$\mathbf{F}^{(n)}=\begin{pmatrix} -\eta_3e_{1,n}^{-1} & -\eta_3e_{1,n} & -\eta_4e_{2,n}^{-1} & -\eta_4e_{2,n} \\ -\eta_5e_{1,n}^{-1} & \eta_5e_{1,n} & -\eta_6e_{2,n}^{-1} & \eta_6e_{2,n} \\ \eta_3e_{1,n+1}^{-1} & \eta_3e_{1,n+1} & \eta_4e_{2,n+1}^{-1} & \eta_4e_{2,n+1} \\ \eta_5e_{1,n+1}^{-1} & -\eta_5e_{1,n+1} & \eta_6e_{2,n+1}^{-1} & -\eta_6e_{2,n+1} \end{pmatrix} \tag{29}$$

where

$$e_{i,j}=e^{\delta\xi_i z_j},\quad i=1, 2;\quad j=1, 2, \ldots, N+1. \tag{30}$$

In Eq. (27), $A^{(n)}$, $B^{(n)}$, $C^{(n)}$, and $D^{(n)}$ denote the arbitrary coefficients corresponding to the nth layer where $z_{n-1}\le z\le z_n$.

In view of Eqs. (23), (24), (28), and (29), the layer stiffness matrix $\mathbf{K}^{(n)}$, which describes the relationship between the $\bar{\mathbf{u}}^{(n)}$ and $\bar{\boldsymbol{\sigma}}^{(n)}$ corresponding to the nth layer, can be expressed as

$$\bar{\boldsymbol{\sigma}}^{(n)}=\mathbf{K}^{(n)}\bar{\mathbf{u}}^{(n)} \tag{31}$$

where

$$\mathbf{K}^{(n)}=\text{symm. }[k_{ij}],\quad i, j=1, 2, 3, 4 \tag{32}$$

$$k_{1j}=-[\eta_3(a_j+b_j\lambda_{1n})+\eta_4(g_j+d_j\lambda_{2n})],\quad j=1, 2, 3, 4 \tag{33}$$

$$k_{2j}=-[\eta_5(a_j-b_j\lambda_{1n})+\eta_6(g_j-d_j\lambda_{2n})],\quad j=2, 3, 4 \tag{34}$$

$$k_{33}=k_{11},\quad k_{34}=-k_{12} \tag{35}$$

$$k_{44}=k_{22} \tag{36}$$

$$\lambda_{in}=e^{-\delta\xi_i h_n},\quad i=1, 2 \tag{37}$$

and the parameters a_i, b_i, g_i, d_i $(i=1, 2, 3, 4)$ are defined in the Appendix. At this stage it is important to note that the layer stiffness matrix $\mathbf{K}^{(n)}$ is a function of only the layer thickness, layer material properties, frequency of excitation, and the Fourier transform parameter ζ. The elements k_{ij} are functions of s_1, s_2, η_i $(i=1, 2, \ldots, 6)$ and λ_{in} $(i=1, 2)$. All these functions are numerically very stable and $\mathbf{K}^{(n)}$ is found to be a well-conditioned matrix for all values of ζ and h_n. Unlike the Thomson-Haskell technique there are no squared large exponential terms that must vanish identically in the numerical evaluation. Only negative exponentials that decrease rapidly with increasing ζ or h_n are involved in k_{ij}.

For the underlying half-plane, the general solutions involves only two coefficients $A^{(N+1)}$ and $C^{(N+1)}$ due to the regularity condition for displacements and stresses at $z\to\infty$. The stiffness matrix of the bottom half-plane can be expressed as

$$\bar{\boldsymbol{\sigma}}^{(N+1)}=\mathbf{K}^{(N+1)}\bar{\mathbf{u}}^{(N+1)} \tag{38}$$

where

$$\bar{\boldsymbol{\sigma}}^{(N+1)}=\langle -i\bar{\sigma}_{xz1}^{(N+1)}\ \ -\bar{\sigma}_{zz1}^{(N+1)}\rangle^T \tag{39}$$

$$\bar{\mathbf{u}}^{(N+1)}=\langle i\bar{u}_x^{(N+1)}\ \ \bar{u}_z^{(N+1)}\rangle^T \tag{40}$$

$$\mathbf{K}^{(N+1)}=\frac{c_{44}\delta}{(s_1-s_2)}\begin{pmatrix} (\eta_3-\eta_4) & (s_2\eta_3-s_1\eta_4) \\ \text{symm.} & (s_2\eta_5-s_1\eta_6) \end{pmatrix}. \tag{41}$$

It is noted that exponential terms are not involved in the

Downloaded 03 May 2010 to 171.66.16.20. Redistribution subject to ASME license or copyright; see http://www.asme.org/terms/Terms_Use.cfm

expression of $\mathbf{K}^{(N+1)}$ and its elements depends on the material properties, frequency of excitation, and the parameter ζ.

Global Stiffness Matrix

The global stiffness matrix of the multilayered half-plane is assembled by using the layer stiffness matrices and continuity condition of traction at layer interfaces. For example, the traction continuity conditions at the nth interface can be expressed as

$$\langle [\bar{\sigma}_{xz2}^{(n-1)} - \bar{\sigma}_{xz1}^{(n)}] \; [\bar{\sigma}_{zz2}^{(n-1)} - \bar{\sigma}_{zz1}^{(n)}] \rangle = \langle \bar{p}_x^{(n)} \quad \bar{p}_z^{(n)} \rangle \qquad (42)$$

where $\bar{p}_i^{(n)}$ is the Fourier transform (defined similar to Eq. (8)) of the externally applied loads in the i-direction ($i=x, z$) at the nth interface.

The consideration of Eq. (42) at each layer interface together with Eqs. (31) and (38) results in the following global equation system:

$$\begin{pmatrix} \mathbf{K}^{(1)} & & & \\ & \mathbf{K}^{(2)} & & \\ & & \mathbf{K}^{(N)} & \\ & & & \mathbf{K}^{(N+1)} \end{pmatrix} \begin{pmatrix} i\bar{u}_x^{(1)} \\ \bar{u}_z^{(1)} \\ \\ i\bar{u}_x^{(N+1)} \\ \bar{u}_z^{(N+1)} \end{pmatrix} = \begin{pmatrix} i\bar{p}_x^{(1)} \\ \bar{p}_z^{(1)} \\ \\ i\bar{p}_x^{(N+1)} \\ \bar{p}_z^{(N+1)} \end{pmatrix}. \qquad (43)$$

The Eq. (43) is solved for discrete values of the Fourier transform parameter ζ and the Eq. (9) with appropriate symmetry or antisymmetry conditions of externally applied loads can be used to compute the displacement at any arbitrary location along the interface. Stresses at the top and bottom interfaces of a layer can be obtained by using Eqs. (31) and (9). If displacements within points in a layer is required, then it is convenient to define a set of fictitious planes through these points and to consider these as additional layers. Alternatively, Eq. (23) can be used to compute $\mathbf{a}^{(n)}$ for a layer and thereafter compute displacements using Eqs. (9), (10), and (11). This, however, may involve the inversion of numerically ill-conditioned matrices such as $\mathbf{G}^{(n)}$ for large values of ζ and consequently loss of precision. If loads are applied within a layer, then fictitious interfaces are considered at the loading levels. It is also noted that the eigenvalues of the stiffness matrix in Eq. (43) correspond directly to the wave numbers (or velocities) of the surface waves of the layered system and the eigenvectors are the corresponding displacements at layer interfaces. In addition, the size of the final equation system (i.e., Eq. (43)) is equal to $2(N+1)$, which is nearly one-half of that corresponding to the classical approach (Thomson, 1950; Mal, 1988a,b) based on the solution of layer arbitrary coefficients $A^{(n)}$, $B^{(n)}$, $C^{(n)}$, and $E^{(n)}$. This reduction of the size of final equation system together with the symmetry of the system and the fact that the displacements are directly determined as the basic unknowns adds to the computational efficiency of the formulation.

Numerical Results and Discussion

The authors have developed a computer code based on the preceeding analysis to evaluate the dynamic response of a multilayered orthotropic elastic half-plane. The tasks performed by the computer code can be described as (a) the computation and assembly of stiffness matrices corresponding to each layer and the underlying half-plane of the multilayered region to establish Eq. (43) for a specified value of ζ; (b) the solution of Eq. (43) to obtain the interlayer displacement vector in the transformed domain; and (c) the evaluation of Fourier-type integrals defined by Eq. (9) by using an adaptive version of Filon's numerical integration scheme (Tranter, 1956). Note that once the values of $\bar{u}_i$ and $\bar{\sigma}_{ij}$ corresponding to a certain evaluation (i.e., z-coordinate) are computed, thereafter the displacements and stresses at any arbitrary epicentral distance (i.e., x-coordinate) at that evaluation can be computed by using Eq. (9). In accordance with reality, materials are assumed to be attenuating (i.e., complex c_{ij} or α, β and κ in Eq. (7) which may be frequency dependent). This also results in the path of integration (i.e., real ζ-axis) free of any singularities. If accurate experimental data is available then a complex moduli can be established for the material. On the other hand, negligible material attenuation (one percent complex part) is assumed in the evaluation of the response of a multilayered medium mainly to facilitate the numerical integration along the real ζ-axis (Schwab, 1970; Aspel and Luco, 1983). This technique with a one percent complex part has been used in the present study to evaluate all integrals.

Table 1 Material constants ($\times 10^9$ N/m^2)

	c_{11}	c_{12}	c_{33}	c_{13}	c_{44}	ρ(g/cm^3)
isotropic	24.0	8.0	24.0	8.0	8.0	2.0
layered soil[1]	6.25	2.19	4.57	1.74	1.40	2.0
beryl rock	4.13	1.47	3.62	1.01	1.0	2.0
Al_2O_3	33.8	14.3	24.5	14.3	5.0	3.96
SiC	50.2	9.5	56.5	5.6	16.9	3.10
nylon	0.168	0.06	0.512	0.104	0.0666	1.135
aluminum[2]	10.9	5.6	10.9	5.6	2.65	2.7

[1] limestone/sandstone layered system; [2] isotropic

Table 2 Thickness distribution of multilayered systems

System No.	Layer thickness h_1/a	h_2/a	h_3/a
1	∞ (layered soil)	—	—
2	0.3 (layered soil)	0.7 (beryl rock)	∞ (isotropic)
3	1.0 (layered soil)	1.0 (beryl rock)	∞ (isotropic)

The numerical stability and the accuracy of the present stiffness matrix technique have been verified through the comparison with the explicit analytical solution for a homogeneous orthotropic half-plane (Rajapakse and Wang, 1991). A homogeneous half-plane consisting of beryl rock (Table 1) under a uniformly distributed load of intensity q_0 and width "$2a$" applied at a depth "a" below the free surface is considered for this purpose. The half-plane is discretized by using two models; the first model has ten layers (uniform thickness $h/a=0.5$) with an underlying half-plane and the second model has 25 layers ($h/a=0.2$) with a bottom half-plane. Comparison of numerical results corresponding to the two multilayered models with the explicit solution (Rajapakse and Wang, 1991) shows less than one percent difference.

In this paper, selected numerical results corresponding to five layered systems are presented. The properties of different materials considered in the numerical study are given in Table 1. The thickness distribution of the first set of layered systems considered in the numerical study is given in Table 2. The three layered systems defined in Table 2 are subjected to vertical and horizontal uniform strip loads of intensity q_0 and width "$2a$." This problem can be considered as an approximation of the response of a flexible strip footing on layered anisotropic soils and pavement systems subjected to dynamic loadings. The numerical results are presented in terms of nondimensional displacements (compliances) $u_{ij}^*(x, z) = u_{ij}(x, z)c_{44}^{(1)}/(aq_0)$, where u_{ij} denotes the displacement in the i-direction ($i=x, z$) due to an applied load acting in the j-direction ($j=x, z$) and $c_{44}^{(1)}$ is the moduli c_{44} of the top layer (Fig. 1). A nondimensional frequency a_0 defined as $a_0 = a\omega[\rho^{(1)}/c_{44}^{(1)}]^{1/2}$ where $\rho^{(1)}$ is the mass

Downloaded 03 May 2010 to 171.66.16.20. Redistribution subject to ASME license or copyright; see http://www.asme.org/terms/Terms_Use.cfm

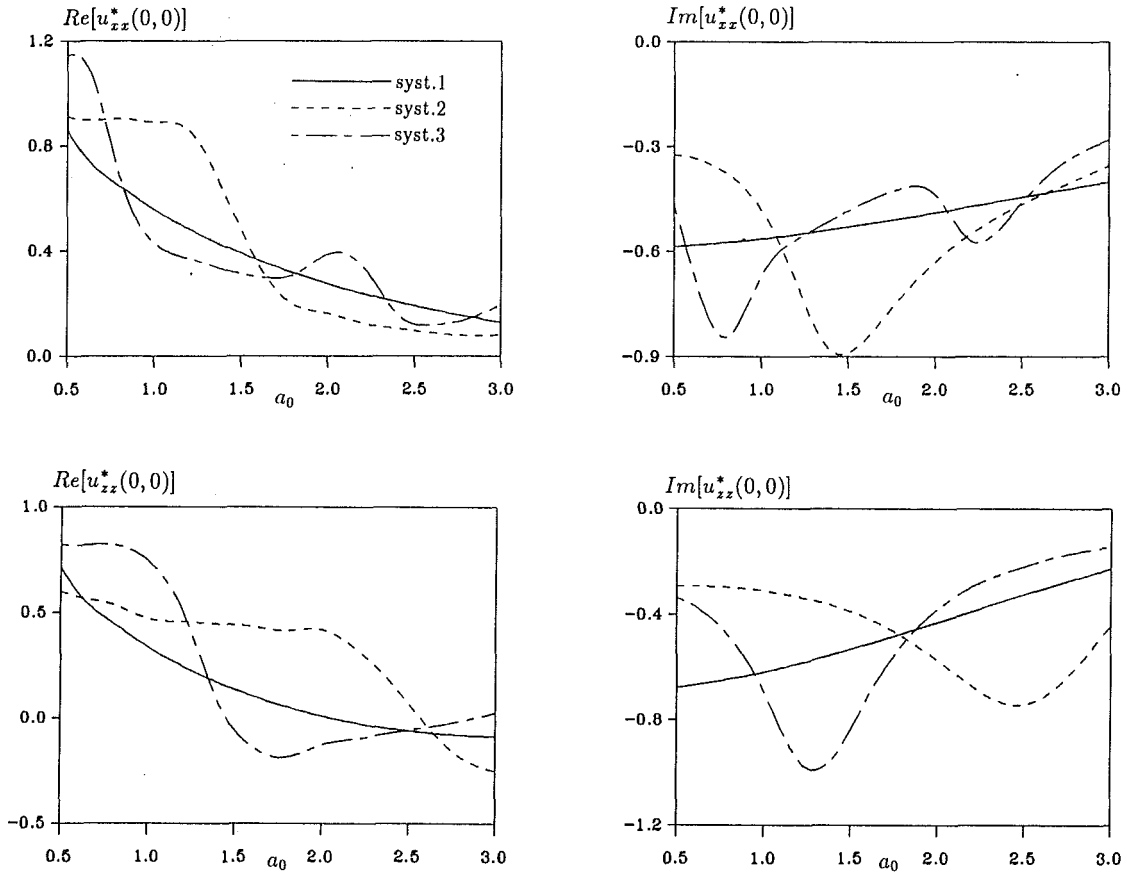


Fig. 2 Normalized displacements u^*_{xx} and u^*_{zz} due to strip loads at $z/a = 0$

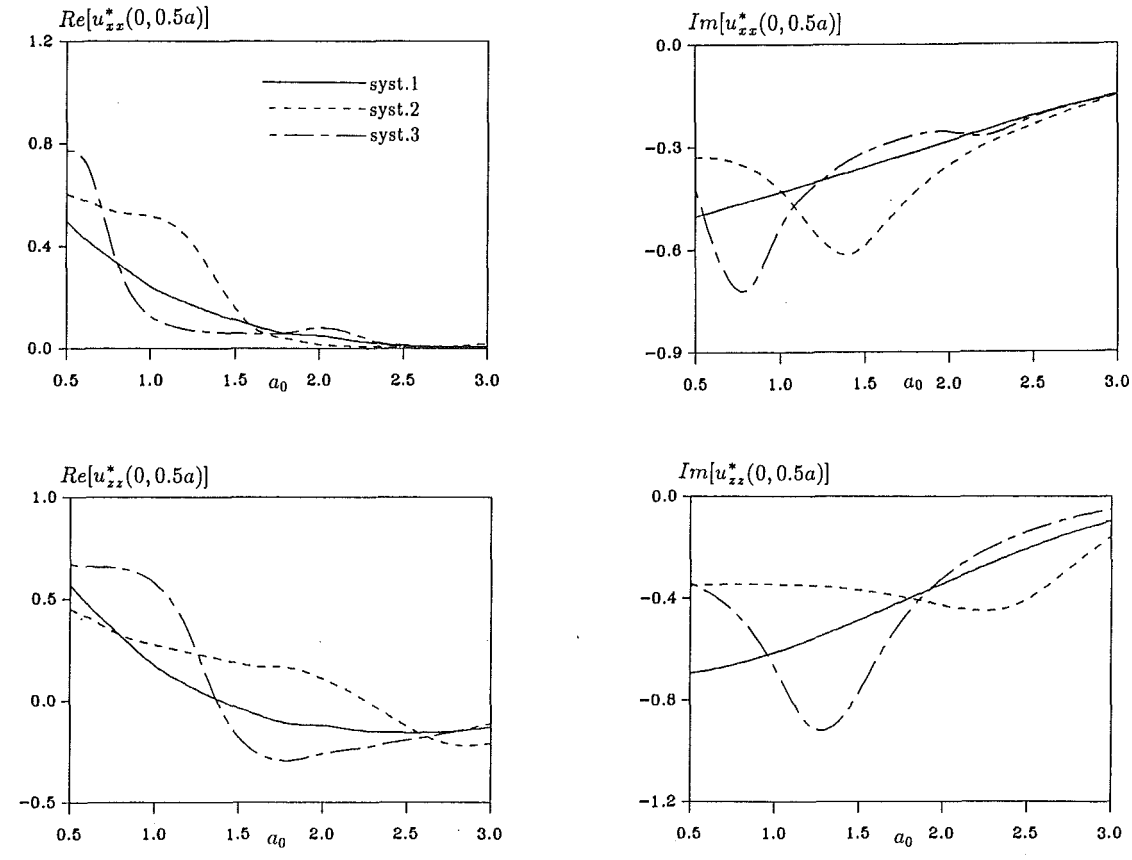


Fig. 3 Normalized displacements u^*_{xx} and u^*_{zz} due to strip loads at $z/a = 0.5a$

Downloaded 03 May 2010 to 171.66.16.20. Redistribution subject to ASME license or copyright; see http://www.asme.org/terms/Terms_Use.cfm

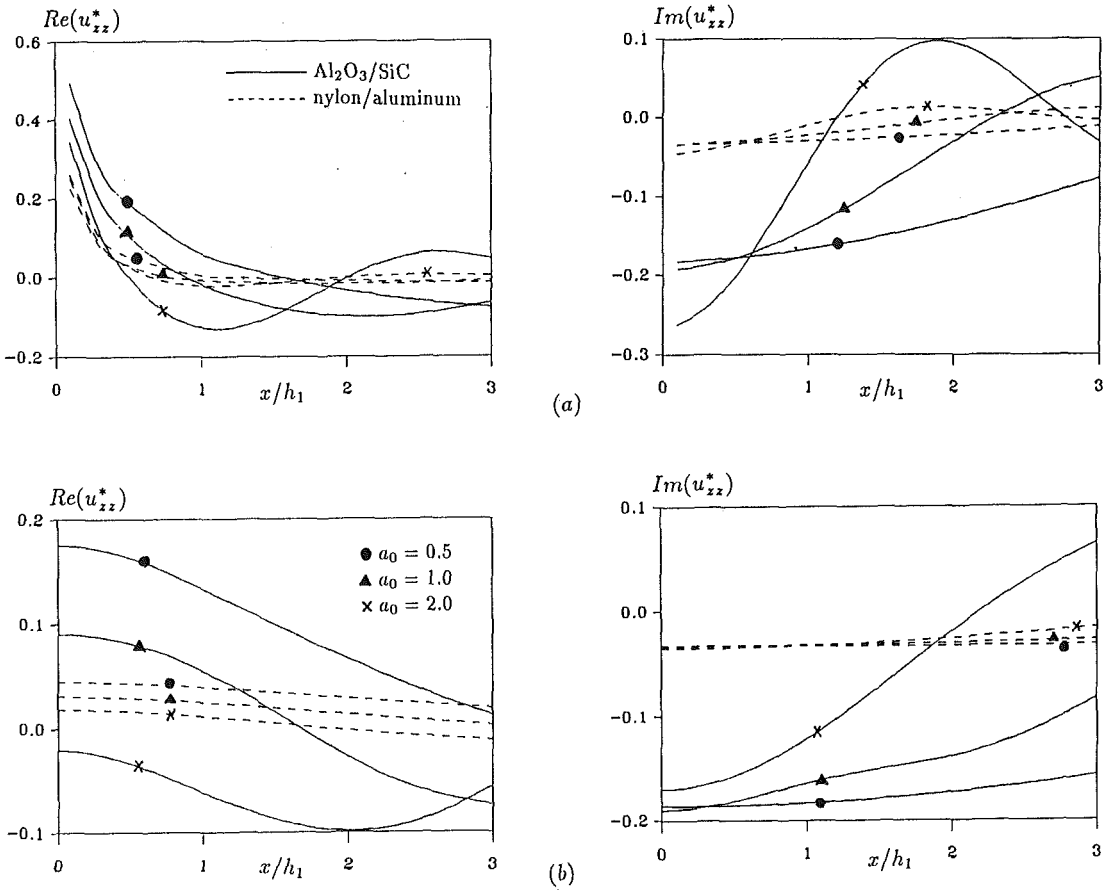


Fig. 4 *Normalized displacement u^*_{zz} of Al_2O_3/SiC and nylon/aluminum systems due to a vertical point load applied at coordinate origin; (a) u^*_{zz} along the surface ($z/h_1 = 0$); (b) u^*_{zz} along the interface ($z/h_1 = 1.0$)*

density of the top layer is also used. Figures 2 and 3 shows the influence of frequency of excitation over the range $0.5 < a_0 < 3.0$ on displacements u^*_{xx} and u^*_{zz} at the center point of a uniform strip loading applied at the surface ($z = 0$) and at a depth $0.5a$ below the surface, respectively. The frequency range $0.5 < a_0 < 3.0$ is selected since most machine foundation vibrations are in this range (Gazetas, 1983). The strong influence of layering on the response is clearly noted in Figs. 2 and 3. Comparison of displacements corresponding to the three soil systems indicates that it is very difficult to relate the influence of degree of anisotropy of materials in a layered system to the features of the response. System 1 is a homogeneous orthotropic medium and the real and imaginary parts of displacements u^*_{xx} and u^*_{zz} vary smoothly with the frequency. In the case of the two layered systems the variation of displacements with the frequency shows considerable oscillations, especially for the imaginary parts. The real parts of the displacements generally decrease with the frequency for all three systems under both vertical and horizontal loadings. Imaginary parts of the displacements increase with the frequency for the homogeneous soil (system 1) but do not follow a definite trend for the other two systems due to oscillatory variations. Comparison of Figs. 2 and 3 indicates that the real parts of displacements for all three systems are higher for surface loading when compared to buried loading. On the other hand, more geometric dissipation occurs under buried loading. However, the general features of compliance profiles shown in Figs. 2 and 3 are quite identical.

The next set of solutions corresponds to two layered systems encountered in computer and electronic devices. The response of a SiC substrate with an Al_2O_3 layer and an aluminum substrate with a nylon layer under a time-harmonic vertical concentrated load applied at coordinate origin (Fig. 1) is studied. Figure 4 shows the variation of nondimensional displacement $u^*_{zz} (= u_{zz} c^{(1)}_{44} h_1 / P_0$, where P_0 is the magnitude of the concentrated load and h_1 is the thickness of the layer) with the horizontal distance at the surface ($z = 0$) and at the material interface. Solutions are presented for three values of nondimensional frequency a_0 $[= h_1 \omega (\rho^{(1)}/c^{(1)}_{44})^{1/2}]$. As can be seen from Fig. 4(a), $u^*_{zz}(0, 0)$ is singular near the origin of the coordinate system for all frequencies due to the fact that loading is applied at the coordinate origin. Surface and interface displacements show relatively smooth variation with the horizontal distance for both layered systems. In the case of Al_2O_3/SiC system, normalized displacements are higher than that corresponding to nylon/aluminum system. Comparison of material properties given in Table 1 indicates that the nylon/aluminum system can be considered as a flexible film on a rigid substrate due to the large difference between material moduli of the two materials. In fact, it can be seen from Fig. 4(b) that the interface displacements of nylon/aluminum system is very close to zero for all three values of frequency. In addition, the surface displacements of nylon/aluminum system is significant only near the loading region $|x/h_1| < 1.0$ indicating the presence of more or less a locally deformed region which is characteristic to a point loaded very flexible layer on a rigid substrate. On the other hand, Al_2O_3/SiC system shows more gradual distribution of the displacements with the horizontal distance and the presence of significant interface displacements. Figure 5 shows the shear and normal stresses along

Downloaded 03 May 2010 to 171.66.16.20. Redistribution subject to ASME license or copyright; see http://www.asme.org/terms/Terms_Use.cfm

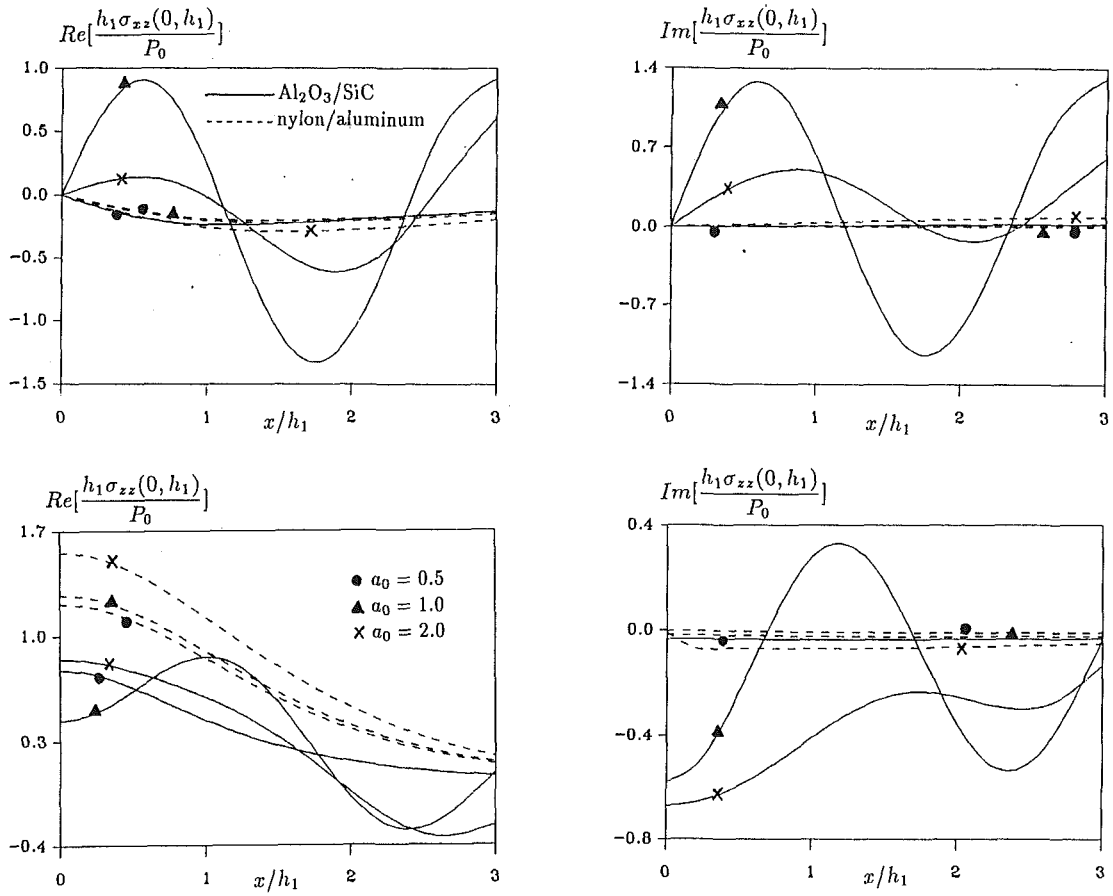


Fig. 5 Normalized stress σ^*_{xz} and σ^*_{zz} along the material interface of Al_2O_3/SiC and nylon/aluminum systems due to a vertical point load applied at coordinate origin

the material interface of Al_2O_3/SiC and nylon/aluminum system under a vertical concentrated load of magnitude P_0 applied at the origin. It is noted from Fig. 5 that the shear stress along the interface is negligible for nylon/aluminum system for all three frequencies. Significant shear stresses are noted along the interface of Al_2O_3/SiC system. The real part of normal stress along the interface of nylon/aluminum system is generally larger than that of Al_2O_3/SiC. It is also noted that the imaginary part of the normal stress is nearly zero for nylon/aluminum system indicating that the loading and the normal stress along the interface are nearly in-phase. A significant imaginary component is noted for normal stress along the interface of Al_2O_3/SiC system. In general, the amplitude of interface vertical stress is higher for the nylon/aluminum system when compared to Al_2O_3/SiC system since the former behave as a flexible layer on a rigid substrate. On the other hand, more shear stress is generated in the Al_2O_3/SiC system along the material interface. The variation of interface stress with the frequency is smoother in the case of nylon/aluminum system but shows complicated oscillatory behavior for the Al_2O_3/SiC system. Generally, the magnitude of both the real and imaginary parts of stress increases with the increasing frequency in the case of nylon/aluminum system. The solutions presented in Figs. 4 and 5 are useful in the study of flaws and material interfaces by using nondestructive testing methods.

A selected set of transient solutions is presented to demonstrate the wide range of applicability of the present scheme. Transient wave propagation problems are becoming increasingly important due to their application in nondestructive evaluation methods (Karim and Kundu, 1988; 1991; Datta et al., 1992; Ju and Datta, 1992), geomechanics (Israil and Banerjee, 1990), and in computer mechanics (Downey and Bogy, 1988). In the present study, the authors consider the case where the three half-plane systems defined in Table 2 are subjected to a uniformly distributed vertical loading of width $2a$ applied at the surface level. The transient character of the loading pulse is represented by the following form (Karim and Kundu, 1991):

$$f(\tau) = \begin{cases} 16q_0\tau^2(\tau-1)^2 & 0 \le \tau \le 1 \\ 0 & \tau > 1 \end{cases} \tag{44}$$

where q_0 is the intensity of the load and τ is a nondimensional time defined as $\tau = (t/a)[\sqrt{c_{44}^{(1)}/\rho^{(1)}}]$. The Fourier transform of Eq. (44) is given by

$$F(a_0) = \frac{32q_0}{a_0^3}\left\{\left[-\frac{6}{a_0} + i\left(1-\frac{12}{a_0^2}\right)\right]e^{ia_0\tau} - \left[\frac{6}{a_0} + i\left(1-\frac{12}{a_0^2}\right)\right]\right\}. \tag{45}$$

It should be noted that the response spectrum corresponding to the above pulse decays fairly rapidly with a_0 due to the presence of terms which are inversely proportional to a_0^n, where $n \ge 3$. An investigation of spectral values of displacements indicates that the values corresponding to $a_0 \ge 5.0$ are negligibly small in the case of the three half-plane systems defined in Table 2. Much more effective filtering of the high-frequency response can be achieved by selecting a transient pulse whose Fourier transform is proportional to an exponential decay with

Downloaded 03 May 2010 to 171.66.16.20. Redistribution subject to ASME license or copyright; see http://www.asme.org/terms/Terms_Use.cfm

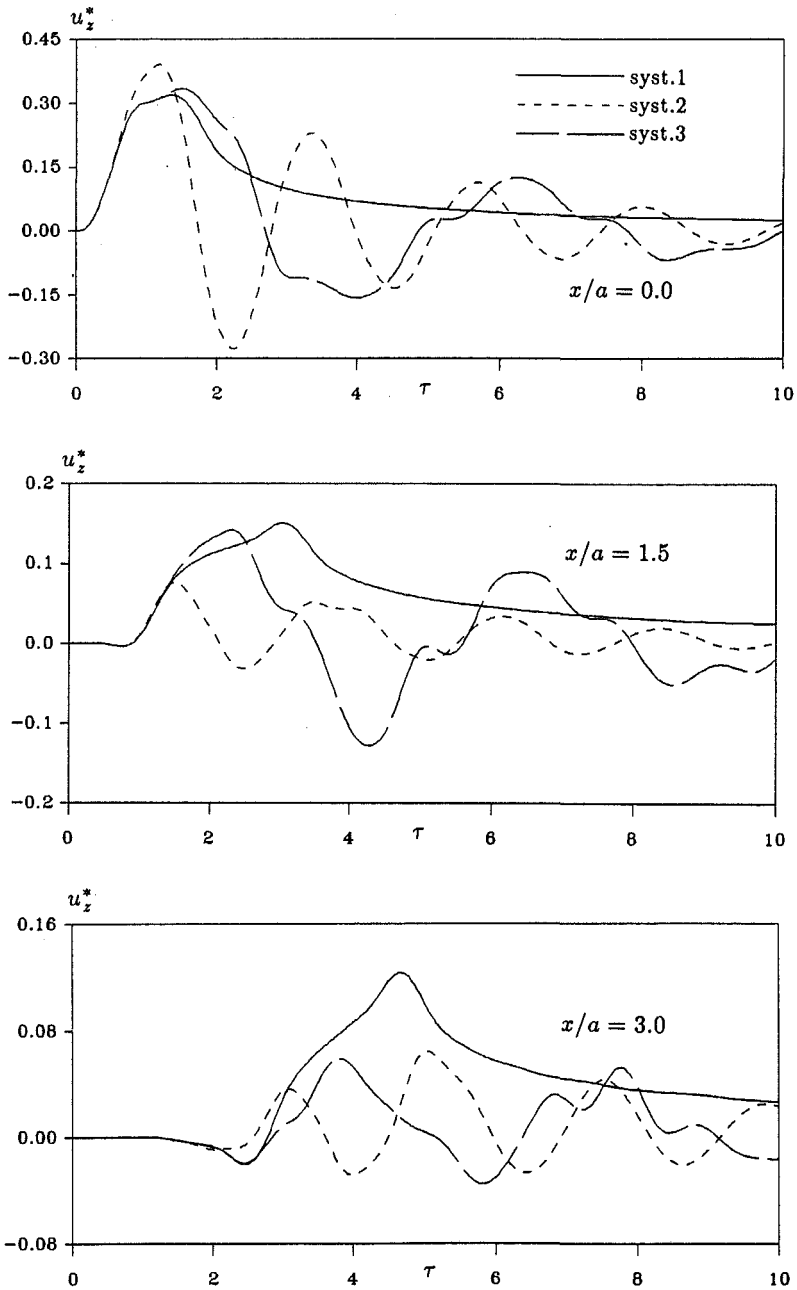


Fig. 6 Normalized vertical displacement of the surface layered systems due to an uniform strip load with time history defined in Eq. (44) applied at the surface

respect to a_0 such as the excitation pulse selected by Datta et al. (1992).

Figure 6 shows the nondimensional vertical displacements $u_z^* = (c_{44}^1 u_z / a q_0)$ at three surface points due to the transient pulse given by Eq. (44). Solutions corresponding to the homogeneous orthotropic half-plane (system 1) at $x = 0.0$ indicates that the vertical displacement increases rapidly during the period $0.0 < \tau < 1.0$ and decreases gradually thereafter. At points outside the loading region (e.g., $x = 1.5$ and 3.0) displacements remains zero for an initial time period. The initial disturbance has a smaller negative value at these points and thereafter increases rapidly with a positive value. Naturally the time to reach the peak vertical displacement increases with the distance from the center of the strip load and the peak magnitude decreases. Numerical solutions for vertical displacements presented by Karim and Kundu (1991) also confirms the presence of a negative displacement initially at points outside the loading. Similar behavior is qualitatively seen in the time-domain boundary element solutions presented by Israil and Banerjee (1990) for a homogeneous isotropic half-plane under a triangular pulse loading. The attenuating part of the response curve at surface points on a homogeneous half-plane is nonoscillatory with time which is also qualitatively similar to the time-domain boundary element solutions given by Israil and Banerjee (1990). However, the transient solutions given by Karim and Kundu (1991) shows some oscillatory variations with time which may arise from numerical instabilities.

Transient displacement profiles corresponding to the two layered systems show features that are completely different to the response of a homogeneous medium. The response of system 2 at $x = 0.0$ shows nearly periodic behavior indicating the dominance of a single surface wave. This fact is also confirmed

Downloaded 03 May 2010 to 171.66.16.20. Redistribution subject to ASME license or copyright; see http://www.asme.org/terms/Terms_Use.cfm

by the comparison of the period of the response at the other two surface points. In addition, the displacements at the three surface points corresponding to the system 2 reach their first peak positive value earlier than the peaks corresponding to the other two half-planes. The response decays less rapidly with time at $x=0.0$ for layered systems when compared to a homogeneous medium. Solutions corresponding to system 3 at $x=0.0$ show irregular oscillations with time indicating contributions due to a number of surface waves. At points outside the loading region (i.e., $x=1.5$ and 3.0), the response of system 2 remains nearly periodic but that of system 3 is still nonperiodic. Comparison of present solutions for orthotropic layered systems with those presented by Israil and Banerjee (1990) for layered isotropic systems shows similar qualitative behavior confirming the oscillatory variation of response with time. A similar oscillatory response was also observed by Downey and Bogy (1988) for layered isotropic viscoelastic half-spaces. These oscillatory variations in the response arise mainly due to the reflection of waves at material interfaces. In a homogeneous half-plane such oscillations do not exist due to the absence of interfaces. The properties of the surface wave field in a layered orthotropic system can be determined by computing the eigenvalues of the global stiffness matrix given by Eq. (43). The presence of a nearly periodic surface response in system 2 is interesting given the fact that the present analysis can be used to model the SASW (Spectral-Analysis-of-Surface-Waves) method (Nazarian et al., 1983) developed for nondestructive evaluation of pavement systems. The SASW method provides accurate evaluation of pavement properties if a single mode surface wave can be established at receiver points through an appropriate test setup. The present numerical solutions confirm that such a behavior can be established in layered orthotropic systems.

Conclusions

A stiffness matrix method based on exact analytical solutions for elastodynamics of plane orthtropic materials is presented to compute displacements and stresses of a multilayered orthotropic elastic half-plane subjected to arbitrary time-harmonic loadings. The Fourier transform of displacements at layer interfaces are considered as the basic unknowns in the analysis. Explicit solutions for stiffness matrices of a layer with a finite thickness and a half-plane are presented. An adaptive version of Filon's numerical integration is used to numerically integrate the Fourier integrals encountered in the analysis. The present method has the advantage that the stiffness matrices involve only negative exponentials and other numerically stable terms. In addition, the size of the final equation system is nearly one-half of that corresponding to the conventional matrix approach based on layer arbitrary coefficients and has a bandwidth equal to four. Selected numerical results presented in this study for five different layered systems indicate that the response of a layered anisotropic medium depend significantly on the frequency of excitation, degree of anisotropy of materials, thickness of layers, and the configuration of layering. Selected time-domain solutions presented in this paper indicate that the surface response due to a transient vertical pulse is nonoscillatory with time in the case of a homogeneous medium whereas a periodic or a nonperiodic response may exist depending on the configuration of the layered system. The present method can be effectively used to compute the kernel functions (Green's functions) required in the application of a boundary integral equation method for layered orthotropic media. It can be also used to verify the accuracy of approximate stiffness methods such as those proposed by Waas (1980), Kausel and Peek (1982), and other numerical techniques. With the aid of computer algebra codes, the present method can be extended to develop a highly stable and computationally efficient stiffness matrix approach for evaluation of static, time-harmonic, and transient responses of layered isotropic and anisotropic half-spaces under three-dimensional loadings.

Acknowledgment

The work presented here was supported by Grant A-6507 from the Natural Sciences and Engineering Research Council of Canada.

References

Apsel, R. J., and Luco, J. E., 1983, "On the Green's Functions for a Layered Half-Space: Part I," *Bull. Seism. Soc. Am.*, Vol. 73, pp. 931–951.

Apsel, R. J., and Luco, J. E., 1987, "Impedance Functions for Foundations Embedded in a Layered Medium: An Integral Equation Approach," *Earth. Engng. Struc. Dyna.*, Vol. 15, pp. 213–231.

Datta, S. K., Ju, T. H., and Shah, A. H., 1992, "Scattering of an Impact Wave by a Crack in a Composite Plate," ASME JOURNAL OF APPLIED MECHANICS, Vol. 59, pp. 596–603.

Downey, H. A., and Bogy, D. B., 1988, "The Normal Impact of a Rod-Mass System on a Viscoelastic Layered Half Space," ASME JOURNAL OF APPLIED MECHANICS, Vol. 55, pp. 879–886.

Gazetas, G., 1983, "Analysis of Machine Foundation Vibrations: State of the Art," *Soil Dyn. Earthquake Eng.*, Vol. 2, pp. 2–42.

Gilbert, F., and Backus, G. E., 1966, "Propagator Matrices in Elastic Wave and Vibration Problems," *Geophysics*, Vol. 31, pp. 326–332.

Haskell, N. A., 1953, "The Dispersion of Surface Waves on Multilayered Media," *Bull. Seism. Soc. Am.*, Vol. 43, pp. 17–34.

Haskell, N. A., 1960, "Crustral Reflection of Plane SH Waves," *J. Geophys. Res.*, Vol. 65, pp. 4147–4150.

Haskell, N. A., 1962, "Crustral Reflection of Plane P and SV Waves," *J. Geophys. Res.*, Vol. 67, pp. 4751–4767.

Israil, A. S. M., and Banerjee, P. K., 1990, "Two-Dimensional Transient Wave-Propagation Problems by Time-Domain BEM," *Int. J. Solids Structure*, Vol. 26, pp. 851–864.

Ju, T. H., and Datta, S. K., 1992, "Pulse Propagation in a Laminated Composite Plate and Nondestructive Evaluation," *Composites Engineering*, Vol. 2, pp. 55–66.

Karim, M. R., and Kundu, T., 1988, "Transient Surface Response of Layered Isotropic and Anisotropic Half-Spaces with Interface Cracks: SH Case," *Int. J. Fracture*, Vol. 37, pp. 245–262.

Karim, M. R., and Kundu, T., 1991, "Dynamic Response of an Orthotropic Half-Space With a Subsurface Crack: In-Plane Case," ASME JOURNAL OF APPLIED MECHANICS, Vol. 58, pp. 988–995.

Kausel, E., and Peek, R., 1982, "Dynamic Loads in the Interior of a Layered Stratum: An Explicit Solution," *Bull. Seism. Soc. Am.*, Vol. 72, pp. 1459–1481.

Knopoff, L., 1964, "A Matrix Method for Elastic Wave Problems," *Bull. Seism. Soc. Am.*, Vol. 54, pp. 431–438.

Lekhnitskii, S. G., 1963, *Theory of Anisotropic Elastic Bodies*, Holden-Day, San Francisco, CA.

Luco, J. E., and Apsel, R. J., 1983, "On the Green's Functions for a Layered Half-Space: Part II," *Bull. Seism. Soc. Am.*, Vol. 73, pp. 909–929.

Mal, A. K., 1988a, "Guided Waves in Layered Solids with Interface Zones," *Int. J. Engng. Sci.*, Vol. 26, pp. 873–881.

Mal, A. K., 1988b, "Wave Propagation in Layered Composite Laminates Under Periodic Surface Loads," *Wave Motion*, Vol. 10, pp. 257–266.

Nazarian, S., Stokoe II, K. H., and Hudson, W. R., 1983, "Use of Spectral Analysis of Surface Waves Method for Determination of Moduli and Thickness of Pavement Systems," *Transportation Research Record*, Vol. 930, pp. 38–45.

Oner, M., and Dong, S. B., 1988, "Analysis of On-Plane Waves in Layered Half-Space by Global-Local Finite Element Method," *Soil Dynamics and Earthquake Engineering*, Vol. 7, pp. 2–8.

Payton, R. G., 1983, *Elastic Wave Propagation in Transversely Isotropic Media*, Martinus, Nijhoff, The Netherlands.

Pestel, E. C., and Leckie, F. A., 1963, *Matrix Methods in Elastomechanics*, McGraw-Hill, New York.

Rajapakse, R. K. N. D., and Wang, Y., 1991, "Elastodynamic Green's Functions of an Orthotropic Half Plane," *J. Engrg. Mechanics*, Vol. 117, pp. 588–604.

Schwab, F., 1970, "Surfaces-Wave Dispersion Computations: Knopoff's Method," *Bull. Seism. Soc. Am.*, Vol. 60, pp. 1491–1520.

Seal, S. H., and Kausel, E., 1989, "Point Loads in Cross-Anisotropic, Layered Halfspaces," *J. Engrg. Mechanics*, Vol. 115, pp. 509–524.

Sneddon, I. N., 1951, *Fourier Transforms*, McGraw-Hill, New York.

Thomson, W. T., 1950, "Transmission of Elastic Waves Through a Stratified Solid Medium," *J. Appl. Phys.*, Vol. 21, pp. 89–93.

Tranter, C. J., 1956, *Integral Transforms in Mathematical Physics*, 2nd ed., John Wiley and Sons, New York.

Wass, G., 1972, "Linear Two-Dimensional Analysis of Soil-Dynamic Problems in Semi-Infinite Layered Media," Ph.D. Thesis, University of California, Berkeley, CA.

Wass, G., 1980, "Dynamics Belastete Fundamente auf Geschichtetemn Baugrund," *Berichte*, Vol. 381, pp. 185–189, in German.

Watson, T. H., 1970, "A Note on Fast Computation of Rayleigh Wave Dispersion in the Multilayered Elastic Half Space," *Bull. Seism. Soc. Am.*, Vol. 60, pp. 161–166.

Downloaded 03 May 2010 to 171.66.16.20. Redistribution subject to ASME license or copyright; see http://www.asme.org/terms/Terms_Use.cfm

APPENDIX

$$a_1=\frac{-c_{44}\delta}{F}[(s_1+s_2)(\lambda_{2n}^2-1)-2s_2(\lambda_{1n}\lambda_{2n}-1)] \tag{A1}$$

$$a_2=\frac{c_{44}\delta}{F}[(s_1+s_2)s_2(\lambda_{2n}^2-1)-2s_2s_1(\lambda_{1n}\lambda_{2n})-1)] \tag{A2}$$

$$a_3=\frac{c_{44}\delta}{F}[(s_1+s_2)\lambda_{1n}(\lambda_{2n}^2-1)-2s_2\lambda_{2n}(\lambda_{1n}\lambda_{2n}-1)] \tag{A3}$$

$$a_4=\frac{-c_{44}\delta}{F}[(s_1+s_2)s_2\lambda_{1n}(\lambda_{2n}^2-1)-2s_1s_2\lambda_{2n}(\lambda_{1n}\lambda_{2n}-1)] \tag{A4}$$

$$g_1=\frac{-c_{44}\delta}{F}[(s_1+s_2)(\lambda_{1n}^2-1)-2s_1(\lambda_{1n}\lambda_{2n}-1)] \tag{A5}$$

$$g_2=\frac{c_{44}\delta}{F}[(s_1+s_2)s_1(\lambda_{1n}^2-1)-2s_2s_1(\lambda_{1n}\lambda_{2n}-1)] \tag{A6}$$

$$g_3=\frac{c_{44}\delta}{F}[(s_1+s_2)\lambda_{2n}(\lambda_{1n}^2-1)-2s_1\lambda_{1n}(\lambda_{1n}\lambda_{2n}-1)] \tag{A7}$$

$$g_4=\frac{-c_{44}\delta}{F}[(s_1+s_2)s_1\lambda_{2n}(\lambda_{1n}^2-1)-2s_1s_2\lambda_{1n}(\lambda_{1n}\lambda_{2n}-1)] \tag{A8}$$

$$b_1=\frac{-c_{44}\delta}{s_1-s_2}[(s_1+s_2)\lambda_{1n}a_1+2s_2\lambda_{2n}c_1-1] \tag{A9}$$

$$b_2=\frac{c_{44}\delta}{s_1-s_2}[(s_1+s_2)\lambda_{1n}a_2+2s_2\lambda_{2n}c_2-s_2] \tag{A10}$$

$$b_3=\frac{-c_{44}\delta}{s_1-s_2}[(s_1+s_2)\lambda_{1n}a_3+2s_2\lambda_{2n}c_3] \tag{A11}$$

$$b_4=\frac{c_{44}\delta}{s_1-s_2}[(s_1+s_2)\lambda_{1n}a_4+2s_2\lambda_{2n}c_4] \tag{A12}$$

$$d_1=\frac{c_{44}\delta}{s_1-s_2}[2s_1\lambda_{1n}a_1+(s_1+s_2)\lambda_{2n}c_1-1] \tag{A13}$$

$$d_2=\frac{-c_{44}\delta}{s_1-s_2}[2s_1\lambda_{1n}a_2+(s_1+s_2)\lambda_{2n}c_2-s_1] \tag{A14}$$

$$d_3=\frac{c_{44}\delta}{s_1-s_2}[2s_1\lambda_{1n}a_3+(s_1+s_2)\lambda_{2n}c_3] \tag{A15}$$

$$d_4=\frac{-c_{44}\delta}{s_1-s_2}[2s_1\lambda_{2n}a_4+(s_1+s_2)\lambda_{2n}c_4] \tag{A16}$$

where

$$F=4s_1s_2(\lambda_{1n}\lambda_{2n}-1)^2-(s_1+s_2)^2(\lambda_{1n}^2-1)(\lambda_{2n}^2-1) \tag{A17}$$

and the expressions of s_1, s_2, and λ_{in} are given by Eqs. (18) and (37), respectively.

Downloaded 03 May 2010 to 171.66.16.20. Redistribution subject to ASME license or copyright; see http://www.asme.org/terms/Terms_Use.cfm

Effective Elastic Moduli of Two-Dimensional Brittle Solids With Interacting Microcracks, Part I: Basic Formulations

J. W. Ju
Associate Professor,
Mem. ASME.

Tsung-Muh Chen
Research Assistant.

Department of Civil and Environmental Engineering,
University of California,
Los Angeles, CA 90024-1593

Statistical micromechanical formulations are presented to investigate effective elastic moduli of two-dimensional brittle solids with interacting slit *microcracks. The macroscopic stress-strain relations of elastic solids with interacting microcracks are micromechanically derived by taking the* ensemble average *over all possible realizations which feature the same material microstructural geometry, characteristics, and loading conditions. Approximate analytical solutions of a two-microcrack interaction problem are introduced to account for microcrack interaction among many randomly oriented and located microcracks. The overall elastic-damage compliances of microcrack-weakened brittle solids under uniaxial and biaxial loads are also derived. Therefore, stationary statistical micromechanical formulation is completed. Moreover, some special cases are investigated by using the proposed framework. At variance with existing phenomenological continuum damage models, the proposed framework does not employ any fitted "material parameters." "Cleavage 1" microcrack growth and "evolutionary damage models" within the proposed context will be presented in Part II of this series. It is emphasized that microstructural statistical informations are already embedded in the proposed ensemble-averaged equations and, therefore, no Monte Carlo simulations are needed.*

I Introduction

The nonlinear mechanical responses of damaged solids due to the existence, growth, and nucleation of microdefects (such as microcracks and microvoids) are of significant importance to engineers, and have been the subject of many investigations. See Krajcinovic (1989) for a literature review on damaged mechanics. For brittle materials (e.g., concrete, rocks, and ceramics), in particular, microcracks often control overall deformation and failure mechanisms. To date, the only exact results derived for microcrack-weakened brittle solids are for dilute microcrack concentrations, where microcrack interactions are entirely neglected (i.e., "Taylor's models"). On the other hand, "effective medium methods" were proposed in the literature to account for interaction effects of microcracks. For example, the "self-consistent method" (Hill, 1965) was first applied to microcrack-weakened solids by Budiansky and O'Connell (1976) with special attention directed to perfectly randomly distributed and *weakly* interacting microcracks. The self-consistent method was further developed by Horii and Nemat-Nasser (1983) to take into account the effects of *closed* microcracks undergoing frictional sliding. Christensen and Lo (1979) proposed a three-phase "generalized self-consistent model." The "differential scheme" was investigated by Roscoe (1952, 1973), McLaughlin (1977), and Hashin (1988). Further, the "Mori-Tanaka method" was developed by Mori and Tanaka (1973), Benveniste (1986), and Zhao, Tandon, and Weng (1989). Some comparisons and assessments for the self-consistent method, the generalized self-consistent method, the Mori-Tanaka method, and/or the differential scheme were also presented by Horii and Sahasakmontri (1990), Laws and Dvorak (1987), Nemat-Nasser and Hori (1990), and Christensen (1990, for pure shear load only). It is noted that the foregoing effective medium methods are only valid for *low* microcrack concentrations since they do *not* depend on locations of microcracks.

All of the aforementioned work can be categorized as "*stationary*" micromechanical models since all microcracks are assumed to be *stationary*; i.e., no microcracks are allowed to grow or nucleated during loading histories. For a constitutive

Contributed by the Applied Mechanics Division of THE AMERICAN SOCIETY OF MECHANICAL ENGINEERS for publication in the ASME JOURNAL OF APPLIED MECHANICS.

Discussion on this paper should be addressed to the Technical Editor, Professor Lewis T. Wheeler, Department of Mechanical Engineering, University of Houston, Houston, TX 77204-4792, and will be accepted until four months after final publication of the paper itself in the ASME JOURNAL OF APPLIED MECHANICS.

Manuscript received by the ASME Applied Mechanics Division, Oct. 8, 1990; final revision, July 22, 1992. Associate Technical Editor: R. M. McMeeking.

Copyright © 1994 by ASME
Downloaded 03 May 2010 to 171.66.16.20. Redistribution subject to ASME license or copyright; see http://www.asme.org/terms/Terms_Use.cfm

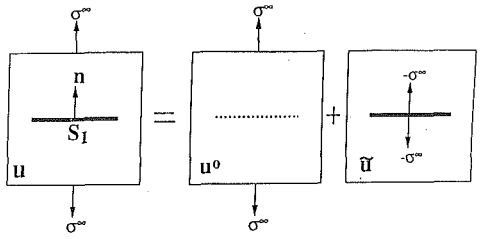


Fig. 1 Superposition of microcrack problem

theory to possess *predictive* capability, however, an "*evolutionary*" micromechanical damage model is warranted to account for "cleavage 1" (pre-existing) microcrack growth and/or "cleavage 2" (new) microcrack nucleation. In the current literature, there are indeed a number of micromechanical "evolutionary" damage models available. See, e.g., Krajcinovic and Fanella (1986), Fanella and Krajcinovic (1988), and Ju (1991b) by using the "Taylor's model," as well as Sumarac and Krajcinovic (1987, 1989), Krajcinovic and Sumarac (1989), Ju (1991a), Ju and Lee (1991), and Lee and Ju (1991) by using the self-consistent method.

When microcrack concentrations are higher and microcrack spacings are closer, *strong* microcrack interactions occur and effective medium theories are no longer appropriate. Emanating from this viewpoint, strong microcrack interaction models were proposed by Gross (1982), Horii and Nemat-Nasser (1985), Hori and Nemat-Nasser (1987) for two-dimensional deterministic microcracks, and by Kachanov and Montagut (1986), Kachanov (1987), Chudnovsky et al. (1987a,b), and Kachanov and Laures (1989) for two and three-dimensional *deterministic* arbitrary microcrack arrays. The foregoing work, nevertheless, are only *stationary* strong microcrack interaction models. Moreover, the work due to Kachanov (1987), Kachanov and Laures (1989) rely on Monte Carlo simulations of deterministic microcrack arrays, and depend on heavy numerical computations of stress "transmission factors." Therefore, it is desirable to develop simple *statistical* micromechanical theories to account for interactions among many randomly located and oriented microcracks. Furthermore, "cleavage 1" microcrack growth models are needed under the condition of microcrack interaction.

The purpose of the present work (Part I and Part II) is to establish a statistical micromechanical framework for deriving "evolutionary" damage models and corresponding constitutive equations for brittle solids containing many interacting, randomly distributed *slit* microcracks. The proposed statistical framework considers the probability and conditional probability density functions of microcrack locations, orientations, lengths, and relative configurations. See Batchelor (1970), Batchelor and Green (1972), Hinch (1977), Willis and Acton (1976), Chen and Acrivos (1978a,b) for references. In addition, the *ensemble-volume* averages of stresses, strains, and compliances are systematically constructed based on analytical micromechanics solutions and probability functions. It is emphasized that the proposed method is very different from that proposed by Hudson (1980, 1981, 1986). Though using the ensemble average approach, Hudson's method is based on a second-order *stiffness* theory and therefore leads to irrational behavior for solids with moderate or high microcrack concentrations (see Sayers and Kachanov, 1991). The proposed approach is free from this anomaly.

A brief outline of this work is as follows. In Section 2, an *ensemble-average* approach to derive damaged stress-strain relations is introduced. Approximate closed-form analytical solutions are subsequently presented for the interaction problem of two arbitrarily located and oriented (but nonintersecting) microcracks. The overall elastic moduli of a statistically representative volume element are then derived. In Section 3, applications are made to a number of special cases. In particular, for the dilute microcrack concentration case, the present approach recovers the well-known Taylor's model by neglecting interactions among microcracks. When all microcracks are *open* and perfectly randomly distributed, the proposed approach shows that the overall compliance matrix becomes isotropic. A comparison between the present method and the self-consistent method is also discussed in this isotropic damage case.

2 An Ensemble-Average Approach to Microcrack Interaction and Effective Moduli

2.1 Background. Consider a statistical realization within a statistical RVE (in the probability space) of a microcrack-weakened solid. The volume of the statistical RVE is V, and the exterior surface is subjected to prescribed traction σ^∞. Let a and n be the average microcrack radius and the average number of microcracks per unit volume, respectively. A typical avenue to describe mechanical responses of a statistical RVE is to relate the volume-averaged strain $\bar{\epsilon}$ to the volume-averaged stress $\bar{\sigma}$. It is well known that

$$\bar{\epsilon} = \mathbf{S}^o : \bar{\sigma} + \frac{1}{V}\int_{S_I} \frac{1}{2}(\llbracket \mathbf{u} \rrbracket \otimes \mathbf{n} + \mathbf{n} \otimes \llbracket \mathbf{u} \rrbracket) dS_I \tag{1}$$

where $\mathbf{S}^o$ is the virgin elastic compliance tensor for the matrix material; $\llbracket \mathbf{u} \rrbracket$ and $\mathbf{n}$ are the microcrack opening displacement vector and the unit normal vector on discontinuity surface, respectively. Moreover, S_I represents the *union* of all discontinuity (microcrack) surfaces (see Fig. 1).

Following the common assumption $\bar{\sigma} \approx \sigma^\infty$, the microcrack-induced strain reads

$$\bar{\epsilon} \approx \frac{1}{V}\int_{S_I} \frac{1}{2}(\llbracket \mathbf{u} \rrbracket \otimes \mathbf{n} + \mathbf{n} \otimes \llbracket \mathbf{u} \rrbracket) dS_I. \tag{2}$$

2.2 Ensemble Average of Microcrack-Induced Strains. In this section, a systematic approach of forming the ensemble-averaged strains and microcrack interaction-induced local *stress perturbations* are presented. The basic idea behind this approach is that the *local* constitutive relation at a typical *point* within a statistical RVE of a microcrack-weakened solid should be obtained by averaging over the ensemble of all *statistical realizations*, including the locations, orientations, lengths, and relative configurations of randomly distributed microcracks. This approach was first applied to the study of fluid suspensions; see Batchelor (1970), Batchelor and Green (1972), and Hinch (1977). The ensemble average approach was later applied to interacting inclusions of solid composite materials by Willis and Acton (1976), and Chen and Acrivos (1978a,b). It is emphasized that local displacements, strains, and stresses vary with *positions* within a RVE. An average over the values of physical quantities occurring in a very large number of realizations is an ensemble average, which will be denoted by angle brackets.

Let us consider a two-phase composite statistical RVE (composed of a linear elastic brittle matrix and inclusions) subjected to external load σ^∞. The local constitutive law at a material point $\mathbf{x}$ may be expressed as

$$\epsilon(\mathbf{x}) = \mathbf{S}^o : \sigma(\mathbf{x}) + \epsilon^*(\mathbf{x}, \mathcal{C}) \tag{3}$$

where ϵ and σ are the local strain and stress, respectively. Furthermore, ϵ^* is a perturbed strain function which is *zero* if $\mathbf{x}$ is a point in the matrix and is nonzero if $\mathbf{x}$ is a point in an inclusion. Obviously, ϵ^* depends on the full configuration of all inclusions (denoted by $\mathcal{C}$). The constitutive law (3) can be easily statistically (ensemble) averaged:

$$\langle \epsilon \rangle(\mathbf{x}) = \mathbf{S}^o : \langle \sigma \rangle(\mathbf{x}) + \langle \epsilon^* \rangle(\mathbf{x}). \tag{4}$$

In addition, the ensemble average of ϵ^* at $\mathbf{x}$ (considered to

Downloaded 03 May 2010 to 171.66.16.20. Redistribution subject to ASME license or copyright; see http://www.asme.org/terms/Terms_Use.cfm

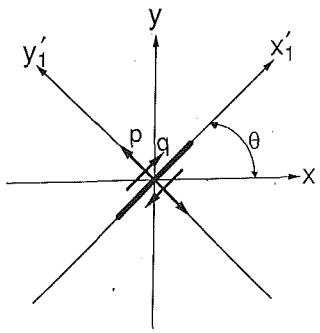


Fig. 2 The local and global coordinates systems

be nonzero because it lies in an inclusion centered at $\mathbf{x}_1$) is (assuming inclusions do *not* intersect one another)

$$\langle \epsilon^* \rangle(\mathbf{x}) = \int_{\mathbf{x} \in \Omega_i} \langle \epsilon^* \rangle(\mathbf{x}|\mathbf{x}_1) f(\mathbf{x}_1) dV_1 \tag{5}$$

where Ω_i is the domain of a single inclusion and the integral is performed over the finite domain such that $\mathbf{x}$ can lie in an inclusion centered at $\mathbf{x}_1$. Further, $f(\mathbf{x}_1)$ is the probability density function (PDF) for a single inclusion being centered at $\mathbf{x}_1$, and $\langle \epsilon^*(\mathbf{x}|\mathbf{x}_1) \rangle$ is the perturbed strain at $\mathbf{x}$ averaged over the subclass of realizations having an inclusion centered at $\mathbf{x}_1$.

At this stage, it is reasonable to restrict composite solids to be *locally homogeneous* (Hinch, 1977). That is, all PDF do not vary under small translation on a macroscopic length scale. With this assumption, $f(\mathbf{x}_1)$ in (5) may be regarded as a constant in the integration and equal to $f(\mathbf{x})$. The statistical "local homogeneity" also allows a small translation of $\mathbf{x} - \mathbf{x}_1$ in the two arguments of $\langle \epsilon^*(\mathbf{x}|\mathbf{x}_1) \rangle$. Namely, we may equate $\langle \epsilon^*(\mathbf{x}|\mathbf{x}_1) \rangle$ to $\langle \epsilon^*(\mathbf{x} + (\mathbf{x} - \mathbf{x}_1)|\mathbf{x}) \rangle$. Thus, Eq. (5) becomes

$$\langle \epsilon^* \rangle(\mathbf{x}) = f(\mathbf{x}) \int_{\mathbf{x}' \in \Omega_i} \langle \epsilon^*(\mathbf{x}'|\mathbf{x}) \rangle dV' \tag{6}$$

where $\mathbf{x}' \equiv 2\mathbf{x} - \mathbf{x}_1$, and the integral extends over all points $\mathbf{x}'$ within an inclusion centered at the position $\mathbf{x}$. By divergence theorem, we have

$$\langle \epsilon^* \rangle(\mathbf{x}) = f(\mathbf{x}) \int_{\partial\Omega_i} \frac{1}{2} \langle \mathbf{u} \otimes \mathbf{n} + \mathbf{n} \otimes \mathbf{u} \rangle(\mathbf{x}'|\mathbf{x}) dS. \tag{7}$$

In the extreme case where inclusions become line microcracks, Eq. (7) can be recast as

$$\langle \epsilon^* \rangle(\mathbf{x}) = f(\mathbf{x}) \int_{\mathcal{G}} \int_{S_I} \frac{1}{2} \langle [\![\mathbf{u}]\!] \otimes \mathbf{n} + \mathbf{n} \otimes [\![\mathbf{u}]\!] \rangle(\mathbf{x}'|\mathbf{x}, \mathcal{G}) f(\mathcal{G}) d\mathcal{G} dS \tag{8}$$

where $\mathcal{G} \equiv (a, \mathbf{n})$ characterizes the microcrack *length* and *orientation* in addition to the information on *location* $\mathbf{x}$; $f(\mathcal{G})$ is the probability function for a microcrack with geometry $\mathcal{G}$. In what follows, for simplicity of demonstration, attention will be focused on two-dimensional plane strain (or plane stress) problems. Accordingly, $\mathcal{G}$ defines the geometric domain (a, θ), where a denotes one half of the microcrack length and θ denotes the angle between the global (reference) coordinate and the local (microcrack) coordinate with $0 \le \theta \le \pi$ (see Fig. 2). It is well known that for a line microcrack in an infinite linear elastic isotropic solid, the *normal* and *tangential* microcrack opening displacements take the form

$$\begin{Bmatrix} [\![u_2']\!] \\ [\![u_1']\!] \end{Bmatrix} = \frac{4(1-\nu^2)}{E} \sqrt{a^2 - x'^2} \begin{Bmatrix} p \\ q \end{Bmatrix} \tag{9}$$

where E and ν are the Young's modulus and Poisson's ratio of the virgin elastic solid, respectively; p and q are the normal and shear external stresses projected on microcrack surface in local coordinate system (see Fig. 2). For plane stress problems, the factor $(1-\nu^2)$ is removed from (9).

By substituting (9) into (8) and using the Voigt's notation for strains, we arrive at

$$\langle \mathbf{e}^* \rangle(\mathbf{x}) \equiv \begin{Bmatrix} \langle e_1^* \rangle \\ \langle e_2^* \rangle \\ \langle e_6^* \rangle \end{Bmatrix} = \begin{Bmatrix} \langle \epsilon_{11}^* \rangle \\ \langle \epsilon_{22}^* \rangle \\ \langle 2\epsilon_{12}^* \rangle \end{Bmatrix} \doteq f(\mathbf{x}) \frac{\pi(1-\nu^2)}{E} \int_{\mathfrak{A}} a^2 \int_{\Theta} \mathbf{g} \cdot \langle \mathbf{T} \rangle f(a, \theta) d\theta \, da \tag{10}$$

where $\mathfrak{A}$ and Θ are the integration domains of microcrack lengths and orientations (for open microcracks), respectively. Further, $\mathbf{g}$ is the transformation matrix relating the global and local coordinates, and $\mathbf{T}$ is *local* stress vector

$$[\mathbf{g}] = \begin{bmatrix} 2\sin^2\theta & -\sin 2\theta \\ 2\cos^2\theta & \sin 2\theta \\ -2\sin 2\theta & 2\cos 2\theta \end{bmatrix}; \quad \mathbf{T} = \begin{Bmatrix} p \\ q \end{Bmatrix}. \tag{11}$$

Following the same arguments in deriving $\langle \mathbf{e}^* \rangle$, the ensemble-average stress field (in the local coordinates) can be shown to be

$$\langle \mathbf{T} \rangle = \begin{Bmatrix} p^\infty \\ q^\infty \end{Bmatrix} + \left\langle \begin{Bmatrix} \tilde{p} \\ \tilde{q} \end{Bmatrix} \right\rangle \equiv \mathbf{T}^\infty + \langle \tilde{\mathbf{T}} \rangle \tag{12}$$

where $\mathbf{T}^\infty$ is the unperturbed local stress field due to remote loading, and $\langle \tilde{\mathbf{T}} \rangle$ is the ensemble average of the perturbation in local stress field due to pairwise microcrack *interactions*:

$$\langle \tilde{\mathbf{T}} \rangle(\mathbf{x}, a, \theta) = \int_{\Xi} \langle \tilde{\mathbf{T}} \rangle(\mathbf{x}, a, \theta | \mathbf{x}_1, a_1, \theta_1) f(\mathbf{x}_1, a_1, \theta_1 | \mathbf{x}, a, \theta) d\theta_1 da_1 d\mathbf{x}_1. \tag{13}$$

Here $\langle \tilde{\mathbf{T}} \rangle(\mathbf{x}, a, \theta | \mathbf{x}_1, a_1, \theta_1)$ is the stress perturbation of a microcrack centered at $\mathbf{x}$ with (a, θ) averaged over the subclass of realizations which have a microcrack centered at $\mathbf{x}_1$ with (a_1, θ_1). In addition, $f(\mathbf{x}_1, a_1, \theta_1 | \mathbf{x}, a, \theta)$ is the conditional probability function for finding a microcrack centered at $\mathbf{x}_1$ with (a_1, θ_1) given one microcrack centered at $\mathbf{x}$ with (a, θ). Since only the ensemble average is considered, the integral in (13) is performed over the domain of a *probabilistic* RVE (in the *probability space*) which is characterized by the two-point probability function $f(\mathbf{x}_1, a_1, \theta_1 | \mathbf{x}, a, \theta)$. Thus, the shape of the physical specimen plays no role here. The active (open) integration domain Ξ also depends on loading conditions and ranges of microcrack interactions.

Assuming that microcracks do *not* intersect one another and that *reasonable randomness* holds (Hinch, 1977), then $f(\mathbf{x}_1, a_1, \theta_1 | \mathbf{x}, a, \theta)$ is simplified to $f(\mathbf{x}_1, a_1, \theta_1)$. Further, by the *local homogeneity* assumption, $f(\mathbf{x}_1, a_1, \theta_1)$ becomes approximately $f(\mathbf{x}, a, \theta)$. Therefore, Eq. (13) can be approximated by the following expression:

$$\langle \tilde{\mathbf{T}} \rangle(\mathbf{x}, a, \theta) = f(\mathbf{x}, a, \theta) \int_{\Xi} \langle \tilde{\mathbf{T}} \rangle(\mathbf{x}, a, \theta | \mathbf{x}_1, a_1, \theta_1) d\theta_1 da_1 d\mathbf{x}_1. \tag{14}$$

The assumption that microcracks do not intersect one another certainly introduces some unknown errors. However, there are no analytical solutions available to accommodate interactions among pairs of arbitrarily *intersected* microcracks. Therefore, following usual simplification made in the literature (Kachanov, 1987; Kachanov and Laures, 1989), we do not consider the cases when microcracks intersect.

2.3 Approximate Analytical Solutions of a Two-Microcrack Interaction Problem. Due to enormous complexity, it is practically impossible to obtain closed-form analytical solutions of strongly interacting *many-microcrack* problems. The

Downloaded 03 May 2010 to 171.66.16.20. Redistribution subject to ASME license or copyright; see http://www.asme.org/terms/Terms_Use.cfm

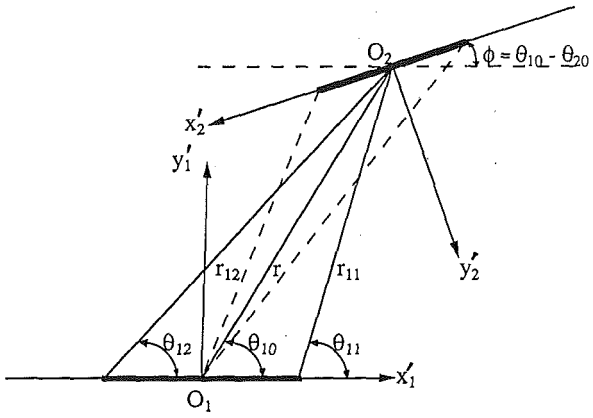


Fig. 3(*a*)

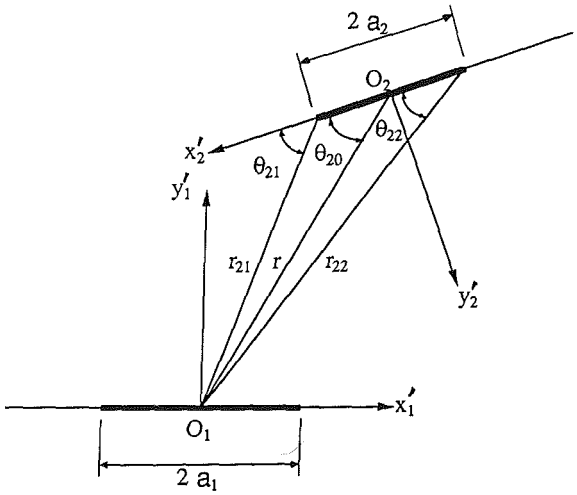


Fig. 3(*b*)

Fig. 3 Definitions of geometric quantities for two neighboring microcracks

formulation of arbitrarily located and oriented many-microcrack interaction problems is actually quite simple; see, e.g., Kachanov (1987) and Kachanov and Laures (1989). Nevertheless, the formulation involves $2N$ (if two-dimensional) or $3N$ (if three-dimensional) linear system of equations, where N designates the number of microcracks in an RVE (say, $N=100$). Clearly, numerical solutions of many-microcrack interaction problems are suitable for the Monte Carlo simulation approach mentioned earlier in Section 1. By contrast, the present work intends to construct closed-form explicit stress solutions ($\tilde{\mathbf{T}}$) and analytical expressions of microcrack-induced strains ($\mathbf{e}^*$) and compliances ($\mathbf{S}^*$) for interacting microcracks within the framework of the *ensemble-average* approach.

In order to construct useful explicit analytical solutions and to gain simple physical insight for interacting microcracks, multiple-microcrack stress *reflections* will be neglected as the first approximation. Namely, we will only consider local stress perturbations based on many (arbitrary) pairwise microcrack interactions. The extension to the higher-order ensemble-average formulation will be presented in Section 4 of Part II.

The *exact* analytical solutions of the boundary value problem of two arbitrarily located and oriented micocracks embedded in an infinite linear elastic isotropic solid are not yet available (except for some special configurations such as collinear microcracks). However, approximate analytical solutions were proposed by several investigators (e.g., Horii and Nemat-Nasser, 1985; Hori and Nemat-Nasser, 1987; Chudnovsky and Kachanov, 1983; Chudnovsky et al., 1987a,b; Kachanov, 1987).

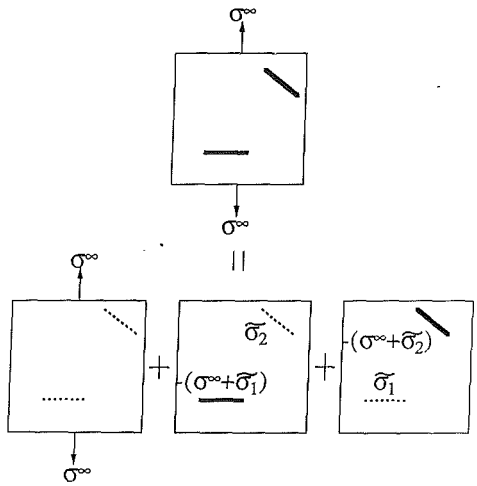


Fig. 4 Decomposition of two-microcrack interaction problem

In the present work, the "pseudo-traction" concept is adopted to find approximate analytical solutions of the two-microcrack interaction problem. For mathematical simplicity, only the *first term* of Taylor's expansion of the local stress field will be used to represent the average stress across the microcrack line.

The local coordinate systems 1 and 2 employed in the two-microcrack interaction problem are given in Figs. 3(*a*) and 3(*b*). The two microcracks have lengths $2a_1$ and $2a_2$, respectively. The y_1' and y_2'-directions are set to be normal to the microcrack lines C_1 and C_2. The original two-microcrack problem is decomposed into a homogeneous problem and two subproblems 1 and 2; see Fig. 4. In the homogeneous problem, an infinite solid without any microcrack is subjected to applied stresses at infinity. In the subproblem j ($j=1, 2$), an infinitely extended solid under zero remote stress at infinity has only one microcrack j, on which the boundary conditions are

$$-p_j+p_j^{\infty}+\tilde{p}_j=0; \quad -q_j+q_j^{\infty}+\tilde{q}_j=0 \quad \text{on} \quad C_j,\ j=1, 2. \tag{15}$$

The quantities $\tilde{p}_j$ and $\tilde{q}_j$ are to be determined in such a way that all boundary conditions of the original problem are satisfied. In the subproblem j, the "exact" stresses are given by (Sneddon and Lowengrub, 1969)

$$\begin{aligned}\sigma_{11}^j &= p_j(-1+E_j-F_j)+q_j(2G_j-H_j)\\ \sigma_{22}^j &= p_j(-1+E_j+F_j)+q_jH_j\\ \sigma_{21}^j &= p_jH_j+q_j(-1+E_j-F_j)\end{aligned} \tag{16}$$

where

$$\begin{aligned}E_j &\equiv \frac{r}{\sqrt{r_{j1}r_{j2}}}\cos\left(\theta_{j0}-\frac{\theta_{j1}+\theta_{j2}}{2}\right)\\ F_j &\equiv \frac{ra_j^2}{(r_{j1}r_{j2})^{3/2}}\sin\theta_{j0}\sin\frac{3}{2}(\theta_{j1}+\theta_{j2})\\ G_j &\equiv \frac{r}{\sqrt{r_{j1}r_{j2}}}\sin\left(\theta_{j0}-\frac{\theta_{j1}+\theta_{j2}}{2}\right)\\ H_j &\equiv \frac{ra_j^2}{(r_{j1}r_{j2})^{3/2}}\sin\theta_{j0}\cos\frac{3}{2}(\theta_{j1}+\theta_{j2}).\end{aligned} \tag{17}$$

See Fig. 3 for the definitions of r_{j1}, r_{j2}, θ_{j1}, and θ_{j2}.

In order to satisfy the original boundary conditions (15), it follows that

$$\begin{aligned}\tilde{p}_j &= \mathbf{e}_{2(i)}^j\cdot\boldsymbol{\sigma}^i\cdot\mathbf{e}_{2(i)}^j\\ \tilde{q}_j &= \mathbf{e}_{2(i)}^j\cdot\boldsymbol{\sigma}^i\cdot\mathbf{e}_{1(i)}^j\end{aligned} \quad i\neq j;\ i, j=1, 2 \text{ (no sum)} \tag{18}$$

where $\mathbf{e}_{1(i)}^j$ and $\mathbf{e}_{2(i)}^j$ are the two unit base vectors for the jth local coordinate system but are expressed in terms of the ith local coordinate components. The subscript i signifies that a quantity is referred to the (x_i', y_i') coordinate system. Sub-

Downloaded 03 May 2010 to 171.66.16.20. Redistribution subject to ASME license or copyright; see http://www.asme.org/terms/Terms_Use.cfm

stitution of Eq. (16) into Eq. (18) yields the local stresses for two microcracks:

$$\begin{Bmatrix} p_1 \\ q_1 \\ p_2 \\ q_2 \end{Bmatrix} = \begin{bmatrix} 0 & 0 & \alpha_1 & \alpha_2 \\ 0 & 0 & \alpha_3 & \alpha_4 \\ \alpha_5 & \alpha_6 & 0 & 0 \\ \alpha_7 & \alpha_8 & 0 & 0 \end{bmatrix} \begin{Bmatrix} p_1 \\ q_1 \\ p_2 \\ q_2 \end{Bmatrix} + \begin{Bmatrix} p_1^\infty \\ q_1^\infty \\ p_2^\infty \\ q_2^\infty \end{Bmatrix} \equiv \boldsymbol{\alpha} \cdot \mathbf{T}_{1-2} + \mathbf{T}_{1-2}^\infty \tag{19}$$

where

$$\begin{aligned} \alpha_1 &= -1 + E_2 + F_2 \cos 2\phi + H_2 \sin 2\phi \\ \alpha_2 &= 2G_2 \sin^2 \phi + H_2 \cos 2\phi - (1 - E_2 + F_2) \sin 2\phi \\ \alpha_3 &= H_2 \cos 2\phi - F_2 \sin 2\phi \\ \alpha_4 &= (G_2 - H_2) \sin 2\phi - (1 - E_2 + F_2) \cos 2\phi \\ \alpha_5 &= -1 + E_1 + F_1 \cos 2\phi - H_1 \sin 2\phi \\ \alpha_6 &= 2G_1 \sin^2 \phi + H_1 \cos 2\phi + (1 - E_1 + F_1) \sin 2\phi \\ \alpha_7 &= H_1 \cos 2\phi + F_1 \sin 2\phi \\ \alpha_8 &= -(G_1 - H_1) \sin 2\phi - (1 - E_1 + F_1) \cos 2\phi \end{aligned} \tag{20}$$

and $\phi \equiv \theta_{10} - \theta_{20}$. It is noteworthy that the "microcrack interaction matrix" $\boldsymbol{\alpha}$ in Eq. (19) actually corresponds to the "transmission factor" matrix $\boldsymbol{\Lambda}$ in Kachanov (1987). In addition, it is convenient to define $\mathbf{T}_{1-2} \equiv (p_1, q_1, p_2, q_2)^T$, $\mathbf{T}_{1-2}^\infty \equiv (p_1^\infty, q_1^\infty, p_2^\infty, q_2^\infty)^T$ and $\tilde{\mathbf{T}}_{1-2} \equiv (\tilde{p}_1, \tilde{q}_1, \tilde{p}_2, \tilde{q}_2)^T$. Since $\mathbf{T}_{1-2} = \mathbf{T}_{1-2}^\infty + \tilde{\mathbf{T}}_{1-2}$, one can solve $\tilde{\mathbf{T}}_{1-2}$ from Eq. (19):

$$\tilde{\mathbf{T}}_{1-2} = \boldsymbol{\alpha} \cdot (\mathbf{I} - \boldsymbol{\alpha})^{-1} \cdot \mathbf{T}_{1-2}^\infty. \tag{21}$$

The comparison of the stress *transmission factors* obtained by using the simple "first-term" approximation (Λ) and the exact solutions (Λ_{ex}) for two collinear microcracks is given in Appendix A for various *normalized* microcrack-tip distance ratios. When $d = 0.25$, it means that the *ratio* of the two microcrack-tip *spacing* to the microcrack *size* ($2a$) is 0.25. It is noted that $\Lambda \equiv 1$ when microcrack interaction is totally neglected. From Table 2 in Appendix A, it is observed that the simple "first-term" approximation is quite acceptable in general except when two microcracks tips are really close to each other (i.e., when $d < 0.1$). It is emphasized that the spatial location of the second microcrack given the first microcrack is random. Therefore, the errors (in Table 2) associated with the proposed approximate analysis should be statistically *averaged* over all possible realizations.

Let us recall that $\tilde{\mathbf{T}} \equiv (\tilde{p}_1, \tilde{q}_1)^T$ and define $\mathbf{K}_1$ as the first two *rows* of the matrix $[\boldsymbol{\alpha} \cdot (\mathbf{I} - \boldsymbol{\sigma})^{-1}]$. Therefore, from Eq. (21), we have

$$\tilde{\mathbf{T}} = \mathbf{K}_1 \cdot \mathbf{T}_{1-2}^\infty. \tag{22}$$

We can now substitute Eq. (22) into (14) and (12) to find the ensemble-average stress of a primary microcrack located at $\mathbf{x}$ over all possible positions and orientations ($\mathbf{x}_1$ and θ_1) of the second neighboring microcrack. In addition, the local and global remote stresses $\mathbf{T}_{1-2}^\infty$ and τ^∞ are related by the following transformation matrix $\mathbf{K}_2$:

$$\begin{Bmatrix} p_1^\infty \\ q_1^\infty \\ p_2^\infty \\ q_2^\infty \end{Bmatrix} = \begin{bmatrix} \sin^2\theta & \cos^2\theta & -\sin 2\theta \\ -1/2 \sin 2\theta & 1/2 \sin 2\theta & \cos 2\theta \\ \sin^2(\theta+\phi) & \cos^2(\theta+\phi) & -\sin 2(\theta+\phi) \\ -1/2 \sin 2(\theta+\phi) & 1/2 \sin 2(\theta+\phi) & \cos 2(\theta+\phi) \end{bmatrix} \begin{Bmatrix} \sigma_{11}^\infty \\ \sigma_{22}^\infty \\ \sigma_{21}^\infty \end{Bmatrix} \equiv \mathbf{K}_2 \cdot \tau^\infty. \tag{23}$$

Therefore, Eq. (22) can be rephrased as

$$\tilde{\mathbf{T}} = \mathbf{K}_1 \cdot \mathbf{K}_2 \cdot \tau^\infty \equiv \mathbf{K} \cdot \tau^\infty \tag{24}$$

where $\mathbf{K} \equiv \mathbf{K}_1 \cdot \mathbf{K}_2$. The detailed *explicit* components of matrix $\mathbf{K}$ are given in Appendix B.

Remark 2.1. It appears that there are some typographical errors in Sneddon and Lowengrub's (1969) solutions. Equations (16) and (17) are the correct formulas after the problem is resolved. ■

2.4 Overall Moduli of Brittle Solids With Interacting Microcracks. By substituting Eqs. (24) and (22) into Eq. (12) and assuming that $\mathbf{x}$ and (a, θ) are statistically independent, one obtains the following expression for the ensemble-average stresses:

$$\langle \mathbf{T} \rangle = \langle \mathbf{T}^\infty + \tilde{\mathbf{T}} \rangle = (\mathbf{K}_0 + f(\mathbf{x}) f(a, \theta) \langle \mathbf{K} \rangle) \cdot \tau^\infty \tag{25}$$

where $\mathbf{T}^\infty \equiv \mathbf{K}_0 \cdot \tau^\infty$, and

$$\mathbf{K}_0 = \begin{bmatrix} \sin^2\theta & \cos^2\theta & -\sin 2\theta \\ -1/2 \sin 2\theta & 1/2 \sin 2\theta & \cos 2\theta \end{bmatrix} \tag{26}$$

$$\langle \mathbf{K} \rangle \equiv \int_{\Xi} \mathbf{K}\, r dr\, d\theta_{10}\, d\theta_{20}\, da_2. \tag{27}$$

Substitution of (25) into (10) then yields the ensemble-average damage-induced strain vector:

$$\langle \mathbf{e}^* \rangle(\mathbf{x}) = \{ \langle \mathbf{S}^{*1} \rangle + \langle \mathbf{S}^{*2} \rangle \} \cdot \tau^\infty \equiv \langle \mathbf{S}^* \rangle \cdot \tau^\infty \tag{28}$$

where

$$\langle \mathbf{S}^{*1} \rangle \equiv \frac{\pi(1-\nu^2)}{E} f(\mathbf{x}) \int_{\mathcal{A}} a^2 \int_{\Theta} \mathbf{g} \cdot \mathbf{K}_0 f(a, \theta) d\theta\, da \tag{29}$$

$$\langle \mathbf{S}^{*2} \rangle \equiv \frac{\pi(1-\nu^2)}{E} f^2(\mathbf{x}) \int_{\mathcal{A}} a^2 \int_{\Theta} \mathbf{g} \cdot \mathbf{K}_0 f^2(a, \theta) d\theta\, da. \tag{30}$$

Clearly, $\langle \mathbf{S}^* \rangle$ is the ensemble-average damage-induced compliance matrix. $f(\mathbf{x})$ and $f(a, \theta)$ depend on material microstructures and loading conditions, and should be specified by experimental observations (e.g., by scanning electron microscopy or computerized tomography).

In what follows, as an illustration for deriving an *explicit* form of overall moduli of microcracked solids, we consider the special case in which: (1) $f(a, \theta) = f(a) f(\theta)$, (2) microcrack orientation is perfectly random (i.e., $f(\theta) = 1/\pi$), (3) the initial microcrack radius a is a constant, and (4) $f(\mathbf{x})$ satisfies

$$\int_A f^2(\mathbf{x}) dA \approx \left\{ \int_A f(\mathbf{x}) dA \right\}^2 / A. \tag{31}$$

Moreover, it is realized that

$$\int_A f(\mathbf{x}) dA = N \tag{32}$$

where N is the total number of microcracks within an RVE (with area A). Since statistical homogeneity (in the probability space) is assumed, the volume average coincides with the ensemble average. The volume average (denoted by an overline) of (28) over an RVE thus takes the form

$$\overline{\langle \mathbf{e}^* \rangle} = \frac{(1-\nu^2)}{E} \left\{ \omega \int_{\Theta} \mathbf{g} \cdot \mathbf{K}_0 d\theta + \frac{\omega^2}{\pi} \int_{\Theta} \mathbf{g} \cdot \langle \hat{\mathbf{K}} \rangle d\theta \right\} \cdot \tau^\infty \tag{33}$$

where

$$\langle \hat{\mathbf{K}} \rangle \equiv \int_{\hat{\Xi}} \mathbf{K}\, r dr d\theta_{10} d\theta_{20} \tag{34}$$

Downloaded 03 May 2010 to 171.66.16.20. Redistribution subject to ASME license or copyright; see http://www.asme.org/terms/Terms_Use.cfm

and $\hat{\Xi}$ is the active (open) probabilistic integration domain for variables r, θ_{10}, and θ_{20}. The effective radius r has been normalized with respect to the microcrack radius a. Further, $\omega \equiv (Na^2/A) \equiv na^2 \equiv \hat{\omega}/\pi$ is a measure of microcrack concentrations. It is emphasized that our definition of microcrack concentration ω differs from the commonly used definition ($\hat{\omega}$) by a multiplier π (see Budiansky and O'Connell, 1976). The integration domains Θ and $\hat{\Xi}$ also depend on loading conditions and range of microcrack interactions.

By substituting Eq. (33) into the volume average of Eq. (4), we finally obtain the following ensemble-volume averaged macroscopic constitutive relation (in Voigt's notation):

$$\overline{\langle \mathbf{e} \rangle} = \overline{\langle \mathbf{S} \rangle} \cdot \boldsymbol{\tau}^{\infty} \tag{35}$$

where

$$\overline{\langle \mathbf{S} \rangle} \equiv \mathbf{S}^{o} + \overline{\langle \mathbf{S}^{*1} \rangle} + \overline{\langle \mathbf{S}^{*2} \rangle}. \tag{36}$$

That is, $\overline{\langle \mathbf{S} \rangle}$ is the ensemble-volume averaged overall effective compliance matrix of a microcracked brittle solid. Specifically, under the *plane-strain* assumption, we write

$$\mathbf{S}^{o} = \frac{(1+\nu)}{E} \begin{bmatrix} 1-\nu & -\nu & 0 \\ -\nu & 1-\nu & 0 \\ 0 & 0 & 2 \end{bmatrix} \tag{37}$$

$$\overline{\langle \mathbf{S}^{*1} \rangle} \equiv \frac{(1-\nu^2)}{E} \omega \int_{\Theta} \mathbf{g} \cdot \mathbf{K}_0 \, d\theta \tag{38}$$

$$\overline{\langle \mathbf{S}^{*2} \rangle} \equiv \frac{(1-\nu^2)}{\pi E} \omega^2 \int_{\Theta} \mathbf{g} \cdot \langle \hat{\mathbf{K}} \rangle \, d\theta. \tag{39}$$

It is noted that $\mathbf{S}^o$ denotes the elastic compliance, $\overline{\langle \mathbf{S}^{*1} \rangle}$ defines the first-order microcrack effects without interaction, and $\overline{\langle \mathbf{S}^{*2} \rangle}$ defines the second-order (in ω^2) microcrack interaction effects.

Remark 2.2. It is interesting to notice that Eq. (28) reveals that physical *nonlocal effects* are brought into constitutive equations through the process of microcrack interaction and *ensemble averaging* (not volume averaging). That is, in Eq. (28), the stress-strain law at a material point within a RVE depends *not only* on the constitutive behavior at the point, but *also* on the constitutive behavior of *neighboring* points. ■

3 Some Special Stationary Examples

In this section, we apply the proposed ensemble-volume average approach to solve three special examples. These examples are all classified as *stationary* micromechanical models. In particular, the first example shows that the proposed method recovers the well-known Taylor's model when microcrack interaction is entirely neglected in Eq. (36). In the second example, we examine the randomly located aligned (parallel) microcracks problem—for transverse cracking phenomenon in laminated composites, for instance. The last example shows that the overall compliance matrix becomes *isotropic* when all microcracks are open. Microcrack locations and orientations are assumed to be perfectly random. In what follows, for simplicity, we further assume that closed microcrack contributions are neglected.

3.1 Dilute Microcracks—Taylor's Model. The *open* microcrack angle domain $\Theta \equiv [\theta_1, \theta_2]$ can be found by solving

$$\sin^2\theta \, \sigma_{11}^{\infty} + \cos^2\theta \, \sigma_{22}^{\infty} - \sin 2\theta \, \sigma_{21}^{\infty} \geq 0 \tag{40}$$

where tensile normal stress is taken as positive. After dropping the interaction term in (36), the overall compliance becomes

$$\overline{\langle \mathbf{S} \rangle} = \mathbf{S}^{o} + \overline{\langle \mathbf{S}^{*1} \rangle} \tag{41}$$

where (by integrating Eq. (38))

$$\overline{\langle \mathbf{S}^{*1} \rangle} = \frac{(1-\nu^2)}{E} \omega \begin{bmatrix} S_{11}^{*1} & 0 & S_{16}^{*1} \\ 0 & S_{22}^{*1} & S_{26}^{*1} \\ S_{61}^{*1} & S_{62}^{*1} & S_{66}^{*1} \end{bmatrix}. \tag{42}$$

Specifically, we have

$$\begin{aligned} S_{11}^{*1} &= \theta_2 - \theta_1 - \frac{1}{2}(\sin 2\theta_2 - \sin 2\theta_1) \\ S_{22}^{*1} &= \theta_2 - \theta_1 + \frac{1}{2}(\sin 2\theta_2 - \sin 2\theta_1) \\ S_{66}^{*1} &= 2(\theta_2 - \theta_1) \\ S_{16}^{*1} &= \sin^2\theta_1 - \sin^2\theta_2 = S_{61}^{*1} = S_{26}^{*1} = S_{62}^{*1}. \end{aligned} \tag{43}$$

For various biaxial loading conditions, we obtain the following results:

(*1*) *Uniaxial or biaxial tension.* All microcracks are open ($\theta_1 = 0$, $\theta_2 = \pi$) and isotropic damage is recovered. The orientation domain is $\Theta \equiv [0, \pi]$. The *nonzero* components in (43) are

$$S_{11}^{*1} = S_{22}^{*1} = \pi; \quad S_{66}^{*1} = 2\pi. \tag{44}$$

(*2*) *Biaxial tension/compression.* We have the axial stress $\sigma_{22}^{\infty} > 0$, the lateral stress $\sigma_{11}^{\infty} < 0$, and shear stress $\sigma_{21}^{\infty} = 0$. The open microcrack angle domain is defined by $\Theta \equiv [0, \theta^*] \cup [\pi - \theta^*, \pi]$, where

$$\theta^* = \tan^{-1} \sqrt{\frac{-\sigma_{22}^{\infty}}{\sigma_{11}^{\infty}}}. \tag{45}$$

The *nonzero* anisotropic components in (43) are

$$S_{11}^{*1} = 2\theta^* - \sin 2\theta^*; \quad S_{22}^{*1} = 2\theta^* + \sin 2\theta^*; \quad S_{66}^{*1} = 4\theta^*. \tag{46}$$

(*3*) *Biaxial tension and shear.* We have $\sigma_{11}^{\infty} = \sigma_{22}^{\infty} > 0$ and $\sigma_{21}^{\infty} \geq \sigma_{22}^{\infty}$. The open domain is defined by $\Theta \equiv [\pi/2, \pi] \cup [0, \theta^*] \cup [\pi/2 - \theta^*, \pi/2]$, where

$$\theta^* = \frac{1}{2} \sin^{-1} \left(\frac{\sigma_{22}^{\infty}}{\sigma_{21}^{\infty}} \right). \tag{47}$$

The *nonzero* components in (43) are

$$\begin{aligned} S_{11}^{*1} &= \frac{\pi}{2} + 2\theta^* = S_{22}^{*1}; \quad S_{66}^{*1} = \pi + 4\theta^* \\ S_{16}^{*1} &= \cos 2\theta^* = S_{61}^{*1} = S_{26}^{*1} = S_{62}^{*1}. \end{aligned} \tag{48}$$

3.2 Aligned Microcracks. Attention is now focused on an array of randomly located aligned (parallel) open microcracks. This class of problems is relevant to the transverse matrix cracking problem in laminated composites (see, for example, Laws, Dvorak, and Hejazi, 1983; Laws and Dvorak, 1987). Since all microcracks have the same orientation, Eq. (17) can be simplified as follows:

$$\begin{aligned} E_1 &= E_2 = \frac{r}{\sqrt{r_1 r_2}} \cos\left(\theta_{10} - \frac{\theta_{11} + \theta_{12}}{2} \right) \\ F_1 &= F_2 = \frac{ra^2}{(r_1 r_2)^{3/2}} \sin\theta_{10} \sin\frac{3}{2}(\theta_{11} + \theta_{12}) \\ G_1 &= G_2 = \frac{r}{\sqrt{r_1 r_2}} \sin\left(\theta_{10} - \frac{\theta_{11} + \theta_{12}}{2} \right) \\ H_1 &= H_2 = \frac{ra^2}{(r_1 r_2)^{3/2}} \sin\theta_{10} \cos\frac{3}{2}(\theta_{11} + \theta_{12}) \end{aligned} \tag{49}$$

where

Downloaded 03 May 2010 to 171.66.16.20. Redistribution subject to ASME license or copyright; see http://www.asme.org/terms/Terms_Use.cfm

$$r_1 = (r^2 - 2ar\cos\theta_{10} + a^2)^{1/2}$$
$$r_2 = (r^2 + 2ar\cos\theta_{10} + a^2)^{1/2}$$
$$\theta_{11} = \cos^{-1}\left(\frac{r\cos\theta_{10} - a}{r_1}\right)$$
$$\theta_{12} = \cos^{-1}\left(\frac{r\cos\theta_{10} + a}{r_1}\right) \tag{50}$$

and $\theta = 0 = \phi \equiv \theta_{10} - \theta_{20}$, $\theta_{10} = \theta_{20}$.

The numerical integration of Eq. (34) will be addressed in Section 3 of Part II of this series. The minimum radius of integration in r (center distance between microcracks) is taken as $2a$. The convergence behavior for the integration in (34) (i.e., $\langle \hat{K}_{ij} \rangle$) with respect to the choice of the maximum integration radius r_{max} is given in Table 1. It is observed that use of $r_{max} = 20a$ is quite acceptable. After numerical Gauss integration of (34) (by using 40 Gauss points), we obtain

$$\langle \hat{\mathbf{K}} \rangle = \begin{bmatrix} 0 & 0.5865 & 0 \\ 0 & 0 & 0.2406 \end{bmatrix}. \tag{51}$$

Accordingly, the transversely isotropic compliance becomes

$$\overline{\langle \mathbf{S} \rangle} = \frac{(1-\nu^2)}{E}\left\{\begin{bmatrix} 1 & \frac{-\nu}{1-\nu} & 0 \\ \frac{-\nu}{1-\nu} & 1 & 0 \\ 0 & 0 & \frac{2}{1-\nu} \end{bmatrix} + \pi \begin{bmatrix} 0 & 0 & 0 \\ 0 & 2\omega + 1.173\omega^2 & 0 \\ 0 & 0 & 2\omega + 0.481\omega^2 \end{bmatrix}\right\}. \tag{52}$$

Clearly, the first-order terms ω in Eq. (52) come from Taylor's model, and the second-order corrections ω^2 in (52) come from the pairwise microcrack interactions.

3.3 Isotropic Damage. Under uniaxial or biaxial tension, all microcracks are typically assumed open. It is also assumed that microcracks are randomly located, randomly oriented, and of uniform size. As a result, the overall behavior is isotropic. The compliance contribution due to the microcrack interaction can be evaluated by performing numerical Gauss integration of Eq. (39). The results are

$$\overline{\langle \mathbf{S}^{*2} \rangle} = \frac{(1-\nu^2)}{E}\pi\omega^2 \begin{bmatrix} 0.373 & 0.041 & 0 \\ 0.041 & 0.373 & 0 \\ 0 & 0 & 0.664 \end{bmatrix}. \tag{53}$$

Therefore, the (plane-strain) overall compliance becomes

$$\overline{\langle \mathbf{S} \rangle} = \frac{(1-\nu^2)}{E}\left\{\begin{bmatrix} 1 & \frac{-\nu}{1-\nu} & 0 \\ \frac{-\nu}{1-\nu} & 1 & 0 \\ 0 & 0 & \frac{2}{1-\nu} \end{bmatrix} + \pi \begin{bmatrix} \omega + 0.373\omega^2 & 0.041\omega^2 & 0 \\ 0.041\omega^2 & \omega + 0.373\omega^2 & 0 \\ 0 & 0 & 2\omega + 0.664\omega^2 \end{bmatrix}\right\}. \tag{54}$$

It is noted that the shear moduli (in 1-2 and 2-1 directions) are changed (nonzero) due to microcrack interaction.

It is very interesting to compare the foregoing overall compliance matrix with that derived by the self-consistent model (e.g., Horii and Nemat-Nasser, 1983). The overall compliance given by the self-consistent method is this isotropic damage case is

$$\overline{\mathbf{S}}^{sc} = \frac{(1-\nu^2)}{E}\begin{bmatrix} \frac{1}{1-\pi\omega} & \frac{-\nu}{1-\nu} & 0 \\ \frac{-\nu}{1-\nu} & \frac{1}{1-\pi\omega} & 0 \\ 0 & 0 & \frac{2}{1-\nu}\frac{1-\pi\nu\omega}{1-\pi\omega} \end{bmatrix}. \tag{55}$$

Obviously, the overall compliance given by the self-consistent method goes to infinity at $\omega = 1/\pi$. An effective medium theory is inherently more suitable for low microcrack concentrations since it does *not* depend on microcrack locations.

For low values of $\omega \ll 1/\pi$, the Taylor's expansion of Eq. (55) renders

$$\overline{\mathbf{S}}^{sc} = \frac{(1-\nu^2)}{E}\left\{\begin{bmatrix} 1 & \frac{-\nu}{1-\nu} & 0 \\ \frac{-\nu}{1-\nu} & 1 & 0 \\ 0 & 0 & \frac{2}{1-\nu} \end{bmatrix} + \pi \begin{bmatrix} \omega + \pi\omega^2 & 0 & 0 \\ 0 & \omega + \pi\omega^2 & 0 \\ 0 & 0 & 2(\omega + \pi\omega^2) \end{bmatrix}\right\}. \tag{56}$$

Apparently, the compliance calculated by the self-consistent method is *higher* than that of the present model. In addition, the self-consistent method predicts *no change* in shear moduli in the 1-2 and 2-1 directions. Finally, it is emphasized that there is no singularity in the present method irrespective of the ω value.

From Eq. (54), it is clear that the relative weight of the second-order terms (in ω^2, due to microcrack interaction) to the first-order terms (in ω) depends on the values of ω. For example, the relative weight is 0.373ω for the 11 and 22 terms in the compliance matrix. If the microcrack density is very small (dilute), the second-order terms are negligible. On the other hand, if the microcrack density is high (e.g., $\omega = 0.5$—corresponding to $\hat{\omega} = 0.5\pi$ defined by Budiansky and O'Connell, 1976), then contributions from the second-order terms are quite significant. It is noted that, however, when micro-

Downloaded 03 May 2010 to 171.66.16.20. Redistribution subject to ASME license or copyright; see http://www.asme.org/terms/Terms_Use.cfm

Table 1. Convergence behavior of $\langle \hat{K}_{ij} \rangle$ versus r_{max}

r_{max}	$\langle \hat{K}_{12} \rangle$	$\langle \hat{K}_{23} \rangle$
$4a$	0.429843	0.173965
$8a$	0.550972	0.225418
$16a$	0.582654	0.238972
$20a$	0.586498	0.240618
$40a$	0.591638	0.242820
$400a$	0.591894	0.243244

crack densities are extremely high, the proposed second-order method may not be accurate enough since higher-order terms should be included; see Section 4 of Part II for extension to the higher-order formulation.

The proposed statistical micromechanical framework is *not* restricted to widely spaced microcrack arrays. From Table 2 in Appendix A, it is seen that the proposed two-microcrack interaction solutions are quite acceptable even when the ratio d is only 0.1 (i.e., when the "microcrack-tip spacing" is only one-tenth of the "microcrack size").

4 Conclusions

A two-dimensional statistical micromechanical theory for microcrack-weakened brittle solids is presented based on the concepts of ensemble-average and pairwise microcrack interaction. The overall compliances are derived by performing ensemble-volume averaged integration over the domain of a statistically representative volume element (in the probability space). Unlike the self-consistent method which introduces a singularity at $\omega = 1/\pi$, our method predicts a smooth increase of effective compliance as ω increases. Further, the proposed microcrack interaction framework does *not* require the use of Monte Carlo simulations. It is emphasized that the proposed second-order terms are second-order in ω^2, not second-order in geometric quantities [such as $(a/r)^2$]. In addition, pairwise interaction effects do not vanish in the event of perfectly randomly distributed microcracks; see Eq. (53). In fact, effects of pairwise microcrack interactions are equally distributed in all directions and therefore the overall behavior is isotropic.

In Part II of this series, we will further investigate issues pertaining to computational aspects of the proposed approach, extension to "evolutionary" micromechanical damage models (with "cleavage 1" microcrack growth), and a higher-order microcrack interaction model. Extension of a three-dimensional statistical micromechanical theory of brittle solids with randomly located, interacting *penny-shaped* microcracks is presented in a separate paper (Ju and Tseng, 1992). Numerical comparisons with the Taylor's model, the self-consistent model, and the differential scheme is also presented in Ju and Tseng (1992).

Acknowledgment

This work was sponsored by the Air Force Office of Scientific Research under Grant No. AFOSR-90-0336, together with the Defense Nuclear Agency. The authors gratefully acknowledge this support and the interest of Dr. Spencer T. Wu, Dr. Paul Senseny, and Dr. Kent L. Goering.

References

Batchelor, G. K., 1970, "The Stress System in a Suspension of Force-Free Particles," *J. Fluid Mech.*, Vol. 41, pp. 545–570.

Batchelor, G. K., and Green, J. T., 1972, "The Determination of the Bulk Stress in a Suspension of Spherical Particles to Order c^2," *J. Fluid Mech.*, Vol. 56, pp. 401–427.

Benveniste, Y., 1986, "On the Mori-Tanaka's Method in Cracked Bodies," *Mech. Res. Comm.*, Vol. 13, pp. 193–201.

Budiansky, B., and O'Connell, R. J., 1976, "Elastic Moduli of a Cracked Solid," *Int. J. Solids & Struct.*, Vol. 12, pp. 81–97.

Chen, H. S., and Acrivos, A., 1978a, "The Solution of the Equations of Linear Elasticity for an Infinite Region Containing Two Spherical Inclusions," *Int. J. Solids & Struct.*, Vol. 14, pp. 331–348.

Chen, H. S., and Acrivos, A., 1978b, "The Effective Elastic Moduli of Composite Materials Containing Spherical Inclusions at Non-Dilute Concentrations," *Int. J. Solids & Struct.*, Vol. 14, pp. 349–364.

Christensen, R. M., 1990, "A Critical Evaluation for a Class of Micromechanics Models," *J. Mech. Phys. Solids*, Vol. 38, No. 3, pp. 379–404.

Christensen, R. M., and Lo, K. H., 1979, "Solutions for Effective Shear Properties in Three Phase Sphere and Cylinder Models," *J. Mech. Phys. Solids*, Vol. 27, pp. 315–330.

Chudnovsky, A., and Kachanov, M., 1983, "Interaction of a Crack with a Field of Microcracks," *Int. J. Eng. Sci.*, Vol. 21, pp. 1009–1018.

Chudnovsky, A., Dolgopolsky, A., and Kachanov, M., 1987a, "Elastic Interaction of a Crack with a Microcrack Array—I. Formulation of the Problem and General Form of the Solution," *Int. J. Solids & Struct.*, Vol. 23, No. 1, pp. 1–10.

Chudnovsky, A., Dolgopolsky, A., and Kachanov, M., 1987b, "Elastic Interaction of a Crack with a Microcrack Array—II. Elastic Solution for Two Crack Configurations," *Int. J. Solids & Struct.*, Vol. 23, No. 1, pp. 11–21.

Fanella, D., and Krajcinovic, D., 1988, "A Micromechanical Model for Concrete in Compression," *Eng. Fract. Mech.*, Vol. 29, No. 1, pp. 49–66.

Gross, D., 1982, "Spannungsintensitatsfaktoren von ribsystemen (Stress Intensity Factors of Systems of Cracks)," *Ing.-Arch.*, Vol. 51, pp. 301–310 (in German).

Hashin, Z., 1988, "The Differential Scheme and Its Application to Cracked Materials," *J. Mech. Phys. Solids*, Vol. 36, pp. 719–734.

Hill, R., 1965, "A Self-Consistent Mechanics of Composite Materials," *J. Mech. Phys. Solids*, Vol. 13, pp. 213–222.

Hinch, E. J., 1977, "An Averaged-Equation Approach to Particle Interactions in a Fluid Suspension," *J. Fluid Mech.*, Vol. 83, pp. 695–720.

Hori, M., and Nemat-Nasser, S., 1987, "Interacting Micro-Cracks Near the Tip in the Process Zone of a Macro-Crack," *J. Mech. Phys. Solids*, Vol. 35, pp. 601–629.

Horii, H., and Nemat-Nasser, S., 1983, "Overall Moduli of Solids with Microcracks: Load-Induced Anisotropy," *J. Mech. Phys. Solids*, Vol. 331, pp. 155–171.

Horii, H., and Nemat-Nasser, S., 1985, "Elastic Fields of Interacting Inhomogeneities," *Int. J. Solids & Struct.*, Vol. 21, pp. 731–745.

Horii, H., and Sahasakmontri, K., 1990, "Mechanical Properties of Cracked Solids: Validity of the Self-Consistent Method," *Micromechanics and Inhomogeneity*, G. J. Weng, M. Taya, and H. Abe, eds., Springer-Verlag, New York, pp. 137–159.

Hudson, J. A., 1980, "Overall Properties of a Cracked Solid," *Math. Proc. Camb. Phil. Soc.*, Vol. 88, pp. 371–384.

Hudson, J. A., 1981, "Wave Speeds and Attenuation of Elastic Waves in Material Containing Cracks," *Geophys. J. R. astr. Soc.*, Vol. 64, pp. 133–150.

Hudson, J. A., 1986, "A Higher Order Approximation to the Wave Propagation Constants for a Cracked Solid," *Geophys. J. R. astr. Soc.*, Vol. 87, pp. 265–274.

Ju, J. W., 1991a, "On Two-Dimensional Self-Consistent Micromechanical Damage Models for Brittle Solids," *Int. J. Solids & Struct.*, Vol. 27, No. 2, pp. 227–258.

Ju, J. W., 1991b, "A Micromechanical Damage Model for Uniaxially Reinforced Composites Weakened by Interfacial Arc Microcracks," ASME JOURNAL OF APPLIED MECHANICS, Vol. 58, pp. 923–930.

Ju, J. W., and Lee, X., 1991, "On Three-Dimensional Self-Consistent Micromechanical Damage Models for Brittle Solids. Part I: Tensile Loadings," *J. Eng. Mech.*, ASCE, Vol. 117, No. 7, pp. 1495–1515.

Ju, J. W., and Tseng, K. W., 1992, "A Three-Dimensional Statistical Micromechanical Theory for Brittle Solids with Interacting Microcracks," *Int. J. Damage Mechanics*, Vol. 1, No. 1, pp. 102–131.

Kachanov, M., 1987, "Elastic Solids with Many Cracks: A Simple Method of Analysis," *Int. J. Solids & Struct.*, Vol. 23, pp. 23–43.

Kachanov, M., and Montagut, E., 1986, "Interaction of a Crack with Certain Microcrack Arrays," *Eng. Fracture Mech.*, Vol. 25, pp. 625–636.

Kachanov, M., and Laures, J.-P., 1989, "Three-Dimensional Problems of Strongly Interacting Arbitrarily Located Penny-Shaped Cracks," *Int. J. of Fract.*, Vol. 41, pp. 289–313.

Krajcinovic, D., 1989, "Damage Mechanics," *Mech. Mater.*, Vol. 8, No. 2–3, pp. 117–197.

Krajcinovic, D., and Fanella, D., 1986, "A Micromechanical Damage Model for Concrete," *Eng. Fract. Mech.*, Vol. 25, pp. 585–596.

Krajcinovic, D., and Sumarac, D., 1989, "A Mesomechanical Model for Brittle Deformation Processes: Part I," ASME JOURNAL OF APPLIED MECHANICS, Vol. 56, pp. 51–62.

Laws, N., and Dvorak, G. J., 1987, "The Effect of Fiber Breaks and Aligned Penny-Shaped Cracks on the Stiffness and Energy Release Rates in Unidirectional Composites," *Int. J. Solids & Struct.*, Vol. 23, No. 9, pp. 1269–1283.

Laws, N., Dvorak, G. J., and Hejazi, M., 1983, "Stiffness Changes in Unidirectional Composites Caused by Crack Systems," *Mech. of Mater.*, Vol. 2, pp. 123–137.

Lee, X., and Ju, J. W., 1991, "On Three-Dimensional Self-Consistent Micromechanical Damage Models for Brittle Solids. Part II: Compressive Loadings," *J. Eng. Mech.*, ASCE, Vol. 117, No. 7, pp. 1516–1537.

McLaughlin, R., 1977, "A Study of the Differential Scheme for Composite Materials," *Int. J. Engng. Sci.*, Vol. 15, pp. 237–244.

Mori, T., and Tanaka, K., 1973, "Average Stress in Matrix and Average Elastic Energy of Materials with Misfitting Inclusions," *Acta Metallurgica*, Vol. 21, pp. 571–574.

Downloaded 03 May 2010 to 171.66.16.20. Redistribution subject to ASME license or copyright; see http://www.asme.org/terms/Terms_Use.cfm

Nemat-Nasser, S., and Hori, M., 1990, "Elastic Solids with Microdefects," *Micromechanics and Inhomogeneity*, G. J. Weng, M. Taya, and H. Abe, eds., Springer-Verlag, New York, pp. 297–320.

Roscoe, R. A., 1952, "The Viscosity of Suspensions of Rigid Spheres," *Brit. J. Appl. Phys.*, Vol. 3, pp. 267–269.

Roscoe, R. A., 1973, "Isotropic Composites with Elastic or Viscoelastic Phases: General Bounds for the Moduli and Solutions for Special Geometries," *Rheol. Acta*, Vol. 12, pp. 404–411.

Sayers, C. M., and Kachanov, M., 1991, "A Simple Technique for Finding Effective Elastic Constants of Cracked Solids for Arbitrary Crack Orientation Statistics," *Int. J. Solids & Struct.*, Vol. 27, No. 6, pp. 671–680.

Sneddon, I. N., and Lowengrub, M., 1969, *Crack Problems in the Classical Theory of Elasticity*, John Wiley and Sons, New York.

Sumarac, D., and Krajcinovic, D., 1987, "A Self-Consistent Model for Microcrack-Weakened Solids," *Mech. Mater.*, Vol. 6, pp. 39–52.

Sumarac, D., and Krajcinovic, D., 1989, "A Mesomechanical Model for Brittle Deformation Processes: Part II," ASME JOURNAL OF APPLIED MECHANICS, Vol. 56, pp. 57–62.

Willis, J. R., and Acton, J. R., 1976, "The Overall Elastic Moduli of a Dilute Suspension of Spheres," *Quart. J. Mech. Appl. Math.*, Vol. 29, No. 2, pp. 163–177.

Zhao, Y. H., Tandon, G. P., and Weng, G. J., 1989, "Elastic Moduli for a Class of Porous Materials," *Acta Mechanica*, Vol. 76, pp. 105–130.

APPENDIX A

Average Stress Field of Two Collinear Microcracks

The problem of two interacting collinear microcracks of equal length in an infinite plate subjected to uniform traction p^∞ at infinity has an exact analytical solution (Sneddon and Lowengrub, 1969). The normalized (nondimensional) distance between the two microcrack tips is denoted by $2k$ (with $k<1$), and the normalized length for each microcrack is designated as $1-k$. For this special configuration, we have

$$\theta_{10}=\theta_{20}=\theta_{ij}=0; \quad i,j=1,2 \tag{57}$$

and $\phi=\theta_{10}-\theta_{20}=0$

$$r=1+k; \quad r_1=\frac{1+3k}{2}=r_{11}=r_{21};$$

$$r_2=\frac{3+k}{2}=r_{12}=r_{22}. \tag{58}$$

Therefore, the only nonzero components in (17) are

$$\Lambda\equiv E_1=E_2=\frac{2(1+k)}{\sqrt{(1+3k)(3+k)}}. \tag{59}$$

Substitution of Eq. (59) into (20) and solution of Eq. (19) then render the approximate *average* normal stress p as follows:

$$p=\frac{p^\infty}{2-\Lambda}. \tag{60}$$

The exact solution for this average normal stress takes the same format as in (60), with Λ replaced by Λ_{ex} (exact; see, e.g., Kachanov, 1987)

$$\Lambda_{ex}=\frac{\sqrt{2+2k}}{1+\sqrt{k}}. \tag{61}$$

Table 2 shows the comparison between Λ and Λ_{ex} for different values of d which is defined as $d\equiv 2k/(1-k)$. It is clear that the error associated with the approximate solution increases as d decreases. This is due to the stress field singularity at microcrack tips.

Table 2 Comparison between Λ and Λ_{ex}

d	exact	approx	error (percent)
10	1.001037	1.001035	0.0002
5	1.00352	1.00349	0.0025
1	1.03528	1.03280	0.2396
0.5	1.07047	1.06066	0.9161
0.25	1.118034	1.091089	2.41
0.1	1.18821	1.122683	5.51
0.05	1.23801	1.13721	8.1419
0.005	1.34863	1.15280	14.52
0.0005	1.39238	1.15451	17.08

APPENDIX B

Components of Matrix K in Eq. (24)

$$\begin{aligned}
K_{11}&=k_1\sin 2\theta+k_2\sin^2\theta+k_3\\
K_{12}&=-k_1\sin 2\theta+k_2\cos^2\theta+k_3\\
K_{13}&=-k_2\sin 2\theta-2k_1\cos 2\theta\\
K_{21}&=k_4\sin 2\theta+k_5\sin^2\theta+k_6\\
K_{22}&=-k_4\sin 2\theta+k_5\cos^2\theta+k_6\\
K_{23}&=-k_5 2\theta-2k_4\cos 2\theta
\end{aligned} \tag{62}$$

where

$$\begin{aligned}
k_1&=\frac{1}{2\Delta}(f_2\sin 2\phi-f_1\cos 2\phi-f_3)\\
k_2&=\frac{1}{2\Delta}(f_2\cos 2\phi+f_1\sin 2\phi+f_4)\\
k_3&=\frac{1}{\Delta}\left(f_2\sin^2\phi-\frac{1}{2}f_1\sin 2\phi\right)\\
k_4&=\frac{1}{2\Delta}(f_6\sin 2\phi-f_5\cos 2\phi-f_7)\\
k_5&=\frac{1}{\Delta}(f_6\cos 2\phi+f_5\sin 2\phi+f_8)\\
k_6&=\frac{1}{\Delta}\left(f_6\sin^2\phi-\frac{1}{2}f_5\sin 2\phi\right)
\end{aligned} \tag{63}$$

and

$$\begin{aligned}
&f_1=(\alpha_1\alpha_4-\alpha_2\alpha_3)\alpha_6+\alpha_2; \quad f_2=-(\alpha_1\alpha_4-\alpha_2\alpha_3)\alpha_8+\alpha_1\\
&f_3=\alpha_1\alpha_6+\alpha_2\alpha_8; \quad f_4=\alpha_2 f_2+\alpha_7 f_1\\
&f_5=-(\alpha_1\alpha_4-\alpha_2\alpha_3)\alpha_5+\alpha_4; \quad f_6=(\alpha_1\alpha_4-\alpha_2\alpha_3)\alpha_7+\alpha_3\\
&f_7=\alpha_1 f_5+\alpha_6 f_6; \quad f_8=\alpha_3\alpha_5+\alpha_4\alpha_7; \quad \Delta=\det(\mathbf{I}-\boldsymbol{\alpha}).
\end{aligned} \tag{64}$$

Downloaded 03 May 2010 to 171.66.16.20. Redistribution subject to ASME license or copyright; see http://www.asme.org/terms/Terms_Use.cfm

Effective Elastic Moduli of Two-Dimensional Brittle Solids With Interacting Microcracks, Part II: Evolutionary Damage Models

J. W. Ju
Associate Professor,
Mem. ASME.

Tsung-Muh Chen
Research Assistant.

Department of Civil and
Environmental Engineering
University of California,
Los Angeles, CA 90024-1593

In Part I of this series, basic formulations of stationary *micromechanical theory and overall responses are presented for two-dimensional brittle solids with randomly dispersed microcracks. The basic formulations hinge on an* ensemble average *approach which includes pairwise microcrack interactions. In this paper, statistical micromechanical* evolutionary models *are proposed to account for "cleavage 1" growth of randomly oriented and located microcracks under microcrack interaction effects. Biaxial tension/compression loadings are also considered to take into account mixed microcrack opening and closure effects. Efficient numerical integration algorithms for the proposed ensemble averaged constitutive equations are subsequently given. Further, uniaxial and biaxial tests are presented to illustrate the proposed models and procedures. Finally, a higher-order microcrack interaction model within the proposed micromechanical framework is discussed.*

I Introduction

A statistical micromechanical ensemble-volume average approach to explicitly derive overall constitutive equations for microcrack-weakened brittle solids has been presented in Part I of this series. The proposed explicit micromechanical approach takes into account interactions among microcracks, random microcrack orientations, locations and densities, and microcrack opening displacements. Damage-induced overall anisotropy can be predicted by the proposed framework. The proposed micromechanical approach is at variance with existing "effective medium theories" such as the self-consistent method (Hill, 1965; Budiansky and O'Connell, 1976; Horii and Nemat-Nasser, 1983), the generalized self-consistent method (Christensen and Lo, 1979), the differential scheme (Roscoe, 1952, 1973; McLaughlin, 1977), and the Mori-Tanaka method (Mori and Tanaka, 1973; Benveniste, 1986), etc. In addition, the proposed framework is different from those micromechanical interaction analyses based on Monte Carlo simulations and numerical computations of stress "transmission factors" (Kachanov, 1987; Kachanov and Laures, 1989). The simple approximate analytical solutions for the two-microcrack interaction problem render *closed-form explicit* expressions for the evaluation of ensemble-average integrals.

Nevertheless, during loading histories of brittle solids, preexisting microcracks may become unstable and *grow* along certain preferred orientations, depending on loading levels, mircocrack configurations and interactions, etc. Therefore, it is important to formulate micromechanical "cleavage 1" (Ashby, 1979) evolutionary damage models to account for both microcrack kinetics and microcrack interactions under specified loads. Some micromechanical "evolutionary" damage models were proposed in the literature for "effective medium theories" (see, e.g., Krajcinovic and Fanella, 1986; Fanella and Krajcinovic, 1988; Sumarac and Krajcinovic, 1987; Ju, 1991; Ju and Lee, 1991; and Lee and Ju, 1991), etc. However, these micromechanical evoluationary damage models are only valid for weak microcrack interactions under low or at most moderate microcrack concentrations. On the other hand, microcrack interaction models due to Kachanov (1987) and Kachanov and Laures (1989) do not consider microcrack growth or nucleation kinetics.

The primary objective of this paper is to extend the framework proposed in Part I to accommodate "cleavage 1" microcrack growth process under microcrack interactions. "Cleavage 1" process implies that only the growth of *preexisting* microcracks is considered. Therefore, microcrack number remains constant during loading histories. Of course, one may also consider "cleavage 2" process (Ashby, 1979) to accommodate *nucleation* of new microcracks. However, that is beyond the scope of the present paper. In Section 2, micromechanical kinetic equations characterizing the "process do-

Contributed by the Applied Mechanics Division of The American Society of Mechanical Engineers for publication in the ASME Journal of Applied Mechanics.

Discussion on this paper should be addressed to the Technical Editor, Professor Lewis T. Wheeler, Department of Mechanical Engineering, University of Houston, Houston, TX 77204-4792, and will be accepted until four months after final publication of the paper itself in the ASME Journal of Applied Mechanics.

Manuscript received by the ASME Applied Mechanics Division, Oct. 3, 1990; final revision, July 22, 1992. Associate Technical Editor: R. M. McMeeking.

Copyright © 1994 by ASME
Downloaded 03 May 2010 to 171.66.16.20. Redistribution subject to ASME license or copyright; see http://www.asme.org/terms/Terms_Use.cfm

mains'' of active (open) microcracks are introduced. These ''process domains'' together with ''open microcrack domains'' completely define the integration domains of the ensemble averaged constitutive equations relating macro-strain and macro-stress. Moreover, various tension/compression loadings are presented in Section 2 to illustrate the proposed approach. Efficient numerical integration algorithms are presented in Section 3 to implement the proposed damage models. A number of uniaxial and biaxial tests are also performed. Finally, discussions on a higher-order microcrack interaction model within the proposed framework is given in Section 4.

2 Evoluationary Models With Microcrack Interaction

Let us consider an ensemble of randomly oriented and located microcracks within a statistically representative volume element. The microcrack number density is denoted by n and the microcrack length is denoted by $2a$. The representative element is subjected to two-dimensional external loading $\tau^\infty = (\sigma^\infty_{11}, \sigma^\infty_{22}, \sigma^\infty_{21})^T$. In accord with Part I of this work, the overall compliance matrix $\overline{\langle \mathbf{S} \rangle}$ can be written as (plane strain with linear elastic matrix)

$$\overline{\langle \mathbf{S} \rangle} = \mathbf{S}^o + \overline{\langle \mathbf{S}^{*1} \rangle} + \overline{\langle \mathbf{S}^{*2} \rangle} \tag{1}$$

where (see Eqs. (37)–(39) in Part I)

$$\mathbf{S}^o = \frac{(1+\nu)}{E}\begin{bmatrix} 1-\nu & -\nu & 0 \\ -\nu & 1-\nu & 0 \\ 0 & 0 & 2 \end{bmatrix} \tag{2}$$

$$\overline{\langle \mathbf{S}^{*1} \rangle} \equiv \frac{(1-\nu^2)}{E} n \int_\Theta a_1^2 \mathbf{g} \bullet \mathbf{K}_0 d\theta \tag{3}$$

$$\overline{\langle \mathbf{S}^{*2} \rangle} \equiv \frac{(1-\nu^2)}{\pi E} n^2 \int_\Theta a_1^4 \mathbf{g} \bullet \langle \hat{\mathbf{K}} \rangle d\theta \tag{4}$$

and (see Eq. (34) in Part I)

$$\langle \hat{\mathbf{K}} \rangle \equiv \int_{\hat{\Xi}} \mathbf{K}\, r dr d\theta_{10} d\theta_{20}. \tag{5}$$

Note that a_1 is the half-length of a primary microcrack and definitions of $\mathbf{g}$, $\mathbf{K}$, and $\mathbf{K}_0$ are given in Eqs. (11), (24), and (26) of Part I, respectively. The effective radius r has been normalized with respect to the microcrack radius a_1. Further, $\hat{\Xi}$ is the current active integration domain, including contributions from open *stationary* or *unstable* microcracks. Contributions due to closed microcracks are not considered in this paper.

For biaxial loadings, the *open* microcrack domain can be approximately defined by finding the domain of tensile (positive) normal stresses on microcrack planes as follows:

$$\sigma^\infty_{11} \sin^2\theta + \sigma^\infty_{22} \cos^2\theta - \sigma^\infty_{21} \sin 2\theta \geq 0. \tag{6}$$

It is noted that Eq. (6) only considers the far-field stresses σ^∞. In some cases, however, the open microcrack domain can be affected by microcrack interaction. That is, some originally *open* microcracks may become closed due to strong microcrack interaction. When this occurs, the *local* stresses σ should be used in (6); i.e., one should check the following ''local (normal) opening condition'' to ensure that a microcrack is indeed open: $\langle p \rangle \geq 0$.

2.1 Kinetic Equations for Microcrack Growth. In continuum damage mechanics, kinetic equations characterizing damage processes are typically postulated on the basis of hypothetical phenomenological arguments and macroscopic observations. However, as shown by Krajcinovic and Fanella (1986), microcrack kinetic equations can be actually derived based on micromechanics, probabilistic configurations of microcracks along certain microstructural weak planes, and fracture energy barriers on the mesoscale. When the *local* stress intensity factor (or strain energy release rate) reaches a certain critical value for the weak plane, a pre-existing microcrack is assumed to become unstable and grows along the weak plane in an unstable manner until reaching a certain characteristic size such as a grain or facet size (Krajcinovic and Fanella, 1986; Sumarac and Krajcinovic, 1987). This idealization is reasonable for *pre-existing* intergranular microcracks or interfacial microcracks (between the matrix and inclusions) in certain brittle materials such as concrete, ceramics, rocks, ice, and some brittle composites, etc. For simplicity, we do not consider microcrack kinking (into the matrix or neighboring weak planes) nor nucleation of new microcracks (see Fanella and Krajcinovic, 1988; Ju and Lee, 1991; and Lee and Ju, 1991) for some recent treatments. In other words, it is assumed that there exists a higher energy barrier serving as a microcrack trapping mechanism (e.g., a higher fracture toughness due to the matrix or due to intergranular kinking). Therefore, the proposed evolutionary damage models are only suitable for pre-peak (not post-peak) behavior of a class of brittle materials aforementioned. ''Run-away instability'' or localized macrocrack growth is *not* considered.

Within the context of microcrack interaction, the *local* stresses σ (not σ^∞) should be employed to compute the stress intensity factors (or strain energy release rates) on pre-existing microcrack tips. This treatment is completely different from existing (''effective medium'') micromechanical evolutionary models which employ far-field stresses σ^∞. Following Krajcinovic and Fanella (1986), we make the following two-stage simplification. It is assumed that the length of a pre-existing microcrack can either be $2a_0$ if the microcrack is stationary, or $2a_f$ if the microcrack is activated. Note that $2a_0$ denotes the average length of an initial microcrack and $2a_f$ signifies the average length of a propagated microcrack (e.g., the grain or facet size). The relation between the initial and final microcrack lengths is assumed to be

$$a_0 = \rho_0 a_f \tag{7}$$

where ρ_0 is a scalar between 0 and 1. The microcrack growth from $2a_0$ and $2a_f$ is assumed to be *instantaneous* once the local fracture energy is reached.

The actual fracture criterion of a material depends on its underlying physics of fracture. This paper does not intend to investigate fracture criteria of all materials. Instead, we attempt to demonstrate possible procedures involved in a micromechanical statistical evolutionary damage formulation. For illustration purpose, the following mixed-mode fracture criterion is employed (see Kanninen and Popelar, 1985, pp. 50–51):

$$\left(\frac{K_I}{K_{Ic}}\right)^2 + \left(\frac{K_{II}}{K_{IIc}}\right)^2 = 1, \tag{8}$$

where K_I and K_{II} are the Mode I and Mode II stress intensity factors of an initial microcrack, respectively. Similarly, K_{Ic} and K_{IIc}, respectively, are the Mode I and Mode II critical stress intensity factors of the weak plane where a pre-existing microcrack is located. The foregoing fracture criterion may be suitable for some materials but modifications are necessary when application to a specific material is sought. In the spirit of statistical ensemble-average stresses, it is reasonable to write the following simple approximations (under *plane strain*):

$$K_I = \langle p \rangle \sqrt{\pi a_0}; \quad K_{II} = \langle q \rangle \sqrt{\pi a_0} \tag{9}$$

where $\langle p \rangle$ and $\langle q \rangle$ = the ensemble-average *local* normal and shear stresses projected on microcrack surfaces in local coordinates. Substitution of (9) into (8) leads to

$$\langle p \rangle^2 + k^2 \langle q \rangle^2 = F_c^2 \tag{10}$$

where

Downloaded 03 May 2010 to 171.66.16.20. Redistribution subject to ASME license or copyright; see http://www.asme.org/terms/Terms_Use.cfm

$$k \equiv \frac{K_{Ic}}{K_{IIc}}; \quad F_c \equiv \frac{K_{Ic}}{\sqrt{\pi a_0}}. \tag{11}$$

For uniformly distributed and oriented microcracks, one has $f(\theta) = 1/\pi$ and $f(\mathbf{x}) = n$. From Eqs. (25)–(27) of Part I, one can write

$$\begin{Bmatrix} \langle p \rangle \\ \langle q \rangle \end{Bmatrix} = \left(\mathbf{K}_0 + \frac{n}{\pi} \langle \mathbf{K} \rangle \right) \cdot \begin{Bmatrix} \sigma_{11}^{\infty} \\ \sigma_{22}^{\infty} \\ \sigma_{12}^{\infty} \end{Bmatrix}. \tag{12}$$

For convenience, let us define

$$\mathbf{M} \equiv \mathbf{K}_0 + \frac{n}{\pi} \langle \mathbf{K} \rangle. \tag{13}$$

It is emphasized that $\langle \mathbf{K} \rangle$ (and thus $\mathbf{M}$) includes microcrack interaction effects. With (12) and (13) at hand, Eq. (10) can be rephrased as follows:

$$\gamma_0 \hat{\sigma}_{11}^{\infty 2} + \gamma_2 \hat{\sigma}_{22}^{\infty 2} + \gamma_3 \hat{\sigma}_{12}^{\infty 2} + 2(\gamma_1 \hat{\sigma}_{11}^{\infty} \hat{\sigma}_{22}^{\infty} + \gamma_4 \hat{\sigma}_{11}^{\infty} \hat{\sigma}_{12}^{\infty} + \gamma_5 \hat{\sigma}_{22}^{\infty} \hat{\sigma}_{12}^{\infty}) = 1 \tag{14}$$

where $\hat{\boldsymbol{\sigma}}^{\infty} \equiv \boldsymbol{\sigma}^{\infty}/F_c$ and

$$\gamma_0 = M_{11}^2 + k^2 M_{21}^2; \quad \gamma_1 = M_{11} M_{12} + k^2 M_{21} M_{22}$$
$$\gamma_2 = M_{12}^2 + k^2 M_{22}^2; \quad \gamma_3 = M_{13}^2 + k^2 M_{23}^2$$
$$\gamma_4 = M_{12} M_{13} + k^2 M_{21} M_{23}; \quad \gamma_5 = M_{12} M_{13} + k^2 M_{22} M_{23}. \tag{15}$$

Equation (14) can be used to solve for the "unstable angle domains" (θ^p) defining the "cleavage 1" unstable microcrack growth domains under a specified far field loading $\boldsymbol{\sigma}^{\infty}$. Conversely, for a specified "unstable growth angle domain," Eq. (14) can be used to obtain the external loading.

2.2 Dilute Case—Taylor's Model. In this case, the overall compliance of a microcrack-weakened solid takes the form

$$\overline{\langle \mathbf{S} \rangle} = \mathbf{S}^o + \overline{\langle \mathbf{S}^{*1i} \rangle} + \overline{\langle \mathbf{S}^{*1p} \rangle} \tag{16}$$

where $\overline{\langle \mathbf{S}^{*1i} \rangle}$ and $\overline{\langle \mathbf{S}^{*1p} \rangle}$ denote the compliance contributions from *initial* microcracks and microcrack *growth*, respectively. $\overline{\langle \mathbf{S}^{*1p} \rangle}$ can be expressed as (cf. (42)–(43) of Part I)

$$\overline{\langle \mathbf{S}^{*1p} \rangle} = \frac{(1-\nu^2)}{E} \omega_0 (\rho_0^{-2} - 1) \begin{bmatrix} S_{11}^{*1p} & 0 & S_{16}^{*1p} \\ 0 & S_{22}^{*1p} & S_{26}^{*1p} \\ S_{61}^{*1p} & S_{62}^{*1p} & S_{66}^{*1p} \end{bmatrix} \tag{17}$$

where $\omega_0 \equiv n a_0^2$ and

$$S_{11}^{*1p} = \theta_2^p - \theta_1^p - \frac{1}{2}(\sin 2\theta_2^p - \sin 2\theta_1^p);$$
$$S_{22}^{*1p} = \theta_2^p - \theta_1^p + \frac{1}{2}(\sin 2\theta_2^p - \sin 2\theta_1^p);$$
$$S_{66}^{*1p} = 2(\theta_2^p - \theta_1^p);$$
$$S_{16}^{*1p} = \sin^2 \theta_1^p - \sin^2 \theta_2^p = S_{26}^{*1p} = S_{26}^{*1p} = S_{62}^{*1p}. \tag{18}$$

In Eq. (18), $\Theta^p \equiv [\theta_1^p, \theta_2^p]$ is the evolutionary angle domain defined by Eq. (14).

(*1*) *Uniaxial tension:* $\hat{\sigma}_{22}^{\infty} > 0$, $\hat{\sigma}_{11}^{\infty} = \hat{\sigma}_{21}^{\infty} = 0$. All microcracks are open but overall responses are *ansiotropic* due to preferred orientations of microcrack growth. Specifically, the process domain is $\Theta^o = [0, \theta^p] \cup [\pi - \theta^p, \pi]$ (see Fig. 1), where θ^p can be solved from (14) for given $\hat{\sigma}_{22}^{\infty}$ (or vice versa):

$$\gamma_2 = \cos^4 \theta^p + k^2 \cos^2 \theta^p \sin^2 \theta^p = \hat{\sigma}_{22}^{\infty 2}. \tag{19}$$

From (18), we have

$$S_{11}^{*1p} = 2\theta^p - \sin 2\theta^p; \quad S_{22}^{*1p} = 2\theta^p + \sin 2\theta^p;$$
$$S_{66}^{*1p} = 4\theta^p; \quad \text{others} = 0. \tag{20}$$

(*2*) *Biaxial tension/compression:* $\hat{\sigma}_{22}^{\infty} > 0$, $\hat{\sigma}_{11}^{\infty} < 0$, $\hat{\sigma}_{21}^{\infty} = 0$. The bound of unstable growth angle domain, θ^p, can be computed from Eq. (14). The process domain is therefore $\Theta^p = [0, \theta^p] \cup [\pi - \theta^p, \pi]$. Conversely, one can obtain the axial external tensile stress $\hat{\sigma}_{22}^{\infty}$ for given lateral external stress $\hat{\sigma}_{11}^{\infty}$ and prescribed angle bound θ^p:

$$\hat{\sigma}_{22}^{\infty} = \left(\frac{-\hat{\sigma}_{11}^{\infty} \gamma_1 + \sqrt{(\gamma_1^2 - \gamma_2 \gamma_0) \hat{\sigma}_{11}^{\infty 2} + \gamma_2}}{\gamma_2} \right). \tag{21}$$

The nonzero components of $\overline{\langle \mathbf{S}^{*1p} \rangle}$ are

$$S_{11}^{*1p} = 2\theta^p - \sin 2\theta^p; \quad S_{22}^{*1p} = 2\theta^p + \sin 2\theta^p; \quad S_{33}^{*1p} = 4\theta^p. \tag{22}$$

Since $\hat{\sigma}_{11}^{\infty} < 0$, it follows that ϵ_{11}^* is *negative* and proportional to the density ω_0. This is due to the fact that Mode II contribution to (contractive) lateral strain is *greater* than Mode I contribution for biaxial tension/compression loads. To wit, let us consider an arbitrary stationary microcrack and compare the contributions of Mode I and Mode II to ϵ_{11}^*:

$$\epsilon_{11}^{*I} = 2 \frac{(1-\nu^2)\pi a_0^2}{E} \sin^2 \theta (\cos^2 \theta \sigma_{22}^{\infty} + \sin^2 \theta \sigma_{11}^{\infty}) \quad \text{(Mode I)} \tag{23}$$

$$\epsilon_{11}^{*II} = -\frac{1}{2} \frac{(1-\nu^2)\pi a_0^2}{E} \sin^2 2\theta (\sigma_{22}^{\infty} - \sigma_{11}^{\infty}) \quad \text{(Mode II)}. \tag{24}$$

The sum of Mode I and Mode II contributions is

$$\epsilon_{11}^* = 2 \frac{(1-\nu^2)\pi a_0^2}{E} \sin^2 \theta \sigma_{11}^{\infty} \le 0. \tag{25}$$

2.3 Uniaxial and Biaxial Tension Loadings. Within the proposed framework, the computation of overall compliances requires information regarding integration domains for microcrack *opening* and *growth*. For uniaxial tension, all microcracks are initially *open* and Eq. (14) becomes (19) in which γ_2 is evaluated by (15). The length of a microcrack is either $a_1 = a_0$ if *stationary* or $a_1 = a_f$ if *unstable*. For a prescribed configuration of microcrack growth domain, $\Theta^p = [0, \theta^p] \cup [\pi - \theta^p, \pi]$, one can systematically explore the status and length (a_2) of a second neighboring random microcrack. The details (27 possible cases) are as follows; see also Fig. 2.

Category I. If $0 \le \theta \le \theta^p$ and $a_1 = a_f$: nine possible cases concerning the length a_2.

$0 < \theta + \theta_{10} \le \theta^p$	a_2	$\theta^p < \theta + \theta_{10} \le \alpha^p$	a_2
(1) If $0 < \theta_{20} \le \theta + \theta_{10} + \theta^p$, then	a_f	(4) If $0 \le \theta_{20} \le \theta + \theta_{10} - \theta^p$, then	a_0
(2) If $\theta + \theta_{10} < \theta_{20} \le \theta + \theta_{10} + \alpha^p$	a_0	(5) If $\theta + \theta_{10} - \theta^p < \theta_{20} \le \theta + \theta_{10} + \theta^p$	a_f
(3) If $\theta + \theta_{10} + \alpha^p < \theta_{20} < \pi$	a_f	(6) If $\theta + \theta_{10} + \theta^p < \theta_{20} \le \pi$	a_0
$\alpha^p < \theta + \theta_{10} \le 2\pi$	a_2		
(7) If $0 < \theta_{20} \le \theta + \theta_{10} - \alpha^p$, then	a_f		
(8) If $\theta + \theta_{10} - \alpha^p < \theta_{20} \le \theta + \theta_{10} - \theta^p$	a_0		
(9) If $\theta + \theta_{10} - \theta^p < \theta_{20} < \pi$	a_f		

Downloaded 03 May 2010 to 171.66.16.20. Redistribution subject to ASME license or copyright; see http://www.asme.org/terms/Terms_Use.cfm

Category II. If $\theta^p < \theta \le \alpha^p$ and $a_1 = a_0$: nine possible cases concerning the length of a_2.

$\theta^p \le \theta + \theta_{10} \le \alpha^p$	a_2	$\alpha^p < \theta + \theta_{10} \le \beta^p$	a_2
(1) If $0 \le \theta_{20} \le \theta + \theta_{10} - \theta^p$, then	a_0	(4) If $0 \le \theta_{20} \le \theta + \theta_{10} - \alpha^p$, then	a_f
(2) If $\theta + \theta_{10} - \theta^p < \theta_{20} \le \theta + \theta_{10} + \theta^p$	a_f	(5) If $\theta + \theta_{10} - \alpha^p < \theta_{20} \le \theta + \theta_{10} - \theta^p$	a_0
(3) If $\theta + \theta_{10} + \theta^p < \theta_{20} \le \pi$	a_0	(6) If $\theta + \theta_{10} - \theta^p < \theta_{20} \le \pi$	a_f
$\beta^p < \theta + \theta_{10} \le 2\pi$	a_2		
(7) If $0 \le \theta_{20} \le \theta + \theta_{10} - \beta^p$, then	a_0		
(8) If $\theta + \theta_{10} - \beta^p < \theta_{20} \le \theta + \theta_{10} - \alpha^p$	a_f		
(9) If $\theta + \theta_{10} - \alpha^p < \theta_{20} \le \pi$	a_0		

Category III. If $\alpha^p \le \theta \le \pi$ and $a_1 = a_f$: nine possible cases concerning the length of a_2.

$\alpha^p < \theta + \theta_{10} \le \beta^p$	a_2	$\beta^p < \theta + \theta_{10}\pi + \alpha^p$	a_2
(1) If $0 \le \theta_{20} \le \theta + \theta_{10} - \alpha^p$, then	a_f	(4) If $0 \le \theta_{20} \le \theta + \theta_{10} - \beta^p$, then	a_0
(2) If $\theta + \theta_{10} - \alpha^p < \theta_{20} \le \theta + \theta_{10} - \theta^p$	a_0	(5) If $\theta + \theta_{10} - \beta^p < \theta_{20} \le \theta + \theta_{10} - \alpha^p$	a_f
(3) If $\theta + \theta_{10} - \theta^p < \theta_{20} \le \pi$	a_f	(6) If $\theta + \theta_{10} - \alpha^p < \theta_{20} \le \pi$	a_0
$\pi + \alpha^p < \theta + \theta_{10} \le 2\pi$	a_2		
(7) If $0 \le \theta_{20} \le \theta + \theta_{10} - \alpha^p - \pi$, then	a_f		
(8) If $\theta + \theta_{10} - \alpha^p - \pi < \theta_{20} \le \theta + \theta_{10} - \beta^p$	a_0		
(9) If $\theta + \epsilon_{10} - \beta^p < \theta_{20} \le \pi$	a_f		

We have employed the definitions $\alpha^p \equiv \pi - \theta^p$ and $\beta^p \equiv \pi + \theta^p$. With the foregoing analysis at hand, one can evaluate the integrals in Eqs. (4)–(5) and the external stress $\hat{\sigma}_{22}^{\infty}$ from (19). For biaxial tension, the foregoing integration domains remain the same and the only difference is the evaluation of θ^p in Eq. (14).

2.4 Biaxial Tension/Compression Loadings. In the case of biaxial tension/compression loadings, some microcracks are open while others are closed. Microcrack *process* and *open* domains are coupled and affect each other. For prescribed lateral stress $\hat{\sigma}_{11}^{\infty}$ and "process angle" θ^p, one has to compute the corresponding normal stress $\hat{\sigma}_{22}^{\infty}$ (evaluated at $\theta = \theta^p$) and the open/closed microcrack angle boundary θ^* by Eqs. (14) and (6) in order to predict progressive *stress-strain* responses. In particular, Eqs. (14) and (6) can be recast as

$$\hat{\sigma}_{22}^{\infty} = \left(\frac{-\hat{\sigma}_{11}^{\infty}\gamma_1 + \sqrt{(\gamma_1^2 - \gamma_2\gamma_0)\hat{\sigma}_{11}^{\infty 2} + \gamma_2}}{\gamma_2} \right)_{(\theta^*, \theta^p, \hat{\sigma}_{11}^{\infty})}; \tag{26}$$

$$\theta^* = \cos^{-1}\left(\sqrt{\frac{\hat{\sigma}_{11}^{\infty}}{-\hat{\sigma}_{22}^{\infty} + \hat{\sigma}_{11}^{\infty}}} \right)_{(\theta^p, \hat{\sigma}_{11}^{\infty})}. \tag{26}$$

As mentioned earlier in Section 2, Eq. (6) (and therefore $(26)_2$) is based on far-field stresses and is therefore an approximation of the local stress formula (in biaxial tension/compression):

$$\langle p \rangle = M_{11}\hat{\sigma}_{11}^{\infty} + M_{12}\hat{\sigma}_{22}^{\infty} \ge 0. \tag{27}$$

From a mathematical viewpoint, use of (26) corresponds to a second-order (in ω^2) accurate interactive microcrack theory. On the other hand, use of $(26)_1$ and (27) produces third and higher-order terms (in ω^3). Since our aim is to develop a second-order theory (in ω^2), Eqs. (26) can be regarded as a good approximation. Nevertheless, Eq. (27) should always be checked against any possible microcrack orientation to ensure that a microcrack is indeed *open*.

The microstructural integration domains can be systematically summarized as follows. Note that there are 76 possible cases in total and $\alpha^* \equiv \pi - \theta^*$ and $\beta^* \equiv \pi + \theta^*$.

Category I. If $0 \le \theta \le \theta^p$ and $a_1 = a_f$: 19 possible cases concerning the length of a_2.

$0 \le \theta + \theta_{10} \le \theta^p$	a_2	$\theta^p < \theta + \theta_{10} \le \theta^*$	a_2
(1) If $0 \le \theta_{20} \le \theta + \theta_{10} + \theta^p$, then	a_f	(5) If $0 \le \theta_{20} \le \theta + \theta_{10} - \theta^p$, then	a_0
(2) If $\theta + \theta_{10} + \theta^p < \theta_{20} \le \theta + \theta_{10} + \theta^*$	a_0	(6) If $\theta + \theta_{10} - \theta^p < \theta_{20} \le \theta + \theta_{10} + \theta^p$	a_f
(3) If $\theta + \theta_{10} - \alpha^* < \theta_{20} \le \theta + \theta_{10} - \alpha^p$	a_0	(7) If $\theta + \theta_{10} + \theta^p < \theta_{20} \le \theta + \theta_{10} + \theta^*$	a_0
(4) If $\theta + \theta_{10} - \alpha^p < \theta_{20} \le \pi$	a_f	(8) If $\theta + \theta_{10} + \alpha^* < \theta_{20} \le \pi$	a_0
$\alpha^* < \theta + \theta_{10} \le \alpha^p$	a_2	$\alpha^p \le \theta + \theta_{10} \le 2\pi$	a_2
(9) If $0 \le \theta_{20} \le \theta + \theta_{10} - \alpha^*$, then	a_0	(13) If $0 \le \theta_{20} \le \theta + \theta_{10} - \alpha^p$, then	a_f
(10) If $\theta + \theta_{10} - \theta^* < \theta_{20} \le \theta + \theta_{10} - \theta^p$	a_0	(14) If $\theta + \theta_{10} - \alpha^p < \theta_{20} \le \theta + \theta_{10} - \alpha^*$	a_0
(11) If $\theta + \theta_{10} - \theta^p < \theta_{20} \le \theta + \theta_{10} + \theta^p$	a_f	(15) If $\theta + \theta_{10} - \theta^* < \theta_{20} \le \theta + \theta_{10} - \theta^p$	a_0
(12) If $\theta + \theta_{10} + \theta^p < \theta_{20} \le \pi$	a_0	(16) If $\theta + \theta_{10} - \theta^p < \theta_{20} \le \pi$	a_f
$\theta^* < \theta + \theta_{10} \le \alpha^*$	a_2		
(17) If $\theta + \theta_{10} - \theta^* \le \theta_{20} \le \theta + \theta_{10} - \theta^p$	a_0		
(18) If $\theta + \theta_{10} - \theta^p < \theta_{20} \le \theta + \theta_{10} + \theta^p$	a_f		
(19) If $\theta + \theta_{10} + \theta^p < \theta_{20} \le \theta + \theta_{10} + \theta^*$	a_0		

Downloaded 03 May 2010 to 171.66.16.20. Redistribution subject to ASME license or copyright; see http://www.asme.org/terms/Terms_Use.cfm

Category II. If $\theta^p < \theta \le \theta^*$ and $a_1 = a_0$: 19 possible cases concerning the length of a_2.

$\theta^p \le \theta + \theta_{10} \le \theta^*$	a_2	$\alpha^* < \theta + \theta_{10} \le \alpha^p$	a_2
(1) If $0 \le \theta_{20} \le \theta + \theta_{10} - \theta^p$, then	a_0	(5) If $0 \le \theta_{20} \le \theta + \theta_{10} - \alpha^*$, then	a_0
(2) If $\theta + \theta_{10} - \theta^p < \theta_{20} \le \theta + \theta_{10} + \theta^p$	a_f	(6) If $\theta + \theta_{10} - \theta^* < \theta_{20} \le \theta + \theta_{10} - \theta^p$	a_0
(3) If $\theta + \theta_{10} + \theta^p < \theta_{20} \le \theta + \theta_{10} + \theta^*$	a_0	(7) If $\theta + \theta_{10} - \theta^p < \theta_{20} \le \theta + \theta_{10} + \theta^p$	a_f
(4) If $\theta + \theta_{10} + \alpha^* < \theta_{20} \le \pi$	a_0	(8) If $\theta + \theta_{10} + \theta^p < \theta_{20} \le \pi$	a_0
$\alpha^p < \theta + \theta_{10} \le \beta^p$	a_2	$\beta^p \le \theta + \theta_{10} \le 2\pi$	a_2
(9) If $0 \le \theta_{20} \le \theta + \theta_{10} - \alpha^p$, then	a_f	(13) If $0 \le \theta_{20} \le \theta + \theta_{10} - \beta^p$, then	a_0
(10) If $\theta + \theta_{10} - \theta^p < \theta_{20} \le \theta + \theta_{10} - \theta^*$	a_0	(14) If $\theta + \theta_{10} - \beta^p < \theta_{20} \le \theta + \theta_{10} - \alpha^p$	a_f
(11) If $\theta + \theta_{10} - \theta^* < \theta_{20} \le \theta + \theta_{10} - \theta^p$	a_0	(15) If $\theta + \theta_{10} - \alpha^p < \theta_{20} \le \theta + \theta_{10} - \alpha^*$	a_0
(12) If $\theta + \theta_{10} - \theta^p < \theta_{20} \le \pi$	a_f	(16) If $\theta + \theta_{10} - \alpha^* < \theta_{20} \le \pi$	a_0
$\theta^* < \theta + \theta_{10} \le \alpha^*$	a_2		
(17) If $\theta + \theta_{10} - \theta^* \le \theta_{20} \le \theta + \theta_{10} - \theta^p$	a_0		
(18) If $\theta + \theta_{10} - \theta^p < \theta_{20} \le \theta + \theta_{10} + \theta^p$	a_f		
(19) If $\theta + \theta_{10} + \theta^p < \theta_{20} \le \theta + \theta_{10} + \theta^*$	a_0		

Category III. If $\alpha^* < \theta \le \alpha^p$ and $a_1 = a_0$: 19 possible cases concerning the length of a_2.

$\alpha^* \le \theta + \theta_{10} \le \alpha^p$	a_2	$\alpha^p < \theta + \theta_{10} \le \beta^p$	a_2
(1) If $0 \le \theta_{20} \le \theta + \theta_{10} - \alpha^*$, then	a_0	(5) If $0 \le \theta_{20} \le \theta + \theta_{10} - \sigma^p$, then	a_f
(2) If $\theta + \theta_{10} - \theta^* < \theta_{20} \le \theta + \theta_{10} - \theta^p$	a_0	(6) If $\theta + \theta_{10} - \sigma^p < \theta_{20} \le \theta + \theta_{10} - \sigma^*$	a_0
(3) If $\theta + \theta_{10} - \theta^p < \theta_{20} \le \theta + \theta_{10} + \theta^p$	a_f	(7) If $\theta + \theta_{10} - \theta^* < \theta_{20} \le \theta + \theta_{10} - \theta^p$	a_0
(4) If $\theta + \theta_{10} + \theta^p < \theta_{20} \le \pi$	a_0	(8) If $\theta + \theta_{10} - \theta^p < \theta_{20} \le \pi$	a_f
$\beta^* < \theta + \theta_{10} \le \beta^*$	a_2	$\pi + \alpha^* < \theta + \theta_{10} \le 2\pi$	a_2
(9) If $0 \le \theta_{20} \le \theta + \theta_{10} - \beta^p$, then	a_0	(13) If $0 \le \theta_{20} \le \theta + \theta_{10} - \alpha^* - \pi$, then	a_0
(10) If $\theta + \theta_{10} - \beta^p < \theta_{20} \le \theta + \theta_{10} - \alpha^p$	a_f	(14) If $\theta + \theta_{10} - \beta^* < \theta_{20} \le \theta + \theta_{10} - \beta^p$	a_0
(11) If $\theta + \theta_{10} - \alpha^p < \theta_{20} \le \theta + \theta_{10} - \alpha^*$	a_0	(15) If $\theta + \theta_{10} - \beta^p < \theta_{20} \le \theta + \theta_{10} - \alpha^p$	a_f
(12) If $\theta + \theta_{10} - \theta^* < \theta_{20} \le \pi$	a_0	(16) If $\theta + \theta_{10} - \alpha^p < \theta_{20} \le \pi$	a_0
$\beta^* < \theta + \theta_{10} \le \pi + \alpha^*$	a_2		
(17) If $\theta + \theta_{10} - \beta^* \le \theta_{20} \le \theta + \theta_{10} - \beta^p$	a_0		
(18) If $\theta + \theta_{10} - \beta^p < \theta_{20} \le \theta + \theta_{10} - \alpha^p$	a_f		
(19) If $\theta + \theta_{10} - \alpha^p < \theta_{20} \le \theta + \theta_{10} - \alpha^*$	a_0		

Category IV. If $\alpha^p < \theta \le \pi$ and $a_1 = a_f$: 19 possible cases concerning the length of a_2.

$\alpha^p \le \theta + \theta_{10} \le \beta^p$	a_2	$\beta^p < \theta + \theta_{10} \le \beta^*$	a_2
(1) If $0 \le \theta_{20} \le \theta + \theta_{10} - \alpha^p$, then	a_f	(5) If $0 \le \theta_{20} \le \theta + \theta_{10} - \beta^*$, then	a_0
(2) If $\theta + \theta_{10} - \alpha^p < \theta_{20} \le \theta + \theta_{10} - \alpha^*$	a_0	(6) If $\theta + \theta_{10} - \beta^p < \theta_{20} \le \theta + \theta_{10} - \alpha^p$	a_f
(3) If $\theta + \theta_{10} - \theta^* < \theta_{20} \le \theta + \theta_{10} - \theta^p$	a_0	(7) If $\theta + \theta_{10} - \alpha^p < \theta_{20} \le \theta + \theta_{10} - \alpha^*$	a_0
(4) If $\theta + \theta_{10} - \theta^p < \theta_{20} \le \pi$	a_f	(8) If $\theta + \theta_{10} - \theta^* < \theta_{20} \le \pi$	a_0
$\pi + \alpha^* < \theta + \theta_{10} \le \pi + \alpha^p$	a_2	$\pi + \alpha^p \le \theta + \theta_{10} \le 2\pi$	a_2
(9) If $0 \le \theta_{20} \le \theta + \theta_{10} - \alpha^* - \pi$, then	a_0	(13) If $0 \le \theta_{20} \le \theta + \theta_{10} - \sigma^p - \pi$, then	a_f
(10) If $\theta + \theta_{10} - \beta^p < \theta_{20} \le \theta + \theta_{10} - \beta^*$	a_0	(14) If $\theta + \theta_{10} - \alpha^p - \pi < \theta_{20} \le \theta + \theta_{10} - \alpha^* - \pi$	a_0
(11) If $\theta + \theta_{10} - \beta^p < \theta_{20} \le \theta + \theta_{10} - \alpha^p$	a_f	(15) If $\theta + \theta_{10} - \beta^* < \theta_{20} \le \theta + \theta_{10} - \beta^p$	a_0
(12) If $\theta + \theta_{10} - \alpha^p < \theta_{20} \le \pi$	a_0	(16) If $\theta + \theta_{10} - \beta^p < \theta_{20} \le \pi$	a_f
$\beta^* < \theta + \theta_{10} \le \pi + \alpha^*$	a_2		
(17) If $\theta + \theta_{10} - \beta^* \le \theta_{20} \le \theta + \theta_{10} - \beta^p$	a_0		
(18) If $\theta + \theta_{10} - \beta^p < \theta_{20} \le \theta + \theta_{10} - \alpha^p$	a_f		
(19) If $\theta + \theta_{10} - \sigma^p < \theta_{20} \le \theta + \theta_{10} - \alpha^*$	a_0		

The foregoing integration domains complete define the integrals in Eqs. (3)–(5), and therefore effective compliances can be computed. In a *strain-driven* algorithm, the axial tensile stress $\hat{\sigma}_{22}^{\infty}$ can also be computed accordingly. It is emphasized that microcrack interactions affect the values of γ_i and thus $\hat{\sigma}_{22}^{\infty}$; see $(26)_1$. In turn $\hat{\sigma}_{22}^{\infty}$ affects the "opening angle" θ^*; see $(26)_2$.

3 Numerical Algorithms and Applications

3.1 Numerical Integration Algorithms. As previously mentioned, one needs to numerically evaluate the integrals involved in Eqs. (3)–(5). Furthermore, one needs to develop efficient numerical algorithm to solve Eq. (26) involving both process and opening domains. First, the numerical integrations of (3)–(5) can be efficiently achieved by using the "Gauss quadrature" scheme. In carrying out the Gauss quadrature numerical scheme, we have chosen the following integration ranges: $[2a, 20a]$ for the distance r, and $[0, \pi]$ for the angle θ_{10}. The integration bounds for θ_{20} and θ are subsequently determined from the systematic analyses presented in Sections 2.3 and 2.4.

Another issue is the number of Gauss points needed for each integration zone aforementioned in Sections 2.3 and 2.4. Table

Downloaded 03 May 2010 to 171.66.16.20. Redistribution subject to ASME license or copyright; see http://www.asme.org/terms/Terms_Use.cfm

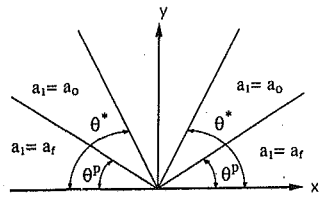


Fig. 1 Schematic sketch for the definitions of process domains (θ^p) and opening domains (θ^*)

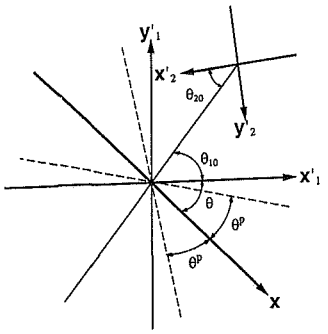


Fig. 2 Schematic sketch for various integration domains, with x denoting the global reference axis (x_1', y_1') denoting the first set of local coordinates, and (x_2', y_2') denoting the second set of local coordinates

Table 1 Convergence behavior ($r_{max} = 20a$)

No. Guass points	$\langle \hat{K}_{12} \rangle$	$\langle \hat{K}_{23} \rangle$
10	0.5862290322	0.2405392992
20	0.5864980549	0.2406183532
30	0.5864981079	0.2406183630
40	0.5864981080	0.2406183630
80	0.5864981080	0.2406183630

Box 1 Numerical integration algorithm

(1) Specify θ^p and $\hat{\sigma}_{11}^{\infty}$, and guess an initial bound of opening domain θ^* (e.g., from Taylor's model analysis).

(2) Integrate (3)–(5) over θ and θ_{10}. Note that

$$a_1 = \begin{cases} a_f, & \text{if } \theta \text{ in process domains;} \\ a_0, & \text{otherwise.} \end{cases}$$

(3) Integrate (3)–(5) over θ_{20} for each value of $\theta + \theta_{10}$. Note that

$$a_2 = \begin{cases} a_f, & \text{if } \theta_{20} \text{ in process domains;} \\ a_0, & \text{otherwise.} \end{cases}$$

(4) Integrate Eqs. (4)–(5) from $r = (a_1 + a_2)$ to $\max(20a_1, 20a_2)$.

(5) For a given fracture criterion, find the corresponding threshold stress $\hat{\sigma}_{22}^{\infty}$ by $(26)_1$. Calculate the updated opening angle bound θ^* by $(26)_2$ or (27). If the difference between the initial guess and the updated θ^*-value is not acceptable, then go back to Step (2) and re-iterate until proper convergence is reached.

(6) Go to Step (1) and specify new θ^p and $\hat{\sigma}_{11}^{\infty}$ values.

1 gives the convergence behavior of Gauss quadrature with respect to the number of Gauss points used for each integration zone for the "aligned microcracks" problem previously considered in Section 3.2 of Part I. Clearly, use of 20 Gauss points in each integration zone is sufficiently accurate. An efficient, iterative numerical integration algorithm to solve Eq. (26) is summarized in Box 1.

Remark 3.1. For uniaxial and biaxial tensile loadings, Eq. (6) is automatically satisfied unless the axial stress goes to infinity; i.e., $\theta^* = \pi/2$. Therefore, the iterative process for finding the opening angle bound θ^* in Step (5) of Box 1 is unnecessary. ■

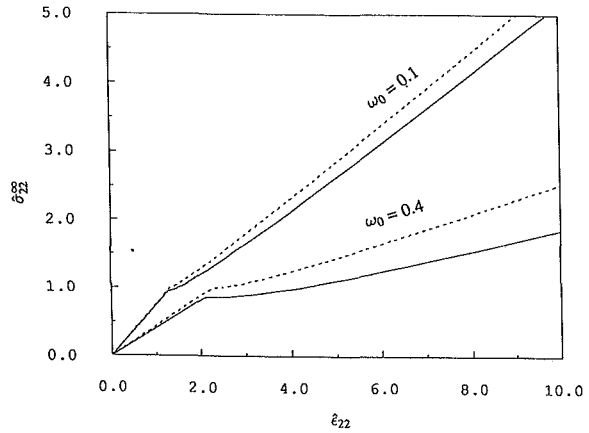


Fig. 3 The normalized axial stress-strain curves for uniaxial tension tests. The dotted lines and solid lines are predictions from Taylor's and the proposed models, respectively.

3.2 Uniaxial Tension Loading Tests. In this section, we consider two (plane-strain) uniaxial tension tests with different initial microcrack concentrations: $\omega_0 \equiv n a_0^2 = 0.1$ (moderate density) and 0.4 (high density). It should be realized that these two concentrations are equal to 0.1π and 0.4π in terms of the commonly used definition ($\hat{\omega} \equiv n\pi a_0^2$). Moreover, the k value in Eq. (11) is taken as 0.5, initial Poisson's ratio $\nu = 0.2$, and $\rho_0 = 0.6$ in. (7). For convenience, all strains are normalized (dimensionless) as follows:

$$\hat{\epsilon} \equiv \frac{\epsilon}{F_c\left(\frac{1-\nu^2}{E}\right)}. \tag{28}$$

The *normalized* stress-strain curves are displayed in Fig. 3. All compliances have also been normalized by dividing the common factor $(1-\nu^2)/E$. We observe that microcrack interactions effectively *lower* the onset (threshold stress) of microcrack propagation. The existence of "corner points" on the axial stress-strain curves in Fig. 3 is a consequence of the *deterministic* fracture criterion (14) and the uniform initial microcrack size a_0. If we employ a *probabilistic* fracture criterion or *nonuniform* initial microcrack sizes, the "corner points" will disappear and be replaced by smooth transitions (c.f. Ju and Lee (199) and Lee and Ju (1991)). It is noted that the axial stress/lateral strain curves are the same for $\omega_0 = 0.1$ and 0.4 for Taylor's model due to the fact that microcracks have no contribution to $\hat{\epsilon}_{11}$. In the case of the proposed microcrack interaction theory, a significant *reduction* in the magnitude of lateral strains is observed. That is, microcrack inteactions enhance Mode I displacements and reduce Mode II displacements, and therefore *reduce* the magnitude of lateral contraction.

Figures 4 and 5 show the *normalized* overall compliance components predicted by both Taylor's and the proposed models. It is noted that Taylor's model does not change either $\langle S_{12} \rangle$ or $\langle S_{21} \rangle$ components despite damage. By contrast, the proposed interaction model shows that the shear components $\langle S_{12} \rangle$ and $\langle S_{21} \rangle$ change. It is also observed that $\langle S_{12} \rangle$ and $\langle S_{21} \rangle$ become slightly different at the microcrack concentration increases. As the normalized axial stress $\hat{\sigma}_{22}^{\infty}$ goes to infinity, one may expect that the overall compliance matrix asymptotically becomes isotropic because all preexisting random microcracks grow to same length a_f. This is indeed the case for Taylor's model and the self-consistent model. However, this may not be always true if microcrack interactions are considered. The reason is that some initially *open* stationary microcracks (a_0) in the very close neighborhood of $\theta = \pi/2$ may become *closed* due to interactions with neighboring propagated

Downloaded 03 May 2010 to 171.66.16.20. Redistribution subject to ASME license or copyright; see http://www.asme.org/terms/Terms_Use.cfm

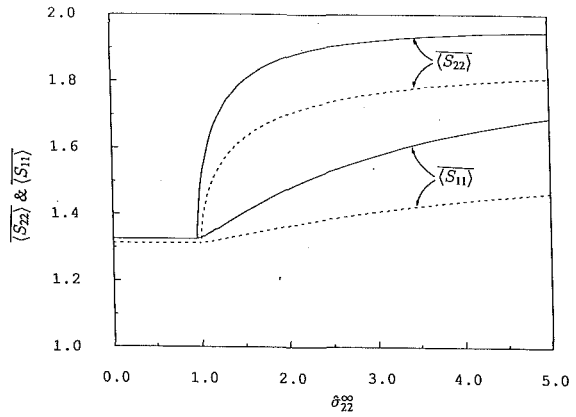


Fig. 4 The normalized $\overline{\langle S_{22}\rangle}$ and $\overline{\langle S_{11}\rangle}$ compliances versus axial stress curves for uniaxial tension tests with $\omega_0 = 0.1$. The compliances have been normalized by the factor $(1-\nu^2)/E$. The dotted lines and solid lines are predictions from Taylor's and the proposed models, respectively.

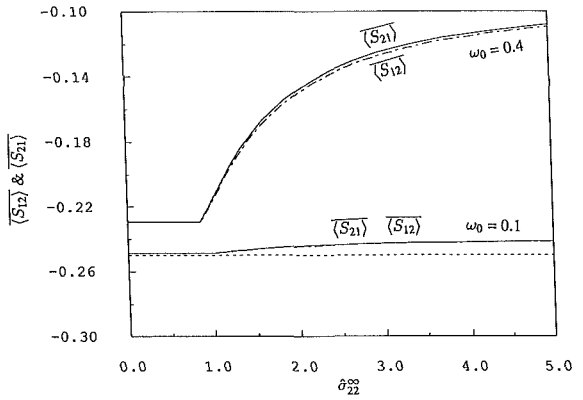


Fig. 5 The normalized $\overline{\langle S_{12}\rangle}$ and $\overline{\langle S_{21}\rangle}$ compliances versus axial stress curves for uniaxial tension tests with $\omega_0 = 0.1$ and $\omega_0 = 0.4$. The dotted line is the prediction from Taylor's model for both $\omega_0 = 0.1$ and $\omega_0 = 0.4$. The dash-dot lines and solid lines are $\langle S_{12}\rangle$ and $\langle S_{21}\rangle$ predictions, respectively, from the proposed model.

microcracks (a_f). Biaxial tension loadings can be treated in a similar fashion and therefore are not repeated here.

3.3 Biaxial Tension/Compression Loading Tests. One has to determine the open domain (θ^*) and the corresponding axial tensile stress $\hat{\sigma}_{22}^{\infty}$ by solving the system of Eqs. (26) for specified values of θ^p and $\hat{\sigma}_{11}^{\infty}$ in order to compute overall compliances. A good initial guess for θ^* can be obtained from Taylor's model by solving Eqs. (6) and (19). With this initial guess $\theta^{*(0)}$, one can obtain the trial value $\hat{\sigma}_{22}^{\infty(1)}$ by using Eq. $(26)_1$. Subsequently, an improved trial value $\theta^{*(1)}$ can be reduced by using $(26)_2$, and so on. In what follows, we adopt the following properties: $\nu = 0.2$, $\rho_0 = 0.6$ and $k = 0.5$.

To illustrate the performance of the proposed numerical algorithm summarized in Box 1, let us consider the *onset* point of the "cleavage 1" microcrack growth. Table 2 shows the convergence behavior of this case for $\omega_0 = 0.1$ and $\hat{\sigma}_{11}^{\infty} = -0.1$. It is observed that remarkable convergence is reached within only two to three iterations.

The *normalized* axial stress-strain curves for four different biaxial tension/compression tests with $\omega_0 = 0.1$, 0.4 and lateral compression $\hat{\sigma}_{11}^{\infty} = -0.1, -0.4$, respectively, are similar to those of the unaxial tension tests in Fig. 3. However, the behavior of axial stress/lateral strain curves depend on $\hat{\sigma}_{11}^{\infty}$ (or the ratio $|\hat{\sigma}_{22}^{\infty}/\hat{\sigma}_{11}^{\infty}|$) and ω_0; see Figs. 6 and 7. The magnitude of lateral (contractive) strains are higher for higher lateral compression $\hat{\sigma}_{11}^{\infty} = -0.4$; compare Figs. 6 and 7. On the other hand, the

Table 2 Convergence behavior

No. of iteration (i)	$\theta^{*(i)}$	$\lvert\theta^{*(i+1)} - \theta^{*(i)}\rvert$
0	1.2645189576	—
1	1.2592833120	5.2356456171E-03
2	1.2592966258	1.3313781921E-05
3	1.2592965919	3.3915545705E-08
4	1.2592965920	9.6395779419E-11
5	1.2592965920	2.1960211427E-13

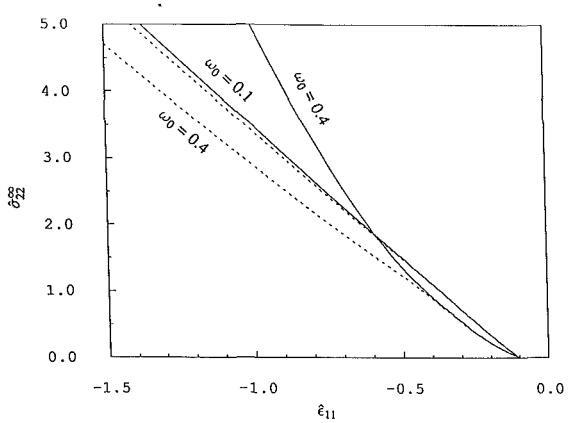


Fig. 6 The normalized axial stress versus lateral strain curves for biaxial tension/compression tests with $\hat{\sigma}_{11}^{\infty} = -0.1$. The dotted lines and solid lines are predictions from Taylor's and the proposed models, respectively.

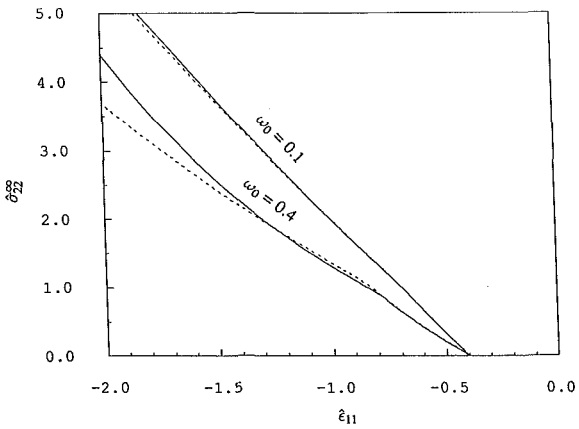


Fig. 7 The normalized axial stress versus lateral strain curves for biaxial tension/compression tests with $\hat{\sigma}_{11}^{\infty} = -0.4$. The dotted and solid lines are predictions from Taylor's and the proposed models, respectively.

loading ratio $|\hat{\sigma}_{22}^{\infty}/\hat{\sigma}_{11}^{\infty}|$ affects the size of the open and process domains. The *sizes* and *orientations* of these open and process domains, in turn, affect the effects of microcrack interaction on lateral strains. In particular, for *higher* loading ratio $|\hat{\sigma}_{22}^{\infty}/\hat{\sigma}_{11}^{\infty}|$, the net effects of microcrack interaction *enhance* the Mode I (dilatational) contributions and *reduce* the Mode II (contractive) contributions. By contrast, when the loading ratio $|\hat{\sigma}_{22}^{\infty}/\hat{\sigma}_{11}^{\infty}|$ is relatively *small*, the net effects of microcrack interaction *enhance* the Mode II (contractive) contributions; see Fig. 7. It is worth mentioning that if $\hat{\sigma}_{22}^{\infty}$ continues to increase in Fig. 7, then the two solid lines in Fig. 7 will also intersect each other just as they do in Fig. 6.

Finally, Fig. 8 displays the normalized $\overline{\langle S_{22}\rangle}$ and $\overline{\langle S_{11}\rangle}$ compliances versus axial stresses for $\omega_0 = 0.4$ and $\hat{\sigma}_{11}^{\infty} = -0.1$. Due to closure of some microcracks, overall compliances are always *anisotropic*. It is also noted that due to microcrack interactions, the overall compliance matrix becomes *nonsymmetric* (i.e., $S_{12} \neq S_{21}$).

Downloaded 03 May 2010 to 171.66.16.20. Redistribution subject to ASME license or copyright; see http://www.asme.org/terms/Terms_Use.cfm

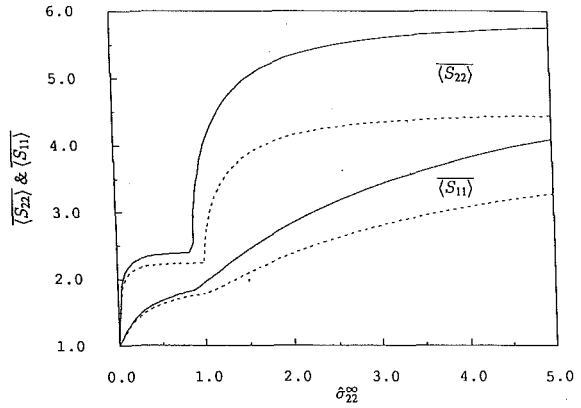


Fig. 8 The normalized $\overline{\langle S_{22}\rangle}$ and $\overline{\langle S_{11}\rangle}$ compliances versus axial stress curves for biaxial tension/compression tests with $\omega_0 = 0.4$ and $\hat{\sigma}_{11}^{\infty} = -0.1$. The dotted lines and solid lines are predictions from Taylor's and the proposed models, respectively.

4 A Higher-Order Microcrack Interaction Model

The statistical micromechanical damage models presented so far are based on the concept of *pairwise* microcrack interaction. This pairwise microcrack mechanism essentially corresponds to a *second-order* damage theory (in ω^2). Within the context of the ensemble-volume average approach, one can systematically incorporate many-microcrack interaction mechanisms into the proposed framework. In essence, one needs to re-derive the ensemble-average of the *perturbation* in local stress field due to n-microcrack *interactions* ($n \geq 3$).

To illustrate the foregoing statements, let us consider a three-microcrack (third-order in ω^3) interaction mechanism. Following the definitions and assumptions described in Part I of this study, one can recast the local ensemble stress perturbation in Eq. (12) of Part I as follows:

$$\langle \tilde{\mathbf{T}} \rangle + \langle \tilde{\tilde{\mathbf{T}}} \rangle \equiv \left\langle \begin{Bmatrix} \tilde{p} \\ \tilde{q} \end{Bmatrix} \right\rangle + \left\langle \begin{Bmatrix} \tilde{\tilde{p}} \\ \tilde{\tilde{q}} \end{Bmatrix} \right\rangle \tag{29}$$

where $\langle \tilde{\mathbf{T}} \rangle$ is the first-order local ensemble stress perturbation due to pairwise microcrack interactions, and $\langle \tilde{\tilde{\mathbf{T}}} \rangle$ is the second-order local ensemble stress perturbation due to the third-order microcrack interactions. In particular, $\langle \tilde{\tilde{\mathbf{T}}} \rangle$ can be expressed as (cf. Eq. (13) of Part I)

$$\langle \tilde{\tilde{\mathbf{T}}} \rangle = \int_{\mathcal{Z}} \langle \tilde{\tilde{\mathbf{T}}} \rangle (\mathbf{x}, a, \theta; \mathbf{x}_1, a_1, \theta_2 | \mathbf{x}_2, a_2, \theta_2) \times f(\mathbf{x}_2, a_2, \theta_2 | \mathbf{x}, a, \theta; \mathbf{x}_1, a_1, \theta_1) d\theta_2 da_2 d\mathbf{x}_2. \tag{30}$$

Here, $\langle \tilde{\tilde{\mathbf{T}}} \rangle (\mathbf{a}, a, \theta; \mathbf{x}_1, a_1, \theta_1 | \mathbf{x}_2, a_2, \theta_2)$ is the second-order *stress perturbation* of a microcrack centered at $\mathbf{x}$ with (a, θ), given a microcrack centered at $\mathbf{x}_1$ with (a_1, θ_1), averaged over the subclass of realizations having a microcrack centered at $\mathbf{x}_2$ with (a_2, θ_2). Further, $f(\mathbf{x}_2, a_2, \theta_2 | \mathbf{x}, a, \theta; \mathbf{x}_1, a_1, \theta_1)$ is the conditional probability function for finding a microcrack centered at $\mathbf{x}_2$ with (a_2, θ_2) given two microcracks fixed at $\mathbf{x}$ with (a, θ) and at $\mathbf{x}_1$ with (a_1, θ_1). $f(\mathbf{x}_2, a_2, \theta_2 | \mathbf{x}, a, \theta; \mathbf{x}_1, a_1, \theta_1)$ can be simplified to $f(\mathbf{x}, a, \theta)$ by the assumptions of local homogeneity and reasonable randomness.

The solutions of $\tilde{\tilde{\mathbf{T}}}$ for a system of three (or many) arbitrarily located and oriented microcracks were previously investigated by Horii and Nemat-Nasser (1985) and Kachanov (1987). In particular, Kachanov (1987) pursued extensive numerical computations in order to obtain the "transmission factors" for local stresses. Alternatively, one can derive approximate analytical solutions for $\tilde{\tilde{\mathbf{T}}}$ by following the procedures presented in Section 2.3 of Part I.

For clarity, let us express $\mathbf{T}$ and $\langle \mathbf{e}^* \rangle (\mathbf{x})$ as follows (cf. Eqs. (25) and (28) of Part I):

$$\langle \mathbf{T} \rangle = \langle \mathbf{T}^{\infty} + \tilde{\mathbf{T}} + \tilde{\tilde{\mathbf{T}}} \rangle = (\mathbf{K}_0 + f(\mathbf{x}) f(a, \theta) \langle \mathbf{K} \rangle + f^2(a, \theta) \langle \mathbf{K}' \rangle) \cdot \boldsymbol{\tau}^{\infty} \tag{31}$$

$$\langle \mathbf{e}^* \rangle (\mathbf{x}) = \{ \langle \mathbf{S}^{*1} \rangle + \langle \mathbf{S}^{*2} \rangle + \langle \mathbf{S}^{*3} \rangle \} \cdot \boldsymbol{\tau}^{\infty} \equiv \langle \mathbf{S}^* \rangle \cdot \boldsymbol{\tau}^{\infty} \tag{32}$$

where $\tilde{\tilde{\mathbf{T}}} \equiv \mathbf{K}' \cdot \boldsymbol{\tau}^{\infty}$ and (see Eqs. (29)–(30) of Part I)

$$\langle \mathbf{S}^{*1} \rangle \equiv \frac{\pi(1-\nu^2)}{E} f(\mathbf{x}) \int_{\mathcal{A}} a^2 \int_{\Theta} \mathbf{g} \cdot \mathbf{K}_0 f(a, \theta) d\theta da \tag{33}$$

$$\langle \mathbf{S}^{*2} \rangle \equiv \frac{\pi(1-\nu^2)}{E} f^2(\mathbf{x}) \int_{\mathcal{A}} a^2 \int_{\Theta} \mathbf{g} \cdot \langle \mathbf{K} \rangle f^2(a, \theta) d\theta da \tag{34}$$

$$\langle \mathbf{S}^{*3} \rangle \equiv \frac{\pi(1-\nu^2)}{E} f^3(\mathbf{x}) \int_{\mathcal{A}} a^2 \int_{\Theta} \mathbf{g} \cdot \langle \mathbf{K}' \rangle f^3(a, \theta) d\theta da. \tag{35}$$

In the above equations, $\mathbf{K}$, $\mathbf{K}_0$, and $\langle \mathbf{K} \rangle$ have been previous defined in Eqs. (24), (26), and (27) of Part I, respectively. Similarly, $\mathbf{K}'$ (or $\tilde{\tilde{\mathbf{T}}}$) can also be constructed as follows. One starts by expanding Eq. (15) of Part I into six linear equations with $j = 1, 2, 3$. Then, one obtains Eqs. (16)–(17) of Part I with the understanding that $j = 1, 2, 3$ and the permutations 1–2, 2–3, 3–1 are involved in Eq. (17). Equation (18) of Part I is modified to include the kth ($k \neq j$ and $k \neq i$) microcrack's contribution to stress perturbations. Subsequently, Eq. (19) of Part I is expanded to a six-equation system with α denoting a six by six coefficient matrix. The components of α are identical to those in Eq. (20) of Part I with the understanding that the 1-2-3 permutations are involved. Therefore, we arrive at explicit formulas similar to Eqs. (21)–(24) in Part I. Finally, it is noted that the computation of $\langle \mathbf{K}' \rangle$ involves integration over the probabilistic domain of all possible positions and orientations of two active neighboring microcracks. Following the standard procedures presented in Section 2.4 of Part I, it can be shown that $\langle \mathbf{S}^{*2} \rangle$ in Eq. (35) introduces third-order terms (in ω^3) to overall compliance. Therefore, a third-order statistical micromechanical model can be constructed. By repeating the foregoing procedures, we can formulate a complete heirarchical family of statistical micromechanical theories of arbitrary order.

5 Conclusions

In this paper, basic two-dimensional formulations presented in Part I of this investigation are further extended to account for "cleavage 1" microcrack growth processes with microcrack interactions. Stemming from a micromechanical viewpoint, a mixed fracture criterion is used to derive microcrack kinetic equations for interacting, randomly located and oriented microcracks. As a result, the proposed approach is capable of predicting the *progressive* stress-strain curves for biaxial loadings. This constitutive predictive capability is not found in the current literature on stationary microcrack interaction models. Both tensile and mixed tensile/compressive loadings are considered in Section 2, including systematic analyses regarding detailed integration domains. Further, efficient numerical integration algorithms are presented for biaxial loadings in Section 3. A number of model predictions and comparisons are also performed. It is shown that load-induced anisotropy and nonsymmetry of overall compliances can be predicted by the proposed micromechanical models. It is emphasized that the proposed models do *not* employ any fitted "material parameters" and do *not* require the use of Monte Carlo simulations.

The proposed pairwise interaction framework is subsequently generalized to a higher-order damage model to account for higher (third- and above-) order microcrack interaction effects in Section 4. However, a higher-order micromechanical damage model requires much more complicated analyses. Experimental validation of the proposed micromechanical evolutionary damage models is needed to further assess their validity for practical engineering problems.

Downloaded 03 May 2010 to 171.66.16.20. Redistribution subject to ASME license or copyright; see http://www.asme.org/terms/Terms_Use.cfm

Acknowledgment

This work was sponsored by the Air Force Office of Scientific Research under Grant No. AFOSR-90-0336, together with the Defense Nuclear Agency. The authors gratefully acknowledge this support and the interest of Dr. Spencer T. Wu, Dr. Paul Senseny, and Dr. Kent L. Goering.

References

Ashby, M. F., 1979, "Micromechanisms of Fracture in Static and Cyclic Failure," *Fracture Mechanics, Current Status, Future Prospects*, R. S. Smith, ed., Pergamon Press, Oxford, Vol. 1, pp. 1–27.

Benveniste, Y., 1986, "On the Mori-Tanaka's Method in Cracked Bodies," *Mech. Res. Comm.*, Vol. 13, pp. 193–201.

Budiansky, B., and O'Connell, R. J., 1976, "Elastic Moduli of a Cracked Solid," *Int. J. Solids & Struct.*, Vol. 12, pp. 81–97.

Christensen, R. M., and Lo, K. H., 1979, "Solutions for Effective Shear Properties in Three Phase Sphere and Cylinder Models," *J. Mech. Phys. Solids*, Vol. 27, pp. 315–330.

Fanella, D., and Krajcinovic, D., 1988, "A Micromechanical Model for Concrete in Compression," *Eng. Fract. Mech.*, Vol. 29, No. 1, pp. 49–66.

Hill, R., 1965, "A Self-Consistent Mechanics of Composite Materials," *J. Mech. Phys. Solids*, Vol. 13, pp. 213–222.

Horii, H., and Nemat-Nasser, S., 1983, "Overall Moduli of Solids with Microcracks: Load-Induced Anisotropy," *J. Mech. Phys. Solids*, Vol. 331, pp. 155–171.

Horii, H., and Nemat-Nasser, S., 1985, "Elastic Fields of Interacting Inhomogeneities," *Int. J. Solids & Struct.*, Vol. 21, pp. 731–745.

Ju, J. W., 1991, "On Two-Dimensional Self-Consistent Micromechanical Damage Models for Brittle Solids," *Int. J. Solids & Struct.*, Vol. 27, No. 2, pp. 227–258.

Ju, J. W., and Lee, X., 1991, "On Three-Dimensional Self-Consistent Micromechanical Damage Models for Brittle Solids. Part I: Tensile Loadings," *J. Eng. Mech.*, ASCE, Vol. 117, No. 7, pp. 1495–1515.

Kachanov, M., 1987, "Elastic Solids with Many Cracks: A Simple Method of Analysis," *Int. J. Solids & Struct.*, Vol. 23, pp. 23–43.

Kachanov, M., and Laures, J.-P., 1989, "Three-Dimensional Problems of Strongly Interacting Arbitrarily Located Penny-Shaped Cracks," *Int. J. of Fract.*, Vol. 41, pp. 289–313.

Kanninen, M. F., and Popelar, C. H., 1985, *Advanced Fracture Mechanics*, Oxford University Press, New York.

Krajcinovic, D., and Fanella, D., 1986, "A Micromechanical Damage Model for Concrete," *Eng. Fract. Mech.*, Vol. 25, pp. 585–596.

Lee, X., and Ju, J. W., 1991, "On Three-Dimensional Self-Consistent Micromechanical Damage Models for Brittle Solids. Part II: Compressive Loadings," *J. Eng. Mech.*, ASCE, Vol. 117, No. 7, pp. 1516–1537.

McLaughlin, R., 1977, "A Study of the Differential Scheme for Composite Materials," *Int. J. Engng. Sci.*, Vol. 15, pp. 237–244.

Mori, T., and Tanaka, K., 1973, "Average Stress in Matrix and Average Elastic Energy of Materials with Misfitting Inclusions," *Acta Metallurgica*, Vol. 21, pp. 571–574.

Roscoe, R. A., 1952, "The Viscosity of Suspensions of Rigid Spheres," *Brit. J. Appl. Phys.*, Vol. 3, pp. 267–269.

Roscoe, R. A., 1973, "Isotropic Composites with Elastic or Viscoelastic Phases: General Bounds for the Moduli and Solutions for Special Geometries," *Rheol. Acta*, Vol. 12, pp. 404–411.

Sumarac, D., and Krajcinovic, D., 1987, "A Self-Consistent Model for Microcrack-Weakened Solids," *Mech. Mater.*, Vol. 6, pp. 39–52.

Downloaded 03 May 2010 to 171.66.16.20. Redistribution subject to ASME license or copyright; see http://www.asme.org/terms/Terms_Use.cfm

Optimal Cool Down in Nonlinear Thermoviscoelasticity With Application to Graphite/Peek (APC-2) Laminates

K. Lee
Graduate Student.

Y. Weitsman[1]
Mem. ASME.

Department of Engineering Science and Mechanics,
The University of Tennessee,
Knoxville, TN 37996-2030

Many thermoplastic resin composite laminates, such as those made of APC-2, undergo a substantial temperature drop during their post-manufacturing cool down. This thermal excursion induces significant residual thermal stresses into the laminate due to the mutual geometric constraints among the multidirectional plies. In view of the considerable time-dependent relaxation which occurs during the cooling process, the residual thermal stresses exhibit strong dependence on the temperature history. However, in view of the high magnitudes of those stresses, the relaxation behavior is viscoelastically nonlinear. This paper demonstrates that it is possible to obtain an optimal cool-down path which minimizes the residual thermal stresses in APC-2 composites upon the termination of the cooling process.

Introduction

APC-2 (graphite/PEEK) composites exhibit substantial time-dependent stress-strain response, especially at high temperatures, and a very large disparity between the longitudinal and transverse coefficients of thermal expansion. In addition, the processing of APC-2 involves cool down from a melt temperature, $T_M \approx 400°C$, down to room temperature, $T_R \approx 20°C$—which is about twice the temperature excursion sustained by graphite/epoxy composites. The above factors produce significant residual thermal stresses in multidirectionally reinforced laminates, which exceed the range of linear behavior. In view of the time-dependent response of PEEK, these stresses are sensitive to temperature history.

The dependence of the residual stresses σ on temperature history $T(t)$ is attributable to two contradictory roles of temperature. On the one hand, upon cooling against geometric constraints, temperature acts as a stress-*inducing* agent. On the other hand, due to the time-temperature analogy in thermoviscoelasticity, temperature enhances the relaxation processes within polymers and thus serves as a stress-*reducing* vehicle. Consequently, since temperature assists in relaxing the very same stresses it generates, it lends itself to an optimization scheme. Accordingly, it is possible to obtain an optimal time-temperature cool-down path $T_\Omega(t)$ which achieves the best interplay between the conflicting roles of temperature and results in minimal residual thermal stresses at the prescribed cooling time t_f, when T reaches the value of T_R.

Optimal temperature cool-down paths were determined by several researchers (Weitsman, 1980; Gurtin and Murphy, 1980; Weitsman and Harper, 1982; and Harper, 1985), assuming several variants of linear thermoviscoelastic material response. However, those optimization formulations are inapplicable to the case of APC-2 composites, because the residual stresses in that material reach magnitudes which lie far beyond the range of linear behavior. The major purpose of this paper is to present an optimization scheme for the cool-down time-temperature path, which yields minimal residual stresses for nonlinear viscoelastic materials.

It seems that the most complete characterization to date of the time-dependent response of PEEK and unidirectionally reinforced APC-2 coupons was obtained by Xiao (1987), with typical creep data at various levels of temperature shown in Fig. 1.[2] These, and supplementary experimental results not shown here, enabled Xiao to represent the time-dependent response of PEEK and APC-2 by means of the nonlinear viscoelastic model of Schapery (1969). However, it is important to note that the creep data of Xiao (1987) were collected under isothermal conditions and were limited to the temperature range of $20°C < T < 200°C$. Consequently, it was necessary to extrapolate the functional representations of those data to temperatures above 200°C in order to determine optimal temperature paths and compute residual thermal stresses. Such extrapolations are obviously undesirable and additional experimental creep data are needed to specify the optimal tem-

[1] Distinguished Scientist, University of Tennessee at Knoxville and Oak Ridge National Laboratory, Oak Ridge, Tennessee.

Contributed by the Applied Mechanics Division of THE AMERICAN SOCIETY OF MECHANICAL ENGINEERS for publication in the ASME JOURNAL OF APPLIED MECHANICS.

Discussion on this paper should be addressed to the Technical Editor, Professor Lewis T. Wheeler, Department of Mechanical Engineering, University of Houston, Houston, TX 77204-4792, and will be accepted until four months after final publication of the paper itself in the ASME JOURNAL OF APPLIED MECHANICS.

Manuscript received by the ASME Applied Mechanics Division, Dec. 11, 1991; final revision, Sept. 24, 1992. Associate Technical Editor: R. M. McMeeking.

[2] The authors thankfully acknowledge the permission of Prof. A. H. Cardon, of the Free University of Brussels, to utilize the data contained in Dr. Xiao's Ph.D. dissertation in the present work.

Copyright © 1994 by ASME
Downloaded 03 May 2010 to 171.66.16.20. Redistribution subject to ASME license or copyright; see http://www.asme.org/terms/Terms_Use.cfm

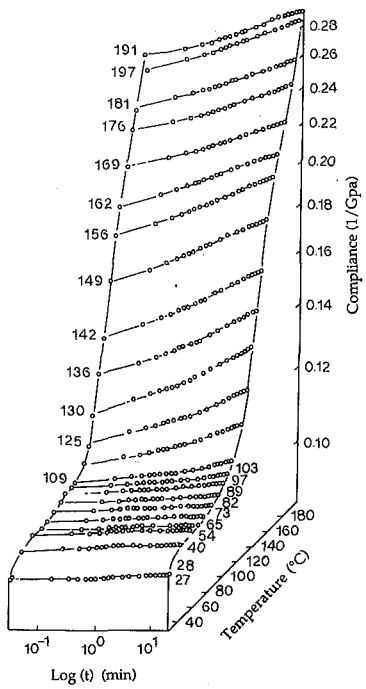


Fig. 1 Temperature dependence of transverse creep compliance of APC-2 unidirectional laminate (Xiao, 1987, p. 109)

perature history $T_\Omega(t)$. Nevertheless, it is reasonable to expect that, in view of its generic nature, the nonlinear optimization scheme developed in this paper would apply to the extended database as well.

In addition to the above-mentioned limited range of isothermal creep data, the full implementation of Schapery's model requires information on two distinct component, $V_1(T)$ and $V_2(T)$, of the so-called vertical shift factor function. It has been shown (Peretz and Weitsman, 1983) that isothermal creep data enable the evaluation of a single function $V(T)$, which is the product of the aforementioned individual components ($V=V_1V_2$), and that the determination of $V_1(T)$ and $V_2(T)$ separately requires the acquisition of creep data under transient temperature conditions. Consequently, Xiao's data contains an uncertain component.

In the present paper the response of APC-2 laminates was formulated by means of classical laminate theory (Jones, 1975), where the nonlinear viscoelastic response of individual APC-2 plies within the laminate was accounted for by means of the quasi-elastic/viscoelastic approximation (Lee, 1991).

2 Basic Equations

The linear thermoelastic response of a unidirectionally reinforced ply undergoing a temperature excursion $\Delta T=T-T_I$ from some stress-free reference temperature T_I (say), is given by (Jones, 1975):

$$\begin{aligned}\epsilon_L-\alpha_L\Delta T&=\sigma_L/E_L-\nu_{TL}\sigma_T/E_T\\ \epsilon_T-\alpha_T\Delta T&=-\nu_{LT}\sigma_L/E_L+\sigma_T/E_T\end{aligned}\tag{1}$$

where standard symbols were used and subscripts L and T denote longitudinal and transverse directions, respectively.

In the particular case of a symmetric balanced cross-ply layup, a straightforward employment of laminate theory yields the following expression for the laminate-level residual thermal stresses $\sigma_T=-\sigma_L=\sigma$:

$$\sigma=-rE_T\alpha\Delta T\tag{2}$$

where

$$\frac{1}{r}=(1+\nu_{TL})\left(1+\frac{1+\nu_{LT}}{1+\nu_{TL}}\frac{E_T}{E_L}\right)\tag{3}$$

and $\alpha=\alpha_T-\alpha_L$.

Note that the form of Eq. (2) remains valid for other symmetric lay-ups (in particular, quasi-isotropic lay-ups), but with different expressions for r.

For APC-2, the most pronounced time dependence occurs in the transverse modulus E_T. However, in view of the following magnitudes $E_L=130$ GPa, 3.3 GPa$<E_T<$10.5 GPa, $\nu_{LT}=0.31$, and $\nu_{TL}=0.0083$, we may ignore the time dependence of r and take $r=0.9125$ to within an error of $\pm$two percent.

Employing a nonlinear viscoelastic model (Schapery, 1969), the counterpart of Eq. (2) reads

$$\sigma(t)=-r\alpha V_1(T)\int_0^t E(\xi(t)-\xi(\tau))[d(V_2(T)\Delta T)/d\tau]d\tau\tag{4}$$

where the product $V(T)=V_1(T)V_2(T)$ is the vertical shift required to coalesce isothermal data (say creep) to form a "master curve."[3] In addition, the "reduced times," $\xi(t)$ and $\xi(\tau)$ in Eq. (4) are given through the expression

$$\xi(u)=\int_0^u dp/a(T;\sigma(p)).\tag{5}$$

In Eq. (5), $a(T;\sigma)$ is the horizontal shift factor required to coalesce isothermal data (say creep) to form a "master curve." Though both "V" and "a" may, in principle, depend on σ, it appears that the nonlinearity of the response of APC-2 can be expressed through $a(T;\sigma)$ alone. Under fluctuating temperatures, i.e., when $T=T(t)$, Eq. (4) should be read with $V_1(T(t))$ and $V_2(T(\tau))$. In this case we also have $\Delta T=\Delta T(\tau)$ in Eq. (4) and $a=a(T(p);\sigma(p))$ in Eq. (5). The quantity $\Delta T=T_I-T$ expresses the temperature drop below the stress-free initial temperature T_I.

3 Optimal Cool Down in the Linear Case

The optimization problem of cool-down history can be stated as follows:

Given an initial temperature T_I, where the composite is stress-free, a final temperature T_R ($T_R<T_I$), a finite time interval t_f, and a thermoviscoelastic stress-strain relation (e.g., Eq. (4)), find the "best" time-temperature history $T=T_\Omega(t)$, which minimizes the residual thermal stresses $\sigma(t_f)$. In all previous studies (Weitsman, 1980; Gurtin and Murphy, 1980; Weitsman and Harper, 1982; and Harper, 1985), which concerned linear behavior, namely $a=a(T)$ in Eq. (5), it was found that $T_\Omega(t)$ underwent sharp drops at $t=o$, from T_I to T_o and at t_f, from $T_\Omega(t_f)=T_F$ to $T=T_R$. Otherwise, $T_\Omega(t)$ varied monotonically and smoothly over the range $o<t<t_f$.

Specifically for the *linear* case expressed in Eq. (4) (namely $a=a(T)\neq a(T;\sigma)$), the initial drop is given by Harper (1985)

$$T_o-T_I=\frac{V_2(T_o)a(T_o)}{a'(T_o)V_2(T_o)-V_2'(T_o)a(T_o)}\tag{6}$$

which is a transcendental equation in the unknown T_o.

Beyond the initial drop, the optimal path $T=T_\Omega(t)$ is governed by the integrodifferential equation

$$\frac{dT(t)}{dt}=-\frac{E''(t,t_f)}{E'(t,t_f)}\times\frac{a'[V_2'(T-T_I)+V_2]}{a\{a''[V_2'(T-T_I)+V_2]-a'[V_2'(T-T_I)+V_2]'\}}.\tag{7}$$

In Eq. (7)

$$E(t,t_f)=E\left(\int_t^{t_f}\frac{ds}{a(T(s))}\right),$$

and primes denote derivatives with respect to the argument, namely, $E'(t,t_f)=dE(t)/dt$ evaluated at

[3] It is obvious from Eq. (4) that for $T=$ constant, $V_1(T)$ can be brought outside the integral and $\sigma(t)$ depends only on $V(T)=V_1(T)V_2(T)$ and not on $V_1(T)$ and $V_2(T)$ separately. This no longer holds for fluctuating temperatures.

Downloaded 03 May 2010 to 171.66.16.20. Redistribution subject to ASME license or copyright; see http://www.asme.org/terms/Terms_Use.cfm

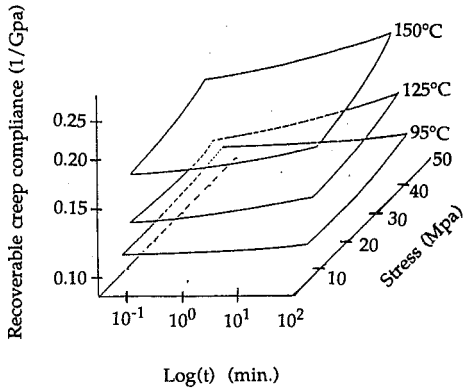


Fig. 2 Transverse tensile compliance-stress-time relationship of typical APC-2 composite laminate (Xiao, 1987, p. 124)

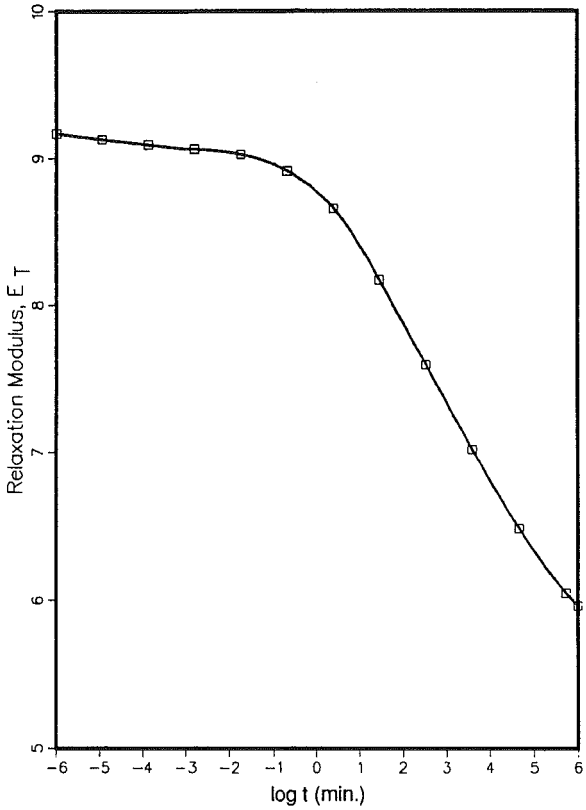


Fig. 3 The relaxation modulus *E(t)* versus log *t*, reduced from experimental creep data (Xiao, 1987)

$$t \to \int_t^{t_f} \frac{ds}{a(T(s))}.$$

Note that due to the presence of $E'(t, t_f)$ and $E''(t, t_f)$, Eq. (7) relates current values of T and T to all past and *future* values of T.

Consequently, that equation must be solved "backwards," from $t = t_f$ towards $t = o$, since $E(t, t_f)$ cannot be evaluated without a priori knowledge of the solution, with the exception of $E(t_f, t_f) = E(o)$—which is known. The procedure is to guess $T_\Omega(t_f) = T_F$, solve Eq. (7) numerically and evaluate $T(o)$, then adjust the guess value of $T_\Omega(t_f)$ iteratively until we obtain $T(o) = T_o$ which matches the root of Eq. (6).

4 The Nonlinear Thermoviscoelastic Response of APC-2

As noted in the Introduction, a comprehensive—albeit incomplete—experimental characterization of the nonlinear thermoviscoelastic response of APC-2 composites was obtained by Xiao (1987). Those experiments consisted of isothermal creep tests under constant uniaxial tension on unidirectionally reinforced APC-2 coupons. The coupons were loaded transversely, as well at an angle of 15 degrees, to the

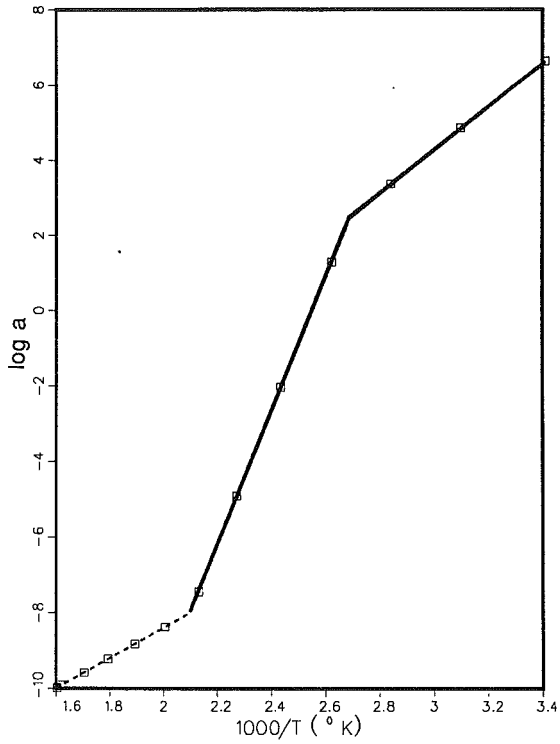


Fig. 4 Horizontal shift factor for transverse compliance of APC-2, reduced from experimental data (Xiao, 1987) and extended by extrapolation (extrapolated values shown by dashed line)

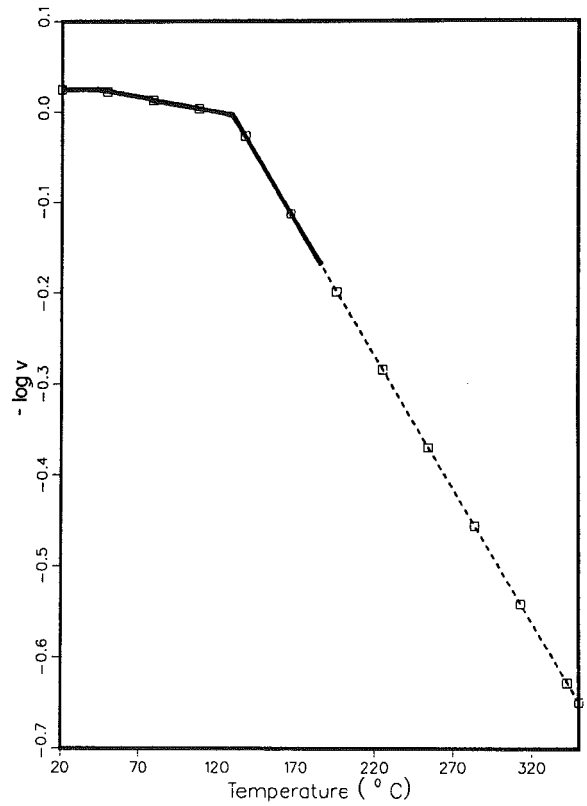


Fig. 5 Vertical shift factor for transverse compliance of APC-2, reduced from experimental data (Xiao, 1987) and extended by extrapolation (extrapolated values shown by dashed line)

Downloaded 03 May 2010 to 171.66.16.20. Redistribution subject to ASME license or copyright; see http://www.asme.org/terms/Terms_Use.cfm

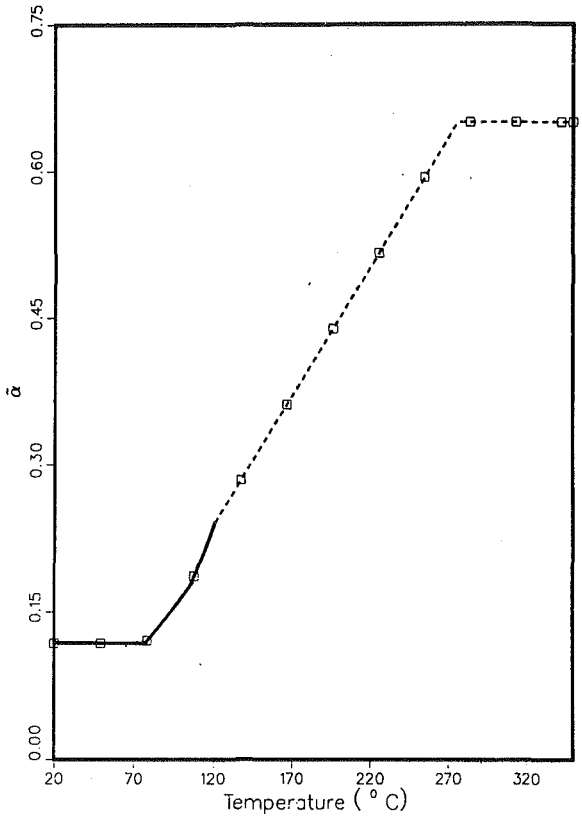


Fig. 6 Nonlinear function $\tilde{\alpha}$, reduced from the experimental data (Xiao, 1987) and extended by extrapolation (extrapolated values shown by dashed line)

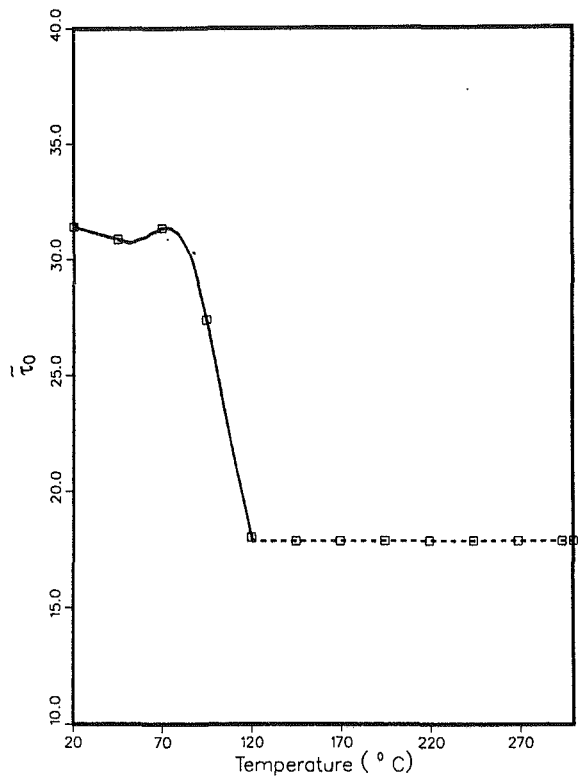


Fig. 7 Nonlinear threshold value $\tilde{\tau}_0$, reduced from the experimental data (Xiao, 1987) and extended by extrapolation (extrapolated values shown by dashed line)

fiber directions. The resulting transverse compliance is drawn in Fig. 1 versus $\log t$, for isothermal temperature values between 27°C and 197°C. Nonlinear effects are illustrated in Fig. 2, where compliances at 95°C, 125°C, and 150°C are sketched at stress levels ranging between 10 and 50 MPa. Further details, as well as procedures and results for data reduction in the context of Schapery's model, are provided in Xiao's dissertation (1987).

For the purpose of the present analysis the aforementioned creep data must be converted to relaxation modulus. In addition, extrapolations to 300°C were constructed in order to assess magnitudes of residual stresses from stress-free temperatures assumed to range in that vicinity. Complete details on data reduction and assumed extrapolations are given elsewhere (Lee, 1991). Results for the relaxation modulus $E(t)$, the horizontal shift factor $a_T(T)$, and the vertical shift factor $V(T)$ are presented in Figs. 3–5, where extrapolated values are shown by dashed lines. The nonlinear effects were incorporated into the horizontal shift factor in the form

$$a(T, \sigma) = a_T(T) a_\sigma(\sigma; T) \tag{8}$$

where $a_\sigma(\sigma; T)$ is expressed in terms of the octahedral shear stress τ_{OCT} (which is an isotropic stress invariant that for uniaxial tension reduces to $(\sqrt{2}/3)\sigma$).

Following Xiao (1987), we selected

$$a_\sigma(\sigma; T) = \begin{cases} \exp[-\tilde{\alpha}(\tau_{OCT} - \tilde{\tau}_0)] & \tau_{OCT} > \tilde{\tau}_0 \\ 1 & \tau_{OCT} \le \tilde{\tau}_0. \end{cases} \tag{9}$$

In expression (9), $\tilde{\alpha}$ and $\tilde{\tau}_0$ are temperature-dependent factor and threshold value, respectively, as shown in Figs. 6 and 7. In those figures, dashed lines correspond to extrapolated values.[4]

[4]The extrapolation of $\tilde{\tau}_0$ in Fig. 7 was motivated, at least partially, by expediency. An extrapolation to values of $\tilde{\tau}_0$ less than 18 MPa would require double precision numerical computations of optimal cooling paths. We found no justification to enmesh ourselves in such complications on the basis of a "free wheeling" extrapolation.

Finally (Barnes and Cogswell, 1987), the coefficients of thermal expansion α_L and α_T, per 1°C, are

$$\alpha_L = \begin{cases} 0.5 \times 10^{-6} \\ 1.0 \times 10^{-6}, \end{cases} \quad \alpha_T = \begin{cases} 30 \times 10^{-6}, & T < 125°C \\ 75 \times 10^{-6}, & T > 125°C. \end{cases} \tag{10}$$

It should be noted that the optimization scheme, as given in Eqs. (6) and (7), requires values of E', E'', a', a'', V', and V''. To generate these values from the curves shown in Figs. 3–7 it was necessary to resort to smoothing operations, employing spline function representations on overlapping segments of the abscissas together with some weighted averaging. Complete details are given elsewhere (Lee, 1991).

5 Optimal Cool Down for Nonlinear Viscoelastic Response

Motivated by the simplified circumstance of the nonlinear standard solid model, where an analytical solution could be matched with results obtained by an iterative numerical scheme (Lee, 1991) we base our iteration procedure on the linear optimization scheme expressed in Eqs. (6) and (7). Accordingly, the scheme follows the steps listed as follows:

Step 1: Consider linear viscoelastic behavior, with response function $E(t)$, α, $V(T)$, and $a(T)$ determined from reduced experimental data together with prescribed initial and final temperatures T_I and T_R, and cooling time t_f. Employ Eq. (6) to determine $T_o = T(o^+)$ and solve Eq. (7) numerically to obtain $T_\Omega(t)$, where $T_F = T_\Omega(t_f^-)$ is chosen iteratively until a solution of Eq. (7) yields $T_\Omega(o^+) = T_o$ which matches Eq. (6). Denote $T_\Omega(t)$ by $T_\Omega^{(o)}(t)$.

Step 2: Employ Eq. (4) to compute the residual thermal stress $\sigma(t)$, denoted by $\sigma^{(o)}(t)$, due to cool-down along $T_\Omega^{(o)}(t)$.

Step 3: Relate $\sigma^{(o)}(t)$ to $T_\Omega^{(o)}(t)$ to form $\sigma^{(o)} = F^{(o)}(T^{(o)})$.

Step 4: Consider the nonlinear shift factor function $a(T; \sigma)$ such as expressed in Eqs. (8) and (9) for APC-2. Along the linear optimal path we have $a(T; \sigma) = a(T^{(o)}; F^{(o)}(T^{(o)}))$ which can be represented as a $^{(1)}(T)$.

Downloaded 03 May 2010 to 171.66.16.20. Redistribution subject to ASME license or copyright; see http://www.asme.org/terms/Terms_Use.cfm

Step 5: Repeat steps 1, 2, 3, and 4 with $a(T)$ replaced by $a^{(1)}(T)$ to obtain $T_\Omega^{(1)}$ with $T_\Omega^{(1)}(t)$, $\sigma^{(1)}(t)$, $\sigma^{(1)}=F^{(1)}(T^{(1)})$ and $a^{(2)}(T)=a(T^{(1)};F^{(1)}(T^{(1)}))$, respectively.

Continue until the attainment of a prescribed convergence, say $T_\Omega^{(n+1)}(t)=T_\Omega^{(n)}(t)+\epsilon(t)$, where $|\epsilon(t)|$ is less than a given tolerance.

In some circumstances the above scheme cannot be employed in a straightforward manner because the range of definition of $a^{(k)}(T)$ in, say, the kth iteration may not suffice for the employment of Eq. (7) to generate $T_\Omega^{(k+1)}(t)$. To illustrate this circumstance, consider Figs. 8 and 9. In those figures the optimal temperature path at the kth iteration, with initial and final values $(T_0)_A$ and $(T_F)_A$, is indicated by "A" in Fig. 8 and the corresponding correlation between $\sigma^{(k)}(t)$ and $T_\Omega^{(k)}(t)$, namely $F^{(k)}(T^{(k)})$ is denoted by the curve "A^*" in Fig. 9. Note that $F^{(k)}(T^{(k)})$ is defined only for temperature T over the range $(T_F)_A<T<(T_0)_A$. This limited range of definition of $F^{(k)}(T^{(k)})$ confines our ability to express $a^{(k)}(T)$ to within the same extent.

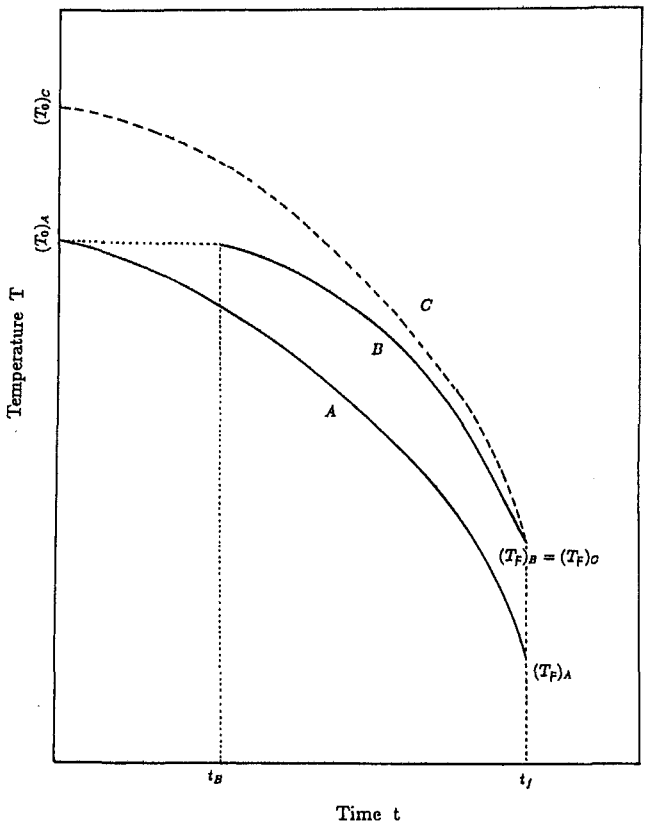


Fig. 8 The construction of the "psuedo" optimal temperature path

Turning to the next iteration, it is necessary to initiate the computation by selecting a new guess value of T_F, say $(T_F)_B$ in Fig. 8. Unfortunately, if $(T_F)_B>(T_F)_A$ it may become impossible to construct a new optimal path by means of Eq. (7) beyond $(T_0)_A$, and the path "B" in Fig. 8 cannot be established for times $t<t_B$.

In order to surmount the above obstacle, we temporarily abandon Eq. (7) and, still using $T_\Omega(t)$ and $\sigma(t)$ at hand, construct functions $F(T)$ and "pseudo" optimal paths $T(t)$ which enable us to proceed with the current iteration. The sole purpose of those "pseudo" paths is to extend the range of definition of $F(T)$.

For that purpose, we select a guess value of T_F, *accompanied by a guess value of* T_0. These values, denoted by $(T_F)_C$ and $(T_0)_C$ in Fig. 8, are then connected by a continuous path $T(t)$, denoted by C in that Figure. The intermediate temperatures $(T_i)_C$ along C are related to $(T_0)_A$, $(T_0)_C$, $(T_F)_A$, $(T_F)_C$ and $(T_i)_A$ according to

$$(T_i)_C=(T_i)_A+\Delta T_i \tag{11}$$

where the intermediate values of ΔT_i were determined from the following relationship based on similar triangles:

$$\frac{\Delta T_0-\Delta T_F}{t_0-t_f}=\frac{\Delta T_i-\Delta T_F}{t_i-t_f}. \tag{12}$$

In Eq. (12), ΔT_0 and ΔT_F refer to the differences between the end values of paths "A" and "C" in Fig. 8, namely

$$\Delta T_0=(T_0)_C-(T_0)_A,\quad \Delta T_F=(T_F)_C-(T_F)_A.$$

We now construct a modified function $F(T)$ by relating the values of $\sigma(t)$, which were computed along $T_\Omega(t)$ of the previous iteration (which are available to us) with $T(t)$ given by Eq. (11). Such a function $F(T)$, sketched by the curve C^* in Fig. 9, is defined over the appropriate range $(T_F)_C<T<(T_0)_C$, which in turn enables the establishment of $\hat{a}(T)=a(T,F(T))$ over the same range. With the above ad hoc values of $\hat{a}(T)$,

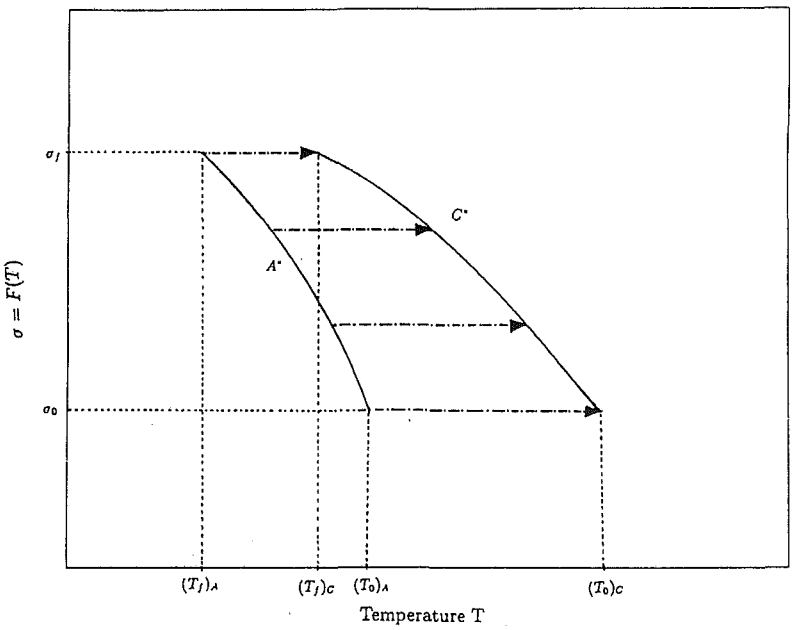


Fig. 9 The function $F(T)$ modified to cover the extended temperature region

Downloaded 03 May 2010 to 171.66.16.20. Redistribution subject to ASME license or copyright; see http://www.asme.org/terms/Terms_Use.cfm

and for the aforementioned guess value of T_F, we now employ Eq. (7) to generate an optimal path $T_\Omega(t)$. Obviously, this $T_\Omega(t)$ cannot rise above $(T_0)_C$ since $\hat{a}(T)$ is undefined for $T > (T_0)_C$. Therefore, if such a circumstance is forced by Eq. (7), we abandon our guess value of $(T_0)_C$ in favor of a revised, higher value. Subsequent guess values of $(T_0)_C$ are introduced iteratively—still retaining the same guess value of $(T_F)_C$—until $(T_0)_C$ matches $T_\Omega(0)$ to within a given tolerance. When this match is achieved, we compute the residual stress $\sigma(t_f^+)_C$ according to Eq. (4), due to cool down along the path $T_\Omega(t)$ which ends at the above guess value of $(T_F)_C$ and is generated through Eq. (7) with the aforementioned, ad hoc, $\hat{a}(T)$.

At this stage we select another guess value of T_F, say $(T_F)_D$, and repeat the procedure, obtaining a corresponding value for the residual stress $\sigma(t_f^+)_D$.

In such manner we obtain a sequence of values $\sigma(t_f^+)$ corresponding to various guess values T_F. Note that all these values are derived from a procedure that uses stresses $\sigma^{(k)}(t)$ along the optimal path of the kth iteration as "guide posts" for the formation of $F(T)$ and $\hat{a}(T)$. No updating of these "guide posts" is affected during the current process.

We now search for the value of T_F which yields a minimal $\sigma(t_f^+)$. This search was performed by means of the IMSL subroutine "UMCGF," which uses a conjugate gradient algorithm and gradients evaluated through finite differences to locate minima of functions.

In this manner we select the "best" T_F as the end point for the current, say $(k+1)$th iteration. For this "best" value of T_F we compute $T_\Omega^{(k+1)}(t)$ and the corresponding stress $\sigma^{(k+1)}(t)$ along $T_\Omega^{(k+1)}(t)$. These two functions are correlated to generate revised listings of $F^{(k+1)}(T)$ and $a^{(k+1)}(T)$. The revised values of $a^{(k+1)}(T)$ form the "guide posts" for the new iteration.

The procedure is repeated until attaining a prescribed convergence criterion such as

$$\frac{1}{t_f}\sqrt{\int_0^{t_f}(T_i^{k+1}(t)-T_i^k(t))^2dt} < \epsilon.$$

Note that in the numerical scheme, as outlined above, we abandoned the use of Eq. (6) and determined the value of T_0 by the search method, which was substituted in its place. As will be noted below, the evaluation of $F(T)$ and hence $\hat{a}(T)$ and, in particular, $\hat{a}'(T)$, near T_0 is not sufficiently reliable to permit the use of Eq. (6).

The selection of nonuniform time intervals Δt_i, adopted for the numerical integration of Eq. (7), was motivated by the results of the nonlinear standard solid model shown elsewhere (Lee, 1991). For that model the temperature T varied most significantly over certain short time intervals. Consequently, at each time step t_i the size of the time interval Δt_i was determined by regulating the temperature increment ΔT_i. It was necessary to regulate ΔT_i because dT/dt along the optimal path $T_\Omega(t)$ varied from extremely large to extremely small values over $0 < t < t_f$, with very rapid variations occurring within short time spans. On the other hand, the time increment was also regulated to avoid undesirably long time intervals when dT/dt was extremely small. It was found that with an appropriate selection of unequal time intervals, sufficient accuracy was obtained for all $T_\Omega(t)$ when the time span t_f was divided into no more than 500 unequal subintervals.

The solution of Eq. (7) is, in general, unstable numerically. The condition $dT/dt < 0$ is required if the temperature T continues to drop monotonically over the time interval $(0, t_f)$. This condition also serves as a requirement for the convergence of the T_Ω. Therefore, several corrections were necessary to avoid the computational instability which occurred when this condition was violated. The solution was Eq. (7) required the values of E', E'', a', a'', and V', which were evaluated by means of interpolating functions. However, inaccurate numerical values were inevitable at certain locations for two reasons: (1) the interpolating functions were generated from a limited number of experimental data and (2) Eq. (7) involved the evaluation of first and second derivatives of functions. Thus certain types of interpolation errors as well as truncational errors were inevitable. On several occasions changes of the sign in dT/dt were encountered during the computations. These were corrected simply by replacing an "unacceptable" value of $(dT/dt)_i$ with $(dT/dt)_{i-1}$ of the previous time step, and continuing the computation accordingly. Numerous trial-and-error tests and the need for ongoing corrections required vigilant attention and judgement during the computation of T_Ω. This requirement for ongoing intervention in the computational process precluded its full automation and ruled out the use of the optimization routines developed as commercial software packages (e.g., IMSL and NAG). Nevertheless, it was possible to accomplish steps 1 and 2 of the computational algorithm in a fairly efficient manner.

The numerical correlation $\sigma = F(T)$ and its incorporation into the horizontal shift factor $a(T;\ \sigma) \rightarrow a(T;\ F(T)) \rightarrow \hat{a}(T)$, which is indicated in Steps 3 and 4 of computational algorithm, required smoothing operations to provide reasonable value for the derivatives of T_Ω to be used in Eq. (7). The interpolating function of $\sigma = F(T)$ was generated with the n sets of paired values (σ_i, T_i) obtained from the previous steps by means of the IMSL routine "CSCON," a shape-preserving interpolation routine. The consequent derivative of $F(T)$ was also generated by means of IMSL routine "CSDER."

It is also noted that $F(T)$ varied significantly with T near $t = 0$ and, moreover, a change of sign of $dF(T)/dT$ occurred due to the initial temperature drop in the immediate vicinity of $t = 0$. To account for this fluctuation with sufficient accuracy it was necessary to generate a suitably appropriate set of paired values of $\sigma_i = \sigma(t_i)$ and $T_i = T(t_i)$ at refined time steps t_i until reliable first derivatives of $\sigma = F(T)$ were obtained near $t = 0$. These procedures resulted in reasonable and consistent values for $\hat{a}(T)$ and all its various derivatives which were needed in the computational scheme for $T_\Omega(t)$.

It should be noted that we have no mathematically grounded proof that the iterated optimization scheme must converge, and obviously no proof of uniqueness. Nevertheless, it is interesting to note that for the APC-2 data at hand, the iterative scheme converged after about five to six iterations.

Efforts to verify our results at least partially were affected in two ways. The first attempt at validation was made by introducing several arbitrary, small disturbances in the optimal path and comparing the ensuing values of $\sigma(t_f^+)$. An upward or a downward perturbation in T_Ω was introduced at selected locations of the optimal path T_Ω. A total of three such locations were examined along T_Ω—at early, intermediate, and late stages in the time interval $(0, t_f)$, respectively. In all cases the resulting values of $\sigma(t_f)$ exceeded the optimal value.

Next, continuous paths adjacent to the optimal path T_Ω were examined, in contrast with the previous perturbations which occurred at localized neighborhoods of T_Ω. Several such adjacent temperature paths were constructed and the consequent values of $\sigma(t_f^+)$ were compared. In some circumstances slightly lower values of $\sigma(t_f^+)$ were obtained for these neighboring temperature paths. However, these lower values were deemed acceptable because they fell within the numerical accuracy of our computations.

6 Numerical Results for APC-2 Laminates

The reduced and extrapolated data, as expressed in Section 4, were utilized in the evaluation of optimal cooling paths for APC-2 composite material. In the computations we employed two values for the initial stress-free temperatures, namely $T_I = 250°C$ and $300°C$. In all cases, we considered a final cool-down temperature $T_R = 30°C$ and a cooling time $t_f = 100$ min. With those two values of T_I, computations were performed for the following three thermorheological subcases:

Downloaded 03 May 2010 to 171.66.16.20. Redistribution subject to ASME license or copyright; see http://www.asme.org/terms/Terms_Use.cfm

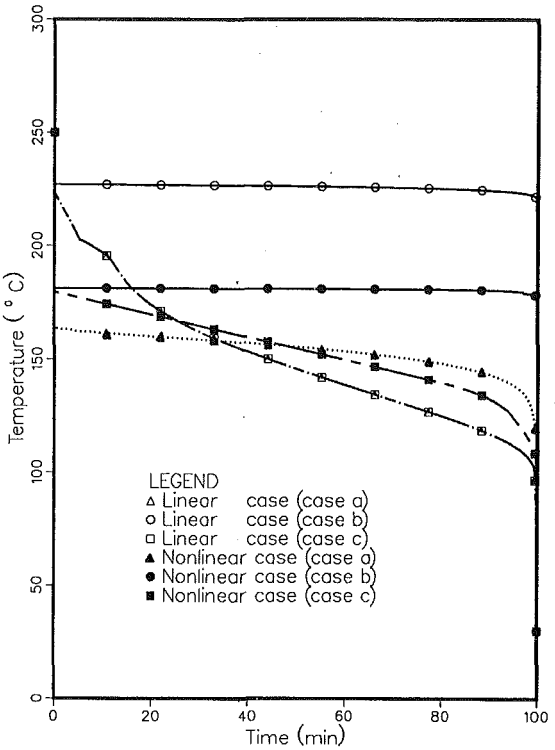


Fig. 10 Optimal temperature paths for APC-2, assuming $T_i = 250°C$

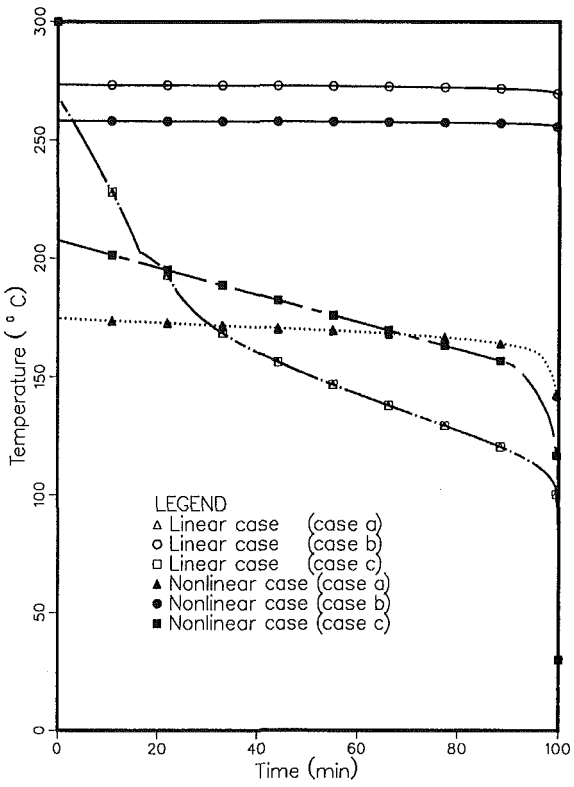


Fig. 11 Optimal temperature paths for APC-2, assuming $T_i = 300°C$

Case a: the thermorheologically simple case ($V = V_1 = V_2 = 1$).

Case b: a thermorheologically complex case with $V = V_2$, and $V_1 = 1$.

Case c: a thermorheologically complex case with $V = V_1$, and $V_2 = 1$.

The results are shown in Figs. 10–13. In all those figures the temperature T is in °C, the stress σ is in MPa, and the time t is in minutes. Results for optimal cool-down paths, $T_\Omega(t)$ versus t, are shown in Figs. 10 and 11 and results for stress histories along the optimal temperature paths, $\sigma(t)$ versus t, are plotted in Figs. 12 and 13.

These figures exhibit the significant role of material nonlinearity during thermal cool down. In addition, the results demonstrate the sensitivity of the nonlinear viscoelastic stresses

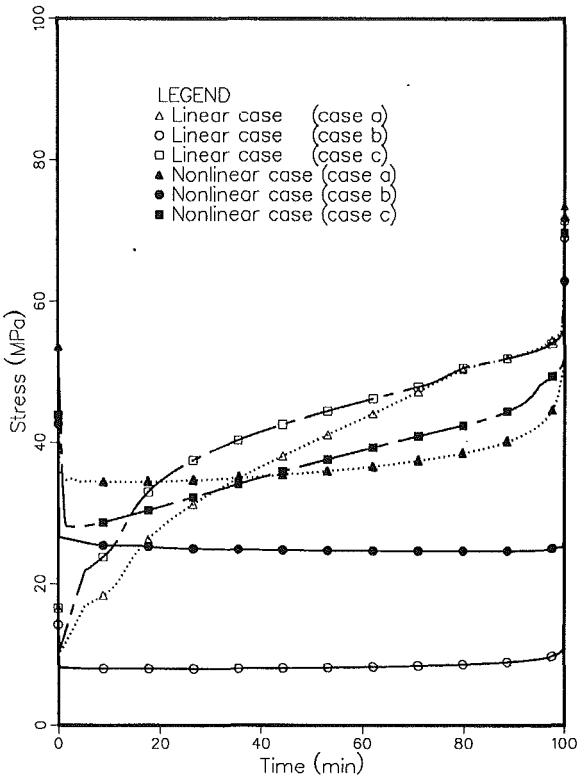


Fig. 12 Stress histories along optimal temperature paths for APC-2, assuming $T_i = 250°C$

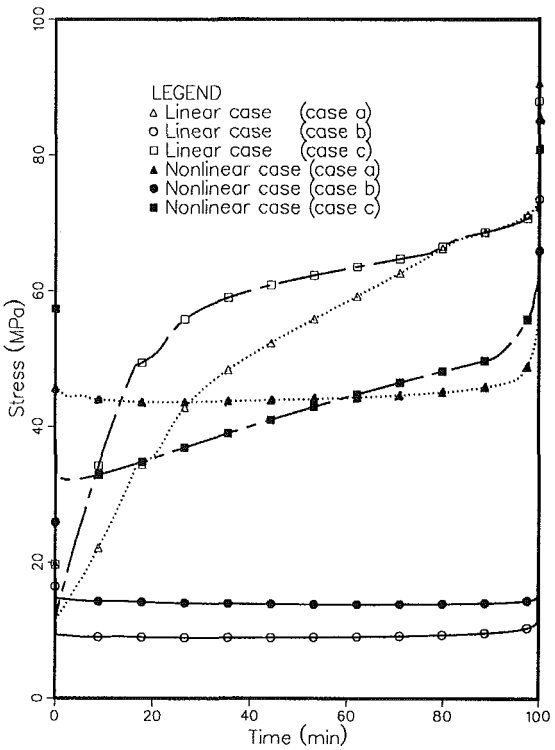


Fig. 13 Stress histories along optimal temperature paths for APC-2, assuming $T_i = 300°C$

Downloaded 03 May 2010 to 171.66.16.20. Redistribution subject to ASME license or copyright; see http://www.asme.org/terms/Terms_Use.cfm

Table 1 Comparison of final stresses for APC-2 composite laminate between linear and nonlinear cases

	Final Stress (MPa)			
	$T_I = 300°C$		$T_I = 250°C$	
Description	Linear	Nonlinear	Linear	Nonlinear
Case a	90.64	85.43	73.57	72.05
Case b	73.47	65.85	68.95	62.81
Case c	87.92	80.86	71.39	69.57

and optimal cooling paths to the detailed characterization of the response functions $V_1(T)$ and $V_2(T)$ as well as to the level of the stress-free temperature T_I.

For Case a, the thermorheologically simple case, the major differences between the optimal temperature paths, as shown in Figs. 10 and 11, was that the nonlinear temperature path resembled a stepwise pattern, while the linear case corresponded to more gradual temperature variations. For Case b, the thermorheologically complex case with $V = V_2$, both linear and nonlinear optimal temperature paths followed stepwise patterns, with the nonlinear paths falling below the linear paths. Regarding Case c, it may be noted that linear optimal paths are identical with those of the Case a since, in Case c, the vertical shift factor is located entirely outside the superposition integral. However, the nonlinear optimal paths corresponding to Cases c and a differed from each other since these paths depended now on stress through $a = a(T, \sigma)$.

Final residual thermal stresses at $t = t_f^+$ for various cases are shown in Table 1. Note that the highest final stress σ_f occurred in the linear Case a which entails horizontal shift only, while the lowest final stress σ_f corresponded to the nonlinear Case b which incorporates the entire vertical shift factor inside the superposition integral.

For all cases note the jump discontinuities at $t = 0$ and $t = t_f$ in both temperatures and stresses. The magnitude of the first jump in temperature, which occurs $t = 0$, depends strictly on the shift-factor function a and the vertical shift factor V_2 and is observed to be directed downward for all cases in our computations. The second jump, which occurs at the terminal $t = t_f$, depends on the prescribed final temperature T_R as well as on $t = t_f$. We note that in the present circumstance all the optimal paths terminate at levels above the room temperature T_R, requiring a downward jump at $t = t_f$.

The values of $\sigma(t_f^+)$ for all cases under consideration are listed in Table 1. It can be noted from that table that for $T_I = 300°C$ nonlinearity can provide up to 37 percent reduction in the final residual stresses, beyond the predictions of linear viscoelastic response. For $T_I = 250°C$ nonlinear can give a 17 percent advantage. Figures 12 and 13 further demonstrate the detailed roles played by the various material functions which relate the thermoviscoelastic behavior of APC-2.

7 Conclusions

The results of this study show that the residual thermal stresses that develop in thermoplastic resin composites, such as APC-2, are affected most substantially by the time-dependent material response of the resin. In addition, it was observed that these stresses reach magnitudes which approach the level of the ultimate transverse strength of the composite ply. Consequently, it is essential to account for nonlinear effects in the evaluation of those stresses and in the determination of optimal temperature paths. Variations among the various viscoelastic material response functions, as well as uncertainties concerning the stress-free temperature, lead to predictions of residual thermal stress which range between 62.7 MPa and 90.7 MPa (as compared with an estimated transverse failure stress $\sigma_T^f \sim 90$ MPa). This unsatisfactory variation in our predictions stems from the incomplete data base for APC-2, which exists at the present time, not from an apparent weakness in our computational scheme. It is therefore desirable to extend the experimental characterization work of Xiao (1987) to include a higher range of temperatures as well as transient temperature response to distinguish between the functions $V_1(T)$ and $V_2(T)$.

It should be noted that the transcrystalline structure of PEEK within the APC-2 composite depends on temperature history and, in particular, on the rate of cooling (Blundell et al., 1985; Blundell and Osborn, 1985). This dependence appears to be rather weak for cooling rates below 500°C/min. Similarly, the transverse modulus of APC-2 exhibits a weak dependence on cooling rates below 3000°C/min (Grossman and Amateau, 1988). Consequently, the optimal paths evaluated in this article should not be affected by the microstructural aspects of PEEK.

Acknowledgment

This work was performed under Contract N00014-90-J-1556 from the office of Naval Research to one of the authors (YW). The authors wish to thank the program manager, Dr. Y. Rajapakse of the Mechanics Division, Engineering Sciences Directorate, for his encouragement and support.

References

Barnes, J. A., and Cogswell, F. N., 1987, "Transverse Flow Processes in Thermoplastic Composite," *International Polymer Processing*, Vol. 1, pp. 157–165.

Blundell, D. J., Chalmers, J. M., Mackenzie, M. W., and Gaskin, W. F., 1985, "Crystalline Morphology of the Matrix of PEEK-Carbon Fiber Aromatic Polymer Composites, I. Assessment of Crystallinity," *Sampe Quarterly*, Vol. 16, pp. 22–30.

Blundell, D. J., and Osborn, B. N., 1985, "Crystalline Morphology of the Matrix of PEEK-Carbon Fiber Aromatic Polymer Composites, II. Crystallization Behavior," *Sampe Quarterly*, Vol. 17, pp. 1–6.

Grossman, S. P., and Amateau, M. F., "The Effect of Processing on Graphite PEEK Thermoplastic Composite," *Proceedings of the 33rd International Sampe Symposium*, Vol. 33, G. Carillo, E. D. Newell, W. D. Brown, and P. Phelan, eds., SAMPE Int. Bus. Off., Covina, pp. 681–692.

Gurtin, M. E., and Murphy, L. F., 1980, "On Optimal Temperature Path for Thermorheologically Simply Viscoelastic Materials," *Quart. App. Math.*, Vol. 38, pp. 179–190.

Harper, B. D., 1985, "Optimal Cooling Paths for a Class of Thermorheologically Complex Viscoelastic Materials," ASME JOURNAL OF APPLIED MECHANICS, Vol. 52, pp. 634–638.

Jones, R. M., 1975, *Mechanics of Composite Materials*, Scripta Book Co., Washington, DC, pp. 147–187.

Lee, K., 1991, "Investigations of the Mechanical Behavior of Graphite/PEEK (APC-2) Composites," Ph.D. Dissertation, The University of Tennessee, Knoxville, TN.

Peretz, D., and Weitsman, Y., 1983, "The Nonlinear Thermoviscoelastic Characterization of a Structural Adhesive," *J. Rheology*, Vol. 27, pp. 97–114.

Schapery, R. A., 1969, "Further Development of the Thermodynamic Constitutive Theory: Stress Formulation," Purdue University Report AA and ES 69-2 (AFML Contract F33615-67-C-1412), Lafayette, Indiana.

Weitsman, Y., 1980, "Optimal Cool-Down in Linear Viscoelasticity," ASME JOURNAL OF APPLIED MECHANICS, Vol. 47, pp. 35–39.

Weitsman, Y., and Harper, B. D., 1982, "Optimal Cool-Down of Cross-Ply Composite Laminates and Adhesive Joints," ASME JOURNAL OF APPLIED MECHANICS, Vol. 49, pp. 735–739.

Xiao, X., 1987, "Viscoelastic Characterization of Thermoplastic Matrix Composites," Ph.D. Thesis, Free University of Brussels.

Downloaded 03 May 2010 to 171.66.16.20. Redistribution subject to ASME license or copyright; see http://www.asme.org/terms/Terms_Use.cfm

Integrated Damping Mechanics for Thick Composite Laminates and Plates

D. A. Saravanos
Senior Research Associate,
Ohio Aerospace Institute,
NASA Lewis Research Center,
21000 Brookpart, MS 49-8,
Cleveland, OH, 44135
Assoc. Mem. ASME

A method for predicting the damped dynamic characteristics of thick composite laminates and plates is presented. Unified damping mechanics relate the damping of composite plates to constituent properties, fiber volume ratio, fiber orientation, laminate configuration, plate geometry, temperature, and moisture. Discrete layer damping mechanics for thick laminates, entailing piecewise continuous displacement fields and including the effects of interlaminar shear damping, are described. A semi-analytical method for predicting the modal damping and natural frequencies of thick simply-supported specialty composite plates is included. Applications demonstrate the validity, merit, and ranges of applicability of the new theory. The applications further illustrate the significance of interlaminar shear damping, and investigate the effects of lamination, thickness aspect ratio, fiber content, and temperature.

Introduction

Passive damping is broadly recognized as an important parameter for improving the elastodynamic performance of many flexible structures, such as large space structures, aircraft panels, engine rotor blades, high-speed machinery, and so forth. Indeed, the existence of material damping may significantly improve vibration and sound control, fatigue endurance, and impact resistance. Composites are already widely preferred as candidate structural materials for many high-performance structures due to their high specific stiffness and strength, and as a result, their damping capacity has received current attention as an added advantage of these materials.

Various damping mechanics theories for unidirectional composites and laminates have been reported by Hashin (1970), Schultz and Tsai (1968, 1969), Adams et al. (1969), Adams and Bacon (1973a, 1973b), Chang and Bert (1973), Siu and Bert (1974), Gibson and Plunkett (1976), Sun et al. (1985), Suarez et al. (1986), and Saravanos and Chamis (1990a, 1990b). Work on the damping of composite beams (Ni and Adams, 1984), composite plates (Lin et al., 1983), and composite plate/shell structures of general geometry and lamination (Saravanos and Chamis, 1991) has been also reported. The research has undoubtedly demonstrated the anisotropy of composite damping and its strong dependence on an array of micromechanical, laminate, structural, and hygrothermal parameters.

The previously mentioned work is mostly limited to the classical laminate theory assumptions which neglect interlaminar shear effects; hence, it is suitable for thin laminates subjected predominantly to pure extension and/or flexure. In all other cases, the damping of the composite is underestimated because the contributions of interlaminar shear damping are neglected. Moreover, interlaminar shear effects are more predominant in composite laminates than in other monolithic materials, as a result of their through-the-thickness inhomogeneity and anisotropy. Therefore, interlaminar shear damping may be a significant source of damping in composites, particularly in laminates of thicker sections; for this reason, integrated damping mechanics need to be developed for its accurate simulation.

Limited research has been reported in this direction (Alam and Asnani, 1986). To overcome these limitations a novel integrated discrete layer laminate damping theory for composite laminates and plates is developed and presented herein. The method assumes piecewise continuous in-plane displacement fields with variable degrees-of-freedom through the laminate thickness. Hence, the effects of interlaminar shear damping are included. In order to establish an upper bound for the accuracy of mechanics, the additional option for piecewise continuous through-the-thickness displacement and three-dimensional elastic continuum constitutive relations is also investigated to account for the contributions of normal through-the-thickness damping and Poisson's effects. These discrete damping theories, although computationally more cumbersome, are particularly suitable for thick composite laminates, or laminates where the representation of local interlaminar shear effects is important.

In addition to laminate damping, a semi-analytical methodology for the prediction of the dynamic properties of simply-

Contributed by the Applied Mechanics Division of THE AMERICAN SOCIETY OF MECHANICAL ENGINEERS for publication in the JOURNAL OF APPLIED MECHANICS.

Discussion on this paper should be addressed to the Technical Editor, Professor Lewis T. Wheeler, Department of Mechanical Engineering, University of Houston, Houston, TX 77204-4792, and will be accepted until four months after final publication of the paper itself in the JOURNAL OF APPLIED MECHANICS.

Manuscript received by the ASME Applied Mechanics Division, Oct. 29, 1991; final revision, Nov. 17, 1992. Associate Technical Editor: G. J. Dvorak.

Copyright © 1994 by ASME
Downloaded 03 May 2010 to 171.66.16.20. Redistribution subject to ASME license or copyright; see http://www.asme.org/terms/Terms_Use.cfm

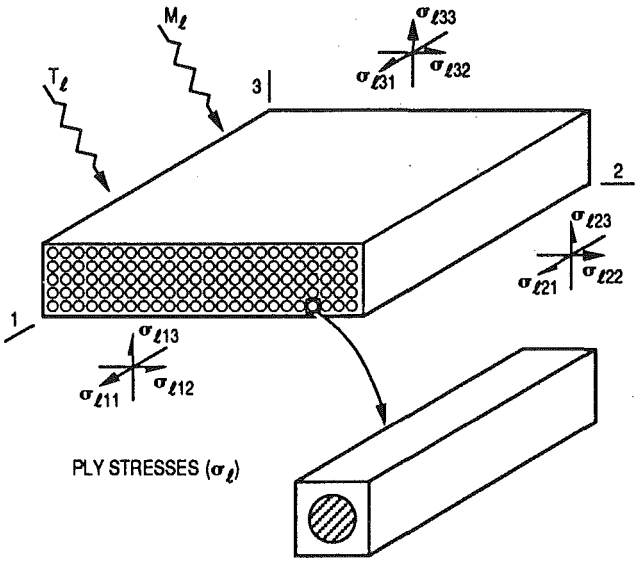


Fig. 1 Unidirectional composite systems

supported (SS) specialty thick composite plates based on the aforementioned laminate mechanics is presented, and results for the modal damping values and frequencies are reported.

Application of the new method, which in the remaining paper will be identified as discrete layer damping theory with constant through-the-thickness displacement, on the damping prediction of composite plates are presented. Additional comparisons with the classical laminate damping theory and a discrete layer damping theory incorporating variable through-the-thickness displacements, illustrate the merit and accuracy of the developed theory, and establish the ranges of applicability for each method. The case studies also quantify the significance of interlaminar shear damping in thick laminates, specific laminate configurations, elevated temperatures, and high-order modes. Moreover, the results provide valuable information and guidelines for either designing composite laminates/plates with good dynamic characteristics or conducting successful measurements of damping in composite laminates.

Composite Damping

This section briefly reviews the synthesis of damping for on-axis (damping along the material axes) and off-axis composites (unidirectional composites loaded at an angle), including the effects of temperature and moisture on composite damping. Additional details are provided by Saravanos and Chamis (1990a). The damping mechanics complement previous work on other composite properties (Murthy and Chamis, 1984).

On-Axis Damping. For a unidirectional composite loaded along the material axes (Fig. 1), closed-form expressions have been developed for the synthesis of damping based on elastic hysteretic damping assumptions (Saravanos and Chamis, 1990a). For orthotropic but transversely isotropic materials, like unidirectional reinforced composites, six damping coefficients will completely characterize the damping of the composite, that is (1) longitudinal damping ψ_{l1} (direction 11), (2) transverse in-plane damping ψ_{l2} (direction 22), (3) transverse through-the-thickness damping, ψ_{l3} (direction 33), (4) in-plane shear damping ψ_{l6} (direction 12), (5) interlaminar shear damping ψ_{l4} (direction 23), and (6) interlaminar shear damping ψ_{l5} (direction 13). These six damping capacities are explicitly related to fiber/matrix moduli and damping values, and the fiber volume ratio. Typical damping predictions and experimental correlations for Gr/Epoxy unidirectional composites are shown by Ni and Adams (1984).

Off-Axis Damping. For the case of off-axis composites, i.e., composites loaded at an angle, a transformation (Saravanos and Chamis, 1990a) provides the equivalent damping capacity of the composite in the structural coordinate system. The damping transformation is extended herein, based on the same principle of invariance of the dissipated energy, to include out-of-plane shear and transverse damping. In such case the off-axis composite damping is best described by the following 6-by-6 damping matrix $[\psi_c]$:

$$[\psi_c] = [R]^T[\psi_l][R]^{-T}. \tag{1}$$

The transformation matrices $[R]^T$ and $[R]^{-T}$ are shown in the Appendix and induce the effect of fiber orientation angle while the diagonal matrix $[\psi_l]$ represents the on-axis damping values

$$[\psi_l] = \begin{bmatrix} \psi_{l1} & 0 & 0 & 0 & 0 & 0 \\ 0 & \psi_{l2} & 0 & 0 & 0 & 0 \\ 0 & 0 & \psi_{l3} & 0 & 0 & 0 \\ 0 & 0 & 0 & \psi_{l4} & 0 & 0 \\ 0 & 0 & 0 & 0 & \psi_{l5} & 0 \\ 0 & 0 & 0 & 0 & 0 & \psi_{l6} \end{bmatrix}. \tag{2}$$

The off-axis ply damping matrix is nondiagonal and has the general form.

$$[\psi_c] = \begin{bmatrix} \psi_{c11} & \psi_{c12} & 0 & 0 & 0 & \psi_{c16} \\ \psi_{c21} & \psi_{c22} & 0 & 0 & 0 & \psi_{c26} \\ 0 & 0 & \psi_{c33} & 0 & 0 & 0 \\ 0 & 0 & 0 & \psi_{c44} & \psi_{c45} & 0 \\ 0 & 0 & 0 & \psi_{c54} & \psi_{c55} & 0 \\ \psi_{c61} & \psi_{c62} & 0 & 0 & 0 & \psi_{c66} \end{bmatrix}. \tag{3}$$

The nondiagonal terms 12 indicate coupling between in-plane extensions, the terms 16 and 26 coupling between the in-plane axial and shear stresses, while the terms 45 indicate the coupling between interlaminar shear stresses. Apparently off-axis loading affects the overall damping capacity of the composite in two ways: (1) by altering the values of the diagonal terms, which is equivalent to altering the dissipative capability of the ply directly associated to normal and shear strains; and (2) by inducing and altering nondiagonal terms.

Hygrothermal Effect. Many mechanical properties of polymers, including damping, are sensitive to hygrothermal variations. In this manner, temperature and moisture may affect the dynamic characteristics of polymer composites. Previous studies (Chamis, 1984) have shown that the hygrothermal effect on most mechanical properties of the matrix can be modeled as

$$\frac{P_M}{P_o} = \left[\frac{T_{gw} - T}{T_{gd} - T_o}\right]^{0.5} \tag{4}$$

where P and T represent matrix properties and temperature; subscript M represents mechanical properties; and subscripts o, gd, gw respectively indicate room, dry glass transition, and wet glass transition conditions. An inverted form of Eq. (4) has been proposed by the authors for the hygrothermal effect on the matrix damping

$$\frac{P_d}{P_p} = \left[\frac{T_{gd} - T_o}{T_{gw} - T}\right]^q. \tag{5}$$

The wet glass transition temperature is

$$T_{gw} = T_{gd}\,(0.005m_l^2 - 0.1m_l + 1) \tag{6}$$

where m_l is the moisture content. The exponent q in Eq. (5) can be correlated to experimental damping data of each in-

Downloaded 03 May 2010 to 171.66.16.20. Redistribution subject to ASME license or copyright; see http://www.asme.org/terms/Terms_Use.cfm

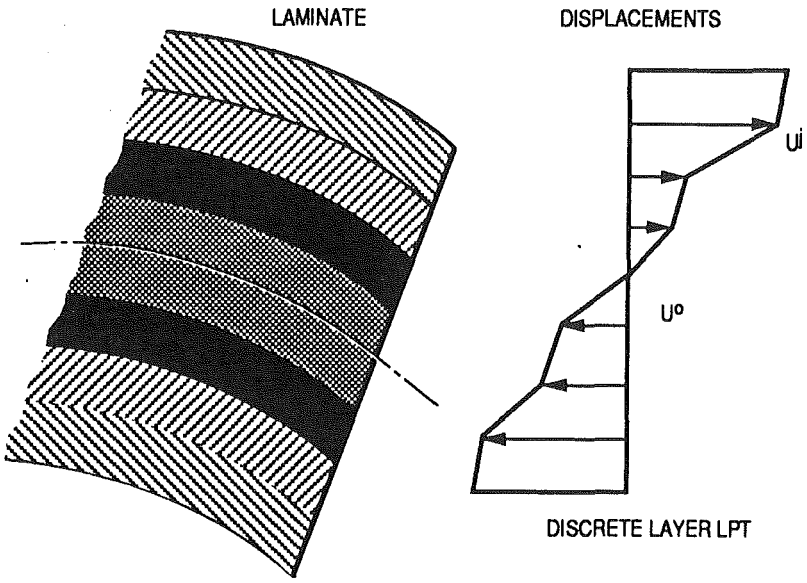


Fig. 2 Kinematic assumptions of discrete layer damping theory

dividual polymer matrix. In the present paper an average value $q=0.5$ is assumed. The effects of temperature and moisture on the composite damping are introduced based on the previously described micromechanics. A similar approach is used for other mechanical properties.

Laminate Damping

A discrete layer damping theory is developed to model the damping of thick laminates, or laminates where the interlaminar shear effects are non-negligible. The present theory assumes a general piecewise continuous in-plane displacement field through the laminate thickness, in addition to the midplane deflections (Fig. 2). The dissipated strain energy in the laminate is defined as

$$\Delta w_L = 1/2 \int_{-h/2}^{h/2} \epsilon_c^T [Q_c][\psi_c]\epsilon_c \, dz \tag{7}$$

and the maximum laminate strain energy as

$$w_L = 1/2 \int_{-h/2}^{h/2} \epsilon_c^T [Q_c]\epsilon_c \, dz \tag{8}$$

where $[Q_c]$ is the off-axis stiffness matrix (see Appendix). The equivalent laminate specific damping capacity then is

$$\psi_L = \Delta w_L / w_L. \tag{9}$$

Discrete layer theories were historically proposed by Grigolyuk and Kogan (1974) and were subsequently generalized (Barbero et al., 1990; also see the review by Noor and Burton, 1990) for the more accurate calculation of stresses in thick laminates. The potential of these theories for accurate damping predictions in thicker laminates, where deviations from the classical laminate damping theory assumptions are expected, is realized herein. Consequently, two types of assumed displacement fields are utilized herein described by the following equations:

$$u(x, y, z, t) = u^o(x, y, t) + \bar{u}(x, y, z, t) \tag{10a}$$

$$v(x, y, z, t) = v^o(x, y, t) + \bar{v}(x, y, z, t) \tag{10b}$$

$$w(x, y, z, t) = w^o(x, y, t) + \gamma \bar{w}(x, y, z, t) \tag{10c}$$

where superscript o represents the uniform through-the-thickness midplane deflection and bar the through-the-thickness variation. γ is a binary constant, such that, if γ equals zero, the through-the-thickness displacement is constant; otherwise, if γ equals to unity, a variable displacement field is assumed. By further assuming a piecewise linear continuous displacement field the previous equations take the form

$$u(x, y, z, t) = u^o(x, y, t) + \sum_{j=1}^{N} u^j(x, y, t) F^j(z) \tag{11a}$$

$$v(x, y, z, t) = v^o(x, y, t) + \sum_{j=1}^{N} v^j(x, y, t) F^j(z) \tag{11b}$$

$$w(x, y, z, t) = w^o(x, y, t) + \gamma \sum_{j=1}^{N} w^j(x, y, t) F^j(z) \tag{11c}$$

where, u^j, v^j, and w^j are displacements along the x, y, and z structural axes, respectively, preferably at the interfaces between various plies, or sublaminates (group of plies). $F^j(z)$ are linear interpolation functions. For γ equal to zero, the piecewise continuous linear displacement field is similar to the one suggested by Barbero et al. (1990). Based on the choice of γ the assumed in-plane displacement field may be as general as possible, in that it may represent either variable in-plane and interlaminar shear strains through-the-laminate thickness ($\gamma=0$) or additionally variable normal strains through-the-thickness and out-of-plane Poisson's effects ($\gamma=1$) in the laminate.

The laminate strains are directly derived from Eqs. (11)

$$\epsilon_{ci} = \epsilon_{ci}^o + \sum_{j=1}^{N} \epsilon_{ci}^j F^j(z) \quad i=1,2,6 \tag{12a}$$

$$\epsilon_{ci} = \epsilon_{ci}^o + \sum_{j=1}^{N} \epsilon_{ci}^j F_{,z}^j(z) + \gamma \sum_{j=1}^{N} \bar{\epsilon}_{ci}^j F^j(z) \quad i=4,5 \tag{12b}$$

$$\epsilon_{c3} = \gamma \sum_{j=1}^{N} \epsilon_{c3}^j F_{,z}^j(z) \tag{12c}$$

where the midplane strains are

$$\epsilon_{c1}^o = u_{,x}^o \; \epsilon_{c2}^o = v_{,y}^o \; \epsilon_{c6}^o = u_{,y}^o + v_{,x}^o \tag{13a}$$

$$\epsilon_{c4}^o = w_{,y}^o \; \epsilon_{c5}^o = w_{,x}^o \tag{13b}$$

and the generalized strains are

$$\epsilon_{c1}^j = u_{,x}^j \; \epsilon_{c2}^j = v_{,y}^j \; \epsilon_{c6}^j = u_{,y}^j + v_{,x}^j \tag{14a}$$

Downloaded 03 May 2010 to 171.66.16.20. Redistribution subject to ASME license or copyright; see http://www.asme.org/terms/Terms_Use.cfm

$$\epsilon^j_{c3}=\gamma w^j\ \epsilon^j_{c4}=v^j\ \epsilon^j_{c5}=u^j \tag{14b}$$

$$\bar{\epsilon}^j_{c4}=\gamma w^j{}_{,y}\ \bar{\epsilon}^j_{c5}=\gamma w^j{}_{,x}. \tag{14c}$$

The comma in the subscripts indicates differentiation.

Combination of Eqs. (7), (12)–(14) ultimately provides the dissipated strain energy per unit area. Depending on the assumption of constant or variable w, the stiffness matrix $[Q_c]$ in Eqs. (7)–(8) may represent plane or three-dimensional stress-strain relations, respectively (see Appendix). Restricting attention in the case of constant w ($\gamma=0$), the dissipated strain energy is

$$\Delta w_L=1/2\left(\epsilon^{oT}_c[A_d]\epsilon^o_c+2\epsilon^{oT}_c\sum_{j=1}^{N}[B^j_d]\epsilon^j_c]+\sum_{j=1}^{N}\sum_{m=1}^{N}\epsilon^{jT}_c[D^{jm}_d]\ \epsilon^m_c\right) \tag{15}$$

where $[A_d]$ is the extensional laminate damping matrix with additional out-of-plane shear terms. The generalized coupling damping matrices $[B^j_d]$ and flexural/shear matrices $[D^{jm}_d]$ are new.

$$[A_d]=\sum_{k=1}^{N_l}\int_{h_{k-1}}^{h_k}[E_c]_k[\psi_c]_k dz \tag{16a}$$

$$(B^j_d)_{in}=\sum_{k=1}^{N_l}\int_{h_{k-1}}^{h_k}([E_c]_k\ [\psi_c]_k)_{in}F^j_{,z}(z)dzi,\ n=1,\ 2,\ 6 \tag{16b}$$

$$(B^j_d)_{in}=\sum_{k=1}^{N_l}\int_{h_{k-1}}^{h_k}([E_c]_k[\psi_c]_k)_{in}\ F^j_{,z}(z)dz\ i,\ n=4,\ 5$$

$$(D^{jm}_d)_{in}=\sum_{k=1}^{N_l}\int_{h_{k-1}}^{h_k}([E_c]_k[\psi_c]_k)_{in}\ F^j(z)F^m(z)dz\ i,\ n=1,\ 2,\ 6$$

$$(D^{jm}_d)_{in}=\sum_{k=1}^{N_l}\int_{h_{k-1}}^{h_k}([E_c]_k[\psi_c]_k)_{in}\ F^j{}_{,z}(z)F^m_{,z}(z)dz\ i,\ n=4,\ 5 \tag{16c}$$

In a similar manner, the maximum strain energy per unit area is

$$w_L=1/2\left(\epsilon^{oT}_c[A]\epsilon^o_c+2\epsilon^{oT}_c\sum_{j=1}^{N}[B^j]\epsilon^j_c+\sum_{j=1}^{N}\sum_{m=1}^{N}\epsilon^{jT}_c[D^{jm}]\epsilon^m_c\right) \tag{17}$$

where $[A]$ is the traditional extension laminate stiffness matrix, however, with additional out-of-plane shear terms. The generalized coupling stiffness matrices $[B^j]$ and flexural/shear matrices $[D^{jm}]$ are (Barbero et al., 1990)

$$[A]=\sum_{k=1}^{N_l}\int_{h_{k-1}}^{h_k}[E_c]_k dz \tag{18a}$$

$$(B^j)_{in}=\sum_{k=1}^{N_l}\int_{h_{k-1}}^{h_k}([E_c]_k)_{in}F^j(z)dz\ i,\ n=1,\ 2,\ 6 \tag{18b}$$

$$(B^j)_{in}=\sum_{k=1}^{N_l}\int_{h_{k-1}}^{h_k}([E_c]_k)_{in}F^j_{,z}(z)dz\ i,\ n=4,\ 5$$

$$(D^{jm})_{in}=\sum_{k=1}^{N_l}\int_{h_{k-1}}^{h_k}([E_c]_k)_{in}F^j(z)F^m\ (z)dz\ i,\ n=1,\ 2,\ 6$$

$$(D^{jm})_{in}=\sum_{k=1}^{N_l}\int_{h_{k-1}}^{h_k}([E_c]_k)_{in}F^j_{,z}(z)F^m_{,z}\ (z)dz\ i,\ n=4,\ 5. \tag{18c}$$

In case of variable $w(\gamma=1)$, Eqs. (15)–(18) will have additional terms. However, because of space limitations and the focus of the paper on the damping theory with constant w, these additional terms are not listed herein.

Structural Damping

The present section describes the procedure followed for analyzing the global damping capacity of composite plates. It is clear from the previous sections, that the damping capacity of the composite plate strongly depends on the deformation of the plate, hence; it is meaningful to consider the modal damping values, that is, the damping of the plate vibrating solely at the respective modal shapes. Since the vibration modes form a complete set representing the elastodynamic structural response of the plate, the modal specific damping capacities provide a complete characterization of the global structural damping.

Thus, the objective of this section is to present the method for synthesizing modal damping. The modal specific damping capacity associated with the mnth-order vibration mode ψ_{mn} of a laminated plate is

$$\psi_{mn}=\frac{\int_A\Delta w_{Lmn}dA}{\int_A w_{Lmn}\ dA} \tag{19}$$

where Δw_{Lmn} and w_{Lmn} are, respectively, the dissipated and maximum laminate modal strain energies of the mnth mode.

Assuming a rectangular α by β symmetric composite plate with negligible coupling ($A_{16}=A_{26}=0$, $B^j_{16}=B^j_{26}=0$, $D^{jm}_{16}=D^{jm}_{26}=0$), the following Navier fundamental solutions form a complete set of mode shapes in the x-y plane:

$$u^o_{mn}(x,\ y,\ t)=U^o_{mn}\cos(ax)\sin(by)\epsilon^{i\omega t} \tag{20a}$$

$$v^o_{mn}(x,\ y,\ t)=V^o_{mn}\sin(ax)\cos(by)\epsilon^{i\omega t} \tag{20b}$$

$$w^o_{mn}(x,\ y,\ t)=W^o_{mn}\sin(ax)\sin(by)\epsilon^{i\omega t} \tag{20c}$$

$$u^j_{mn}(x,\ y,\ t)=U^j_{mn}\cos(ax)\sin(by)\epsilon^{i\omega t} \tag{20d}$$

$$v^j_{mn}(x,\ y,\ t)=V^j_{mn}\sin(ax)\cos(by)e^{i\omega t} \tag{20e}$$

$$w^j_{mn}(x,\ y,\ t)=\gamma W^j_{mn}\sin(ax)\sin(by)e^{i\omega t}. \tag{20f}$$

Where $a=m\pi/\alpha$ and $b=n\pi/\beta$. It is pointed out that Eq. (20f) is used only in the case of variable $w(\gamma=1)$. Combination of Eqs. (13), (14), (20) yields the modal midplane and generalized strains as separable functions of the x, y, coordinates, time, and amplitudes.

$$\{\epsilon^o_{mn}\}=[B^o_{mn}]\{U^o_{mn}\}e^{i\omega t},\ \{\epsilon^j_{mn}\}=[B^j_{mn}]\{U^j_{mn}\}\epsilon^{i\omega t} \tag{21}$$

where the terms in matrices $[B]_{mn}$ are sine/cosine functions of the x, y coordinates and mode order. The displacement amplitudes are $\mathbf{U}^o=\{U^o,\ V^o,\ W^o\}^T$ and $\mathbf{U}^j=\{U^j,\ V^j,\ \gamma W^j\}^T$. The kinetic energy through the thickness h of the plate is

$$K_L=1/2\int_{-h/2}^{h/2}\{\dot{u}\}^T\rho\{\dot{u}\}dz. \tag{22}$$

Considering Eqs. (11), the laminate kinetic energy per unit area takes the form

$$K_L=1/2(\{\dot{u}^o\}^T[A_M]\{\dot{u}^o\}+2\{\dot{u}^o\}^T\sum_{j=1}^{N}[B^j_M]\{\dot{u}^j\}+\sum_{j=1}^{N}\sum_{m=1}^{N}\{\dot{u}^j\}^T[D^{jm}_M]\{\dot{u}^m\}) \tag{23}$$

where the generalized laminate mass matrices are

$$[A_M]=\sum_{k=1}^{N_l}\int_{h_{k-1}}^{h_k}\mathrm{diag}(\rho_k)\ dz \tag{24a}$$

$$[B^j_M]=\sum_{k=1}^{N_l}\int_{h_{k-1}}^{h_k}\mathrm{diag}(\rho_k)F^j(z)\ dz \tag{24b}$$

$$[D^{jm}_M]=\sum_{k=1}^{N_l}\int_{h_{-1}}^{h_k}\mathrm{diag}(\rho_k)F^j(z)F^m(z)dz. \tag{24c}$$

Downloaded 03 May 2010 to 171.66.16.20. Redistribution subject to ASME license or copyright; see http://www.asme.org/terms/Terms_Use.cfm

The term diag(ρ_k) indicates a diagonal matrix, with all diagonal terms equal to the density of the kth ply.

By substituting Eqs. (21) into the strain and kinetic laminate energy, Eqs. (17) and (23), integrating over the plate area, and applying Lagrangian dynamics, it is proved that the undamped modal analysis (free vibration) solution of the plate takes the form

$$-\omega_{mn}^2[M_{mn}]\mathbf{U}_{mn} + [K_{mn}]\mathbf{U}_{mn} = 0 \tag{25}$$

where $\mathbf{U}_{mnb} = \{\mathbf{U}_{mn}^0; \mathbf{U}_{mn}^1, \ldots, \mathbf{U}_{mn}^N\}$. Numerical solution of this eigenvalue problem provides the natural frequencies and the through-the-thickness modes for each order mn of plane modes in the context of Eqs. (20).

The modal damping of each mode is subsequently calculated in accordance with Eq. (19). The integrations over the area of the plate are performed analytically. Only the natural frequencies and the mode shapes through-the-thickness are calculated numerically, hence, the whole procedure is semi-analytical.

An analogous procedure was also developed for the exact analytical solution of modal specific damping capacities in thin rectangular plates based on the classical laminate damping theory assumptions which neglect interlaminar shear. The damping of the plate is calculated from the flexural laminate damping matrix shown in the Appendix. This augments the classical free-vibration solution of undamped composite plates (Whitney, 1987) which provides the natural frequencies and mode shapes. In the remaining paragraphs, predictions with both thick and thin composite damping theories are shown.

Applications and Discussion

The developed methodology is evaluated on various composite plates. In most cases the results are compared with predictions of the classical laminate theory described above in order to validate the new method, illustrate its merits, and quantify the significance of interlaminar shear damping. Additional comparisons with the fully three-dimensional theory ($\gamma = 1$), which are identified herein as discrete layer damping theory-3D, are presented to establish an upper bound of accuracy for the method.

As an initial verification, the prediction midplane displacement w^o at the center of a (0/90/0) rectangular plate ($\beta = 3\alpha$) subject to a sinusoidal distributed load on the top surface are compared towards the exact elasticity solution of Pagano (1970). Such a comparison will reinforce the validity of discrete layer damping theory. The mechanical properties of the composite in this case are: $E_{l11} = 172$ GPa (25 Mpsi), $E_{l22} = 6.9$ GPa (1. Mpsi), $G_{l12} = 3.45$ GPa (0.5 Mpsi), $G_{l23} = 1.38$ GPa (0.2 Mpsi), and $\nu_{l12} = \nu_{l23} = 0.25$. Figure 3 shows the normalized displacements, with respect to classical laminate damping theory predictions, versus the thickness aspect ratio α/h of the plate. The discrete layer damping theory predictions with either constant or variable w, using eight liner segments ($N = 9$), are in excellent agreement with the exact elasticity solution. An asymmetric displacement field w was predicted by discrete layer damping theory-3D at very high thickness with higher displacement at the top of the plate because the load was applied at the top surface. As a result, the discrete layer damping theory-3D seems to slightly underestimate the midplane w^o at very high thicknesses.

In the remaining cases all plates were assumed to be square and have constant thickness of 4.06 mm (0.16 in.), consisting of 16 plies through the thickness, each 0.01 in. thick. The composite material for each ply was assumed 0.50 fiber volume ratio HM-S Graphite/Epoxy for the assumed mechanical properties of the fiber and matrix (see Saravanos and Chamis (1991)). Typical laminate configurations included (1) unidirectional $(0)_{16}$, (2) cross-plies $(0_4/90_4)_s$, and (3) alternating cross-plies $(0/90)_{4s}$. The fibers in the 0-deg are parallel with the x-axis.

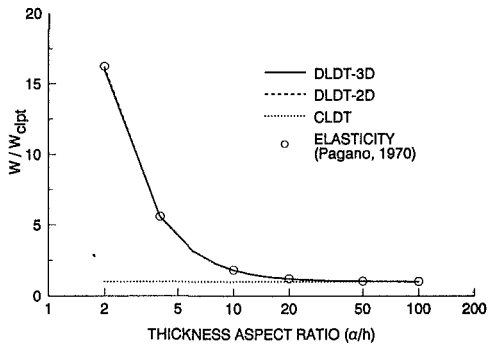


Fig. 3 Predicted midplane displacements at the center of a (0/90/0) rectangular plate ($\alpha = 3\beta$) under sine loading

Sixteen discrete linear displacement segments, one in each ply, were used in the discrete layer damping theory ($N = 17$) to approximate the displacements through the thickness.

Figure 4 shows predictions of the fundamental modal specific damping capacity and natural frequency for the $(0_4/90_4)_s$ and $(0/90)_{4s}$ Gr/Epoxy plates, as functions of thickness aspect ratio α/h. Both plates show very similar trends in their fundamental characteristics. At high aspect ratios both classical laminate damping theory and discrete layer damping theory give comparable predictions, and at the limit (very thin plates, negligible interlaminar shear) the predictions converge to identical values which lends credence to the validity of the discrete layer damping theory. On the other hand, the discrete layer damping theory gives significantly higher predictions of damping for low aspect ratios (thick plates), because the interlaminar shear effects in this regime are important. The damping predictions of classical laminate damping theory are insensitive to thickness because they include only flexural effects. This illustrates the superiority of the developed methodology as well as the significance of interlaminar shear damping. The differences in natural frequency predictions are lower, hence, damping is a more sensitive quantity to interlaminar shear effects. Finally, the difference in the damping predictions between the discrete layer damping theory (constant w) and discrete layer damping theory-3D (variable w) appear rather insignificant within the range of thickness aspect ratios considered. The difference in natural frequency predictions was so small that both lines in Fig. 4 coincide.

The effects of thickness aspect ratio on the damping and frequencies of higher modes (1, 2) (2, 1) and (2, 2) are shown in Figs. 5, 6, and 7, respectively. For both plates, the contributions of interlaminar shear damping are greater in the higher order modes than in the fundamental mode. Interlaminar shear damping appears to be a significant damping source in higher modes at high and intermediate plate thicknesses, because the interlaminar shear damping contributions diminish at higher aspect ratios compared to the fundamental mode. This is clearly seen by comparing the damping curves of modes (1, 1) and (2, 2), which at the limit (negligible shear) converge to the same value of flexural damping, as was expected.

The damping and natural frequency predictions of the discrete layer damping theory (constant w) and discrete layer damping theory-3D (variable w) appear to be in very good agreement also at the higher modes. Hence, it seems that for practical thickness aspect ratios ($\alpha/h \geq 2$) the discrete layer damping theory provides sufficient damping and natural frequency predictions. Some slight underestimation of damping appears at low thicknesses which has been attributed to the inclusion of the through-the-thickness Poisson's effects in the composite stiffness matrix.

The results in Figs. 4 to 7 indicate that classical laminate damping theory predictions may underestimate the modal damping of high-order modes even at high thickness aspect

Downloaded 03 May 2010 to 171.66.16.20. Redistribution subject to ASME license or copyright; see http://www.asme.org/terms/Terms_Use.cfm

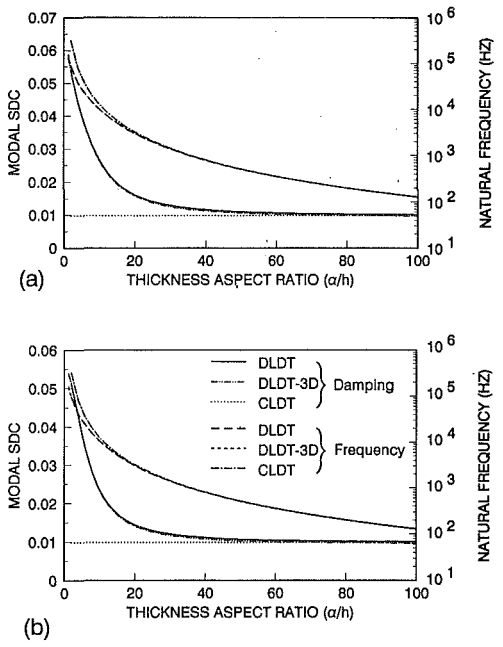


Fig. 4 Effect of thickness aspect ratio on modal characteristics of mode (1, 1). (*a*) $(0_4/90_4)_s$; (*b*) $(0/90)_{4s}$; square HM-S/epoxy plate.

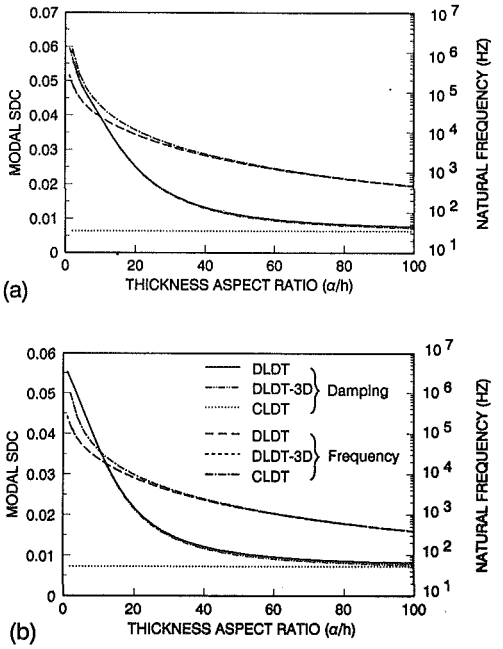


Fig. 6 Effect of thickness aspect ratio on modal characteristics of mode (2, 1). (*a*) $(0_4/90_4)_s$; (*b*) $(0/90)_{4s}$ square HM-S/epoxy plate.

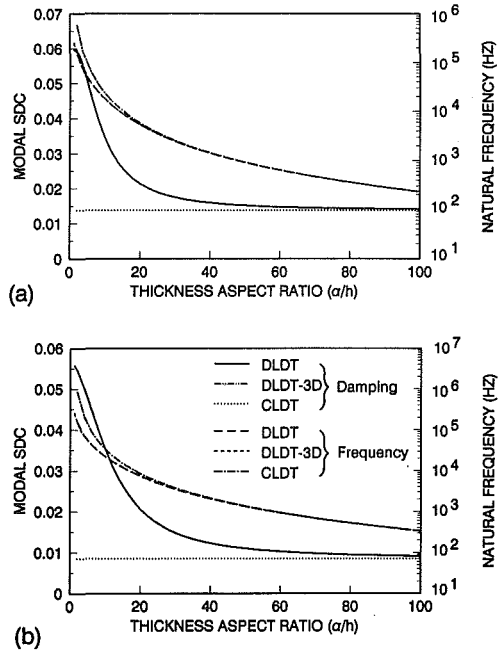


Fig. 5 Effect of thickness aspect ratio on modal characteristics of mode (1, 2). (*a*) $(0_4/90_4)_s$; (*b*) $(0/90)_{4s}$ square HM-S/epoxy plate.

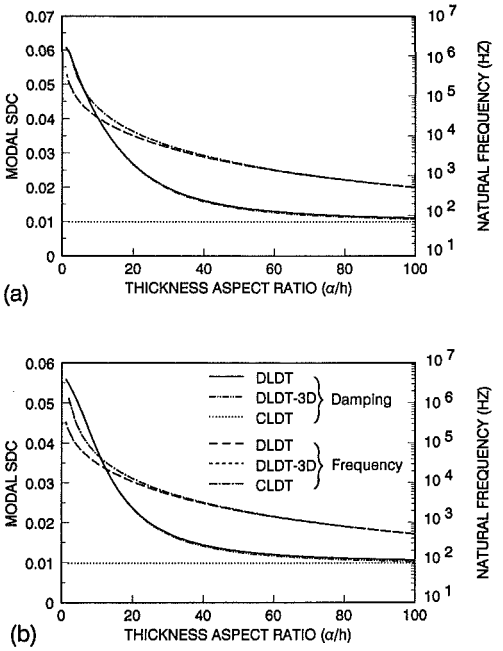


Fig. 7 Effect of thickness aspect ratio on modal characteristics of mode (2, 2). (*a*) $(0_4/90_4)_s$; (*b*) $(0/90)_{4s}$ square HM-S/epoxy plate.

ratios. In order to investigate further the effects of interlaminar shear on the modal damping and natural frequencies of high-order modes, predicted results for the first ten modes of three SS plates based on both the discrete layer damping theory and the classical laminate damping theory are shown in Table 1. The plate dimensions are 406 mm by 406 mm (16 in. by 16 in.); hence, the thickness aspect ratio is rather high ($\alpha/h = 100$). As see, the modal specific damping capacities vary widely with the mode order. In lower modes, the difference between the discrete layer damping theory and the classical laminate damping theory in the prediction of damping of all plates is small, and both theories show good agreement in the prediction of natural frequencies. This validates further the discrete layer damping theory. However, the differences between damping predictions increase in higher order modes. The damping differences are higher in the cross-ply plates than in the unidirectional plate because higher interlaminar shear stresses are developed in the transverse plies in order to balance the normal stresses in the longitudinal plies.

Figure 8 shows the effect of temperature on the fundamental modal damping and natural frequency of $(0_4/90_4)_s$ and $(0/90)_{4s}$, 203 mm by 203 mm (8 in.-by-8 in.) square plates. Predictions of the fundamental specific damping capacity and natural frequency of each plate subjected to uniform through-the-thickness temperature variations are plotted as functions of temperature. Interestingly, the classical laminate damping

Downloaded 03 May 2010 to 171.66.16.20. Redistribution subject to ASME license or copyright; see http://www.asme.org/terms/Terms_Use.cfm

Table 1 Modal characteristics of square simply-supported plates

Mode	(m, n)	Nat. frequency (Hz)		Modal Damping, percent	
		Discrete Layer Damping Theory	Classical Laminate Damping Theory	Discrete Layer Damping Theory	Classical Laminate Damping Theory
(0_{16})	Plate				
1	(1,1)	128.8	129.2	1.035	0.996
2	(1,2)	161.5	161.9	2.561	2.531
3	(1,3)	240.2	240.8	3.861	3.842
4	(1,3)	367.3	368.5	4.399	4.389
5	(2,1)	490.8	496.8	0.761	0.606
6	(2,2)	510.6	516.8	1.148	0.996
7	(1,5)	538.8	541.2	4.582	4.575
8	(2,3)	556.3	562.8	1.827	1.684
9	(2,4)	640.3	647.8	2.654	2.531
10	(2,5)	772.3	780.4	3.390	3.294
$(0_4/90_4)_s$	Plate				
1	(1,1)	128.8	129.2	1.026	0.996
2	(1,2)	231.1	231.9	1.464	1.428
3	(1,3)	449.5	452.8	1.440	1.357
4	(2,1)	461.7	468.2	0.764	0.635
5	(2,2)	510.1	516.8	1.113	0.996
6	(2,3)	652.5	660.5	1.437	1.326
7	(1,4)	767.6	777.5	1.428	1.279
8	(2,4)	914.4	927.7	1.572	1.428
9	(3,1)	1011.0	1043.0	0.845	0.562
10	(3,2)	1041.0	1074.0	1.012	0.736
$(0_4/90_4)_s$	Plate				
1	(1,1)	128.9	129.2	1.019	0.996
2	(1,2)	338.0	340.3	0.931	0.865
3	(2,1)	392.9	396.5	0.823	0.737
4	(2,2)	512.1	516.8	1.076	0.996
5	(1,3)	720.8	730.0	0.904	0.752
6	(2,3)	827.2	839.6	1.103	0.964
7	(3,1)	852.1	869.7	0.837	0.643
8	(3,2)	922.2	940.3	1.025	0.846
9	(3,3)	1140.0	1163.0	1.173	0.996
10	(1,4)	1254.0	1288.0	1.972	0.706

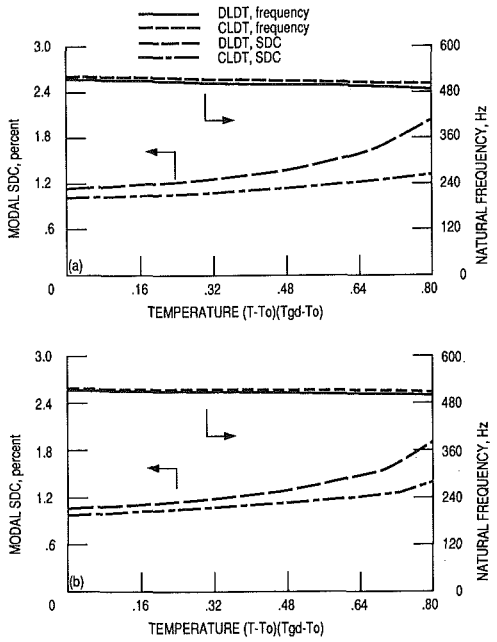


Fig. 8 Effect of temperature on the fundamental modal properties of square HM-S/epoxy plates. (*a*) $(0_4/90_4)_s$; (*b*) $(0/90)_{4s}$.

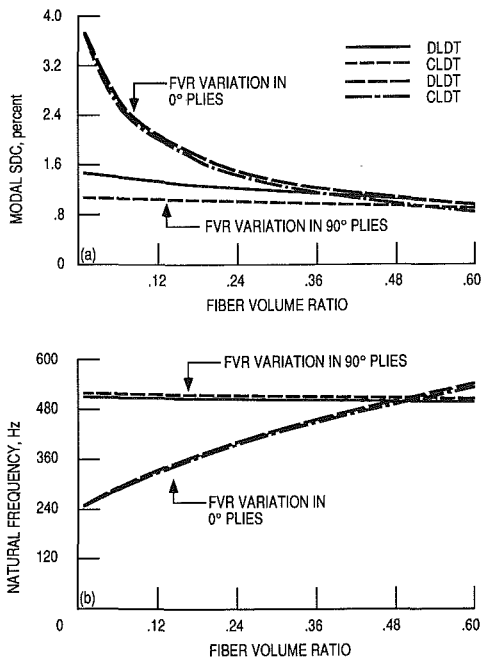


Fig. 9 Effect of fiber volume ratio on the fundamental modal characteristics of a $(0_4/90_4)_s$; HM-S/epoxy plate

theory significantly underestimates the fundamental specific damping capacity at higher temperatures. The underestimation is slightly lower in the second plate. It is recalled that in higher temperatures both the shear modulus of the 90-deg plies decreases and the shear damping increases, respectively. The temperature variation has little effect on the natural frequency.

Finally, the effects of the fiber volume ratio variation, either in the 90-deg plies or the 0-deg plies only, on the fundamental SDC and natural frequency of a 203 mm by 203 mm (8 in. by 8 in)., $(0_4/90_4)_s$ Gr/epoxy plate are shown in Fig. 9. The modal damping is rather insensitive to the fiber volume ratio variation in the 90-deg plies. However, the discrete layer damping theory predicts significantly higher damping at low fiber volume ratio.

Downloaded 03 May 2010 to 171.66.16.20. Redistribution subject to ASME license or copyright; see http://www.asme.org/terms/Terms_Use.cfm

It is recalled that at low fiber volume ratio, the shear modulus G_{l23} is reduced, hence, higher strain energy is stored in the 90-deg plies to balance the bending stress in the 0-deg plies, moreover, the interlaminar shear damping is increased. The variation of the fiber volume ratio in the 0-deg plies has a definite effect on the modal damping and frequency, and both theories provided equivalent results.

The select case studies presented in this section illustrated the capability of the developed damping theory to accurately simulate the damped dynamic response of composite laminates and plates of any thickness. Moreover, they demonstrated the potential of the unified composite mechanics for capturing the effects of a variety of material, structural, and environmental parameters on the dynamic characteristics of composites.

Conclusions

Damping mechanics for thick composite laminates and plates including a discrete-layer damping theory were presented. The damping mechanics included effects from all three stages of material complexity (micromechanical, laminate, and structural), as well as hygrothermal effects and effects of interlaminar shear. Assumed discrete displacement fields enabled the calculation of interlaminar shear strains and the incorporation of interlaminar shear damping. Semi-analytical solutions were developed for the prediction of damped dynamic characteristics of thick composite plates.

Comparisons of the new method with damping mechanics based on classical laminate theory assumptions illustrated that the new damping mechanics predict significantly higher modal damping in the case of higher laminate thickness, modes of higher order, elevated temperatures, and laminates of variable fiber volume ratio through-the-thickness. In this manner, the ranges of applicability of each theory were identified. Additional comparisons with a fully three-dimensional discrete layer damping theory illustrated that the damping mechanics provide sufficient accuracy within the range of practical thickness aspect ratios. In most cases, all theories yielded comparable predictions of natural frequencies, showing that damping is far more sensitive to interlaminar shear than natural frequencies.

Overall, the presented evaluations of the method demonstrated its validity, power, and versatility. The damping mechanics have been incorporated into an in-house research code. Future research will address the dynamic characteristics of thick composite structures with general angle-ply laminations.

Acknowledgment

The authors wants to acknowledge the contributions of Dr. Chirtos C. Chamis, Senior Aerospace Scientist at NASA Lewis Research Center, for his valuable comments and discussions. The work was supported by NASA cooperative agreement NCC3-208/4. This support is gratefully acknowledged.

References

Adams, R. D., Fox, M. A. O., Flood, R. J. L., Friend, R. J., and Hewitt, R. L., 1969, "The Dynamic Properties of Unidirectional Carbon and Glass Fiber-Reinforced Plastics in Torsion and Flexure," *Journal of Composite Materials*, Vol. 3, pp. 594–603.

Adams, R. D., and Bacon, D. G. C., 1973a, "Measurement of the Flexural Damping Capacity and Dynamic Young's Modulus of Metal and Reinforced Plastics," *Journal of Physics, D: Physics*, Vol. 6, pp. 27–41.

Adams, R. D., and Bacon, D. G. C., 1973b, "Effect of Fibre Orientation and Laminate Geometry on the Dynamic Properties of CFRP," *Journal of Composite Materials*, Vol. 7, pp. 402–428.

Alam, N., and Asnani, N. T., 1986, "Vibration and Damping Analysis of Fibre Reinforced Composite Material Plates," *Journal of Composite Materials*, Vol. 20, pp. 2–18.

Barbero, E. J., Reddy, J. N., and Teply, J., 1990, "An Accurate Determination of Stresses in Thick Composite Laminates Using a Generalized Plate Theory," *Int. Journal for Numerical Methods in Engineering*, Vol. 29, pp. 1–14.

Chamis, C. C., 1984, "Simplified Composite Micromechanics Equations for Hygral, Thermal, and Mechanical Properties," *SAMPE Quarterly*, Vol. 15, No. 3, pp. 14–23.

Chang, S., and Bert, C. W., 1973, "Analysis of Damping for Filamentary Composite Materials ," *Composite Materials in Engineering Design, American Society for Metals*, Metals Park, pp. 51–62.

Hashin, Z., 1970, "Complex Moduli of Viscoelastic Composites—II. Fiber Reinforced Composite Materials," *International Journal of Solids and Structures*, Vol. 6, pp. 797–807.

Gibson, R. F., and Plunkett, R., 1976, "Dynamic Mechanical Behavior of Fiber-Reinforced Composites: Measurement and Analysis," *Journal of Composite Materials*, Vol. 10, pp. 325—341.

Grigolyuk, E. I., and Kogan, F. A., 1974, "State-of-the-art of the Theory of Multilayer Shells," *Engl. Translation in Soviet Applied Mechanics*, Vol. 8, No. 6, pp. 583–595.

Lin, D. X., Ni, R. G., and Adams, R. D., 1983, "Prediction and Measurement of the Vibrational Damping Parameters of Carbon and Glass Fibre-Reinforced Plastics Plates," *Journal of Composite Materials*, Vol. 18, pp. 132–152.

Murthy, P. L. N., and Chamis, C. C., 1984, "ICAN: Integrated Composite Analyzer," AIAA Paper 84-0974.

Ni, R. G., and Adams, R. D., 1984, "The Damping and Dynamic Moduli of Symmetric Laminated Composite Beams—Theoretical and Experimental Results," *Journal of Composite Materials*, Vol. 18, pp. 104–121.

Noor, A. K., and Burton, S. W., 1990, "Assessment of Computational Models of Multilayer Composite Shells," ASME *Applied Mechanics Reviews*, Vol. 43, No. 4, pp. 67–96.

Pagano, N. J., 1970, "Exact Solutions for Rectangular Bidirectional Composites and Sandwich Plates," *Journal of Composite Materials*, Vol. 4, pp. 20–34.

Saravanos, D. A., and Chamis, C. C., 1990a, "Unified Micromechanics of Damping for Unidirectional and Off-Axis Fiber Composites," *Journal of Composite Technology and Research*, Vol. 12, No. 1, pp. 31–40.

Saravanos, D. A., and Chamis, C. C., 1990b, "Mechanics of Damping for Fiber Composite Laminates Including Hygro-Thermal Effects," *AIAA Journal*, Vol. 28, No. 10, pp. 1813–1819.

Saravanos, D. A., and Chamis, C. C., 1991, "Computational Simulation of Damping in Composite Structures," *Journal of Reinforced Plastic and Composites*, Vol. 10, pp. 256–278.

Schultz, A. B., and Tsai, S. W., 1968, "Dynamic Moduli and Damping Ratios of Fiber Reinforced Composites," *Journal of Composite Materials*, Vol. 2, No. 3, pp. 368–379.

Schultz, A. B., and Tsai, S. W., 1969, "Measurements of Complex Dynamic Moduli for Laminated Fiber-Reinforced Composites," *Journal of Composite Materials*, Vol. 3, pp. 434–443.

Siu, C. C., and Bert, C. W., 1974, "Sinusoidal Response of Composite-Material Plates with Material Damping," ASME *Journal of Engineering for Industry*, pp. 603–610.

Suarez, S. A., Gibson, R. F., Sun, C. T., and Chaturvedi, S. K., 1986, "The Influence of Fiber Length and Fiber Orientation on Damping and Stiffness of Polymer Composite Materials," *Experimental Mechanics*, Vol. 26, No. 2, pp. 175–184.

Sun, C. T., Chaturvedi, S. K., and Gibson, R. F., 1985, "Internal Damping of Short-Fiber Polymer Matrix Composites," *Computers and Structures*, Vol. 20, No. 1-3, pp. 391–400.

Whitney, J. C., 1987, "Bending of Simply-Supported Rectangular Plates," *Structural Analysis of Laminated Anisotropic Plates*, Technomic Publishing Inc., Lancaster, PA.

APPENDIX

On axis ply stiffness matrix $[Q_1]$ of a transversely isotropic composite:

$$[Q_1] = \begin{bmatrix} Q_{l11} & Q_{l12} & Q_{l13} & 0 & 0 & 0 \\ Q_{l12} & Q_{l22} & Q_{l23} & 0 & 0 & 0 \\ Q_{l13} & Q_{l23} & Q_{l33} & 0 & 0 & 0 \\ 0 & 0 & 0 & Q_{l44} & 0 & 0 \\ 0 & 0 & 0 & 0 & Q_{l55} & 0 \\ 0 & 0 & 0 & 0 & 0 & Q_{l66} \end{bmatrix}. \quad \text{(A1)}$$

DLDT with constant w:

$$\begin{aligned} Q_{l11} &= E_{l11}/\Delta & Q_{l12} &= \nu_{l12}E_{l22}/\Delta \\ Q_{l22} &= E_{l22}/\Delta & Q_{l13} &= Q_{l23} = 0 \\ Q_{l33} &= E_{l33} & Q_{l44} &= G_{l23} \\ Q_{l55} &= G_{l13} & Q_{l166} &= G_{l12} \\ \Delta &= 1 - \nu_{l12}\nu_{l21}. \end{aligned} \quad \text{(A2)}$$

Downloaded 03 May 2010 to 171.66.16.20. Redistribution subject to ASME license or copyright; see http://www.asme.org/terms/Terms_Use.cfm

DLDT with variable w:

$$Q_{l11} = (1-\nu_{l23}^2)E_{l11}/\Delta \qquad Q_{l12} = \nu_{l12}(1+\nu_{l23})E_{l22}/\Delta$$
$$Q_{l13} = \nu_{l13}(1+\nu_{l23})E_{l33}/\Delta \qquad Q_{l22} = (1-\nu_{l13})E_{l22}/\Delta$$
$$Q_{l23} = (\nu_{l23}+\nu_{l12}\nu_{l21})E_{l33}/\Delta \qquad Q_{l33} = (1-\nu_{l12}\nu_{l21})E_{l33}/\Delta$$
$$Q_{l44} = G_{l23} \qquad Q_{l155} = G_{l13}$$
$$Q_{l66} = G_{l12}$$
$$\Delta = (1+\nu_{l23}(1-\nu_{l23}-2\nu_{l12}\nu_{l21}). \tag{A3}$$

Off-axis ply stiffness matrix $[Q_c]$:

$$\{\sigma_c\} = [Q_c]\{e_c\} \tag{A4}$$

$$[Q_c] = [R]^{-1}[Q_l][R]^{-T}. \tag{A5}$$

Transformation matrices:

$$[R] = \begin{bmatrix} m^2 & n^2 & 0 & 0 & 0 & 2mn \\ n^2 & m^2 & 0 & 0 & 0 & -2mn \\ 0 & 0 & 1 & 0 & 0 & 0 \\ 0 & 0 & 0 & n & -n & 0 \\ 0 & 0 & 0 & m & m & 0 \\ -mn & mn & 0 & 0 & 0 & m^2-n^2 \end{bmatrix}, \quad m = \cos\theta,\ n = \sin\theta \tag{A6}$$

$$[R]^{-1} = [R(-\theta)]. \tag{A7}$$

Laminate flexural damping matrix classical laminate damping theory (Saravanos and Chamis, 1990b):

$$[D_{CD}] = \sum_{i=1}^{N_l} \frac{1}{3}(z_t^3 - z_b^3)_i\,[E_c]_i^T[\psi_c]_i. \tag{A8}$$

Downloaded 03 May 2010 to 171.66.16.20. Redistribution subject to ASME license or copyright; see http://www.asme.org/terms/Terms_Use.cfm

Asymptotic Stress Field of a Mode III Crack Growing Along an Elastic/Elastic Power-Law Creeping Bimaterial Interface

C.-Y. Hui

M. T. A. Saif

Department of Theoretical and Applied Mechanics, Cornell University, Ithaca, NY 14853

The asymptotic stress field near the tip of a crack subjected to antiplane shear loading is analysed. The crack is growing quasi-statically along an elastic/elastic power-law creeping bimaterial interface. We find there is a separable solution with the following characteristics: for $n < 3$, *where* n *is the power-law creeping exponent, the asymptotic stress field is dominated by the elastic strain rates and has an inverse square root singularity,* $r^{-1/2}$, *where* r *is the distance from the current crack tip. For* $n \geq 3$, *the near-tip stress and strain fields has a singularity of the form* $r^{-1/(n-1)}$. *The strength of this field is completely specified by the current crack growth rate, besides material properties, and is otherwise independent of the applied load and of the prior crack growth history.*

Introduction

Recent interest in composite materials, such as ceramic-ceramic and metal matrix systems has renewed interest in the studies of the growth of interface cracks along bimaterial systems. The stress field near the tip of a crack between two linear elastic homogeneous materials is well understood (Williams, 1959; Rice and Sih, 1965; England, 1965; Rice, 1988; Shih, 1991). Progress has been made by Shih and Asaro (1988, 1989, 1991), who carried out detail numerical studies to compute the crack-tip fields for a stationary plane-strain crack along the interface between a linearly elastic and a rate-independent plastic material. Analytic study of the crack-tip field has been performed by Wang (1990) and Sharma and Aravas (1991, 1993) for a crack lying along the interface of an elastic and power-law hardening material under plane-strain condition. Champion and Atkinson (1990, 1991) derived asymptotic fields of a crack lying along the interface of two power-law hardening materials. Drugan and Chen (1989) and Chen and Drugan (1991) investigated the stress and deformation fields near the tip of a quasi-statically growing crack through a homogeneous, isotropic, incompressible elastic ideally plastic Prandtl-Reuss-Mises material. Drugan (1991) also studied the fields for a crack quasi-statically growing along the interface of a Prandtl-Reuss-Mises material and a rigid substrate. A recent article by Bose and Castañeda (1992) reports an elegant study of near-tip fields of a quasi-statically growing crack along the interface of two elastoplastic materials characterized by J_2 flow theory of plasticity. The paper also contains a comprehensive literature review on the subject.

Experimental study of the deformation field near a quasi-statically and dynamically growing crack along PMMA/Aluminium interface has been reported by Tippur and Rosakis (1990) who indicate that the experimentally measured stress intensity factors are in good agreement with the numerically evaluated values. Experimental investigations reported by O'Dowd et al. (1992) indicates that the fracture toughness of the interface depends strongly on the load mixity for Aluminium/Niobium interface.

Also, fracture toughness predicted, based on full-field finite element calculations and hoop stress criterion, captures the trend of experimental results.

There is considerably less literature on the problem of the growth of interface cracks along the interface of bimaterial systems of which one of the materials is rate dependent. Such problems may be important for composite material systems like metal matrix composites operating under sufficiently high temperature.

The purpose of this paper is to study analytically the nature of crack-tip fields for a crack lying along the interface of two different materials under antiplane shear (mode III) loading. Mode III loading is chosen for its mathematical simplicity and to provide insight on the crack-tip fields. The crack is growing quasi-statically with velocity $\dot{a}$ along the interface of two homogeneous materials one of which is linearly elastic and the other one is rate dependent. The latter under uniaxial tension deforms as

Contributed by the Applied Mechanics Division of THE AMERICAN SOCIETY OF MECHANICAL ENGINEERS for publication in the ASME JOURNAL OF APPLIED MECHANICS.

Discussion on this paper should be addressed to the Technical Editor, Professor Lewis T. Wheeler, Department of Mechanical Engineering, University of Houston, Houston, TX 77204-4792, and will be accepted until four months after final publication of the paper itself in the ASME JOURNAL OF APPLIED MECHANICS.

Manuscript received by the ASME Applied Mechanics Division, Apr. 15, 1992; final revision, Feb. 19, 1993. Associate Technical Editor: C. F. Shih.

Copyright © 1994 by ASME

Downloaded 03 May 2010 to 171.66.16.20. Redistribution subject to ASME license or copyright; see http://www.asme.org/terms/Terms_Use.cfm

$$\dot{\epsilon} = \frac{\dot{\sigma}}{E} + B\sigma^n. \tag{1}$$

The first term represents the elastic strain rate where E is Young's modulus, and the second term describes power-law secondary creep where B is the creep coefficient and n is the creep exponent. Asymptotic stress field is solved exactly in this case. We show that for $n \geq 3$, the stress and strain singularities are of the form $\sigma, \epsilon \propto r^{-(1/n-1)}$ where r is radial distance from the moving crack tip. This asymptotic field has the remarkable property to be uniquely determined by the current crack growth rate, $\dot{a}$ (besides material properties), independent of the remotely applied load.

Problem Definition

Figure 1 shows the asymptotic view of the crack with a reference frame $(x, y)/(r, \theta)$ moving with the tip with velocity $\dot{a} = da/dt$ along the positive x direction, which coincides with the interface. The z-axis lies along the crack front. Antiplane (mode III) is characterized by the only nonzero out of plane (along z direction) displacement component, w, and the two nonzero stresses and strains $\tau_i = \sigma_{zi}$, and $\gamma_i = 2\epsilon_{zi}$, $i = (x, y)/(r, \theta)$. The magnitude of the resultant shear stress is $\tau_e = (\tau_x^2 + \tau_y^2)^{1/2} = (\tau_\theta^2 + \tau_r^2)^{1/2}$. At any time t, the stresses in (r, θ) coordinates satisfy the equilibrium equation,

$$\frac{\partial \tau_\theta}{r\partial\theta} + \frac{\partial \tau_r}{\partial r} + \frac{\tau_r}{r} = 0, \tag{2}$$

and the strains satisfy the compatibility condition,

$$\frac{\partial \gamma_r}{\partial \theta} - \frac{\partial (r\gamma_\theta)}{\partial r} = 0. \tag{3}$$

The equilibrium equation is identically satisfied by the stress function ψ if

$$\tau_\theta = \frac{\partial \psi}{\partial r}$$

$$\tau_r = -\frac{1}{r}\frac{\partial \psi}{\partial \theta}. \tag{4}$$

The material law for the upper half-plane (UHP), generalized to antiplane shear from Eq. (1), is

$$\dot{\gamma}_i^+ = \frac{\tau_i^+}{G^+} + \overline{B}\tau_e^{+n-1}\tau_i^+ \tag{5}$$

and those for the linear elastic lower half-plane (LHP) are

$$\gamma_i^- = \frac{\tau_i^-}{G^-} \tag{6}$$

where G is the shear modulus, $\overline{B} = (\sqrt{3})^{n+1} B$, and $i = (x, y)/(r, \theta)$. The superscripts $^+$ and $^-$ represent the upper and lower half-planes.

For the time being, consider steady-state crack growth for which

$$\frac{d(\cdot)}{dt} = \frac{d(\cdot)}{dx}\frac{d(x)}{dt} = -\dot{a}\frac{d(\cdot)}{dx} \tag{7}$$

where $(\cdot)$ is a differentiable function of $(x, y)/(r, \theta)$. Using Eqs. (7), (4), and (5) in (3), we get the governing differential equation for ψ^+, which is

$$-\frac{\dot{a}}{G^+}\nabla^2\frac{\partial \psi^+}{\partial x} + \overline{B}\nabla\cdot\{\tau_e^{+n-1}\nabla\psi^+\} = 0 \tag{8}$$

where ∇ is the gradient operator. Similarly, the governing differential equation for ψ^-,

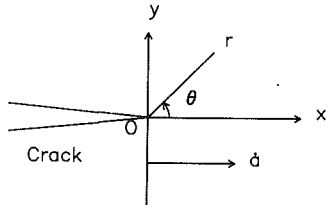


Fig. 1 Crack tip moving with velocity $\dot{a}$ under antiplane shear load (Mode III)

$$\nabla^2\psi^- = 0, \tag{9}$$

is obtained by using Eqs. (7), (4) and (6) in Eq. (3). The boundary conditions for Eqs. (8) and (9) are

(1) traction-free crack surface

$$\frac{\partial \psi^+}{\partial r}(\theta = \pi) = 0$$

$$\frac{\partial \psi^-}{\partial r}(\theta = -\pi) = 0, \tag{10}$$

(2) continuity of traction across the interface

$$\tau_\theta^+(r, \theta = 0) = \tau_\theta^-(r, \theta = 0), \tag{11}$$

(3) continuity of displacement across the interface

$$w(r, \theta = 0^+) = w(r, \theta = 0^-),$$

$$\text{or} \quad \gamma_{r,r}^+(r, \theta = 0) = \gamma_{r,r}^-(r, \theta = 0). \tag{12}$$

Earlier work by Hui and Riedel (1981) shows that the crack-tip stress field of a quasi-statically growing crack under antiplane shear through a *homogeneous* material satisfying Eq. (5) with $n \geq 3$ is given by

$$\tau_i = \left(\frac{\dot{a}}{G^+\overline{B}r}\right)^{\frac{1}{n-1}} f_i(\theta, n) \tag{13}$$

where $f_i(\theta, n)$ is a function of θ and n, and $i = r, \theta$. Note that the stress field given by Eq. (13) satisfies the boundary condition $w = 0$ along $\theta = 0$ and traction-free boundary condition for $\theta = \pi$, which are also the required boundary conditions for the special case where the LHP is rigid. The fact that the elastic strains and creep strains have the same asymptotic behavior as $r \to 0$ when the material is homogeneous, as implied by Eq. (13), leads us to anticipate that if the rigid LHP is replaced by a linearly elastic material, then the nature of the field will be similar to Eq. (13), i.e., separable, and the singularity in the upper and lower half-plane should be the same and equal to $r^{-1/(n-1)}$. We will show that this is indeed the case in the following analysis.

Derivation of ψ^- in the LHP. We will first consider the case of $n \geq 3$. We look for a separable solution, i.e., let

$$\psi^- = r^s\phi^-(\theta) \tag{14}$$

where s is an unknown constant and $\phi^-(\phi)$, a function of θ, is independent of r. Substituting Eq. (14) in Eq. (9), we get

$$\frac{d^2\phi^-(\theta)}{d\theta^2} + s^2\phi^-(\theta) = 0 \tag{15}$$

with the boundary condition that

$$\phi^-(\theta = -\pi) = 0$$

from stress-free crack surface. The general solution of Eq. (15) is

Downloaded 03 May 2010 to 171.66.16.20. Redistribution subject to ASME license or copyright; see http://www.asme.org/terms/Terms_Use.cfm

$$\phi^-(\theta) = A^- \frac{\sin(s(\theta+\pi))}{\cos(s\pi)} \tag{16}$$

and

$$\psi^-(r,\theta) = \frac{A^-}{\cos(s\pi)} r^s \sin\{(s\theta+\pi)\}$$

where A^- is the unknown constant of integration. The stresses are

$$\tau_\theta^-(r,\theta) = \frac{\partial\psi^-}{\partial r} = \frac{A^-}{\cos(s\pi)} sr^{s-1} \sin\{s(\theta+\pi)\} \tag{17}$$

$$\tau_r^-(r,\theta) = -\frac{1}{r}\frac{\partial\psi^-}{\partial\theta} = -\frac{A^-}{\cos(s\pi)} sr^{s-1} \cos\{s(\theta+\pi)\}. \tag{18}$$

Derivation of ψ^+ in the UHP. Motivated by Hui and Riedel (1981) and our anticipation that the stress and strain field will have same order of singularity in both UHP and LHP, we assume

$$\psi^+ = \left(\frac{\dot a}{\bar B G^+}\right)^{1/(n-1)} r^s \phi^+(\theta) \tag{19}$$

where $\phi^+(\theta)$ is independent of r. Using Eq. (4) we get

$$\tau_\theta^+(r,\theta) = \left(\frac{\dot a}{\bar B G^+}\right)^{1/(n-1)} sr^{s-1}\phi^+(\theta) \tag{20}$$

$$\tau_r^+(r,\theta) = -\left(\frac{\dot a}{\bar B G^+}\right)^{1/(n-1)} r^{s-1}\phi^{+\prime}(\theta) \tag{21}$$

and

$$\tau_e^+(r,\theta) = \sqrt{\tau_r^{+2}+\tau_\theta^{+2}} = \left(\frac{\dot a}{\bar B G^+}\right)^{1/(n-1)} r^{s-1}\sqrt{\{\phi^{+\prime}\}^2+\{s\phi^+\}^2} \tag{22}$$

where prime ($'$) denotes derivative with respect to θ.

We now solve for $\phi^+(\theta)$ in the UHP. Substitution of ψ^+ from Eq. (19) in Eq. (8) gives

$$\left(\frac{\dot a}{\bar B G^+}\right)^{1/(n-1)} \frac{\dot a}{G^+} r^{s-3}\{\sin(\theta)\phi^{+\prime\prime\prime} - (s-2)\cos(\theta)\phi^{+\prime\prime} + s^2\sin(\theta)\phi^{+\prime} - (s-2)s^2\cos(\theta)\phi^+\}$$
$$+\bar B\left(\frac{\dot a}{\bar B G^+}\right)^{n/(n-1)} r^{n(s-1)-1}[n(\phi^{+\prime})^2\phi^{+\prime\prime} + (\phi^{+\prime})^2\phi^+\{s^2(2n-1)-s(n-1)\} + s^2\phi^{+\prime\prime}\phi^{+2} + s^2\phi^{+3}\{ns^2-s(n-1)\}] = 0 \tag{23}$$

which is valid for all r only when $s = (n-2)/(n-1)$ (Hui and Riedel, 1981). Equation (23) can be simplified to

$$\sin(\theta)\phi^{+\prime\prime\prime} + (2-s)\cos(\theta)\phi^{+\prime\prime} + s^2\sin(\theta)\phi^{+\prime} - (s-2)s^2\cos(\theta)\phi^+ + (\phi^{+\prime 2}+s^2\phi^{+2})^{(n-3)/2}\{\phi^{+\prime\prime}(s^2\phi^{+2}+n\phi^{+\prime 2}) + s\phi^+\phi^{+\prime 2}(1+2ns-n-s) + s^3\phi^{+3}(1+ns-n)\} = 0 \tag{24}$$

which is the governing differential equation for $\phi^+(\theta)$. Traction-free crack face and displacement and traction continuity across the interface provide the necessary boundary conditions for ϕ^+ as follows.

From the traction-free crack surface boundary condition (Eq. (10)), and using Eq. (20), we have

$$\phi^+(\pi) = 0. \tag{25}$$

Using Eqs. (17) and (20) and continuity of traction across the interface, we obtain

$$A^- = \left(\frac{\dot a}{\bar B G^+}\right)^{1/(n-1)} \frac{\phi_0}{\tan(s\pi)}, \tag{26}$$

where $\phi_0 = \phi^+(\theta = 0)$. Displacement continuity across the interface implies

$$\gamma_{r,r}^+ = \gamma_{r,r}^-, \text{ along } \theta = 0. \tag{27}$$

$\gamma_{r,r}^-(r, \theta = 0)$ can be obtained from Eq. (18),

$$\gamma_{r,r}^-(r,\theta=0) = \frac{\partial}{\partial r}(\tau_r^-/G^-) = -A^-\frac{s(s-1)}{G^-} r^{s-2} \tag{28}$$

whereas $\gamma_{r,r}^+$ can be obtained using Eqs. (5), (7), (20), (21), and (22),

$$\gamma_{r,r}^+(r,\theta=0) = -\frac{1}{G^+}\left(\frac{\dot a}{\bar B G^+}\right)^{1/(n-1)}(s-1)r^{s-2}\phi_0' + \frac{\bar B}{\dot a}\left(\frac{\dot a}{\bar B G^+}\right)^{n/(n-1)} r^{n(s-1)}\phi_0'\{(\phi_0')^2+(s\phi_0)^2\}(n-1)/2 \tag{29}$$

where $\phi_0' = \phi^{+\prime}(\theta = 0)$. Substituting Eqs. (28) and (29) in Eq. (27) and denoting $\beta = G^+/G^-$ we have

$$(s-1)\phi_0' - \phi_0'\{(\phi_0')^2+(s\phi_0)^2\}^{(n-1)/2} = \beta s(s-1)\phi_0\frac{\cos(s\pi)}{\sin(s\pi)}, \tag{30}$$

from which ϕ_0' can be solved numerically for given values of ϕ_0, $\dot a$ and material properties. Note that the left side of Eq. (30) is a monotonically decreasing function of ϕ_0', so that for a given ϕ_0, if a solution for ϕ_0' exists, then it is unique. Also, Eq. (30) includes the boundary condition for the case of a rigid LHP because it gives $\phi_0' = 0$ for $G^- \to \infty$ or $\beta = 0$.

The boundary conditions (25) and (30) are insufficient for solving ϕ^+ because ϕ_0 is not known. However, from the boundedness of stresses at finite distance away from the crack tip, we can find another boundary condition, i.e.,

$$\phi^{+\prime\prime}(\theta=0) = -\frac{ns^2\phi_0 + \{(\phi_0')^2+(s\phi_0)^2\}^{(n-3)/2}\{s\phi_0(\phi_0')^2(n^2-3n+1) - s^3\phi_0^3\}}{n+(n-1)\{s^2\phi_0^2+n(\phi_0')^2\}\{(\phi_0')^2+s^2\phi_0^2\}^{(n-3)/2}}. \tag{31}$$

A discussion of this condition is given by Hui and Riedel (1981) and Delph and Stengle (1989), but for completeness its derivation is given in the Appendix. The boundedness of $\phi^+(\theta = \pi)$ and ϕ^+ $(\theta = \pi)$ has also been shown by Delph and Stengle (1989).

The numerical strategy for solving ϕ^+ can be outlined as follows. For a guessed value of ϕ_0, we solve for ϕ_0' and $\phi^{+\prime\prime}(\theta = 0)$ using Eqs. (30) and (31), respectively. Using ϕ_0 ϕ_0' and $\phi^{+\prime\prime}(\theta = 0)$ as initial conditions, ϕ^+ is solved numerically and $\phi_\pi = \phi^+(\theta = \pi)$ is obtained. ϕ_0 is then varied until the condition $\phi_\pi = 0$ is satisfied.

Summary of Results.

Stresses and Strains in the UHP. With $s = (n-2)/(n-1)$ and ϕ^+ being known according to the scheme outlined above, we have

$$\psi^+ = \left(\frac{\dot a}{\bar B G^+}\right)^{1/(n-1)} r^{(n-2)/(n-1)}\phi^+(\theta) \tag{32}$$

so that stresses are given by

$$\tau_j^+ = \alpha_n\left(\frac{\dot a}{\bar B G^+ r}\right)^{1/(n-1)}\tilde\tau_e$$

and

Downloaded 03 May 2010 to 171.66.16.20. Redistribution subject to ASME license or copyright; see http://www.asme.org/terms/Terms_Use.cfm

$$\tau_e^+ = \alpha_n \left(\frac{\dot{a}}{\bar{B}G^+ r}\right)^{1/(n-1)} \tilde{\tau}_e$$

where $\alpha_n = s\phi_0$, $j = r, \theta$ and

$$\tilde{\tau}_r = \frac{\phi^{+\prime}(\theta)}{s\phi_0}$$

$$\tilde{\tau}_\theta = \frac{\phi^+(\theta)}{\phi_0}$$

$$\tilde{\tau}_e^2 = \tilde{\tau}_\theta^2 + \tilde{\tau}_r^2. \tag{33}$$

The strain-rate field is obtained by inserting the stress field into the material law (Eq. (5)). It has a singularity of the form $\dot{\gamma}_i \propto r^{-n/(n-1)}$. The asymptotic strain field in the UHP is obtained using the steady-state condition. The strain has the same type of singularity as the stress, viz.,

$$\gamma_m = \frac{\alpha_n}{G^+} \left(\frac{\dot{a}}{\bar{B}G^+ r}\right)^{1/(n-1)} \tilde{\gamma}_m(\theta), \tag{34}$$

$m = x, y$. The angular variation of $\gamma_m(r, \theta)$, $\tilde{\gamma}_m(\theta)$, can be written as $\tilde{\gamma}_m = \tilde{\gamma}_m^{el} + \tilde{\gamma}_m^{cr}$, where the elastic part is given by $\tilde{\gamma}_m^{el} = \tilde{\tau}_m$, and the creep part is given by

$$\tilde{\gamma}_m^{+cr} = \frac{\alpha_n^{(n-1)}}{(\sin\theta)^{1/(n-1)}} \int_0^\theta \frac{\tilde{\tau}_e^{n-1}\,\tilde{\tau}_m}{(\sin\theta')^{(n-2)/(n-1)}}\, d\theta' \tag{35}$$

where

$$\tilde{\tau}_x = \tilde{\tau}_r \cos\theta - \tilde{\tau}_\theta \sin\theta$$

$$\tilde{\tau}_y = \tilde{\tau}_r \sin\theta + \tilde{\tau}_\theta \cos\theta,$$

$\tilde{\tau}_r$ and $\tilde{\tau}_\theta$ are given by Eq. (33). The limiting values of $\tilde{\gamma}_x^{+cr}$ and $\tilde{\gamma}_y^{+cr}$ at $\theta = 0$ are $(n-1)\phi_0'(s^2\phi_0^2 + \phi_0'^2)^{(n-1)/2}/\alpha_n$ and $(n-1)(s^2\phi_0^2 + \phi_0'^2)^{(n-1)/2}$, respectively.

Stresses and Strains in the LHP. The stress function in the LHP is obtained by using Eqs. (14), (16), and (26), i.e.,

$$\psi^-(r, \theta) = \left(\frac{\dot{a}}{\bar{B}G^+}\right)^{1/(n-1)} \frac{\phi_0}{\sin(s\pi)}\, r^{(n-2)/(n-1)} \sin\{s(\theta+\pi)\}. \tag{36}$$

The associated stresses and strains are found to be

$$\tau_\theta^-(r, \theta) = \alpha_n \left(\frac{\dot{a}}{\bar{B}G^+ r}\right)^{1/(n-1)} \frac{\sin\{s(\theta+\pi)\}}{\phi_0 \sin(s\pi)}$$

$$\tau_r^-(r, \theta) = -\alpha_n \left(\frac{\dot{a}}{\bar{B}G^+ r}\right)^{1/(n-1)} \frac{\cos\{s(\theta+\pi)\}}{\phi_0 \sin(s\pi)}$$

$$\gamma_j^- = \tau_j^+ / G^-, \quad j = r, \theta.$$

Figure 2(*a–d*) shows the angular functions $\tilde{\tau}_r(\theta)$, $\tilde{\tau}_\theta(\theta)$ and $\tilde{\tau}_e(\theta)$ for $n = 4$, 6 and $\beta = .5$, 1. As expected, for a given value of n, $\tilde{\tau}_r$ at $\theta = 0$ increases monotonically with β, with $\tilde{\tau}_r = 0$ at $\beta = 0$. It is interesting to note that $\tilde{\tau}_\theta(\theta)$ is quite insensitive to n and β. Figure 3 shows that α_n increases with both n and β, which implies that $\tau_\theta^+(r, \theta)$, $\tau_r^+(r, \theta)$ and $\tau_e^+(r, \theta)$ increase with n and β for a given crack speed.

The Case of $1 \le n < 3$

It has been shown by Hui and Riedel (1981) that for $n < 3$, the linear term in Eq. (8) dominates over the nonlinear term as $r \to 0$. The deletion of the nonlinear term from Eq. (8) leads to the elastic stress singularity $\sigma \propto r^{-1/2}$, and the asymptotic solution for both the lower and upper half-planes, $\psi^\pm$, is

$$\psi^\pm = Ar^{1/2} \cos\frac{\theta}{2}, \quad \text{as } r \to 0, \tag{37}$$

where A is an unspecified factor. The solution satisfies the governing differential equation for ψ^+ and ψ^- in the UHP and LHP, the traction-free crack surfaces and continuity of τ_θ across the interface. The factor A in Eq. (37) can be determined by specifying the complete problem including the remote

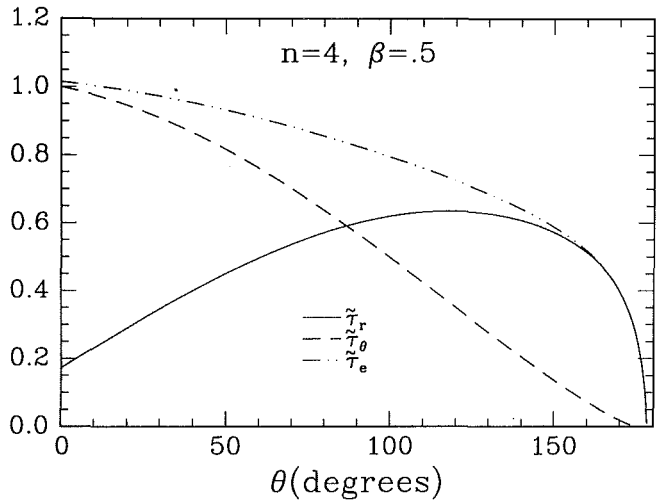


Fig. 2(*a*)

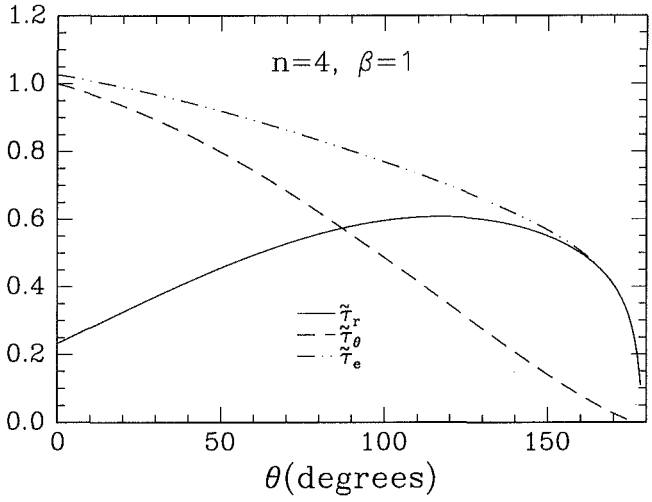


Fig. 2(*b*)

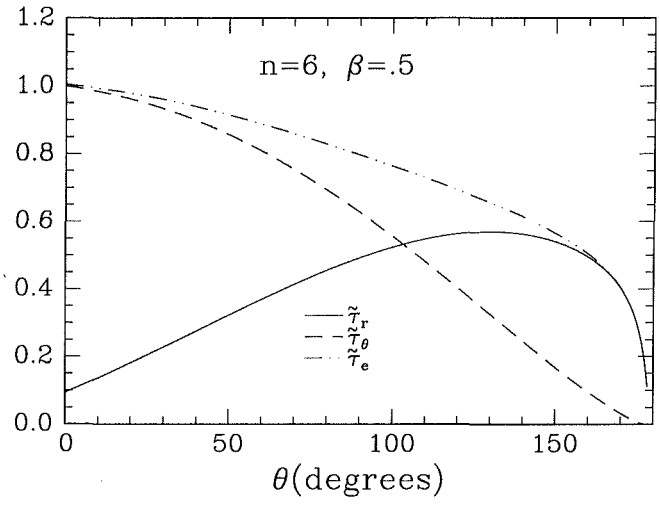


Fig. 2(*c*)

Downloaded 03 May 2010 to 171.66.16.20. Redistribution subject to ASME license or copyright; see http://www.asme.org/terms/Terms_Use.cfm

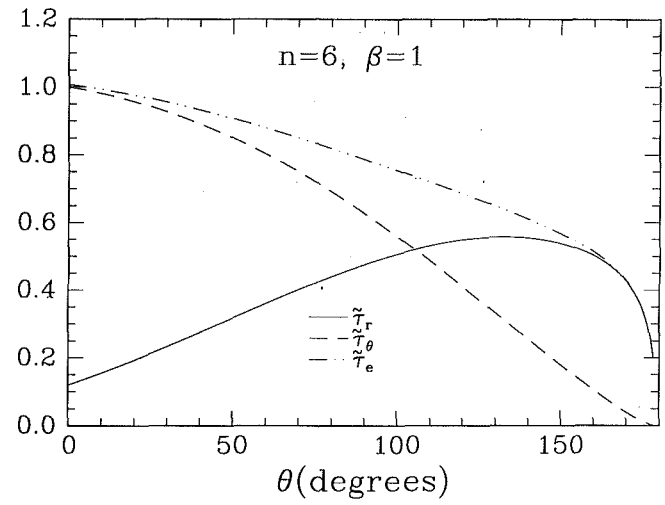


Fig. 2(*d*)

Fig. 2 Angular distribution of the stress components, $\tilde{\tau}_r$ and $\tilde{\tau}_\theta$, and of the equivalent shear stress, $\tilde{\tau}_e$, in the elastic power-law creeping material near the tip of a growing crack in mode III for n = 4, 6 and $\beta = G^+/G^-$ = .5 and 1

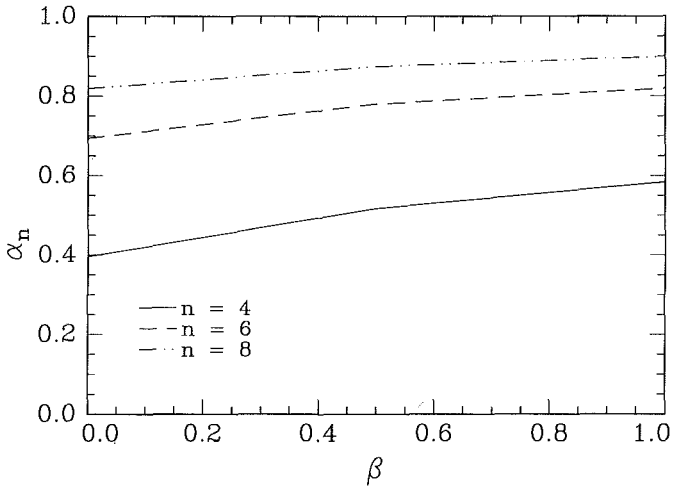


Fig. 3 Variation of $\alpha_n = s\phi_0$ with n and β

boundary conditions. In general, A will be a function of the applied load and the crack growth history.

Nonsteady Crack Growth

The solution for the stress function given in Eqs. (32) and (37) are also asymptotically valid for nonsteady crack growth with a time-dependent growth rate $\dot{a}(t)$. The proof is shown by Hui and Riedel (1981).

Conclusions

The asymptotic stress field near the tip of a quasi-statically growing crack along the interface between a linear elastic and an elastic power-law creeping material subjected to antiplane shear loading has been studied. For $n \geq 3$, the stress and strain field has the form $(\dot{a}/BG^+r)^{1/(n-1)} f_i(\theta, n)$. The amplitude of this asymptotic field is thus independent of remote boundary conditions and crack growth history. For $n < 3$, the stress and strain fields are of the form $Ar^{-1/2}f_i(\theta)$, where the constant A is determined by remote boundary conditions and crack growth history.

Acknowledgments

C.-Y. Hui would like to thank Professor Shih of Brown University for his valuable suggestions. Thanks to the Materials Science Center, Cornell University, for providing computing facilities while conducting this work.

References

Bose, K., and Castañeda, P. Ponte, 1992, "Stable Crack Growth Under Mixed Mode Conditions," *J. Mech. Phys. Solids*, Vol. 40, No. 5, pp. 1053–1103.

Champion, C. R., and Atkinson, C., 1990, "A Mode III Crack at the Interface between Two Nonlinear Materials," *Proc. R. Soc. Lond.*, Vol. A429, pp. 247–257.

Champion, C. R., and Atkinson, C., 1991, "A Crack at the Interface between Two Power-Law Materials Under Plane Strain Loading," *Proc. R. Soc. Lond.*, Vol. A432, p. 547.

Chen, Xing-Yu, and Drugan, W. J., 1991, "Plane Strain Elastic-Ideally Plastic Crack Fields for Mode I Quasi-static Growth at Large Scale Yielding II. Global Analytic Solution for Finite Geometries," *J. of the Mechanics and Physics of Solids*, Vol. 39, No. 7, pp. 895–925.

Delph, T. J., and Stengle, G. A., 1989, "An Analysis of the Hui-Riedel Equation," *International Journal of Fracture*, Vol. 40, pp. 295–305.

Drugan, W. J., and Chen, Xing-Yu, 1989, "Plane Strain Elastic-Ideally Plastic Crack Fields for Mode I Quasi-static Growth at Large Scale Yielding I. A New Family of Asymptotic Solutions," *J. of the Mechanics and Physics of Solids*, Vol. 37, No. 1, pp. 1–26.

Drugan, W. J., 1991, "Near Tip Fields for Quasi-Static Crack Growth Along a Ductile-Brittle Interface," ASME JOURNAL OF APPLIED MECHANICS, Vol. 58, pp. 111–119.

England, A. H., 1965, "A Crack Between Dissimilar Media," ASME JOURNAL OF APPLIED MECHANICS, Vol. 32, pp. 400–402.

Hui, C. Y., and Riedel, H., "The Asymptotic Stress and Strain Field near the Tip of a Growing Crack Under Creep Conditions," *International Journal of Fracture*, Vol. 17, No. 4, Aug. 1981, pp. 409–425.

O'Dowd, N. P., Stout, M. G., and Shih, C. F., 1992, "Fracture Toughness of Alumina/Niobium Interfaces: Experiments and Analyses," *Philosophical Magazine*, Vol. 66, No. 6, pp. 1037–1064.

Rice, J. R., and Sih, G. C., "Plane Problems of Cracks in Dissimilar Media," ASME JOURNAL OF APPLIED MECHANICS, Vol. 32, June 1965, pp. 418–423.

Rice, J. R., 1988, "Elastic Fracture Mechanics Concepts for Interfacial Cracks," ASME JOURNAL OF APPLIED MECHANICS, Vol. 55, pp. 98–103.

Sharma, S. M., and Aravas, N., 1991, "Determination of Higher Order Terms in Asymptotic Elastoplastic Crack Tip Solutions," *J. Mech. Phys. Solids*, Vol. 39, No. 8, pp. 1043–1072.

Sharma, S. M., and Aravas, N., 1993, "On the Development of Variable-Separable Asymptotic Elastoplastic Solutions for Interfacial Cracks," *Int. J. Solids Structures*, Vol. 30, No. 5, pp. 695–732.

Shih, C. F., 1991, "Cracks on Bimaterial Interfaces: Elasticity and Plasticity Aspects," *Materials Science and Engineering*, Vol. A143, pp. 77–90.

Shih, C. F., and Asaro, R. J., 1988, "Elastic-Plastic Analysis of Cracks on Bimaterial Interfaces: Part I—Small Scale Yielding," ASME JOURNAL OF APPLIED MECHANICS, Vol. 55, pp. 299–316.

Shih, C. F., and Asaro, R. J., and O'Dowd, N. P., 1989, "Elastic-Plastic Analysis of Cracks on Bimaterial Interfaces: Part II—Structure of Small Scale Yielding," ASME JOURNAL OF APPLIED MECHANICS, Vol. 56, pp. 763–779.

Shih, C. F., and Asaro, R. J., 1991, "Elastic-Plastic Analysis of Cracks on Bimaterial Interfaces: Part III—Large Scale Yielding," ASME JOURNAL OF APPLIED MECHANICS, June 1991, Vol. 58, pp. 450–463.

Tippur, H. V., and Rosakis, A. J., 1990, "Quasi-Static and Dynamic Crack Growth along Bimaterial Interfaces: A Note on Crack Tip Field Measurements Using Coherent Grading Sensing," SM Report 90-18, Aug., Graduate Aeronautical Laboratories, California Institute of Technology, Pasadena, CA.

Wang, T. C., 1990, "Elastic-Plastic Asymptotic Fields for Cracks on Bimaterial Interfaces," *Engineering Fracture Mechanics*, Vol. 37, No. 3, pp. 527–538.

Williams, M. L., 1959, "The Stresses Around a Fault or Crack in Dissimilar Media," *Bulletin of the Seismological Society of America*, Vol. 49, No. 2, Apr., pp. 199–204.

APPENDIX

Equation (24) suggests that $\phi^+(\theta)$ may have a singularity at $\theta = 0$ due to the vanishing coefficient, $\sin(\theta)$, of $\phi^{+'''}$ and $\phi^{+'}$. However, we do not expect the stresses τ_θ^+ and τ_r^+ to be singular away from the tip at finite values of r. Thus from Eqs. (20) and (21) we conclude that ϕ^+ and $\phi^{+'}$ are bounded at $\theta = 0$. Following Delph and Stengle (1989), we assume that

$$\phi^+ = \phi_0 + \phi_0'\theta + B_2\theta^{1+\alpha_1} + B_3\theta^2 + B_4\theta^{2+\alpha_2} + \cdots$$

Downloaded 03 May 2010 to 171.66.16.20. Redistribution subject to ASME license or copyright; see http://www.asme.org/terms/Terms_Use.cfm

as $\theta \to 0^+$, where B_i, $i = 2, 3, \ldots$ are constants and $0 < \alpha_1, \alpha_2, \ldots < 1$. Then

$$\phi^{+\prime} = \phi_0' + B_2(1+\alpha_1)\theta^{\alpha_1} + 2B_3\theta + B_4(2+\alpha_2)\theta^{1+\alpha_2} + \cdots$$

$$\phi^{\prime\prime +} = B_2(1+\alpha_1)\alpha_1\theta^{\alpha_1-1} + 2B_3 + B_4(2+\alpha_2)(1+\alpha_2)\theta^{\alpha_2} + \cdots$$

$$\phi^{\prime\prime\prime +} = B_2(\alpha_1^2-1)\alpha_1\theta^{\alpha_1-2} + B_4(2+\alpha_2)(1+\alpha_2)\alpha_2\theta^{\alpha_2-1} + \cdots$$

Thus as $\theta \to 0$, $\phi^{+\prime\prime} \sim B_2(1+\alpha_1)\alpha_1\theta^{\alpha_1-1}$ and $(\sin(\theta)\phi^{+\prime\prime\prime}) \sim B_2(\alpha_1^2-1)\alpha_1\theta^{\alpha_1-1}$. Using these asymptotic values in Eq. (24) as $\theta \to 0$ and retaining only the singular terms (order of θ^{α_1-1}), we get

$$\{\alpha_1 - s + 1 + \{(\phi_0^{+\prime})^2 + (s\phi_0)^2\}^{(n-3)/2}\{n(\phi_0')^2 + (s\phi_0)^2\}\}\theta^{\alpha_1-1} = 0$$

and

$$\alpha_1 = s - 1 - \{(\phi_0^{+\prime})^2 + (s\phi_0^{+})^2\}^{(n-3)/2}\{n(\phi_0')^2 + (s\phi_0)^2\}$$

which is less than zero, because $s - 1 = -1/(n-1) < 0$ $(n > 1)$ and the quantities $(\cdot)^2$ are greater than zero. This contradicts our hypothesis of $\alpha_1 > 0$. Thus $\phi^{+\prime\prime}$ must be bounded at $\theta = 0$, i.e., $\phi^{+} = \phi_0 + \phi_0'\theta + B_3\theta^2 + B_4\theta^{2+\alpha_2} + \cdots$, and $(\sin(\theta)\phi^{+\prime\prime}) \sim B_4(2+\alpha_2)(1+\alpha_2)\alpha_2\theta^{\alpha_2}$ + higher order terms of θ, as $\theta \to 0$. Hence $\sin(\theta)\phi^{+\prime\prime} = 0$ at $\theta = 0$ and from Eq. (24),

$$\phi^{+\prime\prime}(\theta = 0) = -\frac{ns^2\phi_0 + \{(\phi_0')^2 + (s\phi_0)^2\}^{(n-3)/2}\{s\phi_0(\phi_0')^2(n^2-3n+1) - s^3\phi_0^3\}}{n + (n-1)\{s^2\phi_0^2 + n(\phi_0')^2\}\{(\phi_0')^2 + s^2\phi_0^2\}^{(n-3)/2}}$$

which gives an additional boundary condition for Eq. (24).

Downloaded 03 May 2010 to 171.66.16.20. Redistribution subject to ASME license or copyright; see http://www.asme.org/terms/Terms_Use.cfm

Two-Dimensional Grained Composites of Extreme Rigidity[1]

S. Vigdergauz
R&D Division,
Israel Electric Corp., Ltd.,
P.O. Box 10,
Haifa 31000, Israel

A thin elastic plate with nonidentical periodical inclusions is considered as an adequate model to optimize mechanical characteristics of a two-phase composite, given the mean stresses and phase volume fraction. Geometrical forms of these inclusions minimizing the total stress energy are obtained explicitly through the analytical solution of a specific boundary value problem so their parametrical equations are expressed in terms of elliptic functions. Such approach is used also to find the effective moduli of the composite. Finally, the similar finite-step procedure is suggested to construct multiphase optimal structure with macroisotropy.

1 Introduction

Let an infinite plate of uniform small thickness contain inclusions of another elastic material, consisting of identical particles of finite size which form a square-mesh network with unit step. The structural periodicity of such a mechanical model of a two-phase composite enables us to focus our analysis on an elementary cell with a single inclusion, given the mean stresses or deformations at its edges, the elastic properties, and the phase volume fraction.

In such a setting we consider a problem of optimizing the configuration of the phase interface, with a view to achieving the absolute possible minimum for the stress energy. Being the strictly positive bilinear form for the cell mean of the stress-strain values under given stresses (or deformations), this minimum corresponds to the minimal deformations (or stresses), hence to the maximum (or minimum) of the overall rigidity of the plate.

The exact value of the minimum energy in the G-closure class of periodic structures of arbitrary geometry (Lurie and Cherkaev, 1984) was determined by Gibianski and Cherkaev (1986) via the Hashin-Shtrikman (1963) approach. The last-named authors as well as others (Avellaneda, 1987, Milton and Kohn, 1988) showed that this minimum is achieved in matrix-type layered composites designed via a multistep asymptotic procedure.

It was established by us that the energy of less complicated grained composites is likewise minimal, when the inclusion boundary is so designed that phase interaction along it is reduced to uniform normal stress. The sought boundary then turns out to be equi-strength, and the stress field within the inclusion is homogeneous. The equi-strength concept was advanced by Cherepanov (1974) and widely used by himself (1974), Banichuk (1983), and the author (1976, 1988, 1989).

It was found that the optimal boundaries really exist when the stress state of the cell is sufficiently closed to all-round compression. Their configuration is then found analytically or numerically.

The effective moduli of the optimal plate are also found in closed form as rational combinations of the given data. Finally, the same approach applies to structural optimization of orthotropic multiphase composites where a central solid inclusion is enclosed by rings of variable thickness, with equi-strength boundary made of assorted materials arranged to a specific sequence—such composites are a macro-generalization of Milton's (1981) well-known asymptotic multicoated-sphere model.

2 Governing Equations

Locate the plate in the infinite plane of a complex variable $z=x+iy$. Let the edges of cells K_{pq}, p, $q=0, \pm 1, \pm 2, \ldots$ be parallel to the axes of the Cartesian coordinate system XOY and the fundamental cell K_{oo} be centered in its origin. Also let the index $j=1, 2$ denote the inclusion and the principal material, respectively. We adopt the following notations: S_j is the part of K occupied by the first or second material, k_j and μ_j are the bulk and shear moduli, c_j is the area of S_j, and, finally, Γ is the smooth boundary of subdomain S_1 (Fig. 1).

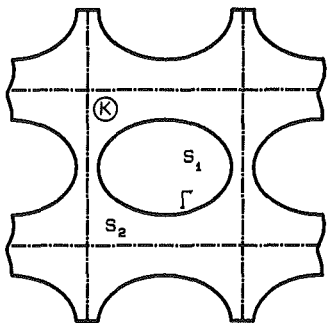


Fig. 1 The schematic picture of two-phase grained composites

[1]The extended summary of this paper was accepted for presentation at the Eighteenth International Congress of Theoretical and Applied Mechanics, (Haifa, Israel, Aug. 22–28, 1992).

Contributed by the Applied Mechanics Division of THE AMERICAN SOCIETY OF MECHANICAL ENGINEERS for publication in the ASME JOURNAL OF APPLIED MECHANICS.

Discussion on this paper should be addressed to the Technical Editor, Professor Lewis T. Wheeler, Department of Mechanical Engineering, University of Houston, Houston, TX 77204-4792, and will be accepted until four months after final publication of the paper itself in the ASME JOURNAL OF APPLIED MECHANICS.

Manuscript received by the ASME Applied Mechanics Division, Aug. 24, 1992; final revision, Mar. 10, 1993. Associate Technical Editor: J. N. Reddy.

Copyright © 1994 by ASME
Downloaded 03 May 2010 to 171.66.16.20. Redistribution subject to ASME license or copyright; see http://www.asme.org/terms/Terms_Use.cfm

As K_{oo} is a unique square, so c_j define the fixed volume fractions of the starting materials in the composite: $c_1 + c_2 = 1$.

Suppose that the fundamental cell is acted upon by the symmetrical tensor $\overline{M}$ of the mean bending moments applied along the edges of K_{oo}, then its stress state is described (Grigolyuk et al., 1982) by the formulae of Kolosov-Muskhelishvili type:

$$M_x(z) + M_y(z) = -4k_j \mathrm{Re}[A\rho(z) + \varphi_j'(z)]$$
$$M_y(z) - M_x(z) + 2iM_{xy}(z) = 2\mu_j[\overline{z}\varphi_j''(z) + \psi_j'(z) + B\rho(z)]$$
$$z \in S_j; \quad j = 1, 2 \tag{1}$$

here $\rho(z)$ is defined as follows: $\rho(z) = 1$, if $z \in S_2$ and $\rho(z) = 0$, if $z \in S_1$.

Two pairs of functions $\varphi_j(z)$, $\psi_j(z)$ holomorphic in the subdomains S_j, respectively, are linked on Γ through the continuous contact conditions (Grigolyuk et al., 1982):

$$[\varphi(t) + t\overline{\varphi'(t)} + \overline{\psi(t)}] = 2At + \overline{Bt}$$
$$[(2k+\mu)\varphi(t) - \mu t\overline{\varphi'(t)} - \mu\overline{\psi(t)}] = 2k_2At - \mu_2\overline{Bt}; \quad t \in \Gamma \tag{2}$$

where the square brackets denote the jump of the bracketed function on Γ: $[f] = f_1 - f_2$; A, B are the certain constants. For clarity, here and henceforth boundary points are denoted by t.

The stress field periodicity results in the specific translation properties of the functions $\varphi_2(z)$, $\psi_2(z)$. In particular, the function $\varphi_2(z)$ is quasi-periodic whereas $\psi_2(z)$ obeys the following relation (Vigdergauz, 1986):

$$\psi_2(z-1) - \psi_2(z) = c_1 b + \lambda_o + i\varphi_2'(z-1)$$
$$\psi_2(z-i) - \psi_2(z) = -c_1 b - \lambda_o + i\varphi_2'(z-i)$$
$$\lambda_o = \pi b/2. \tag{3}$$

The real constant b is defined by (5).

The same considerations lead to relations (Grigolyuk et al., 1982) between tensor $\overline{M}$ and the constants A, B:

$$4k_2A = \frac{\pi\mu_2^2}{k_2+\mu_2}\left(b + \frac{2k_2+\mu_2}{\mu_2}\overline{b}\right) - P - Q$$
$$2\mu_2 B = 2\pi(2k_2+\mu_2)\overline{a} + Q - P + 2iT. \tag{4}$$

Here $P = \overline{M}_x$, $Q = \overline{M}_y$ are the given bending moments, $T = \overline{M}_{xy}$ is the given torque, a, b are the residues at zero point of the functions $\varphi_2(z)$ and $\psi_2(z)$, respectively:

$$a = \frac{1}{2\pi i}\int_\Gamma \varphi_2(t)\,dt, \quad b = \frac{1}{2\pi i}\int_\Gamma \psi_2(t)\,dt. \tag{5}$$

The described periodical structure acts in a smooth external stress field as a homogeneous and, generally speaking, anisotropic elastic medium, which possesses a particular tensor $\overline{C}_o$ of effective bending compliance. Its components are written in the following form (Grigolyuk et al., 1982), on account of relations (4), (5):

$$C_{11} = \gamma[1 - 2\pi\mathrm{Re}(\mu_2 b_x + 2k_2 a_x)], \quad 2\gamma = k_2^{-1} + \mu_2^{-1}$$
$$C_{12} = k_2^{-1} - \gamma[1 + 2\pi\mathrm{Re}(\mu_2 b_y + 2k_2 a_x)]$$
$$C_{21} = k_2^{-1} - \gamma[1 + 2\pi\mathrm{Re}(\mu_2 b_x - 2k_2 a_y)]; \quad C_{21} = C_{12}$$
$$C_{22} = \gamma[1 - 2\pi\mathrm{Re}(\mu_2 b_y - 2k_2 a_x)]$$
$$C_{33} = 4\gamma\left[\frac{2k_2}{k_2+\mu_2} - 2\pi k_2 \mathrm{Im}(a_{xy})\right]. \tag{6}$$

The constants a, b indexed by small letters denote the residues of type (5) for three particular cases of loading, when the corresponding element of tensor $\overline{M}$ equals to one, whereas all the others are zeroed. It is readily verified that $C_{13} = C_{23} = 0$ and $\mathrm{Re}(a_{xy}) = \mathrm{Im}(a_x) = \mathrm{Im}(a_y) = 0$ for any contour Γ symmetric about the X and Y-axes.

Finally, potential energy of cell deformation is written as follows (Grigolyuk et al., 1982):

$$2U = \overline{M}\,\overline{C}_o\,\overline{M} = C_{11}P^2 + 2C_{12}PQ + C_{22}Q^2 + C_{33}T^2. \tag{7}$$

3 Method of Solution

Clearly the averaged functionals (6), (7) depend on the shape of inclusion. For the circular or elliptic configurations they were found by Grigolyuk et al. (1982) numerically using the integral equation equivalent to the boundary conditions (2). It turned out that such an approach involves substantial difficulties. In certain cases, however, the different curves exist, admitting an explicit analytic solution for the problem (2)–(5). Moreover, this solution possesses a certain kind of optimality (see (17)).

To find these curves, let us set

$$P = P_o, \quad Q = Q_o, \quad T = 0 \tag{8}$$

and suppose that the following identities hold along the given contour Γ:

$$M_n(t) = \mathrm{const} = m_o, \quad M_{n\tau}(t) = 0. \tag{9}$$

In other words, we assume the interaction of inclusions and the plate in the specific external field (8) reduces to the normal bending moment, uniformly distributed along Γ. This assumption, permitting us to obtain functions $\varphi_j(z)$ and $\psi_j(z)$ explicitly, will be proved as follows. By virtue of (8), (9) it follows from (2) after some algebra that

$$\psi_1(z) = h_{pq}, \quad \varphi_1(z) = \frac{m_o}{2k_1} + \overline{h}_{pq}\frac{\mu_1-\mu_2}{2k_1+\mu_1+\mu_2}, \quad z \in S_1$$
$$\varphi_2(t) = 0, \quad m_o = A_o\frac{2k_1(k_2+\mu_2)}{(k_1+\mu_2)}$$
$$\psi_2(t) = \frac{m_o}{k_1}\overline{t} - B_o t - 2\overline{A_o t} - 2\lambda\overline{t} + 2h_{pq}\frac{k_1+\mu_1}{2k_1+\mu_1+\mu_2},$$
$$t \in \Gamma. \tag{10}$$

In (10) and henceforth, the index "O" denotes the constants relating to the chosen loading P_o, Q_o.

Here h_{pq} is an arbitrary and, in general, different constant for each cell K_{pq}. It is known (Muskhelishvili, 1975) that these constants are of no importance for the stress field in an elastic body. Thus the set $\{h_{pq}\}$ should be used in order to make the boundary values $\psi_2(z)$ from (10) compatible with (3). Without loss of generality, we may set $h_{oo} = 0$, therefore the boundary condition for the function $\psi_2(z)$ reduces in K_{oo} to the form

$$\psi_2(t) = d_o\overline{t} - B_o t; \quad d_o = 2A_o(k_1+\mu_2)^{-1}(k_2-k_1). \tag{11}$$

It can now be concluded from (10) that $\varphi_2(z) \equiv 0$ everywhere in S_2. Hence, $\psi_2(z)$ becomes a quasi-periodical function in conformity with (3). Furthermore, $\psi_2(z)$ is the only function depending on the configuration Γ (via the relationship between t and $\overline{t}$). We call it the characteristic function of contour Γ and denote $\Omega_o(z)$. The necessary and sufficient condition for its existence in a particular class of curves will be written below, thus ensuring the solvability of the boundary problem (2)–(5) in the form (10), (11).

Substituting (11) into the second relation of (5) and making use of the integral (Muskhelishvili, 1975)

$$\int_\Gamma t\,d\overline{t} = 2ic_1, \tag{12}$$

we obtain

$$b_o = 2c_1A_o\frac{k_2-k_1}{(k_1+\mu_2)}, \tag{13}$$

and certainly $a_o = 0$.

By (4) we have further, on account of (13),

Downloaded 03 May 2010 to 171.66.16.20. Redistribution subject to ASME license or copyright; see http://www.asme.org/terms/Terms_Use.cfm

$$A_o = -\frac{P_o+Q_o}{4\alpha k_2};\quad B_o=\frac{Q_o-P_o}{2\mu_2}$$

$$\alpha = 1 - c_1\frac{\mu_2(k_2-k_1)}{k_2(k_1+\mu_2)} \tag{14}$$

$$m_o = -\frac{k_1(k_2+\mu_2)}{2\alpha k_2(k_1+\mu_2)}(P_o+Q_o). \tag{15}$$

It should be noted that the constants appearing in the relations (11)–(15) do not depend on μ_1—shear modulus of the inclusion. What is more, the uniform bending moment m_o is also independent of dev $\overline{M}=Q_o-P_o$.

Because $\varphi_1(z)$ is linear with respect to z, it follows from (1), that the stress state of inclusions is homogeneous for the given load

$$M_x(z)=M_y(z)=m_o;\quad M_{xy}(z)=0;\quad z\in S_1,$$

and deviation of tensor $M(z)$ is found to be zero.

By identity $\varphi_2(z)\equiv 0$, the tangential moment $M_\tau(t)$ along Γ is determined with allowance for (1), (14), (15):

$$M_\tau(t) = -4k_2A_o - m_o = \frac{P_o+Q_o}{\alpha}\left[1-\frac{k_1(k_2+\mu_2)}{2k_2(k_1+\mu_2)}\right].$$

Uniformity of the moment $M_\gamma(t)$ results from the specific geometrical feature of the closed smooth curve Γ. These curves take the name of equi-strength curves. They were extensively studied in the past (Cherepanov, 1974, Vigdergauz, 1988, see also review by Banichuk, 1983) in the context of the optimization problem for a perforated plate (k_1, $\mu_1=0$). It is evident from the foregoing equations that inclusions bring about no fundamental changes in the solution. Thus, relations (11)–(15) obviously generalize the corresponding results of Vigdergauz (1988), whereas the condition of existence of equi-strength contours, supplementing the proof given by Vigdergauz (1988), can be obtained by analogy from (13):

$$\mu_2|B_o|\le c_2|2k_2A_o-m_o|.$$

By (11), (14), (15) it can be transformed to

$$|Q_o-P_o|\le\left|\frac{\mu_2(k_2-k_1)(P_o+Q_o)}{k_2(k_1+\mu_2)-c_1\mu_2(k_2-k_1)}\right|. \tag{16}$$

This inequality bounding the deviator of given tensor M_o has a clear physical meaning. The discrepancy between the external field with prescribed deviation and the stress state of inclusion whose deviation necessarily vanishes must be sufficiently small to justify the assumption (9).

The smaller difference between elastic moduli of both materials, the more difficult it is to get over this discrepancy. In the limiting case of $k_1=k_2$ (but not necessarily $\mu_1=\mu_2$), the permissible loading interval degenerates into the single point $P_o=Q_o$ complying to all-round compression (see also Vigdergauz, 1989).

The configuration Γ depends parametrically on the quantities appearing in the inequality (16) and hence their permissible values determine the existing class of equi-strong boundaries. Their equations are found analytically (Cherepanov, 1974) via integrals involving elliptic functions or numerically (Vigdergauz, 1986) by solution of an integral equation with Fredholm kernel of a simple type. The given examples show in particular that for $c_1 \ll 1$ the equi-strong contour closely approximates the ellipse with axis ratio $|B_o/2A_o|$.

In view of the linearity of the phases, the following relations are valid:

$$P_oa_x+Q_oa_y=a_o=0,\quad P_ob_x+Q_ob_y=b_o.$$

Combining (6), (7), (13), (14) and performing routine transformations, the cell energy U_o can be found for given moments P_o, Q_o:

$$2U_o-\mu_2^{-1}(P_o-Q_o)^2=[k_2^{-1}-2\pi(k_2^{-1}+\mu_2^{-1})\mu_2b_o](P_o+Q_o)^2$$
$$=\left[k_2^{-1}+c_1\frac{(k_2-k_1)(k_2+\mu_2)}{\alpha k_2^2(k_1+\mu_2)}\right](P_o+Q_o)^2. \tag{17}$$

It is easily shown that the exact lower bound on the cell energy of any two-phase structure (Gibianski and Cherkaev, 1986) coincides with (17), providing $k_1\le k_2$ and the inequality (16) holds. Thus, the smallest possible value of U_o is obtained not only in the matrix-layered materials suggested by Lurie and Cherkaev, but in the grained composites as well. This is true for the tensor $\overline{M}$ of a sufficiently small deviator.

It should be emphasized that the inequality (16) limiting the applicability of expression (17) coincides with those established by Gibianski and Cherkaev (1986) from a quite different consideration. If (16) does not hold, then the absolute energy minimum possesses the different form and thus cannot be attained any more with the equi-strength boundaries. In the opposite case of $k_1\ge k_2$, the optimal problem formulation needs be changed so that the average angles of rotation are given instead of the bending moments. Proceeding by analogy, it can be proved that the piecewise structure with equi-strength inclusions is optimal again attaining the largest possible compliance.

Finally, using the homogeneity of stress field in the subdomain S_1 and recalling (15), we find the deformation energy stored in the inclusion

$$U_1=\frac{m_o^2}{k_1}=k_1\frac{(k_2+\mu_2)(P_o+Q_o)}{4k_2\alpha^2(k_1+\mu_2)^2}.$$

4 The Effective Bulk and Shear Moduli of the Two-Phase Optimal Structures

If the contour Γ is equi-strength for the specific values P_o, Q_o of the bending moments, then the boundary problem (2)–(5) can be also solved explicitly for any given tensor $\overline{M}$ by using the characteristic function $\Omega_o(z)$. To this end let the potentials $\varphi_j(z)$, $\psi_j(z)$ be written in K_{oo} as follows:

$$\varphi_1(z)=R_1z,\quad \psi_1(z)=D_1z,\quad z\in S_1$$
$$\varphi_2(z)=R_2\Omega_o(z)$$
$$\psi_2(z)=D_2\Omega_o(z)-R_2d_o^{-1}[\Omega_o(z)+B_oz]\Omega_o'(z),\quad \in S_2. \tag{18}$$

R_j, D_j, $j=1, 2$ being the four constants sought. The relation for $\psi_2(z)$ is tailored to correspond with the boundary condition (2) and the identity (11). It is readily verified that stress field periodicity in the plate is also provided.

Based on (11), (13), one can find the residues of the functions $\varphi_2(z)$, $\psi_2(z)$ appearing in the relations (4):

$$a=\pi^{-1}c_1d_oR_2,\quad b=\pi^{-1}c_1d_o(D_2+R_2B_o). \tag{19}$$

By virtue of these identities, the boundary condition (2) possesses the form

$$2R_1t+D_1\bar{t}-R_2\Omega_o(t)=\overline{D_2}\,\overline{\Omega_o(t)}-\pi k_2^{-1}bt-\pi\mu_2^{-1}(2k_2+\mu_2)\overline{at}$$
$$=(2\mu_2)^{-1}(Q-P-2iT)\bar{t}-(2k_2)^{-1}(P+Q)t$$
$$2k_1R_1t-\mu_2\overline{Dt}-(2k_2+\mu_2)R_2\Omega_o(t)+\mu_2\overline{D_2\Omega_o(t)}-\pi\mu_2bt$$
$$+(2k_2+\mu_2)\pi\overline{at}=-\frac{P+Q}{2}t-\frac{Q-P-2iT}{2}\bar{t}. \tag{20}$$

The substitution of the expressions (19) and (11) for a, b, $\Omega_o(t)$ in (20), with the coefficients of t and $\bar{t}$ equated, results in a set of linear algebraic equations about the constants R_j, D_j $j=1, 2$:

$$2R_1+R_2B_o-D_2d_o-c_1k_2^{-1}\mu_2d_o(\overline{D}_2+R_2B_o)=-(2k_2)^{-1}(P+Q)$$
$$D_1-d_oR_2-B_o\overline{D}_2-c_1\mu_2^{-1}d_o(2k_2+\mu_2)R_2=(2\mu_2)^{-1}(Q-P-2iT)$$

Downloaded 03 May 2010 to 171.66.16.20. Redistribution subject to ASME license or copyright; see http://www.asme.org/terms/Terms_Use.cfm

$$2k_1R_1+(2k_2+\mu_2)B_oR_2+\mu_2d_o\overline{D}_2$$
$$-c_1\mu_2d_o(\overline{D}_2+B_oR_2)=-\frac{P+Q}{2}$$
$$\mu_1\overline{D}_1+(2k_2+\mu_2)d_oR_2+\mu_2B_o\overline{D}_2-(2k_2+\mu_2)c_1d_oR_2$$
$$=\frac{Q-P-2iT}{2}. \quad (21)$$

The system (21) has a nonzero determinant provided that the inequality (16) holds. It is easy to see that whatever the particular form of its solution may be, the stress field in inclusions is still homogeneous, by virtue of (18), (1), though the deviator of tensor $\overline{M}$ does not vanish anymore.

To find the effective moduli only the constants R_2 and D_2 are required, whose expressions are especially simple when $P_o=Q_o$. In this case the composite is equivalent to a homogeneous and isotropic plate ($C_{11}=C_{22}$). It immediately follows from (21) that

$$R_2=\frac{(\mu_2-\mu_1)(Q-P-iT)}{2d_o[(\mu_1c_1+\mu_2c_2)(2k_2+\mu_1)+\mu_1\mu_2]}$$
$$D_2=\frac{(k_2-k_1)(P+Q)}{2k_2d_o\alpha(k_1+\mu_2)}. \quad (22)$$

Alternately setting each component of the loading to one while setting all the rest to zero, we find by (19) the residues which appear in the coefficients of effective compliance (6). The final results for more practically convenient bulk and shear moduli $k^{-1}=C_{11}+C_{12}$, $\mu^{-1}=C_{11}-C_{12}$, $\mu_*^{-1}=C_{33}$ have the form

$$k^{-1}=k_2^{-1}+\frac{c_1(k_2-k_1)(k_2+\mu_2)}{k_2[k_2k_1+\mu_2(c_1k_1+c_2k_2)]}$$
$$\mu^{-1}=\mu_*^{-1}=\mu_2^{-1}+\frac{2c_1(\mu_2-\mu_1)(k_2+\mu_2)}{\mu_2[c_1\mu_1+c_2\mu_2)(2k_2+\mu_1)+\mu_1\mu_2]}.$$

It should be stressed that the effective bulk modulus k (but not μ!) can also be found through the use of relation (17) for elastic energy of deformation:

$$k=\frac{(P_o+Q_o)^2}{U_o}, \quad P_o=Q_o. \quad (23)$$

Inasmuch as the condition (16) is invariably met for this loading, the value U_o from (17) is the smallest possible and hence the modulus k is also extremal coinciding with the result obtained by Gibiyanski and Cherkaev (1986). To optimize shear moduli μ and μ_* the initial stress state should be set in the form of pure shear (Avellaneda, 1987) conflicting with (16), so their external values are not attained with equi-stress inclusions.

In the limiting case of perforated plates ($k_1=\mu_1=0$) the corresponding formulae for the optimal moduli have previously been reported (Vigdergauz, 1986) as well as numerical examples permitting us to estimate the gain from applying equi-strength contours with those of round shape.

It follows from the foregoing equations that the effective modulus k and μ take the form

$$k^{-1}=k_2^{-1}+f; \quad f=\frac{c_1}{c_2}(k_2^{-1}+\mu_2^{-1})$$
$$\mu^{-1}=\mu_2^{-1}+f; \quad (k_1=\mu_1=0)$$

differing from k_2 and μ_2, respectively, by the same term.

Furthermore, using the defining relations for the Young modulus E and the Poisson ratio ν we obtain

$$E^{-1}=\frac{1}{4}(k^{-1}+\mu^{-1})=\frac{1+c_1}{1-c_1}E_2^{-1}; \quad \nu=\frac{\mu^{-1}-k^{-1}}{\mu^{-1}+k^{-1}}=\frac{1-c_1}{1+c_1}\nu_2.$$

It is easily seen that the effective Young modulus E does not depend on the Poisson ratio ν_2 of the matrix material. In the particular case of circular holes this remarkable fact was originally observed by Day, Snyder, Garboczi, and Thorpe (1991) through numerical simulation. Finally, in their recent paper Cherkaev, Lurie, and Milton (1993) offered rigorous proof that it is generally true for holes of any shape.

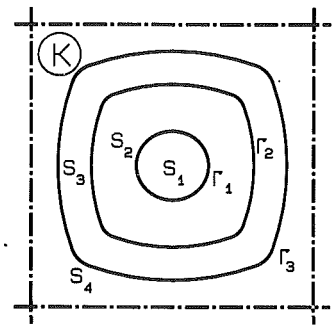


Fig. 2 The schematic picture of multiphase macroisotropic grained structures

5 The Effective Bulk Modulus of Multiphase Macroisotropic Structures

It follows from the second relation (14) that $B_o=0$ in the case of symmetrical structures and hence the boundary value of the characteristic function $\Omega_o(z)$ becomes

$$\Omega_o(t)=d_o\bar{t}, \quad t\in\Gamma.$$

In this case, the solution for the optimization problem depends solely on the geometric parameter c_1, rather than on elastic moduli of materials: $\Omega_o(z)\equiv\Omega_o(z, c_1)$. It is interesting to point out that the central symmetric curve $\Gamma(c_1)$ embraces without contact any other contour which is optimal for lesser c_1 (Cherepanov, 1974, Vigdergauz, 1976). We shall take advantage of this situation to optimize a macroisotropic structure made of m different materials with elastic moduli k_i, μ_i, $i=1, 2, \ldots, m$. For given volume fractions c_i, $c_1+c_2+\ldots+c_m=1$ we now write the ordered numbers $p_i=c_1+c_2+\ldots+c_i$, $p_1\le p_2\le\ldots\le p_m=1$ and bring into use the set of $(m-1)$ enclosed equi-strength contours $\Gamma_i\equiv\Gamma(p_i)$, $i=1, 2, \ldots, m$. Let the first material be placed in subdomain S_1 inside Γ_1, the last one occupies the part of S_m in the exterior of Γ_m and the rest be located in the annular subdomains S_i between the adjacent curves Γ_{i-1} and Γ_i, $i=2, 3, \ldots, m-1$ (Fig. 2).

Again as before, the potentials $\varphi_i(z)$, $\psi_i(z)$ for subdomains S_i are written in the form

$$\varphi_1(z)=A_1z, \quad \psi_1(z)=0, \quad z\in S_1$$
$$\varphi_i(z)=A_i(z)=B_i\Omega_i(z), \quad z\in S_i, \quad i=2, 3, \ldots, m. \quad (24)$$

Here the quasi-periodical function $\Omega_i\equiv d_o^{-1}\Omega_o(z, p_i)$ is defined in the exterior of Γ_i by the boundary condition

$$\Omega_i(t)=\bar{t}, \quad t\in\Gamma_i. \quad (25)$$

The last constant A_m depends immediately upon the given symmetric loading $P_o=Q_o=1$ and can be determined in the following manner:

$$A_m=\pi\frac{\mu_mb_m-2}{2k_m}; \quad b_m=B_m\int_{\Gamma_m}\Omega_m(t)dt=\pi^{-1}p_mB_m. \quad (26)$$

The remaining constants have to be found from $2(m-1)$ contact conditions of the pair of adjoining materials (in accordance with (24) A_m is included in the jump):

$$[\varphi(t)+t\overline{\varphi'(t)}+\overline{\psi(t)}=0, \quad t\in\Gamma_i, \quad i=1, 2, \ldots, m-1$$
$$[(2k+\mu)\varphi(t)-\mu t\overline{\varphi'(t)}-\mu\overline{\psi(t)}]=0. \quad (27)$$

In contrast with the two-phase material, we should now predetermine the value of each function $\Omega_i(z)$ along the outer boundary Γ_{i+1} of its definition area, $i=2, 3, \ldots, m-1$. To

Downloaded 03 May 2010 to 171.66.16.20. Redistribution subject to ASME license or copyright; see http://www.asme.org/terms/Terms_Use.cfm

this end let us consider the real subharmonic function $\omega_i(z) = |\Omega_i'(z)|$. In accordance with (25) it becomes a constant on Γ_i:

$$\omega_i(t) = \left|\frac{d\bar{t}}{dt}\right| = 1, \quad t \in \Gamma_i. \tag{28}$$

We next find another level line γ of the function $\omega_i(z)$ for the prescribed value u_i which satisfies the inequalities $0 < u_i < 1$, following from the maximum principle of subharmonic functions. The function $u_i^{-1}\omega_i(z)$ equals to one identically along γ and thus, by virtue of the fact that parameter c_1 describes exhaustively the inverse problem solution (Cherepanov, 1974), this curve coincides of necessity with equi-strength contour for the value $c_1 > p_i$. In particular, $\gamma = \Gamma_{i+1}$ for $c_1 = p_{i+1}$ and so the following relation is valid:

$$u_i^{-1}\Omega_i'(t) = \Omega_{i+1}'(t), \quad t \in \Gamma_{i+1}.$$

This identity is easily integrated along Γ_{i+1}. Due to the symmetry of Γ_{i+1} about X and Y-axes, integration constants must be equal to zero, hence the functions $u_i^{-1}\Gamma_i(z)$, $\Gamma_{i+1}(z)$ themselves coincide on Γ_{i+1} and consequently they are identical everywhere in its exterior as their common domain of definition.

Our problem here is to find the constant u_i. To this end we note that the difference of the values $\Omega_i(z)$ in the adjacent vertices of the square K_{oo} equals to $\pi c_1 (1-c_1)^{-1}$ (Vigdergauz, 1988). Hence we obtain

$$u_i = p_i(1-p_{i+1})p_{i+1}^{-1}(1-p_i)^{-1}$$
$$\Omega_i(t) = u_i t, \quad t \in \Gamma_{i+1}, \quad i = 1, 2, \ldots, m-1. \tag{29}$$

Substituting (24) into (27) we have, on account of (26), (29),

$$2A_i + u_i B_i - 2A_{i+1} - B_{i+1} = 0 \tag{30}$$

$$2k_i A_i - \mu_i u_i B_i - 2k_{i+1}A_{n+1} + \mu_{i+1}B_{i+1} = 0$$
$$i = 1, 2, \ldots, m-2$$
$$2A_{m-1} + u_{m-1}B_{m-1} - \left(\frac{\mu_m p_m}{k_m} + 1\right)B_m = -2k_m^{-1}$$
$$2k_{m-1}A_{m-1} - \mu_{m-1}u_{m-1}B_{m-1} + (1-p_m)\mu_m B_m = -1.$$

The set of $2(m-1)$ linear algebraic equations about coefficients A_i, B_{i+1}, $i = 1, 2, \ldots, m-1$ is of band type. For determining the bulk modulus k of macroisotropic multiphase composite it suffices to know the coefficient B_m only, as may be inferred from (17), (23), and (26). This coefficient can be obtained from (30) by the bidirectional method.

To complete the suggested structure optimization we should also establish the order of materials in alternation. They can be assorted as was done by Lurie and Cherkaev (1984) in the similar case of permeability optimization for matrix-layered composites, that is the central subdomain S_1 must be invariably occupied by the available phase of the extremal bulk modulus, while the rest are filled successfully by other materials according to relations between their volume fractions and elastic moduli. In doing so, the situation may occur when the same intermediate material occupies several separate rings S_i with given total area.

6 Concluding Remarks

The basic difference between the proposed class of optimal grained structures and their layered counterparts is that the latter fall on the boundary of the G-closure introduced in order to ensure feasibility of a solution to the optimization problem. Infinitely frequent alternation of the phases in them corresponds to a sliding regime of control for the properties of the composites, whereas the grained ones fall strictly within the G-closure and are no-trivial case of smooth control. Extremal physical properties in similar piecewise inhomogeneous materials are far from obvious, since the possibilities of optimization of layered structures—hence also its range of results—are at first glance considered wider. Thus, for example, in grained materials the principal axes of the effective tensor are from the outset parallel to the edges of the network by virtue of the given symmetry of the structures, whereas in layered structures the orientation of the axes serves as a supplementary variable optimization parameter.

Acknowledgment

I wish to express my thanks to R. V. Kohn, A. V. Cherkaev, and L. V. Gibiyansky of the Courant Mathematical Institute, New York, for useful and inspiring discussion.

References

Avellaneda, M., 1987, "Optimal Bounds ad Microgeometries for Elastic Two-Phase Composites," *SIAM J. Appl. Math.*, Vol. 49, pp. 824–837.

Banichuk, N. V., 1983, *Problems and Methods of Optimal Structural Design*, Plenum Press, New York, pp. 1–318.

Cherepanov, G. P., 1974, "Inverse Problem of the Plane Theory of Elasticity," *Journal Appl. Math. Mech.*, Vol. 38, pp. 915–931.

Cherkaev, A. V., Lurie, K. A., and Milton, G. M., 1993, "Invariant Properties of the Stress in Plane Elasticity and Equivalence Classes of Composites," *Proc. Roy. Soc. London A*, in press.

Day, A. R., Snyder, K. A., Garboczi, E. J., and Thorpe, M. F., 1991, "The Elastic Moduli of a Sheet Containing Circular Holes," *J. Mech. Phys. Solids*, Vol. 39, pp. 1031–1051.

Gibiansky, L. V., and Cherkaev, A. V., 1986, "Design of Composite Plates of Extremal Rigidity," preprint No. 914, A. F. Ioffe Physical-Technical Institute, Academy of Science, USSR, Leningrad.

Grigolyuk, E. I., Gringauz, M. G., Dolgikh V. M., and Fil'shtinskii, L. A., 1982, "Bending of Elastic Plates with a Regular Structure," *Mechanics of Solids*, Vol. 17, No. 3, pp. 110–115.

Hashin, Z., and Shtrikman, S., 1963, "A Variational Approach to the Theory of the Elastic Behavior of Multiphase Materials," *J. Mech. Phys. Solids*, Vol. 11, pp. 127–140.

Lurie, K. A., and Cherkaev, A. V., 1984, "G-Closure for Some Particular Set of Admissible Material Characteristics for the Problem of Bending of Thin Elastic Plates," *Journal of Optimization Theory Appl.*, Vol. 42, pp. 305–318.

Milton, G. W., 1981, "Bounds on the Transport and Optical Properties of a Two-Component Composite Material," *J. Appl. Phys.*, Vol. 52, pp. 5294–5304.

Milton, G. W., and Kohn, R. V., 1988, "Variational Bounds on the Effective Moduli of Anisotropic Composites," *J. Mech. Phys. Solids*, Vol. 36, pp. 597–629.

Muskhelishvili, N. I., 1975, *Some Basic Problems of the Mathematical Theory of Elasticity*, Noordhoff Int. Publ., Leiden, The Netherlands, pp. 1–368.

Vigdergauz, S. B., 1976, "Integral Equation of the Inverse Problem of the Plane Theory of Elasticity," *Journal Appl. Math. Mech.*, Vol. 40, pp. 518–521.

Vigdergauz, S. B., 1986, "Effective Elastic Parameters of a Plate With a Regular System of Equal-Strength Holes," *Mech. Solids*, Vol. 21, No. 2, pp. 165–169.

Vigdergauz, S. B., 1988, "The Geometrical Characteristics of Equally Strong Boundaries of Elastic Bodies," *Journal Appl. Math. Mech.*, Vol. 21, pp. 371–376.

Vigdergauz, S. B., 1989, "Piecewise Homogeneous Plates of Extremal Rigidity," *Journal Appl. Math. Mech.*, Vol. 53, pp. 78–82.

Downloaded 03 May 2010 to 171.66.16.20. Redistribution subject to ASME license or copyright; see http://www.asme.org/terms/Terms_Use.cfm

Effect of Constitutive Parameters on Formation of a Spherical Void in a Compressible Nonlinear Elastic Material

Shiro Biwa[1]

Eiji Matsumoto

Toshinobu Shibata

Department of Mechanical Engineering,
Kyoto University,
Kyoto 606-01, Japan

Void formation in materials under isotropic tension is considered within the theory of finite elasticity. This phenomenon is described as the bifurcation of the solution containing a spherical cavity from the state of homogeneous deformation of a solid hyperelastic sphere. The equation giving the bifurcation point is derived, and the critical stretch and stress are numerically calculated for a special class of compressible nonlinear elastic materials for which the strain energy function was proposed by Hill. The effects of constitutive parameters on the post-bifurcation behavior as well as on the critical stretch and stress are discussed.

1 Introduction

The attempt to treat analytically the void formation in materials under isotropic tension within the framework of finite elasticity was first formulated by Ball (1982). In this theory, the spherically symmetric deformations of a solid hyperelastic sphere subjected to uniform radial stretch are considered and as a result, the sphere deforms homogeneously until the stretch reaches a certain critical value, while the solution which contains a spherical cavity bifurcates from the state of homogeneous deformation at the critical stretch. This cavity can be regarded as an idealized model of a void formed in the material due to isotropic tension.

This bifurcation problem has been thoroughly examined for incompressible materials. On the other hand, in the case of compressible materials, even if we assume the spherical symmetry, the deformation must be, in general, determined by solving the equation of equilibrium considering the constitutive relation. This makes the problem formidable. So far, however, some mathematical questions such as the existence and the stability of the solution with a cavity have been examined by Stuart (1985), Sivaloganathan (1986a, b), and Podio-Guidugli et al., (1986). Furthermore, the bifurcation point corresponding to the critical state has been calculated for specific materials. See Horgan and Abeyaratne (1986), Ertan (1988), Haughton (1990), Tian-Hu (1990), and Horgan (1992) for spherically or cylindrically symmetric problems and Hou and Abeyaratne (1992) for a nonsymmetric problem. And comparison with experimental results for rubbery materials has been made by Stringfellow and Abeyaratne (1989).

In order to relate this bifurcation problem with the phenomena of void formation in real materials, it is important to consider the effect of material parameters in the constitutive relation on the existence of the cavitating solution, its properties, and the critical stretch or stress corresponding to the bifurcation point.

In this paper we consider the effect of certain constitutive parameters, which are the constants essentially expressing the resistances to one-directional extension, one-directional contraction, and isotropic volume change, on the post-bifurcation behavior as well as on the critical stretch and stress. A corresponding problem about the effect of a similar parameter for incompressible materials has been examined by Chou-Wang and Horgan (1989). Since mathematical aspects of this bifurcation problem have been extensively discussed in the aforementioned studies, we assume that the cavitating solution exists and seek for the critical value of the stretch and the stress numerically, which will be meaningful from the engineering point of view.

In Section 2, we formulate the boundary value problem to be analyzed, and the homogeneous solution without a cavity is presented in Section 3. In Section 4, the equation giving the bifurcation point is derived by making use of the method developed by Stuart (1985) in his attempt to examine the existence of the cavitating solution. In Section 5, specific materials for which the strain energy function has been proposed by Hill (1978) are introduced and the critical stretch and stress are numerically calculated. The post-bifurcation behavior, which exhibits, due to the void formation, the change in macroscopic stress-stretch relation under isotropic tension, is also calculated. In Section 6, the energy functionals for both ho-

[1]Presently on leave at the Department of Solid Mechanics, Royal Institute of Technology, S-100 44 Stockholm, Sweden.

Contributed by the Applied Mechanics Division of THE AMERICAN SOCIETY OF MECHANICAL ENGINEERS for publication in the ASME JOURNAL OF APPLIED MECHANICS.

Discussion on this paper should be addressed to the Technical Editor, Professor Lewis T. Wheeler, Department of Mechanical Engineering, University of Houston, Houston, TX 77204-4792, and will be accepted until four months after final publication of the paper itself in the ASME JOURNAL OF APPLIED MECHANICS.

Manuscript received by the ASME Applied Mechanics Division, Sept. 14, 1992; final revision, Mar. 8, 1993. Associate Technical Editor: R. Abeyaratne.

Copyright © 1994 by ASME
Downloaded 03 May 2010 to 171.66.16.20. Redistribution subject to ASME license or copyright; see http://www.asme.org/terms/Terms_Use.cfm

mogeneous and cavitating solutions are compared and it is shown that the cavitating solution is energetically favorable for a wide range of constitutive parameters.

2 Formulation

We consider the radial deformations of a solid sphere with radius A, under which a material point with the position vector $\mathbf{X}$ moves to a point with the position vector $\mathbf{x}(\mathbf{X})$ in the deformed configuration. The deformation can be expressed in the form

$$\mathbf{x}(\mathbf{X}) = \frac{r(R)}{R}\,\mathbf{X}, \tag{1}$$

where $R = |\mathbf{X}|$ and $r(R) = |\mathbf{x}(\mathbf{X})|$. We have $r(R) > 0$ for $0 < R \leqq A$. If $r(0) = \lim_{R\to 0} r(R) > 0$, a spherical cavity with radius $r_c = r(0)$ is formed at the center, otherwise the sphere remains solid. The corresponding deformation gradient $\mathbf{F}$ is written in the following way:

$$\mathbf{F} = \frac{dr}{dR}\,\hat{\mathbf{r}}\otimes\hat{\mathbf{r}} + \frac{r}{R}\,(\hat{\theta}\otimes\hat{\theta} + \hat{\phi}\otimes\hat{\phi}), \tag{2}$$

where $\hat{\mathbf{r}} = \mathbf{X}/|\mathbf{X}|$ and the two unit vectors $\hat{\theta}$ and $\hat{\phi}$ are perpendicular to $\hat{\mathbf{r}}$. These three vectors are selected so that they constitute an orthonormal basis. Thus the deformation gradient is diagonal with respect to this basis and the principal stretches λ_i $(i = 1, 2, 3)$ are

$$\lambda_1 = \lambda_r = \frac{dr}{dR},\ \lambda_2 = \lambda_3 = \lambda_\theta = \lambda_\phi = \frac{r}{R}. \tag{3}$$

In the following discussion we use the notation $r' = dr/dR$. Since it is required that

$$J = \frac{r' r^2}{R^2} > 0,\ 0 < R \leqq A, \tag{4}$$

where J is the Jacobian, r' must be positive for $0 < R \leqq A$.

We assume that the sphere is composed of a homogeneous, isotropic, and compressible hyperelastic material. The strain energy function W of isotropic materials is the symmetric function of the principal stretches and written as

$$W = W(\lambda_1, \lambda_2, \lambda_3). \tag{5}$$

Thus the Cauchy stress tensor τ associated with the above radial deformation is given as follows:

$$\tau = \tau_r \hat{\mathbf{r}}\otimes\hat{\mathbf{r}} + \tau_\theta(\hat{\theta}\otimes\hat{\theta} + \hat{\phi}\otimes\hat{\phi}), \tag{6}$$

$$\tau_r(R) = \frac{R^2}{r^2}\,W_1\left(r', \frac{r}{R}, \frac{r}{R}\right),$$

$$\tau_\theta(R) = \frac{R}{r' r}\,W_2\left(r', \frac{r}{R}, \frac{r}{R}\right), \tag{7}$$

where τ_r and τ_θ are the principal stresses and

$$W_i(\lambda_1, \lambda_2, \lambda_3) = \frac{\partial}{\partial\lambda_i}\,W(\lambda_1, \lambda_2, \lambda_3),\ i = 1,2. \tag{8}$$

In the radial deformation, the equation of equilibrium reduces to

$$\frac{d\tau_r}{dR} + 2\,\frac{r'}{r}\,(\tau_r - \tau_\theta) = 0,\ 0 < R < A. \tag{9}$$

Since we suppose that the surface of the sphere is subject to uniform stretch, the boundary condition at the surface is given as

$$r(A) = \lambda A,\ \lambda > 1, \tag{10}$$

where λ denotes the prescribed stretch, i.e., the ratio of deformed to undeformed radius of the sphere. If $r(0) > 0$, a cavity is formed at the center and assumed to be traction-free, so the boundary condition at the center can be expressed in the following way:

$$r(0) = 0 \text{ or } \tau_r(0) = \lim_{R\to 0} \tau_r(R) = 0. \tag{11}$$

In summary, we seek for the deformation $r(R)$ which satisfies $r(R) > 0$ and $r'(R) > 0$ for $0 < R \leqq A$ as well as the equation of equilibrium (9), the constitutive equations (7), and the boundary conditions (10) and (11). Especially, attention will be focussed on the description of the solution with a cavity and the numerical calculation of the bifurcation point and the post-bifurcation behavior for a wide variety of materials.

3 Homogeneous Solution

First, we consider the following homogeneous deformation,

$$r(R) = \lambda R. \tag{12}$$

The corresponding principal stretches and the principal Cauchy stresses are given as

$$\lambda_r = \lambda_\theta = \lambda, \tag{13}$$

$$\tau_r = \tau_\theta = \frac{1}{\lambda^2}\,W_1(\lambda, \lambda, \lambda). \tag{14}$$

Thus the equation of equilibrium (9) and the two boundary conditions (10) and (11) are satisfied. Since $r(0) = 0$ the sphere remains solid.

4 Cavitating Solution

Next we seek for the solution with $r(0) > 0$, which we call cavitating solution. For this purpose it is convenient to transform the variable R to

$$t = \frac{r(R)}{R}, \tag{15}$$

which represents the principal stretch in the direction perpendicular to $\hat{\mathbf{r}}$. This is possible since

$$\frac{dt}{dR} = \frac{1}{R}\left(r' - \frac{r}{R}\right) < 0 \tag{16}$$

for the cavitating configuration (for a detailed proof see Sivaloganathan, 1986b). From the boundary condition (10), we have $t = \lambda$ at the surface $R = A$ and t increases monotonically from λ to infinity as R varies from A to 0. Set

$$s = r'(R) \tag{17}$$

and we can regard s as a function of t and it is written as $s = s(t)$. For $t > \lambda$ we have $0 < s(t) < t$ as stated above. By the above transformation of the variable, the equation of equilibrium (9) reduces to the following first-order nonlinear ordinary differential equation for $s(t)$, i.e.,

$$W_{11}(s(t), t, t)\,\frac{ds(t)}{dt} = -2\left(\frac{W_2(s(t), t, t) - W_1(s(t), t, t)}{t - s(t)} + W_{12}(s(t), t, t)\right), \tag{18}$$

where

$$W_{1i}(\lambda_1, \lambda_2, \lambda_3) = \frac{\partial^2 W}{\partial\lambda_i\partial\lambda_1}\,(\lambda_1, \lambda_2, \lambda_3),\ i = 1,2. \tag{19}$$

Let α denote the value of s at $t = \lambda$. Here α represents the radial principal stretch at the surface of the sphere and α must satisfy $0 < \alpha < \lambda$. We assume that the differential Eq. (18) can be solved for $t \in [\lambda, \infty)$ with $s(\lambda) = \alpha$ as the initial condition. The solution constructed in this way will be denoted by $s(t; \alpha)$ hereafter.

Downloaded 03 May 2010 to 171.66.16.20. Redistribution subject to ASME license or copyright; see http://www.asme.org/terms/Terms_Use.cfm

Similar transformation of variable can be applied to the boundary condition (11). Using (7) and (9), we obtain

$$\frac{d\tau}{dR} = -2\left(\frac{R}{r}\right)^3 f\left(r', \frac{r}{R}\right)\frac{d}{dR}\left(\frac{r}{R}\right), \tag{20}$$

where

$$f\left(r', \frac{r}{R}\right) = \frac{r' W_1\left(r', \frac{r}{R}, \frac{r}{R}\right) - \frac{r}{R} W_2\left(r', \frac{r}{R}, \frac{r}{R}\right)}{r' - \frac{r}{R}}. \tag{21}$$

In this study, we assume that the strain energy function satisfies the Baker-Ericksen inequality, which requires that the greater principal stress should occur always in the direction of the greater principal stretch (Truesdell and Noll, 1965), so that the above function f is positive. If we integrate (20) using (15) and the fact $t = \lambda$ at $R = A$, the boundary condition (11) for the cavitating solution reduces to

$$\frac{1}{\lambda^2} W_1(\alpha, \lambda, \lambda) = 2\int_\lambda^\infty \frac{f(s(t;\alpha), t)}{t^3}\, dt. \tag{22}$$

If there exists α $(0 < \alpha < \lambda)$ which satisfies (22), then the cavitating solution exists and its deformation is determined by (15) and (16), which will be presented afterwards.

It has been known that the cavitating solution bifurcates from the homogeneous one when the prescribed stretch exceeds a certain critical value. Now we can proceed to determine the bifurcation point from the homogeneous solution to the cavitating one. At the bifurcation point, the radial principal stretch α takes the value λ, so we can obtain, in the limit where $\alpha \to \lambda$ in (22), the equation giving the critical stretch λ_{CR}, i.e.,

$$\frac{1}{\lambda_{CR}^2} W_1(\lambda_{CR}, \lambda_{CR}, \lambda_{CR}) = 2\int_{\lambda_{CR}}^\infty \frac{f(s(t;\lambda_{CR}), t)}{t^3}\, dt. \tag{23}$$

In the above expression, $s(t; \lambda_{CR})$ should be determined by the differential Eq. (18) with the condition $s(\lambda_{CR}) = \lambda_{CR}$. The foregoing formula was originally obtained by Stuart (1985) in his attempt to examine mathematically the existence of the cavitating solution. It should be noted that $f(s(t; \lambda_{CR}), t)/t^3$ must be integrable at infinity in order for the critical stretch to exist. We can determine λ_{CR} by solving this equation, though not only the left-hand side of the equation is the function of λ_{CR} but also the right-hand side depends on λ_{CR} through the interval of integration and through the initial condition for the differential Eq. (18). This means that it is highly difficult to solve it analytically. Afterwards the numerical calculation will be carried out to determine λ_{CR}.

Once λ_{CR} is determined, the critical value of the radial Cauchy stress τ_r at the surface, denoted by p_{CR}, is given by (7) as follows:

$$p_{CR} = \frac{1}{\lambda_{CR}^2} W_1(\lambda_{CR}, \lambda_{CR}, \lambda_{CR}) = 2\int_{\lambda_{CR}}^\infty \frac{f(s(t;\lambda_{CR}), t)}{t^3}\, dt. \tag{24}$$

Here we consider the limit in which the material behaves incompressibly. In this limiting case the homogeneous solution is written as $r(R) = R$ by the internal constraint of incompressibility and the critical stretch λ_{CR} is equal to unity, if the cavitating solution exists. Furthermore, $s(t)$ is determined as

$$s(t) = \frac{1}{t^2}, \tag{25}$$

without solving (18). Then the integral in (24) approaches, as $\lambda_{CR} \to 1$, to

$$2\int_1^\infty \frac{f(s(t),t)}{t^3}\, dt = 2\int_1^\infty \frac{1}{t^3}\frac{tW_2(t^{-2}, t, t) - t^{-2}W_1(t^{-2}, t, t)}{t - t^{-2}}\, dt = \int_1^\infty \frac{\frac{d}{dt} W(t^{-2}, t, t)}{t^3 - 1}\, dt. \tag{26}$$

Consequently, substitution of (26) into (24) leads to

$$p_{CR} = \int_1^\infty \frac{\frac{d}{dt}\hat{W}(t)}{t^3 - 1}\, dt, \tag{27}$$

where

$$\hat{W}(t) = W(t^{-2}, t, t). \tag{28}$$

This expression was first given by Ball (1982) for incompressible materials.

In the incompressible case the existence of the cavitating solution requires the boundedness of the integral in (27), imposing a certain restriction on the given strain energy function (Chou-Wang and Horgan, 1989). In the compressible case, however, the situation is not so simple. Without going too much into mathematical detail, we could state that the strain energy function must have the following properties, i.e., (i) the radial equilibrium Eq. (18) is solvable for $t \in [\lambda, \infty)$, $\lambda > 1$; (ii) the integral in (22) is finite; and (iii) for given $\lambda > \lambda_{CR}$ there exists α, $0 < \alpha < \lambda$, satisfying (22) as well as λ_{CR} satisfying (23).

We make a qualitative consideration on (ii) for a special class of materials in the next section, but (i) and (iii) will not be pursued here but assumed to be satisfied when numerical calculations are carried out.

5 Results for a Special Class of Nonlinear Elastic Materials

5.1 Hill's Strain Energy Function. Hill (1978) proposed the following strain energy function for compressible hyperelastic materials:

$$W = \sum_i \frac{c_i}{m_i}\left\{\lambda_1^{m_i} + \lambda_2^{m_i} + \lambda_3^{m_i} - 3 + \frac{1}{n}\left(J^{-m_i n} - 1\right)\right\}, \tag{29}$$

where c_i, m_i, and n are material constants. By taking appropriate pairs of these constants, that is, (c_i, m_i), the behavior of materials is well expressed. The method of determining these constants and the properties of this function have been discussed by Storåkers (1986).

However, we consider for simplicity the next form:

$$W = \sum_{i=1}^{2} \frac{c_i}{m_i}\left\{\lambda_1^{m_i} + \lambda_2^{m_i} + \lambda_3^{m_i} - 3 + \frac{1}{n}\left(J^{-m_i n} - 1\right)\right\}, \tag{30}$$

where m_1 and c_1 are assumed to be positive and m_2 and c_2 negative. Also we assume $3n + 1 > 0$. On these assumptions the classical inequality, which requires that the shear modulus and the bulk modulus for the infinitesimal deformation should be positive (Truesdell and Noll, 1965), and the Baker-Ericksen inequality previously mentioned are satisfied automatically. The elastic constants for the infinitesimal deformations are as follows:

$$E_0 = \frac{3n+1}{2n+1}\sum_{i=1}^{2} m_i c_i,\ \nu_0 = \frac{n}{2n+1},$$

$$\mu_0 = \frac{1}{2}\sum_{i=1}^{2} m_i c_i,\ K_0 = \left(n + \frac{1}{3}\right)\sum_{i=1}^{2} m_i c_i, \tag{31}$$

where E_0, ν_0, μ_0, and K_0 are Young's modulus, Poisson's ratio, shear modulus, and bulk modulus, respectively.

Downloaded 03 May 2010 to 171.66.16.20. Redistribution subject to ASME license or copyright; see http://www.asme.org/terms/Terms_Use.cfm

In the above strain energy function, m_1, $-m_2$ and n represent mainly the stiffnesses for one-directional extension, one-directional contraction, and isotropic volume change, respectively. Note that m_1 also contributes to the stiffness for volume contraction and m_2 to the one for volume expansion, since they appear as exponents of J in (30). Moreover, if n increases to infinity, it is equivalent to impose the constraint of incompressibility, $J = 1$, and we obtain the strain energy function for incompressible materials, i.e.,

$$W=\sum_{i=1}^{2}\frac{c_i}{m_i}\left(\lambda_1^{m_i}+\lambda_2^{m_i}+\lambda_3^{m_i}-3\right). \tag{32}$$

5.2 Bifurcation Point. Before calculating the bifurcation point numerically, a consideration will be made to narrow the range of parameters to be considered. Using the strain energy function (30), the Eq. (23) giving the critical stretch reduces to

$$\sum_{i=1}^{2}\frac{c_i}{\lambda_{CR}^{3-m_i}}\left(1-\lambda_{CR}^{-m_i(3n+1)}\right) = 2\sum_{i=1}^{2}c_i\int_{\lambda_{CR}}^{\infty}\frac{t^{m_i}-\{s(t;\lambda_{CR})\}^{m_i}}{t^3\{t-s(t;\lambda_{CR})\}}\,dt. \tag{33}$$

For this equation to be solved it is necessary that the integral in the right-hand side is bounded. The integrand is a continuous function of t, so it is enough to consider its behavior as $t \to \lambda_{CR}$ and as $t \to \infty$, respectively. First, since $s(t; \lambda_{CR}) \to \lambda_{CR}$ as $t \to \lambda_{CR}$, by l'Hôspital's rule, the integrand converges to the next value:

$$\lim_{t\to\lambda_{CR}}\frac{t^{m_i}-\{s(t;\lambda_{CR})\}^{m_i}}{t^3\{t-s(t;\lambda_{CR})\}} = \lim_{\frac{s}{t}\to 1} t^{m_i-4}\,\frac{\{s(t;\lambda_{CR})/t\}^{m_i}-1}{s(t;\lambda_{CR})/t-1} = m_i\lambda_{CR}^{m_i-4}. \tag{34}$$

Moreover, as $t \to \infty$, if the order of the integrand satisfies

$$\frac{1}{t^3}\,\frac{t^{m_i}-\{s(t;\lambda_{CR})\}^{m_i}}{t-s(t;\lambda_{CR})} = O\left(\frac{1}{t^{\beta}}\right),\ \beta>1, \tag{35}$$

the integral will be convergent. This is equivalent to

$$m_1<3 \text{ and } \frac{\{s(t;\lambda_{CR})\}^{m_2}}{t^4} = O\left(\frac{1}{t^{\beta}}\right),\ \beta>1, \tag{36}$$

since we assumed m_1 to be positive and m_2 negative (see the Appendix for the proof). Note that the derived condition (36) is sufficient for the boundedness of the integral in (33) but not for the existence of the cavitating solution. It indicates that the material has to be soft enough for one-directional extension and contraction in order to form a void.

If the integral is finite, then the matter is whether there exists a value of λ_{CR} satisfying (33) or not, which will be examined numerically. The critical stretch is calculated for some combinations of constitutive parameters by solving (33) numerically, which can be easily done by the iterative method. For this purpose we use new parameters c, γ_1, and γ_2 which are related with c_1 and c_2 in the following way:

$$c=c_1+|c_2|>0,\ \gamma_1=c_1/c>0,\ \gamma_2=c_2/c<0. \tag{37}$$

Once the critical stretch is determined by (33), the critical value of the radial Cauchy stress is given by

$$\frac{p_{CR}}{c}=\sum_{i=1}^{2}\frac{\gamma_i}{\lambda_{CR}^{3-m_i}}\left(1-\lambda_{CR}^{-m_i(3n+1)}\right). \tag{38}$$

Numerical results are shown in Fig. 1 and Fig. 2. As far as demonstrated in the figures, the critical stretch exists and depends monotonically on m_1, that is, the large value of m_1 gives the large critical stretch. This indicates that the material with the small stiffness for one-directional extension forms a void at the small value of stretch. On the other hand, the critical stretch seems to have a minimum with respect to m_2 and increases as $|m_2|$ decreases to 0. Furthermore, large n, which means the large resistance against volume change, gives the small critical stretch. The critical stress also depends monotonically on m_1, m_2, and n, that is, the material with the large stiffnesses against one-directional extension, one-directional contraction, and volume change forms a void at the large value of isotropic stress (Fig. 2). Observe that as $m_2 \to 0$, the critical stretch increases but the critical stress decreases. This behavior can be interpreted in the sense that the isotropic expansion prior to the void formation becomes larger for the smaller value of $|m_2|$, because the sphere gets softer for volume expansion.

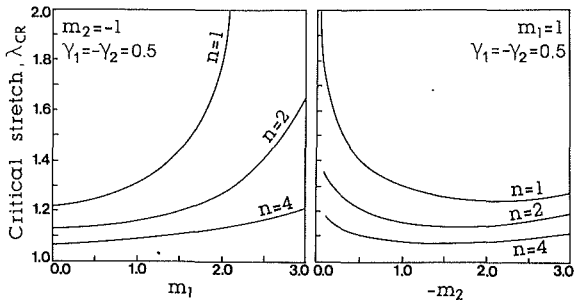


Fig. 1 Variation of the critical stretch with m_1 and m_2 for different values of n. $\gamma_1 = -\gamma_2 = 0.5$ (left; $m_2 = -1$, right; $m_1 = 1$).

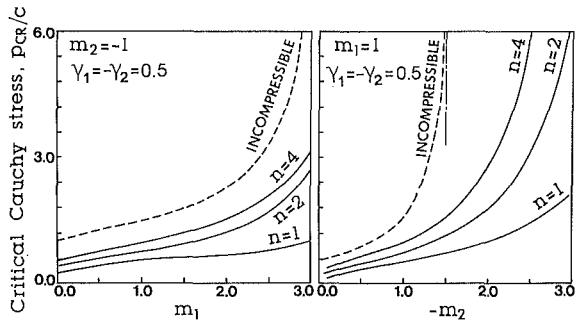


Fig. 2 Variation of the critical stress with m_1 and m_2 for different values of n. $\gamma_1 = -\gamma_2 = 0.5$ (left; $m_2 = -1$, right; $m_1 = 1$).

Also in the figure is shown the critical stress in the case $n \to \infty$, in which the material becomes incompressible, numerically calculated by the formula (27). The integral in (27) is finite if $0 < m_1 < 3$ and $-3/2 < m_2 < 0$ (see also Chou-Wang and Horgan, 1989). In the incompressible case the critical stress increases infinitely as $m_1 \to 3$ or $m_2 \to -3/2$, while in the compressible case the critical stress exists as far as numerically calculated for $0 < m_1 < 3$ and $-3 < m_2 < 0$, which indicates that the compressibility promotes the void formation.

Ertan (1988) considered the void formation problem for a slightly different class of materials. Ertan concluded that the critical stretch and stress are smaller when the material is softer and that according as the material becomes less compressible, the critical stretch approaches to unity while the critical stress increases. It is not easy to compare this result with the present one directly because the constitutive settings are different between the two analyses, but Ertan's result is qualitatively similar to ours, especially concerning the compressibility dependence.

Furthermore, if we put $c_1 = 0$, $c_2 = -\mu$ and $m_2 = -2$ in (30) we obtain the strain energy function for the Blatz-Ko foam rubber. The critical stretch and stress for this material were calculated by Horgan and Abeyaratne (1986) by obtaining the

Downloaded 03 May 2010 to 171.66.16.20. Redistribution subject to ASME license or copyright; see http://www.asme.org/terms/Terms_Use.cfm

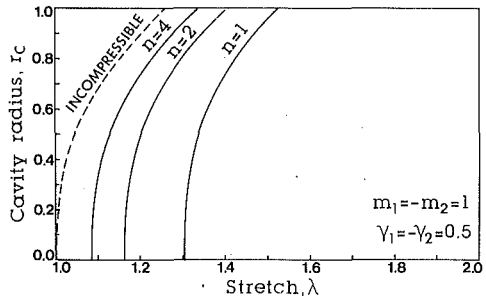


Fig. 3 Relation between the stretch and the cavity radius for different values of n. $m_1 = -m_2 = 1$ and $\gamma_1 = -\gamma_2 = 0.5$.

closed-form solution of the equilibrium equation. This analysis was reconfirmed by Tian-Hu (1990). The analytical values thus obtained, however, can be calculated by the present method and we have confirmed that the agreement is well.

5.3 Post-Bifurcation Behavior. For the stretch λ which exceeds the critical value λ_{CR}, there exists, in addition to the homogeneous solution without a cavity, the solution containing a spherical cavity at the center. For the latter solution, the principal stretches at the surface are

$$\lambda_r = \alpha < \lambda, \quad \lambda_\theta = \lambda, \tag{39}$$

where α is related to λ by the condition that the first-order nonlinear ordinary differential Eq. (18) for $s = s(t)$ solved with the initial condition $s(\lambda) = \alpha$ should satisfy the traction-free boundary condition (22). Once α is determined for the specific value of λ, $s = s(t)$ and consequently the deformation $r = r(R)$ can be determined.

The deformation $r = r(R)$ is given in the following way. From (16) the next expression is obtained:

$$\frac{1}{R}\frac{dR}{dt} = \frac{1}{s(t) - t}, \tag{40}$$

which is integrated to give, with the fact that $R = A$ at $t = \lambda$,

$$R(t) = A \exp\left\{\int_\lambda^t \frac{d\tau}{s(\tau;\alpha) - \tau}\right\}. \tag{41}$$

In a similar fashion, we obtain

$$r(t) = \lambda A \exp\left\{\int_\lambda^t \frac{s(\tau;\alpha)/\tau}{s(\tau;\alpha) - \tau}\, d\tau\right\}. \tag{42}$$

The preceding two equations give the parametric representation for the deformation $r = r(R)$. Now the radius r_c of the cavity at the center is given by

$$r_c = \lim_{t\to\infty} r(t) = \lambda A \exp\left\{\int_\lambda^\infty \frac{s(\tau;\alpha)/\tau}{s(\tau;\alpha) - \tau}\, d\tau\right\}. \tag{43}$$

The relation between the stretch λ and the cavity radius r_c is calculated and presented in Fig. 3. As $n \to \infty$, the critical stretch approaches to unity and the relation between λ and r_c to the next relation

$$\lambda^3 - (r_c/A)^3 = 1, \tag{44}$$

which is the result from the internal constraint of incompressibility.

The relation between the stretch λ and the radial Cauchy stress at the surface, $p \equiv \tau_r(A) = W_1(\alpha, \lambda, \lambda)/\lambda^2$, is also calculated (Fig. 4). This can be regarded as giving the macroscopic stress-stretch relation of the sphere under isotropic tension and it is shown that the void formation causes the change in this relation, i.e., after the cavity is formed, the same stretch is accompanied by the smaller value of the radial stress for the cavitating solution than for the homogeneous

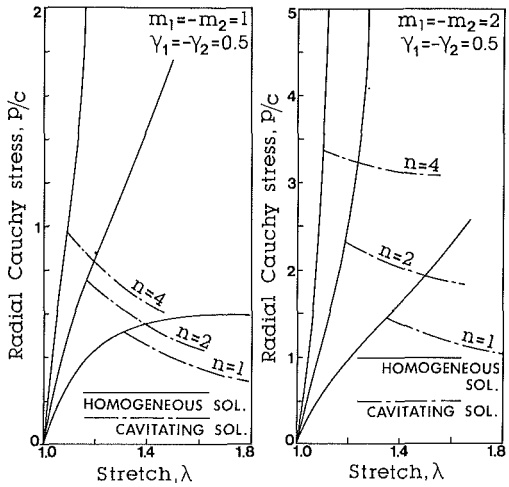


Fig. 4 Relation between the stretch and the radial Cauchy stress for different values of n. $\gamma_1 = -\gamma_2 = 0.5$ (left; $m_1 = -m_2 = 1$, right; $m_1 = -m_2 = 2$).

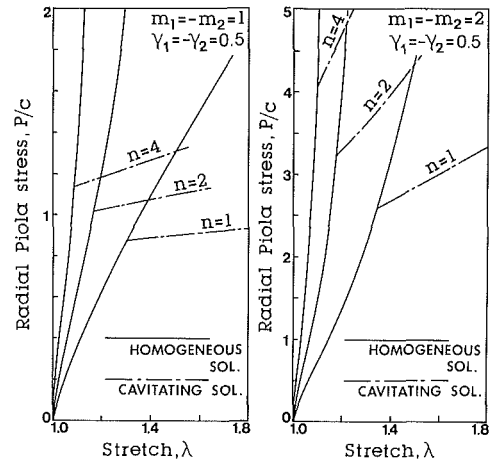


Fig. 5 Relation between the stretch and the radial Piola stress for different values of n. $\gamma_1 = -\gamma_2 = 0.5$ (left; $m_1 = -m_2 = 1$, right; $m_1 = -m_2 = 2$).

one. This change may be describing qualitatively well-known phenomena that materials soften due to the formation of voids. The relation between the stretch λ and the radial first Piola-Kirchhoff stress (simply referred to as Piola stress) at the surface, $P = \lambda^2 p$, which is essentially the normalized radial load applied at the surface, is also presented in Fig. 5. It is shown that, according as the cavity grows, the radial Cauchy stress decreases while the radial Piola stress increases.

6 Remark on Energy

In the preceding sections, it has been assumed that, for appropriate strain energy functions, there exist two types of spherically symmetric solutions, i.e., the homogeneous solution in which the sphere remains solid, and the cavitating solution in which the sphere forms a cavity, for sufficiently large stretch prescribed at the surface. The critical stretch and stress have been calculated for a special class of compressible nonlinear elastic materials. If two solutions are possible, however, we may expect that the energetically favorable one would actually appear. Now the energy stored in the sphere for both homogeneous and cavitating solutions are calculated and compared.

In the case that the stretch at the surface is prescribed, the energy functional is given as follows:

Downloaded 03 May 2010 to 171.66.16.20. Redistribution subject to ASME license or copyright; see http://www.asme.org/terms/Terms_Use.cfm

$$E=\int_B WdV=4\pi\int_0^A R^2W\left(r',\frac{r}{R},\frac{r}{R}\right)dR. \quad (45)$$

Clearly, for the homogeneous solution, we obtain from (13),

$$E_{\text{hom}}=4\pi\int_0^A R^2W(\lambda,\lambda,\lambda)dR=\frac{4}{3}\pi A^3W(\lambda,\lambda,\lambda). \quad (46)$$

On the other hand, for the cavitating solution using the formula

$$\frac{d}{dR}\left[R^3\left\{W\left(r',\frac{r}{R},\frac{r}{R}\right)+\left(\frac{r}{R}-r'\right)W_1\left(r',\frac{r}{R},\frac{r}{R}\right)\right\}\right]=3R^2W\left(r',\frac{r}{R},\frac{r}{R}\right), \quad (47)$$

which is originally due to Green (1973), the functional (45) reduces to

$$E_{\text{cav}}=\frac{4\pi}{3}\left[R^3\left\{W\left(r',\frac{r}{R},\frac{r}{R}\right)+\left(\frac{r}{R}-r'\right)W_1\left(r',\frac{r}{R},\frac{r}{R}\right)\right\}\right]_{R=0}^{R=A}. \quad (48)$$

In the above expression the term with $R \to 0$ is zero (for the proof see Sivaloganathan, 1986a). Thus we obtain

$$E_{\text{cav}}=\frac{4\pi}{3}A^3\left\{W(\alpha,\lambda,\lambda)+(\lambda-\alpha)W_1(\alpha,\lambda,\lambda)\right\}. \quad (49)$$

Therefore, the difference between the energy functional for both solutions is given by

$$E_{\text{hom}}-E_{\text{cav}}=\frac{4\pi}{3}A^3\left\{W(\lambda,\lambda,\lambda)-W(\alpha,\lambda,\lambda)+(\alpha-\lambda)W_1(\alpha,\lambda,\lambda)\right\}. \quad (50)$$

Next, the above quantity will be estimated for the specific material given by (30). Substituting (30) into the above expression, we obtain

$$\frac{E_{\text{hom}}-E_{\text{cav}}}{\frac{4\pi}{3}A^3}=\sum_{i=1}^{2}\frac{c_i}{m_i}\left\{\lambda^{m_i}-\alpha^{m_i}+\frac{1}{n}\lambda^{-2m_in}(\lambda^{-m_in}-\alpha^{-m_in})\right\}+\sum_{i=1}^{2}c_i(\alpha-\lambda)(\alpha^{m_i-1}-\alpha^{-m_in-1}\lambda^{-2m_in}). \quad (51)$$

If, for fixed λ, we regard this to be a function of α and write it as $\Delta E(\alpha;\lambda)$, the following equations are obtained:

$$\lim_{\alpha\to\lambda}\Delta E(\alpha;\lambda)=0, \quad (52)$$

$$\frac{d}{d\alpha}\Delta E(\alpha;\lambda)=(\alpha-\lambda)\sum_{i=1}^{2}\left\{c_i(m_i-1)\alpha^{m_i-2}+c_i(m_in+1)\lambda^{-2m_in}\alpha^{-m_in-2}\right\}. \quad (53)$$

Then, if

$$c_i(m_i-1)\geqq 0,\ c_i(m_in+1)\geqq 0,\ i=1,2 \quad (54)$$

and either one of the above four is positive, $\Delta E(\alpha;\lambda)$ will be positive for $0<\alpha<\lambda$, i.e., $E_{\text{hom}}>E_{\text{cav}}$. Thus the cavitating solution is energetically favorable. Since the above condition is essentially equivalent to the tension-extension inequality (Truesdell and Noll, 1965, see also Sivaloganathan, 1986b), materials which satisfy this inequality would indeed form a void under sufficiently large stretch. This result has been proved mathematically by Sivaloganathan (1986b).

Next, the case will be considered in which this inequality is not necessarily satisfied, and here we consider the behavior at the critical point. If we set $\lambda \to \lambda_{\text{CR}}$, we get

$$\lim_{\alpha\to\lambda_{\text{CR}}}\Delta E(\alpha;\lambda_{\text{CR}})=0, \quad (55)$$

$$\lim_{\alpha\to\lambda_{\text{CR}}}\frac{d}{d\alpha}\Delta E(\alpha;\lambda_{\text{CR}})=0, \quad (56)$$

$$\lim_{\alpha\to\lambda_{\text{CR}}}\frac{d^2}{d\alpha^2}\Delta E(\alpha;\lambda_{\text{CR}})=\sum_{i=1}^{2}\left\{c_i(m_i-1)\lambda_{\text{CR}}^{m_i-2}+c_i(m_in+1)\lambda_{\text{CR}}^{-3m_in-2}\right\}. \quad (57)$$

So $E_{\text{hom}} > E_{\text{cav}}$ near the critical stretch λ_{CR} if and only if

$$\sum_{i=1}^{2}\left\{c_i(m_i-1)\lambda_{\text{CR}}^{m_i-2}+c_i(m_in+1)\lambda_{\text{CR}}^{-3m_in-2}\right\}>0. \quad (58)$$

This condition is numerically estimated to show that, as long as calculated and illustrated in the figures, the inequality (58) holds and it is energetically favorable for the sphere to form a spherical void at the bifurcation point.

7 Conclusion

In this paper the void formation in compressible nonlinear elastic materials under isotropic tension was considered. A method was presented to calculate the critical stretch and stress for a wide variety of strain energy functions. As a result, the critical stress increases as the stiffness for one-directional extension, one-directional contraction, or volume change increases. Also, the post-bifurcation behavior was calculated and the cavitating solution was revealed to be energetically favorable for a wide range of constitutive parameters. Finally it is noted that we have been concerned in this paper with the spherically symmetric deformations. Since for the cavitating solution the deformation in the neighborhood of the cavity is in a quite localized state, it is possible for the sphere to take asymmetric configurations such as surface instabilities or shear bands, which must be analyzed within a different framework.

Acknowledgment

The authors are grateful to the reviewers of this paper for their constructive criticism.

References

Ball, J. M., 1982, "Discontinuous Equilibrium Solutions and Cavitation in Nonlinear Elasticity," *Philosophical Transactions of the Royal Society of London*, Vol. A306, pp. 557–611.

Chou-Wang, M.-S., and Horgan, C. O., 1989, "Void Nucleation and Growth for a Class of Incompressible Nonlinearly Elastic Materials," *International Journal of Solids and Structures*, Vol. 25, No. 11, pp. 1239–1254.

Ertan, N., 1988, "Influence of Compressibility and Hardening on Cavitation," *ASCE Journal of Engineering Mechanics*, Vol. 114, No. 7, pp. 1231–1244.

Green, A. E., 1973, "On Some General Formulae in Finite Elastostatics," *Archive for Rational Mechanics and Analysis*, Vol. 50, pp. 73–80.

Haughton, D. M., 1990, "Cavitation in Compressible Elastic Membranes," *International Journal of Engineering Science*, Vol. 28, No. 2, pp. 163–168.

Hill, R., 1978, "Aspects of Invariance in Solid Mechanics," *Advances in Applied Mechanics*, C.-S. Yih, ed., Vol. 18, Academic Press, pp. 1–75.

Horgan, C. O., 1992, "Void Nucleation and Growth for Compressible Non-Linearly Elastic Materials: An Example," *International Journal of Solids and Structures*, Vol. 29, No. 3, pp. 279–291.

Horgan, C. O., and Abeyaratne, R., 1986, "A Bifurcation Problem for a Compressible Nonlinearly Elastic Medium: Growth of a Micro-Void," *Journal of Elasticity*, Vol. 16, pp. 189–200.

Hou, H.-S., and Abeyaratne, R., 1992, "Cavitation in Elastic and Elastic-Plastic Solids," *Journal of the Mechanics and Physics of Solids*, Vol. 40, No. 3, pp. 571–592.

Podio-Guidugli, P., Vergara Caffarelli, G., and Virga, E. G., 1986, "Dis-

Downloaded 03 May 2010 to 171.66.16.20. Redistribution subject to ASME license or copyright; see http://www.asme.org/terms/Terms_Use.cfm

continuous Energy Minimizers in Nonlinear Elastostatics: An Example of J. Ball Revisited," *Journal of Elasticity*, Vol. 16, pp. 75–96.

Sivaloganathan, J., 1986a, "Uniqueness of Regular and Singular Equilibria for Spherically Symmetric Problems of Nonlinear Elasticity," *Archive for Rational Mechanics and Analysis*, Vol. 96, pp. 97–136.

Sivaloganathan, J., 1986b, "A Field Theory Approach to Stability of Radial Equilibria in Nonlinear Elasticity," *Mathematical Proceedings of the Cambridge Philosophical Society*, Vol. 99, pp. 589–604.

Storåkers, B., 1986, "On Material Representation and Constitutive Branching in Finite Compressible Elasticity," *Journal of the Mechanics and Physics of Solids*, Vol. 34, No. 2, pp. 125–145.

Stringfellow, R., and Abeyaratne, R., 1989, "Cavitation in an Elastomer: Comparison of Theory with Experiment," *Materials Science and Engineering*, Vol. A112, pp. 127–131.

Stuart, C. A., 1985, "Radially Symmetric Cavitation for Hyperelastic Materials," *Annales de l'Institut Henri Poincaré-Analyse non linéaire*, Vol. 2, No. 1, pp. 33–66.

Tian-Hu, H., 1990, "A Theory of the Appearance and Growth of the Micro-Spherical Void," *International Journal of Fracture*, Vol. 43, pp. R51–55.

Truesdell, C., and Noll, W., 1965, "The Non-Linear Field Theories of Mechanics," *Encyclopedia of Physics*, Vol. 3, No. 3, S. Flügge, ed., Springer-Verlag, Berlin.

APPENDIX

We show briefly the proof of (36). For $i = 1$, note $m_1 > 0$. The left-hand side of (35) is written as

$$\frac{t^{m_1}\{1-(s/t)^{m_1}\}}{t^4(1-s/t)},\ 0<\frac{s}{t}<1. \tag{A1}$$

Clearly, unless $s/t \to 1$ as $t \to \infty$, it is integrable when $m_1 < 3$. If $s/t \to 1$ as $t \to \infty$, by l'Hôspital's rule, (A1) converges to $m_1 t^{m_1-4}$, leading to the same result.

For $i = 2$, note $m_2 < 0$. If $s/t \to 1$ as $t \to \infty$, the left-hand side of (35) converges to $m_2 t^{m_2-4}$ and it is integrable. Otherwise it is integrable when

$$\frac{s^{m_2}}{t^4}=O\left(\frac{1}{t^\beta}\right),\ \beta>1. \tag{A2}$$

Thus we obtained (36), which is equivalent to (35).

Downloaded 03 May 2010 to 171.66.16.20. Redistribution subject to ASME license or copyright; see http://www.asme.org/terms/Terms_Use.cfm

Electron Beam Moiré Study of Fracture of a Glass Fiber Reinforced Plastic Composite

D. T. Read
Materials Reliability Division,
National Institute of Standards
and Technology,
Boulder, CO 80303

J. W. Dally
Mechanical Engineering Department,
University of Maryland,
College Park, MD 20742

Using the method of electron beam moiré, a small region at an interface of a $[O_2/90]_s$ glass fiber reinforced plastic composite has been examined during tensile testing. The tensile test was conducted inside a scanning electron microscope, with a high spatial frequency line grating (10,000 lines/mm) at the interface between a longitudinal ply and a transverse ply. During the test, this region was observed at a magnification of 1900×. Local strain measurements were made by interpreting the moiré fringe patterns over gage lengths that varied from 10 to 30 μm. The magnitude and distribution of the local strains depended on the damage that occurred with monotonically increasing load. Load shedding by the transverse ply was evident from the fringe patterns. Extremely high local strains were observed: longitudinal fiber strains up to three percent, normal strains up to three percent, and shear strains up to 40 percent in the epoxy matrix.

Introduction

Glass fiber reinforced plastic fabricated from several layers or plies is classified as a laminated composite. Although each layer is orthotropic, and the layers may have different orientations, the laminate acts as a single body with a global stiffness that is related to the stiffness and orientation of the individual plies (Halpin, 1984). In a structural analysis of a laminated composite, planes through a typical cross-section are assumed to remain plane after deformations due to tensile or bending loads (Tsai and Hahn, 1981, and Vinson and Sierakowski, 1986). Stresses vary from ply to ply because of changing elastic constants, but the displacements are continuous across the interfaces. Experiments with tension members, beams, plates, and shells (Halpin, 1984) confirm that the results of analysis using laminate theory are not always adequate, and more involved micromechanics theories (Chamis, 1974) are necessary to predict the loss of stiffness and strength. Here we report experimental results showing some deviations from the plane sections remain plane assumption of the simple laminate theory even prior to extensive ply damage. The need for micromechanics theory when damage occurs is clearly established.

Electron beam (e-beam) moiré (Kishimoto et al., 1991; Dally and Read, 1992) was used to study displacement and strains in a tensile specimen fabricated from a $[O_2/90]_s$ glass fiber reinforced epoxy. Displacement and strain were measured on a microscale during four phases of loading:

(1) prior to cross ply cracking,
(2) after cross ply cracking,
(3) after extensive damage, but before delamination, and
(4) after delamination, prior to rupture.

The analysis was performed with a high-frequency line grating (10,000 lines/mm) that was written with an e-beam over an area 50 × 80 μm. The patch of grating was positioned at an interface between a cross ply and a longitudinal ply. The measurement field included three rows of fibers associated with the cross ply, the resin-rich interface, and several fibers in the longitudinal ply.

Background. Some experimental studies of the deformation and failure of composite materials have utilized detailed observations of the behavior of specimens under load. To cite an outstanding example, D. Post and colleagues presented moiré interferometry data showing the shear strain differences among 0 deg plies, 90 deg plies, and resin-rich regions between plies (Post et al., 1989). They have applied well-developed techniques to a series of issues in the behavior of composite materials and interfaces (Post et al., 1987a, Post et al., 1987b, Post and Wood, 1989). In particular, the stiffness difference between fiber and matrix-produced zig-zag fringes (Post et al., 1987a).

High-magnification observation of fracture surfaces was used by Bandyopadhyay et al. (1989) to support their explanation of the difference in fracture toughness between two types of carbon fiber composites. The techniques of Raman spectroscopy (Galiotis et al., 1988) and of speckle interferometry (Anastasi et al., 1987) have also been used to map stresses and deformations in composites at lower spatial resolution.

Detailed theoretical models of the micromechanical behavior

Contributed by the Applied Mechanics Division of THE AMERICAN SOCIETY OF MECHANICAL ENGINEERS for publication in the ASME JOURNAL OF APPLIED MECHANICS.

Discussion on this paper should be addressed to the Technical Editor, Professor Lewis T. Wheeler, Department of Mechanical Engineering, University of Houston, Houston, TX 77204-4792, and will be accepted until four months after final publication of the paper itself in the ASME JOURNAL OF APPLIED MECHANICS.

Manuscript received by the ASME Applied Mechanics Division, Oct. 1, 1992; final revision, Feb. 23, 1993. Associate Technical Editor: W. N. Sharpe, Jr.

Copyright © 1994 by ASME
Downloaded 03 May 2010 to 171.66.16.20. Redistribution subject to ASME license or copyright; see http://www.asme.org/terms/Terms_Use.cfm

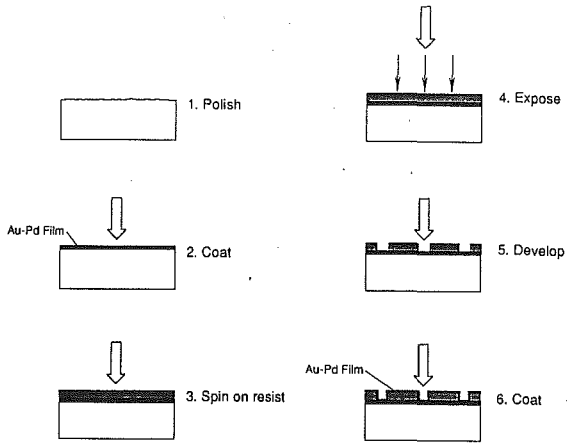


Fig. 1 Electron-beam lithography procedure to produce line gratings for electron beam moiré on the GFRP tensile specimen

of composites have been formulated (Lee et al., 1989), but their verification has relied on macroscopic observations. It is well recognized that demonstration of the macroscopic usefulness of such models does not constitute proof of their micromechanical assumptions.

e-Beam Moiré. e-Beam moiré is similar to optical moiré except that an electron beam is used to produce the line gratings and a scanning electron beam is then employed to generate the moiré fringe pattern. The technique for producing the line grating is shown in Fig. 1. We first prepared the surface of the specimen by grinding it smooth and flat with a series of water-lubricated abrasive papers ending with 5 μm grit. The final polish was achieved by finishing with 3 and then 1 μm diamond particles. The second step was the application of a very thin (10 to 20 nm) gold palladium coating by plasma sputtering. This metallic coating is necessary to render the specimen surface conductive, to prevent a surface charge from developing on the glass fiber reinforced plastic specimen under the electron beam.

The specimens were then coated with polymethylmethacrylate (PMMA) which serves as an electron beam resist. The PMMA solution used for coating was two percent PMMA, molecular weight of 950,000, with chlorobenzene as the solvent. The PMMA resist was spun on the specimens, at a speed of 3000 RPM for 30 seconds. The specimens were then baked on a hot plate for 30 minutes at 160°C. This process produces a cured layer of PMMA resist that is approximately 100 nm thick.

The specimen was mounted on a specimen stage in a digitally controlled scanning electron microscope equipped with a Faraday cup and a beam blanker. The scanning electronic microscope was operated with an accelerating voltage of 20 kV and a 50 μm aperture. The probe current was adjusted to 10 pA, which produces a focussed beam of electrons 10 to 15 nm in diameter. The e-beam in the scanning electronic microscope was computer controlled and patterns were written in the PMMA resist with programmed instructions. These instructions defined both the geometry of the pattern and the electron dosage.

After the patterns were written, the specimen was developed in a solution consisting of three parts (by volume) of isopropyl alcohol to one part of methyl isobutyl ketone for 40 s. The specimen was immediately rinsed in isopropyl alcohol for 20 s followed by a second rinse in deionized water for 30 s. The development of the resist is an etching process; precise control of the development is critical. Finally, the specimen was coated again with a very thin layer (10 to 20 nm) of a gold palladium alloy to provide a conductive surface on top of the PMMA.

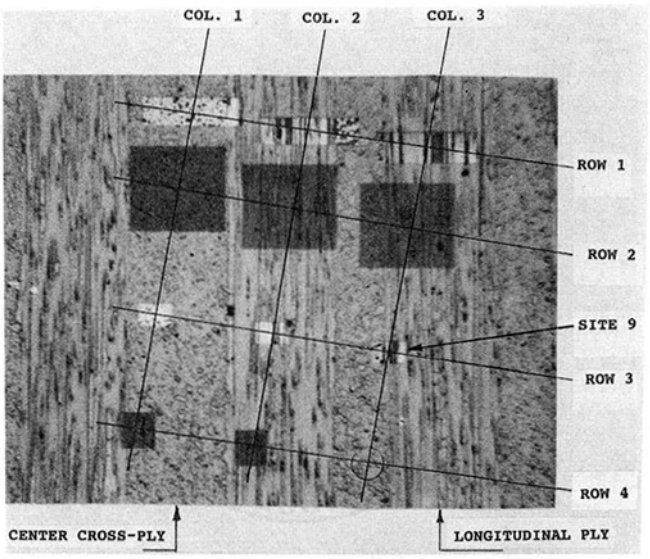


Fig. 2 LIne and dot gratings on the tensile specimen

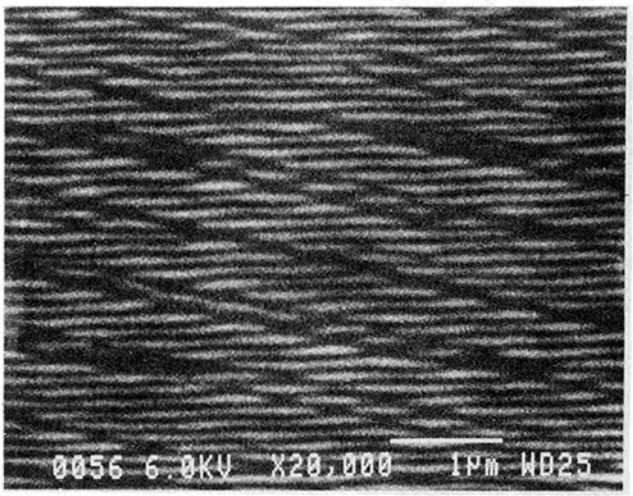


Fig. 3 An SEM micrograph of the moiré grating used in this study with pitch p_s = 100 nm

Twelve different patterns were written on the specimen as illustrated in Fig. 2. The top three patterns, along row 1, are lines 250 μm long on 200 nm centers. The next three patterns, along row 2, are dots placed in a rectangle 240 × 200 μm in size on 200 nm centers. The three patterns on row 3 are lines 80 μm long on 100 nm centers; 500 lines are included in each pattern. Two dot patterns placed in an 80 μm square on 100 nm centers are shown along row 4. The third pattern located at column 3 in row 4 was underexposed. The difference in the shading indicates different line densities and exposures of the patterns.

The pattern at site 9, the third pattern in the third row, was selected for observation in the study. This pattern, having a density of 10,000 lines/mm, was located at an interface between a cross ply and a longitudinal ply. Also, the line array provided 80 or more lines across each of several glass fibers (8 to 10 μm in diameter) which was enough to investigate intraply and intrafiber deformations. Finally, the quality of the line grating was sufficient to produce scanning moiré fringes with good contrast.

A scanning electron microscope micrograph of the moiré grating at site 9 taken at 20,000×, presented in Fig. 3, shows the detail of the line array. The thin dark lines correspond to

Downloaded 03 May 2010 to 171.66.16.20. Redistribution subject to ASME license or copyright; see http://www.asme.org/terms/Terms_Use.cfm

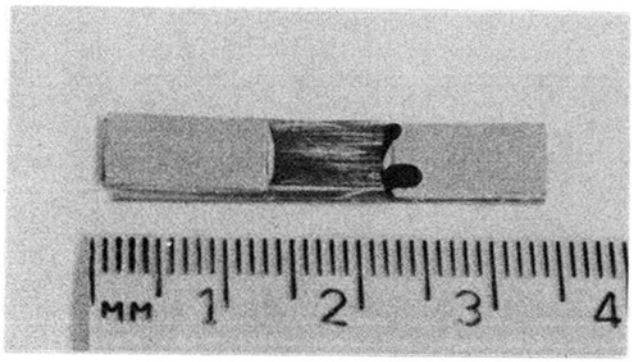


Fig. 4(*a*) Tensile specimen after failure. The black drops are conductive paste, which electrically grounds the specimen surface to the grips.

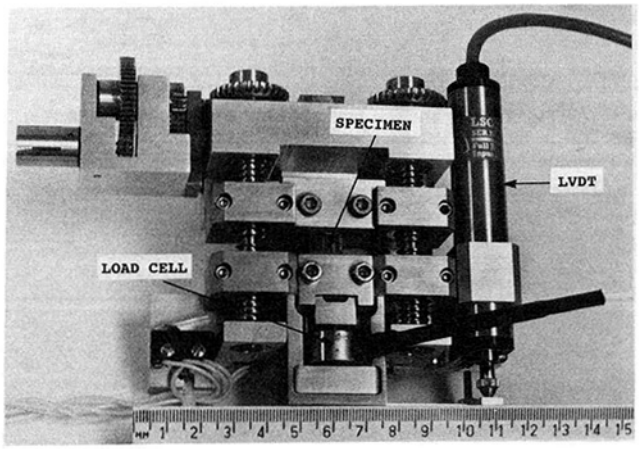


Fig. 4(*b*) Tensile testing stage for the scanning electron microscope

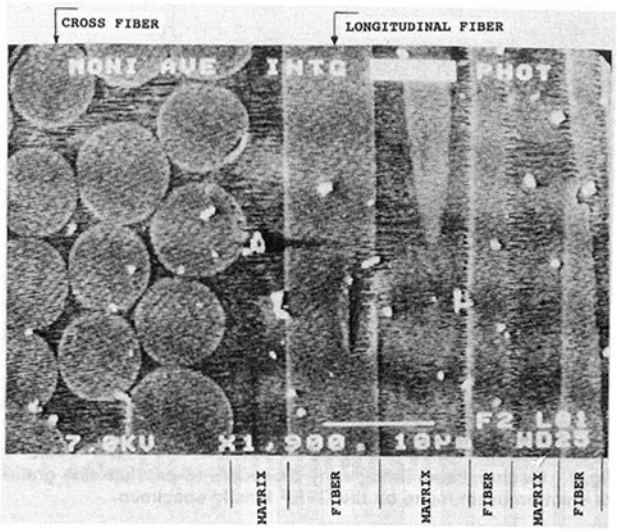


Fig. 5 Moiré fringe pattern at an interface between a longitudinal ply and a cross ply, at initial load

trenches in the PMMA resist formed by etching the regions exposed by the electron beam. The wider light lines are ridges in the resist. The dark lines on a diagonal are due to a malfunction in the e-beam control during the exposure of the resist. Fortunately, the primary lines, which are horizontal and on 100 nm centers, are dominant since they cover about 85 percent of the area. Although the grating was flawed, it produced well-defined moiré fringes with good contrast.

Moiré fringe patterns are formed by scanning the grating lines with the electron beam in a scanning electron microscope. The pitch p_r of the raster scan in the SEM can be controlled by adjusting either the magnification M or the number of scan lines used to form the image. In these experiments the number of scan lines was held constant at 500 and the reference pitch p_r was adjusted with the magnifications setting. At a magnification of 1900×, p_r = 98 nm and is nearly equal to the pitch p_s of the specimen grating. The signal from the secondary electrons which is sensed by a detector in the scanning electron microscope is strongly affected by the difference in frequencies, $f_s - f_r = 1/p_s - 1/p_r$ of the two line arrays. When this frequency difference is small, a pattern of light and dark bands corresponding to moiré fringes is formed. Since these fringes are formed by electrons, the method is not limited by the wavelength of light, and microscale measurements at high magnification are possible.

Specimen and Load Fixture

The composite material investigated is a glass fiber reinforced epoxy known as 52/3501-6. The panels were laid up by hand and cured in an autoclave. The lay-up included 48 layers of prepreg oriented $[0_2/90]_s$. The lay-up was symmetrical, with a surface to midplane sequence of 0/0/90/0/0/90 . . . . 0/0/90. The finished panels were 6.22 mm thick, with a void content of less than one percent.

A thin strip 2 mm thick and 33 mm long oriented in the longitudinal 0-deg direction was cut from the composite panel by using an abrasive cutoff wheel flooded with water. The strip was turned on its side to show the cross-section of the laminate and adhesively bonded to a polishing block. The strip was reduced to a thickness of 0.406 mm by sanding and polishing with standard metallographic polishing equipment. The high-density gratings were written on the specimen surface at the sites defined in Fig. 2.

The ends of the specimen were reinforced by bonding aluminum plates to both surfaces as shown in Fig. 4(*a*). The specimen was placed in a small universal testing machine that was designed to fit into the vacuum chamber of a scanning electron microscope. This testing machine, shown in Fig. 4(*b*), employs clamped wedge grips for specimen attachment. Both spur and worm gears are used to turn a pair of lead screws that drive both loading platens at equal speeds. The applied load and platen displacement were measured with a load cell and a LVDT, respectively.

Strain Field Development With Load

Before Cross Ply Cracking. The glass fiber reinforced plastic tensile specimen was mounted on a scanning electron microscope loading machine, and a small initial load of 75 N was applied. The moiré pattern at site 9 was brought into focus at a magnification of 1900×. At this magnification, the pitch of the specimen gratings p_s and the pitch of the scanning electron beam p_r, which serves as the reference grating, were nearly equal. The electron beam raster lines and the specimen grating lines were aligned. The small difference between p_r and p_s produced the mismatch fringes presented in Fig. 5. This figure shows the interface between a 90-deg or cross ply and a 0-deg or longitudinal ply. The three columns of circles are fiber ends in the 90-deg ply that range in diameter from 8 to 10 μm. The resin-rich area at the interface varies in thickness from 3.5 to 5.3 μm. Portions of five different fibers and two resin regions from the 0-deg ply can be identified in Fig. 5.

The next moiré fringe pattern, presented in Fig. 6, corresponds to a nominal tensile stress of 347 MPa. The fringes are continuous across the interface, indicating that the deformations are continuous from the 90-deg to the 0-deg ply. The continuity of the displacements across the interface is consistent

Downloaded 03 May 2010 to 171.66.16.20. Redistribution subject to ASME license or copyright; see http://www.asme.org/terms/Terms_Use.cfm

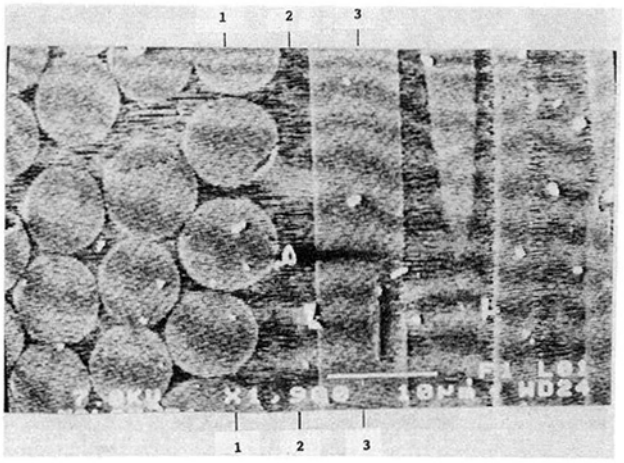


Fig. 6 Moiré fringe pattern prior to cross-ply cracking, at a stress of 347 MPa

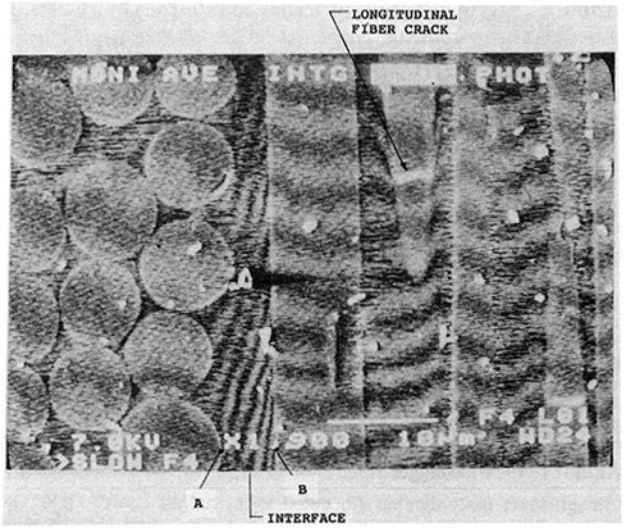


Fig. 7 Moiré fringe pattern after cross-ply cracking, at a stress of 524 MPa

Table 1 Strain distribution across an interface in a $0_2/90$ glass fiber reinforced plastic composite prior to 90-deg ply failure

σ = 347 MPa

Ply	Strain ϵ_y
90 deg	8.6×10^{-3}
Interface	9.5×10^{-3}
0 deg	10.1×10^{-3}

with elementary laminate theory. However, the gradient dN/dy of the fringe field differs among the 90-deg ply, the interface, and the 0-deg ply, indicating a strain gradient $d\epsilon_y/dx$ across this interface. This strain gradient is not consistent with the plane section assumption of elementary laminate theory.

The strain at any location in the field is given by

$$\epsilon_y = \frac{v}{L} = \frac{\Delta N p_r}{L} \tag{1}$$

where v is the displacement along the axis of the specimen and normal to the grating lines, p_r = 98.3 nm is the reference pitch at 1900×, and L is a gage length.

The fringe order difference ΔN is

$$\Delta N = N_p - N_0 \tag{2}$$

where N_p is the number of fringes at load P and N_0 is the number of fringes at initial load.

Combining Eqs. (2) and (3) gives

$$\epsilon_y = (N_p' - N_0')p_r \tag{3}$$

where N_p' and N_0' are fringe gradients $\Delta N/\Delta y$ at load P and the initial load.

The fringe gradients N_p' and N_0' were determined over a gage length Δy of 25 to 30 μm along the lines 1, 2, and 3 defined in Fig. 6. These lines refer to the first column of fibers in the 90-deg ply, the resin-rich interface, and the first longitudinal fiber in the-deg ply. The results are given in Table 1.

The distance between lines 1 and 3 was 12.9 μm and the strain difference across the interface was 1.5×10^{-3}. Thus, the strain gradient from fiber center line to fiber center line across the interface was $d\epsilon_y/dx = 0.12 \times 10^{-3}\ (\mu\text{m})^{-1}$.

Next, a local elastic modulus E_l was determined from

$$E_l = \sigma/\epsilon_{\text{ave}} \tag{4}$$

where the applied tensile stress σ = 347 MPa, and the average strain is

$$\epsilon_{\text{ave}} = (2\epsilon_0 + \epsilon_{90})/3 = 9.6\times10^{-3}. \tag{5}$$

The form of the numerator in Eq. (5) was employed because the laminate was fabricated with two 0-deg plies for every 90-deg ply.

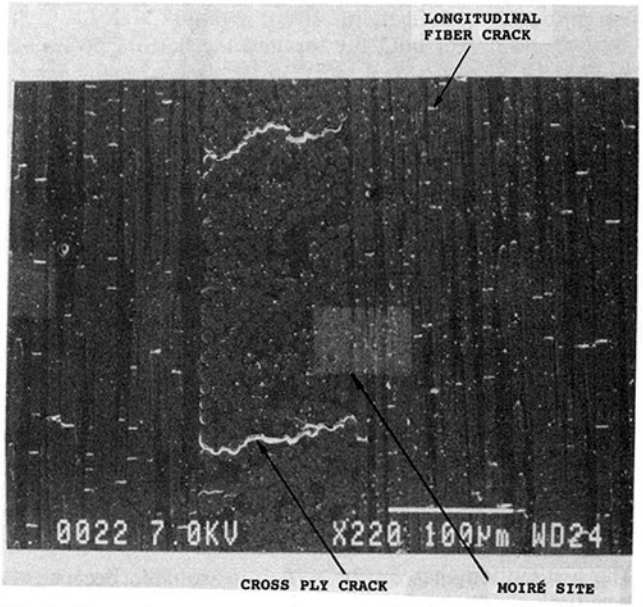


Fig. 8 Cross-ply cracking near the grating and longitudinal fiber cracks over the whole field, at a stress of 700 MPa

The value of the local modulus was 36.1 GPa, which is within five percent of the expected global modulus of 37.9 GPa.

After Cross-Ply Cracking. The moiré fringe pattern presented in Fig. 7 shows a dramatic change in the deformations across the same interface. A cursory inspection of the fringe pattern shows that (a) the strain in the 90-deg ply has decreased, (b) the strain in the 0-deg ply has increased, and (c) significant shearing strain has occurred over the resin-rich area at the interface. Failures in the 90-deg ply above and below the grating area are shown in Fig. 8. This cross-ply cracking markedly degraded the contribution of the 90-deg ply to the tensile stiffness of the composite.

Analysis of Fig. 7 gives the results presented in Table 2. The strains in the 90-deg ply have decreased to about ten percent of their former value, although the global stress on the specimen increased from 347 to 524 MPa. Clearly, the cross-ply cracking has nearly eliminated the load-carrying capability of

Downloaded 03 May 2010 to 171.66.16.20. Redistribution subject to ASME license or copyright; see http://www.asme.org/terms/Terms_Use.cfm

Table 2 Strain distribution across an interface in a $0_2/90$ glass fiber reinforced plastic composite after 90-deg ply failure

σ = 524 MPa

Ply	Strain, ϵ_y
90 deg	8.9×10^{-4}
0 deg	10.9×10^{-3}

Table 3 Strains at several locations near the interface

σ = 700 MPa

Location	Strain	
	ϵ_y	γ_{xy}
Cross ply	-3.9×10^{-4}	—
Interface	13.5×10^{-3}	0.093
First longitudinal fiber	13.5×10^{-3}	—
Second longitudinal fiber	16.7×10^{-3}	—
Resin between first and second fiber	17.6×10^{-3}	0.014
Resin by crack in dagger fiber	—	0.133

the 90-deg plies. The strain in the first fiber of the 0-deg ply varies over its length in the field of view. Over the bottom portion of this fiber, the strain is 13.5×10^{-3}, but over the top portion of this fiber, the strain is only 8.7×10^{-3}. The average strain over both the top and the bottom portions is 10.9×10^{-3}, which represents an increase of eight percent over strains due to the previous load. Because the globally applied stress was increased by 51 percent, the damage in the cross plies and other fractures of individual fibers has affected the strain distribution in the local region being analyzed.

The effect of damage is most evident at the interface, where moiré fringes that are inclined 17 deg to the vertical indicate significant shear in the resin-rich region between the 0-deg and 90-deg plies. The engineering shear strain is defined as

$$\gamma_{xy} = \left(\frac{\partial v}{\partial x} + \frac{\partial u}{\partial y}\right). \tag{6}$$

If we assume that $\partial u/\partial y$ is small enough relative to $\partial v/\partial x$ to be neglected in the interface region, the engineering shear strain can be approximated as

$$\gamma_{xy} \cong \frac{\Delta v}{\Delta x}. \tag{7}$$

The assumption that $\partial u/\partial y \approx 0$ is reasonable because the longitudinal fibers adjacent to the interface are observed to remain straight under axial tensile stresses. Using Eq. (7), γ_{xy} is determined by noting a shift of five fringe orders across the interface from point A to point B in Fig. 7. This shift due to shear gives $\Delta v = \Delta N p_r = 0.49\ \mu$m. The thickness of the resin-rich area at the lower fiber, corresponding to Δx in Eq. (7), is 5.29 μm. The resulting engineering shear strain γ_{xy} = 9.3 percent. Clearly, a very large shearing strain is supported by the matrix material, preventing delamination.

A final feature, evident in Fig. 7, is a crack in one of the longitudinal fibers. This fiber was not perfectly planar in the lay-up and appears with a dagger shape after polishing. One observes rotation of the moiré fringes to the left of the crack, indicating another localized shear strain. Measurements of Δv and Δx indicate that γ_{xy} in the matrix material just above and to the left of the crack was about 4.5 percent.

Extension of Shearing into the 0-deg Ply. Moiré patterns in Figs. 9(*a*), 9(*b*), and 9(*c*) show the effect of increasing the tensile stress in the presence of 90-deg ply damage. A cursory inspection of Fig. 9(*a*), which corresponds to σ = 700 MPa, shows the unloading of the 90-deg ply and the extension of the shearing strains from the interface into the resin-rich areas of the 0-deg ply. Measurements were made of the normal strains ϵ_y in the fibers and the shear strains γ_{xy} in the regions of epoxy between the fibers. The results are presented in Table 3.

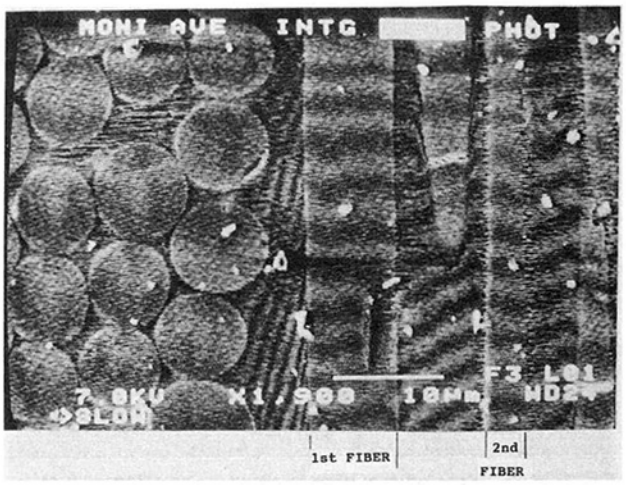


Fig. 9(*a*) Moiré fringe pattern showing development of shear at the interface between the longitudinal ply and the cross ply, at a stress of 700 MPa

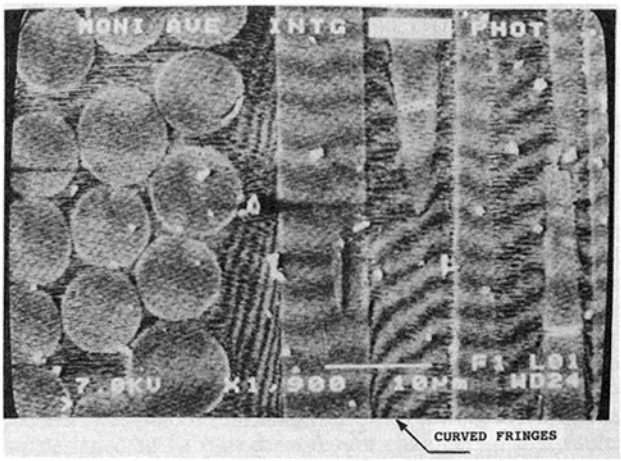


Fig. 9(*b*) Moiré fringe pattern showing extending shear deformation into the longitudinal ply, at a stress of 828 MPa

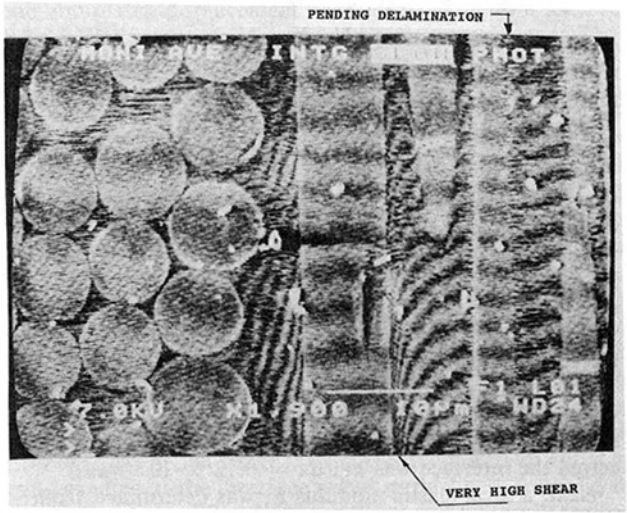


Fig. 9(*c*) Moiré fringe pattern prior to delamination cracking at the location marked, at a stress of 933 MPa

Downloaded 03 May 2010 to 171.66.16.20. Redistribution subject to ASME license or copyright; see http://www.asme.org/terms/Terms_Use.cfm

Table 4 Strains at several locations near the interface

σ = 828 MPa

Location	Strain ϵ_y	Strain γ_{xy}
Cross ply	9.8×10^{-4}	—
Interface	16.0×10^{-3}	0.119
First longitudinal fiber	16.0×10^{-3}	—
Second longitudinal fiber	22.8×10^{-3}	—
Resin between first and second fibers		
adjacent first fiber	—	0.084
center of region	21.4×10^{-3}	0.055
adjacent second fiber	—	0
Resin near crack in dagger-like fiber	—	0.133

Table 5 Strains at several locations near the interface

σ = 993 MPa

Location	Strain ϵ_y	Strain γ_{xy}
Cross ply	3.93×10^{-4}	—
Interface	12.4×10^{-3}	0.072
First longitudinal fiber	12.4×10^{-3}	—
Second longitudinal fiber	25.4×10^{-3}	—
Resin between first and second fibers		
adjacent first fiber	—	0.167
center of region	25.7×10^{-3}	—
adjacent second fiber	—	0

The compressive strain indicated in the cross ply is not real. The magnitude of this strain, $\epsilon_y = 3.9 \times 10^{-4}$, shows the resolution of the method. It is believed that the cross ply is totally unloaded at this load increment. The shear strain at the interface did not change as the applied tensile stress increased from 524 to 700 MPa. The strain ϵ_y in the first longitudinal fiber has increased but not in proportion to the loading. The strains in the second longitudinal fiber and the resin between the first and second fibers are nearly the same, and both are higher than the strain in the first longitudinal fiber.

Shearing strains of 1.36 percent were measured between the first two fibers in the resin region below the dagger-shaped longitudinal fiber. Shearing strains near the crack in the dagger-shaped fiber were 13.3 percent on the left side and higher than this value on the right side.

The moiré fringe pattern shown in Fig. 9(*b*) corresponds to a tensile stress of 828 MPa. The normal and shear strains at several locations are shown in Table 4.

The strains in the longitudinal fibers and the shear strains at the interface all increased on this increment of the load. However, the increases in strains were not all proportional to the increase in the load. The strain in the second longitudinal fiber exceeds two percent and the strain in the first longitudinal fiber is 1.6 percent. Another crack in a longitudinal fiber to the far right in Fig. 9(*b*) is evident. The curvature of the fringes in the resin region between the first and second fibers is due to a decrease in the value of the shearing strain across the region. The shearing strain is a maximum adjacent to the first fiber and is nearly zero adjacent to the second fiber.

The final moiré pattern in this series, Fig. 9(*c*), corresponds to a tensile stress of 993 MPa, an increase of 20 percent from 828 MPa. The strains at several locations are shown in Table 5. While the applied stress increased 20 percent from Fig. 9(*b*) to Fig. 9(*c*), the shearing strains at the interface and the normal strains in the first longitudinal fiber decreased markedly, because these regions were beginning to unload. The interface has shifted to the right side of the first longitudinal fiber. This shift is apparent from the sharp increase in the shear strain (to 16.7 percent) in the resin region adjacent to and to the right of the first fiber. The normal strain in the resin region and in the second longitudinal fiber has increased to 2.5 percent. The

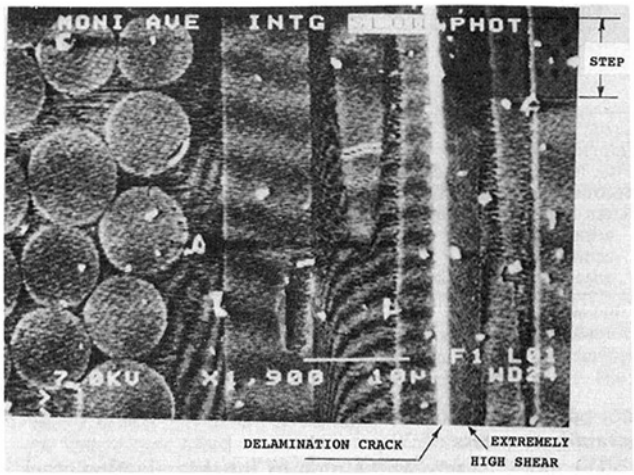


Fig. 10(*a*) Fringe pattern after 0-deg ply delamination cracking, at a stress of 1075 MPa

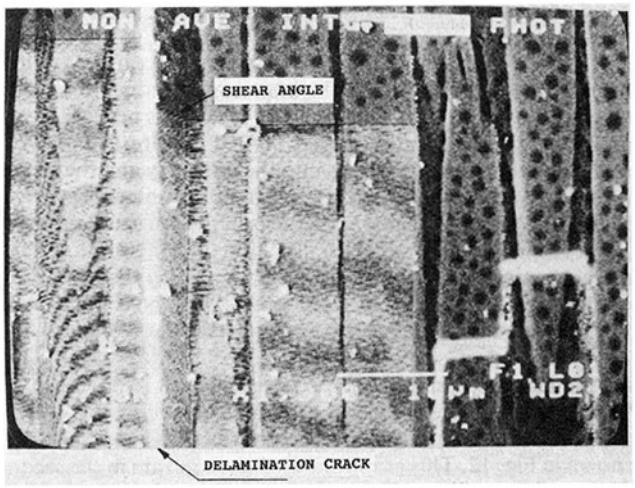


Fig. 10(*b*) Moiré pattern to the right of the delamination crack, at a stress of 1075 MPa

shifting of load from the first to the second fiber is due to extensions of the cross-ply cracks, above and below the moiré grating, that cut across the first longitudinal fiber (see Fig. 11).

Finally, a pending delamination plane is marked in Fig. 9(*c*), just to the right of the second complete longitudinal fiber. At this interface, continuous moiré fringes are observed that indicate high normal strain (2.5 percent) but relatively small shearing strains.

Longitudinal Ply Failure by Delamination. On the next load increment, to σ = 1075 MPa, a delamination crack appeared in the moiré grating as shown in Fig. 10(*a*). The delamination produced a step-like deformation of the top edge of the moiré grating as illustrated in Fig. 10(*b*), although the specimen continued to support the applied load. An analysis of the regions to the left of the delamination crack gave the strains presented in Table 6.

The delamination did not markedly affect the trends under way at locations to the left of the longitudinal crack. The cross ply at the site is essentially free. The interface and the first longitudinal fiber continue to unload. The strains in the region between the first and second fibers and in the second fiber continue to increase, exceeding 3.2 percent. The shear strain adjacent to the first longitudinal fiber is so high that it was

Downloaded 03 May 2010 to 171.66.16.20. Redistribution subject to ASME license or copyright; see http://www.asme.org/terms/Terms_Use.cfm

Table 6 Strains at several locations after delamination

σ = 1075 MPa

Location	Strain ϵ_y	γ_{xy}
Cross ply	1.96×10^{-4}	—
Interface	7.66×10^{-3}	0.067
First longitudinal fiber	7.66×10^{-3}	—
Second longitudinal fiber	33.4×10^{-3}	—
Resin between first and second fibers		
adjacent first fiber	—	~0.2*
center of region	32.3×10^{-3}	—
adjacent second fiber	—	**

* too large to resolve
** small

not possible to resolve the fringes. It is believed that the shear strain is in excess of 20 percent.

The moiré pattern to the right of the delamination crack is shown in Fig. 10(*b*). The normal strains in the longitudinal fibers are nearly zero. A very high shearing strain exists to the right of the delamination crack. Measurements of the angle of top boundary of the grating across the 2.35 μm wide shear band adjacent to the delamination crack give a shear strain of 41.4 percent.

A photograph at 160× in Fig. 11 shows the different types of damage developed during the monotonic loading to a global tensile stress of 1075 MPa. The cross-ply cracks near the measurement site and in an adjacent 90-deg ply are evident. Extension of the cross-ply cracks into the 0-deg ply and the failure of the first longitudinal fiber explains its unloading at the higher stress levels. Transverse cracks in the longitudinal fibers occur at many locations. These cracks in the longitudinal fibers are to be expected because local strains in the fibers of 3.3 percent give local uniaxial fiber stresses of about 2400 MPa. Delamination cracks have formed between the 0-deg and 90-deg plies and at several locations in the 0-deg plies. These delaminations produce step discontinuities as large as 7.5 μm in the v displacement field.

The distribution of strain ϵ_y across the measurement site is shown in Fig. 12. This graph shows that the strain in the second fiber and the adjacent resin region increased monotonically with the applied stress. Tensile strain in the transverse ply increased at first, then decreased because of cracking in that ply. The resin between the longitudinal and transverse plies had a similar history.

The shear strains measured locally in the epoxy resin were very large. Before delamination, shear strains of 16.7 percent were measured. After delamination, the shear strains were 41.4 percent in a shear band 2.35 μm wide adjacent to a longitudinal crack in the 0-deg ply. Neglecting biaxial effects, the normal stresses in the epoxy in resin-rich areas between fibers are estimated to be at least 1100 MPa.

Following this delamination, the specimen was unloaded and found to be intact. It was then reloaded until failure occurred at a nominal tensile stress of σ = 1220 MPa.

Discussion and Conclusions

The e-beam moiré method with a high-frequency line grating (10,000 lines/mm) enabled an examination of a small region about 45 μm square at an interface of a $[O_2/90]_s$ glass fiber reinforced plastic. The examination, performed at 1900×, permitted measurement of normal and shearing strains in the cross ply, in the resin-rich region between plies, in the longitudinal fibers, and in resin regions between these longitudinal fibers. The specimen was loaded in uniaxial tension until failure occurred at 1220 MPa. Local strain measurements were made by interpreting the moiré fringe patterns over gage lengths ranging from 10 to 30 μm.

The magnitude and the distribution of the strains depended

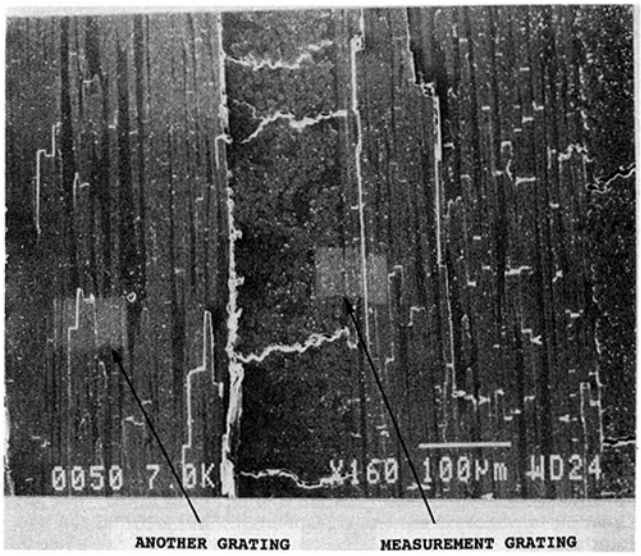


Fig. 11 Cross ply, longitudinal fiber, and longitudinal ply cracking. Also, intraply delamination.

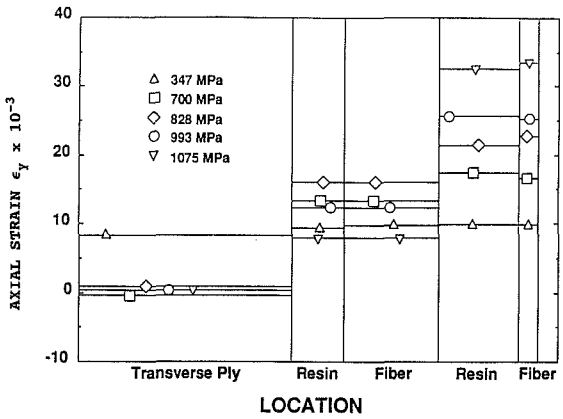


Fig. 12 Strain distribution across the grating for several different applied stress levels

on the damage that occurred in the specimen as the load was increased and on the location of the damage. From several local strain measurements at a number of locations the following conclusions have been drawn:

(1) Before the failure of the 90-deg ply, there was a difference of 14 percent in ϵ_y across the interface between 0-deg and 90-deg plies with the higher strains in the 0-deg ply. At a nominal stress of 347 MPa, the gradient $d\epsilon_y/dx = 1.2 \times 10^{-4}$ μm^{-1}. Higher strains in the 0-deg ply may indicate that very isolated 90-deg cracking occurred at even lower global stress.

(2) Before failure of the 90-deg ply, we measured a local modulus E_1 = 36.1 GPa over a gage length of about 25 μm.

(3) When the 90-deg ply failed by transverse cracking, its load-carrying capability effectively vanished.

(4) Failure of the 90-deg ply produced shearing strains in the resin-rich area between the 0-deg and 90-deg plies. These shearing strains were large and increased with load to 11.9 percent before they were relieved by fracture of adjacent fibers in the 0-deg ply.

(5) Isolated transverse cracks occurred in large numbers in longitudinal fibers at nominal stresses as low as 347 MPa. These cracks produced shearing strains in the epoxy which increased with load to about 13 percent.

(6) After failure of the 90-deg ply, the strain increments at different locations were not proportional to the increments

Downloaded 03 May 2010 to 171.66.16.20. Redistribution subject to ASME license or copyright; see http://www.asme.org/terms/Terms_Use.cfm

of the applied (global) stress. The increasing numbers of cracks in the 90-deg plies and in the longitudinal fibers produced a new local geometry at each load increment. This progressive damage by cracking resulted in strain redistribution.

(7) Cross-ply cracks extended into the 0-deg ply and effectively shifted the interface between plies. This shift produced shear strains as large as 16.7 percent in the matrix between longitudinal fibers.

(8) Local delamination occurred due to cracking between 0-deg and 90-deg plies and cracking between longitudinal fibers in the 0-deg ply. However, the specimen remained intact and supported the applied load.

(9) After delamination in the 0-deg ply at $\sigma = 1075$ MPa, fiber strains of 3.34 percent were measured. The corresponding fiber stress, neglecting biaxial effects, was 2400 MPa, which was 2.23 percent larger than the global applied tensile stress.

(10) A delamination crack passing through the moiré grating produced a step discontinuity of 7.5 displacement field. This slippage is consistent with crack-opening displacements associated with transverse cracks in the adjacent 90-deg ply.

(11) A localized shear band was evident in the epoxy matrix material adjacent to the delamination crack. This band was 2.35 μm wide and was produced by an average shearing strain of 41.4 percent.

(12) The epoxy matrix between longitudinal fibers supported normal strains as large as 3.23 percent, which corresponds to a local tensile strength in excess of 1100 MPa if biaxial effects are neglected.

(13) While these experimental results are typical, they are not unique. The strain distributions at each load are clearly dependent on the many different types of damage and the location of each damage site relative to the measurement position.

(14) It is always difficult to specify the accuracy of a measurement and this statement is particularly true when the experimental method is as new as e-beam moiré. The results were obtained from Eq. (3) and involved measuring fringe gradients. It is estimated that the gradients could be determined to $\pm$ 4 ($\pm$ 0.2 fringes in a count of five percent over a gage length of 20 to 30 μm). A second source of error is in the reference pitch p_r. The value of p_r depends on the magnification which was fixed at 1900$\times$ to produce all of the moiré fringe patterns. Variations in the magnification due to electronic instabilities in the scanning electron microscope are known to occur, but they have not been studied to date.

(15) Measurements of the strain ϵ_y in the cross ply at high loads after the region was essentially stress-free indicate that the resolution of the measurements was about $\pm$ 1000 $\mu\epsilon$ or $\pm$ 0.1 percent.

Acknowledgments

Thanks are due to R. E. Harris and J. Martinis for the use of the lithographic facility in the Electromagnetic Technology Division at NIST, and to Greg Zimmerli for introducing us to electron beam lithography.

References

Anastasi, R. F., Serabian, S. M., Shuford, R. J., and Das-Gupta, D., 1987, "Nondestructive Detection of Simulated Delaminations in Composite Laminates by Laser-Speckle Shearography," *Experimental Techniques*, Vol. 11, No. 6, June, pp. 28–31.

Bandyopadhyay, S., Gellert, E. P., Silva, V. M., and Underwood, J. H., 1989, "Microscopic Aspects of Failure and Fracture in Cross-Ply Fibre Reinforced Composite Laminates," *Journal of Composite Materials*, Vol. 23, Dec., pp. 1216–1231.

Chamis, C. C., 1974, "Micromechanics Strength Theories for Composite Materials," *Fracture and Fatigue*, Vol. 5, L. J. Broutman, ed., Academic Press, New York, pp. 93–151.

Dally, J. W., and Read, D. T., 1993, "Electron Beam Moiré," *Experimental Mechanics*, Vol. 33, No. 4, Dec., pp. 270–277.

Galiotis, C., Melanitis, N., Batchelder, D. N., Robinson, I. M., and Peacock, J. A., 1988, "Residual Strain Mapping in Carbon Fibre/PEEK Composites," *Composites*, Vol. 19, No. 4, July, pp. 312–324.

Halpin, J. C., 1984, *Primer on Composite Materials: Analysis*, Technomic, Lancaster, PA.

Kishimoto, S., Egashir, M., Shinya, N., and Carolan, R. A., "Local Micro-Deformation Analysis by Means of Microgrid and Electron Beam Moiré Fringe Method," *Proceedings of the Sixth International Conference on Mechanical Behavior of Materials*, M. Jono and T. Inoue, eds., Kyoto, Japan, Vol. 4, pp. 661–666, pp. 1991.

Lee, J-W., Allen, D. H., and Harris, C. E., 1989, "Internal State Variable Approach for Predicting Stiffness Reductions in Fibrous Laminated Composites with Matrix Cracks," *Journal of Composite Materials*, Vol. 23, Dec., pp. 1273–1291.

Post, D., Czarnek, R., Joh, D., Jo, J., and Guo, Y., 1987a, "Experimental Study of Metal-Matrix Composite," *Experimental Mechanics*, Vol. 27, No. 2, June, pp. 190–194.

Post, D., Czarnek, R., and Joh, D., 1987b, "Shear Strains in a Graphite/PEEK Beam by Moiré Interferometry," *Experimental Mechanics*, Vol. 27, No. 3, Sept., pp. 246–249.

Post, D., and Wood, J. D., "Determination of Thermal Strains by Moiré Interferometry," *Experimental Mechanics*, Vol. 29, No. 3, Sept., pp. 318–322.

Post, D., Dai, F. L., Guo, Y., and Ifju, P., 1989, "Interlaminar Shear Moduli of Cross-ply Laminates: An Experimental Analysis," *Journal of Composite Materials*, Vol. 23, No. 3, pp. 264–279.

Tsai, S. W., and Hahn, H. T., 1980, *Introduction to Composite Materials*, Technomic, Lancaster, PA, 1980.

Vinson, J. R., and Sierakowski, R. L., 1986, *The Behavior of Structures Composed of Composite Materials*, Martinus Nijhoff, Boston, MA.

Downloaded 03 May 2010 to 171.66.16.20. Redistribution subject to ASME license or copyright; see http://www.asme.org/terms/Terms_Use.cfm

Free-Edge Effects in Anisotropic Laminates Under Extension, Bending and Twisting, Part I: A Stress-Function-Based Variational Approach[1]

W.-L. Yin
School of Civil Engineering,
Georgia Institute of Technology,
Atlanta, GA 30332

A variational method involving Lekhnitskii's stress functions is used to determine the interlaminar stresses in a multilayered strip of laminate subjected to arbitrary combinations of axial extension, bending, and twisting loads. The stress functions in each layer are approximated by polynomial functions of the thickness coordinate. The equilibrium equations, the traction-free boundary conditions, and the continuity conditions of the interlaminar stresses are exactly satisfied in the present analysis, while the compatibility equations and the continuity of the displacements across the interfaces are enforced in an averaged sense by applying the principle of complementary virtual work. This yields an eigenvalue problem for the interfacial values of the stress functions and their normal derivatives. Interlaminar stresses for all three distinct loading cases may be obtained, in a single solution process, by combining the eigenfunctions with appropriate particular solutions (peculiar to each loading case) so as to ensure satisfaction of the traction-free boundary condition at the free edge.

1 Introduction

Composite laminates are prone to severe interlaminar stresses along a free edge. Theoretical studies based on the assumption of layer-wise homogeneity and linearly elastic behavior suggest that a singularity of the stress field generally exists at the intersection of a free edge with an interface between two dissimilar materials (Bogy, 1968; Ting and Chou, 1981). From a practical point of view, the presence of a stress singularity and its effect on the region outside the immediate neighborhood of the singularity may be of greater importance than the precise mathematical form of the singularity (deduced by strictly applying the simplifying assumptions of layerwise homogeneity and linear elasticity to a corner region of very small size, and thereby producing idealized and unrealistic local results). This is because a singularity actually indicates a region of severe stress gradient in which the stress field is affected significantly by nonlinear and inelastic material response and microscopic heterogeneity. This is especially true if, as in the case of free edges of laminates composed of thin plies, the regions of high stress gradient are only one order of magnitude greater than the characteristic length of the microstructure—the diameter of the reinforcing fibers and the spacing between adjacent fibers.

It follows from this reasoning that, when assessing the detrimental effects of free-edge interlaminar stresses, one should not pay too much attention to the minute details of the computed local stress near a mathematical singularity based on simplifying constitutive assumptions and layer-wise homogenization. It is more important to extract from the computed results certain quantities which manifest the overall mechanical effects and characteristics of a small, severly stressed region—quantities whose values do not change appreciably with refinement in material and computational modeling over the region. Examples of such global measures include the well-known path-independent integrals. They also include the maximum values of certain stress functions and their derivatives along an interface, which are introduced in Part II of this paper.

Approximate solutions of the free-edge interlaminar stress problem may be obtained by directly solving the governing differential equations, for example, through the use of the

[1]A preliminary version of this paper was presented in AIAA/ASME/ASCE/AHS/ASC 32nd Structures, Structural Dynamics and Materials Conference, Apr. 1991, Baltimore, MD.

Contributed by the Applied Mechanics Division of THE AMERICAN SOCIETY OF MECHANICAL ENGINEERS for publication in the ASME JOURNAL OF APPLIED MECHANICS.

Discussion on this paper should be addressed to the Technical Editor, Professor Lewis T. Wheeler, Department of Mechanical Engineering, University of Houston, Houston, TX 77204-4792, and will be accepted until four months after final publication of the paper itself in the ASME JOURNAL OF APPLIED MECHANICS.

Manuscript received by the ASME Applied Mechanics Division, Oct. 16, 1992; final revision, Apr. 14, 1993. Associate Technical Editor: F. Y. M. Wan.

Copyright © 1994 by ASME
Downloaded 03 May 2010 to 171.66.16.20. Redistribution subject to ASME license or copyright; see http://www.asme.org/terms/Terms_Use.cfm

finite difference method (Pipes and Pagano, 1970; Altus et al., 1980) or (complex) series expansion in conjunction with boundary collocation (Wang and Choi, 1982; Zwiers et al., 1982). While such solution methods have been applied to laminates composed of a small number of layers, they are not suitable for efficient solution of multilayered laminates.

An attractive and practical alternative approach to the interlaminar stress problem is provided by the variational method. Most of the previous works in this area, including a large number of studies using finite element discretization, were based on the displacement formulation and the principle of minimum potential energy. Other researchers used the displacement/stress hybrid formulation and Reissner's variational principle (Pagano, 1978a,b; Pagano and Soni, 1989; the last reference includes selected references to important works on edge effects). However, since the present concern is with the stress concentration near the free edge and not with the displacement solution, a pure stress formulation based on the complementary virtual work principle should be a preferred, natural choice which leads logically and efficiently to better overall estimates for the stress field (a similar viewpoint was expressed by Bar-Yoseph and Pian, 1981).

In this work, Lekhnitskii's stress functions are introduced in each anisotropic layer of a composite laminate. This ensures that the approximate solutions of the present approach satisfy *exactly* the equilibrium equations in all parts of the laminate, including the interfacial corner regions with steep stress gradients. Furthermore, the traction-free boundary conditions and the continuity of interlaminar stresses are *exactly* satisfied (the latter on entire interfaces, including the short segments adjacent to the free edge), while the compatibility of strain and the interfacial continuity of displacements are enforced in an averaged sense through the condition of stationary complementary energy. These exact requirements upon the stress solutions in the present analysis scheme help to avoid or alleviate difficulties that might arise in a displacement-based approach, whose solutions are liable to significant violation of the equilibrium equations and the continuity of tractions in small but critical regions of severe stress (see Spilker, 1980, for a discussion concerning the importance of satisfying free-edge traction conditions in finite element analysis).

Besides the constitutive assumption of linear anisotropic elasticity for individual layers, the only assumption introduced in the present analysis is that the stress functions in each layer are polynomial functions of the thickness coordinate. No a priori assumption is made concerning the dependence of the stress functions on the coordinate parallel to the interface. Rather, it follows as a consequence of the stationary complementary energy principle that the form of dependence is governed by a system of linear ordinary differential equations with constant coefficients. This system of equations together with the homogeneous boundary conditions along the free edges define an eigenvalue problem. The solution of the eigenvalue problem is an appropriate combination of the eigenfunctions with a particular solution. The latter represents the *limiting* interior stress field away from the free edge and is a function of the thickness coordinate only. There is one particular solution unique to each one of the three fundamental cases of strain loading—axial extension, bending, and twisting. However, the eigenvalues and the eigenfunctions are the same for all three types of loading. Thus the present approach has the additional advantage that the solutions to all loading cases may be obtained simultaneously. In contrast, implementation of the finite element and other numerical solution procedures usually must be repeated for each loading case.

The present analysis method is applicable, in principle, to a laminated strip composed of different anisotropic layers with arbitrary combinations of layer thicknesses, orientation angles and elastic properties. Sample solutions are obtained in Part II of this paper for symmetric, four-layer, angle-ply, and cross-ply laminates under various strain loads, and the accuracy of the results for the interlaminar stresses is confirmed by comparison with existing numerical solutions for the loading case of axial extension. Superior accuracy may be achieved by using higher-degree polynomial expansions of the stress functions in each layer.

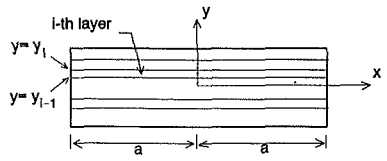


Fig. 1 A multilayered laminate

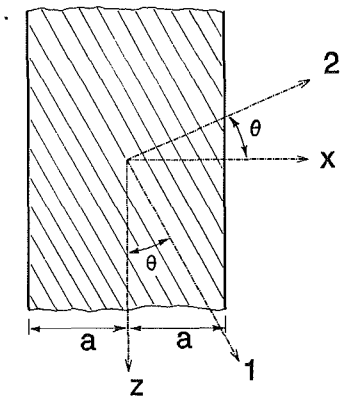


Fig. 2 Transformation of coordinates in a layer

2 Elasticity of an Orthotropic Layer Referred to the Global Coordinates of the Laminate

Consider a laminated strip of thickness $t = 2y^*$, with two parallel free edges at $x = \pm a$, and consisting of $n + 1$ unidirectional, fiber-reinforced composite layers separated by n planar interfaces. The layers and their interfaces will be numbered from the bottom up. Thus the ith layer is bounded below by the $(i - 1)$th interface, $y = y_{i-1}$, and bounded above by the ith interface, $y = y_i$, where the coordinate y is referred to the middle plane of the laminate (Fig. 1). The layer has the thickness $h_i = y_i - y_{i-1}$. Each unidirectional layer will be regarded in the present analysis as a homogeneous, orthotropic, linearly elastic medium with the extensional elastic modulus E_1 along the fiber direction and moduli E_2 and E_3 along the other two orthotropic directions. Other material moduli needed to characterize the elasticity of the layer are ν_{23}, ν_{31}, ν_{12}, G_{23}, G_{31}, and G_{12} (Lekhnitskii, 1963, pp. 20–21). It is more convenient for the present analysis to use the compliance coefficients $S_{ij}(i, j = 1, \ldots, 6)$ to define the constitutive equation of the layer as follows:

$$\epsilon_i = \sum_{j=1}^{3} S_{ij}\sigma_j \quad (i = 1, 2, 3) \tag{1a}$$

$$\gamma_{23} = S_{44}\tau_{23}, \quad \gamma_{13} = S_{55}\tau_{13}, \quad \gamma_{12} = S_{66}\tau_{12}. \tag{1b}$$

If the elastic properties of the layer are transversely isotropic in the plane perpendicular to the fiber direction, then $E_2 = E_3$, $\nu_{12} = \nu_{13}$ and $G_{12} = G_{13}$. Furthermore, $S_{11} = 1/E_1$, $S_{22} = S_{33} = 1/E_2$, $S_{12} = S_{13} = -\nu_{12}/E_1 = -\nu_{21}/E_2$, $S_{23} = -\nu_{23}/E_2$, $S_{44} = 1/G_{23}$ and $S_{55} = S_{66} = 1/G_{12}$.

The thickness direction of all layers (i.e., the y-axis) is an orthotropic direction and this direction will be taken as the 3-direction in every layer. Within the plane of the layer, the fiber direction is oriented at a constant angle θ with respect to the

Downloaded 03 May 2010 to 171.66.16.20. Redistribution subject to ASME license or copyright; see http://www.asme.org/terms/Terms_Use.cfm

z-direction (the direction parallel to the free edges, see Fig. 2). Transformation of the stress components from the (z, x, y) coordinate system to the orthotropic material system (1, 2, 3) follows the relation

$$\begin{Bmatrix} \sigma_1 \\ \sigma_2 \\ \sigma_3 \\ \tau_{23} \\ \tau_{13} \\ \tau_{12} \end{Bmatrix} = \begin{bmatrix} \cos^2\theta & \sin^2\theta & 0 & 0 & 0 & \sin 2\theta \\ \sin^2\theta & \cos^2\theta & 0 & 0 & 0 & -\sin 2\theta \\ 0 & 0 & 1 & 0 & 0 & 0 \\ 0 & 0 & 0 & \cos\theta & -\sin\theta & 0 \\ 0 & 0 & 0 & \sin\theta & \cos\theta & 0 \\ -\frac{1}{2}\sin 2\theta & \frac{1}{2}\sin 2\theta & 0 & 0 & 0 & \cos 2\theta \end{bmatrix} \begin{Bmatrix} \sigma_z \\ \sigma_x \\ \sigma_y \\ \tau_{xy} \\ \tau_{yz} \\ \tau_{xz} \end{Bmatrix}$$

The tensorial strain components transform in exactly the same manner. For simplicity we denote the matrix of transformation in the last equation by $\mathbf{H}(\theta)$ and the matrix of Eq. (1) by $\mathbf{S}$. Then $\mathbf{H}(-\theta)$ is the inverse matrix of $\mathbf{H}(\theta)$. Furthermore,

$$\{\epsilon_z, \epsilon_x, \epsilon_y, \gamma_{xy}/2, \gamma_{yz}/2, \gamma_{xz}/2\}^t = \mathbf{H}(-\theta)\mathbf{SH}(\theta) \times \{\sigma_z, \sigma_x, \sigma_y, \tau_{xy}, \tau_{yz}, \tau_{xz}\}^t, \quad (2)$$

where the superscript t denotes the transpose operation. The 6×6 symmetric compliance matrix $[a_{ij}]$ of the layer (referred to the global axes x, y, and z) may then be obtained from the matrix $\mathbf{H}(-\theta)\mathbf{SH}(\theta)$ according to

$$[a_{ij}] = \Lambda\mathbf{H}(-\theta)\mathbf{SH}(\theta), \quad (3)$$

in which Λ is the diagonal matrix with the elements 1, 1, 1, 2, 2, and 2.

From the first row of Eq. (2) one obtains $\sigma_z = (\epsilon_z - a_{12}\sigma_x - a_{13}\sigma_y - a_{16}\tau_{xz})/a_{11}$. Substitution into Eq. (2) yields

$$\begin{Bmatrix} \sigma_z \\ \epsilon_x \\ \epsilon_y \\ \gamma_{xy} \\ \gamma_{yz} \\ \gamma_{xz} \end{Bmatrix} = \begin{bmatrix} 1/a_{11} & -a_{12}/a_{11} & -a_{13}/a_{11} & 0 & 0 & -a_{16}/a_{11} \\ a_{12}/a_{11} & \beta_{22} & \beta_{23} & 0 & 0 & \beta_{26} \\ a_{13}/a_{11} & \beta_{23} & \beta_{33} & 0 & 0 & \beta_{36} \\ 0 & 0 & 0 & \beta_{44} & \beta_{45} & 0 \\ 0 & 0 & 0 & \beta_{45} & \beta_{55} & 0 \\ a_{16}/a_{11} & \beta_{26} & \beta_{36} & 0 & 0 & \beta_{66} \end{bmatrix} \begin{Bmatrix} \epsilon_z \\ \sigma_x \\ \sigma_y \\ \tau_{xy} \\ \tau_{yz} \\ \tau_{xz} \end{Bmatrix} \quad (4)$$

where the coefficients $\beta_{ij} \equiv a_{ij} - a_{1i}a_{1j}/a_{11}$ (for $i, j \neq 1$) were introduced by Lekhnitskii (1963, p. 109).

3 Generalized Plane Deformation of a Laminated Strip

For a homogeneous, anisotropic elastic medium of cylindrical shape with the generators parallel to the z-direction, Lekhnitskii (1963, pp. 107–108) investigated the class of infinitesimal deformations for which the stress tensor is independent of the z-coordinate. He found that the class consists of deformations with the displacements

$$\begin{aligned} w(z, x, y) &= (A\,x - B\,y + C)z + W(x, y) + \omega_1 y - \omega_2 x + w_o, \\ u(z, x, y) &= -A\,z^2/2 - \Theta\,y\,z + U(x, y) + \omega_2 z - \omega_3 y + u_o, \\ v(z, x, y) &= B\,z^2/2 + \Theta\,x\,z + V(x, y) + \omega_3 x - \omega_1 z + v_o. \end{aligned} \quad (5)$$

Starting from a plane deformation $U(x, y)$ and $V(x, y)$, one may obtain generalized plane deformations of Eq. (5) by superposing rigid-body translations, rotations, shearing along the z-axis (characterized by the function $W(x, y)$), uniform extension and twisting along the same axis (the constants C and Θ), and uniform bending deformation with respect to the y and x-axes (the constants A and B, respectively).

In the present work, we study the interlaminar stresses in a thin laminated strip bounded by two parallel free edges ($x = \pm a$) under mechanical loads at the two ends ($z = 0, l$). The end loads are such that the resulting stress in the strip depends only on x and y but not on the axial coordinate z. In each layer of the laminated strip, the displacement functions have the form given by Eq. (5). In order to satisfy the interfacial continuity of the displacements, either exactly or in an averaged sense, it is necessary that the set of constants A, B, C, and Θ be the same for all layers.

It is well known that intense interlaminar stresses are localized in the vicinity of the free edges. Along a free edge $x = \pm a$, the in-plane normal and shearing stress resultants N_x and N_{xz} vanish, and so does the normal bending moment M_x and the transverse shearing force V_x. The nonvanishing force and moments are N_z, M_z, and M_{zx}, and their conjugate kinematical variables (in the strain energy density function of the classical laminate theory) are the axial extensional strain in the middle plane, $\epsilon_z^o = C$, the bending curvature $\kappa_z = B$, and the twisting curvature $\kappa_{zx} = \Theta$. Bending with respect to the y-axis introduces a large in-plane strain in the laminate, and this usually does not happen (or becomes unstable) unless the thickness and width of the laminated strip ($2y^*$ and $2a$) are comparable in magnitude. Hence, for a thin laminate, the local states of loading and deformation near $x = a$ are characterized by the free-edge condition and the three constant parameters B, C, and Θ.

4 Stress Functions: Interface and Boundary Conditions

A stress field in the ith layer, depending only on x and y and satisfying the differential equations of equilibrium, may

Downloaded 03 May 2010 to 171.66.16.20. Redistribution subject to ASME license or copyright; see http://www.asme.org/terms/Terms_Use.cfm

be expressed in terms of a pair of stress functions $F^{(i)}(x, y)$ and $\Psi^{(i)}(x, y)$ in the following manner:

$$\sigma_x^{(i)} = F^{(i)}{}_{,yy}, \quad \sigma_y^{(i)} = F^{(i)}{}_{,xx}, \quad \tau_{xy}^{(i)} = -F^{(i)}{}_{,xy}$$
$$\tau_{xy}^{(i)} = \Psi^{(i)}{}_{,y}, \quad \tau_{yz}^{(i)} = -\Psi^{(i)}{}_{,x} \tag{6}$$

Obviously, an arbitrary bilinear function of x and y and an arbitrary constant may be added to the first and the second stress function, respectively, without affecting the resulting stress field in the layer. The first row of Eq. (3) yields

$$\sigma_z^{(i)} = (\epsilon_z - a_{12}^{(i)} F^{(i)}{}_{,yy} - a_{13}^{(i)} F^{(i)}{}_{,xx} - a_{16}^{(i)} \Psi^{(i)}{}_{,y})/a_{11}^{(i)}. \tag{7}$$

The continuity of the normal and shearing stresses across the ith interface requires that $(F^{(i+1)} - F^{(i)})_{,xx}$, $(F^{(i+1)}{}_{,y} - F^{(i)}{}_{,y})_{,x}$ and $(\Psi^{(i+1)} - \Psi^{(i)})_{,x}$ vanish along the interface. Hence we may appropriately choose an additive bilinear function and an additive constant for the stress functions in the $(i + 1)$th layer so that, along the interface $y = y_i$,

$$F^{(i+1)} = F^{(i)}, \quad F^{(i+1)}{}_{,y} = F^{(i)}{}_{,y}, \quad \Psi^{(i+1)} = \Psi^{(i)}. \tag{8}$$

Furthermore, without loss of generality the stress functions in the bottom layer may be chosen in such a way that, over the lower surface of the laminate, $y = -y^*$, one has

$$F^{(1)} = 0, \quad F^{(1)}{}_{,y} = 0, \quad \Psi^{(1)} = 0. \tag{9}$$

By integrating σ_x and τ_{xz} through the thickness of all layers, and making use of the continuity of $F_{,y}$ and Ψ across the interfaces, one finds that the stress resultants N_x and N_{xz} are equal, respectively, to the values of $F_{,y}$ and Ψ on the upper surface of the laminate. Let the values be denoted by G^* and Ψ^*, i.e.,

$$N_x = \sum_i \int \sigma_x^{(i)} dy = \sum_i \int F^{(i)}{}_{,yy}\, dy$$
$$= \sum_i F^{(i)}{}_{,y} \Big|_{y = y_{i-1}}^{y = y_i} = F^{(n+1)}{}_{,y} \Big|_{y = y_0}^{y = y^*} = G^*,$$
$$N_{xz} = \sum_i \int \tau_{xz}^{(i)} dy = \sum_i \int \Psi^{(i)}{}_{,y}\, dy = \Psi^*.$$

Similarly, the stress moment M_x has the expression $M_x = F^* - y^* G^*$, where F^* is the value of the stress function F on the top surface. For the case considered in the present work, N_x, N_{xz}, and M_x all vanish because of the free-edge conditions. Hence,

$$F^* = G^* = \Psi^* = 0. \tag{10}$$

Finally, the absence of surface tractions along the free edges $x = \pm a$ implies that $F_{,yy} = -F_{,xy} = \Psi_{,y} = 0$. Integration with respect to the thickness coordinate yields the following results on $x = \pm a$,

$$F = F_{,x} = \Psi = 0. \tag{11}$$

Equations (8), (9), (10), and (11) imply that, for the present problem, the stress functions in the layers may be chosen in such a way that F, Ψ, and $\partial F/\partial n$ vanish on the boundary surfaces $x = \pm a$ and $y = \pm y^*$, and are continuous across all layer interfaces.

5 The Principle of Complementary Virtual Work

A variation of the stress field in the ith layer satisfies the equilibrium equations $\delta\sigma_{ij,j} = 0$ as well as the free-edge condition and the continuity of δF, $\delta F_{,y}$ and $\delta\Psi$ across the upper and lower interfaces. Hence,

$$0 = \int\int\int u_i \delta\sigma_{ij,j}\, dx\, dy\, dz$$
$$= \int\int\int \{(u_i \delta\sigma_{ij})_{,j} - u_{i,j}\delta\sigma_{ij}\}\, dx\, dy\, dz$$
$$= \oint\!\!\oint u_i \delta\sigma_{ij} n_j dA - \int\int\int \frac{1}{2}(u_{i,j} + u_{j,i})\delta\sigma_{ij}\, dx\, dy\, dz. \tag{12}$$

Since the stresses in all layers are independent of the axial coordinate z, it is sufficient to consider only those variations of the stresses which are also independent of z. Furthermore, one needs only consider an interval of the laminated strip of unit length along the axial direction, $0 \le z \le 1$. By summing Eq. (12) over all layers, and making use of the traction-free boundary conditions and the interfacial continuity of the interlaminar stresses, one obtains

$$\sum \int\int (\Delta u\ \delta\tau_{xz} + \Delta v\ \delta\tau_{yz} + \Delta w\ \delta\sigma_z)dx\, dy - \sum \int ([u]_i \delta\tau_{xy}$$
$$+ [v]_i \delta\sigma_y + [w]_i \delta\tau_{yz})dx = \sum \int\int \epsilon_{ij}\ \delta\sigma_{ij}\, dx\, dy, \tag{13}$$

where the double integrals are summed over all layers and the single integrals are summed over all interfaces $y = y_i$. The bracket symbol, $[\ ]_i$, denotes the jump of the quantity inside the bracket across the ith interface. Δu, Δv, and Δw stand for the differences of the displacements at $z = 1$ and $z = 0$. They may be obtained from Eq. (5) with $A = 0$:

$$\Delta u = -\Theta y + \omega_2, \quad \Delta v = B/2 + \Theta x - \omega_1, \quad \Delta w = C - B\, y.$$

Equations (6) and (7) yield, in each layer,

$$\delta\tau_{xz} = \delta\Psi_{,y}, \quad \delta\tau_{yz} = -\delta\Psi_{,x},$$
$$\delta\sigma_z = -(a_{12}\delta F_{,yy} + a_{13}\delta F_{,xx} + a_{16}\delta\Psi_{,y})/a_{11}. \tag{14}$$

Hence the double integrals on the left-hand side of Eq. (13) yield, after integration by parts,

$$-\sum (B\, a_{16}/a_{11} - 2\Theta)\int\int \delta\Psi\, dx\, dy$$
$$+ B\sum [a_{12}/a_{11}]_i \int \delta F_i\, dx + \sum (C - B\, y_i)\int ([a_{12}/a_{11}]_i \delta G_i$$
$$+ [a_{16}/a_{11}]_i)\delta\Psi_i dx - \sum \int [\omega_2]_i \delta\Psi_i dx,$$

while the single integrals in Eq. (13) yield

$$-\sum \int ([u_{,x}]_i \delta G_i + [v_{,xx}]_i \delta F_i$$
$$+ [u_{,z} + w_{,x}]_i \delta\Psi_i)dx + \sum \int [\omega_2]_i \delta\Psi_i dx.$$

Here F_i, G_i, and Ψ_i stand for the values of F, $F_{,y}$, and Ψ, respectively, on the ith interface. Substituting the preceding results into Eq. (13) and imposing the conditions of interfacial continuity of the tangential strains ϵ_x, γ_{xz} and of the curvature $v_{,xx}$, one obtains

$$\sum \int\int \epsilon_{ij}\delta\sigma_{ij}\, dx\, dy + \sum (B\, a_{16}^{(i)}/a_{11}^{(i)} - 2\Theta)\int\int \delta\Psi\, dx\, dy$$
$$- \sum (C - By_i) \int ([a_{12}/a_{11}]_i \delta G_i + [a_{16}/a_{11}]_i \delta\Psi_i)dx$$
$$- B\sum [a_{12}/a_{11}]_i \int \delta F_i dx = 0. \tag{15a}$$

The first term of the preceding equation may be expressed in terms of the stress functions. Let $\{\sigma\} = \{F_{,yy}, F_{,xx}, -F_{,xy}, -\Psi_{,x}, \Psi_{,y}\}^t$ and let $\mathbf{B}$ denote the 5×5 submatrix obtained from the matrix of Eq. (4) by removing the first row and the first column. Then Eqs. (4), (6), and (14) yield

$$\sum \int\int \epsilon_{ij}\delta\sigma_{ij}\, dx\, dy = \sum \int\int \{\sigma\}^t \mathbf{B}\delta\{\sigma\}\, dx\, dy. \tag{15b}$$

6 Polynomial Approximations of the Stress Functions

In a variational method of solution, the stress functions F and Ψ in all layers are to be determined within a class of

Downloaded 03 May 2010 to 171.66.16.20. Redistribution subject to ASME license or copyright; see http://www.asme.org/terms/Terms_Use.cfm

admissible functions satisfying the traction-free boundary conditions (Eqs. (9)–(11)) and the interfacial continuity of F, $F_{,y}$ and Ψ. The criterion of selection is that Eq. (15) should be satisfied for arbitrary admissible variations δF and $\delta\Psi$. The criterion ensures, in an averaged sense, the compatibility of strain in all layers and the continuity of the displacements across all interfaces. If the layers constituting the laminate are very thin, one may approximate the stresses in each layer by polynomial functions of the thickness coordinate. Then the class of admissible stress functions consists of polynomial functions of y, with the coefficients depending on x.

In the ith layer, we define the nondimensional thickness coordinate η by

$$\eta = (y - y_{i-1})/(y_i - y_{i-1}).$$

In the classical plate theory the in-plane stresses vary linearly in the thickness direction. This feature is approximately valid in each thin layer of a laminated plate, except in regions close to the free edges. Hence, the stress function $F(x, y)$ in each layer may be approximated by a polynomial function of degree three in the normalized thickness coordinate η. Now the stress function in the ith layer must assume values $F_i(x)$ and $F_{i-1}(x)$, respectively, on the interface $y = y_i$ and y_{i-1}, and the y-derivative of the stress function must assume values $G_i(x)$ and $G_{i-1}(x)$ on these interfaces. Hence the cubic polynomial approximation of the stress function in the ith layer must have the following expression:

$$F^{(i)}(x, \eta) = (1 - 3\eta^2 + 2\eta^3)F_{i-1}(x) + (\eta - 2\eta^2 + \eta^3)h_i G_{i-1}(x) + (3\eta^2 - 2\eta^3)F_i(x) + (\eta^3 - \eta^2)h_i G_i(x) \quad (i = 1, 2, \ldots, n+1) \quad (16)$$

where $F_o(x) \equiv G_o(x) \equiv F_{n+1}(x) \equiv G_{n+1}(x) \equiv 0$ in view of Eqs. (9) and (10).

These approximate expressions of the stress function yield interlaminar stresses σ_y, τ_{xy} and in-plane stress σ_x with cubic, quadratic and linear dependence on η, respectively, in each layer. For the sake of consistency the interlaminar shearing stress τ_{yz} and the in-plane stress τ_{xz} will be approximated, respectively, by quadratic and linear functions of η. Then, according to Eq. (6), the stress function $\Psi^{(i)}$ depends quadratically on y and has the expression

$$\Psi^{(i)}(x, \eta) = (1 - \eta^2)\Psi_{i-1}(x) + \eta^2\Psi_i(x) + (\eta - \eta^2)h_i H_{i-1}(x), \quad (i = 1, 2, \ldots, n+1) \quad (17)$$

where $\Psi_o(x) \equiv \Psi_{n+1}(x) \equiv 0$, $H_0(x)$ is the value of $\Psi_{,y}$ on the bottom surface, $\Psi_i(x)$ is the value of Ψ on the ith interface and $H_i(x)$ is the value of $\Psi_{,y}$ on the *upper* side of the same interface (notice that, although Ψ is continuous across each interface, $\Psi_{,y}$ is generally discontinuous). Improved approximate solutions for the interlaminar stresses may be obtained by using higher-degree polynomial expansions of the stress functions. A solution that yields polynomial expansions of the fifth, fourth, and third degree in η, respectively, for the interlaminar stresses σ_y, τ_{xy}, and τ_{yz}, is obtained in Part II of this paper for a symmetric, four-layer, cross-ply laminate, in addition to less elaborate variational solutions based on Eqs. (16) and (17).

7 An Eigenvalue Problem for the Functions F_i, G_i, Ψ_i, and H_i

According to the approximation of Eqs. (16) and (17), the stress functions in all layers are completely determined by $3n$ functions $F_i(x)$, $G_i(x)$, $\Psi_i(x)$ $(i = 1, 2, \ldots, n)$ and $n + 1$ functions $H_i(x)$ $(i = 0, 1, \ldots, n)$. Let this set of $4n + 1$ functions be arranged as the components of a column vector $\{X\}$ according to

$$X_i = F_i(x), \quad X_{i+n} = G_i(x), \quad X_{i+2n} = \Psi_i(x), \quad (i = 1, 2, \ldots, n)$$
$$X_{i+3n+1} = H_i(x) \quad (i = 0, 1, \ldots, n). \quad (18a)$$

Substituting Eqs. (16) and (17) into Eq. (15), performing the integration with respect to η, and integrating by parts with respect to x, we obtain

$$\{\delta X\}^t \left\{ \left(\mathbf{W} \frac{d^4}{dx^4} + \mathbf{V} \frac{d^2}{dx^2} + \mathbf{U} \right) \{X\} - \{b\} \right\} = 0, \quad (19)$$

where

$$b_i = B[a_{12}/a_{11}]_i, \quad b_{i+n} = (C - By_i)[a_{12}/a_{11}]_i$$
$$b_{i+2n} = (C - By_i)[a_{16}/a_{11}]_i + 2h_{i+1}(2\Theta - B\, a_{16}^{(i+1)}/a_{11}^{(i+1)})/3 + h_i(2\Theta - Ba_{16}^{(i)}/a_{11}^{(i)})/3, \quad (i = 1, 2, \ldots, n)$$
$$b_{i+3n+1} = h_{i+1}^2(2\Theta - B\, a_{16}^{(i+1)}/a_{11}^{(i+1)})/6 \quad (i = 0, 1, \ldots, n). \quad (18b)$$

In Eq. (19), $\mathbf{U}$, $\mathbf{V}$, and $\mathbf{W}$ are constant real symmeteric matrices determined completely by the integral expressions in Eq. (15*b*). It is clear from Eq. (15*b*) that the fourth-order derivatives in Eq. (19) arise only from the integrals $\Sigma \int\int \beta_{33}^{(i)} F^{(i)}{}_{,xx}\delta F^{(i)}{}_{,xx}\, dx\, dy$, i.e., they only involve the stress functions $F^{(i)}$ but not $\Psi^{(i)}$. Hence, by virtue of the representation of Eq. (16), the coefficient matrix $\mathbf{W}$ of the operator d^4/dx^4 has nonvanishing elements only in a $2n \times 2n$ square submatrix in the upper left corner.

The elements of the three matrices have lengthy and complex expressions and it is impractical to obtain these expressions without using symbolic algebraic programs. In the present analysis, the symbolic algebraic program MACSYMA (1988) is used to obtain the compliance coefficients $\beta_{ij}^{(i)}$ of each layer from Eqs. (1)–(4), and to generate the matrices $\mathbf{U}$, $\mathbf{V}$, and $\mathbf{W}$ from Eqs. (15*b*), (16), and (17).

Equation (19) is satisfied for arbitrary variations δH_0, δF_1, $\delta G_1, \delta\Psi_1, \ldots$ and δH_n if and only if $\{X\}$ satisfies the following Euler-Lagrange equation:

$$\left(\mathbf{W} \frac{d^4}{dx^4} + \mathbf{V} \frac{d^2}{dx^2} + \mathbf{U} \right) \{X\} = \{b\}. \quad (20)$$

Equation (20) and the homogeneous boundary conditions at the free edges

$$H_0 = 0 \quad \text{and} \quad F_i = F_i' = G_i = G_i' = \Psi_i = H_i = 0 \quad (i = 1, 2, \ldots, n) \quad \text{at} \quad x = \pm a \quad (21)$$

(where the primes indicate differentiation with respect to x) define an eigenvalue problem where the eigenvalues are the roots of the characteristic equation (Ince, 1927)

$$\text{Determinant}(\mathbf{W}\lambda^4 + \mathbf{V}\lambda^2 + \mathbf{U}) = 0. \quad (22)$$

The eigenvector corresponding to each eigenvalue may be determined from the homogeneous differential equation associated with Eq. (20). The eigenfunctions have the form $\{c\}\exp(\pm\lambda_k x)$, where $\{c\}$ is a constant vector with real or complex components depending on whether λ_k is a real or complex eigenvalue.

When the eigenvalue problem of Eqs. (20) and (21) has been solved for $\{X\}$, the stress functions in the successive layers are given analytically by Eqs. (16) and (17) and the stress field in each layer is given by Eq. (6). However, the interlaminar stresses along the ith interface may be directly obtained by differentiating the functions F_i, G_i, and Ψ_i.

$$\sigma_y = F_i''(x), \quad \tau_{xy} = -G_i'(x), \quad \tau_{yz} = -\Psi_i'(x). \quad (23)$$

It is important to emphasize that no extraneous numerical error is introduced in the evaluation of Eq. (23) because the derivatives are obtained analytically through differentiation of exponential and sinusoidal functions. This is in contrast with

Downloaded 03 May 2010 to 171.66.16.20. Redistribution subject to ASME license or copyright; see http://www.asme.org/terms/Terms_Use.cfm

numerical differentiation of finite element displacement solutions to obtain strain and stress fields, where each step of differentiation may introduce additional errors besides those that are inherent in the original displacement solution.

The preceding analysis reduces the interlaminar stress problem of a multilayered laminate into a purely mathematical eigenvalue problem by means of the variational method. Solutions are obtained in Part II of this paper for the classical problem of symmetric, four-layer laminates under the three fundamental types of strain loads.

Acknowledgment

This article is based partially on research work performed under a U.S. Army Research Office contract to Georgia Institute of Technology and partially on work supported by a contract from the NASA Langley Research Center to Lockheed Aeronautical Systems Company.

References

Altus, E., Rotem, A., and Shmueli, M., 1980, "Free Edge Effect in Angle Ply Laminates—A New Three Dimensional Finite Difference Solution," *J. Composite Mat.*, Vol. 14, pp. 21–30.

Bar-Yoseph, P., and Pian, T. H. H., 1981, "Calculation of Interlaminar Stress Concentration in Composite Laminate," *J. Composite Mat.*, Vol. 15, pp. 225–239.

Bogy, D. B., 1968, "Edge-Bonded Dissimilar Orthogonal Elastic Wedges Under Normal and Shear Loading," ASME JOURNAL OF APPLIED MECHANICS, Vol. 35, pp. 460–466.

Ince, E. L., 1927, *Ordinary Differential Equations*, Dover, New York, pp. 144–148.

Lekhnitskii, S. G., 1963, *Theory of Elasticity of an Anisotropic Elastic Body*, Holden-Day, San Francisco, CA.

MACSYMA Reference Manual, 1988, Version 13, Symbolics, Inc., Burlington, MA.

Pagano, N. H., 1978a, "Stress Fields in Composite Laminates," *Int. J. Solids Struc.*, Vol. 14, pp. 385–400.

Pagano, N. J., 1978b, "Free Edge Stress Fields in Composite Laminates," *Int. J. Solids Struc.*, Vol. 14, pp. 401–406.

Pagano, N. J., and Soni, S. R., 1989, "Models for Studying Free-Edge Effects," *Interlaminar Response of Composite Materials*, N. J. Pagano, ed., Elsevier, Amsterdam.

Pipes, R. B., and Pagano, N. J., 1970, "Interlaminar Stresses in Composite Laminates Under Uniform Axial Extension," *J. Composite Mat.*, Vol. 4, pp. 538–548.

Spilker, R. L., 1980, "Edge Effects in Symmetric Composite Laminates: Importance of Satisfying the Traction-Free-Edge Condition," *J. Composite Materials*, Vol. 14, pp. 2–20.

Ting, T. C. T., and Chou, S. C., 1981, "Edge Singularities in Anisotropic Composites," *Int. J. Solids Struc.*, Vol. 17, pp. 1057–1068.

Wang, S. S., and Choi, I., 1982, "Boundary-Layer Effects in Composite Laminates—I. Free-Edge Stress Singularities—II. Free-Edge Stress Solutions and Basic Characteristics," ASME JOURNAL OF APPLIED MECHANICS, Vol. 49, pp. 541–560.

Zwiers, R. I., Ting, T. C. T., and Spilker, R. L., 1982, "On the Logarithmic Singularity of Free-Edge Stress in Laminated Composites Under Uniform Extension," ASME JOURNAL OF APPLIED MECHANICS, Vol. 49, pp. 561–569.

Downloaded 03 May 2010 to 171.66.16.20. Redistribution subject to ASME license or copyright; see http://www.asme.org/terms/Terms_Use.cfm

Free-Edge Effects in Anisotropic Laminates Under Extension, Bending, and Twisting, Part II: Eigenfunction Analysis and the Results for Symmetric Laminates

W.-L. Yin
School of Civil Engineering,
Georgia Institute of Technology,
Atlanta, GA 30332

The eigenvalue problem associated with the determination of the interlaminar stresses in a laminated strip is examined and physical interpretations are given to the (constant) particular solutions and the complementary solutions of the problem. The case of symmetric laminates is considered in detail, and variational solutions are computed for four-layer, symmetric, cross-ply, and angle-ply laminates subjected to the three fundamental types of strain loads. Solutions based on two sets of stress functions with polynomial expansions of different degrees are compared with each other and with the existing solutions to assess the accuracy. The interfacial values of the stress functions and their derivatives are identified as the resultant peeling and shearing forces over end intervals of the interface.

1 Introduction

In Part I of this paper, we derived, without approximation, a variational equation for the Lekhnitskii stress functions F and Ψ in the various layers of a laminated strip with two parallel free edges along $x = \pm a$. The variational equation contains three strain load parameters B, C, and Θ characterizing, respectively, axial extension, bending and twisting of the strip. In this equation,

$$\sum\int\int \epsilon_{ij}\delta\sigma_{ij}dxdy+\sum (Ba_{16}^{(i)}/a_{11}^{(i)}-2\Theta)\int\int \delta\Psi\, dxdy$$
$$-\sum (C-By_i)\int ([a_{12}/a_{11}]_i\delta G_i+[a_{16}/a_{11}]_i\delta\Psi_i)dx$$
$$-B\sum [a_{12}/a_{11}]_i\int \delta F_i dx=0, \quad (1)$$

the double integrals are summed over all layers and the single integrals are summed over all interfaces. The functions $F_i(x)$, $G_i(x)$ and $\Psi_i(x)$ denote, respectively, the values of $F(x, y)$, $F_{,y}(x, y)$ and $\Psi(x, y)$ on the ith interface $y = y_i$. The bracket symbol $[\ ]_i$ stands for the jump of the quantity inside the bracket across the ith interface. There are $n + 1$ generally anisotropic layers separated by n interfaces.

When the stress functions in each layer are approximated by polynomial expansions in terms of the thickness coordinate, and when the expansions are substituted into the variational equation, we obtain the Euler-Lagrange equation of the following form:

$$\left(\mathbf{W}\frac{d^4}{dx^4}+\mathbf{V}\frac{d^2}{dx^2}+\mathbf{U}\right)\{X\}=\{b\}, \quad (2)$$

where the vector $\{b\}$ is known in terms of the three strain loads and where the coefficient functions in $\{X\}$ satisfy the homogeneous boundary conditions at the free edges $x = \pm a$:

$$F_i=F_i'=G_i=G_i'=\Psi_i=H_i=0,\ (i=1,2,\ldots,n),\ H_0=0. \quad (3)$$

Thus, the analysis of Part I reduces the interlaminar stress problem of the laminated strip to a mathematical problem, which governs the coefficient functions of the polynomial expansions of the stress functions. In this part of the paper, the eigenvalue problem associated with Eqs. (2) and (3) is examined, and solutions are obtained for the interlaminar stresses in angle-ply and cross-ply symmetric laminates using two different polynomial expansions of the stress functions (one lower order and another higher order). The results of the present solutions are compared with previous solutions by other authors (for the case of axial extension load) and found to be in close agreement. It should be mentioned that, while there is a larger number of numerical solutions in the literature concerning the interlaminar stresses in a symmetric four-layer laminate loaded under axial strain, existing results for the bending

Contributed by the Applied Mechanics Division of THE AMERICAN SOCIETY OF MECHANICAL ENGINEERS for publication in the ASME JOURNAL OF APPLIED MECHANICS.

Discussion on this paper should be addressed to the Technical Editor, Professor Lewis T. Wheeler, Department of Mechanical Engineering, University of Houston, Houston, TX 77204-4792, and will be accepted until four months after final publication of the paper itself in the ASME JOURNAL OF APPLIED MECHANICS.

Manuscript received by the ASME Applied Mechanics Division, Oct. 16, 1992; final revision, Apr. 14, 1993. Associate Technical Editor: F. Y. M. Wan.

Copyright © 1994 by ASME
Downloaded 03 May 2010 to 171.66.16.20. Redistribution subject to ASME license or copyright; see http://www.asme.org/terms/Terms_Use.cfm

and twisting cases are scarce (for the case of bending loads, see Salamon, 1978; Ye, 1990; for the twisting case see Chan and Ochoa, 1987 and Li, 1992. See also Murthy and Chamis, 1989). The present analysis method generally yields the solutions for all three distinct cases of strain loads in terms of the same set of eigenfunctions[1].

2 The Particular Solution

Let the laminated strip $-a \le x \le a$ be extended in imagination to a (fictitious) infinite laminate and let this infinite laminate be subjected to a deformation characterized by

$$\sigma_y \equiv \tau_{xy} \equiv \tau_{yz} \equiv 0, \tag{4}$$

$$\epsilon_x = \epsilon_x^o - y\kappa_x, \quad \epsilon_z = C - By, \quad \gamma_{xz} = \gamma_{xz}^o - \Theta y, \tag{5}$$

where ϵ_x^o, γ_{xz}^o, and κ_x are three constants chosen in such a way as to yield vanishing resultants N_x, N_{xy}, and M_x in the infinite laminate:

$$N_x \equiv \Sigma \int \sigma_x^{(i)} dy = 0, \quad N_{xz} \equiv \Sigma \int \tau_{xz}^{(i)} dy = 0,$$

$$M_x \equiv -\Sigma \int \sigma_x^{(i)} y dy = 0. \tag{6}$$

The integrals in these expressions are summed over all layers and $\sigma_x^{(i)}$ and $\tau_{xz}^{(i)}$ denote the stresses in the ith layer determined by Eqs. (4) and (5). Notice that the strain and stress fields of the infinite laminate as determined by Eqs. (4)–(6) are functions only of the thickness coordinate y. Hence, the corresponding stress functions $F^{(i)}$ and $\Psi^{(i)}$ in the various layers are also functions of y only.

Since the strain components ϵ_x, ϵ_z, and γ_{xz} of Eq. (5) depend linearly on y, the stresses in the infinite laminate must be piecewise linear in y. Hence $F^{(i)}$ and $\Psi^{(i)}$ are expressed *exactly* by equations of the form (16) and (17) in Part I, except that F_i, G_i, Ψ_i, and H_i are constants rather than functions of x. With all the stress and strain components independent of x, the variational Eq. (1) for the fictitious infinite laminate reduces to

$$\sum \int\int \{F_{,yy}, \Psi_{,y}\} \begin{bmatrix} \beta_{22} & \beta_{26} \\ \beta_{26} & \beta_{66} \end{bmatrix} \begin{Bmatrix} \delta F_{,yy} \\ \delta \Psi_{,y} \end{Bmatrix} dxdy$$

$$+ \sum \{B a_{16}^{(i)}/a_{11}^{(i)} - 2\Theta\} \int \delta\Psi^{(i)} dy - \sum (C - By_i) \{[a_{12}/a_{11}]_i \times \delta G_i + [a_{16}/a_{11}]_i \delta\Psi_i\} - B \sum [a_{12}/a_{11}]_i \delta F_i = 0.$$

The corresponding Euler-Lagrange equation becomes

$$\mathbf{U}\{X\} = \{b\}. \tag{7}$$

Thus, although the differential equation for the finite strip, Eq. (2), is only approximately valid because it is based on polynomial approximations of stress functions, the governing Eq. (7) for the fictitious infinite laminate is, in contrast, *exactly* valid. Furthermore, the unique solution of the infinite laminate problem is characterized by

$$\{X\}^p = \mathbf{U}^{-1}\{b\}. \tag{8}$$

Because the solution of the infinite laminate problem may be obtained by solving ϵ_x^o, γ_{xz}^o and κ_x from the system of equations in Eq. (6) and then calculating the stresses $\sigma_x^{(i)}(y)$ and $\tau_{xz}^{(i)}(y)$ and the stress functions $F^{(i)}(y)$ and $\Psi^{(i)}(y)$, the invertibility of the matrix $\mathbf{U}$ is ensured. $\{X\}^p$ as given by Eq. (8) is a particular solution of the governing equation, Eq. (2), for the finite strip.

[1]For an exception to this statement, see the remark on cross-ply laminates in the last paragraph of Section 3.

3 Solution of the Eigenvalue Problem

The first step in solving the eigenvalue problem associated with Eqs. (2) and (3) is the determination of *all* real and complex roots of the characteristic equation

$$\text{Determinant } (\mathbf{W}\lambda^4 + \mathbf{V}\lambda^2 + \mathbf{U}) = 0. \tag{9}$$

This equation is of the form usually found in vibration problems of a damped system. However, while the matrix $\mathbf{U}$ is always nonsingular and $\mathbf{V}$ is generally nonsingular, the nonzero elements of $\mathbf{W}$ are confined to a submatrix in the upper left corner. Thus, if the laminate has $n + 1$ layers and if the stress functions $F^{(i)}$ and $\Psi^{(i)}$ in each layer are approximated, respectively, by cubic and quadratic functions of the thickness coordinate (see Eqs. (16) and (17) of Part I), the matrices $\mathbf{U}$ and $\mathbf{V}$ have the dimension $4n + 1$ while $\mathbf{W}^*$, the nonvanishing submatrix of $\mathbf{W}$, has the dimension $2n$. Equation (9) is a polynomial equation of the degree $2 \times 2n + 2n + 1 = 6n + 1$ in the variable λ^2. Hence there are $6n + 1$ pairs of real and complex eigenvalues, with each pair consisting of eigenvalues which differ only in algebraic sign. Considered as an equation for λ^2, the characteristic equation yields no solutions λ^2 with negative real parts. Hence there are no purely imaginary eigenvalues.

Equation (9) can be transformed, through algebraic manipulations, into a characteristic equation of the standard form

$$\text{Determinant } (\mathbf{M} - \lambda^{-2}\mathbf{I}_{6n+1}) = 0, \tag{10}$$

which is associated with a real square matrix $\mathbf{M}$ of dimension $6n + 1$, defined as the product of two matrices in the following manner:

$$\mathbf{M} = \begin{bmatrix} -\mathbf{U}^{-1} & \mathbf{O} \\ \mathbf{O} & \mathbf{I}_{2n} \end{bmatrix} \cdot \left[\begin{array}{cc:c} \multicolumn{2}{c:}{\multirow{2}{*}{$\mathbf{V}$}} & \mathbf{W}^* \\ & & \mathbf{O} \\ \hdashline \mathbf{I}_{2n} & \mathbf{O} & \mathbf{O} \end{array}\right]. \tag{11}$$

The transformation to Eq. (10) allows commercial and public-domain computer programs to be readily used for determining all real and complex roots.

Once a real or complex eigenvalue λ_k has been computed, the corresponding eigenvector $\{c\}_k$ (which determines the eigenfunction $\{c\}_k \exp(\lambda_k x)$) may be obtained by solving the algebraic equations $(\mathbf{W}\lambda_k^4 + \mathbf{V}\lambda_k^2 + \mathbf{U})\{c\}_k = \{0\}$. The eigenfunctions are combined linearly to form the complementary solution. The latter decays rapidly away from the two free edges and has a vanishing effect on the stresses in the interior of the laminate. The coefficients in the complementary solution are appropriately chosen so as to cancel exactly the tractions of the particular solution at the free edges. Hence, the free-edge conditions are exactly satisfied while the stress field in the interior region away from the free edges is closely approximated by the particular solution (i.e., the solution of the fictitious infinite laminate subjected to the same strain load).

In the case of a cross-ply laminate with the material axes parallel and perpendicular to the free edges, the solution space of the eigenvalue problem decomposes orthogonally into subspaces of dimensions $8n$ and $4n + 2$. The two subspaces are associated, respectively, with the two stress functions F and Ψ (Notice that there is no coupling between F and Ψ in the Euler-Lagrange equation because the elastic compliance coefficients $\beta_{26}^{(i)}$, $\beta_{36}^{(i)}$, $\beta_{45}^{(i)}$, and $a_{16}^{(i)}$ (see Eq. (4), Part I) vanish in every layer of a cross-ply laminate). Consequently, Eq. (2) uncouples into a system of $2n$ *fourth-order* differential equations for the functions F_i and G_i and another system of $2n + 1$ *second-order* equations for the functions Ψ_i and H_i. The first system of equations determines the solutions under axial extension and bending while the second system of equations determines the solutions associated with the twisting deformation.

Downloaded 03 May 2010 to 171.66.16.20. Redistribution subject to ASME license or copyright; see http://www.asme.org/terms/Terms_Use.cfm

4 The Case of Symmetric Laminates

If the laminate is symmetric with respect to the middle plane $y = 0$, then all stiffness and compliance coefficients of the layers are even functions of y. In particular, there is no discontinuity in a_{12}/a_{11} or a_{16}/a_{11} across the plane $y = 0$ if that plane is artificially regarded as an interface. Hence there are no contributions to the single integrals of Eq. (1) from the interface $y = 0$.

For a symmetric laminate loaded under a uniform axial strain only (i.e., $B = \Theta = 0$ and $\epsilon_z^o = C \neq o$), the deformation and the stress in the laminate are symmetric with respect to the middle plane. Hence F is an even function of y while $F_{,y}$ and Ψ are odd functions. In particular, $G = \Psi = 0$ on $y = 0$. Setting $B = \Theta = 0$ in Eq. (1), one finds that the regions of the laminate above and below the middle plane make equal contributions to the sum of integrals.

The last conclusion may also be reached for a symmetric laminate subjected to bending and twisting ($C = 0$, while B and Θ do not both vanish). In such loading cases, F is an odd function of y while $F_{,y}$ and Ψ are even functions. In particular, $F = \Psi_{,y} = 0$ on $y = 0$. Because a_{16}/a_{11} is an even function of y while the interfacial jumps $[a_{12}/a_{11}]$ and $[a_{16}/a_{11}]$ are odd in y, the sum of integrals in Eq. (1) receives equal contributions from the regions above and below the middle plane.

Hence, in the case of a symmetric laminate, the number of unknown functions in Eq. (2) may be significantly reduced. Only the functions F_i, G_i, Ψ_i, and H_i associated with the interfaces on and above the middle plane need be included in the vector $\{X\}$. Let these interfaces be renumbered in the ascending order, starting with interface 0 on $y = 0$. Then, for the uniform axial strain load (i.e., $C \neq 0$ and $B = \Theta = 0$), the required set of unknown functions include F_i, G_i, Ψ_i, and H_i (for $i \geq 1$) and the functions F_0 and H_0. Under bending and twisting loads (i.e., $C = 0$), F_0 and H_0 are replaced by G_0 and Ψ_0.

For the classical problem of a symmetric, four-layer laminate under an axial strain load, there is only one interface in the upper half of the laminate and the stress functions in the two layers in the upper region (renumbered as layers 1 and 2) have expressions

$$F^{(1)}(x,\eta) = (1-3\eta^2+2\eta^3)F_0(x) + (3\eta^2-2\eta^3)F_1(x) + (\eta^3-\eta^2)h_1G_1(x), \quad (12a)$$

$$F^{(2)}(x,\eta) = (1-3\eta^2+2\eta^3)F_1(x) + (\eta-2\eta^2+\eta^3)h_2G_1(x), \quad (12b)$$

$$\Psi^{(1)}(x,\eta) = \eta^2\Psi_1(x) + (\eta-\eta^2)h_1H_0(x), \quad (12c)$$

$$\Psi^{(2)}(x,\eta) = (1-\eta^2)\Psi_1(x) + (\eta-\eta^2)h_2H_1(x). \quad (12d)$$

The vectors $\{X\}$ and $\{b\}$ become, respectively, $\{F_0(x), F_1(x), G_1(x), \Psi_1(x), H_0(x), H_1(x)\}^t$ and $\{0, 0, C[a_{12}/a_{11}]_1, C[a_{16}/a_{11}]_1, 0, 0\}^t$.

In the cases of bending and twisting loads one has $C = 0$. The stress functions in layer 2 are still given by Eqs. (12*b*) and (12*d*) while Eqs. (12*a*) and (12*c*) are replaced by

$$F^{(1)}(x,\eta) = (\eta-2\eta^2+\eta^3)h_1G_0(x) + (3\eta^2-2\eta^3)F_1(x) + (\eta^3-\eta^2)h_1G_1(x), \quad (13a)$$

$$\Psi^{(1)}(x,\eta) = (1-\eta^2)\Psi_0(x) + \eta^2\Psi_1(x). \quad (13b)$$

Furthermore, the vectors $\{X\}$ reduces to $\{F_1(x), G_0(x), G_1(x), \Psi_0(x), \Psi_1(x), H_1(x)\}^t$ and $\{b\}$ has the components $b_1 = B[a_{12}/a_{11}]_1$, $b_2 = 0$, $b_3 = -Bh_1[a_{12}/a_{11}]_1$, $b_4 = 2(2\Theta - Ba_{16}^{(1)}/a_{11}^{(1)})h_1/3$, $b_5 = -Bh_1[a_{16}/a_{11}]_1 + (2\Theta - Ba_{16}^{(1)}/a_{11}^{(1)})h_1/3 + 2(2\Theta - Ba_{16}^{(2)}/a_{11}^{(2)})h_2/3$ and $b_6 = (h_2^2/6)(2\Theta - Ba_{16}^{(2)}/a_{11}^{(2)})$.

5 Results for Symmetric Four-Layer Laminates

When the stress functions are approximated by polynomial expansions such as given in Eq. (12) or (13), the analytical expressions of the constant matrices **U**, **V**, and **W** are obtained in terms of the layer elasticity, thicknesses, and orientation angles by using the symbolic program *MACSYMA* (1988). Fortran codes are developed for solving the eigenvalue problem and evaluating the interlaminar stresses along the interfaces under the various strain loads. In the case of a four-layer laminate, execution of the Fortran program takes about one second on a 486 personal computer.

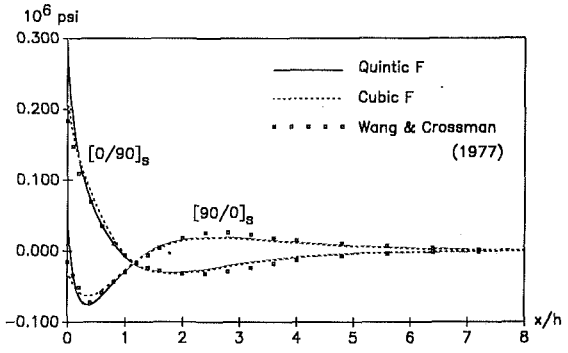


Fig. 1 σ_y on $y = h$ in cross-ply laminates under $\epsilon_z = 1$

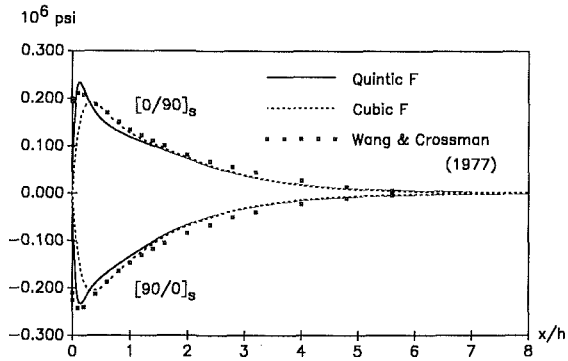


Fig. 2 τ_{xy} on $y = h$ in cross-ply laminates under $\epsilon_z = 1$

For convenience of comparison with the existing solutions in the literature, approximate solutions are obtained by the present method for symmetric, four-layer laminates composed of unidirectional plies with the same thickness h and with the elastic moduli $E_{11} = 20 \times 10^6$ psi, $E_2 = E_3 = 2.1 \times 10^6$ psi, $\nu_{12} = \nu_{13} = \nu_{23} = 0.21$ and $G_{12} = G_{13} = G_{23} = 0.85 \times 10^6$ psi. The distance between the pair of free edges is $w = 2a = 16h$.

We first consider four-layer symmetric *cross-ply* laminates with the ply configurations $[0/90]_s$ and $[90/0]_s$. For the case of a unit axial strain load ($C = 1$ and $B = \Theta = 0$), the interlaminar stresses σ_y and τ_{xy} on the interface $y = h$ are shown by the broken curves in Figs. 1 and 2, respectively. An additional set of improved variational solutions, based on quintic polynomial expansions of $F^{(i)}$ and cubic expansions of $\Psi^{(i)}$, is also obtained and the results are shown by solid curves in the same figures. The difference between the two set of solutions is insignificant except in the immediate neighborhood of the free edge. Solutions based on the higher-order polynomial expansions of the stress functions yield steeper stress gradients near the free edge. These solutions are in very close agreement with the numerical solutions of Wang and Crossman (1977). The latter are shown in the same figures by open square symbols. We note that the x-coordinate in all figures has been shifted so that $x = 0$ denotes the left free edge of the laminated strip.

For the $[0/90]_s$ laminate under unit bending and twisting deformations ($B = 1/h$ and $\Theta = 1/h$, respectively), the nonvanishing interlaminar stresses on the interface $y = h$ (based

Downloaded 03 May 2010 to 171.66.16.20. Redistribution subject to ASME license or copyright; see http://www.asme.org/terms/Terms_Use.cfm

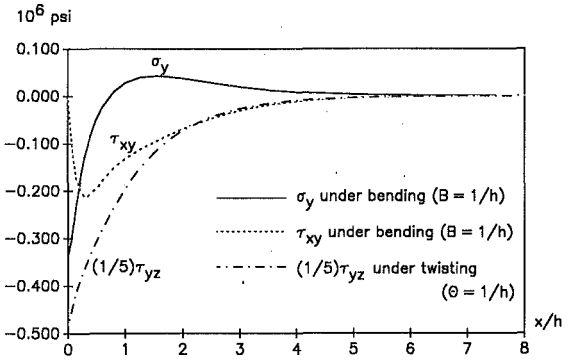


Fig. 3 $[0/90]_s$ laminate under bending and twisting

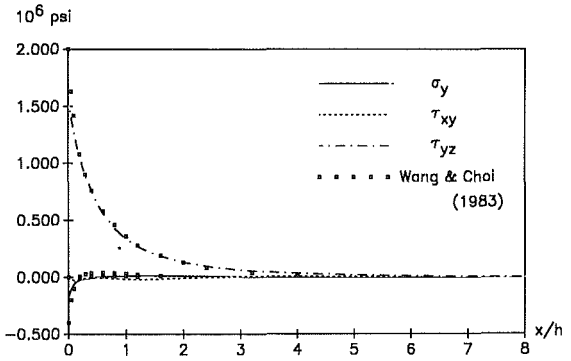


Fig. 4 $[45/-45]_s$ laminate under unit extension ($\epsilon_z = 1$)

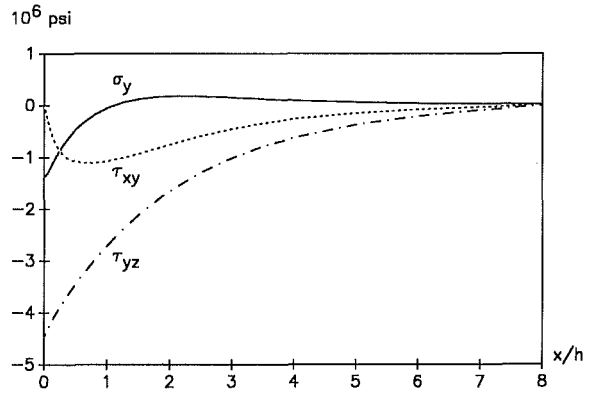


Fig. 5 $[45/-45]_s$ laminate under twisting deformation ($\Theta = 1/h$)

on Eqs. (12) and (13)) are shown in Fig. 3. The results for the bending deformation is close to that for the axial strain load, except for a reversal of algebraic signs. This may be expected because a bending curvature $B = 1/h$ yields an axial strain $\epsilon_z = -1$ on the interface $y = h$. The mode III interlaminar stress τ_{yz} produced by the twisting load, $\Theta = 1/h$, is found to be an order of magnitude greater than the mode I and mode II interlaminar stresses produced by a unit axial strain or by the bending curvature $B = 1/h$. This is also not surprising because the shearing strain near the free edge caused by $\Theta = 1/h$ is of the order $2a/h$, i.e., an order of magnitude greater than unity.

In the case of $[45/-45]_s$ angle-ply laminates, the solution space of the governing differential equation is not orthogonally decomposable. Hence, all three components of the interlaminar stresses generally occur in each one of the loading cases. The interlaminar stresses on the interface $y = h$ are shown in Figs. 4 and 5, respectively, for the extension and twisting loads, and the results in Fig. 4 are compared with the solutions of Wang and Choi (1982). Additional results may be found in Yin (1991a). Here again a twisting deformation ($\Theta = 1/h$) produces a very large mode III interlaminar stress. Notice that, according to the linear elasticity solution, all six stress components approach infinite limits as one approaches the singular point along the interface from the interior of the laminate. This discontinuous behavior can be approximated by the continuous fields of the present solutions (and those of finite element solutions) in a limiting sense only, when an increasingly large number of terms are included in the polynomial representations of the stress functions.

6 Physical Meanings of the Functions $F_i'(x)$, $G_i(x)$ and $\Psi_i(x)$

The values of the stress functions and their y-derivatives along the ith interface, given by the functions $F_i(x)$, $\Psi_i(x)$, $G_i(x)$, and $H_i(x)$, are related to the resultant forces and moments of the normal and shearing interlaminar stresses over interfacial intervals of varying lengths adjacent to the free edge. That is, over the interval $[0, x]$ of the ith interface (where the origin $x = 0$ has been shifted to the left free edge) we have

$$\int \sigma_y dx = \int F_i'' dx = F_i'(x), \quad \int \tau_{xy} dx = -\int G_i' dx = -G_i(x)$$

$$\int x\,\sigma_y dx = xF_i'(x) - F_i(x), \quad \int \tau_{yz} dx = -\int \Psi_i' dx = -\Psi_i(x). \tag{14}$$

In particular, the maximum absolute values of G_i and Ψ_i, reached at the centerline of the strip, are equal to the resultant forces of the interlaminar shearing stresses τ_{xy} and τ_{yz}, respectively, over one half of the ith interface. In most cases, G_i and Ψ_i change monotonically from zero to their maximum or minimum values at the centerline of the strip. If G_i or Ψ_i attains a large value in a very short distance from the free edge, then an intense interlaminar shearing action (of mode II or III, respectively) occurs in a very short interval from the free edge. This situation is susceptible to delamination failure under the shear fracture mode.

The behavior of the function $F_i'(x)$ has a similar implication for the interlaminar normal stress. This function usually increases from zero at the free edge to a maximum or minimum value in a short distance from the edge. It then decays slowly to zero at the midpoint of the beam. If F_i' increases from zero to a large maximum value in a narrow boundary interval, then an intense interlaminar normal stress acts in that short end interval, and the resultant peeling force is balanced by an equal compressive force distributed over the remaining portion of the half interface. This situation is susceptible to delamination failure under the peeling fracture mode.

Over short end segments of an interface, the average values of intense peeling and shearing stresses are provided by the ratios of F_i', G_i, and Ψ_i to the segment length. These average values are meaningful measures of the criticality of interlaminar action, and may be used as parameters in the interlaminar fracture criteria for the peeling and shearing modes of failure. Being global measures, they are less affected by deviation of material behavior from the assumption of linear elasticity, and by the crudeness or refinement of the approximate analysis, than the pointwise values of the interlaminar stresses. That is, a relatively simple analysis (involving low-degree polynomial approximations of the stress functions) may provide unreliable results for the detailed interlaminar stress distribution along the interface, but may still yield accurate results for the maximum values of F_i', G_i, and Ψ_i.

Figures 6 and 7 show, respectively, the functions $F_1'(x)$ and $G_1(x)$ for the four-layer symmetric cross-ply laminates under a unit axial strain load. The differences between the solutions with cubic and quintic polynomial expansion of $F^{(i)}$ are considerably smaller than the differences between the correspond-

Downloaded 03 May 2010 to 171.66.16.20. Redistribution subject to ASME license or copyright; see http://www.asme.org/terms/Terms_Use.cfm

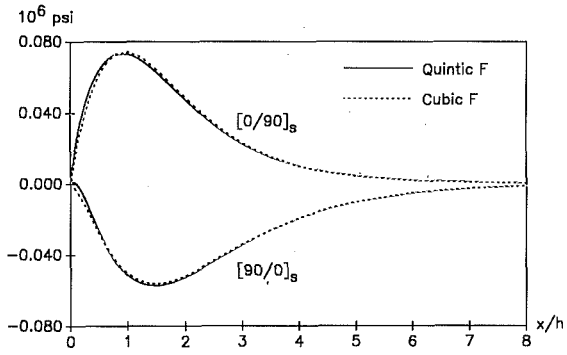


Fig. 6 $F_1'(x)/h$ in cross-ply laminates under $\epsilon_z = 1$

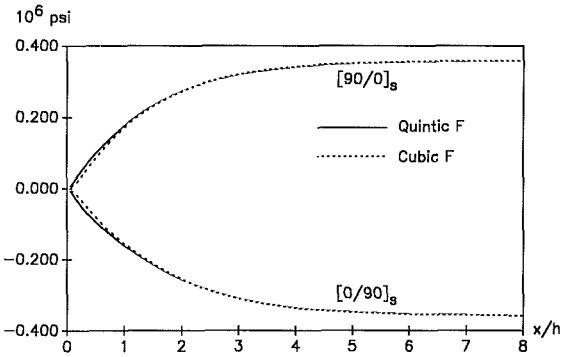


Fig. 7 $G_1(x)/h$ in cross-ply laminates under $\epsilon_z = 1$

ing results for the interlaminar stresses (Figs. 1 and 2). This and other comparisons (for a laminated beam subjected to temperature loads, see Yin, 1992a) demonstrate that the resultant peeling and shearing forces over end segments of an interface are predicted with satisfactory accuracy by the variational solutions using lower-degree polynomial expansions of the stress functions, even though such solutions may yield poor results for the pointwise values of the interlaminar stresses near the free edge.

7 The Effect of Laminate Width

It was mentioned previously that the characteristic Eq. (9) has two sets of eigenvalues which differ only in algebraic sign. The eigenfunctions corresponding to eigenvalues with positive (negative) real parts decay exponentially away from the right (left) free edge of the laminate. If the width-to-thickness ratio of the layers is large, then the first (second) set of eigenfunctions make negligible contribution to the solution away from the right (left) free edge. That is, the solutions in the left and right halves of the laminate are approximately uncoupled. Hence, for sufficiently large values of w/h, the interlaminar stress distribution near a free edge is not appreciably dependent on w/h. This conclusion is substantiated by the results for $[0/45]_s$ laminates with $w/h = 4$, 8, 16, and 50 (see Fig. 9 of Yin, 1991a for the results under the unit axial strain load). The interlaminar stress distributions approach limiting patterns as w/h increases. The ratio has a significant effect on the interlaminar stresses only if the width $w = 2a$ becomes comparable to the laminate thickness. The present conclusion, while in agreement with the results of Salamon (1981), is contrary to the contention of Murthy and Chamis (1989) concerning the effect of laminate width.

8 Concluding Remarks

A systematic approximate method has been developed for determining the free-edge interlaminar stresses in a multilayered anisotropic laminate subjected to combined axial strain, bending and twisting deformation. The method is based on the complementary virtual work principle with the use of Lekhnitskii's stress functions.

Aside from using polynomial expansions of the stress functions, the present analysis introduces no extraneous assumptions and is mathematically rigorous within the context of the variational approach. The method is also conceptually simple, and straightforward in practical implementation. The latter feature is due largely to the complete avoidance of explicit use of displacement variables, which are not needed for evaluating the interlaminar stresses. Not only is the number of unknown functions significantly reduced in comparison with an alternative variational method based on the Reissner principle (which yields approximate solutions with comparable accuracy for a four-layer laminate, see Pagano, 1978), the present analysis is also free from the occurrence of zero eigenvalues associated with rigid displacement modes that have no effect upon the solution for the interlaminar stresses.

In the ith layer, the first-order partial derivatives of the stress function F and the value of the stress function Ψ provide useful measures of the severity of the interlaminar action near the free edge. These values are less affected by the degree of refinement of the approximate analysis method than the detailed distributions of the interlaminar stresses are. They may be used as parameters in fracture criteria for the initiation of delamination failure.

The present analysis method has been implemented on personal computers. It requires very simple preparation of input data, and is ideally suited for parametric studies and repeated executions in design and optimization of laminates. The results for the interlaminar stresses, obtained here for symmetric four-layer laminates, are comparable in accuracy to refined finite-element solutions involving several hundreds of degrees-of-freedom (with the possible use of special corner elements). If the laminate has a large number of layers, a sublaminate/layer approach developed in a companion study (Yin, 1992b) may be used to reduce the eigenvalue problem to a fixed size independent of the number of layers. In this approach, two interior layers adjacent to a particular interface are modeled as anisotropic elastic media, while all remaining layers are grouped into an upper and a lower sublaminate. The sublaminate/layer modeling and analysis takes into account the combined stiffness matrices of the remote layers, as well as the distinct elastic properties of the two adjacent layers (the latter affect directly the nature of stress singularity of the elasticity solution).

Using the superposition method, the present analysis procedure may be modified to calculate the interlaminar stresses in a multilayered laminate caused by humidity and temperature loads. The analysis procedure of hygrothermal stresses has been developed in the special case of a laminated beam (Yin, 1991b), and suggested for the general case of a laminated strip (Yin, 1993b). Furthermore, if the stress functions in each layer are expressed in terms of oblique cartesian coordinates, the present analysis method may be adapted to determine interlaminar stresses near inclined free edges (Yin, 1993a). Appropriate choices of the edge inclination angles may result in more dispersed patterns of interlaminar stresses on critical interfaces.

Acknowledgments

This article is based partially on research work performed under a U.S. Army Research Office contract to Georgia Institute of Technology and partially on work supported by a contract from the NASA Langley Research Center to Lockheed Aeronautical Systems Company.

References

Chan, W. S., and Ochoa, O. O., 1987, "Assessment of Free-Edge Delami-

Downloaded 03 May 2010 to 171.66.16.20. Redistribution subject to ASME license or copyright; see http://www.asme.org/terms/Terms_Use.cfm

nation Due to Torsion," *Proceedings of the Second Technical Conference*, American Society for Composites, Lancaster, PA, pp. 469–478.

Li, J., 1992, "Free-Edge Interlaminar Stress Analysis in Laminated Composites under Combined Loading," *Proc. AIAA/ASME/ASCE/AHS/ASC Structures, Structural Dynamics and Materials Conference*, Part 2, Dallas, TX, pp. 698–706.

MACSYMA Reference Manual, 1988, Version 13, Symbolics, Burlington, MA.

Murthy, P. L. N., and Chamis, C. C., 1989, "Free-Edge Delamination: Laminate Width and Loading Conditions Effects," *J. Composite Tech. & Research*, Vol. 11, pp. 15–22.

Pagano, N. J., 1978, "Free Edge Stress Fields in Composite Laminates," *Int. J. Solids Struct.*, Vol. 14, pp. 401–406.

Salamon, N. J., 1978, "Interlaminar Stresses in a Layered Composite Laminate in Bending," *Fibre Sci. Tech.*, Vol. 11, pp. 305–317.

Salamon, N. J., 1981, "Stress Distribution in Sandwich Beams in Uniform Bending," *Test Methods and Design Allowables for Fibrous Composites*, ASTM STP-734, C. C. Chamis, ed., ASTM, Philadelphia, PA.

Wang, A. S. D., and Crossman, F. W., 1977, "Some New Results on Edge Effects in Symmetric Composite Laminates," *J. Composite Mat.*, Vol. 11, pp. 92–106.

Wang, S. S., and Choi, I., 1982, "Boundary-Layer Effects in Composite Laminates—I. Free-Edge Stress Singularities,—II. Free-Edge Stress Solutions and Basic Characteristics," ASME JOURNAL OF APPLIED MECHANICS, Vol. 49, pp. 541–560.

Ye, L., 1990, "Some Characteristics of Distributions of Free-Edge Interlaminar Stresses in Composite Laminates," *Int. J. Solids Struc.*, Vol. 26, pp. 331–351.

Yin, W.-L.,, 1991a, "Free-Edge Effects in Laminates Under Extension, Bending and Twisting, Part I: A Stress Function Approach," *Proc. AIAA/ASME/ASCE/AHS/ASC 32nd Structures, Structural Dynamics and Materials Conference*, Part 2, Baltimore, MD, pp. 985–995.

Yin, W.-L. 1991b, "Thermal Stresses and Free-Edge Effects in Laminated Beams: A Variational Approach Using Stress Functions," ASME *Journal of Electronic Packaging*, Vol. 113, pp. 68–75.

Yin, W.-L., 1992a, "Refined Variational Solutions of the Interfacial Thermal Stresses in a Laminated Beam," ASME *Journal of Electronic Packaging*, Vol. 114, pp. 193–198.

Yin, W.-L., 1992b, "Free-Edge Effects in Laminates Under Extension, Bending and Twisting, Part II: Sublaminate/layer Modeling and Analysis," *Proc. AIAA/ASME/ASCE/AHS/ASC 33rd Structures, Structural Dynamics and Materials Conference*, Part 2, Dallas, TX, pp. 48–58.

Yin, W.-L., 1993a, "The Effects of Inclined Free Edges on the Thermal Stresses in a Layered Beam," ASME *Journal of Electronic Packaging*, Vol. 115, pp. 208–213.

Yin, W.-L., 1993b, "Analysis of the Interlaminar Thermal Stresses in Multilayered Structures," *Thermal Stress and Strain in Microelectronic Packaging*, J. Lau, ed., Van Nostrand Reinhold, New York, pp. 95–138.

Downloaded 03 May 2010 to 171.66.16.20. Redistribution subject to ASME license or copyright; see http://www.asme.org/terms/Terms_Use.cfm

Z. Xia

F. Ellyin
Mem. ASME.

Department of Mechanical Engineering,
University of Alberta,
Edmonton, AB T6G 2G8, Canada

Biaxial Ratcheting Under Strain or Stress-Controlled Axial Cycling With Constant Hoop Stress

Strain or stress-controlled tension-compression cyclic tests were conducted on pressurized thin-walled tubular specimens of 304 stainless steel. In strain-controlled mode ratcheting strains in hoop direction, and under stress-controlled mode ratcheting in both hoop and axial directions, were observed. To predict the observed ratcheting behavior, an additional evolution rule for the stress memory surface has been introduced in the constitutive model developed recently by the authors. Qualitative and quantitative comparisons with the test results indicate a fairly good agreement in predicting ratcheting deformations.

1 Introduction

Mechanical ratcheting behavior of materials is one of the problems which has recently attracted considerable interest. Structures under certain loading conditions, for example, pressure vessels subjected simultaneously to an internal pressure and a cyclic axial loading (thermal loading, etc.), may develop a fair amount of ratcheting deformation. On the other hand, correctly predicting ratcheting behavior of materials is still a challenge for most constitutive models. According to Chaboche and Nouailhas (1989a), two types of ratcheting could be distinguished: one is quasi-reversed cycling loading which is related to cyclic plasticity; the other is quasi-repeated loading condition with high mean-stress in which the ratcheting is mainly due to the normal creep. In this paper we will focus on the tests and modeling of the first type of ratcheting.

Most multiaxial ratcheting tests reported in the literature were conducted under combined constant tension and cyclic shear loading condition.[1] As indicated by Ellyin and Xia (1991) this type of multiaxial test provides a relatively narrow range of possible stress combinations in the σ_1-σ_2 stress plane, whereas biaxial pull-push tests may cover all quadrants of the principal stress plane. Another advantage of the latter type of test is that coupling effects between principal directions may be exhibited. This characteristic has been shown more clearly through the stress-controlled biaxial ratcheting tests (see Section 2.3).

A comparison study of ten types of constitutive models was made by Inoue et al. (1989a, b). The study revealed that most constitutive models have a poor capability of predicting ratcheting strain in uniaxial and multiaxial cases. Chaboche and Nouailhas (1989b) discussed the possibility of improving the ratcheting predictions by introducing additional linear and nonlinear kinematic hardening rules. Further models developed to predict ratcheting are those of McDowell and Lamar (1989) and Blanchard and Lemoine (1988), among others.

To simulate practical loading conditions of pressure vessel structures we chose two testing programs on thin-walled tubular specimens. A constant internal pressure is first applied to specimens. Subsequently, a strain or stress-controlled cyclic loading is added in the axial direction. The test results are presented in Section 2.3. A constitutive model with an additional evolution rule for the stress memory surface, and a comparison between test results and model predictions are discussed in Sections 3 and 4.

2 Biaxial Tension-Compression Ratcheting Test

2.1 Testing Equipment. Thin-walled tubular specimens were used in this investigation. The geometry of specimens is shown in Fig. 1. The material tested is type 304 stainless steel. After machining the specimens, they were annealed in an argon environment at 1093°C for 90 minutes.

The tests are carried out on a servo-controlled electro-hydraulic closed-loop system—a modified MTS system. The specimens were subjected to an internal pressure and an axial load. For a schematic of the test facility see Ellyin et al. (1991).

2.2 Testing Procedure. From a stress-free state, the internal pressure is increased to a value which produces a constant hoop stress of 80 MPa. To keep axial strain at zero, an axial stress of 20 MPa is applied to the specimen ($\nu = 0.25$) for the strain-controlled tests. Strain cycling with an amplitude of

[1] After completion of this work, our attention was drawn to a recent paper by Hassan, Corona, and Kyriakides (*Int. J. Plasticity*, Vol. 8, pp. 117–146, 1992) who presented experimental and modeling results of biaxial ratcheting on 1026 steel.

Contributed by the Applied Mechanics Division of THE AMERICAN SOCIETY OF MECHANICAL ENGINEERS for publication in the ASME JOURNAL OF APPLIED MECHANICS.

Discussion on this paper should be addressed to the Technical Editor, Professor Lewis T. Wheeler, Department of Mechanical Engineering, University of Houston, Houston, TX 77204-4792, and will be accepted until four months after final publication of the paper itself in the ASME JOURNAL OF APPLIED MECHANICS.

Manuscript received by the ASME Applied Mechanics Division, Sept. 14, 1992; final revision, Feb. 23, 1993. Associate Technical Editor: W. N. Sharpe, Jr.

Copyright © 1994 by ASME
Downloaded 03 May 2010 to 171.66.16.20. Redistribution subject to ASME license or copyright; see http://www.asme.org/terms/Terms_Use.cfm

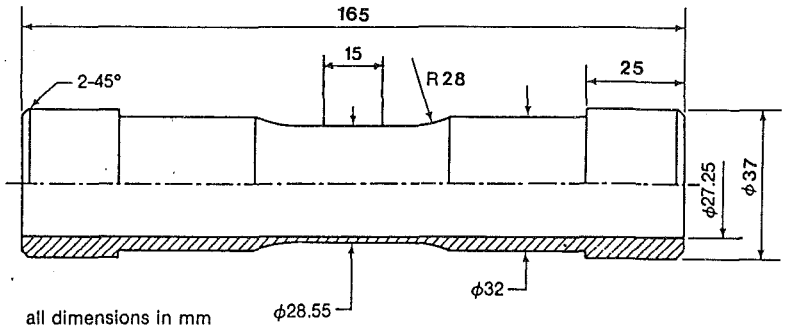


Fig. 1 Geometry of the specimen

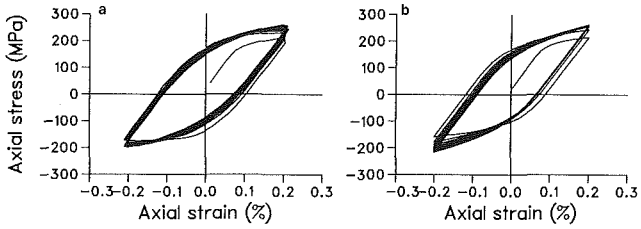


Fig. 2 Axial stress-strain response for strain-controlled ratcheting test; (*a*) test result; (*b*) predicted result

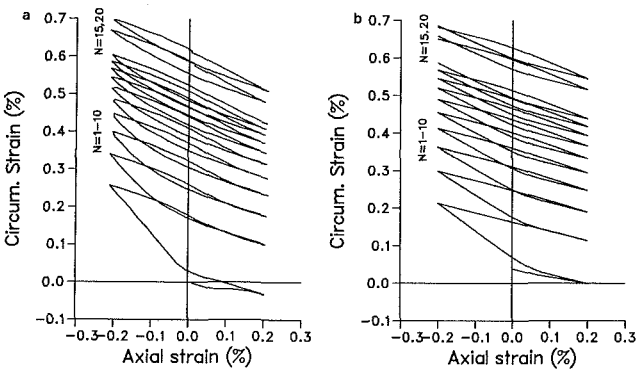


Fig. 3 Circumferential strain versus axial strain for strain-controlled ratcheting test; (*a*) test result; (*b*) predicted result

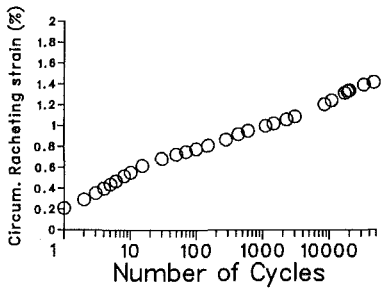


Fig. 4 Circumferential ratcheting strain versus number of cycles (strain-control)

± 0.2 percent is then superimposed in the axial direction. The cycling follows a triangle wave, the frequency is 0.025 s^{-1} ($\dot{\epsilon} = 2 \times 10^{-4}\ s^{-1}$) for the first 450 cycles and is subsequently increased to $f = 0.1\ s^{-1}$ ($\dot{\epsilon} = 8 \times 10^{-4}\ s^{-1}$). The test continued until failure of the specimen at number of cycles $N_f = 44507$. A crack penetrating through the thickness was found on the specimens and the internal pressure, therefore, could not be maintained (see Fig. 9(*a*)).

For the stress-controlled tests, the initial axial stress is zero whereas the initial axial strain is -9.89×10^{-5}, as a result of the applied hoop stress of 80 MPa. A cyclic axial stress with an amplitude of ± 182 MPa is then applied to the specimen. The loading frequency is 0.025 s^{-1} ($\dot{\sigma} = 18.2$ MPa/s) for the first 450 cycles and is increased to $f = 0.1\ s^{-1}$ ($\dot{\sigma} = 72.8$ MPa/s) thereafter. The test ran until 6000 cycles when the ratcheting rate became very small. The stress amplitude was subsequently increased to ± 252 MPa. Under this larger stress amplitude the test lasted only 785 cycles when an instability occurred and the specimen collapsed.

2.3 Test Results. Typical test results for the strain-controlled tests are shown in Figs. 2 to 4. From the axial strain-axial stress response (Fig. 2(*a*)) it is seen that after a transient hardening stage (first 20–30 cycles) the stress-strain loops become stable. It is noted that there is a stable tensile mean stress value (≈ 20 MPa). The ratcheting strain in the hoop direction is shown in Figs. 3(*a*) and 4 which indicate that the ratcheting strain per cycle (ratcheting rate) decreases with the increasing number of cycles. But the ratcheting rate does not appear to approach asymptotically a constant value. In the diagram of ratcheting strain-logarithm of number of cycles (Fig. 4) a linear relation appears to fit the experimental data with good approximation. From the axial strain-hoop strain diagram (Fig. 3(*a*)) one observes that the ratcheting strain is mostly developed during the unloading path from $+0.2$ percent to -0.2 percent. With increasing cycles the ratcheting per cycle is decreasing and the axial strain-hoop strain loops tend to reach a stable shape. When comparing number of cycles to failure in these tests with our previous fatigue test data, Ellyin et al. (1991), it is noted that the fatigue life is reduced to less than one half of the uniaxial fatigue tests without a constant hoop stress.

For the stress-controlled tests, it is observed that ratcheting occurs in both axial and hoop directions, i.e., a positive ratcheting strain in the hoop direction and a negative one in the axial direction (Figs. 5–7). It seems that a constant hoop stress has a similar effect as a negative mean stress in axial direction and causes negative axial ratcheting strain. Such a coupling effect between the two principal directions cannot be observed in biaxial tension-torsion tests. Under a small stress amplitude (± 182 MPa), the characteristic of the accumulated ratcheting strains is similar to the strain-controlled test. The ratcheting rate is decreased with increasing cycles. There is no indication that the ratcheting rate reaches a finite asymptotic value (Fig. 5). From the diagrams of axial stress-axial strain and axial stress-hoop strain (Figs. 6(*a*), 7(*a*)) it is seen that both ratcheting strains are mostly developed during the unloading path from $+182$ MPa to -182 MPa. The shape of the two stress-strain loops seems to stabilize after a few tens of cycles.

Upon increasing the axial stress amplitude to ± 254 MPa, it is observed that for the first ten cycles the ratcheting rates in both directions are decreasing with increasing cycles. Subsequently, the ratcheting rates gradually tend to increase with the increasing cycles and eventually the specimen collapses (Figs. 8 and 9(*b*)). The occurrence of such an instability may be explained as follows. At the previous stage ($\Delta\sigma/2 = 182$

Downloaded 03 May 2010 to 171.66.16.20. Redistribution subject to ASME license or copyright; see http://www.asme.org/terms/Terms_Use.cfm

MPa) the residual deformation had accumulated to about +1.5 percent in hoop (or radial) direction. Under larger stress range ($\Delta\sigma/2 = 245$ MPa), the ratcheting process did accelerate and the profile in the middle part of the specimen gradually changed into a barrel shape. Although the axial load was still kept at a constant range, the actual stress range in the specimen increased due to additional bending effect of the barrel shape. This barreling effect becomes greater with increased ratcheting deformation and eventually causes the collapse of the specimen (Fig. 9(*b*)).

By comparing the strain and stress-controlled test results, it is clear that the stress-controlled biaxial ratcheting could accelerate the damage process since accumulated deformations in two principal directions can develop simultaneously.

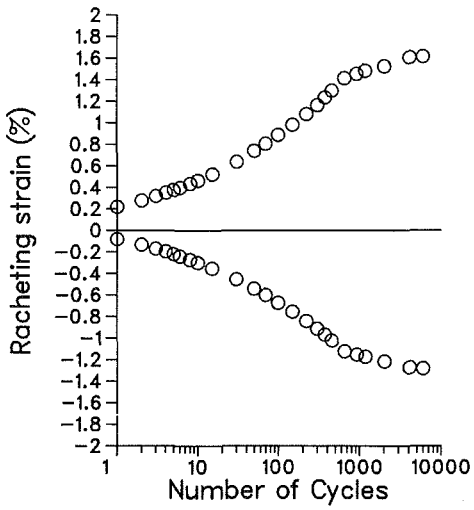


Fig. 5 Ratcheting strains versus number of cycles (stress-control)

3 Description of Constitutive Model

Recently, Ellyin and Xia (1989, 1991) have presented a hierarchy of constitutive models including rate-independent, rate-dependent, and creep models. In this paper we extend the constitutive model by introducing an additional evolution rule for the stress memory surface. This greatly improves predictive capability of the model for the ratcheting deformation. For those cases without ratcheting deformation, the previous model is recovered.

It is known that the type 304 stainless steel is a rate-sensitive material even at room temperature. In our previous paper, Ellyin and Xia (1991), a rate-dependent constitutive model has been presented to simulate various rate-dependent behaviors of this material. The model is formulated based on a family of rate-dependent uniaxial stress-strain curves. In the case of loading with a constant strain-rate or a constant stress-rate, as in the present ratcheting tests, the rate-dependent model reduces to a rate-independent one, provided that the calculation is based on a uniaxial stress-strain curve corresponding to this particular strain or stress rate. Therefore, for the sake of simplicity, the following description of constitutive model is presented within the context of the rate-independent behavior.

We define two hypersurfaces in the stress space, a yield surface and a stress memory surface:

$$\phi_y = f_y(\sigma_{ij} - \alpha_{ij}) - q^2 = 0, \tag{1}$$

$$\phi_m^\sigma = f_m^\sigma(\sigma_{ij} - \beta_{ij}) - R^2(\sigma_{e,\max}) = 0. \tag{2}$$

In the foregoing equations, α_{ij} and q specify the center and radius of the yield surface. The size of the stress memory

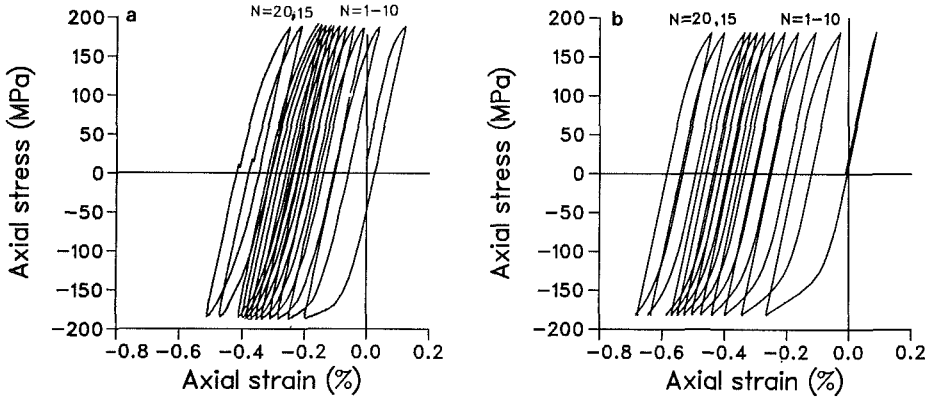


Fig. 6 Axial strain versus axial stress for stress-controlled ratcheting test; (*a*) test result; (*b*) predicted result

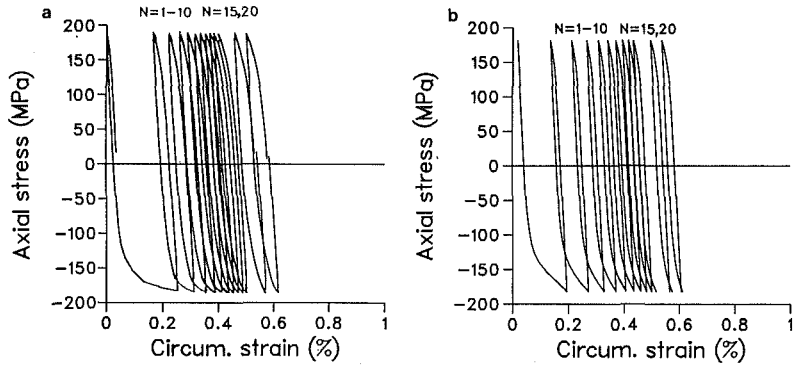


Fig. 7 Circumferential strain versus axial stress for stress-controlled ratcheting test; (*a*) test result; (*b*) predicted result

Downloaded 03 May 2010 to 171.66.16.20. Redistribution subject to ASME license or copyright; see http://www.asme.org/terms/Terms_Use.cfm

surface, R, is determined by the maximum equivalent stress level experienced by the material during its previous loading history. In our earlier constitutive model, the stress memory surface was defined as an isotropic one, i.e., $\beta_{ij} \equiv 0$. Now we introduce a variable to represent anisotropy of the stress memory surface. Under certain loading conditions, the stress memory surface may become anisotropic, or the β_{ij} may gradually move to a new location in the stress space. Details of the evolution rule of β_{ij} will be described later on.

It is assumed that the total strain increment can be decomposed into elastic and plastic parts, i.e.,

$$d\epsilon_{ij} = d\epsilon^e_{ij} + d\epsilon^p_{ij}. \tag{3}$$

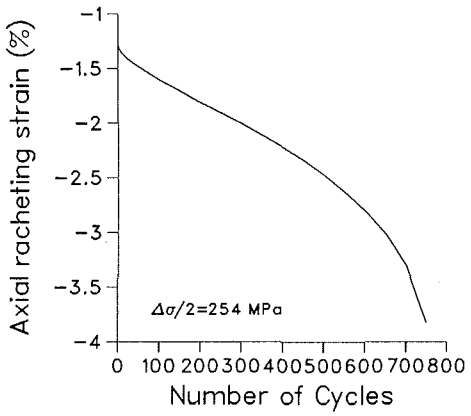


Fig. 8 Axial ratcheting strain versus number of cycles for stress-controlled test with increased stress range $\Delta\sigma/2 = 254$ MPa

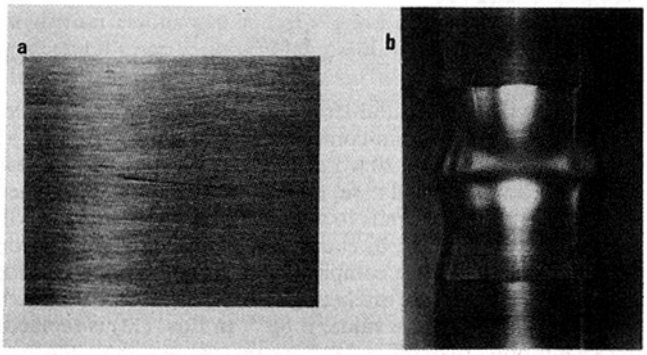


Fig. 9 Photographs of failed specimens; (*a*) strain-controlled test, a crack has penetrated the thickness; (*b*) stress-controlled test, collapsed surface

The increment of elastic strain is related to the stress increment through the generalized Hooke's law, and the increment of plastic strain is written as

$$d\epsilon^p_{ij} = g \frac{\partial f_y}{\sigma_{ij}} \frac{\partial f_y}{\partial \sigma_{kl}} d\sigma_{kl}. \tag{4}$$

In the case of von Mises yield condition,

$$d\epsilon^p_{ij} = 9g(s_{ij} - \alpha_{ij})(s_{kl} - \alpha_{kl}) d\sigma_{kl}, \tag{5}$$

where s_{ij} is the deviatoric stress tensor, g can be determined by specializing (5) to the uniaxial case. We thus obtain

$$g = \frac{1}{4q^2}\left(\frac{1}{E_t} - \frac{1}{E}\right), \tag{6}$$

where E is the elastic modulus and E_t is the instantaneous tangent modulus.

In this model two types of plastic loading are distinguished by the introduction of the stress memory surface. The first type is called monotonic loading (ML) in which the stress memory surface expands with the movement of the yield surface and the two surfaces remain tangent to each other. The second type is termed plastic reloading (RL). For this case the plastic deformation takes place after an elastic unloading and the current stress point is inside the stress memory surface. When the current stress point touches the memory surface again, it moves by expansion, and we incorporate the latter stage into the ML case.

The evolution rule of the yield surface and the calculation of the tangent modulus, E_t, are also different for the two plastic loading cases.

For the ML case, a Ziegler type of evolution rule is adopted, i.e.,

$$d\sigma_{ij} = d\mu(\sigma_{ij} - \alpha_{ij}). \tag{7}$$

For the RL case, it is assumed that

$$d\alpha_{ij} = d\mu(\sigma^m_{ij} - \sigma^y_{ij}), \tag{8}$$

where σ^y_{ij} is the current stress point on the yield surface, C', σ^m_{ij} is a point on the stress memory surface, D', whose exterior normal is parallel to the outward normal at the point σ^y_{ij} (see Fig. 10(*b*)). By using the consistency condition,

$$d\phi_y = \frac{\partial f_y}{\partial \sigma_{ij}}(d\sigma_{ij} - d\alpha_{ij}) - 2q\,dq = 0, \tag{9}$$

and one of the Eqs. (7) or (8), the $d\alpha_{ij}$ is completely determined.

The tangent modulus is defined as a function of the equivalent stress, $\sigma_e = [3s_{ij}s_{ij}/2]^{1/2}$, in the ML case. The function relation is obtained from the uniaxial stress-strain curve. In the RL case, it is obvious that the effective stress value is no longer a proper variable to calculate the E_t. For most metals

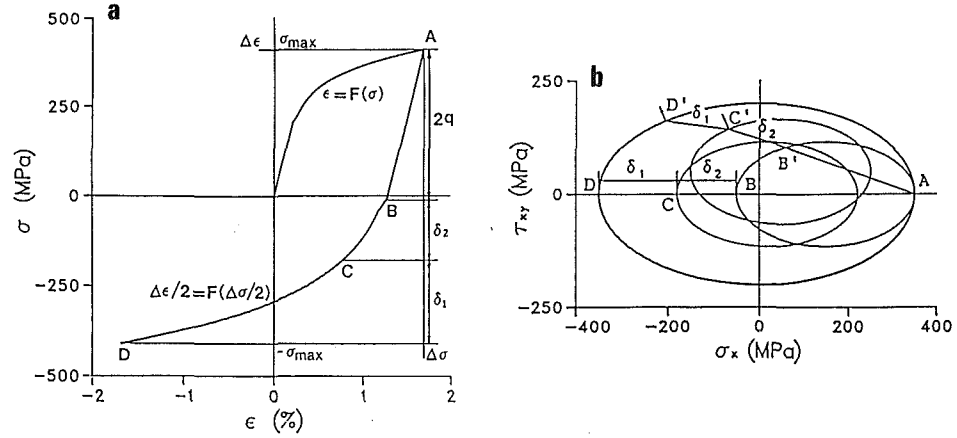


Fig. 10 Evolution rule of yield surface and calculation of tangent modulus for two types of plastic loading

Downloaded 03 May 2010 to 171.66.16.20. Redistribution subject to ASME license or copyright; see http://www.asme.org/terms/Terms_Use.cfm

it is found that the unloading branch can be described approximately by a uniaxial curve magnified by a factor of two. If the uniaxial curve is expressed as $\epsilon = F(\sigma)$, the unloading curve can be represented by $\Delta\epsilon/2 = F(\Delta\sigma/2)$, (see Fig. 10(*a*)). Let us first consider the uniaxial unloading case as shown in Fig. 10(*b*). From the maximum stress point A to point B, the unloading is elastic and upon further unloading reversed plastic flow will take place. From Fig. 10(*a*, *b*) we can see that a ratio $r = \delta_1/\delta_2$ uniquely determines a corresponding point on the unloading curve. At point B, $\delta_2 = 0$, $r = \infty$ and $E_t = E$ (elastic modulus); at point D, $\delta_1 = 0$, $r = 0$ and $E_t = E_t^{(D)}$. The above can easily be extended to nonproportional loading (see Fig. 10(*b*)) whereby the distance δ_1 is measured from the current stress point C' (σ_{ij}^{y}) to a corresponding point on the memory surface, D', as described above. The distance δ_2 is measured from the point of the onset of plastic flow B' (σ_{ij}^{0}) to the point C' (σ_{ij}^{y}). Therefore, at any instant of plastic reloading (current stress point being inside the stress memory surface) we can find the ratio r and then a corresponding point on the uniaxial curve and subsequently determine the value of E_t. It is noted that the point B' (σ_{ij}^{0}) should be updated after every elastic unloading process. If the current stress point touches the memory surface again, then the memory surface moves by expansion, and the loading type switches to the ML case.

The above rule for the determination of the tangent modulus is straightforward and it is preferable to the ones described elsewhere. In a review of various approaches for correlating the modulus function, McDowell (1987) concluded that the distance "δ" has to be normalized with respect to a parameter which is a function of loading history. The dimensionless parameter r has the required properties relating previous loading history to the current one.

The transient hardening is reflected in a change of q and E_t. This is specified by

$$\frac{\partial q}{\partial l_p} = k_1 (q_{st} - q), \tag{10}$$

$$\frac{\partial E_t}{\partial l_p} = k_1 (E_{t,\,st} - E_t), \tag{11}$$

where k_1 is a material constant, the subscript "*st*" refers to the stable (saturated) state, and l_p is the accumulated plastic length,

$$l_p = \int \left(\frac{2}{3} d\epsilon_{ij}^{p} \, d\epsilon_{ij}^{p} \right)^{1/2}. \tag{12}$$

Equations (10) and (11) are equivalent to a family of uniaxial curves which evolves from a virgin state to a saturated state with the increasing l_p (Fig. 11). The model also considers extra hardening effect of nonproportional loading path by introducing a ratio of two areas defined in the strain Π-plane. The procedure to determine the ratio as well as other details of the model can be found in Xia and Ellyin (1991).

We now turn to the formulation of evolution rule for the stress memory surface, which is essential in properly predicting the ratcheting deformation. From the experimental observations (Section 2.3), we find that the axial strain-hoop strain loop (in the strain-controlled tests) or the axial stress-axial strain, and axial stress-hoop strain loops (in the stress-controlled tests) all tend to a stable shape after a transient stage. This indicates that q and E_t do not change significantly after the transient stage. Both sets of tests also show that ratcheting mainly develops in one direction of the loading path (i.e., in the decreasing direction). This implies that the instantaneous values of E_t for two loading directions in a cycle are different. This asymmetry decreases with the increasing cycles. It was indicated earlier that the value of E_t is related to a ratio of two distances in the stress space, which is dependent on the relative position of the yield and memory surfaces. It is to be noted also that a certain mean stress state is required for the development of ratcheting deformation. An isotropic stress memory surface ($\beta_{ij} = 0$) introduces asymmetry for a cyclic loading path with a nonzero mean stress. If the stress memory surface remains isotropic ($\beta_{ij} = 0$), then the ratcheting rate will converge to a constant value. To simulate a decreasing ratcheting rate the stress memory surface must gradually evolve to a symmetrical configuration with respect to the cyclic loading path. This implies that the mean stress point will be the limiting location of the β_{ij}. We thus specify the following rule for the evolution of the stress memory surface center,

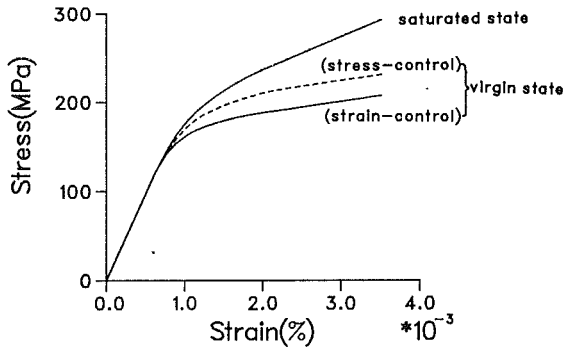


Fig. 11 Uniaxial curves used in the calculations

$$\frac{\partial \beta_{ij}}{\partial l_p} = k_2 (\sigma_{ij}^{\text{mean}} - \beta_{ij}), \tag{13}$$

where the mean stress $\sigma_{ij}^{\text{mean}}$ is defined as the geometric center of the cyclic stress path in the stress space. In general, the cyclic stress path is represented by a closed spatial curve in the stress space. The geometrical center of the cyclic stress path can be expressed as

$$\sigma_{ij}^{\text{mean}} = \frac{\oint_L \sigma_{ij} dl}{\oint_L dl} \tag{14}$$

where dl is the differential length of the curve. For example, in the case of the strain-controlled test, we can choose the initial stress value, $\sigma_a = 20$ MPa, $\sigma_t = 80$ MPa as $\sigma_{ij}^{\text{mean}}$, whereas for the stress-controlled case, $\sigma_a = 0$, $\sigma_t = 80$ MPa. Thus, when the number of cycles tends to a large value, the ratcheting will eventually stop. In fact, by choosing a proper function relation we can simulate a more complicated decreasing process of the ratcheting rate, and the ratcheting rate can be adjusted to reach an asymptotically finite value, if $\sigma_{ij}^{\text{mean}}$ in Eqs. (13) is replaced by a value other than the real mean stress value in the ratcheting process. Another advantage of such a rule is that for a loading case without ratcheting ($\sigma_{ij}^{\text{mean}} = 0$), our previous model is recovered. In other words, the material constant, k_2, is independent of all other material constants, it affects only the ratcheting behavior and has no effect on other types of materials response. This is not the case in some proposed constitutive models in which an additional evolution rule does effect the prediction for other loading cases (e.g., see Chaboche and Nouaihas, 1989b).

4 Comparison With Experimental Results

From the description of the constitutive model in the previous section we note that two uniaxial curves (virgin and saturated) are needed. These two curves are shown in Fig. 11. In fact, the two curves were obtained from the strain-controlled test (Fig. 2(*a*)). From these curves the elastic modulus ($E = 1.94 \times 10^5$ MPa), two interpolating tables representing function relations between the tangent modulus, E_t, and the equivalent stress, σ_e, could be easily obtained. Other material constants for the calculation are taken as

$$\nu = 0.25 \quad q_0 = q_{st} = 123.8 \text{ MPa}, \quad k_1 = 150, \quad k_2 = 45.$$

Downloaded 03 May 2010 to 171.66.16.20. Redistribution subject to ASME license or copyright; see http://www.asme.org/terms/Terms_Use.cfm

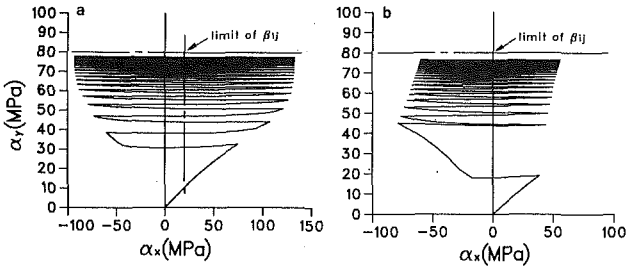


Fig. 12 The predicted trajectory of back stress α during the first 20 cycles; (*a*) strain-controlled test; (*b*) stress-controlled test

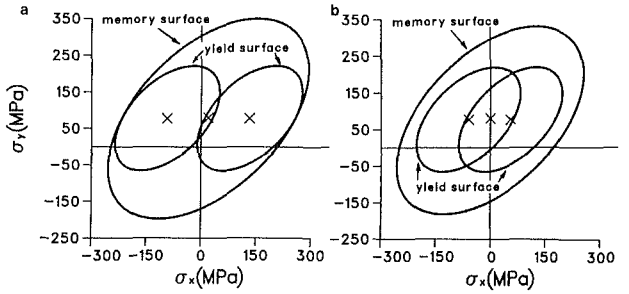


Fig. 13 The relative position of stress memory surface and yield surface at the 20th cycle predicted by the model; (*a*) strain-controlled test; (*b*) stress-controlled test

Figures 2(*b*), 3(*b*), 12(*a*), and 13(*a*) show the prediction of the model for the strain-controlled tests. It can be seen that the prediction results are in fairly good agreement with the experimental observations. Figure 13(*a*) shows the relative position of the yield and memory surfaces at 20th cycle. In the limiting case ($l_p \to \infty$), the yield surface will move completely symmetric with respect to the stress memory surface ($\beta_a = 20$ MPa, $\beta_l = 80$ MPa), in which case the ratcheting stops.

Figures 6(*b*), 7(*b*), 12(*b*), and 13(*b*) are the predicted results for the stress-controlled tests. It was mentioned in Section 3 that type 304 stainless steel is a rate-dependent material. The uniaxial curves at strain or stress-controlled modes are different. Usually the uniaxial curve tends to have a more gradual and large transition zone at the constant stress rate in comparison to the strain-controlled one (see Ellyin and Xia, 1991). The stress-controlled uniaxial curve (dashed curve, Fig. 11) with a larger transition zone is used as the virgin uniaxial curve for the stress-controlled test in the subsequent calculations. Comparing Figs. 6(*b*) and 7(*b*) with Figs. 6(*a*) and 7(*a*), we again see that there is a good agreement between the predicted and experimental results. Figure 13(*b*) shows the trend towards a symmetric position between yield and stress memory surfaces. Here the predicted results for the first 20 cycles are provided. After the first 20 cycles, the transient (isotropic) hardening process is almost complete. The only parameter which influences the rate of ratcheting is k_2 in Eq. (13). If we want to accurately correlate the accumulated ratcheting strain for the whole ratcheting process (up to hundreds or thousands of cycles), instead of taking a constant value for the k_2, a certain function form of $k_2 = k_2(l_p)$ has to be specified. Incorporation of this adjustment into the model presents no difficulty.

To further examine the capability of the model to predict other ratcheting tests we also present the results for a uniaxial cyclic test (with a constant mean stress) and a combined constant tension-cycle torsion test by using the same set of material constants (see Figs. 14 and 15). The trends shown in these figures are very similar to the experimental observation reported in the literature.

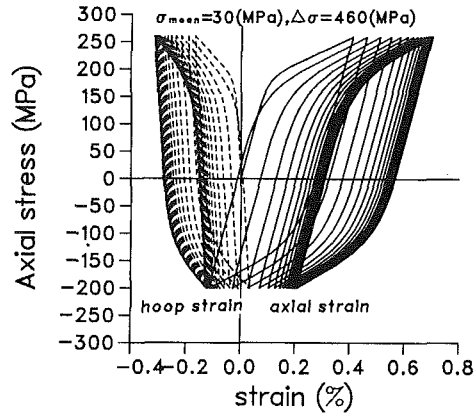


Fig. 14 Predicted ratcheting strains for uniaxial cyclic test with $\sigma_{mean} = 30$ MPa, $\Delta\sigma = 460$ MPa

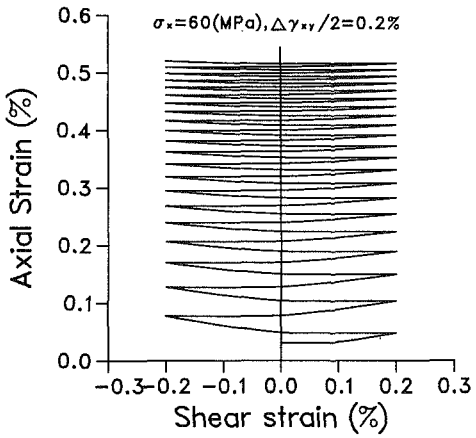


Fig. 15 Predicted ratcheting strain for cyclic shear test with $\sigma_x = 60$ MPa, $\Delta\gamma_{xy}/2 = 0.2$ percent

5 Conclusions

Results of biaxial strain or stress-controlled ratcheting test of type 304 stainless steel are presented. The following conclusions are reached:

(1) The rate of ratcheting is a decreasing function of number of cycles and there is no indication that the ratcheting rate asymptotically reaches a nonzero stable value.

(2) The stress-controlled biaxial ratcheting test can accumulate ratcheting deformation in both principal directions. Such a loading condition is more dangerous since it may accelerate material damage or lead to the collapse of components.

By introducing a simple additional evolution rule for the stress memory surface we have developed a constitutive model which shows the capability to correctly predict ratcheting behavior of materials.

6 Acknowledgments

The work reported herein is part of a general investigation into material behavior under multiaxial states of stress and adverse environments. The research is supported, in part, by the Natural Sciences and Engineering Research Council of Canada (NSERC Grant A-3808). We would like to thank the staff of the machine shop, A. Muir, Supervisor, for preparation of specimens, and B. Faulkner and I. Buttar in caring for the multiaxial test facility.

References

Blanchard, P., and Lemoine, P., 1988, "Constitutive Modelling of 17-12 Mo SPH Stainless Steel Behaviour at High Temperature," ASME *Journal of Pressure Vessel Technology*, Vol. 110, pp. 51–58.

Downloaded 03 May 2010 to 171.66.16.20. Redistribution subject to ASME license or copyright; see http://www.asme.org/terms/Terms_Use.cfm

Chaboche, J. L., and Nouailhas, D., 1989a, "Constitutive Modelling of Ratcheting Effects—Part I: Experimental Facts and Properties of the Classical Models," ASME *Journal of Engineering Materials and Technology*, Vol. 8, pp. 384–392.

Chaboche, J. L., and Nouailhas, D., 1989b, "Constitutive Modelling of Ratcheting Effects—Part II: Possibilities of Some Additional Kinematic Rules," ASME *Journal of Engineering Materials and Technology*, Vol. 8, pp. 409–416.

Ellyin, F., 1989, "An Anisotropic Hardening Rule for Elastoplastic Solids Based on Experimental Observations," ASME JOURNAL OF APPLIED MECHANICS, Vol. 56, pp. 499–507.

Ellyin, F., Golos, K., and Xia, Z., 1991, "In-Phase and Out-of-Phase Multiaxial Fatigue," ASME *Journal of Engineering Materials and Technology*, Vol. 113, pp. 112–118.

Ellyin, F., and Xia, Z., 1989, "A Rate-Independent Constitutive Model for Transient Non-Proportional Loading," *J. Mech. Phys. Solids*, Vol. 37, No. 1, pp. 71–91.

Ellyin, F., and Xia, F., 1991, "A Rate-Dependent Inelastic Constitutive Model—Part I: Elastic-Plastic Flow," ASME *Journal of Engineering Materials and Technology*, Vol. 113, pp. 314–323.

Inoue, T., Ohno, N., et al., 1989a, "Evaluation of Inelastic Constitutive Models under Plasticity-Creep Interaction for 2¼ Cr-1Mo Steel at 600°C," *Nuclear Engng. Design*, Vol. 114, pp. 295–309.

Inoue, T., Yoshida, F., et al., 1989b, "Plasticity-Creep Behaviour of 2¼ Cr-1Mo Steel at 600°C in Multiaxial Stress State," *Structural Design for Elevated Temperature Environment—Creep, Ratchet, Fatigue and Fracture*, PVP, Vol. 163, ASME, New York, pp. 101–107.

McDowell, D. L., 1989, "An Evaluation of Recent Developments in Hardening, and Flow Rules for Rate-Independent, Nonproportional Cyclic Plasticity," ASME JOURNAL OF APPLIED MECHANICS, Vol. 54, pp. 323–334.

McDowell, D. L., and Lamar, A. B., 1989, "Modelling Ratcheting and Anisotropic Deformation with Hardening Dynamic Recovery Format Models," *Proc. of Plasticity 89, 2nd Int. Symp. on Plasticity and Its Current Applications*, Tsu, Japan, A. S. Khan and M. Tokuda, eds., Pergamon, Oxford, U.K., pp. 247–251.

Xia, Z., and Ellyin, F., 1991, "Nonproportional Multiaxial Cyclic Loading: Experiments and Constitutive Modelling," ASME JOURNAL OF APPLIED MECHANICS, Vol. 58, pp. 317–325.

Downloaded 03 May 2010 to 171.66.16.20. Redistribution subject to ASME license or copyright; see http://www.asme.org/terms/Terms_Use.cfm

R. L. Weaver
Department of Theoretical and Applied Mechanics, University of Illinois at Urbana-Champaign, Urbana, IL 61801

W. Sachse
Department of Theoretical and Applied Mechanics Cornell University, Ithaca, NY 14853

Asymptotic Viscoelastic Rays in a Thick Plate

The high-frequency behavior of generalizd ray arrivals is discussed with a view towards material characterization by means of measurements of the dispersion of ultrasonic pulses. The effect of beam spreading is treated exactly. Signal processing algorithms are developed. They are demonstrated with a synthetic signal obtained in an elastic material.

Introduction

The dispersive and attenuating properties of elastic waves in solids are receiving increasing attention as a means for characterizing a variety of geological and high-technology materials. The existing methods utilized in most laboratory measurements have focused on plane wave studies. In these, a pulse or a burst of plane waves is propagated through a known thickness of the material and the dispersion of the pulse on reception are ascertained, usually as a function of frequency (Papadakis, 1976; Sachse et al., 1979; Winkler and Plona, 1982; Plona et al., 1987). An essential assumption in such methods is that plane waves are generated and detected in the specimen. The results can, however, be complicated in actual measurement situations by the lack of true plane waves. Beam spreading and the uncertainties in calibrating transducers of finite aperture complicate the plane wave analysis and introduce uncertainties into the data processing and measurement results (Truell et al., 1969). It has been proposed (Sachse and Kim, 1986; 1987a; 1987b) that the use of point sources and point receivers, with their consequent spherical waves, may be free of these uncertainties. However, spherical elastic waves possess a geometric dispersion and attenuation and the processing of the detected ultrasonic, spherical wave signals must correct for these geometric effects in order to extract the correct wave propagation characteristics. It is to be hoped that the geometric effects from a simple point source, though greater than those from a wide aperture transducer, may be more easily understood and corrected for in the detected signals.

This paper deals with the frequency-dependent phase of a detected ultrasonic signal and the procedures for properly extracting the material's dispersion relation from them. In the next section the standard analysis of a plane viscoelastic longitudinal pulse traveling through the thickness of a plate specimen is reviewed and the basic features of the dispersion determination process described. The *P*-ray arrival at epicenter in a plate is presented in Section 3. Instead of the usual evaluation of the wave amplitude in the time domain by the Cagniard method, it is evaluated asymptotically in the frequency domain. A formula similar to that of the plane wave case is developed and the correction factor for the different geometry determined. The effect of the correction factor on dispersion and attenuation assessments is discussed. A similar formula for the *S*-ray is presented and the use of other ray arrivals is also discussed. A synthetic signal corresponding to an elastic material is employed in Section 4 in order to illustrate the procedure for recovery of the dispersion relation of the material.

Contributed by the Applied Mechanics Division of THE AMERICAN SOCIETY OF MECHANICAL ENGINEERS for publication in the ASME JOURNAL OF APPLIED MECHANICS.

Discussion on this paper should be addressed to the Technical Editor, Professor Lewis T. Wheeler, Department of Mechanical Engineering, University of Houston, Houston, TX 77204-4792, and will be accepted until four months after final publication of the paper itself in the ASME JOURNAL OF APPLIED MECHANICS.

Manuscript received by the ASME Applied Mechanics Division, June 30, 1988; final revision, Mar. 25, 1993. Associate Technical Editor: R. M. Christensen.

2 Plane Waves in a Plate

We consider a homogeneous viscoelastic flat plate of thickness $2h$ $(=L)$ subjected to a step traction of magnitude τ applied on one face at $z=-h$. The normal displacement response at $z=h$ is sought. We assume that the material behavior is well described by the density ρ and the generalized complex Lamé moduli $\lambda(\omega)$ and $\mu(\omega)$. Thus the results to be presented will strictly apply only to effectively homogeneous, isotropic, local, and viscoelastic materials. The stated problem is equivalent to a symmetrized problem of forces applied simultaneously on both faces of the plate with the ray arrivals from the extra source discarded. The symmetrized problem has the equation of motion in the spatial domain

$$\rho\omega^2\hat{u}(z)+(\lambda+2\mu)\frac{d^2\hat{u}(z)}{dz^2}=0 \tag{1}$$

with the displacements subject to the surface tractions τ at the boundary

$$(\lambda+2\mu)\frac{d\hat{u}(z)}{dz}\bigg|_{z=\pm h}=-\tau/(-i\omega). \tag{2}$$

The Fourier transform of the longitudinal displacements is given by

Copyright © 1994 by ASME
Downloaded 03 May 2010 to 171.66.16.20. Redistribution subject to ASME license or copyright; see http://www.asme.org/terms/Terms_Use.cfm

$$\hat{u}(\omega, z) \equiv \int_{-\infty}^{\infty} u(t, z) e^{i\omega t} dt$$

and the symmetric solution to the equation of motion is then

$$\hat{u}(\omega, z) = -i \frac{\tau \sin \mathbf{k}z}{\omega \mathbf{k}(\lambda + 2\mu) \cos \mathbf{k}h} \tag{3}$$

where the complex dispersion relation is given by

$$\mathbf{k}(\omega) = \frac{\omega}{\mathbf{c}_P(\omega)} = \omega \sqrt{\frac{\rho}{(\lambda + 2\mu)}} \tag{4}$$

in which $\mathbf{c}_P(\omega)$ is the complex longitudinal wavespeed of the material.

At $z = h$ the response can be written as a sum of powers of e^{2ihk}, each of which corresponds to a separate ray arrival, with the even powers corresponding to the arrivals from the fictitious source. The term in e^{2ihk} to the first power is the first P-ray arrival. Its amplitude is

$$\hat{u}_P(\omega, z) = \frac{-2\tau e^{2ihk}}{\omega^2 \rho \mathbf{c}_P} \tag{5}$$

The explicit inverse ω^2 dependence given in Eq. (5) is characteristic of a ramp function in the time domain. The Fourier transform of the first signal arrival has, for large thicknesses, a significant frequency dependence via the factor e^{2ihk}. Different schemes can be used to extract the desired complex dispersion relation $\mathbf{k}(\omega)$ which is strongly material dependent (Sachse and Pao, 1978; Ting and Sachse, 1978). Ideally, the measurement should be repeated with plate specimens of different thicknesses. The Fourier transforms of the first wave arrivals of the respective signals are divided and the algebraic dependencies related to the tractions, τ, frequency, ω, and longitudinal wave speed, $\mathbf{c}_P$, thereby eliminated. Alternatively, with well-characterized sources and receivers, or at large thicknesses, the factor e^{2ihk}, or at least its phase, can be extracted directly. We now wish to consider how the above is modified if, instead of a distributed force resulting in a plane wave signal, the source is a point force resulting in a spherical wave signal.

3 The Viscoelastic P-Ray at Epicenter

In an elastic plate, the P-ray from a step surface normal point force gives rise to a displacement response at epicenter directly across the thickness dimension of the flat plate which consists of a step discontinuity followed by a smooth rise (Knopoff, 1958). The highest frequencies are found predominantly in the step, corresponding to the arrival of the signal corresponding to the P-ray. The response at lower frequencies includes a substantially larger contribution from the subsequent ramp-like behavior and thus appears to be delayed relative to the high-frequency components. The result is an apparent, geometric dispersion which has nothing to do with the properties of the material. The rise is at a rate such that on time scales comparable to transit times, the displacement achieves a level appreciably different from its initial level. This is an indication that geometric dispersion should be unimportant at high frequencies, that is, for signals whose wavelengths are short compared to the thickness of the plate specimen.

We consider here the symmetrized problem of an elastic slab subjected to simultaneous normal step inward forces $FH(t)$ on opposite sides of a plate specimen, at $z = \pm h$. Following the notation of Achenbach (Achenbach, 1973), we can write, for the Hankel and Fourier transforms of the symmetric displacement potentials

$$\hat{\bar{\phi}}^{H0} = A \cos pz; \quad \hat{\bar{\phi}}^{H1} = B \sin qz,$$

where $p^2 \equiv \omega^2/\mathbf{c}_P^2 - k^2$, and $q^2 \equiv \omega^2/\mathbf{c}_S - k^2$. Here, $\mathbf{c}_P(\omega)$ and $\mathbf{c}_S(\omega)$ are the longitudinal and transverse complex wave speeds and k is the Hankel transform variable. The double transform of the z-displacement field is

$$\hat{\bar{u}}^{H0} = kB \sin qz - Ap \sin pz \tag{6}$$

and the double-transformed boundary conditions related to the normal and shear tractions are

$$\hat{\bar{\tau}}_z^{H0}|_{z=\pm h} = \mu \left\{ (2k^2 - \omega^2/\mathbf{c}_S^2)\hat{\bar{\phi}}^{H0} + 2k \frac{d}{dz} \hat{\bar{\psi}}^{H1} \right\}_{z=\pm h} = \frac{-iF}{2\pi\mu\omega}$$

$$\hat{\bar{\tau}}_{zr}|_{z=\pm h} = -\mu \left\{ 2k \frac{d}{dz} \hat{\bar{\phi}}^{H0} + (2k^2 - \omega^2/\mathbf{c}_S^2)\hat{\bar{\psi}}^{H1} \right\}_{z=\pm h} = 0. \tag{7}$$

The boundary conditions can be solved for the coefficients A and B, and the response $\hat{\bar{u}}$ evaluated at $z = -h$. We obtain

$$\hat{\bar{u}}^{H0}|_{z=-h} = \frac{iF}{2\pi\mu\omega} \left(\frac{p\omega^2}{\mathbf{c}_S^2} \right) \frac{\sin qh \sin ph}{R} \tag{8}$$

where

$$R \equiv (2k^2 - \omega^2/\mathbf{c}_S^2)^2 \cos ph \sin qh + 4k^2 pq \cos qh \sin ph. \tag{9}$$

The Hankel transform is then inverted to give the Fourier transform of the response at $z = -h$ at a distance r from epicenter

$$\hat{u}(\omega) = \int_0^{\infty} kJ_0(kr)\hat{\bar{u}}^{H0}(k, \omega) dk. \tag{10}$$

For a receiver point at epicenter, $r = 0$, we obtain

$$\hat{u}(\omega) = \frac{iF\omega}{2\pi\mu\mathbf{c}_S^2} \int_0^{\infty} \frac{pk\, dk}{R} \sin qh \sin ph. \tag{11}$$

This expression is analogous to Eq. (3) and it can also be decomposed into a ray sum where the term of form e^{2iph} corresponds to the P-ray. Some algebra yields

$$\hat{u}_P(\omega) = \frac{F\omega}{\pi\mu\mathbf{c}_S^2} \int_0^{\infty} pk\, dk\, e^{2iph} \frac{(2k^2 - \omega^2/\mathbf{c}_S^2)^2}{[(2k^2 - \omega^2/\mathbf{c}_S^2)^2 + 4k^2 pq]^2}. \tag{12}$$

The procedure thus far is standard and with some changes can be found in the literature (Achenbach, 1973). The significant difference is that in Eq. (12) we understand $\mathbf{c}_P$ and $\mathbf{c}_S$ to be complex and frequency dependent. The usual next step, taken in the case $\mathbf{c}_P$ and $\mathbf{c}_S$ are constant, is evaluation of the inverse Hankel and Fourier transforms simultaneously by means of the Cagniard method. This is probably not possible for the general viscoelastic case, but here the time domain response is not needed, rather, it is the frequency domain response. That is, an equation analogous to Eq. (5), which was for plane waves, is required.

An exact analytic evaluation of the integral appearing in Eq. (12) is probably not possible either. However, from the remarks made at the beginning of this section it is clear that it is the high-frequency behavior that is relevant. Thus, the integral comprising Eq. (12) should be evaluated asymptotically, for large pL, with the end point at $k = 0$ corresponding to the arrival of the harmonic P-ray at the phase velocity $c_P(\omega)$.

A change of variables specified by

$$\phi = \frac{\mathbf{c}_P p}{\omega} = \sqrt{1 - \left(\frac{\mathbf{c}_P k}{\omega} \right)^2} \tag{13}$$

and a deformation of the contour gives

$$\hat{u}_P(\omega) = -\frac{F\mathbf{c}_S^2}{\pi\mu\mathbf{c}_P^3} \int_1^{\infty} \phi^2 d\phi \left(1 - 2(1 - \phi^2) \frac{\mathbf{c}_S^2}{\mathbf{c}_P^2} \right) e^{2ih(\omega/c_P)\phi}$$
$$\times \left[\left(1 - 2(1 - \phi^2) \left(\frac{\mathbf{c}_S^2}{\mathbf{c}_P^2} \right) \right)^2 \right.$$
$$\left. - 4 \left(\frac{\mathbf{c}_S}{\mathbf{c}_P} \right)^4 \phi(1 - \phi^2) \left(\left(\frac{\mathbf{c}_P}{\mathbf{c}_S} \right)^2 - 1 + \phi^2 \right)^{1/2} \right]^{-2}. \tag{14}$$

The term ϕ can now be interpreted as a dimensionless measure

Downloaded 03 May 2010 to 171.66.16.20. Redistribution subject to ASME license or copyright; see http://www.asme.org/terms/Terms_Use.cfm

of time, that is $\phi = tc_P/2h$. Application of the usual asymptotic formula

$$\int_1 g(\phi)e^{ix\phi}d\phi \sim e^{ix}[-ig(1)/x + g'(1)/x^2 + ig''(1)/x^3 + \cdots] \tag{15}$$

gives for the displacements of the P-wave amplitude

$$\hat{u}_P(\omega) = \frac{iF}{\pi\rho 2h\omega \mathbf{c}_P^2} e^{2ih\omega/c_P}\left[1 + i\frac{\mathbf{A}}{(2h\omega/\mathbf{c}_P)} + \cdots\right]. \tag{16}$$

The correction factor is specified by $\mathbf{A}$ which is given by

$$\mathbf{A} = 2 - 8\left(\frac{\mathbf{c}_S}{\mathbf{c}_P}\right)^2 + 16\left(\frac{\mathbf{c}_S}{\mathbf{c}_P}\right)^3. \tag{17}$$

For materials whose Poisson ratio is 1/3, the value of $\mathbf{A}$ is equal to 2. While the correction factor, in fact, depends on the unknown and potentially frequency-dependent wave speeds, it is worth noting that any extra frequency dependence in the correction term beyond the explicit ω would be of second order in the dispersion. A good initial estimate for the correction factor can be obtained by using nominally real and constant wavespeeds c_P and c_S, yielding a real and constant value A.

It follows from Eq. (16) that the Fourier phase function of the velocity signal corresponding to the P-wave arrival is given by

$$\phi(\omega) = kL + \frac{A}{kL} \tag{18}$$

Here $k(\omega)$ $(=\omega/c_P)$ corresponds to the dispersion relation. The first term of the phase function is identical to that derived for plane waves by Sachse and Pao (1978). The phase functions of other source types are expected to exhibit a similar form. It is seen from Eq. (16) that the value of A in the correction term is proportional to the slope of the displacement rise in the time domain immediately subsequent to the ray arrival.

The results contained in Eq. (16) can be compared with Eq. (5). In both cases the important behavior for large thicknesses is in the exponential term. The inverse ω scaling appearing in Eq. (16) is characteristic of a step function in the time domain. However, at lower frequencies, the inverse ω scaling is contaminated by an ω^{-2} term, characteristic of a ramp function in the time domain.

A naïve application of methods based on Eq. (5) for extraction of the dispersion relation, $k(\omega)$, may be seriously compromised by the curvature correction factor which is given by $1 + iA/(2h\omega/c_P) + \cdots$. Even for fairly large specimen thicknesses, where this factor is close to 1, the curvature correction factor has a nonzero phase and may affect the determination of the dispersion relation. This is particularly true if the material dispersion is small.

A comparison of the dispersion relation determined from the plane and the spherical wave analysis methods is now made. If the $k(\omega)$ evaluation is carried out using the formula based on Eq. (5), then from the displacement signal amplitudes determined on two plates of differing thicknesses, say x and $x+\Delta x$, the signal processing would conclude with an estimate for $k(\omega)$ to be $k_e(\omega)$ given by

$$k_e(\omega) = -\frac{i}{\Delta x}\log_e\left[\frac{\hat{u}(x+\Delta x)}{\hat{u}(x)}\right]. \tag{19}$$

Substitution of Eq. (16) into Eq. (20) gives the estimated dispersion relation at large kx.

$$k_e(\omega) = k + \frac{A}{\Delta x}\left[\frac{1}{k(x+\Delta x)} - \frac{1}{kx}\right] \neq k \tag{20}$$

It is seen that the estimated phase velocity, $c_e = \omega/k_e$ possesses an apparent frequency dependence even in the absence of any material dispersion. That is, the estimated phase velocity will be

$$c_e = c\left[1 + \frac{-A}{x(x+\Delta x)}\left(\frac{c}{\omega}\right)^2\right] \tag{21}$$

Alternatively, if the phase function of a received signal from an experiment on a flat plate of fixed thickness $x = 2h$ is set equal to $k_e x$, as is appropriate in the plane wave case, an incorrect determination of dispersion is recovered from a measurement utilizing spherical waves. That is

$$k_e L = \phi(\omega) = kL + A/kL$$

where the $\pi/2$ term in the phase from the factor i in Eq. (16) has been absorbed into the receiver calibration and does not appear in the measured phase. It is seen from the above that the values for k_e are overestimated, hence leading to an underestimate of the phase velocity. As expected, the lower frequency components of the signal possess an apparent velocity which is lower than the higher frequency components.

Clearly, to obtain a correct result, the received epicentral phase spectra must be corrected by dividing out the geometric factor before initiating the standard signal processing which was previously used to analyze the signals obtained in plane wave experiments. It is noted, however, that the geometric correction factor is accurate only to the second term in an asymptotic series and hence is not exact. The lack of an exact correction term may force measurements made on materials having a small dispersion to be extended to higher frequencies or carried out in thicker slabs.

The epicentral responses have the additional virtue of including a signal corresponding to the S-ray as well. Because of this, it should be possible to determine the shear wave dispersion as well as that of the P-wave signal from a single measurement. The arrival of the S-ray is approximately a ramp function and has no step discontinuities; it thus lacks strong high-frequency content. Nevertheless, its asymptotic spectral behavior is given here for possible application. The S-ray is given by the e^{2iqh} term in the ray series expansion of Eq. (11). Manipulations similar to those previously used to derive Eq. (16) give for the asymptotic form of the S-ray arrival a result similar to that given by Eq. (16) with the correction factor specified by $\mathbf{B}$, where

$$\mathbf{B} = 32\left(\frac{\mathbf{c}_S}{\mathbf{c}_P}\right) + 4\left(\frac{\mathbf{c}_P}{\mathbf{c}_S}\right)^2 - 27. \tag{22}$$

The value of B is 5.00 for materials whose Poisson ratio is 1/3. The Fourier phase function of the displacement or the negative of acceleration signal corresponding to the S-wave arrival is given by $\phi_S(\omega) = kL + B/kL$. This result pertains to the asymptotic form of only the S-ray arrival and assumes no contribution from the tail of the P-ray.

The application of Eq. (16) to experimental waveforms requires that only the signal from the desired ray be processed. Strictly speaking this is of course impossible; the actual waveforms are superpositions of all rays. The undesired rays, however, usually contribute no discontinuities near the arrival time of the ray of interest, and therefore they do not contribute at high frequencies. We are thus led to suggest that the waveform in the vicinity of the relevant ray arrival time be smoothly gated, resulting in a windowed waveform containing, at high frequencies, only information related to the ray of interest. The windowing must be carried out carefully to minimize any sharp truncations of the waveform in the time domain before a spectrum analysis is made which could result in spurious, high-frequency amplitudes. The windowing function should be as wide as possible in the time domain in order to preserve maximal moderate frequency information and in order to incorporate all constituents of a possibly heavily dispersed pulse. On the other hand, it should be sufficiently short to exclude any contamination from other rays. Elementary analysis tells

Downloaded 03 May 2010 to 171.66.16.20. Redistribution subject to ASME license or copyright; see http://www.asme.org/terms/Terms_Use.cfm

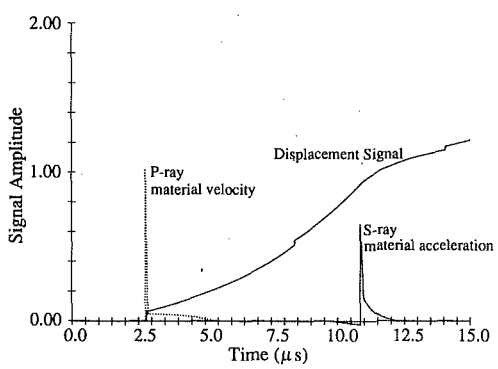


Fig. 1 Epicentral displacement response (solid line) of an elastic plate of thickness 2.5 cm to a step load as calculated by generalized ray theory. c_P was taken to be 0.8871 cm/μs and c_S as 0.2288 cm/μs. The windowed *P*-ray arrival material velocity is shown as the dotted line. The dash-dot line shows the negative of the material acceleration associated with the *S*-ray.

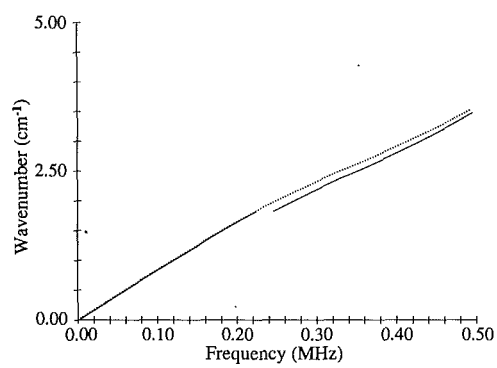


Fig. 2 Values of $k_P(\omega)$ as recovered from the phase function, ϕ of the Fourier phase function of the windowed *P*-waveform shown in Fig. 1. The function $k(\omega)$ as constructed from $k=\phi/L$ is shown in the dotted line; $k(\omega)$ as constructed from $k=\phi/L - A/kL^2$ is shown in the solid line.

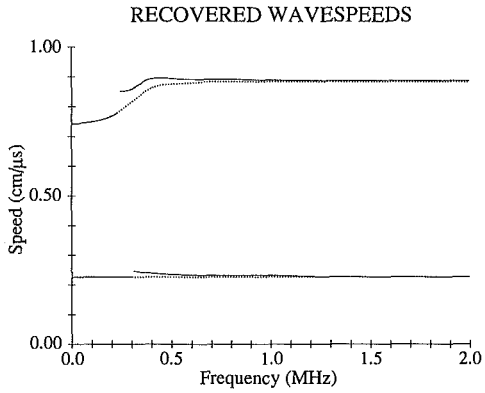


Fig. 3 *P* and *S*-wavephase velocities as obtained from $c=\omega/k$ with k recovered as in Fig. 2. The solid lines are based on the $k(\omega)$ recovered using the full formula, with correction term. The dotted lines are based on the plane wave formula.

us that a window function with no discontinuity except at its second and higher derivatives will introduce spurious terms in the resulting spectrum of order ω^{-3}, which is negligible at high frequencies, negligible that is, compared with the asymptotics of a ray arrival which is itself of stronger discontinuity. Such a window function is provided by a cosine bell.

While the *P* and *S*-rays at epicenter are probably the least difficult to treat analytically and identify experimentally, it appears that in principle any generalized ray arrival could be used for laboratory assessments of dispersion. The 3*P*-ray, for example, though diminished in amplitude compared to the 1*P* signal, might be more useful because its extra path length would give it greater sensitivity to dispersion. All the early generalized rays in a slab, on and off epicenter, have been calculated for the case of elastic materials (Knopoff, 1958; Ceranoglu and Pao, 1981). It would be a straightforward matter to extract from these calculations the asymptotic behavior of the viscoelastic rays should they be judged useful for experimental assessments of material dispersion and attenuation.

4 Example

To demonstrate the phase analysis procedure for determining the dispersion of point-source generated signals, a numerical experiment was carried out. Using known longitudinal and shear wavespeeds as input data, a solution to the forward problem, that is, the epicentral displacement signal corresponding to a point force, step excitation, was found. This signal was then processed according to the algorithm presented in the previous section to recover the frequency-dependent wavespeeds.

In this example, the input wavespeeds are constant and real for all frequencies, with $c_P = 0.8871$ cm/μs and $c_S = 0.2288$ cm/μs. The synthetic epicentral displacement signal resulting from a step force normal to the surface of the plate is shown in Fig. 1. Also shown in the figure are the *P*-ray velocity signal portion and the negative of the *S*-ray acceleration signal portion of the waveform, gated out according to the procedure specified in the previous section.

If the signals are assumed to have been generated by a plane wave source, the dispersion can be found from the Fourier phase function, ϕ, of the gated portion of the signal; $\phi(\omega) = kL$. If a spherical wave source is correctly assumed, the dispersion relation can be found from the Fourier phase function according to Eq. (18). It is assumed here that the attenuation of the material is sufficiently low that the dispersion relation can be approximated by its real part, i.e., $\mathbf{k}(\omega) \simeq k(\omega)$.

A comparison of the dispersion relations, $k(\omega)$, recovered by the two methods is shown in Fig. 2. The corresponding phase velocities ω/k are shown in Fig. 3. It is noted that a solution to Eq. (18) is only obtained for sufficiently large values of ϕ, corresponding to sufficiently high frequencies. Inasmuch as Eq. (18) is only asymptotic, it is only valid for these frequencies anyway.

The dispersion relation and corresponding phase velocities were obtained with and without the use of the correction terms A/kL and B/kL in order to assess the importance and accuracy of the correction terms. The correction term was, however, deleted for those low frequencies such that ϕ was less than $\sqrt{12A}$ (or $\sqrt{12B}$), where the correction term is sufficiently large that one might question the validity of the asymptotics, hence the discontinuities in Figs. 2 and 3. These discontinuities mark our estimated limit of validity of the asymptotic formulae.

In all four cases the correct wave speeds are recovered for all frequencies above 1.5 MHz. For the *P*-ray case, the wave speed as recovered by the full formula (solid line) is as accurate or more accurate than the plane wave formula (dotted line) for all frequencies. It does, however, show some slight unphysical structure that is related to illegitimacy of the asymptotics at low frequencies. The *S*-ray velocities are recovered more accurately by the full formula above 750 kHz, but less accurately at lower frequencies. In this particular simulation, the *S*-ray velocities are in fact quite accurately recovered over the entire frequency range by the plane wave formula.

The chief conclusion which we draw from this example is that the simple plane wave formula is not excessively inac-

Downloaded 03 May 2010 to 171.66.16.20. Redistribution subject to ASME license or copyright; see http://www.asme.org/terms/Terms_Use.cfm

curate. We further conclude that for higher frequencies where the correction term provides a clear increase in accuracy, it is not very significant. At lower frequencies where the correction term is more significant, the asymptotics is losing its validity. It is probably most fair to use the "correction" term, not as a *correction* term to the plane wave formula, but as a test for the accuracy of the plane wave formula. As in the usual asymptotic recipe, one states that the plane wave formula $\phi = kL$ has an error estimated to be of the order of the first term neglected, that is A/kL or B/kL.

5 Acknowledgments

This work has been supported by grants from the Solid Mechanics Program of the National Science Foundation. The work of RLW has been supported by Grant MSM-8412178 and that of WS by Grant MSM-8405466. Additional support also came from the Solid Mechanics Program of the Office of Naval Research.

References

Achenbach, J. D., 1973, *Wave Propagation in Elastic Solids*, North-Holland, Amsterdam, Chapter 8.

Ceranoglu, A. N., and Pao, Y. H., 1981, "Propagation of Elastic Pulses and Acoustic Emission in a Plate," ASME JOURNAL OF APPLIED MECHANICS, Vol. 48, pp. 125–147.

Knopoff, L., 1958, "Surface Motions of a Thick Plate," *J. Appl. Phys.*, Vol. 24, pp. 661–670.

Papadakis, E. P., 1976, "Ultrasonic Velocity and Attenuation: Measurement Methods with Scientific and Technical Applications," in *Physical Acoustics*, Vol. 12, W. P. Mason and R. N. Thurston, eds., Academic Press, New York, pp. 277–374.

Plona, T. J., Winkler, K. W., and Schoenberg, M., 1987, "Acoustic Waves in Alternating Fluid/Solid Layers," *J. Acoust. Soc. Am.*, Vol. 81, pp. 1227–1234.

Sachse, W., and Kim, K. Y., 1986, "Point-Source/Point-Receiver Materials Testing," *Review of Quantitative Nondestructive Evaluation*, Vol. 6A, D. O. Thompson and D. E. Chimenti, eds., Plenum Press, New York, pp. 311–320; also 1987a, in *Ultrasonic Materials Characterization II*, J. Boussière, J. P. Monchalin, C. O. Ruud, and R. E. Green, eds., Plenum Press, New York, pp. 707–715.

Sachse, W., and Kim, K. Y., 1987b, "Quantitative Acoustic Emission and Failure Mechanics of Composite Materials," *Ultrasonics*, Vol. 25, pp. 195–203.

Sachse, W., and Pao, Y. H., 1978, "On the Determination of Phase and Group Velocities of Dispersive Waves in Solids," *J. Appl. Phys.*, Vol. 49, No. 8, pp. 4320–4327.

Sachse, W., Ting, C. S., and Hemenway, A., 1979, "Dispersion of Elastic Waves and the Nondestructive Testing of Composite Materials," *Composite Materials: Testing and Design*, (Fifth Conference), ASTM STP 674, S. W. Tsai, ed., ASTM, Philadelphia, PA, pp. 165–183.

Ting, C. S., and Sachse, W., 1978, "Measurement of Ultrasonic Dispersion by Phase Comparison of Continuous Harmonic Waves," *J. Acoust. Soc. Am.*, Vol. 64, No. 3, pp. 852–857.

Truell, R., Elbaum, C., and Chick, B., 1969, *Ultrasonic Methods in Solid State Physics*, Academic Press, New York, pp. 53–158.

Winkler, K. W., and Plona, T. J., 1982, "Technique for Measuring Ultrasonic Velocity and Attenuation Spectra in Rocks under Pressure," *J. Geophys. Res.*, Vol. 87, pp. 10,776–10,780.

Downloaded 03 May 2010 to 171.66.16.20. Redistribution subject to ASME license or copyright; see http://www.asme.org/terms/Terms_Use.cfm

Imposition of Constraints

S. Djerassi
Rafael,
P.O. Box 2250,
Haifa, Israel

This paper deals with problems in dynamics in which a moving system is subjected to imposition (or relaxation) of constraints. Three phases of motion are associated with these types of problems: an unconstrained motion, imposition of constraints, and constrained motion. The equations governing each of the phases are derived and an algorithm for combining these into one coherent computer code is built and used in connection with an illustrative example.

1 Introduction

The system depicted in Fig. 1 can be used to introduce the idea of imposition of constraints on a moving system. The system consists of unconstrained rigid bodies A and B moving in N, a Newtonian reference frame. At time $t=t_1$, a point R of A hits a point $\overline{R}$ of B. The rise and fall of contact forces and of constraint forces take place during a short time period, starting at $t=t_1$ and terminating at $t=t_2$. When $t>t_2$, point R remains in contact with P, a plane containing point $\overline{R}$ and perpendicular to $\mathbf{b}_3$, a unit vector fixed in B. Accordingly, S undergoes three consecutive phases of motion in N: (a) an unconstrained motion $(0\leqq t<t_1)$; (b) imposition of constraints $(t_1\leqq t\leqq t_2)$; and (c) constrained motion $(t_2<t)$. It is required to formulate equations governing the motion of S throughout phases (a), (b), and (c). To this end, one may take the following steps: derive the equations of motion of S in phase (a); derive constraint equations and use them to generate equations governing the motion of S in phase (c); and, take account of the imposition of constraints in phase (b) by deriving algebraic equations relating values of generalized speeds at $t=t_1$ to values of generalized speeds at $t=t_2$.

These steps are taken in Sec. 2 in connection with a generic system S, and applied to the example just described in Sec. 3. An algorithm for combining the three phases of motion into one coherent computer code is constructed and used to simulate the entire motion of S in N. Results of one such simulation are reported in Sec. 4. A short discussion in Sec. 5 concludes this paper.

2 Theory

Let the three phases associated with imposition of constraint be applied to S, a system of ν particles P_i $(i=1, \ldots, \nu)$, and assume that in phase (a) S is a holonomic system, possessing n generalized coordinates $q_1, \ldots, q_n$ and n generalized speeds $u_1, \ldots, u_n$ in N. Let $\mathbf{v}^{Pi}$ be the velocity of P_i in N, and note that $\mathbf{v}^{Pi}$ can be expressed as (Kane, 1985, Eq. (2.14.2))

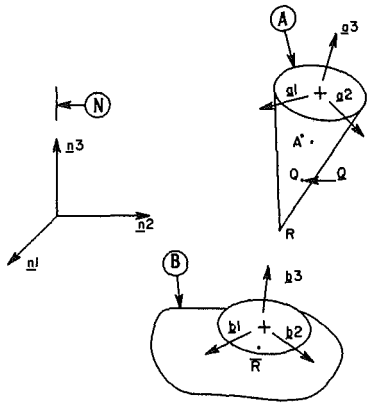


Fig. 1 A system undergoing imposition of constraints

$$\mathbf{v}^{Pi}=\sum_{r=1}^{n}\mathbf{v}_r^{Pi}u_r+\mathbf{v}_t^{Pi}\quad(i=1, \ldots, \nu)\tag{1}$$

where $\mathbf{v}_r^{Pi}$, called the rth partial velocity of P_i, and $\mathbf{v}_t$ are functions of $q_1, \ldots, q_n$ and t; and let

$$F_r+F_r^*=0\quad(r=1, \ldots, n)\tag{2}$$

where F_r is the rth generalized active force for S, and F_r^* is the rth generalized inertia force for S in N, be the dynamical equations governing the motion of S in N in phase (a). Assume that motion constraints are imposed on S, a process starting at $t=t_1$, and terminating at $t=t_2$, so that at $t=t_2$ the following m linear relations between $u_1, \ldots, u_n$ come into play:

$$u_k=\sum_{r=1}^{p}C_{kr}u_r+D_k\quad(k=p+1, \ldots, n)\tag{3}$$

where C_{kr} and D_k are functions of $q_1, \ldots, q_n$ and t. Under these circumstances, the dynamical equations governing the motion of S in N when $t>t_2$ are

$$F_r+F_r^*+\sum_{k=p+1}^{n}C_{kr}(F_k+F_r^*)=0\quad(r=1, \ldots, p).\tag{4}$$

Proof (Wampler, 1985; Djerassi, 1985): Rewriting Eqs. (1) as

$$\mathbf{v}^{Pi}=\sum_{i=1}^{p}\mathbf{v}_r^{Pi}u_r+\sum_{k=p+1}^{n}\mathbf{v}_k^{Pi}u_k+\mathbf{v}_t\quad(i=1, \ldots, \nu)\tag{5}$$

Contributed by the Applied Mechanics Division of THE AMERICAN SOCIETY OF MECHANICAL ENGINEERS for publication in the ASME JOURNAL OF APPLIED MECHANICS.

Discussion on this paper should be addressed to the Technical Editor, Professor Lewis T. Wheeler, Department of Mechanical Engineering, University of Houston, Houston, TX 77204-4792, and will be accepted until four months after final publication of the paper itself in the ASME JOURNAL OF APPLIED MECHANICS.

Manuscript received by the ASME Applied Mechanics Division, Aug. 10, 1992; final revision, Jan. 13, 1993. Associate Technical Editor: D. J. Inman.

Copyright © 1994 by ASME
Downloaded 03 May 2010 to 171.66.16.20. Redistribution subject to ASME license or copyright; see http://www.asme.org/terms/Terms_Use.cfm

and using Eqs. (3) to eliminate u_k $(k=p+1, \ldots, n)$ from Eqs. (5), one has, after rearrangement,

$$\mathbf{v}^{Pi}=\sum_{r=1}^{p}\left(\mathbf{v}_r^{Pi}+\sum_{k=p+1}^{n} C_{kr}\mathbf{v}_k^{Pi}\right)u_r + \sum_{k=p+1}^{n} D_k\mathbf{v}_k^{Pi}+\mathbf{v}_t^{Pi} \quad (i=1, \ldots, \nu). \quad (6)$$

Now, in connection with phase (a),

$$F_r+F_r^*=\sum_{i=1}^{\nu}\mathbf{v}_r^{Pi}\cdot(\mathbf{F}^{Pi}+\mathbf{F}^{*Pi}) \quad (r=1, \ldots, n), \quad (7a)$$

and in connection with phase (c),

$$\tilde{F}_r+\tilde{F}_r^*=\sum_{i=1}^{\nu}\tilde{\mathbf{v}}_r^{Pi}\cdot(\mathbf{F}^{Pi}+\mathbf{F}^{*Pi}) \quad (r=1, \ldots, p), \quad (7b)$$

where $\mathbf{F}^{Pi}$ and $\mathbf{F}^{*Pi}$ are, respectively, the active force and the inertia force acting on P_i, $\mathbf{v}_r^{Pi}$ $(r=1, \ldots, n)$ and $\tilde{\mathbf{v}}_r^{Pi}$ $(r=1, \ldots, p)$ are the coefficients of u_r in Eqs. (1) and (6), respectively, and $\tilde{F}_r$ and $\tilde{F}_r^*$ are the generalized active force and the generalized inertia force associated with S in phase (c), respectively (Kane, 1985).

In view of Eqs. (6),

$$\tilde{\mathbf{v}}_r^{Pi}=\mathbf{v}_r^{Pi}+\sum_{k=p+1}^{n} C_{kr}\mathbf{v}_k^{Pi} \quad (r=1, \ldots, p).$$

Hence, with $\tilde{F}_r+\tilde{F}_r^*=0$ $(r=1, \ldots, p)$ (Kane, 1985), the dynamical equations of the constrained system are

$$\sum_{i=1}^{\nu}\left(\mathbf{v}_r^{Pi}+\sum_{k=p+1}^{n} C_{kr}\mathbf{v}_k^{Pi}\right)\cdot(\mathbf{F}^{Pi}+\mathbf{F}^{*Pi})=0 \quad (r=1, \ldots, p) \quad (8)$$

and these are equivalent, in view of Eqs. (7), with Eqs. (4).

Integration of Eqs. (2) yields numerical values of $u_1, \ldots, u_n$, the independent generalized speeds in phase (a), whereas integration of Eqs. (4) yields numerical values for $u_1, \ldots, u_p$, the independent generalized speeds in phase (c); and substitution in Eqs. (3) yields numerical values for $u_{p+1}, \ldots, u_n$, the dependent generalized speeds in phase (c). The task undertaken next is that of relating $u_r(t_2)$ $(r=1, \ldots, n)$ to $u_r(t_1)$ $(r=1, \ldots, n)$. To this end, the theory of imposition of constraints is developed. The theory is based on the following assumption: (t_2-t_1) is "small," e.g., relative to time constants associated with S, and, consequently, the configuration of S in N does not change when $t_1 \leqq t \leqq t_2$. This means that, during phase (b)

$$q_r(t)=\text{Const} \quad t_1 \leqq t \leqq t_2 \quad (r=1, \ldots, n). \quad (9)$$

When phase (b) is regarded as a continuation of phase (a), one is justified in writing,

$$\int_{t_1}^{t_2}(F_r+F_r^*)dt=0 \quad (r=1, \ldots, n). \quad (10)$$

By the same token, one may regard phase (c) as a continuation of phase (b), and hence

$$\int_{t_1}^{t_2}\left[(F_r+F_r^*)+\sum_{k=p+1}^{n} C_{kr}(F_k+F_k^*)\right]dt = 0 \quad (r=1, \ldots, p). \quad (11)$$

Thus, both Eqs. (10) and Eqs. (11) are valid statements.

Now, Kane shows (1985, Sec. 7.8) that, defining $p_r(t)$ $(r=1, \ldots, n)$, called generalized momentum, as

$$p_r(t) \triangleq \sum_{i=1}^{\nu} m_i\mathbf{v}_r^{Pi}\cdot\mathbf{v}^{Pi} \quad (r=1, \ldots, n) \quad (12)$$

where m_i is the mass of P_i, one has

$$\int_{t_1}^{t_2}F_r^*dt=-[p_r(t_2)-p_r(t_1)] \quad (r=1, \ldots, n) \quad (13)$$

or, since (Kane, 1985, Sec. 7.8)

$$p_r=\frac{\partial K}{\partial u_r} \quad (r=1, \ldots, n), \quad (14)$$

where K is the kinetic energy for S in N,

$$\int_{t_1}^{t_2}F_r^*dt=-\left[\frac{\partial K(t_2)}{\partial u_r}-\frac{\partial K(t_1)}{\partial u_r}\right] \quad (r=1, \ldots, n). \quad (15)$$

Noting, in view of Eq. (1), that

$$K=\frac{1}{2}\sum_{i=1}^{\nu} m_i\left(\sum_{s=1}^{n}\mathbf{v}_s^{Pi}u_s+\mathbf{v}_t^{Pi}\right)^2, \quad (16)$$

one has

$$\frac{\partial K}{\partial u_r}=\sum_{i=1}^{\nu}\sum_{s=1}^{n} m_i\mathbf{v}_r^{Pi}\cdot\mathbf{v}_s^{Pi}u_s+\sum_{i=1}^{\nu} m_i\mathbf{v}_r^{Pi}\cdot\mathbf{v}_t^{Pi} \quad (r=1, \ldots, n) \quad (17)$$

and, defining m_{rs} as

$$m_{rs} \triangleq \sum_{i=1}^{\nu} m_i\mathbf{v}_r^{Pi}\cdot\mathbf{v}_s^{Pi} \quad (r,s=1, \ldots, n), \quad (18)$$

one obtains

$$\frac{\partial K}{\partial u_r}=\sum_{s=1}^{n} m_{rs}u_s+\sum_{i=1}^{\nu} m_i\mathbf{v}_r^{Pi}\cdot\mathbf{v}_t^{Pi} (r=1, \ldots, n). \quad (19)$$

As $\mathbf{v}_r^{Pi}$ and $\mathbf{V}_t^{Pi}$ $(r=1, \ldots, n, i=1, \ldots, \nu)$ are functions of $q_1, \ldots, q_n$ and t, then, in view of Eqs. (9), substitution from Eqs. (19) into Eqs. (15) leads to

$$\int_{t_1}^{t_2}F_r^*dt=-\sum_{s=1}^{n} m_{rs}[u_s(t_2)-u_s(t_1)] \quad (r=1, \ldots, n), \quad (20)$$

and similarly, in connection with Eqs. (11),

$$\int_{t_1}^{t_2}\left(F_r^*+\sum_{k=p+1}^{n} C_{kr}F_k^*\right)dt=-\sum_{s=1}^{n} m_{rs}[u_s(t_2)-u_s(t_1)] - \sum_{k=p+1}^{n} C_{kr}\sum_{s=1}^{n} m_{ks}[u_s(t_2)-u_s(t_1)]$$

or

$$\int_{t_1}^{t_2}\left(F_r^*+\sum_{k=p+1}^{n} C_{kr}F_k^*\right)dt = -\sum_{s=1}^{n}\left(m_{rs}+\sum_{k=p+1}^{n} C_{kr}m_{ks}\right)[u_s(t_2)-u_s(t_1)] \quad (r=1, \ldots, p). \quad (21)$$

Now, I_r, the rth generalized impulse, is defined (Kane, 1985, Sec. 7.8)

$$I_r \triangleq \sum_{i=1}^{\nu}\mathbf{v}_r^{Pi}(t_1)\cdot\int_{t_1}^{t_2}\mathbf{F}^{Pi}dt \quad (r=1, \ldots, n), \quad (22)$$

and, since $\mathbf{v}_r^{Pi}$ is a function of quantities remaining constant when $t_1 \leqq t \leqq t_2$, then

$$I_r=\int_{t_1}^{t_2}F_r dt \quad (r=1, \ldots, n). \quad (23)$$

Downloaded 03 May 2010 to 171.66.16.20. Redistribution subject to ASME license or copyright; see http://www.asme.org/terms/Terms_Use.cfm

Table 1 The governing equations at phases (*a*), (*b*), and (*c*)

Phase	Equations (Imposition)	Equations (Relaxation)
(*a*)	(2)	(4), (3)
(*b*)	(29), (9)	(29), (9)
(*c*)	(4), (3)	(2)

In connection with the problem at hand, I_r is the rth generalized impulse related to the unconstrained system. On the other hand, $\tilde{I}_r$, defined similarly to I_r, with $\tilde{\mathbf{v}}_r(t_2)$ replacing $\mathbf{v}_r(t_1)$ in Eqs. (22), is given by

$$\tilde{I}_r = \int_{t_1}^{t_2} \left(F_r + \sum_{k=p+1}^{n} C_{kr} F_k \right) dt \quad (r=1, \ldots, p), \tag{24}$$

and is the generalized impulse related to the constrained system. Assuming that the only forces contributing to I_r in Eqs. (23) are external forces associated with the imposition, and noting that these forces are nonworking when regarded as acting on the constrained system, one may conclude that

$$\tilde{I}_r = 0 \quad (r=1, \ldots, p) \tag{25}$$

and that, consequently, the linear and angular momenta of S in N remain unaltered in phase (*b*). In view of Eqs. (25), (24), (11), and (21), this means that

$$\sum_{s=1}^{n} \left(m_{rs} + \sum_{k=p+1}^{n} C_{kr} m_{ks} \right) [u_s(t_2) - u_s(t_1)] = 0 \quad (r=1, \ldots, p). \tag{26}$$

In addition, Eq. (2) is satisfied at $t=t_2$, namely,

$$u_k(t_2) = \sum_{r=1}^{p} C_{kr} u_r(t_2) + D_k \quad (k=p+1, \ldots, n). \tag{27}$$

Thus, Eqs. (26) and (27) are n algebraic equations enabling evaluation of $u_r(t_2)$ $(r=1, \ldots, n)$, given $u_r(t_1)$ $(r=1, \ldots, n)$.

Equations (26) and (27) can be arranged in a matrix form. To do this, let $\overline{C}$ be an $m \times p$ matrix having C_{kr} as its entries, and let $\overline{m}_r$ $(r=1, \ldots, p)$ be a $1 \times n$ row matrix having

$$m_{rs} + \sum_{k=p+1}^{n} C_{kr} m_{ks}$$

as its sth element. Let $\overline{M}$, $\overline{N}$ and $\overline{D}$ be the following $n \times n$, $n \times n$, and $n \times 1$ matrices, respectively:

$$\overline{M} \triangleq \left| \begin{array}{c|c} \begin{matrix} \overline{m}_1 \\ \vdots \\ \overline{m}_p \end{matrix} & \\ \hline \overline{C} & \begin{matrix} -1 & \cdots & 0 \\ \vdots & & \vdots \\ 0 & \cdots & -1 \end{matrix} \end{array} \right| ; \quad \overline{N} \triangleq \left| \begin{array}{c|c} \begin{matrix} \overline{m}_1 \\ \vdots \\ \overline{m}_p \end{matrix} & \\ \hline & \begin{matrix} 0 & \cdots & 0 \\ \vdots & & \vdots \\ 0 & \cdots & 0 \end{matrix} \end{array} \right| ; \quad \overline{D} \triangleq \left| \begin{array}{c} 0 \\ \vdots \\ 0 \\ \hline D_{p+1} \\ \vdots \\ D_n \end{array} \right| . \tag{28}$$

Accordingly, Eqs. (26) and (27) can be written as

$$\overline{M} | u_1(t_2), \ldots, u_n(t_2) |^T = \overline{N} | u_1(t_1), \ldots, u_n(t_1) |^T + \overline{D}. \tag{29}$$

To summarize, the equations indicated in columns 2 and 3 of Table 1 govern the respective phases of the motion indicated in column 1; and the flowchart in Fig. 2 outlines the main steps in constructing an algorithm for simulating a motion of the type under consideration.

The following comments are in order:

(a) Equations (4) involve $u_{p+1}, \ldots, u_n$ and $\dot{u}_{p+1}, \ldots, \dot{u}_n$. These can be eliminated from Eqs. (4) with the aid of Eqs. (3), noting that

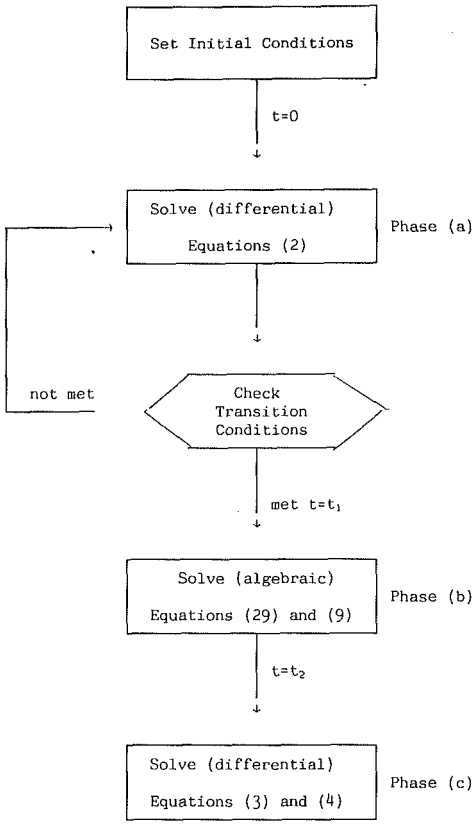


Fig. 2 Imposition of constraints: algorithm flowchart

$$\dot{u}_k = \sum_{r=1}^{p} C_{kr} \dot{u}_r + \sum_{r=1}^{p} \dot{C}_{kr} u_r + \dot{D}_k \quad (k=p+1, \ldots, n) \tag{30}$$

where $\dot{C}_{kr}$ and $\dot{D}_k$ are functions of $q_1, \ldots, q_n$ $\dot{q}_1, \ldots, \dot{q}_n$ and t. One then has p differential equations for p unknowns $u_1, \ldots, u_p$. Alternatively, one can regard Eqs. (4) and (30) as n differential equations for n unknowns $u_1, \ldots, u_n$. The latter approach is advantageous in connection with numerical integration.

(b) The derivations above are not limited to systems which are holonomic in phase (*a*). For, in the event that S is initially a nonholonomic system, one may regard n as representing the number of independent generalized speeds of the nonholonomic system, noting that the number of generalized coordinates is greater than n, say n', and that additional $(n'-n)$ nonholonomic constraint equations exist. These, however, play no part in the present analysis.

(c) Motion of systems undergoing a series of events each of which is regarded as an imposition of constraints, can, in view of comment *b*, be simulated by applying the above procedure as many times as needed. Examples of such systems are spacecraft deploying panels or antennas, missiles deploying lift surfaces, etc.

(d) t_1 is defined as a point in time when certain conditions regarding the configuration, the kinematics, or the kinetics of S, are met. These conditions, called transition conditions, form a part of the formulation of the imposition of constraints problem (as shown in Fig. 2).

(e) Replacing Eqs. (2) with Langrange's equations of the first kind, and u_r $(r=1, \ldots, n)$ in Eqs. (3) with $\dot{q}_r$ $(r=1, \ldots, n)$, one can obtain Eqs. (26) with $\dot{q}_s(t_2)$ and $\dot{q}_s(t_1)$ replacing $u_s(t_2)$ and $u_s(t_1)$, $(s=1, \ldots, n)$, respectively. To do so, one must choose $\dot{q}_1, \ldots, \dot{q}_n$ to be generalized speeds, a choice generally leading to more complex equations of motion than equations obtained when generalized speeds

Downloaded 03 May 2010 to 171.66.16.20. Redistribution subject to ASME license or copyright; see http://www.asme.org/terms/Terms_Use.cfm

are defined as (certain) linear combination of $\dot{q}_1, \ldots, \dot{q}_n$ and t (Kane, 1980).

3 Example

Let S be the system described in Fig. 1 and assume, for simplicity, that B is fixed in N[1]. Then six generalized coordinates for S in N, q_r $(r=1, \ldots, 6)$, can be defined as follows: Let $\mathbf{n}_1$, $\mathbf{n}_2$, and $\mathbf{n}_3$ be a set of dexteral, mutually perpendicular unit vectors fixed in N, and $\mathbf{a}_1$, $\mathbf{a}_2$, and $\mathbf{a}_3$ a similar set fixed in A and parallel to central principal axes of A. Let $\mathbf{a}_i$ be initially aligned with $\mathbf{n}_i$ $(i=1, 2, 3)$, and subject A to three successive rotations of q_1 about $\mathbf{a}_1$, q_2 about $\mathbf{a}_2$, and q_3 about $\mathbf{a}_3$. Thus A is brought to a general orientation in N. Let q_4, q_5, and q_6 be the cartesian measure numbers of $\mathbf{p}^{A^*}$, the position vector of the mass center A^* of A in N. Let C_{ij} be defined as

$$C_{ij} \triangleq \mathbf{n}_i \cdot \mathbf{a}_j \quad (i,j=1, 2, 3) \tag{31}$$

so that the 3×3 matrix C, having C_{ij} $(i,j=1, 2, 3)$ as elements, is given by

$$C = \begin{vmatrix} C_2C_3 & -C_2S_3 & S_2 \\ S_1S_2C_3+S_3C_1 & -S_1S_2S_3+C_3C_1 & -S_1C_2 \\ -C_1S_2C_3+S_3S_1 & C_1S_2S_3+C_3S_1 & C_1C_2 \end{vmatrix} \tag{32}$$

where $C_2=\cos q_2$, $S_3=\sin q_3$, etc.

Let six quantities u_r $(r=1, \ldots, 6)$ be defined

$$u_i \triangleq {}^N\mathbf{w}^A \cdot \mathbf{a}_i \quad (i=1, 2, 3) \tag{33}$$

$$u_{i+3} \triangleq {}^N\mathbf{v}^{A^*} \cdot \mathbf{n}_i \quad (i=1, 2, 3) \tag{34}$$

where ${}^N\mathbf{w}^A$ is the angular velocity of A in N, and ${}^N\mathbf{v}^{A^*}$ is the velocity in N of A^*, so that

$${}^N\mathbf{w}^A = u_1\mathbf{a}_1 + u_2\mathbf{a}_2 + u_3\mathbf{a}_3 \tag{35}$$

$${}^N\mathbf{v}^{A^*} = u_4\mathbf{n}_1 + u_5\mathbf{n}_2 + u_6\mathbf{n}_3. \tag{36}$$

Let ${}^A\mathbf{p}^Q$, the position vector of point Q in A, and $\mathbf{Q}$, an external force exerted on A at Q, be expressed as

$${}^A\mathbf{p}^Q = p_1\mathbf{a}_1 + p_2\mathbf{a}_2 + p_3\mathbf{a}_3 \tag{37}$$

and

$$\mathbf{Q} = Q_1\mathbf{a}_1 + Q_2\mathbf{a}_2 + Q_3\mathbf{a}_3 \tag{38}$$

where p_i and Q_i $(i=1, 2, 3)$ are constants.

Noting that the velocity of Q in N is given by

$${}^N\mathbf{v}^Q = {}^N\mathbf{v}^{A^*} + {}^N\mathbf{w}^A \times {}^A\mathbf{p}^Q$$

$${}^N\mathbf{v}^Q = u_4\mathbf{n}_1 + u_5\mathbf{n}_2 + u_6\mathbf{n}_3 + (u_2p_3 - u_3p_2)\mathbf{a}_1 + (u_3p_1 - u_1p_3)\mathbf{a}_2 + (u_1p_2 - u_2p_1)\mathbf{a}_3, \tag{39}$$

and using Eqs. (2) with $r=6$, one can show that the motion of S in N is governed by the following six dynamical equations:

$$-I_1\dot{u}_1 - u_3u_2(I_3-I_2) - p_3Q_2 + p_2Q_3 = 0 \tag{40}$$

$$-I_2\dot{u}_2 - u_1u_3(I_1-I_3) - p_1Q_3 + p_3Q_1 = 0 \tag{41}$$

$$-I_3\dot{u}_3 - u_2u_1(I_2-I_1) - p_2Q_1 + p_1Q_2 = 0 \tag{42}$$

$$-M\dot{u}_4 + C_{11}Q_1 + C_{12}Q_2 + C_{13}Q_3 = 0 \tag{43}$$

$$-M\dot{u}_5 + C_{21}Q_1 + C_{22}Q_2 + C_{23}Q_3 = 0 \tag{44}$$

$$-M\dot{u}_6 + C_{31}Q_1 + C_{32}Q_2 + C_{33}Q_3 = 0 \tag{45}$$

where I_1, I_2, and I_3 are the central principal moments of inertia for A, and M is the mass of A. Suppose the position vector ${}^A\mathbf{p}^R$ of point R of A is given with respect to A^* by

$${}^A\mathbf{p}^R = r\mathbf{a}_3 \tag{46}$$

where r is a constant, and hence, that ${}^N\mathbf{v}^R$, the velocity of R in N, is given by

$${}^N\mathbf{v}^R = u_4\mathbf{n}_1 + u_5\mathbf{n}_2 + u_6\mathbf{n}_3 + u_2r\mathbf{a}_1 - u_1r\mathbf{a}_2. \tag{47}$$

After hitting point $\overline{R}$, point R remains in contact with P plane fixed N and perpendicular to $\mathbf{n}_3$. Thus, a motion constraint is imposed on S, namely,

$${}^N\mathbf{v}^R \cdot \mathbf{n}_3 = 0 \tag{48}$$

or, when Eq. (47) is used,

$$u_6 = r(u_1C_{32} - u_2C_{31}). \tag{49}$$

Equation (49) is cast in the form of Eqs. (3), and hence C_{kr} and D_k $(k=6, r=1, \ldots, 5)$ can be readily identified as

$$C_{61} = rC_{32} \quad C_{62} = -rC_{31}$$

$$C_{63} = C_{64} = C_{65} = 0; \quad D_6 = 0 \tag{50}$$

and used in connection with Eqs. (4) to derive the dynamical equations governing the motion of the constrained system in N. The first two equations are

$$-I_1\dot{u}_1 - Mr^2C_{32}(\dot{u}_1C_{32} - \dot{u}_2C_{31}) - u_3u_2(I_3-I_2) - Mr^2C_{32}(u_1\dot{C}_{32} - u_2\dot{C}_{31}) + rC_{32}(C_{31}Q_1 + C_{32}Q_2 + C_{33}Q_3) - p_3Q_2 + p_2Q_3 = 0 \tag{51}$$

$$-I_2\dot{u}_2 + Mr^2C_{31}(\dot{u}_1C_{32} - \dot{u}_2C_{31}) - u_1u_3(I_1-I_3) + Mr^2C_{31}(u_1\dot{C}_{32} - u_2\dot{C}_{31}) - rC_{31}(C_{31}Q_1 + C_{32}Q_2 + C_{33}Q_3) - p_1Q_3 + p_3Q_1 = 0 \tag{52}$$

obtained after eliminating $\dot{u}_6$ with the aid of Eq. (49); and the last three equations are identical with Eqs. (42)–(44). Equations (51), (52), and (42)–(44) are five differential equations for $u_1, \ldots, u_5$.

Alternatively, Eqs. (4) can be used to obtain for $r=1$, [2]

$$\underset{(40)}{-I_1\dot{u}_1} - u_3u_2(I_3-I_2) - p_3Q_2 + p_2Q_3 + \underset{(50)}{rC_{32}}\Big(\underset{(45)}{-M\dot{u}_6} + C_{31}Q_1 + C_{32}Q_2 + C_{33}Q_3\Big) = \underset{(4)}{0} \tag{53}$$

$$\underset{(41)}{-I_2\dot{u}_2} - u_1u_3(I_1-I_3) - p_1Q_3 + p_3Q_1 + \underset{(50)}{(-rC_{31})}\Big(\underset{(45)}{-M\dot{u}_6} + C_{31}Q_1 + C_{32}Q_2 + C_{33}Q_3\Big) = \underset{(4)}{0}. \tag{54}$$

These equations, together with Eqs. (42)–(44) and with

$$\underset{(49)}{\dot{u}_6} = r(\dot{u}_1C_{32} - \dot{u}_2C_{31}) + r(u_1\dot{C}_{32} - u_2\dot{C}_{31}) \tag{55}$$

constitute a set of six differential equations for $u_1, \ldots, u_6$.

Values of $u_r(t_2)$ $(r=1, \ldots, 6)$ are obtained by reference to Eq. (29). Substitution from Eqs. (40)–(45) and (50) into Eq. (29) leads to the following matrix equation:

$$\left[\begin{array}{cccccc} -I_1 & 0 & 0 & 0 & 0 & -MrC_{32} \\ 0 & -I_2 & 0 & 0 & 0 & MrC_{31} \\ 0 & 0 & -I_3 & 0 & 0 & 0 \\ 0 & 0 & 0 & -M & 0 & 0 \\ 0 & 0 & 0 & 0 & -M & 0 \\ \hline rC_{32} & -rC_{31} & 0 & 0 & 0 & -1 \end{array}\right] \left|\begin{array}{c} u_1(t_2) \\ u_2(t_2) \\ u_3(t_2) \\ u_4(t_2) \\ u_5(t_2) \\ u_6(t_2) \end{array}\right| = \left[\begin{array}{cccccc} -I_1 & 0 & 0 & 0 & 0 & -MrC_{32} \\ 0 & -I_2 & 0 & 0 & 0 & MrC_{31} \\ 0 & 0 & -I_3 & 0 & 0 & 0 \\ 0 & 0 & 0 & -M & 0 & 0 \\ 0 & 0 & 0 & 0 & -M & 0 \\ \hline 0 & 0 & 0 & 0 & 0 & 0 \end{array}\right] \left|\begin{array}{c} u_1(t_1) \\ u_2(t_1) \\ u_3(t_1) \\ u_4(t_1) \\ u_5(t_1) \\ u_6(t_1) \end{array}\right|. \tag{56}$$

[1] Strictly speaking, such an assumption violates Eqs. (25). It can be shown, however, that if the mass properties of B significantly exceed those of A, as when B is Earth and A is a top, then the errors introduced in calculating $u_r(t_2)$ $(r=1, \ldots, n)$, with B fixed in N, are negligible.

[2] Numbers beneath signs of equality or beneath other symbols refer to equations numbered correspondingly.

Downloaded 03 May 2010 to 171.66.16.20. Redistribution subject to ASME license or copyright; see http://www.asme.org/terms/Terms_Use.cfm

Table 2 The governing equation in the example

Phase	Equations
(*a*)	(40)–(45)
(*b*)	(56)
(*c*)	(53), (54), (42)–(44), (55)

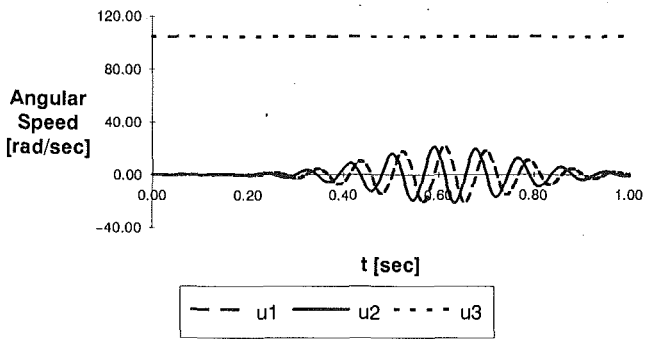


Fig. 3 u_1, u_2, and u_3 as functions of time

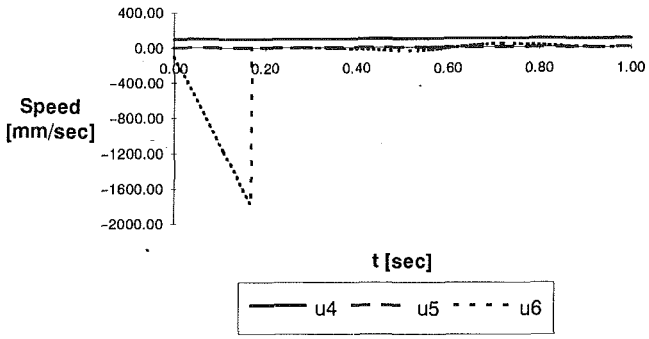


Fig. 4 u_4, u_5, and u_6 as functions of time

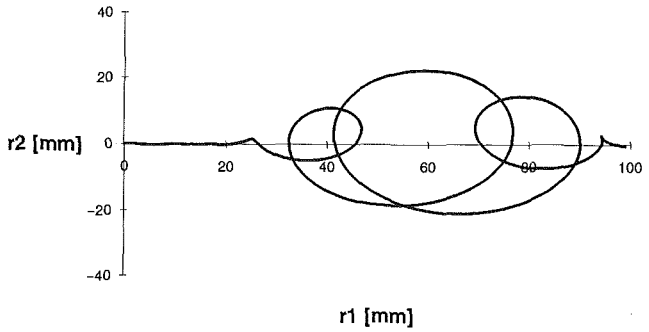


Fig. 5 The projection of point R on plane P

Hence, the equations indicated in column 2 of Table 2 govern the respective phases of motion indicated in column 1.

Lastly, the transition conditions must be formulated. To this end, let q_r ($r=4, 5, 6$) be defined as u_r ($r=4, 5, 6$), so that ${}^N\mathbf{p}^{A^*}$ and ${}^N\mathbf{p}^R$, the position vectors of A^* and of R in N, can be expressed as

$$ {}^N\mathbf{p}^{A^*} = q_4\mathbf{n}_1 + q_5\mathbf{n}_2 + q_6\mathbf{n}_3 \tag{57} $$

$$ {}^N\mathbf{p}^R = {}^N\mathbf{p}^{A^*} + {}^A\mathbf{p}^R = q_4\mathbf{n}_1 + q_5\mathbf{n}_2 + q_6\mathbf{n}_3 + r\mathbf{a}_3. \tag{58} $$

The transition condition (46) is

$$ r_3 \triangleq {}^N\mathbf{p}^R \cdot \mathbf{n}_3 = 0 \tag{59} $$

or, with the aid of Eqs. (58), (31) and (32),

$$ r_3 = q_6 + rC_{33} = 0. \tag{60} $$

Thus, with $t=t_1$ as the point in time at which Eq. (60) is satisfied, all the ingredients needed to simulate the motion of S in N are at hand.

4 Simulation

Let A be a cone-shaped top with D as its base diameter, H as its height; and R as the point located at its vertex. Let the top be tossed on a horizontal plane P containing $\overline{R}$. Set $D=40$ mm, $H=60$ mm, $M=0.00001$ Kgf-mm^{-1}-sec, and let the initial conditions be $u_1(0)=u_2(0)=0.2$ rad/sec, $u_3(0)=104.72$ rad/sec, $u_4(0)=100$ mm/sec, $u_5(0)=0$, and $u_6(0)=-100$ mm/sec. Finally, let $\mathbf{a}_i$ coincide with $\mathbf{n}_i$ ($i=1, 2, 3$) at $t=0$, $q_4(0)=q_5(0)=0$ and $q_6(0)=200$ mm.

Figure 3 shows $u_1(t)$, $u_2(t)$, and $u_3(t)$, whereas Fig. 4 shows $u_4(t)$, $u_5(t)$, and $u_6(t)$. Because $u_5=0$ at all times, A moves in N so that A^* remains in a plane perpendicular to $\mathbf{n}_2$ throughout the motion. Figure 5 shows the projection of R on P (obtained by plotting $r_2 \triangleq {}^N\mathbf{p}^R \cdot \mathbf{n}_2$, versus $r_1 \triangleq {}^N\mathbf{p}^R \cdot \mathbf{n}_1$). This projection becomes the actual path of R in P after R hits $\overline{R}$. Here, $r_2(t_1)=0$ and $r_1(t_1)=20$ mm.

Results indistinguishable from those displayed in Figs. 3, 4, and 5 are obtained if B, representing Earth, undergoes an unconstrained motion in N, and if q_r and u_r ($r=1, \ldots, 6$) describe the motion of A and B.

5 Discussion

Equation (48) implies that a mechanism exists which prevents R from losing contact with P, once a contact has been established. If such a mechanism is absent from the actual system, then Eq. (48) fails to represent the state of affairs, and an impact of A with N must be considered. One may then invoke an impact theory (e.g., Kane, 1985), simulating the behavior of S while undergoing a series of impacts. However, since the coefficient of restitution is practically smaller than 1, a point in time $\bar{t}$ will eventually be reached such that for $t>\bar{t}$, $r_3(t)<\epsilon$ where ϵ is an arbitrarily small constant. Then the approximation in applying the theory of imposition of constraints at $t_1=t$ will be acceptable.

It is essential to accentuate the intrinsic difference between an impact theory and the imposition (relaxation) of constraints theory. The former involves no change in the number of independent generalized speeds whereas the latter is associated with either an increase (relaxation) or a decrease (imposition) of that number. Thus, the solution of problems where an impact occurs between $t=t_1$ and $t=t_2$ involves the evaluation of $u_1(t_2), \ldots, u_n(t_2)$ as functions of $u_1(t_1), \ldots, u_n(t_1)$. On the other hand, the solution of problems where imposition (relaxation) of constraints occurs between $t=t_1$ and $t=t_2$ involves the evaluation of $u_1(t_2), \ldots, u_p(t_2)$ as functions of $u_1(t_1), \ldots, u_n(t_1)$, where $p \neq n$.

The two theories are similar only in that the events involved are of short duration (hence the assumption that the configuration of systems undergoing these events do not change) and are associated with large rates of change of reaction forces, giving, however, no indication as to the time histories of these forces for $t_1 \leqq t \leqq t_2$.

Lastly, consider the example once more, and suppose a spring of constant k and a damper of constant b attach point R to A. In addition, suppose that both the spring and the damper are inactive as long as $r_3>0$. When $r_3 \leqq 0$, the spring and the damper are active, adding to the existing generalized active forces contributions from the active forces exerted on A by the spring and the damper. Thus, no change of phases of motion in the sense discussed above takes place, and S possesses six independent generalized speeds throughout the motion. The indicated suppositions may represent an actual system, such

Downloaded 03 May 2010 to 171.66.16.20. Redistribution subject to ASME license or copyright; see http://www.asme.org/terms/Terms_Use.cfm

as a landing aircraft. Frequently, however, when imposition of constraints occurs, then springs and dampers are introduced for the sole purpose of keeping the number of independent generalized speeds, and hence, the number of dynamical equations, unchanged. This may lead either to erroneous results (e.g., if k is too small) or to time-consuming simulations (e.g., if k is too large) or to both. The three phases of motion described here may offer the best approximation for the type of problems under consideration.

References

Djerassi, S., and Kane, T. R., 1985, "Equations of Motion Governing the Deployment of a Flexible Linkage from a Spacecraft," *The Journal of Astronautical Sciences*, Vol. 33, No. 4.

Kane, T. R., and Levinson, D. A., 1980, "Formulation of Equations of Motion for Complex Spacecraft," *J. of Guidance and Control*, Vol. 3, No. 2.

Kane, T. R., and Levinson, D. A., 1985, *Dynamics: Theory and Application*, McGraw-Hill, New York.

Wampler, C., Buffinton, K., and Shu-hui, J., 1985, "Formation of Equations of Motion for Systems Subject to Constraints," ASME JOURNAL OF APPLIED MECHANICS, Vol. 52.

Downloaded 03 May 2010 to 171.66.16.20. Redistribution subject to ASME license or copyright; see http://www.asme.org/terms/Terms_Use.cfm

Motion and Force Prediction of a Pushed Object by Maximum Dissipation Method

Hiroshi Sakurai
Department of Mechanical Engineering,
Colorado State University,
Fort Collins, CO 80523
Mem. ASME

When an object on a horizontal surface is pushed hard enough to overcome the friction between the object and the surface, the object moves. It was proved by interpreting Kuhn-Tucker's optimality condition that when a pusher moves an object, the motion and the friction force of the pushed object corresponding to the pusher motion are those that maximize the power dissipated to friction under Coulomb's friction law. This is different from the principles of maximum and minimum dissipation postulated in the past in that it involves the pusher motion too whereas the principles do not. It allows us to treat the prediction of the motion and the friction force of a pushed object as an optimization problem. Since this optimization can be performed with linear programming within any desired accuracy, it offers us a simple, robust, and fast method to predict the motion and the friction force of a pushed object. The method was verified with an experiment of pushing a wooden block. It was applied to the estimation of the necessary clamping force in fixturing for machining.

1 Introduction

When an object on a horizontal surface is pushed hard enough to overcome the friction between the object and the surface, the object moves. This motion is the combination of translation and rotation unless the line of the pushing force goes through the center of friction. Yet at any instant, the motion can be described as the rotation around an instantaneous center of rotation on the surface. If the object moves slowly enough, the inertial force can be neglected. Even with the assumption of negligible inertial force, it is not easy to find the instantaneous center of rotation. To show this difficulty, we try to find the instantaneous center of rotation by solving the force and moment equilibrium equations. Figure 1 shows an object being pushed and moving on a horizontal surface. The horizontal surface is called support surface hereafter. The pushing occurs at the point of contact between the pusher and the object. This point of contact is called push point hereafter and its position is denoted by $\mathbf{r}_p$.

First we neglect the friction between the pusher and the object for the moment. Then the pushing force applied at $\mathbf{r}_p$ is $F_p\mathbf{n}$ where $\mathbf{n}$ is the normal at the push point and F_p is the magnitude of the pushing force. When the object rotates around the center of rotation $\mathbf{r}_0$ at the angular velocity of ω, the differential element dA located at $\mathbf{r}$ generates a differential friction force where A is the area of contact between the object and the support surface. Its magnitude is $\mu(\mathbf{r})p(\mathbf{r})dA$ where $\mu(\mathbf{r})$ and $p(\mathbf{r})$ are the friction coefficient and the pressure at $\mathbf{r}$, respectively. Its direction is opposite to that of the motion of the differential element. In the rest of the paper, $[a\ b]^T \cdot [c\ d]^T$ denotes the scalar product of the two vectors, i.e., $(ac + bd)$. $[a\ b]^T \times [c\ d]^T$ denotes the vector product of the vectors $[a\ b\ 0]^T$ and $[c\ d\ 0]^T$ and represents only the third component of the result, i.e., $(ad - bc)$. $\mathbf{k} \otimes [a\ b]^T$ denotes the vector product of the vectors $[0\ 0\ 1]^T$ and $[a\ b\ 0]^T$ and represents only the first and second component of the result, i.e., $[-b\ a]^T$. $\mathbf{k} \otimes$ rotates a vector by 90 degrees. sign(ω) denotes the sign of ω. It is 1 when ω is positive (counterclockwise) and -1 when ω is negative (clockwise). Then the force and moment equilibrium equations are

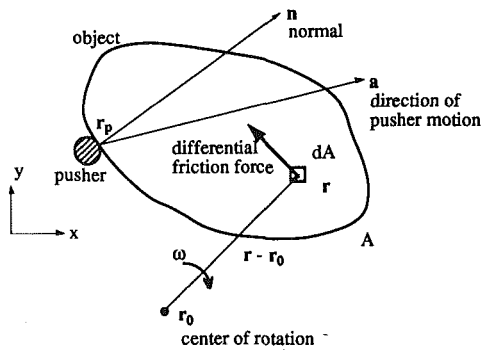


Fig. 1 An object being pushed

Contributed by the Applied Mechanics Division of THE AMERICAN SOCIETY OF MECHANICAL ENGINEERS for publication in the ASME JOURNAL OF APPLIED MECHANICS.

Discussion on this paper should be addressed to the Technical Editor, Professor Lewis T. Wheeler, Department of Mechanical Engineering, University of Houston, Houston, TX 77204-4792, and will be accepted until four months after final publication of the paper itself in the ASME JOURNAL OF APPLIED MECHANICS.

Manuscript received by the ASME Applied Mechanics Division, Jan. 5, 1993; final revision, Mar. 29, 1993. Associate Technical Editor: R. L. Huston.

Copyright © 1994 by ASME
Downloaded 03 May 2010 to 171.66.16.20. Redistribution subject to ASME license or copyright; see http://www.asme.org/terms/Terms_Use.cfm

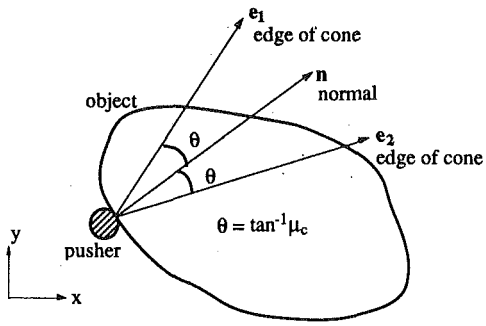


Fig. 2 Friction cone

$$\mathbf{n}F_p = -\operatorname{sign}(\omega)\int_A \frac{\mathbf{k}\otimes(\mathbf{r}-\mathbf{r}_0)}{|\mathbf{r}-\mathbf{r}_0|}\,\mu(\mathbf{r})p(\mathbf{r})dA$$

$$\mathbf{r}_p\times\mathbf{n}F_p = -\operatorname{sign}(\omega)\int_A \frac{\mathbf{r}\times[\mathbf{k}\otimes(\mathbf{r}-\mathbf{r}_0)]}{|\mathbf{r}-\mathbf{r}_0|}\,\mu(\mathbf{r})p(\mathbf{r})dA. \quad (1)$$

The unknowns are F_p and $\mathbf{r}_0$. Solving these equations analytically or even numerically for the unknowns F_p and $\mathbf{r}_0$ is generally difficult.

Now we make the problem discrete by assuming that the object is supported at discrete points instead of by an area. Let $\mathbf{r}_i$ denote the position of the ith support point, μ_i and N_i denote the friction coefficient and the support force at the ith support point, and n denote the number of the support points. The force and moment equilibrium equations are

$$\mathbf{n}F_p = -\operatorname{sign}(\omega)\sum_{i=1}^{n}\frac{\mathbf{k}\otimes(\mathbf{r}_i-\mathbf{r}_0)}{|\mathbf{r}_i-\mathbf{r}_0|}\,\mu_i N_i$$

$$\mathbf{r}_p\times\mathbf{n}F_p = -\operatorname{sign}(\omega)\sum_{i=1}^{n}\frac{\mathbf{r}_i\times[\mathbf{k}\otimes(\mathbf{r}_i-\mathbf{r}_0)]}{|\mathbf{r}_i-\mathbf{r}_0|}\,\mu_i N_i. \quad (2)$$

Solving analytically these equations for the unknowns F_p and $\mathbf{r}_0$ is very difficult and solving them by numerical methods lacks robustness since numerical methods for the above equations do not converge reliably unless the initial guess is very close to the solution (Mason, 1985). Also it must be checked beforehand if one of the support point coincides with the center of rotation since in that case $\mathbf{r}_i - \mathbf{r}_0$ becomes zero for the support point and the above equations contain 0/0 terms. Thus it is not simple to find the instantaneous center of rotation for the sliding object even if the friction between the pusher and the object is neglected.

Since there usually exists friction between the pusher and the object, the problem is more complicated. The direction of the pushing force is unknown and thus there are five unknowns (F_p, $\mathbf{n}$ and $\mathbf{r}_0$) for three equations in equation sets (1) or (2). Friction cone defines the possible range of the direction of the pushing force as shown in Fig. 2. The half angle of the cone is equal to $\tan^{-1}\mu_c$ where μ_c is the friction coefficient between the pusher and the object. When the pushing force lies inside the cone, there is no slipping between the pusher and the object. This is called fixed contact mode. In fixed contact mode, the push point on the object moves with the pusher. When the force lies on one of the edges of the friction cone, there is slipping between the pusher and the object. This is called slipping contact mode. There is no good way to incorporate this additional information into the equation sets (1) or (2).

In this work, the problem was formulated as follows.

Find the instantaneous center of rotation and the friction force of an object under the following conditions:

(1) The object is supported at discrete points on a horizontal surface. It is being pushed by a pusher and is moving.

(2) There is friction between the object and the support surface and between the pusher and the object. The friction obeys Coulomb's law.

(3) The inertial force is negligible.

(4) The support forces at the support points are known.

In this work, the problem was solved by maximizing the power dissipated to friction. The method is based on the maximum dissipation principle for a pushed object proved in this work and it is simple, robust and fast. The maximum dissipation principle for a pushed object is as follows: When a pusher moves an object, the motion and the friction force of the object corresponding to the pusher motion are those that maximize the power dissipated to friction under Coulomb's law. In other words, the object being pushed resists the pusher as much as possible.

In the following, related work on friction and sliding object is reviewed first. Then the maximum dissipation method is presented. Then the motion predicted with the method for a wooden block is compared with the experiment result. Next, the application of the method to fixturing for machining is presented. The proof of the maximum dissipation principle for a pushed object is given in the Appendix.

2 Related Work

Though the treatment of friction in textbooks is limited to the cases of single-degree of freedom, i.e., an object either translates linearly or rotates around a known point (Kane, 1985), various studies of friction have been conducted by many researchers and a detailed bibliography can be found in (Goyal, 1989).

Moreau interpreted Coulomb's law as the principle of maximum dissipation: The friction force corresponding to a given motion is the one that maximizes the power dissipated to friction (Moreau, 1979). Then by applying convex analysis, he derived the principle of minimum dissipation: The motion corresponding to a given friction force is the one which minimizes the power dissipated to friction. These two principles seemingly contradict each other, but they do not. In the principle of maximum dissipation, the dissipated power is maximized in terms of friction force under the constraint that the friction force at each point of contact is less than or equal to the maximum, i.e., $|\mathbf{f}_i| \le \mu_i N_i$. In the principle of minimum dissipation, the dissipated power is minimized in terms of the motion under the constraint that the friction force at each point of contact is the maximum, i.e., $|\mathbf{f}_i| = \mu_i N_i$. So the maximum and minimum occur under different constraints. Now the major difference between Moreau's principle of maximum dissipation and the author's maximum dissipation principle is that Moreau's principle requires the motion of the sliding object to be known and thus cannot be applied to the problem of predicting motion whereas the author's principle does not require the motion of the sliding object and thus can be applied to the problem of predicting motion.

Recently, the general motion of an object on a planar surface attracted attention in robotics. Mason studied the planar motion of a pushed object (Mason, 1985, 1986). He developed a numerical method to find the location of the center of rotation of a pushed object supported at discrete points. With his method, the rotation centers are calculated for various directions of pusher motion under the assumption of fixed contact mode. In fixed contact mode, the center of rotation lies on a line that goes through the contact point and is perpendicular to the direction of pusher motion. Thus the assumption reduces the number of unknowns to one and the numerical method to solve the problem is more reliable than the one to solve the equation set (2). For each calculated center of rotation, the direction of the pushing force is calculated. Then by interpolating them, he generates the locus of the rotation centers labeled both with the directions of pushing motions and the

Downloaded 03 May 2010 to 171.66.16.20. Redistribution subject to ASME license or copyright; see http://www.asme.org/terms/Terms_Use.cfm

directions of pushing forces. Now the rotation center for a given direction of the pusher motion is obtained by intersecting the locus with the direction of the pusher motion. If the direction of the pushing force of the obtained rotation center is outside the friction cone, the contact is in slipping mode. The correct rotation center is obtained by intersecting the locus with one of the edges of the friction cone, which is the direction of the pushing force in slipping contact mode. Compared with this complicated method, the maximum dissipation method given later is much simpler and more robust.

Peshkin determined the quantitative bounds on the possible motions for all possible support distributions between the object and the support surface (Peshkin, 1988). In doing so, he proved the principle of minimum dissipation, which he calls the minimum power principle, in a different way (Peshkin, 1989) and applied it only to derive the equation sets (1) and (2) which do not include the pusher motion. He solved the equation set (2) by a numerical method which, he says, usually converges quickly if the initial guess is "sufficiently close" to the correct answer.

Goyal extended Moreau's principle of maximum dissipation for the case of a sliding object and developed the concept of limit surface. A limit surface is an ellipsoid-like surface in three-dimensional load space (two force components and moment) and characterizes the relationship between the friction load and the motion. During slip, the load is on this surface and the direction of motion is the normal to this surface. When no slip is occurring, the load is within or on the surface. As limit surface cannot be expressed analytically and as neither the load nor the motion is known in our problem, we cannot use limit surface to find out the load and the motion.

Trinkle analyzed robotic grasping (Trinkle, 1988). Since both of his work and the work presented in this paper involve planar motion of an object and both use linear programming, the two may look similar. But his work assumes that there is no friction and the focus of this work is friction. There is no overlap between his work and this work.

3 Motion and Force Prediction by the Maximum Dissipation Method

The maximum dissipation principle is repeated here: When a pusher moves an object, the motion and the friction force of the object corresponding to the pusher motion are those that maximize the power dissipated to friction under Coulomb's law. The power dissipated to friction is equal to the power exerted by the pusher which is the dot product of the pushing force and the velocity of the pusher. Since the pushing force is equal in magnitude and opposite in direction to the resultant friction force between the object and the support surface, the power dissipated is equal to the negative of the dot product of the resultant friction force and the pusher velocity. Since the pusher speed is not a parameter of the maximization, we use the direction of the pusher motion instead of the pusher velocity. With the normal $\mathbf{n}$ and the friction coefficient μ_c, the directions of the two edges of the friction cone are expressed as $\mathbf{e}_1 = [n_x - \mu_c n_y, \mu_c n_x + n_y]^T/\sqrt{1+\mu_c^2}$ and $\mathbf{e}_2 = [n_x + \mu_c n_y, -\mu_c n_x + n_y]^T/\sqrt{1+\mu_c^2}$ where $\mathbf{n} = [n_x, n_y]^T$. Now the maximization of the power dissipated to friction is expressed as follows:

$$\text{Maximize} \quad P(\mathbf{f}) = -\mathbf{a} \cdot \sum_{i=1}^{n} \mathbf{f}_i$$

$$\text{subject to} \quad g_i(\mathbf{f}) = |\mathbf{f}_i|^2 - (\mu_i N_i)^2 \le 0 \quad i = 1, \ldots, n$$

$$g_{n+1}(\mathbf{f}) = -\mathbf{e}_1 \times \sum_{i=1}^{n} \mathbf{f}_i \le 0$$

$$g_{n+2}(\mathbf{f}) = \mathbf{e}_2 \times \sum_{i=1}^{n} \mathbf{f}_i \le 0$$

$$h(\mathbf{f}) = \sum_{i=1}^{n} [(\mathbf{r}_i - \mathbf{r}_p) \times \mathbf{f}_i] = 0 \tag{3}$$

where $\mathbf{f}$ is the vector of all the friction forces, and $\mathbf{a}$ is the direction of the pusher motion. The objective function $P(\mathbf{f})$ is the power dissipated to friction. Each inequality constraint $g_i(\mathbf{f})$ represents Coulomb's law. The inequality constraints $g_{n+1}(\mathbf{f})$ and $g_{n+2}(\mathbf{f})$ together represent that the negative of the resultant friction force lies inside or on the friction cone. The equality constraint $h(\mathbf{f})$ means that the resultant friction moment around the push point is zero. When the objective function $P(\mathbf{f})$ is maximum, the pusher is moving the object. The proof of this is given in the Appendix. By solving this maximization problem, we can obtain as the maximizer the friction force at each support point when the pusher is moving the object. Then by intersecting the lines which go through the support points and are perpendicular to the friction forces, the center of rotation is obtained. The resultant friction force is obtained by summing the friction forces at all the support points.

The above formulation is a nonlinear constrained optimization which generally is difficult to solve. But since each of inequality constraints $g_i(\mathbf{f})$ is a circular disk, it can be easily approximated with a regular polygon to the desired accuracy. Then the optimization problem becomes a linear programming problem. When the number of support points is large and a highly accurate result is desired, the linear programming problem becomes too large. To avoid this problem, each $g_i(\mathbf{f})$ is approximated first with a hexagon and the maximization with linear programming is performed. Then each $g_i(\mathbf{f})$ is approximated with finer facets only at the vicinity of the obtained friction force and the maximization with linear programming is performed again. This process of the finer approximation and maximization is repeated until the desired accuracy is achieved.

In this method, there is no need to first find the contact mode and then treat the problem differently depending on the contact mode found. The center of rotation is found by simply solving the above optimization problem. Thus the method is simple. Since the method uses linear programming, it is fast and it does not have any difficulty of convergence. It does not require any initial guesses. Simplicity, robustness, and speed are the advantages of this method.

Though the maximum dissipation method was formulated for the case of a given pusher motion, it can be used for the case of a given pushing force direction. Let $\mathbf{c}$ denote the direction of the pushing force and $\mathbf{r}_f$ denote the location the force is applied. Then by replacing $\mathbf{n}$ and $\mathbf{a}$ with $\mathbf{c}$ and $\mathbf{r}_p$ with $\mathbf{r}_f$, the method becomes the maximization of the frictional dissipation for the case of a given pushing force direction. The maximization of $P(\mathbf{f})$ leads us to the motion and the friction force of the object. This is equivalent to calculating the point on the limit surface of the object for the given direction of the load.

Moreau's principle of maximum dissipation and Goyal's limit surface are the interpretation of friction law and tell that the friction force corresponding to a given motion of a sliding object is the one that maximizes the frictional dissipation. In the light of the maximum dissipation principle for a pushed object presented here and the principle of minimum dissipation, the author guesses that it may be possible to formulate the principle of maximum dissipation in a more general way: When an object moves under whatever external forces and constraints, the frictional dissipation is maximum. The object select both the motion and the friction force so that the power dissipated to friction is maximum. This statement and the principle of minimum dissipation are complementary to each other. The frictional dissipation is maximum under the constraint of $|\mathbf{f}_i| \le \mu_i N_i$ at each point of contact and it is minimum under the constraint of $|\mathbf{f}_i| = \mu_i N_i$ at each point of contact.

Downloaded 03 May 2010 to 171.66.16.20. Redistribution subject to ASME license or copyright; see http://www.asme.org/terms/Terms_Use.cfm

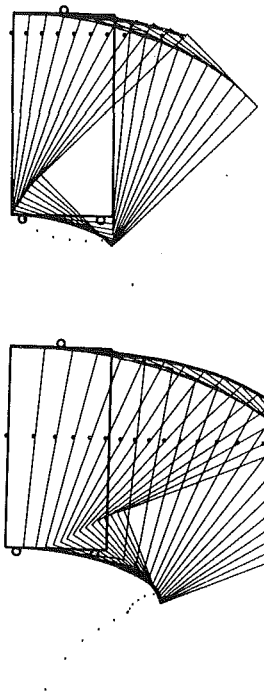


Fig. 3 Comparison with the experiment results

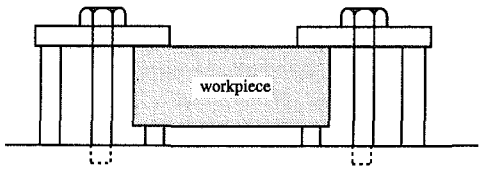


Fig. 4 Down-holding clamping scheme

4 Comparison With the Experiment Result

An experiment of pushing was performed with a 40 mm × 80 mm wooden block supported on a piece of paper by three round-head nails. Three point support was selected since the exact normal forces at the support points can be obtained easily from force and moment equilibrium. The uniformity of the friction coefficient among the support points was verified by seeing that the block linearly translated whenever it was pushed in such a way that the line of pushing went through the center of gravity of the block. The block was pushed with a thin stick and its locus was recorded. The friction coefficient between the pusher and the block was found by pushing the pusher against the block, gradually tilting the block and measuring the angle when the pusher started slipping. The tangent of the angle is the friction coefficient and it was 0.325. The friction coefficient between the block and the support surface does not affect the motion of the block.

Then the simulation of pushing the block was performed by repeating the calculation of the center of rotation and the rotation of the block around the calculated center of rotation. Figure 3 shows the comparison of the simulation results with the experiment results. The two cases are different only in the initial distance of the pushing lines from the center of gravity of the block. In each figure, the rectangle drawn with the thick lines shows the block in the initial position, the three circles show the support points in the initial position, the series of large solid dots shows the locus of the push point, the series of the rotated rectangles shows the locus of the block, the series of small solid dots show the locus of the center of rotation, and the thick curve shows the locus of the upper left corner of the block obtained from the experiment. The block

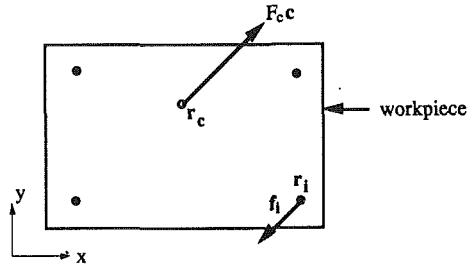


Fig. 5 Model of the clamping scheme

was rotated by 1.5 degrees around each calculated center of rotation in the simulation and it was shown in the figures for every 4.5-deg rotation. The time required for the simulation is about 10 seconds for each case. The simulation results match the experiment results very well. It also can be said that the motion of a pushed object is predictable if the pressure distribution and the friction coefficient are controlled carefully.

5 Estimation of Necessary Clamping Force in Fixturing

The maximum dissipation method was originally developed by the author for the estimation of necessary clamping force in automatic fixture design (Sakurai, 1992). Figure 4 shows a commonly used clamping scheme in fixturing for machining called down-holding clamping.

The workpiece is supported by the locators. The clamps are applied exactly above the locators to avoid the workpiece deformation. This scheme relies solely on the friction force in preventing the workpiece from moving under the horizontal cutting force. Clamping force must be large enough to generate enough friction force and must be small enough not to deform the workpiece. Necessary clamping force is not calculated in the current machine shop practice though inadequate clamping force sometimes causes inaccuracy of finished parts. The down-holding clamping in Fig. 4 is modeled as shown in Fig. 5.

$\mathbf{r}_c$, $\mathbf{c}$, and F_c are the position, the direction, and the magnitude of the horizontal cutting force, respectively. $\mathbf{r}_i$ is the position of the ith clamp and $\mathbf{f}_i$ is the friction force at the ith clamp. It is assumed that all the clamps and locators exert the same clamping force onto the workpiece.

By replacing $\mathbf{r}_p$ with $\mathbf{r}_c$, $\mathbf{n}$ and $\mathbf{a}$ with $\mathbf{c}$ and setting $\mu_c = 0$ in the maximization formulation (3), we transform the constraints $g_{n+1}(\mathbf{f})$ and $g_{n+2}(\mathbf{f})$ into an equality constraint that constrains the resultant friction force in the direction parallel to $\mathbf{c}$. We set $N_i = 1$ to find the resultant friction force F_f which the unit clamping force at all the clamps can generate. F_f is obtained as the maximum of the objective function $P(\mathbf{f})$. Then the necessary clamping force is $F_c/2F_f$. This estimation was implemented in an automatic setup planning and fixture design system. The estimation takes 0.2 second on Silicon Graphics IRIS 4D/20 for the case of four clamps and the angular accuracy of friction forces within 0.01 deg. This high speed is desirable since estimation of clamping force must be repeated for different cutting forces at different locations.

There has been one research effort beside the author's work in estimating necessary clamping force (Lee, 1991). They approximate the limit surface of a clamped workpiece with an ellipsoid and calculate the intersection between the line of cutting load (force and moment) and the ellipsoid. Since a limit surface cannot be expressed analytically, the accuracy of the approximation is difficult to control.

7 Conclusions

The maximum dissipation principle for a pushed object was proved by interpreting Kuhn-Tucker's optimality condition. This principle is different from other similar principles on

Downloaded 03 May 2010 to 171.66.16.20. Redistribution subject to ASME license or copyright; see http://www.asme.org/terms/Terms_Use.cfm

frictional dissipation in that it includes the pusher motion whereas others do not. The principle was implemented as the maximum dissipation method to predict the motion and the friction force of a pushed object when the pusher motion is given. The method is simple, robust and fast. The validity of the method was verified by comparing the predicted locus of a pushed block with the experiment result. The method is used for the estimation of the necessary clamping force in fixturing.

References

Goyal, S., 1989, "Planar Sliding of a Rigid Body with Dry Friction: Limit Surfaces and Dynamics of Motion," Ph.D. Thesis, Cornell University, Ithica, NY.

Lee, S. H., and Cutkosky, M. R., 1991, "Fixture Planning With Friction," ASME *Journal of Engineering for Industry*, Vol. 113, pp. 320–327.

Kane, T. R., and Levinson, D. A., 1985, *Dynamics: Theory and Applications*, McGraw-Hill, New York, pp. 118–124.

Mason, M. T., and Salisbury, J. K., 1985, *Robot Hands and the Mechanics of Manipulation*, Cambridge: The MIT Press, Cambridge, MA.

Mason, M. T., 1986, "Mechanics and Planning of Manipulator Pushing Operations," *International Journal of Robotics Research*, Vol. 5, No. 3, pp. 53–70.

Moreau, J. J., 1979, "Application of Convex Analysis to Some Problems of Dry Friction," *Trends in Application of Pure Mathematics to Mechanics*, Vol. 2, pp. 263–280.

Peshkin, M. A., and Sanderson, A. C., 1988, "The Motion of a Pushed, Sliding Workpiece," *IEEE Journal of Robotics and Automation*, Vol. 4, No. 6, pp. 569–598.

Peshkin, M. A., and Sanderson, A. C., 1989, "Minimization of Energy in Quasi-Static Manipulation," *IEEE Journal of Robotics and Automation*, Vol. 5, No. 1, pp. 53–60.

Sakurai, H., 1992, "Automatic Setup Planning and Fixture Design for Machining," *Journal of Manufacturing Systems*, Vol. 11, No. 1, pp. 30–37.

Trinkle, J. C., Abel, J. M., and Paul, R. P., 1988, "An Investigation of Frictionless Enveloping Grasping in the Plane," *The International Journal of Robotics Research*, Vol. 7, No. 3, pp. 33–51.

APPENDIX

Proof of the Maximum Dissipation Principle

In this Appendix, the maximum dissipation principle for a pushed object is proved by interpreting Kuhn-Tucker's optimality condition. The coordinate system is changed to the one shown in Fig. 6. The origin is located at the push point. The y-axis coincides with the normal of the object at the push point. Then $\mathbf{r}_p = \mathbf{0}$, $\mathbf{e}_1 = [-\mu_c, 1]^T/\sqrt{1+\mu_c^2}$ and $\mathbf{e}_2 = [\mu_c, 1]^T/\sqrt{1+\mu_c^2}$ in the formulation (3).

Since this optimization is a convex program, Kuhn-Tucker's optimality condition is necessary and sufficient for the global maximum. Kuhn-Tucker's optimality condition for the maximization formulation (3) is as follows:

There exist vectors $\mathbf{f}$, α, and a scalar β that satisfy the constraints in (3), and

$$\nabla P(\mathbf{f}) - \sum_{i=1}^{n+2} \alpha_i \nabla g_i(\mathbf{f}) - \beta \nabla h(\mathbf{f}) = 0$$

$$\alpha_i g_i(\mathbf{f}) = 0 \quad i = 1, \ldots, n+2$$

$$\alpha_i \geq 0 \quad i = 1, \ldots, n+2.$$

This is the necessary and sufficient condition for the maximum, not just for the optimum. By rewriting these conditions in more detail, we obtain the following for the ith support point:

$$\begin{bmatrix} -\beta y_i + a_x + \alpha_{n+1} - \alpha_{n+2} \\ \beta x_i + a_y + \mu_c \alpha_{n+1} + \mu_c \alpha_{n+2} \end{bmatrix} + 2\alpha_i \mathbf{f}_i = 0 \tag{A1}$$

$$\alpha_i [|\mathbf{f}_i|^2 - (\mu_i N_i)^2] = 0 \tag{A2}$$

$$\alpha_{n+1} \left[\mathbf{e}_1 \times \sum_{i=1}^{n} \mathbf{f}_i \right] = 0 \tag{A3}$$

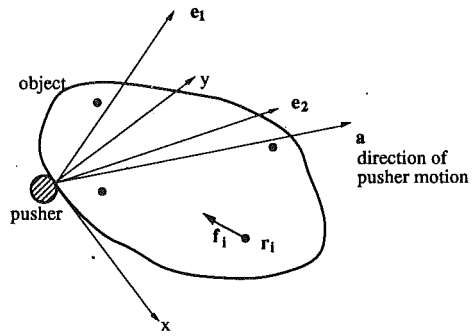


Fig. 6 Coordinate system

$$\alpha_{n+2} \left[-\mathbf{e}_2 \times \sum_{i=1}^{n} \mathbf{f}_i \right] = 0 \tag{A4}$$

$$\alpha_i \geq 0. \tag{A5}$$

First, we prove that when $P(\mathbf{f})$ is maximum, the pusher is moving the object.

(1) When $\beta \neq 0$, Eq. (A1) can be rewritten as

$$\mathbf{k} \otimes (\mathbf{r}_i - \mathbf{r}_0) + \frac{2\alpha_i}{\beta} \mathbf{f}_i = 0 \tag{A6}$$

where

$$\mathbf{r}_0 = \begin{bmatrix} -(a_y + \mu_c \alpha_{n+1} + \mu_c \alpha_{n+2})/\beta \\ (a_x + \alpha_{n+1} - \alpha_{n+2})/\beta \end{bmatrix}. \tag{A7}$$

Let's assume $\alpha_i \neq 0$ for all the support points. From Eq. (A2), we can conclude $|\mathbf{f}_i|^2 - (\mu_i N_i)^2 = 0$. The object is moving. By taking the scalar product between Eq. (A6) and $\mathbf{k} \otimes \mathbf{f}_i$, we obtain

$$\mathbf{f}_i \cdot (\mathbf{r}_i - \mathbf{r}_0) = 0. \tag{A8}$$

By taking the vector product between Eq. (A6) and the vector $\mathbf{r}_i - \mathbf{r}_0$, we obtain

$$|\mathbf{r}_i - \mathbf{r}_0|^2 = -\frac{2\alpha_i}{\beta} (\mathbf{r}_i - \mathbf{r}_0) \times \mathbf{f}_i.$$

By multiplying this equation with the similar equation for the jth support point, we obtain

$$[(\mathbf{r}_i - \mathbf{r}_0) \times \mathbf{f}_i][(\mathbf{r}_j - \mathbf{r}_0) \times \mathbf{f}_j] = \frac{\beta^2}{4\alpha_i \alpha_j} |\mathbf{r}_i - \mathbf{r}_0|^2 |\mathbf{r}_j - \mathbf{r}_0|^2 > 0. \tag{A9}$$

Equation (A8) means that at any support point the friction force is perpendicular to the vector from $\mathbf{r}_0$ to the support point $\mathbf{r}_i$, and Eq. (A9) means that all the friction forces are directed in the same sense around $\mathbf{r}_0$. We can conclude that the object is rotating around $\mathbf{r}_0$.

Now we show that this is the rotation for the object pushed at the origin in the direction $\mathbf{a}$.

(1.1) When $g_{n+1}(\mathbf{f}) < 0$ and $g_{n+2}(\mathbf{f}) < 0$, the pushing force is inside the friction cone. Since $\alpha_{n+1} = \alpha_{n+2} = 0$ from Eqs. (A3) and (A4), we obtain from Eq. (A7)

$$\mathbf{r}_0 = \frac{1}{\beta} \begin{bmatrix} -a_y \\ a_x \end{bmatrix}$$

and hence

$$\mathbf{a} \cdot \mathbf{r}_0 = \frac{-a_x a_y + a_x a_y}{\beta} = 0.$$

This means that the push point is moving in the direction $\mathbf{a}$ in fixed contact mode and that the rotation is for the object pushed at the origin in the direction $\mathbf{a}$.

(1.2) When $g_{n+1}(\mathbf{f}) = 0$ and $g_{n+2}(\mathbf{f}) < 0$, the pushing force is in the direction $\mathbf{e}_1$. We show that the equation set (2) is

Downloaded 03 May 2010 to 171.66.16.20. Redistribution subject to ASME license or copyright; see http://www.asme.org/terms/Terms_Use.cfm

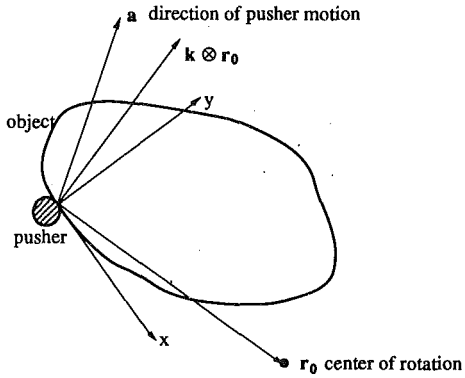


Fig. 7 The relation between the pusher motion and the object motion

satisfied for $\mathbf{n} = \mathbf{e}_1$. $h(\mathbf{f}) = 0$ means that the second equation of the equation set (2) is satisfied. Since $g_{n+1}(\mathbf{f}) = 0$, the resultant friction force is parallel to $\mathbf{e}_1$. Since $g_{n+2}(\mathbf{f}) < 0$, $\alpha_{n+2} = 0$. From Eq. (A6), we obtain

$$[\mathbf{k}\otimes\mathbf{r}_0]\times\mathbf{a}=\frac{a_x\mu_c-a_y}{\beta}\,\alpha_{n+1} \text{ and } \mathbf{r}_0\times\mathbf{e}_1=\frac{a_x\mu_c-a_y}{\beta\sqrt{1+\mu_c^2}}.$$

From these two equations, we obtain

$$\alpha_{n+1}=\frac{1}{\sqrt{1+\mu_c^2}}\,\frac{[\mathbf{k}\otimes\mathbf{r}_0]\times\mathbf{a}}{\mathbf{r}_0\times\mathbf{e}_1}>0. \tag{A10}$$

Since there is slipping between the pusher and the object, the relation between the directions of the pusher motion and the motion of the push point on the object is as shown in Fig. 7. Thus $[\mathbf{k} \otimes \mathbf{r}_0] \times \mathbf{a} > 0$. From this and Eq. (A10), $\mathbf{r}_0 \times \mathbf{e}_1 > 0$. The rotation center is on the right side of $\mathbf{e}_1$. The object is rotating clockwise and the resultant friction force is opposite to $\mathbf{e}_1$. Thus the first equation of the equation set (2) is satisfied. The rotation is for the object pushed at the origin in the direction $\mathbf{a}$.

If $\alpha_i = 0$, from Eq. (A6) $\mathbf{r}_i = \mathbf{r}_0$. The object is rotating around the ith support point.

(2) When $\beta = 0$, Eq. (A1) reduces to

$$\mathbf{b}+2\alpha_i\mathbf{f}_i=0 \text{ where } \mathbf{b}=\begin{bmatrix} a_x+\alpha_{n+1}-\alpha_{n+2} \\ a_y+\mu_c\alpha_{n+1}+\mu_c\alpha_{n+2}\end{bmatrix}. \tag{A11}$$

Let's assume $\alpha_i = 0$. Then $\mathbf{b} = \mathbf{0}$ and thus $a_y = -\mu_c(\alpha_{n+1} + \alpha_{n+2}) \leq 0$. But $a_y > 0$ since the object is being pushed. So, α_i cannot be 0. Then, from Eqs. (A2) and (A11), we obtain

$$|\mathbf{f}_i|^2-(\mu_iN_i)^2=0 \text{ and } \mathbf{f}_i=-\frac{1}{2\alpha_i}\,\mathbf{b}. \tag{A12}$$

The object is translating in the direction $\mathbf{b}$. Now we show that this is the motion for the object pushed in the direction $\mathbf{a}$.

(2.1) When $g_{n+1}(\mathbf{f}) < 0$ and $g_{n+2}(\mathbf{f}) < 0$, the pushing force is inside the friction cone. From $\alpha_{n+1} = \alpha_{n+2} = 0$ and Eq. (A12), we obtain $\mathbf{f}_i = -\mu_iN_i\mathbf{a}$. The object is translating in the direction $\mathbf{a}$ in fixed contact mode.

(2.2) When $g_{n+1}(\mathbf{f}) = 0$ and $g_{n+2}(\mathbf{f}) < 0$, the pushing force is parallel to $\mathbf{e}_1$. Using $\alpha_{n+2} = 0$, we find $\mathbf{b} \cdot \mathbf{e}_1 = \mathbf{a} \cdot \mathbf{e}_1 > 0$. The friction forces are opposite to $\mathbf{e}_1$ and $\mathbf{f}_i = -\mu_iN_i\mathbf{e}_1$. The object is translating in the direction $\mathbf{e}_1$ in slipping contact mode.

The reverse (when the pushed object is moving, $P(\mathbf{f})$ is maximum) was also proved by interpreting the directions of the friction forces when the object pushed is moving. For example, when the object is translating linearly in fixed contact mode, the friction force is

$$\mathbf{f}_i=-\mu_iN_i\mathbf{a}.$$

By rewriting this, we get

$$\mathbf{a}+\frac{1}{\mu_iN_i}\,\mathbf{f}_i=0$$

By comparing this equation with Eq. (A6), we select the following values for the Lagrange multipliers.

$$\beta=0,\ \alpha_{n+1}=0,\ \alpha_{n+2}=0, \text{ and } \alpha_i=\frac{1}{2\mu_iN_i}>0$$

Obviously, all the constraints in (3) and the conditions (A1) through (A5) are satisfied, and $P(\mathbf{f})$ is maximum. Similar arguments can be made in other cases of the object movement.

Downloaded 03 May 2010 to 171.66.16.20. Redistribution subject to ASME license or copyright; see http://www.asme.org/terms/Terms_Use.cfm

N. Sri Namachchivaya
Department of Aeronautical and Astronautical Engineering, University of Illinois at Urbana-Champaign, Urbana, IL 61801
Mem. ASME

H. J. Van Roessel
Department of Mathematics, University of Alberta, Edmonton, Alberta, Canada

S. Talwar
Department of Aeronautical and Astronautical Engineering, University of Illinois at Urbana-Champaign, Urbana, IL 61801

Maximal Lyapunov Exponent and Almost-Sure Stability for Coupled Two-Degree-of-Freedom Stochastic Systems

In this paper, a perturbation approach is used to calculate the asymptotic growth rate of stochastically coupled two-degree-of-freedom systems. The noise is assumed to be white and of small intensity in order to calculate the explicit asymptotic formulas for the maximum Lyapunov exponent. The Lyapunov exponents and rotation number for each degree-of-freedom are obtained in the Appendix. The almost-sure stability or instability of the four-dimensional stochastic system depends on the sign of the maximum Lyapunov exponent. The results presented here match those presented by the first author and others using the method of stochastic averaging, where approximate Itô equations in amplitudes and phase are obtained in the sense of weak convergence.

1 Introduction

For linear Itô stochastic differential equations, a general method of obtaining the necessary and sufficient conditions for almost-sure asymptotic stability was presented by Khasminskii (1967). The essence of this method is the projection of the system in R^n onto the surface of an n-dimensional sphere such that the stochastic differential equation for $\log \|x\|$ can be written explicitly as a function of only $n-1$ independent angles. The top Lyapunov exponent, defined by

$$\lambda = \lim_{t \to \infty} \sup \frac{1}{t} \log \|x(t, x_o)\|, \tag{1}$$

can then be obtained. These results have been applied to second-order systems by Kozin and Prodromou (1971) and Mitchell and Kozin (1974). A complete study of second-order systems, taking into consideration all possible singularities that can exist in one-dimensional diffusion, was presented by Nishioka (1976). However, there are very few results for the case in which the noise is ergodic and non-white. These results are due to Arnold et al. (1986) and Pardoux and Wihstutz (1987), where almost-sure asymptotic stability of a second-order system with a colored noise process was considered. For the case in which the noise is a Markov process with finitely many states, the top Lyapunov exponent was obtained by Pinsky (1986). A survey of known results on the asymptotics of Lyapunov exponents and rotation number for general two-dimensional systems driven by white or real noise is given by Pinsky and Wihstutz (1991). More recently, Sri Namachchivaya (1991) obtained analytic results for almost-sure asymptotic stability of multi-degree-of-freedom linear systems excited by combined stochastic and harmonic excitation. These results were derived under the assumption that one of the degrees-of-freedom is critically damped, while the remaining degrees-of-freedom are strongly stable. Here, the method of extended averaging (Sri Namachchivaya and Lin, 1988) was used to obtain a lower dimensional Itô stochastic equation: almost-sure stability for these equations was then derived.

In most of the studies reported thus far, the necessary and sufficient conditions were obtained only for a second-order system or multi-degree-of-freedom system with single critical mode. However, to understand most physical phenomena, it is necessary to obtain results for multi-degree-of-freedom systems. The level of mathematical difficulty encountered in this type of analysis, due to the associated multidimensional diffusion problem, has restricted major developments in this area. This problem was overcome by a new approach initiated by Ariaratnam and Xie (1991) and Sri Namachchivaya and Ariaratnam (1990) to study two coupled oscillators with small noise. These results were extended by Sri Namachchivaya and Talwar (1993) to the study of general three and four-dimensional systems under small noise excitations. The method presented in these manuscripts has three important steps. As a first step, approximate Itô equations in amplitudes and phases are obtained assuming the fluctuating coupling terms have zero mean with auto-correlation that goes to zero rapidly for large times. The second step involves the Khasminskii transformation and examination of the diffusion on the appropriate domain by

Contributed by the Applied Mechanics Division of THE AMERICAN SOCIETY OF MECHANICAL ENGINEERS for publication in the ASME JOURNAL OF APPLIED MECHANICS.

Discussion on this paper should be addressed to the Technical Editor, Professor Lewis T. Wheeler, Department of Mechanical Engineering, University of Houston, Houston, TX 77204-4792, and will be accepted until four months after final publication of the paper itself in the ASME JOURNAL OF APPLIED MECHANICS.

Manuscript received by the ASME Applied Mechanics Division, Oct. 16, 1992; final revision, Apr. 27, 1993. Associate Technical Editor: D. J. Inman.

Copyright © 1994 by ASME
Downloaded 03 May 2010 to 171.66.16.20. Redistribution subject to ASME license or copyright; see http://www.asme.org/terms/Terms_Use.cfm

making use of the boundary behavior of the singular points. Finally, the maximum Lyapunov exponent is evaluated using the stationary density of the ergodic diffusive process.

In this paper, we present an alternative method to calculate maximal Lyapunov exponent for stochastically coupled two-degree-of-freedom systems. The noise is assumed white and of small intensity such that one can obtain an asymptotic growth rate. Here we apply a modified version of the perturbation theoretic approach given by Arnold et al. (1986) to obtain the top Lyapunov exponent. In addition, the top Lyapunov exponent for each degree-of-freedom, along with an alternative procedure to calculate the maximal Lyapunov exponent of the complete four-dimensional system, are given in the Appendix. The results pertaining to the maximal Lyapunov exponents of the two-degree-of-freedom system obtained here using an asymptotic expansion of the associated diffusion are exactly the same as those obtained by Ariaratnam and Xie (1992) and Sri Namachchivaya and Talwar (1993) using the method of averaging. The method presented here can easily be extended to incorporate real-noise excitations with specific generators $G(\xi)$. These results are presented in Sri Namachchivaya and Van Roessel (1993).

2 Statement of the Problem and Formulation

Consider linear oscillatory systems described by equations of motion of the form

$$\ddot{q}_i + \omega_i^2 q_i + \epsilon 2\zeta\omega_i \dot{q}_i + \epsilon^{1/2}\sum_{j=1}^{2} k_{ij} q_j \xi(t) = 0 \quad i, j = 1, 2 \qquad (2)$$

where q_i's are generalized coordinates, ω_i is the ith natural frequency and $\epsilon\zeta$ represents small viscous damping coefficients. It is assumed that the natural frequencies are *not commensurable*. The stochastic term $\epsilon^{1/2}\xi(t)$ is a white-noise process with small intensity. In the subsequent analysis, repeated subscripts do not imply summation unless summation is explicitly indicated. The stability of the equilibrium state $q = \dot{q} = 0$ is to be investigated. Since the excitation is white noise, the above equations can be represented in the first-order form by a set of Stratonovich differential equations.

$$dx = Ax\,dt + \epsilon^{1/2} B_x \circ dW_t \quad x(0) = x_o \in R^4 \qquad (3)$$

where $x_{2i-1} = q_i$, $x_{2i} = \omega_i^{-1}\dot{q}_i$, A and B are constant 4×4 matrices given by

$$A = \begin{bmatrix} 0 & \omega_1 & 0 & 0 \\ -\omega_1 & -\epsilon 2\zeta\omega_1 & 0 & 0 \\ 0 & 0 & 0 & \omega_2 \\ 0 & 0 & -\omega_2 & -\epsilon 2\zeta\omega_2 \end{bmatrix}$$

$$B = \begin{bmatrix} 0 & 0 & 0 & 0 \\ -\dfrac{k_{11}}{\omega_1} & 0 & -\dfrac{k_{12}}{\omega_1} & 0 \\ 0 & 0 & 0 & 0 \\ -\dfrac{k_{21}}{\omega_2} & 0 & -\dfrac{k_{22}}{\omega_2} & 0 \end{bmatrix}$$

and W_t is the standard Weiner process. According to Oseledec's (1968) multiplicative ergodic theory (see Arnold and Wihstutz, 1986), for stationary stochastic process and initial random variable $x_o \neq 0$, the Lyapunov exponent (i.e., the exponential growth rate) of the corresponding solution $x(t; x_o)$ of Eq. (3) is given by

$$\lambda(x_o) = \lim_{t\to\infty} \frac{1}{t} \log \|x(t; x_o)\| \quad \text{w.p. 1.}$$

Moreover, for an ergodic random process, the random variable $\lambda(x_o)$ takes on non-random values

$$\lambda^{\min} = \lambda_p < \lambda_{p-1} < \cdots < \lambda_1 = \lambda^{\max}$$

with non-random multiplicities which add up to four in our case. The top Lyapunov exponent $\lambda^{\max}$ which will be denoted as λ henceforth, defines the sample stability or instability of the trivial solution of Eq. (3). However, the explicit evaluation of λ in terms of system parameters, which as we shall show in this section is given by an integral over the unit sphere with respect to the invariant measure of an associated diffusion, is usually difficult. Due to this, we only present an asymptotic expansion of λ in terms of intensity of the noise and damping which are assumed small. As a first step, we use the following transformation:

$$x_1 = r\cos\phi_1\cos\theta \qquad x_3 = r\cos\phi_2\sin\theta$$
$$x_2 = -r\sin\phi_1\cos\theta \qquad x_4 = -r\sin\phi_2\sin\theta$$

where

$$0 \le \phi_i \le 2\pi \qquad 0 \le \theta \le \frac{\pi}{2}.$$

In the above transformation, r represents the norm of the response, ϕ_1 and ϕ_2 are the angles of the first and second oscillators, respectively, and θ describes the coupling or exchange of energy between the first and second oscillators. The physical meaning of this transformation is more transparent from an alternative procedure given in the Appendix. Letting $\rho = \ln\|x\|$, we can write the stochastic differential equations for ρ, ϕ_1, ϕ_2, and θ as

$$d\rho = \epsilon[\tilde{q}_1(\phi, \theta)]dt + \epsilon^{1/2}[q_1(\phi, \theta)] \circ dW_t$$
$$d\theta = \epsilon[\tilde{q}_2(\phi, \theta)]dt + \epsilon^{1/2}[q_2(\phi, \theta)] \circ dW_t$$
$$d\phi_i = [\omega_i + \epsilon\tilde{h}_i(\phi, \theta)]dt + \epsilon^{1/2}]h_i(\phi, \theta)] \circ dW_t \qquad (4)$$

where

$$\tilde{q}_1 = -[\eta_1(1 - \cos 2\phi_1)\cos^2\theta + \eta_2(1 - \cos 2\phi_2)\sin^2\theta]$$

$$\tilde{q}_2 = \frac{1}{2}[\eta_1(1 - \cos 2\phi_1) - \eta_2(1 - \cos 2\phi_2)]\sin 2\theta$$

$$q_1 = \frac{1}{2}[(p_{21}\cos\phi_1\sin\phi_2 + p_{12}\sin\phi_1\cos\phi_2)\sin 2\theta + p_{22}\sin 2\phi_2\sin^2\theta + p_{11}\sin 2\phi_1\cos^2\theta]$$

$$q_2 = \frac{1}{4}[(p_{22}\sin 2\phi_2 - p_{11}\sin 2\phi_1)\sin 2\theta + 4p_{21}\cos\phi_1\sin\phi_2\cos^2\theta - 4p_{12}\sin\phi_1\cos\phi_2\sin^2\theta]$$

$$h_1 = p_{11}\cos^2\phi_1 + p_{12}\cos\phi_1\cos\phi_2\tan\theta$$

$$h_2 = p_{22}\cos^2\phi_2 + p_{21}\cos\phi_1\cos\phi_2\cot\theta$$

$$\tilde{h}_i = -\eta_i\sin 2\phi_i, \quad p_{ij} = \frac{k_{ij}}{\omega_i}, \quad \eta_i = \zeta\omega_i. \qquad (5)$$

Since the processes (θ, ϕ_1, ϕ_2) do not depend on ρ, the processes (θ, ϕ_1, ϕ_2) alone form a diffusive Markov process and the associated generator is given by

$$L^\epsilon = L^o + \epsilon L^1 \qquad (6)$$

where

$$L^o = \sum_{i=1}^{2} \omega_i \frac{\partial}{\partial\phi_i}$$

$$L^1 = \tilde{q}_2\frac{\partial}{\partial\theta} + \sum_{i=1}^{2}\tilde{h}_i\frac{\partial}{\partial\phi_i} + \frac{1}{2}\left(q_2\frac{\partial}{\partial\theta} + \sum_{i=1}^{2} h_i\frac{\partial}{\partial\phi_i}\right)^2.$$

Employing the Wong and Zakai correction for the ρ equation, the drift term can be written as

$$Q^\epsilon = \epsilon\left[\tilde{q}_1 + \frac{1}{2}\left(\frac{\partial q_1}{\partial\theta}q_2 + \sum_{i=1}^{2}\frac{\partial q_1}{\partial\phi_i}h_i\right)\right] \qquad (7)$$

Downloaded 03 May 2010 to 171.66.16.20. Redistribution subject to ASME license or copyright; see http://www.asme.org/terms/Terms_Use.cfm

Integrating the Itô equation for ρ with Q^ϵ as the drift term, yields

$$\|x(t;\, x_o)\| = \|x_o\| \exp\left\{ \int_o^t Q(\theta(\tau),\, \varphi(\tau))d\tau + \int_o^t q_1(\theta(\tau),\, \varphi(\tau))dw(\tau)d\tau \right\}.$$

Making use of Eq. (1) and the above equation it is obvious that, according to Oseledec's (1968) multiplicative ergodic theory, the top Lyapunov exponent is given by

$$\lambda^\epsilon = \langle Q^\epsilon,\, p^\epsilon \rangle \equiv \int_0^{\pi/2} \int_0^{2\pi} \int_0^{2\pi} Q^\epsilon(\theta,\, \phi_1,\, \phi_2)\, p^\epsilon(\theta,\, \phi_1,\, \phi_2)\, d\phi_1\, d\phi_2 d\theta \quad (8)$$

where p^ϵ is the unique ergodic invariant probability measure given by

$$L^{\epsilon *} p^\epsilon = 0$$

provided L^ϵ is hypoelliptic, and (*) represents the adjoint operator.

3 Method of Asymptotic Expansion

In order to obtain the solution given by the integral (8), we expand

$$Q^\epsilon = Q^o + \epsilon Q^1$$

and suppose we construct a formal expansion of $p^\epsilon = p^o + \epsilon p^1 + \cdots \epsilon^N p^N + \cdots$ so that the Fokker-Planck equation

$$L^{\epsilon *} p^\epsilon = (L^o + \epsilon L^1)(p^o + \epsilon p^1 + \cdots) = 0$$

yields

$$L^{o*} p^o = 0, \quad L^{o*} p^1 = -L^{1*} p^o, \quad L^{o*} p^2 = -L^{1*} p^1, \quad \cdots.$$

By constructing an expansion for the adjoint problem $L^\epsilon F^\epsilon = Q^\epsilon$, we want to show that we have an asymptotic expansion for the maximal Lyapunov exponent as

$$\lambda^\epsilon = \langle Q^o,\, p^o \rangle + \epsilon(\langle Q^o,\, p^1 \rangle + \langle Q^1,\, p^o \rangle) + \cdots. \quad (9a)$$

To this end, we construct an adjoint expansion for $L^\epsilon F^\epsilon = Q^\epsilon$ with $F^\epsilon = F^o + \epsilon F^1 + \cdots + \epsilon^N F^N$ such that

$$(L^o + \epsilon L^1)(F^o + \epsilon F^1 + \cdots + \epsilon^N F^N) = Q^\epsilon - (q^o + \epsilon q^1 + \cdots + \epsilon^N q^N) + \epsilon^{N+1} L^1 F^N.$$

Here $q^o, q^1, \cdots, q^N$ are constants and are chosen so that the sequence of problems

$$L^o F^o = Q^o - q^o, \quad L^o F^1 + L^1 F^o = Q^1 - q^1, \quad \cdots, \quad L^o F^N + L^1 F^{N+1} = -q^N$$

are solvable, which implies via the Fredholm alternative

$$\langle (Q^o - q^o),\, p^o \rangle = 0, \quad \langle (Q^1 - q^1 - L^1 F^o),\, p^o \rangle = 0, \quad \cdots, \quad \langle -(L^1 F^{N-1} + q^N),\, p^o \rangle = 0$$

where $L^{o*} p^o = 0$. Then by defining for convenience $\tilde{p}^\epsilon = p^o + \epsilon p^1 + \cdots + \epsilon^N p^N$ and using the Poisson equations, yields

$$L^{\epsilon *} \tilde{p}^\epsilon = \epsilon^{N+1} L^{1*} p^N.$$

Taking the inner product of Q^ϵ with respect to p^ϵ and $\tilde{p}^\epsilon$ yields

$$\langle Q^\epsilon,\, p^\epsilon \rangle = \langle q^\epsilon,\, p^\epsilon \rangle - \epsilon^{N+1} \langle L^1 F^N,\, p^\epsilon \rangle$$

$$\langle Q^\epsilon,\, \tilde{p}^\epsilon \rangle = \langle q^\epsilon,\, \tilde{p}^\epsilon \rangle + \epsilon^{N+1} [\langle L^{1*} p^N,\, F^\epsilon \rangle - L^1 F^N,\, \tilde{p}^\epsilon \rangle]$$

Subtracting one equation from the other, and using the fact that both p^ϵ and $\tilde{p}^\epsilon$ are probability density functions leads to

$$\langle Q^\epsilon,\, p^\epsilon \rangle - [\langle Q^o,\, p^o \rangle + \epsilon\{\langle Q^o,\, p^1 \rangle + \langle Q^1,\, p^o \rangle\} + \cdots + \epsilon^N \{\langle Q^o,\, p^N \rangle + \langle Q^1,\, p^{N-1} \rangle\}] = \epsilon^{N+1} [\langle L^1 F^N,\, \tilde{p}^\epsilon \rangle + \langle Q^1,\, p^N \rangle - \langle L^1 F^N,\, p^\epsilon \rangle - \langle L^1 F^\epsilon,\, p^N \rangle].$$

Suppose that $p^o, p^1, \cdots, p^N$ and $F^o, F^1, \cdots, F^N$ are such that inner products on the rhs of the above equations are well defined and, due to the fact that p^ϵ is unknown, assume the existence of the following bound

$$\sup_{\varphi,\theta,\xi} |L^1 F^N| \le K_1 < \infty.$$

Then it is clear, using the above estimate, that the asymptotic expansion for a fixed $N \ge 0$ given by Eq. (9a) is valid. Since $Q^o \equiv 0$, the first-order approximation of Eq. (9a) reduces to

$$\lambda^\epsilon = \epsilon \langle Q^1,\, p^o \rangle + 0(\epsilon^2) = \epsilon \lambda^1 + 0(\epsilon^2) \quad (9b)$$

and

$$L^{o*} p^o = 0, \quad L^{o*} p^1 = -L^{1*} p^o \quad (10)$$

with the boundary conditions

$$p(\theta,\, \phi_i + 2\pi,\, \phi_j) = p(\theta,\, \phi_i,\, \phi_j), \quad i \ne j.$$

It is important to point out that in addition to smooth functions, p^o and p^1 can be generalized functions due to certain singularities. In this work, all possible solutions for p^o will be determined in order to calculate the first order approximation of Lyapunov exponent. It is clear from the first of Eq. (10) that the general solution of p^o is of the form

$$p^o = F(\theta,\, \psi), \quad \psi = \omega_2 \phi_1 - \omega_1 \phi_2.$$

However, the boundary conditions

$$p^o(\theta,\, \phi_1 + 2\pi,\, \phi_2) = p^o(\theta,\, \phi_1,\, \phi_2), \quad p^o(\theta,\, \phi_1,\, \phi_2 + 2\pi) = p^o(\theta,\, \phi_1,\, \phi_2)$$

imply

$$F(\theta,\, \psi + 2\pi\omega_2) = F(\theta,\, \psi), \quad F(\theta,\, \psi + 2\pi\omega_1) = F(\theta,\, \psi).$$

Since it is assumed that the frequencies are noncommensurable (i.e., $m_1\omega_1 + m_2\omega_2 \ne 0$ for $m_i \in Z$), it is obvious $F(\theta, \psi) = F(\theta)$. Thus, the stationary solution satisfying the periodic boundary conditions can be written as

$$p^o = \frac{F(\theta)}{4\pi^2} \quad (11)$$

where $F(\theta)$ is yet to be determined. In the work of Arnold et al. (1986), both p^o and L^o are functions of the same independent variables. However, in our case L^o is only a function of (φ_1, φ_2) where as p^o depends in general on φ_1, φ_2, and θ. Thus, one cannot completely determine p^o by solving the 0(1) equation. In order to calculate p^o completely, it is necessary to consider the ϵ order Poisson equation along with its adjoint problem, i.e.,

$$L^{o*} p^1 = -L^{1*} p^o \quad \text{and} \quad L^o u^1 = 0. \quad (12)$$

The solution of the first equation requires that $L^{1*} p^o$ must satisfy the solvability condition

$$\langle u^1,\, L^{1*} p^o \rangle = 0 \quad \forall u^1 \in \ker(L^o) = \{\text{arbitrary function of } \theta\},$$

i.e.,

$$\int_0^{\pi/2} \int_0^{2\pi} \int_0^{2\pi} u^1(\theta) L^{1*} p^o d\phi_1 d\phi_2 d\theta = 0.$$

If this is to hold for an arbitrary $u^1(\theta)$ we require

$$\int_0^{2\pi} \int_0^{2\pi} L^{1*} p^o d\phi_1 d\phi_2 = 0. \quad (13)$$

It is important to note that since the integrations in the foregoing equations are taken with respect to φ_i, $i = 1, 2$, the possibility of generalized functions being the solution of p^o is

Downloaded 03 May 2010 to 171.66.16.20. Redistribution subject to ASME license or copyright; see http://www.asme.org/terms/Terms_Use.cfm

not excluded. The integrand in Eq. (13) can be explicitly written as

$$L^{1*}p^o=\frac{1}{4\pi^2}\Bigg\{-\frac{\partial}{\partial\theta}[m_\theta F(\theta)]-\sum_{i=1}^{2}\left\{\frac{\partial m_{\phi_i}}{\partial\phi_i}\right\}F(\theta)+S_o\Bigg[\sum_{i=1}^{2}\left\{\frac{\partial}{\partial\phi_i}\frac{\partial}{\partial\theta}[q_2h_iF(\theta)]\right\}+\frac{1}{2}\frac{\partial^2}{\partial\theta^2}[q_2q_2F(\theta)]+\frac{1}{2}\sum_{i,j=1}^{2}\left\{\frac{\partial^2[h_ih_j]}{\partial\phi_i\partial\phi_j}F(\theta)\right\}\Bigg]\Bigg\}$$

where

$$S_o=2\int_0^\infty E[f(t)\cdot f(t+\tau)]d\tau$$

is the spectrum of the white noise excitation.

Although the maximal Lyapunov exponent and stationary probability density will be presented for the original Eq. (2), to avoid lengthy calculations, the analysis presented in this section considers the special case where $p_{11}=p_{22}=0$.

$$Q^1+\tilde{q}_1(\theta,\ \phi_1,\ \phi_2)+\frac{S_o}{2}p_{21}^2\cos^2\phi_1\cos^2\theta(1-2\sin^2\theta\sin^2\phi_2)+\frac{S_o}{2}p_{12}^2\cos^2\phi_2\sin^2\theta(1-2\cos^2\theta\sin^2\phi_1)-\frac{S_o}{8}p_{12}p_{21}\sin 2\phi_1\sin 2\phi_2\sin^2 2\theta$$

$$m_\theta=\tilde{q}_2(\theta,\ \phi_1,\ \phi_2)+\frac{S_o}{2}p_{21}^2\cos^2\phi_1\cos^2\theta(\cos^2\phi_2\cot\theta-\sin^2\phi_2\sin 2\theta)+\frac{S_o}{2}p_{12}^2\cos^2\phi_2\sin^2\theta(\sin^2\phi_1\sin 2\theta-\cos^2\phi_1\tan\theta)-\frac{S_o}{16}p_{12}p_{21}\sin 2\phi_1\sin 2\phi_2\sin 4\theta$$

$$m_{\phi_1}=-\frac{S_o}{2}p_{12}^2\tan^2\theta\sin 2\phi_1\cos^2\phi_2+\tilde{h}_1(\theta,\ \phi_1,\ \phi_2)$$

$$m_{\phi_2}=-\frac{S_o}{2}p_{21}^2\cot^2\theta\sin 2\phi_2\cos^2\phi_1+\tilde{h}_2(\theta,\ \phi_1,\ \phi_2)$$

$$q_2q_2=p_{21}^2\cos^4\theta\cos^2\phi_1\sin^2\phi_2+p_{12}^2\sin^4\theta\sin^2\phi_1\cos^2\phi_2-\frac{1}{8}p_{12}p_{21}\sin^2 2\theta\sin 2\phi_1\sin 2\phi_2$$

$$q_2h_1=\frac{1}{4}p_{12}p_{21}\sin 2\theta\cos^2\phi_1\sin 2\phi_2-\frac{1}{2}p_{12}^2\frac{\sin^3\theta}{\cos\theta}\sin 2\phi_1\cos^2\phi_2$$

$$q_2h_2=\frac{1}{2}p_{21}^2\frac{\cos^3\theta}{\sin\theta}\cos^2\phi_1\sin 2\phi_2-\frac{1}{4}p_{12}p_{21}\sin 2\theta\sin 2\phi_1\cos^2\phi_2$$

$$h_1h_1=p_{12}^2\tan^2\theta\cos^2\phi_1\cos^2\phi_2$$

$$h_2h_2=p_{21}^2\cot^2\theta\cos^2\phi_1\cos^2\phi_2$$

$$h_1h_2=p_{12}p_{21}\cos^2\phi_1\cos^2\phi_2$$

Since m_{ϕ_i} is 2π-periodic in ϕ_i, it is obvious that the second term in the solvability condition yields

$$\frac{1}{4\pi^2}\int_0^{2\pi}\int_0^{2\pi}\frac{\partial}{\partial\phi_i}[m_{\phi_i}(\theta,\ \phi_1,\ \phi_2)F(\theta)]d\phi_1\,d\phi_2=0,\quad i=1,\ 2.$$

Similarly, due to the fact that the terms in q_2h_i are 2π-periodic in either ϕ_1 or ϕ_2, we have

$$\frac{1}{4\pi^2}\int_0^{2\pi}\int_0^{2\pi}\frac{\partial^2}{\partial\theta\,\partial\phi_i}[q_2h_iF(\theta)]d\phi_1\,d\phi_2=0,\quad i=1,\ 2.$$

The expressions for h_ih_j contain constant terms in addition to 2π-periodic terms. However, due to the differentiation, the constant terms vanish and the last term in the solvability condition yields

$$\frac{1}{4\pi^2}\int_0^{2\pi}\int_0^{2\pi}\frac{\partial^2}{\partial\phi_i\,\partial\phi_j}[h_ih_jF(\theta)]d\phi_1\,d\phi_2=0,\quad i,\ j=1,\ 2.$$

Thus we have

$$\int_0^{2\pi}\int_0^{2\pi}L^{1*}p^o d\phi_1\,d\phi_2=\frac{-1}{4\pi^2}\Bigg[\int_0^{2\pi}\int_0^{2\pi}\frac{\partial}{\partial\theta}[m_\theta(\theta,\ \phi_1,\ \phi_2)F(\theta)]d\phi_1\,d\phi_2+\frac{S_o}{2}\int_0^{2\pi}\int_0^{2\pi}\frac{\partial^2}{\partial\theta^2}[q_2q_2F(\theta)]d\phi_1\,d\phi_2\Bigg]=0.$$

The equation governing the arbitrary function $F(\theta)$ is then determined from the solvability condition as

$$-\frac{\partial}{\partial\theta}[\Omega(\theta)F(\theta)]+\frac{1}{2}\frac{\partial^2}{\partial\theta^2}[\Psi^2(\theta)F(\theta)]=0 \tag{14}$$

where

$$\Omega(\theta)=\frac{1}{2}(\eta_1-\eta_2)\sin 2\theta+\frac{S_o}{4}[\cot 2\theta(p_{12}^2\sin^4\theta+p_{21}^2\cos^4\theta)]$$

and

$$\Psi^2(\theta)=\frac{S_o}{4}[p_{12}^2\sin^4\theta+p_{21}^2\cos^4\theta].$$

Since the solvability condition of Eq. (12) yields the condition on p^1 which is of the order (ϵ), it is not surprising that we need to use the properties of the process with $\epsilon\neq 0$ to determine p^o. The solution of Eq. (14) is given by

$$F(\theta)=m(\theta)[c_1S(\theta)+c_2]$$

where c_1 and c_2 are determined by the boundary and normalization conditions, and

$$S(\theta)=\int^\theta s(\eta)d\eta,\quad s(\theta)=\exp[-B(\theta)],\quad m(\theta)=[\Psi^2(\theta)s(\theta)]^{-1}$$

$$B(\theta)=\ln|\sin 2\theta|+\frac{4}{S_o}(\eta_1-\eta_2)\begin{cases}\dfrac{1}{p_{12}p_{21}}\tan^{-1}\left[\dfrac{\alpha^--\alpha^+\cos 2\theta}{2p_{12}p_{21}}\right] & p_{12}p_{21}\neq 0\\ \dfrac{-2}{\alpha^--\alpha^+\cos 2\theta} & p_{12}p_{21}=0\end{cases}$$

with

$$\alpha^+=p_{12}^2+p_{21}^2,\quad \alpha^-=p_{12}^2-p_{21}^2.$$

As mentioned earlier, the procedure presented so far has not restricted p^o to be a smooth function in θ. In general, it is possible to have singularities in θ. Thus, some justification is needed in order to ensure p^o is a bounded positive density. Even though it is clear from the diffusion term that there is no singularity in the open interval $\theta\in(0,\ \pi/2)$, it is important to make sure p^o could not represent a point mass at 0 or $\pi/2$. To this end, it is obvious from the transformation that $\theta=0$ implies $r_1=0$ and $\theta=\pi/2$ implies $r_2=0$. Physically, however, it is clear that unless the coupling coefficients p_{12} and p_{21} are both zero, it is not possible to have a solution with either r_1 or r_2 identically zero. Thus, there is no accumulation of mass at either $\theta=0$ or $\theta=\pi/2$ and p^o will not represent a point mass at 0 or $\pi/2$. Moreover, this assertion can also be justified by applying the Feller classification based on scale and speed measures for the $F(\theta)$ process. It can easily be shown that $(\varphi_i,\ \theta=0)$ and $(\varphi_i,\ \theta=\pi/2)$ are entrance boundaries (Sri Namachchivaya and Ariaratnam, 1990), and it is required that

Downloaded 03 May 2010 to 171.66.16.20. Redistribution subject to ASME license or copyright; see http://www.asme.org/terms/Terms_Use.cfm

$c_1 = 0$ in order to maintain $p^o(\theta)$ positive and finite throughout $\theta = (0, \pi/2)$. In the expression for $F(\theta)$, $c_2 = C$ is chosen to satisfy the normality condition. The stationary probability density for this special case ($p_{11} = p_{22} = 0$) is given by

$$p^o(\theta, \psi_1, \psi_2) = \frac{1}{4\pi^2} F(\theta)$$

where

$$F(\theta) = \begin{cases} \dfrac{C \sin 2\theta}{\psi^2(\theta)} \exp\left(\dfrac{4(\eta_1 - \eta_2)}{S_o p_{12} p_{21}} \tan^{-1}\left[\dfrac{\alpha^- - \alpha^+ \cos 2\theta}{2 p_{12} p_{21}} \right] \right) & p_{12} p_{21} \neq 0 \\ \dfrac{C \sin 2\theta}{\psi^2(\theta)} \exp\left(\dfrac{8(\eta_2 - \eta_1)}{S_o(\alpha^- - \alpha^+ \cos 2\theta)} \right) & p_{12} p_{21} = 0 \end{cases}$$

$$C = \left[M\left(\frac{\pi}{2}\right) - M(0) \right]^{-1}$$

and

$$M(\theta) = \begin{cases} \dfrac{1}{(\eta_1 - \eta_2)} \exp\left(\dfrac{4(\eta_1 - \eta_2)}{S_o p_{12} p_{21}} \tan^{-1}\left[\dfrac{\alpha^- - \alpha^+ \cos 2\theta}{2 p_{12} p_{21}} \right] \right) & p_{12} p_{21} \neq 0 \\ \dfrac{1}{(\eta_1 - \eta_2)} \exp\left(\dfrac{8(\eta_2 - \eta_1)}{S_o(\alpha^- - \alpha^+ \cos 2\theta)} \right) & p_{12} p_{21} = 0. \end{cases}$$

Thus, the first approximation of the maximal Lyapunov exponent can be calculated using

$$\lambda^1 = \langle Q^1, p^o \rangle = \frac{1}{4\pi^2} \int_0^{\pi/2} \int_0^{2\pi} \int_0^{2\pi} Q^1(\theta, \phi_1, \phi_2) F(\theta) d\phi_1 d\phi_2 d\theta = \int_0^{\pi/2} Q(\theta) F(\theta) d\theta$$

where

$$Q(\theta) = -(\eta_1 \cos^2\theta + \eta_2 \sin^2\theta) + \psi^2(\theta).$$

This yields

$$\lambda^1 = -\frac{1}{2}(\eta_1 - \eta_2) + \frac{1}{2}(\eta_1 - \eta_2) \frac{M(\pi/2) + M(0)}{M(\pi/2) - M(0)}. \quad (15)$$

This is precisely the result obtained by Sri Namachchivaya and Ariaratnam (1990) using the method of stochastic averaging where approximate Itô equations in amplitudes and phase are obtained assuming the fluctuating coupling terms have zero mean with autocorrelation that goes to zero rapidly for large times. For this four-dimensional case, the amplitude processes are decoupled from the phase processes and the Khasminskii transformations are applied on a quarter circle and the diffusion on its domain was examined by making use of the boundary behavior of the singular points. Furthermore, it was shown diffusion is ergodic and the maximal Lyapunov exponent is evaluated using the stationary density of the ergodic diffusive process. This provides the almost-sure asymptotic stability condition, and thus the stability boundary in the system parameter space.

For the original problem given in Eq. (2) with $p_{11} \neq 0$, $p_{22} \neq 0$, the general procedure explained above yields the following:

$$Q(\theta) = \lambda_1 \cos^2(\theta) + \lambda_2 \sin^2(\theta) + \psi^2(\theta)$$

$$\Omega(\theta) = \frac{1}{2}[\lambda_2 - \lambda_1 + (\alpha_{12} - \alpha_{21})] \sin 2\theta + \frac{1}{2}\gamma \sin 4\theta + \frac{1}{2}(\alpha_{12} + \alpha_{21}) \cot 2\theta + \frac{1}{2}(\alpha_{21} - \alpha_{12}) \csc 2\theta$$

$$\psi^2(\theta) = \frac{1}{2}(\alpha_{12} + \alpha_{21}) + \frac{1}{2}(\alpha_{21} - \alpha_{12}) \cos 2\theta + \gamma \sin^2(2\theta)$$

where

$$\beta_i = \frac{S_o}{8} p_{ii}^2, \quad \alpha_{ij} = \frac{S_o}{4} p_{ij}^2, \quad i \neq j$$

$$\gamma = \frac{1}{4}(\beta_1 + \beta_2) - \frac{1}{4}(\alpha_{12} + \alpha_{21}), \quad \lambda_i = -\eta_i + \beta_i$$

As before, the diffusion is nonsingular and the Lyapunov exponent reduces to

$$\lambda^1 = \frac{1}{2}(\lambda_1 + \lambda_2) - \frac{1}{2}(\lambda_1 - \lambda_2) \frac{M(\pi/2) + M(0)}{M(\pi/2) - M(0)} \quad (16)$$

where

$$M(\theta) = \begin{cases} \dfrac{1}{(\lambda_2 - \lambda_1)} \exp\left(\dfrac{2(\lambda_1 - \lambda_2)}{\sqrt{-\Delta}} \tanh^{-1}\left[\dfrac{b + 2c\cos 2\theta}{\sqrt{-\Delta}} \right] \right) & \Delta < 0 \\ \dfrac{1}{(\lambda_2 - \lambda_1)} \exp\left(\dfrac{2(\lambda_1 - \lambda_2)}{b + 2c\cos 2\theta} \right) & \Delta = 0 \\ \dfrac{1}{(\lambda_2 - \lambda_1)} \exp\left(\dfrac{2(\lambda_2 - \lambda_1)}{\sqrt{\Delta}} \tan^{-1}\left[\dfrac{b + 2c\cos 2\theta}{\sqrt{\Delta}} \right] \right) & \Delta > 0 \end{cases}$$

$a = -2\gamma - (\alpha_{12} + \alpha_{21})$, $b = (\alpha_{12} - \alpha_{21})$, $c = 2\gamma$, $\Delta = 4ac - b^2$.

These are once again the results obtained by the method of stochastic averaging in Ariaratnam and Xie (1991) and Sri Namachchivaya and Talwar (1993). Alternative procedure to calculate the top Lyapunov exponent along with Lyapunov exponents of each degree-of-freedom are given in the Appendix.

4 Conclusion

In this paper, an alternative perturbative method introduced in Arnold et al. (1986) is presented to calculate the top Lyapunov exponent of a coupled white noise driven, two-degree-of-freedom system. It is shown that the results in the first approximation are precisely the same as those obtained by the method of stochastic averaging (Sri Namachchivaya and Ariaratnam, 1990), where the stochastic averaging gives rise to an approximate Itô equation in a weak sense. The asymptotic analysis presented in this paper leads to a sequence of linear Poisson equations to be solved at each order in ϵ. To completely

Downloaded 03 May 2010 to 171.66.16.20. Redistribution subject to ASME license or copyright; see http://www.asme.org/terms/Terms_Use.cfm

determine the solution at any particular order requires that a solvability condition be met at the subsequent order in ϵ. At the leading order this solvability condition leads integration of the right-hand side of the first order of Poisson equation with respect to φ_1 and φ_2. Thus, it is natural that Eq. (14), for diffusion in θ, that we obtained is similar to that obtained using stochastic averaging. It is also clear from this analysis that stochastic averaging yields the first term in the asymptotic expansion of Lyapunov exponent. Furthermore, this method can be easily extended to obtain the second-order approximation of the Lyapunov exponent. However, the results presented in Ariaratnam and Xie (1992) and Sri Namachchivaya and Talwar (1992) are more general in the sense that they can be applied to problems with real noise provided the excitation intensity is small. In the real noise case, the diffusion in θ can be singular and more detailed analysis must be carried out as shown in Ariaratnam and Xie (1992).

The Lyapunov exponents for each degree-of-freedom, λ_i^1, were obtained in the Appendix by examining the asymptotic growth rate of $\ln r_i$. These do not reflect the coupling that is present in the four-dimensional system. Furthermore, these quantities are the same as the Lyapunov exponent of each decoupled degree-of-freedom. Thus, the top Lyapunov exponent of the coupled two-degree-of-freedom system cannot be obtained by finding the maximum of λ_1^1 and λ_2^1. However, it may be possible to obtain the maximal Lyapunov exponent of the coupled system by this method if one obtains higher order approximations of the individual Lyapunov exponents λ_i. It is also shown that for the white noise excitation the first-order approximation of the rotation number, α_i^1, is identically zero.

Acknowledgments

The authors would like to acknowledge Prof. Mark Pinsky for the discussions and suggestions regarding the method presented in the Appendix, and Professors Ludwig Arnold, Wolfgang Kliemann, and Volker Wihstutz for their various helpful discussions. The first author would like to acknowledge the support of AFOSR through Grant 91-0041 and the National Science Foundation through Grant MSS 90-57437 PYI.

References

Ariaratnam, S. T., and Xie, W. C., 1992, "Lyapunov Exponents and Stochastic Stability of Coupled Linear Systems under Real Noise Excitation," to appear in ASME JOURNAL OF APPLIED MECHANICS.

Arnold, L., and Wihstutz, V., eds., 1986, *Lyapunov Exponents* (Lecture Notes in Mathematics, No. 1186), Springer-Verlag, Berlin.

Arnold, L., Papanicolaou, G., and Wihstutz, V., 1986, "Asymptotic Analysis of Lyapunov Exponent and Rotation Number of the Random Oscillator and Applications," *SIAM Journal of Applied Mathematics*, Vol. 46, No. 3, pp. 427–450.

Khasminskii, R. Z., 1967, "Necessary and Sufficient Conditions for the Asymptotic Stability of Linear Stochastic Systems," *Theory of Probability and Applications*, Vol. 21, No. 1, pp. 144–147.

Kozin, F., 1963, "Almost-Sure Stability of Linear Stochastic Systems with Random Coefficients," *Journal of Mathematics and Physics*, Vol. 42, pp. 59–67.

Kozin, F., and Prodromou, S., 1971, "Necessary and Sufficient Conditions for Almost-Sure Sample Stability of Linear Itô Equations," *SIAM Journal of Applied Mathematics*, Vol. 21, No. 2, pp. 413–424.

Mitchell, R. R., and Kozin, F., 1974, "Sample Stability of Second Order Linear Differential Equations with Wide-Band Noise Coefficients," *SIAM Journal of Applied Mathematics*, Vol. 274, No. 4, pp. 571–604.

Nishioka, K., 1976, "On the Stability of Two-Dimensional Linear Stochastic Systems," *Kodai Mathematics Seminar*, Rep. 27, pp. 211–230.

Oseledec, V. I., 1968, "A Multiplicative Ergodic Theorem Lyapunov Characteristic Numbers for Dynamical Systems," *Transaction of Moscow Mathematical Society*, Vol. 19, pp. 197–231.

Pardoux, E., and Wihstutz, V., 1987, "Lyapunov Exponent and Rotation Number of Two-Dimensional Linear Stochastic Systems with Small Diffusion," *SIAM Journal of Applied Mathematics*, Vol. 48, No. 2, pp. 442–457.

Pinsky, M. A., 1986, "Instability of Harmonic Oscillators with Small Noise," *SIAM Journal of Applied Mathematics*, Vol. 46, No. 3, pp. 451–463.

Pinsky, M. A., and Wihstutz, V., 1991, "Lyapunov Exponents for White and Real Noise Driven Two-Dimensional Systems," *Lectures in Applied Mathematics*, Vol. 27, pp. 201–213.

Sri Namachchivaya, N., and Lin, Y. K., 1988, "Application of Stochastic Averaging for System With High Damping," *Journal of Probabilistic Engineering Mechanics*, Vol. 3, No. 3, pp. 185–196.

Sri Namachchivaya, N., and Ariaratnam, S. T., 1990, "Almost-Sure Asymptotic Stability of Stochastically Coupled Two Degree of Freedom Mechanical Systems," Report UILU ENG 90-0502, University of Illinois at Urbana-Champaign.

Sri Namachchivaya, N., 1991, "Almost-Sure Stability of Stochastic Systems With Applications to Rotor Blade Dynamics in Forward Flight," *Journal of Sound and Vibration*, Vol. 151, No. 1, pp. 77–90.

Sri Namachchivaya, N., and Talwar, S., 1993, "Maximal Lyapunov Exponents for Stochastically Perturbed Co-Dimension Two Bifurcations," *Journal of Sound and Vibration*, Vol. 169, No. 3, pp. 349–372.

Sri Namachchivaya, N., and Van Roessel, H., 1993, "Maximal Lyapunov Exponent and Rotation Numbers for Two Coupled Oscillators Driven by Real Noise," *Journal of Statistical Physics*, Vol. 71, No. 4.

APPENDIX A

The procedure given in the main text yields the maximal Lyapunov exponent of the whole system, however, it is possible to determine the top Lyapunov exponents for each degree-of-freedom along with their rotation numbers. To this end, the usual transformation is introduced to the original system (3), i.e.,

$$x_{2i-1} = r_i \cos\phi_i, \quad x_{2i} = -r_i \sin\phi_i, \quad \rho_i = \ln(r_i)$$

which yields

$$d\rho_i = \epsilon[\tilde{p}_i(\phi)]dt + \epsilon^{1/2}[p_i(\exp(\rho_j - \rho_i), \phi)] o\, dW_t$$
$$d\phi_i = [\omega_i + \epsilon\tilde{h}_i(\phi)]dt + \epsilon^{1/2}[h_i(\exp(\rho_j - \rho_i), \phi)] o\, dW_t$$

where p_i and h_i contain terms of the form $\exp(\rho_j - \rho_i)$ for $i \neq j$. These terms are due to the stochastic coupling between the first and the second degree-of-freedom. Due to the fact $\exp(\rho_j - \rho_i) = r_j/r_i$ is always positive, one can introduce a one-to-one mapping $\exp(\rho_2 - \rho_1) = \tan\theta$ where $0 \le \theta \le \pi/2$. Now, the Stratonovich equation can be written as

$$d\rho_i = \epsilon[\tilde{p}_i(\phi)]dt + \epsilon^{1/2}[p_i(\theta, \phi)] o\, dW_t$$
$$d\phi_i = [\omega_i + \epsilon\tilde{h}_i(\phi)]dt + \epsilon^{1/2}[h_i(\theta, \phi)] o\, dW_t$$
$$d\theta = \epsilon[\tilde{q}_2(\phi)]dt + \epsilon^{1/2}[q_2(\theta, \phi)] o\, dW_t \tag{17}$$

where

$$\tilde{p}_i = -\eta_i(1 - \cos 2\phi_i)$$
$$p_1 = p_{11}\cos\phi_1 \sin\phi_1 + p_{12}\tan\theta \sin\phi_1 \cos\phi_2$$
$$p_2 = p_{21}\cot\theta \cos\phi_1 \sin\phi_2 + p_{22}\cos\phi_2 \sin\phi_2.$$

The remaining quantities $\tilde{h}_i$, h_i, $\tilde{q}_i$, and q_2 are as defined in Eq. (5). The Lyapunov exponents of each degree-of-freedom can now be calculated using the ideas of Pinsky (1986). Accordingly, one introduces bounded functions f and g along with real numbers λ and α. The bounded functions f and g are defined as

$$f_i^\epsilon(\rho, \theta, \phi) = \rho_i + \epsilon f_i(\theta, \phi) + \epsilon^2 \tilde{f}_i(\theta, \phi) + \cdots$$
$$g_i^\epsilon(\rho, \theta, \phi) = \phi_i + \epsilon g_i(\theta, \phi) + \epsilon^2 \tilde{g}_i(\theta, \phi) + \cdots$$

such that the real numbers are given by

$$\tilde{L}^\epsilon f_i^\epsilon = \lambda_i^\epsilon, \quad \tilde{L}^\epsilon g_i^\epsilon = \alpha_i^\epsilon$$

where $\tilde{L}^\epsilon$ is the generator for the complete system including ρ, i.e.,

$$\tilde{L}^\epsilon = \tilde{L}^o + \epsilon\tilde{L}^1, \quad \tilde{L}^o = \tilde{L}^o_\phi = L^o, \quad \tilde{L}^1 = \tilde{L}^1_{\rho,\phi,\theta} \neq L^1. \tag{18}$$

Applying the Itô Lemma, it can be shown that

$$f_i^\epsilon(\rho, \theta, \phi) = \rho_i + \epsilon f_i(\theta, \phi) + \epsilon^2 \tilde{f}_i(\theta, \phi) + \cdots$$
$$= f_i(0) + \int^t \tilde{L}^\epsilon f_i^\epsilon d\tau + M_{\lambda_i}(t)$$
$$g_i^\epsilon(\rho, \theta, \phi) = \phi_i + \epsilon g_i(\theta, \phi) + \epsilon^2 \tilde{g}_i(\theta, \phi) + \cdots$$
$$= g_i(0) + \int^t \tilde{L}^\epsilon g_i^\epsilon d\tau + M_{\alpha_i}(t)$$

Downloaded 03 May 2010 to 171.66.16.20. Redistribution subject to ASME license or copyright; see http://www.asme.org/terms/Terms_Use.cfm

where $\rho=\rho(t)$, $\theta=\theta(t)$, and $\phi=\phi(t)$ are stochastic processes, $M_{\lambda_i}(t)$ and $M_{\alpha_i}(t)$ are Itô stochastic integrals of bounded functions, hence

$$\lim_{t\to\infty}\frac{1}{t}M_{\lambda_i}(t)=0 \quad \text{and} \quad \lim_{t\to\infty}\frac{1}{t}M_{\alpha_i}(t)=0.$$

Now dividing the Itô integral equations by t and taking the limit yields

$$\lim_{t\to\infty}\frac{1}{t}[\rho_i(t)]=\lambda_i^\epsilon \quad \text{and} \quad \lim_{t\to\infty}\frac{1}{t}[\phi_i(t)]=\alpha_i^\epsilon.$$

In order to determine the first approximation of λ_i^ϵ, we expand the expression

$$\tilde{L}^\epsilon f_i^\epsilon=\lambda_i^\epsilon$$

where $\tilde{L}^\epsilon$ is the generator of the complete system as given in Eq. (18). The expansion of the Lyapunov exponent for each degree-of-freedom is given by

$$\lambda_i^\epsilon=\lambda_i^o+\epsilon\lambda_i^1+\epsilon^2\lambda_i^2+\cdots$$

where it is clear that $\lambda_i^o=0$ and λ_i^1 is to be determined. This procedure yields

$$\tilde{L}^o f_i(\phi,\theta)=-Q_i^1+\lambda_i^1, \quad \tilde{L}^o\tilde{f}_i(\phi,\theta)=-\tilde{L}^1 f_i(\phi,\theta)+\lambda_i^2, \ \cdots$$

where $\tilde{L}^o$, $\tilde{L}^1$ are defined in Eq. (6) and

$$Q_i^1=\tilde{p}_i+\frac{1}{2}\left[\frac{\partial p_i}{\partial\theta}q_2+\sum_{j=1}^{2}\frac{\partial p_i}{\partial\phi_j}h_j\right]$$
$$=-\eta_i+\cos 2\phi_i\left[\eta_i+\frac{S_o}{2}(p_{ii}\cos\phi_i+p_{ij}\cos\phi_j(\cot\theta)^{(-1)^j})^2\right].$$

The solvability condition yields the first approximation to the Lyapunov exponent for each degree-of-freedom as

$$\lambda_i^1=\langle Q_i^1, p^o\rangle.$$

Once again, p^o is the solution of the adjoint problem given by Eq. (10), whose solution is given by Eq. (11) as

$$p^o=\frac{F(\theta)}{4\pi^2}.$$

However, in this calculation due to the form of Q_i^1 it is not necessary to determine $F(\theta)$ explicitly as before, and the Lyapunov exponents for each degree of freedom is given by

$$\lambda_i^1=-\eta_i+\frac{S_o}{8}p_{ii}$$

It is worth noting that these are exactly the maximum Lyapunov exponent of each decoupled degree-of-freedom (i.e., $p_{12}=p_{21}=0$). Similarly, to determine the first approximation of α_i^ϵ, we expand the expression

$$L^\epsilon g_i^\epsilon=\alpha_i^\epsilon.$$

Following the general procedure given above, one obtains

$$\alpha_i^\epsilon=\langle H_i^1, p^o\rangle$$

where

$$H_i^1=\tilde{h}_i+\frac{1}{2}\left[\frac{\partial h_i}{\partial\theta}q_2+\sum_{j=1}^{2}\frac{\partial h_i}{\partial\phi_j}h_j\right]$$
$$=-\sin 2\phi_i\left[\eta_i+\frac{S_o}{2}(p_{ii}\cos\phi_i+p_{ij}\cos\phi_j(\cot\theta)^{(-1)^j})^2\right].$$

Since $\alpha_i^1=0$, in the first approximation the rotation number is $\alpha_i^\epsilon=\omega_i+0(\epsilon^2)$.

In order to determine the top Lyapunov exponent, we can once again make use of the Stratonovich Eqs. (17). Since

$$\ln\|x\|=\ln(r_1^2+r_2^2)^{1/2}=\ln r_1+\ln(\sec\theta)=\rho_1+z.$$

The Itô equations for ρ_1 and z are required and found to be

$$d\rho_1=\epsilon[Q_1^1(\theta,\phi)]dt+\epsilon^{1/2}[p_1(\theta,\phi)]dW$$
$$dz=\epsilon[Q_z^1(\theta,\phi)]dt+\epsilon^{1/2}[q_z(\theta,\phi)]dW$$

where using Itô's formula for a change of variables

$$Q_z^1=Q_\theta^1\tan\theta+\frac{1}{2}q_z^2\sec^2\theta, \quad q_z=q_2\tan\theta$$
$$Q_\theta^1=\tilde{q}_2(\phi,\theta)+\frac{1}{2}\left[\frac{\partial q_2}{\partial\theta}q_2+\sum_{i=1}^{2}\frac{\partial q_2}{\partial\phi_i}h_i\right].$$

The remaining quantities $\tilde{q}_2$, q_2, and h_i have been defined previously in Eq. (5). To simplify the expressions, the analysis presented below considers the special case of $p_{11}=p_{22}=0$. For this case, the Itô equation coefficients are

$$Q_z^1=\eta_1\sin^2\theta(1-\cos 2\phi_1)-\eta_2\sin^2\theta(1-\cos 2\phi_2)$$
$$+\frac{1}{4}p_{21}^2S_o(1+\cos 2\phi_1)\left(\cos^4\theta+\frac{1}{4}\cos 2\phi_2\sin^2 2\theta\right)$$
$$+\frac{1}{4}p_{12}^2S_o(1+\cos 2\phi_1)\left(\sin^4\theta+\cos 2\phi_1\left(\frac{1}{4}\sin^2 2\theta+\tan^2\theta\right)\right)$$
$$-\frac{1}{8}p_{12}p_{21}S_o\sin 2\phi_1\sin 2\phi_2\sin^2 2\theta$$

$$q_z=\frac{1}{2}\sin^2\theta(p_{22}\sin 2\phi_2-p_{11}\sin 2\phi_1)+\frac{1}{2}p_{21}\cos\phi_1\sin\phi_2\sin 2\theta$$
$$-p_{12}\sin\phi_1\cos\phi_2\sin^3\theta\sec\theta.$$

It is clear that the top Lyapunov exponent is given by

$$\lambda^1=\lim_{t\to\infty}\frac{1}{t}\ln\|x\|=E[Q_1^1(\theta,\phi)]+E[Q_z^1(\theta,\phi)].$$

Upon substitution, the maximal Lyapunov exponent is

$$\lambda^1=\int_o^{\pi/2}F(\theta)\left[-\eta_1\cos^2\theta-\eta_2\sin^2\theta\right.$$
$$\left.+\frac{S_o}{4}(p_{12}^2\sin^4\theta+p_{21}^2\cos^4\theta)\right]d\theta$$

which is precisely that obtained in Eq. (15). Similarly, the top Lyapunov exponent for the general case presented in Eq. (16) can be obtained using Eq. (19).

Downloaded 03 May 2010 to 171.66.16.20. Redistribution subject to ASME license or copyright; see http://www.asme.org/terms/Terms_Use.cfm

On the Boltzmann-Hamel Equations of Motion: A Vectorial Treatment

J. G. Papastavridis
Associate Professor of Mechanics,
School of Mechanical Engineering,
Georgia Institute of Technology,
Atlanta, GA 30332

This paper presents a direct vectorial derivation of the famous Boltzmann-Hamel equations of motion of discrete mechanical systems, in general nonlinear nonholonomic coordinates and under general nonlinear (velocity) nonholonomic constraints. The connection between particle and system vectors is stressed throughout, in all relevant kinematic and kinetic quantities/principles/theorems. The specialization of these results to the common case of linear nonholonomic coordinates and linear nonholonomic (i.e., Pfaffian) constraints is carried out in the paper's Appendix.

1 Introduction

The equations of motion of discrete mechanical systems under Pfaffian (possibly nonholonomic (= noncompletely integrable)) constraints and in nonholonomic, or quasi-coordinates, given in definitive form by Hamel in 1903–1904 and called (not quite accurately) today "the Boltzmann-Hamel (BH) equations," constitute the theoretical pinnacle of Lagrangean-type analytical dynamics. Unfortunately, their few expositions in English (e.g., Desloge, 1982; Feiyue and Bainum, 1991; Kilmister, 1964, 1967; Meirovitch, 1970; Neimark and Fufaev, 1972; Whittaker, 1937) are exclusively and uniformly algebraic, and thus reinforce the widespread but incorrect notion that analytical dynamics is somehow nonvectorial; and such an incomplete understanding contributes significantly, no doubt, to the current (undeserved) lack of interest toward this important topic.

The purpose of this paper is to try to remedy this situation by rederiving the BH equations using as much as possible particle and system vectors. Such a (differential) geometric approach should, hopefully, improve our grasp of these fundamental equations. Also, in the process, and in pointing out their differences from the ordinary (i.e., holonomic coordinate) Lagrangean equations, we will be able to see clearly the most general geometrical structure generated by, or needed in, the Lagrangean mechanics formalism.

This discussion elaborates, complements, and clarifies the fundamental (but virtually unknown) paper by Schaefer (1951); the latter has inspired this investigation.

Contributed by the Applied Mechanics Division of THE AMERICAN SOCIETY OF MECHANICAL ENGINEERS for publication in the ASME JOURNAL OF APPLIED MECHANICS.

Discussion on this paper should be addressed to the Technical Editor, Professor Lewis T. Wheeler, Department of Mechanical Engineering, University of Houston, Houston, TX 77204-4792, and will be accepted until four months after final publication of the paper itself in the ASME JOURNAL OF APPLIED MECHANICS.

Manuscript received by the ASME Applied Mechanics Division, Oct. 29, 1992; final revision, Mar. 15, 1993. Associate Technical Editor: P. D. Spanos.

2 Kinematics

Consider a mechanical system S whose configurations of interest are completely and uniquely determined by the n holonomic positional system parameters ("generalized coordinates") $q = (q_1, \ldots, q_n)$, so that the inertial *position* vector $\mathbf{r}$ of a typical of its particles P is expressible as (t = *time*):

$$\mathbf{r} = \mathbf{r}(P;\, t,\, q) \equiv \mathbf{r}(t,\, q). \tag{1}$$

Then the (inertial) *virtual displacement, velocity*, and *acceleration* (vectors) of P (with all latin indices (except D and I and of course t = *time*) running from 1 to n) will equal, respectively:

$$\text{(i)} \qquad \delta\mathbf{r} = \sum_k (\partial\mathbf{r}/\partial q_k)\delta q_k = \sum_k \mathbf{e}_k \delta q_k; \tag{2a}$$

$$\text{(ii)} \qquad \mathbf{v} \equiv d\mathbf{r}/dt = \sum_k (\partial\mathbf{r}/\partial q_k)\dot{q}_k + \partial\mathbf{r}/\partial t$$

$$\equiv \sum_k \dot{q}_k \mathbf{e}_k + \mathbf{e}_t; \tag{2b}$$

$$\text{(iii)} \quad \mathbf{a} \equiv d\mathbf{v}/dt = \sum_k (\partial\mathbf{r}/\partial q_k)\ddot{q}_k + 2\sum_{k,l} (\partial^2\mathbf{r}/\partial q_k \partial q_l)\dot{q}_k\dot{q}_l + \sum_k (\partial^2\mathbf{r}/\partial t \partial q_k)\dot{q}_k + \partial^2\mathbf{r}/\partial t^2$$

$$\equiv \sum_k \ddot{q}_k \mathbf{e}_k + 2\sum_{k,l} \dot{q}_k\dot{q}_l \mathbf{e}_{k,l} + \sum_k \dot{q}_k \mathbf{e}_{k,t} + \mathbf{e}_{t,t}$$

$$\equiv \sum_k \ddot{q}_k \mathbf{e}_k + \ldots$$

$$(\ldots \equiv \text{terms not containing } \ddot{q}); \tag{2c}$$

where the fundamental holonomic *particle and system* vectors $\mathbf{e}_k$ and $\mathbf{e}_t$ are defined by

$$\mathbf{e}_k = \mathbf{e}_k(t,\, q) \equiv \partial\mathbf{r}/\partial q_k \text{ and } \mathbf{e}_t = \mathbf{e}_t(t,\, q) \equiv \partial\mathbf{r}/\partial t, \tag{3}$$

and $(\ldots)_{,k} \equiv \partial(\ldots)/\partial q_k$. From the above we readily deduce the following kinematical identities ("Helmholtz's rules"):

Copyright © 1994 by ASME
Downloaded 03 May 2010 to 171.66.16.20. Redistribution subject to ASME license or copyright; see http://www.asme.org/terms/Terms_Use.cfm

(i) $$\frac{\partial \mathbf{r}}{\partial q_k}=\frac{\partial \mathbf{v}}{\partial \dot{q}_k}=\frac{\partial \mathbf{a}}{\partial \ddot{q}_k}=\ldots\equiv \mathbf{e}_k, \tag{4}$$

(ii) $$\frac{\partial \mathbf{v}}{\partial q_k}=\frac{\partial}{\partial q_k}\left(\frac{d\mathbf{r}}{dt}\right)=\frac{d}{dt}\left(\frac{\partial \mathbf{r}}{\partial q_k}\right)=\frac{d\mathbf{e}_k}{dt}, \tag{5}$$

and from them the *integrability* conditions:

(i) $$\begin{aligned} E_k(\mathbf{v}) &\equiv \frac{d}{dt}\left(\frac{\partial \mathbf{v}}{\partial \dot{q}_k}\right)-\frac{\partial \mathbf{v}}{\partial q_k} \\ &=\frac{d}{dt}\left(\frac{\partial \mathbf{r}}{\partial q_k}\right)-\frac{\partial}{\partial q_k}\left(\frac{d\mathbf{r}}{dt}\right) \\ &=\frac{d}{dt}\left(\frac{\partial \mathbf{r}}{\partial q_k}\right)-\frac{d}{dt}\left(\frac{\partial \mathbf{r}}{\partial q_k}\right) \\ &=\frac{d\mathbf{e}_k}{dt}-\frac{\partial \mathbf{v}}{\partial q_k}=\mathbf{0}, \end{aligned} \tag{6}$$

(ii) $$\mathbf{e}_{k,l}=\mathbf{e}_{l,k}\equiv \partial^2\mathbf{r}/\partial q_k\partial q_l \text{ and } \mathbf{e}_{t,k}=\mathbf{e}_{k,t}. \tag{7}$$

Let us further assume that S is subject to $m(<n)$ independent, and generally nonintegrable, velocity constraints:

$$f_D(t, q, \dot{q})=0;\ D=1, \ldots, m(<n). \tag{8}$$

Remark: For most practical purposes (e.g., problems of rigid body rolling) the constraints (8) have the Pfaffian form

$$\sum_k a_{Dk}\dot{q}_k+a_D=0,$$

$$\{a_{Dk}, a_D: \text{ functions of } q \text{ and } t\}. \tag{9}$$

Here, however, the utilization of the general nonlinear case (8) will allow us to see more clearly the formal structure of the resulting equations as well as their differences from (5)–(8); and we can at any point specialize from (8) to (9) if needed (see Appendix).

To make further progress, i.e., express $\dot{q}$, δq, and then $\delta\mathbf{r}$, $\mathbf{v}$, $\mathbf{a}$ in terms of independent (= unconstrained) "velocity parameters", and following Hamel (1938, 1949) we introduce the n quasi-velocities $\omega = (\omega_1, \omega_2, \ldots, \omega_n)$ by the following n (assumed *invertible*) "natural" (= decoupled) equations

$$\omega_D=f_D(t, q, \dot{q})=0\ [D=1, \ldots, m(<n): \text{ dependent}],$$

$$\omega_I\equiv f_I(t, q, \dot{q})\neq 0\ [I=m+1, \ldots, n: \text{ independent}],$$

$$\omega_{n+1}\equiv \dot{q}_{n+1}=\dot{t}=1 \text{ (always)}. \tag{10}$$

Solving (10) for the n of the $\dot{q}$'s we find

$$\dot{q}_k=\dot{q}_k(t, q, \omega_D, \omega_I)|_{\omega_D=0}=\dot{q}_k(t, q, \omega_I). \tag{11}$$

The $(n-m)$ $f_I(\ldots)$ are arbitrary, except that when the $\dot{q}$ from (11) are inserted back into (8) they must satisfy them identically. Hence we have the following *compatibility* equations (δ_{kl} = Kronecker delta):

$$\sum_s\left(\frac{\partial \omega_k}{\partial \dot{q}_s}\right)\left(\frac{\partial \dot{q}_s}{\partial \omega_l}\right)=\delta_{kl} \text{ and } \sum_l\left(\frac{\partial \dot{q}_s}{\partial \omega_l}\right)\left(\frac{\partial \omega_l}{\partial \dot{q}_k}\right)=\delta_{sk}. \tag{12}$$

Now, to attach the constraints (8), (9) to Lagrange's kinetic variational equations (see Kinetics, below) we need their virtual forms, i.e., define $\delta\theta$ (where $\omega_k \equiv d\theta_k/dt$, θ_k = quasi-coordinate) and relate it to δq via a *linear and homogeneous transformation*. It has been shown (see e.g., Hamel, 1949) that in this case, the n δq must satisfy the m (nontrivial and nonobvious!) Appell-Chetaev-Hamel conditions

$$\sum_k (\partial f_D/\partial \dot{q}_k)\delta q_k=0. \tag{13}$$

In view of these results, the virtual form of (10) is

$$\delta\theta_D\equiv\sum_k (\partial\omega_D/\partial\dot{q}_k)\delta q_k(=0),$$

$$\delta\theta_I\equiv\sum_k (\partial\omega_I/\partial\dot{q}_k)\delta q_k(\neq 0),$$

$$\delta\theta_{n+1}\equiv\delta q_{n+1}=\delta t=0. \tag{14}$$

Inverting these equations we obtain

$$\delta q_k=\sum_l (\partial\dot{q}_k/\partial\omega_l)\delta\theta_l \xrightarrow{(14)_1} \sum_I (\partial\dot{q}_k/\partial\omega_I)\delta\theta_I. \tag{15}$$

The representations (14), (15) are fundamental to all subsequent developments; they establish a one-to-one correspondence among the $\delta\theta$ and δq, just like Eqs. (10) do for the ω and $\dot{q}$.

Remark: In what follows, for algebraic convenience, and to stress coordinates rather than constraints, we shall allow the indices of ω and $\delta\theta$ to run (like those of $\dot{q}$ and δq) from 1 to n. The satisfaction of the constraints $(10)_1$ and $(14)_1$ can be done at any time by simply setting there $\omega_D = 0$ and $\delta\theta_D = 0$ (plus appropriate Lagrangean multipliers, if needed—see Kinetics Section); i.e., by restricting the ω indices to run over the independent range $I = m+1, \ldots, n$ only; similarly we may use, if desired for extra clarity, the notation $(\ldots)|_{\omega_D=0} \equiv (\ldots)_0$. Let us now express the particle kinematics in terms of system rates of change. With the help of the notation $f(t, q, \dot{q}) = f[t, q, \dot{q}(t, q, \omega)] \equiv f^*(t, q, \omega)$, we obtain the nonholonomic variable counterparts of (2):

(i) $$\begin{aligned} \delta\mathbf{r}&=\sum_{k,l}\frac{\partial\mathbf{r}}{\partial q_k}\left(\frac{\partial\dot{q}_k}{\partial\omega_l}\delta\theta_l\right)=\sum_{l,k}\left(\frac{\partial\mathbf{r}}{\partial q_k}\frac{\partial\dot{q}_k}{\partial\omega_l}\right)\delta\theta_l \\ &\equiv\sum_l\frac{\partial\mathbf{r}}{\partial\theta_l}\delta\theta_l\equiv\sum_k\mathbf{a}_k\delta\theta_k(\equiv\delta\mathbf{r}^*) \end{aligned} \tag{16a}$$

from which and (14), (15) the $\{\mathbf{e}_k\} \leftrightarrow \{\mathbf{a}_k\}$ transformation law follows:

$$\mathbf{a}_l=\sum_k(\partial\dot{q}_k/\partial\omega_l)\mathbf{e}_k \leftrightarrow \mathbf{e}_k=\sum_l(\partial\omega_l/\partial\dot{q}_k)\mathbf{a}_l, \tag{16b}$$

where we have introduced the symbolic "quasi-chain rule" notation

$$\frac{\partial(\ldots)^*}{\partial\theta_l}\equiv\sum_k\frac{\partial(\ldots)^*}{\partial q_k}\frac{\partial\dot{q}_k}{\partial\omega_l}\leftrightarrow\frac{\partial(\ldots)^*}{\partial q_k}\equiv\sum_l\frac{\partial(\ldots)^*}{\partial\theta_l}\frac{\partial\omega_l}{\partial\dot{q}_k}. \tag{16c}$$

(ii) $$\mathbf{v}=\sum_k\dot{q}_k(t, q, \omega)\mathbf{e}_k+\mathbf{e}_t=\sum_k\omega_k\mathbf{a}_k+\mathbf{a}_t\equiv\mathbf{v}^*$$

(definition of $\mathbf{a}_t$), (16d)

from which

$$\begin{aligned} \mathbf{a}_t&=\mathbf{e}_t+\sum_k(\dot{q}_k\mathbf{e}_k-\omega_k\mathbf{a}_k) \\ &=\mathbf{e}_t+\sum_k\dot{q}_k\mathbf{e}_k-\sum_k\omega_k\left(\sum_l\frac{\partial\dot{q}_l}{\partial\omega_k}\mathbf{e}_l\right) \\ &=\ldots=\mathbf{e}_t+\sum_k\underbrace{\left(\dot{q}_k-\sum_l\frac{\partial\dot{q}_k}{\partial\omega_l}\omega_l\right)}_{\neq 0, \text{ in general}}\mathbf{e}_k. \end{aligned} \tag{16e}$$

(iii) $$\begin{aligned} \mathbf{a}&=\sum_k\mathbf{e}_k\ddot{q}_k+\ldots=\sum_k\mathbf{e}_k\left(\dot{q}_k(t, q, \omega)\right)^{\cdot}+\ldots \\ &=\sum_k\frac{\partial\mathbf{v}}{\partial\dot{q}_k}\left(\sum_l\frac{\partial\dot{q}_k}{\partial\omega_l}\dot{\omega}_l\right)+\ldots(\ldots\equiv\text{ no }\dot{\omega}-\text{terms}) \end{aligned}$$

Downloaded 03 May 2010 to 171.66.16.20. Redistribution subject to ASME license or copyright; see http://www.asme.org/terms/Terms_Use.cfm

$$= \sum_l \left(\sum_k \frac{\partial \mathbf{v}}{\partial \dot{q}_k} \frac{\partial \dot{q}_k}{\partial \omega_l} \right) \dot{\omega}_l + \dots$$

$$\equiv \sum_l \frac{\partial \mathbf{v}^*}{\partial \omega_l} \dot{\omega}_l + \dots \equiv \sum_k \dot{\omega}_k \mathbf{a}_k + \dots$$

$$\equiv \mathbf{a}^*(t, q, \omega, \dot{\omega}) \equiv \mathbf{a}^*, \tag{16f}$$

i.e.,

$$\frac{\partial \mathbf{v}^*}{\partial \omega_l} = \sum_k \frac{\partial \mathbf{v}}{\partial \dot{q}_k} \frac{\partial \dot{q}_k}{\partial \omega_l}. \tag{17}$$

Note the difference between the definition (16*c*) and the (covariant) vector transformation (17)! From the above we immediately obtain the nonholonomic counterpart of (4):

$$\frac{\partial \mathbf{r}}{\partial \theta_k} = \frac{\partial \mathbf{r}^*}{\partial \theta_k} = \frac{\partial \mathbf{v}^*}{\partial \omega_k} = \frac{\partial \mathbf{a}^*}{\partial \dot{\omega}_k} = \dots \equiv \mathbf{a}_k. \tag{18}$$

However, here contrary to (5), by (16*c*), (17) and since $\mathbf{v} = \mathbf{v}(t, q, \dot{q}) = \mathbf{v}[t, q, \dot{q}(t, q, \omega)] = \mathbf{v}^*(t, q, \omega) \equiv \mathbf{v}^*$, we have

$$\frac{\partial \mathbf{v}^*}{\partial \theta_k} \equiv \sum_l \frac{\partial \mathbf{v}^*}{\partial q_l} \frac{\partial \dot{q}_l}{\partial \omega_k} = \sum_l \left(\frac{\partial \mathbf{v}}{\partial q_l} + \sum_r \frac{\partial \mathbf{v}}{\partial \dot{q}_r} \frac{\partial \dot{q}_r}{\partial q_l} \right) \left(\frac{\partial \dot{q}_l}{\partial \omega_k} \right)$$

$$= \sum_l \frac{\partial \mathbf{v}}{\partial q_l} \frac{\partial \dot{q}_l}{\partial \omega_k} + \sum_l \frac{\partial \mathbf{v}}{\partial \dot{q}_l} \frac{\partial \dot{q}_l}{\partial \theta_k},$$

whereas

$$\frac{d}{dt} \left(\frac{\partial \mathbf{r}}{\partial \theta_k} \right) = \frac{d}{dt} \left(\frac{\partial \mathbf{v}^*}{\partial \omega_k} \right) = \frac{d}{dt} \left(\sum_l \frac{\partial \mathbf{v}}{\partial \dot{q}_l} \frac{\partial \dot{q}_l}{\partial \omega_k} \right)$$

$$= \sum_l \frac{d}{dt} \left(\frac{\partial \mathbf{v}}{\partial \dot{q}_l} \right) \frac{\partial \dot{q}_l}{\partial \omega_k} + \sum_l \frac{\partial \mathbf{v}}{\partial \dot{q}_l} \frac{d}{dt} \left(\frac{\partial \dot{q}_l}{\partial \omega_k} \right), \tag{20}$$

and therefore

$$E_k^*(\mathbf{v}^*) \equiv \frac{d}{dt} \left(\frac{\partial \mathbf{v}^*}{\partial \omega_k} \right) - \frac{\partial \mathbf{v}^*}{\partial \theta_k}$$

$$= \sum_l \left[\frac{d}{dt} \left(\frac{\partial \mathbf{v}}{\partial \dot{q}_l} \right) - \frac{\partial \mathbf{v}}{\partial q_l} \right] \left(\frac{\partial \dot{q}_l}{\partial \omega_k} \right) + \sum_l \left[\frac{d}{dt} \left(\frac{\partial \dot{q}_l}{\partial \omega_k} \right) - \frac{\partial \dot{q}_l}{\partial \theta_k} \right] \left(\frac{\partial \mathbf{v}}{\partial \dot{q}_l} \right)$$

$$= \sum_l \underbrace{E_l(\mathbf{v})}_{=0, \text{ by (6)}} \frac{\partial \dot{q}_l}{\partial \omega_k} + \sum_l E_k^*(\dot{q}_l) \frac{\partial \mathbf{v}}{\partial \dot{q}_l} \neq \mathbf{0}, \tag{21}$$

or finally

$$\gamma_k \equiv E_k^*(\mathbf{v}^*) = \frac{d\mathbf{a}_k}{dt} - \frac{\partial \mathbf{v}^*}{\partial \theta_k}$$

$$= \sum_l E_k^*(\dot{q}_l) \left(\frac{\partial \mathbf{v}}{\partial \dot{q}_l} \right)^* = \sum_l E_k^*(\dot{q}_l) \mathbf{e}_l^*$$

$$= \sum_l E_k^*(\dot{q}_l) \left(\sum_r \frac{\partial \omega_r}{\partial \dot{q}_l} \mathbf{a}_r \right) \equiv \sum_r H_{kr} \mathbf{a}_r, \tag{22}$$

where $H_{kr} \equiv \sum_l E_k^*(\dot{q}_l) \frac{\partial \omega_r}{\partial \dot{q}_l}$.

We note that here $\mathbf{e}_l \equiv \partial \mathbf{v} / \partial \dot{q}_l \to (\partial \mathbf{v} / \partial \dot{q}_l)^* \equiv \mathbf{e}_l^*$ = function of t, q, ω. The key (non) integrability Eqs. (21), (22) result from the nonholonomicity of the "coordinates" θ; *consequently they have nothing to do with constraints*. The vector γ_k is the *particle* equivalent of the "nonholonomic deviation" of Schieldrop (1925) and Johnsen (1936, 1937, 1941).

Alternative Derivation of (21), (22). We have successively

$$\gamma_k \equiv E_k^*(\mathbf{v}^*) = \frac{d}{dt} \left(\frac{\partial \mathbf{v}^*}{\partial \omega_k} \right) - \frac{\partial \mathbf{v}^*}{\partial \theta_k}$$

$$\equiv \frac{d\mathbf{a}_k}{dt} - \frac{\partial \mathbf{v}^*}{\partial \theta_k} \text{ (invoking (16}b\text{))}$$

$$= \frac{d}{dt} \left(\sum_l \frac{\partial \dot{q}_l}{\partial \omega_k} \mathbf{e}_l \right) - \sum_l \frac{\partial \mathbf{v}^*}{\partial q_l} \frac{\partial \dot{q}_l}{\partial \omega_k}$$

$$= \sum_l \frac{d}{dt} \left(\frac{\partial \dot{q}_l}{\partial \omega_k} \right) \mathbf{e}_l + \sum_l \frac{\partial \dot{q}_l}{\partial \omega_k} \frac{d\mathbf{e}_l}{dt} - \sum_l \left[\frac{\partial}{\partial q_l} \underbrace{\left(\sum_s \dot{q}_s \mathbf{e}_s + \mathbf{e}_t \right)}_{\nu^* = \nu} \right] \frac{\partial \dot{q}_l}{\partial \omega_k}$$

$$= \dots + \dots - \sum_l \left[\sum_s \left(\frac{\partial \dot{q}_s}{\partial q_l} \mathbf{e}_s + \dot{q}_s \frac{\partial \mathbf{e}_s}{\partial q_l} \right) + \frac{\partial \mathbf{e}_t}{\partial q_l} \right] \frac{\partial \dot{q}_l}{\partial \omega_k}$$

$$= \dots + \dots - \sum_{l,s} \frac{\partial \dot{q}_s}{\partial q_l} \frac{\partial \dot{q}_l}{\partial \omega_k} \mathbf{e}_s - \sum_{l,s} \dot{q}_s \frac{\partial \dot{q}_l}{\partial \omega_k} \frac{\partial \mathbf{e}_s}{\partial q_l} - \sum_l \frac{\partial \dot{q}_l}{\partial \omega_k} \frac{\partial \mathbf{e}_t}{\partial q_l}$$

(invoking the integrability conditions (7))

$$= \dots + \dots - \sum_l \left[\underbrace{\sum_s \left(\frac{\partial \mathbf{e}_l}{\partial q_s} \dot{q}_s \right) + \frac{\partial \mathbf{e}_l}{\partial t}}_{= d\mathbf{e}_l / dt} \right] \left(\frac{\partial \dot{q}_l}{\partial \omega_k} \right) - \sum_s \frac{\partial \dot{q}_s}{\partial \theta_k} \mathbf{e}_s$$

$$= \dots + \dots - \sum_l \frac{\partial \dot{q}_l}{\partial \omega_k} \frac{d\mathbf{e}_l}{dt} - \sum_l \frac{\partial \dot{q}_l}{\partial \theta_k} \mathbf{e}_l$$

(second and third sums cancel)

or finally

$$\gamma_k = \sum_l \left[\frac{d}{dt} \left(\frac{\partial \dot{q}_l}{\partial \omega_k} \right) - \frac{\partial \dot{q}_l}{\partial \theta_k} \right] \mathbf{e}_l, \tag{21, 22}$$

as before.

3 Kinetics

The equations of motion of a typical particle P of mass dm, of the system S, is Newton's "second law of motion" (in continuum form for the particle quantities, for extra clarity, i.e., to reserve the indices for the system variables) is

$$dm\mathbf{a} = d\mathbf{f}, \; d\mathbf{f} = d\mathbf{F} + d\mathbf{R}, \tag{23}$$

where

$d\mathbf{f}$ = *total* force on P,
$d\mathbf{F}$ = total *impressed* (or acting, or physical, or known), force on P,
$d\mathbf{R}$ = total *constraint reaction* (or geometrical) force on P. (24)

The fundamental principle of Lagrangean analytical mechanics (actually a *constitutive* postulate, like Hooke's law in elasticity and Navier-Stokes law in fluid mechanics, etc.—and as such not a law of nature like $(23)_1$) states that for *bilateral* (or reversible, or two-sided, or equality) constraints, like (8), (9):

$$-\delta' W_R \equiv \int (-d\mathbf{R}) \cdot \delta \mathbf{r} = 0, \tag{25}$$

where $\int \dots$ is a sum over the system particles (like a Stieltjes' integral), for a given time; i.e., *the total* (first-order) *virtual work of the "lost" forces* $\{-d\mathbf{R}\}$, $-\delta' W_R$, *vanishes*. Then

Downloaded 03 May 2010 to 171.66.16.20. Redistribution subject to ASME license or copyright; see http://www.asme.org/terms/Terms_Use.cfm

(23) leads to the familiar *Lagrange's Principle* (LP) (or "principle of D'Alembert in Lagrange's form"):

$$\underbrace{\int dm\mathbf{a}\bullet\delta\mathbf{r}}_{\equiv\delta' I}=\underbrace{\int d\mathbf{F}\bullet\delta\mathbf{r}}_{\equiv\delta' W}, \tag{26}$$

where, as in (25), the accents signify *absence of perfect differentials*; i.e., in general no $W_R/W/I$ exist but only $\delta' W_R/\delta' W/\delta' I$. (Similarly in (14), etc., we should have written $\delta'\theta$, if θ = quasi-coordinate; we hope no confusion will occur from this minor inconsistency.) All conceivable equations of motion follow from (25), (26); plus the method of Lagrangean multipliers, if desired and needed. Indeed:

(i) substituting (2*a*) into (26) yields its *holonomic* system variable counterpart:

$$\underbrace{\sum_k I_k\delta q_k}_{\delta' I}=\underbrace{\sum_k Q_k\delta q_k}_{\delta' W} \tag{27}$$

where (using (4), (5))

$$I_k\equiv\int dm\mathbf{a}\bullet\mathbf{e}_k=\ldots=E_k(T)\equiv\left(\frac{\partial T}{\partial\dot q_k}\right)^{\cdot}-\frac{\partial T}{\partial q_k}$$

$$=\textit{holonomic}\ (k)\text{th component of } \textit{system}\ \text{"inertia force,"}$$

$$Q_k\equiv\int d\mathbf{F}\bullet\mathbf{e}_k=\textit{holonomic}\ (k)\text{th component of system impressed force,} \tag{28}$$

while substituting (16*a*) into (26) yields its *nonholonomic* system variable counterpart

$$\underbrace{\sum_k I_k^*\delta\theta_k}_{\delta' I}=\underbrace{\sum_k\Theta_k\delta\theta_k}_{\delta' W} \tag{29}$$

where

$$I_k^*\equiv\int dm\mathbf{a}\bullet\mathbf{a}_k\equiv\int dm\mathbf{a}^*\bullet\mathbf{a}_k=\ldots\ \text{(see Section 4)}$$

$$=\textit{nonholonomic}\ (k)\text{th component of system inertia force,}$$

$$\Theta_k\equiv\int d\mathbf{F}\bullet\mathbf{a}_k=\textit{nonholonomic}\ (k)\text{th component of system impressed force.} \tag{30}$$

(Here, in exception to our earlier $(\ldots)^*$ convention, $I_k^*\equiv$ as defined by $(30)_1$; i.e., $(I_k)^*\neq I_k^*$).

From the invariant equation (27), (29), $\delta' I=\delta' W$, and (14), (15), or from (28), (30) and the transformation equations (16*b*), we readily obtain the system components transformation equations

$$I_k^*\equiv\int dm\mathbf{a}\bullet\left(\sum_l\frac{\partial\dot q_l}{\partial\omega_k}\mathbf{e}_l\right)=\sum_l\frac{\partial\dot q_l}{\partial\omega_k}I_l\leftrightarrow I_l=\sum_k\frac{\partial\omega_k}{\partial\dot q_l}I_k^*,$$

$$\Theta_k=\int d\mathbf{F}\bullet\left(\sum_l\frac{\partial\dot q_l}{\partial\omega_k}\mathbf{e}_l\right)=\sum_l\frac{\partial\dot q_l}{\partial\omega_k}Q_l\leftrightarrow Q_l=\sum_k\frac{\partial\omega_k}{\partial\dot q_l}\Theta_k. \tag{30a}$$

Now: (i) Under the $m(<n)$ constraints $(8)/(10)_1$, $\omega_D\equiv f_D=0$, Eq. (27) plus method of Lagrangean multipliers $\{\lambda_D=\lambda_D(t);\ D=1,\ldots,m\}$ produces the n Lagrange-Routh (LR) equations:

$$I_k\equiv E_k(T)=Q_k+\sum_D\lambda_D\frac{\partial f_D}{\partial\dot q_k}. \tag{31}$$

(ii) Under the constraints $(14)_1$, $\delta\theta_D=0$ (or $1\bullet\delta\theta_D=0$), Eq. (29) plus method of Lagrangean multipliers produces the two *uncoupled* sets of Hamel equations

$$I_D^*=\Theta_D+\lambda_D\quad(\delta\theta_D=0,\ \lambda_D\neq0;\ \text{"kinetostatic" equations}),$$
$$I_I^*=\Theta_I\quad(\delta\theta_I\neq0,\ \lambda_I=0;\ \text{"kinetic" equations}). \tag{32}$$

(It can be easily shown that the Lagrangean multipliers in both (31) and (32) coincide, and that $\lambda_k=\int d\mathbf{R}\bullet\mathbf{a}_k$ – see e.g., Papastavridis (1990).) The reduction of I_k to system variables, i.e., Lagrange's identity $(28)_1$

$$I_k\equiv\int dm\mathbf{a}\bullet\frac{\partial\mathbf{r}}{\partial q_k}=\int dm\mathbf{a}\bullet\frac{\partial\mathbf{v}}{\partial\dot q_k}=\int dm\mathbf{a}\bullet\frac{\partial\mathbf{a}}{\partial\ddot q_k}=\ldots$$

$$=E_k(T)\equiv\frac{d}{dt}\left(\frac{\partial T}{\partial\dot q_k}\right)-\frac{\partial T}{\partial q_k}, \tag{28}_1$$

depends critically on the holonomic variable identities (4), (5): $\partial\mathbf{r}/\partial q_k=\partial\mathbf{v}/\partial\dot q_k$, and $\partial\mathbf{v}/q_k=d/dt(\partial\mathbf{r}/\partial q_k)=d\mathbf{e}_k/dt$. The details of its derivation are available in every Lagrangean dynamics exposition. In the next section we carry out this task for I_k^*; as we shall see there: $I_k^*\neq E_k^*(T^*)$.

4 Transformation of Nonholonomic Inertia Force

We find successively

$$I_k^*\equiv\int dm\mathbf{a}\bullet\mathbf{a}_k=\int dm\mathbf{a}^*\bullet\mathbf{a}_k=\int dm\mathbf{a}^*\bullet\frac{\partial\mathbf{v}^*}{\partial\omega_k}$$

$$=\frac{d}{dt}\int\left(dm\mathbf{v}^*\bullet\frac{\partial\mathbf{v}^*}{\partial\omega_k}\right)-\underbrace{\int dm\mathbf{v}^*\bullet\frac{d}{dt}\left(\frac{\partial\mathbf{v}^*}{\partial\omega_k}\right)}_{=\int dm\mathbf{a}^*\bullet(d\mathbf{a}_k/dt)}$$

[adding and subtracting $\int dm\mathbf{v}^*\bullet(\partial\mathbf{v}^*/\partial\theta_k)$]

$$=\frac{d}{dt}\int dm\mathbf{v}^*\bullet\frac{\partial\mathbf{v}^*}{\partial\omega_k}-\int dm\mathbf{v}^*\bullet\frac{\partial\mathbf{v}^*}{\partial\theta_k}$$
$$-\int dm\mathbf{v}^*\bullet\left[\frac{d}{dt}\left(\frac{\partial\mathbf{v}^*}{\partial\omega_k}\right)-\frac{\partial\mathbf{v}^*}{\partial\theta_k}\right]$$

(invoking (21), (22))

$$=\frac{d}{dt}\left[\frac{\partial}{\partial\omega_k}\int\frac{1}{2}dm\mathbf{v}^*\bullet\mathbf{v}^*\right]$$
$$-\frac{\partial}{\partial\theta_k}\int\frac{1}{2}dm\mathbf{v}^*\bullet\mathbf{v}^*-\int dm\mathbf{v}^*\bullet E_k^*(\mathbf{v}^*)$$

$$=\frac{d}{dt}\frac{\partial T^*}{\partial\omega_k}-\frac{\partial T^*}{\partial\theta_k}-\Gamma_k, \tag{33}$$

where

$$T=T(t,q,\dot q)=T[t,q,\dot q(t,q,\omega)]$$
$$\equiv T^*(t,q,\omega)=T^*\equiv\int\frac{1}{2}dm\mathbf{v}^*\bullet\mathbf{v}^*, \tag{34}$$

$$\Gamma_k\equiv\int dm\mathbf{v}^*\bullet\left[\frac{d}{dt}\left(\frac{\partial\mathbf{v}^*}{\partial\dot\omega_k}\right)-\frac{\partial\mathbf{v}^*}{\partial\theta_k}\right]$$

$$\equiv\int dm\mathbf{v}^*\bullet\left[\frac{d}{dt}\left(\frac{\partial\mathbf{r}}{\partial\theta_k}\right)-\frac{\partial}{\partial\theta_k}\left(\frac{d\mathbf{r}}{dt}\right)\right]$$

$$\equiv\int dm\mathbf{v}^*\bullet\left(\frac{d\mathbf{a}_k}{dt}-\frac{\partial\mathbf{v}^*}{\partial\theta_k}\right)\equiv\int dm\mathbf{v}^*\bullet E_k^*(\mathbf{v}^*)\equiv\int dm\mathbf{v}^*\bullet\boldsymbol{\gamma}_k$$

(invoking (21), (22))

Downloaded 03 May 2010 to 171.66.16.20. Redistribution subject to ASME license or copyright; see http://www.asme.org/terms/Terms_Use.cfm

$$= \int dm\mathbf{v}^* \cdot \left[\sum_l E_k^*(\dot{q}_l)\mathbf{e}_l^* \right] = \sum_l E_k^*(\dot{q}_l) \left(\int dm\mathbf{v} \cdot \mathbf{e}_l \right)^*$$

$$\equiv \sum_l \left(\frac{\partial T}{\partial \dot{q}_l} \right)^* E_k^*(\dot{q}_l) = \sum_l p_l^* E_k^*(\dot{q}_l), \tag{35}$$

and $p_l \equiv \partial T/\partial \dot{q}_l \to p_l^* = (\partial T/\partial \dot{q}_l)^*$; that is, after the $\dot{q}$ differentiations, the $\dot{q}$ are replaced by $\dot{q} = \dot{q}(t, q, \omega)$: $p_l = p_l(t, q, \dot{q}) = p_l[t, q, \dot{q}(t, q, \omega)] \equiv p_l^*(t, q, \omega)$ = *holonomic* $(l)th$ component of system (generalized) *momentum*, but expressed in nonholonomic variables.

Alternatively,

$$\Gamma_k \equiv \int dm\mathbf{v}^* \cdot \left[\sum_{r,l} E_k^*(\dot{q}_l) \frac{\partial \omega_r}{\partial \dot{q}_l} \mathbf{a}_r \right]$$

$$= \sum_{r,l} E_k^*(\dot{q}_l) \frac{\partial \omega_r}{\partial \dot{q}_l} \underbrace{\left(\int dm\mathbf{v}^* \cdot \mathbf{a}_r \right)}_{\partial T^*/\partial \omega_r \equiv P_r}$$

$$= \sum_l E_k^*(\dot{q}_l) \underbrace{\left(\sum_r \frac{\partial \omega_r}{\partial \dot{q}_l} P_r \right)}_{\dot{p}_l^*}, \tag{35a}$$

where

$$P_r \equiv \int dm\mathbf{v}^* \cdot \mathbf{a}_r = \int dm\mathbf{v}^* \cdot \frac{\partial \mathbf{v}^*}{\partial \omega_r} = \frac{\partial T^*}{\partial \omega_r}$$

$$= nonholonomic\ (r)\text{th component of system (generalized) momentum}$$

$$\neq p_r^* \equiv (\partial T/\partial \dot{q}_r)^*. \tag{36}$$

Clearly

$$P_k = \sum_l \frac{\partial \dot{q}_l}{\partial \omega_k} p_l \mapsto p_l = \sum_k \frac{\partial \omega_k}{\partial \dot{q}_l} P_k, \tag{37}$$

while $\partial T^*/\partial \dot{q}_k$ is, as yet, undefined. (For additional (system) forms of Γ_k see Hamel (1938, 1949).)

We repeat: equation

$$\int dm\mathbf{v}^* \cdot \frac{d\mathbf{a}_k}{dt} = \frac{\partial T^*}{\partial \theta_k} + \underbrace{\int dm\mathbf{v}^* \cdot \gamma_k}_{\Gamma_k} \tag{38}$$

is a purely *kinematical* result that has nothing to do with constraints, but with nonholonomic *coordinates*. In holonomic coordinates $\mathbf{v}^* = \mathbf{v}$, $\mathbf{a}_k \to \mathbf{e}_k$, $T^* = T$, $\theta_k \to q_k$, $\gamma_k = \mathbf{0}$, $\Gamma_k = 0$, and (38) reduces to the familiar

$$\int dm\mathbf{v} \cdot \frac{d\mathbf{e}_k}{dt} = \int dm\mathbf{v} \cdot \frac{d}{dt} \left(\frac{\partial \mathbf{r}}{\partial q_k} \right) = \int dm\mathbf{v} \cdot \frac{\partial \mathbf{v}}{\partial q_k} = \frac{\partial T}{\partial q_k}, \tag{39}$$

(= 0, if for, e.g., $d\mathbf{e}_k/dt = \mathbf{0}$, i.e., *rectilinear* coordinates). (This author would welcome a good notation and name for $\partial T/\partial q_k$; similar to $p_k \equiv \partial T/\partial \dot{q}_k$ for the generalizated system momentum. Hildebrand (1965) has already suggested the names: "associated inertia force" and "momental inertia force".)

Historical Remarks: The earliest nonholonomic equations of motion are due to Ferrers (1873). They are a very special case of the kinetic Eqs. $(32)_2$: for linear velocity constraints in the form

$$\dot{q}_D = \sum_l b_{Dl}\dot{q}_l + b_D$$

$$\{b_{Dl} \text{ and } b_D = \text{functions of } q \text{ and } t\}, \tag{40}$$

i.e., with the choice of $\omega_l \equiv \dot{q}_l$ $(\neq 0)$ and $\omega_D \equiv \dot{q}_D - \Sigma_l\, b_{Dl}\dot{q}_l - b_D$ $(= 0)$, with $\mathbf{v}$ and $\mathbf{a}$ in rectangular Cartesian coordinates, and with I_k^* (actually I_l^*) in the "intermediate" form

$$I_k^* = \frac{d}{dt} \int dm\mathbf{v}^* \cdot \frac{\partial \mathbf{v}^*}{\partial \omega_k} - \int dm\mathbf{v}^* \cdot \frac{d}{dt} \left(\frac{\partial \mathbf{v}^*}{\partial \omega_k} \right)$$

$$= \frac{d}{dt} \left(\frac{\partial T^*}{\partial \omega_k} \right) - \int dm\mathbf{v}^* \cdot \frac{d\mathbf{a}_k}{dt}. \tag{41}$$

Such equations were also arrived at (most likely independently) by Carvallo (1900, 1901), in connection with his classic monocycle and bicycle dynamics studies. (See also, e.g., Auerbach (1908) and Marcolongo and Timerding (1912).) Some authors, probably after Whittaker (1937), erroneously call Ferrers' equations the Lagrange-Routh Eqs. (31). In sum: *the first nonholonomic equations in history were multiplierless*, (i.e., reactionless) *and in quasi-coordinates.*

Acknowledgment

The author would like to thank the unknown reviewers for their constructive comments on an earlier version of this paper.

References

Auerbach, F., 1908, "Kinematik und Dynamik," *Handbuch der Physik*, Vol. 1, M. Winkelmann, ed., Barth, Leipzig, p. 327.

Carvallo, M. E., 1900–1901, "Théorie du Mouvement du Monocycle et de la Bicyclette," *Journal de l'École Polytechnique II Serie*, Cinquième Cahier (1900), pp. 119–118; Sixième Cahier (1901), pp. 1–48, especially pp. 34–36.

Desloge, E. A., 1982, *Classical Mechanics*, Vols. 1 and 2, John Wiley and Sons, New York, pp. 715–719.

Feiyue, L., and Bainum, P. M., 1991, "On the Lagrangian Equations for Quasi-coordinates," *Proceedings of the Second Pan American Congress of Applied Mechanics* (PACAM), American Academy of Mechanics, pp. 158–161.

Ferrers, N. M., 1873, "Extension of Lagrange's Equations," *The Quarterly Journal of Pure and Applied Mathematics*, Vol. 12, pp. 1–5.

Fischer, V., and Stephan, W., 1972, *Prinzipien und Methoden der Dynamik*, VEB Fachbuchverlag, Leipzig, pp. 71–76.

Johnsen, L., 1941, "Dynamique Générale des Systèmes Non-holonomes," *Skrifter Utgitt av det Norske Videnskaps-Akademi i Oslo I. Mat.-Naturv. Klass.*, No. 4, pp. 1–75.

Johnsen, L., 1936, "Allgemeine Quasikoordinaten," *Avhandlingen Utgitt av det Norske Videnskaps-Akademi i Oslo, I. Mat.-Naturv. Klasse*, No. 11, pp. 1–13.

Johnsen, L., 1937, "Sur la Reduction au Nombre Minimum des Équations du Mouvement d'um Système Non-Holonome," *Avhandlingen Utgitt av det Norske Videnskaps-Akademi i Oslo, I. Mat.-Naturv. Klasse*, No. 11, pp. 1–14.

Hamel, G., 1949, *Theoretische Mechanik*, Springer, Berlin, pp. 473–482; 495–499.

Hamel, G., 1938, "Nichtholonome Systeme höherer Art," *Sitzungsberichte der Berliner Mathematischen Gesellschaft*, Vol. 37, pp. 41–52.

Hildebrand, F. B., 1965, *Methods of Applied Mathematics*, 2nd ed., Prentice-Hall, Englewood Cliffs, NJ, p. 156.

Kilmister, C. W., 1964, *Hamiltonian Dynamics*, John Wiley and Sons, New York, pp. 40–46.

Kilmister, C. W., 1967, *Lagrangian Dynamics: An Introduction for Students*, Logos Press/Elek Books, London, pp. 121–125.

Marcolongo, R., and Timerding, H. E., (editor of German edition), 1912, *Theoretische Mechanik, Vol. 2: Dynamik*, Teubner, Leipzig, pp. 104–105.

Meirovitch, L., 1970, *Methods of Analytical Dynamics*, McGraw-Hill, New York, pp. 157–160.

McGill, D. J., and Shiau, J.-F., 1972, "On the Use of Kinetic Energy to Determine Generalized Inertia Forces in Nonholonomic Systems," ASME Journal of Applied Mechanics, Vol. 39, pp. 923–926.

Neimark, J. I., and Fufaev, N. A., 1972, *Dynamics of Nonholonomic Systems*, American Mathematical Society, Providence, RI, pp. 120–135.

Papastavridis, J. G., 1990, "Maggi's Equations of Motion and the Determination of Constraint Reactions," *Journal of Guidance, Control and Dynamics*, Vol. 13, pp. 213–220.

Papastavridis, J. G., 1991, "On Energy Rate Theorems for Linear First-Order Nonholonomic Systems," ASME Journal of Applied Mechanics, Vol. 58, pp. 536–544.

Papastavridis, J. G., 1992, "On the Transitivity Equations of Rigid-Body Dynamics," ASME Journal of Applied Mechanics, Vol. 59, pp. 955–962.

Schieldrop, E. B., 1925, "Sur une Notion de Déviation Non Holonome," *Den sjette skandinaviske Matematikerkongres i Kobenhavn, Beretniger*, pp. 281–307.

Downloaded 03 May 2010 to 171.66.16.20. Redistribution subject to ASME license or copyright; see http://www.asme.org/terms/Terms_Use.cfm

Schaefer, H., 1951, "Die Bewegungsgleichungen nichtholonomer Systeme," *Abhandlungen der Braunschweig Wiss. Ges.*, Vol. 3, pp. 116–121.
Whittaker, E. T., 1937, *Analytical Dynamics*, 4th ed., Cambridge University Press, Cambridge, pp. 41–44, 215.

APPENDIX

Specialization to the Linear First-Order (Possibly) Nonholonomic, i.e., Pfaffian, Constraints

Assume that the constraints (8) have the special Pfaffian form (9)

$$\sum_k a_{Dk}\dot{q}_k + a_D = 0, \text{ with rank } (a_{Dk}) = m. \tag{A1}$$

Then (10) reduces to

$$\omega_D \equiv \sum_k a_{Dk}\dot{q}_k + a_D (=0),\ D = 1, \ldots, m (<n),$$

$$\omega_I \equiv \sum_k a_{Ik}\dot{q}_k + a_I (\neq 0),\ I = m+1; \ldots, n,$$

$$\omega_{n+1} \equiv \dot{q}_{n+1} = \dot{t} = 1 \text{ (always)}, \tag{A2}$$

where the $(n - m)$ Eqs. $(A2)_2$ are arbitrary, except that when the $n \times n$ system $(A2)_{1,2}$ is solved for the n $\dot{q}$ in terms of the ω, etc., and the result is inserted into $(A2)_1$ it satisfies them identically; i.e., analytically:

$$\dot{q}_k = \sum_l A_{kl}\omega_l + A_k \rightarrow \sum_I A_{kI}\omega_I + A_k, \tag{A3}$$

where (a_{kl}) and (A_{kl}) are inverse matrices (see also Papastavridis (1990, Eqs. (21*a*, *b*))

$$\sum_k a_{lk}A_{kr} = \delta_{lr} \text{ and } \sum_l a_{lk}A_{rl} = \delta_{kr} \tag{A4}$$

(linear counterparts of (12)). The virtual forms of the above (linear counterparts of (13), (14), (15)) are, respectively,

$$\delta\theta_D \equiv \sum_k a_{Dk}\delta q_k (=0),$$

$$\delta\theta_I \equiv \sum_k a_{Ik}\delta q_k (\neq 0),$$

$$\delta\theta_{n+1} \equiv \delta q_{n+1} = \delta t = 0, \tag{A5}$$

$$\delta q_k = \sum_l A_{kl}\delta\theta_l \rightarrow \sum_I A_{kI}\delta\theta_I (\neq 0), \tag{A6}$$

while the Pfaffian counterparts of (2) and (16) are, respectively,

$$\delta\mathbf{r} = \sum_k \mathbf{e}_k\delta q_k = \sum_k \mathbf{a}_k\delta\theta_k \rightarrow \sum_I \mathbf{a}_I\delta\theta_I \equiv \delta\mathbf{r}^*,$$

$$\mathbf{a}_l = \mathbf{a}_l(t, q) = \sum_k A_{kl}\mathbf{e}_k \leftrightarrow \mathbf{e}_k = \mathbf{e}_k(t, q) = \sum_l a_{lk}\mathbf{a}_l,$$

$$\frac{\partial(\ldots)^*}{\partial\theta_l} \equiv \sum_k A_{kl}\frac{\partial(\ldots)^*}{\partial q_k} \leftrightarrow \frac{\partial(\ldots)^*}{\partial q_k} = \sum_l a_{lk}\frac{\partial(\ldots)^*}{\partial\theta_l}, \tag{A7a}$$

$$\mathbf{v} = \mathbf{v}(t, q) = \sum_k \dot{q}_k\mathbf{e}_k + \mathbf{e}_t$$

$$= \sum_k \omega_k\mathbf{a}_k + \mathbf{a}_t = \sum_I \omega_I\mathbf{a}_I + \boldsymbol{\alpha}_t \equiv \mathbf{v}^*(t, q, \omega) \equiv \mathbf{v}^*, \tag{A7b}$$

$$\mathbf{a}_t = \mathbf{e}_t + \sum_k A_k\mathbf{e}_k = \mathbf{e}_t + \sum_k A_k\left(\sum_l a_{lk}\mathbf{a}_l\right)$$

$$= \mathbf{e}_t + \sum_l \left(\sum_k a_{lk}A_k\right)\mathbf{a}_l \text{ (see Papastavridis, 1990, Eq. (21}b\text{))}$$

$$= \mathbf{e}_t + \sum_k (-a_k)\mathbf{a}_k = \ldots = \mathbf{e}_t + \sum_k (A_k)\mathbf{e}_k, \tag{A7c}$$

$$\mathbf{a} = \sum_k \ddot{q}_k\mathbf{e}_k + \ldots = \sum_k \dot{\omega}_k\mathbf{a}_k + \ldots \rightarrow \sum_I \dot{\omega}_I\mathbf{a}_I + \ldots$$

$$\equiv \mathbf{a}^*(t, q, \omega, \dot{\omega}) \equiv \mathbf{a}^* \ (\ldots \equiv \text{no } \ddot{q}, \dot{\omega} \text{ terms}), \tag{A7d}$$

$$\frac{\partial\mathbf{v}^*}{\partial\omega_l} = \sum_k A_{kl}\frac{\partial\mathbf{v}}{\partial\dot{q}_k} \leftrightarrow \frac{\partial\mathbf{v}}{\partial\dot{q}_k} = \sum_l a_{lk}\frac{\partial\mathbf{v}^*}{\partial\omega_l}. \tag{A7e}$$

(Note the difference between this and definition (A7*a*)).

From now on, for algebraic simplicity, let us take the scleronomic constraint case of (A2), i.e., $a_k = 0$ and $a_{kl} = a_{kl}(q) \rightarrow A_k = 0$ and $A_{kl} = A_{kl}(q)$. Then $\mathbf{e}_k = \mathbf{e}_k(q)$ and $\mathbf{a}_k = \mathbf{a}_k(q)$. (This is no loss of generality really, since, formally, the time can be taken as the $(n + 1)$th "coordinate": $q_{n+1} \equiv \theta_{n+1} = t$, that also satisfies the constraint $\omega_{n+1} \equiv \dot{q}_{n+1} = 1$, or $\omega_{n+1} \equiv \dot{q}_{n+1} - 1 = 0$ (velocity form), and $\delta q_{n+1} \equiv \delta\theta_{n+1} = \delta t = 0$ (virtual form). Thus the equations presented below hold for the general rheonomic case with appropriate extension of the latin indices to $n + 1$).

Now, recalling (19),

$$\frac{\partial\mathbf{v}^*}{\partial\theta_k} = \sum_l \left(\frac{\partial\mathbf{v}^*}{\partial q_l}\right)\left(\frac{\partial\dot{q}_l}{\partial\omega_k}\right) = \sum_l \frac{\partial}{\partial q_l}\left[\sum_r \omega_r\mathbf{a}_r(t, q)\right]\left(\frac{\partial\dot{q}_l}{\partial\omega_k}\right)$$

$$= \sum_{l,r} \omega_r\left[\left(\frac{\partial\mathbf{a}_r}{\partial q_l}\right)\left(\frac{\partial\dot{q}_l}{\partial\omega_r}\right)\right] = \sum_r \omega_r\frac{\partial\mathbf{a}_r}{\partial\theta_k},$$

and therefore the Pfaffian counterpart of (21), (22) is written successively:

$$\boldsymbol{\gamma}_k \equiv E_k^*(\mathbf{v}^*) = \frac{d\mathbf{a}_k}{dt} - \frac{\partial\mathbf{v}^*}{\partial\theta_k}$$

$$= \sum_l \dot{q}_l\frac{\partial\mathbf{a}_k}{\partial q_l} - \frac{\partial}{\partial\theta_k}\left(\sum_l \omega_l\mathbf{a}_l\right)$$

$$= \sum_l \dot{q}_l\left(\sum_r \frac{\partial\omega_r}{\partial\dot{q}_l}\frac{\partial\mathbf{a}_k}{\partial\theta_r}\right) - \sum_r \omega_r\frac{\partial\mathbf{a}_r}{\partial\theta_k}$$

$$= \sum_r \left(\sum_l \frac{\partial\omega_r}{\partial\dot{q}_l}\dot{q}_l\right)\frac{\partial\mathbf{a}_k}{\partial\theta_r} - \sum_r \omega_r\frac{\partial\mathbf{a}_r}{\partial\theta_k}$$

$$= \sum_r \frac{\partial\mathbf{a}_k}{\partial\theta_r}\underbrace{\left(\sum_l A_{rl}\dot{q}_l\right)}_{=\omega_r} - \sum_r \frac{\partial\mathbf{a}_r}{\partial\theta_k}\omega_r,$$

or finally

$$\boldsymbol{\gamma}_k \equiv \frac{d}{dt}\left(\frac{\partial\mathbf{v}^*}{\partial\omega_k}\right) - \frac{\partial\mathbf{v}^*}{\partial\theta_k} = \sum_{l,s} \gamma_{lk}^s\omega_l\mathbf{a}_s, \tag{A8}$$

where the famous three-index "Hamel transitivity (or transpositional) coefficients" γ_{lk}^s $(= -\gamma_{kl}^s)$ are defined by the *nonintegrability* equation:

$$\frac{\partial\mathbf{a}_k}{\partial\theta_l} - \frac{\partial\mathbf{a}_l}{\partial\theta_k} = \sum_s \gamma_{lk}^s\mathbf{a}_s. \tag{A9}$$

Then (recalling (35), (36)),

$$\Gamma_k \equiv \int dm\mathbf{v}^* \cdot \left(\frac{d\mathbf{a}_k}{dt} - \frac{\partial\mathbf{v}^*}{\partial\theta_k}\right) = \sum_l \left(\int dm\mathbf{v}^* \cdot \left(\frac{\partial\mathbf{a}_k}{\partial\theta_l} - \frac{\partial\mathbf{a}_l}{\partial\theta_k}\right)\right)\omega_l$$

Downloaded 03 May 2010 to 171.66.16.20. Redistribution subject to ASME license or copyright; see http://www.asme.org/terms/Terms_Use.cfm

$$= \sum_{l,s} \left(\int dm \mathbf{v}^* \cdot \mathbf{a}_s \right) \gamma^s_{lk} \omega_l = \sum_{l,s} \gamma^s_{lk} P_s \omega_l,$$

$$P_s \equiv \partial T^* / \partial \omega_s, \quad \text{(A10)}$$

and so the inertia term (38) becomes

$$\int dm \mathbf{v}^* \cdot \frac{d\mathbf{a}_k}{dt} = \int dm \mathbf{v}^* \cdot \frac{\partial \mathbf{v}^*}{\partial \theta_k} + \int dm \mathbf{v}^* \cdot \underbrace{\left(\frac{d\mathbf{a}_k}{dt} - \frac{\partial \mathbf{v}^*}{\partial \theta_k} \right)}_{\gamma_k}$$

$$= \frac{\partial T^*}{\partial \theta_k} + \sum_{l,s} \gamma^s_{lk} P_s \omega_l. \quad \text{(A11)}$$

Accordingly, and since $\gamma^s_{lk} = -\gamma^s_{kl}$ (and this is the reason we raised the index s—to stress the skew-symmetry in l and k), we ultimately obtain the Hamel form of 1903–1904:

$$I^*_k \equiv \int dm \mathbf{a}^* \cdot \mathbf{a}_k = \frac{d}{dt} \int dm \mathbf{v}^* \cdot \mathbf{a}_k - \int dm \mathbf{v}^* \cdot \frac{d\mathbf{a}_k}{dt}$$

$$= \frac{d}{dt} \left(\frac{\partial T^*}{\partial \omega_k} \right) - \frac{\partial T}{\partial \theta_k} - \sum_{l,s} \gamma^s_{lk} \frac{\partial T^*}{\partial \omega_s} \omega_l$$

$$\equiv E^*_k (T^*) + \sum_{l,s} \gamma^s_{kl} \frac{\partial T^*}{\partial \omega_s} \omega_l$$

$$\equiv \dot{P}_k - \frac{\partial T^*}{\partial \theta_k} + \sum_{l,k} \gamma^s_{kl} P_s \omega_l. \quad \text{(A12)}$$

Other definitions of the (system) coefficients γ^s_{lk}, equivalent to (A9), as well as concrete algebraic expressions of them in terms of a_{kl}, A_{kl} and their q-gradients exist in the literature—see, e.g., Papastavridis (1991) and references therein. This Appendix generalizes and considerably simplifies an earlier vectorial treatment by McGill and Shiau (1972).

Downloaded 03 May 2010 to 171.66.16.20. Redistribution subject to ASME license or copyright; see http://www.asme.org/terms/Terms_Use.cfm

F. Dai[1]
Assoc. Mem. ASME

M. M. Khonsari[2]
William Kepler Whiteford Faculty Fellow,
Mem. ASME

Department of Mechanical Engineering,
University of Pittsburgh,
648 Benedum Engineering Hall,
Pittsburgh, PA 15261

Generalized Reynolds Equation for Solid-Liquid Lubricated Bearings

The continuum theory of mixture was employed to derive a generalized form of the Reynolds equation for the lubrication problems involving lubricants that contain solid particles. The derivation of the governing equations and the boundary conditions are presented. The governing equations are two coupled partial differential equations that must be solved simultaneously for the solid volume fraction and the pressure distribution in a hydrodynamic bearing. The boundary conditions allow the particles to slip at the boundary surfaces. The formulation takes the interaction between the solid and the fluid constituents into consideration. Extensive numerical results are presented for the performance parameters in finite journal bearings lubricated with granular powder mixed with Newtonian oil.

1 Introduction

Over a century has passed since the publication of Osborne Reynolds' original paper on the fluid mechanics of lubricating oil flowing within the clearance space of a bearing. His ingenious derivation of the governing equation for pressure distribution gave birth to the theory of hydrodynamic lubrication and what is known as the classical Reynolds equation. The solution to the Reynolds equation yields a remarkably accurate pressure distribution from which the load-carrying capacity, friction force, and many other bearing performance parameters are easily obtainable, hence the practicality and the realism of the formulation. Nevertheless, the derivation is based on a number of restrictive assumptions. One assumption asserts that the fluid is linearly viscous or Newtonian and that a single parameter μ adequately characterizes its viscosity. There is a growing number of applications where the classification of the lubricant as Newtonian may be questionable. Examples include situations where variety of additives are intentionally inserted into a carrier fluid such as the conventional oil for the purpose of enhancement of lubrication characteristics. The particulate matter added to the fluid may be made of solid lubricants powder or they may be fluidic-type additives such as polymers.

The purpose of this paper is to characterize the behavior of a class of bi-component lubricants in a hydrodynamic bearing. In particular, we shall concentrate on lubricants that contain a mixture of solids and liquid. The lubrication effectiveness of such a mixture is clearly dependent upon the constitutive relationship of the fluid, the constitutive equation of the solid, and their respective interaction. We shall therefore focus our attention to a particular class of solids and fluid mixture with a known material constitutive relationship. Guided by the principles of continuum mechanics, we present the derivation of a "generalized Reynolds equation" for lubricant containing the mixture of incompressible powder granular-type solid inserted into a liquid lubricant which is assumed to exhibit Newtonian behavior.

Developments reported in the present paper are based on several preceding articles. First, perturbation solutions were reported for situations where the solid volume fraction was assumed to be small and that at the boundaries the solid particles conform to the velocity of the moving and stationary surfaces so that the classical no-slip boundary condition was applicable (Dai and Khonsari, 1991). A variation of the solutoin method which accounted for the particle slippage at the moving boundary was later reported (Dai and Khonsari, 1992). Finally, the restriction on the solid volume fractin was relaxed and extensive numerical solutions were reported for both slider bearings and journal bearings (Dai and Khonsari, 1993). A common assumption made in these articles was that flow is two-dimensional, owing to an imposed geometrical restriction known as the infinitely long bearing. As a result, the pressure was assumed to remain constant in the axial direction. Therefore, the governing equation for the pressure distribution was only one dimensional.

The governing equations and solutions presented in the present paper are generalized so that they can be used for three-dimensional flows, i.e., applicable to bearings of finite length. Furthermore, the volume fraction of the solid particles is not restricted to small values and the slippage at the boundaries is taken into consideration. Extensive numerical solutions are presented for the prediction of the performance parameters of a journal bearing.

2 Formulation

Consider the lubrication problem of a journal bearing where the bearing length and the diameter are both of finite length.

[1]Current address: Department of Mechanical Engineering, University of California at Berkeley, Berkeley, CA 94720.

[2]To whom all correspondence should be addressed.

Contributed by the Applied Mechanics Division of THE AMERICAN SOCIETY OF MECHANICAL ENGINEERS for publication in the ASME JOURNAL OF APPLIED MECHANICS.

Discussion on this paper should be addressed to the Technical Editor, Professor Lewis T. Wheeler, Department of Mechanical Engineering, University of Houston, Houston, TX 77204-4792, and will be accepted until four months after final publication of the paper itself in the ASME JOURNAL OF APPLIED MECHANICS.

Manuscript received by the ASME Applied Mechanics Division, May 7, 1992; final revision, Mar. 10, 1993. Associate Technical Editor: S. A. Berger.

Copyright © 1994 by ASME
Downloaded 03 May 2010 to 171.66.16.20. Redistribution subject to ASME license or copyright; see http://www.asme.org/terms/Terms_Use.cfm

The fluid mechanics of finite bearings involves three-dimensional flow analyses. In this paper, we shall restrict our formulation to steady state, and assume that all kinematic quantities are continuous functions of x, y, and z for both the fluid and the solid constituents. This consideration requires the following velocity components:

fluid constituent

$$u_x = u_x(x, y, z), \quad u_y = u_y(x, y, z), \quad u_z = u_z(x, y, z), \tag{1}$$

solid constituent

$$w_x = w_x(x, y, z), \quad w_y = w_y(x, y, z), \quad w_z = w_z(x, y, z). \tag{2}$$

An order-of-magnitude analysis shows that the governing equations for the conservation of momentum for each constituent can be written as follows (cf. Dai and Khonsari, 1993):

momentum equations for the *fluid constituent*

$$\frac{\partial p}{\partial x} = \frac{\partial}{\partial y}\left[\mu_f(\nu)\frac{\partial u_x}{\partial y}\right] + \alpha_3(\nu)(w_x - u_x), \tag{3}$$

$$\frac{\partial p}{\partial y} = 0, \tag{4}$$

$$\frac{\partial p}{\partial z} = \frac{\partial}{\partial y}\left[\mu_f(\nu)\frac{\partial u_z}{\partial y}\right] + \alpha_3(\nu)(w_z - u_z), \tag{5}$$

and *momentum equations* for the *solid constituent*

$$\frac{\partial}{\partial x}\left[\beta_1(\nu)\left(\frac{\partial \nu}{\partial y}\right)^2\right] + \frac{\partial}{\partial y}\left[\mu_s(\nu)\frac{\partial w_x}{\partial y} + \beta_3(\nu)\frac{\partial \nu}{\partial x}\frac{\partial \nu}{\partial y}\right] - \alpha_3(\nu)(w_x - u_x) = 0, \tag{6}$$

$$\frac{\partial}{\partial y}\left[\beta_1(\nu)\left(\frac{\partial \nu}{\partial y}\right)^2\right] + \frac{\partial}{\partial y}\left[\beta_3(\nu)\left(\frac{\partial \nu}{\partial y}\right)^2\right] = 0, \tag{7}$$

$$\frac{\partial}{\partial z}\left[\beta_1(\nu)\left(\frac{\partial \nu}{\partial y}\right)^2\right] + \frac{\partial}{\partial y}\left[\mu_s(\nu)\frac{\partial w_z}{\partial y} + \beta_3(\nu)\frac{\partial \nu}{\partial z}\frac{\partial \nu}{\partial y}\right] - \alpha_3(\nu)(w_z - u_z) = 0, \tag{8}$$

where p, ν are the pressure and the solid volume fraction, respectively. μ_f and μ_s are coefficients of viscosity associated with the fluid and the solid. The parameter α_3 is the interaction coefficient which is similar to the drag force coefficient that Saffman (1962) used. Parameters β_1 and β_3 appear in the constitutive equations of the granular material as prescribed by Cowin (1974) and Savage (1979). These parameters are dependent upon the solid volume fraction, ν. The interested reader is referred to Dai and Khonsari (1993) for the details of the derivation of the above equations.

The reader may recognize the similarity between Eq. (3) and the momentum equation used by Saffman (1962) for external flow of dusty gas over a plane with $dp/dx = 0$. Equation (4) essentially asserts that the pressure is constant across the film which is typical for most lubrication problem. In the absence of the interaction term $\alpha_3(\nu)(w_i - u_i)$ and when the solid volume fraction $\nu = 0$, Eqs. (3) and (5) reduce to their linearly viscous counterparts. Using these equations, together with the conservation of mass, one can proceed to derive the classical Reynolds equation. In the present case, however, these equations are coupled to the momentum equations for the solid constituent through the velocity components and the solid volume fraction.

We recall that the coefficients α_3, μ_s, β_1, and β_3 are all functions of the solid volume fraction. Therefore, the solution to Eqs. (3) through (8) depend upon the functional form of these coefficients. These functions depend on the material properties and for a given type of granular material most appropriately should be evaluated experimentally. Because of the lack of sufficient experimental data in the open literature and the fact that the *form* of the material functions is unknown, *as a first approximation*, we linearize the material parameters in the neighborhood of the volume fraction. This idea was utilized in our previous paper (Dai and Khonsari, 1991) for the situation where the solid volume fraction is small. There we gave additional references where the approach was first introduced for a problem involving larger volume fractions. Expanding the material functions in the Taylor series and retaining only first-order terms yield

$$\mu_f(\nu) = \mu(1 - \nu), \tag{9}$$

$$\mu_s(\nu) = \mu_s^0 \nu, \tag{10}$$

$$\beta_1(\nu) = \beta_1^0 + \beta_1^1 \nu, \tag{11}$$

$$\beta_3(\nu) = \beta_3^0 + \beta_3^1 \nu, \tag{12}$$

$$\alpha_3(\nu) = \alpha^2 \nu, \tag{13}$$

where μ is the viscosity of the pure fluid and the parameters, μ_s^0, β_1^0, β_1^1, β_3^0, β_3^1 and α, are constants.

Making use of Eqs. (9)–(13), the governing equations for the conservation of momentum becomes the following:

fluid constituent

$$\frac{\partial p}{\partial x} = \mu\frac{\partial}{\partial y}\left[(1 - \nu)\frac{\partial u_x}{\partial y}\right] + \alpha^2 \nu(w_x - u_x), \tag{14}$$

$$\frac{\partial p}{\partial y} = 0, \tag{15}$$

$$\frac{\partial p}{\partial z} = \mu\frac{\partial}{\partial y}\left[(1 - \nu)\frac{\partial u_z}{\partial y}\right] + \alpha^2 \nu(w_z - u_z), \tag{16}$$

solid constituent

$$\frac{\partial}{\partial x}\left[(\beta_1^0 + \beta_1^1\nu)\left(\frac{\partial \nu}{\partial y}\right)^2\right] + \frac{\partial}{\partial y}\left[\mu_s^0 \nu\frac{\partial w_x}{\partial y} + (\beta_3^0 + \beta_3^1\nu)\frac{\partial \nu}{\partial x}\frac{\partial \nu}{\partial y}\right] - \alpha^2\nu(w_x - u_x) = 0, \tag{17}$$

$$\frac{\partial}{\partial y}\left\{\left[\beta_1^0 + \beta_3^0 + (\beta_1^1 + \beta_3^1)\nu\right]\left(\frac{\partial \nu}{\partial y}\right)^2\right\} = 0, \tag{18}$$

$$\frac{\partial}{\partial z}\left[(\beta_1^0 + \beta_1^1\nu)\left(\frac{\partial \nu}{\partial y}\right)^2\right] + \frac{\partial}{\partial y}\left[\mu_s^0 \nu\frac{\partial w_z}{\partial y} + (\beta_3^0 + \beta_3^1\nu)\frac{\partial \nu}{\partial z}\frac{\partial \nu}{\partial y}\right] - \alpha^2\nu(w_z - u_z) = 0. \tag{19}$$

3 Solutions

The system of equations given in (14)–(19) consists of a set of coupled nonlinear partial differential equations. Generally, this system has to be solved by numerical method.

For the case of an infinitely long bearing, we recently reported a solution procedure using the perturbation method under the premise of small ν assumption (Dai and Khonsari, 1991). In that reference, we discussed the boundary conditions involved and presented some results for small solid volume fractions. In problems involving mixtures, the formulation of boundary conditions is a difficult task. Experimental measurements would have to be conducted in order to establish the behavior of particles at the boundary. This would indeed be an extremely difficult undertaking since in lubrication problems one is confronted with a very thin film gap. Due to the uncertainties in the state of affair insofar as the boundary conditions involved, we propose to assume that the volume fraction remains uniform across the film gap. This assumption can be justified based on the computer simulations of Campbell and Brennen (1985) who provided extensive simulations for rapidly flowing granular material between two parallel surfaces. Their solutions, generated based on random collision of many particles, showed that for a class of boundary conditions, the volume fraction remains nearly uniform across the gap between the two plates. We therefore assume that when

Downloaded 03 May 2010 to 171.66.16.20. Redistribution subject to ASME license or copyright; see http://www.asme.org/terms/Terms_Use.cfm

the flow becomes steady, the solid volume fraction varies along x and z only, i.e.,

$$\nu = \nu(x, z). \tag{20}$$

Having made this assumption, it is easy to see that Eq. (18) is automatically satisfied and that governing equations are greatly simplified. We shall now set out to derive a generalized Reynolds equation that can be readily applied to lubrication problems involving a mixture of fluid and solid powder based upon the assumptions discussed heretofore.

Eliminating the term $\alpha^2\nu(w_x - u_x)$ from Eqs. (14) and (17), we have

$$\mu_s^0\nu \frac{\partial^2 w_x}{\partial y^2} + \mu(1-\nu)\frac{\partial^2 u_x}{\partial y^2} - \frac{\partial p}{\partial x} = 0. \tag{21}$$

Solving Eq. (14) for w_x, we obtain

$$w_x = \frac{1}{\alpha^2\nu}\left\{\frac{\partial p}{\partial x} - \mu\frac{\partial}{\partial y}\left[(1-\nu)\frac{\partial u_x}{\partial y}\right]\right\} + u_x \tag{22}$$

and substituting Eq. (22) into (21) and rearranging the result, we arrive at

$$\frac{\mu_s^0\mu(1-\nu)}{\alpha^2}\frac{\partial^4 u_x}{\partial y^4} - G(x, z)\frac{\partial^2 u_x}{\partial y^2} + \frac{\partial p}{\partial x} = 0, \tag{23}$$

where

$$G(x, z) = \mu_s^0\nu + \mu(1-\nu). \tag{24}$$

Integration of Eq. (23) over y yields the following expression for the velocity component of the fluid phase, u_x:

$$u_x = C_1(x, z)e^{\alpha k(x, z)y} + C_2(x, z)e^{-\alpha k(x, z)y} + \frac{C_3(x, z) + C_4(x, z)y}{G(x, z)} + \frac{1}{G(x, z)}\left[\frac{y^2}{2} + \frac{\mu_s^0\mu(1-\nu)}{\alpha^2 G(x, z)}\right]\frac{\partial p}{\partial x}, \tag{25}$$

where C_1 through C_4 are arbitrary functions of x and z resulting from the integration, and

$$k(x, z) = \sqrt{\frac{G(x, z)}{\mu_s^0\mu(1-\nu)}}. \tag{26}$$

Furthermore, substituting Eq. (25) into Eq. (22) yields the solution for the velocity component of the solid phase, w_x, as shown below:

$$w_x = \left\{\frac{1}{\alpha^2\nu}\left[1 - \frac{\mu(1-\nu)}{G(x, z)}\right] + \frac{\mu_s^0\mu(1-\nu)}{\alpha^2 G^2(x, z)} + \frac{y^2}{2G(x, z)}\right\}\frac{\partial p}{\partial x} + \frac{C_3(x, z) + C_4(x, z)y}{G(x, z)} + C_1(x, z)\left[1 - \frac{\mu(1-\nu)k^2(x, z)}{\nu}\right]e^{\alpha k(x, z)y} + C_2(x, z) \times \left[1 - \frac{\mu(1-\nu)k^2(x,z)}{\nu}\right]e^{-\alpha k(x, z)y}. \tag{27}$$

The arbitrary functions C_1 through C_4 should be determined from the boundary conditions of u_x and w_x.

In a hydrodynamic bearing, normally one surface is stationary and one moves at an imposed velocity U. For the problem under consideration, we adopt the classical no-slip boundary condition for the fluid constituent but make provisions for the possibility of particle slippage on the surfaces. The above consideration yields the following boundary conditions:

$$u_x|_{y=0} = U,\ u_x|_{y=h(x)} = u_y|_{y=0} = u_y|_{y=h(x)} = u_z|_{y=0} = u_z|_{y=h(x)} = 0, \tag{28}$$

$$w_x|_{y=0} = B_1(x, z),\ w_x|_{y=h(x)} = B_2(x, z),\ w_y|_{y=0} = 0,\ w_y|_{y=h(x)} = B_2(x, z)\frac{dh(x)}{dx}, \tag{29}$$

$$w_z|_{y=0} = B_3(x, z),\ w_z|_{y=h(x)} = B_4(x, z), \tag{30}$$

where h is the film gap between the sliding surface and the stationary surface whose form depends on the geometry of the bearing. Parameter $B_i(x, z)$, $i = 1, 4$, represent the functional forms of the particle slippage on the boundary.

Application of the above boundary conditions to evaluate the constants in Eqs. (25) and (27) yields

$$u_x = U\left[1 - \frac{y}{h(x)}\right] + \frac{1}{G(x, z)}\left[\frac{y^2 - h(x)y}{2} - \frac{(\mu_s^0)^2\nu}{G(x, z)}\frac{\phi_1(x, y, z)}{\alpha^2}\right]\frac{\partial p}{\partial x} - \frac{\mu_s^0\nu[U - B_1(x, z)]}{G(x, z)} \times \left[1 - \frac{y}{h(x)} - \phi_2(x, y, z)\right] + \frac{\mu_s^0\nu B_2(x, z)}{G(x, z)}\left[\frac{y}{h(x)} + \phi_3(x, y, z)\right], \tag{31}$$

$$w_x = U\left[1 - \frac{y}{h(x)}\right] + \frac{1}{G(x, z)}\left[\frac{y^2 - h(x)y}{2} + \frac{\mu_s^0\mu(1-\nu)}{G(x, z)}\frac{\phi_1(x, y, z)}{\alpha^2}\right]\frac{\partial p}{\partial x} - \frac{U - B_1(x, z)}{G(x, z)}\left\{\mu_s^0\nu\left[1 - \frac{y}{h(x)}\right] + \mu(1-\nu)\phi_2(x, y, z)\right\} + \frac{B_2(x, z)}{G(x, z)}\left[\frac{\mu_s^0\nu y}{h(x)} - \mu(1-\nu)\phi_3(x, y, z)\right], \tag{32}$$

where

$$\phi_1(x, y, z) = 1 - \frac{e^{\alpha k(x, z)y}}{1 + e^{\alpha k(x, z)h(x)}} - \frac{e^{-\alpha k(x, z)y}}{1 + e^{-\alpha k(x, z)h(x)}},$$

$$\phi_2(x, y, z) = \left[\frac{e^{\alpha k(x, z)y}}{1 + e^{\alpha k(x, z)h(x)}} - \frac{e^{\alpha k(x, z)[h(x) - y]}}{1 + e^{-\alpha k(x, z)h(x)}}\right]\frac{1}{1 - e^{\alpha k(x, z)h(x)}},$$

$$\phi_3(x, y, z) = \left[\frac{e^{\alpha k(x, z)[h(x) + y]}}{1 + e^{\alpha k(x, z)h(x)}} - \frac{e^{-\alpha k(x, z)y}}{1 + e^{-\alpha k(x, z)h(x)}}\right]\frac{1}{1 - e^{\alpha k(x, z)h(x)}}.$$

Similarly, from Eqs. (16) and (19), and the corresponding boundary conditions for u_z and w_z in (28)–(30), we obtain expressions for the fluid and solid velocity components in the z direction. The result is given as follows:

$$u_z = \frac{1}{G(x, z)}\left[\frac{y^2 - h(x)y}{2} - \frac{(\mu_s^0)^2\nu}{G(x, z)}\frac{\phi_1(x, y, z)}{\alpha^2}\right]\frac{\partial p}{\partial z} + \frac{\mu_s^0\nu B_3(x, z)}{G(x, z)}\left[1 - \frac{y}{h(x)} - \phi_2(x, y, z)\right] + \frac{\mu_s^0\nu B_4(x, z)}{G(x, z)}\left[\frac{y}{h(x)} + \phi_3(x, y, z)\right], \tag{33}$$

$$w_z = \frac{1}{G(x, z)}\left[\frac{y^2 - h(x)y}{2} + \frac{\mu_s^0\mu(1-\nu)}{G(x, z)}\frac{\phi_1(x, y, z)}{\alpha^2}\right]\frac{\partial p}{\partial z} + \frac{B_3(x, z)}{G(x, z)}\left\{\mu_s^0\nu\left[1 - \frac{y}{h(x)}\right] + \mu(1-\nu)\phi_2(x, y, z)\right\} + \frac{B_4(x, z)}{G(x, z)}\left[\frac{\mu_s^0\nu y}{h(x)} - \mu(1-\nu)\phi_3(x, y, z)\right]. \tag{34}$$

It can be seen from the above equations that the velocity components of the solid and fluid constituents, u_x and w_x, consist of four portions: the first portion is generated by the pressure gradient and the second and the third portions are

Downloaded 03 May 2010 to 171.66.16.20. Redistribution subject to ASME license or copyright; see http://www.asme.org/terms/Terms_Use.cfm

contributed by the slippage of the granules on the sliding surface and the stationary surface, respectively. The fourth portion is due to the motion of the sliding surface. The velocity components, u_z and w_z, are composed of the first three portions mentioned above.

Under the steady-state condition, the statements of *conservation of mass* for the fluid and solid constituents translate to the following equations:

$$\frac{\partial}{\partial x}[(1-\nu)u_x]+\frac{\partial}{\partial y}[(1-\nu)u_y]+\frac{\partial}{\partial z}[(1-\nu)u_z]=0, \quad (35)$$

$$\frac{\partial}{\partial x}(\nu w_x)+\frac{\partial}{\partial y}(\nu w_y)+\frac{\partial}{\partial z}(\nu w_z)=0. \quad (36)$$

Integrating Eqs. (35) and (36) over y from 0 to h and using Leibnitz's general integration rule results in the following two equations:

$$\frac{\partial}{\partial x}\int_0^{h(x)}(1-\nu)u_x dy+\frac{\partial}{\partial z}\int_0^{h(x)}(1-\nu)u_z dy=0. \quad (37)$$

$$\frac{\partial}{\partial x}\int_0^{h(x)}\nu w_x dy+\frac{\partial}{\partial z}\int_0^{h(x)}\nu w_z dy=0. \quad (38)$$

Finally, substituting for the velocity components from Eqs. (31)–(34) and performing the integration results in the two coupled partial differential equations listed as follows:

$$\frac{\partial}{\partial x}\left\{\frac{h^3(x)}{6}\frac{\partial p}{\partial x}-Uh(x)G(x,z)-\mu_s^0 h(x)\nu\left[B_1(x,z)+B_2(x,z)-U\right]\right\}+\frac{\partial}{\partial z}\left\{\frac{h^3(x)}{6}\frac{\partial p}{\partial z}-\mu_s^0 h(x)\nu\left[B_3(x,z)+B_4(x,z)\right]\right\}=0, \quad (39)$$

$$\frac{\partial}{\partial x}\left\{\frac{1}{G(x,z)}\left[\frac{h^3(x)}{6}+\frac{2\mu_s^0(\mu_s^0-\mu)\nu(1-\nu)}{G(x,z)}\frac{\psi_1(x,z)}{\alpha^2}\right]\frac{\partial p}{\partial x}-Uh(x)-\frac{\nu[B_1(x,z)+B_2(x,z)-U]}{G(x,z)}\psi_2(x,z)\right\}+\frac{\partial}{\partial z}\left\{\frac{1}{G(x,z)}\left[\frac{h^3(x)}{6}+\frac{2\mu_s^0(\mu_s^0-\mu)\nu(1-\nu)}{G(x,z)}\frac{\psi_1(x,z)}{\alpha^2}\right]\frac{\partial p}{\partial z}-\frac{\nu[B_3(x,z)+B_4(x,z)]}{G(x,z)}\psi_2(x,z)\right\}=0, \quad (40)$$

where

$$\psi_1(x,z)=h(x)-\frac{2}{\alpha k(x,z)}\frac{1-e^{-\alpha k(x,z)h(x)}}{1+e^{-\alpha k(x,z)h(x)}},$$

$$\psi_2(x,z)=\mu_s^0 h(x)-\frac{2(\mu_s^0-\mu)(1-\nu)}{\alpha k(x,z)}\frac{1-e^{-\alpha k(x,z)h(x)}}{1+e^{-\alpha k(x,z)h(x)}}.$$

Equations (39) and (40) represent the generalized Reynolds equations. They must be solved simultaneously for volume fraction and pressure distribution by numerical method. These equations reduce to the classical Reynolds equation when the solid volume fraction vanishes. Before we discuss the numerical procedure, we shall present expressions for important bearing performance parameters and some special cases of the generalized Reynolds equations.

4 Friction Force, Load-Carrying Capacity, and Friction Coefficient

To evaluate the frictional characteristics of the mixture flow we must now turn our attention to the total stress field in the mixture, **T**,

$$\mathbf{T}=-p\begin{pmatrix}1&0&0\\0&1&0\\0&0&1\end{pmatrix}+\begin{pmatrix}0&\tau_{xy}&0\\\tau_{xy}&0&\tau_{yz}\\0&\tau_{yz}&0\end{pmatrix}, \quad (41)$$

where

$$\tau_{xy}=\mu(1-\nu)\frac{\partial u_x}{\partial y}+\mu_s^0\nu\frac{\partial w_x}{\partial y},\ \tau_{yz}=\mu(1-\nu)\frac{\partial u_z}{\partial y}+\mu_s^0\nu\frac{\partial w_z}{\partial y},$$

and the higher order terms of C/R have been neglected where C is the radial clearance and R the radius of the journal.

It follows from Eqs. (31), (32), and (41) that the pressure and shear stress of the mixture flow, T_{yy} and T_{xy}, take the forms

$$T_{yy}=-p, \quad (42)$$

$$T_{xy}=\frac{2y-h(x)}{2}\frac{\partial p}{\partial x}-\frac{UG(x,z)}{h(x)}+\frac{\mu_s^0\nu}{h(x)}[B_2(x,z)+U-B_1(x,z)]. \quad (43)$$

Evaluating Eq. (43) at $y = 0$ we have

$$T_{xy}|_{y=0}=-\frac{1}{h(x)}\left\{\frac{h^2(x)}{2}\frac{\partial p}{\partial x}+UG(x,z)-\mu_s^0\nu[B_2(x,z)+U-B_1(x,z)]\right\}. \quad (44)$$

The friction coefficient of the mixture flow, f_m, is defined as

$$f_m=\frac{F_m}{W_m}, \quad (45)$$

where F_m and W_m are the friction force and load-carrying capacity of the mixture flow which are defined as

$$F_m=\int_A T_{xy}|_{y=0}dA,\ W_m=\int_A p dA, \quad (46)$$

where A is the area of the sliding surface.

5 Special Cases

5.1 No-Slip Boundary Conditions. Suppose that we adopt the no-slip boundary conditions for the particles similar to that of the fluid phase, that is $B_1 = U$, $B_2 = 0$ and $B_3 = B_4 = 0$. Physically this would best describe the situation where the stationary and sliding surface are rough. Equations (31)–(34), (39), (40), and (44) reduce to the following:

$$u_x=U\left[1-\frac{y}{h(x)}\right]+\frac{1}{G(x,z)}\left[\frac{y^2-h(x)y}{2}-\frac{(\mu_s^0)^2\nu}{G(x,z)}\frac{\phi_1(x,y,z)}{\alpha^2}\right]\frac{\partial p}{\partial x}, \quad (47)$$

$$w_x=U\left[1-\frac{y}{h(x)}\right]+\frac{1}{G(x,z)}\left[\frac{y^2-h(x)y}{2}+\frac{\mu_s^0\mu(1-\nu)}{G(x,z)}\frac{\phi_1(x,y,z)}{\alpha^2}\right]\frac{\partial p}{\partial x}, \quad (48)$$

$$u_z=\frac{1}{G(x,z)}\left[\frac{y^2-h(x)y}{2}-\frac{(\mu_s^0)^2\nu}{G(x,z)}\frac{\phi_1(x,y,z)}{\alpha^2}\right]\frac{\partial p}{\partial z}, \quad (49)$$

$$w_z=\frac{1}{G(x,z)}\left[\frac{y^2-h(x)y}{2}+\frac{\mu_s^0\mu(1-\nu)}{G(x,z)}\frac{\phi_1(x,y,z)}{\alpha^2}\right]\frac{\partial p}{\partial z}, \quad (50)$$

$$\frac{\partial}{\partial x}\left[\frac{h^3(x)}{6}\frac{\partial p}{\partial x}-Uh(x)G(x,z)\right]+\frac{\partial}{\partial z}\left[\frac{h^3(x)}{6}\frac{\partial p}{\partial z}\right]=0, \quad (51)$$

Downloaded 03 May 2010 to 171.66.16.20. Redistribution subject to ASME license or copyright; see http://www.asme.org/terms/Terms_Use.cfm

$$\frac{\partial}{\partial x}\left\{\frac{1}{G(x,z)}\left[\frac{h^3(x)}{6}+\frac{2\mu_s^0(\mu_s^0-\mu)\nu(1-\nu)}{G(x,z)}\frac{\psi_1(x,z)}{\alpha^2}\right]\frac{\partial p}{\partial x}-Uh(x)\right\}$$
$$+\frac{\partial}{\partial z}\left\{\frac{1}{G(x,z)}\left[\frac{h^3(x)}{6}+\frac{2\mu_s^0(\mu_s^0-\mu)\nu(1-\nu)}{G(x,z)}\frac{\psi_1(x,z)}{\alpha^2}\right]\frac{\partial p}{\partial z}\right\}=0, \tag{52}$$

$$T_{xy}|_{y=0}=-\frac{1}{h(x)}\left[\frac{h^2(x)}{2}\frac{\partial p}{\partial x}+UG(x,z)\right]. \tag{53}$$

5.2 Pure Fluid Flow Case. In pure fluid flow case, we have $\nu(x, z) = 0$. It then follows from Eqs. (24) and (26) that

$$G(x,z)=\mu. \tag{54}$$

Suppressing $\nu(x, z)$ from Eqs. (47), (49), (51), (or (52)) and (53), and noting the foregoing equations, we obtain

$$u_x=U\left[1-\frac{y}{h(x)}\right]+\frac{y^2-h(x)y}{2\mu}\frac{\partial p}{\partial x}, \tag{55}$$

$$u_z=\frac{y^2-h(x)y}{2\mu}\frac{\partial p}{\partial z}, \tag{56}$$

$$\frac{\partial}{\partial x}\left[\frac{h^3(x)}{6}\frac{\partial p}{\partial x}-U\mu h(x)\right]+\frac{\partial}{\partial z}\left[\frac{h^3(x)}{6}\frac{\partial p}{\partial z}\right]=0, \tag{57}$$

$$T_{xy}|_{y=0}=-\frac{1}{h(x)}\left[\frac{h(x)}{2}\frac{\partial p}{\partial x}+U\mu\right]. \tag{58}$$

The above expressions are exactly those that one encounters in the classical lubrication theory for three-dimensional flows with Newtonian fluids. Equation (57) is known as the Reynolds equation.

5.3 The Case Where $\alpha \to \infty$. This limiting case physically corresponds to the situation where the solid particles are carried by the fluid at the same velocity, that is $\mathbf{u} = \mathbf{w}$. Note that

$$\lim_{\alpha\to\infty}\frac{\phi_1(x,y,z)}{\alpha^2}$$
$$=\lim_{\alpha\to\infty}\frac{1}{\alpha^2}\left[1-\frac{e^{\alpha k(x,z)y}}{1+e^{\alpha k(x,z)h(x)}}-\frac{e^{-\alpha k(x,z)y}}{1+e^{-\alpha k(x,z)h(x)}}\right]\to 0, \tag{59}$$

$$\lim_{\alpha\to\infty}\frac{\psi_1(x,z)}{\alpha^2}=\lim_{\alpha\to\infty}\frac{1}{\alpha^2}\left[h(x)-\frac{2}{\alpha k(x,z)}\frac{e^{-\alpha k(x,z)h(x)}}{1+e^{-\alpha k(x,z)h(x)}}\right]\to 0. \tag{60}$$

From Eqs. (47)–(53) we obtain

$$u_x=w_x=U\left[1-\frac{y}{h(x)}\right]+\frac{y^2-h(x)y}{2G(x,z)}\frac{\partial p}{\partial x}, \tag{61}$$

$$u_z=w_z=\frac{y^2-h(x)y}{2G(x,z)}\frac{\partial p}{\partial z}, \tag{62}$$

$$\frac{\partial}{\partial x}\left[\frac{h^3(x)}{6}\frac{\partial p}{\partial x}-Uh(x)G(x,z)\right]+\frac{\partial}{\partial z}\left[\frac{h^3(x)}{6}\frac{\partial p}{\partial z}\right]=0, \tag{63}$$

$$\frac{\partial G(x,z)}{\partial x}\frac{\partial p}{\partial x}+\frac{\partial G(x,z)}{\partial z}\frac{\partial p}{\partial z}-\frac{6UG(x,z)}{h^2(x)}\frac{\partial G(x,z)}{\partial x}=0, \tag{64}$$

$$T_{xy}|_{y=0}=-\frac{1}{h(x)}\left[\frac{h^2(x)}{2}\frac{\partial p}{\partial x}+UG(x,z)\right]. \tag{65}$$

Equations (61)–(63) and (65) can be obtained from the results for the pure fluid flow case, Eqs. (55)–(58), by replacing ν with G.

6 Numerical Procedure and Results

In this section, we shall present numerical solutions for the special case of the generalized Reynolds equations in the absence of particle slippage at the boundaries. The equations we wish to solve are given in Section 5.1

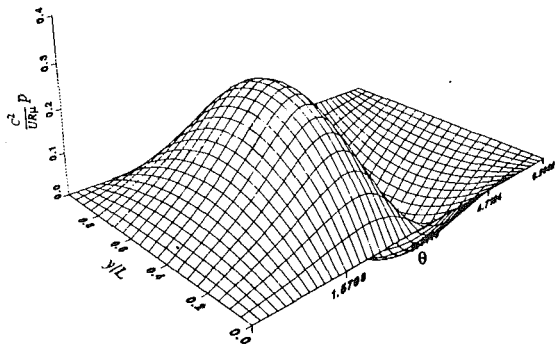


Fig. 1 Pressure distributions

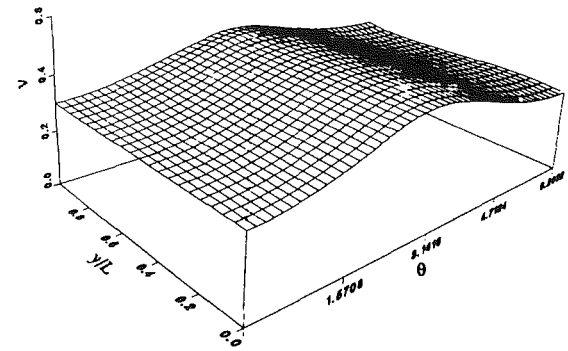


Fig. 2 Distribution of solid volume fraction

Equations (51) and (52) were discretized and solved simultaneously using the finite difference method. A brief description of the method follows. For an assumed pressure distribution, as an initial guess, Eq. (51) was solved for the volume fraction distribution along the direction of motion x and in the axial direction z. Once the solution for ν is available, Eq. (52) is solved for the pressure distribution. This equation is an elliptic partial differential equation and is solved using the successive-over-relaxation method. The values of pressure and their gradients are then used subsequently to update the volume fraction distribution, by solving Eq. (51). This cycle is repeated until the solutions for both ν and p converge. That is, the relative error between two successive iterations falls below a specified tolerance.

The solutions presented in this paper are for a steadily loaded journal bearing without any misalignment in the axial direction. The film thickness profile is therefore a function of x, only. Specifically,

$$h=C(1+\epsilon\cos\theta),$$

where $\theta(=x/R)$ is the circumferential coordinate and $\epsilon\ (=e/C)$ is the eccentricity ratio.

The simulations presented in this paper, unless stated otherwise, correspond to a bearing with $R/L = 1.0$, $\epsilon = 0.3$, $\alpha = 0.5$, $\nu(0, z) = 0.3$ and $\bar{\mu}_s = \mu_s/\mu = 0.8$. The four other parameters used in this paper, fluid mass flux rate, solid mass flux rate, fluid flow leakage rate, and solid flow leakage rate, are defined below, respectively,

$$Q=\int_0^L\int_0^h\left[(1-\nu)u_x\right]|_{x=0}dzdy,\quad M=\int_0^L\int_0^h(\nu w_x)|_{x=0}dzdy,$$

$$Q_L=2\int_0^{2\pi}\int_0^h\left[(1-\nu)u_y\right]|_{y=0}dzd\theta,$$

$$M_L=2\int_0^{2\pi}\int_0^h(\nu w_y)|_{y=0}dzd\theta.$$

Downloaded 03 May 2010 to 171.66.16.20. Redistribution subject to ASME license or copyright; see http://www.asme.org/terms/Terms_Use.cfm

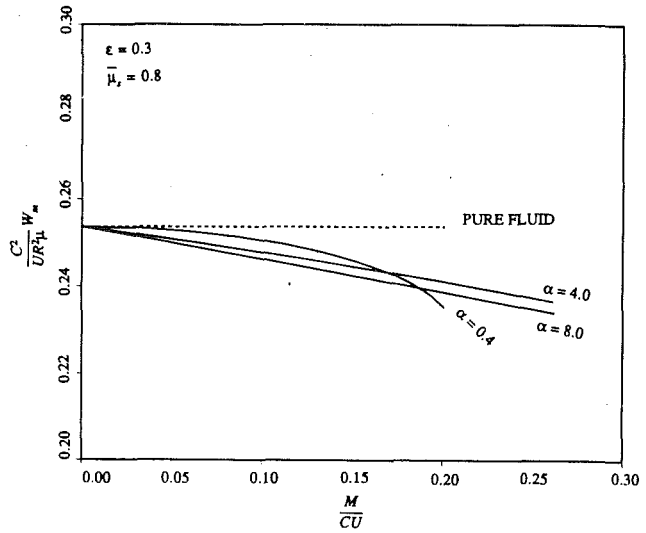


Fig. 3 Load-carrying capacity versus solid mass flow rate

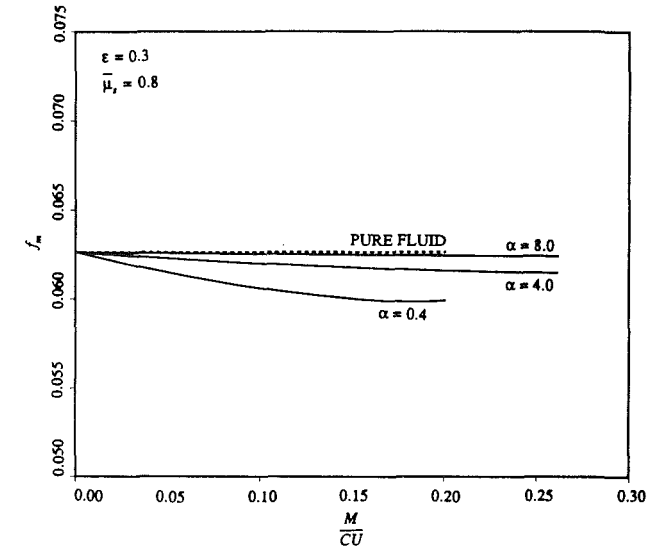


Fig. 4 Friction coefficient versus solid mass flow rate for various interaction coefficients

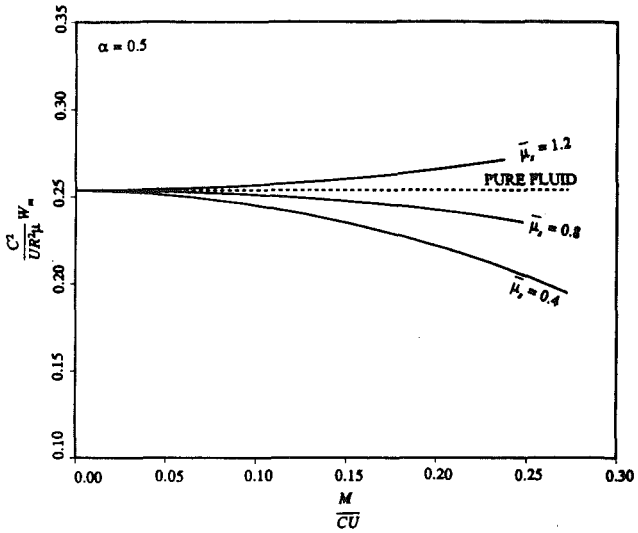


Fig. 5 Load-carrying capacity versus solid mass flow rate for various solid viscosity coefficients

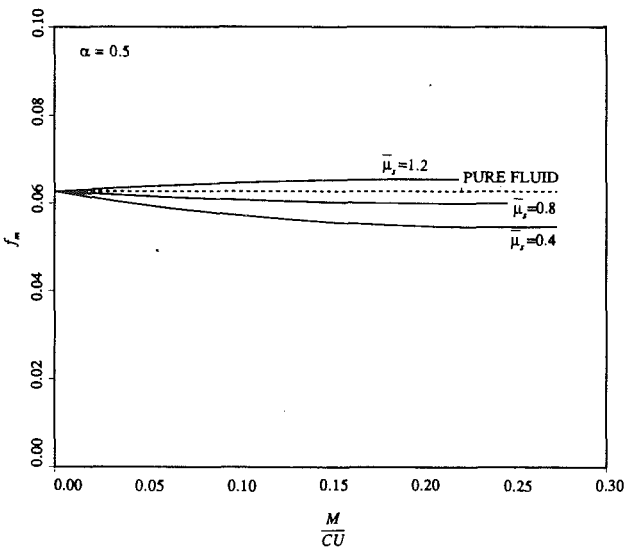


Fig. 6 Friction coefficient versus solid mass flow rate for various solid viscosity coefficients

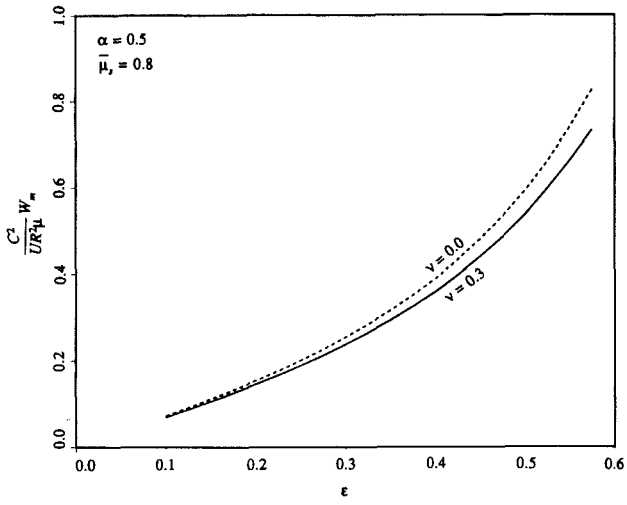


Fig. 7 Load-carrying capacity versus eccentricity ratio

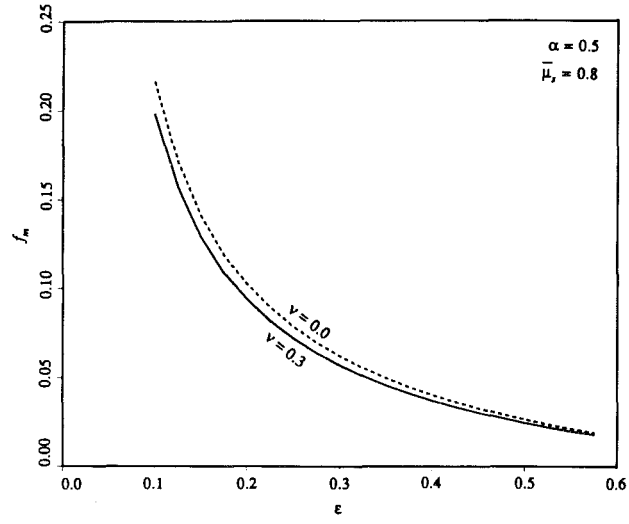


Fig. 8 Friction coefficient versus eccentricity ratio

Downloaded 03 May 2010 to 171.66.16.20. Redistribution subject to ASME license or copyright; see http://www.asme.org/terms/Terms_Use.cfm

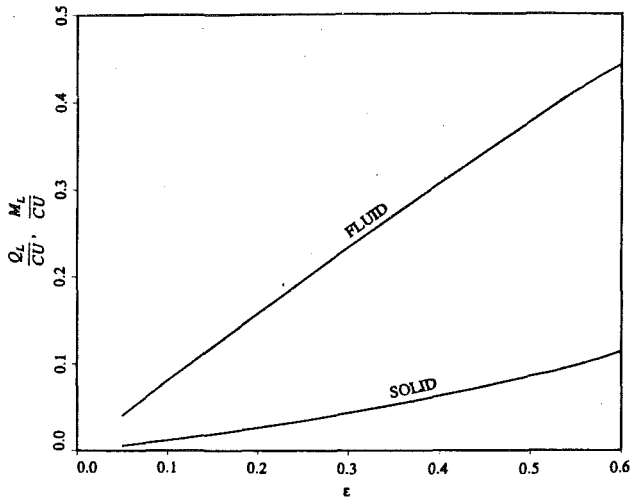


Fig. 9 Leakage flow rate versus eccentricity ratio

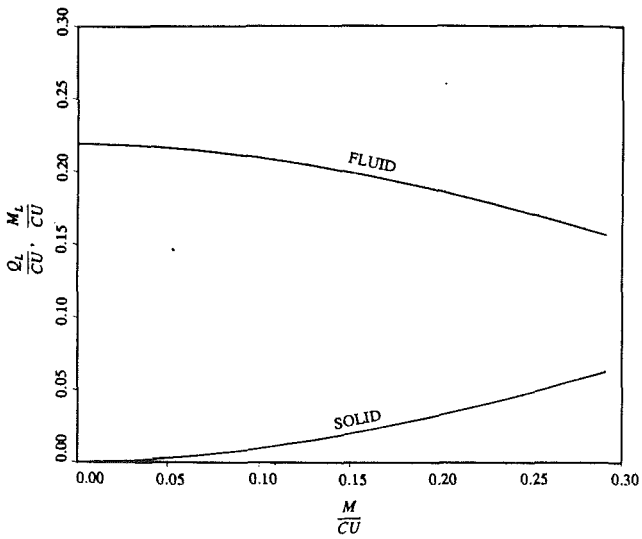


Fig. 10 Leakage flow rate versus solid mass flow rate

Figures 1 and 2 show a typical pressure profile and volume fraction distribution. The pressure at inlet is assumed to be equal to that of the atmosphere. Pressure steadily increases from the inlet in the direction of motion, reaches a maximum value and then drops below the atmospheric pressure according to the Sommerfeld boundary condition assumed in the simulations. Such "negative pressures" occur when the fluid enters the divergent region at $\theta \geq \pi$. The divergent region of the bearing does not contribute positively to the load-carrying capacity and is usually neglected in classical solutions dealing with pure fluid.

The volume fraction profile increases in the convergent portion of the film, for the film gap becomes narrow in the region $0 \leq \theta \leq \pi$. In the divergent region of the flow, the volume fraction gradually decreases. The distribution of the volume fraction in the axial direction is fairly uniform due to the absence of misalignment as expected.

Figures 3–8 deal with the trend of the load-carrying capacity and the friction coefficient under various conditions. The solid lines correspond to the performance of the mixture and the dashed lines represent the pure fluid case, shown for purpose of comparison.

Figure 3 concentrates on the influence of the interaction coefficient on the load-carrying capacity for specified solid mass flow rates at the inlet. These simulations show that the interaction coefficient plays an important role on the load-carrying capacity. It is recalled that in these simulations the solid viscosity coefficient is assumed to be $\overline{\mu}_s = 0.8$. With this value of $\overline{\mu}_s$, the load-carrying capacity shows a reduction when compared to that of a pure fluid. Similar results were reported for infinitely long bearings (cf. Dai and Khonsari, 1993). To show the importance of $\overline{\mu}_s$, Fig. 5 is presented. In that figure, the interaction coefficient α was kept constant and $\overline{\mu}_s$ was varied for specified solid mass flow rates. We note that when $\overline{\mu}_s = 1.2$, the model predicts an enhancement in the load-carrying capacity.

Figures 4 and 6 show the variation of coefficient of friction corresponding to the conditions described in Figs. 3 and 5. These figures show that the friction coefficient is affected by the interaction coefficient α and the solid viscosity coefficient $\overline{\mu}_s$. While the model predicts an improvement in the load-carrying capacity for $\overline{\mu}_s = 1.2$, this situation would result in an increase in the coefficient of friction relative to pure lubricant case.

Thus far the simulations were restricted to an eccentricity ratio of $\epsilon = 0.3$. In Figs. 7 and 8, we show the load-carrying capacity and friction coefficient vary with increasing the eccentricity. The values of $\alpha = 0.5$ and $\overline{\mu}_s = 0.8$ are assumed and the simulation results are shown for the solid mass flow rate of $\nu = 0.3$ along with that of the pure fluid. Under these conditions, the model predicts that friction coefficient is improved when a lubricant is made up of a mixture of solid powder added to Newtonian fluid. Figures 9 and 10 show the variations of the fluid flow leakage rate and the solid flow leakage rate with eccentricity ratio and solid mass flow rate, respectively.

Acknowledgments

The authors wish to acknowledge the National Science Foundation (NSF), and Pittsburgh Supercomputing Center (PSC), and NASA Lewis Research Center for partial support of this research.

References

Campbell, C. S., and Brennen, C. E., 1985, "Computer Simulation of Granular Shear Flows," *J. Fluid Mech.*, Vol. 151, p. 167.

Cowin, S. C., 1974, "A Theory for the Flow of Granular Materials," *Powder Technol.*, p. 61.

Dai, F., and Khonsari, M. M., 1991, "On the Solution of a Lubrication Problem with Particulate Solids," *Int. J. Engng. Sci.*, Vol. 29, p. 1019.

Dai, F., and Khonsari, M. M., 1992, "Analytical Solution for a Mixture of a Newtonian Fluid and Granules in Hydrodynamic Bearings," *Wear*, Vol. 156, p. 327.

Dai, F., and Khonsari, M. M., 1993, "A Continuum Theory of a Lubrication Problem With Solid Particles," ASME JOURNAL OF APPLIED MECHANICS, Vol. 60, pp. 48–58.

Saffman, P. G., 1962, "On the Stability of Laminar Flow of a Dusty Gas," *J. Fluid Mech.*, Vol. 13, p. 120.

Savage, S. B., 1979, "Gravity Flow of Cohesionless Granular Materials in Chutes and Channels," *J. Fluid Mech.*, Vol. 92, p. 53.

Downloaded 03 May 2010 to 171.66.16.20. Redistribution subject to ASME license or copyright; see http://www.asme.org/terms/Terms_Use.cfm

Journal of Applied Mechanics

Brief Notes

A Brief Note is a short paper that presents a specific solution of technical interest in mechanics but which does not necessarily contain new general methods or results. A Brief Note should not exceed 1500 words *or equivalent* (a typical one-column figure or table is equivalent to 250 words; a one line equation to 30 words). Brief Notes will be subject to the usual review procedures prior to publication. After approval such Notes will be published as soon as possible. The Notes should be submitted to the Technical Editor of the JOURNAL OF APPLIED MECHANICS. Discussions on the Brief Notes should be addressed to the Editorial Department, ASME, United Engineering Center, 345 East 47th Street, New York, N. Y. 10017, or to the Technical Editor of the JOURNAL OF APPLIED MECHANICS. Discussions on Brief Notes appearing in this issue will be accepted until two months after publication. Readers who need more time to prepare a Discussion should request an extension of the deadline from the Editorial Department.

Accurate Data for Stress Intensity Factors at Infinitesimal Kinks

S. Melin[1]

1 Introduction

The stress intensity factors at the tip of a straight crack terminating in an infinitesimal kink are calculated from a matrix formulation of a Hilbert problem following the work of Khrapkov (1971). These stress intensity factors are expressed in terms of the stress intensity factors of the crack in absence of a kink. This method provides very accurate results and the values presented here might be of interest for determination of the accuracy of other methods.

2 Posing the Problem

Consider a straight crack in a large plate of a linearly elastic material terminating in an infinitesimal kink according to Fig. 1. The loading consists of the remote stresses σ_x^∞, σ_y^∞, and τ_{xy}^∞, assumed to be chosen so that the crack surfaces do not touch each other. Plane conditions are assumed.

The stress intensity factors k_I and k_{II} at the tip of the kink, forming an angle α to the main crack, will be calculated in terms of the stress intensity factors K_I and K_{II} at the tip of the crack in absence of a kink. Here only a brief review of the method will be given. Details are found in Melin (1985).

Instead of assuming the kink length to be infinitesimal, it will be assumed to be of unit length, implying a semi-infinite main crack. Furthermore, a homogeneous stress field $\sigma_x = -\sigma_x^\infty$, $\sigma_y = -\sigma_y^\infty$ and $\tau_{xy} = -\tau_{xy}^\infty$ is superimposed everywhere. This implies introduction of tractions on the crack surfaces.

Now introduce a local coordinate system (θ, r) according to Fig. 1. In each of the segments $(0 \le \theta \le \theta_1, 0 \le r < \infty)$ and $(-\theta_2 \le \theta \le 0, 0 \le r < \infty)$, where $\theta_1 = \pi - \alpha$ and $\theta_2 = \pi + \alpha$, the equations of equilibrium and Hooke's law holds.

The boundary conditions at the kink surfaces and along the line $\theta = 0$ are

$$\theta = 0\pm \quad r<1:\ \sigma_\theta(0\pm,r) = -\sigma_0(\alpha,r);\ \tau_{r\theta}(0\pm,r) = -\tau_0(\alpha,r) \tag{1}$$

$$\theta = 0\pm \quad r>1:\ \frac{\partial}{\partial r}\left[u_\theta(0+,r) - u_\theta(0-,r)\right] = 0;$$

$$\frac{\partial}{\partial r}\left[u_r(0+,r) - u_r(0-,r)\right] = 0$$

$$\sigma_\theta(0+,r) - \sigma_\theta(0-,r) = 0;\ \tau_{r\theta}(0+,r) - \tau_{r\theta}(0-,r) = 0 \tag{2}$$

with $\sigma_0(\alpha, r)$ and $\tau_0(\alpha, r)$ known. By the notations $\theta+$ and $\theta-$ are meant the limiting values as θ is approached from the positive and negative side, respectively.

The conditions along the surfaces of the main crack are

$$\theta = \theta_1\ 0 \le r < \infty:\ \sigma_\theta(\theta_1,r) = 0;\ \tau_{r\theta}(\theta_1,r) = 0 \tag{3}$$

$$\theta = -\theta_2\ 0 \le r < \infty:\ \sigma_\theta(-\theta_2,r) = 0;\ \tau_{r\theta}(-\theta_2,r) = 0. \tag{4}$$

By assuming for a while $\partial u_\theta/\partial r$, $\partial u_r/\partial r$, σ_θ, and $\tau_{r\theta}$ to be known for $\theta = 0\pm$, $r > 1$, a solution will be sought for each of the segments $0 \le \theta \le \theta_1$ and $-\theta_2 \le \theta \le 0$. Thereupon the solutions will be matched to each other through the boundary conditions at $\theta = \pm 0$, $r > 1$.

3 Formulation and Solution of a Hilbert Problem

The problem will be solved by employing the Mellin transform. The Mellin transform of a function $g(\theta, r)$ is defined by the expression

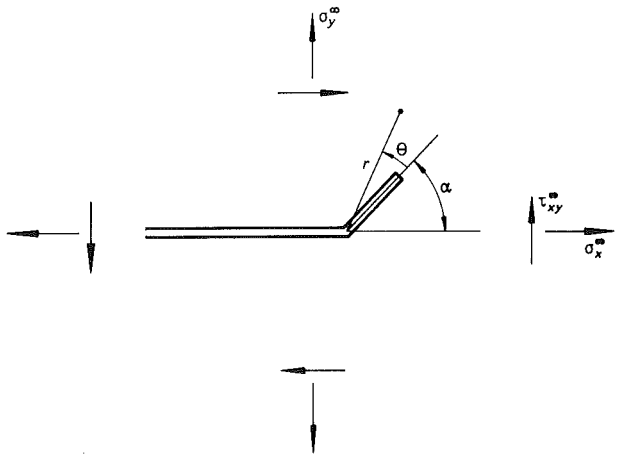


Fig. 1 A straight crack terminating in an infinitesimal kink, forming an angle α to the main crack. The remote stresses are σ_x^∞, σ_y^∞ and τ_{xy}^∞.

[1]Division of Solid Mechanics, Lund Institute of Technology, Box 118, S-221 00 Lund, Sweden.

Contributed by the Applied Mechanics Division of THE AMERICAN SOCIETY OF MECHANICAL ENGINEERS for publication in the ASME JOURNAL OF APPLIED MECHANICS. Manuscript received by the ASME Applied Mechanics Division, Apr. 3, 1991; final revision, Nov. 1, 1993. Associate Technical Editor: C. F. Shih.

Copyright © 1994 by ASME
Downloaded 03 May 2010 to 171.66.16.20. Redistribution subject to ASME license or copyright; see http://www.asme.org/terms/Terms_Use.cfm

$$\bar{g}(\theta,\rho)=\int_0^{\infty} r^{\rho} g(\theta,r)\,dr \tag{5}$$

with a bar indicating the transformed function. The transform is decomposed into two parts:

$$\bar{g}_-(\theta,\rho)=\int_0^{1} r^{\rho} g(\theta,r)\,dr;\ \bar{g}_+(\theta,\rho)=\int_1^{\infty} r^{\rho} g(\theta,r)\,dr. \tag{6}$$

This transform is applied to the equations of equilibrium, Hooke's law and to the boundary conditions. Reduction of the obtained system of equations results in the following boundary value problem:

$$X_+ = A(\rho)X_-(\rho)+A(\rho)S_+(\rho) \tag{7}$$

where

$$X_+(\rho)=\frac{4G}{1+\kappa}\begin{bmatrix}\bar{u}_{\theta,r+}(0,\rho)\\ \bar{u}_{r,r+}(0,\rho)\end{bmatrix};\ X_-(\rho)=\begin{bmatrix}\bar{\sigma}_{\theta-}(0,\rho)\\ \bar{\tau}_{r\theta-}(0,\rho)\end{bmatrix} \tag{8}$$

$$S_+(\rho)=\begin{bmatrix}\bar{\sigma}_{\theta+}(0,\rho)\\ \bar{\tau}_{r\theta+}(0,\rho)\end{bmatrix};\ A(\rho)=\begin{bmatrix}a_{11}(\rho) & a_{12}(\rho)\\ a_{21}(\rho) & a_{22}(\rho)\end{bmatrix} \tag{9}$$

G is the shear modulus. $\kappa = (3-\nu)/(1+\nu)$ in plane stress and $\kappa = (3-4\nu)$ in plane strain with ν denoting Poissons ratio.

The coefficients of the matrix $A(\rho)$ are given by

$$a_{11}(\rho)=\frac{\sin\rho\theta_1\cos\rho\theta_1+\rho\sin\theta_1\cos\theta_1}{D_1(\rho)}+\frac{\sin\rho\theta_2\cos\rho\theta_2+\rho\sin\theta_2\cos\theta_2}{D_2(\rho)}$$

$$a_{12}(\rho)=\rho(\rho-1)\left[\frac{\sin^2\theta_1}{D_1(\rho)}-\frac{\sin^2\theta_2}{D_2(\rho)}\right]$$

$$a_{21}(\rho)=\rho(\rho+1)\left[-\frac{\sin^2\theta_1}{D_1(\rho)}+\frac{\sin^2\theta_2}{D_2(\rho)}\right]$$

$$a_{22}(\rho)=\frac{\sin\rho\theta_1\cos\rho\theta_1-\rho\sin\theta_1\cos\theta_1}{D_1(\rho)}+\frac{\sin\rho\theta_2\cos\rho\theta_2-\rho\sin\theta_2\cos\theta_2}{D_2(\rho)} \tag{10}$$

with $D_i(\rho)=\rho^2\sin^2\theta_i-\sin^2\rho\theta_i$, $i=1,4$, and the restriction that $a_{11}(\rho)\neq a_{22}(\rho)$.

Equation (7) constitutes a nonhomogeneous Hilbert problem. It is valid along any arbitrary line $\Re\rho=\rho_0$ in the strip $\rho^*<\Re\rho<0$, where $\Re$ denotes the real part and ρ^* the largest of the negative zeros of the denominators $D_1(\rho)$ and $D_2(\rho)$.

After consideration of physical acceptable results, the solution to Eq. (7) is given by

$$X(\rho)=\frac{1}{2\pi i}H(\rho)\int_{\rho_0-i\infty}^{\rho_0+i\infty}\frac{1}{p-\rho}H_-^{-1}(\rho)S_+(p)\,dp \tag{11}$$

where $H(\rho)=H_{\pm}(\rho)$ is a piece-wise regular matrix with $H_+(\rho)$ regular in the half-plane $\Re\rho\geq\rho_0$ and $H_-(\rho)$ regular in the half-plane $\Re\rho\leq\rho_0$. $H_-^{-1}(\rho)$ denotes the inverse to $H_-(\rho)$. The problem is solved with the imaginary axes, i.e., the line $\Re\rho_0=0-$, chosen as the line of discontinuity.

4 Stress Intensity Factors at the Tip of the Kink

The stress intensity factors k_{I} and k_{II} at the tip of the kink are given by the limiting values

$$\begin{bmatrix}k_{\mathrm{I}}\\ k_{\mathrm{II}}\end{bmatrix}=\sqrt{2\pi}\lim_{r\to 1+0}\left\{\sqrt{r-1}\begin{bmatrix}\sigma_\theta(0,r)\\ \tau_{r\theta}(0,r)\end{bmatrix}\right\} \tag{12}$$

which implies, that k_{I} and k_{II} can be obtained directly from the transformed quantities through the relations

$$\begin{bmatrix}k_{\mathrm{I}}\\ k_{\mathrm{II}}\end{bmatrix}=i\sqrt{2}\lim_{\rho\to-\infty}\left\{|\rho|^{1/2}\begin{bmatrix}\bar{\sigma}_{\theta-}(0,\rho)\\ \bar{\tau}_{r\theta-}(0,\rho)\end{bmatrix}\right\}=i\sqrt{2}\lim_{\rho\to-\infty}[|\rho|^{1/2}X_-(\rho)] \tag{13}$$

i.e., only the limiting values as $|\rho|\to\infty$ are of interest. Insertion of $X_-(\rho)$, obtained from Eq. (11) gives

$$\begin{bmatrix}k_{\mathrm{I}}\\ k_{\mathrm{II}}\end{bmatrix}=-\frac{1}{\sqrt{2\pi}}\begin{bmatrix}\cos q & \sin q\\ -\sin q & \cos q\end{bmatrix}\int_{-i\infty}^{+i\infty}H_-^{-1}(p)S_+(p)\,dp \tag{14}$$

with q determined by the integral

$$q=\frac{1}{2\pi}\int_{-\infty}^{+\infty}\frac{\epsilon(i\tau)}{\sqrt{\operatorname{cosec}^2\theta_1+\tau^2}}\,d\tau \tag{15}$$

and

$$2\epsilon(i\tau)=\ln\left\{\frac{\sinh 2\tau\theta_1}{2D_1(i\tau)}+\frac{\sinh 2\tau\theta_2}{2D_2(i\tau)}+\left[\frac{\sin 2\theta_1}{2D_1(i\tau)}+\frac{\sin 2\theta_2}{2D_2(i\tau)}\right]\tau\sqrt{\operatorname{cosec}^2\theta_1+\tau^2}\tan\theta_1\right\}$$
$$-\ln\left\{\frac{\sinh 2\tau\theta_1}{2D_1(i\tau)}+\frac{\sinh 2\tau\theta_2}{2D_2(i\tau)}-\left[\frac{\sin 2\theta_1}{2D_1(i\tau)}+\frac{\sin 2\theta_2}{2D_2(i\tau)}\right]\tau\sqrt{\operatorname{cosec}^2\theta_1+\tau^2}\tan\theta_1\right\}. \tag{16}$$

After insertion of $S_+(\rho)$ in Eq. (14), the integral can be evaluated by taking the residual value at $p=-1/2$:

$$\begin{bmatrix}k_{\mathrm{I}}\\ k_{\mathrm{II}}\end{bmatrix}=\frac{-1}{2\pi^{3/2}}\begin{bmatrix}\cos q & \sin q\\ -\sin q & \cos q\end{bmatrix}\times H_-^{-1}(-1/2)\begin{bmatrix}\frac{1}{2}(1+\cos\alpha)\cos\frac{\alpha}{2}K_{\mathrm{I}}-\frac{3}{2}\sin\alpha\cos\frac{\alpha}{2}K_{\mathrm{II}}\\ \frac{1}{2}\sin\alpha\cos\frac{\alpha}{2}K_{\mathrm{I}}+\frac{1}{2}(3\cos\alpha-1)\cos\frac{\alpha}{2}K_{\mathrm{II}}\end{bmatrix} \tag{17}$$

where

$$H_-^{-1}(-1/2)=\Lambda_-^{-1/2}(-1/2)\left\{E\cosh\left[\sqrt{1+\frac{3}{4}\tan^2\theta_1}\,\beta_-(-1/2)\right]-B(-1/2)\frac{\sinh\left[\sqrt{1+\frac{3}{4}\tan^2\theta_1}\,\beta_-(-1/2)\right]}{\sqrt{1+\frac{3}{4}\tan^2\theta_1}}\right\}. \tag{18}$$

E denotes the 2×2 unit matrix and

$$B(-1/2)=\begin{bmatrix}1 & -\frac{3}{2}\tan\theta_1\\ -\frac{1}{2}\tan\theta_1 & 1\end{bmatrix} \tag{19}$$

Downloaded 03 May 2010 to 171.66.16.20. Redistribution subject to ASME license or copyright; see http://www.asme.org/terms/Terms_Use.cfm

Table 1 Values of the functions $R_{ij}(\alpha)$ that determine the stress intensity factors at the tip of an infinitesimal kink forming an angle α to the main crack

α	R_{11}	R_{12}	R_{21}	R_{22}
0	1.	0.	0.	1.
1	.9998857	−2.617781E-2	8.725816E-3	.9997622
2	.9995432	−5.234285E-2	1.744666E-2	.9990495
3	.9989724	−7.848238E-2	2.615756E-2	.9978619
4	.9981738	−.1045837	3.485356E-2	.9962006
5	.9971479	−.1306340	4.352972E-2	.9940667
6	.9958952	−.1566206	5.218108E-2	.9914613
7	.9944164	−.1825310	6.080276E-2	.9883870
8	.9927129	−.2083527	6.938987E-2	.9848456
9	.9907851	−.2340729	7.793754E-2	.9808394
10	.9886345	−.2596795	8.644097E-2	.9763714
11	.9862623	−.2851599	9.489535E-2	.9714449
12	.9836699	−.3105021	.1032959	.9660633
13	.9808590	−.3356938	.1116381	.9602303
14	.9778311	−.3607229	.1199170	.9539500
15	.9745883	−.3855777	.1281283	.9472271
16	.9711322	−.4102464	.1362673	.9400662
17	.9675651	−.4347172	.1443296	.9324721
18	.9635893	−.4589787	.1523107	.9244508
19	.9595065	−.4830195	.1602062	.9160069
20	.9552199	−.5068287	.1680121	.9071472
21	.9507316	−.5303948	.1757239	.8978775
22	.9460444	−.5537073	.1833376	.8882045
23	.9411609	−.5767556	.1908491	.8781347
24	.9360843	−.5995293	.1982546	.8676753
25	.9308172	−.6220178	.2055500	.8568337
26	.9253629	−.6442114	.2127317	.8456172
27	.9197244	−.6661000	.2197960	.8340335
28	.9139053	−.6876742	.2267392	.8220907
29	.9079087	−.7089247	.2335578	.8097973
30	.9017382	−.7298421	.2402485	.7971613
31	.8953973	−.7504176	.2468080	.7841920
32	.8888895	−.7706427	.2532330	.7708979
33	.8822187	−.7905088	.2595206	.7572880
34	.8753887	−.8100076	.2656676	.7433718
35	.8684033	−.8291317	.2716714	.7291589
36	.8612664	−.8478730	.2775292	.7146587
37	.8539820	−.8662244	.2832381	.6998811
38	.8465542	−.8841786	.2887959	.6848361
39	.8389872	−.9017289	.2942000	.6695340
30	.8312851	−.9188689	.2994483	.6539847
41	.8234521	−.9355922	.3045385	.6381990
42	.8154928	−.9518928	.3094686	.6221871
43	.8074110	−.9677650	.3142367	.6059601
44	.7992114	−.9832036	.3188410	.5895284
45	.7908983	−.9982030	.3232797	.5729030
46	.7824766	−1.012759	.3275516	.5560952
47	.7739500	−1.026867	.3316550	.5391153
48	.7653235	−1.040523	.3355885	.5219749
49	.7566018	−1.053723	.3393514	.5046851
50	.7477889	−1.066462	.3429421	.4872572
51	.7388897	−1.078739	.3463600	.4697023
52	.7299089	−1.090549	.3496042	.4520319
53	.7208509	−1.101891	.3526740	.4342573
54	.7117203	−1.112761	.3555690	.4163896
55	.7025218	−1.123159	.3582885	.3984407
56	.6932599	−1.133080	.3608325	.3804216
57	.6839392	−1.142526	.3632007	.3623438
58	.6745642	−1.151494	.3653929	.3442186
59	.6651397	−1.159982	.3674093	.3260573
60	.6556703	−1.167992	.3692501	.3078712
61	.6461603	−1.175522	.3709154	.2896716
62	.6366143	−1.182572	.3724058	.2714698
63	.6270368	−1.189142	.3737218	.2532769
64	.6174324	−2.295234	.3748640	.2351039
65	.6078054	−1.200848	.3758332	.2169619
66	.5981602	−1.205984	.3766300	.1988619
67	.5885013	−1.210645	.3772559	.1808146
68	.5788329	−1.214832	.3777114	.1628308
69	.5691593	−1.218547	.3779979	.1449214
70	.5594851	−1.221792	.3781169	.1270967
71	.5498140	−1.224569	.3780695	.1093671
72	.5401504	−1.226881	.3778572	9.174311E-2
73	.5304984	−1.228732	.3774819	7.423477E-2
74	.5208619	−1.230123	.3769448	5.685227E-2
75	.5112604	−1.231097	.3762593	3.960662E-2
76	.5016518	−1.231545	.3753933	2.250408E-2
77	.4920860	−1.231582	.3743826	5.557768E-3
78	.4825515	−1.231175	.3732181	−1.122402E-2
79	.4730519	−1.230329	.3719015	−2.783193E-2
80	.4636095	−1.229097	.3704501	−4.425862E-2

Table 1 Continued

81	.4541724	−1.227337	.3688219	−6.048987E-2
82	.4447998	−1.225202	.3670636	−7.652216E-2
83	.4354763	−1.222646	.3651625	−9.234505E-2
84	.4262055	−1.219676	.3631214	−.1079503
85	.4170122	−1.216358	.3609614	−.1233358
86	.4078357	−1.212514	.3586296	−.1384748
87	.3987428	−1.208333	.3561842	−.1533783
88	.3897156	−1.203762	.3536092	−.1680321
89	.3807569	−1.198806	.3509079	−.1824292
90	.3718838	−1.193511	.3480953	−.1965741

$H_-^{-1}(-1/2)$ further contains the following integrals:

$$\Lambda_-(-1/2)=\frac{1}{\sqrt{2}}\exp\left[-\frac{1}{4\pi}\int_0^\infty \frac{1}{\tau^2+\frac{1}{4}}\ln|\Delta(i\tau)|\,d\tau\right] \tag{20}$$

$$\beta_-(-1/2)=-\frac{1}{2\pi}\cot\theta_1\int_0^\infty \frac{\epsilon(i\tau)}{\left(\tau^2+\frac{1}{4}\right)\sqrt{\operatorname{cosec}^2\theta_1+\tau^2}}\,d\tau \tag{21}$$

with $\epsilon(i\tau)$ according to Eq. (16) and

$$\Delta(i\tau)=-\left[\frac{\sinh 2\tau\theta_1+\tau\sin 2\theta_1}{2D_1(i\tau)}+\frac{\sinh 2\tau\theta_2+\tau\sin 2\theta_2}{2D_2(i\tau)}\right]\times\left[\frac{\sinh 2\tau\theta_1-\tau\sin 2\theta_1}{2D_1(i\tau)}+\frac{\sinh 2\tau\theta_2-\tau\sin 2\theta_2}{2D_2(i\tau)}\right]+\tau^2(\tau^2+1)\left[\frac{1-\cos 2\theta_1}{2D_1(i\tau)}-\frac{1-\cos 2\theta_2}{2D_2(i\tau)}\right] \tag{22}$$

$2D_j(i\tau)=\cosh 2\tau\theta_j-2\tau^2\sin^2\theta_j-1,\ j=1,2.$

The integrals can be calculated numerically with any desired degree of accuracy. Thus the stress intensity factors k_I and k_{II} at the tip of the kink are expressed as functions of the stress intensity factors K_I and K_{II} of the main crack as

$$\begin{cases}k_I=R_{11}(\alpha)K_I+R_{12}(\alpha)K_{II}\\ k_I=R_{21}(\alpha)K_I+R_{22}(\alpha)K_{II}\end{cases} \tag{23}$$

where α is the angle between the kink and the main crack.

5 Results

The functions $R_{ij}(\alpha)$ of relations (23), determining the stress intensity factors at the tip of the kink, are listed in Table 1 for values of α in the interval $0 \le \alpha \le 90$ deg.

In the case of pure mode I loading, i.e., $K_{II}=0$, k_I and k_{II} are determined by $R_{II}(\alpha)$ and $R_{21}(\alpha)$. In this case k_I decreases monotonically with increasing α whereas k_{II} has a maximum $k_{II}\approx .378121\ K_I$ at $\alpha\approx 70.22$ deg.

For the case of pure mode II loading, k_I and k_{II} are determined by $R_{12}(\alpha)$ and $R_{22}(\alpha)$ since $K_I=0$. The maximum value of k_I, approximately $1.23162\,|K_{II}|$, is obtained for a kink angle $\alpha\approx 76.58$ deg. The mode II stress intensity factor k_{II} increases monotonically with α and passes through zero at $\alpha\approx 77.3301$ deg. This result agrees with Bilby et al. (1975, 1977), although it is here more accurately determined.

The values of $R_{ij}(\alpha)$ might be useful for control and estimate of the accuracy of other methods, dealing with curved cracks.

References

Bilby, B. A., and Cardew, G. E., 1975, *International Journal of Fracture*, Vol. 11, pp. 708–712.

Downloaded 03 May 2010 to 171.66.16.20. Redistribution subject to ASME license or copyright; see http://www.asme.org/terms/Terms_Use.cfm

Bilby, B. A., Cardew, G. E., and Howard, I. C., 1977, *Fracture 1977*, Vol. 3, ICF4, Waterloo, Canada, June 19–24.
Khrapkov, A. A., 1971, *International Journal of Fracture*, Vol. 7, pp. 373–382.
Melin, S., 1985, "The Infinitesimal Kink," Report from Division of Solid Mechanics, Lund, Sweden.

On the Use of Variational Principles to Derive Beam Boundary Conditions

Hui Fan[2] and G. E. O. Widera[3]

1 Introduction

Almost all engineering type beam theories have, as their basis, a variational principle from which the control equations and corresponding boundary conditions can be obtained. The difference between the exact elasticity theory and the variationally derived one is minimized under energy meanings. In a previous paper by the authors (Fan and Widera, 1992), a formal asymptotic expansion procedure was developed for a beam from which the expansions which are valid in the interior region (outer expansion) and boundary layers (inner expansion) can be obtained. The proper boundary conditions for the outer expansion were derived without a consideration of the inner solution by adopting Gregory and Wan's technique (1984). There have been previous attempts (see, for example, Fan, 1989) to derive the outer expansion boundary conditions through use of a variational principle. In the following, several of these principles are considered and it will be shown that the boundary conditions given in Fan and Widera (1992) cannot all be derived by the application of variational principles.

The nomenclature and notation employed in Fan and Widera (1992) as well as some of the results obtained there will be made use of in the following.

2 Derivation of Boundary Conditions

For the case where only stress components are prescribed (Case A of Fan and Widera, 1992) at the end plane, the Theorem of Minimum Potential Energy is employed to derive the boundary conditions for the outer expansion. From (see Washizu, 1975)

$$\Pi_v = \int_D W(v_{i,j})dV - \int_{\partial D_t} \bar{t}_i v_i dA = MIN$$

where $W(v_{i,j})$ is the strain energy density in terms of the derivatives of the displacements, we obtain

$$\int_{S_0} (\tau_{3i}^e - \bar{\tau}_{3i})\delta v_i dA = 0 \tag{1}$$

where here and hereafter the superscript e represents the expansion solution and a bar the prescribed data. Not having employed the decay analysis given in Fan and Widera (1992), previous authors (see, for example, Logan and Widera (1980) and Widera and Fan (1988)) employed the outer expansion to obtain the variations δv_i:

$$\delta v_1^{(n)} = \frac{\nu}{2}(x_1^2 - x_2^2)\delta d_{,33}^{(n-2)}(x_3) + \delta d^{(n)}(x_3) \tag{2a}$$

$$\delta v_2^{(n)} = \nu x_1 x_2 \delta d_{,33}^{(n-2)}(x_3) \tag{2b}$$

$$\delta v_3^{(n)} = \chi(x_1, x_2)\delta d_{,333}^{(n-2)}(x_3) - x_1 \delta d_{,3}^{(n)}(x_3). \tag{2c}$$

Substituting (2) into (1), one obtains

$$\int_{S_0} (\tau_{31}^e - \bar{\tau}_{31})dA = 0 \tag{3a}$$

$$\int_{S_0} x_1(\tau_{33}^e - \bar{\tau}_{33})dA = 0. \tag{3b}$$

Equations (3*a*, *b*) are well-known forms which correspond to shear force and moment balance, respectively. They are identical to the results of the decay analysis (Fan and Widera, 1992, Eqs. (34) and (37)).

Next, use is made of the Theorem of Complementary Energy to discuss displacement conditions (Case D of Fan and Widera, 1992). From

$$\Pi_\tau = \int_D W(\tau_{ij})dV - \int_{\partial D_v} t_i \bar{v}_i dA = MIN$$

we have

$$\int_{S_0} (v_i^e - \bar{v}_i)\delta t_i dA = 0. \tag{4}$$

Setting $\delta\Pi_\tau = 0$ is incontroversial, as one uses the variations of the outer expansion as stress variations. One thus obtains

$$\int_{S_0} \left\{ (v_1^e - \bar{v}_1)\left[\frac{\nu}{2}(x_1^2 - x_2^2) + \chi_{,1}\right] + (v_2^e - \bar{v}_2)(\nu x_1 x_2 + \chi_{,2}) \right\} dA = 0 \tag{5a}$$

$$\int_{S_0} x_1(v_3^e - \bar{v}_3)dA = 0. \tag{5b}$$

Apparently, these boundary conditions for displacement data have a different meaning than those of Eqs. (47) and (49) of Fan and Widera (1992), which were obtained by the use of decay analysis.

Recall that the St. Venant solutions are used in the mixed data cases (Cases B and C of Fan and Widera, 1992). One may thus expect that a variational principle would yield the proper boundary conditions for these prescribed data. The Reissner variational principle

$$\delta\Pi_R = \delta\left[\int_D (v_{i,j}\tau_{ij} - W(\tau_{ij}))dV - \int_{\partial D_t} v_i \bar{t}_i dA + \int_{\partial D_v} t_i(v_i - \bar{v}_i)dA \right]$$

is adopted here for these two cases.

For Case B, one has

$$\int_{S_0} \{(\tau_{3\alpha}^e - \bar{\tau}_{3\alpha})\delta v_\alpha - (v_3^e - \bar{v}_3)\delta\tau_{33}\} dA = 0. \tag{6}$$

As previously mentioned, the variation of the displacement and stress are taken in the outer expansion thusly:

$$\delta v_1^{(n)} = \frac{\nu}{2}(x_1^2 - x_2^2)\delta d_{,33}^{(n-2)}(x_3) + \delta d^{(n)}(x_3) \tag{7a}$$

$$\delta v_2^{(n)} = \nu x_1 x_2 \delta d_{,33}^{(n-2)}(x_3) \tag{7b}$$

$$\delta\tau_{33}^{(n)}(x_3) = -x_1 \delta d_{,33}^{(n)}(x_3). \tag{7c}$$

[2]Nanyang Technological University, Singapore 2263. Assoc. Mem. ASME.
[3]Mechanical and Industrial Engineering Department, Marquette University, Milwaukee, WI 53233. Fellow ASME.

Contributed by the Applied Mechanics Division of THE AMERICAN SOCIETY OF MECHANICAL ENGINEERS for publication in the ASME JOURNAL OF APPLIED MECHANICS. Manuscript received by the ASME Applied Mechanics Division, Aug. 20, 1990; final revision, April 12, 1993. Associate Technical Editor: F. Y. M. Fan.

Downloaded 03 May 2010 to 171.66.16.20. Redistribution subject to ASME license or copyright; see http://www.asme.org/terms/Terms_Use.cfm

Bilby, B. A., Cardew, G. E., and Howard, I. C., 1977, *Fracture 1977*, Vol. 3, ICF4, Waterloo, Canada, June 19–24.

Khrapkov, A. A., 1971, *International Journal of Fracture*, Vol. 7, pp. 373–382.

Melin, S., 1985, "The Infinitesimal Kink," Report from Division of Solid Mechanics, Lund, Sweden.

On the Use of Variational Principles to Derive Beam Boundary Conditions

Hui Fan[2] and G. E. O. Widera[3]

1 Introduction

Almost all engineering type beam theories have, as their basis, a variational principle from which the control equations and corresponding boundary conditions can be obtained. The difference between the exact elasticity theory and the variationally derived one is minimized under energy meanings. In a previous paper by the authors (Fan and Widera, 1992), a formal asymptotic expansion procedure was developed for a beam from which the expansions which are valid in the interior region (outer expansion) and boundary layers (inner expansion) can be obtained. The proper boundary conditions for the outer expansion were derived without a consideration of the inner solution by adopting Gregory and Wan's technique (1984). There have been previous attempts (see, for example, Fan, 1989) to derive the outer expansion boundary conditions through use of a variational principle. In the following, several of these principles are considered and it will be shown that the boundary conditions given in Fan and Widera (1992) cannot all be derived by the application of variational principles.

The nomenclature and notation employed in Fan and Widera (1992) as well as some of the results obtained there will be made use of in the following.

2 Derivation of Boundary Conditions

For the case where only stress components are prescribed (Case A of Fan and Widera, 1992) at the end plane, the Theorem of Minimum Potential Energy is employed to derive the boundary conditions for the outer expansion. From (see Washizu, 1975)

$$\Pi_v = \int_D W(v_{i,j})dV - \int_{\partial D_t} \bar{t}_i v_i dA = MIN$$

where $W(v_{i,j})$ is the strain energy density in terms of the derivatives of the displacements, we obtain

$$\int_{S_0} (\tau^e_{3i} - \bar{\tau}_{3i})\delta v_i dA = 0 \tag{1}$$

where here and hereafter the superscript e represents the expansion solution and a bar the prescribed data. Not having employed the decay analysis given in Fan and Widera (1992), previous authors (see, for example, Logan and Widera (1980) and Widera and Fan (1988)) employed the outer expansion to obtain the variations δv_i:

$$\delta v_1^{(n)} = \frac{\nu}{2}(x_1^2 - x_2^2)\delta d_{,33}^{(n-2)}(x_3) + \delta d^{(n)}(x_3) \tag{2a}$$

$$\delta v_2^{(n)} = \nu x_1 x_2 \delta d_{,33}^{(n-2)}(x_3) \tag{2b}$$

$$\delta v_3^{(n)} = \chi(x_1, x_2)\delta d_{,333}^{(n-2)}(x_3) - x_1 \delta d_{,3}^{(n)}(x_3). \tag{2c}$$

Substituting (2) into (1), one obtains

$$\int_{S_0} (\tau^e_{31} - \bar{\tau}_{31})dA = 0 \tag{3a}$$

$$\int_{S_0} x_1(\tau^e_{33} - \bar{\tau}_{33})dA = 0. \tag{3b}$$

Equations (3*a*, *b*) are well-known forms which correspond to shear force and moment balance, respectively. They are identical to the results of the decay analysis (Fan and Widera, 1992, Eqs. (34) and (37)).

Next, use is made of the Theorem of Complementary Energy to discuss displacement conditions (Case D of Fan and Widera, 1992). From

$$\Pi_\tau = \int_D W(\tau_{ij})dV - \int_{\partial D_v} t_i \bar{v}_i dA = MIN$$

we have

$$\int_{S_0} (v_i^e - \bar{v}_i)\delta t_i dA = 0. \tag{4}$$

Setting $\delta\Pi_\tau = 0$ is incontroversial, as one uses the variations of the outer expansion as stress variations. One thus obtains

$$\int_{S_0} \left\{ (v_1^e - \bar{v}_1)\left[\frac{\nu}{2}(x_1^2 - x_2^2) + \chi_{,1}\right] + (v_2^e - \bar{v}_2)(\nu x_1 x_2 + \chi_{,2}) \right\} dA = 0 \tag{5a}$$

$$\int_{S_0} x_1(v_3^e - \bar{v}_3)dA = 0. \tag{5b}$$

Apparently, these boundary conditions for displacement data have a different meaning than those of Eqs. (47) and (49) of Fan and Widera (1992), which were obtained by the use of decay analysis.

Recall that the St. Venant solutions are used in the mixed data cases (Cases B and C of Fan and Widera, 1992). One may thus expect that a variational principle would yield the proper boundary conditions for these prescribed data. The Reissner variational principle

$$\delta\Pi_R = \delta\left[\int_D (v_{i,j}\tau_{ij} - W(\tau_{ij}))dV - \int_{\partial D_t} v_i \bar{t}_i dA + \int_{\partial D_v} t_i(v_i - \bar{v}_i)dA \right]$$

is adopted here for these two cases.

For Case B, one has

$$\int_{S_0} \{(\tau^e_{3\alpha} - \bar{\tau}_{3\alpha})\delta v_\alpha - (v_3^e - \bar{v}_3)\delta\tau_{33}\} dA = 0. \tag{6}$$

As previously mentioned, the variation of the displacement and stress are taken in the outer expansion thusly:

$$\delta v_1^{(n)} = \frac{\nu}{2}(x_1^2 - x_2^2)\delta d_{,33}^{(n-2)}(x_3) + \delta d^{(n)}(x_3) \tag{7a}$$

$$\delta v_2^{(n)} = \nu x_1 x_2 \delta d_{,33}^{(n-2)}(x_3) \tag{7b}$$

$$\delta\tau_{33}^{(n)}(x_3) = -x_1 \delta d_{,33}^{(n)}(x_3). \tag{7c}$$

[2]Nanyang Technological University, Singapore 2263. Assoc. Mem. ASME.

[3]Mechanical and Industrial Engineering Department, Marquette University, Milwaukee, WI 53233. Fellow ASME.

Contributed by the Applied Mechanics Division of THE AMERICAN SOCIETY OF MECHANICAL ENGINEERS for publication in the ASME JOURNAL OF APPLIED MECHANICS. Manuscript received by the ASME Applied Mechanics Division, Aug. 20, 1990; final revision, April 12, 1993. Associate Technical Editor: F. Y. M. Fan.

Copyright © 1994 by ASME

Downloaded 03 May 2010 to 171.66.16.20. Redistribution subject to ASME license or copyright; see http://www.asme.org/terms/Terms_Use.cfm

With these variations, (6) yields

$$\int_{S_0} (\tau_{31}^e - \bar{\tau}_{31}) dA = 0 \tag{8a}$$

and

$$\int_{S_0} \left[(v_3^e - \bar{v}_3) x_1 + \epsilon \frac{\nu}{2} (x_1^2 - x_2^2)(\tau_{31}^e - \bar{\tau}_{31}) + \epsilon \nu x_1 x_2 (\tau_{32}^e - \bar{\tau}_{32}) \right] dA = 0. \tag{8b}$$

The other mixed data, Case C, is formulated in a similar way. Here, we have

$$\int_{S_0} \{(\tau_{33}^e - \bar{\tau}_{33}) \delta v_3 - (v_\alpha^e - \bar{v}_\alpha) \delta \tau_{3\alpha}\} dA = 0. \tag{9}$$

The variations in the form of the outer expansion then provide

$$\int_{S_0} x_1 (\tau_{33}^e - \bar{\tau}_{33}) dA = 0 \tag{10a}$$

$$\int_{S_0} \left[(v_1^e - \bar{v}_1) \left(\frac{\nu}{2} (x_1^2 - x_2^2) + \chi_{,1} \right) + (v_2^e - \bar{v}_2)(\nu x_1 x_2 + \chi_{,2}) - 2(1+\nu)\epsilon \chi (\tau_{33}^e - \bar{\tau}_{33}) \right] dA = 0. \tag{10b}$$

Comparing (8) with Eqs. (38) and (41) of Fan and Widera (1992), and (10) with (43) and (45) of the same paper, one notices that, in the mixed data cases, the Reissner variational principle provides the same conditions for the outer expansion as does the decay analysis.

3 Conclusion

All the preceding formulations can be summarized as follows: The use of variational principles provides the correct boundary conditions for the mixed data (Cases B and C) as well as for the stress data cases, where one obtains the desired conditions (3). As for the displacements prescribed case, Eq. (5) derived by use of a variational principle is not consistent with that obtained from decay analysis (Fan and Widera, 1992). The authors are not aware of anyone having determined an estimate for the error introduced by using Eq. (5).

Usually, refined theories derived from variational principles are compared with elasticity theory solutions having prescribed stress data boundary conditions. The comparison for these conditions is generally fairly good. A much larger difference results if displacement data is prescribed. This was shown in a numerical example by Gregory and Wan (1984) where the use of a variational principle based plate theory yielded an unacceptable error for all boundaries for which displacement data is prescribed.

In papers by Gregory and Wan (1984) and the present authors (1992) the correct boundary conditions for displacement data have been formulated for the problems of a plane strain strip and for a circular cross-section beam, respectively. The procedure employed in these papers does not, however, recommend itself for engineering applications. It is a rather unfortunate fact that variational principle based plate (beam) theories are easily used without needing to consider the three-dimensional solution; an unknown error is, however, introduced when displacement prescribed conditions are present. On the other hand, decay analysis provides the correct condition for the displacement data, but the gap between this formulation and engineering applications is too wide to bridge given the present stage of research in this field.

References

Fan, H., 1989, "On the Foundations of Beam Theory," Ph.D. Dissertation, University of Illinois at Chicago, Chicago, IL.

Fan, H., and Widera, G. E. O., 1992, "On the Proper Boundary Conditions for Beam Theory," ASME Journal of Applied Mechanics, Vol. 59, pp. 915–922.

Gregory, R. D., and Wan, F. Y. M., 1984, "Decaying States of Plane Strain in a Semi-Infinite Strip and Boundary Conditions for Plate Theory," *J. Elasticity*, Vol. 14, pp. 27–64.

Logan, D., and Widera, G. E. O., 1980, "Refined Theories for Nonhomogeneous Anisotropic Cylindrical Shells: Part I—Derivation," *J. Engineering Mechanics Div. ASCE*, Vol. 106, No. EM6, pp. 1053–1074.

Washizu, K., 1975, *Variational Methods in Elasticity and Plasticity*, 2nd ed., Pergamon Press.

Widera, G. E. O., and Fan, H., 1988, "On the Asymptotic Formulation for Plates and Shells," *Computational Mechanics '88*, Vol. 1, Springer-Verlag, New York.

APPENDIX

(1) St. Venant bending solution

$$U_1 = \frac{1}{2}[x_3^2 + \epsilon^2 \nu (x_1^2 - x_2^2)]$$
$$U_2 = \nu \epsilon^2 x_1 x_2$$
$$U_3 = -\epsilon x_1 x_2$$
$$\tau_{\alpha\beta} = 0, \quad \tau_{3\alpha} = 0$$
$$\tau_{33} = -\epsilon x_1. \tag{A1}$$

(2) St. Venant flexure solution

$$U_1 = -\frac{x_3^3}{6} + k_1 x_3 = \epsilon^2 \left[-\frac{\nu}{2} (x_1^2 - x_2^2) x_3 \right]$$
$$U_2 = \epsilon^2 \nu x_1 x_2 x_3$$
$$U_3 = \epsilon x_1 \left[\frac{c_3^2}{6} - k_1 \right] - \epsilon^2 \chi(x_1, x_2)$$
$$\tau_{\beta\alpha} = 0$$
$$\tau_{31} = \frac{\epsilon^2}{2(1+\nu)} \left[\frac{\nu}{2} (x_1^2 - x_2^2) + \chi_{,1} \right]$$
$$\tau_{32} = \frac{\epsilon^2}{2(1+\nu)} (\nu x_1 x_2 + \chi_{,2})$$
$$\tau_{33} = -x_1 \ell \epsilon. \tag{A2}$$

On the Double Cantilever Beam Specimen for Mode-I Interface Delamination

B. Balendran[4]

A compliance model is presented for a DCB specimen for mode-I interface delamination. The undelaminated part of the specimen is modeled by using Reissner's mixed variational principle from which the rotation of the cross-section at the

[4]Center of Excellence for Advanced Materials, Department of Advanced Materials, Department of Applied Mechanics and Engineering Sciences, University of California, San Diego, La Jolla, CA 92093-0411.

Contributed by the Applied Mechanics Division of The American Society of Mechanical Engineers for publication in the ASME Journal of Applied Mechanics. Manuscript received by the ASME Applied Mechanics Division, Aug. 30, 1991; final revision, Apr. 13, 1993. Associate Technical Editor: M. E. Fourney.

Downloaded 03 May 2010 to 171.66.16.20. Redistribution subject to ASME license or copyright; see http://www.asme.org/terms/Terms_Use.cfm

With these variations, (6) yields

$$\int_{S_0} (\tau_{31}^e - \bar{\tau}_{31}) dA = 0 \tag{8a}$$

and

$$\int_{S_0} \left[(v_3^e - \bar{v}_3) x_1 + \epsilon \frac{\nu}{2} (x_1^2 - x_2^2)(\tau_{31}^e - \bar{\tau}_{31}) + \epsilon \nu x_1 x_2 (\tau_{32}^e - \bar{\tau}_{32}) \right] dA = 0. \tag{8b}$$

The other mixed data, Case C, is formulated in a similar way. Here, we have

$$\int_{S_0} \{(\tau_{33}^e - \bar{\tau}_{33}) \delta v_3 - (v_\alpha^e - \bar{v}_\alpha) \delta \tau_{3\alpha}\} dA = 0. \tag{9}$$

The variations in the form of the outer expansion then provide

$$\int_{S_0} x_1 (\tau_{33}^e - \bar{\tau}_{33}) dA = 0 \tag{10a}$$

$$\int_{S_0} \left[(v_1^e - \bar{v}_1) \left(\frac{\nu}{2} (x_1^2 - x_2^2) + \chi_{,1} \right) + (v_2^e - \bar{v}_2)(\nu x_1 x_2 + \chi_{,2}) - 2(1+\nu)\epsilon \chi (\tau_{33}^e - \bar{\tau}_{33}) \right] dA = 0. \tag{10b}$$

Comparing (8) with Eqs. (38) and (41) of Fan and Widera (1992), and (10) with (43) and (45) of the same paper, one notices that, in the mixed data cases, the Reissner variational principle provides the same conditions for the outer expansion as does the decay analysis.

3 Conclusion

All the preceding formulations can be summarized as follows: The use of variational principles provides the correct boundary conditions for the mixed data (Cases B and C) as well as for the stress data cases, where one obtains the desired conditions (3). As for the displacements prescribed case, Eq. (5) derived by use of a variational principle is not consistent with that obtained from decay analysis (Fan and Widera, 1992). The authors are not aware of anyone having determined an estimate for the error introduced by using Eq. (5).

Usually, refined theories derived from variational principles are compared with elasticity theory solutions having prescribed stress data boundary conditions. The comparison for these conditions is generally fairly good. A much larger difference results if displacement data is prescribed. This was shown in a numerical example by Gregory and Wan (1984) where the use of a variational principle based plate theory yielded an unacceptable error for all boundaries for which displacement data is prescribed.

In papers by Gregory and Wan (1984) and the present authors (1992) the correct boundary conditions for displacement data have been formulated for the problems of a plane strain strip and for a circular cross-section beam, respectively. The procedure employed in these papers does not, however, recommend itself for engineering applications. It is a rather unfortunate fact that variational principle based plate (beam) theories are easily used without needing to consider the three-dimensional solution; an unknown error is, however, introduced when displacement prescribed conditions are present. On the other hand, decay analysis provides the correct condition for the displacement data, but the gap between this formulation and engineering applications is too wide to bridge given the present stage of research in this field.

References

Fan, H., 1989, "On the Foundations of Beam Theory," Ph.D. Dissertation, University of Illinois at Chicago, Chicago, IL.

Fan, H., and Widera, G. E. O., 1992, "On the Proper Boundary Conditions for Beam Theory," ASME Journal of Applied Mechanics, Vol. 59, pp. 915–922.

Gregory, R. D., and Wan, F. Y. M., 1984, "Decaying States of Plane Strain in a Semi-Infinite Strip and Boundary Conditions for Plate Theory," *J. Elasticity*, Vol. 14, pp. 27–64.

Logan, D., and Widera, G. E. O., 1980, "Refined Theories for Nonhomogeneous Anisotropic Cylindrical Shells: Part I—Derivation," *J. Engineering Mechanics Div. ASCE*, Vol. 106, No. EM6, pp. 1053–1074.

Washizu, K., 1975, *Variational Methods in Elasticity and Plasticity*, 2nd ed., Pergamon Press.

Widera, G. E. O., and Fan, H., 1988, "On the Asymptotic Formulation for Plates and Shells," *Computational Mechanics '88*, Vol. 1, Springer-Verlag, New York.

APPENDIX

(1) St. Venant bending solution

$$U_1 = \frac{1}{2}[x_3^2 + \epsilon^2 \nu (x_1^2 - x_2^2)]$$
$$U_2 = \nu \epsilon^2 x_1 x_2$$
$$U_3 = -\epsilon x_1 x_2$$
$$\tau_{\alpha\beta} = 0, \quad \tau_{3\alpha} = 0$$
$$\tau_{33} = -\epsilon x_1. \tag{A1}$$

(2) St. Venant flexure solution

$$U_1 = -\frac{x_3^3}{6} + k_1 x_3 = \epsilon^2 \left[-\frac{\nu}{2} (x_1^2 - x_2^2) x_3 \right]$$
$$U_2 = \epsilon^2 \nu x_1 x_2 x_3$$
$$U_3 = \epsilon x_1 \left[\frac{c_3^2}{6} - k_1 \right] - \epsilon^2 \chi(x_1, x_2)$$
$$\tau_{\beta\alpha} = 0$$
$$\tau_{31} = \frac{\epsilon^2}{2(1+\nu)} \left[\frac{\nu}{2} (x_1^2 - x_2^2) + \chi_{,1} \right]$$
$$\tau_{32} = \frac{\epsilon^2}{2(1+\nu)} (\nu x_1 x_2 + \chi_{,2})$$
$$\tau_{33} = -x_1 \ell \epsilon. \tag{A2}$$

On the Double Cantilever Beam Specimen for Mode-I Interface Delamination

B. Balendran[4]

A compliance model is presented for a DCB specimen for mode-I interface delamination. The undelaminated part of the specimen is modeled by using Reissner's mixed variational principle from which the rotation of the cross-section at the

[4]Center of Excellence for Advanced Materials, Department of Advanced Materials, Department of Applied Mechanics and Engineering Sciences, University of California, San Diego, La Jolla, CA 92093-0411.

Contributed by the Applied Mechanics Division of The American Society of Mechanical Engineers for publication in the ASME Journal of Applied Mechanics. Manuscript received by the ASME Applied Mechanics Division, Aug. 30, 1991; final revision, Apr. 13, 1993. Associate Technical Editor: M. E. Fourney.

Copyright © 1994 by ASME
Downloaded 03 May 2010 to 171.66.16.20. Redistribution subject to ASME license or copyright; see http://www.asme.org/terms/Terms_Use.cfm

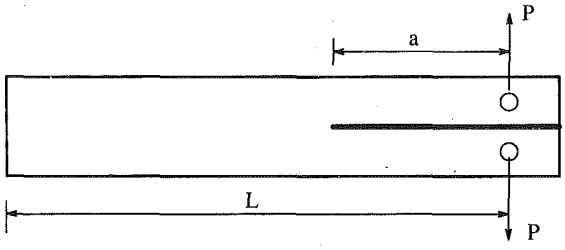


Fig. 1 Double cantilever beam specimen

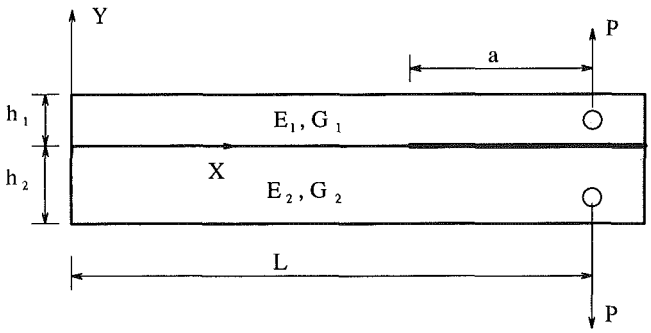


Fig. 2 Double cantilever beam specimen for interface delamination

tip of the crack and the shear stress at the interface are evaluated. The results for a homogeneous beam with midplane crack are deduced and shown to be in better agreement with the experimental and finite element results than any of the existing models.

1 Introduction

The double cantilever beam (DCB) specimen has been used extensively to evaluate the mode-I critical strain energy release rate (G_{Ic}) of a crack in homogeneous materials (see Fig. 1). The critical strain energy release rate is related to the critical load and the compliance by

$$G_{Ic}=\frac{P_c^2}{2B}\frac{dC}{da}, \tag{1}$$

where C is the compliance function, P_c is the critical load, a is the crack length, and B is the width of the beam. The critical load is obtained from experiments. This method requires an expression relating the specimen compliance to the crack length. (See Davies and Benzeggagh (1989) for a complete review of the existing models relating compliance to the crack length.) They show that the results for the compliance and the critical strain energy release rate, obtained from all the existing models, differ considerably from those obtained experimentally for highly orthotropic materials such as glass/epoxy, where the Young's modulus in the axial direction is about ten times higher than the transverse shear modulus. Most of the existing models treat each arm of the specimen as a built-in cantilever beam of length equal to the length of the crack. The rotation of the cross-sections at the tip of the crack is neglected in these models. However, in highly orthotropic materials, the effect of shear deformation is significant, and hence the rotation of the cross-sections at the tip of the crack is crucial in determining the compliance of the specimen. This rotation can be obtained only by considering the undelaminated part of the specimen also in the analysis.

In this paper we consider a bicomposite cantilever beam specimen with an initial interface delamination on the free end to evaluate the critical strain energy release rate at the interface (see Fig. 2). The delaminated parts of the specimen are modeled by Timoshenko beam theory. The undelaminated part of the specimen is modeled by using Reissner's (1984) mixed variational principle. The compliance function and an expression for strain energy release rate are derived. The results are reduced for a homogeneous specimen with a midplane crack and are compared with existing models.

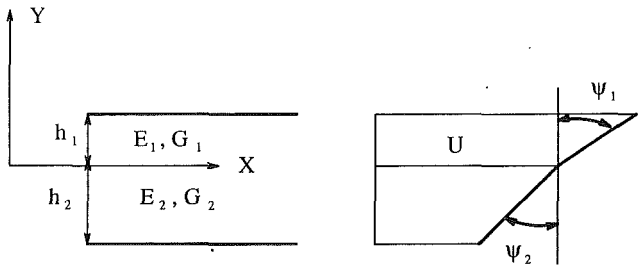


Fig. 3 Assumed displacement field in the undelaminated part of the specimen

2 Compliance Model for a Bicomposite Beam

First we consider the bending of a bicomposite beam of unit width to model the undelaminated part of the specimen. Axial displacement is assumed to be linear across the thickness in each beam. Continuity of the displacement at the interface is imposed. The transverse displacement is assumed to be a constant across the thickness. The assumed displacement field is (see Fig. 3)

$$u_i(x, y)=U(x)+y\psi_i(x), \quad v(x, y)=V(x), \quad i=1, 2. \tag{2a,b}$$

The subscript or superscript 1 and 2 denote the beam at top and bottom, respectively. The nonvanishing strain components are then given by

$$\epsilon_{xx}^i=\frac{dU}{dx}+y\frac{d\psi_i}{dx}, \quad \gamma_{xy}^i=\psi_i+\frac{dV}{dx} \quad i=1, 2. \tag{3a,b}$$

Constitutive equations are in the form

$$\sigma_{xx}^i=E_i\epsilon_{xx}^i, \quad \sigma_{xy}^i=G_i\gamma_{xy}^i, \quad i=1, 2. \tag{4a,b}$$

The trial transverse stresses are assumed to be in the form

$$\sigma_{yy}^1=\sigma_{yy}^2=0,$$

$$\sigma_{xy}^1=\frac{\tau}{h_1^2}(y-h_1)(3y-h_1)-\frac{6Q_1}{h_1^3}y(y-h_1),$$

$$\sigma_{xy}^2=\frac{\tau}{h_2^2}(y+h_2)(3y+h_2)-\frac{6Q_2}{h_2^3}y(y+h_2), \tag{5a-d}$$

where τ is the interface shear stress and Q_i is the shear force in the beam i, $i=1, 2$. Introducing these trial displacement field and the transverse shear stresses in the Reissner's mixed variational principle, and using the boundary condition for the problem in Fig. 2, the displacement field, the transverse shear forces and the interface shear stress in the undelaminated part of the specimen ($0<x<b$, $b\equiv L-a$) are obtained as

$$\psi_1=-P\frac{D_1a\alpha}{1+\beta}\frac{\cosh\alpha x}{\sinh\alpha b}, \quad \psi_2=P\frac{\beta D_1a\alpha}{1+\beta}\frac{\cosh\alpha x}{\sinh\alpha b},$$

$$Q_1=-Pa\alpha\frac{\cosh\alpha x}{\sinh\alpha b}, \quad Q_2=Pa\alpha\frac{\cosh\alpha x}{\sinh\alpha b},$$

$$\tau=P\frac{3(G_1-G_2)a\alpha}{4(G_1h_2+G_2h_1)}\frac{\cosh\alpha x}{\sinh\alpha b}, \quad V=PD_2a\frac{\sinh\alpha x}{\sinh\alpha b},$$

$$U=P\frac{(E_1h_1^2+\beta E_2h_2^2)}{2(E_1h_1+E_2h_2)}\frac{D_1a\alpha}{1+\beta}\frac{(\cosh\alpha x-1)}{\sinh\alpha b},$$

for $0<x<b$ (6a-g)

Downloaded 03 May 2010 to 171.66.16.20. Redistribution subject to ASME license or copyright; see http://www.asme.org/terms/Terms_Use.cfm

where

$$D_1=\frac{6}{5}\left(\frac{1}{G_1h_1}+\frac{1}{G_2h_2}\right)-\frac{3}{40}\frac{(G_1-G_2)^2}{G_1G_2(G_1h_2+G_2h_1)},$$

$$\alpha=\sqrt{\frac{(C_{11}+C_{22}+2C_{12})}{D_1(C_{11}C_{22}-C_{12}^2)}},\quad \beta=\frac{C_{11}+C_{12}}{C_{22}+C_{12}},$$

$$C_{11}=\frac{E_1h_1^3}{12}\frac{(E_1h_1+4E_2h_2)}{(E_1h_1+E_2h_2)},\quad C_{22}=\frac{E_2h_2^3}{12}\frac{(E_2h_2+4E_1h_1)}{(E_1h_1+E_2h_2)},$$

$$C_{12}=\frac{E_1E_2h_1^2h_2^2}{4(E_1h_1+E_2h_2)},$$

$$D_2=\frac{D_1}{1+\beta}-\frac{6}{5G_2h_2}+\frac{3}{40}\frac{G_1-G_2}{G_2(G_1h_2+G_2h_1)}. \qquad (7a\text{-}g)$$

Knowing the rotation and the transverse displacements at the tip of the crack, the transverse displacements at the free end can be obtained from a Timoshenko beam theory. Hence the compliance and the critical strain energy release rate for the specimen can be obtained as

$$C=\frac{6a}{5B}\left(\frac{1}{G_1h_1}+\frac{1}{G_2h_2}\right)+\frac{4a^3}{B}\left(\frac{1}{E_1h_1^3}+\frac{1}{E_2h_2^3}\right)+\frac{\alpha a^2}{D_1B}\coth\alpha b, \qquad (8a)$$

$$G_{Ic}=\frac{6P_c^2a^2}{B^2}\left(\frac{1}{E_1h_1^3}+\frac{1}{E_2h_2^3}\right)+\frac{3P_c^2}{5B^2}\left(\frac{1}{G_1h_1}+\frac{1}{G_2h_2}\right)+\frac{\alpha aP_c^2}{D_1B^2}\left(\coth\alpha b+\frac{\alpha a}{2\sinh^2\alpha b}\right). \qquad (8b)$$

3 Reduction to Homogeneous Beam with Midplane Crack

For a homogeneous beam with midplane crack, ($E_1=E_2=E$, $G_1=G_2=G$, $h_1=h$), the parameters α, β, D_1, and D_2 are reduced to

$$D_1=\frac{12}{5Gh},\quad \alpha=\sqrt{\frac{10G}{Eh^2}},\quad \beta=1,\quad D_2=0. \qquad (9a,b)$$

The compliance and the critical strain energy release rate are then given by

$$C=\frac{8a^3}{EBh^3}+\frac{12a}{5GBh}(1+\alpha a\coth\alpha b), \qquad (10a)$$

$$G_{Ic}=\frac{12P_c^2a^2}{EB^2h^3}+\frac{6P_c^2}{5GB^2h}\left(1+2\alpha a\coth\alpha b+\frac{\alpha a^2}{\sinh^2\alpha b}\right). \qquad (10b)$$

In a review, Davies and Benzeggagh (1989) compare the results from the eixsting models for thin and thick specimen of glass/epoxy and carbon/epoxy with the experimental and finite element results. Kanninen's (1974) model seems to be the best among them to correlate with the experimental and finite element results. The results from the present model for the same data are hence compared with the results from the experiments, finite element method, and Kanninen's model, in Tables 1 and 2 for compliances and in Tables 3 and 4 for critical strain energy release rates. The tables show that the results from the present model are in better agreement with the experimental and finite element results than any of the existing models for both thin and thick specimens.

Table 1 Comparison of different model values of C ($mN^{-1}\times10^{-5}$) for glass/epoxy), ($E=46{,}000$ MPa, $G=5{,}000$ MPa, $B=20$ mm, $L=150$ mm); *from Davies and Benzeggagh (1989)

	Thin (4.6 mm)			Thick (20mm)		
a (mm)	51.5	71.0	101.0	41.0	56.0	91.0
Experiment*	11.67	30.17	86.4	0.155	0.324	1.131
FEM*				0.131	0.278	0.975
Present	11.07	28.04	78.57	0.112	0.245	0.884
Kanninen (1974)	10.5	27.27	73.66	0.087	0.201	0.780

Table 2 Comparison of different model values of C ($mN^{-1}\times10^{-5}$) for carbon/epoxy, ($E=130{,}000$ MPa, $G=5{,}300$ MPa, $B=20$ mm, $L=150$ mm); *from Davies and Benzeggagh (1989)

	Thin (5.2 mm)			Thick (20 mm)		
a (mm)	38	55	71	40	55	80
Experiment*	1.42	3.90	7.60	0.064	0.138	0.322
FEM*				0.063	0.123	0.290
Present	1.30	3.61	7.41	0.052	0.107	0.268
Kanninen (1974)	1.07	3.14	6.65	0.029	0.068	0.192

Table 3 Comparison of different model values of G_{IC} (J/m^2) for glass/epoxy, ($E=46{,}000$ MPa, $G=5{,}000$ MPa, $B=20$ mm, $L=150$ mm); *from Davies and Benzeggagh (1989)

	Thin (4.6 mm)			Thick (20 mm)		
a (mm)	51.5	71.0	101.0	41.0	56.0	91.0
Experiment*	267	258	228	245	222	216
FEM*				211	195	190
Present	248	239	206	175	176	186
Kanninen (1974)	239	233	202	148	154	172

Table 4 Comparison of different model values of G_{IC} (J/m^2) for carbon/epoxy, ($E=130{,}000$ MPa, $G=5{,}300$ MPa, $B=20$ mm, $L=150$ mm); *from Davies and Benzeggagh (1989)

	Thin (5.2 mm)			Thick (20 mm)		
a (mm)	38	55	71	40	55	80
Experiment*	190	175	175	168	181	175
FEM*				172	169	169
Present	180	176	184	126	140	156
Kanninen (1974)	158	161	172	84	103	124

4 Conclusion

A compliance model has been presented for a DCB specimen for mode-I interface delamination based on the first-order shear deformation theory but to include the effect of the undelaminated part of the specimen. The results for the midplane delamination in a homogeneous beam specimen is reduced and shown to be in better agreement with the experimental and finite element results than any of the existing models.

References

Davies, P., and Benzeggagh, M. L., 1989, "Interlaminar Mode-I Fracture Testing," *Application of Fracture Mechanics to Composite Materials*, K. Friedrich, ed., Elsevier, New York, pp. 81-112.

Kanninen, M. F., 1974, "A Dynamic Analysis of Unstable Crack Propagation and Arrest in the DCB Test Specimen," *Int. J. Fract.*, Vol. 10, pp. 415-430.

Reissner, E., 1984, "On Certain Mixed Variational Theorem and a Proposed Application," *Int. J. Numerical Methods in Engineering*, Vol. 20, pp. 1366-1368.

Downloaded 03 May 2010 to 171.66.16.20. Redistribution subject to ASME license or copyright; see http://www.asme.org/terms/Terms_Use.cfm

Electroelastic Field Concentrations In and Around Inhomogeneities in Piezoelectric Solids

M. L. Dunn[5,6] and M. Taya[5,7]

1 Introduction

The study of stress concentrations around inhomogeneities in piezoelectric solids has received attention recently, however, analyses have primarily been devoted to two-dimensional problems (see Sosa, 1991, and the references contain therein). It appears that only the works of Deeg (1980) and Wang (1992) address the problem of three-dimensional inclusions in piezoelectric solids. Deeg generalized the classical formation of Eshelby (1957) to accommodate piezoelectric inclusions, however, he did not obtain concentration factors. Recently Dunn and Taya (1993) extended Deeg's work and obtained expressions for tensors analogous to Eshelby's tensor in elasticity which can be used to easily solve piezoelectric inclusion and inhomogeneity problems. Here the analytical approach of Deeg (1980) and Dunn and Taya (1993) is furthered to obtain the electroelastic field concentrations around ellipsoidal inhomogeneities in piezoelectric solids. These are obtained without solving the complicated electroelastic fields *outside* the inhomogeneity. Instead, the jump conditions at the interface of an elastic inclusion (Hill, 1962; Walpole, 1967; Mura and Cheng, 1977) are generalized to coupled electroelastic behavior and the electroelastic fields just outside the inhomogeneity is expressed in terms of the interior electroelastic fields of an *equivalent inclusion*.

2 Fundamental Equations

In the absence of body forces and free charge, the field equations for the stationary linear response of a piezoelectric solid consist of the following.

Divergence Equations.

$$\sigma_{ij,j}=0 \quad D_{i,i}=0 \tag{1}$$

Gradient Equations.

$$\epsilon_{ij}=\frac{1}{2}(u_{i,j}+u_{j,i}) \quad E_i=-\phi_{,i} \tag{2}$$

Constitutive Equations.

$$\sigma_{ij}=C_{ijmn}\epsilon_{mn}+e_{nij}\phi_{,n} \quad D_i=e_{imn}\epsilon_{mn}-\kappa_{in}\phi_{,n} \tag{3}$$

where σ_{ij}, ϵ_{ij}, u_i, D_i, E_i, and $\phi_{,i}$ are the stress, strain, elastic displacement, electric displacement, electric field, and electric potential gradient, respectively, and unless otherwise noted conventional indicial notation is utilized. In Eqs. (3), C_{ijmn}, e_{nij}, and κ_{in} are the elastic (measured in a constant electric field), piezoelectric (measured at a constant strain or electric field) and the dielectric (measured at a constant strain) moduli, respectively.

In the solution of piezoelectric problems, it is convenient to utilize the notation introduced by Barnett and Lothe (1975). This notation is identical to conventional indicial notation with the exception that both lower and uppercase subscripts are used which take on the range $1\rightarrow 3$ and $1\rightarrow 4$, respectively. With this notation the field variables are identified as follows.

Elastic Displacement and Electric Potential.

$$U_M=\begin{cases} u_m & M=1,\ 2,\ 3 \\ \phi & M=4 \end{cases} \tag{4}$$

Elastic Strain and Electric Field.

$$Z_{Mn}=\begin{cases} \epsilon_{mn} & M=1,\ 2,\ 3 \\ \phi_{,n} & M=4 \end{cases} \tag{5}$$

Stress and Electric Displacement.

$$\Sigma_{iJ}=\begin{cases} \sigma_{ij} & J=1,\ 2,\ 3 \\ D_i & J=4 \end{cases} \tag{6}$$

Electroelastic Moduli.

$$E_{iJMn}=\begin{cases} C_{ijmn} & J,\ M=1,\ 2,\ 3 \\ e_{nij} & J=1,\ 2,\ 3;\ M=4 \\ e_{imn} & J=4;\ M=1,\ 2,\ 3 \\ -\kappa_{in} & J,\ M=4 \end{cases} \tag{7}$$

With this shorthand notation, the constitutive Eqs. (3) can be unified as

$$\Sigma_{iJ}=E_{iJMn}Z_{Mn}. \tag{8}$$

3 Interior Electroelastic Fields: Equivalent Inclusion Approach

Consider an infinite piezoelectric body (with electroelastic moduli E_{iJKl}) and containing a perfectly bonded ellipsoidal inhomogeneity (with principal axes a_1, a_2, a_3 and electroelastic moduli E^i_{iJKl}) oriented such that the a_3 and x_3-axes coincide. The piezoelectric body is subjected to boundary conditions compatible with a uniform far-field stress and electric displacement, Σ^o_{iJ}.

Utilizing the equivalent inclusion method (Deeg, 1980; Dunn and Taya, 1993), the stress and electric displacement in the inhomogeneity can be simulated by those in an equivalent inclusion with the electroelastic coefficients of the matrix and a fictitious eigenstrain and eigenelectric field, Z^*_{Mn}:

$$\Sigma^{\text{in}}_{iJ}=\Sigma^o_{iJ}+\Sigma_{iJ}=E^i_{iJKl}[Z^o_{Kl}+Z_{Kl}]=E_{iJKl}[Z^o_{Kl}+Z_{Kl}-Z^*_{Kl}] \tag{9}$$

where Σ_{iJ} is the disturbance of the otherwise uniform stress and electric displacement $\Sigma^o_{iJ}=E_{iJKL}Z^o_{Kl}$. The disturbance fields, Z_{Kl}, are related to the fictitious eigenfields by

$$Z_{Mn}=S_{MnAb}Z^*_{Ab}, \tag{10}$$

where the four tensors S_{MnAb} are the piezoelectric analog of Eshelby's tensor and are functions of the shape of the inhomogeneity and the electroelastic coefficients of the matrix. The tensors S_{MnAb} have been given explicitly by Dunn and Taya (1993). Equations (9) and (10) can be solved to obtain Σ^{in}_{iJ} and Z^*_{Ab} which are the key quantities necessary to obtain the electroelastic field concentrations at the interface of the matrix and inhomogeneity. It is noted that as in the uncoupled elastic and electric problems, the electroelastic fields are uniform inside the inhomogeneity.

4 Electroelastic Field Concentrations

Here the jump conditions at the interface of an elastic inclusion (Hill, 1962; Walpole, 1967; Mura and Cheng, 1977) are generalized to the electroelastic case so that the stress and electric displacement just outside the inhomogeneity can be expressed in terms of the known Σ^{in}_{iJ} and Z^*_{Mn}. The traction and normal component of the electric displacement are con-

[5] Department of Mechanical Engineering, FU-10, University of Washington, Seattle, WA 98195.
[6] Assoc. Mem. ASME.
[7] Mem. ASME.

Contributed by the Applied Mechanics Division of The American Society of Mechanical Engineers for publication in the ASME Journal of Applied Mechanics. Manuscript received by the ASME Applied Mechanics Division, Jan. 27, 1992; final revision, Feb. 2, 1993. Associate Technical Editor: R. M. McMeeking.

Copyright © 1994 by ASME
Downloaded 03 May 2010 to 171.66.16.20. Redistribution subject to ASME license or copyright; see http://www.asme.org/terms/Terms_Use.cfm

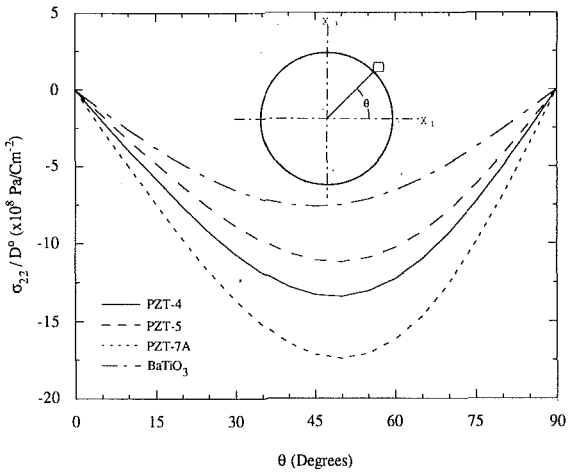


Fig. 1 Stress concentrations at the interface of a spherical cavity in a various piezoelectric materials subjected to the applied electric displacement, $D_1^o = D^o$.

tinuous across the interface between two different materials, i.e., $(\Sigma_{iJ}^{\text{out}} - \Sigma_{iJ}^{\text{in}})\ n_i = 0$ where n_i is the unit outward normal to the surface of the inhomogeneity and the superscripts "out" and "in" denote quantities just outside and just inside the inhomogeneity, respectively. By use of the continuity requirements of the elastic displacement ($u_i^{\text{out}} = u_i^{\text{in}}$) and electric field ($\gamma_{ijk}\, n_i\, E_k^{\text{out}} = \gamma_{ijk}\, n_i\, E_k^{\text{in}}$, where γ_{ijk} is the permutation tensor), the jump conditions for the strain and electric field are obtained:

$$[Z_{Kl}] = Z_{Kl}^{\text{out}} - Z_{Kl}^{\text{in}} = \Lambda_K n_l \tag{10}$$

where $[\bullet]$ denotes the jump in a quantity and Λ_K ($=\lambda_k$ for $K = 1, 2, 3$ and $=\delta$ for $K = 4$) are the unknown magnitudes of the jumps. To solve for Λ_K, recall from the equivalent inclusion solution

$$\Sigma_{iJ}^{\text{in}} = E_{iJKl}^{i} Z_{Kl}^{\text{in}} = E_{iJKl}[Z_{Kl}^{\text{in}} - Z_{Kl}^{*}] \tag{11}$$

$$\Sigma_{iJ}^{\text{out}} = E_{iJKl} Z_{Kl}^{\text{out}}. \tag{12}$$

Substituting Eqs. (11) and (12) into the traction-electric displacement continuity requirement and using Eq. (10) yields a set of four algebraic simultaneous equations for the four unknowns Λ_K which can be solved to yield

$$\Lambda_K = -K_{MK}^{-1} E_{pMNq} Z_{Nq}^{*} n_p \tag{13}$$

where K_{MK}^{-1} is the inverse of $K_{JK} = K_{KJ} = E_{iJKl} n_l n_i$.

With the jumps Λ_K obtained from Eq. (13), the stress and electric displacement just outside the inclusion readily follow as

$$\Sigma_{iJ}^{\text{out}} = \Sigma_{iJ}^{\text{in}} + E_{iJKl}[-E_{pQMn} Z_{Mn}^{*} K_{QK}^{-1} n_p n_l + Z_{Kl}^{*}]. \tag{14}$$

Thus the stress and electric displacement just outside the inhomogeneity are completely determined from the solution for the stress and electric displacement inside the inhomogeneity and Z_{Mn}^{*}. When piezoelectric coupling is absent, Eq. (14) reduces to the uncoupled elastic and electric results (Mura and Cheng, 1977).

5 Results and Discussion

The electroelastic moduli used in the following computations are given in Table 1 (Berlincourt, 1964, 1971) where the well-known two-index notation is utilized (Nye, 1957).

Through a complex variable approach, Sosa (1991) obtained the electroelastic fields at the surface of an elliptical cavity ($a_2 = \infty$) with its generatrix parallel to the isotropic plane of an infinite PZT-4 matrix for an applied mechanical load. Sosa showed that when piezoelectric coupling is *ignored*, the maximum stresses predicted by an elastic analysis differ from those

Table 1 Electroelastic material properties

	C_{11} (GPa)	C_{12} (GPa)	C_{13} (GPa)	C_{33} (GPa)	C_{44} (GPa)	e_{31} (C/m^2)	e_{33} (C/m^2)	e_{15} (C/m^2)	κ_{11}^{*}/κ_o	κ_{33}^{*}/κ_o
PZT-4	139	77.8	74.3	115	25.6	-5.2	15.1	12.7	730	635
PZT-5	121	75.4	75.2	111	21.1	-5.4	15.8	12.3	916	830
PZT-7A	148	76.2	74.2	131.0	25.4	-2.1	9.5	9.7	460	235
$BaTiO_3$	150	66	66	146	44	-4.35	17.5	11.4	1115	1260

* $\kappa_o = 8.85$ E-12 $\frac{C^2}{Nm^2}$ = permittivity of free space.

of an electroelastic analysis by as much as 18 percent for a cavity aspect ratio, $a_1/a_3 = 0.1$. It has been verified numerically that the present approach recovers Sosa's result for two-dimensional elliptical inclusions.

Unlike Sosa's (1991) approach, the present solution is also applicable to three-dimensional cavities and inhomogeneities. As an example, Fig. 1 shows the distribution of σ_{22} around the surface (in the x_1-x_3 plane as shown in the inset) of a spherical cavity in various piezoelectric solids subjected to an applied electric displacement of $D_1^o = D^o$. The electroelastic material properties of the various piezoelectric materials represent varying degrees of electroelastic coupling and material anisotropy (although all are transeversely isotropic). It is seen that the maximum stress induced varies widely between the materials. In addition, the location, θ, of the maximum stress component appears to be a function of the electroelastic material properties of the piezoelectric material. Finally, it is noted that numerous additional geometric and loading configurations can be easily analyzed with the proposed approach. Unfortunately space requirements limit their presentation here.

Note Added to Proof: The piezoelectric inhomogeneity problem has also been studied recently by Benveniste (1992) and Chen (1993).

References

Barnett, D. M., and Lothe, J., 1975, "Dislocations and Line Charges in Anisotropic Piezoelectric Insulators," *Physica Statis Solid* (*b*), Vol. 67, pp. 105–111.

Benveniste, Y., 1992, "The Determination of the Elastic and Electric Fields in a Piezoelectric Inhomogeneity," *J. Appl. Phys.*, Vol. 72, ,pp. 1086–1095.

Berlincourt, D. A., Curran, D. R., and Jaffe, H., 1964, "Piezoelectric and Piezomagnetic Materials and Their Function in Transducers," *Physical Acoustics: Principle and Methods*, W. P. Mason, ed., pp. 169–270.

Berlincourt, D. A., 1971, "Piezoelectric Crystals and Ceramics," *Ultrasonic Transducer Materials*, O. E. Mattiat, ed., pp. 63–119.

Chen, T., 1993, "An Invariant Treatment of Interfacial Discontinuities in Piezoelectric Media," *International Journal of Engineering Science*, Vol. 31, No. 7, pp. 1061–1072.

Deeg, W. F., 1980, "The Analysis of Dislocation, Crack, and Inclusion Problems in Piezoelectric Solids," Ph.D. Dissertation, Stanford University.

Dunn, M. L., and Taya, M., 1993, "An Analysis of Piezoelectric Composite Materials Containing Ellipsoidal Inhomogeneities," *Proceedings of the Royal Society, London*, Vol. A443, pp. 265–287.

Dunn, M. L., 1994, "Electroelastic Green's Functions for Transversely Isotropic Piezoelectric Media and Their Application to the Solution of Inclusion and Inhomogeneity Problems," *International Journal of Engineering Science*, Vol. 32, pp. 119–131.

Eshelby, J. D., 1957, "The Determination of the Elastic Field of an Ellipsoidal Inclusion, and Related Problems," *Proceedings of the Royal Society of London*, Vol. A241, pp. 376–396.

Hill, R., 1961, "Discontinuity Relations in Mechanics of Solids," *Progress in Solid Mechanics*, I. N. Sneddon and R. H. Hill, eds., Vol. 2, pp. 245–276.

Mura, T., and Cheng, P. c., 1977, "The Elastic Field Outside an Ellipsoidal Inclusion," ASME Journal of Applied Mechanics, Vol. 44, pp. 591–594.

Mura, T., 1987, *Micromechanics of Defects in Solids*, Martinus Nijhoff, Amsterdam.

Nye, J. F., 1957, *Physical Properties of Crystals*, Oxford University Press, Oxford, U.K.

Sosa, H., 1991, "Plane Problems in Piezoelectric Media with Defects," *International Journal of Solids and Structures*, Vol. 28, No. 4, pp. 491–505.

Walpole, L. J., 1967, "The Elastic Field of an Inclusion in an Anisotropic Medium," *Proceedings of the Royal Society of London*, Vol. A300, pp. 270–289.

Wang, B., 1992, "Three-Dimensional Analysis of an Ellipsoidal Inclusion in a Piezoelectric Material," *International Journal of Solids and Structures*, Vol. 29, No. 3, pp. 293–308.

Downloaded 03 May 2010 to 171.66.16.20. Redistribution subject to ASME license or copyright; see http://www.asme.org/terms/Terms_Use.cfm

Material Instability for Fiber Composites

R. M. Christensen[8]

The objective here is to directly use the governing differential equations to derive the well-known ideal, or classical instability criterion, for fiber composites $\sigma_c = -\mu_L$, first derived by Rosen (1965). The derivation given here is consistent with Biot (1965). Take the fibers as aligned in the direction of the 1-axis, or later the x-axis. The macroscopic level equations of equilibrium, without body force are given by $\sigma_{ij,j} = 0$ in terms of rectangular cartesian coordinates. Consider strain states with $\epsilon_{33} = \epsilon_{23} = \epsilon_{31} = 0$ and take a pre-existing state of stress in the 1 direction. Converting to x, y, z coordinates with z being in the 3 direction, then the governing relations are

$$\frac{\partial \sigma_{xx}}{\partial x} + \frac{\partial \sigma_{xy}}{\partial y} + \sigma_c \frac{\partial^2 u}{\partial x^2} = 0$$

$$\frac{\partial \sigma_{xy}}{\partial x} + \frac{\partial \sigma_{yy}}{\partial y} + \sigma_c \frac{\partial^2 v}{\partial x^2} = 0 \tag{1}$$

where σ_c is the pre-existing state of stress in the x, or fiber direction, u and v are the displacements in the x and y directions, and σ_{xx}, σ_{yy}, and σ_{xy} are additional stresses due to a further state of small deformation beyond that causing σ_c. These equations are obtained from the full nonlinear forms. The terms involving σ_c in the equilibrium equations must be of the same order as the other terms, for any solution of interest, as will occur here.

Take the stress constitutive equations as those for a transversely isotropic, elastic material, with five independent effective properties. Appropriate to the deformation state, the constitutive equations take the reduced form

$$\begin{bmatrix} \sigma_{xx} \\ \sigma_{yy} \\ \sigma_{xy} \end{bmatrix} = \begin{bmatrix} C_{11} & C_{12} & 0 \\ C_{12} & C_{22} & 0 \\ 0 & 0 & 2\mu_L \end{bmatrix} \begin{bmatrix} \epsilon_{xx} \\ \epsilon_{yy} \\ \epsilon_{xy} \end{bmatrix} \tag{2}$$

where μ_L is the longitudinal shear modulus of the fiber composite and the C_{ij}'s are the other appropriate properties. These properties result from volume averages of deformation states taken over dimensions that are large compared with the characteristic dimensions of fiber diameter and fiber spacing. Only a slight reinterpretation of (2) is needed for application to orthotropic materials.

Combining (1) and (2) with the strain-displacement relations gives

$$(\sigma_c + C_{11}) \frac{\partial^2 u}{\partial x^2} + (C_{12} + \mu_L) \frac{\partial^2 v}{\partial x \partial y} + \mu_L \frac{\partial^2 u}{\partial y^2} = 0$$

and

$$(\sigma_c + \mu_L) \frac{\partial^2 v}{\partial x^2} + (C_{12} + \mu_L) \frac{\partial^2 u}{\partial x \partial y} + C_{22} \frac{\partial^2 v}{\partial y^2} = 0. \tag{3}$$

For C_{11}, much larger than the other properties, σ_c must be negligible compared with C_{11} to have terms of consistent order. Taking $u(x, y) = 0$ leaves

$$(C_{12} + \mu_L) \frac{\partial^2 v}{\partial x \partial y} = 0$$

and

$$(\sigma_c + \mu_L) \frac{\partial^2 v}{\partial x^2} + C_{22} \frac{\partial^2 v}{\partial y^2} = 0. \tag{4}$$

A nontrivial solution of (4) is possible. This solution is given by

$$\sigma_c = -\mu_L$$

and

$$v = Ay + f(x) \tag{5}$$

with $f(x)$ arbitrary. Note that no solution of (4) is possible for $\sigma_c > -\mu_L$ except that of homogeneous deformation. Thus relation (5) provides the material instability criterion. At the critical compressive stress level of (5), in the fiber direction, the material bifurcates and can sustain a shear deformation of arbitrary form for $f(x)$ in relation (5).

Although the material instability criterion (5) was found from a two-dimensional deformation field, the result has fully three-dimensional applicability. That is, the result (5) applies to materials with three-dimensional microstructures as well as two-dimensional microstructures. Most previous analyses with intended application to fiber composites have actually proceeded by assuming and then analyzing a two-dimensional, layered media-type microstructure, e.g., Rosen (1965), Kulkarni, Rice, and Rosen (1975), Steif (1987), Lagoudas, Tadjbakhsh, and Fares (1992), Minahen and Knauss (1989), etc. The macroscopic implications of the result were inferred after completing the analysis, but was still restricted to a two-dimensional microstructure. The nature of the result here is that this sequence is reversed. First, the material instability criterion is found at the macroscopic level with no restriction to either a two-dimensional or a three-dimensional microstructure. Thereafter, the result (5) can be evaluated for any two-dimensional or a three-dimensional microstructure of interest.

In view of the demonstrated sensitivity of critical compressive strength to interface integrity it is useful to establish upper and lower bounds of behavior. Consider the boundary value problem which must be posed to determine the effective longitudinal shear modulus, μ_L, for any model of fiber reinforcement. This is an antiplane problem with displacements taken in the form

$$w = w(x, y)$$
$$u = v = 0 \tag{6}$$

where the z-axis is now in the fiber direction. The equations of equilibrium reduce to the form

$$\nabla^2 w = 0. \tag{7}$$

In the case of perfect bonding between fibers and matrix, the appropriate condition is w = constant over all fiber-matrix interfaces for very stiff fibers. Far-field conditions involve imposing $w(x, y)$ relative to a state of shear.

Now consider the case of no bonding whatsoever between the fiber and matrix phases. In this situation the only nonvanishing matrix stresses are

$$\sigma_{yz} \neq 0$$

$$\sigma_{zx} \neq 0. \tag{8}$$

The governing equilibrium equation

$$\frac{\partial \sigma_{yz}}{\partial y} + \frac{\partial \sigma_{zx}}{\partial x} = 0 \tag{9}$$

is satisfied by introduction of the stress function

[8]Chemistry and Materials Science Department, Department of Applied Science, Lawrence Livermore National Laboratory, University of California, P.O. Box 808, Livermore, CA 94550. Honorary Member, ASME.

Contributed by the Applied Mechanics Division of THE AMERICAN SOCIETY OF MECHANICAL ENGINEERS for publication in the ASME JOURNAL OF APPLIED MECHANICS. Manuscript received by the ASME Applied Mechanics Division, Feb. 17, 1992; final revision, Apr. 5, 1993. Associate Technical Editor: A. K. Noor.

Copyright © 1994 by ASME
Downloaded 03 May 2010 to 171.66.16.20. Redistribution subject to ASME license or copyright; see http://www.asme.org/terms/Terms_Use.cfm

$$\sigma_{yz}=\frac{\partial\psi}{\partial x}$$

$$\sigma_{zx}=-\frac{\partial\psi}{\partial y}. \tag{10}$$

The resulting compatibility equation can be shown to be

$$\nabla^2\psi=0. \tag{11}$$

Consideration of the traction-free surfaces at the interface between fibers and matrix can be shown to yield the condition, ψ = constant, on these interfaces.

Comparison of the governing Eq. (7) for the case of perfect interfaces with rigid fibers and Eq. (11) for unbonded interfaces, shows these two problems to be formally identical in terms of w and ψ. Now form the strain energies and complementary energies for these two problems. The two local forms are given by

$$U_{\text{strain}}=\mu_m\left[\left(\frac{\partial w}{\partial x}\right)^2+\left(\frac{\partial w}{\partial y}\right)^2\right]$$

and

$$U_{\text{compl.}}=J_m\left[\left(\frac{\partial\psi}{\partial x}\right)^2+\left(\frac{\partial\psi}{\partial y}\right)^2\right] \tag{12}$$

where J_m is the shear compliance of the matrix material, $J_m = 1/\mu_m$. Following the usual method of determining the effective properties for the two problems we see that the problems of determining μ_L and J_L are formally identical. The solution for the effective shear modulus can be written as

$$\frac{\mu_L}{\mu_m}=F(c)\ \text{(perfect bonding)} \tag{13}$$

where $F(c)$ is a function of fiber volume fraction, which results from any particular micromechanics model of interest. It follows that the solution for J_L in the second problem is identical with that for μ_L in the first problem with the same function, $F(c)$. That is, for unbonded fibers

$$\frac{J_L}{J_m}=F(c)\ \text{(no bonding)}. \tag{14}$$

It also follows from $J_L = 1/\mu_L$ and from (5) that the critical compressive stress is bounded by

$$-\mu_m F(c)\le\sigma_c\le\frac{-\mu_m}{F(c)}. \tag{15}$$

The range in between these two limits would correspond to partial debonding. Under concentrated conditions $F(c)$ in (13) is typically up to an order of magnitude larger than 1 in size. Thus, the difference between the two limits in (15) is up to two orders of magnitude for typical polymeric, fiber composite materials. It follows that the compressive material strength due to instability is very sensitive to interface conditions, and the level of compressive material strength can be severely degraded by poor interfaces. This characteristic has been understood for some time; however, (15) directly allows estimates of the maximum size of the effect. Further, these results show that there could be a very energetically favorable mechanism for bond rupture at or near the fiber-matrix interface when composites are loaded in axial compression.

Acknowledgment

The author is appreciative of support from Dr. Y. D. S. Rajapakse, the Office of Naval Research. A helpful discussion with Dr. S. J. DeTeresa was appreciated. The work was performed under the auspices of the U.S. Department of Energy by the Lawrence Livermore National Laboratory under contract number W7405-ENG-48.

Note Added to Proof: See also the work of Geymonat et al. (1993).

References

Biot, M. A., 1965, *Mechanics of Incremental Deformations*, John Wiley and Sons, New York.

Geymonat, G., Muller, S., and Triantafyllidis, N., 1993, "Homogenization of Nonlinearly Elastic Materials, Microscopic Bifurcation and Macroscopic Loss of Rank-One Convexity," *Arch. Rational Mech. Anal.*, Vol. 122, pp. 231-290.

Kulkarni, S. V.,, Rice, J. S., and Rosen, B. W., 1975, "An Investigation of the Compressive Strength of Kevlar 49/Epoxy Composites," *Composites*, Vol. 6, pp. 217-225.

Lagoudas, D. C., Tadjbakhsh, I., and Fares, N., 1991, "A New Approach to Microbuckling of Fibrous Composites," ASME JOURNAL OF APPLIED MECHANICS, Vol. 58, pp. 473-479.

Minahen, T. M., and Knauss, W. G., 1989, "A Note on Microbuckling in Unidirectional Fibrous Composites," ASME JOURNAL OF APPLIED MECHANICS, Vol. 56, pp. 983-985.

Rosen, B. W., 1965, "Mechanics of Composite Strengthening," *Fiber Composite Materials*, ASM, Metals Park, OH, Chapter 3.

Steif, P. S., 1987, "An Exact Two-Dimensional Approach to Fiber Micro-Buckling," *Int. Journal of Solids and Structures*, Vol. 23, pp. 1235-1246.

Stability of a Fluid-Conveying Pipe With Flow-Dependent Support Stiffness

A. Guran[9] and R. H. Plaut[10]

Introduction

The stability of pipes conveying fluid has been studied extensively (Chen, 1987; Païdoussis, 1987). The behavior is especially interesting if the downstream end is free, so that the system is nonconservative. A standard example is a cantilevered pipe, for which the upstream end is clamped. In actuality, however, most supports have some rotational flexibility. The effect of such flexibility at the upstream end of the pipe, as depicted in Fig. 1, is analyzed in this Note. Earlier studies involving pipes with flexible end supports include Chen (1971), Liu and Mote (1974), Lin and Chen (1976), Païdoussis et al. (1980), Noah and Hopkins (1980), and Jendrzejczyk and Chen (1985).

In the present investigation, the rotational stiffness at the support is assumed to be constant or to increase as the flow increases (due to the induced compressive load acting on the support). The cantilevered pipe is a special case when the rotational stiffness is infinite. The case of zero stiffness is inherently unstable, since a rigid rotation about the upstream end is possible.

Analysis

The uniform elastic pipe shown in Fig. 1 is considered. It has length L, bending stiffness EI, and mass per unit length M, while the fluid has mass per unit length m and constant

[9]Department of Civil and Environmental Engineering, Rensselaer Polytechnic Institute, Troy, NY 12180-3590. Currently at Virginia Polytechnic Institute and State University.

[10]Department of Civil Engineering, Virginia Polytechnic Institute and State University, Blacksburg, VA 24061-0105. Fellow ASME.

Contributed by the Applied Mechanics Division of THE AMERICAN SOCIETY OF MECHANICAL ENGINEERS for publication in the ASME JOURNAL OF APPLIED MECHANICS. Manuscript received by the ASME Applied Mechanics Divison, Mar. 23, 1992 final revision, June 1, 1993. Associate Technical Editor: A. K. Noor.

Downloaded 03 May 2010 to 171.66.16.20. Redistribution subject to ASME license or copyright; see http://www.asme.org/terms/Terms_Use.cfm

$$\sigma_{yz}=\frac{\partial\psi}{\partial x}$$

$$\sigma_{zx}=-\frac{\partial\psi}{\partial y}. \tag{10}$$

The resulting compatibility equation can be shown to be

$$\nabla^2\psi=0. \tag{11}$$

Consideration of the traction-free surfaces at the interface between fibers and matrix can be shown to yield the condition, ψ = constant, on these interfaces.

Comparison of the governing Eq. (7) for the case of perfect interfaces with rigid fibers and Eq. (11) for unbonded interfaces, shows these two problems to be formally identical in terms of w and ψ. Now form the strain energies and complementary energies for these two problems. The two local forms are given by

$$U_{\text{strain}}=\mu_m\left[\left(\frac{\partial w}{\partial x}\right)^2+\left(\frac{\partial w}{\partial y}\right)^2\right]$$

and

$$U_{\text{compl.}}=J_m\left[\left(\frac{\partial\psi}{\partial x}\right)^2+\left(\frac{\partial\psi}{\partial y}\right)^2\right] \tag{12}$$

where J_m is the shear compliance of the matrix material, $J_m = 1/\mu_m$. Following the usual method of determining the effective properties for the two problems we see that the problems of determining μ_L and J_L are formally identical. The solution for the effective shear modulus can be written as

$$\frac{\mu_L}{\mu_m}=F(c)\ \text{(perfect bonding)} \tag{13}$$

where $F(c)$ is a function of fiber volume fraction, which results from any particular micromechanics model of interest. It follows that the solution for J_L in the second problem is identical with that for μ_L in the first problem with the same function, $F(c)$. That is, for unbonded fibers

$$\frac{J_L}{J_m}=F(c)\ \text{(no bonding)}. \tag{14}$$

It also follows from $J_L = 1/\mu_L$ and from (5) that the critical compressive stress is bounded by

$$-\mu_m F(c)\le\sigma_c\le\frac{-\mu_m}{F(c)}. \tag{15}$$

The range in between these two limits would correspond to partial debonding. Under concentrated conditions $F(c)$ in (13) is typically up to an order of magnitude larger than 1 in size. Thus, the difference between the two limits in (15) is up to two orders of magnitude for typical polymeric, fiber composite materials. It follows that the compressive material strength due to instability is very sensitive to interface conditions, and the level of compressive material strength can be severely degraded by poor interfaces. This characteristic has been understood for some time; however, (15) directly allows estimates of the maximum size of the effect. Further, these results show that there could be a very energetically favorable mechanism for bond rupture at or near the fiber-matrix interface when composites are loaded in axial compression.

Acknowledgment

The author is appreciative of support from Dr. Y. D. S. Rajapakse, the Office of Naval Research. A helpful discussion with Dr. S. J. DeTeresa was appreciated. The work was performed under the auspices of the U.S. Department of Energy by the Lawrence Livermore National Laboratory under contract number W7405-ENG-48.

Note Added to Proof: See also the work of Geymonat et al. (1993).

References

Biot, M. A., 1965, *Mechanics of Incremental Deformations*, John Wiley and Sons, New York.

Geymonat, G., Muller, S., and Triantafyllidis, N., 1993, "Homogenization of Nonlinearly Elastic Materials, Microscopic Bifurcation and Macroscopic Loss of Rank-One Convexity," *Arch. Rational Mech. Anal.*, Vol. 122, pp. 231–290.

Kulkarni, S. V.,, Rice, J. S., and Rosen, B. W., 1975, "An Investigation of the Compressive Strength of Kevlar 49/Epoxy Composites," *Composites*, Vol. 6, pp. 217–225.

Lagoudas, D. C., Tadjbakhsh, I., and Fares, N., 1991, "A New Approach to Microbuckling of Fibrous Composites," ASME JOURNAL OF APPLIED MECHANICS, Vol. 58, pp. 473–479.

Minahen, T. M., and Knauss, W. G., 1989, "A Note on Microbuckling in Unidirectional Fibrous Composites," ASME JOURNAL OF APPLIED MECHANICS, Vol. 56, pp. 983–985.

Rosen, B. W., 1965, "Mechanics of Composite Strengthening," *Fiber Composite Materials*, ASM, Metals Park, OH, Chapter 3.

Steif, P. S., 1987, "An Exact Two-Dimensional Approach to Fiber Micro-Buckling," *Int. Journal of Solids and Structures*, Vol. 23, pp. 1235–1246.

Stability of a Fluid-Conveying Pipe With Flow-Dependent Support Stiffness

A. Guran[9] and R. H. Plaut[10]

Introduction

The stability of pipes conveying fluid has been studied extensively (Chen, 1987; Païdoussis, 1987). The behavior is especially interesting if the downstream end is free, so that the system is nonconservative. A standard example is a cantilevered pipe, for which the upstream end is clamped. In actuality, however, most supports have some rotational flexibility. The effect of such flexibility at the upstream end of the pipe, as depicted in Fig. 1, is analyzed in this Note. Earlier studies involving pipes with flexible end supports include Chen (1971), Liu and Mote (1974), Lin and Chen (1976), Païdoussis et al. (1980), Noah and Hopkins (1980), and Jendrzejczyk and Chen (1985).

In the present investigation, the rotational stiffness at the support is assumed to be constant or to increase as the flow increases (due to the induced compressive load acting on the support). The cantilevered pipe is a special case when the rotational stiffness is infinite. The case of zero stiffness is inherently unstable, since a rigid rotation about the upstream end is possible.

Analysis

The uniform elastic pipe shown in Fig. 1 is considered. It has length L, bending stiffness EI, and mass per unit length M, while the fluid has mass per unit length m and constant

[9]Department of Civil and Environmental Engineering, Rensselaer Polytechnic Institute, Troy, NY 12180-3590. Currently at Virginia Polytechnic Institute and State University.

[10]Department of Civil Engineering, Virginia Polytechnic Institute and State University, Blacksburg, VA 24061-0105. Fellow ASME.

Contributed by the Applied Mechanics Division of THE AMERICAN SOCIETY OF MECHANICAL ENGINEERS for publication in the ASME JOURNAL OF APPLIED MECHANICS. Manuscript received by the ASME Applied Mechanics Divison, Mar. 23, 1992 final revision, June 1, 1993. Associate Technical Editor: A. K. Noor.

Copyright © 1994 by ASME
Downloaded 03 May 2010 to 171.66.16.20. Redistribution subject to ASME license or copyright; see http://www.asme.org/terms/Terms_Use.cfm

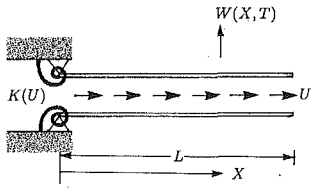


Fig. 1 Geometry of pipe

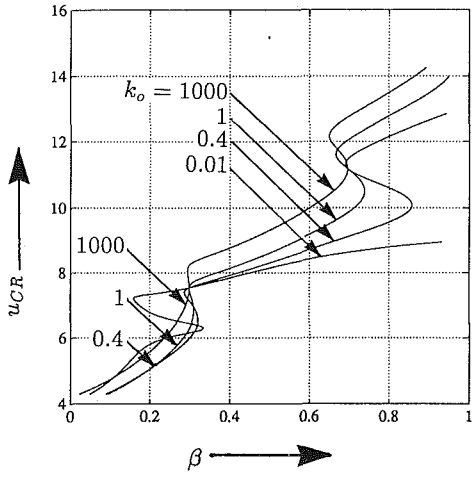


Fig. 2 Critical velocity u_{CR} (lowest branch) versus mass parameter β for $\alpha = 0.1$

velocity U. The rotational spring at $X=0$ has stiffness K, and the transverse deflection is $W(X,T)$ where T denotes time. It is convenient to define the nondimensional quantities

$$x=X/L, \quad w=W/L, \quad t=(T/L^2)\sqrt{EI/(M+m)},$$
$$\beta=\sqrt{M/(M+m)}, \quad u=UL\sqrt{M/EI}, \quad k=KL/EI \qquad (1)$$

and to assume motion of the form

$$w(x,t)=y(x)e^{i\omega t}, \quad i=\sqrt{-1}. \qquad (2)$$

Then $y(x)$ is governed by the equation (Chen, 1987)

$$y''''+u^2y''+2i\sqrt{\beta}u\omega y'-\omega^2 y=0 \qquad (3)$$

and the boundary conditions are

$$y(0)=0, \quad y''(0)-ky'(0)=0, \quad y''(1)=0, \quad y'''(1)=0. \qquad (4)$$

When the compressive load on a column is increased, the rotational stiffness at the base may increase (Picard and Beaulieu, 1985). For a pipe, the flowing fluid induces an "effective compressive load" at the upstream end, proportional to the square of the velocity (Païdoussis and Issid, 1974). Therefore, the rotational stiffness at the upstream end in Fig. 1 may increase as the flow velocity increases. In order to include this type of behavior, the nondimensional stiffness k is assumed to have the form

$$k(u)=k_o(1+\alpha u^2). \qquad (5)$$

In other words, the spring stiffness is constant if $\alpha=0$ and increases linearly with the effective compressive load if the stiffening rate α is positive.

The governing equations are solved numerically. All motions decay if u is less than the critical flow velocity u_{CR}, and dynamic instability (i.e., flutter) occurs if $u>u_{CR}$. At u_{CR}, a periodic motion is possible, but there is no associated classical normal mode which keeps the same shape during each period (Chen, 1987). If k is sufficiently small, this periodic motion has only positive or negative deflection at any time. If k is sufficiently large, the deflection changes sign at a location which varies during the motion.

The influence of the mass parameter β on u_{CR} is shown in Fig. 2. Curves are plotted for $\alpha=0.1$ and $k_o=0.01$, 0.4, 1, and 1,000. At a fixed value of β on the abscissa, if the curve is not single valued, the lowest point on the curve gives u_{CR}. As for the cantilevered pipe (Chen, 1987), u_{CR} may change discontinuously as β is varied.

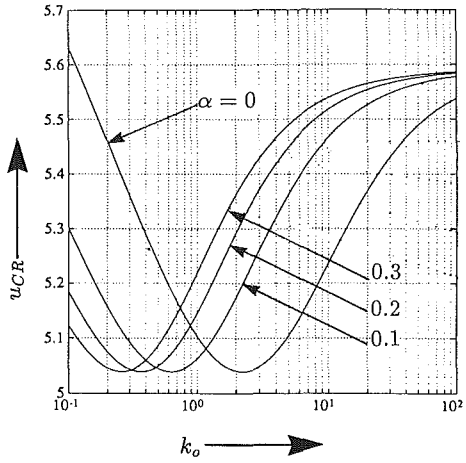


Fig. 3 Critical velocity u_{CR} versus initial stiffness k_o for $\beta = 0.2$ and fixed α

The influence of the spring stiffness parameter k_o on u_{CR} is depicted in Fig. 3 for the case $\beta=0.2$ and the spring stiffening rates $\alpha=0$, 0.1, 0.2, and 0.3. As $k_o\to\infty$, u_{CR} approaches the value 5.59 of the critical velocity for a cantilevered pipe with $\beta=0.2$, for any value $\alpha\geq 0$. As $k_o\to 0$, u_{CR} approaches 6.12. As k_o is increased from the value $k_o=0.1$, u_{CR} decreases to the minimum value 5.04 and then increases. This minimum critical velocity is independent of α and only depends on the value of β. It occurs at $k_o=2.232$ if $\alpha=0$ and at smaller values of k_o if $\alpha>0$.

In Fig. 3, it is surprising to see that the critical velocity for the cantilevered pipe ($k=\infty$) is not always an upper bound for that of a pipe with a flexible support; higher critical velocities can occur for very small support stiffnesses. It is also unexpected that there is a range of support stiffness in which an increase of stiffness causes the critical velocity to decrease. Perhaps the most important finding is the existence of a minimum critical velocity that is independent of the support stiffness function $k(u)$ and only dependent on the ratio between the pipe and fluid masses per unit length. Knowledge of this minimum value is useful since the flexibility characteristics of an actual support may not be known precisely.

References

Chen, S. S., 1971, "Flow-Induced Instability of an Elastic Tube," ASME Paper 71-Vibr-39.

Chen, S. S., 1987, *Flow-Induced Vibration of Circular Cylindrical Structures, Hemisphere*, Washington, D.C.

Jendrzejczyk, J. A., and Chen, S. S., 1985, "Experiments on Tubes Conveying Fluid," *Thin-Walled Structures*, Vol. 3, pp. 109–134.

Lin, H. C., and Chen, S. S., 1976, "Vibration and Stability of Fluid-Conveying Pipes," *Shock and Vibration Bulletin*, Vol. 46, Part 2, pp. 267–283.

Liu, H. L., and Mote, Jr., C. D., 1974, "Dynamic Response of Pipes Transporting Fluids," *Journal of Engineering for Industry*, Vol. 96, pp. 591–596.

Noah, S. T., and Hopkins, G. R., 1980, "Dynamic Stability of Elastically Supported Pipes Conveying Fluid," *Journal of Sound and Vibration*, Vol. 71, pp. 103–116.

Païdoussis, M. P., 1987, "Flow-Induced Instabilities of Cylindrical Structures," ASME *Applied Mechanics Reviews*, Vol. 40, pp. 163–175.

Païdoussis, M. P., and Issid, N. T., 1974, "Dynamic Stability of Pipes Conveying Fluid," *Journal of Sound and Vibration*, Vol. 33, pp. 267–294.

Païdoussis, M. P., Issid, N. T., and Tsui, M., 1980, "Parametric Resonance Oscillations of Flexible Slender Cylinders in Harmonically Perturbed Axial Flow, Part 1: Theory," ASME JOURNAL OF APPLIED MECHANICS, Vol. 47, pp. 709–714.

Picard, A., and Beaulieu, D., 1985, "Behaviour of a Simple Column Base Connection," *Canadian Journal of Civil Engineering*, Vol. 12, pp. 126–136.

Downloaded 03 May 2010 to 171.66.16.20. Redistribution subject to ASME license or copyright; see http://www.asme.org/terms/Terms_Use.cfm

Both Bounds to Buckling Loads and Fundamental Frequencies

R. Schmidt[11]

A simple procedure for improving the Krylov-Bogolyubov-Weinstein-Isaacson-Keller (KBWIK) lower bound and the Rayleigh upper bound to the first eigenvalue is described and illustrated by examples. The procedure makes use of the method of successive approximations, the Rayleigh-Schwarz quotients, the Krylov-Bogolyubov enclosure theorem, and the Temple inequality.

Introduction

For engineering purposes, the difficulties in obtaining an exact solution to an eigenvalue problem can often be circumvented by determining tight lower and upper bounds to the first eigenvalue, such as the critical buckling load or the fundamental frequency of vibration. A sufficiently accurate upper bound can usually be determined with the aid of the well-known Rayleigh, Ritz, Galërkin, and least-squares methods, and the procedures described by Schmidt (1989a, 1989b, 1990); however, despite many attempts, no simple satisfactory procedure has been devised for calculating a tight lower bound. The well-known Temple lower-bound formula (Temple and Bickley, 1956; Wang, 1953; Collatz, 1948) can yield accurate lower bounds to the first eigenvalue, but, unfortunately, requires a prerequisite knowledge of a lower bound to the second eigenvalue. The KBWIK lower-bound formula (Collatz, 1948; Isaacson and Keller, 1966) is less dependent on the second eigenvalue, but that is only because of its frequent less than satisfactory accuracy.

Of course, Temple and Bickley (1956) endeavored to alleviate the aforementioned difficulty by devising a method for calculating a (rough) lower bound L_2 to the second eigenvalue $k_2 \equiv E_2$ with the aid of the Green function—a method clearly inaccessible to the average engineer. Herein we suggest a simple procedure for estimating L_2 and calculating both bounds, the lower L and the upper U, to the first eigenvalue $k_1 \equiv E_1 \equiv E$. The efficacy of the procedure will depend to a certain degree on the judicious choice of the approximation to the first eigenfunction. Of course, the same is true in all other methods mentioned heretofore.

Formulas

The aforementioned Temple lower-bound formulas read

$$E \geq L_{TE} = \frac{T(E_2 - R)}{E_2 - T} > L_T = \frac{T(L_2 - R)}{L_2 - T}, \quad \text{if } L_2 > R, \quad (1)$$

where E denotes the exact value of the first eigenvalue k_1; L_{TE} and L_T are the Temple lower bounds to E; L_2 is a lower bound to the second eigenvalue $E_2 \equiv k_2$; and R and T are, respectively, the Rayleigh and the Schwarz (or Timoshenko) quotients, which are known always to be upper bounds, i.e., $R \geq T \geq E$.

The KBWIK lower-bound formula has the form (Isaacson and Keller, 1966)

$$E \geq L_{KB} = T - \sqrt{T(R-T)}, \text{ if } E_2 - T > T - E. \quad (2)$$

If the assumed shape function $u(x)$ used to calculate R is improved by one cycle of successive approximations applied to the (Sturm-type) differential equation (Temple and Bickley, 1956; Collatz, 1948), and the new shape function obtained (free of k) is denoted by $v(x)$, then, with the new Rayleigh quotient S, obtained by using v, Eqs. (1) and (2) may be replaced by more accurate formulas, viz.:

$$E \geq L_{SE} = \frac{S(E_2 - T)}{E_2 - S} > L_S = \frac{S(L_2 - T)}{L_2 - S}, \quad \text{if } E_2 > L_2 > T, \quad (3)$$

(see Temple and Bickley (1956) or Wang (1953) for a method of proof), and

$$E \geq L_{KS} = S - \sqrt{S(T-S)}, \quad \text{if } E_2 - S > S - E. \quad (4)$$

(There are extant many methods for the calculation of the Rayleigh-Schwarz (Timoshenko) quotients $R > T > S$; see references.)

To be able to use these formulas with confidence, we must know either the second eigenvalue $E_2 \equiv k_2$ or its lower bound $L_2 < E_2$ (the formulas (1) and (3) frequently yield a lower bound to $E \equiv E_1$ even when E_2 is replaced by one of its upper bounds!). Under certain limiting conditions, a rough value of L_2 can be arrived at in a very simple fashion. If the formula in (2) is definitely valid, then, if $L_{TE} > L_{KB}$ (which is usually the case in practical problems), we obtain an equipotent inequality

$$E_2 > T + \sqrt{T(R-T)} > E \quad (5)$$

by means of a simple manipulation of (1) and (2). Temple's auxiliary condition $E_2 > L_2 > R$ in (1) makes (5) definitely valid if $E_2 \geq 2T$ (a simple inspection of the formula provides the proof). The condition $E_2 \geq 2T$ is sufficient but not necessary for the validity of the lower bound in (5), nor is it very stringent in most engineering problems (according to Temple and Bickley 1956, E_2/T "is usually greater than 2"). (The second inequality in (5) is part of the aforementioned Krylov-Bogolyubov enclosure theorem, and so is (2).) Substituting formula (5) for L_2 in (3), we obtain a usually tight lower bound to the first eigenvalue E.

A tight upper bound to E can be easily calculated by the formula derived from (1) and (3) by Schmidt (1990, 1989), viz.,

$$U = a - \sqrt{a^2 - b^2} > E, \quad (6)$$

where

$$a = \frac{T(R-S)}{2(T-S)}, \quad b^2 = \frac{ST(R-T)}{T-S}. \quad (7)$$

The proposed procedure will now be demonstrated by means of simple illustrative problems with known exact solutions.

Euler's Column or Vibrating String

For clarity and fast verification by the reader, let us consider a very simple eigenvalue problem, viz.,

$$y'' + ky = 0, \quad y(0) = y(1) = 0, \quad (8)$$

which describes the buckled Euler column and the free vibration of a taut string. The exact eigenvalues are $k_1 \equiv E_1 \equiv E = \pi^2 = 9.869604$, $k_2 \equiv E_2 = 4\pi^2 = 39.478418, \ldots$ Since Eq. (8) is the Euler equation of the functional

$$F = \int_0^1 (y'^2 - ky^2)\,dx, \quad (9)$$

we have

[11]Professor of Engineering Mechanics, College of Engineering and Science, University of Detroit, Detroit, MI 48221. Mem. ASME.

Contributed by the Applied Mechanics Division of THE AMERICAN SOCIETY OF MECHANICAL ENGINEERS for publication in the ASME JOURNAL OF APPLIED MECHANICS. Manuscript received by the ASME Applied Mechanics Division, June 2, 1992; final revision, Mar. 4, 1993. Associate Technical Editor: F. Y. M. Wan.

Copyright © 1994 by ASME
Downloaded 03 May 2010 to 171.66.16.20. Redistribution subject to ASME license or copyright; see http://www.asme.org/terms/Terms_Use.cfm

$$R=\frac{\int u'^2dx}{\int u^2dx}, \quad T=\frac{\int u'v'dx}{\int uvdx}, \quad S=\frac{\int v'^2dx}{\int v^2dx}, \tag{10}$$

where the integrals extend from $x = 0$ to $x = 1$. Assuming a simple shape function $u = x - x^2$ and then rewriting Eq. (8) as $y'' \approx cv'' \approx -ky \approx -ku = -k(x - x^2)$, integrating, and determining the constants of integration by using the boundary conditions of (8), we obtain an improved shape function v (after setting $c = k/12$ in this one cycle of successive approximations), $v = x - 2x^3 + x^4$. With these two functions, Eqs. (10), (2), (4), (5), and (6) yield $R = 10$, $T = 168/17 = 9.882353$, $S = 306/31 = 9.870968$, $L_{KB} = 8.804100$, $L_{KS} = 9.535732$, $E_2 > 10.960606$, and $U = 9.869750$, respectively. Substituting the value $10.960606 < E_2$ for L_2 in Eq. (3), we obtain $L_S = 9.767830$. Thus we have bracketed the first eigenvalue E by $L_S = 9.767830 < E = 9.869604 < U = 9.869750$. A fairly tight lower bound has been obtained despite the great inaccuracy in L_2.

Encouraged by the good accuracy of the lower bound we venture now to improve on it. Selecting a simple polynomial $u_i = x - 3x^2 + 2x^3$ satisfying the orthogonality condition $\int_0^1 uu_i dx = 0$ of the modes and proceeding as before, we obtain $v_i = x - 10x^3 + 15x^4 - 6x^5$ (which turns out to be orthogonal to v), $R_i = 42$, $T_i = 40$, $S_i = 39.6$, $U_i = 38.695048$, and $(L_{KS})_i = S_i - [S_i(T_i - S_i)]^{1/2} = 35.620050$. Taking this last value for L_2 in (3) and also using $T = 168/17$ and $S = 306/31$, we obtain $L_S = 9.866603 < E = 9.869604$, a very tight lower bound to the first eigenvalue.

Vibrating Tapered Cantilever Beam

We place the origin of coordinates at the free tip and consider free flexural vibrations in the plane of the taper. The governing differential equation is (McLachlan, 1951)

$$(x^3y'')'' - kxy = 0, \quad k = \omega^2 l^4 \rho A_m / \bar{E} I_m, \tag{11}$$

which is accompanied by the boundary conditions $(x^3y'')' = x^3y'' = 0$ at $x = 0$ and $y = y' = 0$ at $x = 1$. It is easy to see that its functional is

$$F=\int_0^1 (x^3y''^2 - kxy^2)dx, \tag{12}$$

and hence (Schmidt, 1989b)

$$R=\frac{\int x^3u''^2dx}{\int xu^2dx}, \quad T=\frac{\int x^3u''v''dx}{\int xuvdx}, \quad S=\frac{\int x^3v''^2dx}{\int xv^2dx}. \tag{13}$$

Assuming $y \approx u = 1 - 2x + x^2$, we obtain $v = 29 - 72x + 60x^2 - 20x^3 + 3x^4$ by using the method of successive approximations. With these shape functions, Eqs. (13) and (6) yield $R = 30$, $T = 20160/709 = 28.434415$, $S = 63810/2257 = 28.272043$, and $U = 28.253387$, as compared with the exact value of $k_1 \equiv E = (5.315)^2 \approx 28.25$ (Kirchhoff, 1882). Equations (2), (4), and (5) now yield $L_{KB} = 21.762346$, $L_{KS} = 26.129476$, and $L_2 = 35.106484$. Substituting the values of L_2, S, and T into (3), we obtain $L_S = 27.600357$ for the lower bound to E.

References

Collatz, L., 1948, *Eigenwertprobleme*, Chelsea Publishing Co., New York.

Isaacson, E., and Keller, H. B., 1966, *Analysis of Numerical Methods*, John Wiley and Sons, New York.

Kirchhoff, G. R., 1882, Gesammelte Abhandlungen, Leipzig.

McLachlan, N. W., 1951, *Theory of Vibrations*, Dover Publications, New York.

Schmidt, R., 1989a, "A Way of Accurately Estimating Eigenvalues," ASME JOURNAL OF APPLIED MECHANICS, Vol. 56, pp. 224–226.

Schmidt, R., 1989b, "Accurate Fundamental Frequencies of Vibrating Beams via a Ritz-Rayleigh-Sturm-Liouville Approach," *Industrial Mathematics*, Vol. 39, Part 1, pp. 37–46.

Schmidt, R., 1990, "Accurate Upper Bounds to Eigenvalues via Temple's Lower-Bound Formula," *Industrial Mathematics*, Vol. 40, Part 1, pp. 11–18.

Temple, G., and Bickley, W. G., 1956, *Rayleigh's Principle*, Dover Publications, New York.

Wang, C.-T., 1953, *Applied Elasticity*, McGraw-Hill, New York.

Finite Element Simulation of the Hardness Testing of Ion-Implanted Materials

J. P. Blanchard[12]

1 Introduction

Ion implantation has been shown to be an effective process for improving the wear, corrosion, and fatigue properties of metals. Characterization of surfaces which have been altered by ion implantation is difficult, because the properties vary with depth from the surface and because the affected material is at extremely shallow depths (on the order of 0.1 microns). Hardness testing provides a simple method for assessing the effectiveness of ion-implantation in improving certain properties of a metal. It provides information about increased strength near the surface, indicating possible improvements in wear resistance and/or corrosion resistance. The interpretation of such tests, though, is complicated by the fact that the properties of ion-implanted materials vary with depth from the surface.

Finite element simulation can enhance the understanding of hardness tests in surface-modified materials by providing a link between the results of the test and the actual changes induced by the implantation. It can, for instance, indicate the position of the peak in the hardness, relative to the position of the peak in the profile of the implanted ions, as studied by Was (1990). It can also be used to determine the change in the strength of the implanted material by comparing the simulation to the test data (Bourcier et al., 1991). This is made possible by the fact that the effects of ion implantation are modeled as a change in yield strength in the implanted region. The implantation hardens the surface both by producing damage in the lattice and by producing hard compounds such as nitrides and carbides, thus altering the yield strength in the implanted layer. This paper provides the results of a generic study of the simulation of ion-implanted materials, including a discussion of the error introduced by the discretization of the surface and the dependence of the depth of the peak in the measured hardness on the depth of the peak in the yield strength distribution.

2 Model

Because indentation causes large-strain plastic deformation, there is little one can do analytically to study the problem. Hence, finite element methods are used here to simulate hardness tests. In previous studies, several investigators (Shih et al., 1990; Bhattacharya and Nix, 1988a) have used the finite

[12]Department of Nuclear Engineering and Engineering Physics, University of Wisconsin, 1500 Johnson Drive, Madison, WI 53706-1687. Assoc. Mem. ASME.

Contributed by the Applied Mechanics Division of THE AMERICAN SOCIETY OF MECHANICAL ENGINEERS for publication in the ASME JOURNAL OF APPLIED MECHANICS. Manuscript received by the ASME Applied Mechanics Division, June 12, 1992; final revision, Mar. 29, 1993. Associate Technical Editor: A. K. Noor.

Downloaded 03 May 2010 to 171.66.16.20. Redistribution subject to ASME license or copyright; see http://www.asme.org/terms/Terms_Use.cfm

$$R=\frac{\int u'^2dx}{\int u^2dx}, \quad T=\frac{\int u'v'dx}{\int uvdx}, \quad S=\frac{\int v'^2dx}{\int v^2dx}, \tag{10}$$

where the integrals extend from $x = 0$ to $x = 1$. Assuming a simple shape function $u = x - x^2$ and then rewriting Eq. (8) as $y'' \approx cv'' \approx -ky \approx -ku = -k(x - x^2)$, integrating, and determining the constants of integration by using the boundary conditions of (8), we obtain an improved shape function v (after setting $c = k/12$ in this one cycle of successive approximations), $v = x - 2x^3 + x^4$. With these two functions, Eqs. (10), (2), (4), (5), and (6) yield $R = 10$, $T = 168/17 = 9.882353$, $S = 306/31 = 9.870968$, $L_{KB} = 8.804100$, $L_{KS} = 9.535732$, $E_2 > 10.960606$, and $U = 9.869750$, respectively. Substituting the value $10.960606 < E_2$ for L_2 in Eq. (3), we obtain $L_S = 9.767830$. Thus we have bracketed the first eigenvalue E by $L_S = 9.767830 < E = 9.869604 < U = 9.869750$. A fairly tight lower bound has been obtained despite the great inaccuracy in L_2.

Encouraged by the good accuracy of the lower bound we venture now to improve on it. Selecting a simple polynomial $u_i = x - 3x^2 + 2x^3$ satisfying the orthogonality condition $\int_0^1 uu_i dx = 0$ of the modes and proceeding as before, we obtain $v_i = x - 10x^3 + 15x^4 - 6x^5$ (which turns out to be orthogonal to v), $R_i = 42$, $T_i = 40$, $S_i = 39.6$, $U_i = 38.695048$, and $(L_{KS})_i = S_i - [S_i(T_i - S_i)]^{1/2} = 35.620050$. Taking this last value for L_2 in (3) and also using $T = 168/17$ and $S = 306/31$, we obtain $L_S = 9.866603 < E = 9.869604$, a very tight lower bound to the first eigenvalue.

Vibrating Tapered Cantilever Beam

We place the origin of coordinates at the free tip and consider free flexural vibrations in the plane of the taper. The governing differential equation is (McLachlan, 1951)

$$(x^3y'')'' - kxy = 0, \quad k = \omega^2 l^4 \rho A_m / \bar{E} I_m, \tag{11}$$

which is accompanied by the boundary conditions $(x^3y'')' = x^3y'' = 0$ at $x = 0$ and $y = y' = 0$ at $x = 1$. It is easy to see that its functional is

$$F=\int_0^1 (x^3y''^2 - kxy^2)dx, \tag{12}$$

and hence (Schmidt, 1989b)

$$R=\frac{\int x^3u''^2dx}{\int xu^2dx}, \quad T=\frac{\int x^3u''v''dx}{\int xuvdx}, \quad S=\frac{\int x^3v''^2dx}{\int xv^2dx}. \tag{13}$$

Assuming $y \approx u = 1 - 2x + x^2$, we obtain $v = 29 - 72x + 60x^2 - 20x^3 + 3x^4$ by using the method of successive approximations. With these shape functions, Eqs. (13) and (6) yield $R = 30$, $T = 20160/709 = 28.434415$, $S = 63810/2257 = 28.272043$, and $U = 28.253387$, as compared with the exact value of $k_1 \equiv E = (5.315)^2 \approx 28.25$ (Kirchhoff, 1882). Equations (2), (4), and (5) now yield $L_{KB} = 21.762346$, $L_{KS} = 26.129476$, and $L_2 = 35.106484$. Substituting the values of L_2, S, and T into (3), we obtain $L_S = 27.600357$ for the lower bound to E.

References

Collatz, L., 1948, *Eigenwertprobleme*, Chelsea Publishing Co., New York.

Isaacson, E., and Keller, H. B., 1966, *Analysis of Numerical Methods*, John Wiley and Sons, New York.

Kirchhoff, G. R., 1882, Gesammelte Abhandlungen, Leipzig.

McLachlan, N. W., 1951, *Theory of Vibrations*, Dover Publications, New York.

Schmidt, R., 1989a, "A Way of Accurately Estimating Eigenvalues," ASME JOURNAL OF APPLIED MECHANICS, Vol. 56, pp. 224–226.

Schmidt, R., 1989b, "Accurate Fundamental Frequencies of Vibrating Beams via a Ritz-Rayleigh-Sturm-Liouville Approach," *Industrial Mathematics*, Vol. 39, Part 1, pp. 37–46.

Schmidt, R., 1990, "Accurate Upper Bounds to Eigenvalues via Temple's Lower-Bound Formula," *Industrial Mathematics*, Vol. 40, Part 1, pp. 11–18.

Temple, G., and Bickley, W. G., 1956, *Rayleigh's Principle*, Dover Publications, New York.

Wang, C.-T., 1953, *Applied Elasticity*, McGraw-Hill, New York.

Finite Element Simulation of the Hardness Testing of Ion-Implanted Materials

J. P. Blanchard[12]

1 Introduction

Ion implantation has been shown to be an effective process for improving the wear, corrosion, and fatigue properties of metals. Characterization of surfaces which have been altered by ion implantation is difficult, because the properties vary with depth from the surface and because the affected material is at extremely shallow depths (on the order of 0.1 microns). Hardness testing provides a simple method for assessing the effectiveness of ion-implantation in improving certain properties of a metal. It provides information about increased strength near the surface, indicating possible improvements in wear resistance and/or corrosion resistance. The interpretation of such tests, though, is complicated by the fact that the properties of ion-implanted materials vary with depth from the surface.

Finite element simulation can enhance the understanding of hardness tests in surface-modified materials by providing a link between the results of the test and the actual changes induced by the implantation. It can, for instance, indicate the position of the peak in the hardness, relative to the position of the peak in the profile of the implanted ions, as studied by Was (1990). It can also be used to determine the change in the strength of the implanted material by comparing the simulation to the test data (Bourcier et al., 1991). This is made possible by the fact that the effects of ion implantation are modeled as a change in yield strength in the implanted region. The implantation hardens the surface both by producing damage in the lattice and by producing hard compounds such as nitrides and carbides, thus altering the yield strength in the implanted layer. This paper provides the results of a generic study of the simulation of ion-implanted materials, including a discussion of the error introduced by the discretization of the surface and the dependence of the depth of the peak in the measured hardness on the depth of the peak in the yield strength distribution.

2 Model

Because indentation causes large-strain plastic deformation, there is little one can do analytically to study the problem. Hence, finite element methods are used here to simulate hardness tests. In previous studies, several investigators (Shih et al., 1990; Bhattacharya and Nix, 1988a) have used the finite

[12]Department of Nuclear Engineering and Engineering Physics, University of Wisconsin, 1500 Johnson Drive, Madison, WI 53706-1687. Assoc. Mem. ASME.

Contributed by the Applied Mechanics Division of THE AMERICAN SOCIETY OF MECHANICAL ENGINEERS for publication in the ASME JOURNAL OF APPLIED MECHANICS. Manuscript received by the ASME Applied Mechanics Division, June 12, 1992; final revision, Mar. 29, 1993. Associate Technical Editor: A. K. Noor.

Copyright © 1994 by ASME
Downloaded 03 May 2010 to 171.66.16.20. Redistribution subject to ASME license or copyright; see http://www.asme.org/terms/Terms_Use.cfm

element method to study the indentation of homogeneous materials, and one study (Bhattacharya and Nix, 1988b) considered the hardness testing of coatings. These studies have established good agreement between the codes and hardness measurements in homogeneous materials, so this paper makes no attempt to reestablish the ability of the finite element method to accurately represent such tests. This work relies heavily on the results of these previous studies in modeling ion-implanted materials.

The simulations described in this paper were carried out using the finite element code NIKE2D (Hallquist, 1986). This is an implicit, finite deformation, large strain code for plane strain, plane stress, and axisymmetric analyses. The simulations were run on a CRAY-II, with typical execution times on the order of 15 minutes of CPU time.

The model used for most of the analyses consisted of 2466 four-node quadrilateral elements and 2579 nodes. The analysis was conducted in axisymmetric mode, thus modeling a conical indenter. The indenters used in hardness tests are rarely conical, but the use of conical indenters to reduce simulation models to two dimensions has been shown to produce adequate results (Bhattacharya and Nix, 1988a). The included angle of the conical indenter was 136 deg. (That is, the angle between the indenter and the surface of the specimen was 22 deg.) The boundary conditions are identical to those employed by Bhattacharya and Nix (1988a,b), i.e., symmetry conditions were imposed on the centerline of the model and sliding conditions were imposed on the bottom and side of the indented specimen. It is presumed that the bottom and side of the specimen are sufficiently removed from the indent region as to not affect the hardness. This was verified by conducting additional simulations for larger specimens and comparing the hardness results. The contact between the indenter and the specimen surface was modeled using a slideline (adopting the terminology of the NIKE codes) and the indenter was modeled using 66 elements. (The author was forced to model the indenter because the code could not be made to model the contact between a string of coupled nodes and another surface.) The contact surface was assumed to be frictionless. The material model used for the specimen was linearly elastic-perfectly plastic, as the modeling of strain hardening has been shown to be relatively unimportant for hardness simulation (Bhattacharya and Nix, 1988a). The indenter was modeled as an elastic material with a stiffness (elastic modulus) 40 times that of the specimen. Higher stiffnesses tended to cause the simulation to fail.

The nominal properties used for the analysis are as follows: $E=127$ GPa, $\nu=0.278$, and $\sigma_{ys}=2070$ MPa, where E is the elastic modulus, ν is Poisson's ratio, and σ_{ys} is the yield strength. These properties were taken from an earlier work (Bhattacharya and Nix, 1988b) in order to allow verification of our results for indentation of unimplanted materials. The properties are for silicon. In cases where an implanted surface is simulated, the effect of the implantation is modeled by varying the yield strength of the specimen with depth from the surface. For most of the analyses, the peak yield stress in the implanted layer was chosen to be about 3.6 times that of the unimplanted material in order to produce hardness effects that exceed the noise resulting from errors in the simulation. This ratio is significantly smaller than the ratio of nearly 100 found previously in implanted aluminum (Bourcier et al., 1991), but it should be sufficient for demonstration of the distributions expected in typical ion-implanted samples.

In the ion-implanted materials, the yield stress was assumed to peak below the surface of the specimen. The actual distribution was bilinear, such that the yield stress was equal to that of the unimplanted material everywhere except in a local region of high strength (induced by the implantation). In this region, the strength was assumed to rise linearly to a peak value, and then decrease linearly to the value for the unimplanted material. This distribution implicitly assumes that the property changes are dominated by the formation of hard phases, such as carbides or nitrides, so that the property distribution follows the implanted ion distribution. The peaks in the yield stress were produced using eight sets of material properties, each with a different yield stress. The elastic modulus was not changed. Because eight materials were used, implanted layers with peaks below the surface were 15 elements wide while those with peaks at the surface were eight elements wide.

3 Model Verification

In order to test the ability of this model (and the NIKE-2D code) to simulate a hardness test, comparisons were made to previous simulations by Bhattacharya and Nix (1988a,b) who also compared their simulations to experimental hardness measurements. Hence, there is an implicit comparison to experimental results here. First, comparisons were made for the case of the hardness testing of a homogeneous material using selected properties from Bhattacharya and Nix (1988a). This previous work used a different code (ABAQUS), so it provides an independent test of NIKE-2D's ability to model hardness tests. The results from this simulation agreed with those from previous simulations within the error estimates established in the next section. In order to verify the ability of NIKE-2D to simulate specimens for which the yield stress varies with depth, comparisons were made to the results in Bhattacharya and Nix (1988b) in which the hardness of coatings are simulated. Again, comparison of results from NIKE-2D to results from previous analyses agreed within the expected error. Hence, NIKE-2D is capable of simulating hardness testing in both homogeneous and coated materials. The author is not aware of any previous simulations of ion-implanted materials.

4 Discretization Error

One of the most significant errors introduced by the finite element simulation technique lies in the inability of the method to determine the contact radius to better than the width of the elements. Because contact between the indenter and the specimen is given only at the nodes it cannot be determined more closely than the element width. Therefore, error is introduced and the error increases with decreasing contact area, as shown below.

If hardness is defined as

$$H=\frac{P}{\pi r^2}, \tag{1}$$

where H is the hardness, P is the applied load, and r is the radius of the projected contact area (a circle for conical indenters), then an error (δr) in the determination of the radius gives

$$H=\frac{P}{\pi(r+\delta r)^2}. \tag{2}$$

If the error in the radius is fixed by the element width in the region neighboring the contact area, then the error in the calculated hardness is a maximum when r is a minimum, i.e., for smaller loads (smaller contact areas).

The error due to this phenomenon can be bounded by using the full element width for the error in the radius. The results of two such calculations in a homogeneous material are shown in Fig. 1. One result is for a relatively coarse mesh (1144 nodes and 1066 elements) while the other is for a finer mesh (2579 nodes and 2466 elements). Two results of note can be extracted from this curve. First, the error decreases for increasing load due to the effects discussed previously. This supports the conclusions of Yost (1983), who used Monte Carlo simulations to generate similar results for the depth-dependence of errors incurred during hardness tests. The second conclusion exhib-

Downloaded 03 May 2010 to 171.66.16.20. Redistribution subject to ASME license or copyright; see http://www.asme.org/terms/Terms_Use.cfm

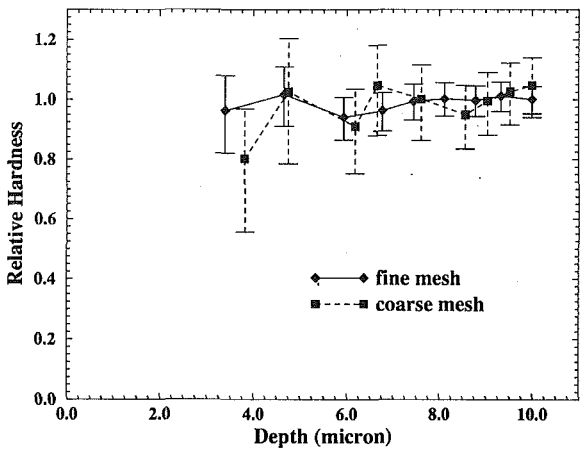


Fig. 1 Depth dependence of the relative hardness of a homogeneous material simulated using both a fine mesh and a coarse mesh

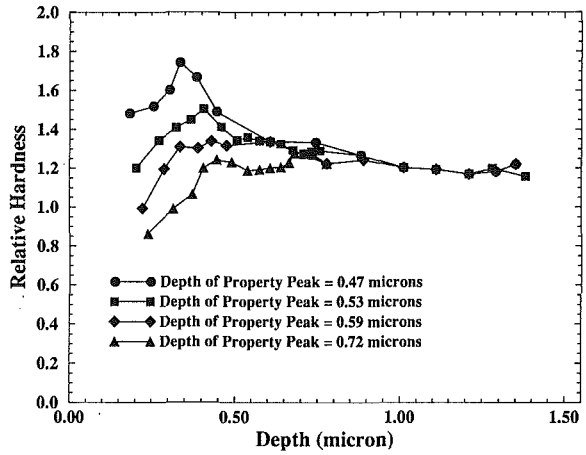


Fig. 2 Distribution of relative hardness for implanted layers which produce yield stress peaks of constant width with distributions of varying depth

ited by this curve is that within the error bars, the hardness of this homogeneous material is independent of depth. Assuming a constant hardness, the relative hardness here lies somewhere between 0.91 and 1.05 for the coarse mesh and between 0.96 and 1.02 for the finer mesh. The conclusion that the hardness is independent of depth agrees with the conclusion of previous simulations (Bhattacharya and Nix, 1988a). For reference, the smallest elements in the coarse-mesh calculation have a width of 0.083 microns while the width of the smallest elements in the fine-mesh calculation is 0.041 microns. This is significantly smaller than the largest indentation depth, which is on the order of ten microns. These element widths were reduced even further for the rest of the simulations presented in this paper. This reduction was such that the ratio of the smallest element width to the peak indentation depth was held roughly constant (~ 0.004).

It should be noted that this discretization is not the sole error encountered in such simulations. Large-strain plastic behavior is difficult to model, and much error is introduced by this fact. The above discussion merely indicates the importance of the choice of the element size in the neighborhood of the contact region. The curves in Fig. 1 do seem to indicate that this discretization error dominates the random errors produced by the inability of the code to simulate the contact at resolutions finer than the element width.

5 Property Changes at Various Depths

This section considers the simulation of ion-implanted samples by varying the yield stress distribution as described earlier. The depth of the peak in the strength is varied parametrically to model deeper ion penetration (higher ion energies). The results of this study are shown in Fig. 2. As expected, the depth of the peak in the hardness increases as the depth of the property distribution increases.

Another result that can be inferred from Fig. 2 is that the height of the hardness peak decreases with the depth of the peak in the properties, even though the height of the yield stress peak does not change. This likely occurs because as the yield stress peak deepens, the effects of this peak on the hardness can be spread over a wider area. (For reference, the relative hardness of a homogeneous material with a yield stress equal to that of the peak in the yield stress distribution used in these analyses is 2.64.) This phenomenon exhibits the ability of the hardness test to spread localized property changes over larger areas. Another notable result is that the hardness at the surface seems to decrease as the depth increases. The curve representing the deepest peak in the yield stress indicates that the normalized hardness is below unity at the surface, which is not an expected result. However, taking into account the errors discussed earlier, these relative hardness values are essentially unity, so no conclusive statements can be made here.

6 Conclusions

The hardness distribution in ion-implanted surfaces has been simulated using finite element analysis. The following conclusions can be deduced from the results of the study:

(1) The error due to the inability of finite element codes to resolve the contact area to better than the element width decreases with increasing penetration depth. This results from the same phenomenon that causes large experimental error in low-load hardness tests.

(2) As the depth of the property distribution increases, the height of the peak in the hardness distribution decreases and the width of the hardness distribution increases.

This latter point is significant, as hardness tests which increase the strength by the same amount but at different depths may exhibit distinctly different distributions in hardness. Hence, one must take care in comparing hardness tests of implanted surfaces for which the implantation depth is not identical.

Acknowledgments

This work was supported by the National Science Foundation via the Presidential Young Investigator Award Program, and by NSF Grant #ECD-8721545.

References

Bhattacharya, A. K., and Nix, W. D., 1988a, "Analysis of Elastic and Plastic Deformation Associated With Indentation Testing of Thin Films on Substrates," *International Journal of Solids and Structures*, Vol. 24, p. 1287.

Bhattacharya, A. K., and Nix, W. D., 1988b, "Finite Element Simulation of Indentation Experiments," *International Journal of Solids and Structures*, Vol. 24, p. 881.

Bourcier, R. J., Follstaedt, D. M., Dugger, M. T., and Myers, S. M., "Mechanical Characterization of Several Ion-Implanted Alloys: Nanoindentation Testing, Wear Testing and Finite Element Modeling," *Nuclear Instruments and Methods*, Vol. B59/60, p. 905.

Hallquist, J. O., 1986, "NIKE-2D—A Vectorized Implicit, Finite Deformation Finite Element Code for Analyzing the Static and Dynamic Response of 2-D Solids With Interactive Rezoning and Graphics," Lawrence Livermore National Laboratory Report, UCID-19677.

Shih, C. W., Yang, M., and Li, J. C. M., 1991, "Effect of Tip Radius on Nanoindentation," *Journal of Materials Research*, Vol. 6, p. 2623.

Was, G. S., 1990, "Surface Mechanical Properties of Aluminum Implanted Nickel and Co-Evaporated Ni-Al on Nickel," *Journal of Materials Research*, Vol. 5, p. 1668.

Yost, F. G., 1983, "On the Definition of Hardness," *Metallurgical Transactions A*, Vol. 14, p. 947.

Downloaded 03 May 2010 to 171.66.16.20. Redistribution subject to ASME license or copyright; see http://www.asme.org/terms/Terms_Use.cfm

Torsion of Rectangular Bars With Multiple Cylindrical Reinforcement or Cavities

A. K. Naghdi[13]

In recent years, the problems of torsion of rectangular bars with or without reinforcement have been investigated in a few occasions. Among the investigations are the works of Naghdi (1983, 1990) and Kuo and Conway (1980). Naghdi obtained solutions for torsion of rectangular bars with two and four cavities, and Kuo and Conway solved the problem of a square bar with four cylindrical reinforcement using Howland functions (1935). Employing a special class of basis functions, in the present work, the problems of torsion of rectangular bars with $4N$ cylindrical reinforcement are solved. Each set of cavities for reinforcement material are symmetrical with respect to the two axes of symmetry of the rectangular section. However, the radii of cavities in various sets are independent of one another. The convergence of the series solutions involved is very much improved. Numerical results are presented.

Method of Solution

In the following, we shall discuss the case of torsion of a rectangular prismatic bar with reinforcement in four cavities ($N=1$), and the fundamental sets of basis functions suitable for the solution. The basic functions for $N=2, 3, \ldots$ corresponding, respectively, to eight, twelve, . . . reinforcement cavities are obtained by placing the poles of the fundamental sets at the centers of the cavities and thus generating the appropriate solution. the solution for torsion of rectangular bars with $4N$ cavities with no reinforcement can be found from the former solutions by obtaining the limits when the modulus of rigidity of the reinforcing material tends to zero.

Consider a prismatic bar whose cross-section is a multiply connected rectangular region a by b having four equal and symmetrically located circular cutouts reinforced by cylinders of a different material. Choose the nondimensional coordinate axes of symmetry $\xi=X/a$, $\eta=y/a$, $\rho=r/a$, and denote by subscripts 1 and 2 for symbols related to rectangular and reinforcing regions, respectively, as shown in Fig. 1. According to the St. Venant theory of torsion of prismatic bars given by Sokolnikoff (1956), the equations

$$\frac{\partial^2\psi_1}{\partial\xi^2}+\frac{\partial^2\psi_1}{\partial\eta^2}=0 \quad \text{in region 1,} \tag{1}$$

$$\frac{\partial^2\psi_2}{\partial\rho^2}+\frac{1}{\rho}\frac{\partial\psi_2}{\partial\rho}+\frac{1}{\rho^2}\frac{\partial^2\psi_2}{\partial\Phi^2}=0 \quad \text{in region 2,} \tag{2}$$

must be satisfied and the following boundary conditions have to be fulfilled:

$$\psi_1=\frac{1}{2}(\xi^2+\eta^2) \quad \text{on the outer boundary,} \tag{3}$$

$$\psi_1-\frac{G_2}{G_1}\psi_2=\frac{1}{2}\left(1-\frac{G_2}{G_1}\right)(\xi^2+\eta^2)+K, \quad \text{on } \rho=\rho_0 \tag{4}$$

$$\frac{\partial\psi_1}{\partial\rho}=\frac{\partial\psi_2}{\partial\rho}, \tag{5}$$

in which G_1 and G_2 are the moduli of shear for the material of the rectangular bar and cylindrical reinforcement, respectively, and K is a constant to be determined. In addition, it is required that the following conditions be satisfied.

$$\oint_{c_2}\frac{\partial\psi_1}{\partial\rho}\,ds=0, \tag{6}$$

$$\oint_{c_2}\frac{\partial\psi_2}{\partial\rho}\,ds=0, \tag{7}$$

in which c_2 is the boundary of any of the four circular regions for reinforcement and ds is the element of arc length. The function ψ_2 satisfying Eq. (2) is written in the usual way

$$\psi_2=\sum_{n=1}^{\infty}[\overline{A}_n\rho^n\cos n\Phi+\overline{B}_n\rho^n\sin n\Phi], \tag{8}$$

in which $\overline{A}_n$ and $\overline{B}_n$ are the unknown constants of integration. The function ψ_1 is now sought in the form

$$\psi_1=\overline{\psi}+A_0\psi_0^*+A_1\psi_1^*+A_2\psi_2^*+\ldots+B_1\psi_1^0+B_2\psi_2^0+\ldots. \tag{9}$$

where $\overline{\psi}$ is the stress function for torsion of a solid rectangular cross-section bar given by Sokolnikoff (1956) and ψ_j^* and ψ_j^0 are sets of linearly independent basic functions of Laplace's equation, which automatically vanish on the outer boundary, and have singularities at the centers of the cutouts. The unknown constants A_j, B_j as well as $\overline{A}_n$, $\overline{B}_n$, and K are to be determined from the conditions (4), (5), (6), and (7). For the derivation of ψ_n^* and ψ_n^0 the following technique is employed. First, the solution of Poisson's equation, suitable for the problem under considerations,

$$\frac{\partial^2\tilde{\psi}}{\partial\xi^2}+\frac{\partial^2\tilde{\psi}}{\partial\eta^2}=\sum_{n=1,3,5}^{\infty}S_n^*[\delta(\eta-\eta_0)+\delta(\eta+\eta_0)]\cos(n\pi\xi), \tag{10}$$

in which S_n^* are the Fourier coefficients, δ is the unit impulse function, and η_0 is showing in Fig. 1 is sought in the form

$$\tilde{\psi}=\sum_{n=1,3,5}^{\infty}g_n(\eta)\cos(n\pi\xi). \tag{11}$$

Substituting (11) in (10), employing the homogeneous boundary condition for $\tilde{\psi}$ at $\eta=\pm b/2a$, and considering that the function $\tilde{\psi}$ must be continuous at $\eta=\pm\eta_0$, the function $\tilde{\psi}$ is obtained in the usual way. The Fourier coefficients S_n^* are now selected in such a way that $\tilde{\psi}$ represents the solution for the case of four unit concentrated positive sources at $\xi=\pm\xi_0$ $\eta=\pm\eta_0$. The results are

$$\tilde{\psi}=\sum_{n=1,3,5}^{\infty}\frac{4\cosh(n\pi\eta_0)\sinh[n\pi(\eta-b/2a)]}{(n\pi)\cosh(n\pi b/2a)}\times\cos(n\pi\xi_0)\cos(n\pi\xi) \quad \text{for } b/2a\geq\eta>\eta_0, \tag{12}$$

$$\tilde{\psi}=\sum_{n=1,3,5}^{\infty}\frac{4\cosh(n\pi\eta)\sinh[h\pi(\eta_0-b/2a)]}{(n\pi)\cosh(n\pi b/2a)}\times\cos(n\pi\xi_0)\cos(n\pi\xi) \quad \text{for } \eta_0>\eta>-\eta_0, \tag{13}$$

$$\tilde{\psi}=\sum_{n=1,3,5}^{\infty}\frac{-4\cosh(n\pi\eta_0)\sinh[n\pi(\eta+b/2a)]}{(n\pi)\cosh(n\pi b/2a)}\times\cos(n\pi\xi_0)\cos(n\pi\xi) \quad \text{for } -b/2a\leq\eta<-\eta_0. \tag{14}$$

[13]Professor of Mechanical Engineering and Mathematical Sciences, Department of Mechanical Engineering, Purdue University, Indianapolis, IN 46202-5132.

Contributed by the Applied Mechanics Division of THE AMERICAN SOCIETY OF MECHANICAL ENGINEERS for publication in the ASME JOURNAL OF APPLIED MECHANICS. Manuscript received by the ASME Applied Mechanics Division, June 29, 1992; final revision, May 19, 1993. Associate Technical Editor: X. Markenscoff.

Copyright © 1994 by ASME
Downloaded 03 May 2010 to 171.66.16.20. Redistribution subject to ASME license or copyright; see http://www.asme.org/terms/Terms_Use.cfm

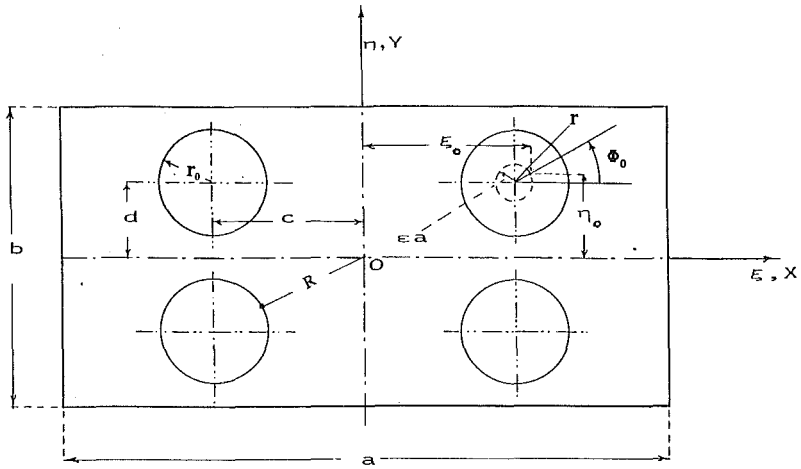


Fig. 1 Cross-section of a rectangular bar with cylindrical reinforcement subject to torque

Next, we shall generate certain basic functions ψ_j^* and ψ_j^0 from the following integrals

$$\psi_j^* = \oint \tilde{\psi}(\xi, \eta, \xi_0, \eta_0)\epsilon \cos J\Phi_0 d\Phi_0 \quad \text{for } J=0,1,2,3, \ldots, \quad (15)$$

$$\psi_j^0 = \oint \tilde{\psi}(\xi, \eta, \xi_0, \eta_0)\epsilon \sin j\Phi_0 d\Phi_0 \quad \text{for } J=1, 2, 3, \ldots, \quad (16)$$

in which the path of integration in around the center of one of the four inner circular cutouts with parametric equations (see Fig. 1):

$$\xi_0 = \bar{c} + \epsilon \cos \Phi_0, \quad \bar{c} = c/a,$$
$$\eta_0 = \bar{d} + \epsilon \sin \Phi_0, \quad \bar{d} = d/a,$$
$$\epsilon = a \text{ small positive number.} \quad (17)$$

Substituting (17) in (12), (13), (14), expanding terms such as

$$\cosh(n\pi\eta_0)\cos(n\pi\xi_0)$$

in powers of ϵ, we integrate (15) and (16). Finally we shrink to zero the radius of path of integration ϵ and retain the dominating term. Discarding coefficients which can eventually be absorbed into $A_0, A_1, \ldots, B_1, B_2, \ldots$ given in (9), we obtain the desired linearly independent basic functions which automatically satisfy the homogeneous outer boundary condition. Those basic functions are written in different forms depending on various regions for η. We shall give only the results for the region $b/2a \geq \eta > \bar{d}$:

$$\psi_{2L}^* = (-1)^L \sum_{n=1,3,5}^{\infty} \frac{(n)^{2L-1}\cos(n\pi\bar{c})\cosh(n\pi\bar{d})}{\cosh(n\pi b/2a)} f_1(\xi, \eta)$$
$$f_1(\xi, \eta) = \sinh[n\pi(\eta - b2a)]\cos(n\pi\xi), \quad L=0, 1, 2, \ldots, \quad (18)$$

$$\psi_{2L-1}^* = (-1)^L \sum_{n=1,3,5}^{\infty} \frac{(n)^{2L-2}\sin(n\pi\bar{c})\cosh(n\pi\bar{d})}{\cosh(n\pi b/2a)} f_1(\xi, \eta), \quad (19)$$

$$\psi_{2L}^0 = (-1)^{L+1} \sum_{n=1,3,5}^{\infty} \frac{(n)^{2L-1}\sin(n\pi\bar{c})\sinh(n\pi\bar{d})}{\cosh(n\pi b/2a)} f_1(\xi, \eta), \quad (20)$$

$$\psi_{2L-1}^0 = (-1)^L \sum_{n=1,3,5}^{\infty} \frac{(n)^{2L-2}\cos(n\pi\bar{c})\sinh(n\pi\bar{d})}{\cosh(n\pi b/2a)} f_1(\xi, \eta), \quad L=1, 2, 3, \ldots. \quad (21)$$

The main problem with the series given in (18) through (21) and similar series is slow rate of convergence when $|\eta - \bar{d}| << 1$. To eliminate this difficulty, note that

$$\frac{1}{\cosh(n\pi b/2a)} = \frac{1}{\frac{1}{2}e^{(n\pi b/2a)}[1 + e^{-n\pi b/a}]}$$
$$= 2[e^{-n\pi b/2a} - e^{-3(n\pi b/2a)} + e^{-5(n\pi b/2a)} - \ldots]. \quad (22)$$

Employing (22) in the series such as those given in (18) through (21) and writing the hyperbolic sine and cosine terms in exponential forms, we obtain the basic functions as the sum of two series: one which has a very rapid convergence property, and a number of other series which are written in the form

$$\sum_{n=1,3,5}^{\infty} n^J e^{-n\lambda} \frac{\sin(n\Phi_0)}{\cos(n\Phi_0)}, \quad (23)$$

in which λ is a positive number. We shall employ the following technique in order to write the summation (23) in closed form. Consider the analytic function given by Gradshteyn and Ryzhik (1965)

$$F(Z) = \frac{1}{2} + \sum_{n=1}^{\infty} e^{-nZ} = \frac{1}{2}\coth(Z/2),$$
$$Z = \lambda + i\Phi_0, \; i = \sqrt{-1}. \quad (24)$$

Since the derivatives of an analytic function are still analytic functions, we differentiate (24) many times to obtain

$$\sum_{n=1}^{\infty} ne^{-nz} = \frac{1}{4}\frac{1}{\sinh^2(Z/2)},$$
$$\sum_{n=1}^{\infty} n^2 e^{-nZ} = \frac{1}{4}\frac{\cosh(Z/2)}{\sinh^3(Z/2)},$$
$$\ldots\ldots\ldots$$
$$\ldots\ldots\ldots \quad (25)$$

The real and imaginary parts of the relations in (25) give the closed-form representations for series (23). We have developed a recurrence formula for the nth derivative of the

Downloaded 03 May 2010 to 171.66.16.20. Redistribution subject to ASME license or copyright; see http://www.asme.org/terms/Terms_Use.cfm

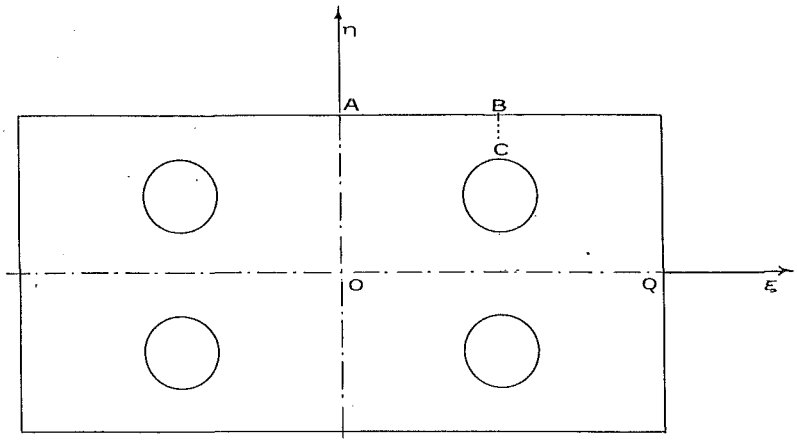


Fig. 2 Positions of line segments *AB*, *CB*, and *OQ* along which $\tau^*_{\zeta\xi}$ and $\tau^*_{\zeta\eta}$ are given

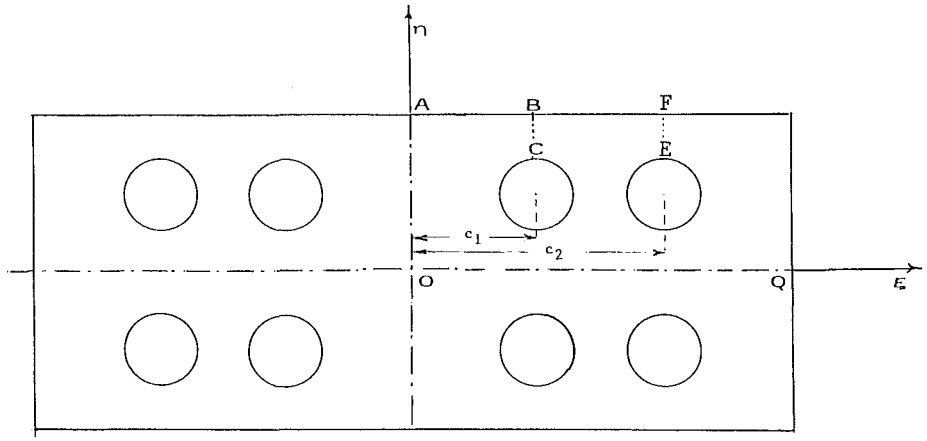


Fig. 3 Positions of line segments *AB*, *CB*, *FE*, and *OQ* along which $\tau^*_{\zeta\xi}$ and $\tau^*_{\zeta\eta}$ are given

function $F(Z)$ and programmed it. Thus the basic function ψ^*_J and ψ^0_J in the series form with rapid convergence property are available for any given J.

Numerical Results

Since the outer boundary condition (3) for the problem under consideration is automatically satisfied by function ψ_1, it is sufficient to satisfy only the inner boundary conditions (4) and (5) as well as the conditions (6). It is not too difficult to show that the condition (6) is satisfied if

$$A_0 = 0. \tag{26}$$

Also, it can be easily seen that the condition (7) is automatically satisfied by ψ_2 given in (8). The rest of the unknown constants $A_1, A_2, \ldots, B_1, B_2, \ldots, \overline{A}_1, \overline{A}_2, \ldots, \overline{B}_1, \overline{B}_2, \ldots$ and K are determined by the point-by-point satisfaction of the inner boundary conditions and the employment of method of least square error given by Hildebrand (1956). Define the nondimensional shear stresses $\overline{\tau}_{\zeta\Phi}$ and $\tau^*_{\zeta\Phi}$ as follows:

$$\overline{\tau}_{\zeta\Phi} = \frac{\tau_{\zeta\Phi}}{G\alpha a^2}, \quad \tau^*_{\zeta\Phi} = \frac{\overline{\tau}_{\zeta\Phi}}{\overline{D}}, \tag{27}$$

in which ζ is the axis perpendicular to ξ, η axes and $\tau_{\zeta\Phi}$ is the shear stress in $\xi\eta$-plane in the direction of Φ, α is the angle of twist per unit length. The quantity $\overline{D}$ is the nondimensional torsional rigidity defined as

$$\overline{D} = \int\int_{\text{Region 1}} \left(\xi \frac{\partial \psi_1}{\partial \xi} + \eta \frac{\partial \psi_1}{\partial \eta}\right) d\xi d\eta$$

$$+ \frac{G_2}{G_1} \int\int_{\text{Region 2}} \left(\xi \frac{\partial \psi_2}{\partial \xi} + \eta \frac{\partial \psi_2}{\partial \eta}\right) d\xi d\eta$$

$$= \frac{1}{2a^2} \oint_{C^*} \varphi_1 d(R^2) + \frac{1}{2a^2} \frac{G_2}{G_1} \oint_{c_2} \varphi_2 d(R^2), \tag{28}$$

in which φ_1 and φ_2 are the dimensionless warping functions for regions 1 and 2, respectively, R is shown in Fig. 2, and C^* is the complete boundary of region 1 consisting of the outer rectangle and the inner circles. Knowing that φ_1 and φ_2 are equal of c_2, expression (28) can be somewhat simplified. In Tables 1, 2, 3, and 4 the values of the nondimensional shear stress $\tau^*_{\zeta\xi}$ and $\tau^*_{\zeta\eta}$ are presented for the case of $N=1$ along *AB*, *CB*, and *OQ* (See Fig. 2) for values of $G_2/G_1 = 30$, 15, and 5, 0, respectively. In Tables 5, and 6 the values of dimensionless shear stresses $\overline{\tau}_{\zeta\Phi}$ on the inner boundary are presented for the special case of square bar, $N=1$, and $G_2/G_1 = 5$ and 0, respectively. Finally, in Table 7, the values of $\tau^*_{\zeta\xi}$ and $\tau^*_{\zeta\eta}$ are given for the case of $N=2$ (8 cavities), $G_2/G_1 = 0$ along *AB*, *CB*, *FE*, and *OQ* (see Fig. 3). For all the cases presented here, the values of $\overline{D}$ are also given.

Downloaded 03 May 2010 to 171.66.16.20. Redistribution subject to ASME license or copyright; see http://www.asme.org/terms/Terms_Use.cfm

Table 1 The values of dimensionless shear stresses $\tau^*_{\xi\xi}$ and $\tau^*_{\xi\eta}$ for the case of $N = 1$, $\rho_0 = 0.0625$, $\bar{c} = 0.25$, $\bar{d} = 0.125$, $b/a = 0.5$, and $G_2/G_1 = 30$. $\bar{D} = 0.0351$.

ξ	0	0.03947	0.07895	0.1184	0.1579	0.1974	0.25
$\tau^*_{\xi\xi}$ Along AB	-14.41	-14.38	-14.27	-13.95	-13.17	-11.60	-9.343
η	0.1875	0.1974	0.2072	0.2171	0.2270	0.2368	0.25
$\tau^*_{\xi\xi}$ Along CB	-2.193	-4.230	-5.694	-6.822	-7.736	-8.501	-9.343
ξ	0	0.07895	0.1579	0.2368	0.3158	0.3947	0.5
$\tau^*_{\zeta\eta}$ Along OQ	0	0.4144	1.226	2.939	3.807	5.544	10.27

Table 2 The values of dimensionless shear stresses $\tau^*_{\xi\xi}$ and $\tau^*_{\xi\eta}$ for the case of $N = 1$, $\rho_0 = 0.0625$, $\bar{c} = 0.25$, $\bar{d} = 0.125$, $b/a = 0.5$, and $G_2/G_1 = 15$. $\bar{D} = 0.0334$.

ξ	0	0.03947	0.07895	0.1184	0.1579	0.1974	0.25
$\tau^*_{\xi\xi}$ Along AB	-15.04	-15.02	-14.90	-14.58	-13.79	-12.23	-9.971
η	0.1875	0.1974	0.2072	0.2171	0.2270	0.2368	0.25
$\tau^*_{\xi\xi}$ Along CB	-2.709	-4.750	-6.225	-7.370	-8.305	-9.093	-9.971
ξ	0	0.07895	0.1579	0.2368	0.3158	0.3947	0.5
$\tau^*_{\zeta\eta}$ Along OQ	0	0.4422	1.282	3.021	3.976	5.836	10.80

Table 3 The values of dimensionless shear stresses $\tau^*_{\xi\xi}$ and $\tau^*_{\xi\eta}$ for the case of $N = 1$, $\rho_0 = 0.0625$, $\bar{c} = 0.25$, $\bar{d} = 0.125$, $b/a = 0.5$, and $G_2/G_1 = 5$. $\bar{D} = 0.0316$.

ξ	0	0.03947	0.07895	0.1184	0.1579	0.1974	0.25
$\tau^*_{\xi\xi}$ Along AB	-15.61	-15.57	-15.46	-15.16	-14.46	-13.12	-11.13
η	0.1875	0.1974	0.2072	0.2171	0.2270	0.2368	0.25
$\tau^*_{\xi\xi}$ Along CB	-4.359	-6.151	-7.483	-8.547	-9.442	-10.22	-11.13
ξ	0	0.07895	0.1579	0.2368	0.3158	0.3947	0.5
$\tau^*_{\zeta\eta}$ Along OQ	0	0.4931	1.336	2.968	4.128	6.222	11.49

Table 4 The values of dimensionless shear stresses $\tau^*_{\xi\xi}$ and $\tau^*_{\xi\eta}$ for the case of $N = 1$, $\rho_0 = 0.0625$, $\bar{c} = 0.25$, $\bar{d} = 0.125$, $b/a = 0.5$, and $G_2/G_1 = 0$. $\bar{D} = 0.0247$.

ξ	0	0.03947	0.07895	0.1184	0.1579	0.1974	0.25
$\tau^*_{\xi\xi}$ Along AB	-17.15	-17.12	-16.99	-16.95	-17.43	-18.76	-20.35
η	0.1875	0.1974	0.2072	0.2171	0.2270	0.2368	0.25
$\tau^*_{\xi\xi}$ Along CB	-21.92	-20.03	-19.18	-18.93	-19.06	-19.48	-20.35
ξ	0	0.07895	0.1579	0.2368	0.3158	0.3947	0.5
$\tau^*_{\zeta\eta}$ Along OQ	0	0.8629	1.569	1.923	4.580	8.377	15.27

Table 5 The values of dimensionless shear stresses $\bar{\tau}_{\zeta\Phi}$ on the inner boundary for the case of $N = 1$, $\rho_0 = 0.125$, $\bar{c} = \sqrt{2}/8$, $\bar{d} = \sqrt{2}/8$, $b/a = 1$, and $G_2/G_1 = 5$. $\bar{D} = 0.1644$.

Φ rad	$\pi/48$	$5\pi/48$	$9\pi/48$	$13\pi/48$	$17\pi/48$	$21\pi/48$
$\bar{\tau}_{\zeta\Phi}$	0.3058	0.2980	0.3040	0.2910	0.1918	0.04641
Φ rad	$25\pi/48$	$29\pi/48$	$33\pi/48$	$37\pi/48$	$41\pi/48$	$45\pi/48$
$\bar{\tau}_{\zeta\Phi}$	-0.06818	-0.1200	-0.1025	-0.01780	0.1193	0.2522

Table 6 The values of dimensionless shear stresses $\bar{\tau}_{\zeta\Phi}$ on the inner boundary for the case of $N = 1$, $\rho_0 = 0.125$, $\bar{c} = \sqrt{2}/8$, $\bar{d} = \sqrt{2}/8$, $b/a = 1$, and $G_2/G_1 = 0$. $\bar{D} = 0.1235$.

Φ rad	$\pi/48$	$5\pi/48$	$9\pi/48$	$13\pi/48$	$17\pi/48$	$21\pi/48$
$\bar{\tau}_{\zeta\Phi}$	0.4215	0.4141	0.4231	0.3854	0.1862	-0.04133
Φ rad	$25\pi/48$	$29\pi/48$	$33\pi/48$	$37\pi/48$	$41\pi/48$	$45\pi/48$
$\bar{\tau}_{\zeta\Phi}$	-0.1461	-0.2160	-0.1870	-0.1039	0.06025	0.3038

Table 7 The values of dimensionless shear stresses $\tau^*_{\xi\xi}$ and $\tau^*_{\xi\eta}$ for the case of $N = 2$, $\rho_0 = 0.0625$, $\bar{c}_1 = 0.16$, $\bar{c}_2 = 0.33$, $\bar{d} = 0.125$, $b/a = 0.5$, and $G_2/G_1 = 0$. $\bar{D} = 0.0207$.

ξ	0	0.02723	0.05447	0.08170	0.1089	0.1362	0.16
$\tau^*_{\xi\xi}$ Along AB	-26.41	-26.62	-27.24	-28.22	-29.24	-29.53	-28.56
η	0.1875	0.1981	0.2088	0.2194	0.2301	0.2407	0.25
$\tau^*_{\xi\xi}$ Along CB	-29.07	-27.16	-26.51	-26.55	-27.00	-27.74	-28.56
η	0.1875	0.1981	0.2088	0.2194	0.2301	0.2407	0.25
$\tau^*_{\xi\xi}$ Along FE	-12.17	-12.42	-13.00	-13.75	-14.61	-15.55	-16.43
ξ	0	0.08511	0.1702	0.2553	0.3404	0.4255	0.5
$\tau^*_{\zeta\eta}$ Along OQ	0	1.958	4.764	5.802	11.12	10.40	14.83

Discussion

Numerical results obtained in this investigation are very accurate and well within the ordinary engineering approximations. Using 40 linear equations and 25 unknowns for the cases presented in Tables 1, 2, and 3, an accuracy of at least four significant figures in satisfaction of the inner boundary conditions is obtained. Furthermore, to justify the correctness of the solution, another method is utilized for the case of torsion of square bars. This latter method uses solutions of Laplace's equation in polar coordinates and employs numerical technique on both inner and outer boundary conditions. The results of the two independent methods are in very good agreement. Comparing the values of stresses given in Tables 5 and 6 with those presented in the form of graphs by Kuo and Conway (1980), the following observations are made. Considering the nondimensionalizing factors, and different coordinate systems in the two articles, it is seen that the results in Table 5 are of the same order of magnitude as those given by the mentioned authors but are not close. However, the results given in Table 6 are completely different from those presented by Kuo and Conway (1980).

It is believed that the results obtained by these authors are in error. Also, the authors claim that the torsional rigidity is little affected by the presence of the reinforcing rods, and it is close to that of an unreinforced shaft. This statement does not seem to be true and the results given in the present paper show the dependence of $\bar{D}$ on G_2/G_1. For example, the results from Tables 4 and 3 show that $\bar{D}$ increases from 0.0247 to 0.0316 as G_2/G_1 varies from 0 to 5. This is an increase of almost 28 percent for $\bar{D}$. For the cases presented in Tables 5 and 6, an increase of 33 percent in torsional rigidity $\bar{D}$ is observed.

References

Gradshteyn, I. S., and Ryzhik, I. M., 1965, *Table of Integrals Series and Products*, New York and London.

Hildebrand, F. B., 1956, *Introduction to Numerical Analysis*, McGraw-Hill, New York.

Howland, R. C. J., 1935, "Potential Functions with Periodicity in One Co-

Downloaded 03 May 2010 to 171.66.16.20. Redistribution subject to ASME license or copyright; see http://www.asme.org/terms/Terms_Use.cfm

ordinate," *Proceedings of The Cambridge Philosophical Society, London*, Vol. A30, pp. 315–326.

Kuo, Y-M., and Conway, H. D., 1980, "Torsion of Reinforced Square Cylinder," *Journal of The Engineering Mechanics Division*, ASCE, Vol. 106, No. EM6, pp. 1341–1347.

Naghdi, A. K., 1990, "Torsion of a Rectangular Bar with Multiple Cylindrical Cutouts," Proceedings of The 15th South Eastern Conference on Theoretical and Applied Mechanics, pp. 327–332.

Naghdi, A. K., 1983, "Torsion of a Rectangular Bar with Two Circular Holes," *Journal of Engineering Mechanics*, ASCE, Vol. 109, No. 2, pp. 643–648.

Sokolnikoff, S., 1956, *Mathematical Theory of Elasticity*, McGraw-Hill, New York.

Diffusive Transport Across a Wavy Plate Composed of Annular Sectors

C. Y. Wang[14]

Introduction

Diffusive transport across a plate or barrier is fundamental to heat and mass transfer. Let the temperature (or concentration) be at different constant levels on the two surfaces of a plate of uniform thickness. Simple exact solutions exist if the plate is in the shape of a flat layer or a circular annulus (Crank, 1956). Perturbation solution is possible if the plate is not flat, but with small curvature compared to the thickness (Wang, 1982). For plates with large curvature, either complex transform (if at all possible) or tedious numerical integration of the partial differential equations is necessary.

This Note uses a simple, highly efficient, semianalytical method to treat a wavy plate composed of joined annular sectors (Fig. 1). Practical applications of diffusion through wavy surfaces include walls which enhance heat transfer (Webb, 1987) and the internal folds of the small intestine (Hendrix, 1974). We shall illustrate the solution to this diffusion problem using the terminology of heat conduction.

Solution Method

Normalize all lengths by the thickness of the plate h. Each period of the plate consists of two annular sectors (I and II) both with opening angle 2β and inner and outer radii b and $1+b$, respectively. We normalize the temperature T by the exterior temperature T_e and interior temperature T_i as follows:

$$\tau = 2\left(\frac{T-T_i}{T_e-T_i}\right) - 1. \tag{1}$$

The governing equation is the Laplace equation in cylindrical coordinates

$$\frac{\partial^2\tau}{\partial r^2}+\frac{1}{r}\frac{\partial\tau}{\partial r}+\frac{1}{r}\frac{\partial^2\tau}{\partial\theta^2}=0. \tag{2}$$

The boundary conditions are that on the top surface $\tau=1$ and on the bottom surface $\tau=-1$. Use separation of variables on Eq. (2) and set the sign of the separation constant such that eigenfunctions exist in the radical direction.

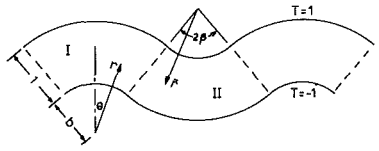


Fig. 1 The coordinate system

For Sector I, the following form of solution is obtained:

$$\tau_I(r,\theta)=\tau_0(r)+\sum_1^\infty B_n \sin\left[\lambda \ln\left(\frac{r}{b}\right)\right]\cosh(\lambda\theta). \tag{3}$$

Here $\lambda\equiv n\pi/\ln(1+1/b)$ are eigenvalues, B_n are constants to be determined, and τ_0 is the axisymmetric solution satisfying the boundary conditions

$$\tau_0(r)=1-2\frac{\ln\left(\frac{b+1}{r}\right)}{\ln\left(1+\frac{1}{b}\right)}. \tag{4}$$

Again, considering symmetry, the solution to Sector II is

$$\tau_{II}(\bar r,\theta)=-\tau_I(r,\theta). \tag{5}$$

Now both temperature and flux are equal at the joints

$$\tau_I(r,\beta)=\tau_{II}(\bar r,\beta)|_{\bar r=2b+1-r}=-\tau_I(2b+1-r,\beta) \tag{6}$$

$$\frac{1}{r}\frac{\partial\tau_I}{\partial\theta}(r,\beta)=$$

$$-\frac{1}{\bar r}\frac{\partial\tau_{II}}{\partial\theta}(\bar r,\beta)|_{\bar r=2b+1-r}=\frac{1}{2b+1-r}\frac{\partial\tau_I}{\partial\theta}(2b+1-r,\beta). \tag{7}$$

It is not possible to solve analytically for B_n from Eqs. (6) and (7), thus collocation of N points is used, yielding $2N$ coefficients of B_n. The problem is further simplified by noting symmetry, such that the N points can be distributed in the smaller region $b<r<b+1/2$. The linear system of equations to be solved are

$$\sum_1^{2N} B_n\cosh(\lambda\beta)\left\{\sin\left[\lambda\ln\left(\frac{r_j}{b}\right)\right]+\sin\left[\lambda\ln\left(\frac{2b+1-r_j}{b}\right)\right]\right\}$$
$$=-\tau_0(r_j)-\tau_0(2b+1-r_j) \tag{8}$$

$$\sum_1^{2N} B_n\lambda\sinh(\lambda\beta)\left\{\frac{1}{r_j}\sin\left[\lambda\ln\left(\frac{r_j}{b}\right)\right]-\frac{1}{2b+1-r_j}\sin\left[\lambda\ln\left(\frac{2b+1-r_j}{b}\right)\right]\right\}=0 \tag{9}$$

$$r_j=b+j/(2N+1),\quad j=1,\ldots,N. \tag{10}$$

After B_n are found, the error of truncation is determined by checking the symmetry at the joint:

$$e=\max|\tau_I(r,\beta)-\tau_I(2b+r-1,\beta)|. \tag{11}$$

For a typical case $b=0.5$, $\beta=90$ deg, we find e is less than 1.5 percent for $N=5$ and the error decreases to 0.2 percent when $N=10$. Convergence is extremely fast. In our calculations $N=20-30$ is found to be adequate.

Results and Discussion

The temperature distribution for $b=0.5$, $\beta=90$ deg is shown in Fig. 2. The isotherms meander from side to side, showing local heat transfer is not even. The local rate of heat transfer, normalized by $k(T_e-T_i)/h$, (k = thermal conductivity) is

[14]Professor, Department of Mathematics and Mechanical Engineering, Michigan State University, East Lansing, MI 48824. Mem. ASME.

Contributed by the Applied Mechanics Division of The American Society of Mechanical Engineers for publication in the ASME Journal of Applied Mechanics. Manuscript received by the ASME Applied Mechanics Division, Sept. 1, 1992; final revision; Feb. 8, 1993. Associate Technical Editor: R. M. Bowen.

Downloaded 03 May 2010 to 171.66.16.20. Redistribution subject to ASME license or copyright; see http://www.asme.org/terms/Terms_Use.cfm

ordinate," *Proceedings of The Cambridge Philosophical Society, London*, Vol. A30, pp. 315–326.

Kuo, Y-M., and Conway, H. D., 1980, "Torsion of Reinforced Square Cylinder," *Journal of The Engineering Mechanics Division*, ASCE, Vol. 106, No. EM6, pp. 1341–1347.

Naghdi, A. K., 1990, "Torsion of a Rectangular Bar with Multiple Cylindrical Cutouts," Proceedings of The 15th South Eastern Conference on Theoretical and Applied Mechanics, pp. 327–332.

Naghdi, A. K., 1983, "Torsion of a Rectangular Bar with Two Circular Holes," *Journal of Engineering Mechanics*, ASCE, Vol. 109, No. 2, pp. 643–648.

Sokolnikoff, S., 1956, *Mathematical Theory of Elasticity*, McGraw-Hill, New York.

Diffusive Transport Across a Wavy Plate Composed of Annular Sectors

C. Y. Wang[14]

Introduction

Diffusive transport across a plate or barrier is fundamental to heat and mass transfer. Let the temperature (or concentration) be at different constant levels on the two surfaces of a plate of uniform thickness. Simple exact solutions exist if the plate is in the shape of a flat layer or a circular annulus (Crank, 1956). Perturbation solution is possible if the plate is not flat, but with small curvature compared to the thickness (Wang, 1982). For plates with large curvature, either complex transform (if at all possible) or tedious numerical integration of the partial differential equations is necessary.

This Note uses a simple, highly efficient, semianalytical method to treat a wavy plate composed of joined annular sectors (Fig. 1). Practical applications of diffusion through wavy surfaces include walls which enhance heat transfer (Webb, 1987) and the internal folds of the small intestine (Hendrix, 1974). We shall illustrate the solution to this diffusion problem using the terminology of heat conduction.

Solution Method

Normalize all lengths by the thickness of the plate h. Each period of the plate consists of two annular sectors (I and II) both with opening angle 2β and inner and outer radii b and $1+b$, respectively. We normalize the temperature T by the exterior temperature T_e and interior temperature T_i as follows:

$$\tau = 2\left(\frac{T-T_i}{T_e-T_i}\right) - 1. \tag{1}$$

The governing equation is the Laplace equation in cylindrical coordinates

$$\frac{\partial^2\tau}{\partial r^2} + \frac{1}{r}\frac{\partial\tau}{\partial r} + \frac{1}{r}\frac{\partial^2\tau}{\partial\theta^2} = 0. \tag{2}$$

The boundary conditions are that on the top surface $\tau = 1$ and on the bottom surface $\tau = -1$. Use separation of variables on Eq. (2) and set the sign of the separation constant such that eigenfunctions exist in the radical direction.

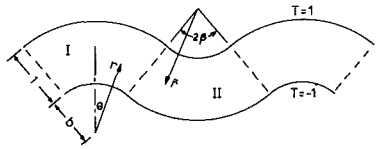


Fig. 1 The coordinate system

For Sector I, the following form of solution is obtained:

$$\tau_I(r,\theta) = \tau_0(r) + \sum_1^\infty B_n \sin\left[\lambda \ln\left(\frac{r}{b}\right)\right]\cosh(\lambda\theta). \tag{3}$$

Here $\lambda \equiv n\pi/\ln(1+1/b)$ are eigenvalues, B_n are constants to be determined, and τ_0 is the axisymmetric solution satisfying the boundary conditions

$$\tau_0(r) = 1 - 2\frac{\ln\left(\frac{b+1}{r}\right)}{\ln\left(1+\frac{1}{b}\right)}. \tag{4}$$

Again, considering symmetry, the solution to Sector II is

$$\tau_{II}(\bar{r},\theta) = -\tau_I(r,\theta). \tag{5}$$

Now both temperature and flux are equal at the joints

$$\tau_I(r,\beta) = \tau_{II}(\bar{r},\beta)|_{\bar{r}=2b+1-r} = -\tau_I(2b+1-r,\beta) \tag{6}$$

$$\frac{1}{r}\frac{\partial\tau_I}{\partial\theta}(r,\beta) =$$

$$-\frac{1}{\bar{r}}\frac{\partial\tau_{II}}{\partial\theta}(\bar{r},\beta)|_{\bar{r}=2b+1-r} = \frac{1}{2b+1-r}\frac{\partial\tau_I}{\partial\theta}(2b+1-r,\beta). \tag{7}$$

It is not possible to solve analytically for B_n from Eqs. (6) and (7), thus collocation of N points is used, yielding $2N$ coefficients of B_n. The problem is further simplified by noting symmetry, such that the N points can be distributed in the smaller region $b<r<b+1/2$. The linear system of equations to be solved are

$$\sum_1^{2N} B_n \cosh(\lambda\beta)\left\{\sin\left[\lambda\ln\left(\frac{r_j}{b}\right)\right] + \sin\left[\lambda\ln\left(\frac{2b+1-r_j}{b}\right)\right]\right\} = -\tau_0(r_j) - \tau_0(2b+1-r_j) \tag{8}$$

$$\sum_1^{2N} B_n\lambda\sinh(\lambda\beta)\left\{\frac{1}{r_j}\sin\left[\lambda\ln\left(\frac{r_j}{b}\right)\right] - \frac{1}{2b+1-r_j}\sin\left[\lambda\ln\left(\frac{2b+1-r_j}{b}\right)\right]\right\} = 0 \tag{9}$$

$$r_j = b + j/(2N+1), \quad j = 1, \ldots, N. \tag{10}$$

After B_n are found, the error of truncation is determined by checking the symmetry at the joint:

$$e = \max|\tau_I(r,\beta) - \tau_I(2b+r-1,\beta)|. \tag{11}$$

For a typical case $b=0.5$, $\beta=90$ deg, we find e is less than 1.5 percent for $N=5$ and the error decreases to 0.2 percent when $N=10$. Convergence is extremely fast. In our calculations $N=20-30$ is found to be adequate.

Results and Discussion

The temperature distribution for $b=0.5$, $\beta=90$ deg is shown in Fig. 2. The isotherms meander from side to side, showing local heat transfer is not even. The local rate of heat transfer, normalized by $k(T_e-T_i)/h$, (k = thermal conductivity) is

[14]Professor, Department of Mathematics and Mechanical Engineering, Michigan State University, East Lansing, MI 48824. Mem. ASME.

Contributed by the Applied Mechanics Division of The American Society of Mechanical Engineers for publication in the ASME Journal of Applied Mechanics. Manuscript received by the ASME Applied Mechanics Division, Sept. 1, 1992; final revision; Feb. 8, 1993. Associate Technical Editor: R. M. Bowen.

Copyright © 1994 by ASME
Downloaded 03 May 2010 to 171.66.16.20. Redistribution subject to ASME license or copyright; see http://www.asme.org/terms/Terms_Use.cfm

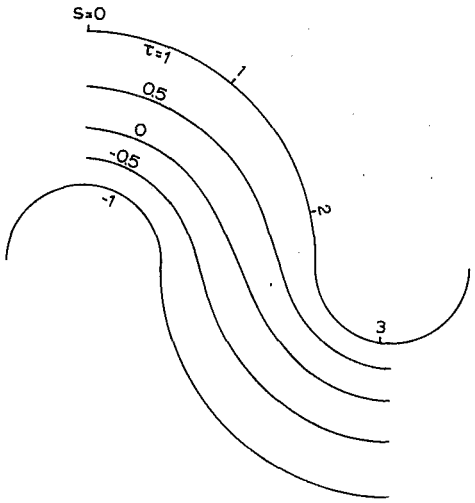


Fig. 2 Isotherms for $b=0.5$, $\beta=90$ deg

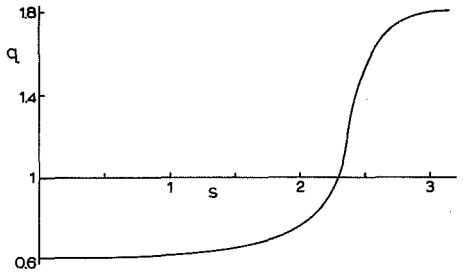


Fig. 3 Local rate of heat transfer. Refer to Fig. 2 for location s.

$$q|_{r=1+b}=\frac{1}{2}\frac{\partial\tau}{\partial r}|_{r=1+b}$$

$$=\frac{1}{(1+b)}\left[\frac{1}{\ln\left(1+\frac{1}{b}\right)}+\frac{1}{2}\sum B_n\lambda(-1)^n\cosh(\lambda\theta)\right] \quad (12)$$

$$q|_{r=b}=\frac{1}{b}\left[\frac{1}{\ln\left(1+\frac{1}{b}\right)}+\frac{1}{2}\sum B_n\lambda\cosh(\lambda\theta)\right]. \quad (13)$$

The rate of heat transfer along the exterior surface as a function of arc length s is plotted in Fig. 3 for $b=0.5$, $\beta=90$ deg. The heat transfer rate is almost three times higher at a locally concave site than that at a convex site. Also of interest is the total heat flux Q per period per depth

$$Q=\int_{-\beta}^{\beta}k\left(\frac{\partial T}{\partial r}r\right)_{r=1+b}d\theta+\int_{-\beta}^{\beta}\left(k\frac{\partial T}{\partial r}r\right)_{r=b}d\theta$$

$$=4k(T_e-T_i)\left[\frac{\beta}{\ln\left(1+\frac{1}{b}\right)}+\frac{1}{4}\sum B_n(1+(-1)^n)\sinh(\lambda\beta)\right]. \quad (14)$$

If the plate were flat, the flux for the same center line length (or same amount of material) is

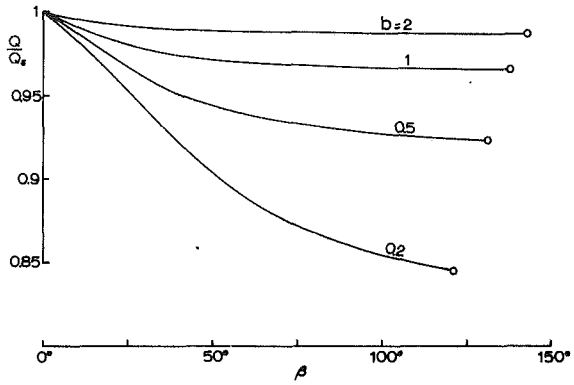


Fig. 4 Total heat flux ratio Q/Q_s. Circles denote $\beta=\beta^*$.

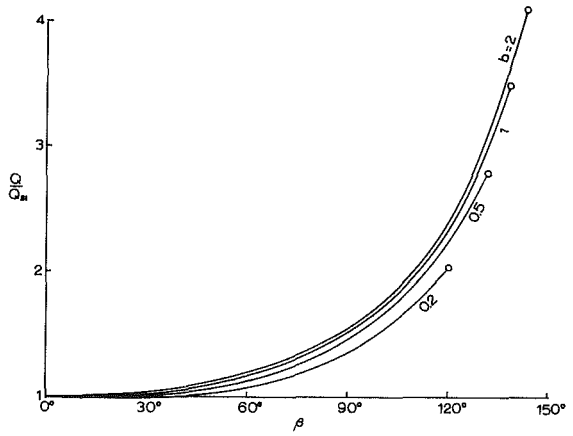


Fig. 5 Total heat flux ratio Q/Q_{s_1}.

$$Q_s=4k(T_e-T_i)\beta\left(b+\frac{1}{2}\right). \quad (15)$$

The ratio Q/Q_s is plotted in Fig. 4. As compared to a flat plate, the total heat flux is slightly less for the wavy plate of same volume. The curves end at β^*, when the plate touches itself at periodic points

$$\beta^*=\sin^{-1}\left(\frac{b+1}{2b+1}\right)>\frac{\pi}{2}. \quad (16)$$

The decisive advantage for utilizing wavy plates is in the increase in surface area for diffusion. In comparison to a flat plate of same nominal size, the transfer of flux is increased by a factor of $(\beta/\sin\beta)$. This increase more than compensates for the slight decrease in Q/Q_s. Let Q_{s_1} be the heat flux across a flat plate of the same nominal size. Figure 5 shows the heat flux Q of a wavy plate may be several fold larger than Q_{s_1}, especially at larger β angles. Thus convoluted surfaces are highly desirable in both biological and mechanical systems which require diffusive transport.

We comment that the direct use of finite differences may not be as efficient for the present problem since discretizations in both r and θ directions would involve the square of the number of computations used in the present paper.

References

Crank, J., 1956, *The Mathematics of Diffusion*, Clarendon Press, Oxford, U.K.

Hendrix, T. R., 1974, "The Absorptive Function of the Alimentary Canal," *Medical Physiology*, Vol. 2, V. B. Mountcastle, ed., Mosby, St. Louis, MO, Chapter 50.

Downloaded 03 May 2010 to 171.66.16.20. Redistribution subject to ASME license or copyright; see http://www.asme.org/terms/Terms_Use.cfm

Wang, C. Y., 1982, "Diffusive Transport Across Corrugated Plates and Tubes," *AIChE Journal*, Vol. 28, pp. 1016-1019.

Webb, R. L., 1987, "Enhancement of Single-Phase Heat Transfer," *Handbook of Single-Phase Convective Heat Transfer*, S. Kakac, R. K. Shah, and W. Aung, eds., John Wiley and Sons, New York, Chapter 17.

Torsion of a Tube With Longitudinal Corrugations

C. Y. Wang[15]

Introduction and Formulation

Torsion of cylindrical bars has always been an important topic in elasticity. Exact and approximate solutions have been found for various solid cross-sectional shapes using conformal mapping, separation of variables, or direct numerical integration. More difficult are the problems of torsion of hollow cylinders where solutions are few (Roark and Young, 1975). This paper studies the torsion of a tube with small longitudinal wavy corrugations on the surfaces. These corrugations may be due to imprecise machining or maybe intentional, such as those which enhance the gripping of a coupling. Our aim is to determine the effect of the corrugations on the torsional rigidity and the maximum shear stress.

We normalize all lengths by the mean outer radius R such that the outer and inner boundaries are given by

$$r_1 = 1 + h\epsilon \sin(n\theta) \tag{1}$$

$$r_2 = b + k\epsilon \sin(m\theta + \alpha). \tag{2}$$

Here, n, m are integers, α is a phase shift, b, h, k are 0(1) non-negative numbers less than unity, $\max(h, k) = 1$, $0 < \epsilon < < 1$, and $0 \le r_2 < r_1$.

In terms of Prandtl stress function ψ (see Sokolnikoff, 1956), the torsion problem is

$$\nabla^2\psi = -2 \tag{3}$$

$$\psi = 0 \text{ on } r_1, \quad \psi = K \text{ on } r_2 \tag{4, 5}$$

$$\oint_{r_1} \frac{\partial\psi}{\partial\eta}\, ds = -2(\text{Area enclosed by } r_1). \tag{6}$$

Here K is an unknown constant determined by Eq. (6), η is the normal, and s is the arc length. This geometry precludes the use of conformal mapping or separation of variables. Due to the unknown K, numerical integration is also not feasible.

Perturbation Solution

When $\epsilon = 0$, the problem becomes the torsion of a hollow circular tube which has an exact solution. We shall perturb from such a state. Let

$$\psi(r, \theta) = \psi_0(r) + \epsilon\psi_1(r, \theta) + \epsilon^2\psi_2(r, \theta) + \ldots \tag{7}$$

$$K = K_0 + \epsilon K_1 + \epsilon^2 K_2 + \ldots, \tag{8}$$

where

$$\psi_0 = \frac{1}{2}(1 - r^2), \; K_0 = \frac{1}{2}(1 - b^2). \tag{9}$$

Equation (3) yields

$$\nabla^2\psi_1 = 0, \; \nabla^2\psi_2 = 0. \tag{10, 11}$$

The boundary conditions are more complicated. Let $S \equiv \sin(n\theta)$, $S' \equiv \sin(m\theta + \alpha)$. Equation (4) is expanded as

$$0 = \psi|_{r=1+\epsilon hS} = \psi|_1 + \epsilon hS \frac{\partial\psi}{\partial r}|_1 + \frac{\epsilon^2 h^2 S^2}{2} \frac{\partial^2\psi}{\partial r^2}|_1 \ldots$$

$$= \psi_0(1) + \epsilon[\psi_1(1, \theta) + hS\psi_{0r}(1)] + \epsilon^2\left[\psi_2(1, \theta) + hS\psi_{1r}(1, \theta) + \frac{1}{2}h^2S^2\psi_{0rr}(1)\right] + \ldots. \tag{12}$$

This gives

$$\psi_1(1, \theta) = -hS\psi_{0r}(1) \tag{13}$$

$$\psi_2(1, \theta) = -hS\psi_{1r}(1, \theta) - \frac{1}{2}h^2S^2\psi_{0rr}(1). \tag{14}$$

Similarly, Eq. (5) yields

$$\psi_1(b, \theta) = K_1 - kS'\psi_{0r}(b) \tag{15}$$

$$\psi_2(b, \theta) = K_2 - kS'\psi_{1r}(b) - \frac{1}{2}k^2S'^2\psi_{0rr}(b). \tag{16}$$

Since ψ_0 is known, Eqs. (10), (14), (15) are solved to yield

$$\psi_1 = \left(\frac{r^n - b^{2n}r^{-n}}{1 - b^{2n}}\right)hS + \frac{b^{m+1}kS'}{1 - b^{2m}}(r^{-m} - r^m) + K_1\frac{\ell nr}{\ell nb}. \tag{17}$$

The conditions on ψ_2 then become

$$\psi_2(1, \theta) = -\frac{hK_2S}{\ell nb} + \left[\frac{1}{2} - \frac{n(1 + b^{2n})}{(1 - b^{2n})}\right]h^2S^2 + \frac{2mkhb^{m+1}}{1 - b^{2m}}SS' \tag{18}$$

$$\psi_2(b, \theta) = K_2 - \frac{kK_1S'}{b\ell nb} + \left[\frac{1}{2} + \frac{m(1 + b^{2m})}{(1 - b^{2m})}\right]k^2S'^2 - \frac{2nkhb^{n-1}}{1 - b^{2n}}SS'. \tag{19}$$

The solution of Eqs. (11), (18), (19) is

$$\psi_2(r, \theta) = A_0(r) + A_1(r)S + A_2(r)S' + A_3(r)\cos 2n\theta + A_4(r)\cos(2m\theta + 2\alpha) + A_5(r)\cos[(n - m)\theta - \alpha] + A_6(r)\cos[(n + m)\theta + \alpha],$$

where

$$A_0 = \left[\frac{1}{2} - \frac{n(1 + b^{2n})}{(1 - b^{2n})}\right]\frac{h^2}{2} + \left\{K_2 + \left[\frac{1}{2} + \frac{m(1 + b^{2m})}{(1 - b^{2m})}\right]\frac{k^2}{2} - \left[\frac{1}{2} - \frac{n(1 + b^{2n})}{(1 - b^{2n})}\right]\frac{h^2}{2}\right\}\frac{\ell nr}{\ell nb} \tag{20}$$

$$A_1 = -\frac{(r^n - b^{2n}r^{-n})}{(1 - b^{2n})}\frac{hK_1}{\ell nb}, \quad A_2 = -\left(\frac{r^m - r^{-m}}{b^m - b^{-m}}\right)\frac{kK_1}{b\ell nb} \tag{21}$$

$$A_3 = -\left(\frac{r^{2n} - b^{4n}r^{-2n}}{1 - b^{4n}}\right)\left[\frac{1}{2} - \frac{n(1 + b^{2n})}{(1 - b^{2n})}\right]\frac{h^2}{2} \tag{22}$$

$$A_4 = -\left(\frac{r^{2m} - r^{-2m}}{b^{2m} - b^{-2m}}\right)\left[\frac{1}{2} + \frac{m(1 + b^{2m})}{(1 - b^{2n})}\right]\frac{k^2}{2} \tag{23}$$

[15]Departments of Mathematics and Mechanical Engineering, Michigan State University, East Lansing, MI 48824. Mem. ASME.

Contributed by the Applied Mechanics Division of THE AMERICAN SOCIETY OF MECHANICAL ENGINEERS for publication in the ASME JOURNAL OF APPLIED MECHANICS. Manuscript received by the ASME Applied Mechanics Division, Sept. 28, 1992; final revision, Mar. 4, 1993. Associate Technical Editor: F. Y. M. Wan.

Downloaded 03 May 2010 to 171.66.16.20. Redistribution subject to ASME license or copyright; see http://www.asme.org/terms/Terms_Use.cfm

Wang, C. Y., 1982, "Diffusive Transport Across Corrugated Plates and Tubes," *AIChE Journal*, Vol. 28, pp. 1016-1019.

Webb, R. L., 1987, "Enhancement of Single-Phase Heat Transfer," *Handbook of Single-Phase Convective Heat Transfer*, S. Kakac, R. K. Shah, and W. Aung, eds., John Wiley and Sons, New York, Chapter 17.

Torsion of a Tube With Longitudinal Corrugations

C. Y. Wang[15]

Introduction and Formulation

Torsion of cylindrical bars has always been an important topic in elasticity. Exact and approximate solutions have been found for various solid cross-sectional shapes using conformal mapping, separation of variables, or direct numerical integration. More difficult are the problems of torsion of hollow cylinders where solutions are few (Roark and Young, 1975). This paper studies the torsion of a tube with small longitudinal wavy corrugations on the surfaces. These corrugations may be due to imprecise machining or maybe intentional, such as those which enhance the gripping of a coupling. Our aim is to determine the effect of the corrugations on the torsional rigidity and the maximum shear stress.

We normalize all lengths by the mean outer radius R such that the outer and inner boundaries are given by

$$r_1 = 1 + h\epsilon \sin(n\theta) \tag{1}$$

$$r_2 = b + k\epsilon \sin(m\theta + \alpha). \tag{2}$$

Here, n, m are integers, α is a phase shift, b, h, k are 0(1) non-negative numbers less than unity, $\max(h, k) = 1$, $0 < \epsilon < < 1$, and $0 \le r_2 < r_1$.

In terms of Prandtl stress function ψ (see Sokolnikoff, 1956), the torsion problem is

$$\nabla^2\psi = -2 \tag{3}$$

$$\psi = 0 \text{ on } r_1, \quad \psi = K \text{ on } r_2 \tag{4, 5}$$

$$\oint_{r_1} \frac{\partial\psi}{\partial\eta}\, ds = -2(\text{Area enclosed by } r_1). \tag{6}$$

Here K is an unknown constant determined by Eq. (6), η is the normal, and s is the arc length. This geometry precludes the use of conformal mapping or separation of variables. Due to the unknown K, numerical integration is also not feasible.

Perturbation Solution

When $\epsilon = 0$, the problem becomes the torsion of a hollow circular tube which has an exact solution. We shall perturb from such a state. Let

$$\psi(r, \theta) = \psi_0(r) + \epsilon\psi_1(r, \theta) + \epsilon^2\psi_2(r, \theta) + \ldots \tag{7}$$

$$K = K_0 + \epsilon K_1 + \epsilon^2 K_2 + \ldots, \tag{8}$$

where

$$\psi_0 = \frac{1}{2}(1 - r^2), \; K_0 = \frac{1}{2}(1 - b^2). \tag{9}$$

Equation (3) yields

$$\nabla^2\psi_1 = 0, \; \nabla^2\psi_2 = 0. \tag{10, 11}$$

The boundary conditions are more complicated. Let $S \equiv \sin(n\theta)$, $S' \equiv \sin(m\theta + \alpha)$. Equation (4) is expanded as

$$0 = \psi|_{r=1+\epsilon hS} = \psi|_1 + \epsilon hS \frac{\partial\psi}{\partial r}|_1 + \frac{\epsilon^2 h^2 S^2}{2} \frac{\partial^2\psi}{\partial r^2}|_1 \ldots$$

$$= \psi_0(1) + \epsilon[\psi_1(1, \theta) + hS\psi_{0r}(1)] + \epsilon^2\left[\psi_2(1, \theta) + hS\psi_{1r}(1, \theta) + \frac{1}{2}h^2S^2\psi_{0rr}(1)\right] + \ldots. \tag{12}$$

This gives

$$\psi_1(1, \theta) = -hS\psi_{0r}(1) \tag{13}$$

$$\psi_2(1, \theta) = -hS\psi_{1r}(1, \theta) - \frac{1}{2}h^2S^2\psi_{0rr}(1). \tag{14}$$

Similarly, Eq. (5) yields

$$\psi_1(b, \theta) = K_1 - kS'\psi_{0r}(b) \tag{15}$$

$$\psi_2(b, \theta) = K_2 - kS'\psi_{1r}(b) - \frac{1}{2}k^2S'^2\psi_{0rr}(b). \tag{16}$$

Since ψ_0 is known, Eqs. (10), (14), (15) are solved to yield

$$\psi_1 = \left(\frac{r^n - b^{2n}r^{-n}}{1 - b^{2n}}\right)hS + \frac{b^{m+1}kS'}{1 - b^{2m}}(r^{-m} - r^m) + K_1\frac{\ell nr}{\ell nb}. \tag{17}$$

The conditions on ψ_2 then become

$$\psi_2(1, \theta) = -\frac{hK_2S}{\ell nb} + \left[\frac{1}{2} - \frac{n(1 + b^{2n})}{(1 - b^{2n})}\right]h^2S^2 + \frac{2mkhb^{m+1}}{1 - b^{2m}}SS' \tag{18}$$

$$\psi_2(b, \theta) = K_2 - \frac{kK_1S'}{b\ell nb} + \left[\frac{1}{2} + \frac{m(1 + b^{2m})}{(1 - b^{2m})}\right]k^2S'^2 - \frac{2nkhb^{n-1}}{1 - b^{2n}}SS'. \tag{19}$$

The solution of Eqs. (11), (18), (19) is

$$\psi_2(r, \theta) = A_0(r) + A_1(r)S + A_2(r)S' + A_3(r)\cos 2n\theta + A_4(r)\cos(2m\theta + 2\alpha) + A_5(r)\cos[(n - m)\theta - \alpha] + A_6(r)\cos[(n + m)\theta + \alpha],$$

where

$$A_0 = \left[\frac{1}{2} - \frac{n(1 + b^{2n})}{(1 - b^{2n})}\right]\frac{h^2}{2} + \left\{K_2 + \left[\frac{1}{2} + \frac{m(1 + b^{2m})}{(1 - b^{2m})}\right]\frac{k^2}{2} - \left[\frac{1}{2} - \frac{n(1 + b^{2n})}{(1 - b^{2n})}\right]\frac{h^2}{2}\right\}\frac{\ell nr}{\ell nb} \tag{20}$$

$$A_1 = -\frac{(r^n - b^{2n}r^{-n})}{(1 - b^{2n})}\frac{hK_1}{\ell nb}, \quad A_2 = -\left(\frac{r^m - r^{-m}}{b^m - b^{-m}}\right)\frac{kK_1}{b\ell nb} \tag{21}$$

$$A_3 = -\left(\frac{r^{2n} - b^{4n}r^{-2n}}{1 - b^{4n}}\right)\left[\frac{1}{2} - \frac{n(1 + b^{2n})}{(1 - b^{2n})}\right]\frac{h^2}{2} \tag{22}$$

$$A_4 = -\left(\frac{r^{2m} - r^{-2m}}{b^{2m} - b^{-2m}}\right)\left[\frac{1}{2} + \frac{m(1 + b^{2m})}{(1 - b^{2n})}\right]\frac{k^2}{2} \tag{23}$$

[15]Departments of Mathematics and Mechanical Engineering, Michigan State University, East Lansing, MI 48824. Mem. ASME.

Contributed by the Applied Mechanics Division of THE AMERICAN SOCIETY OF MECHANICAL ENGINEERS for publication in the ASME JOURNAL OF APPLIED MECHANICS. Manuscript received by the ASME Applied Mechanics Division, Sept. 28, 1992; final revision, Mar. 4, 1993. Associate Technical Editor: F. Y. M. Wan.

Copyright © 1994 by ASME
Downloaded 03 May 2010 to 171.66.16.20. Redistribution subject to ASME license or copyright; see http://www.asme.org/terms/Terms_Use.cfm

$$A_5=\begin{cases}\dfrac{kh}{b^{-n+m}-b^{n-m}}\left\{\left(\dfrac{nb^{n-1}}{1-b^{2n}}+\dfrac{mb^{2m-n}}{1-b^{2m}}\right)r^{n-m}-\left(\dfrac{nb^{n-1}}{1-b^{2n}}+\dfrac{mb^{1+n}}{1-b^{2m}}\right)r^{m-n}\right\}, & m\neq n\\ \dfrac{nkhb^n}{1-b^{2n}}\left[b-\left(b-\dfrac{1}{b}\right)\dfrac{\ell nr}{\ell nb}\right], & m=n\end{cases} \tag{24}$$

$$A_6=\frac{-kh}{b^{-n-m}-b^{n+m}}\left\{\left(\frac{nb^{n-1}}{1-b^{2n}}+\frac{mb^{1-m}}{1-b^{2m}}\right)r^{n+m}-\left(\frac{nb^{n-1}}{1-b^{2n}}+\frac{mb^{2m+1+n}}{1-b^{2m}}\right)r^{-n-m}\right\}. \tag{25}$$

The normal derivative on the surface $r=f(\theta)$ is

$$\frac{\partial\psi}{\partial\eta}=\eta\cdot\nabla\psi=\frac{\nabla(r-f)\cdot\nabla\psi}{|\nabla(r-f)|}=\frac{f\psi_r-f'\psi_\theta/f}{\sqrt{f^2+(f')^2}}. \tag{26}$$

Thus Eq. (6) gives

$$\begin{aligned}0&=\oint\left[\frac{f\psi_r-f'\psi_\theta/f}{\sqrt{f^2+(f')^2}}\right]\sqrt{f^2+(f')^2}\,d\theta+2\oint\frac{1}{2}f^2d\theta\\&=\oint\{[(1+h\epsilon S)(\psi_{0r}+\epsilon\psi_{1r}+\epsilon^2\psi_{2r})-h\epsilon^2n\cos(n\theta)\psi_{1\theta}]_{r=1+\epsilon hS}\\&\qquad+(1+h\epsilon S)^2\}d\theta+0(\epsilon^3)\\&=\oint\left\{\left[\psi_{0r}+\epsilon(\psi_{1r}+hS\psi_{0rr}+hS\psi_{0r})+\epsilon^2(\psi_{2r}+hS\psi_{1rr}\right.\right.\\&\qquad\left.+\frac{1}{2}h^2S^2\psi_{0rrr})+hS\psi_{1r}+h^2S^2\psi_{0rr}-hn\cos(n\theta)\psi_{1\theta}\right]_{r=1}\\&\qquad\left.+(1+\epsilon 2hS+\epsilon^2h^2S^2)\right\}d\theta+0(\epsilon^3).\end{aligned} \tag{27}$$

Equating equal powers of ϵ, we find $K_1=0$ and

$$K_2=\left[\frac{1}{2}-\frac{n(1+b^{2n})}{1-b^{2n}}\right]\frac{h^2}{2}-\left[\frac{1}{2}+\frac{m(1+b^{2m})}{1-b^{2m}}\right]\frac{k^2}{2}+\delta_{mn}\cos\alpha\frac{nkhb^n}{1-b^{2n}}\left(b+\frac{1}{b}\right), \tag{28}$$

where δ_{mn} is the Kronecker delta.

Results and Discussion

The torsional rigidity, normalized by $2\mu R^4$ (μ = Lamé constant), is

$$\begin{aligned}D&=\int\int\psi dA+KA_2\\&=\oint\left[\int_{b+k\epsilon S'}^{1+h\epsilon S}\psi r dr\right]d\theta+K\frac{1}{2}\oint(b+k\epsilon S')^2d\theta\\&=\oint\left[\int_b^1\psi r dr+h\epsilon S\psi|_1-k\epsilon S'\psi|_b b+\frac{h^2\epsilon^2S^2}{2}(\psi_r)_r|_1\right.\\&\qquad\left.-\frac{k^2\epsilon^2S'^2}{2}(\psi_r)_r|_b+\frac{K_0}{2}(b+k\epsilon S')^2+\epsilon^2\frac{K_2}{2}b^2\right]d\theta+0(\epsilon^3).\end{aligned} \tag{29}$$

Substituting Eqs. (7), (28) into Eq. (29)

$$D=\frac{\pi}{4}(1-b^4)[1+\epsilon^2(h^2\phi_1+k^2\phi_2+\delta_{mn}hk\cos\alpha\,\phi_3)], \tag{30}$$

where

$$\phi_1=\left[3-\frac{2n(1+b^{2n})}{(1-b^{2n})}\right]\frac{1}{(1-b^4)} \tag{31}$$

$$\phi_2=-\left[2+b^2+\frac{2b^2m(1+b^{2m})}{(1-b^{2m})}\right]\frac{1}{(1-b^4)} \tag{32}$$

$$\phi_3=\frac{8nb^{n+1}}{(1-b^{2n})(1-b^4)}. \tag{33}$$

The parameter ϕ_1 represents the effect of the exterior corrugations. Figure 1 shows, except for $n=1$ and $b<1/\sqrt{5}$, ϕ_1 is negative, or in general a decrease in torsional rigidity. Figure 2 shows ϕ_2, that the effect of interior corrugations always decreases rigidity. The parameter ϕ_3 represents the interaction of interior and exterior corrugations and is present only if $m=n$. This interaction always increases rigidity (Fig. 3). In the case where the inside and outside surfaces are both corrugated with the same amplitude ($h=k=1$), the same number of waves ($m=n$) and no phase lag ($\alpha=0$), the relative increase in torsional rigidity is proportional to $(\phi_1+\phi_2+\phi_3)$. This sum is shown in Fig. 4. Notice the large decreases in rigidity for both ϕ_1 and ϕ_2 at large b, since portions of the tube wall become too thin. This defect is alleviated when both walls are corrugated and in phase as shown in Fig. 4. The range of validity for Figs. 1–4 is $|\phi|<<1/\epsilon^2$. From these results for given mean inside and outside radii of the tube, we can conclude the following:

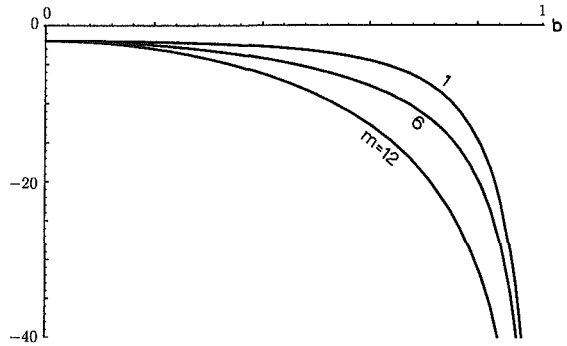


Fig. 1 The function ϕ_1

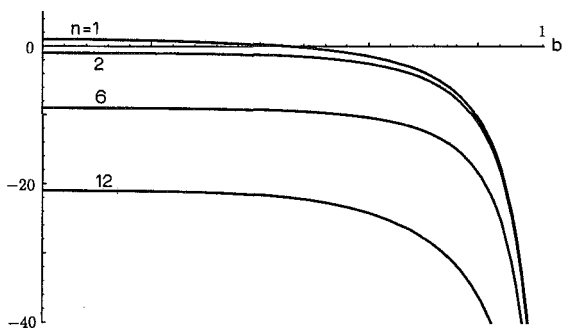


Fig. 2 The function ϕ_2

Downloaded 03 May 2010 to 171.66.16.20. Redistribution subject to ASME license or copyright; see http://www.asme.org/terms/Terms_Use.cfm

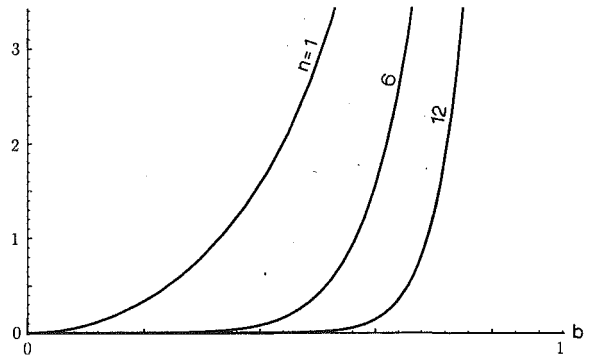


Fig. 3 The function ϕ_3

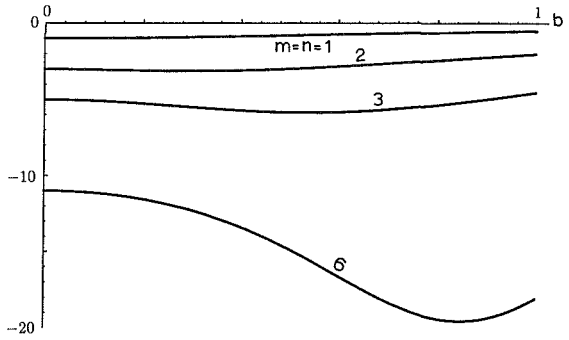


Fig. 4 The function $\phi_1+\phi_2+\phi_3$

1 For given $n=m$, $\phi_2>\phi_1$ for low b and $\phi_1>\phi_2$ for large b. Thus if only one surface needs to be corrugated, it is better to make it the inside surface if the tube wall is thick and the outside surface if the tube wall is thin.

2 Higher rigidity is achieved by using the lowest possible number of waves.

3 When both surfaces are corrugated it is best to use the same phase, same wave number, and same amplitude such that the beneficial interaction effect is fully utilized. This effect is dominant at large b.

The normalized maximum shear stress, occurring on the outer boundary, is

$$\frac{\partial\psi}{\partial\eta}|_{1+\epsilon aS}=\psi_{0r}|_1+\epsilon(\psi_{1r}|_1+hS\psi_{0rr}|_1)+0(\epsilon^2)$$

$$=-1+\epsilon(t_1hS-t_2kS')+0(\epsilon^2) \tag{34}$$

$$t_1=\frac{n(1+b^{2n})}{1-b^{2n}}-1>0,\quad t_2=\frac{2mb^{m+1}}{1-b^{2m}}>0. \tag{35}$$

If only the outside surface is corrugated, the maximum shear stress is at a trough ($\theta=-\pi/2n$) with the value $-1-\epsilon t_1$. If only the inside surface is corrugated, the maximum shear stress is $-1-\epsilon t_2$ on the smooth outside at $\theta=[(\pi/2)-\alpha]/m$. If both surfaces are corrugated with the same phase, wave number, and amplitude, the maximum shear stress is $-1-\epsilon(t_1-t_2)$ at an outside trough.

References

Roark, R. J., and Young, W. C., 1975, *Formulas for Stress and Strain*, 5th ed., McGraw-Hill, New York.

Sokolnikoff, I. S., 1956, *Mathematical Theory of Elasticity*, 2nd ed., McGraw-Hill, New York.

The Buckling Behavior of Rectangular-Bar Helical Compression Springs

L. E. Becker[16] and W. L. Cleghorn[17]

Buckling design charts are presented for rectangular-bar helical compression springs with clamped ends, demonstrating the effect of the number of turns of the spring.

1 Introduction

The buckling behavior of rectangular-bar helical compression springs has been investigated by Haringx (1948), whose model consisted of a prismatic rod with rigidities corresponding to those of unclosed circular rings. Becker and Cleghorn (1992) developed a new set of dynamic, partial differential equations for helical compression springs, and found numerical solutions for clamped ends and circular cross-section using the transfer matrix method to produce buckling design charts. The present article is an extension of the latter for rectangular cross-sections.

2 Method of Solution

Figure 1 shows a long, thin helical compression spring in its unloaded state and its critical pre-buckling configuration due to a determinate axial compressive load P. For a rectangular cross-section with side length $2a$ perpendicular to the spring axis, and side length $2b$ parallel to the axis, we define

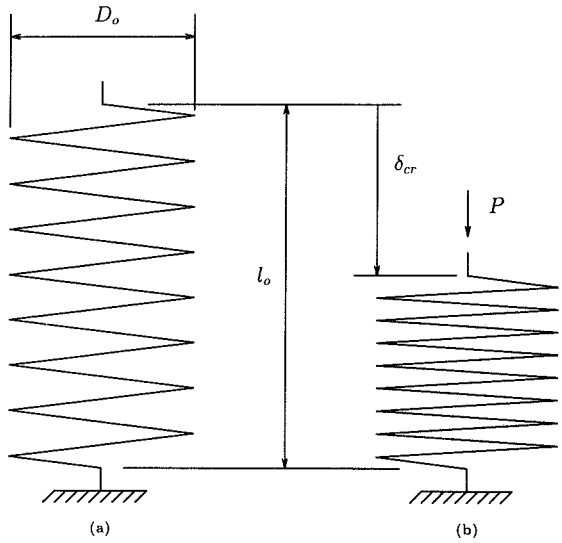


Fig. 1 Definition diagram

[16] Graduate Student, Division of Applied Sciences, Harvard University, Cambridge, MA 02138.

[17] Associate Professor, Department of Mechanical Engineering, University of Toronto, Ontario, M5S 1A4, Canada.

Contributed by the Applied Mechanics Division of THE AMERICAN SOCIETY OF MECHANICAL ENGINEERS for publication in the ASME JOURNAL OF APPLIED MECHANICS. Manuscript received by the ASME Applied Mechanics Division, Oct. 1, 1992; final revision, Jan. 28, 1993. Associate Technical Editor: R. L. Huston.

Downloaded 03 May 2010 to 171.66.16.20. Redistribution subject to ASME license or copyright; see http://www.asme.org/terms/Terms_Use.cfm

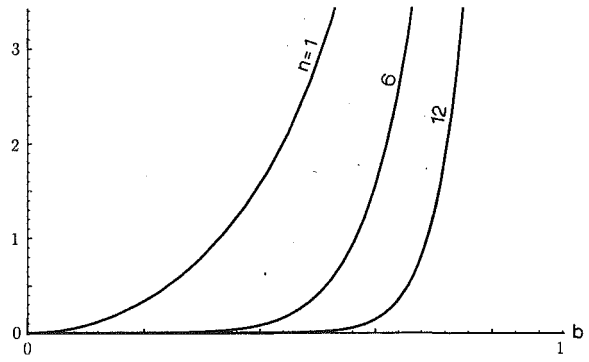


Fig. 3 The function ϕ_3

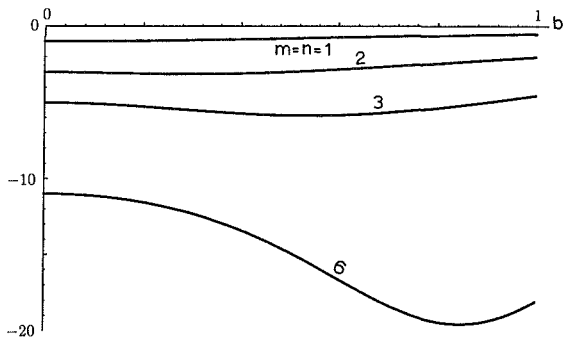


Fig. 4 The function $\phi_1+\phi_2+\phi_3$

1 For given $n=m$, $\phi_2>\phi_1$ for low b and $\phi_1>\phi_2$ for large b. Thus if only one surface needs to be corrugated, it is better to make it the inside surface if the tube wall is thick and the outside surface if the tube wall is thin.

2 Higher rigidity is achieved by using the lowest possible number of waves.

3 When both surfaces are corrugated it is best to use the same phase, same wave number, and same amplitude such that the beneficial interaction effect is fully utilized. This effect is dominant at large b.

The normalized maximum shear stress, occurring on the outer boundary, is

$$\frac{\partial\psi}{\partial\eta}|_{1+\epsilon aS}=\psi_{0r}|_1+\epsilon(\psi_{1r}|_1+hS\psi_{0rr}|_1)+0(\epsilon^2)$$

$$=-1+\epsilon(t_1hS-t_2kS')+0(\epsilon^2) \tag{34}$$

$$t_1=\frac{n(1+b^{2n})}{1-b^{2n}}-1>0,\quad t_2=\frac{2mb^{m+1}}{1-b^{2m}}>0. \tag{35}$$

If only the outside surface is corrugated, the maximum shear stress is at a trough ($\theta=-\pi/2n$) with the value $-1-\epsilon t_1$. If only the inside surface is corrugated, the maximum shear stress is $-1-\epsilon t_2$ on the smooth outside at $\theta=[(\pi/2)-\alpha]/m$. If both surfaces are corrugated with the same phase, wave number, and amplitude, the maximum shear stress is $-1-\epsilon(t_1-t_2)$ at an outside trough.

References

Roark, R. J., and Young, W. C., 1975, *Formulas for Stress and Strain*, 5th ed., McGraw-Hill, New York.

Sokolnikoff, I. S., 1956, *Mathematical Theory of Elasticity*, 2nd ed., McGraw-Hill, New York.

The Buckling Behavior of Rectangular-Bar Helical Compression Springs

L. E. Becker[16] and W. L. Cleghorn[17]

Buckling design charts are presented for rectangular-bar helical compression springs with clamped ends, demonstrating the effect of the number of turns of the spring.

1 Introduction

The buckling behavior of rectangular-bar helical compression springs has been investigated by Haringx (1948), whose model consisted of a prismatic rod with rigidities corresponding to those of unclosed circular rings. Becker and Cleghorn (1992) developed a new set of dynamic, partial differential equations for helical compression springs, and found numerical solutions for clamped ends and circular cross-section using the transfer matrix method to produce buckling design charts. The present article is an extension of the latter for rectangular cross-sections.

2 Method of Solution

Figure 1 shows a long, thin helical compression spring in its unloaded state and its critical pre-buckling configuration due to a determinate axial compressive load P. For a rectangular cross-section with side length $2a$ perpendicular to the spring axis, and side length $2b$ parallel to the axis, we define

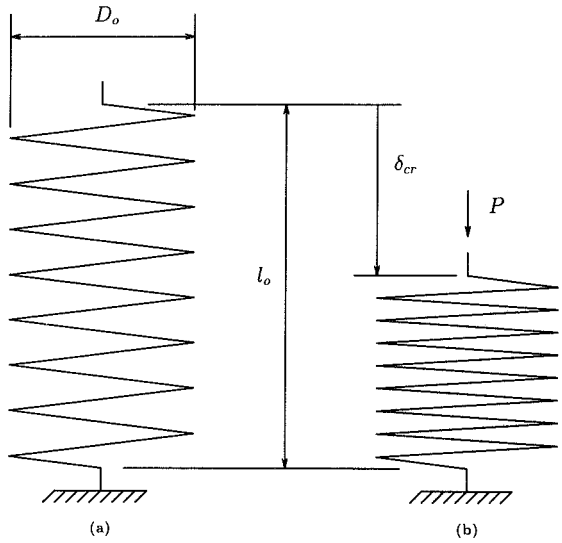


Fig. 1 Definition diagram

[16] Graduate Student, Division of Applied Sciences, Harvard University, Cambridge, MA 02138.

[17] Associate Professor, Department of Mechanical Engineering, University of Toronto, Ontario, M5S 1A4, Canada.

Contributed by the Applied Mechanics Division of THE AMERICAN SOCIETY OF MECHANICAL ENGINEERS for publication in the ASME JOURNAL OF APPLIED MECHANICS. Manuscript received by the ASME Applied Mechanics Division, Oct. 1, 1992; final revision, Jan. 28, 1993. Associate Technical Editor: R. L. Huston.

Copyright © 1994 by ASME

Downloaded 03 May 2010 to 171.66.16.20. Redistribution subject to ASME license or copyright; see http://www.asme.org/terms/Terms_Use.cfm

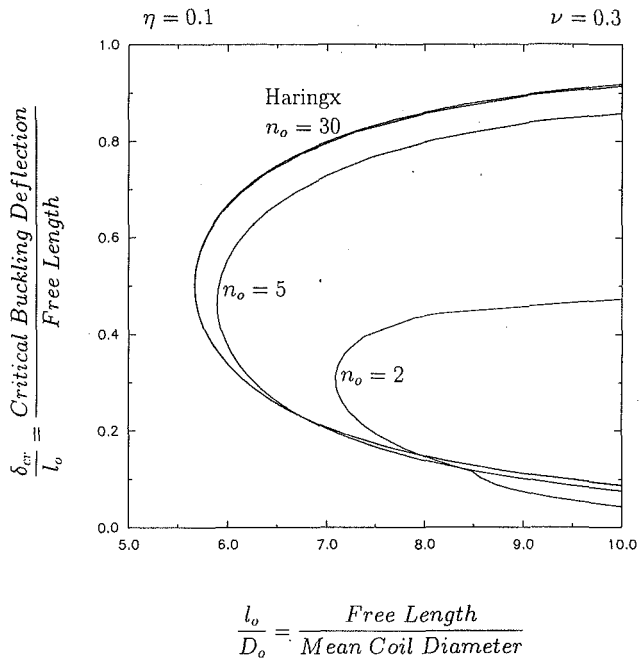


Fig. 2 Buckling curves for n_o = 30, 5, and 2 (η = 0.1)

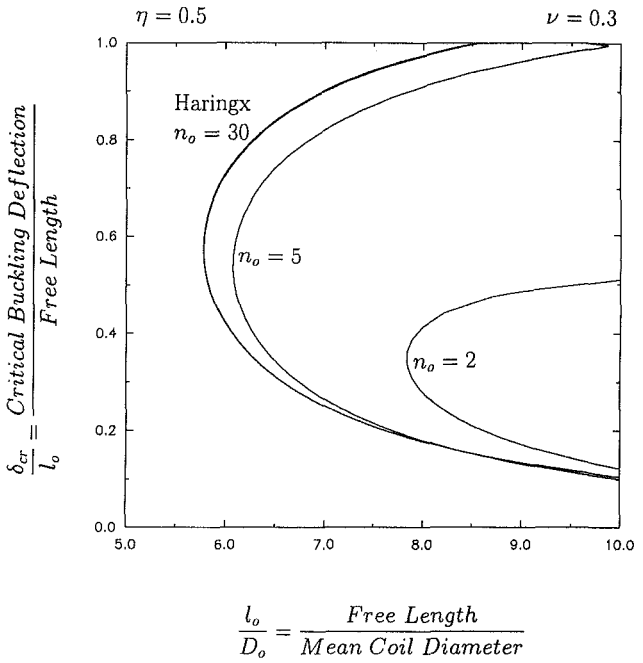


Fig. 3 Buckling curves for n_o = 30, 5, and 2 (η = 0.5)

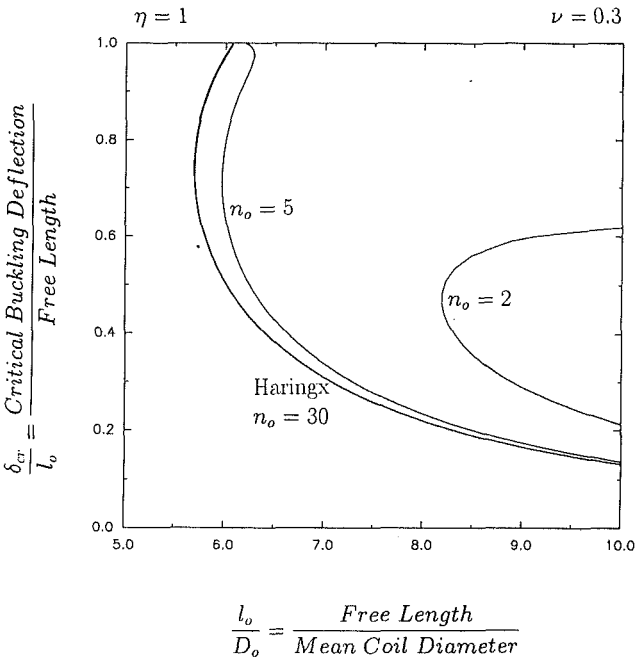


Fig. 4 Buckling curves for n_o = 30, 5, and 2 (η = 1)

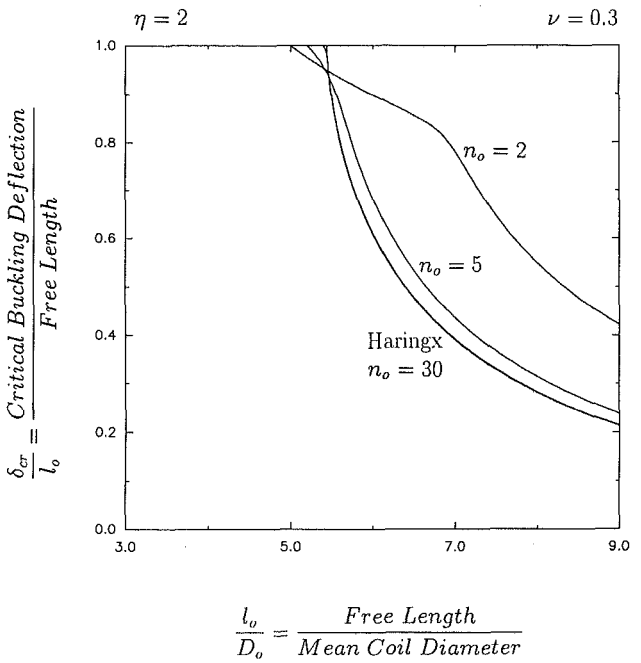


Fig. 5 Buckling curves for n_o = 30, 5, and 2 (η = 2)

$$\eta = \frac{b}{a}, \tag{1}$$

and a spring index

$$c = \frac{R}{\sqrt{ab}}, \tag{2}$$

where R is the coil radius at the critical state. Following the procedure given by Becker and Cleghorn (1992), buckling design charts are generated.

3 Results

Figures 2 to 6 give buckling curves for η = 0.1, 0.5, 1, 2, and 10, where Poisson's ratio ν = 0.3. Each figure compares the results by Haringx (1948) to the present model for n_o = 30, 5, and 2, the number of turns of the unloaded spring. As found previously by the authors, the results conform to the theory presented by Haringx for large numbers of turns, and their dependence on c is negligible.

For $n_o < 2$, l_o/D_o and δ_{cr}/l_o begin to move towards infinity and zero, respectively, as n_o approaches some critical value, n_{oc}, beyond which no buckling can occur regardless of initial configuration. With η = 1, we find n_{oc} = 1, as for circular cross-sections. As η increases, n_{oc} increases up to a limiting value of 1.42.

Figure 7 shows curves for various $\eta < 1$ with n_o = 1. As

Downloaded 03 May 2010 to 171.66.16.20. Redistribution subject to ASME license or copyright; see http://www.asme.org/terms/Terms_Use.cfm

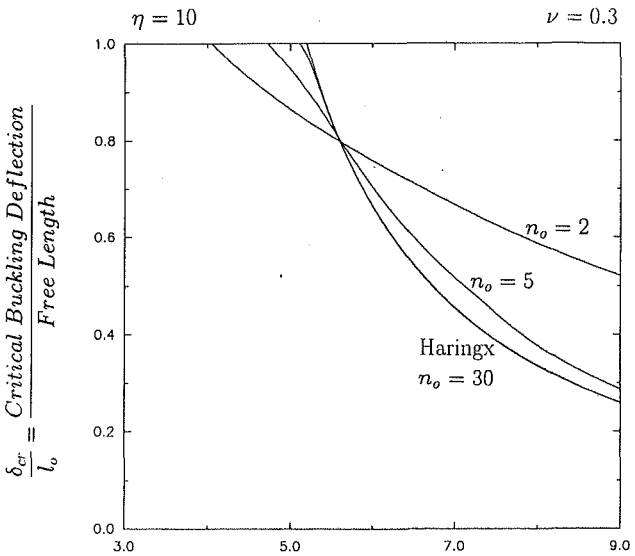


Fig. 6 Buckling curves for n_o = 30, 5, and 2 (η = 10)

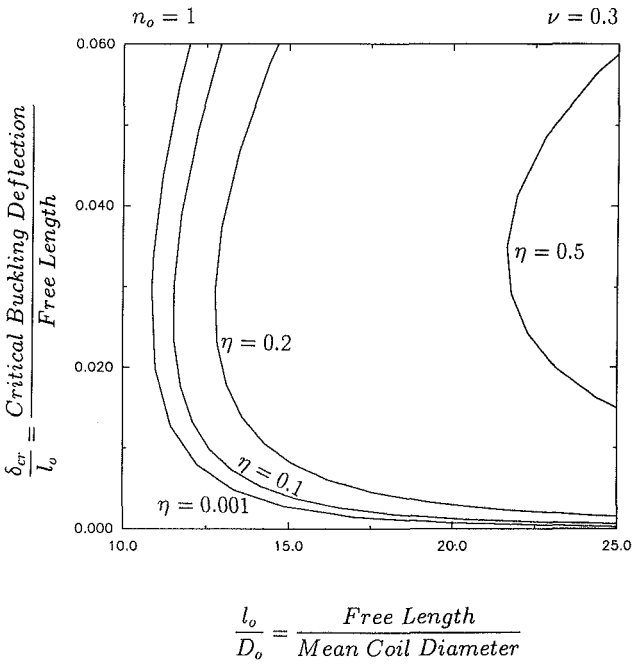


Fig. 7 Buckling curves for n_o = 1 (η = 0.5, 0.2, 0.1, and 0.001)

n_o is decreased further, δ_{cr}/l_o quickly becomes smaller by several orders of magnitude, but there is a progressively smaller shift along the l_o/D_o axis for lower values of η. For $\eta < 1$, n_{oc} is close to zero, violating the assumption of long, thin helices, and hence was not investigated further.

References

Becker, L. E., and Cleghorn, W. L., 1992, "On the Buckling of Helical Compression Springs," *Int. J. Mech. Sci.*, Vol. 34, pp. 275-282.

Haringx, J. A., 1948, "On Highly Compressible Helical Springs and Rubber Rods, and Their Application for Vibration-Free Mountings," *Philips Res. Rep.*, Vol. 3, pp. 401-449.

Longitudinal Impact of a Shaped Projectile on a Hopkinson Bar

C. Bacon[18]

A computational method is developed to calculate numerically the normal force generated by the impact of a nonuniform linearly elastic projectile on a Hopkinson bar. One-dimensional relations are used. In order to assess the validity of the method, it is compared with an analytical solution in the case of the impact of a truncated cone on a rigid half-space. Then some practical applications are performed to predict the force generated by the impact of different truncated cones on a Hopkinson bar. We show that a perfect ramp load is only generated by the impact of a truncated cone on a rigid half-space.

Nomenclature

$A(x)$ = cross-sectional area (m^2)
c = wave propagation speed (m/s)
E = Young's modulus (GPa)
$F(x, t)$ = normal force (N)
L = length of the projectile (m)
t = time (s)
T = transit time (s)
$v(x, t)$ = particle velocity (m/s)
x = abscissa (m)
$Z(x)$ = $A\rho c$ = mechanical impedance (kg/s)
ρ = density (kg/m^3)

1 Introduction

Generally, the split Hopkinson pressure bars technique uses the longitudinal impact of a cylindrical projectile to generate a rectangular incident pulse. That pulse allows one to dynamically load the specimen sandwiched between the two Hopkinson bars. However, if we want to study the influence of the strain rate on the mechanical properties of the specimen, it is useful to be able to change the profile of the incident wave. In order to do this, some noncylindrical projectiles must be used. Then, if we want to calculate the incident wave propagating in the Hopkinson bar, the propagation of the generated elastic wave in the projectile must be known.

To study many different cases it is convenient to use a numerical approach instead of an analytical one. A finite element analysis could be carried out but that method is relatively complicated to perform and it needs a large computational time. Generally, it is easier to use one-dimensional relations.

This paper outlines a computational method to calculate numerically the normal force generated by the impact of a nonuniform projectile on a Hopkinson bar. One-dimensional relations will be used. A calculation will be carried out to predict the incident wave generated by the impact of a truncated cone.

2 Mathematical Analysis

For the calculation, we assume that the projectile and the

[18]Laboratoire Matériaux En wmagement Fiabilité, E.N.S.A.M. Bordeaux, 33 405 Talence Cedex, France. Presently at the Laboratoire de Mécanique Physique, Université Bordeaux I, 33 605 Talence Cedex, France.

Contributed by the Applied Mechanics Division of THE AMERICAN SOCIETY OF MECHANICAL ENGINEERS for publication in the ASME JOURNAL OF APPLIED MECHANICS. Manuscript received by the ASME Applied Mechanics Division, Oct. 26, 1992; final revision, Apr. 6, 1993. Associate Technical Editor: J. N. Reddy.

Downloaded 03 May 2010 to 171.66.16.20. Redistribution subject to ASME license or copyright; see http://www.asme.org/terms/Terms_Use.cfm

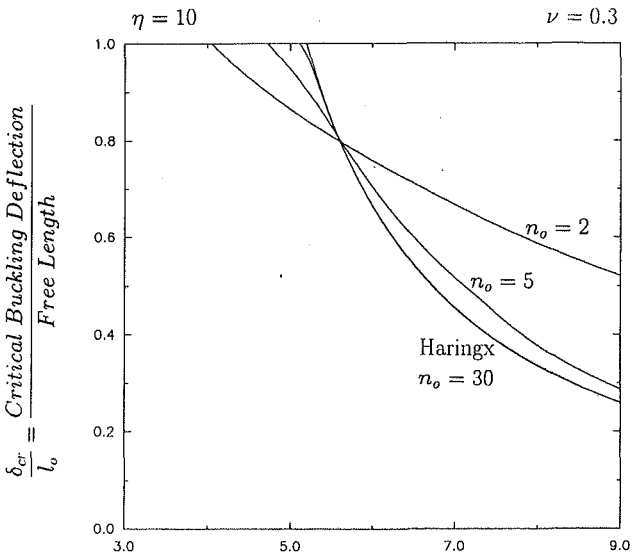


Fig. 6 Buckling curves for n_o = 30, 5, and 2 (η = 10)

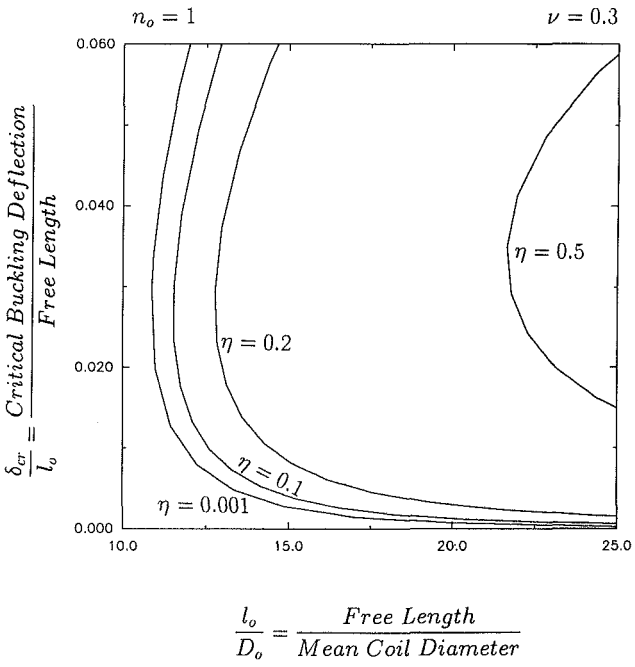


Fig. 7 Buckling curves for n_o = 1 (η = 0.5, 0.2, 0.1, and 0.001)

n_o is decreased further, δ_{cr}/l_o quickly becomes smaller by several orders of magnitude, but there is a progressively smaller shift along the l_o/D_o axis for lower values of η. For $\eta < 1$, n_{oc} is close to zero, violating the assumption of long, thin helices, and hence was not investigated further.

References

Becker, L. E., and Cleghorn, W. L., 1992, "On the Buckling of Helical Compression Springs," *Int. J. Mech. Sci.*, Vol. 34, pp. 275-282.

Haringx, J. A., 1948, "On Highly Compressible Helical Springs and Rubber Rods, and Their Application for Vibration-Free Mountings," *Philips Res. Rep.*, Vol. 3, pp. 401-449.

Longitudinal Impact of a Shaped Projectile on a Hopkinson Bar

C. Bacon[18]

A computational method is developed to calculate numerically the normal force generated by the impact of a nonuniform linearly elastic projectile on a Hopkinson bar. One-dimensional relations are used. In order to assess the validity of the method, it is compared with an analytical solution in the case of the impact of a truncated cone on a rigid half-space. Then some practical applications are performed to predict the force generated by the impact of different truncated cones on a Hopkinson bar. We show that a perfect ramp load is only generated by the impact of a truncated cone on a rigid half-space.

Nomenclature

$A(x)$ = cross-sectional area (m^2)
c = wave propagation speed (m/s)
E = Young's modulus (GPa)
$F(x, t)$ = normal force (N)
L = length of the projectile (m)
t = time (s)
T = transit time (s)
$v(x, t)$ = particle velocity (m/s)
x = abscissa (m)
$Z(x)$ = $A\rho c$ = mechanical impedance (kg/s)
ρ = density (kg/m^3)

1 Introduction

Generally, the split Hopkinson pressure bars technique uses the longitudinal impact of a cylindrical projectile to generate a rectangular incident pulse. That pulse allows one to dynamically load the specimen sandwiched between the two Hopkinson bars. However, if we want to study the influence of the strain rate on the mechanical properties of the specimen, it is useful to be able to change the profile of the incident wave. In order to do this, some noncylindrical projectiles must be used. Then, if we want to calculate the incident wave propagating in the Hopkinson bar, the propagation of the generated elastic wave in the projectile must be known.

To study many different cases it is convenient to use a numerical approach instead of an analytical one. A finite element analysis could be carried out but that method is relatively complicated to perform and it needs a large computational time. Generally, it is easier to use one-dimensional relations.

This paper outlines a computational method to calculate numerically the normal force generated by the impact of a nonuniform projectile on a Hopkinson bar. One-dimensional relations will be used. A calculation will be carried out to predict the incident wave generated by the impact of a truncated cone.

2 Mathematical Analysis

For the calculation, we assume that the projectile and the

[18]Laboratoire Matériaux En wmagement Fiabilité, E.N.S.A.M. Bordeaux, 33 405 Talence Cedex, France. Presently at the Laboratoire de Mécanique Physique, Université Bordeaux I, 33 605 Talence Cedex, France.

Contributed by the Applied Mechanics Division of THE AMERICAN SOCIETY OF MECHANICAL ENGINEERS for publication in the ASME JOURNAL OF APPLIED MECHANICS. Manuscript received by the ASME Applied Mechanics Division, Oct. 26, 1992; final revision, Apr. 6, 1993. Associate Technical Editor: J. N. Reddy.

Copyright © 1994 by ASME
Downloaded 03 May 2010 to 171.66.16.20. Redistribution subject to ASME license or copyright; see http://www.asme.org/terms/Terms_Use.cfm

impacted body are linearly elastic, the projectile with a non-uniform impedance can be divided into segments with constant impedances, and the wave propagation speed and the impedance are given by (one-dimensional solution):

$$c=\sqrt{\frac{E}{\rho}} \text{ and } Z(x)=A(x)\rho c \tag{1}$$

where E, ρ, and $A(x)$ are, respectively, the Young's modulus, the material density, and the cross-sectional area of the bodies. Only the cross-sectional area of the projectile changes with the position x on the projectile.

Now, we want to determine a convenient formulation of the normal force and the particle velocity for a projectile with a piecewise constant impedance since we have assumed that we can divide the projectile with a nonuniform impedance into segments with constant impedances.

Then it can be shown (Bacon, 1993) that the normal force at the time t and the cross-section i is given by

$$F(x,\,t)=\frac{Z_{i+1}F(x-cT,\,t-T)+Z_iF(x)+cT,\,t-T)+Z_iZ_{i+1}[v(x+cT,\,t-T)-v(x-cT,\,t-T)]}{Z_i+Z_{i+1}} \tag{2}$$

and the particle velocity by

$$v(x,\,t)=\frac{F(x+cT,\,t-T)-F(x-cT,\,t-T)+Z_iv(x-cT,\,t-T)+Z_{i+1}v(x+cT,\,t-T)}{Z_i+Z_{i+1}} \tag{3}$$

where T is the transit time of the wave into each segment. So, if the initial conditions and the boundary conditions on the normal force and the particle velocity are known, the histories of the normal force and the particle velocity of any cross-section between two segments with constant impedances can be calculated.

So, for a projectile with a piecewise constant impedance, the obtained solution is the exact one-dimensional solution. For a projectile with a continuous variation of the impedance, we must divide that projectile into a sufficient number of uniform segments. Then the solution is not exact, but converges towards the exact solution when the number of segments grows. Then there is a need to validate the method by comparing with an analytical solution.

3 Numerical Results: Generation of Ramp Loads

At first, to validate the computational method in the case of a projectile with a continuous non-uniform impedance divided into uniform segments, we wish to compare a numerical result with an analytical solution.

A one-dimensional analytical solution has been determined by Lundberg and Lesser for the impact of a truncated cone on a rigid half-space (Lundberg and Lesser, 1978).

The cross-sectional area of a truncated cone is given by

$$A(x)=A(0)\left(1+\frac{x}{ct_0}\right)^2 \tag{4}$$

where $A(0)$ is the cross-sectional area of the contact section.

For such a truncated cone, the authors have demonstrated that the normalized impact force is represented by the following ramp function:

$$F(0,\,t)/F(0,\,0)=1+\frac{t}{t_0}. \tag{5}$$

In the numerical calculation, the chosen impedance of the bar is 100,000 times the impedance of the contact section of the projectile to simulate an almost rigid half-space.

The calculation has been performed by dividing the projectile into 80 cylindrical segments. The numerical result is compared with the analytical solution of Lundberg and Lesser in Fig. 1. The normalized normal force is defined as the ratio between the applied impact force and the initial impact force.

We can notice a good agreement between the two curves. The steps on the numerical result are due to the partition of the projectile into cylindrical segments.

The previous analytical solution is not available in the case of the impact of a truncated cone on a real Hopkinson bar since the impedance of such a bar is always finite. Now we wish to know whether a truncated cone generates a ramp incident wave in the practical case of the impact on a real Hopkinson bar. We have chosen a projectile whose area is given by the relation (4).

We have performed five calculations with different values of ct_0. We can notice that the more the value ct_0 increases the less the projectile is conical: $ct_0 = \infty$ would correspond to a cylindrical projectile. For the numerical calculations, the projectile is divided into 80 cylindrical segments. The normalized generated forces versus the normalized time ct/L are plotted in Fig. 2 where L is the length of the projectile.

By referring to Fig. 2, we can see that, unlike the previous case, we have no longer a ramp load when the value ct_0 decreases. However, we can notice that the more the projectile is conical the more the loading rate increases.

We point out that the numerical prediction allows us to study the profile of the impact force after the wave makes a round trip in the projectile. It is not possible with the analytical solution which considers that the projectile is a semi-infinite truncated cone.

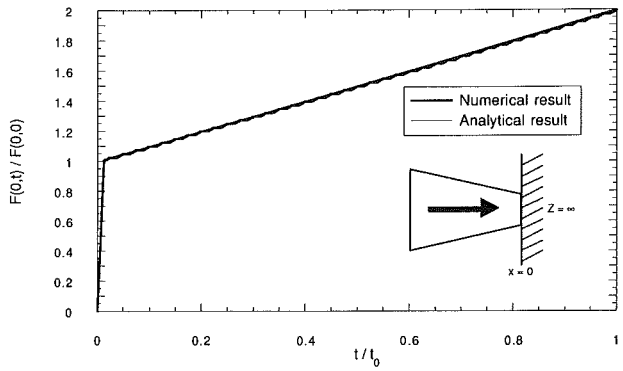


Fig. 1 Comparison between the computational result and the analytical solution for the impact of a truncated cone on a rigid half-space

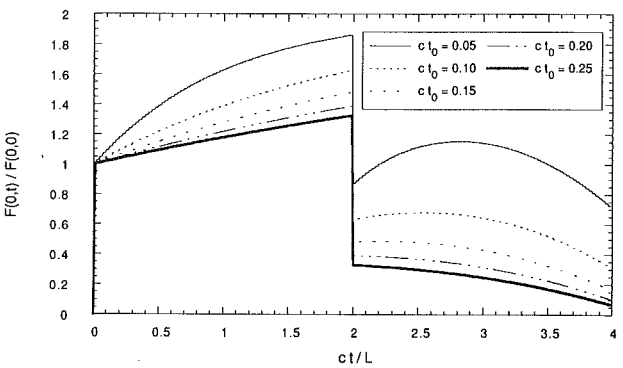


Fig. 2 Normalized impact force generated by the impact of different truncated cones

Downloaded 03 May 2010 to 171.66.16.20. Redistribution subject to ASME license or copyright; see http://www.asme.org/terms/Terms_Use.cfm

4 Conclusion

In this paper, we have seen a one-dimensional computational method to calculate the force generated by the impact of nonuniform projectile on a Hopkinson bar. That method is very easy to implement in a personal computer.

To test whether the partition of the nonuniform projectile into uniform segments is a reasonable approximation, we have compared a computed calculation with a known analytical solution. The result shows good accuracy of the method.

Although the impact of a truncated cone on a rigid half-space generates a ramp load, we have seen that it is not exactly the case for the impact of a truncated cone on a Hopkinson bar. However, we have noticed that the more the projectile is conical the more the loading rate increases. This fact allows us to study the influence of the strain rate on the mechanical compressive behavior of the Hopkinson specimen by changing the profile of the incident wave generated by the impact.

References

Bacon, C., 1993, "Numerical Prediction of the Propagation of Elastic Waves in Longitudinally Impacted Rods: Application to Hopkinson Testing," *International Journal of Impact Engineering*, Vol. 13, No. 4, pp. 527–539.

Lunberg, B., and Lesser, M., 1978, "On Impactor Synthesis," *Journal of Sound and Vibration*, Vol. 58, No. 1, pp. 5–14.

Longitudinal Shear and Torsion of Bimaterial Solids

Xiangzhou Zhang[19] and Norio Hasebe[20]

Introduction

Owing to the increasing use of composite materials in engineering practice, the stress analysis of heterogeneous media has intensively been studied in recent years. In order to obtain a general description of stress distribution in a heterogeneous medium, one can usually resort to the approach of effective moduli (Christensen and Lo, 1979), which idealized the heterogeneous medium into an isotropic or anisotropic homogeneous one. On the other hand, when there is a need for the detailed information of deformation around an interface of an heterogeneous medium, a solution to the problem derived from the heterogeneous medium per se is usually required.

This Note is concerned with the longitudinal shear and torsion of a bimaterial solid, one of typical models in the elastic stress analysis of composite materials. A general solution procedure is provided, by which the exact solution for every particular problem can easily be constructed from homogeneous elastic solutions. Two special cases, relating to the elastic deformation around an interface in bimaterial solids with a cylindrical circular hole or a penny-shaped crack, are treated rigorously to illustrate the application of the solution procedure.

[19]Department of Aircraft Engineering, Northwestern Polytechnical University, Xian 710072, China.

[20]Department of Civil Engineering, Nagoya Institute of Technology, Nagoya 466, Japan.

Contributed by the Applied Mechanics Division of THE AMERICAN SOCIETY OF MECHANICAL ENGINEERS for publication in the ASME JOURNAL OF APPLIED MECHANICS. Manuscript received by the ASME Applied Mechanics Division, Oct. 23, 1992; final revision, Mar. 29, 1993. Associate Technical Editor: J. N. Reddy.

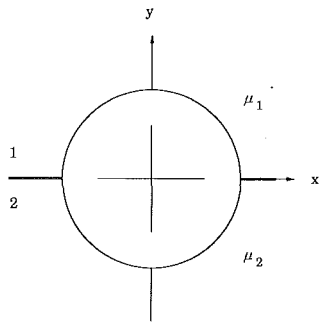


Fig. 1 The bimaterial solid

Problem and Solution Procedure

Consider the longitudinal shear of a bimaterial solid with a cylindrical hole, as depicted in Fig. 1, composed of two dissimilar half-spaces, with μ_1 and μ_2 being the shear moduli of the upper and lower half-spaces, respectively. The solid is symmetric in geometry with respect to the interface, which lies in the xz-plane, otherwise the geometry can be arbitrary. The longitudinal displacement of the solid, when its boundary value is prescribed, should satisfy the following equations:

$$\frac{\partial^2 w_i}{\partial x^2}+\frac{\partial^2 w_i}{\partial y^2}=0,\ i=1,\ 2 \tag{1}$$

$$x^2+y^2\to\infty,\ w_i=0,\ i=1,\ 2 \tag{2}$$

$$w_i=g(x_0,\ y_0),\ i=1,\ 2,\ \text{on the boundary} \tag{3}$$

$$w_1=w_2,\ \mu_1\frac{\partial w_1}{\partial y}=\mu_2\frac{\partial w_2}{\partial y},\ \text{at the interface} \tag{4a, b}$$

where x_0 and y_0 stand for the coordinates of a point on the boundary; subscripts 1 and 2 are used to distinguish quantities related to the upper and lower half-spaces, respectively; $g(x_0, y_0)$ stands for a given function. As a rule, $g(x_0, y_0)$ can be divided into two portions such that

$$g(x_0,\ y_0)=g_s(x_0,\ y_0)+g_a(x_0,\ y_0), \tag{5}$$

with g_s and g_a representing the boundary displacement symmetric and antisymmetric with respect to the xz-plane, respectively.

To solve the problem we first work out a preliminary solution, $w_{i1}(x, y)$, to Eq. (1)–(4a, b) on condition that $\mu_1=\mu_2$ in Eq. (4b) and $g=g_s$ in Eq. (5). This is a homogeneous solution easily obtainable; meantime, it is incomplete since it does not meet the real boundary condition (3).

Likewise, we prepare another preliminary solution to the problem on condition that $\mu_1=\mu_2$ in Eq. (4b) and $g=g_a$ in Eq. (3). This homogeneous solution, denoted by $w_{i2}(x, y)$, has a defect that it can not satisfy the real stress continuation condition at the interface, Eq. (4b), due to the presence of the antisymmetric component of the displacement. Therefore, another solution, $w_{i3}(x, y)$, should be sought via the following condition at the interface:

$$\mu_1\left(\frac{\partial w_{12}}{\partial y}+\frac{\partial w_{13}}{\partial y}\right)=\mu_2\left(\frac{\partial w_{22}}{\partial y}+\frac{\partial w_{23}}{\partial y}\right) \tag{6}$$

and added to w_{i1} and w_{i2} so that the stress continuation at the interface can be true. For this purpose we prescribe $w_{i3}(x, y)$ in such a way that

$$w_{13}(x,\ y)=\frac{\mu_2-\mu_1}{\mu_1+\mu_2}\,w_{12}(x,\ y) \tag{7}$$

$$w_{23}(x,\ y)=\frac{\mu_1-\mu_2}{\mu_1+\mu_2}\,w_{22}(x,\ y). \tag{8}$$

It is easily seen that with such form of $w_{i3}(x, y)$, Eq. (6) is

Downloaded 03 May 2010 to 171.66.16.20. Redistribution subject to ASME license or copyright; see http://www.asme.org/terms/Terms_Use.cfm

4 Conclusion

In this paper, we have seen a one-dimensional computational method to calculate the force generated by the impact of nonuniform projectile on a Hopkinson bar. That method is very easy to implement in a personal computer.

To test whether the partition of the nonuniform projectile into uniform segments is a reasonable approximation, we have compared a computed calculation with a known analytical solution. The result shows good accuracy of the method.

Although the impact of a truncated cone on a rigid half-space generates a ramp load, we have seen that it is not exactly the case for the impact of a truncated cone on a Hopkinson bar. However, we have noticed that the more the projectile is conical the more the loading rate increases. This fact allows us to study the influence of the strain rate on the mechanical compressive behavior of the Hopkinson specimen by changing the profile of the incident wave generated by the impact.

References

Bacon, C., 1993, "Numerical Prediction of the Propagation of Elastic Waves in Longitudinally Impacted Rods: Application to Hopkinson Testing," *International Journal of Impact Engineering*, Vol. 13, No. 4, pp. 527–539.

Lunberg, B., and Lesser, M., 1978, "On Impactor Synthesis," *Journal of Sound and Vibration*, Vol. 58, No. 1, pp. 5–14.

Longitudinal Shear and Torsion of Bimaterial Solids

Xiangzhou Zhang[19] and Norio Hasebe[20]

Introduction

Owing to the increasing use of composite materials in engineering practice, the stress analysis of heterogeneous media has intensively been studied in recent years. In order to obtain a general description of stress distribution in a heterogeneous medium, one can usually resort to the approach of effective moduli (Christensen and Lo, 1979), which idealized the heterogeneous medium into an isotropic or anisotropic homogeneous one. On the other hand, when there is a need for the detailed information of deformation around an interface of an heterogeneous medium, a solution to the problem derived from the heterogeneous medium per se is usually required.

This Note is concerned with the longitudinal shear and torsion of a bimaterial solid, one of typical models in the elastic stress analysis of composite materials. A general solution procedure is provided, by which the exact solution for every particular problem can easily be constructed from homogeneous elastic solutions. Two special cases, relating to the elastic deformation around an interface in bimaterial solids with a cylindrical circular hole or a penny-shaped crack, are treated rigorously to illustrate the application of the solution procedure.

[19]Department of Aircraft Engineering, Northwestern Polytechnical University, Xian 710072, China.

[20]Department of Civil Engineering, Nagoya Institute of Technology, Nagoya 466, Japan.

Contributed by the Applied Mechanics Division of THE AMERICAN SOCIETY OF MECHANICAL ENGINEERS for publication in the ASME JOURNAL OF APPLIED MECHANICS. Manuscript received by the ASME Applied Mechanics Division, Oct. 23, 1992; final revision, Mar. 29, 1993. Associate Technical Editor: J. N. Reddy.

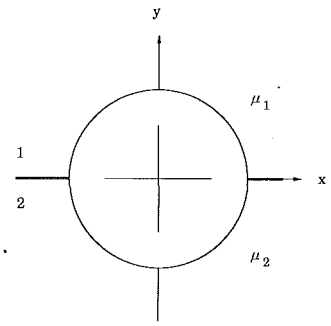


Fig. 1 The bimaterial solid

Problem and Solution Procedure

Consider the longitudinal shear of a bimaterial solid with a cylindrical hole, as depicted in Fig. 1, composed of two dissimilar half-spaces, with μ_1 and μ_2 being the shear moduli of the upper and lower half-spaces, respectively. The solid is symmetric in geometry with respect to the interface, which lies in the xz-plane, otherwise the geometry can be arbitrary. The longitudinal displacement of the solid, when its boundary value is prescribed, should satisfy the following equations:

$$\frac{\partial^2 w_i}{\partial x^2}+\frac{\partial^2 w_i}{\partial y^2}=0,\ i=1,\ 2 \tag{1}$$

$$x^2+y^2\to\infty,\ w_i=0,\ i=1,\ 2 \tag{2}$$

$$w_i=g(x_0,\ y_0),\ i=1,\ 2,\ \text{on the boundary} \tag{3}$$

$$w_1=w_2,\ \mu_1\frac{\partial w_1}{\partial y}=\mu_2\frac{\partial w_2}{\partial y},\ \text{at the interface} \tag{4a, b}$$

where x_0 and y_0 stand for the coordinates of a point on the boundary; subscripts 1 and 2 are used to distinguish quantities related to the upper and lower half-spaces, respectively; $g(x_0, y_0)$ stands for a given function. As a rule, $g(x_0, y_0)$ can be divided into two portions such that

$$g(x_0,\ y_0)=g_s(x_0,\ y_0)+g_a(x_0,\ y_0), \tag{5}$$

with g_s and g_a representing the boundary displacement symmetric and antisymmetric with respect to the xz-plane, respectively.

To solve the problem we first work out a preliminary solution, $w_{i1}(x, y)$, to Eq. (1)–(4a, b) on condition that $\mu_1=\mu_2$ in Eq. (4b) and $g=g_s$ in Eq. (5). This is a homogeneous solution easily obtainable; meantime, it is incomplete since it does not meet the real boundary condition (3).

Likewise, we prepare another preliminary solution to the problem on condition that $\mu_1=\mu_2$ in Eq. (4b) and $g=g_a$ in Eq. (3). This homogeneous solution, denoted by $w_{i2}(x, y)$, has a defect that it can not satisfy the real stress continuation condition at the interface, Eq. (4b), due to the presence of the antisymmetric component of the displacement. Therefore, another solution, $w_{i3}(x, y)$, should be sought via the following condition at the interface:

$$\mu_1\left(\frac{\partial w_{12}}{\partial y}+\frac{\partial w_{13}}{\partial y}\right)=\mu_2\left(\frac{\partial w_{22}}{\partial y}+\frac{\partial w_{23}}{\partial y}\right) \tag{6}$$

and added to w_{i1} and w_{i2} so that the stress continuation at the interface can be true. For this purpose we prescribe $w_{i3}(x, y)$ in such a way that

$$w_{13}(x,\ y)=\frac{\mu_2-\mu_1}{\mu_1+\mu_2}\,w_{12}(x,\ y) \tag{7}$$

$$w_{23}(x,\ y)=\frac{\mu_1-\mu_2}{\mu_1+\mu_2}\,w_{22}(x,\ y). \tag{8}$$

It is easily seen that with such form of $w_{i3}(x, y)$, Eq. (6) is

Copyright © 1994 by ASME
Downloaded 03 May 2010 to 171.66.16.20. Redistribution subject to ASME license or copyright; see http://www.asme.org/terms/Terms_Use.cfm

satisfied. Besides, the displacement w_{i3} continues at the interface. On the other hand, w_{i3} produces a displacement distribution $w_{i3}(x_0, y_0)$ on the boundary, which in general is not but should be vanishing. In view of this, a fourth solution, $w_{i4}(x, y)$, specified by Eqs. (1), (2), (4*a*, *b*) (with $\mu_1 = \mu_2$) and the boundary condition

$$w_{i4}(x_0, y_0) = -w_{i3}(x_0, y_0), \quad i = 1, 2 \tag{9}$$

should be added to the preceding three solutions to complete the final solution. Since w_{i4} is symmetric with respect to the xz-plane, it behaves like w_{i1} and is virtually a homogeneous solution.

Combining the above result, the final solution to the heterogeneous problem is written as the sum of four homogeneous solutions:

$$w_i = w_{i1} + w_{i2} + w_{i3} + w_{i4}, \quad i = 1, 2. \tag{10}$$

Now consider the elastic torsion of a bi-material solid containing a cavity of axisymmetric geometry. This solid can also be represented by Fig. 1, with the understanding that the diagram shown stands for a cross-section of the solid which contains the axis of symmetry y. A cylindrical coordinate system (r, ϕ, y) is used to formulate the problem. The governing equation and boundary conditions of the problem are

$$\frac{\partial^2 w_i}{\partial r^2} + \frac{1}{r} \cdot \frac{\partial w_i}{\partial r} - \frac{w_i}{r^2} + \frac{\partial^2 w_i}{\partial y^2} = 0, \; i = 1, 2 \tag{11}$$

$$r^2 + y^2 \to \infty, \; w_i = 0, \; i = 1, 2 \tag{12}$$

$$w_i = g(r_0, y_0), \; i = 1, 2, \text{ on the boundary} \tag{13}$$

$$w_1 = w_2, \; \mu_1 \frac{\partial w_1}{\partial y} = \mu_2 \frac{\partial w_2}{\partial y}, \text{ at the interface.} \tag{14a, b}$$

The solution to this problem can also be expressed as a sum of four homogeneous solutions:

$$w_i = w_{i1} + w_{i2} + w_{i3} + w_{i4}, \quad i = 1, 2 \tag{15}$$

where w_{ij} $(i = 1, 2; j = 1, 2, 3, 4)$ should be worked out via a way similar to that for the antiplane shear problem. For instance, $w_{i2}(r, y)$ and $w_{i3}(r, y)$ are also related to each other by an equation identical to Eq. (6) in form.

The above formulation for the longitudinal shear and torsion problems is developed in terms of displacement boundary conditions. When the boundary is under a prescribed traction condition, the solution procedure is also applicable with only minor modifications.

A Bimaterial Solid Having a Cylindrical Circular Cavity at the Interface

A composed solid, made up of two half-spaces of dissimilar materials, with a cylindrical circular hole of radius a at the interface is considered. This solid represents a model of composite materials containing a cylindrical circular defect at an interface.

To describe and solve the problem, the polar coordinates, (r, θ), are used. The boundary displacement on the cavity surface in its most general form is expressed by

$$w_i(a, \theta) = \sum_{n=0}^{\infty} (a_n \cos n\theta + b_n \sin n\theta), \quad i = 1, 2 \tag{16}$$

whereas the displacement at infinity vanishes. For simplicity in the following, only two typical terms, $a_n \cos n\theta$ and $b_j \sin j\theta$ in Eq. (16), will be considered. Using conventional methods available in standard reference books (Carslaw and Jaeger, 1959; Sneddon, 1951), the following homogeneous solutions are obtained:

$$w_{i1} = \frac{a_n a^n \cos n\theta}{r^n}, \; w_{i2} = \frac{b_j a^j \sin j\theta}{r^j}, \; i = 1, 2 \tag{17a, b}$$

$$w_{13} = \frac{\mu_2 - \mu_1}{\mu_1 + \mu_2} \cdot \frac{b_j a^j \sin j\theta}{r^j}, \; w_{23} = \frac{\mu_1 - \mu_2}{\mu_1 + \mu_2} \cdot \frac{b_j a^j \sin j\theta}{r^j} \tag{18a, b}$$

$$w_{i4} = \frac{\mu_1 - \mu_2}{\mu_1 + \mu_2} \left[\frac{C_0}{2} + \sum_{n=1}^{\infty} \frac{C_n \cos n\theta}{r^n} \right], \; i = 1, 2 \tag{19}$$

$$C_n = \begin{cases} 0, & j + n = \text{even} \\ \dfrac{4jb_j a^n}{\pi(j^2 - n^2)}, & j + n = \text{odd.} \end{cases} \tag{20a, b}$$

By making use of Eqs. (10), (17*a*, *b*)–(20*a*, *b*), the final form of $w_1(r, \theta)$ and $w_2(r, \theta)$ can easily be constructed by superposition.

A Bimaterial Solid Containing a Penny-Shaped Crack at the Interface

Consider a bimaterial solid having a penny-shaped crack of unit radius embedded in the interface plane and centered at the origin. External load at the infinity vanishes and on the crack boundary the displacement is prescribed antisymmetrically to the interface plane. It is known that the homogeneous solution to this problem takes the following form (Kassir and Sih, 1975)

$$w_{12}(r, y) = \int_0^{\infty} C(s) J_1(rs) e^{-sy} ds \tag{21}$$

for the upper half-space, where the unknown function $C(s)$ should be sought from the following condition

$$\int_0^{\infty} C(s) J_1(rs) ds = w_{12}(r, 0^+) = \begin{cases} f(r), & 0 \le r \le 1 \\ 0, & 1 < r \end{cases} \tag{22a, b}$$

where $f(r)$ is a given continuous function with $f(1) = 0$. Solving the above integral equation we obtain

$$C(s) = s \int_0^1 r f(r) J_1(sr) dr. \tag{23}$$

Substituting Eq. (23) into (21), the explicit expressions for $w_{12}(r, y)$ can be obtained. The shear stresses and stress intensity factors can be determined subsequently. In this problem, $w_{22}(r, y) = -w_{12}(r, -y)$ and $w_{11}(r, y) = w_{21}(r, -y) = 0$, because the given displacement on the boundary does not contain component symmetric to the interface.

The third solution, w_{i3}, can be obtained simply via Eqs. (6)–(8). To finally complete the solution the fourth solution w_{i4} is needed. However, in case the main interest of investigation is to obtain the stress intensity factor, this is not necessary; since in the solution w_{i4} the stress intensity factor vanishes.

Finally, the stress intensity factor for this problem can be expressed as

$$K_3 = \frac{2\mu_1 \mu_2 K_{30}}{\mu_0(\mu_1 + \mu_2)}. \tag{24}$$

That is, the stress intensity factor for the bimaterial solid equals that of a homogeneous solid (which is denoted by K_{30}) multiplied by a factor $2\mu_1\mu_2/[\mu_0(\mu_1 + \mu_2)]$, with μ_0 being the shear modulus of the homogeneous material. It is seen that the factor depends on material constants. Therefore, the recognition that K_3 is independent of material constants in bimaterial solid problems (Kassir and Sih, 1975) is valid only within the scope of traction boundary condition, and is not a general conclusion.

Downloaded 03 May 2010 to 171.66.16.20. Redistribution subject to ASME license or copyright; see http://www.asme.org/terms/Terms_Use.cfm

References

Carslaw, H. S., and Jaeger, J. C., 1959, *Conduction of Heat in Solids*, Oxford University Press, Oxford, U.K.

Christensen, R. M., and Lo, K. H., 1979, "Solution for Effective Shear Properties in Three Phase Sphere and Cylinder Models," *Journal of Mechanics and Physics of Solids*, Vol. 27, pp. 315–330.

Kassir, M. K., and Sih, G. C., 1975, *Three Dimensional Crack Problems*, Noordhoff, Leyden.

Sneddon, I. N., 1951, *Fourier Transforms*, McGraw-Hill, New York.

Bending of Plates on Thin Compressible Foundations

C. W. Bert[21]

Introduction

There has been a great variety of continuum models to describe the behavior of flexible foundations more accurately than the classical Winkler (1867) and Pasternak (1954) models (cf., Bharatha and Levinson (1980) and Kerr (1984)). One of the more recent models was presented by Dillard (1989) to describe elastomeric foundations, which were assumed to be incompressible. However, many materials used as flexible foundations are *not* incompressible. The purpose of this paper is to develop a model for a foundation of linear elastic isotropic material having an arbitrary Poisson's ratio, ν.

Analysis

The system considered consists of a plate perfectly bonded to a compressible interlayer, which in turn is perfectly bonded to an underlying rigid support; see Fig. 1. If the plate is thin, homogeneous, isotropic, and undergoes small deflection (w), its governing differential equation can be expressed as

$$D\nabla^4 w = p - q \tag{1}$$

where D is the plate rigidity, p is the applied normal pressure, q is the resisting pressure due to the interlayer, and x and y are Cartesian coordinates of the plate middle surface.

The problem is now reduced to determination of the resisting pressure q. If the interlayer is isotropic, very thin, and perfectly bonded, it can be assumed that the three normal stress components are approximately equal with a magnitude q (see Gent and Meinecke (1970) and Holownia (1972)). The relative volume change ($\Delta V/V_o$) in the interlayer can be expressed as

$$\bar{\epsilon}_x + \bar{\epsilon}_y + \bar{\epsilon}_z = \Delta V/V_o = -3(1-2\nu)(q/E) \tag{2}$$

where E is Young's modulus of the interlayer, $\bar{\epsilon}_x$ and $\bar{\epsilon}_y$ are the in-plane normal strains in the midplane of the interlayer, and $\bar{\epsilon}_z$ is the thickness normal strain.

Assuming that the in-plane normal strains are distributed parabolically through the interlayer thickness (h), and that the thickness normal strain is uniformly distributed, one may write

$$\bar{\epsilon}_x = \frac{2}{3}\frac{\partial u_o}{\partial x}, \quad \bar{\epsilon}_y = \frac{2}{3}\frac{\partial v_o}{\partial y}, \quad \bar{\epsilon}_z = -\frac{w}{h} \tag{3}$$

where u_o and v_o are the midplane displacements. (See the Appendix.)

Substituting Eqs. (3) into Eq. (2) yields

$$\frac{\partial u_o}{\partial x} + \frac{\partial v_o}{\partial y} = \frac{3}{2}\frac{w}{h} - \frac{9(1-2\nu)}{2E}q. \tag{4}$$

The equations of equilibrium in the respective x and y directions are

$$\frac{\partial \sigma_x}{\partial x} + \frac{\partial \tau_{xz}}{\partial z} = 0, \quad \frac{\partial \sigma_y}{\partial y} + \frac{\partial \tau_{yz}}{\partial z} = 0 \tag{5}$$

where the conventional notation for stress components has been used. However,

$$\sigma_x \approx \sigma_y \approx -q$$

$$\tau_{xz} = G\gamma_{xz} = G\frac{\partial u}{\partial z} = -\frac{8Gu_o}{h^2}z$$

$$\tau_{yz} = G\gamma_{yz} = G\frac{\partial v}{\partial z} = -\frac{8Gv_o}{h^2}z \tag{6}$$

where G is the shear modulus of the interlayer, and the γ_{ij} are engineering shear strains. (See the Appendix.)

Substitution of Eqs. (6) into Eqs. (5) yields

$$\frac{\partial q}{\partial x} = -\frac{8G}{h^2}u_o, \quad \frac{\partial q}{\partial y} = -\frac{8G}{h^2}v_o. \tag{7}$$

Also, for isotropic interlayer material, E and G must be related by

$$G = \frac{E}{2(1+\nu)}. \tag{8}$$

Taking the appropriate first partial derivatives of u_o and v_o as given by Eqs. (7) and using Eq. (8), one obtains

$$\frac{\partial u_o}{\partial x} = -\frac{(1+\nu)h^2}{4E}\frac{\partial^2 q}{\partial x^2}, \quad \frac{\partial v_o}{\partial y} = -\frac{(1+\nu)h^2}{4E}\frac{\partial^2 q}{\partial y^2} \tag{9}$$

Finally, substitution of Eqs. (9) into Eq. (4) yields the following governing differential equation for the resisting pressure q:

$$(\nabla^2 - C)q = \frac{-6E}{(1+\nu)h^3}w \tag{10}$$

where

$$C = \frac{1-2\nu}{1+\nu}\frac{18}{h^2}. \tag{11}$$

Equation (10) is equivalent to Eq. (24) of a recent paper by Lai et al. (1992).

For the case of an incompressible interlayer, as treated by Dillard (1989), $\nu = 1/2$ and C vanishes. This is consistent with Dillard's work.

Substituting Eq. (10) into Eq. (1), one gets

$$D\nabla^4 w - \frac{6E}{(1+\nu)h^3}(\nabla^2 - C)^{-1}(w) = p. \tag{12}$$

If one seeks an approximate solution by the Galerkin method, for instance, then one must work with integrodifferential Eq. (12); see Batdorf (1969). However, if one seeks an exact solution, one may escalate the order of the governing Eq. (12) by operating on both sides of it with the operator $(\nabla^2 - C)$. The result is

$$(\nabla^2 - C)D\nabla^4 w - \frac{6E}{(1+\nu)h^3}w = (\nabla^2 - C)p. \tag{13}$$

[21]Benjamin H. Perkinson Chair Professor of Engineering and Director, School of Aerospace and Mechanical Engineering, The University of Oklahoma, 865 Asp Avenue, Room 212, Norman, OK 73019-0601. Fellow ASME.

Contributed by the Applied Mechanics Division of THE AMERICAN SOCIETY OF MECHANICAL ENGINEERS for publication in the ASME JOURNAL OF APPLIED MECHANICS. Manuscript received by the ASME Applied Mechanics Division, Jan. 5, 1993; final revision, Apr. 19, 1993. Associate Technical Editor: A. K. Noor.

Downloaded 03 May 2010 to 171.66.16.20. Redistribution subject to ASME license or copyright; see http://www.asme.org/terms/Terms_Use.cfm

References

Carslaw, H. S., and Jaeger, J. C., 1959, *Conduction of Heat in Solids*, Oxford University Press, Oxford, U.K.

Christensen, R. M., and Lo, K. H., 1979, "Solution for Effective Shear Properties in Three Phase Sphere and Cylinder Models," *Journal of Mechanics and Physics of Solids*, Vol. 27, pp. 315–330.

Kassir, M. K., and Sih, G. C., 1975, *Three Dimensional Crack Problems*, Noordhoff, Leyden.

Sneddon, I. N., 1951, *Fourier Transforms*, McGraw-Hill, New York.

Bending of Plates on Thin Compressible Foundations

C. W. Bert[21]

Introduction

There has been a great variety of continuum models to describe the behavior of flexible foundations more accurately than the classical Winkler (1867) and Pasternak (1954) models (cf., Bharatha and Levinson (1980) and Kerr (1984)). One of the more recent models was presented by Dillard (1989) to describe elastomeric foundations, which were assumed to be incompressible. However, many materials used as flexible foundations are *not* incompressible. The purpose of this paper is to develop a model for a foundation of linear elastic isotropic material having an arbitrary Poisson's ratio, ν.

Analysis

The system considered consists of a plate perfectly bonded to a compressible interlayer, which in turn is perfectly bonded to an underlying rigid support; see Fig. 1. If the plate is thin, homogeneous, isotropic, and undergoes small deflection (w), its governing differential equation can be expressed as

$$D\nabla^4 w = p - q \tag{1}$$

where D is the plate rigidity, p is the applied normal pressure, q is the resisting pressure due to the interlayer, and x and y are Cartesian coordinates of the plate middle surface.

The problem is now reduced to determination of the resisting pressure q. If the interlayer is isotropic, very thin, and perfectly bonded, it can be assumed that the three normal stress components are approximately equal with a magnitude q (see Gent and Meinecke (1970) and Holownia (1972)). The relative volume change ($\Delta V/V_o$) in the interlayer can be expressed as

$$\bar{\epsilon}_x + \bar{\epsilon}_y + \bar{\epsilon}_z = \Delta V/V_o = -3(1-2\nu)(q/E) \tag{2}$$

where E is Young's modulus of the interlayer, $\bar{\epsilon}_x$ and $\bar{\epsilon}_y$ are the in-plane normal strains in the midplane of the interlayer, and $\bar{\epsilon}_z$ is the thickness normal strain.

Assuming that the in-plane normal strains are distributed parabolically through the interlayer thickness (h), and that the thickness normal strain is uniformly distributed, one may write

$$\bar{\epsilon}_x = \frac{2}{3}\frac{\partial u_o}{\partial x}, \quad \bar{\epsilon}_y = \frac{2}{3}\frac{\partial v_o}{\partial y}, \quad \bar{\epsilon}_z = -\frac{w}{h} \tag{3}$$

where u_o and v_o are the midplane displacements. (See the Appendix.)

Substituting Eqs. (3) into Eq. (2) yields

$$\frac{\partial u_o}{\partial x} + \frac{\partial v_o}{\partial y} = \frac{3}{2}\frac{w}{h} - \frac{9(1-2\nu)}{2E}q. \tag{4}$$

The equations of equilibrium in the respective x and y directions are

$$\frac{\partial \sigma_x}{\partial x} + \frac{\partial \tau_{xz}}{\partial z} = 0, \quad \frac{\partial \sigma_y}{\partial y} + \frac{\partial \tau_{yz}}{\partial z} = 0 \tag{5}$$

where the conventional notation for stress components has been used. However,

$$\sigma_x \approx \sigma_y \approx -q$$

$$\tau_{xz} = G\gamma_{xz} = G\frac{\partial u}{\partial z} = -\frac{8Gu_o}{h^2}z$$

$$\tau_{yz} = G\gamma_{yz} = G\frac{\partial v}{\partial z} = -\frac{8Gv_o}{h^2}z \tag{6}$$

where G is the shear modulus of the interlayer, and the γ_{ij} are engineering shear strains. (See the Appendix.)

Substitution of Eqs. (6) into Eqs. (5) yields

$$\frac{\partial q}{\partial x} = -\frac{8G}{h^2}u_o, \quad \frac{\partial q}{\partial y} = -\frac{8G}{h^2}v_o. \tag{7}$$

Also, for isotropic interlayer material, E and G must be related by

$$G = \frac{E}{2(1+\nu)}. \tag{8}$$

Taking the appropriate first partial derivatives of u_o and v_o as given by Eqs. (7) and using Eq. (8), one obtains

$$\frac{\partial u_o}{\partial x} = -\frac{(1+\nu)h^2}{4E}\frac{\partial^2 q}{\partial x^2}, \quad \frac{\partial v_o}{\partial y} = -\frac{(1+\nu)h^2}{4E}\frac{\partial^2 q}{\partial y^2} \tag{9}$$

Finally, substitution of Eqs. (9) into Eq. (4) yields the following governing differential equation for the resisting pressure q:

$$(\nabla^2 - C)q = \frac{-6E}{(1+\nu)h^3}w \tag{10}$$

where

$$C = \frac{1-2\nu}{1+\nu}\frac{18}{h^2}. \tag{11}$$

Equation (10) is equivalent to Eq. (24) of a recent paper by Lai et al. (1992).

For the case of an incompressible interlayer, as treated by Dillard (1989), $\nu = 1/2$ and C vanishes. This is consistent with Dillard's work.

Substituting Eq. (10) into Eq. (1), one gets

$$D\nabla^4 w - \frac{6E}{(1+\nu)h^3}(\nabla^2 - C)^{-1}(w) = p. \tag{12}$$

If one seeks an approximate solution by the Galerkin method, for instance, then one must work with integrodifferential Eq. (12); see Batdorf (1969). However, if one seeks an exact solution, one may escalate the order of the governing Eq. (12) by operating on both sides of it with the operator $(\nabla^2 - C)$. The result is

$$(\nabla^2 - C)D\nabla^4 w - \frac{6E}{(1+\nu)h^3}w = (\nabla^2 - C)p. \tag{13}$$

[21]Benjamin H. Perkinson Chair Professor of Engineering and Director, School of Aerospace and Mechanical Engineering, The University of Oklahoma, 865 Asp Avenue, Room 212, Norman, OK 73019-0601. Fellow ASME.

Contributed by the Applied Mechanics Division of THE AMERICAN SOCIETY OF MECHANICAL ENGINEERS for publication in the ASME JOURNAL OF APPLIED MECHANICS. Manuscript received by the ASME Applied Mechanics Division, Jan. 5, 1993; final revision, Apr. 19, 1993. Associate Technical Editor: A. K. Noor.

Copyright © 1994 by ASME
Downloaded 03 May 2010 to 171.66.16.20. Redistribution subject to ASME license or copyright; see http://www.asme.org/terms/Terms_Use.cfm

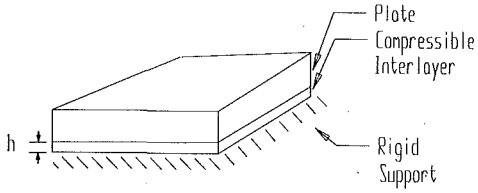


Fig. 1 Schematic diagram of a plate with a compressible interlayer and a rigid support

Application to a Square Plate on a Compressible Foundation

Here, the same example is selected as was used by Dillard (1989): a square plate of isotropic material, simply supported on all four edges, and resting on an elastic foundation. A Navier solution is sought in the form

$$w(x, y) = \sum_m \sum_n W_{mn} \sin \frac{m\pi x}{a} \sin \frac{n\pi y}{a}. \tag{14}$$

The loading is taken to be

$$p(x, y) = \sum_m \sum_n P_{mn} \sin \frac{m\pi x}{a} \sin \frac{n\pi y}{a} \tag{15}$$

where

$$P_{mn} = \frac{4}{ab} \int_0^a \int_0^a p(x, y) \sin \frac{m\pi x}{a} \sin \frac{n\pi y}{a} \, dy dx. \tag{16}$$

Thus,

$$W_{mn} = \frac{(P_{mn}/D)(\alpha_m^2 + \beta_n^2 + C)}{(\alpha_m^2 + \beta_n^2)^3 + C(\alpha_m^2 + \beta_n^2)^2 + F} \tag{17}$$

where C is as defined in Eq. (11) and $F \equiv 12\, G/Dh^3$, $\alpha_m \equiv m\pi/a$, $\beta_n \equiv n\pi/a$.

The deflection influence coefficient, K, is defined as the deflection at (x, y) due to a unit load applied at (ζ, η). For the case of the deflection at the plate center $(a/2, a/2)$ due to a unit load applied at the same point, the dimensionless influence coefficient, $\bar{K}$, is

$$\bar{K} \equiv KD/a^4$$

or

$$\bar{K} = 4 \sum_m \sum_n \frac{\pi^2 (m^2 + n^2) + \bar{C}}{\pi^6 (m^2 + n^2)^3 + \pi^4 (m^2 + n^2)^2 \bar{C} + \bar{F}} \tag{18}$$

where

$$\bar{C} \equiv Ca^2 = 18 (a/h)^2 (1 - 2\nu)/(1 + \nu);$$
$$\bar{F} \equiv Fa^6 = 144 (a/h)^6 (1 - \nu_p^2)(G/E_p)$$

and E_p and ν_p are the elastic modulus and Poisson's ratio of the plate. For the incompressible case considered by Dillard, one needs only to set $\bar{C} = 0$. The analogous result for the case of a plate on a Winkler foundation is

$$\bar{K} = 4 \sum_m \sum_n \frac{1}{\pi^2 (m^2 + n^2)^2 + \bar{F}}. \tag{19}$$

Results and Discussion

Numerical results are shown in Table 1 for the same plate properties and interlayer shear modulus as were considered by Dillard, namely, $E_p = 210$ GPa, $\nu_p = 0.3$, $G = 1.3$ MPa. The interlayer Poisson's ratio (ν) is varied, and the geometry is defined by $a/h = 15$. It is noted that the present compressible solution predicts an increase in $\bar{K}$ of 29.5 percent as ν is changed only a very little from the incompressible case ($\nu = 0.5$) to $\nu = 0.49$. The Winkler foundation is slightly more than three times stiffer than the incompressible foundation.

Table 1 Values of the dimensionless deflection influence coefficients, $\bar{K}$, for a thin plate supported by various elastic interlayers

Plate with:	$\bar{K}$
No foundation	0.01699
Winkler foundation	0.003534
Incompressible foundation	0.01100
Compressible foundations:	
ν = -0.9	0.01466
ν = 0	0.01679
ν = 0.25	0.01670
ν = 0.40	0.01644
ν = 0.45	0.01606
ν = 0.48	0.01518
ν = 0.49	0.01425
ν = 0.495	0.01324
ν = 0.499	0.01164

It is interesting that in the case of a compressible interlayer, the largest deflection occurs for $\nu = 0$, although the dropoff is very small between $\nu = 0$ and -0.9. Negative values of ν are included here not only because they fall within the theoretical limits (-1 to $+0.5$) for isotropic material, but also because they have been observed experimentally (cf. Lakes (1987)).

It should also be mentioned that to obtain a solution which is converged so that the last term added produces a change of approximately 0.05 percent from the preceding result, the convergence was slowest (i.e., the most terms were required) for the Winkler foundation (81 terms) and fastest for the compressible foundation in the range -0.9 to 0.48 (36 terms).

Conclusion

A simple continuum model has been developed to describe the behavior of a compressible elastic interlayer (i.e., one of arbitrary Poisson's ratio).

Acknowledgments

Helpful discussions with Prof. Victor Birman of the University of Missouri and the skillful typing of Susan Wierimaa are gratefully acknowledged.

References

Batdorf, S. B., 1969, "On the Application of Inverse Differential Operators to the Solution of Cylinder Buckling and Other Problems," *AIAA/ASME 10th Structures, Structural Dynamics and Materials Conference*, New Orleans, LA, ASME, New York, pp. 386–391.

Bharatha, S., and Levinson, M., 1980, "A Theory of Elastic Foundations," *Archive for Rational Mechanics and Analysis*, Vol. 74, pp. 249–266.

Dillard, D. A., 1989, "Bending of Plates on Thin Elastomeric Foundations," ASME JOURNAL OF APPLIED MECHANICS, Vol. 56, pp. 382–386.

Gent, A. N., and Meinecke, E. A., 1970, "Compression, Bending, and Shear of Bonded Rubber Blocks," *Polymer Engineering and Science*, Vol. 10, pp. 48–53.

Holowania, B. P., 1972, "Effect of Poisson's Ratio on Bonded Rubber Blocks," *Journal of Strain Analysis*, Vol. 7, pp. 236–242.

Kerr, A. D., 1984, "On the Formal Development of Elastic Foundation Models," *Ingenieur-Archiv*, Vol. 54, pp. 455–464.

Lai, Y. H., Dillard, D. A., and Thornton, J. S., 1992, "The Effect of Compressibility on the Stress Distributions in Thin Elastomeric Blocks and Annular Bushings," ASME JOURNAL OF APPLIED MECHANICS, Vol. 59, pp. 902–908.

Lakes, R. S., 1987, "Negative Poisson's Ratio Materials," *Science*, Vol. 238, p. 551.

Downloaded 03 May 2010 to 171.66.16.20. Redistribution subject to ASME license or copyright; see http://www.asme.org/terms/Terms_Use.cfm

Pasternak, P. L., 1954, "On a New Method of Analysis of an Elastic Foundation by Means of Two Foundation Constants," (in Russian), *Gosudarstvennge Izdatelstvo Literaturi po Stroitelstvu i Arkhitekture*, Moscow, Russia.

Winkler, E., 1867, *Die Lehre von der Elasticität und Festigkeit*, Dominicus, Prague, p. 182.

APPENDIX

Derivation of Eqs. (3) and (6)

Assume that the normal strain in the x direction is parabolically distributed through the interlayer thickness h, i.e.,

$$\epsilon_x(x, y, z) = [1-(2z/h)^2]\epsilon_{xo}(x, y) \tag{A1}$$

where

$$\epsilon_{xo} = \epsilon_x|_{z=0} = \frac{\partial u_o}{\partial x}. \tag{A2}$$

The corresponding mean strain averaged through the interlayer thickness is

$$\bar{\epsilon}_x = \frac{1}{h}\int_{-h/2}^{h/2} \epsilon_x dz = \frac{1}{h}\int_{-h/2}^{h/2} [1-(2z/h)^2]\epsilon_{xo} dz$$

or

$$\bar{\epsilon}_x = \frac{2}{3}\epsilon_{xo} = \frac{2}{3}\frac{\partial u_o}{\partial x}. \tag{A3}$$

This is the first of Eqs. (3); the second one is obtained in an analogous fashion and the third one is trivial.

From Eqs. (A1) and (A2) it is clear that

$$u(x, y, z) = [1-(2z/h)^2]u_o(x, z).$$

Thus,

$$\frac{\partial u}{\partial z} = -\frac{8u_o}{h^2}z$$

or

$$\tau_{xz} = -\frac{8Gu_o}{h^2}z. \tag{A4}$$

This is the second of Eqs. (6); the third one is obtained in a similar manner and the first one is trivial.

Identities for Torsion of Cylinders

Zhengxian Bai[22] and R. T. Shield[23]

1 Introduction

In a cylinder for which the only nonzero stresses are the two shearing stresses associated with the axial direction, equilibrium requires that the stresses be independent of the axial coordinate. We suppose also that the lateral surface is free from traction, corresponding to a state of pure torsion. In Section 2 we give a simple method for generating identities on the stresses involving integrals over the cross-section using only the equilibrium equation and the boundary condition satisfied by the stresses. Although the material properties are not utilized, it is to be expected that the main use of the method will be to generate identities for small strain elastic or elastic-plastic torsion.

As a first use of the approach, it is shown in Section 2 that each of the rectangular shearing stresses contributes one half of the twisting moment, a result independent of the material properties of the cylinder. The result has been given previously by Timoshenko and Goodier (1951, 1970) in the context of elastic torsion, and it was shown earlier by Thomson and Tait (1912) to hold for elastic torsion of an isotropic bar with a very narrow rectangular section.

A known identity for elastic torsion is considered in Section 3 as an illustration of the method. The motivation for this work arose in an investigation of second-order elastic torsion, extension, and bending of short and long cylinders (Bai, 1991), in which it was found that certain identities on the St. Venant warping function were required to justify the analysis. The identities in question are given in Section 4.

A similar approach could be used to generate identities for other problems involving quantities governed by field equations and boundary conditions.

2 Cylinder in Torsion and Generation of Identities

We consider an equilibrium state of a cylinder composed of a material which is homogeneous in the axial direction, the z-direction of the coordinate system (x, y, z). We suppose that τ_{xz} and τ_{yz} are the only nonzero stresses and that there is no traction on the lateral surface. The stresses are then independent of z and we have

$$\frac{\partial \tau_{xz}}{\partial x} + \frac{\partial \tau_{yz}}{\partial y} = 0 \text{ on } A, \tag{1}$$

$$\tau_{xz}n_x + \tau_{yz}n_y = 0 \text{ on } L, \tag{2}$$

where A is the cross-section of the cylinder and L is the boundary.

From these equations it follows that there is no transverse force on a cross-section of the cylinder. We have

$$\int_A \tau_{xz} dA = \int_A \left[\tau_{xz} + x\left(\frac{\partial \tau_{xz}}{\partial x} + \frac{\partial \tau_{yz}}{\partial y}\right)\right] dA$$

$$= \int_L x(\tau_{xz}n_x + \tau_{yz}n_y) ds = 0, \tag{3}$$

and it can similarly be shown that there is no resultant force in the y-direction. (These results also follow from overall equilibrium of a portion of the cylinder and the absence of any bending moments, τ_{zz} being zero. Some writers, Love (1927) and Sokolnikoff (1956) for example, involve material properties by using the warping function for elastic torsion to deduce the results.)

The only moment acting on a cross-section is a twisting moment M given by

$$M = \int_A (x\tau_{yz} - y\tau_{xz}) dA. \tag{4}$$

We can generate identities involving integrals over the cross-section by using the boundary condition (2), the divergence theorem, and the equilibrium Eq. (1). For any continuously differentiable function $f(x, y)$ we have

$$\int_L f(x, y)[\tau_{xy}n_x + \tau_{yz}n_y] ds = 0,$$

which leads to

[22]Advanced Engineering, General Motors Technical Center, Warren, MI 48090-9010.

[23]1 Fork Point Lane, Oriental, NC 28571. Fellow ASME.

Contributed by the Applied Mechanics Division of THE AMERICAN SOCIETY OF MECHANICAL ENGINEERS for publication in the JOURNAL OF APPLIED MECHANICS. Manuscript received by the ASME Applied Mechanics Division, Jan. 12, 1993; final revision, Apr. 5, 1993. Associate Technical Editor: J. W. Rudnicki.

Downloaded 03 May 2010 to 171.66.16.20. Redistribution subject to ASME license or copyright; see http://www.asme.org/terms/Terms_Use.cfm

Pasternak, P. L., 1954, "On a New Method of Analysis of an Elastic Foundation by Means of Two Foundation Constants," (in Russian), *Gosudarstvennge Izdatelstvo Literaturi po Stroitelstvu i Arkhitekture*, Moscow, Russia.

Winkler, E., 1867, *Die Lehre von der Elasticität und Festigkeit*, Dominicus, Prague, p. 182.

APPENDIX

Derivation of Eqs. (3) and (6)

Assume that the normal strain in the x direction is parabolically distributed through the interlayer thickness h, i.e.,

$$\epsilon_x(x, y, z) = [1-(2z/h)^2]\epsilon_{xo}(x, y) \tag{A1}$$

where

$$\epsilon_{xo} = \epsilon_x|_{z=0} = \frac{\partial u_o}{\partial x}. \tag{A2}$$

The corresponding mean strain averaged through the interlayer thickness is

$$\bar{\epsilon}_x = \frac{1}{h}\int_{-h/2}^{h/2} \epsilon_x dz = \frac{1}{h}\int_{-h/2}^{h/2} [1-(2z/h)^2]\epsilon_{xo} dz$$

or

$$\bar{\epsilon}_x = \frac{2}{3}\epsilon_{xo} = \frac{2}{3}\frac{\partial u_o}{\partial x}. \tag{A3}$$

This is the first of Eqs. (3); the second one is obtained in an analogous fashion and the third one is trivial.

From Eqs. (A1) and (A2) it is clear that

$$u(x, y, z) = [1-(2z/h)^2]u_o(x, z).$$

Thus,

$$\frac{\partial u}{\partial z} = -\frac{8u_o}{h^2}z$$

or

$$\tau_{xz} = -\frac{8Gu_o}{h^2}z. \tag{A4}$$

This is the second of Eqs. (6); the third one is obtained in a similar manner and the first one is trivial.

Identities for Torsion of Cylinders

Zhengxian Bai[22] and R. T. Shield[23]

1 Introduction

In a cylinder for which the only nonzero stresses are the two shearing stresses associated with the axial direction, equilibrium requires that the stresses be independent of the axial coordinate. We suppose also that the lateral surface is free from traction, corresponding to a state of pure torsion. In Section 2 we give a simple method for generating identities on the stresses involving integrals over the cross-section using only the equilibrium equation and the boundary condition satisfied by the stresses. Although the material properties are not utilized, it is to be expected that the main use of the method will be to generate identities for small strain elastic or elastic-plastic torsion.

As a first use of the approach, it is shown in Section 2 that each of the rectangular shearing stresses contributes one half of the twisting moment, a result independent of the material properties of the cylinder. The result has been given previously by Timoshenko and Goodier (1951, 1970) in the context of elastic torsion, and it was shown earlier by Thomson and Tait (1912) to hold for elastic torsion of an isotropic bar with a very narrow rectangular section.

A known identity for elastic torsion is considered in Section 3 as an illustration of the method. The motivation for this work arose in an investigation of second-order elastic torsion, extension, and bending of short and long cylinders (Bai, 1991), in which it was found that certain identities on the St. Venant warping function were required to justify the analysis. The identities in question are given in Section 4.

A similar approach could be used to generate identities for other problems involving quantities governed by field equations and boundary conditions.

2 Cylinder in Torsion and Generation of Identities

We consider an equilibrium state of a cylinder composed of a material which is homogeneous in the axial direction, the z-direction of the coordinate system (x, y, z). We suppose that τ_{xz} and τ_{yz} are the only nonzero stresses and that there is no traction on the lateral surface. The stresses are then independent of z and we have

$$\frac{\partial \tau_{xz}}{\partial x} + \frac{\partial \tau_{yz}}{\partial y} = 0 \text{ on } A, \tag{1}$$

$$\tau_{xz}n_x + \tau_{yz}n_y = 0 \text{ on } L, \tag{2}$$

where A is the cross-section of the cylinder and L is the boundary.

From these equations it follows that there is no transverse force on a cross-section of the cylinder. We have

$$\int_A \tau_{xz} dA = \int_A \left[\tau_{xz} + x\left(\frac{\partial \tau_{xz}}{\partial x} + \frac{\partial \tau_{yz}}{\partial y}\right)\right] dA$$

$$= \int_L x(\tau_{xz}n_x + \tau_{yz}n_y) ds = 0, \tag{3}$$

and it can similarly be shown that there is no resultant force in the y-direction. (These results also follow from overall equilibrium of a portion of the cylinder and the absence of any bending moments, τ_{zz} being zero. Some writers, Love (1927) and Sokolnikoff (1956) for example, involve material properties by using the warping function for elastic torsion to deduce the results.)

The only moment acting on a cross-section is a twisting moment M given by

$$M = \int_A (x\tau_{yz} - y\tau_{xz}) dA. \tag{4}$$

We can generate identities involving integrals over the cross-section by using the boundary condition (2), the divergence theorem, and the equilibrium Eq. (1). For any continuously differentiable function $f(x, y)$ we have

$$\int_L f(x, y)[\tau_{xy}n_x + \tau_{yz}n_y] ds = 0,$$

which leads to

[22]Advanced Engineering, General Motors Technical Center, Warren, MI 48090-9010.

[23]1 Fork Point Lane, Oriental, NC 28571. Fellow ASME.

Contributed by the Applied Mechanics Division of THE AMERICAN SOCIETY OF MECHANICAL ENGINEERS for publication in the JOURNAL OF APPLIED MECHANICS. Manuscript received by the ASME Applied Mechanics Division, Jan. 12, 1993; final revision, Apr. 5, 1993. Associate Technical Editor: J. W. Rudnicki.

Copyright © 1994 by ASME
Downloaded 03 May 2010 to 171.66.16.20. Redistribution subject to ASME license or copyright; see http://www.asme.org/terms/Terms_Use.cfm

$$\int_A \left[\frac{\partial f}{\partial x} \tau_{xz} + \frac{\partial f}{\partial y} \tau_{yz} \right] dA = 0. \quad (5)$$

If we set $f = xy$ we get

$$\int_A (y\tau_{xz} + x\tau_{yz}) dA = 0, \quad (6)$$

and comparison with (4) shows that *each of the rectangular components of stress provides one half of the twisting moment*,

$$\int_A x\tau_{yz} dA = -\int_A y\tau_{xz} dA = \frac{1}{2} M. \quad (7)$$

This result follows from equilibrium and the lack of traction on the lateral surface and so is independent of the material properties.

The result (7) has been shown previously for particular cases. Timoshenko and Goodier (1951, 1970) used the Prandtl stress function, whose existence is implied by (1), to show that τ_{xz}, τ_{yz} each contribute half of the torque. The argument is given for a simply connected cross-section and for elastic torsion but it does not make use of any material properties. Goodier (1962) also used the Prandtl stress function but showed that the result holds for a multiply connected section. Thomson and Tait (1912) used the series solution for elastic torsion of a bar of narrow rectangular section to show that in the limit as the ratio of the lengths of the sides tends to zero, the stress components parallel to the sides each contribute one half of the moment, the contribution of the stress parallel to the shorter sides coming entirely from the ends of the section. This result is also implied by the approximate membrane analogy solution for a narrow rectangular section as discussed by Timoshenko and Goodier (1951, 1970).

Identity (6) is a special case of the identity

$$\int_A (nx^{n-1}y^m \tau_{xz} + mx^n y^{m-1} \tau_{yz}) dA = 0. \quad (8)$$

3 Elastic Torsion

For elastic torsion of a cylinder of isotropic material, the stresses are related to the St. Venant warping function $\phi(x, y)$ through

$$\tau_{xz} = \mu\alpha\left(\frac{\partial\phi}{\partial x} - y\right), \quad \tau_{yz} = \mu\alpha\left(\frac{\partial\phi}{\partial y} + x\right), \quad (9)$$

where α is the angle of twist per unit length and μ is the shear modulus. If we use these relations in (5), we get

$$\int_L \left[\frac{\partial f}{\partial x}\left(\frac{\partial\phi}{\partial x} - y\right) + \frac{\partial f}{\partial y}\left(\frac{\partial\phi}{\partial y} + x\right) \right] ds = 0. \quad (10)$$

Love (1927) and Diaz and Weinstein (1948) derive the identity

$$\int_A \left[\left(\frac{\partial\phi}{\partial x}\right)^2 + \left(\frac{\partial\phi}{\partial y}\right)^2 \right] dA = \int_A \left(y\frac{\partial\phi}{\partial x} - x\frac{\partial\phi}{\partial y} \right) dA \quad (11)$$

by using the properties of the warping function. The identity was used by Love to show that the energy per unit length of the cylinder is $1/2C\alpha^2$, where C is the torsional rigidity, while Diaz and Weinstein used it to show that $C \le \mu J$, where J is the polar moment of inertia of the section about the axis of torsion.

The identity (11) follows immediately from (10) by replacing f by ϕ.

4 Identities for Second-Order Effects in Torsion, Extension, and Bending

In treating second-order elastic effects in the torsion, extension, and bending of short and long cylinders of isotropic material, it was found that in order for solutions for second-order displacements to exist, it was necessary for the St. Venant warping function to satisfy certain identities (Bai, 1991). In addition to the identities obtained by using (9) in (3), (6) and the identity on τ_{yz} corresponding to (3), the following identities were needed:

$$\int_A x\left(\frac{\partial\phi}{\partial x} - y\right) dA = \int_A y\left(\frac{\partial\phi}{\partial y} + x\right) dA = 0, \quad (12)$$

$$\frac{1}{2}\int_A (x^2 - y^2)\left(\frac{\partial\phi}{\partial x} - y\right) dA = \int_A xy\left(\frac{\partial\phi}{\partial y} + x\right) dA, \quad (13)$$

$$\frac{1}{2}\int_A (y^2 - x^2)\left(\frac{\partial\phi}{\partial y} + x\right) dA = \int_A xy\left(\frac{\partial\phi}{\partial x} + y\right) dA, \quad (14)$$

$$\int_A x\left[\frac{\partial\phi}{\partial x}\left(\frac{\partial\phi}{\partial x} - y\right) + \frac{\partial\phi}{\partial y}\left(\frac{\partial\phi}{\partial y} + x\right)\right] dA = -\int_A \phi\left(\frac{\partial\phi}{\partial x} - y\right) dA, \quad (15)$$

$$\int_A y\left[\frac{\partial\phi}{\partial x}\left(\frac{\partial\phi}{\partial x} - y\right) + \frac{\partial\phi}{\partial y}\left(\frac{\partial\phi}{\partial y} + x\right)\right] dA = -\int_A \phi\left(\frac{\partial\phi}{\partial y} + x\right) dA. \quad (16)$$

It is easily seen that these identities follow simply from (10) by replacing f in turn by x, y, $x^3/6 - xy^2/2$, $y^3/6 - x^2y/2$, $x\phi$, and $y\phi$.

References

Bai, Z., 1991, "Overall Results in Second-Order Elasticity," Ph.D. Dissertation, University of Illinois at Urbana-Champaign, Urbana, IL.

Diaz, J. B., and Weinstein, A., 1948, "The Torsional Rigidity and Variational Methods," *American Journal of Mathematics*, Vol. 70, pp. 107–116.

Goodier, J. N., 1962, "Torsion," *Handbook of Engineering Mechanics*, W. Flügge ed., McGraw-Hill, New York, Chap. 36, pp. 4–5.

Love, A. E. H., 1927, *The Mathematical Theory of Elasticity*, 4th ed., Cambridge University Press, Cambridge, England, pp. 312–313.

Sokolnikoff, I. N., 1956, *Mathematical Theory of Elasticity*, 2nd ed., McGraw-Hill, New York, p. 112.

Thomson, W., and Tait, P. G., 1912, *A Treatise on Natural Philosophy*, Vol. 2, Cambridge University Press, Cambridge, U.K., pp. 267–268.

Timoshenko, S. P., and Goodier, J. N., 1951, *Theory of Elasticity*, 2nd ed., McGraw-Hill, New York, pp. 262, 273–274.

Timoshenko, S. P. and Goodier, J. N., 1970, *Theory of Elasticity*, 3rd ed, McGraw-Hill, New York, pp. 296, 308–309.

Downloaded 03 May 2010 to 171.66.16.20. Redistribution subject to ASME license or copyright; see http://www.asme.org/terms/Terms_Use.cfm

Journal of Applied Mechanics

Discussion

On the Approximate Solution of Nonclassically Damped Linear Systems[1]

S. M. Shahruz[2]. The authors propose and study an iterative approach by which an approximate solution for nonclassically damped linear systems is obtained.

In Section 3, the authors start with (14) and after many steps arrive at (40). One can, however, obtain (40) in a few easy steps as follows. From (5) and $q_a(0) = q(0)$ and $\dot{q}_a(0) = \dot{q}(0)$, one obtains

$$\hat{q}_a(s) = \hat{F}(s)\hat{g}(s) + \hat{F}(s)[(sI_n + \Lambda)q(0) + \dot{q}(0)], \qquad \text{(D1)}$$

where $\hat{F}(s)$ is given by (32). From (14), one obtains

$$\hat{e}(s) = \hat{H}(s)\hat{e}(s) + \hat{H}(s)\hat{q}_a(s) + \hat{F}(s)Rq(0), \qquad \text{(D2)}$$

where $\hat{H}(s)$ is given by (31). Substituting $\hat{q}_a(s)$ from (D1) into (D2), one obtains (40).

The authors let $q(0) = \dot{q}(0) = 0$ in (40) and arrive at (41), in which $\|\hat{H}(s)\|$ and $\|\hat{F}(s)\|$ are given by (42) and (43), respectively. The norms in (42) and (43) are not valid induced norms, because the maximum of the right-hand sides of (42) and (43) over all $1 \le i \le n$ cannot be computed if the supremum of the functions of s in (42) and (43) over all $s \in C$ is not computed for each i. Using (42) and (43), the authors derive inequality (48). Then, by applying the inverse Laplace transform to (48), they obtain inequality (49) in the time domain. This step is questionable, because applying the inverse Laplace transform to inequalities in the Laplace domain and obtaining inequalities in the time domain is not justified. Assuming that (49) is correct, it provides an upper bound on the magnitude of the error in the approximate solution of the system. Computing the error bound in (49) is not simple, contrary to the authors' claim. Furthermore, the authors state that the error bound (49) is generally sharper than that given by (9) and (10). This statement is not proved rigorously; it is only confirmed by simulation for one particular example in Section 5.

In Section 4, the authors propose an iterative approach that results in an approximate solution for nonclassically damped systems. The authors give an estimate of the number of iterations required to achieve a specified error tolerance; this estimate is given by (77). Estimates obtained by (77) can be *extremely conservative.* For instance, consider a system for which

$$D = \begin{bmatrix} 0.9899 & 0.190 & -0.190 & 0.185 & -0.190 \\ 0.190 & 1.0000 & -0.190 & -0.190 & 0.185 \\ -0.190 & -0.190 & 1.0049 & 0.185 & 0.190 \\ 0.185 & -0.190 & 0.185 & 1.0099 & -0.190 \\ -0.190 & 0.185 & 0.190 & -0.190 & 1.0198 \end{bmatrix},$$

$$\Omega = \text{diag}[(0.9899)^2, (1)^2, (1.0049)^2, (1.0099)^2, (1.0198)^2],$$

and the input vector is $g(t) = [1\ 1\ 1\ 1\ 1]^T \sin t$ for all $t \ge 0$. For this system, the damping ratio is 0.5 for all five modes. Using (10), (11), and (12) in the paper, one obtains $\|\bar{H}\| = 0.9956$.

Now, let the error tolerance be 0.05. By (77), an estimate of the number of iterations required to achieve the 0.05 error tolerance is $N \ge 1910$. This estimate is extremely conservative, because of the following: For the third mode, (i) compute the starting-step solution of the iteration, which is the same as the solution obtained by the approximate decoupling, $q_{a3}(\cdot)$; (ii) solve the system by numerical integration to obtain $q_3(\cdot)$; (iii) plot the error $e_3(\cdot) := q_3(\cdot) - q_{a3}(\cdot)$, which is the largest. Due to space limitation, our figure of e_3 is deleted. Having the error plotted, it becomes evident that *no* iteration is necessary, and the starting-step solution of the iteration meets an even tighter error tolerance of 0.02. Estimates obtained by (77) can be extremely conservative, because in computing the norm $\|\bar{H}\|$ the signs of the off-diagonal elements of the normalized damping matrix are not considered. It turns out that the signs of the off-diagonal elements play an important role in the magnitude of the approximation error (Shahruz and Packard, 1993).

Reference

Shahruz, S. M., and Packard, A. K., 1993, "Approximate Decoupling of Weakly Nonclassically Damped Linear Second-Order Systems Under Harmonic Excitations," ASME *Journal of Dynamic Systems, Measurement, and Control*, Vol.115, pp. 214–218.

Authors' Closure[3]

A common procedure in the solution of a nonclassically damped linear system is to neglect the off-diagonal elements of the associated modal damping matrix. The purpose of our paper is to derive a quadrature formula for the error of approximation, and to outline an iterative scheme to improve the accuracy of the approximate solution. The issues brought up in the discussion by Dr. S. M. Shahruz are rather minor and stylistic. These issues are clarified in the following paragraphs.

The aim of our iterative derivation of Eq. (40) is to highlight the structure of the associated iterative scheme. It permits a similar iterative scheme to be brought up in Section 4 without elaboration, since questions such as the convergence of the vectors e_k and u_k have already been addressed in the derivation of Eq. (40). Several other equations in our paper could be established more directly if this were the sole intention.

For every s with which the right-hand side of Eqs. (42) and (43) are finite, $\|\hat{H}(s)\|$ and $\|\hat{F}(s)\|$ are valid norms. Those singular values in s with which expressions (42) and (43) are indeterminate do not have any relevance to subsequent manipulations. Equation (49) is valid when some mild mathe-

[1] By J. H Hwang and F. Ma and published in the Sept. 1993 issue of the ASME JOURNAL OF APPLIED MECHANICS, Vol. 60, pp. 695–701.

[2] Research Scientist, Berkeley Engineering Research Institute, P.O. Box 9984, Berkeley, CA 94709.

[3] J. H. Hwang and F. Ma, Department of Mechanical Engineering, University of California, Berkeley, CA 94720.

Copyright © 1994 by ASME
Downloaded 03 May 2010 to 171.66.16.20. Redistribution subject to ASME license or copyright; see http://www.asme.org/terms/Terms_Use.cfm

Journal of Applied Mechanics

Book Reviews

Mechanics of Composite Structures, by Valery V. Vasiliev (English edition edited by Robert M. Jones and translated from the 1988 Russian edition, by Lucia I. Man). Taylor and Francis, Basingstoke, Hampshire, UK and Bristol, PA, 1993. 508 pp. Price: 71 pounds.

REVIEWED BY C. W. BERT[1]

As the field of composite materials and structures continues to mature, there is a continuing need for both text and reference books. As for the mechanics aspects of the subject, most of the classic texts, such as those of R. M. Jones (*Mechanics of Composite Materials*, Scripta, 1975) and R. M. Christensen (*Mechanics of Composite Materials*), Wiley, 1979) do not go into the structural aspects in very much depth. An exception in *The Behavior of Structures Composed of Composite Materials* by J. R. Vinson and R. L. Sierakowski (Martinus Nijhoff, 1986). The present book may serve as a text for a graduate-level course or as a reference for practicing design engineers and researchers. It is unique in that it covers for the first time in an English-language composites text, the subjects of ring structures and thin-walled beams.

Chapter 1 is an introduction to the structural properties of composite materials including anisotropic elastic behavior. Chapter 2 presents a very general development of the equations of an orthotropic elastic medium and their specialization to thin-walled structures. Special mention is made of stiffened structures, varying thickness, hygrothermal effects, material and geometric nonlinearity, buckling, and dynamic response. The material nonlinearities considered include both elastic-plastic and nonlinear elastic behavior.

Composite beams, columns, and circular rings are treated in Chapter 3. This work is distinct from other texts in that it includes postbuckling behavior of columns, vibrational behavior of shear deformable beams, and bending and deflection of rings. Chapter 4 deals with thin-walled beams, including those with open cross-sections, and single and double-cell closed cross-sections, including bending, twisting, and warping.

Chapter 4 covers composite plates, including unstiffened and stiffened rectangular plates and circular plates. Deflection, buckling, and post-buckling are all treated. The importance of transverse shear deformation is included via first-order shear deformation theory. Many of the numerical results are compared with experimental results for validation.

Circular cylindrical shells are analyzed in Chapter 6 for deflection, buckling, and free vibration. Both complete cylinders and cylindrically curved panels are treated. In addition to first-order shear deformable theory, classical thin-shell, membrane, and semi-membrane theories are discussed. Both linear and geometrically nonlinear behavior is analyzed. The final chapter (7) is devoted to axisymmetric deformation of shells of revolution, including both linear and geometrically nonlinear analysis, and design of membranes of revolution.

The book is very clearly written and illustrated. The only criticism, a very minor one, is the limited number of references (48), some of which refer to Russian editions of journal articles, even in cases in which English translation editions exist.

This book is highly recommended to all engineers, designers, and researchers concerned with composite structures.

Introduction to the Thermodynamics of Solids, by J. L. Ericksen, Chapman and Hall, New York, 1991. 204 pages. Price $49.95.

REVIEWED BY YI-CHAO CHEN[2]

Classical thermodynamics was developed primarily for systems composed of gases and liquids, with minimum consideration given to mechanical aspects, such as motion, deformation, and stresses. Such considerations are of great importance in the study of solids. While there has been a large number of works in thermoelasticity, thermoplasticity, etc., many of them routinely apply basic principles of thermodynamics to solids without questioning the validity of these principles in the specific context. Most modern treatments of these theories require mathematics at advanced levels, and may not be readily accessible to those who are just beginning research in these areas.

Professor Ericksen has devoted his career to research in theoretical physics, including thermodynamics. His expertise in virtually every area of mechanics enables him, in the present volume, to illustrate the use of fundamental ideas of thermodynamics to analyze nonlinear phenomena in solids, and to pinpoint the difficulties involved as well as possible solutions. Considering the depth of thought shown in this work, it is quite remarkable that it was developed from a series of lecture notes for seniors and beginning graduate students, and uses elementary mathematics.

Some general notions and basic principles of thermodynamics are stated in Chapter 1, that exposes, as do the following chapters, the reader to various controversial ideas. Constitutive theory of heat transfer is discussed in Chapter 2 with the aid of Clausius-Duhem inequality, reflecting the author's view that energy and entropy are well defined for many nonequilibrium processes.

Equilibrium theories for solids of simple geometries, i.e., bars and plates, are discussed in Chapters 3 and 4. Clearly demonstrated is the application of thermodynamics to examining stability and phase transitions in solids subject to various loading conditions and thermal settings. The essentially one-dimensional analyses allow for an exposition with a high concentration of ideas for the amount of mathematics required. Similar practices are exercised in Chapters 5 and 6,

[1]Benjamin H. Perkinson Chair and Director, School of Aerospace and Mechanical Engineering, The University of Oklahoma, Norman, OK 73019-0601. Fellow ASME.

[2]Professor, Department of Mechanical Engineering, University of Houston, Houston, TX 77204-4792.

Copyright © 1994 by ASME
Downloaded 03 May 2010 to 171.66.16.20. Redistribution subject to ASME license or copyright; see http://www.asme.org/terms/Terms_Use.cfm